

Extraction of Single and Double Differential Cross-Sections on Argon for CC1 μ 2p0 π Event Topologies in the SBND

Emilio Peláez Cisneros

August 2, 2024

Abstract

The precise measurement of cross-sections for a variety of interactions is critical to the success of upcoming flagship neutrino experiments. Of special interest are neutrino interactions that leave the nucleus in a 2-particle 2-hole state (2p2h). This note will present cross-section measurements for the production of 2p2h states on Argon. Using SBND data collected from the **period** of operation, we select events corresponding to a charged-current ν_μ interaction that left the Argon nucleus in a 2p2h state. These interactions produce a topology with one muon and two protons in the final state (CC1 μ 2p0 π). This analysis targets both single differential and double differential cross-section measurements for CC1 μ 2p0 π event topologies in a variety of kinematic variables. Comparisons are made to a set of theoretical models that explore different cross-section modeling configurations. Code for this analysis is available on [GitHub](#).

Contents

1	Introduction and motivation	2
2	Generator analysis	2
2.1	Signal definition	2
2.2	Generators	2
2.3	Variables definition	3
2.4	Pre-FSI events	16
2.5	Double differential plots	16
2.6	Pure MEC events	16
3	SBND analysis	32
3.1	Fiducial volume	32
3.2	Signal definition	32
3.3	Variable plots	33
3.4	Interaction and topology breakdown	36
3.5	Signal efficiency	36
3.6	Migration and response matrices	45
3.7	Systematics	52
3.8	Closure test	52
4	Cross-section results	57
5	Appendices	58
5.1	Cross section systematics	58
5.2	Flux systematics	325
5.3	Statistical systematics	417
6	References	425

1 Introduction and motivation

2 Since many current and next generation neutrino oscillation experiments will utilize dense nuclear targets,
3 such as liquid argon (LAr), it is critical to characterize the impact of nuclear effects on neutrino cross-sections.
4 One area of interest are neutrino events that eject 2 nucleons from the nucleus, leaving it with 2 holes: known
5 as 2-particle 2-hole states (2p2h). The general picture is that the neutrino has a charged-current interaction
6 with a neutron in the nucleus, producing a proton with significant momentum; this proton interacts with
7 another proton, producing the 2p2h state. While the majority of 2p2h states are caused by Meson Exchange
8 Currents (MEC) [15], some nuclear effects, such as Short-Range Nucleon-Nucleon correlations (SRC) [10],
9 can also produce these states. In an accelerator-based liquid argon time projection chamber (LArTPC)
10 experiment, such as SBND, a charged-current (CC) muon neutrino (ν_μ) interaction that results in a 2p2h
11 state would have a final state topology of 1 muon, 2 protons, and no charged or neutral pions. While
12 there are existing measurements of CC1 μ 2p0 π events on argon, the analyses were statistically limited and
13 no cross-sections were extracted [1, 19]. There was a previous report with single differential cross-section
14 measurements from the MicroBooNE detector [20], but this document presents the first double differential
15 cross-section measurements of CC1 μ 2p0 π topologies on argon, using data collected from the period of SBND
16 operations.

17 2 Generator analysis

18 2.1 Signal definition

19 We choose charged-current muon neutrino interactions that result in one muon, two protons, no charged pions
20 with $P_\pi > 70$ MeV/c, no neutral pions or heavier mesons, and any number of neutrons. These interactions
21 are denoted as CC1 μ 2p0 π . We require the momentum of the muon and protons to be in the following ranges
22 (in MeV/c):

$$100 < P_P < 1200 \quad 300 < P_\mu < 1000 \quad (1)$$

23 2.2 Generators

24 The following generators are used to create events, which are then discriminated using the signal definition
25 above: NuWro, GiBUU, NEUT, GENIE G18, GENIE AR23. Information about these generators is
26 summarized in Table 1.

Name	Generator/Configuration
G18	GENIE v3.0.6 G18_10a_02_11a
AR23	G18 with SuSAv2 MEC model
NuWro	NuWro 19.02.1
NEUT	NEUT v5.4.0
GiBUU	GiBUU 2021

Table 1: Generator and configuration data.

27 The GENIE configurations we used are:

- 28 (i) GENIE G18 [2, 3]: This modern model configuration uses the local Fermi gas (LFG) model [9],
29 the Nieves CCQE scattering prescription [23], which includes Coulomb corrections for the outgoing
30 muon [11], and random phase approximation (RPA) corrections [22]. Additionally, it uses the
31 Nieves MEC model [25], the KuzminLyubushkin-Naumov Berger-Sehgal RES [6, 28, 16], Berger-Sehgal
32 COH [7] and Bodek-Yang DIS [29] scattering models with the PYTHIA [26] hadronization part, and
33 the hA2018 FSI model [4].
- 34 (ii) GENIE AR23: Same as the G18 model configuration but using the SuSAv2 MEC model.

35 The alternative event generators are:

- 36 (i) NuWro [12]: Includes the LFG model [9], the Llewellyn Smith model for QE events [18], the Nieves
37 model for MEC events [24], the AdlerRarita-Schwinger formalism to calculate the Δ resonance explicitly [13],
38 the Berger-Sehgal (BS) COH [7] scattering model, an intranuclear cascade model for FSI [24],
39 and a coupling to PYTHIA [26] for hadronization.
- 40 (ii) NEUT [14]: Corresponds to the combination of the LFG model [8, 9], the Nieves CCQE scattering
41 prescription [23], the Nieves MEC model using a lookup table [25], the Berger Sehgal RES [6, 13, 5]
42 and BS COH [7] scattering models, FSI with medium corrections for pions [2, 3], and PYTHIA [26]
43 purposes.
- 44 (iii) GiBUU [21]: Uses similar models to GENIE, but they are implemented in a coherent way by solving
45 the Boltzmann-Uehling-Uhlenbeck transport equation [21]. The modeling includes the LFG model [9],
46 a standard CCQE expression [17], an empirical MEC model, and a dedicated spin dependent resonance
47 amplitude calculation following the MAID analysis [21]. The DIS model is from PYTHIA [26]. GiBUU's
48 FSI treatment propagates the hadrons through the residual nucleus in a nuclear potential consistent
49 with the initial state.

50 2.3 Variables definition

51 Given the momentum vectors for the leading proton \vec{p}_L , recoil proton \vec{p}_R , and muon \vec{p}_μ , we define several
52 variables. First, we define the momenta and opening angle of each variable, denoted as $|\vec{p}|$ and $\cos(\theta_{\vec{p}})$, with
53 the appropriate index for each momentum vector. These variables are plotted in Figure 1.

54 We also define variables relating the multiple momentum vectors. First, the opening angle between the
55 protons in the lab frame, given by

$$\cos(\theta_{\vec{p}_L, \vec{p}_R}) = \frac{\vec{p}_L \cdot \vec{p}_R}{|\vec{p}_L| |\vec{p}_R|}. \quad (2)$$

56 Then, the opening angle between the total proton momentum ($\vec{p}_{\text{sum}} = \vec{p}_L + \vec{p}_R$) and the muon, given by

$$\cos(\theta_{\vec{p}_\mu, \vec{p}_{\text{sum}}}) = \frac{\vec{p}_\mu \cdot \vec{p}_{\text{sum}}}{|\vec{p}_\mu| |\vec{p}_{\text{sum}}|}. \quad (3)$$

57 The momentum transverse to the direction of the neutrino beam, which we denote $\delta\vec{P}_T$ and is given by

$$\delta\vec{P}_T = \vec{p}_T^\mu + \vec{p}_T^L + \vec{p}_T^R. \quad (4)$$

58 For the transverse momentum, we will be interested in its magnitude $|\delta\vec{P}_T|$. Finally, the angular orientation
59 of the transverse momentum with respect to the transverse muon is defined as

$$\delta\alpha_T = \cos^{-1} \left(\frac{-\vec{p}_T^\mu \cdot \delta\vec{P}_T}{|\vec{p}_T^\mu| |\delta\vec{P}_T|} \right). \quad (5)$$

60 We plot the differential cross sections of these variables for the given generators in Figure 2. We can also
61 see the cross section by event type for all variables and all generators in Figures 3 to 12.

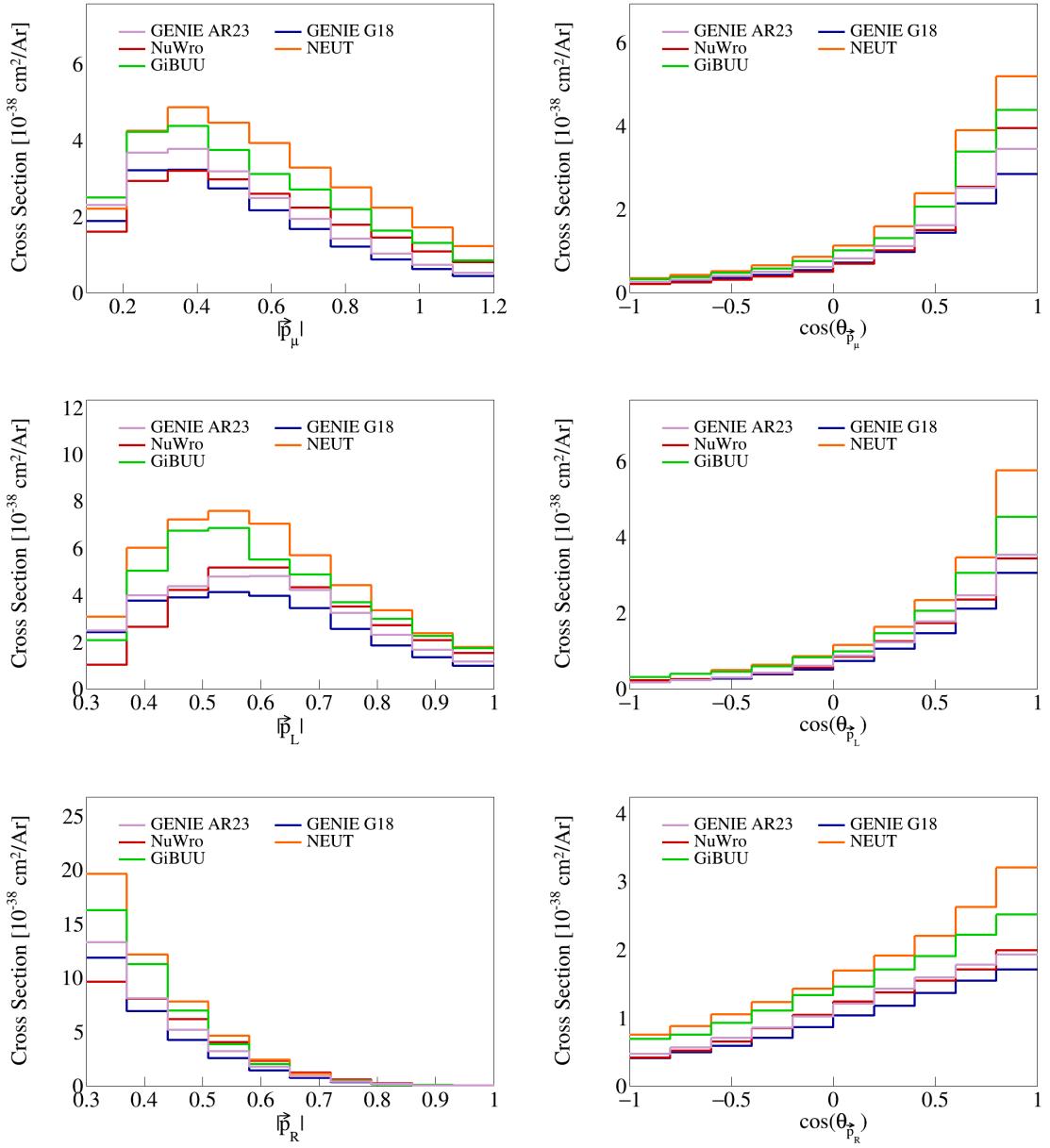


Figure 1: Cross sections for momentum and opening angles of individual particles.

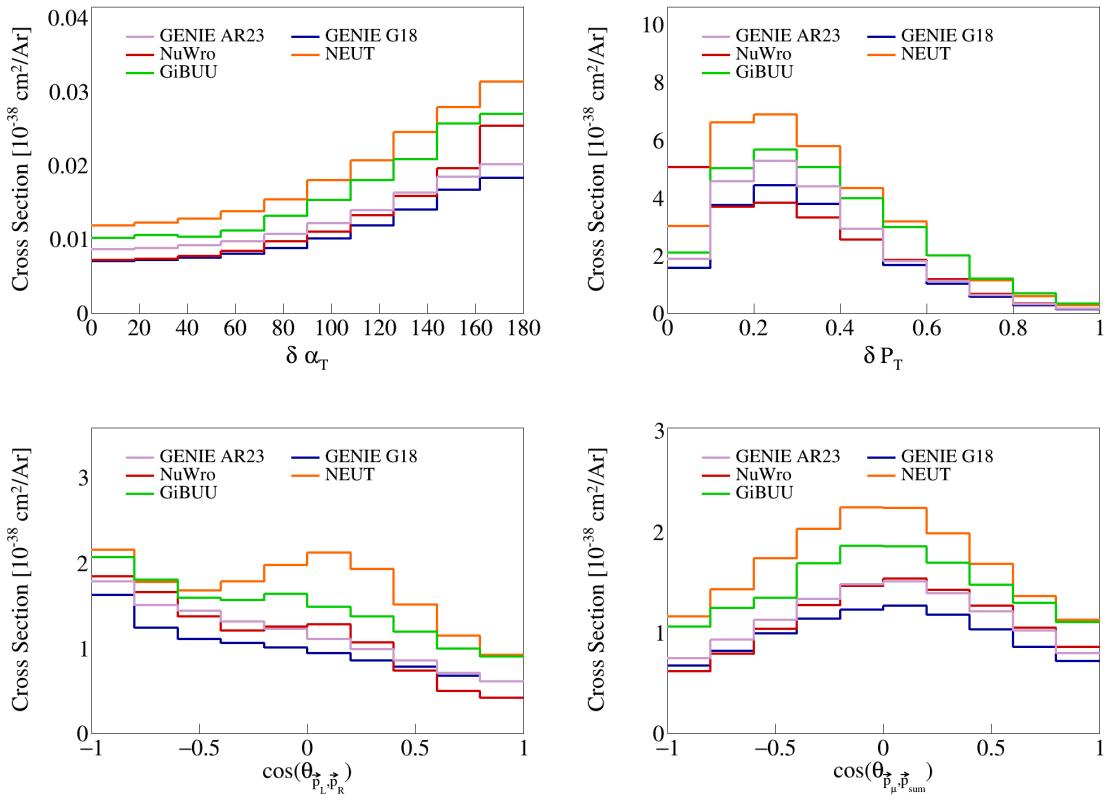


Figure 2: Cross sections for opening angles and transverse momentum.

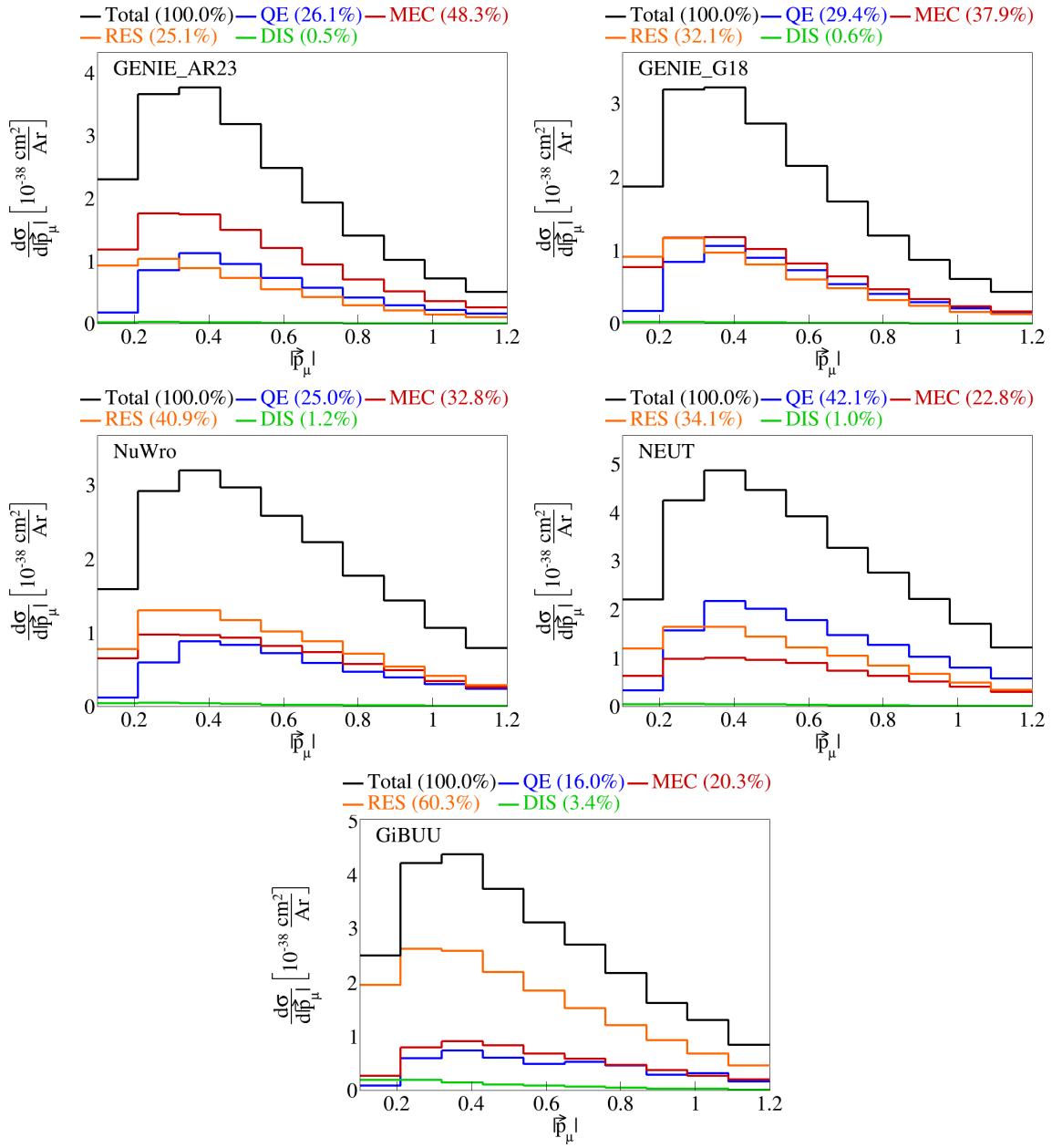


Figure 3: Event interaction breakdown for $|\vec{p}_\mu|$.

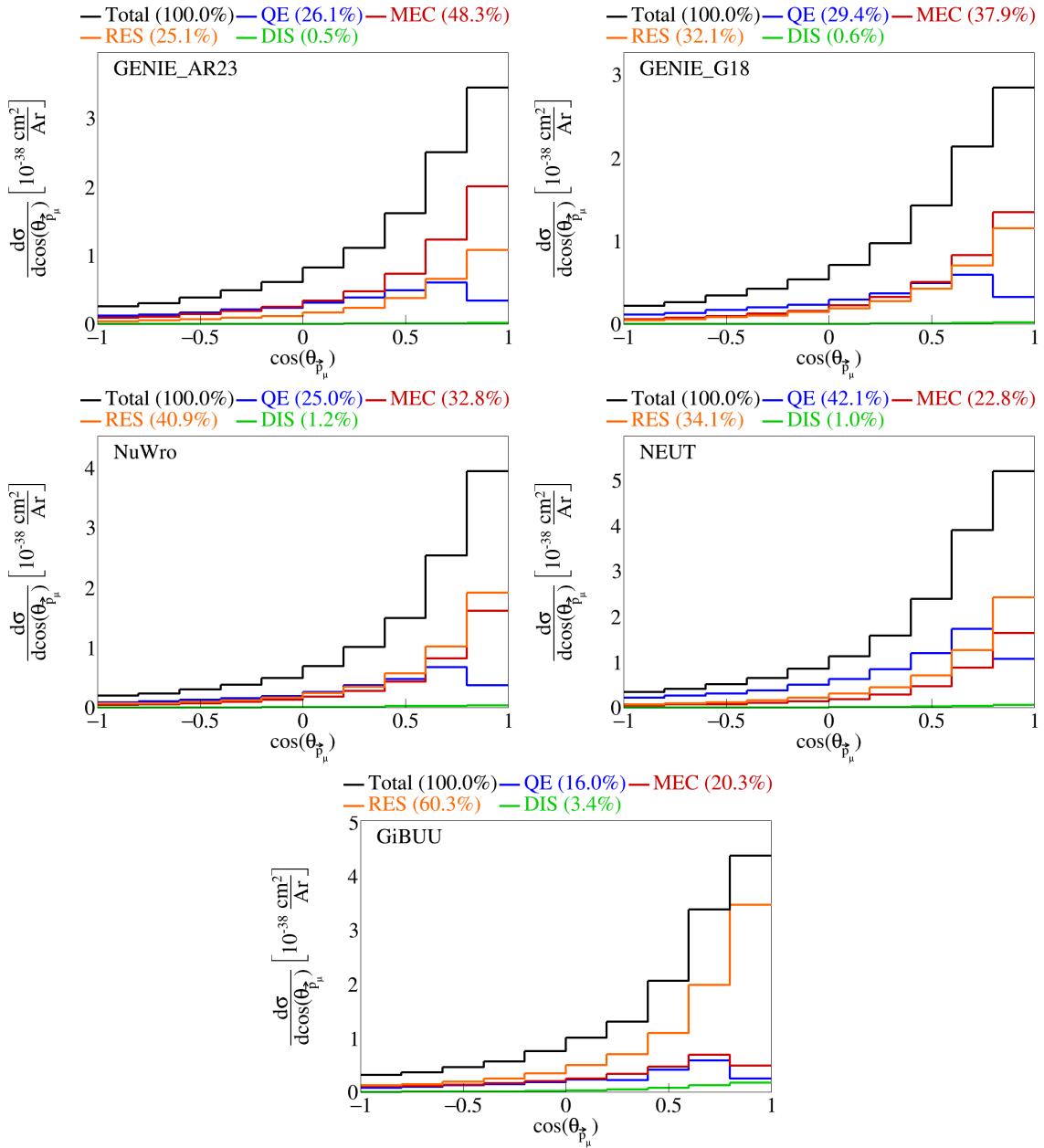


Figure 4: Event interaction breakdown for $\cos(\theta_{\vec{p}_\mu})$.

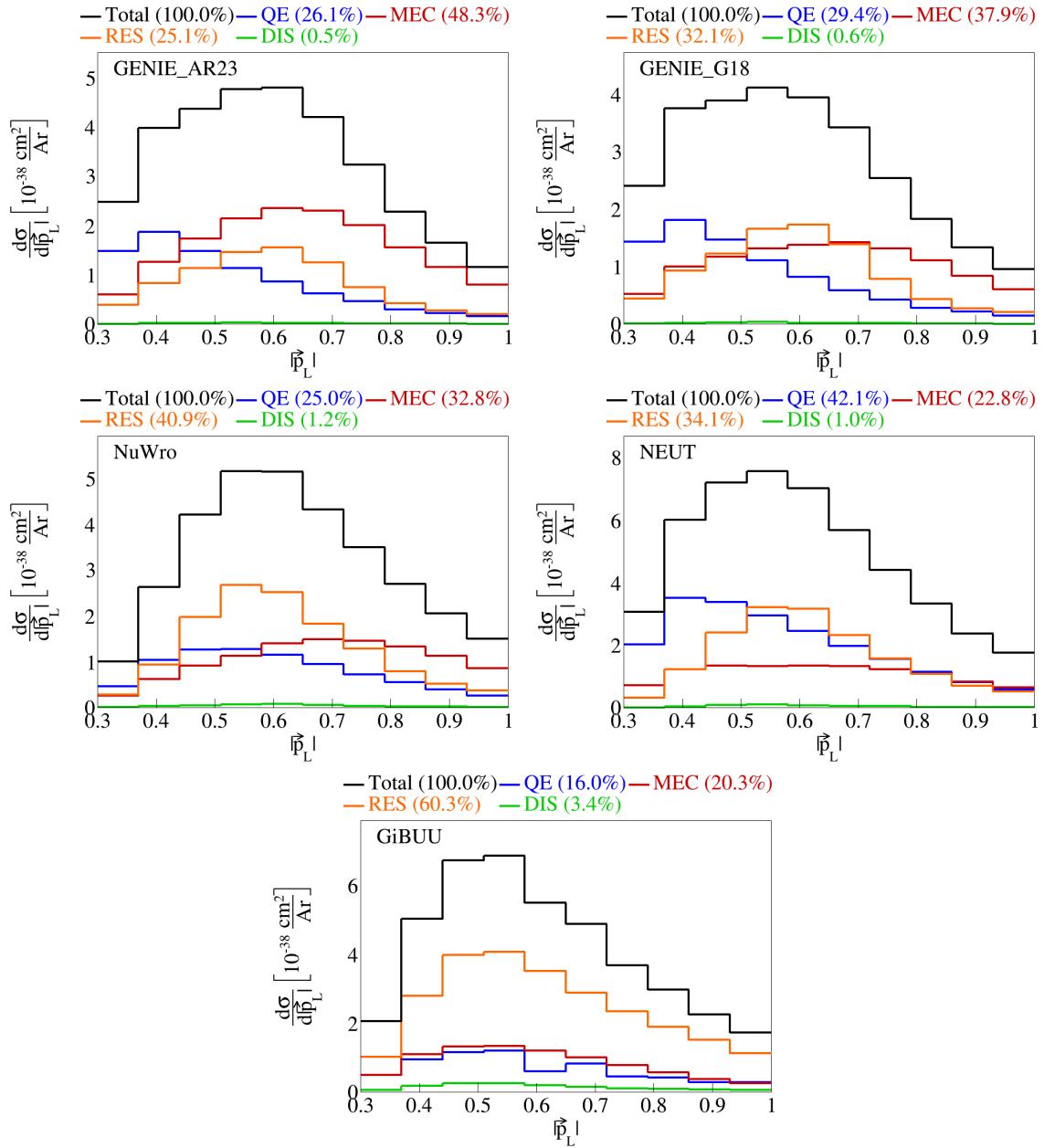


Figure 5: Event interaction breakdown for $|\vec{p}_L|$.

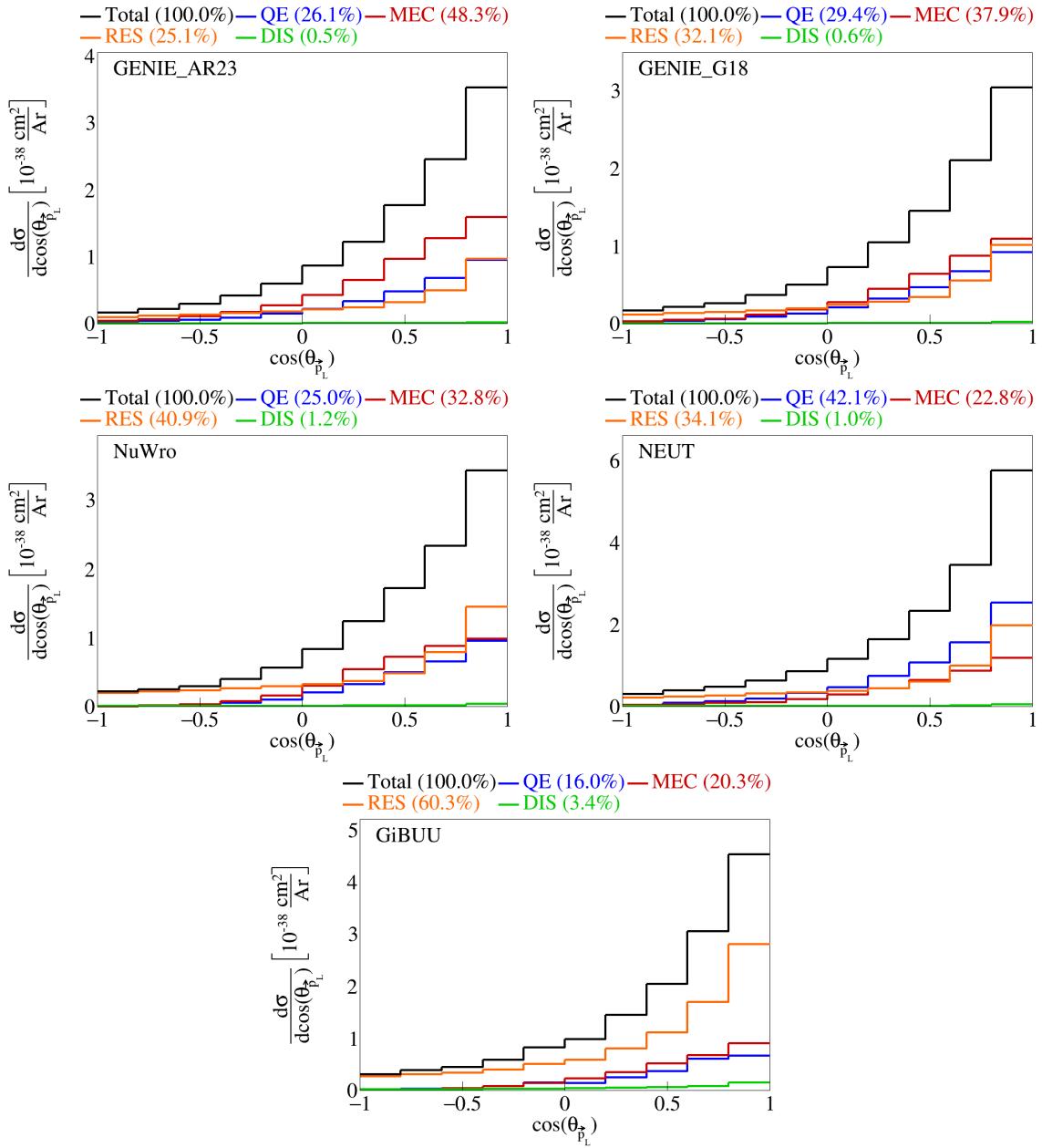


Figure 6: Event interaction breakdown for $\cos(\theta_{\vec{p}_L})$.

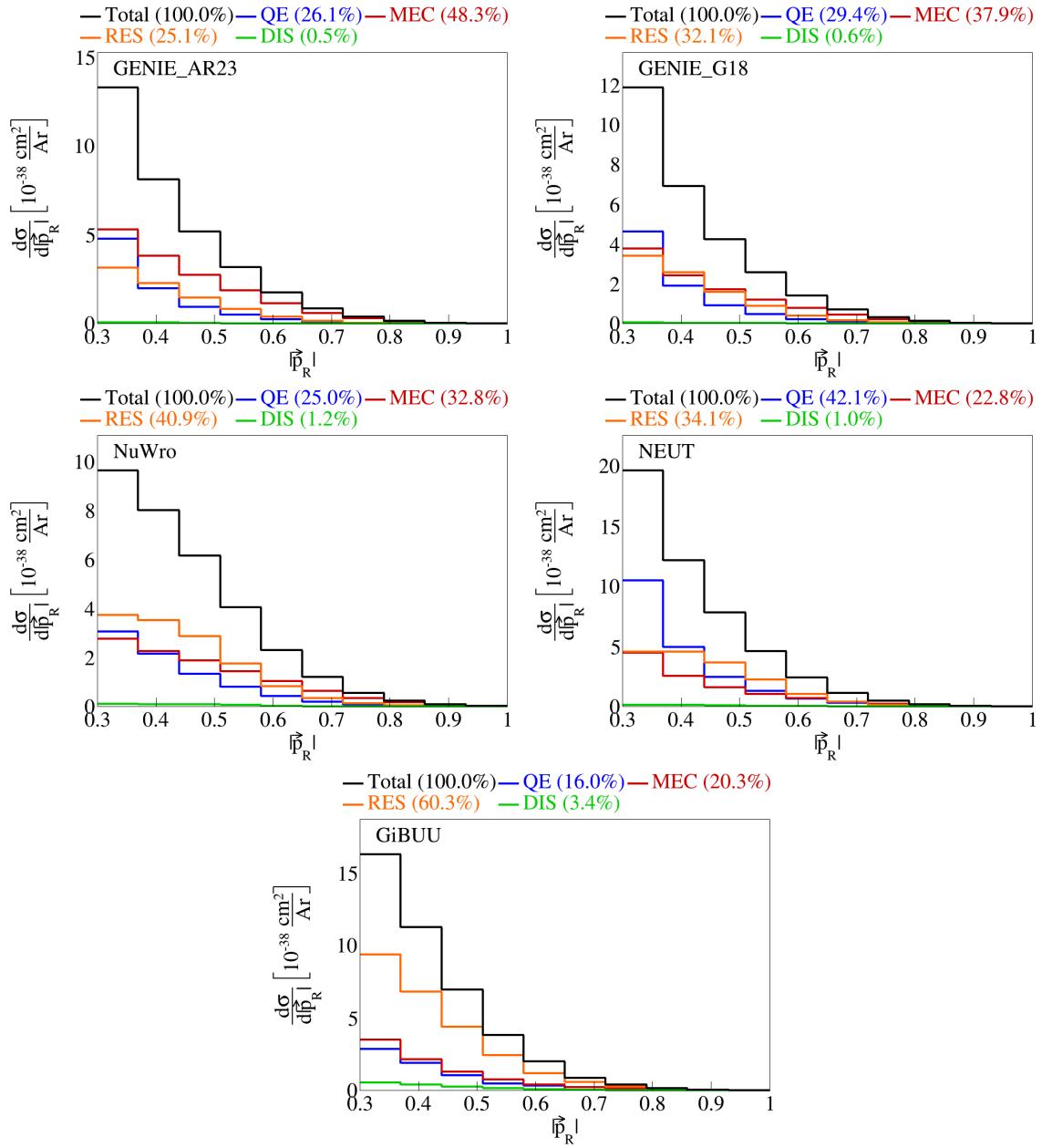


Figure 7: Event interaction breakdown for $|\vec{p}_R|$.

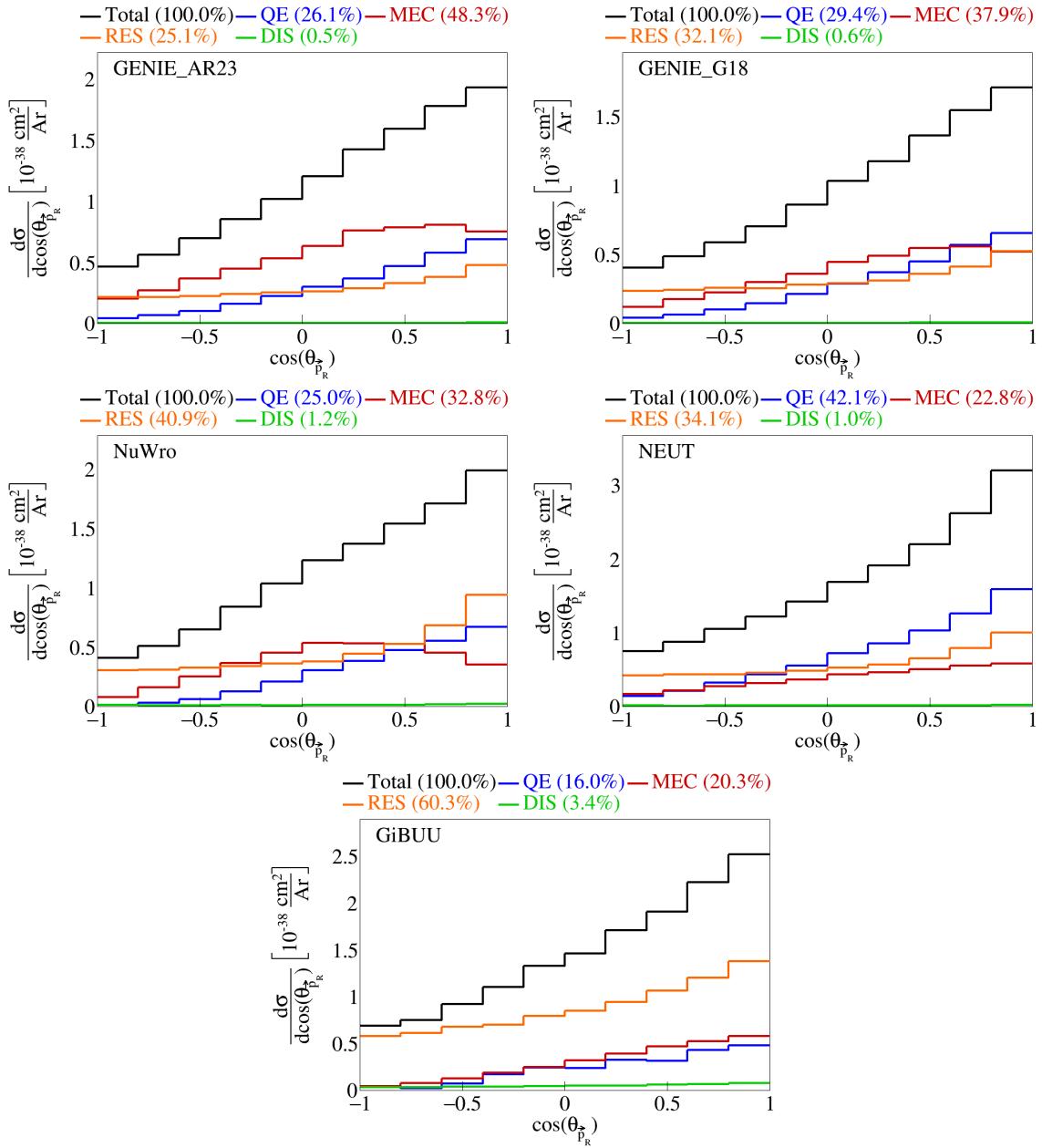


Figure 8: Event interaction breakdown for $\cos(\theta_{\vec{p}_R})$.

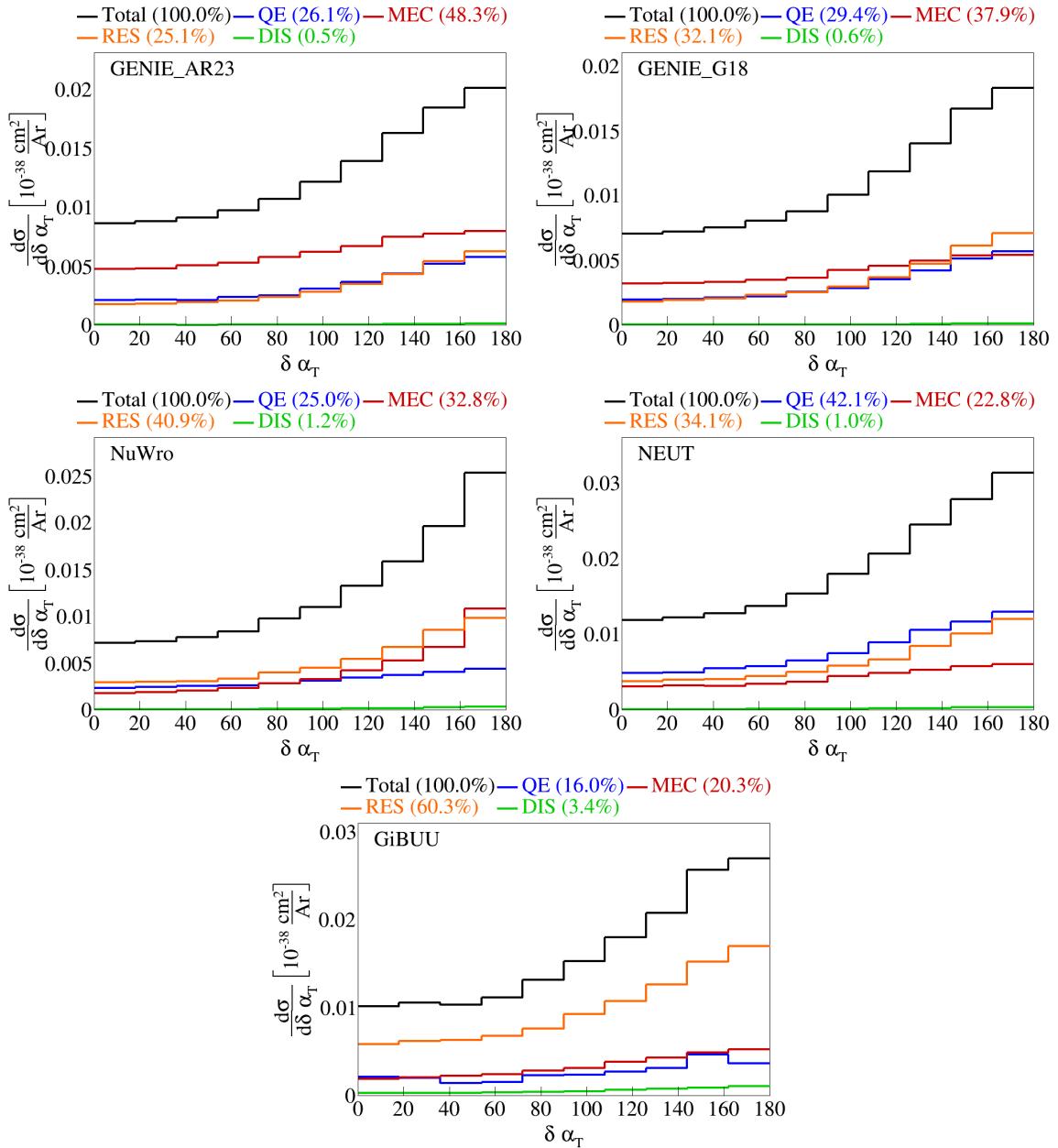


Figure 9: Event interaction breakdown for $\delta \alpha_T$.

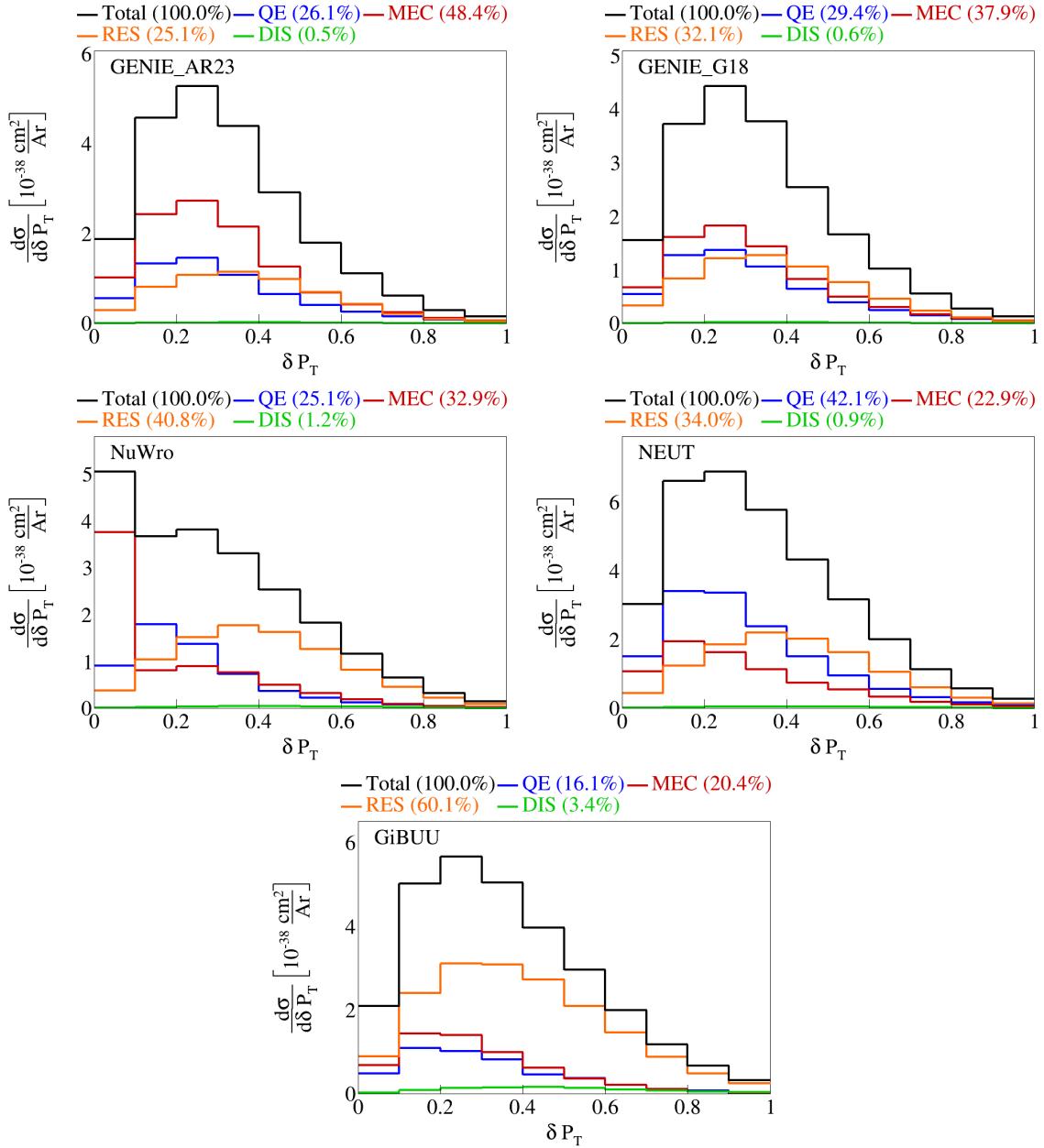


Figure 10: Event interaction breakdown for $|\delta \vec{P}_T|$.

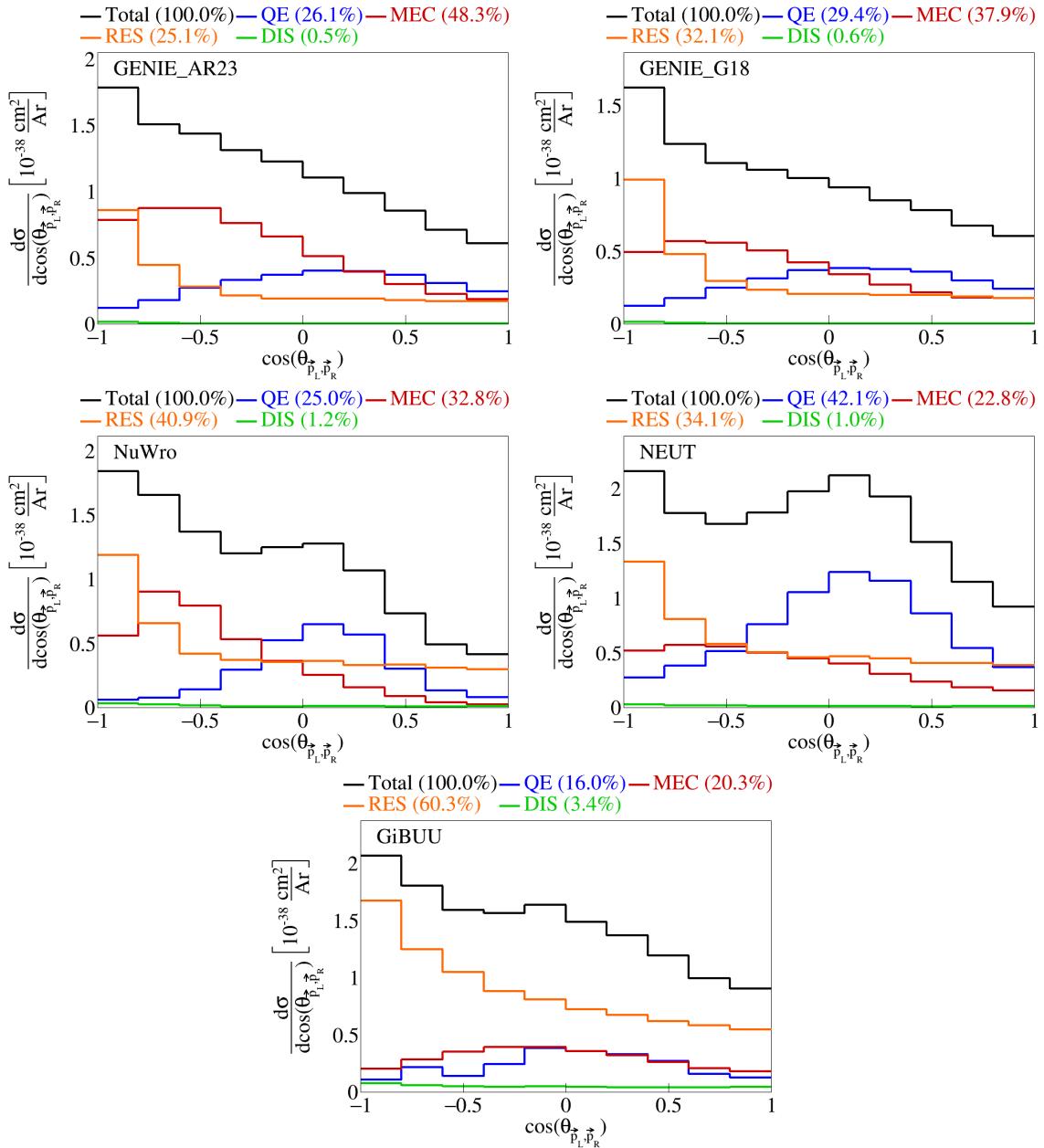


Figure 11: Event interaction breakdown for $\cos(\theta_{\vec{p}_L, \vec{p}_R})$.

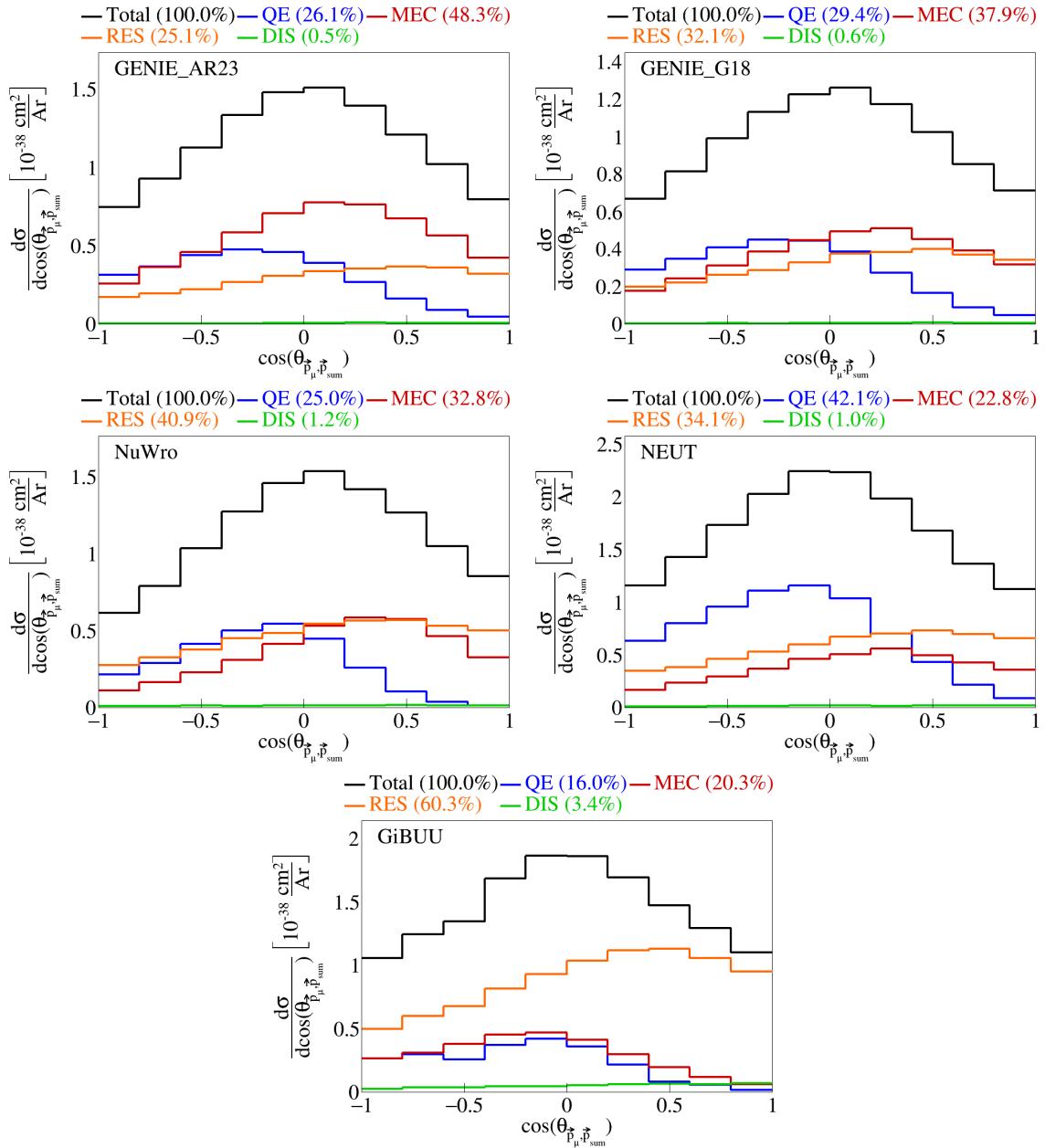


Figure 12: Event interaction breakdown for $\cos(\theta_{\vec{p}_\mu, \vec{p}_{\text{sum}}})$.

62 **2.4 Pre-FSI events**

63 To investigate why the percentage of MEC events for some generators is low, we performed event selection
64 before any final state interactions took place and plotted the interaction breakdown. For both GENIE tunes,
65 NEUT, and NuWro, we got 100% MEC events pre-FSI. For GiBUU, only 4.1% MEC versus 76.2% RES and
66 16% DIS events pre-FSI. The interaction breakdown for $|\vec{p}_\mu|$ for all the generators are shown in Figure 13.
67 Since GiBUU is the outlier, we checked the specific interaction mode for the resonance events. We got that
68 10 has 39.3%, 11 has 34.7%, 12 has 0.0136%, 13 has 26 %, and 27, 22, and 23 all have zero percent of the
69 resonance events. We also checked the event interaction breakdown for GiBUU samples generated without
70 final state interactions, in which we found that 100% of the events are MEC, shown in Figure 14.

71 Note that the difference between these two GiBUU samples is that in the former, the samples were
72 generated with final state interactions, and then we look at the state before the final state interactions
73 reportedly took place, and in the latter the event generation was done without any final state interactions.

74 **2.5 Double differential plots**

75 For our double differential variables, we look at δP_T , $\delta \alpha_T$, $\cos(\theta_{\vec{p}_L, \vec{p}_R})$, and $\cos(\theta_{\vec{p}_\mu, \vec{p}_{\text{sum}}})$ in $\cos(\theta_{\vec{p}_\mu})$. We
76 have two bins for $\cos(\theta_{\vec{p}_\mu})$, the first one going from -1 to 0.5 and the second from 0.5 to 1. Therefore, these
77 are irregular bins, with the first holding a larger range than the second. These plots are shown in Figure 15.
78 Note that, in these plots, the horizontal axis is defined by bin number of the double differential measurement,
79 not the value of the variable. This is because we are representing two variables in a single axis, but we can
80 slice the plots to get our usual horizontal axis.

81 We slice the double differential plots into two plots each, so that we have the variable of interest in the
82 horizontal axis instead of bin numbers, and each slice corresponds to one bin of $\cos(\theta_{\vec{p}_\mu})$. These plots are
83 shown in Figure 16, and the plots broke down by interaction are in Figures 17 to 20. In these plots, the
84 bins contents have been reweighted appropriately, by dividing the content of each bin by the width of the
85 bin for the variable in the axis multiplied by the width of the $\cos(\theta_{\vec{p}_\mu})$ slice. Note that the plots for the
86 $0.5 < \cos(\theta_{\vec{p}_\mu}) < 1$ slice have more events in general, although they span a smaller phase space of $\cos(\theta_{\vec{p}_\mu})$,
87 as it can be seen by the scale of the vertical axis. We performed the same double differential analysis for
88 the events before final state interactions. These are shown in Figure 21, and the corresponding interaction
89 breakdown plots are in Figures 22 to 25.

90 **2.6 Pure MEC events**

91 We also generated pure meson exchange current events using different configurations to get the MEC splines.
92 These were all generated using different tunes of GENIE: AR23, G18 with Empirical MEC model, and G18
93 with Nieves MEC model. The plots for the transverse kinematic variables are shown in Figure 26. The sliced
94 double differential plots are shown in Figure 27.

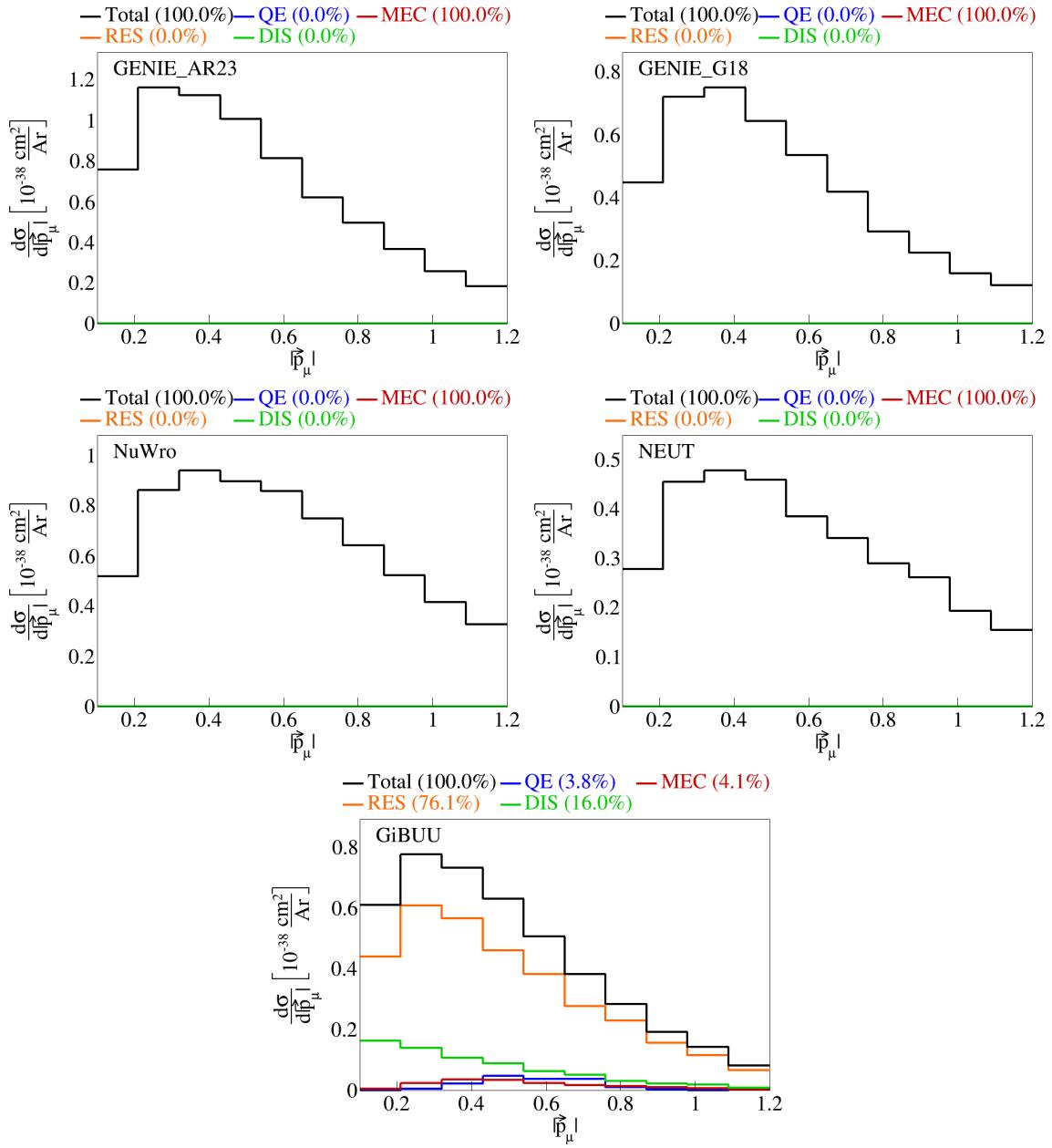


Figure 13: Event interaction breakdown of $|\vec{p}_\mu|$ before final state interactions.

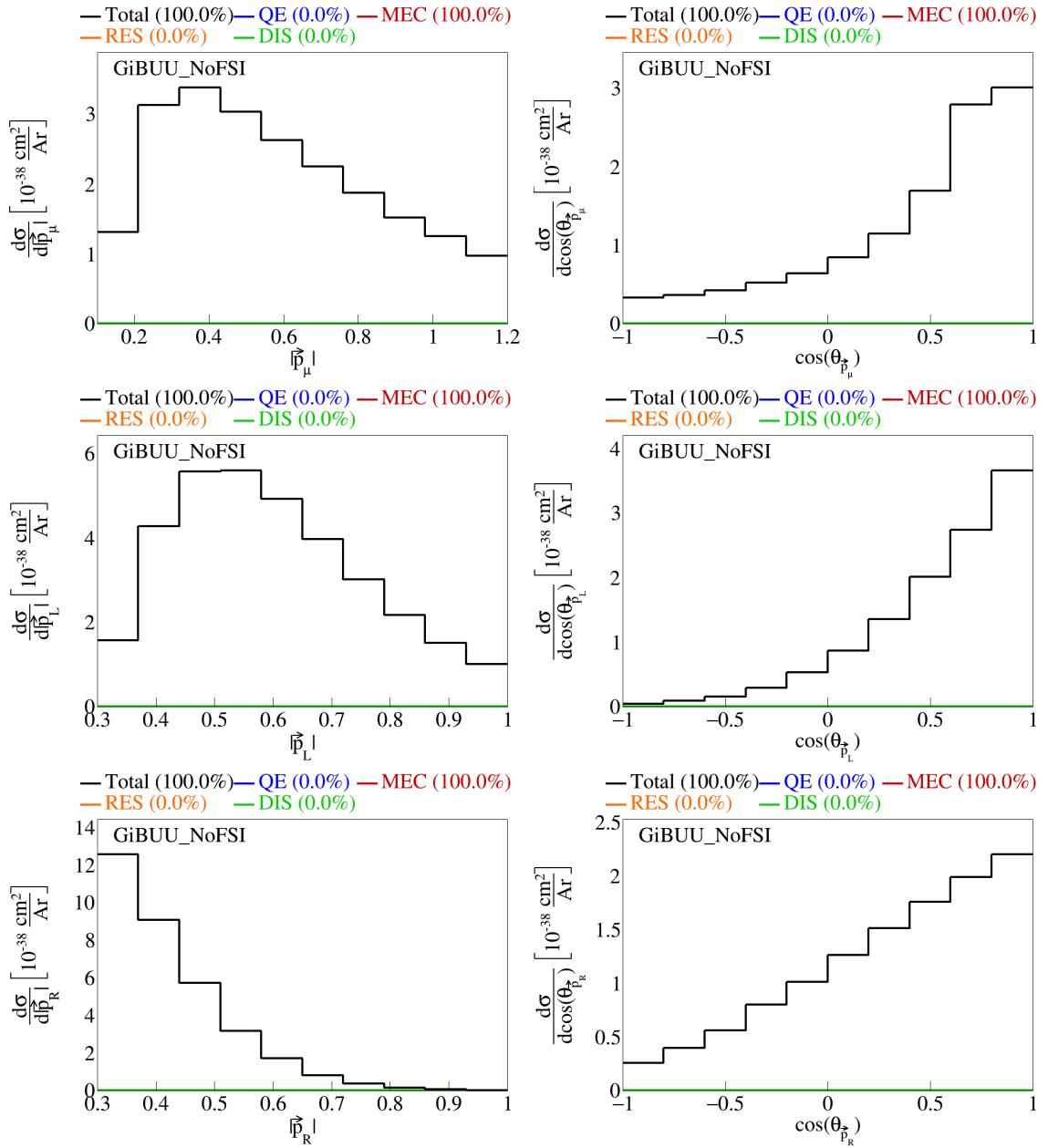


Figure 14: Event interaction breakdown for final events from GiBUU events with no FSI.

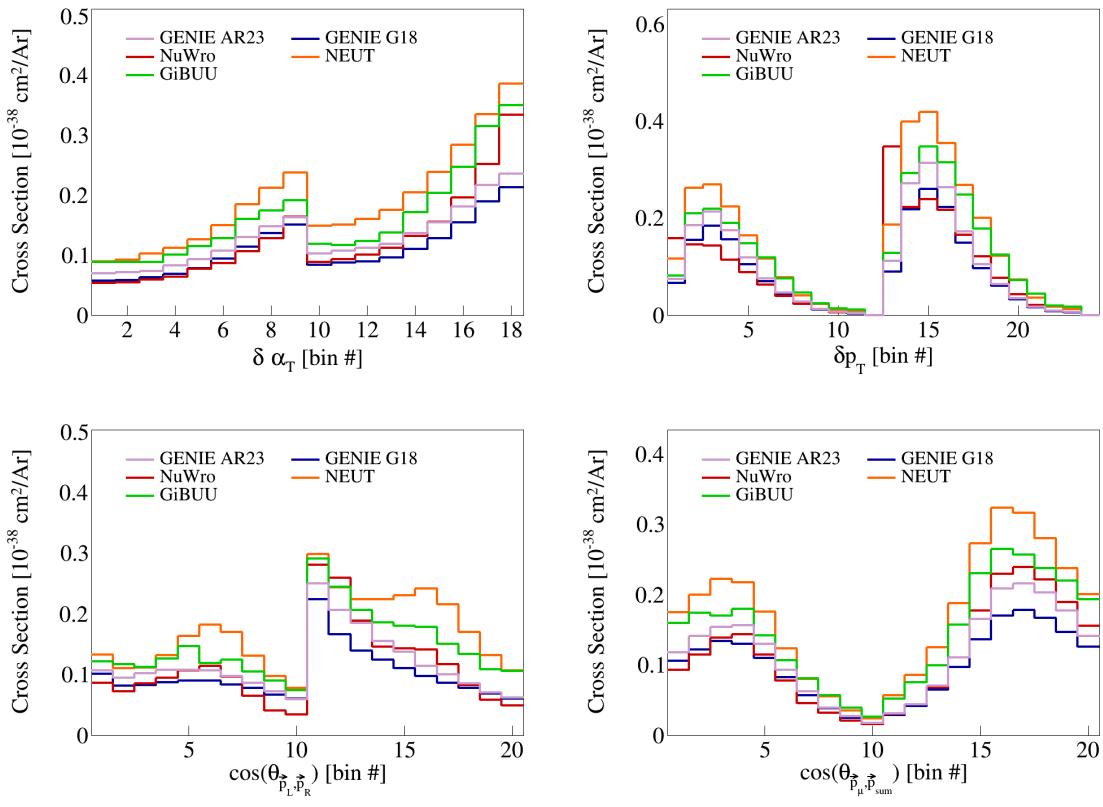


Figure 15: Double differential serial plots, all in $\cos(\theta_{\vec{p}_\mu})$.

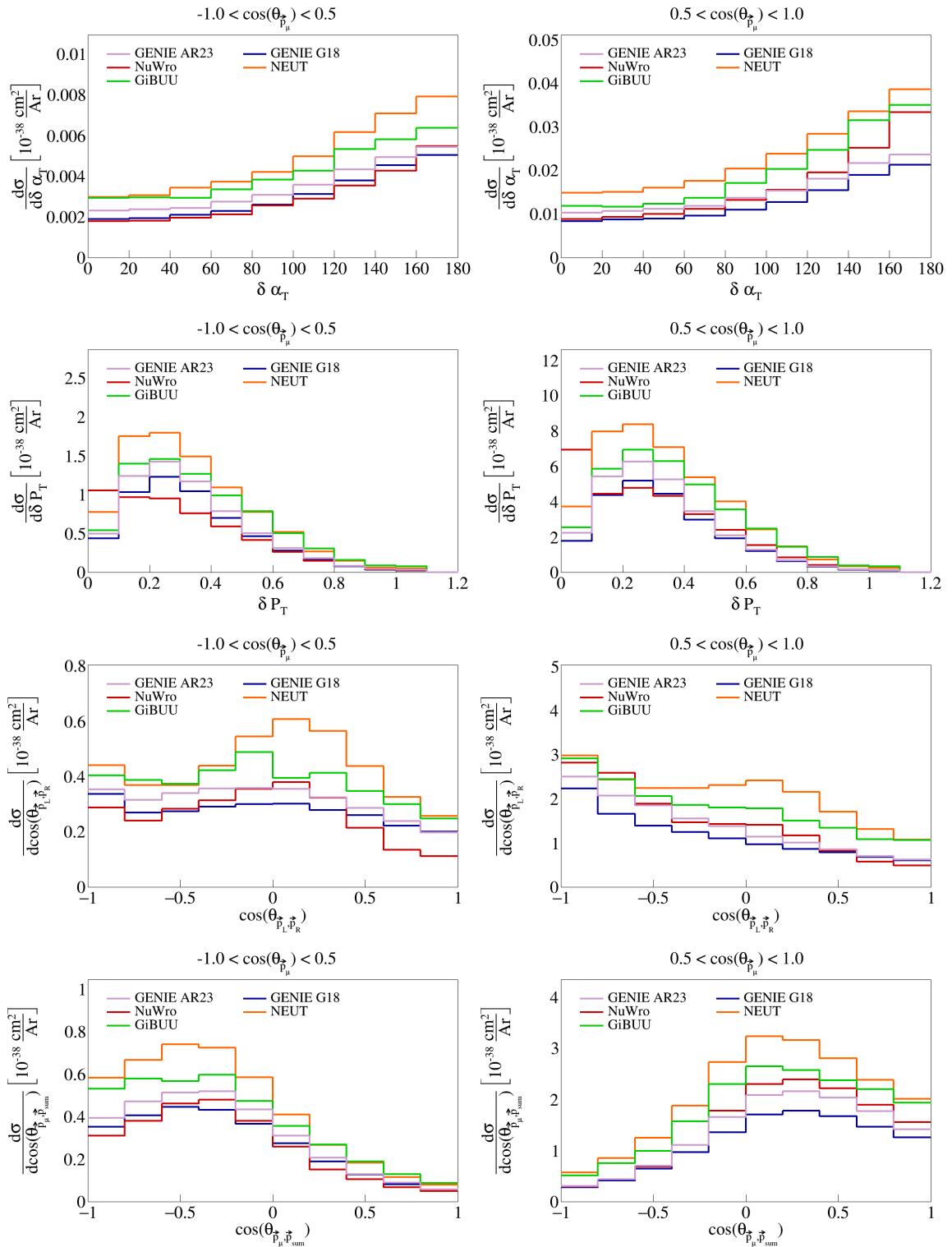


Figure 16: Sliced double differential plots.

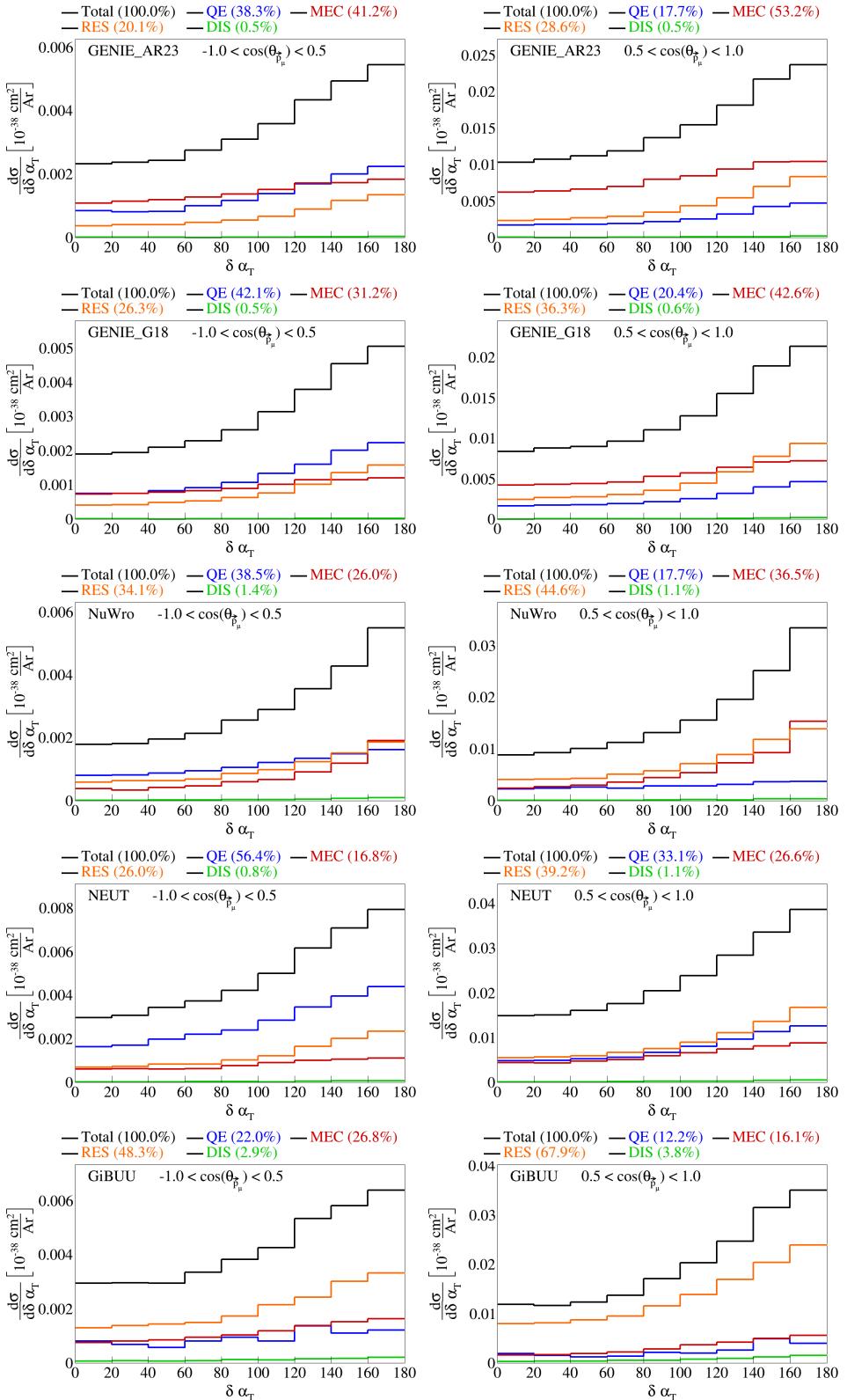


Figure 17: Interaction breakdown for sliced double differential plots for $\delta\alpha_T$ in $\cos(\theta_{\vec{p}_\mu})$.

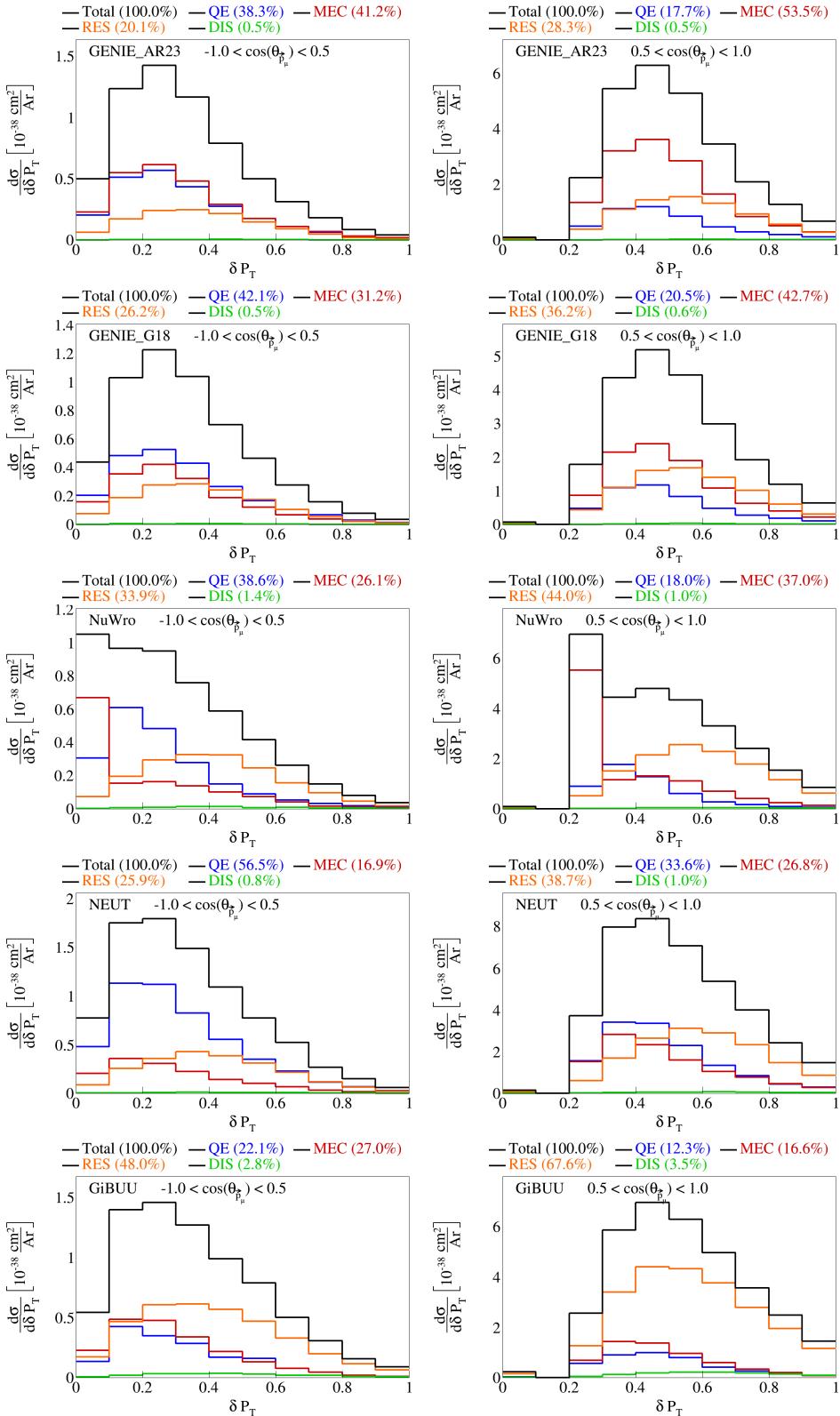


Figure 18: Interaction breakdown for sliced double differential plots for $|\delta \vec{P}_T|$ in $\cos(\theta_{\vec{p}_\mu})$.

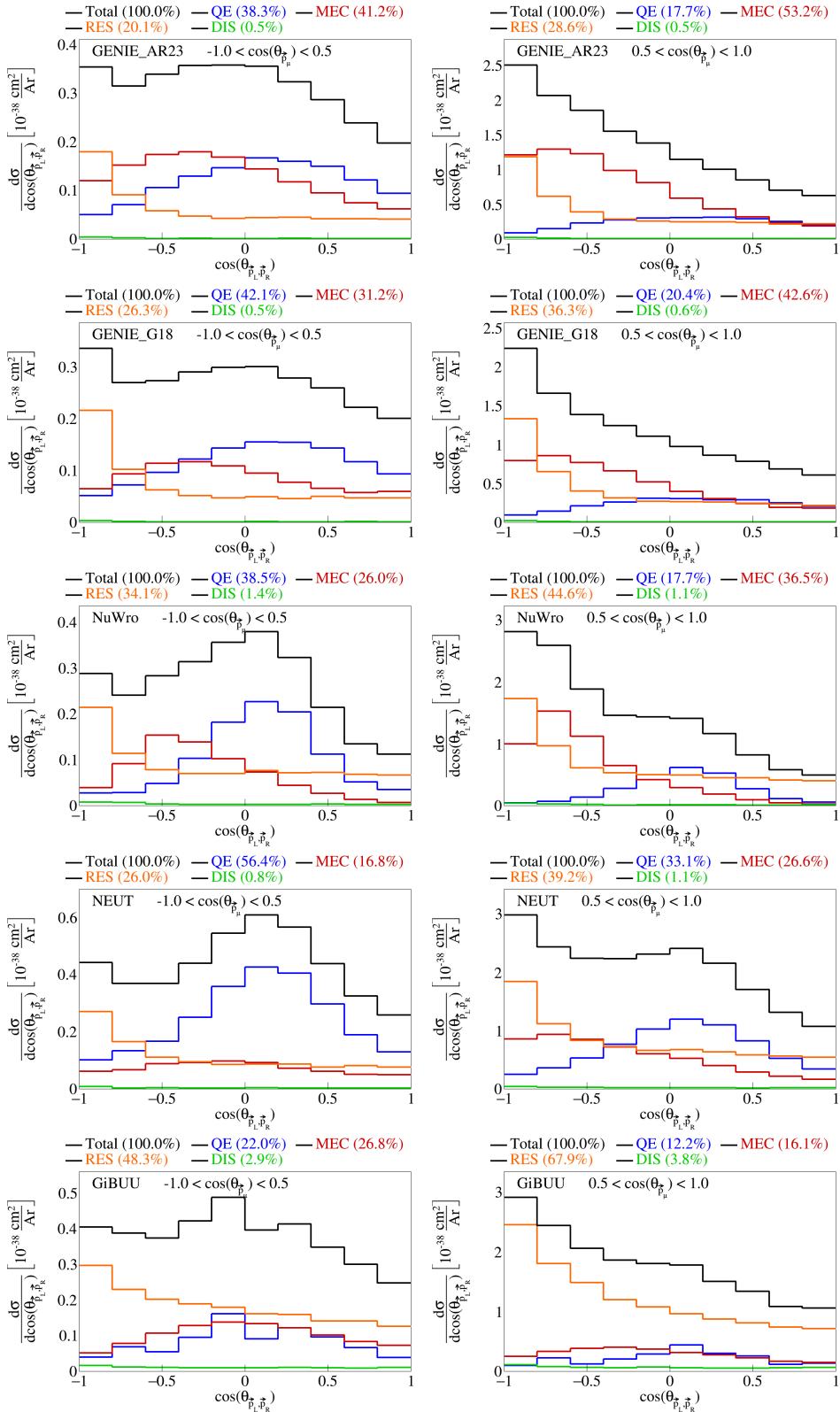


Figure 19: Interaction breakdown for sliced double differential plots for $\cos(\theta_{\vec{p}_L, \vec{p}_R})$ in $\cos(\theta_{\vec{p}_\mu})$.

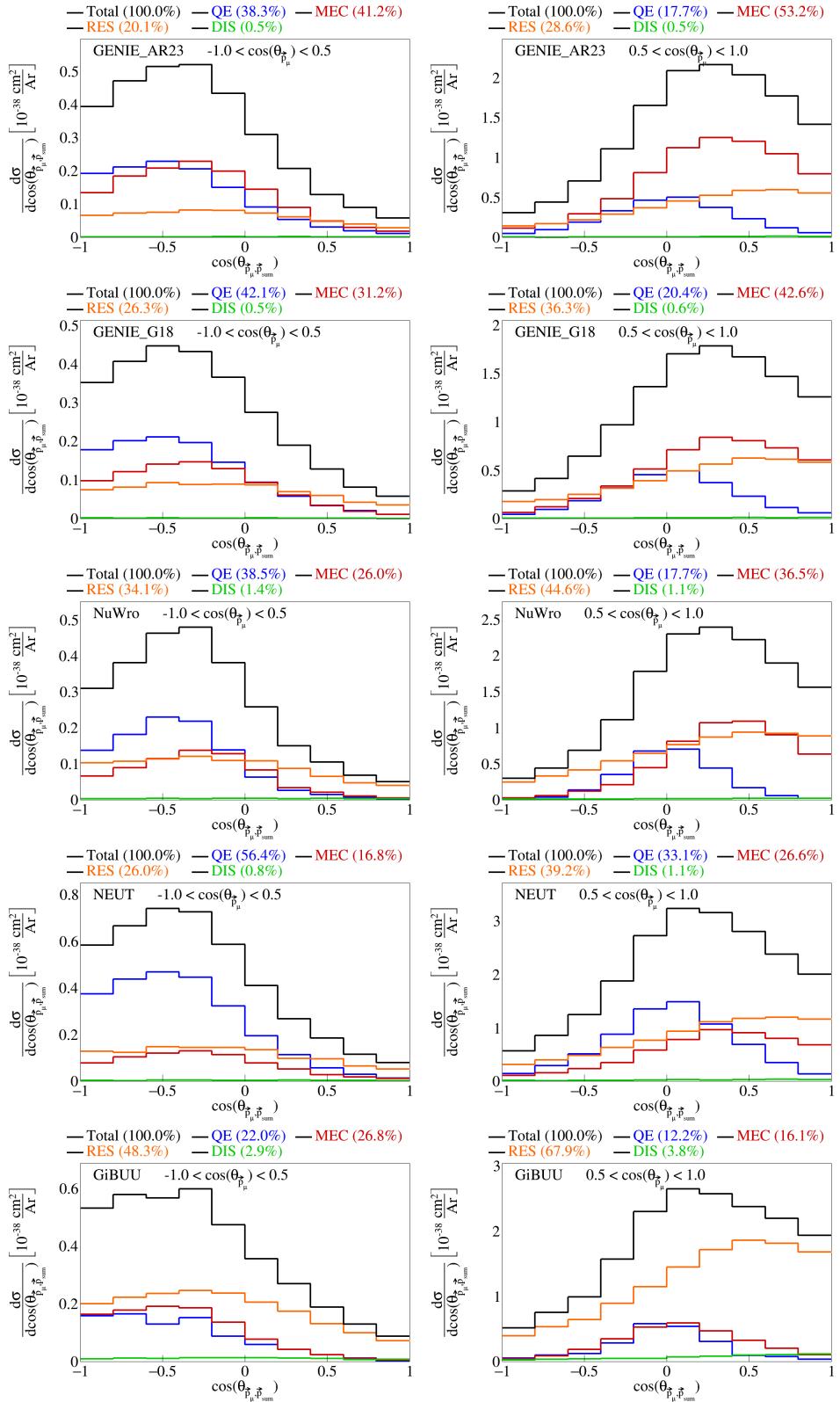


Figure 20: Interaction breakdown for sliced double differential plots for $cos(\theta_{\vec{p}_\mu}, \vec{p}_{sum})$ in $cos(\theta_{\vec{p}_\mu})$.

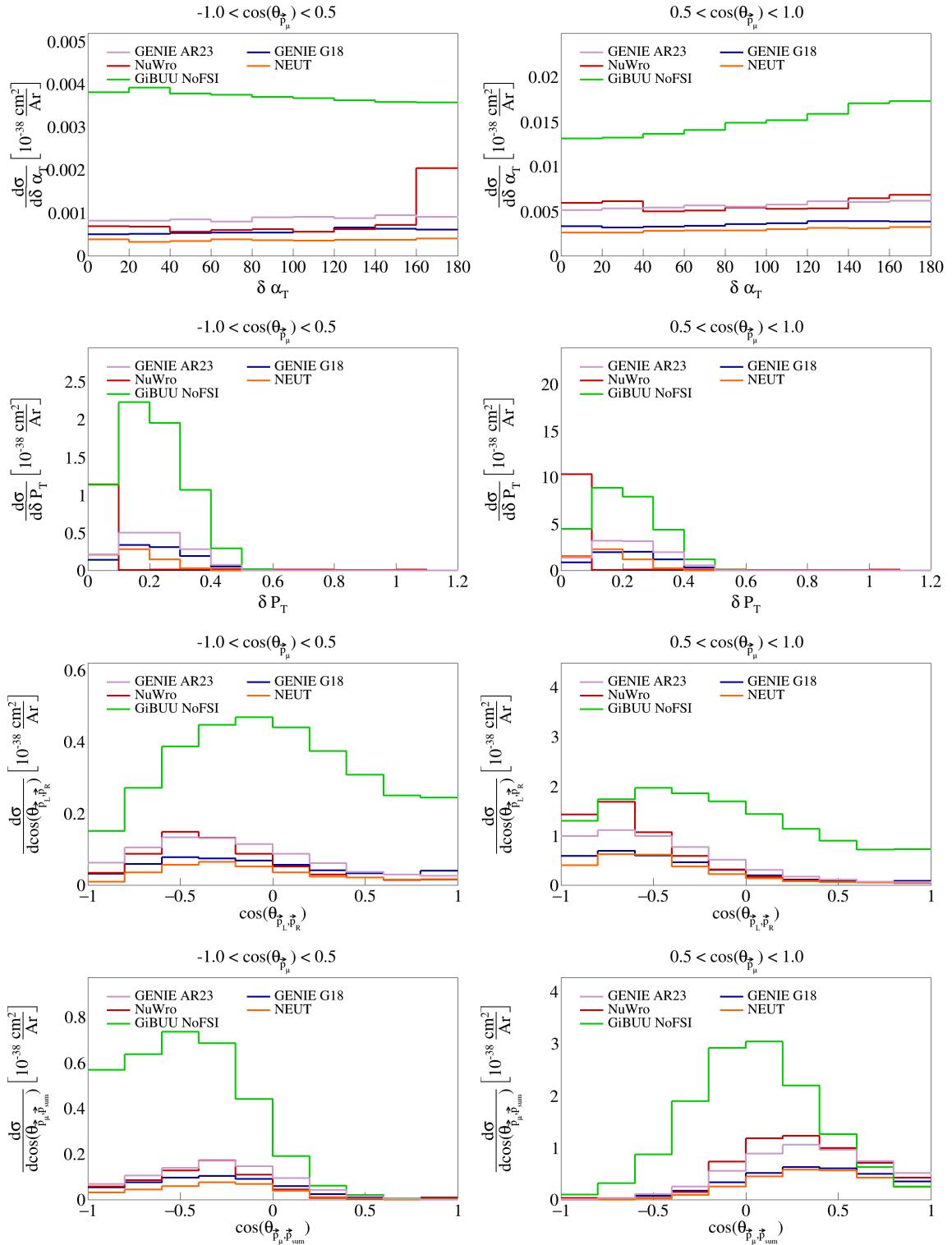


Figure 21: Sliced double differential plots for pre-FSI events.

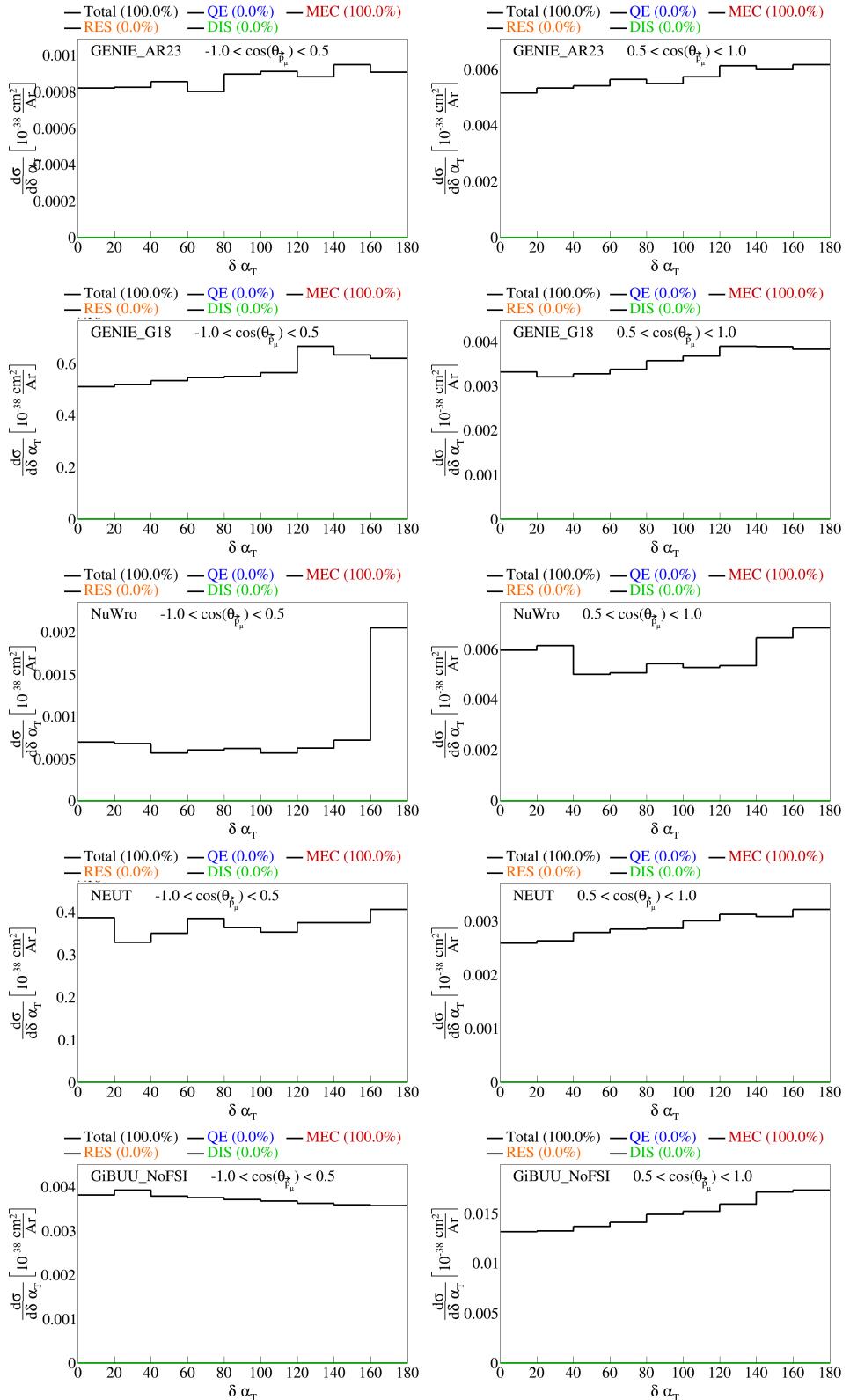


Figure 22: Interaction breakdown for sliced double differential plots for pre-FSI $\delta\alpha_T$ in $\cos(\theta_{\bar{p}_\mu})$.

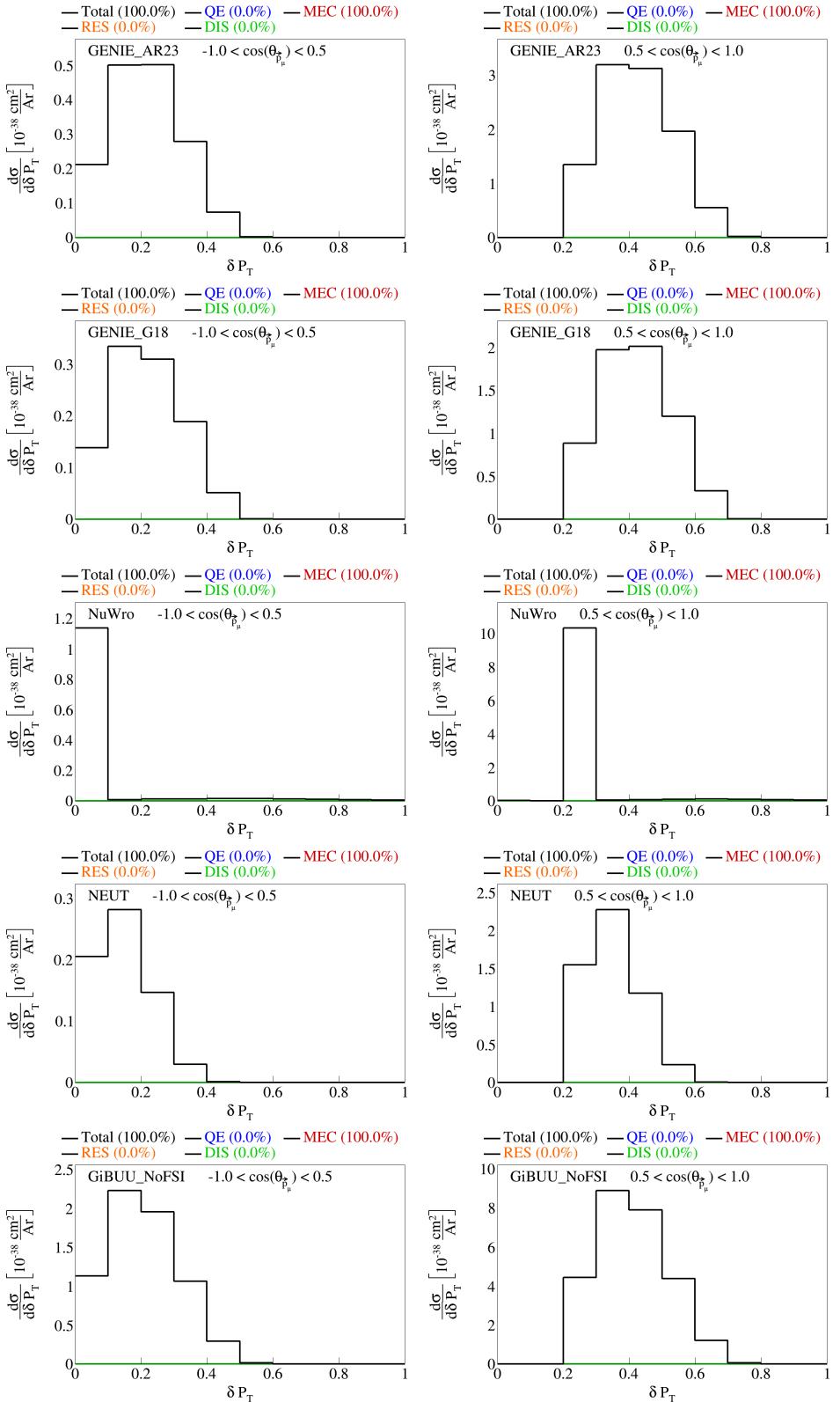


Figure 23: Interaction breakdown for sliced double differential plots for pre-FSI $|\delta \vec{P}_T|$ in $\cos(\theta_{\vec{P}_\mu})$.

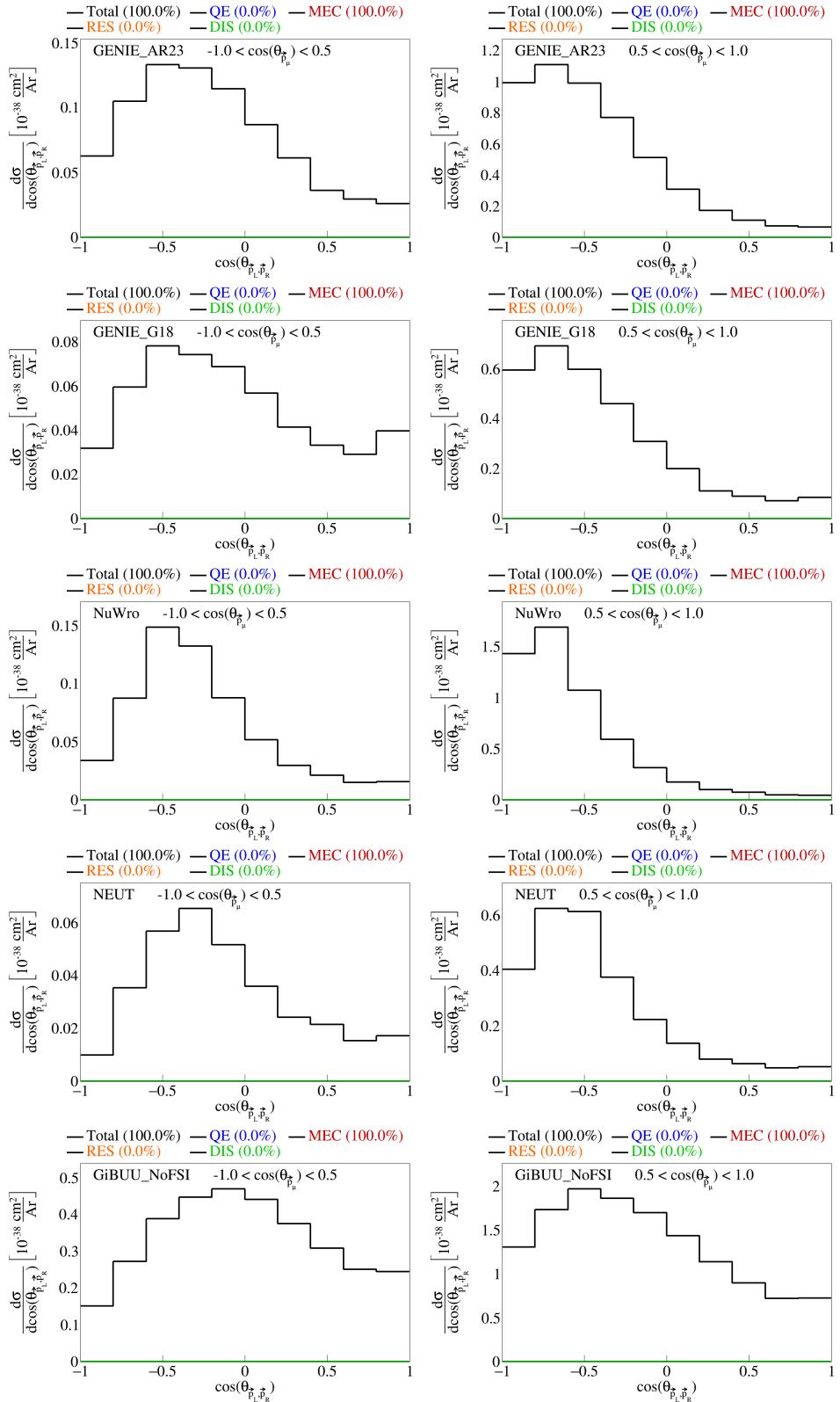


Figure 24: Interaction breakdown for sliced double differential plots for pre-FSI $\cos(\theta_{\vec{p}_L, \vec{p}_R})$ in $\cos(\theta_{\vec{p}_\mu})$.

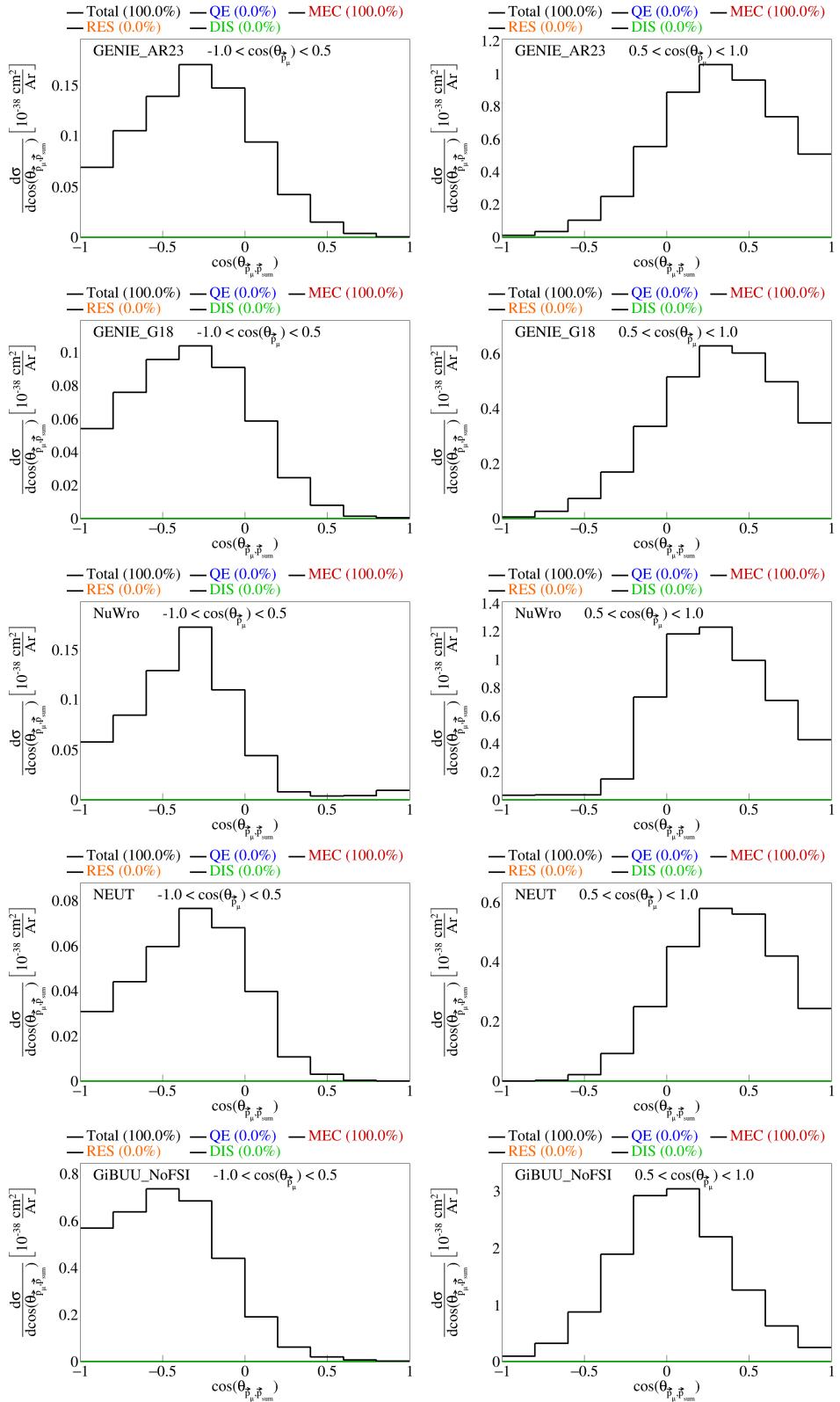


Figure 25: Interaction breakdown for sliced double differential plots for pre-FSI $\cos(\theta_{\vec{p}_\mu, \vec{p}_{\text{sum}}})$ in $\cos(\theta_{\vec{p}_\mu})$.

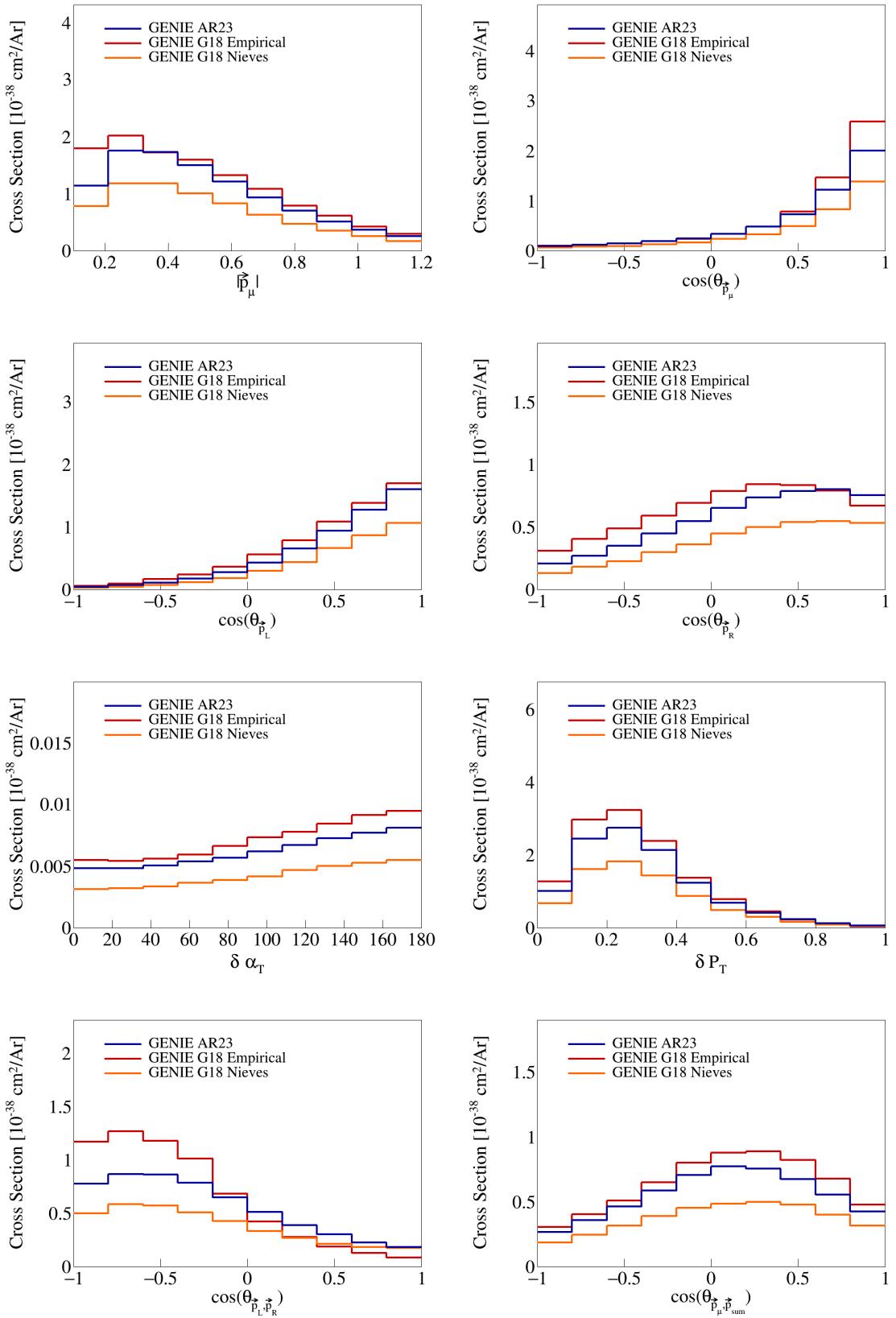


Figure 26: Variable plots for pure MEC events.

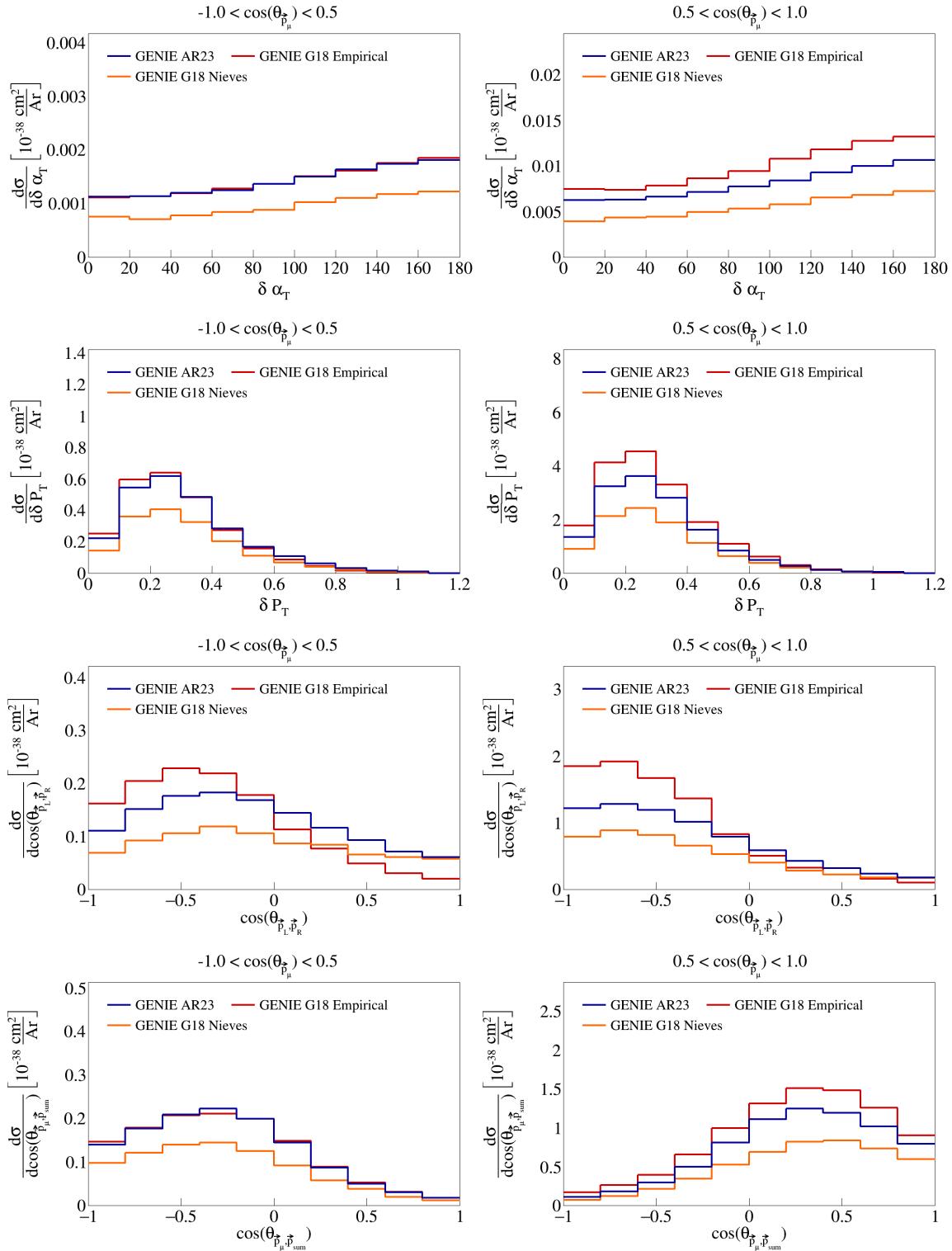


Figure 27: Sliced double differential plots for pure MEC events.

95 3 SBND analysis

96 The CAF files used for this analysis are available in the Fermilab gpvms at the path

97 `/pnfs/sbnd/persistent/users/twester/sbnd/v09_78_04/cv/*.flat.caf.root`

98 where the asterisk means that all the files in the directory with the extension `.flat.caf.root` will be used.

99 3.1 Fiducial volume

100 To perform the analysis of SBND data, we have to define the fiducial volume of the detector, which represents
101 a central part of the detector in which we will accept signals. The fiducial volume is given by the following
102 ranges:

$$5 < |x| < 180 \quad |y| < 180 \quad 10 < z < 450 \quad (6)$$

103 where x , y , and z are the coordinates in the detector frame, all in centimeters.

104 3.2 Signal definition

105 To perform analysis on experiment data, we will be using the CAFAna framework. This allows us to perform
106 cuts based on the reconstructed and Monte Carlo data (if available, i.e., only in the case of dealing with
107 simulated events), to discriminate events. To discriminate events based on their Monte Carlo data, we
108 perform a simple `TruthCut` that checks the following:

- 109 (i) That the neutrino interaction takes place in the fiducial volume.
- 110 (ii) That the neutrino is a muon neutrino.
- 111 (iii) That the interaction is a charged current interaction.
- 112 (iv) That there is only one muon in our allowed momentum range.
- 113 (v) That there are only two protons in our allowed momentum range.
- 114 (vi) That there are no charged/neutral pions in our defined momenta ranges.

115 Using the reconstructed event data, the cut we have to use is not as simple as in the Monte Carlo data
116 case. We now have to use a `Cut` that looks at different variables of the reconstructed event to determine if
117 it is a signal event. We perform the following cuts:

- 118 (i) Cosmic: that the event is not a cosmic event by Pandora's criteria, i.e., requiring `nu_score > 0.4` to
119 check how neutrino-like the event is, and `fmatch.score < 7` with $0 < fmatch.time < 1.8$ to check the
120 event comes from the beam.
- 121 (ii) Vertex in FV: that the reconstructed vertex for the neutrino interaction takes place in the fiducial
122 volume defined above.
- 123 (iii) One muon: that there is one muon track with $L_{\text{track}} > 50$ cm, starting point in the fiducial volume,
124 $\chi^2_\mu < 30$, $\chi^2_p > 60$, with momentum in our allowed range; if there are multiple candidate tracks, the
125 one with the longest track length is chosen.
- 126 (iv) Two protons: that there are two proton tracks with $\chi^2_p < 100$, full track in the fiducial volume, and
127 that these have momentum in our allowed range.
- 128 (v) No charged pions: that there are no other reconstructed tracks with momentum in the allowed range
129 for charged pions inside the fiducial volume.
- 130 (vi) No neutral pions: that there are no reconstructed particles with a positive `trackScore` less than 0.5
131 indicating a shower, so we don't allow any neutral pions.

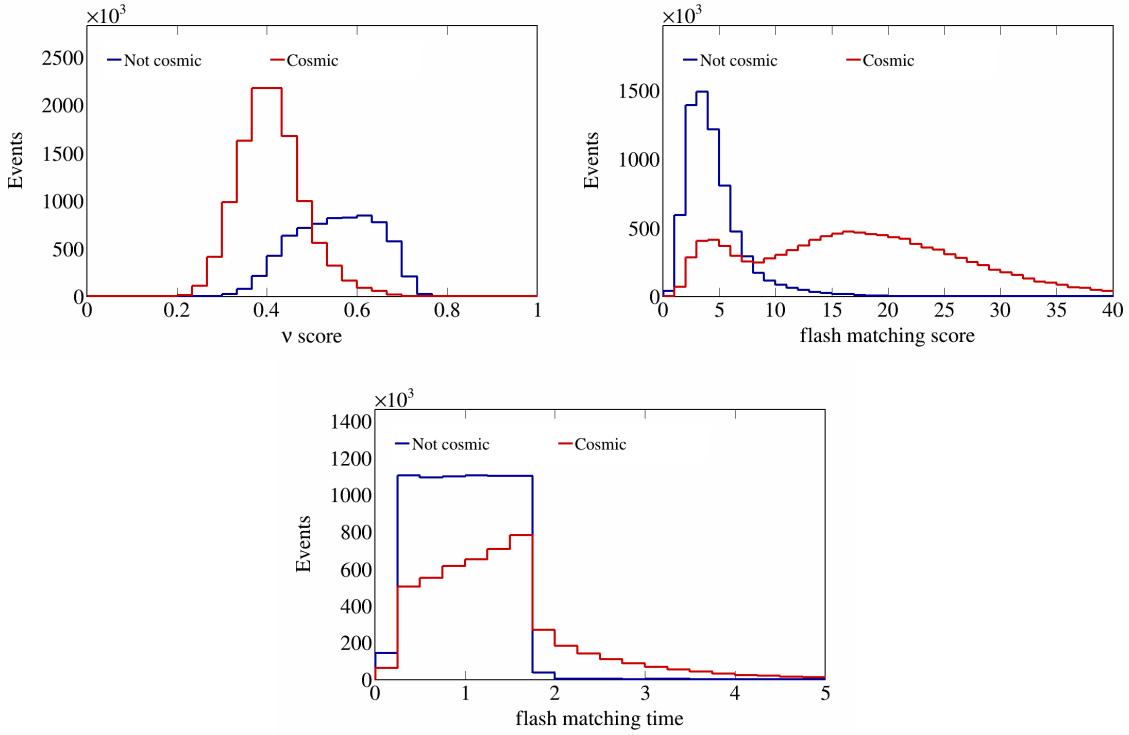


Figure 28: Cosmic cut variables before rejecting cosmic events.

Using these two discriminators on simulated events, the reconstructed events that satisfy the signal definition, and distinguish between true signal events and background events. To get a better sense of what values the variables chosen to do the cuts take on for each true particle, we plot the flash matching score, time, and ν score in Figures 28, and the χ^2 values for muons and protons in Figure 29.

We use a one-bin histogram with lower bound 0 and upper bound of 3 in the true energy variable to get total counts of generated events, true signal events, all reconstructed events, and efficiency and purity data after each of the cuts described above is applied to the reconstructed events. These results are shown in Table 2. Counts are obtained using ROOT’s command `Histo->Integral()`. Global efficiency is defined as the ratio between events that pass the cut and reconstructed events, signal efficiency as the ratio between true events that pass the cut and all true signal events, and purity as the ratio between true signal events that pass the cut and all events that pass the cut. The numbers reported in this table are POT normalized to 6.6×10^{20} .

3.3 Variable plots

Using all the variable definitions as we did when studying the event generators, and the signal definition based on the cuts described in the previous section, we can generate plots for SBND data. The reconstructed single differential variables corresponding to vector opening angles and magnitudes are shown in Figure 30. In these figures, three lines are shown, corresponding to: all reconstructed (all the reconstructed events that pass our signal definition), signal (reconstructed events that pass signal definition and are true signal events as determined by the `TruthCut` from our previous section), and background (reconstructed events that pass signal definition but are not true signal events) events. Similarly, the variables relating multiple vectors are shown in Figure 31, and double differential sliced variables are shown in Figure 32.

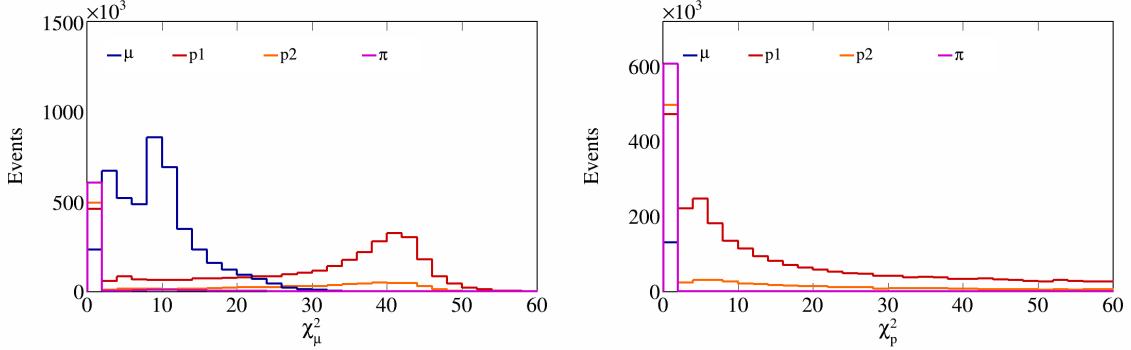


Figure 29: Muon and proton χ^2 values for all particles.

Cut	Number of events	Global efficiency	Signal efficiency	Purity
All	$1.3938 \cdot 10^7$	-	-	-
True signal events	272161	-	-	-
All reco events	$7.09465 \cdot 10^6$	100%	-	-
Cosmic cut	$5.74938 \cdot 10^6$	81.0381%	89.6205%	4.24241%
Vertex in FV cut	$3.23953 \cdot 10^6$	45.6616%	88.2885%	7.41734%
One muon cut	$2.20417 \cdot 10^6$	31.068%	70.5202%	8.70753%
Two protons cut	146443	2.06413%	17.517%	32.5549%
No charged pions cut	67441.8	0.9506%	12.6665%	51.1156%
No neutral pions cut	54514.3	0.768385%	11.3094%	56.4617%

Table 2: Global efficiency, selection efficiency, and purity for cuts made in signal definition.

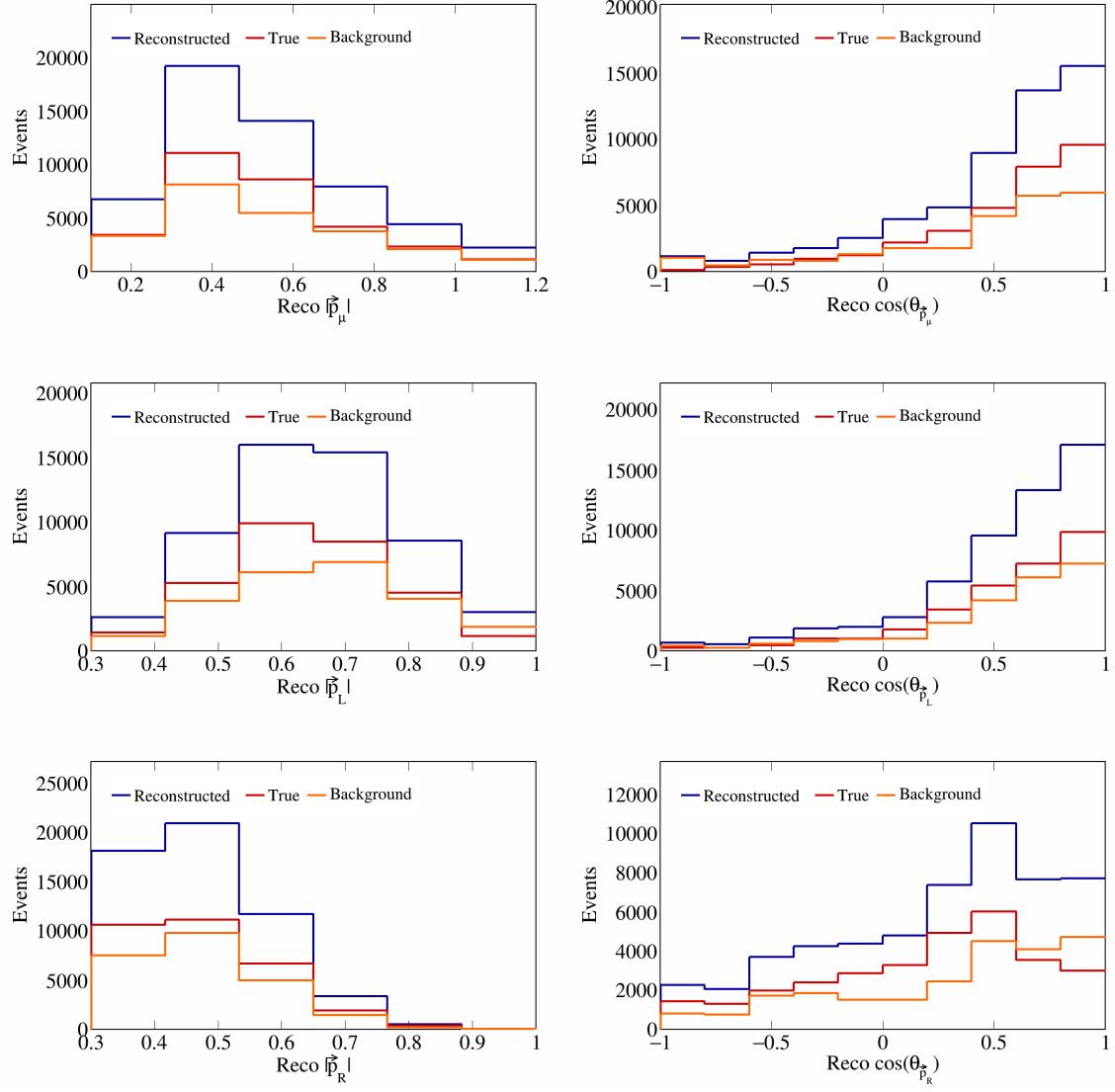


Figure 30: Vector directions and magnitudes for SBND data.

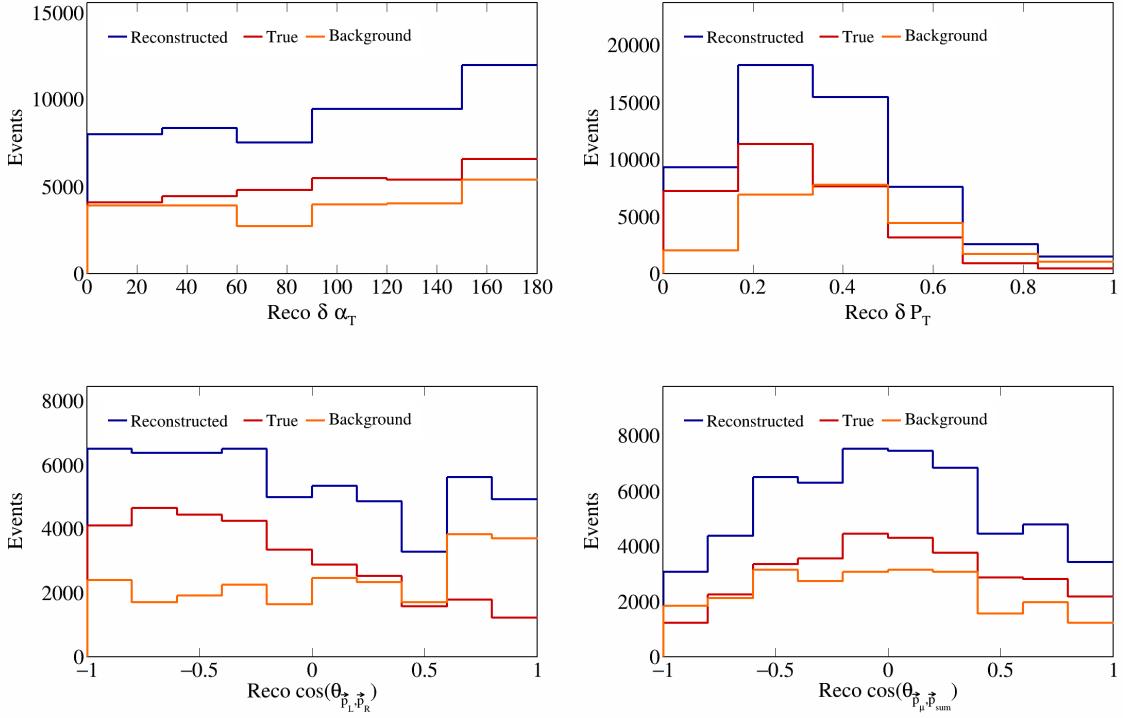


Figure 31: Vector opening angles and transverse momentum for SBND data.

153 3.4 Interaction and topology breakdown

154 We perform an interaction and topology breakdown for the SBND data. For these breakdowns, we look at
 155 the reconstructed events that pass our signal definitions cuts and see what percentage of these are generated
 156 from different interaction modes and topologies. This helps us get a better idea of what our background
 157 signal is composed of. For the interaction breakdown, we look at quasielastic (QE), MEC (meson-exchange
 158 current), RES (resonance), and DIS (deep inelastic scattering) events. For the topology breakdown, we look
 159 at the number of protons, pions, and muons in the final state. The topologies we label are CC2p0pi (our
 160 signal definition), CC1p0pi, CC($N > 2$)p0pi, CC($N \geq 0$)p1pi, and CC0p0pi. Any other topology is labeled
 161 as “Other”. These breakdowns are shown in Figures 33 to 36.

162 3.5 Signal efficiency

163 Using the truth information about reconstructed events, we can also compute signal efficiency on a bin-by-
 164 bin basis. To be precise, signal definition on a bin i is defined as the ratio between the number of events
 165 generated in bin i and reconstructed in any bin over the number of events generated in bin i . These plots
 166 are shown in Figure 37 and Figure 38 for single-differential variables and Figure 39 for double differential
 167 variables.

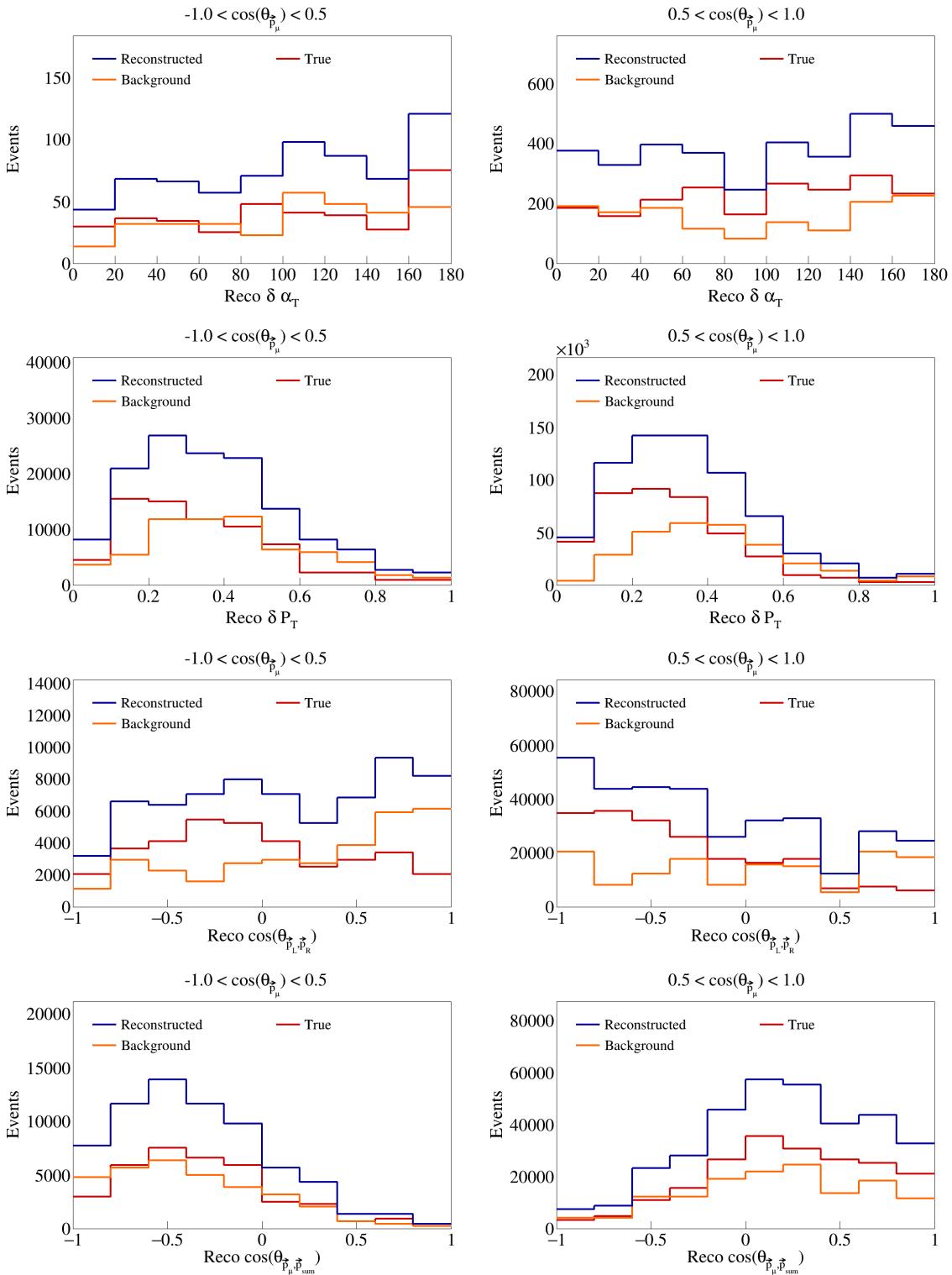


Figure 32: Sliced double differential plots for SBND events.

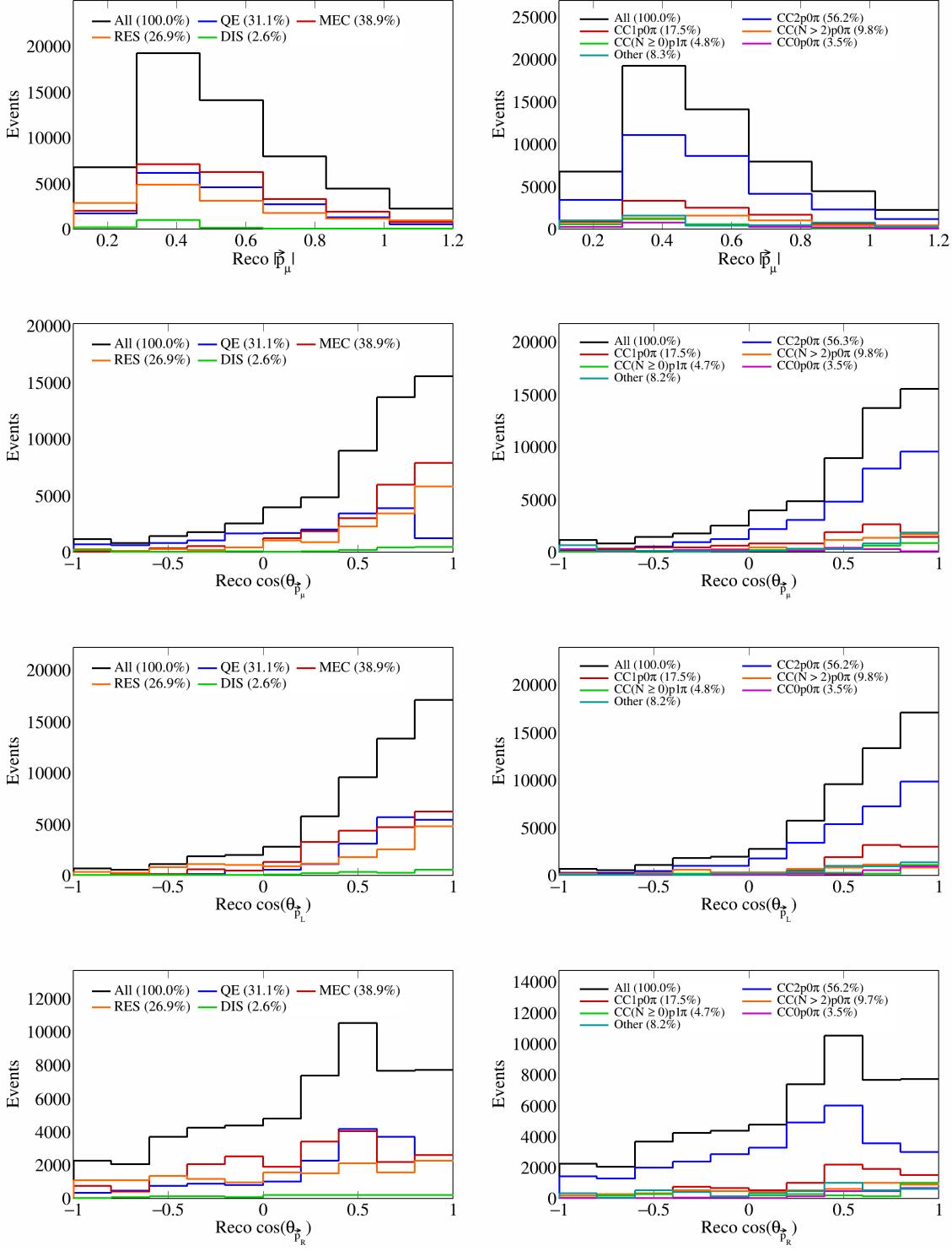


Figure 33: Interaction and topology breakdown for vector directions and magnitudes.

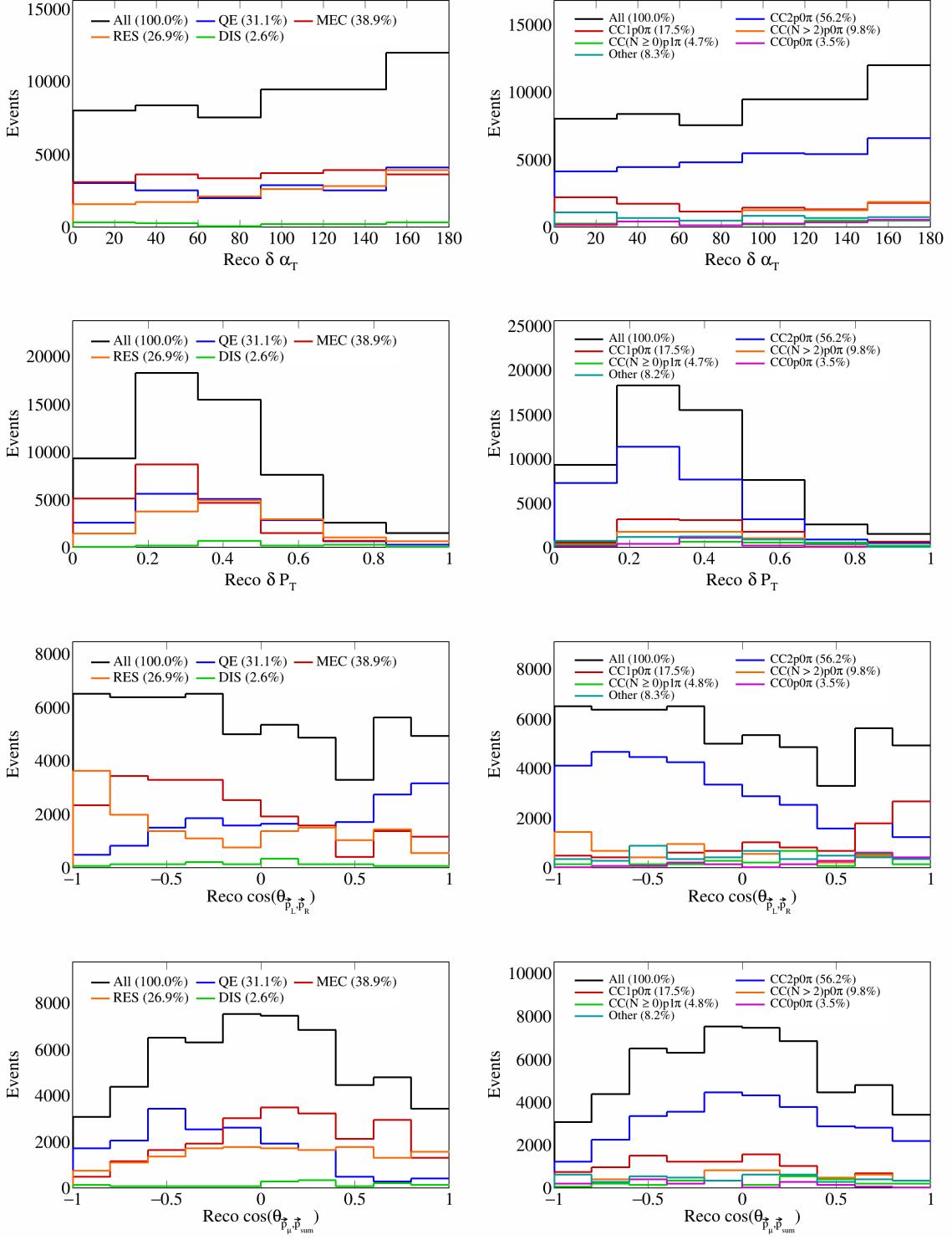


Figure 34: Interaction and topology breakdown for opening angles and transverse variables.

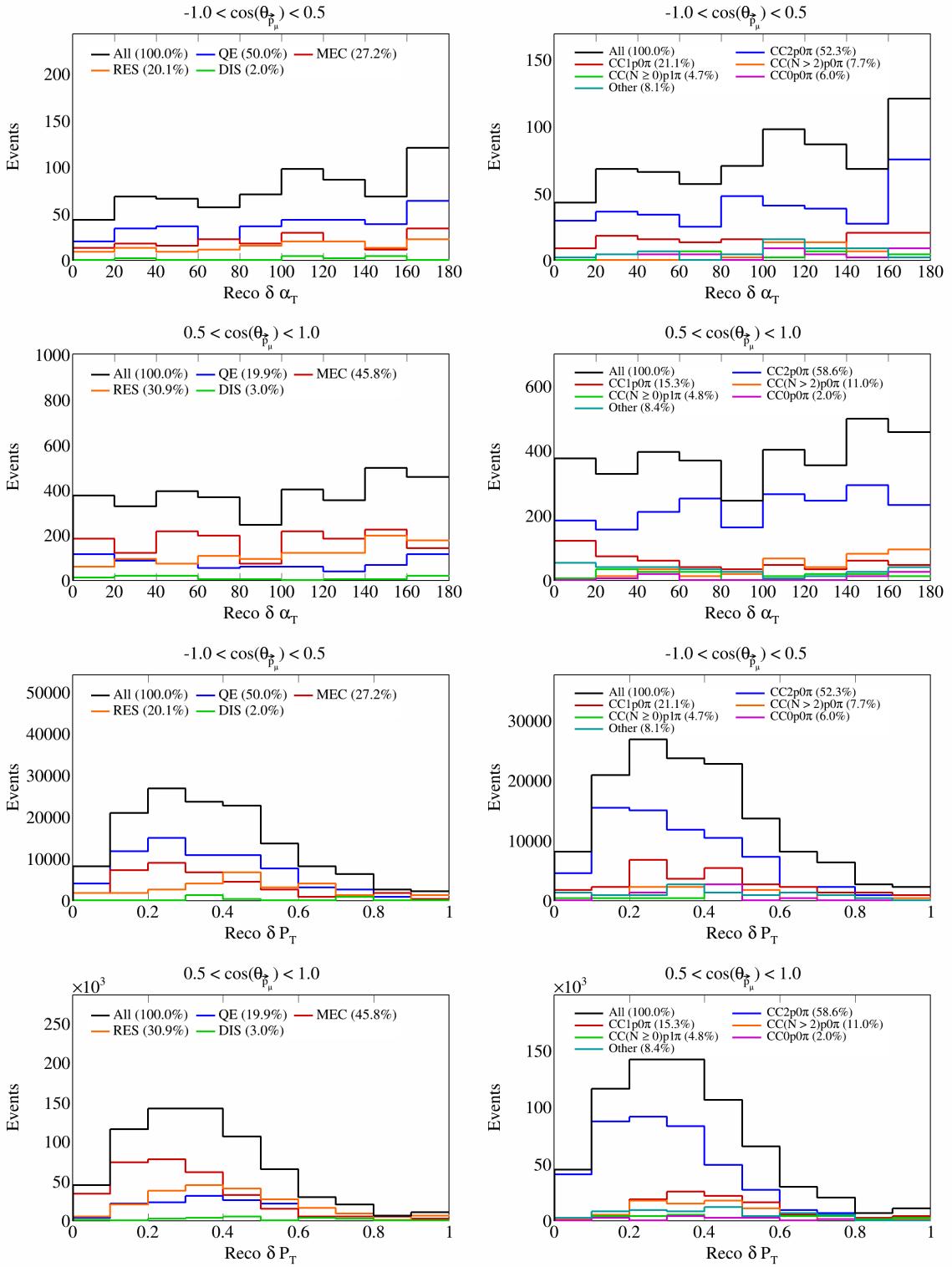


Figure 35: Interaction and topology breakdown for double differential transverse variables.

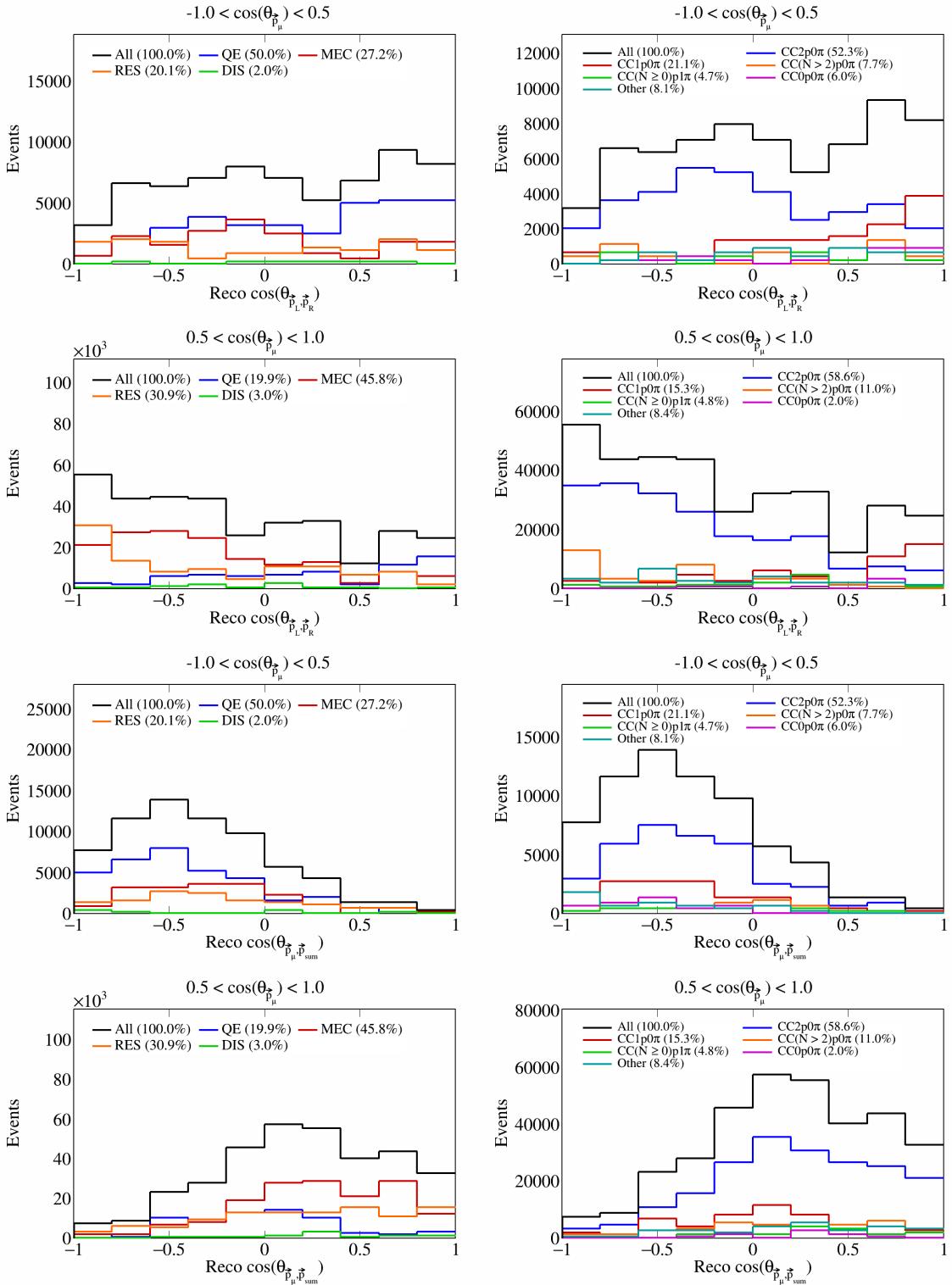


Figure 36: Interaction and topology breakdown for double differential opening angles.

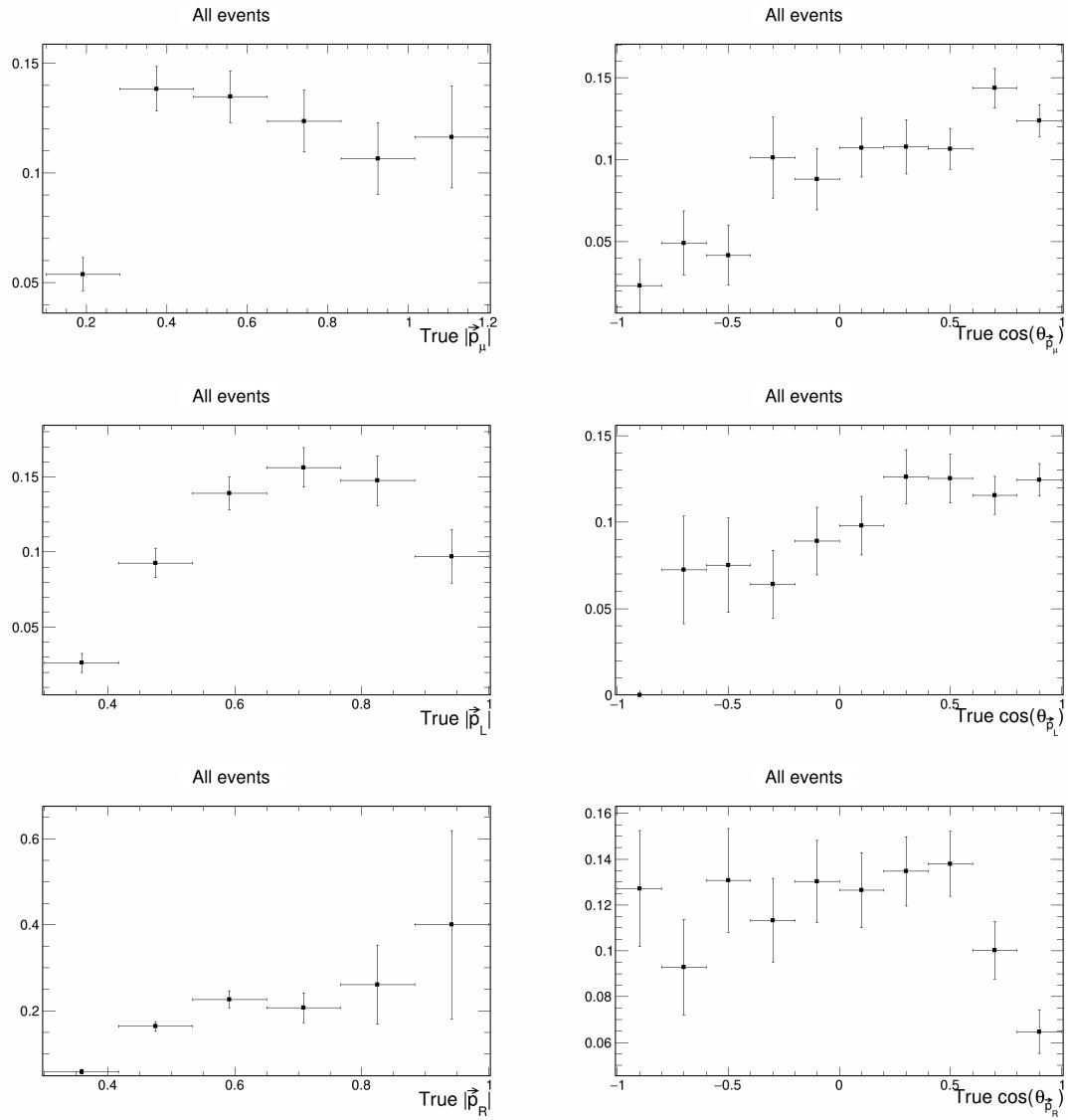


Figure 37: Signal efficiency plots for single differential vector directions and magnitudes.

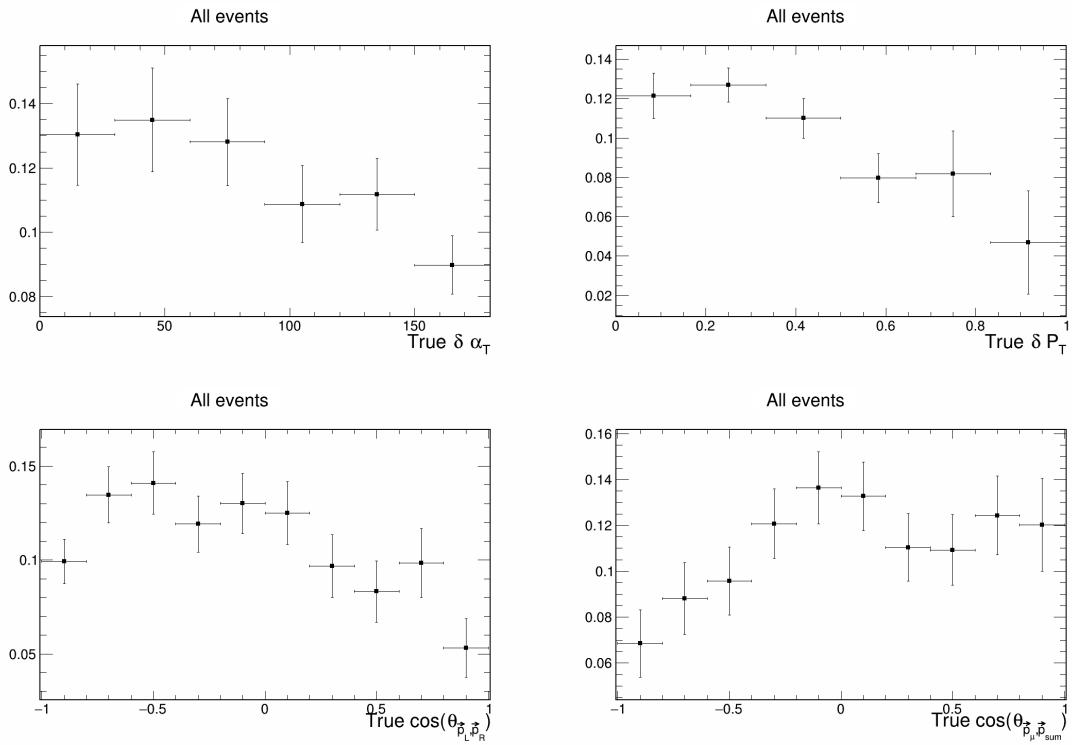


Figure 38: Signal efficiency plots for single differential vector opening angles and transverse momentum.

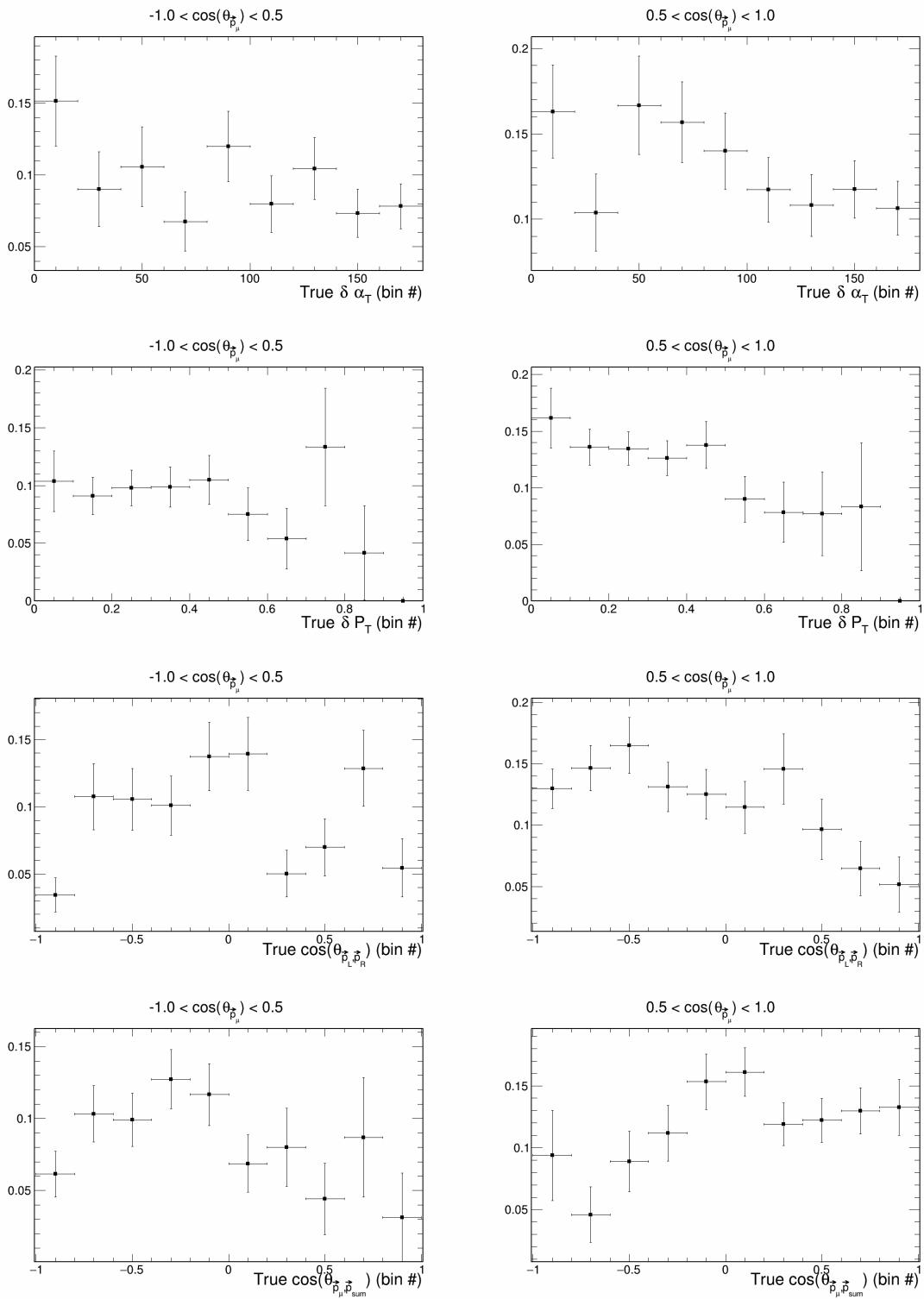


Figure 39: Signal efficiency plots for double differential variables.

168 **3.6 Migration and response matrices**

169 Further, we compute migration matrices which give us a measure of how reliable our reconstructed variables
170 are. A given column in this matrix represents a bin of the truth variable, i.e., the value with which the
171 event was generated. Then, each row corresponds to a reconstructed bin of the same variable, and each cell
172 corresponds to the probability that an event generated with the truth value corresponding to the column gets
173 reconstructed with the value corresponding to the row. For the migration matrix, we consider true signal
174 events that were reconstructed and satisfy our signal definition in the denominator. Therefore, the values in
175 each column must add up to 1. The migration matrices for the single differential variables are presented in
176 Figure 40 and Figure 41. The migration matrices for the double differential variables (given in terms of the
177 bin number) are presented in Figure 42.

178 Response matrices are computed in a similar manner, but using the total number of generated events in the
179 denominator when computing the ratios, i.e., without requiring the events to be successfully reconstructed.
180 Therefore, for these matrices, the columns of the response matrices do not have to add up to 1. The response
181 matrices for single differential variables are presented in Figure 43 and Figure 44, and the double differential
182 response matrices are given in Figure 45.

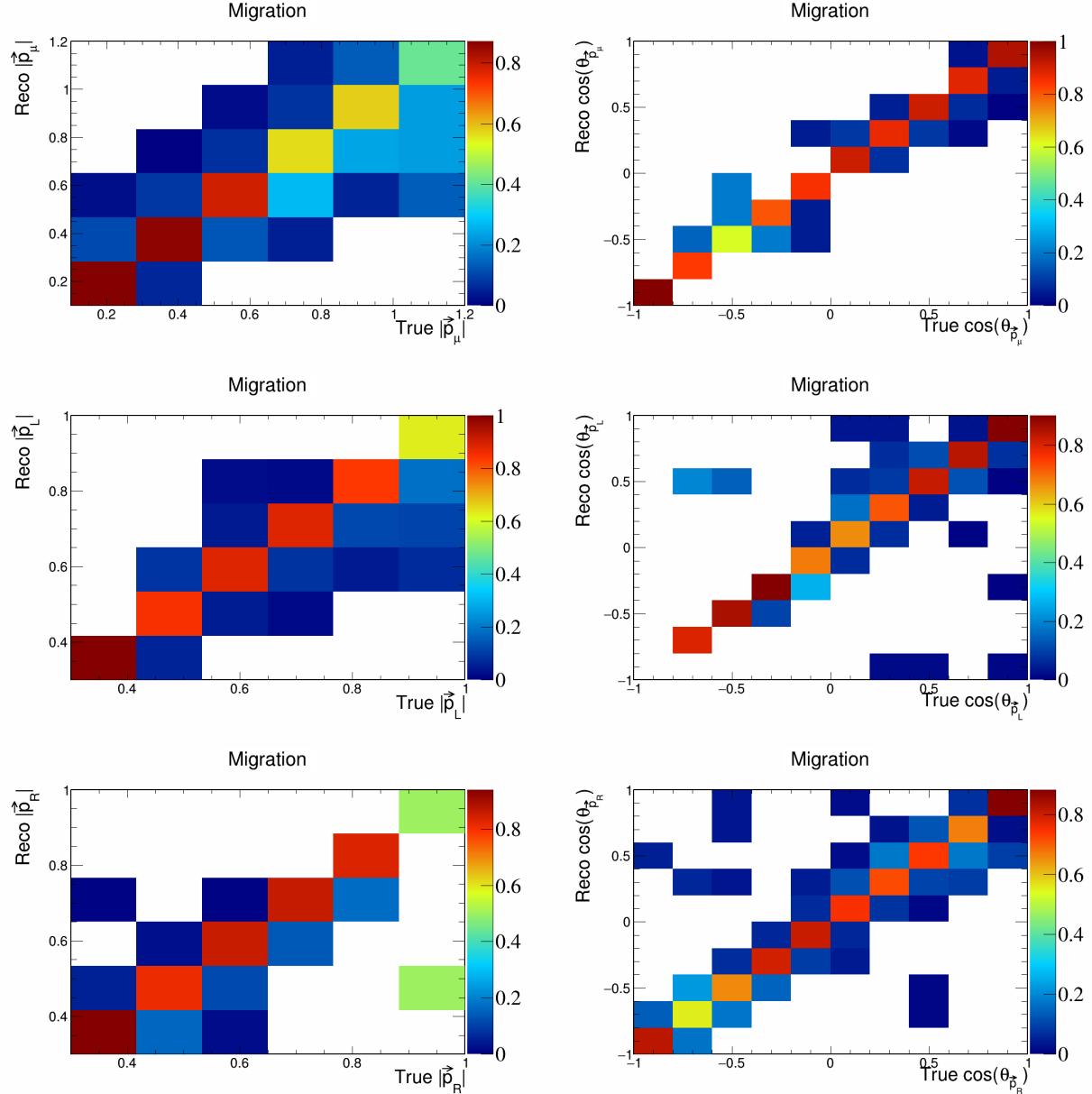


Figure 40: Migration matrices for signal differential vector directions and magnitudes.

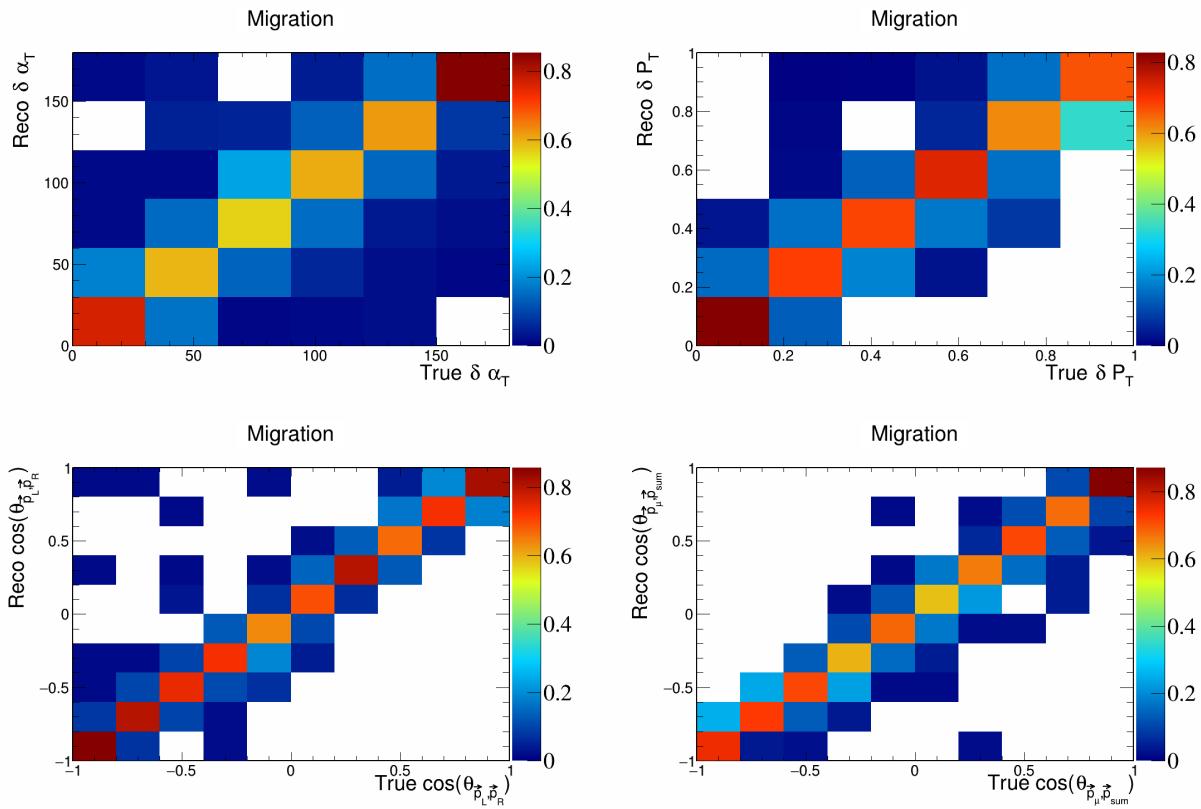


Figure 41: Migration matrices for signal differential vector opening angles and transverse momentum.

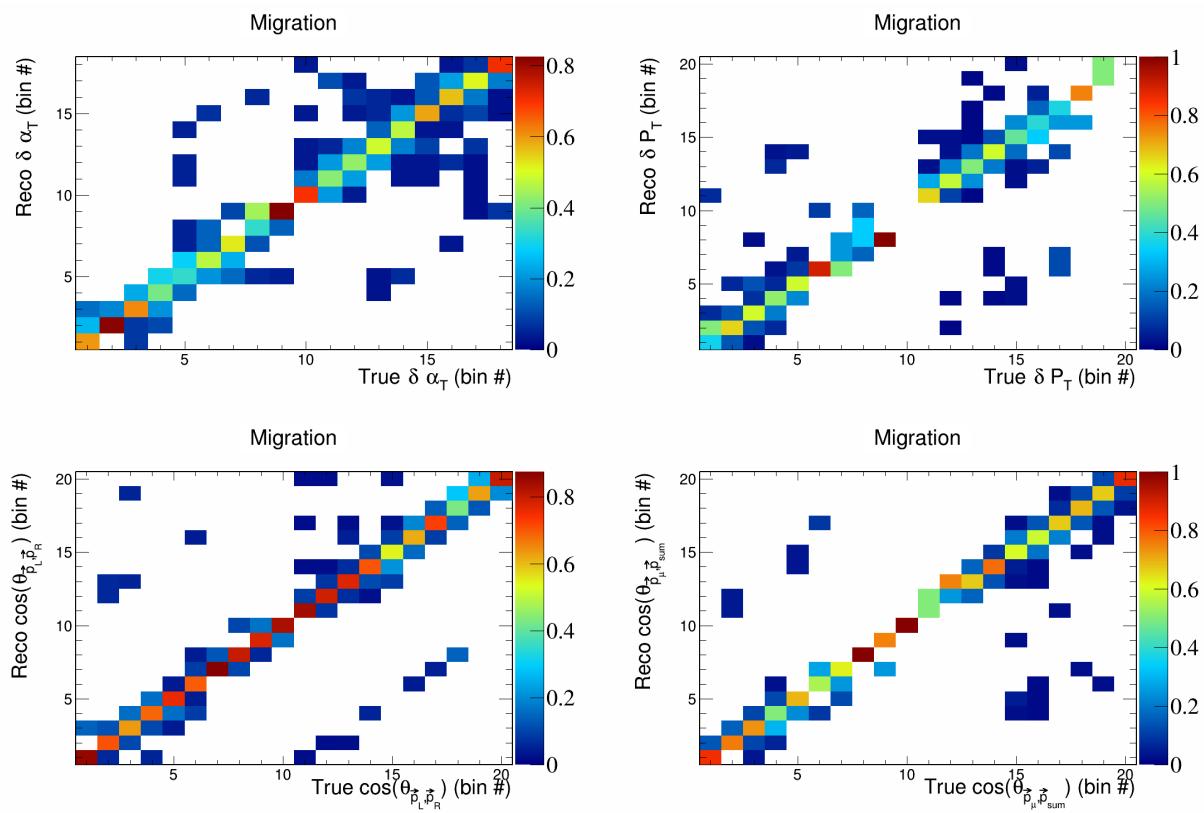


Figure 42: Migration matrices for double differential variables.

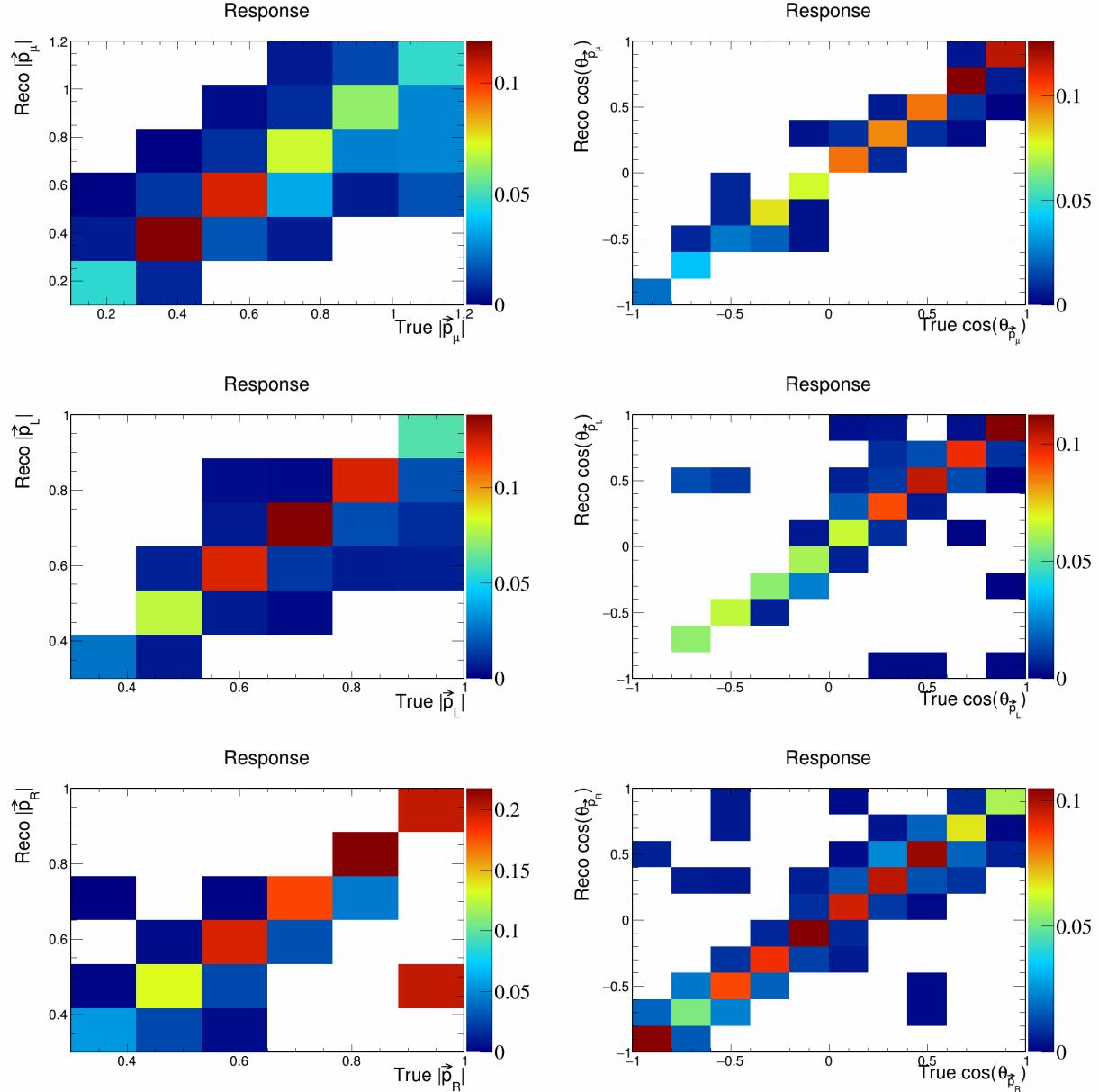


Figure 43: Response matrices for signal differential vector directions and magnitudes.

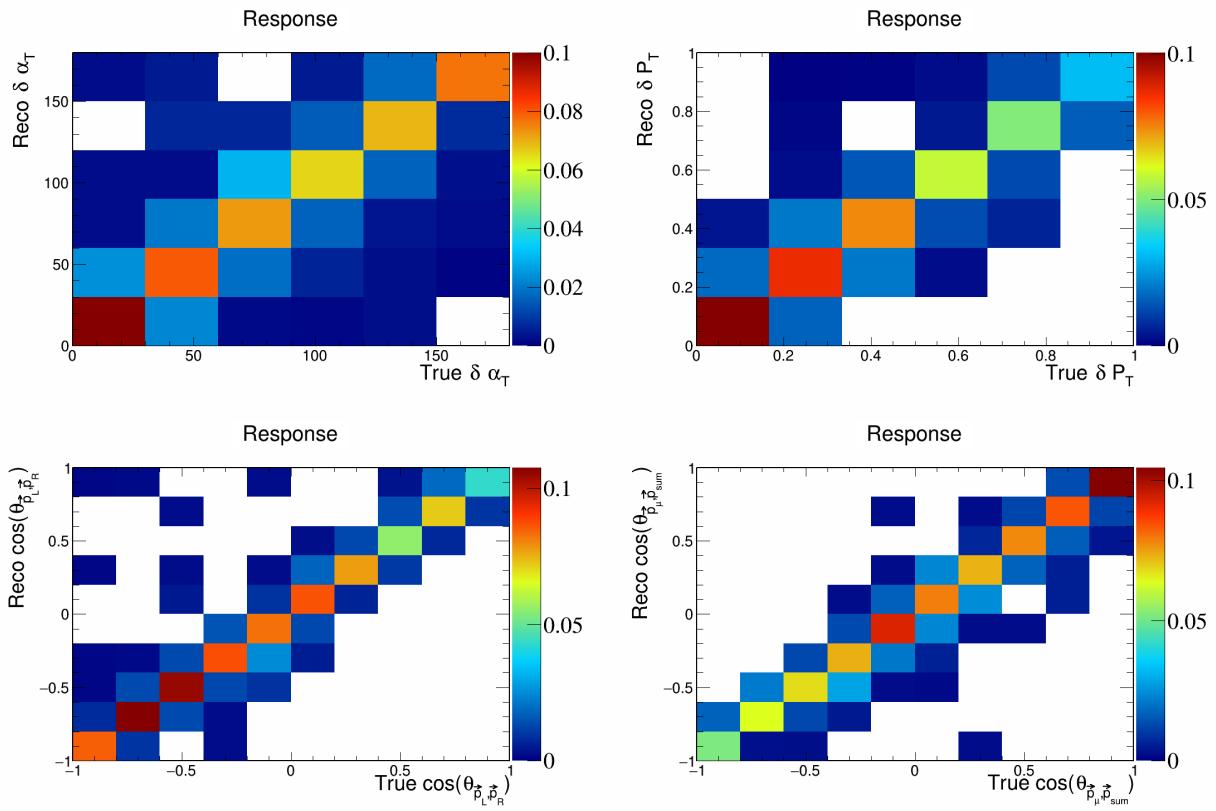


Figure 44: Response matrices for signal differential vector opening angles and transverse momentum.

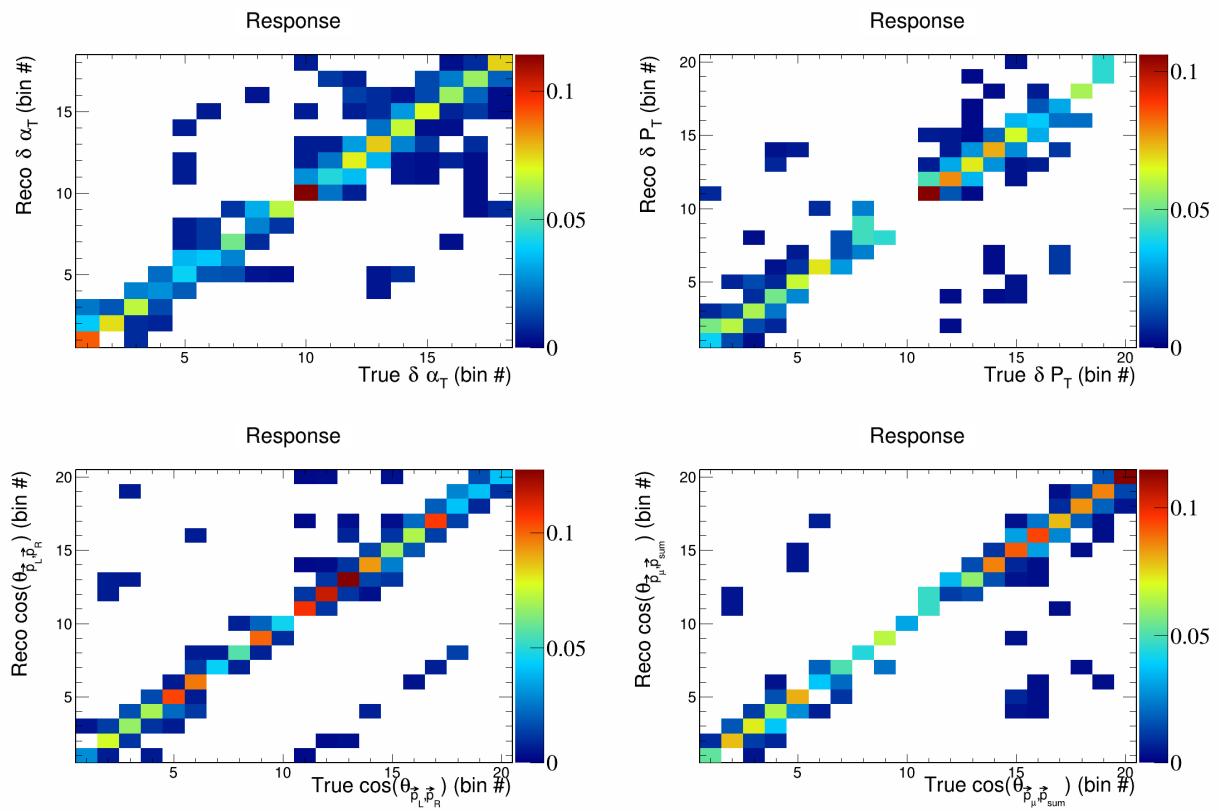


Figure 45: Response matrices for double differential variables.

183 **3.7 Systematics**

184 To include systematic uncertainties in our study, we first consider cross sectional systematics. These are
 185 variations in the cross section models used to generate the events. They can be of two types: multisigma
 186 and multisim. For the former, we consider a 1σ variation of the affected parameters, and in the latter we
 187 consider one hundred universes, each with a random variation picked from a Gaussian distribution between
 188 0σ and 1σ . From these variations, we compute the covariance matrix as

$$E_{i,j} = \frac{1}{N_{\text{Univ}}} \sum_{s=1}^{N_{\text{Univ}}} (\tilde{\sigma}_i^{\text{Var},s} - \tilde{\sigma}_i^{\text{CV}})(\tilde{\sigma}_j^{\text{Var},s} - \tilde{\sigma}_j^{\text{CV}}) \quad (7)$$

189 where $\tilde{\sigma}_i^{\text{Var},s}$ represents the variation cross section of the variable in the i -th bin in the s -th universe, and
 190 $\tilde{\sigma}_i^{\text{CV}}$ is the central value (without any variation) of the cross section in the i -th bin. Then, the fractional
 191 covariance matrix is defined as

$$F_{i,j} = \frac{E_{i,j}}{\tilde{\sigma}_i^{\text{CV}} \tilde{\sigma}_j^{\text{CV}}}. \quad (8)$$

192 And the correlation matrix is defined as

$$\rho_{i,j} = \frac{E_{i,j}}{\sqrt{E_{i,i} E_{j,j}}}. \quad (9)$$

193 In the case of a multisigma systematic, $N_{\text{Univ}} = 1$, and for a multisim systematic, $N_{\text{Univ}} = 100$. The plots
 194 for all the individual cross sectional systematics are shown in Appendix 5.1. Flux systematics are computed
 195 in the same way, but each universe varies a flux parameter. The corresponding plots for the individual
 196 flux systematics are shown in Appendix 5.2. Finally, we also consider statistical systematics. This are
 197 straightforward to compute, as the covariance matrix is given by the square root of the number of elements
 198 in the corresponding bin in the histogram. These statistical covariance matrices are shown in Appendix 5.3.
 199 The total covariance matrices for each variable are shown in Figures 46 and 47.

200 **3.8 Closure test**

201 We use the total covariance matrices obtained from all the systematics and shown in the previous section
 202 to unfold our data. We perform this unfolding following the Wiener-SVD method [27], which for a given
 203 variable takes as input a response matrix, true signal histogram, a reconstructed signal histogram, and the
 204 covariance matrix. The output is the unfolded spectrum and a smearing matrix that can be used to smear
 205 true signal histograms.

206 To ensure that the unfolding techniques that we will implement work correctly, we perform a closure test,
 207 meaning that we will perform the unfolding on simulated true signal events and check that the unfolded
 208 data matches the true signal data with added smearing. We can see that the plots that perform this test
 209 in Figure 48 and Figure 49. We also note that the overall shape and magnitude of our histograms match
 210 previously reported MicroBooNE analyses.

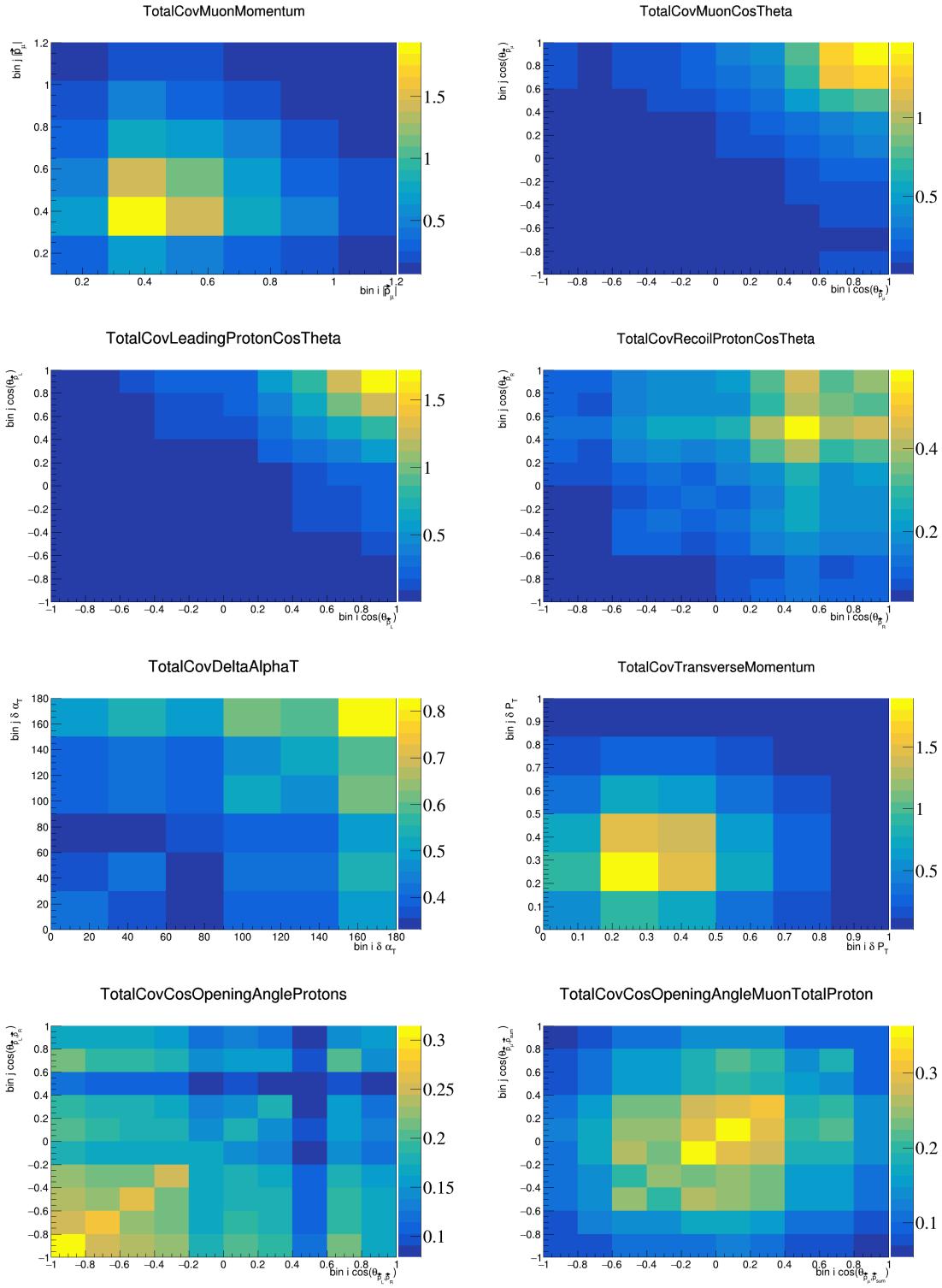


Figure 46: Total covariance matrices for single differential variables.

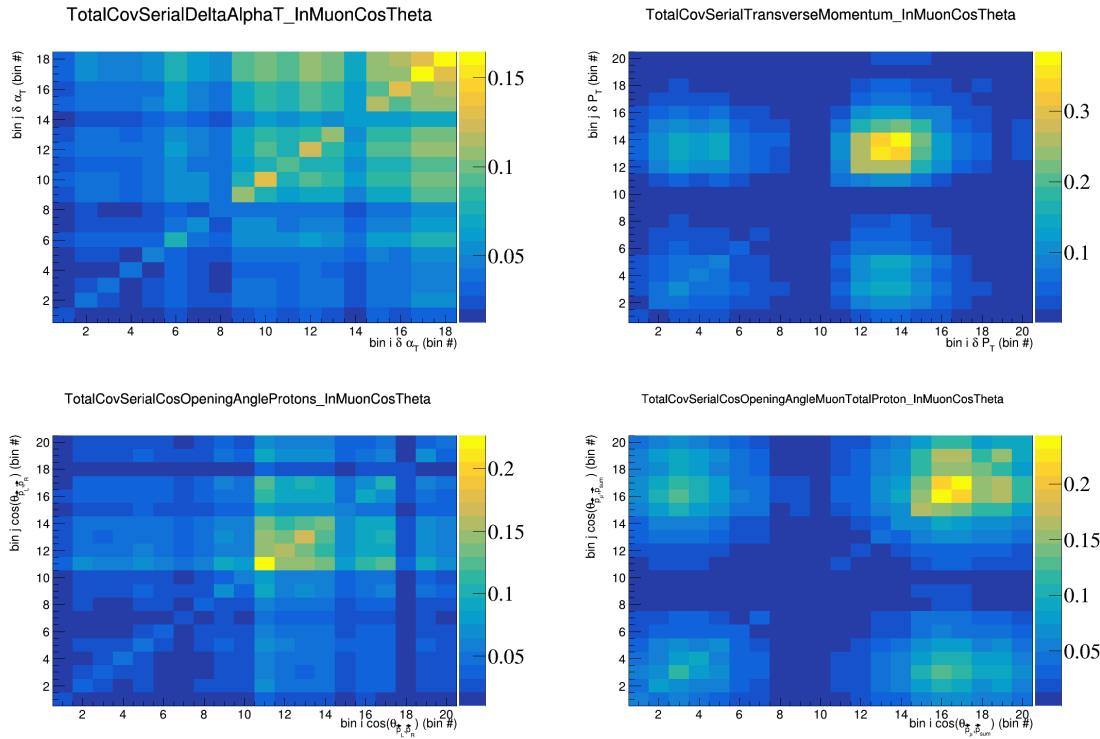


Figure 47: Total covariance matrices for double differential variables.

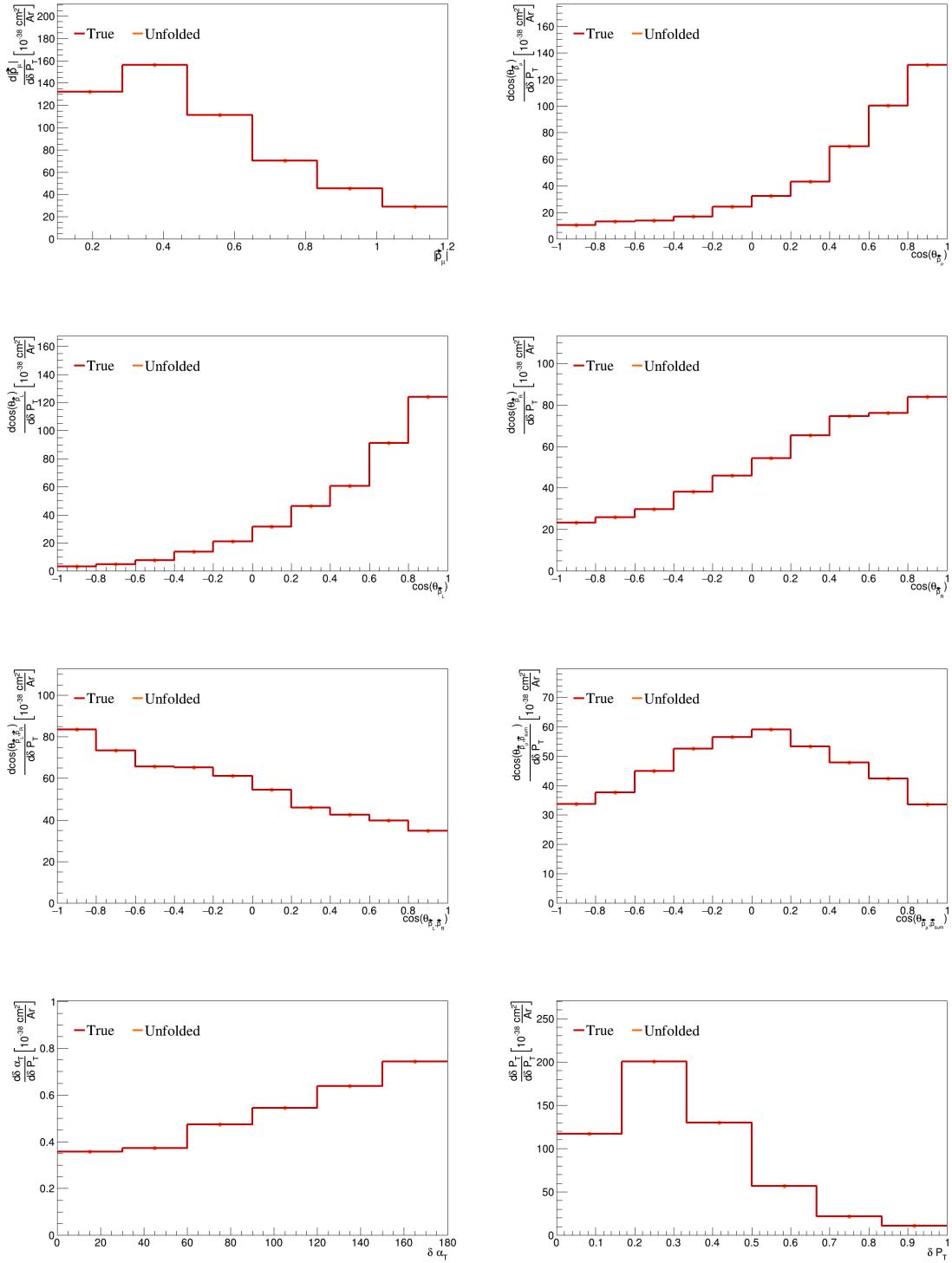


Figure 48: Closure test single differential plots.

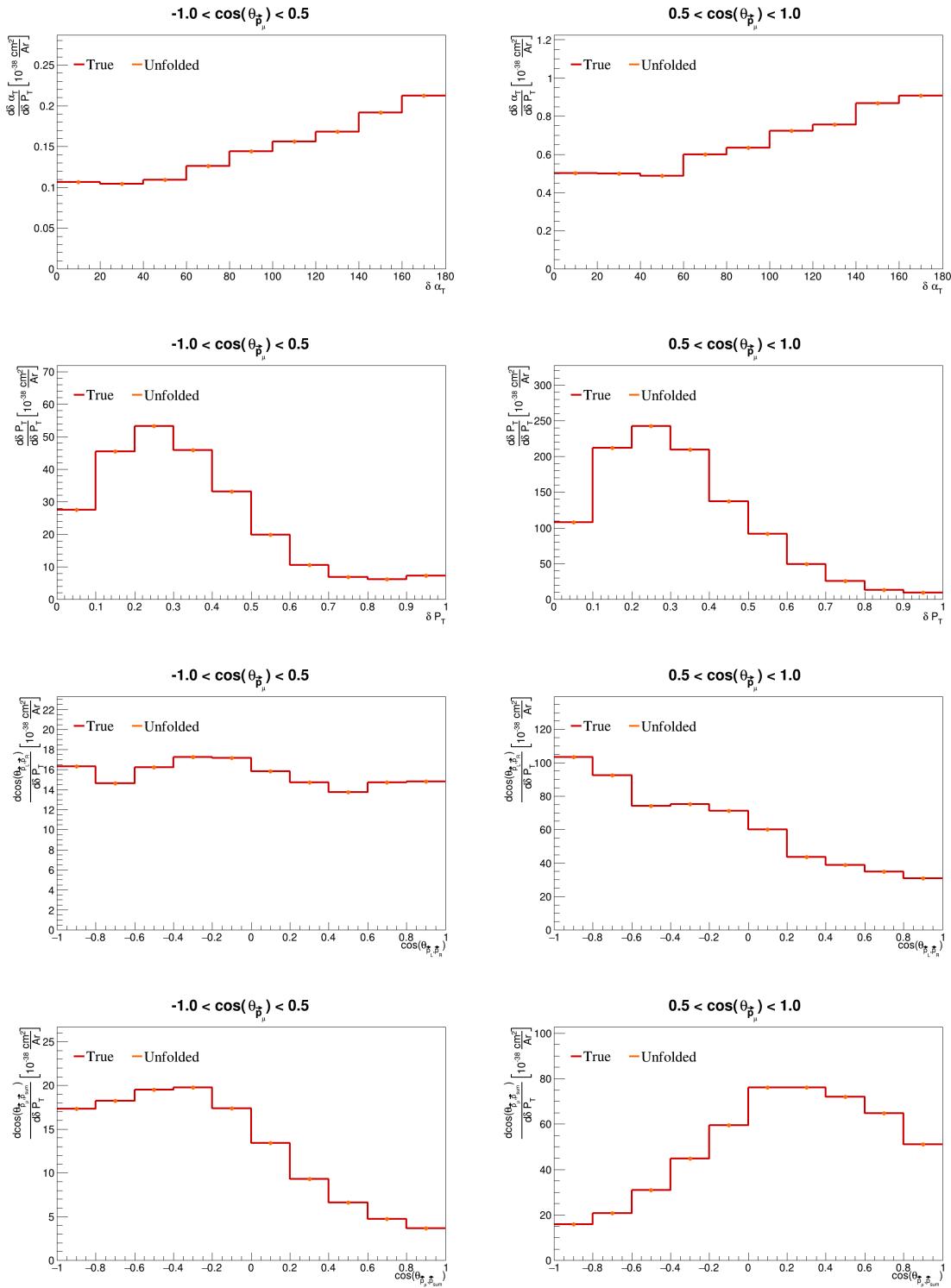


Figure 49: Closure test double differential plots.

₂₁₁ **4 Cross-section results**

₂₁₂ Placeholder.

213 **5 Appendices**

214 **5.1 Cross section systematics**

215 In this appendix, the variations, covariance matrices, fractional covariance matrices, and correlation matrices
 216 are plotted for all of the cross section systematics and variables.

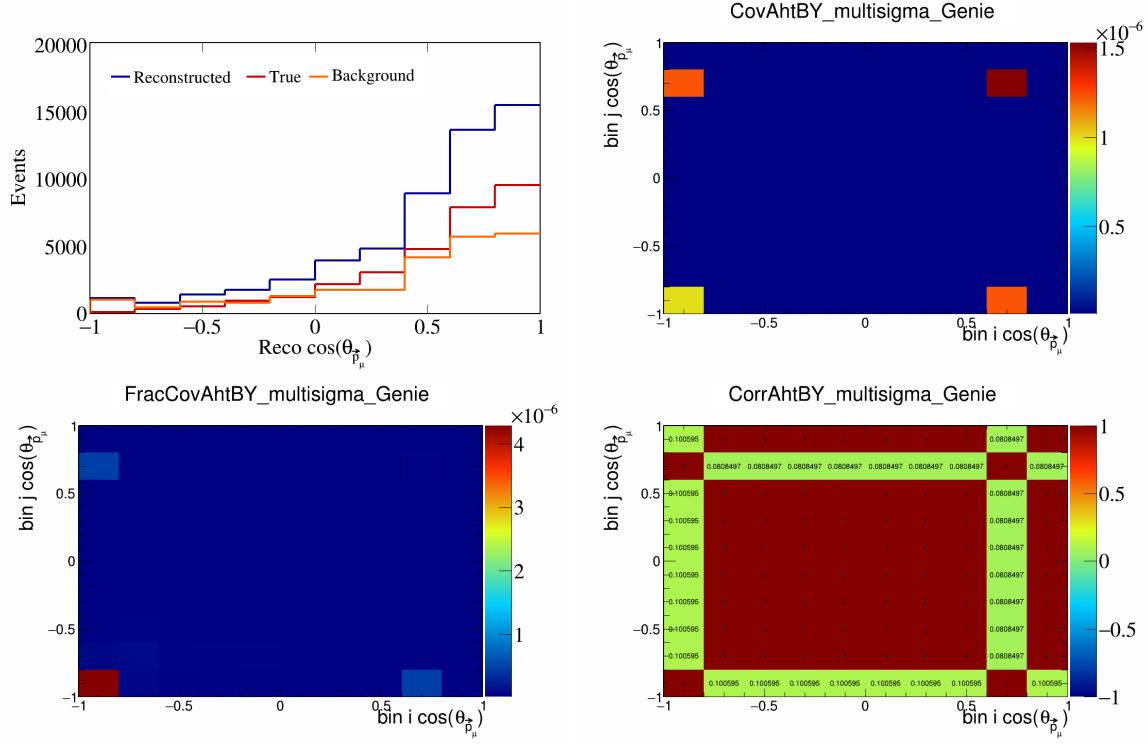


Figure 50: AhtBY variations for $\cos(\theta_{\vec{p}_\mu})$.

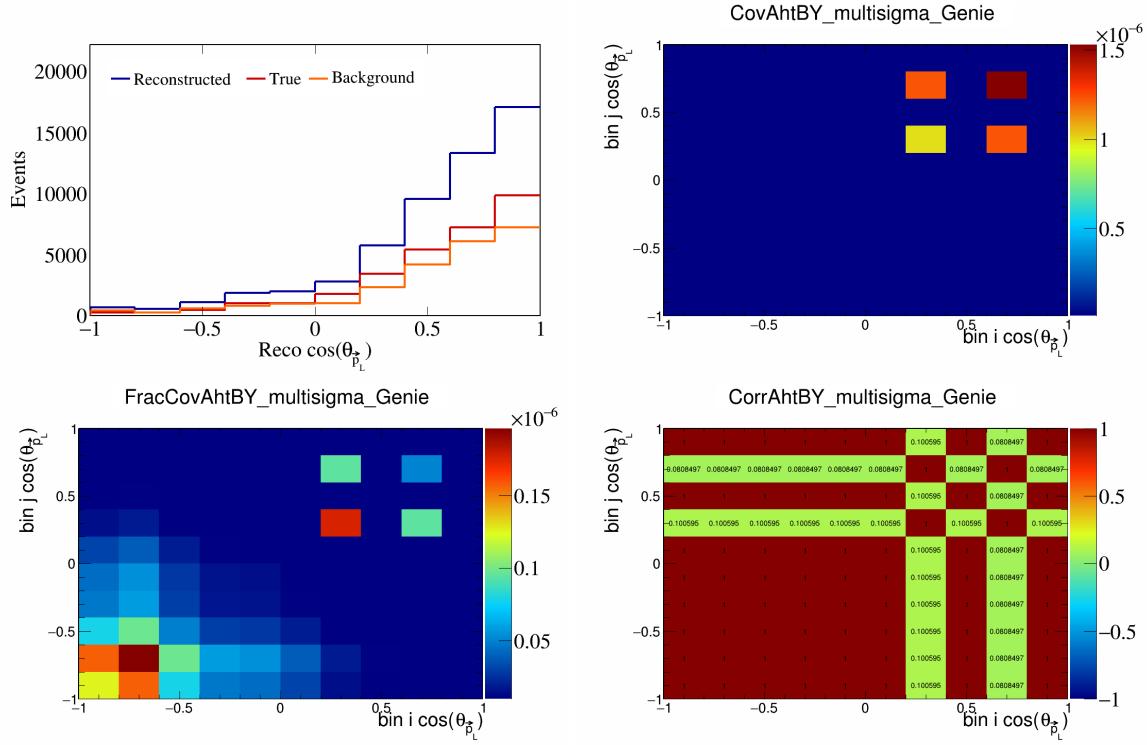


Figure 51: AhtBY variations for $\cos(\theta_{\vec{p}_L})$.

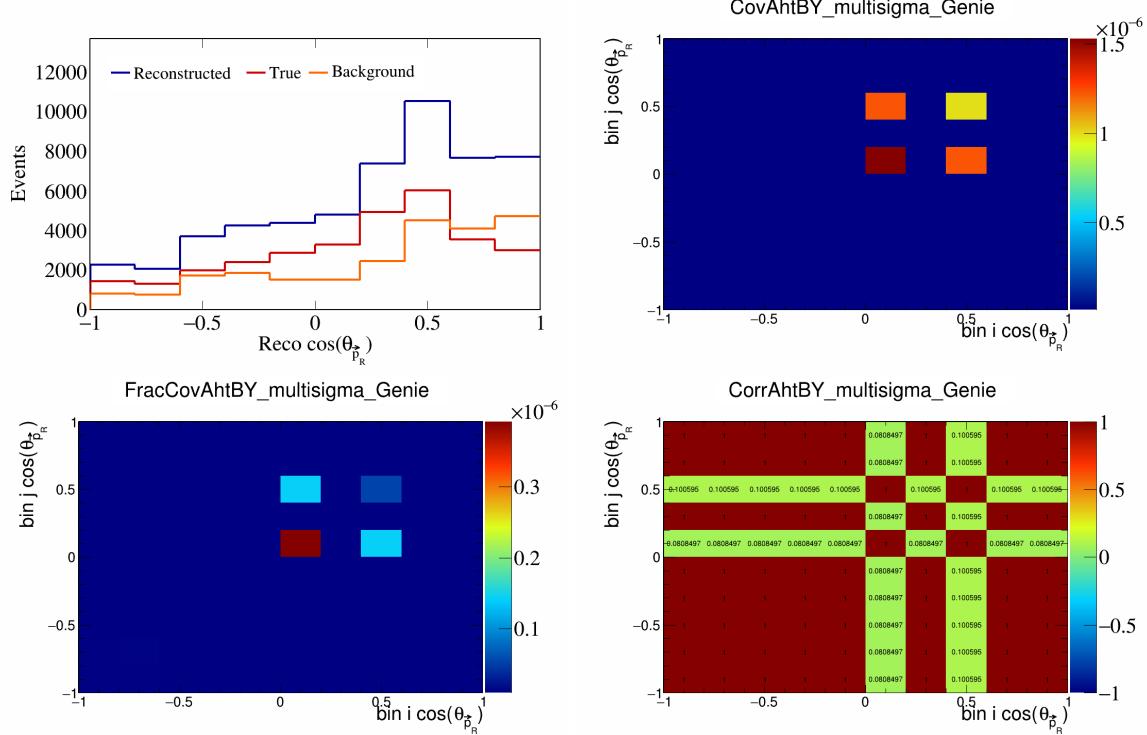


Figure 52: AhtBY variations for $\cos(\theta_{\vec{p}_R})$.

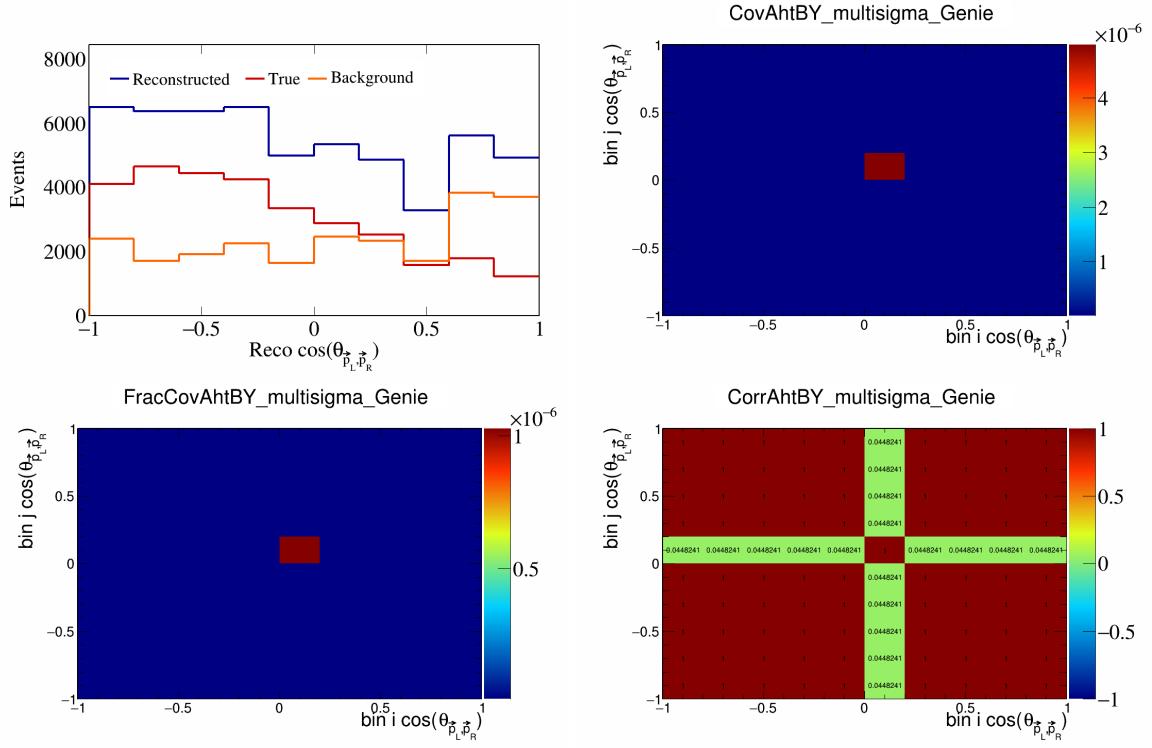


Figure 53: AhtBY variations for $\cos(\theta_{\vec{p}_L, \vec{p}_R})$.

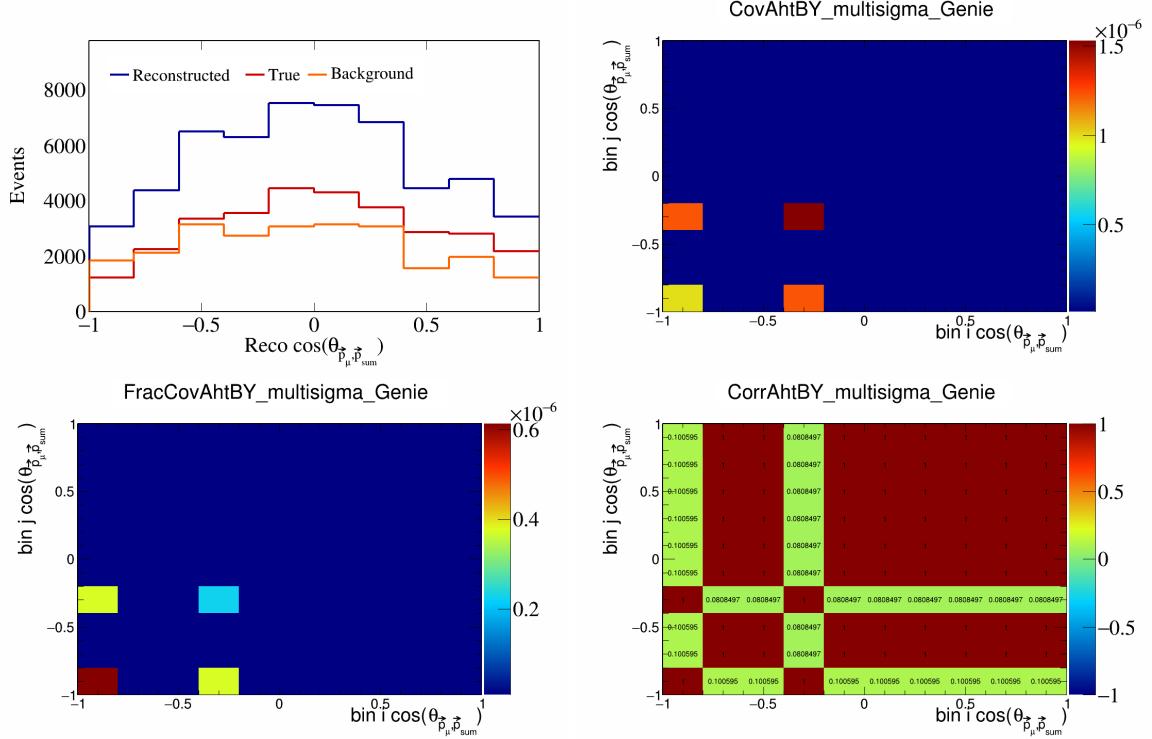


Figure 54: AhtBY variations for $\cos(\theta_{\vec{p}_\mu, \vec{p}_{\text{sum}}})$.

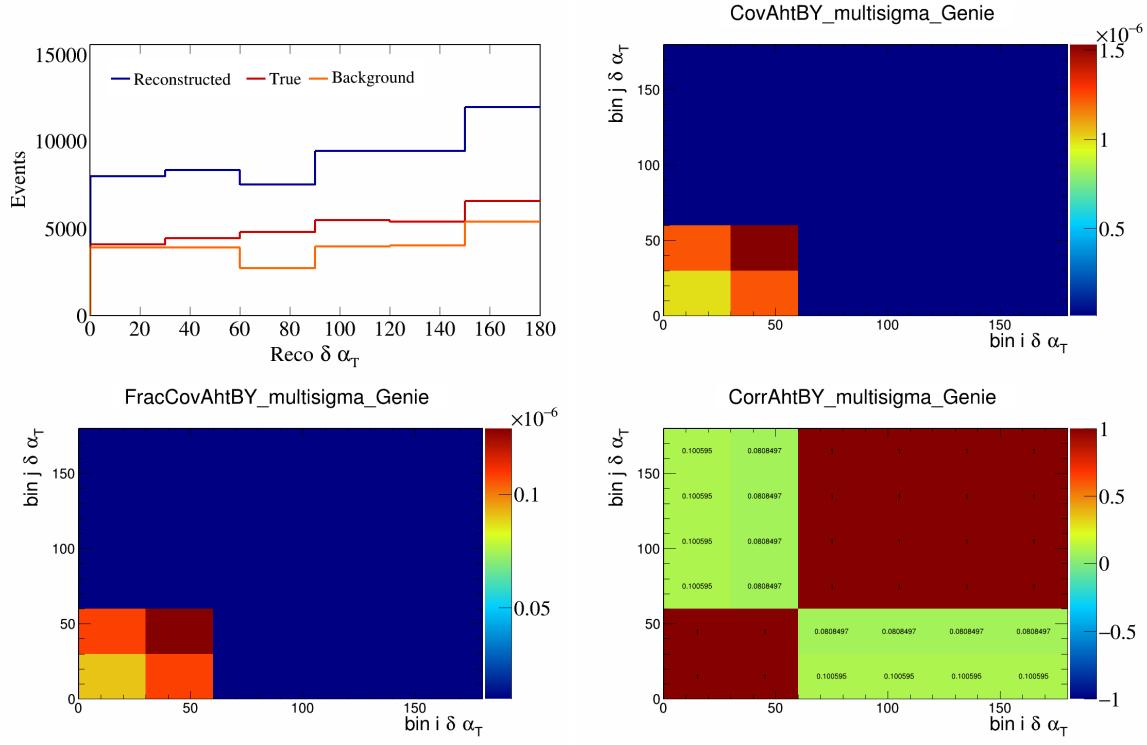


Figure 55: AhtBY variations for $\delta\alpha_T$.

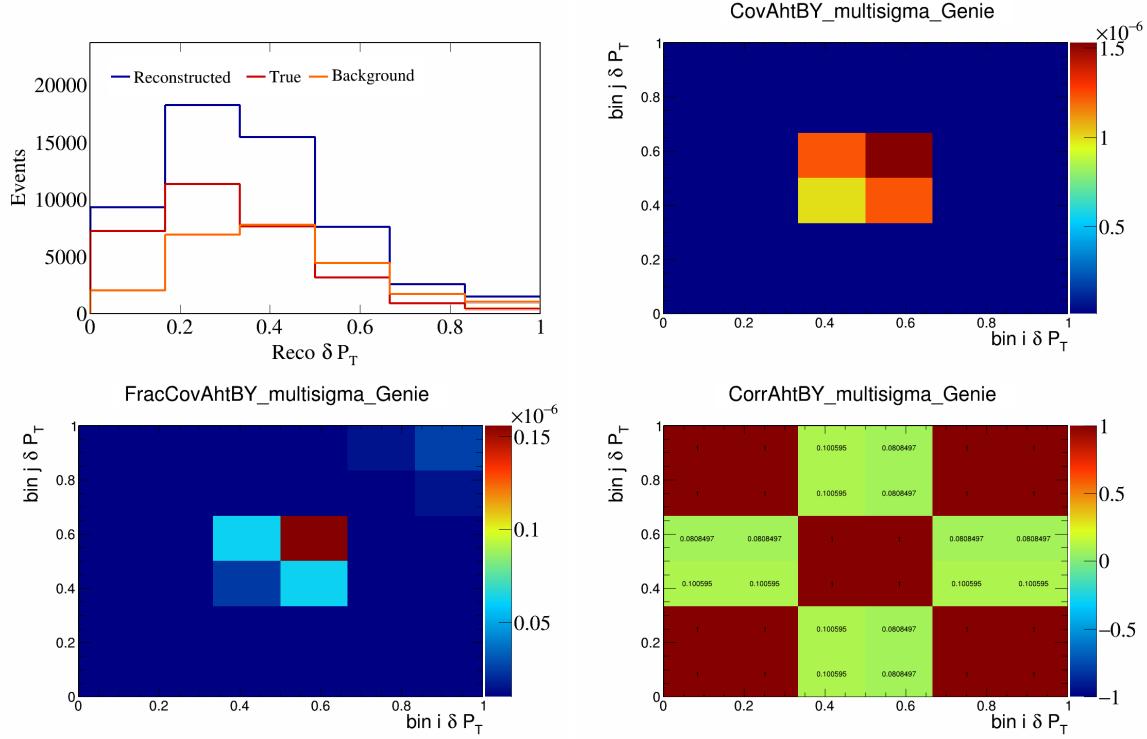


Figure 56: AhtBY variations for δP_T .

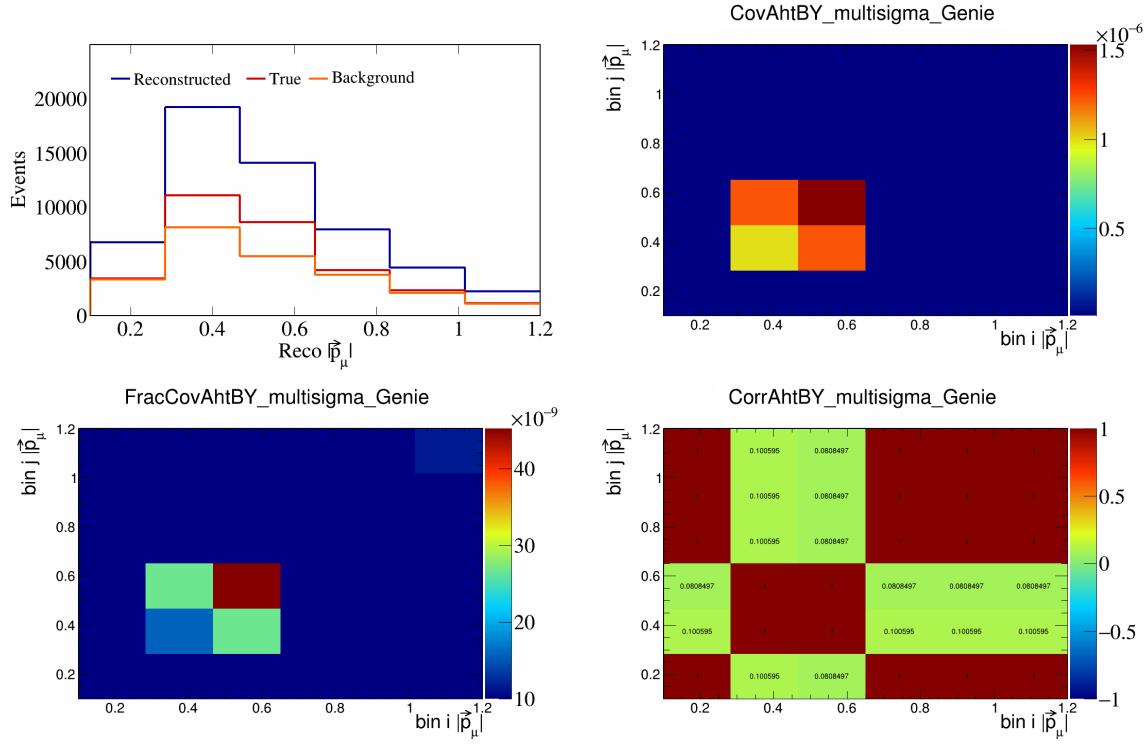


Figure 57: AhtBY variations for $|\vec{p}_\mu|$.

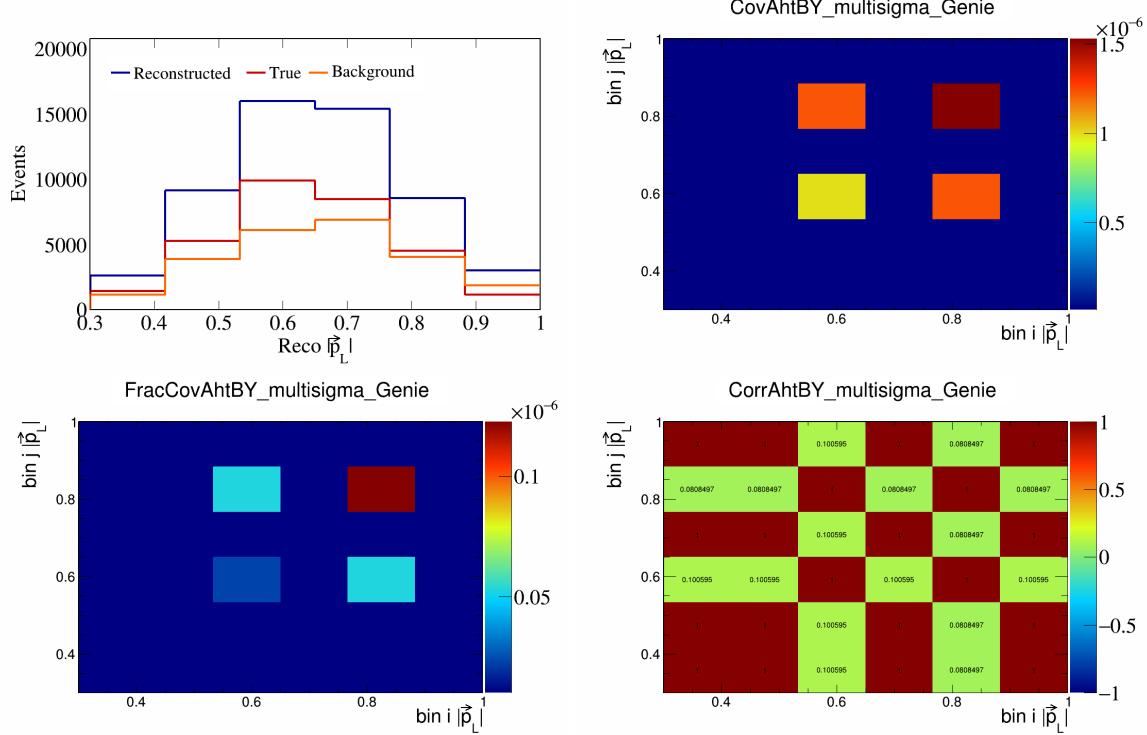


Figure 58: AhtBY variations for $|\vec{p}_L|$.

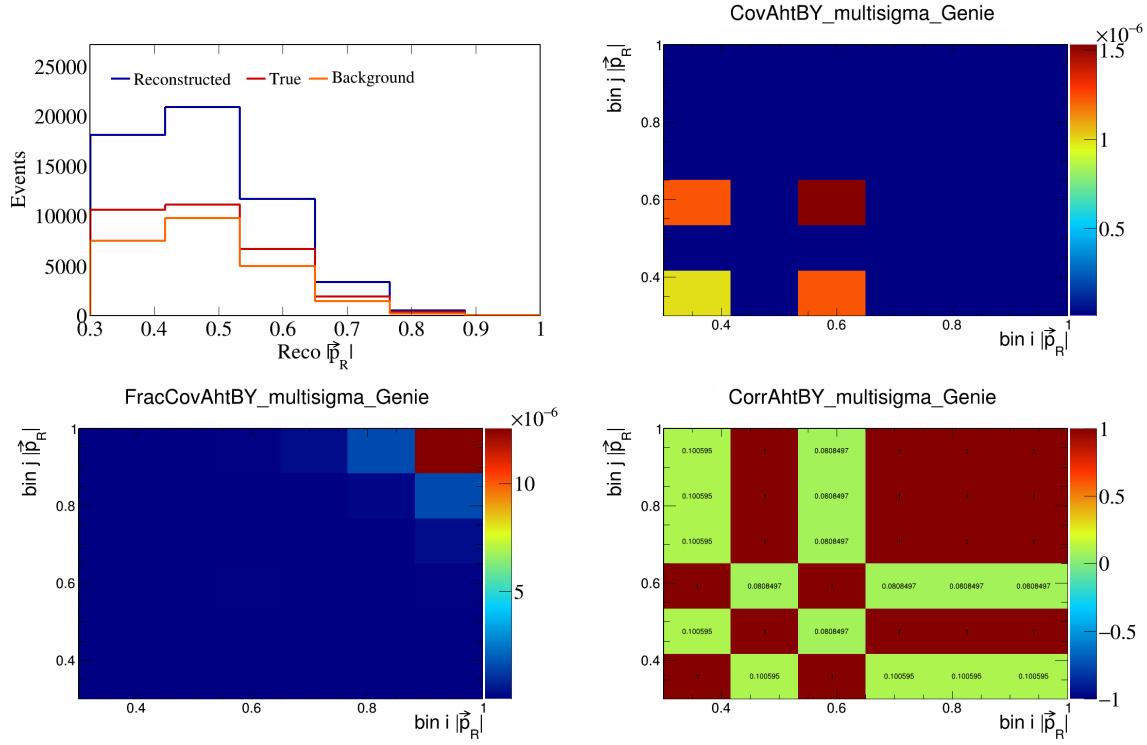


Figure 59: AhtBY variations for $|\vec{p}_R|$.

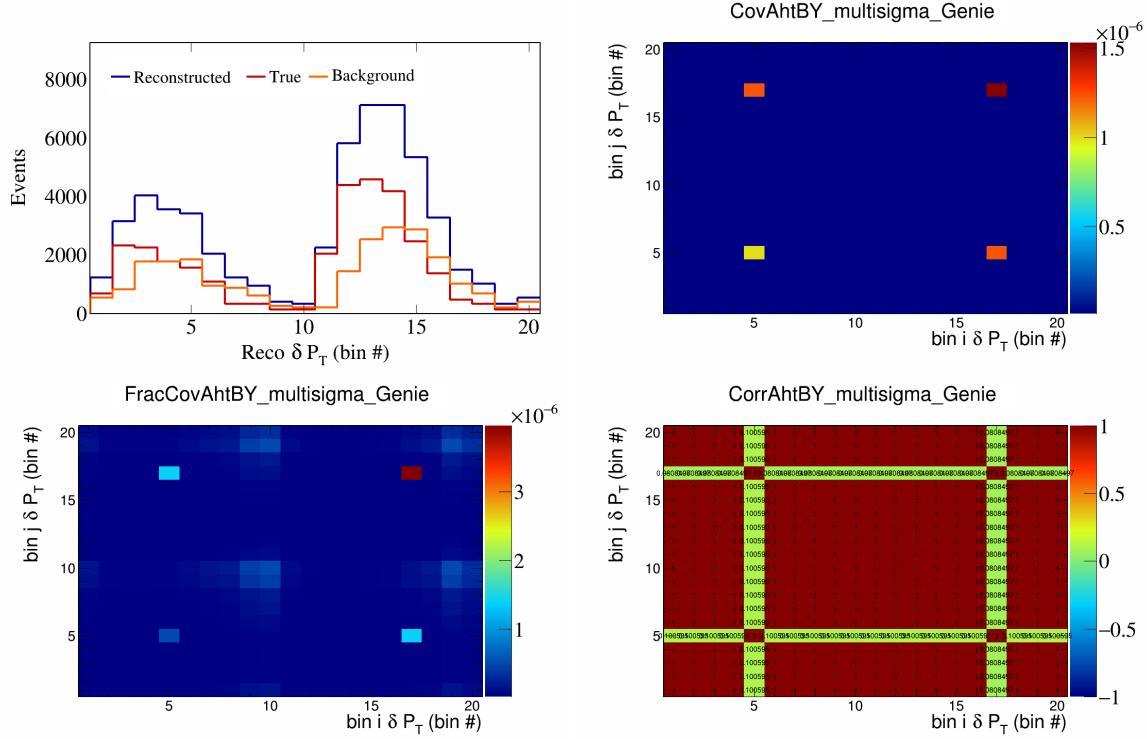


Figure 60: AhtBY variations for δP_T in $\cos(\theta_{\vec{p}_\mu})$.

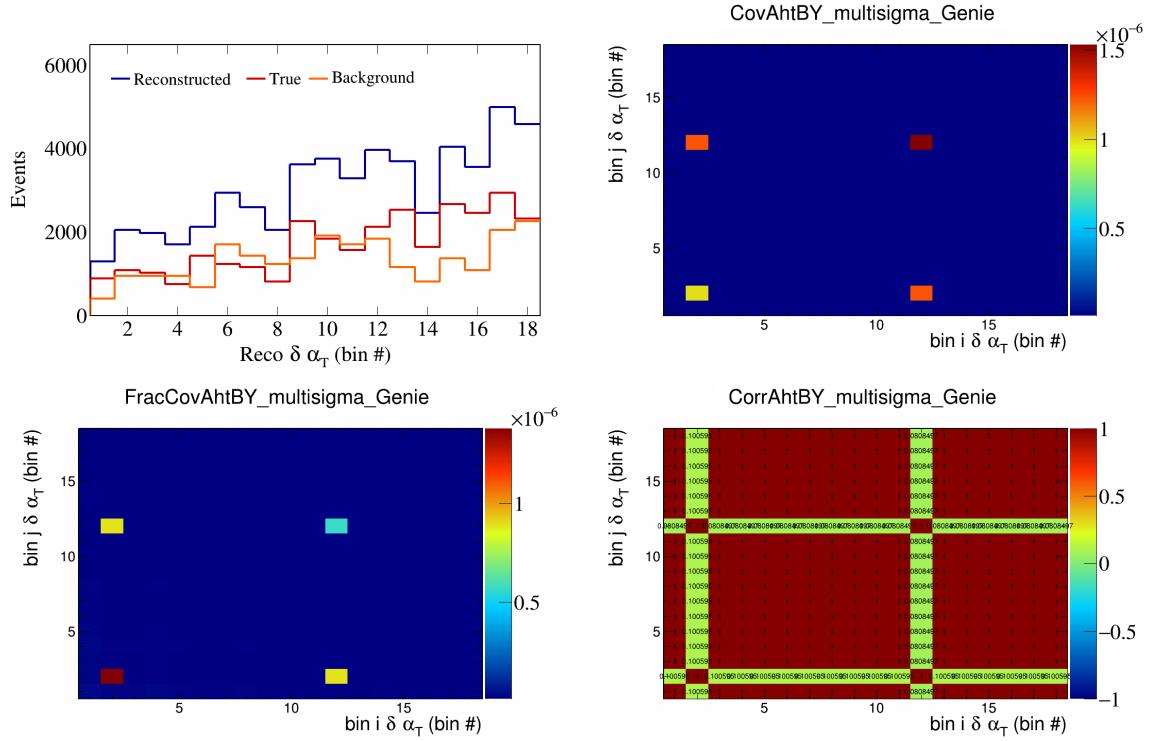


Figure 61: AhtBY variations for $\delta\alpha_T$ in $\cos(\theta_{\vec{p}_\mu})$.

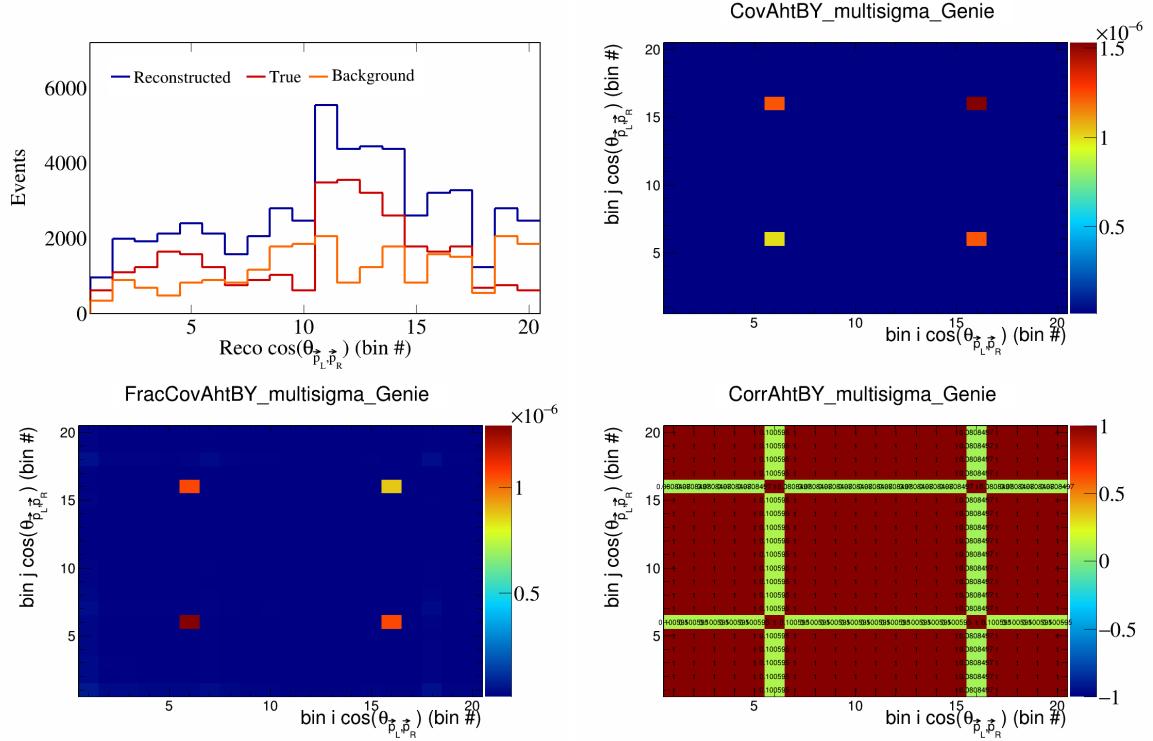


Figure 62: AhtBY variations for $\cos(\theta_{\vec{p}_L, \vec{p}_R})$ in $\cos(\theta_{\vec{p}_\mu})$.

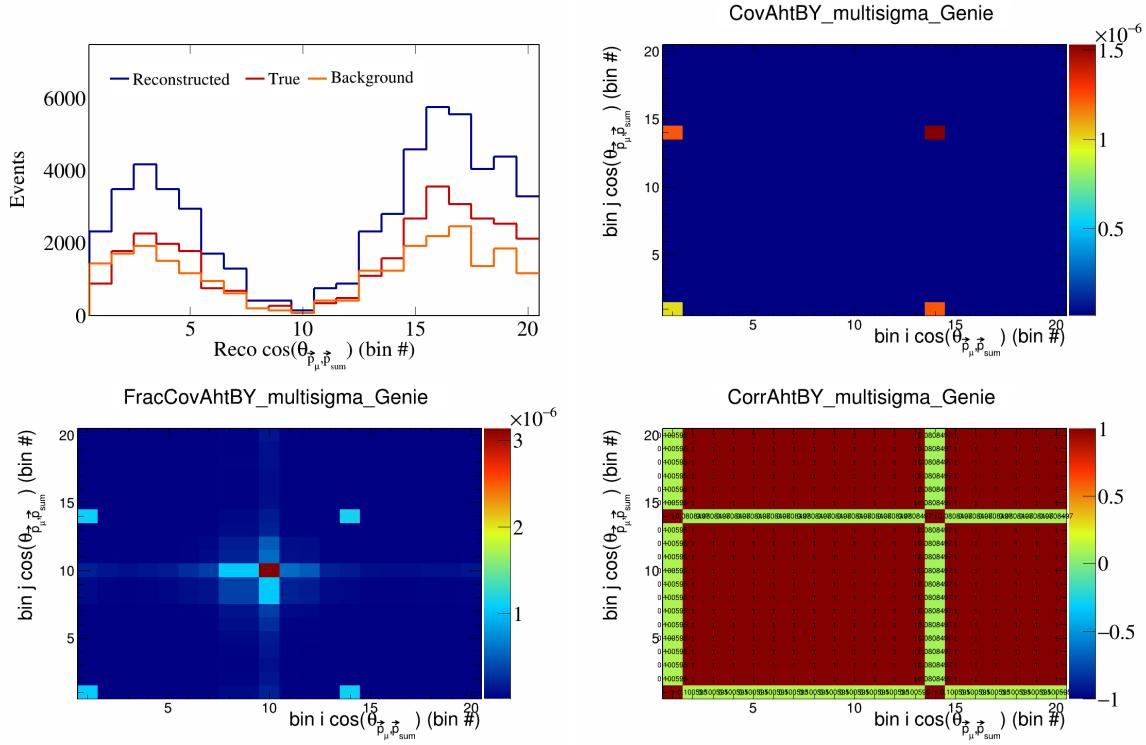


Figure 63: AhtBY variations for $\cos(\theta_{\vec{p}_\mu}^r)$ in $\cos(\theta_{\vec{p}_\mu})$.

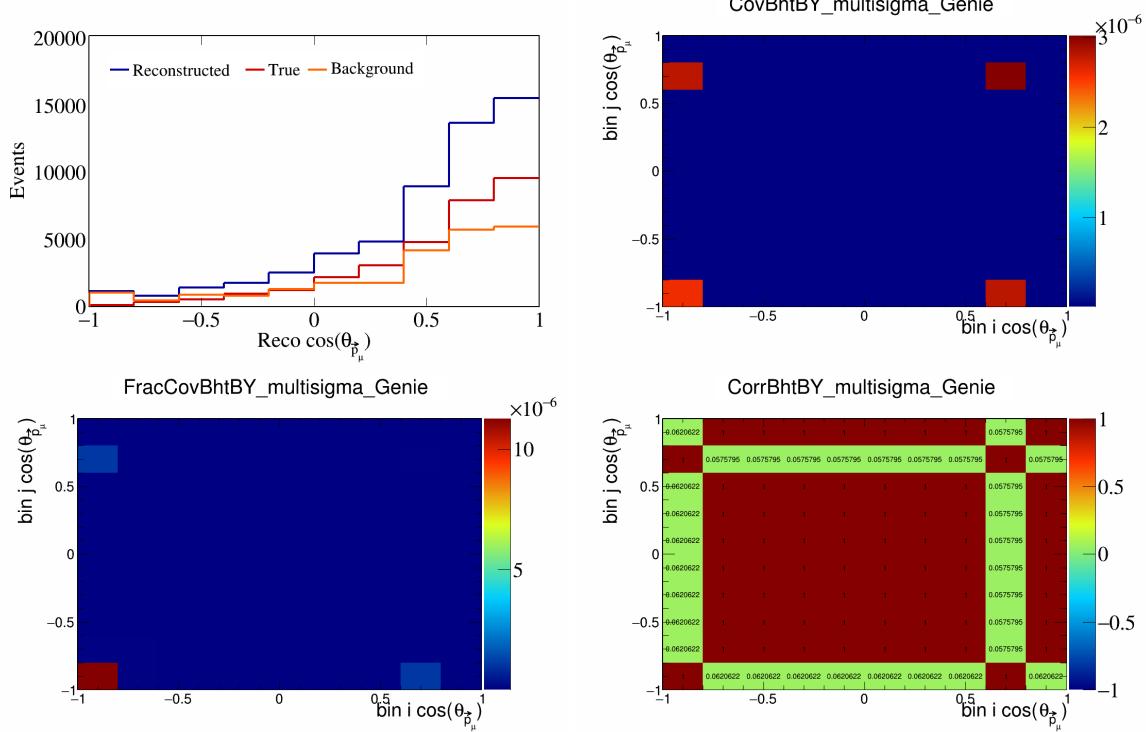


Figure 64: BhtBY variations for $\cos(\theta_{\vec{p}_\mu}^r)$.

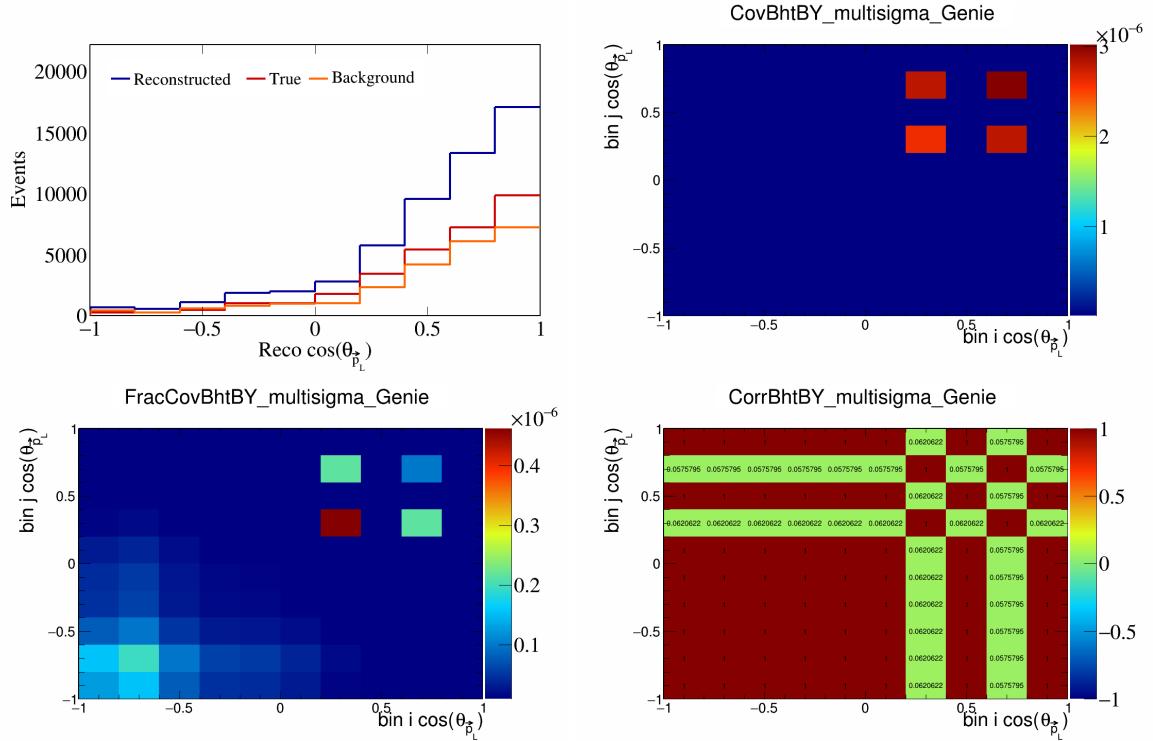


Figure 65: BhtBY variations for $\cos(\theta_{\vec{p}_L})$.

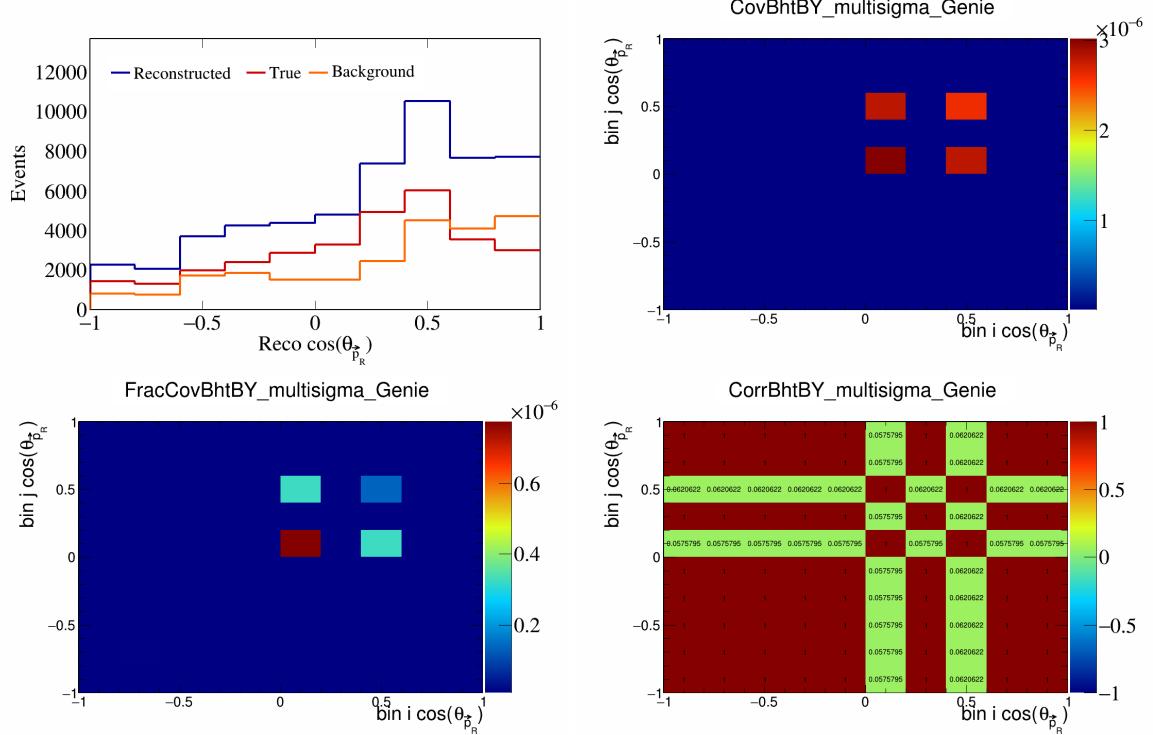


Figure 66: BhtBY variations for $\cos(\theta_{\vec{p}_R})$.

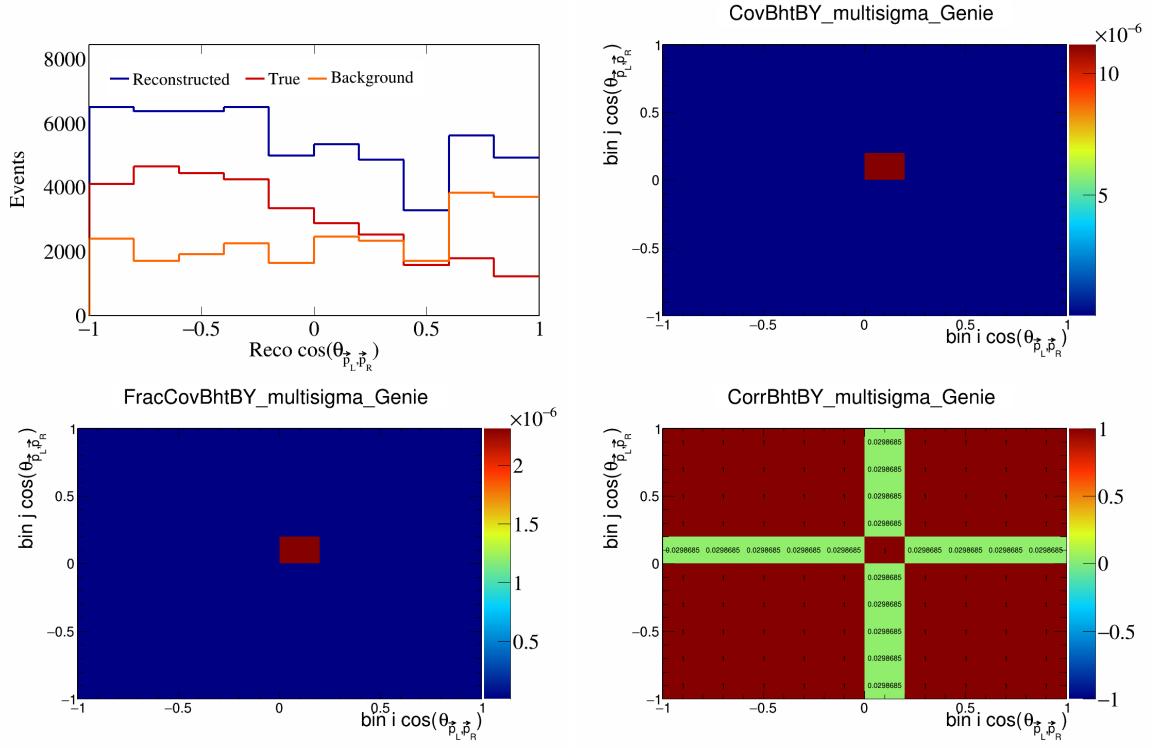


Figure 67: BhtBY variations for $\cos(\theta_{\vec{p}_L, \vec{p}_R})$.

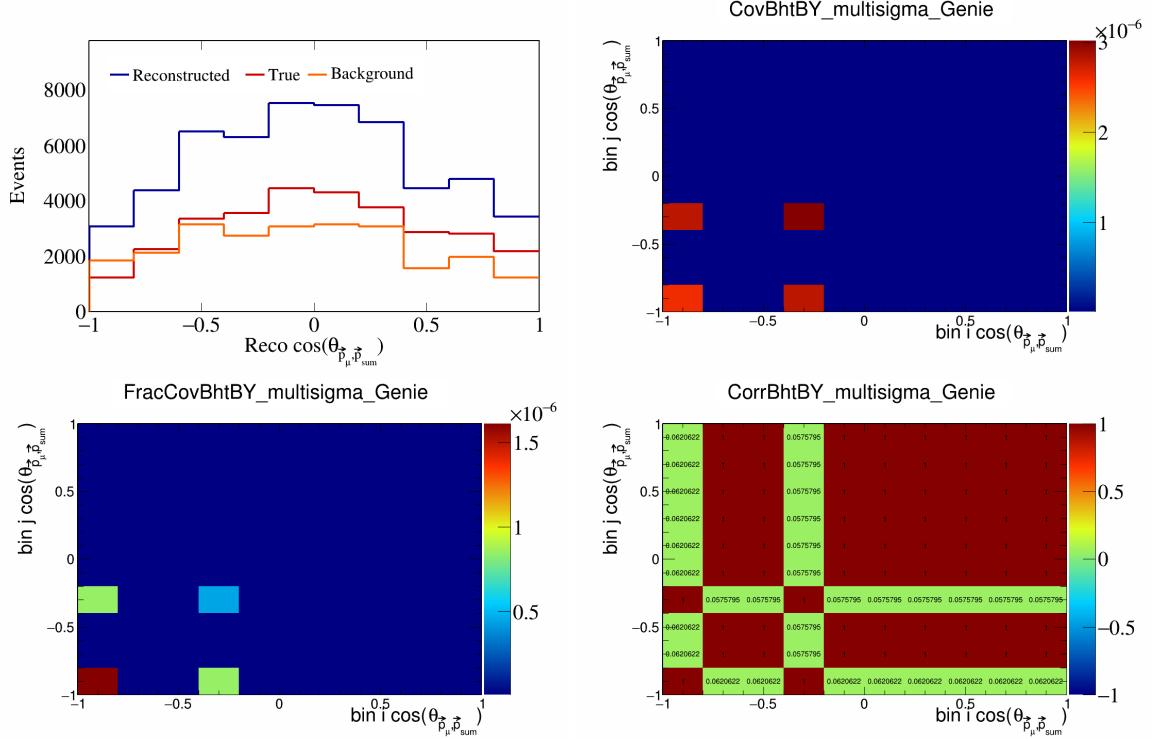


Figure 68: BhtBY variations for $\cos(\theta_{\vec{p}_\mu, \vec{p}_{\text{sum}}})$.

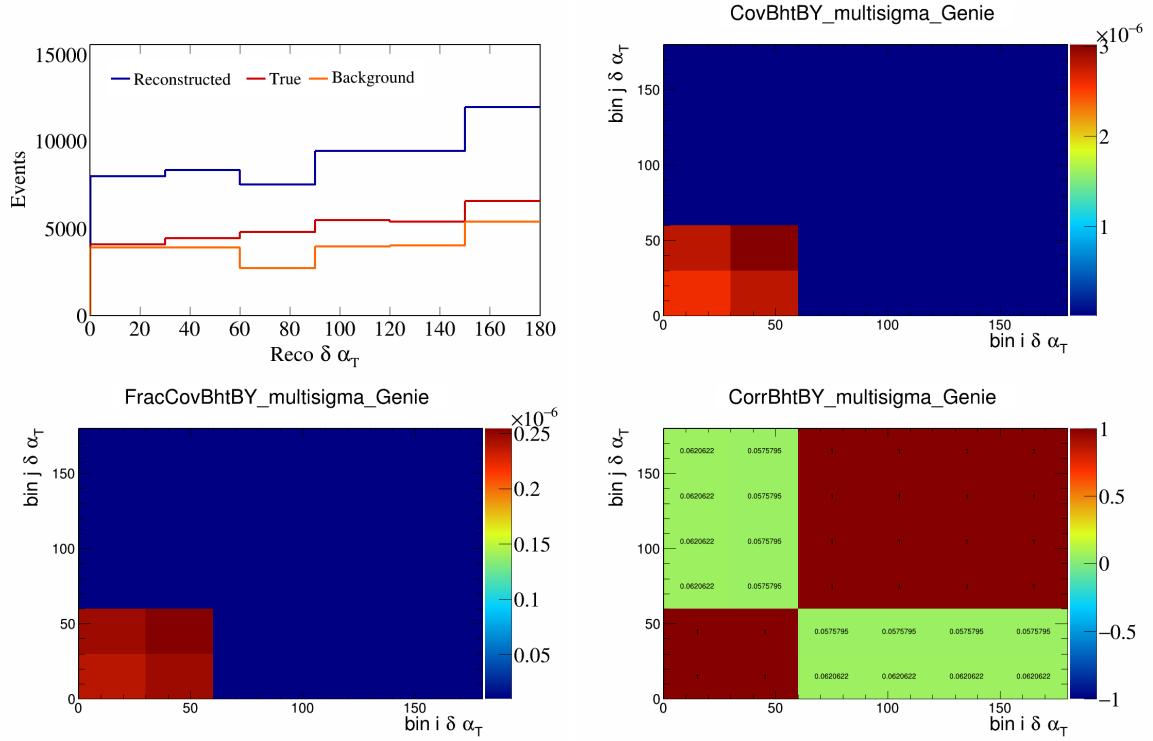


Figure 69: BhtBY variations for $\delta\alpha_T$.

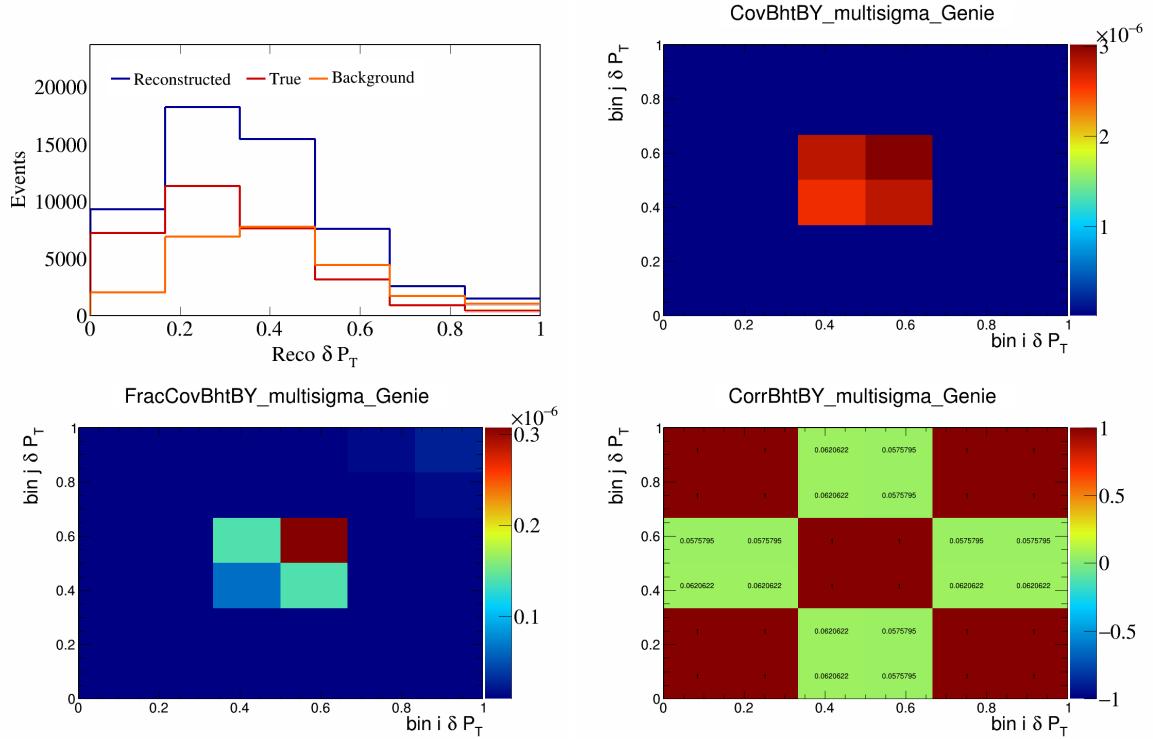


Figure 70: BhtBY variations for δP_T .

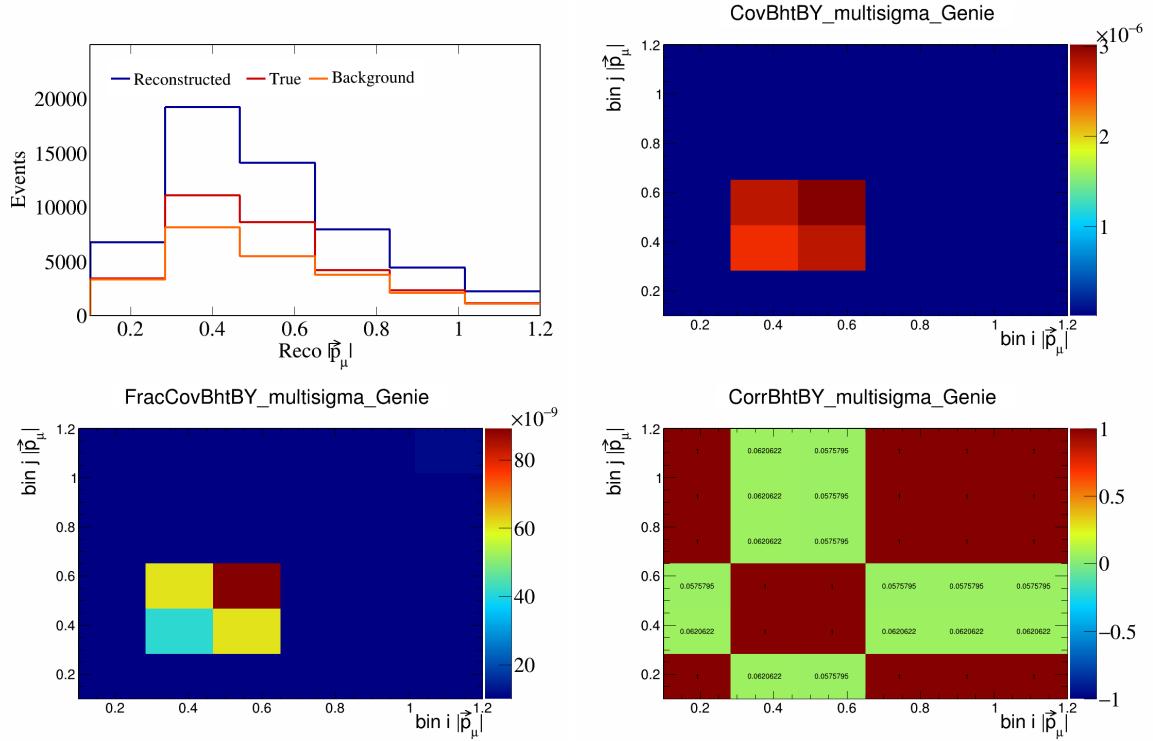


Figure 71: BhtBY variations for $|\vec{p}_\mu|$.

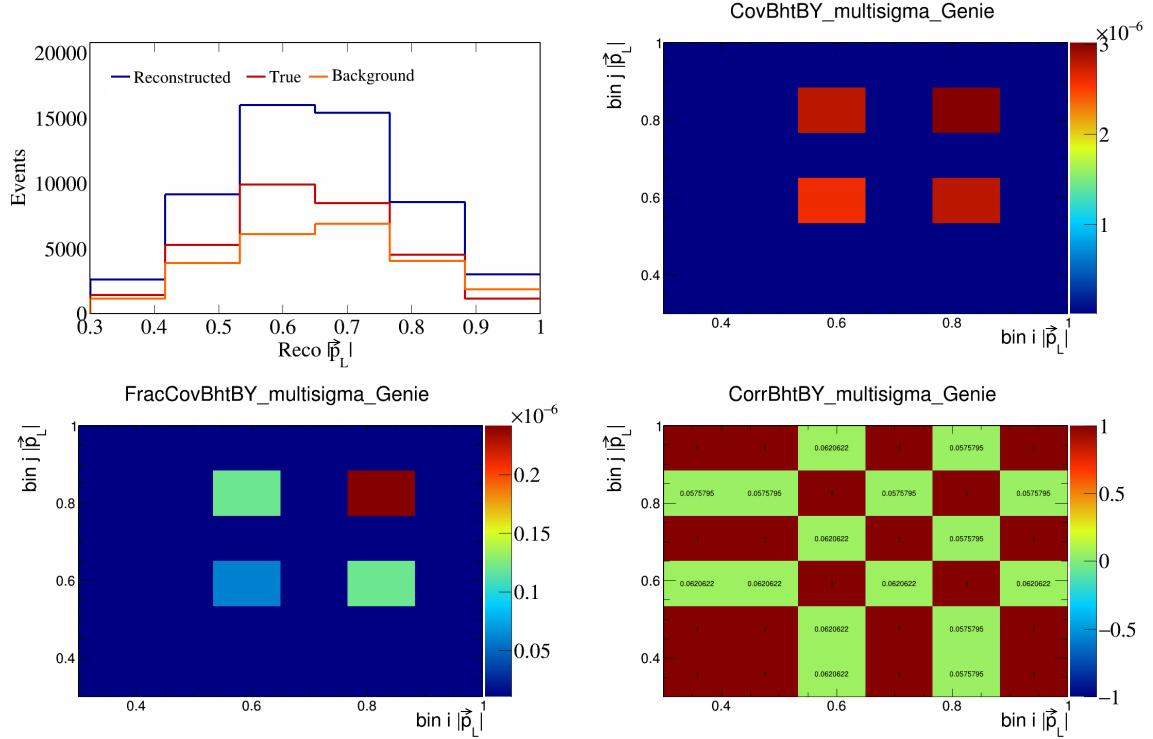


Figure 72: BhtBY variations for $|\vec{p}_L|$.

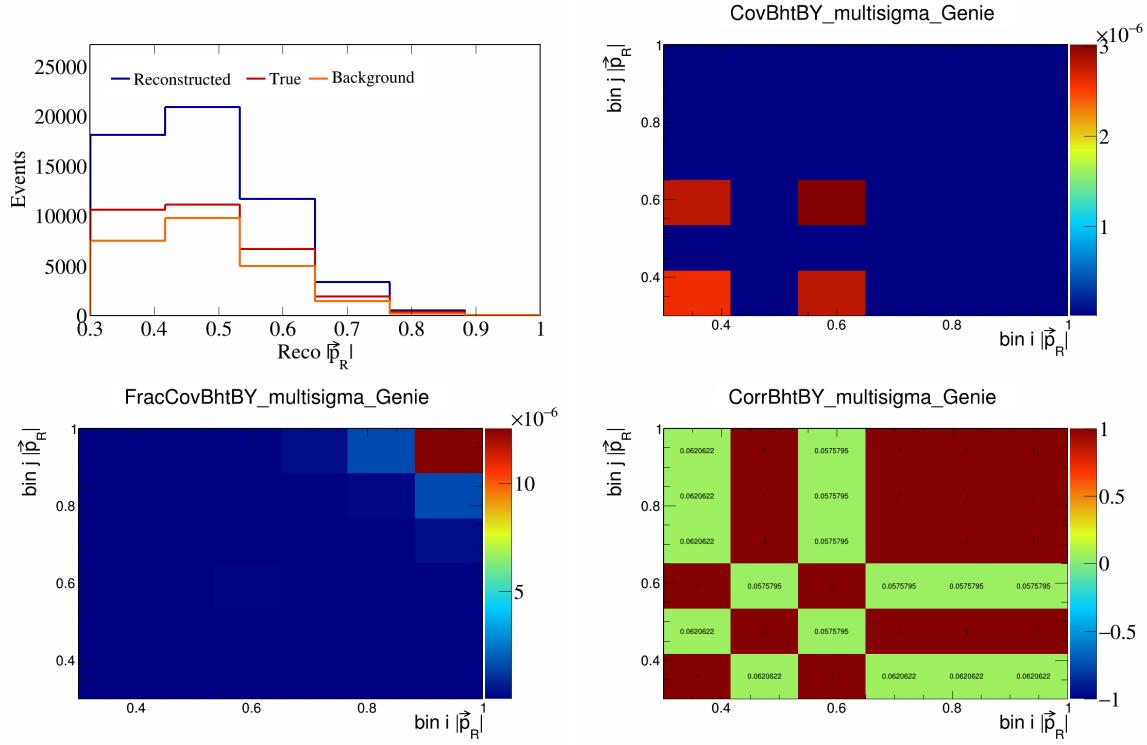


Figure 73: BhtBY variations for $|\vec{p}_R|$.

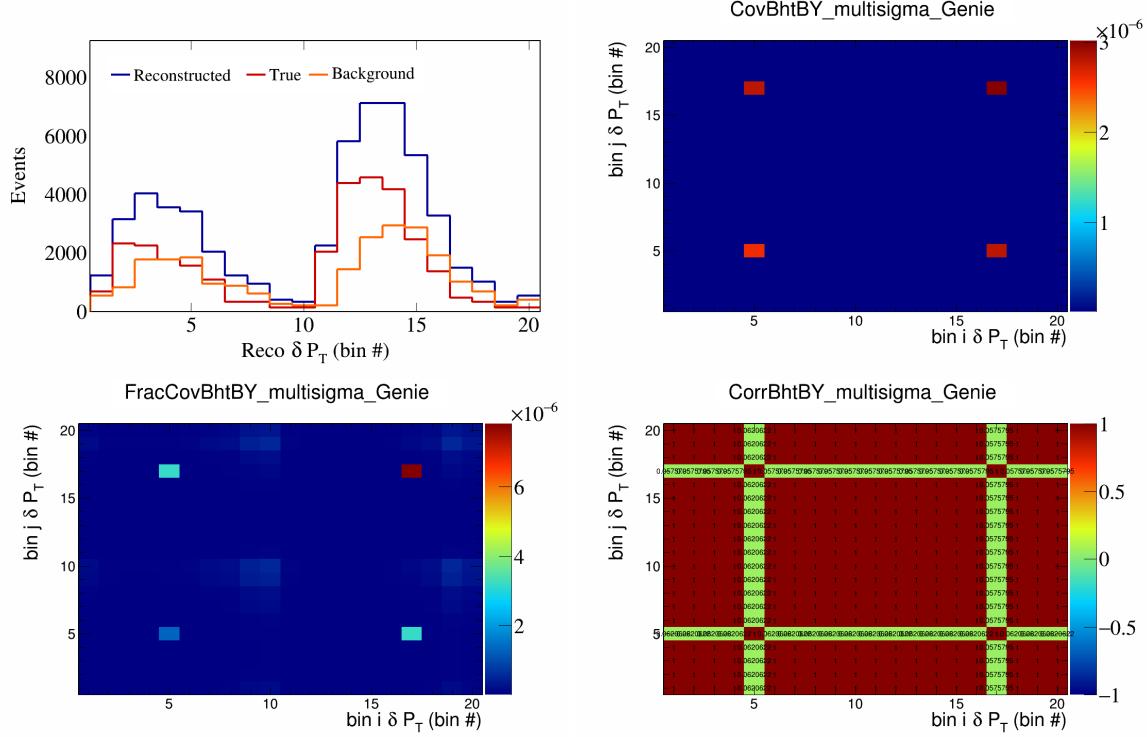


Figure 74: BhtBY variations for δP_T in $\cos(\theta_{\vec{p}_\mu})$.

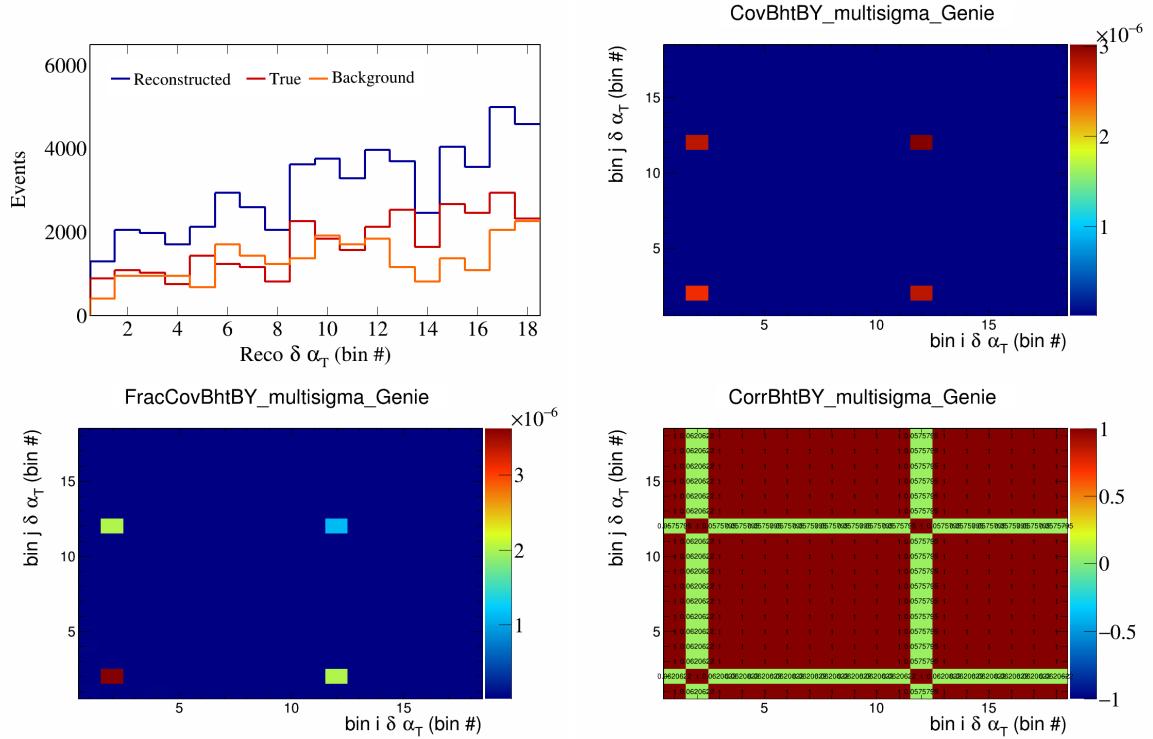


Figure 75: BhtBY variations for $\delta\alpha_T$ in $\cos(\theta_{\vec{p}_\mu})$.

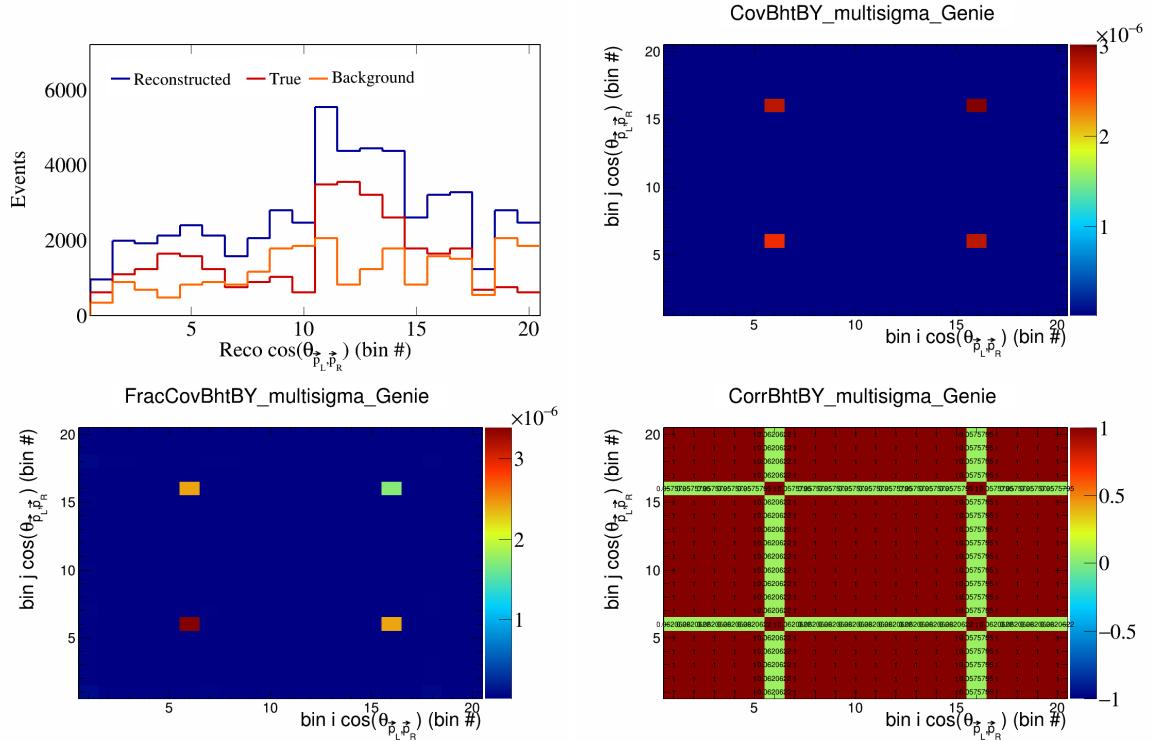


Figure 76: BhtBY variations for $\cos(\theta_{\vec{p}_L, \vec{p}_R})$ in $\cos(\theta_{\vec{p}_\mu})$.

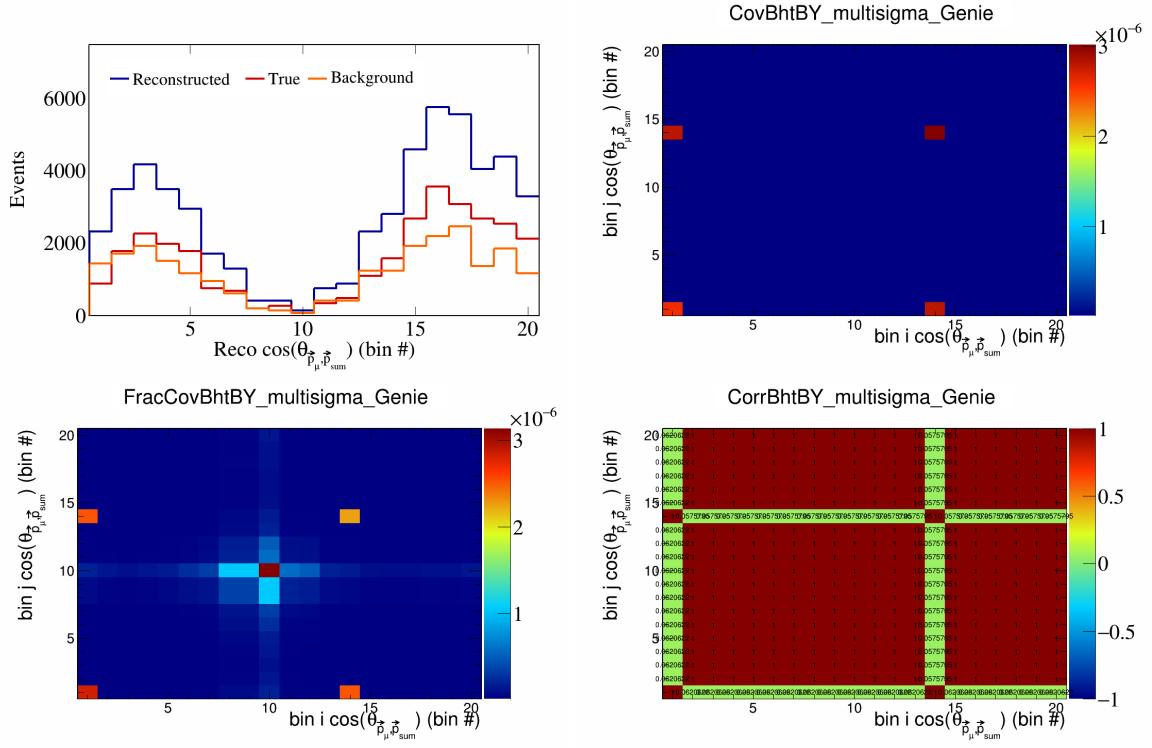


Figure 77: BhtBY variations for $\cos(\theta_{\vec{p}_\mu}^j)$ in $\cos(\theta_{\vec{p}_\mu}^i)$.

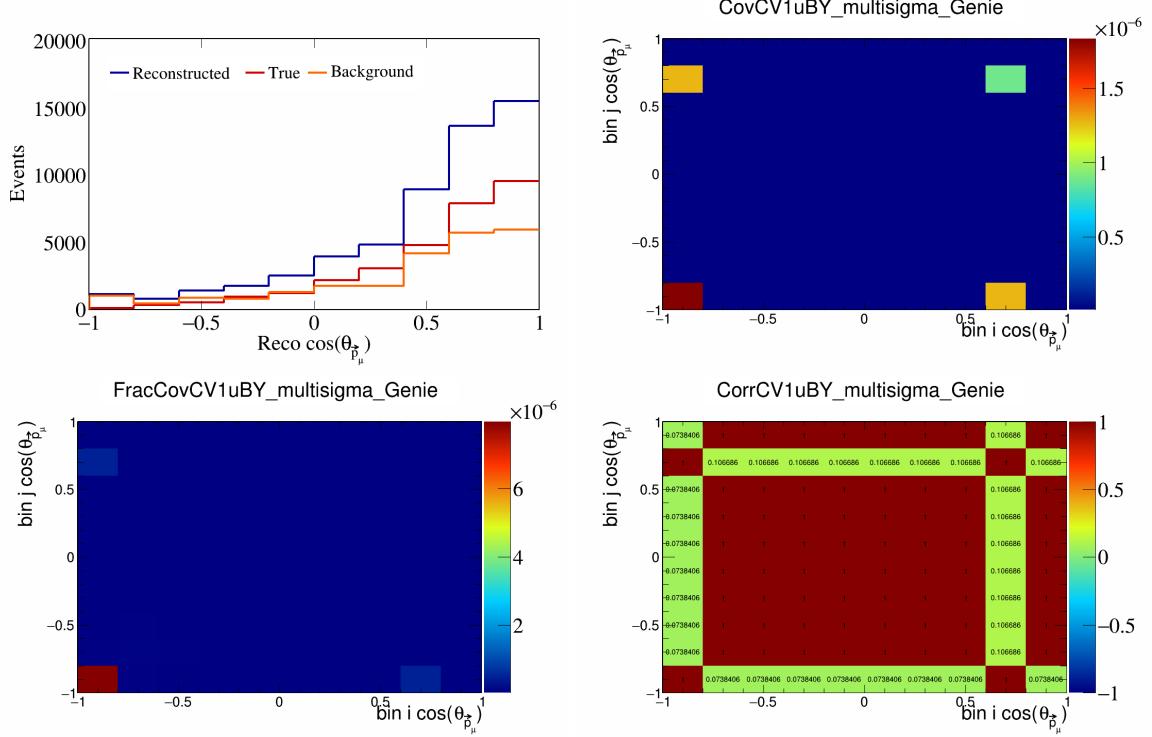


Figure 78: CV1uBY variations for $\cos(\theta_{\vec{p}_\mu}^j)$.

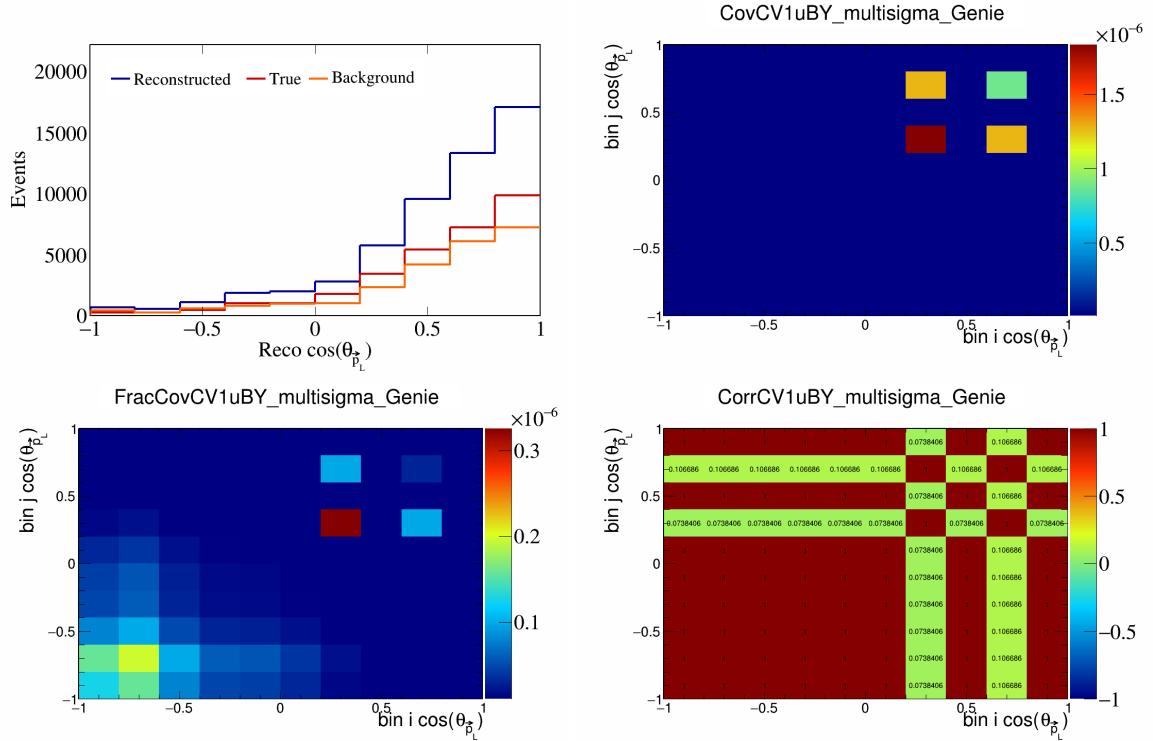


Figure 79: CV1uBY variations for $\cos(\theta_{\vec{p}_L})$.

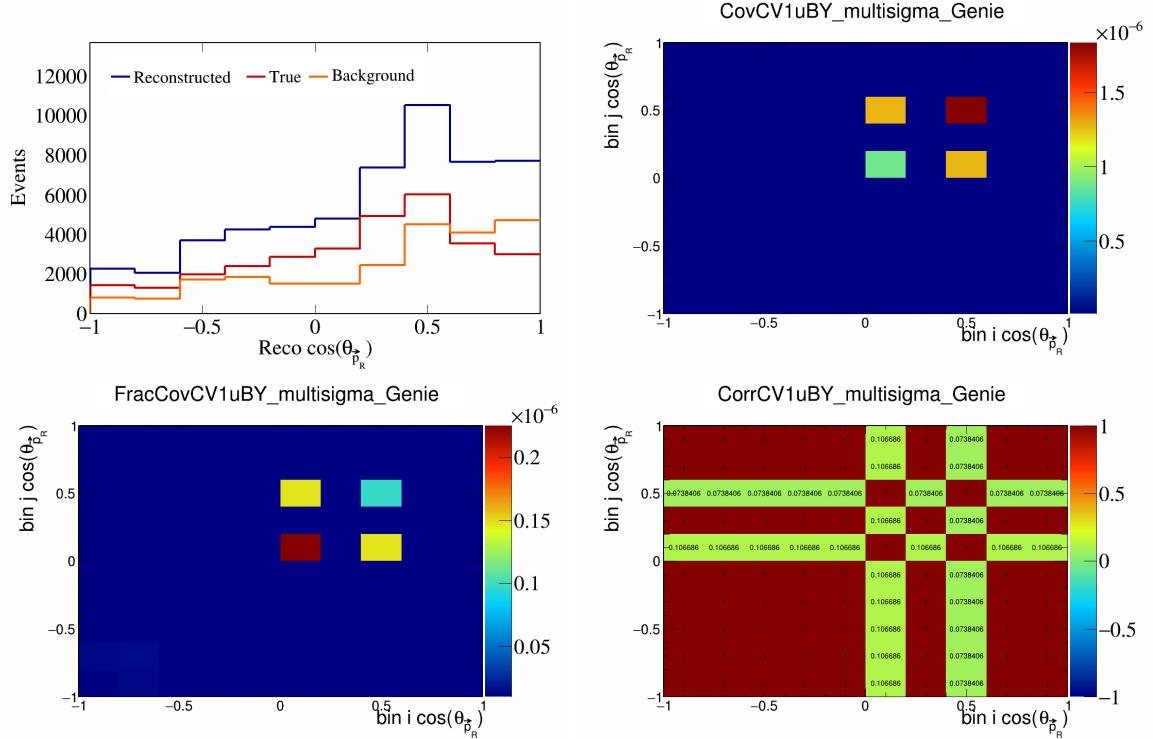


Figure 80: CV1uBY variations for $\cos(\theta_{\vec{p}_R})$.

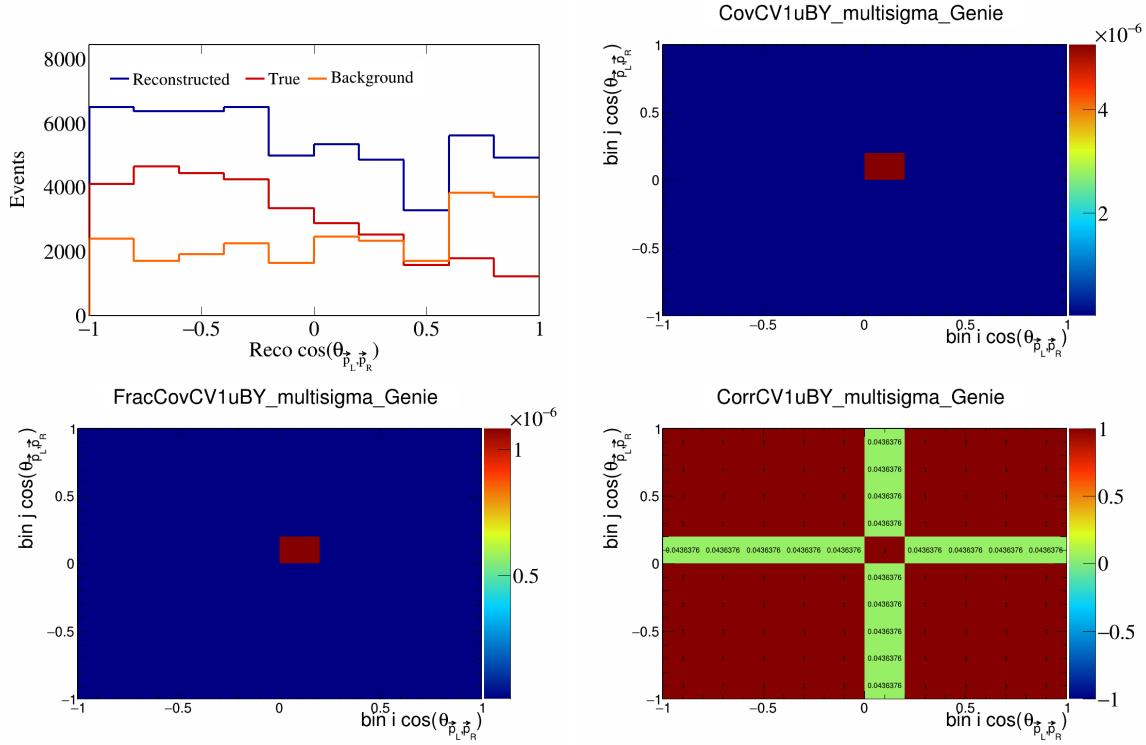


Figure 81: CV1uBY variations for $\cos(\theta_{\vec{p}_L, \vec{p}_R})$.

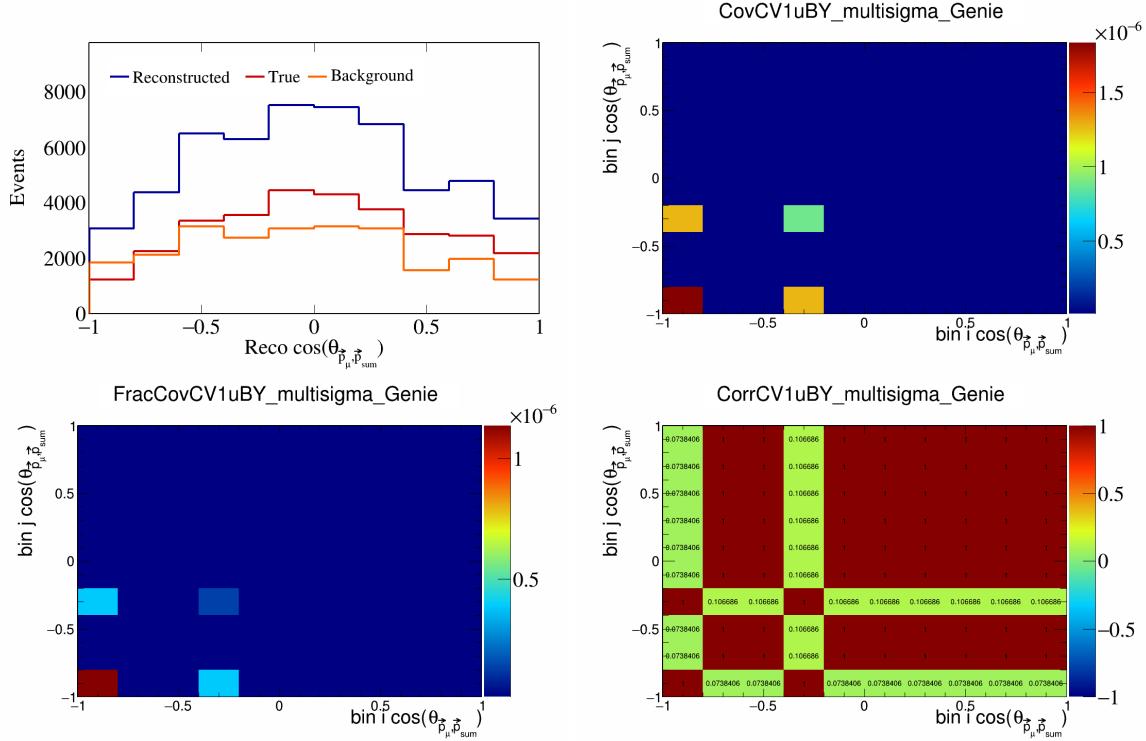


Figure 82: CV1uBY variations for $\cos(\theta_{\vec{p}_\mu, \vec{p}_{\text{sum}}})$.

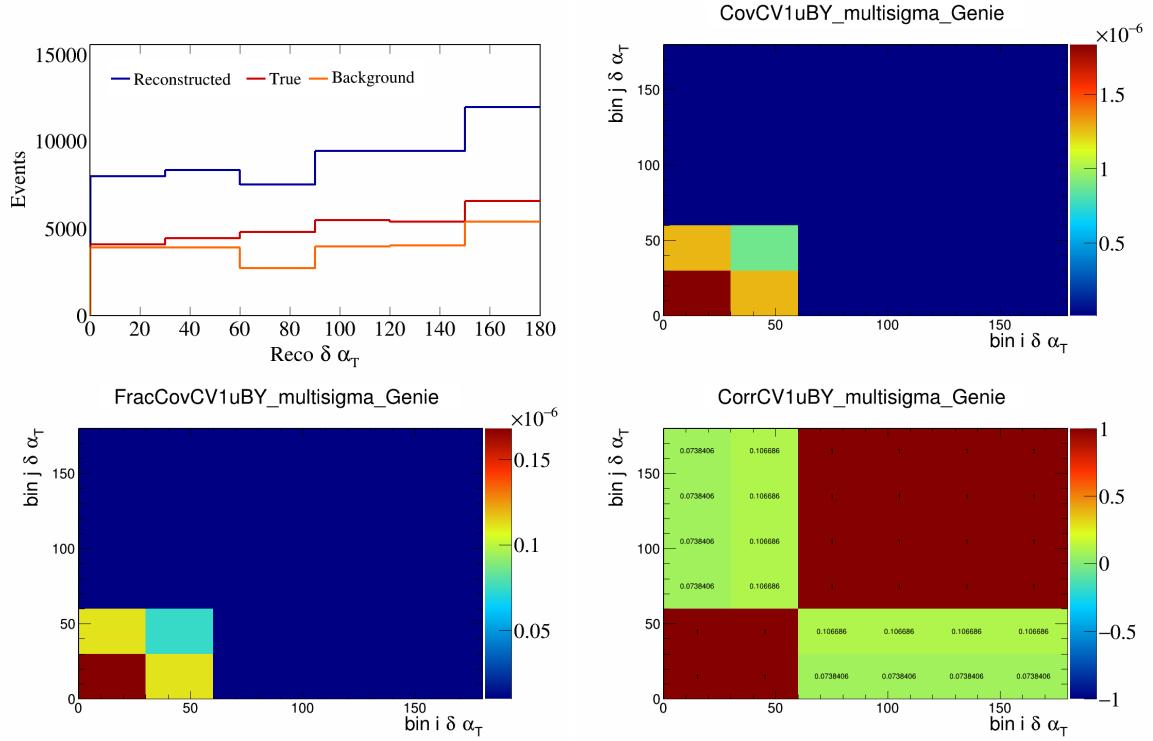


Figure 83: CV1uBY variations for $\delta\alpha_T$.

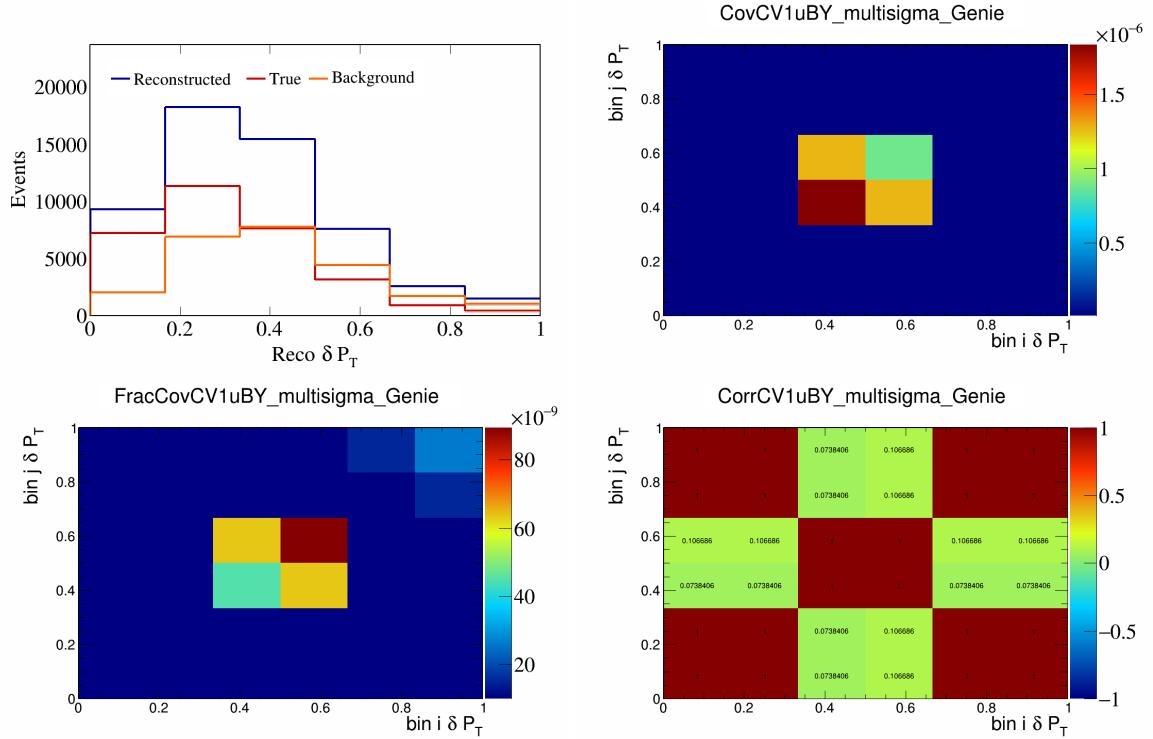


Figure 84: CV1uBY variations for δP_T .

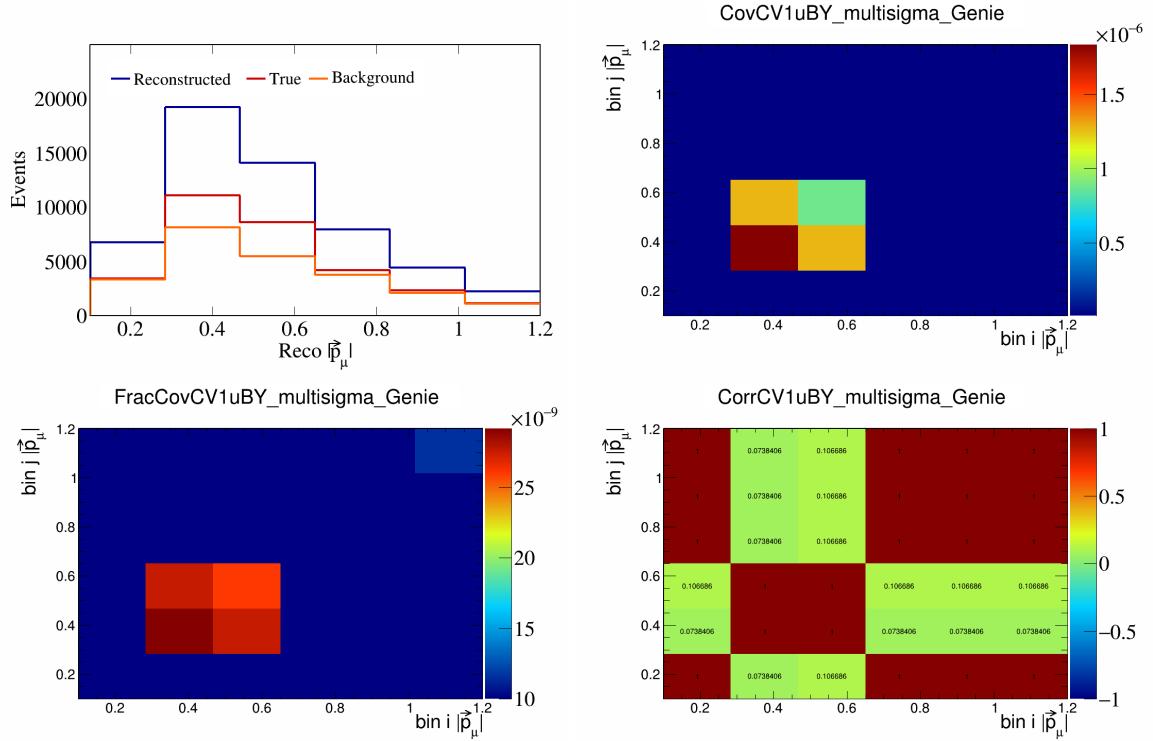


Figure 85: CV1uBY variations for $|\vec{p}_\mu|$.

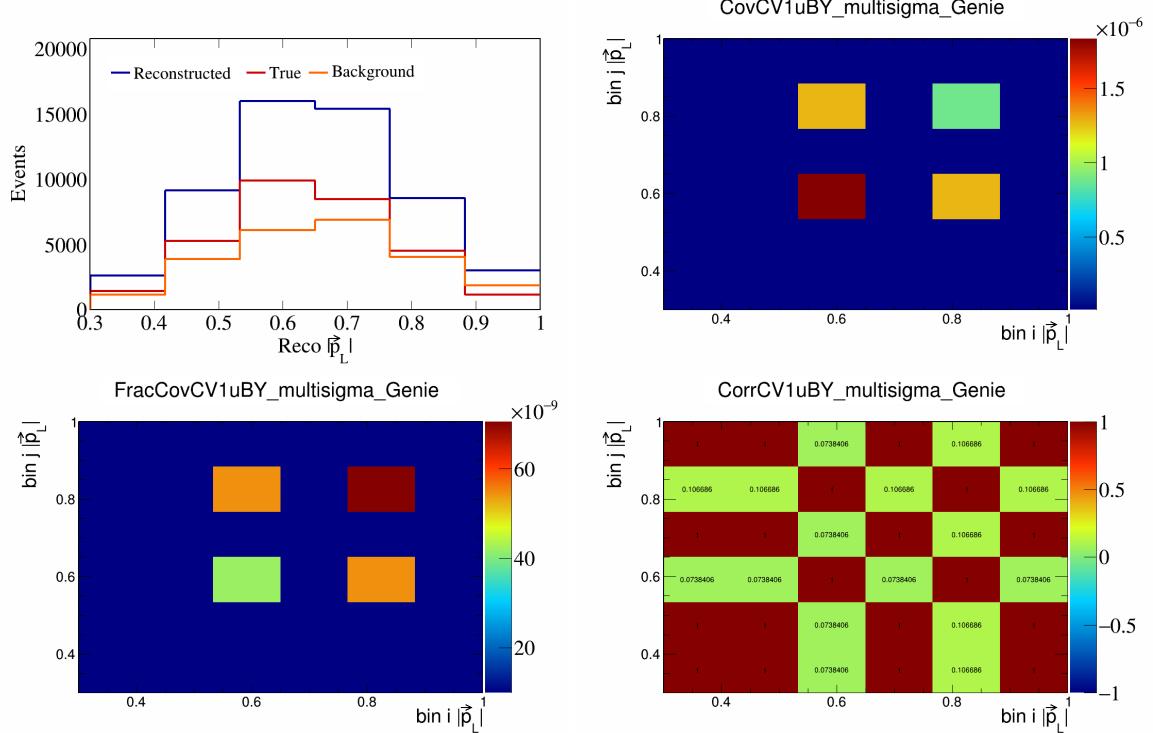


Figure 86: CV1uBY variations for $|\vec{p}_L|$.

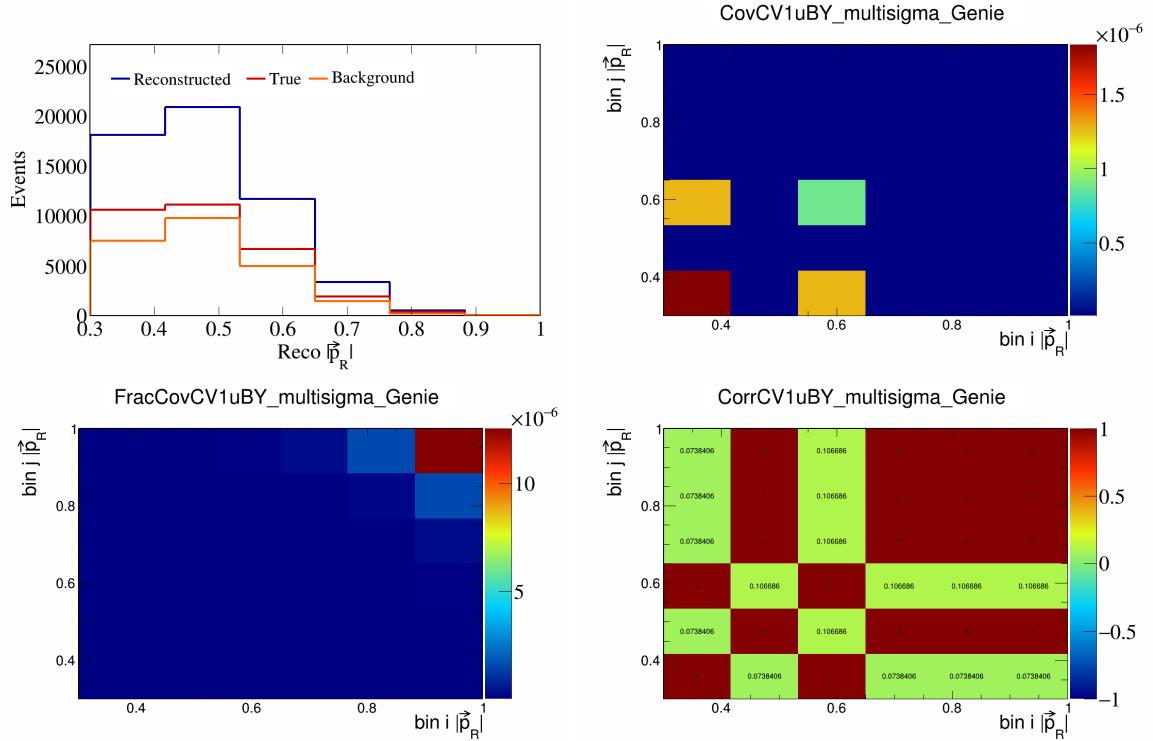


Figure 87: CV1uBY variations for $|\vec{p}_R|$.

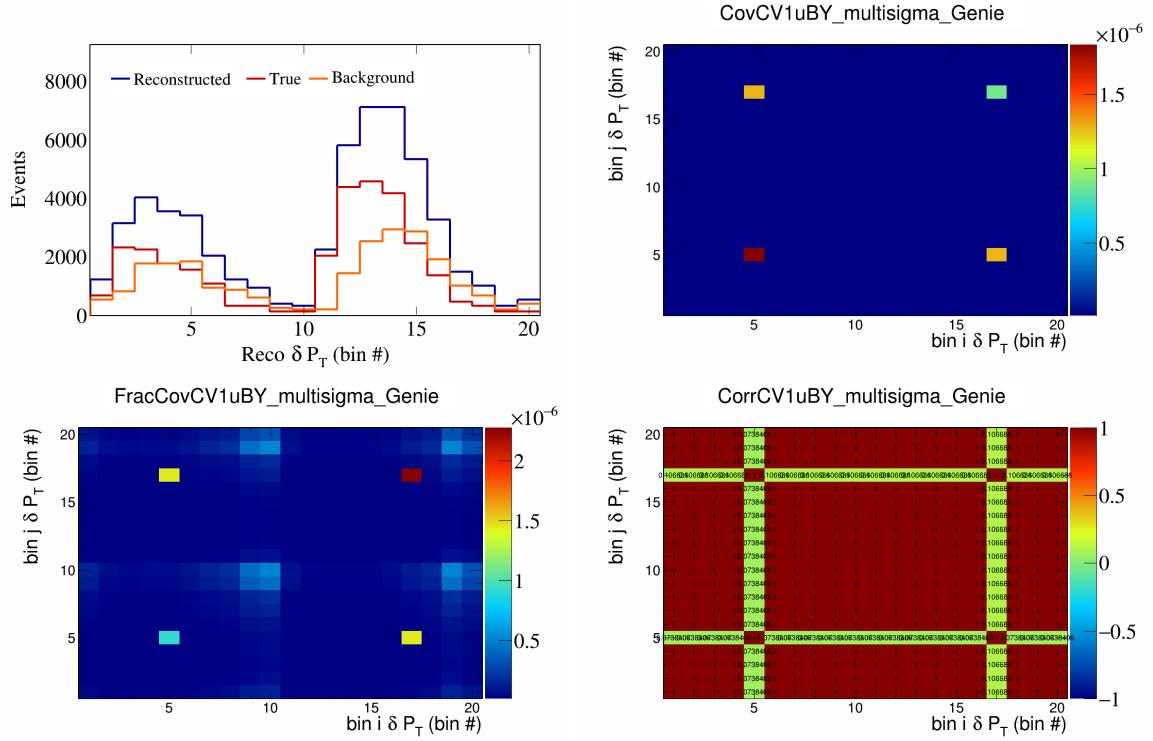


Figure 88: CV1uBY variations for δP_T in $\cos(\theta_{\vec{p}_\mu})$.

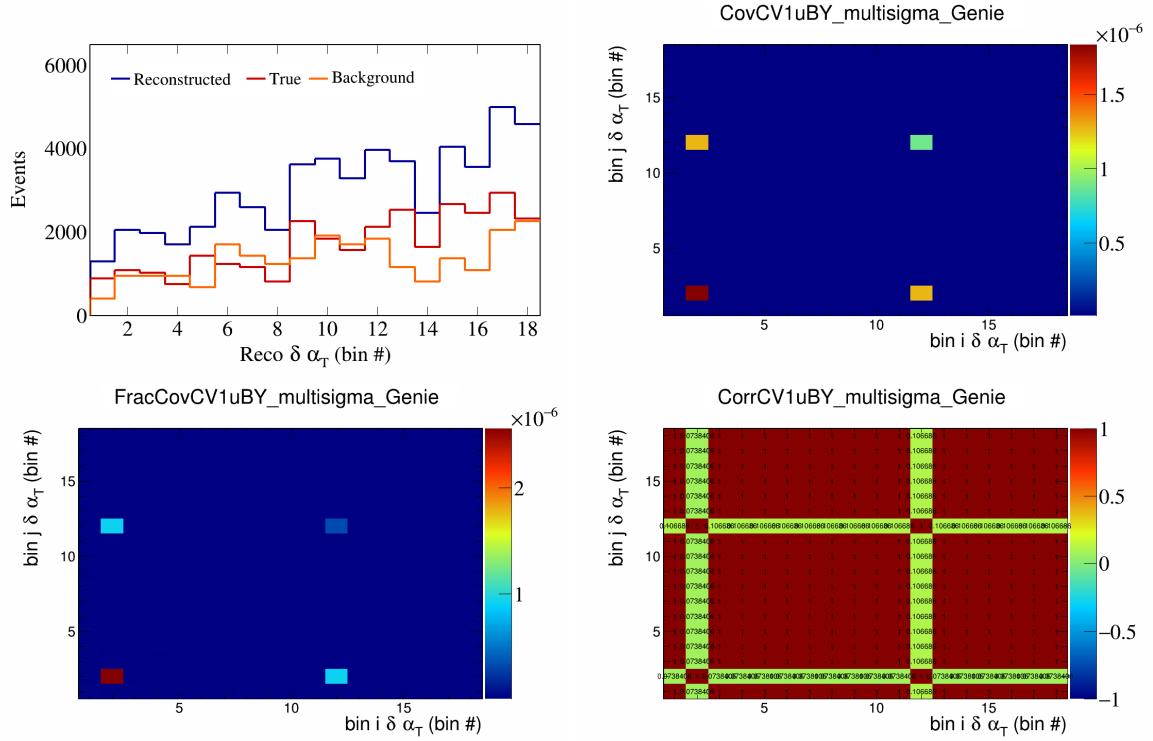


Figure 89: CV1uBY variations for $\delta\alpha_T$ in $\cos(\theta_{\vec{p}_\mu})$.

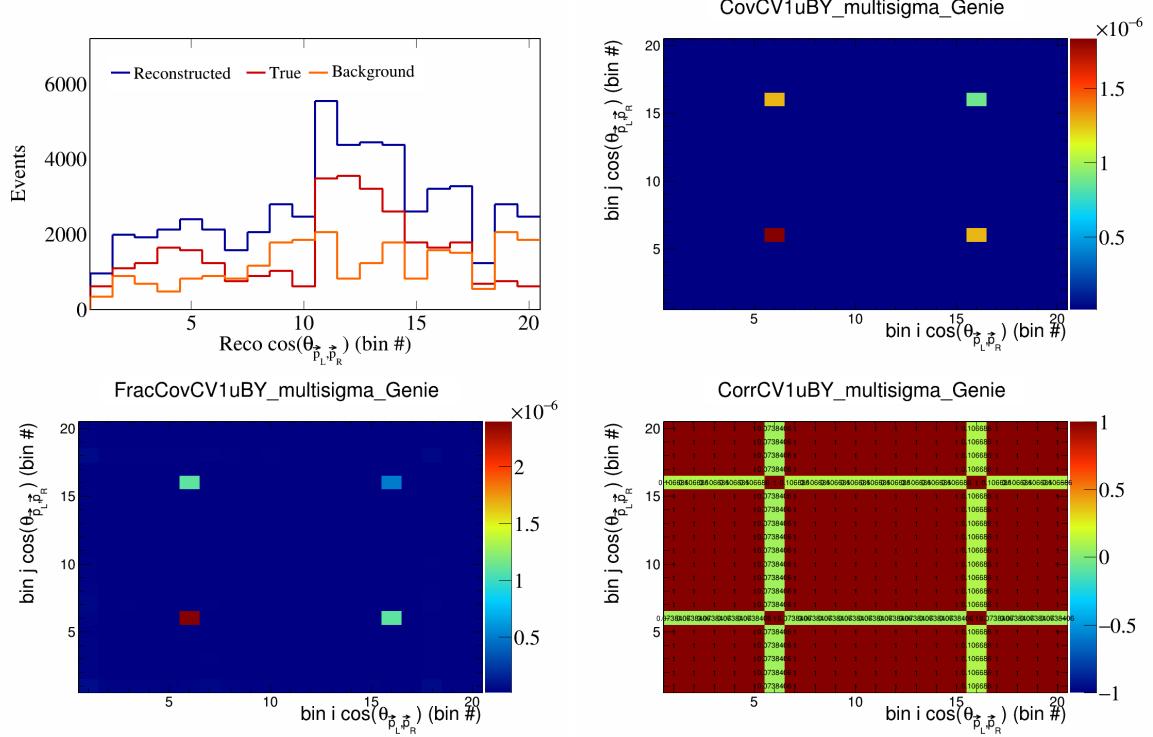


Figure 90: CV1uBY variations for $\cos(\theta_{\vec{p}_L, \vec{p}_R})$ in $\cos(\theta_{\vec{p}_\mu})$.

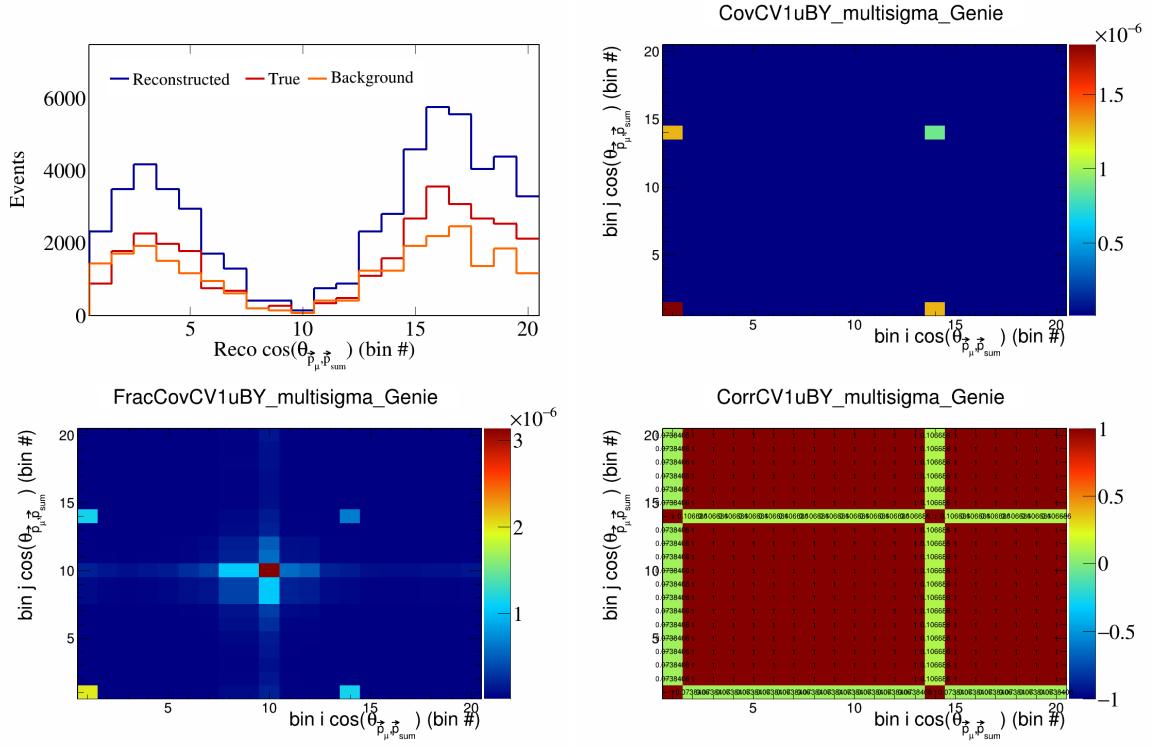


Figure 91: CV1uBY variations for $\cos(\theta_{\vec{p}_\mu, \vec{p}_{\text{sum}}})$ in $\cos(\theta_{\vec{p}_\mu})$.

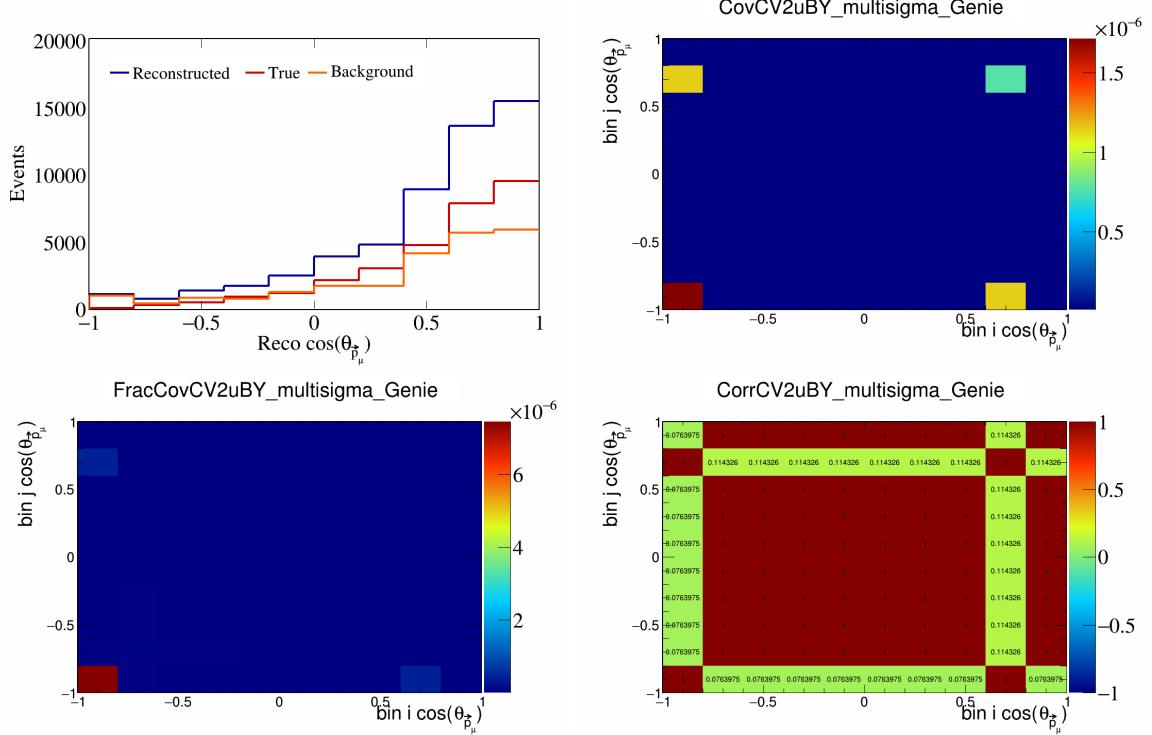


Figure 92: CV2uBY variations for $\cos(\theta_{\vec{p}_\mu})$.

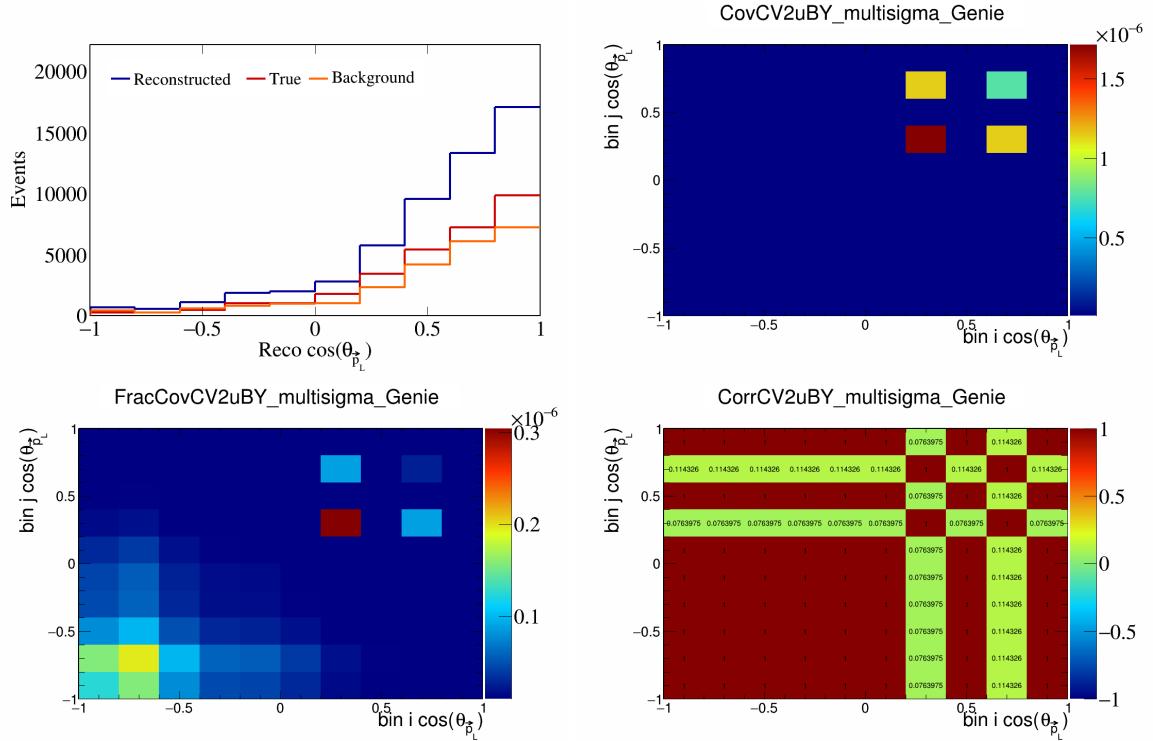


Figure 93: CV2uBY variations for $\cos(\theta_{\vec{p}_L})$.

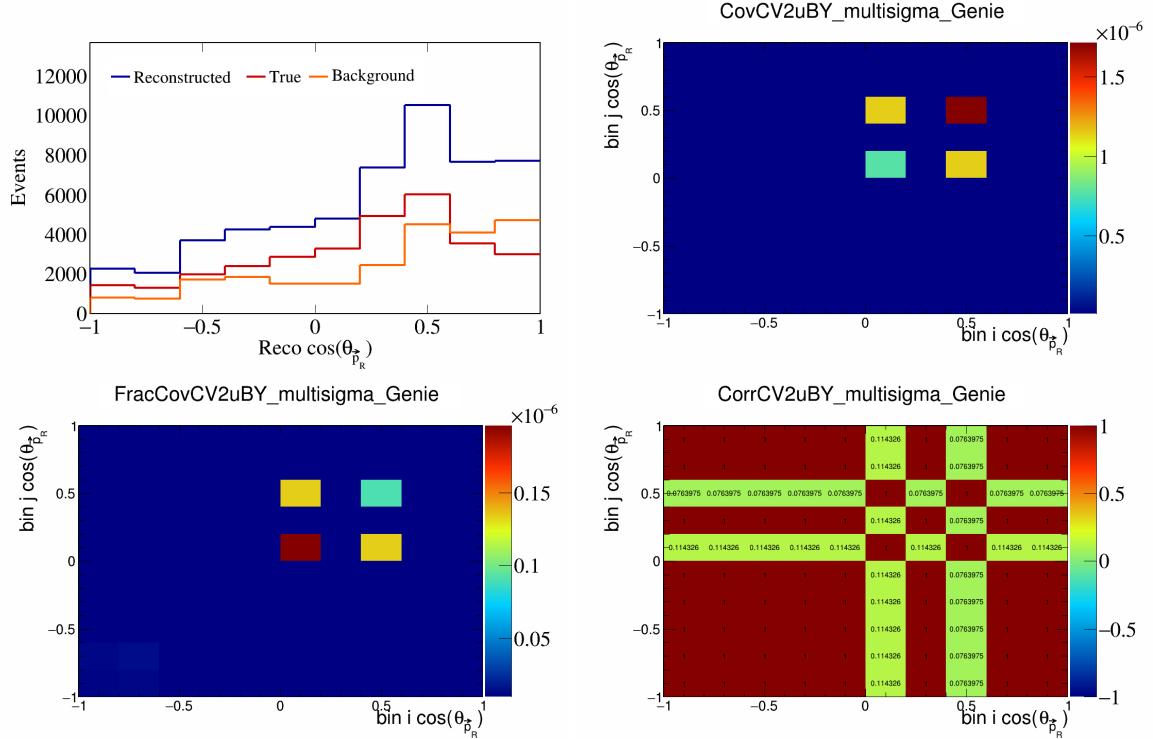


Figure 94: CV2uBY variations for $\cos(\theta_{\vec{p}_R})$.

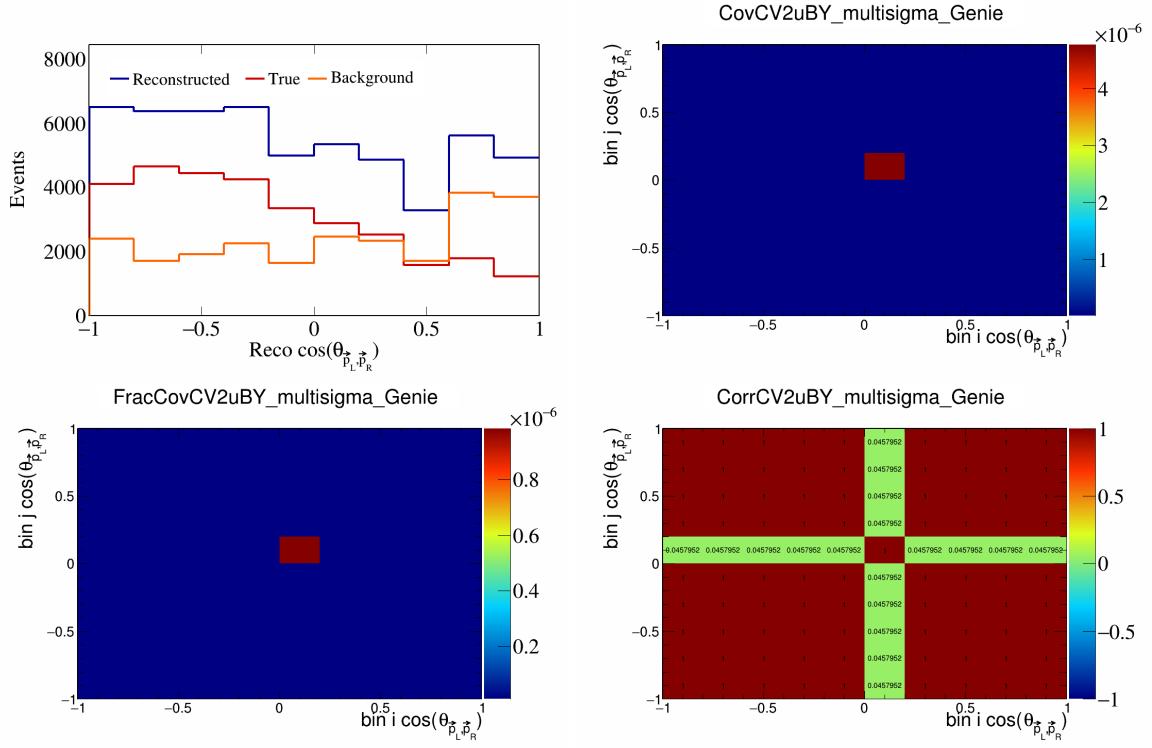


Figure 95: CV2uBY variations for $\cos(\theta_{\vec{p}_L, \vec{p}_R})$.

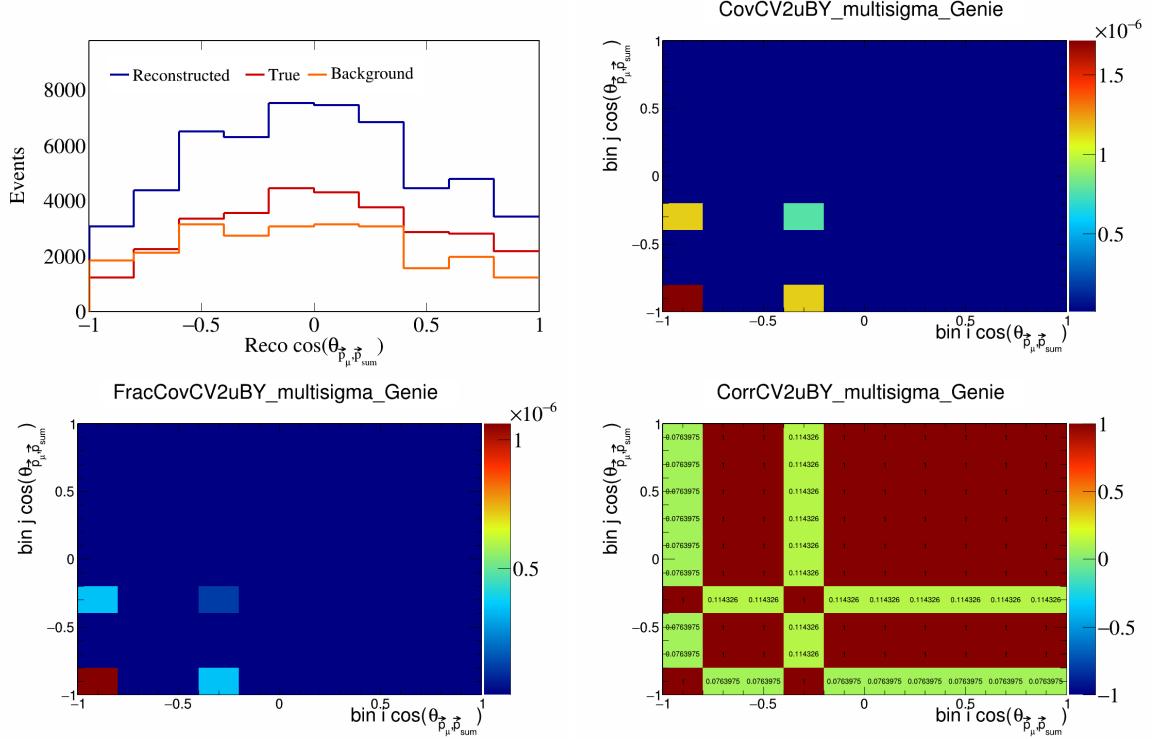


Figure 96: CV2uBY variations for $\cos(\theta_{\vec{p}_\mu, \vec{p}_{\text{sum}}})$.

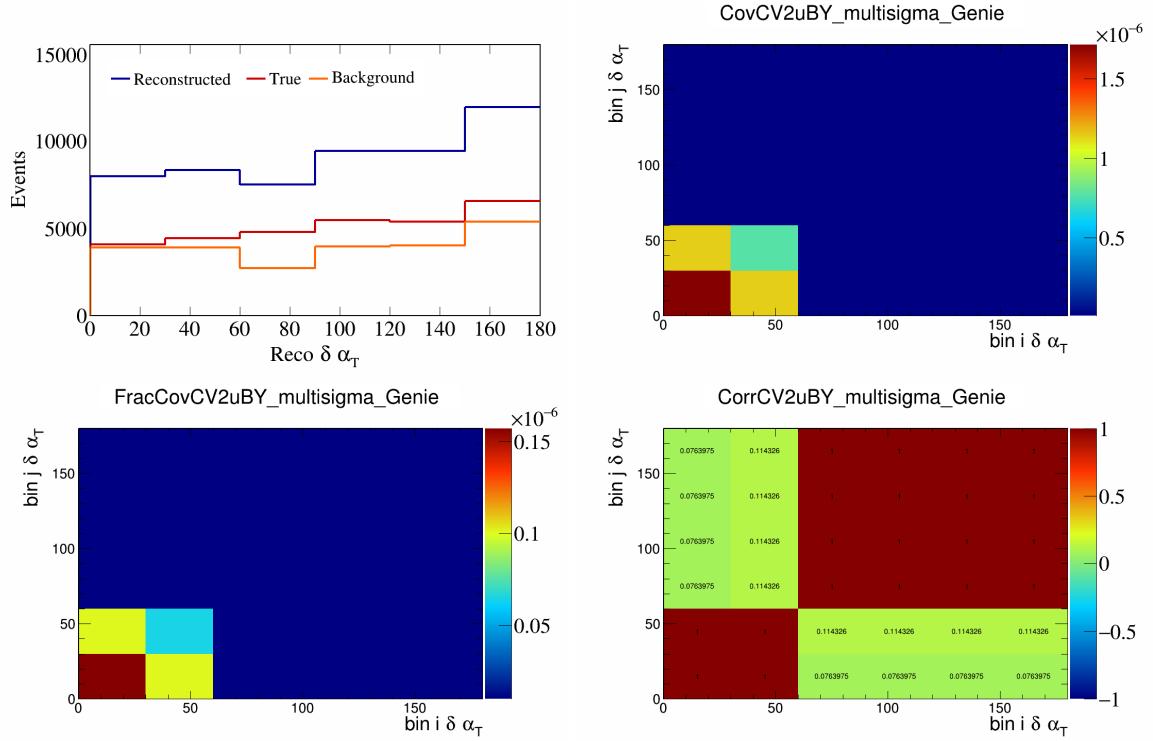


Figure 97: CV2uBY variations for $\delta\alpha_T$.

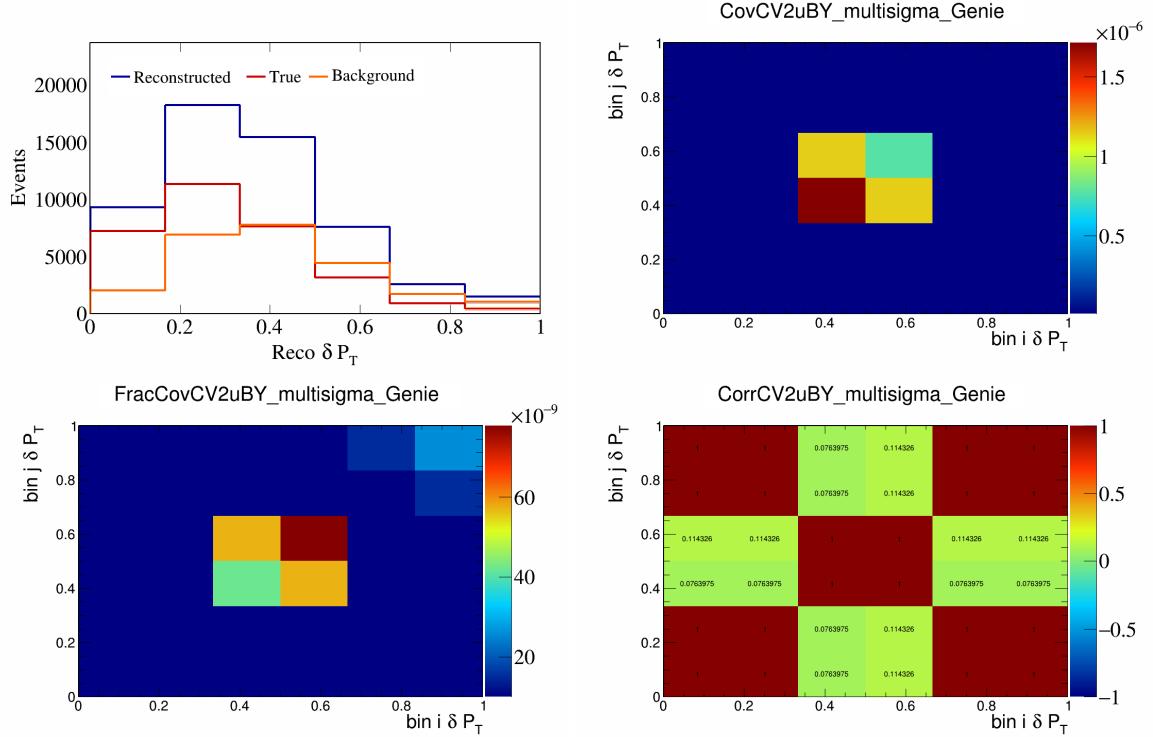


Figure 98: CV2uBY variations for δP_T .

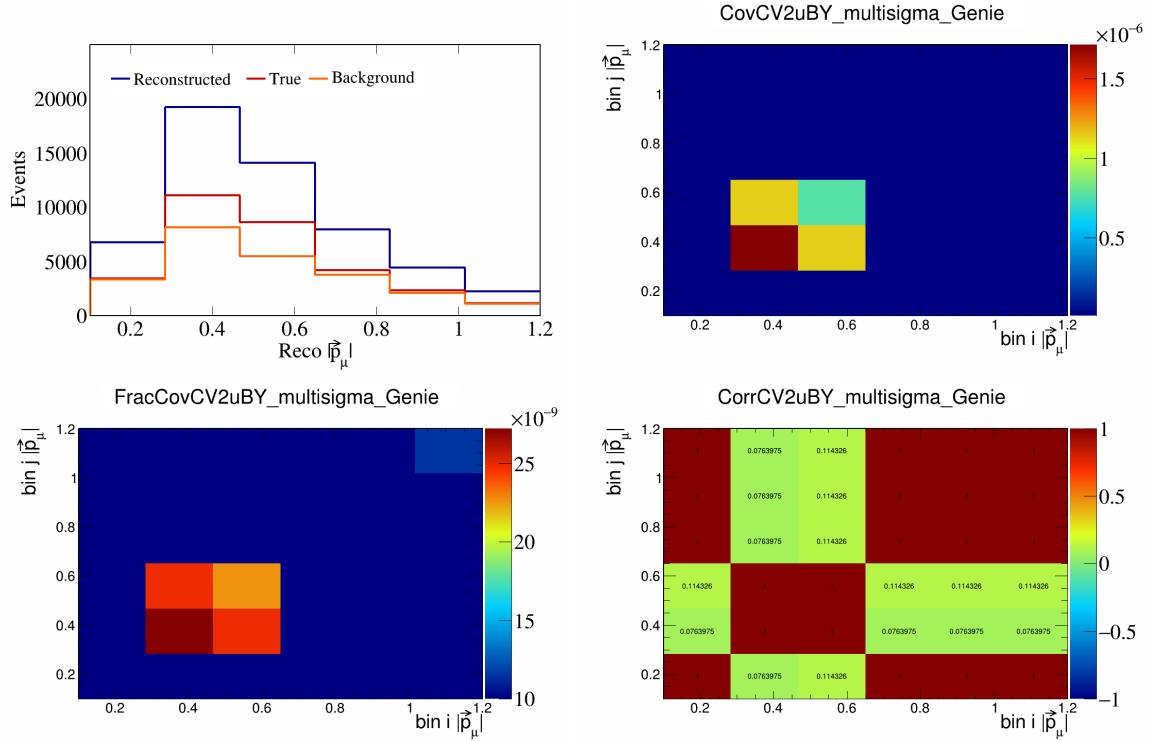


Figure 99: CV2uBY variations for $|\vec{p}_\mu|$.

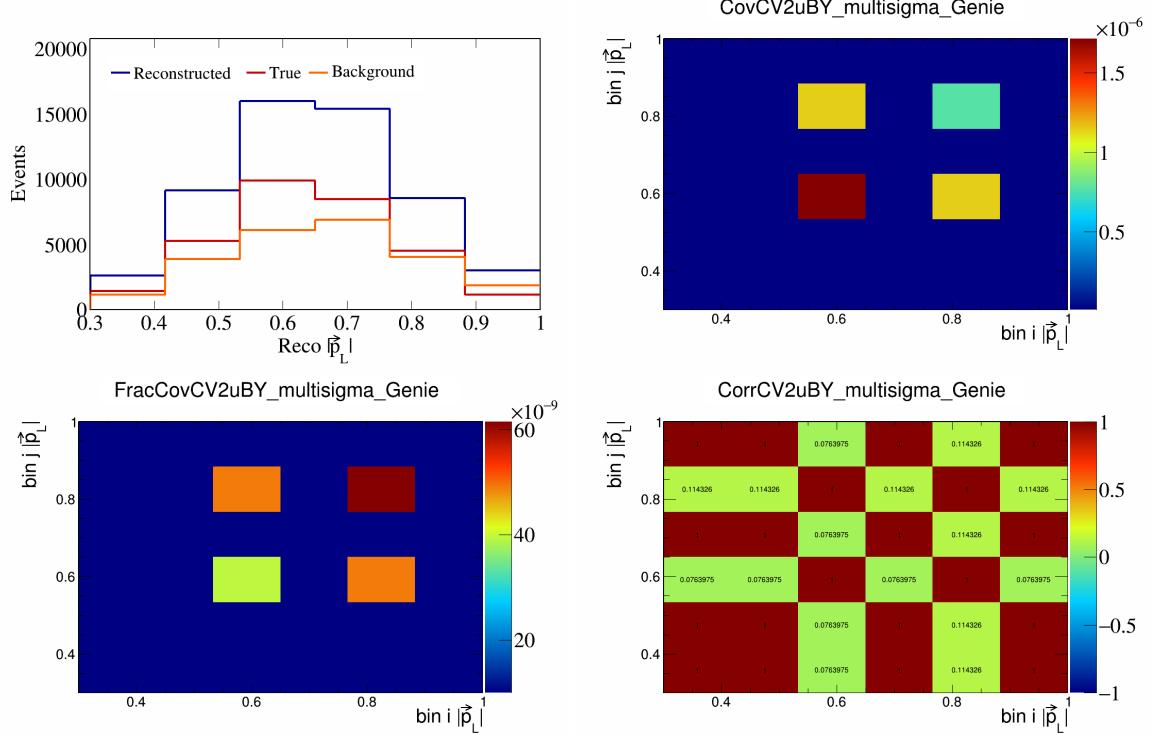


Figure 100: CV2uBY variations for $|\vec{p}_L|$.

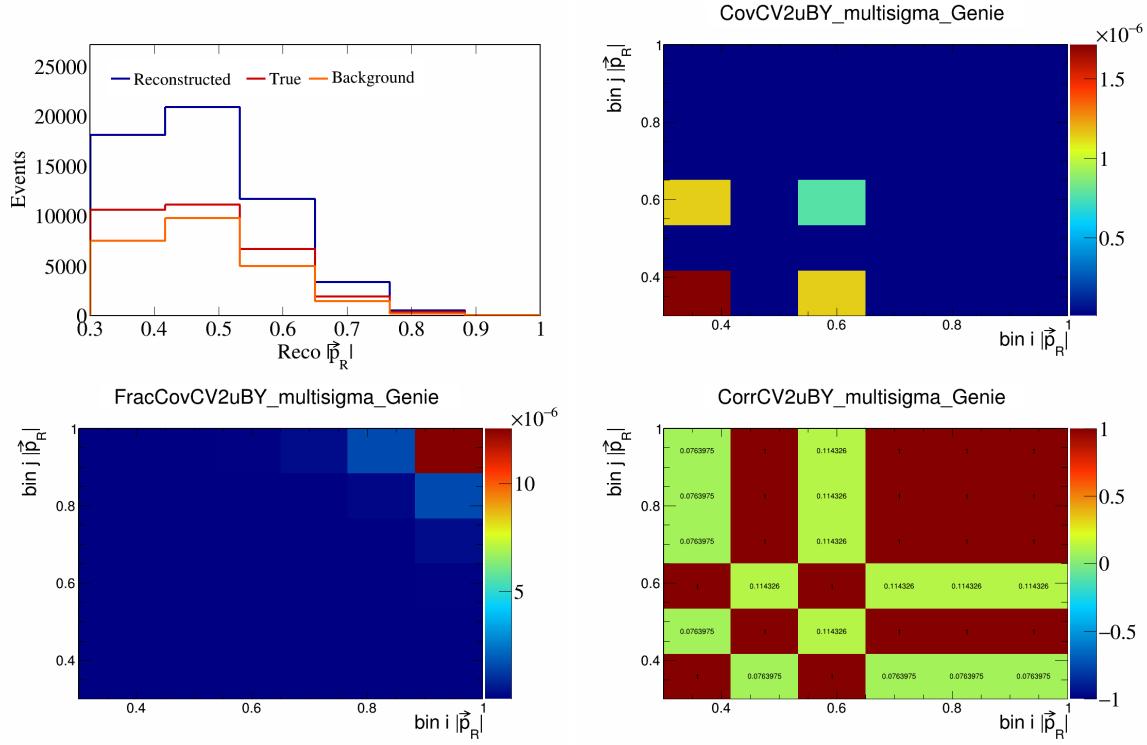


Figure 101: CV2uBY variations for $|\vec{p}_R|$.

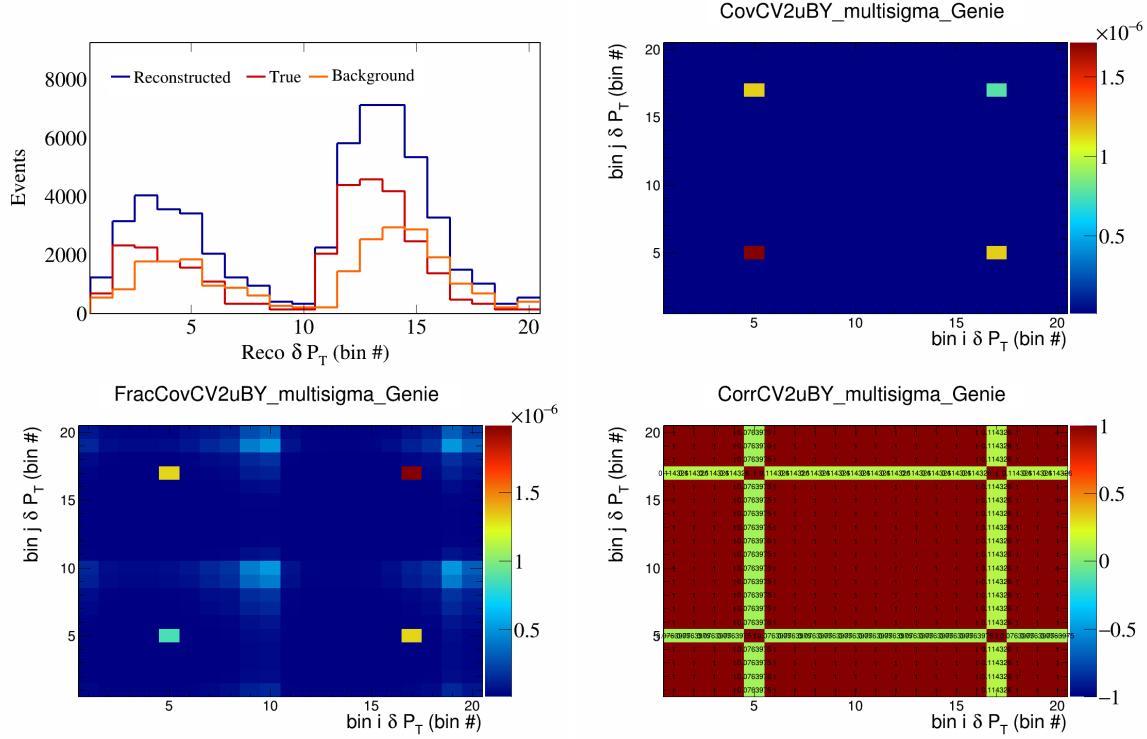


Figure 102: CV2uBY variations for δP_T in $\cos(\theta_{\vec{p}_\mu})$.

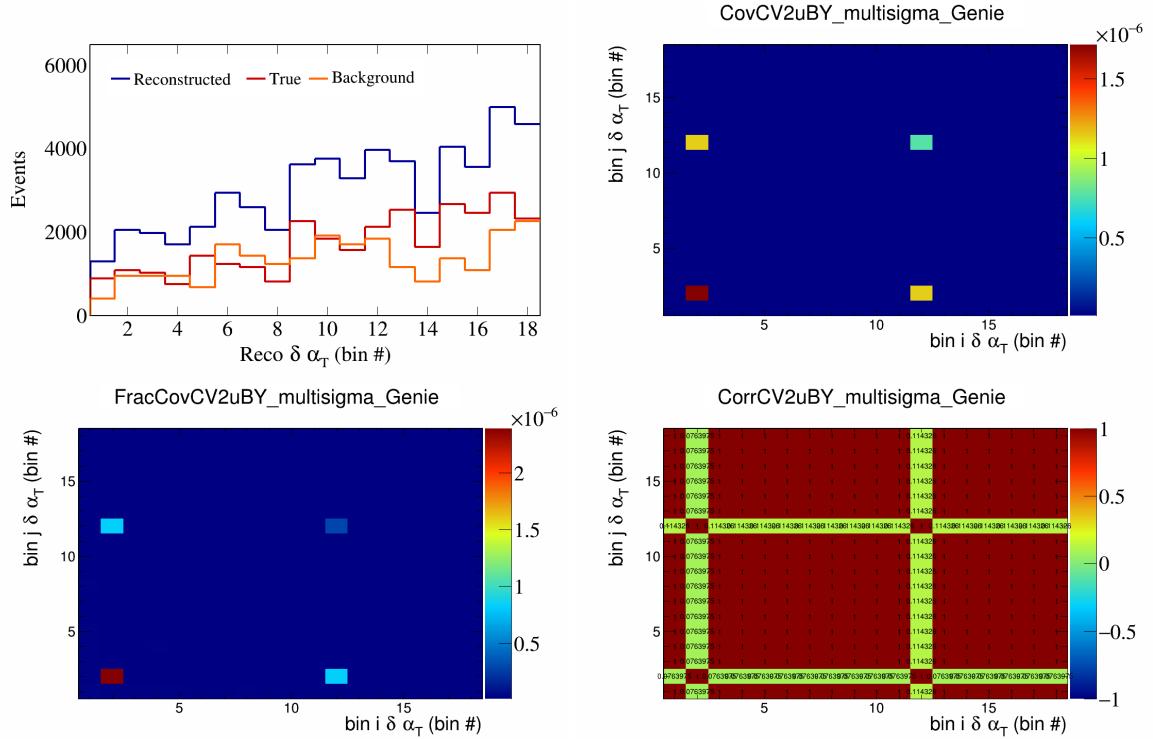


Figure 103: CV2uBY variations for $\delta \alpha_T$ in $\cos(\theta_{\vec{p}_\mu})$.

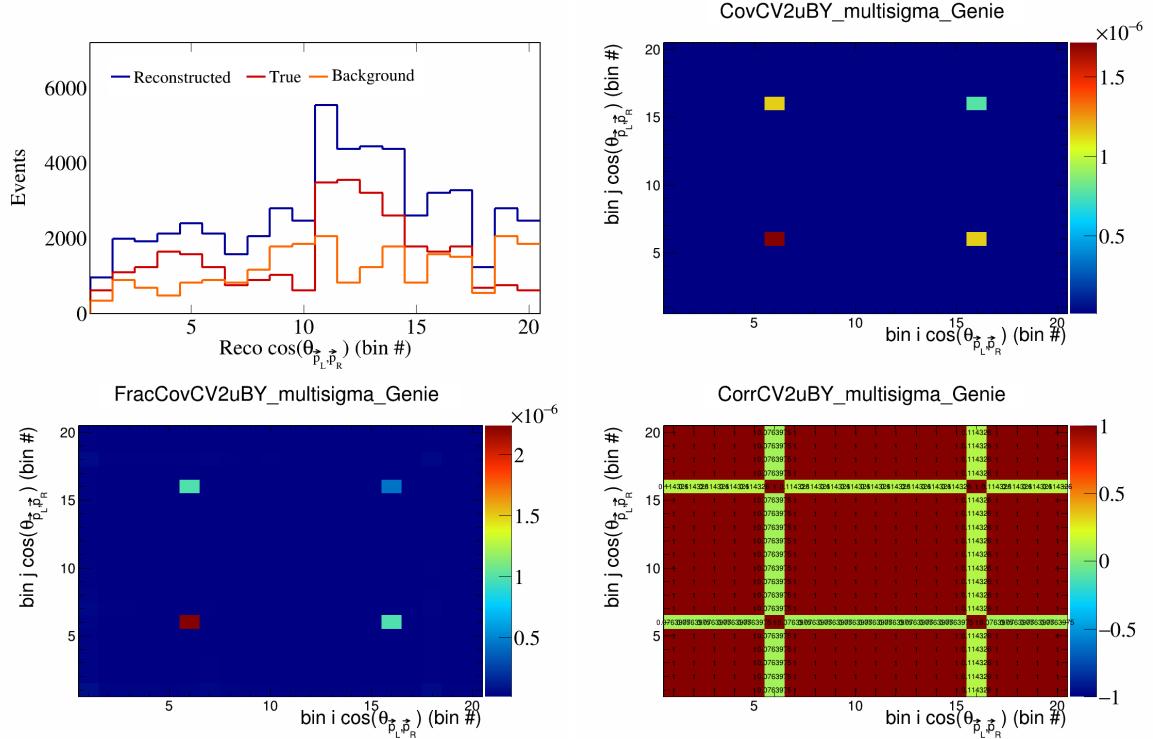


Figure 104: CV2uBY variations for $\cos(\theta_{\vec{p}_L, \vec{p}_R})$ in $\cos(\theta_{\vec{p}_\mu})$.

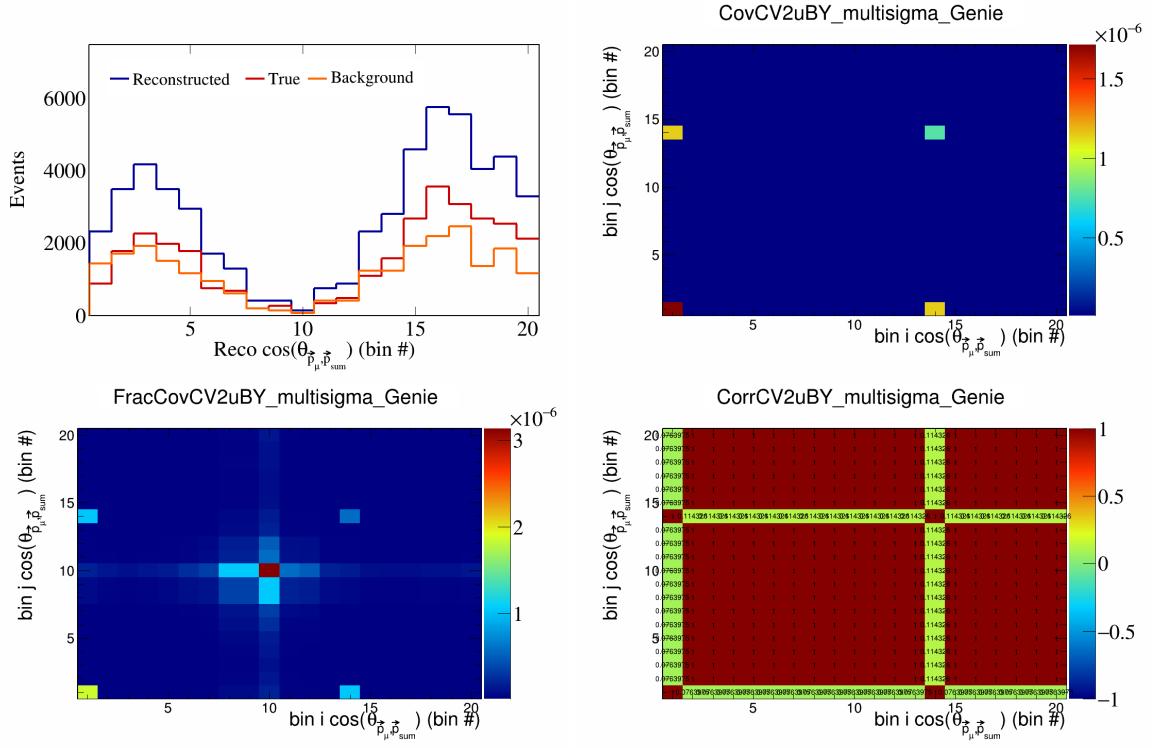


Figure 105: CV2uBY variations for $\cos(\theta_{\vec{p}_\mu, \vec{p}_{\text{sum}}})$ in $\cos(\theta_{\vec{p}_\mu})$.

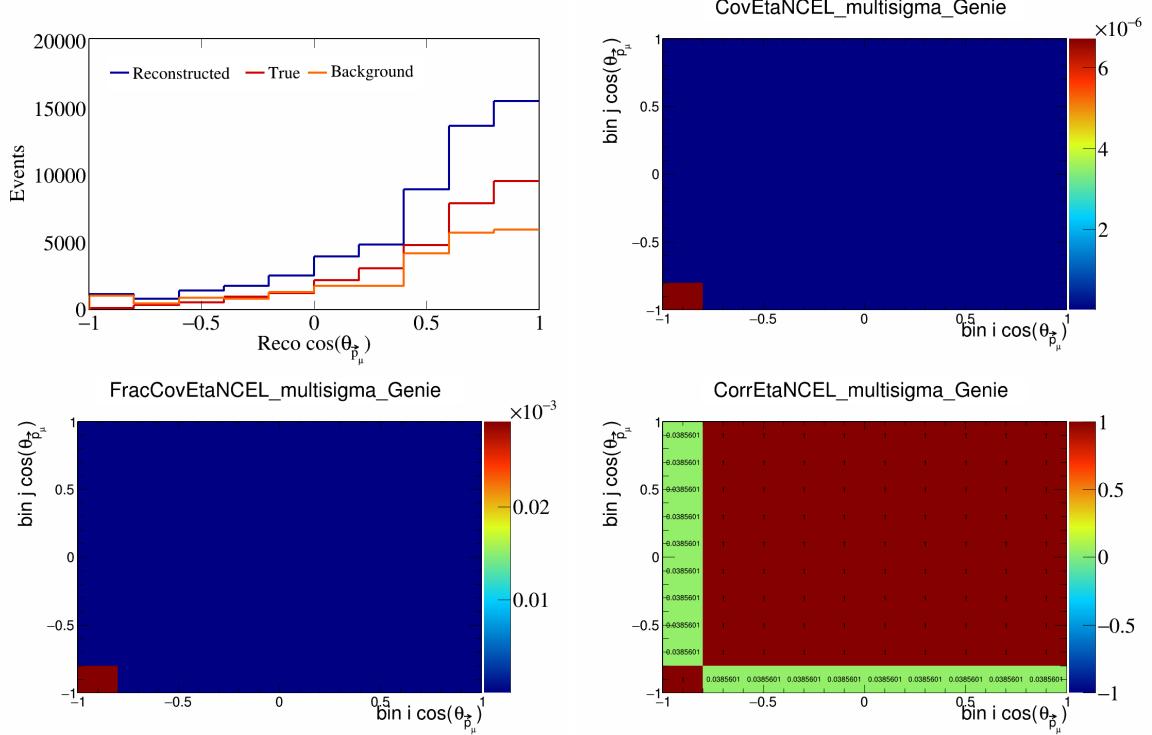


Figure 106: EtaNCEL variations for $\cos(\theta_{\vec{p}_\mu})$.

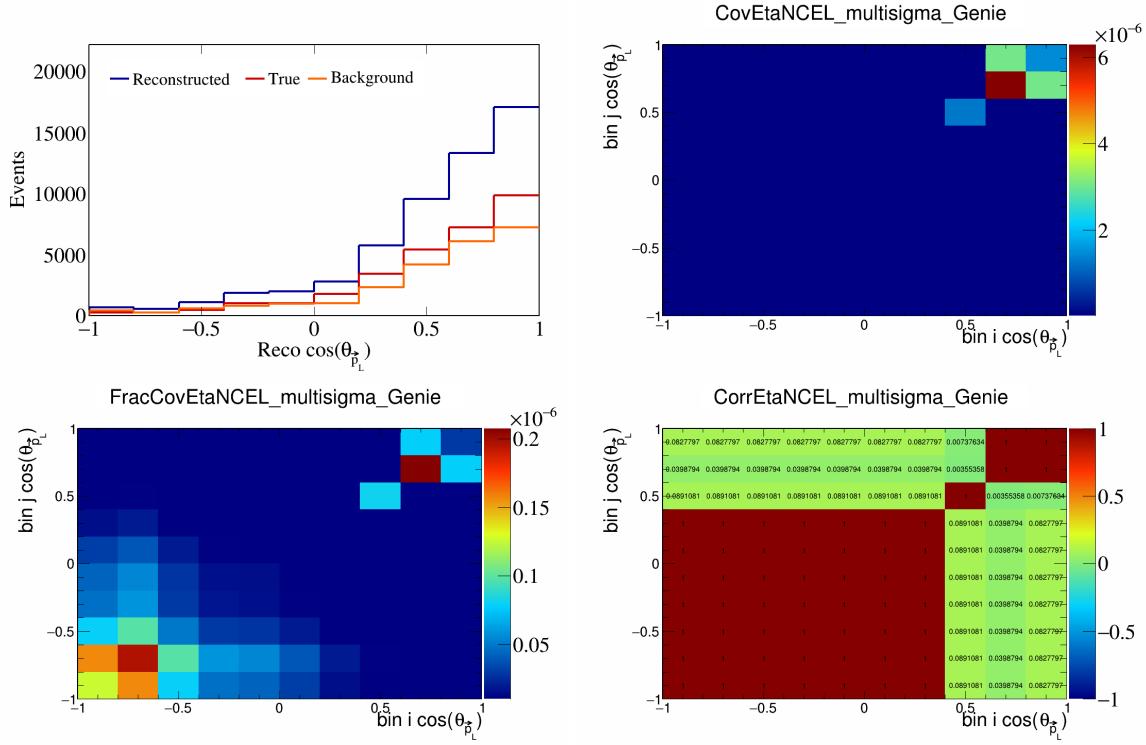


Figure 107: EtaNCEL variations for $\cos(\theta_{\vec{p}_L})$.

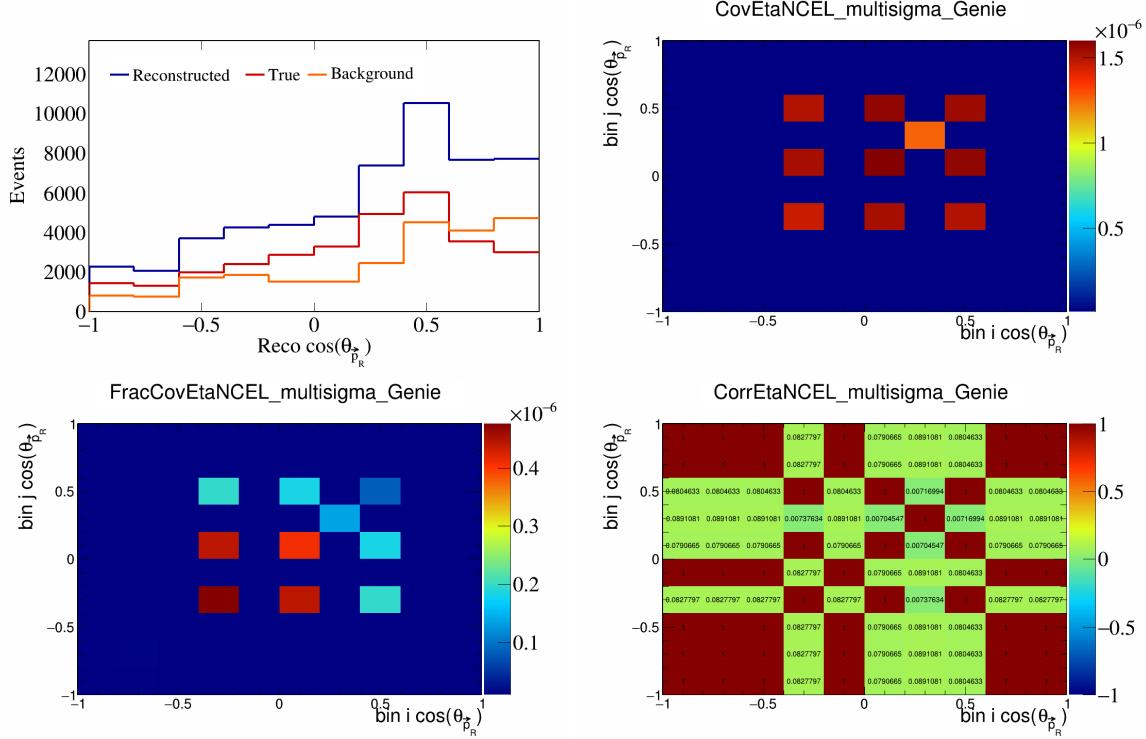


Figure 108: EtaNCEL variations for $\cos(\theta_{\vec{p}_R})$.

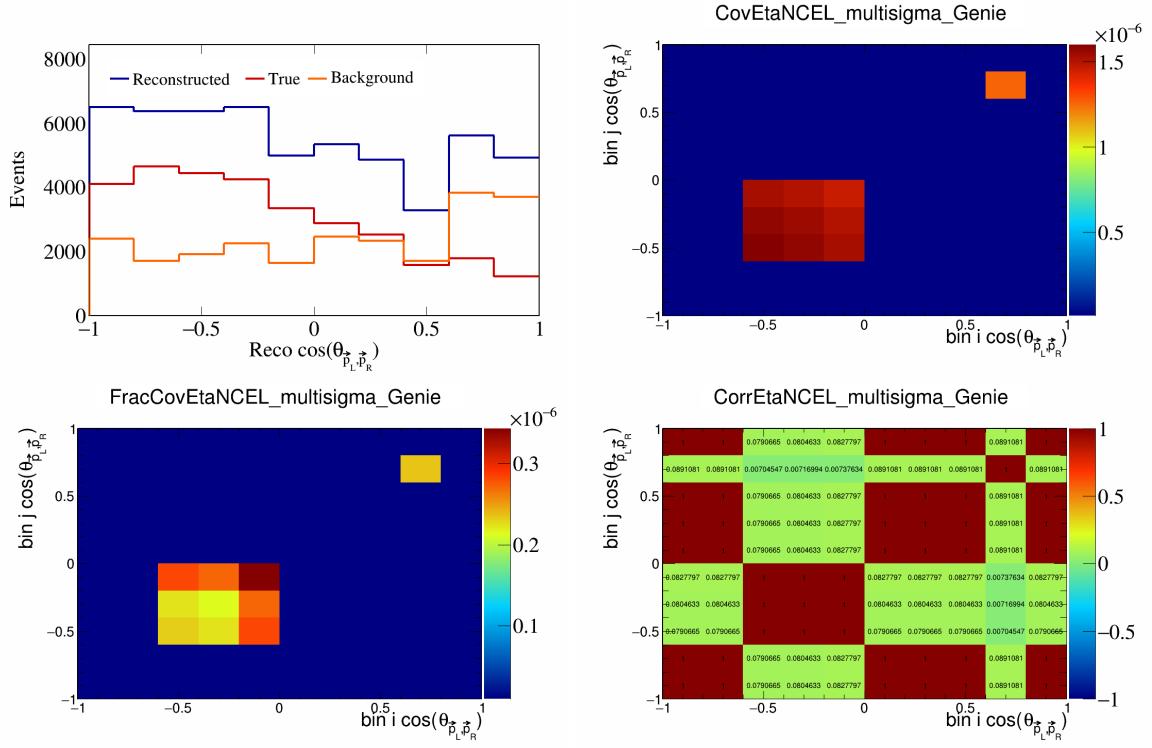


Figure 109: EtaNCEL variations for $\cos(\theta_{\vec{p}_L, \vec{p}_R})$.

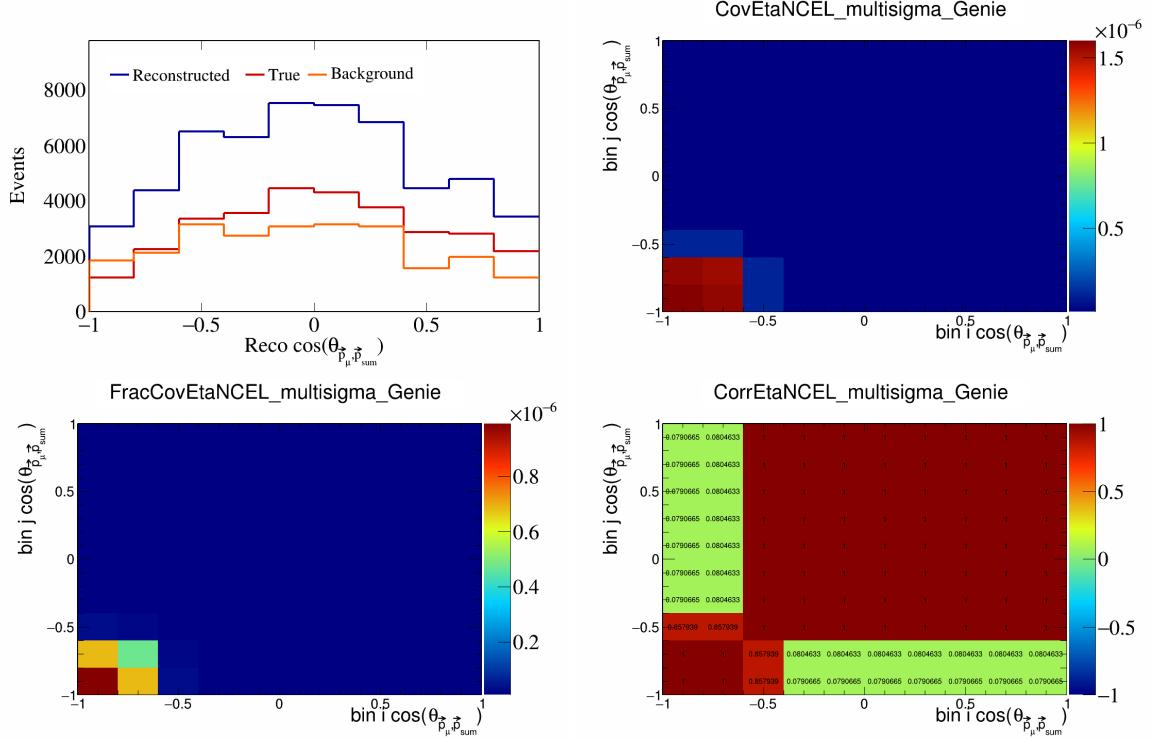


Figure 110: EtaNCEL variations for $\cos(\theta_{\vec{p}_\mu, \vec{p}_{\text{sum}}})$.

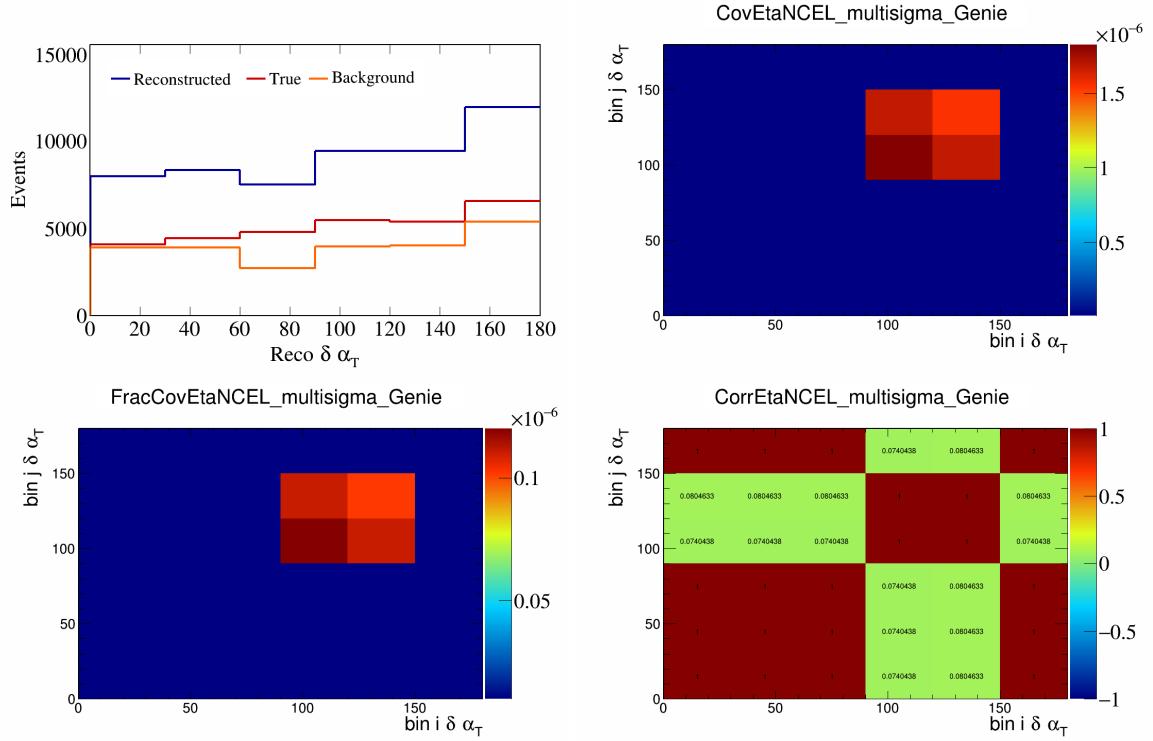


Figure 111: EtaNCEL variations for $\delta\alpha_T$.

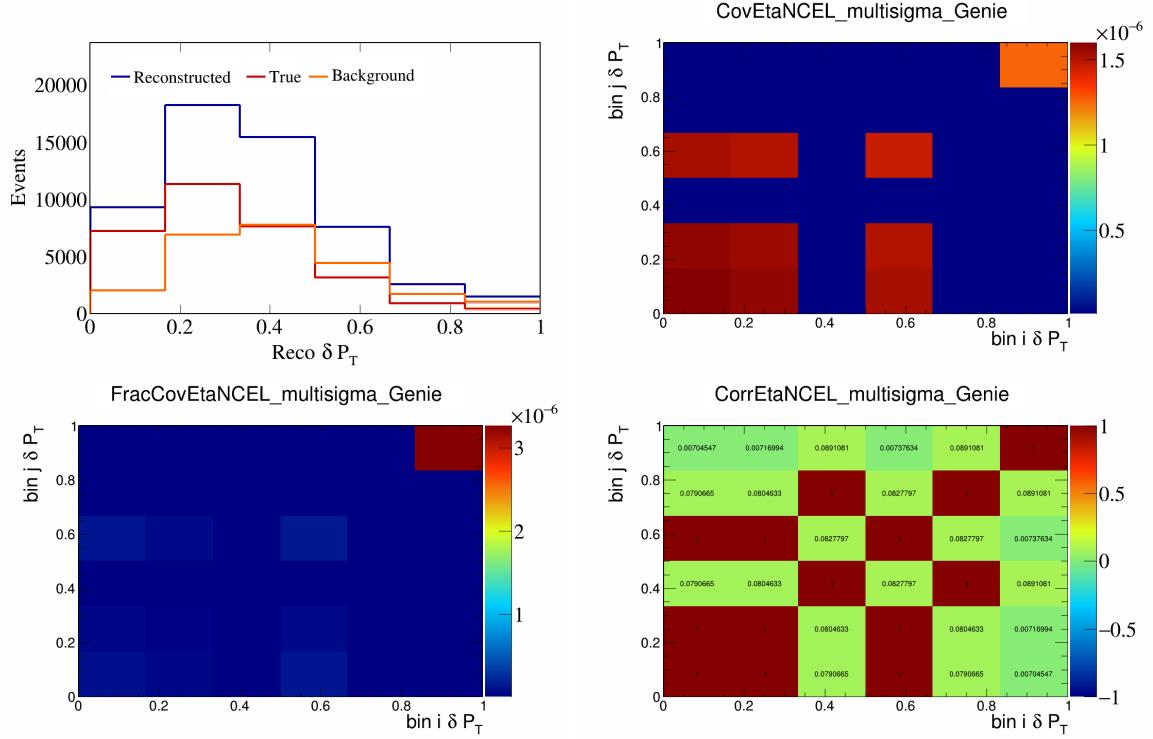


Figure 112: EtaNCEL variations for δP_T .

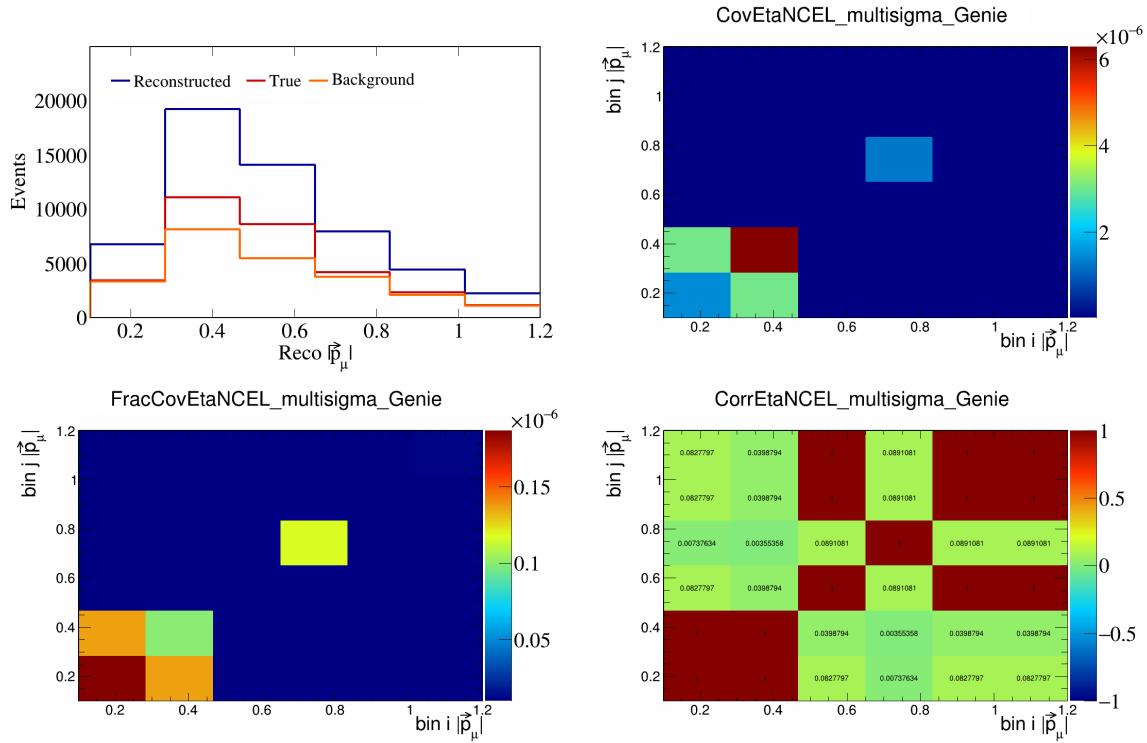


Figure 113: EtaNCEL variations for $|\vec{p}_\mu|$.

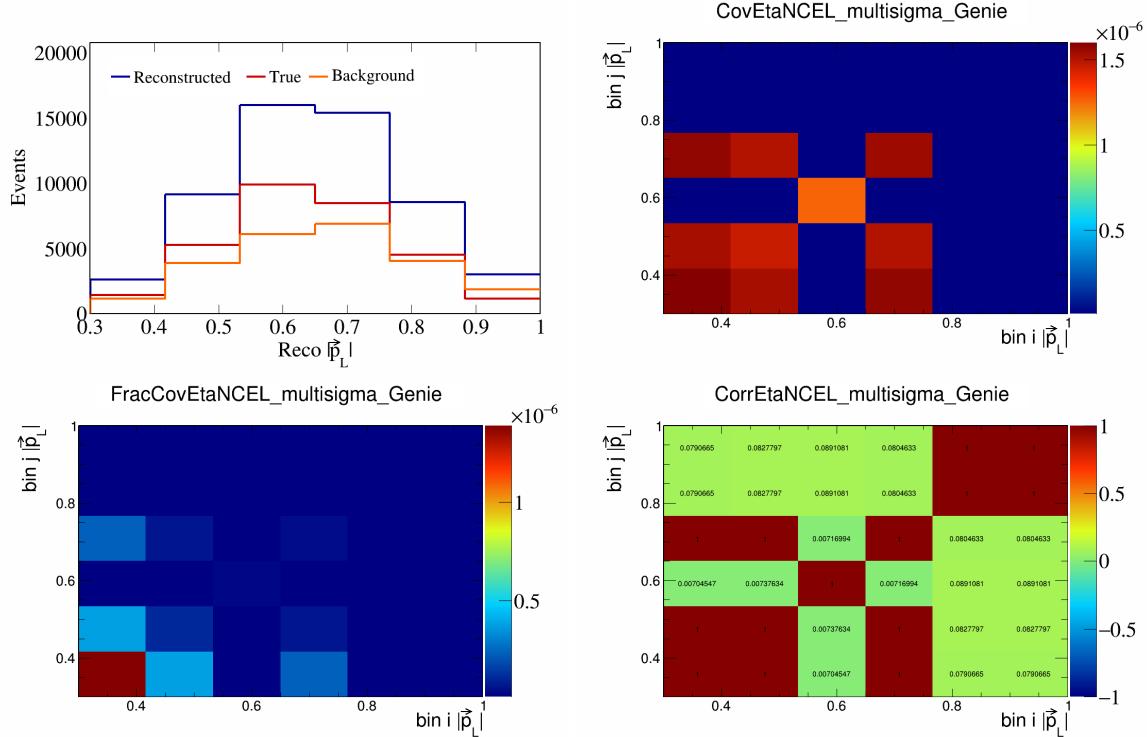


Figure 114: EtaNCEL variations for $|\vec{p}_L|$.

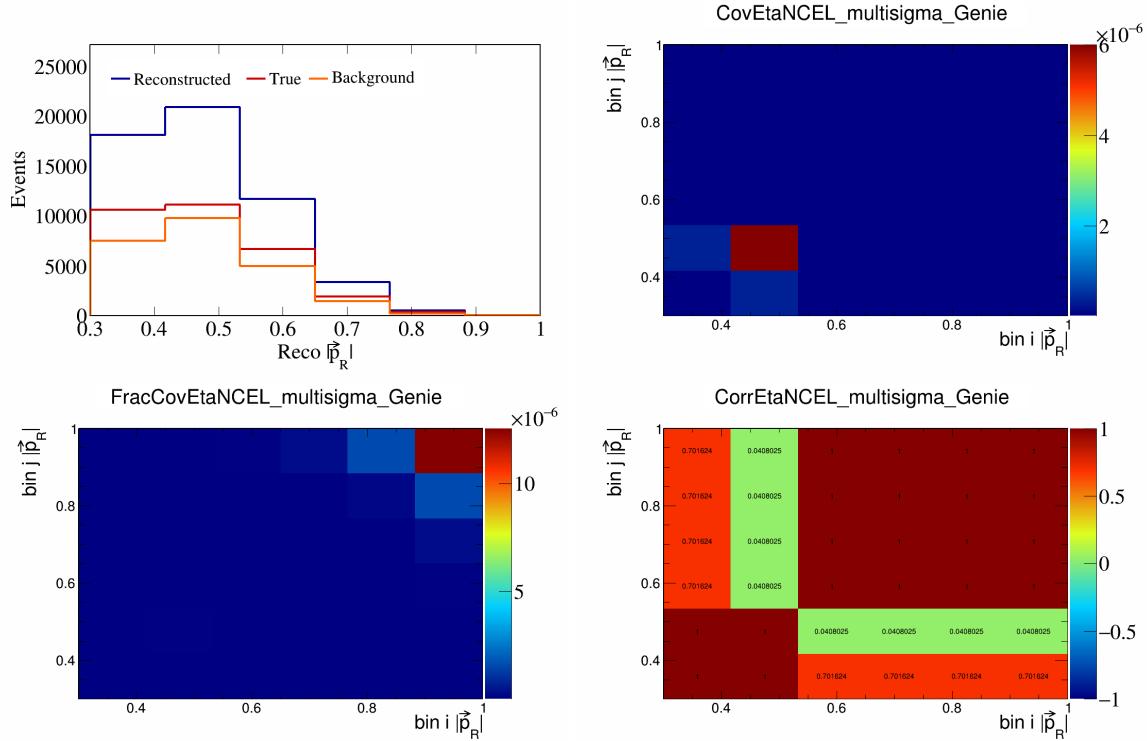


Figure 115: EtaNCEL variations for $|\vec{p}_R|$.

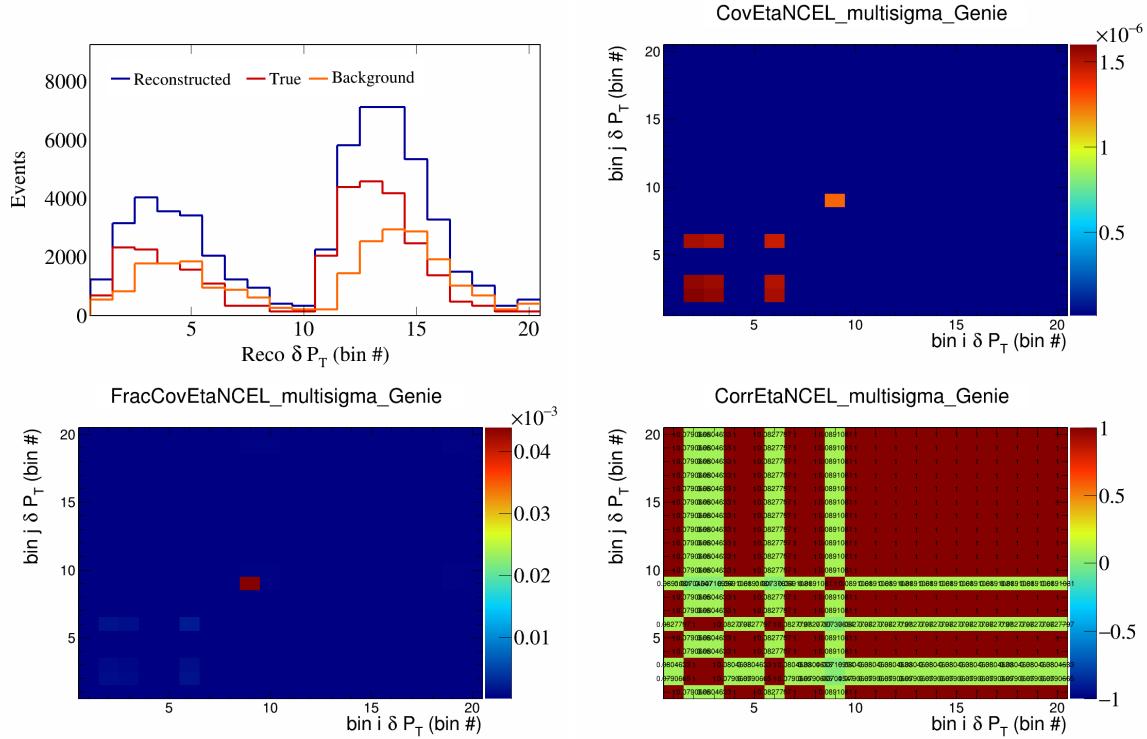


Figure 116: EtaNCEL variations for δP_T in $\cos(\theta_{\vec{p}_\mu})$.

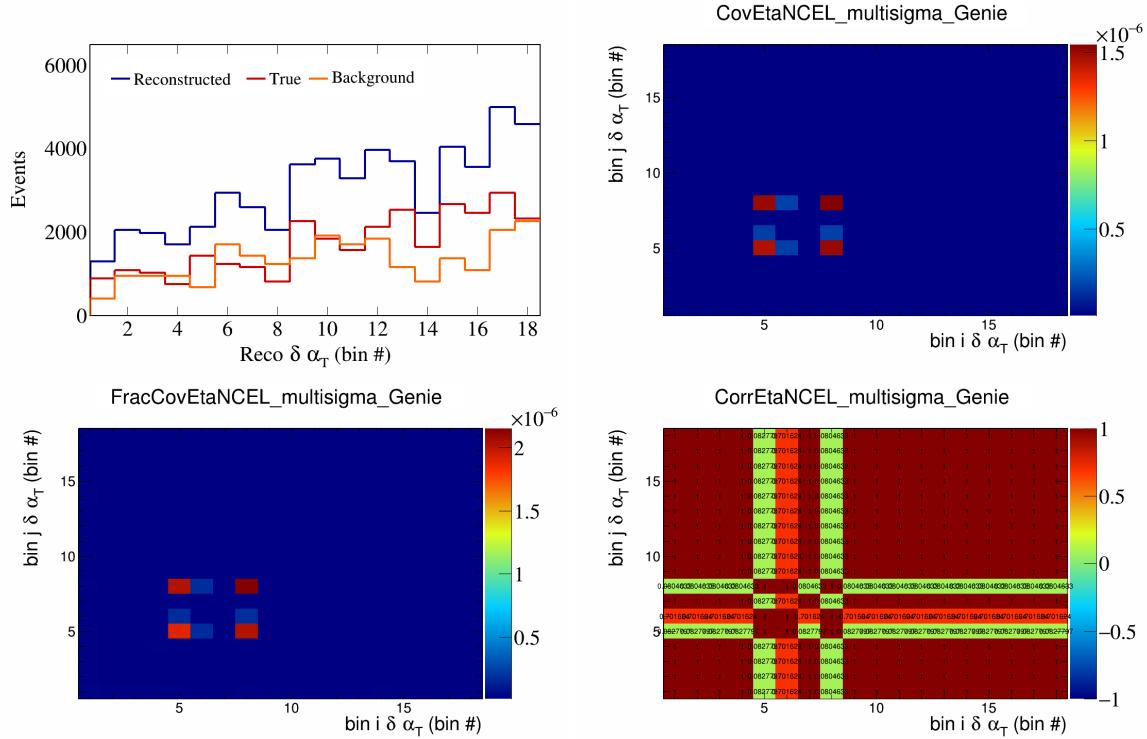


Figure 117: EtaNCEL variations for $\delta\alpha_T$ in $\cos(\theta_{\vec{p}_\mu})$.

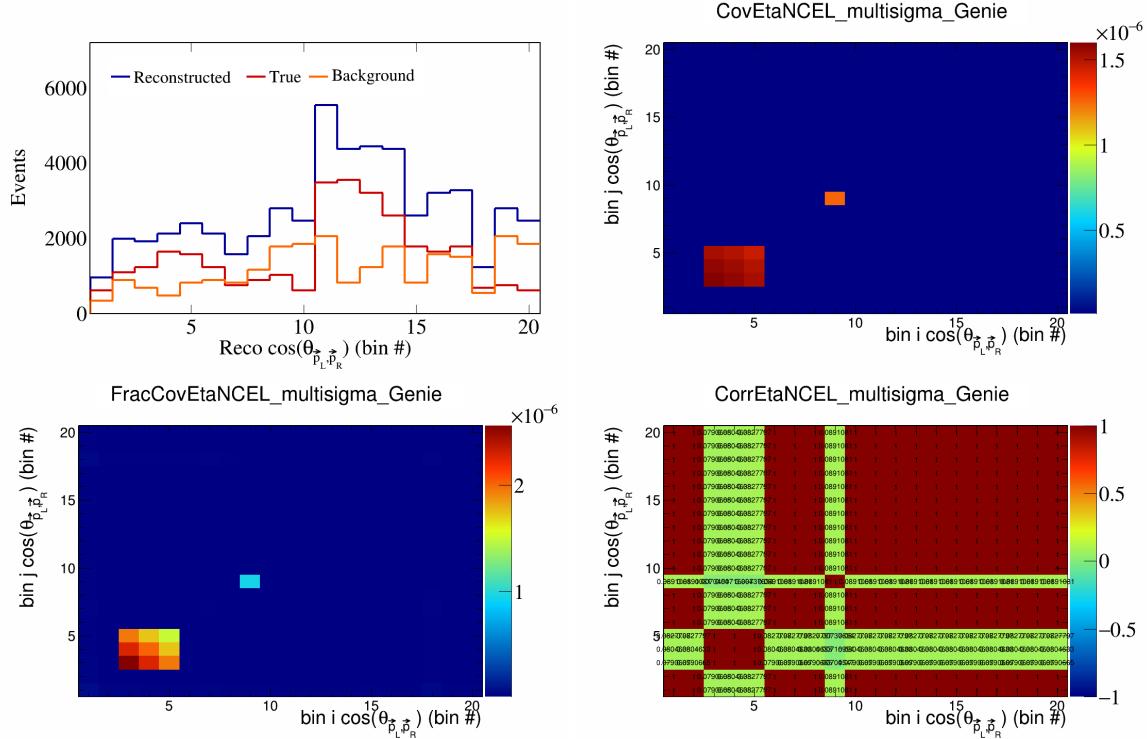


Figure 118: EtaNCEL variations for $\cos(\theta_{\vec{p}_L, \vec{p}_R})$ in $\cos(\theta_{\vec{p}_\mu})$.

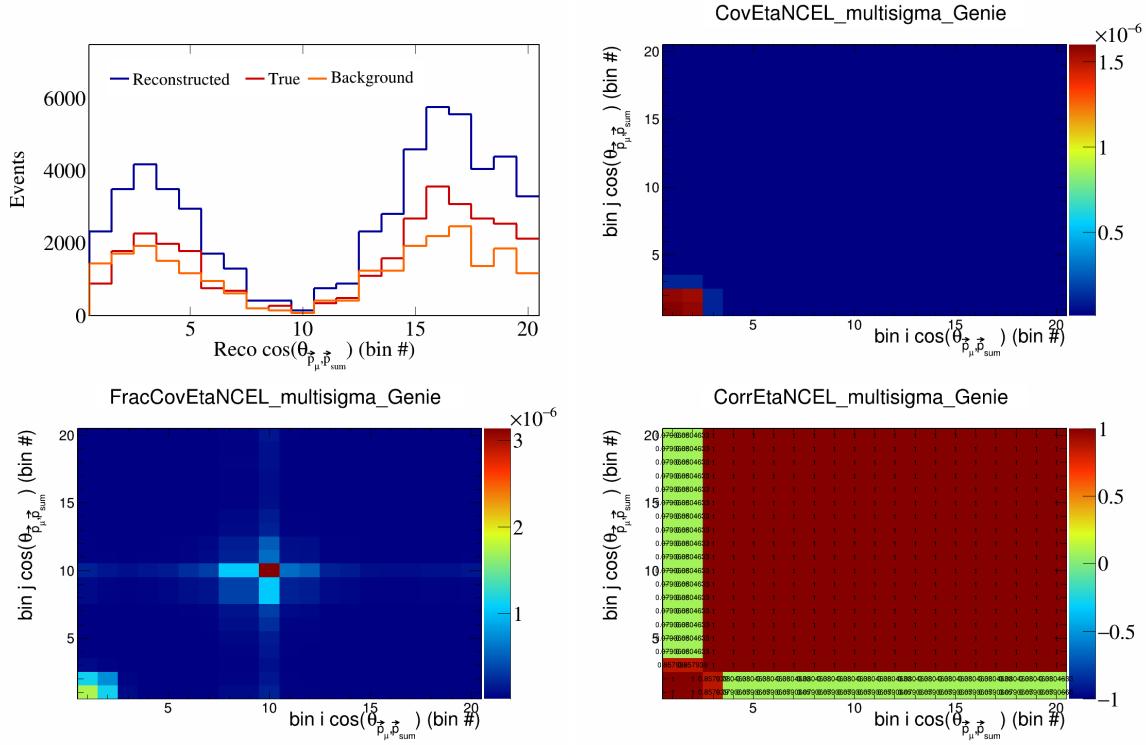


Figure 119: EtaNCEL variations for $\cos(\theta_{\vec{p}_\mu, \vec{p}_{\text{sum}}})$ in $\cos(\theta_{\vec{p}_\mu})$.

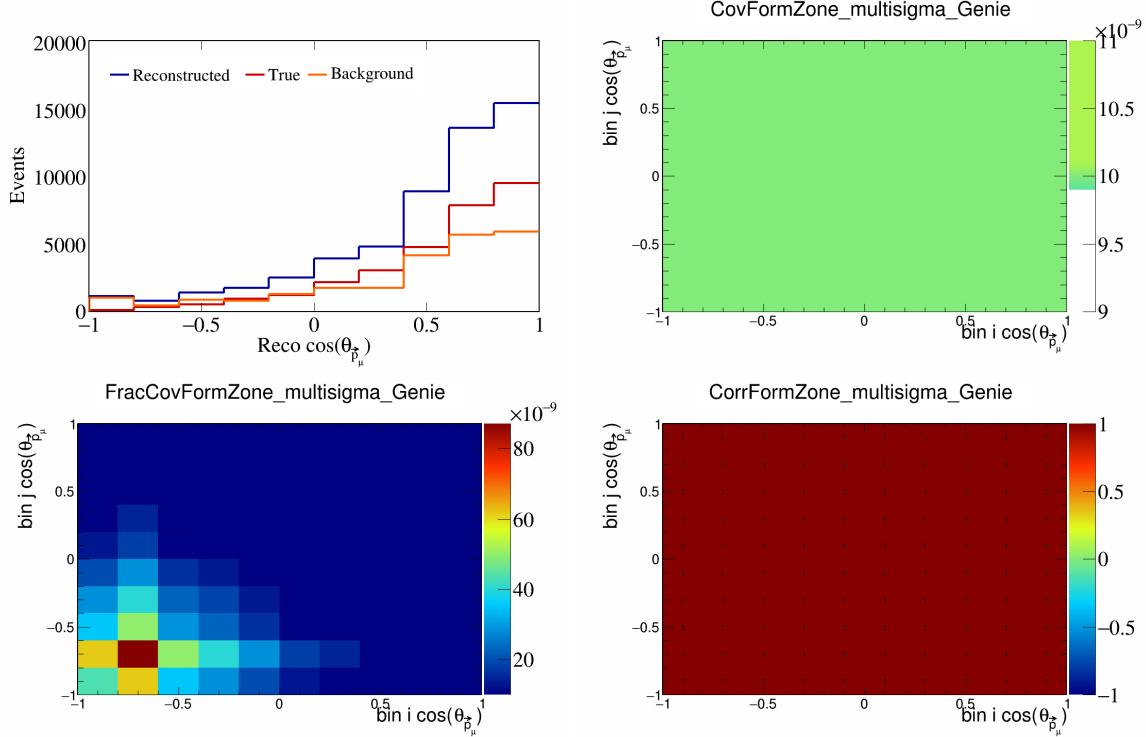


Figure 120: FormZone variations for $\cos(\theta_{\vec{p}_\mu})$.

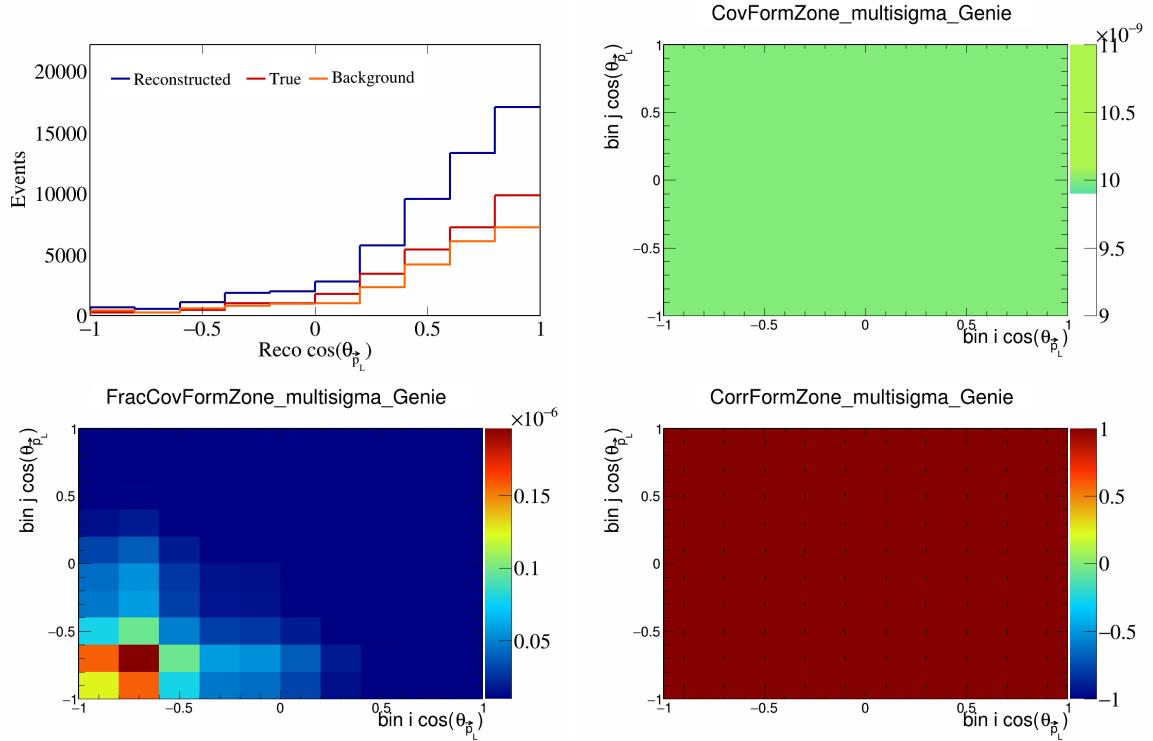


Figure 121: FormZone variations for $\cos(\theta_{\vec{p}_L})$.

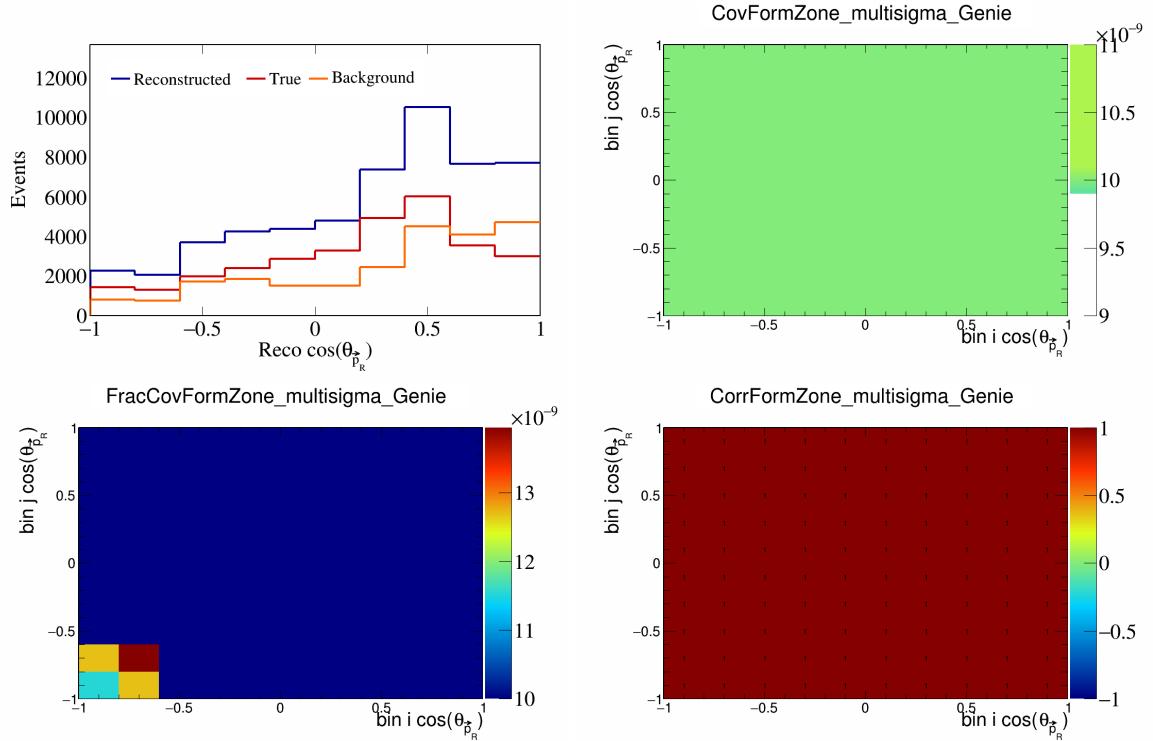


Figure 122: FormZone variations for $\cos(\theta_{\vec{p}_R})$.

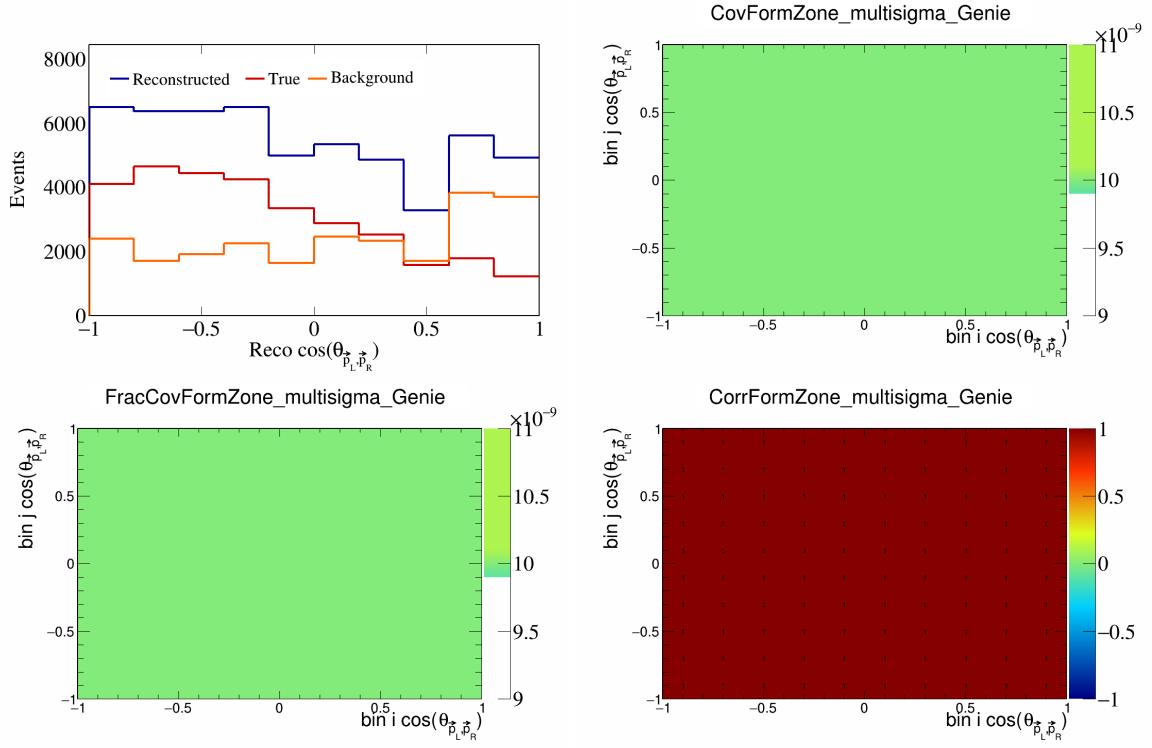


Figure 123: FormZone variations for $\cos(\theta_{\vec{p}_L, \vec{p}_R})$.

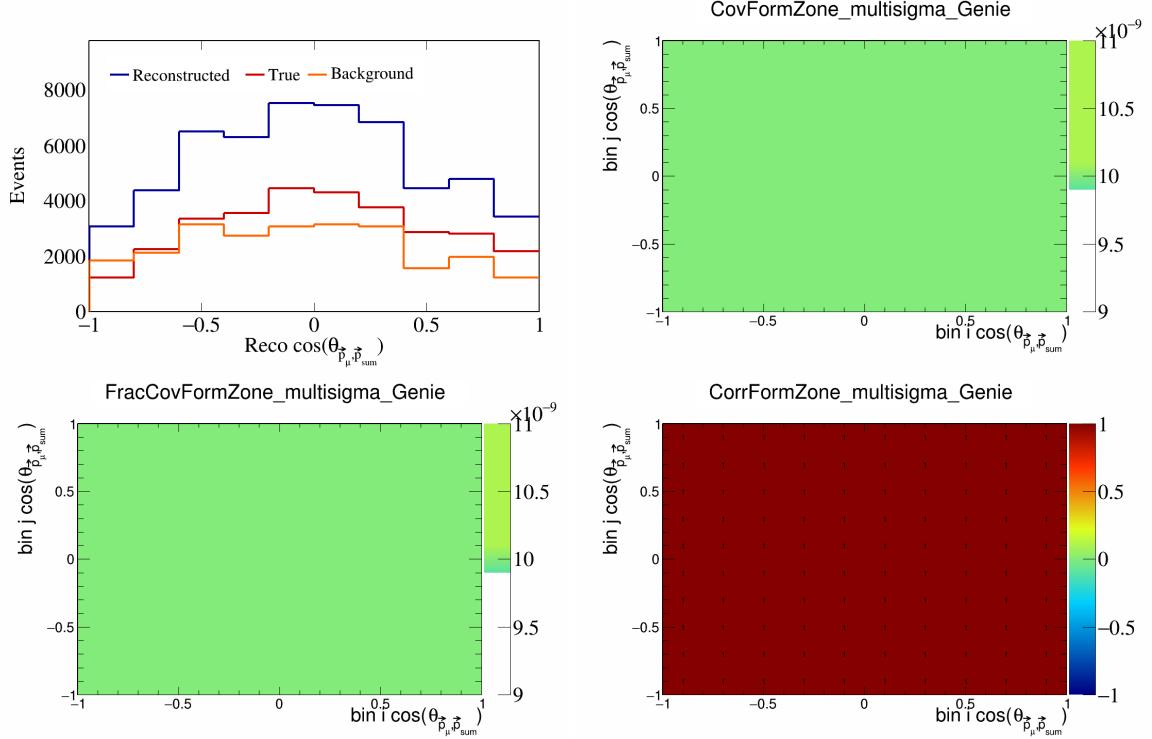


Figure 124: FormZone variations for $\cos(\theta_{\vec{p}_\mu, \vec{p}_{\text{sum}}})$.

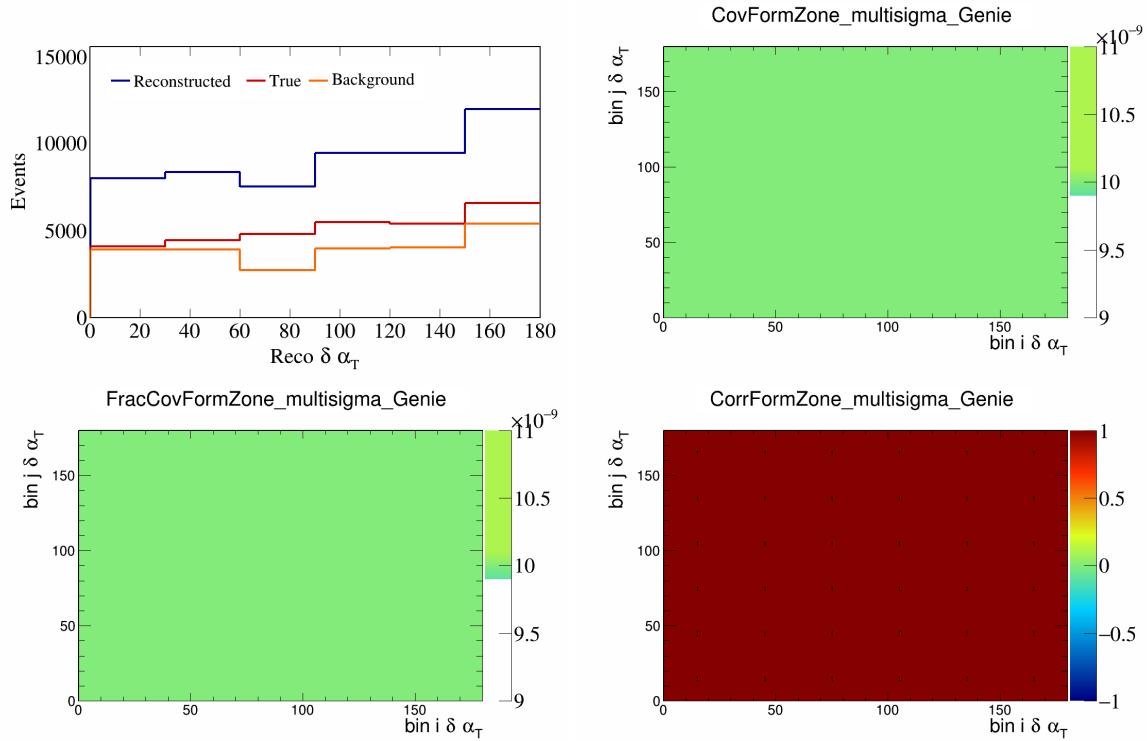


Figure 125: FormZone variations for $\delta\alpha_T$.

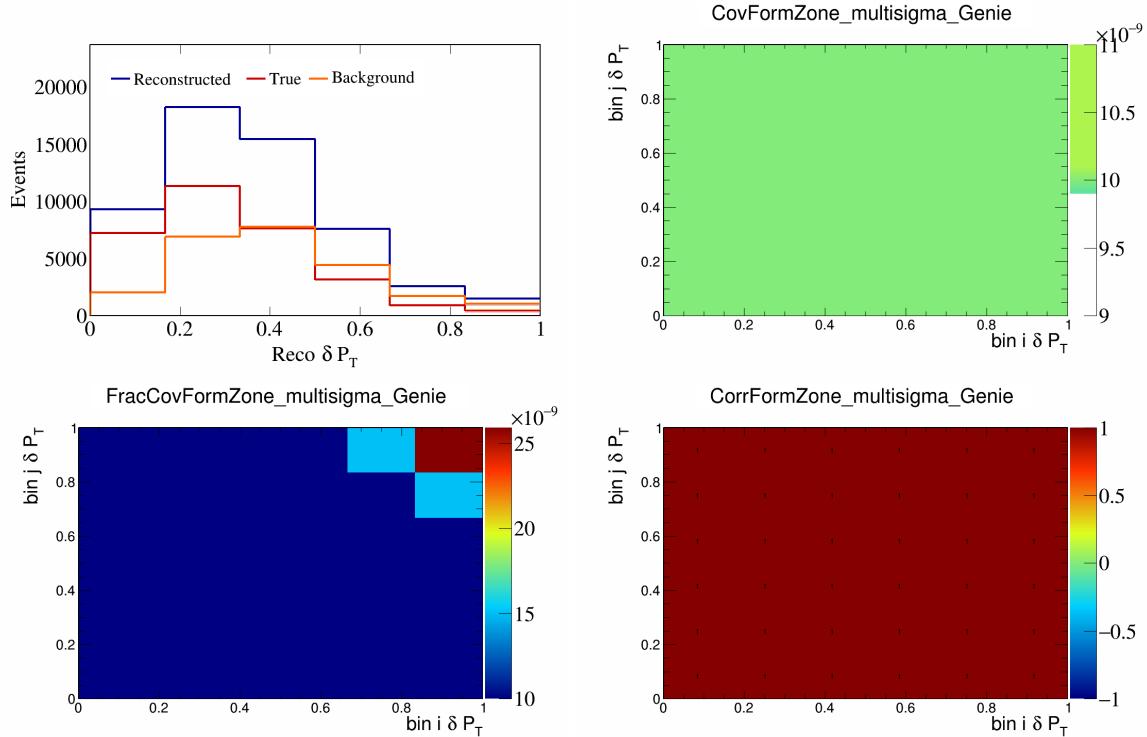


Figure 126: FormZone variations for δP_T .

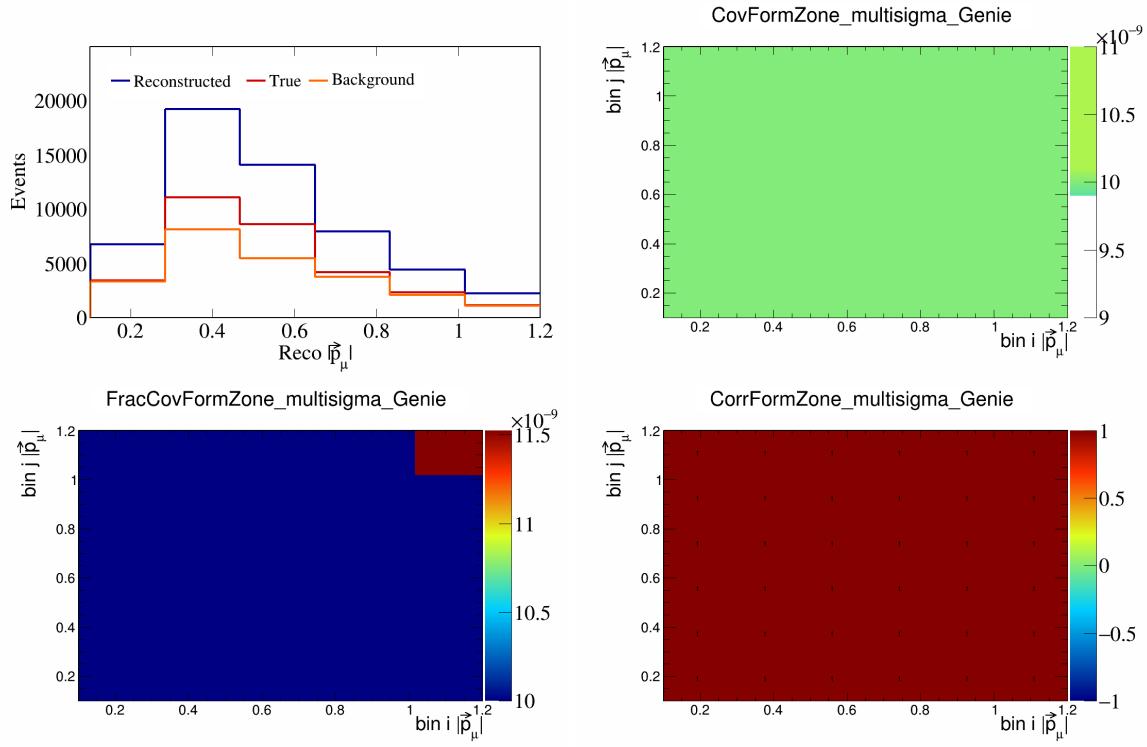


Figure 127: FormZone variations for $|\vec{p}_\mu|$.

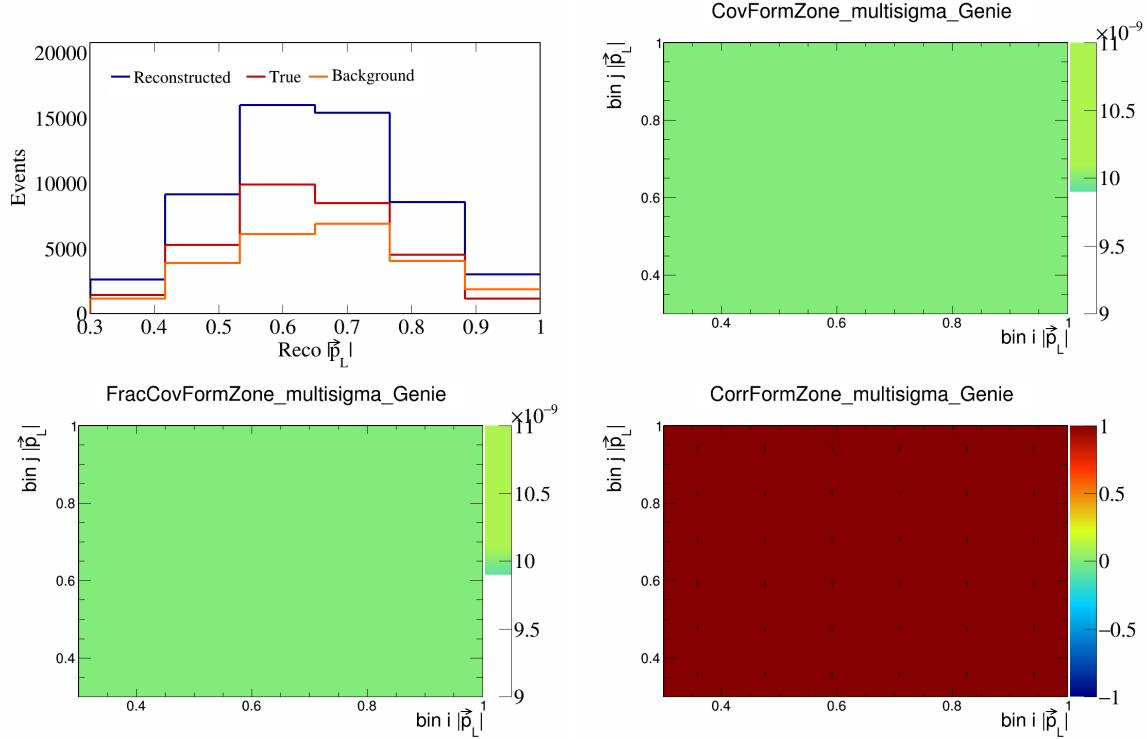


Figure 128: FormZone variations for $|\vec{p}_L|$.

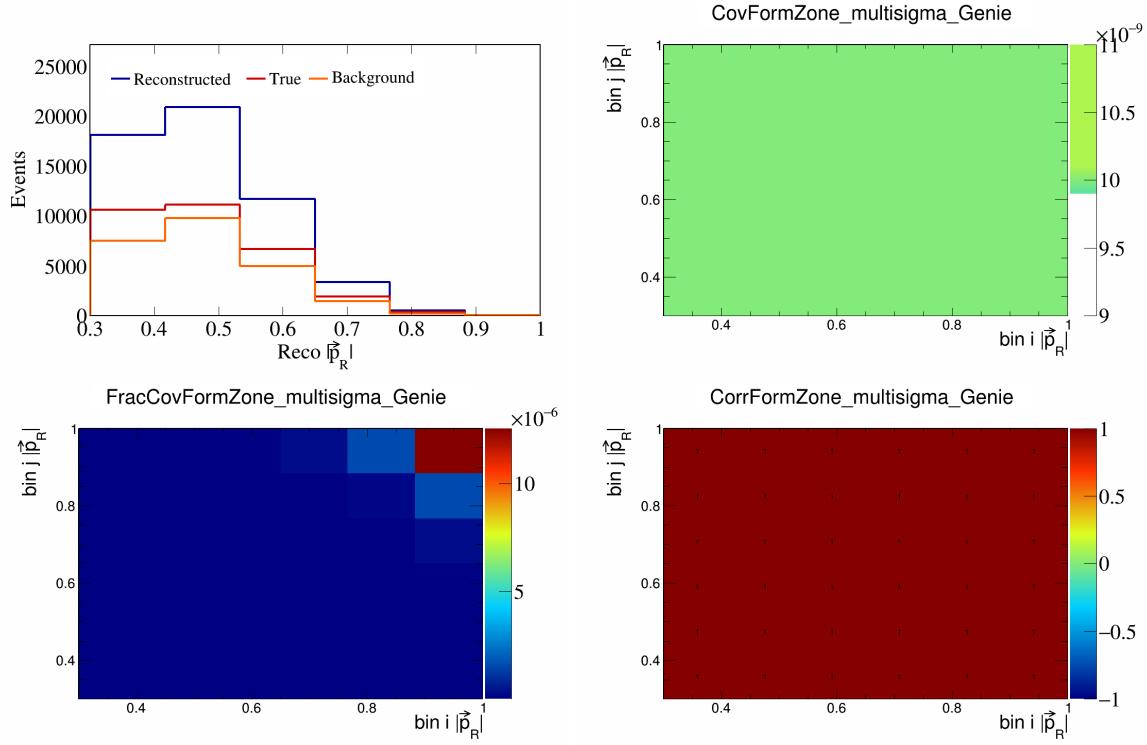


Figure 129: FormZone variations for $|\vec{p}_R|$.

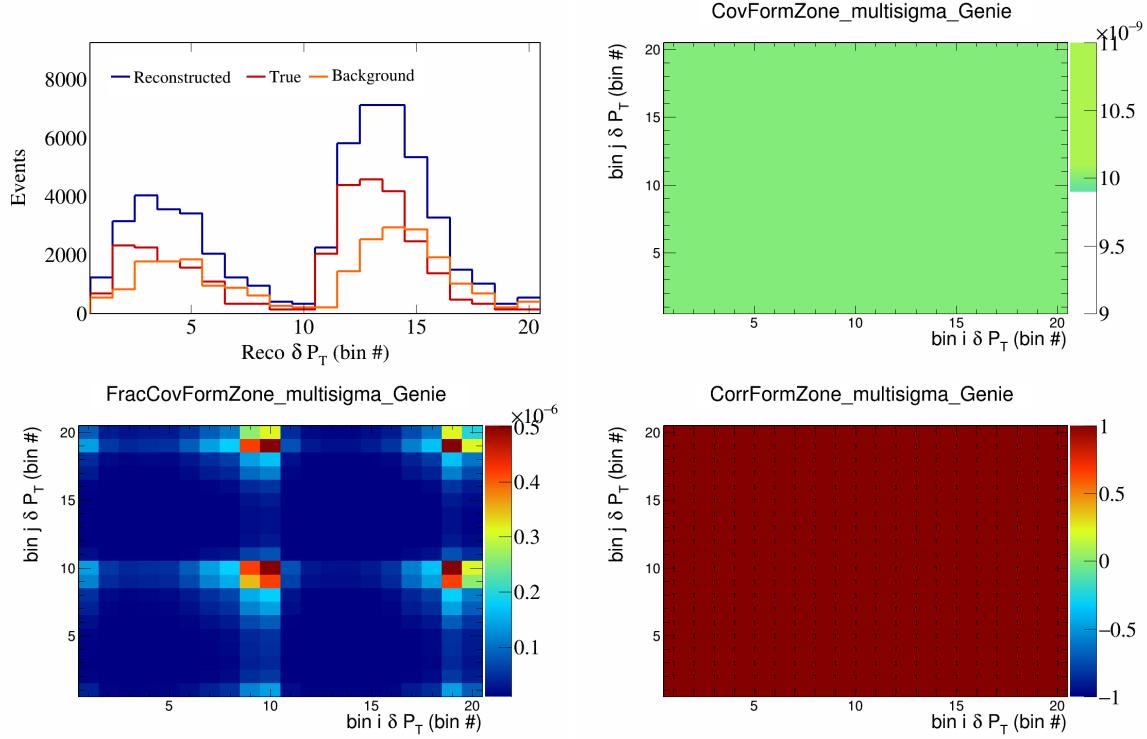


Figure 130: FormZone variations for δP_T in $\cos(\theta_{\vec{p}_\mu})$.

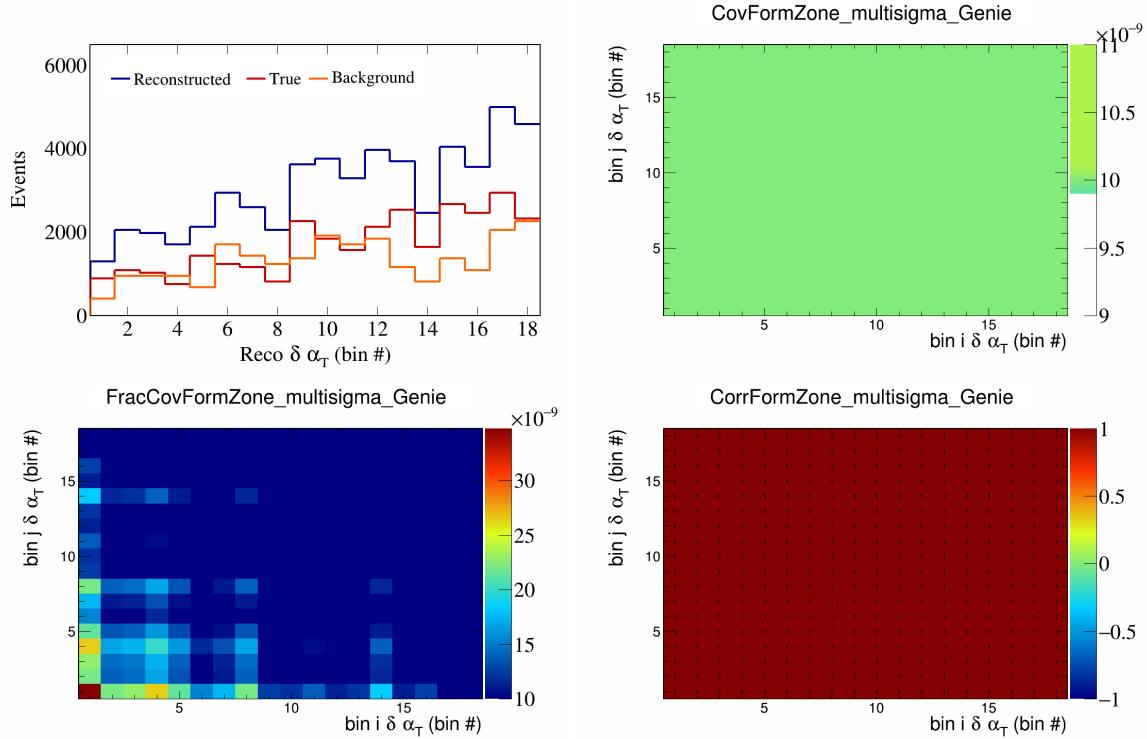


Figure 131: FormZone variations for $\delta \alpha_T$ in $\cos(\theta_{\vec{p}_\mu})$.

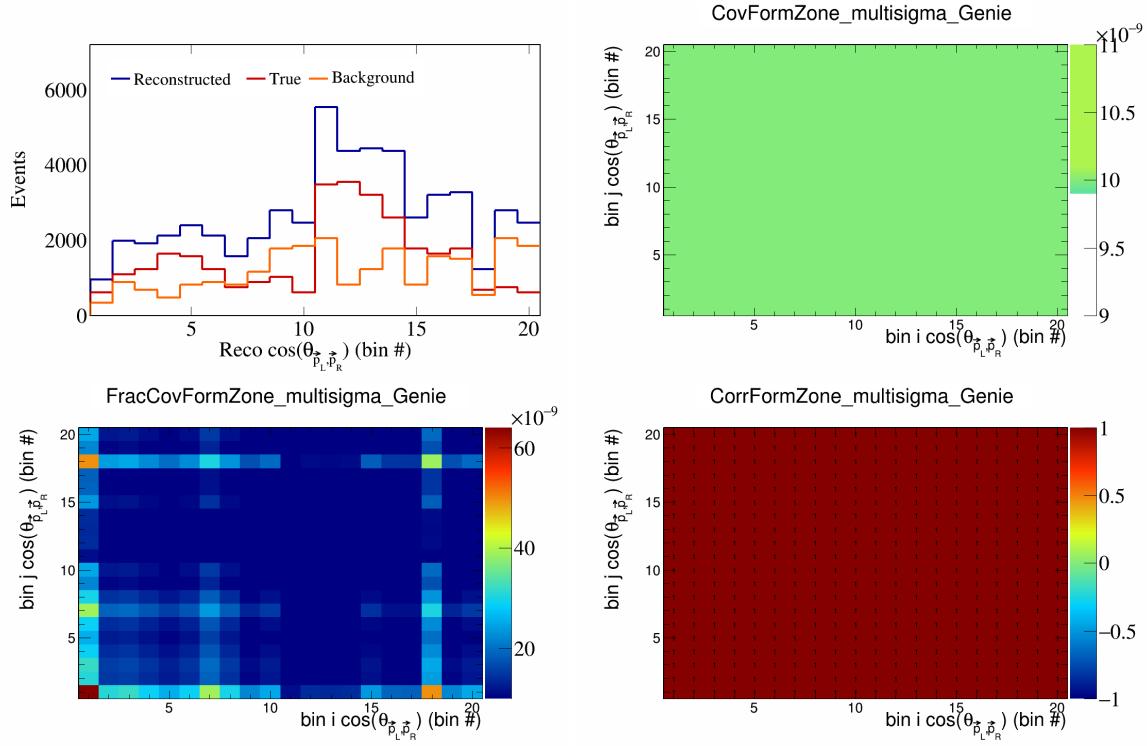


Figure 132: FormZone variations for $\cos(\theta_{\vec{p}_L, \vec{p}_R})$ in $\cos(\theta_{\vec{p}_\mu})$.

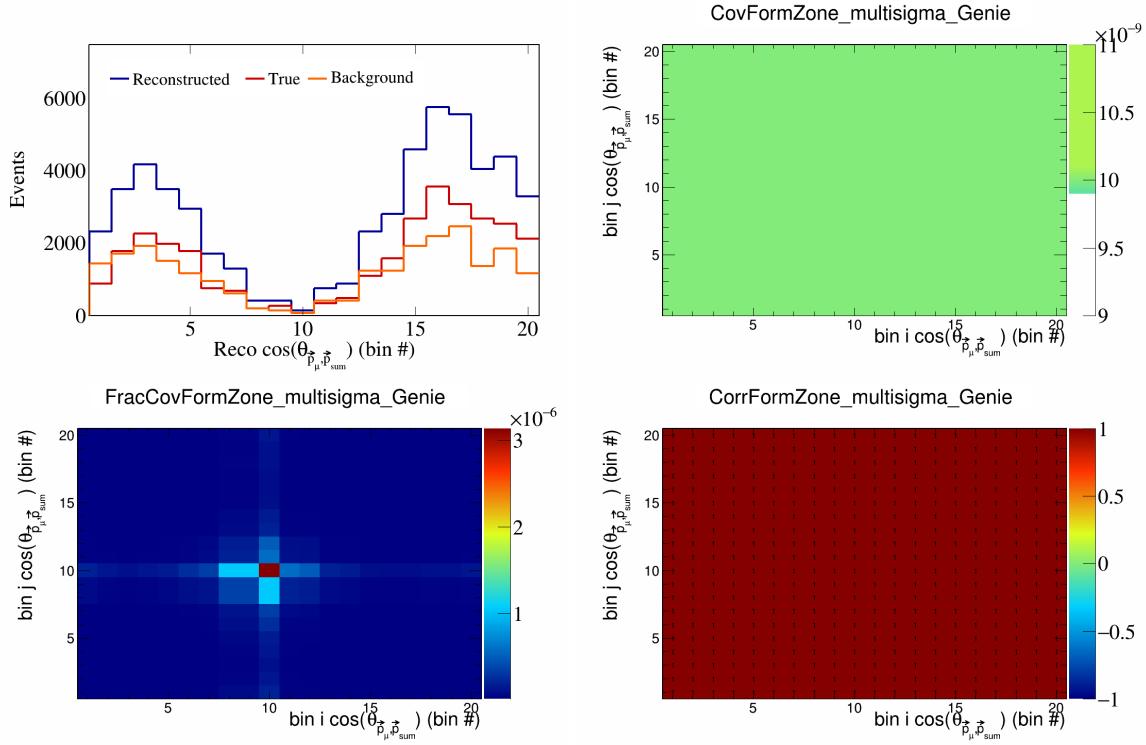


Figure 133: FormZone variations for $\cos(\theta_{\vec{p}_\mu} \cdot \vec{p}_{\text{sum}})$ in $\cos(\theta_{\vec{p}_\mu})$.

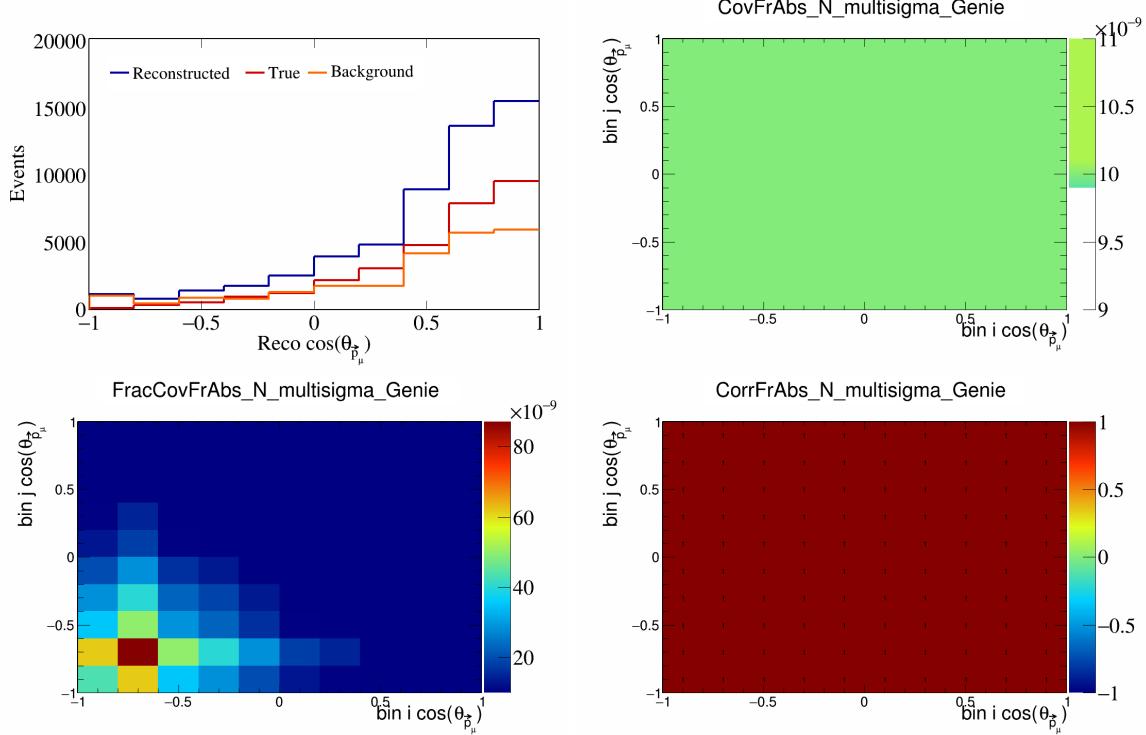


Figure 134: FrAbsN variations for $\cos(\theta_{\vec{p}_\mu})$.

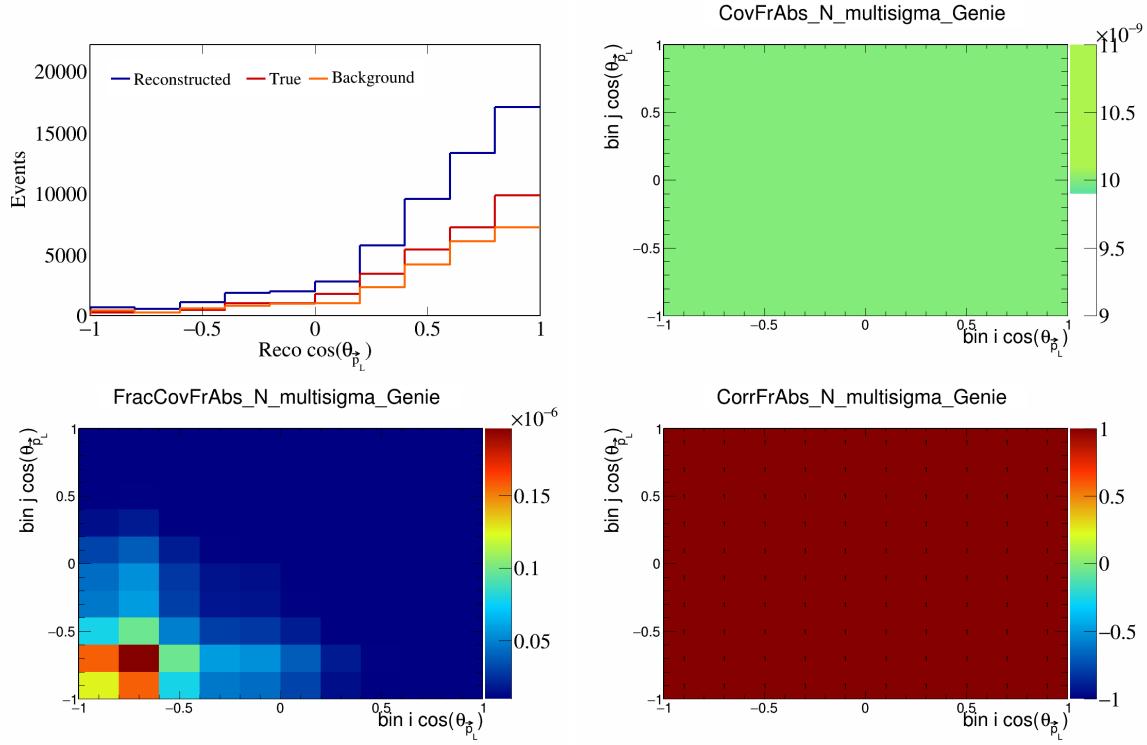


Figure 135: FrAbsN variations for $\cos(\theta_{\vec{p}_L})$.

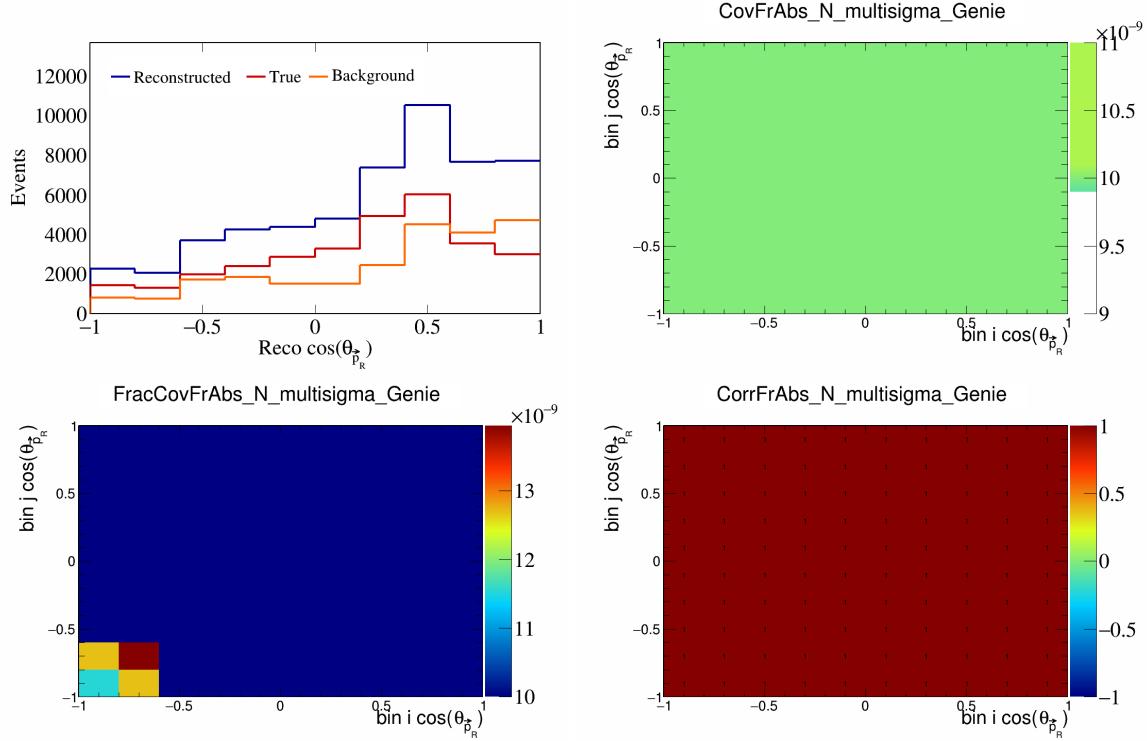


Figure 136: FrAbsN variations for $\cos(\theta_{\vec{p}_R})$.

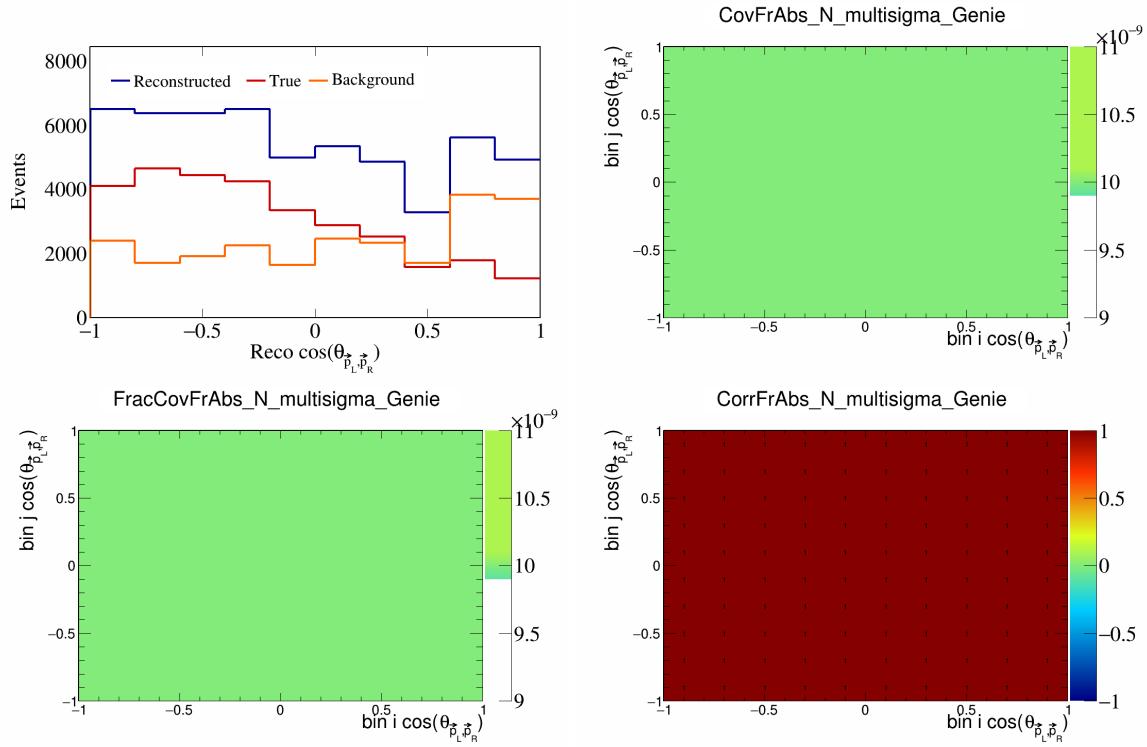


Figure 137: FrAbsN variations for $\cos(\theta_{\vec{p}_L, \vec{p}_R})$.

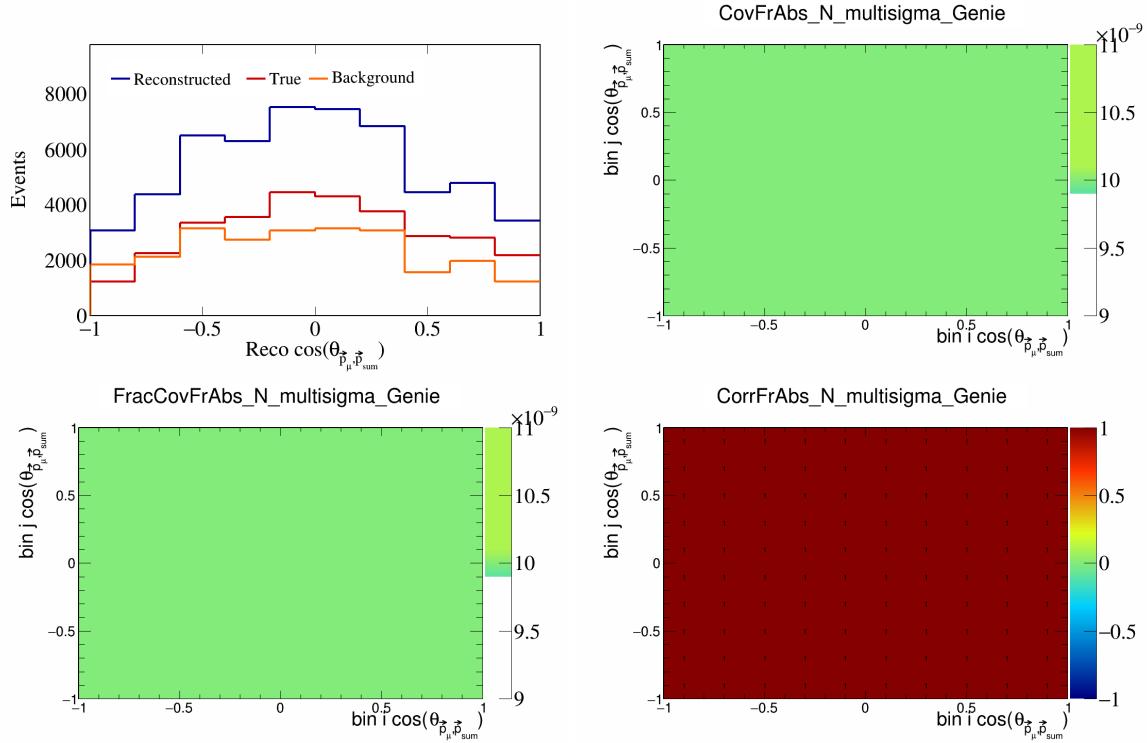


Figure 138: FrAbsN variations for $\cos(\theta_{\vec{p}_\mu, \vec{p}_{\text{sum}}})$.

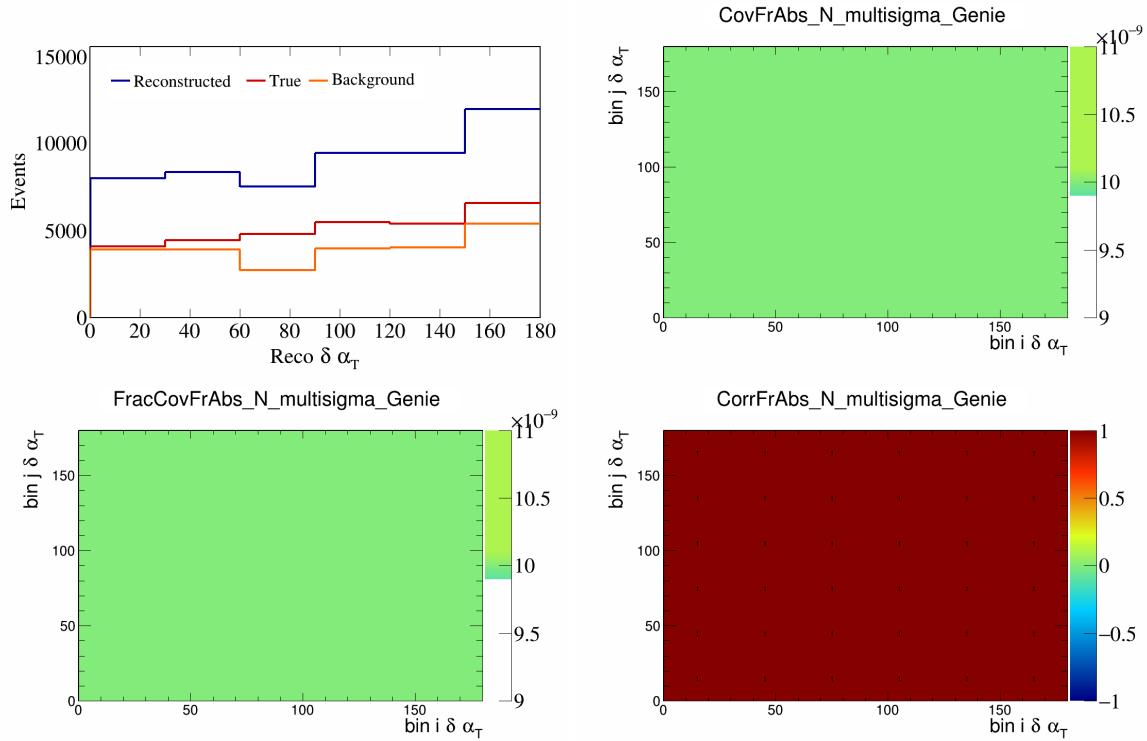


Figure 139: FrAbsN variations for $\delta\alpha_T$.

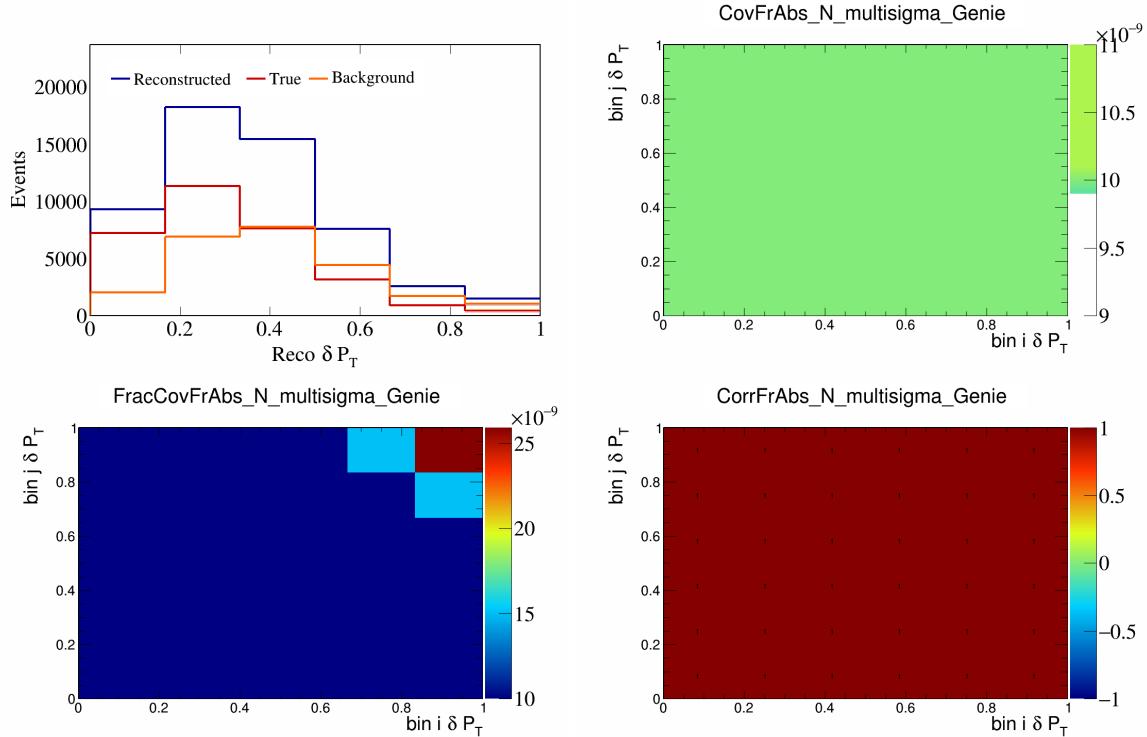


Figure 140: FrAbsN variations for δP_T .

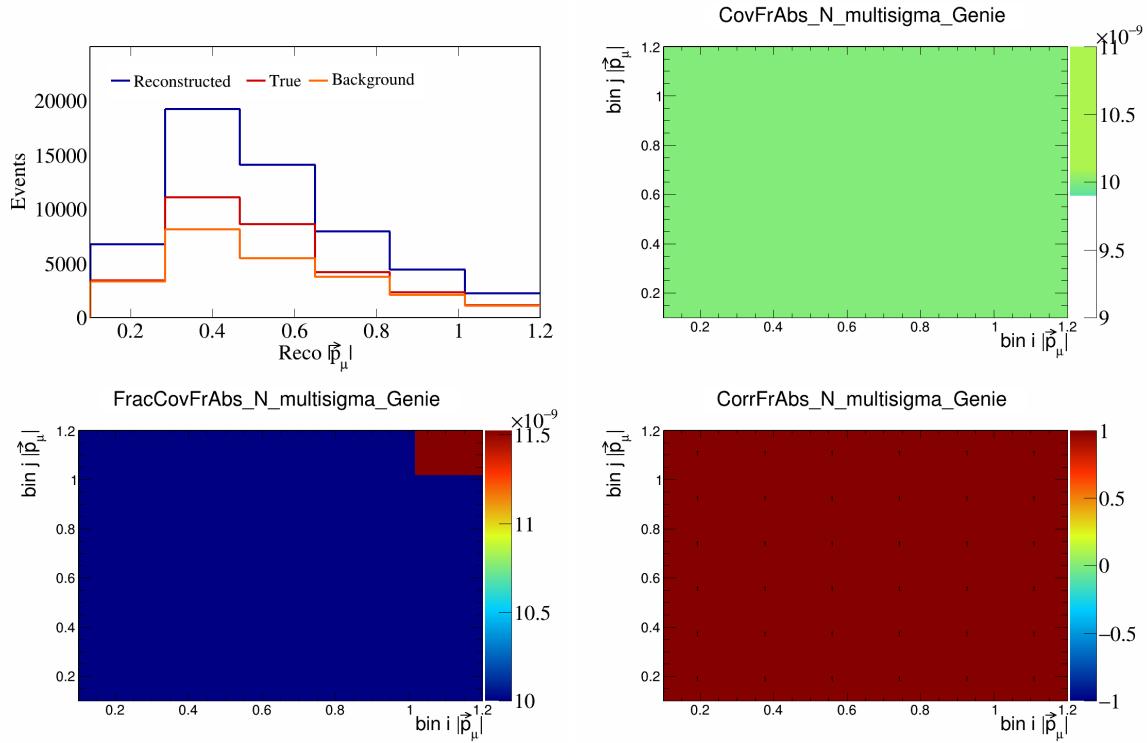


Figure 141: FrAbsN variations for $|\vec{p}_\mu|$.

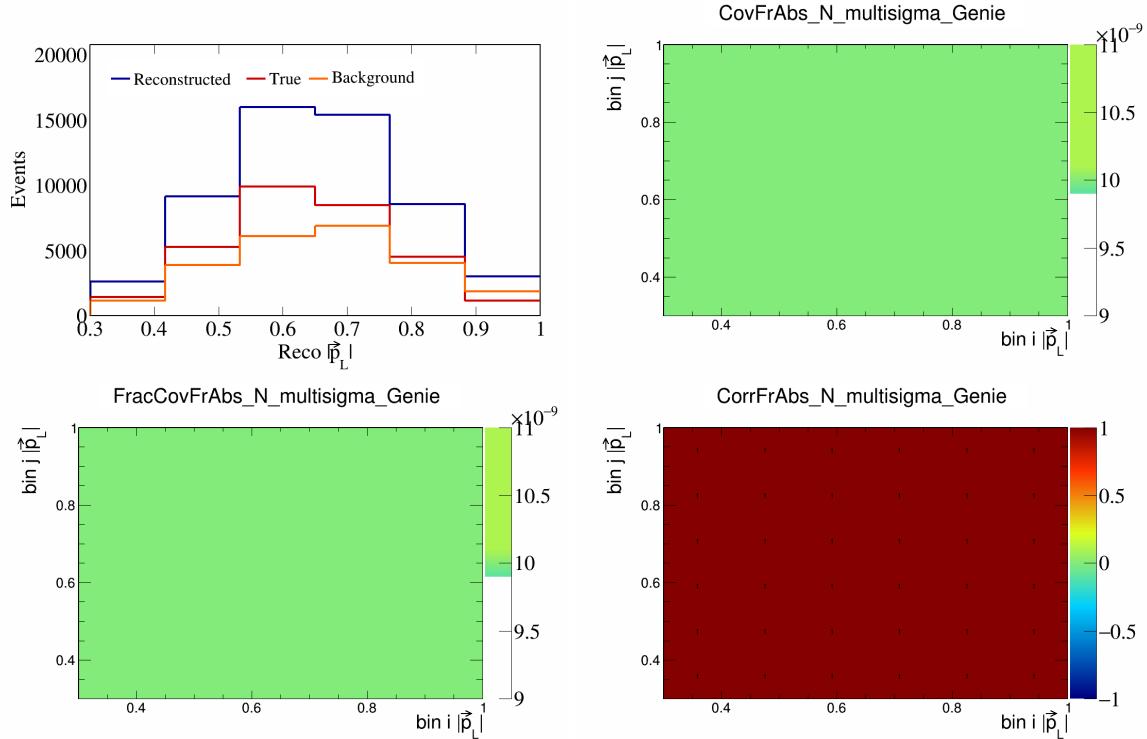


Figure 142: FrAbsN variations for $|\vec{p}_L|$.

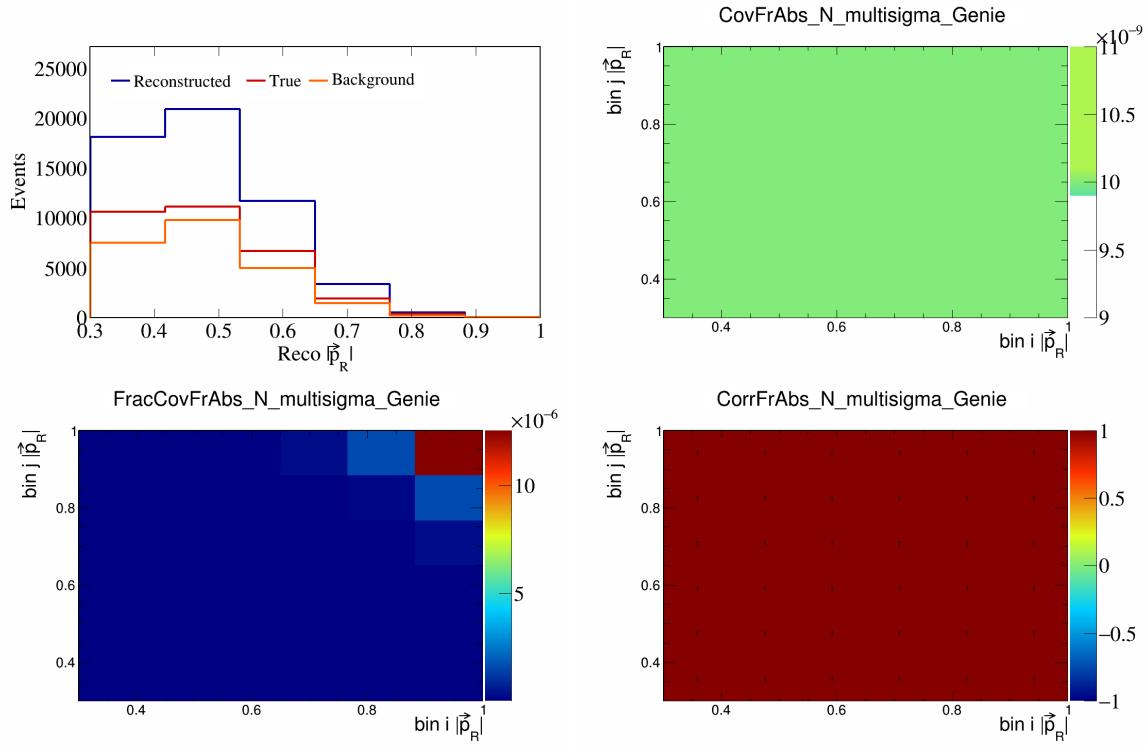


Figure 143: FrAbsN variations for $|\vec{p}_R|$.

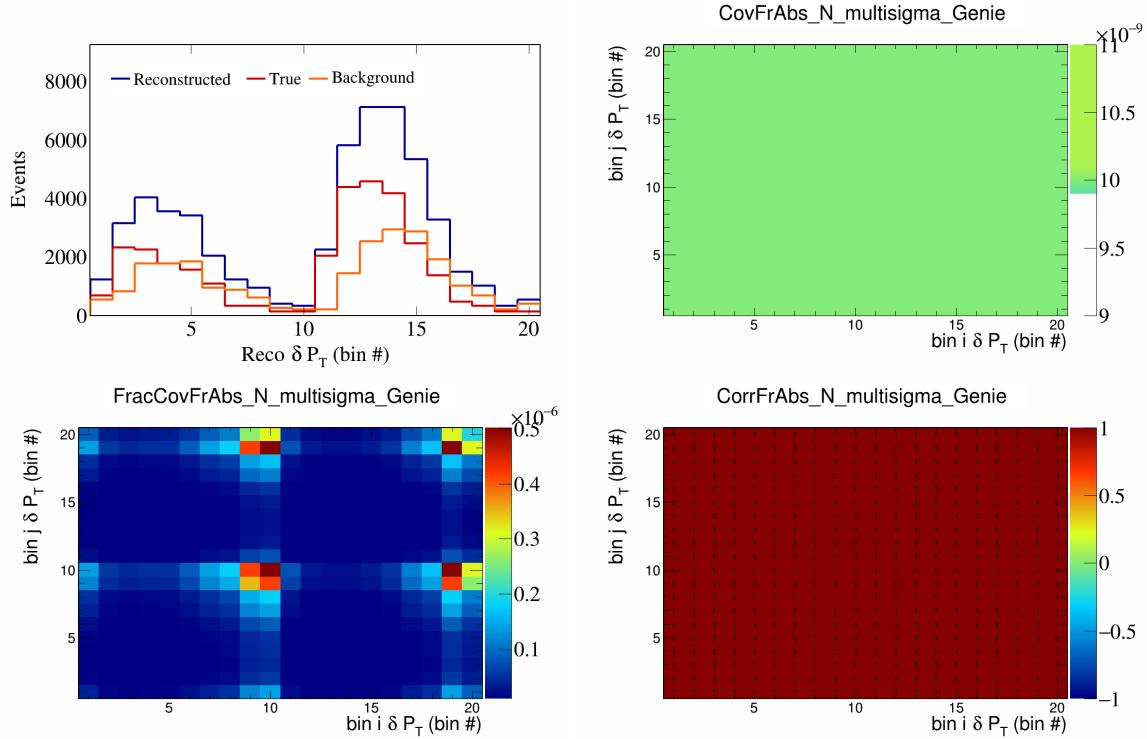


Figure 144: FrAbsN variations for δP_T in $\cos(\theta_{\vec{p}_\mu})$.

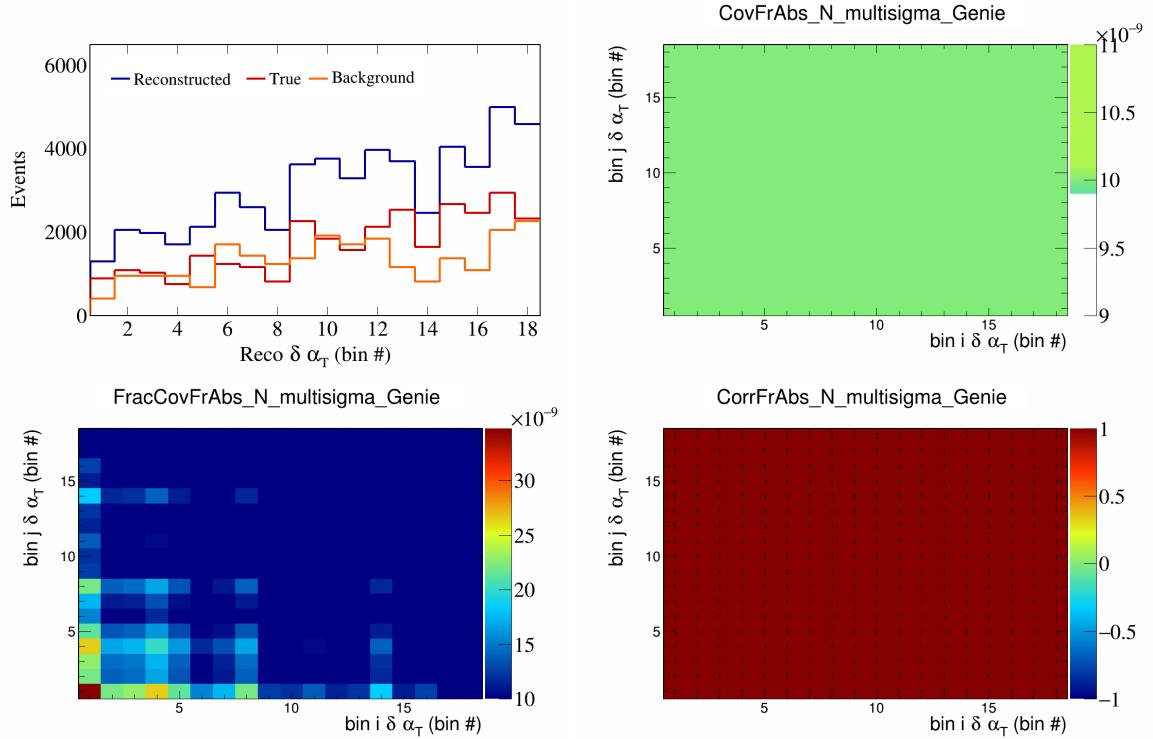


Figure 145: FrAbsN variations for $\delta\alpha_T$ in $\cos(\theta_{\vec{p}_\mu})$.

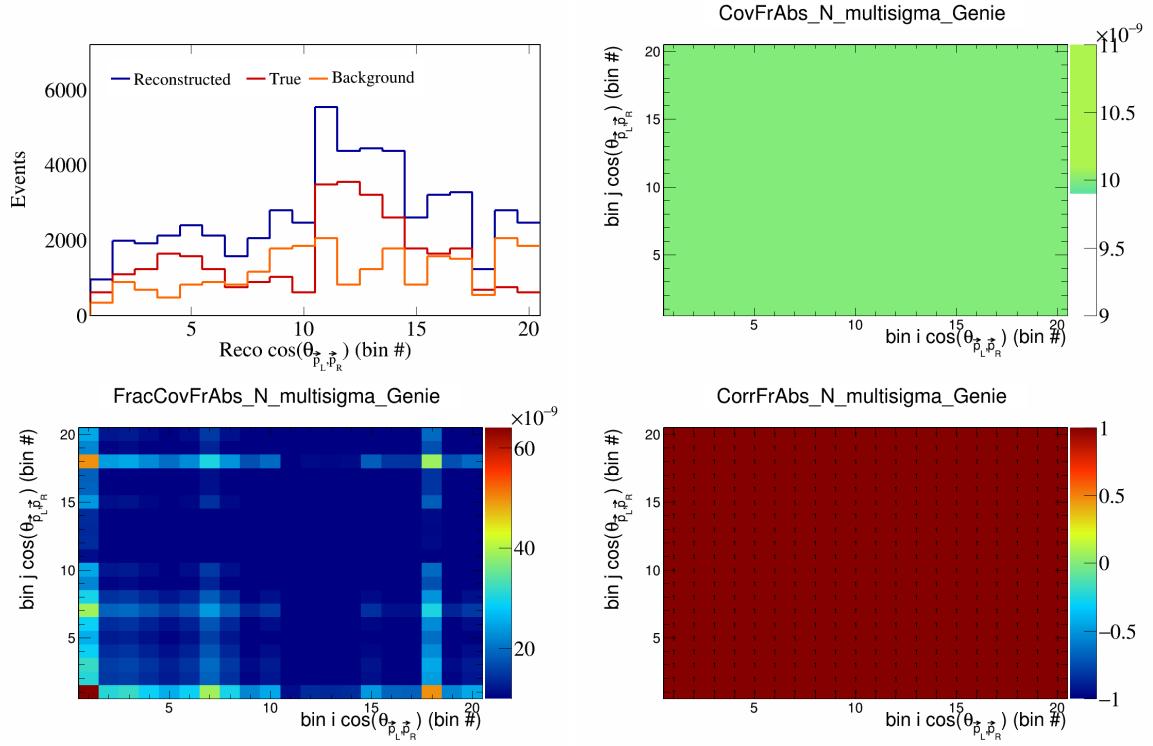


Figure 146: FrAbsN variations for $\cos(\theta_{\vec{p}_L, \vec{p}_R})$ in $\cos(\theta_{\vec{p}_\mu})$.

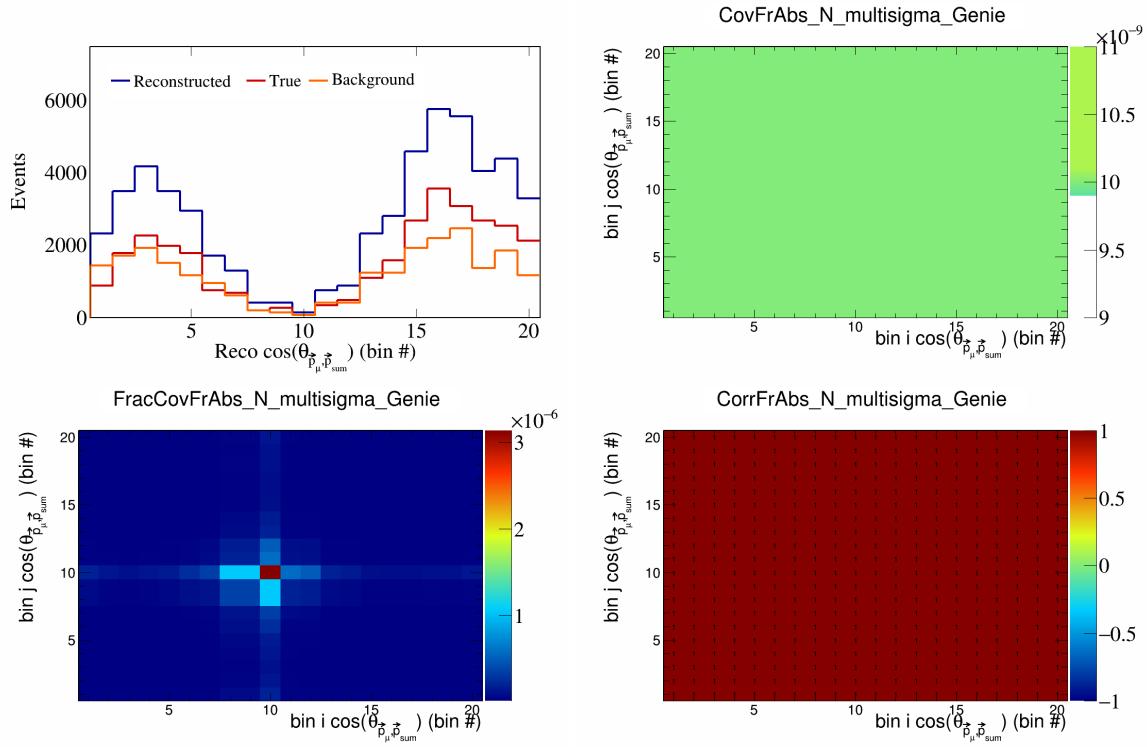


Figure 147: FrAbsN variations for $\cos(\theta_{\vec{p}_\mu})$ in $\cos(\theta_{\vec{p}_\mu})$.

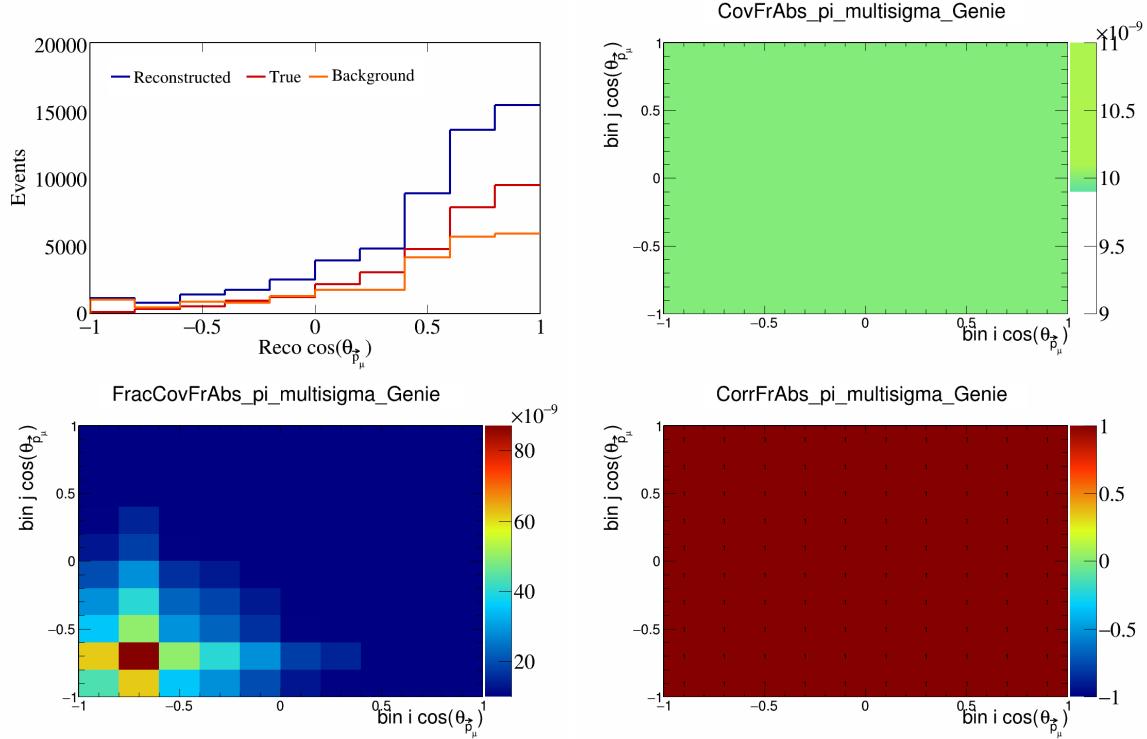


Figure 148: FrAbspi variations for $\cos(\theta_{\vec{p}_\mu})$.

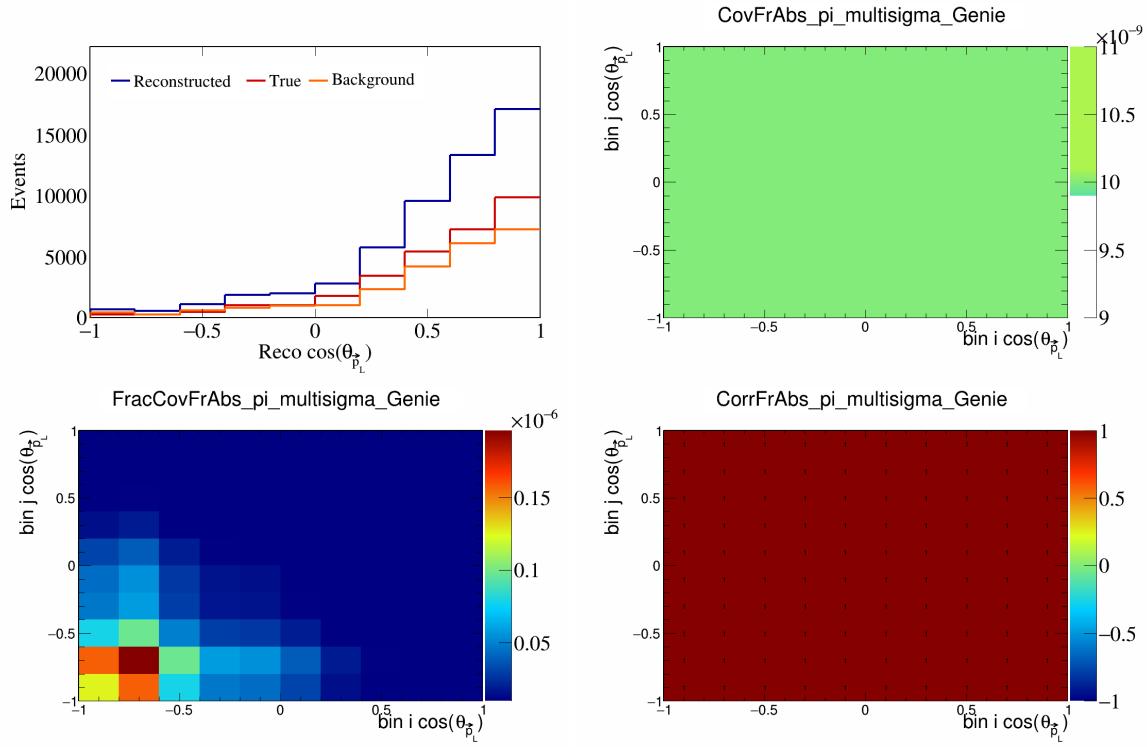


Figure 149: FrAbspi variations for $\cos(\theta_{\vec{p}_L})$.

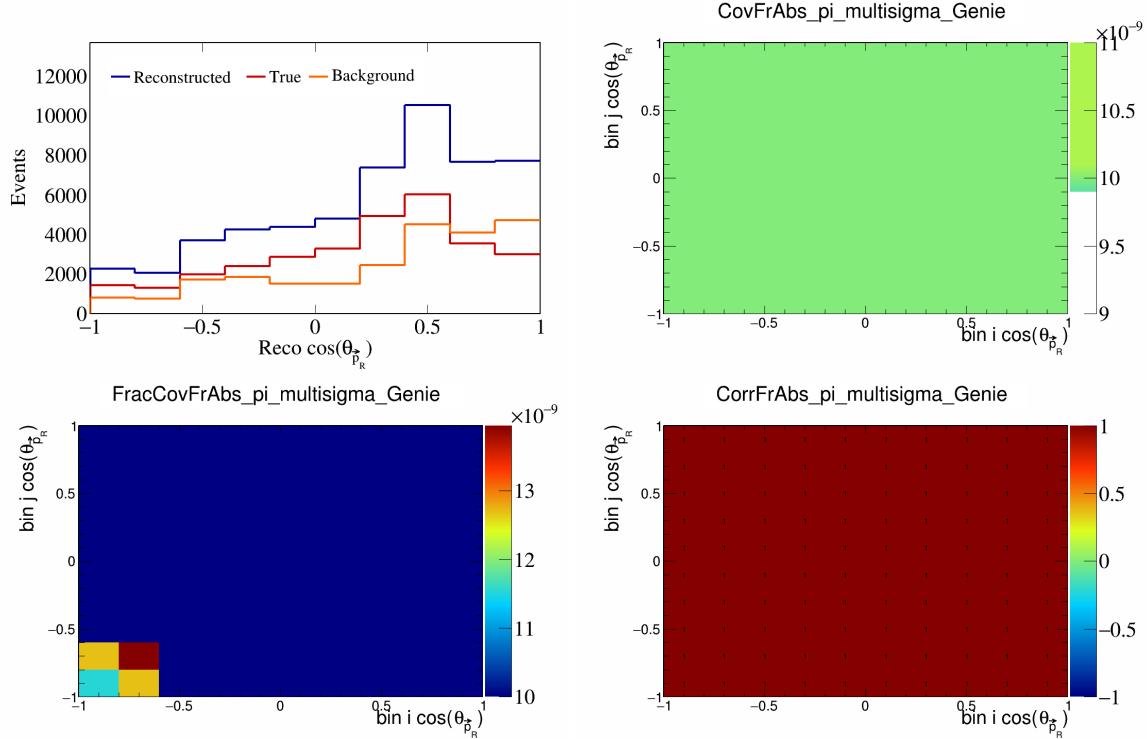


Figure 150: FrAbspi variations for $\cos(\theta_{\vec{p}_R})$.

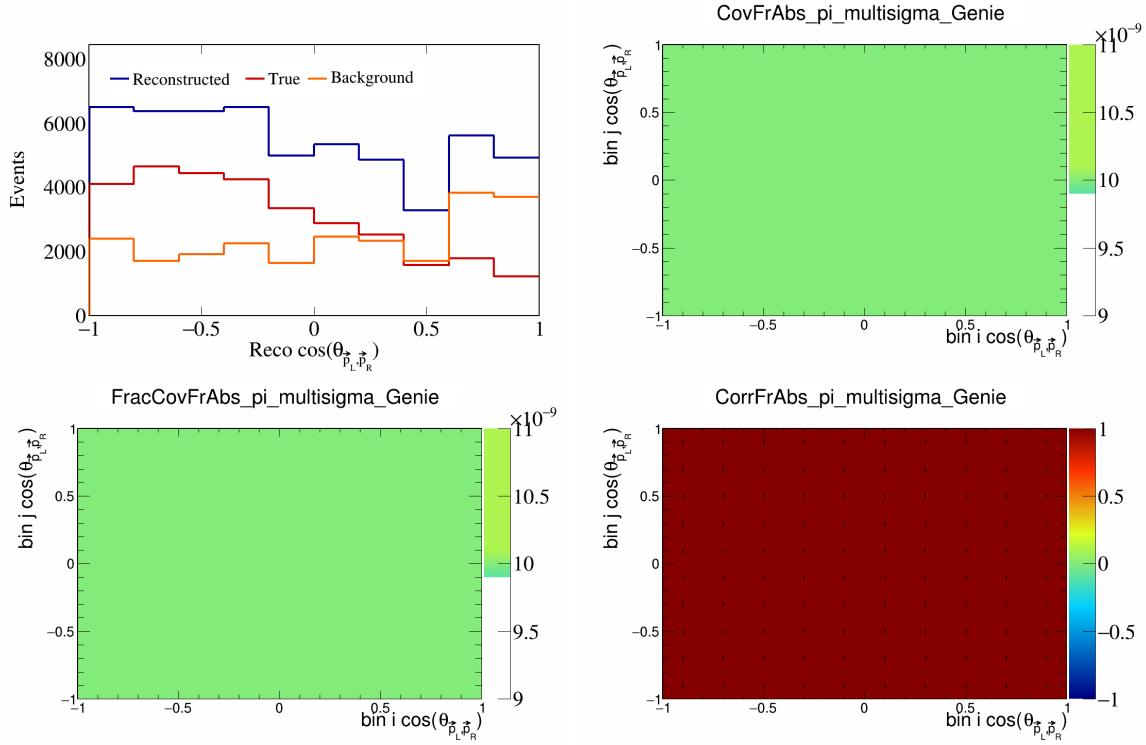


Figure 151: FrAbspi variations for $\cos(\theta_{\vec{p}_L, \vec{p}_R})$.

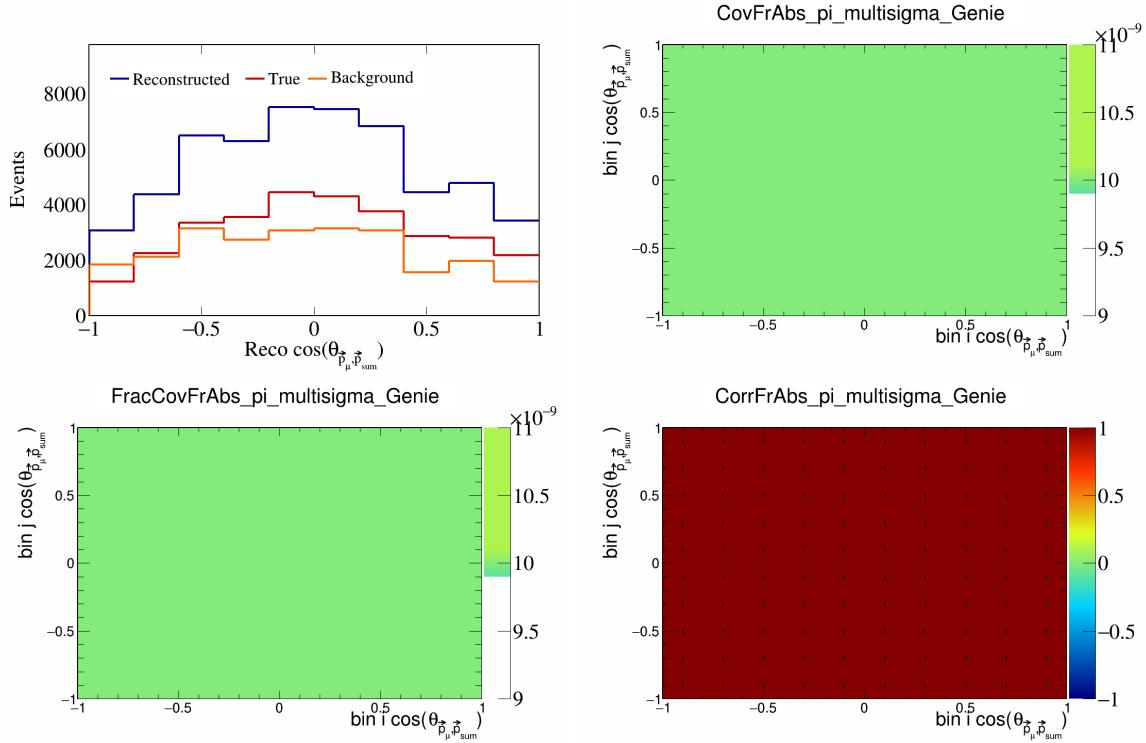


Figure 152: FrAbspi variations for $\cos(\theta_{\vec{p}_\mu, \vec{p}_{\text{sum}}})$.

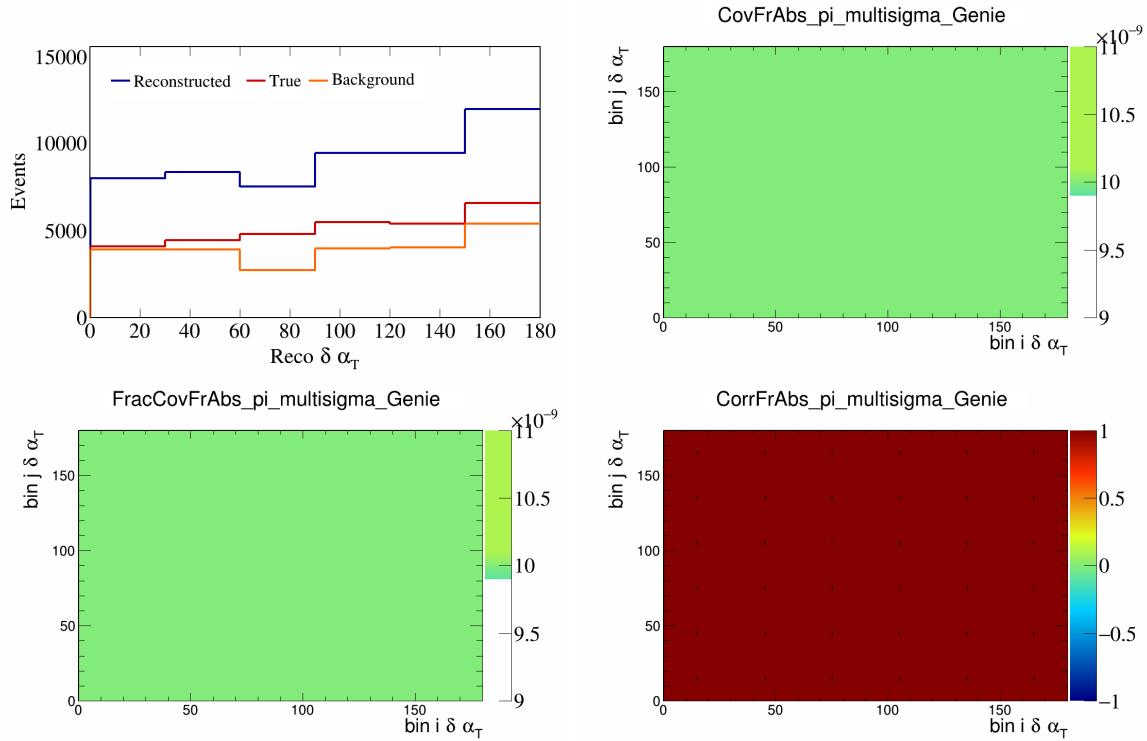


Figure 153: FrAbspi variations for $\delta\alpha_T$.

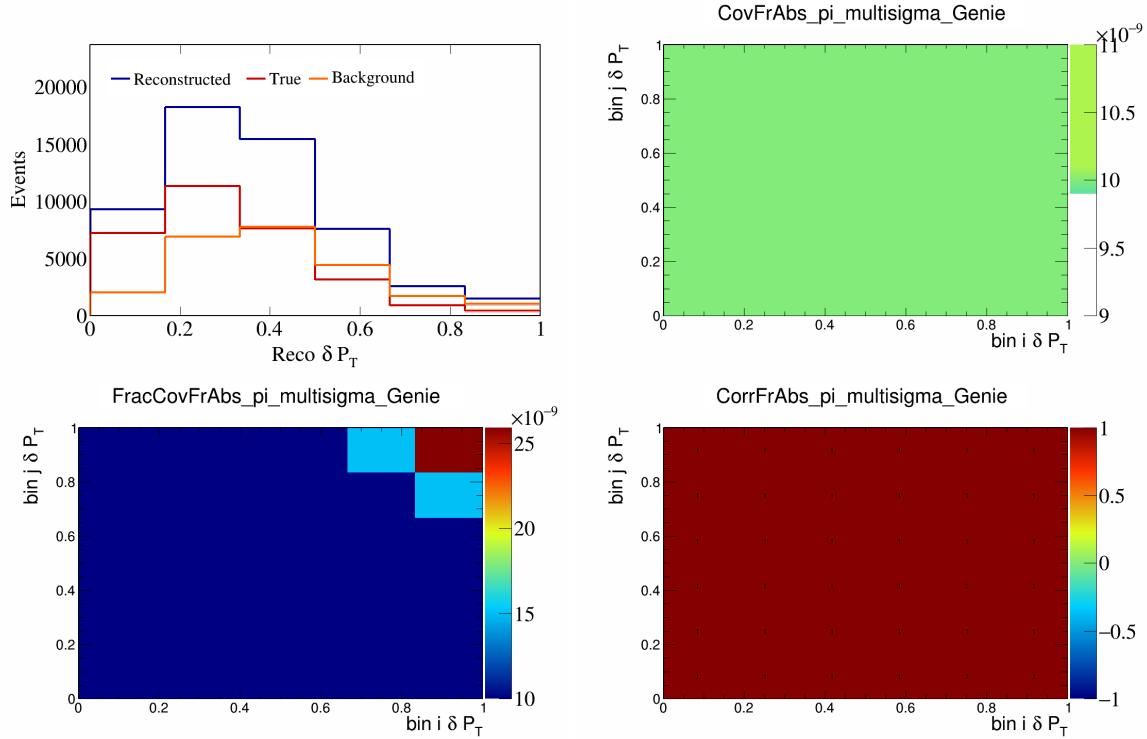


Figure 154: FrAbspi variations for δP_T .

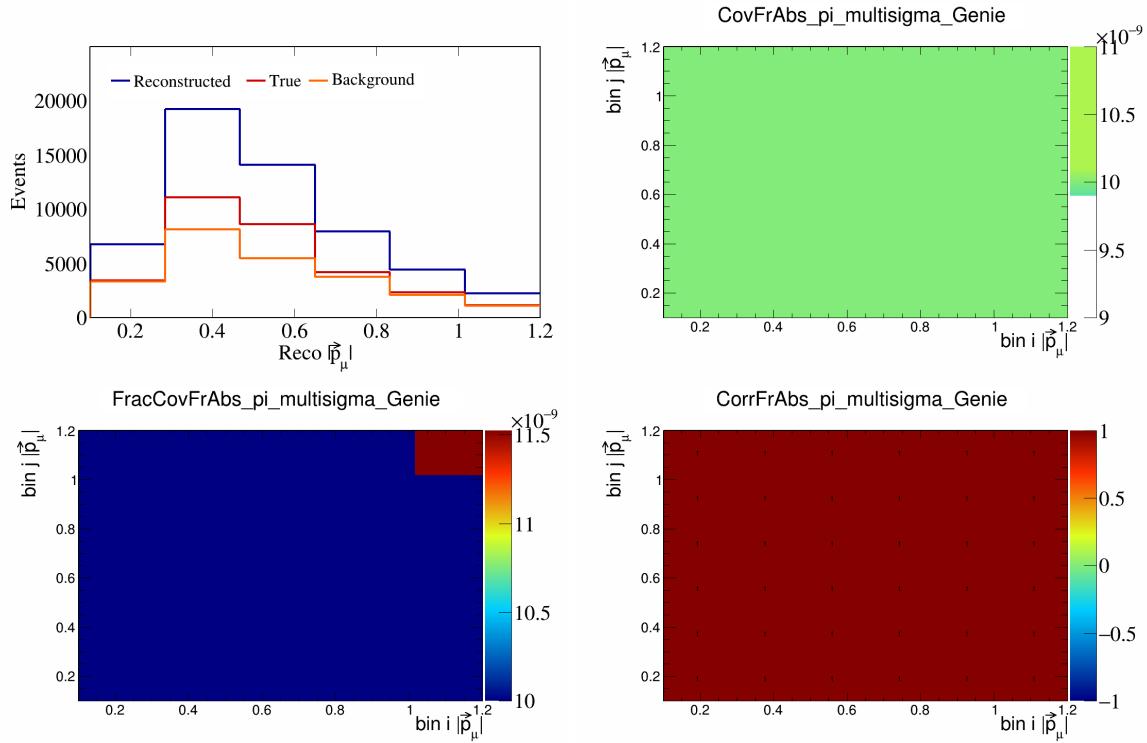


Figure 155: FrAbspi variations for $|\vec{p}_\mu|$.

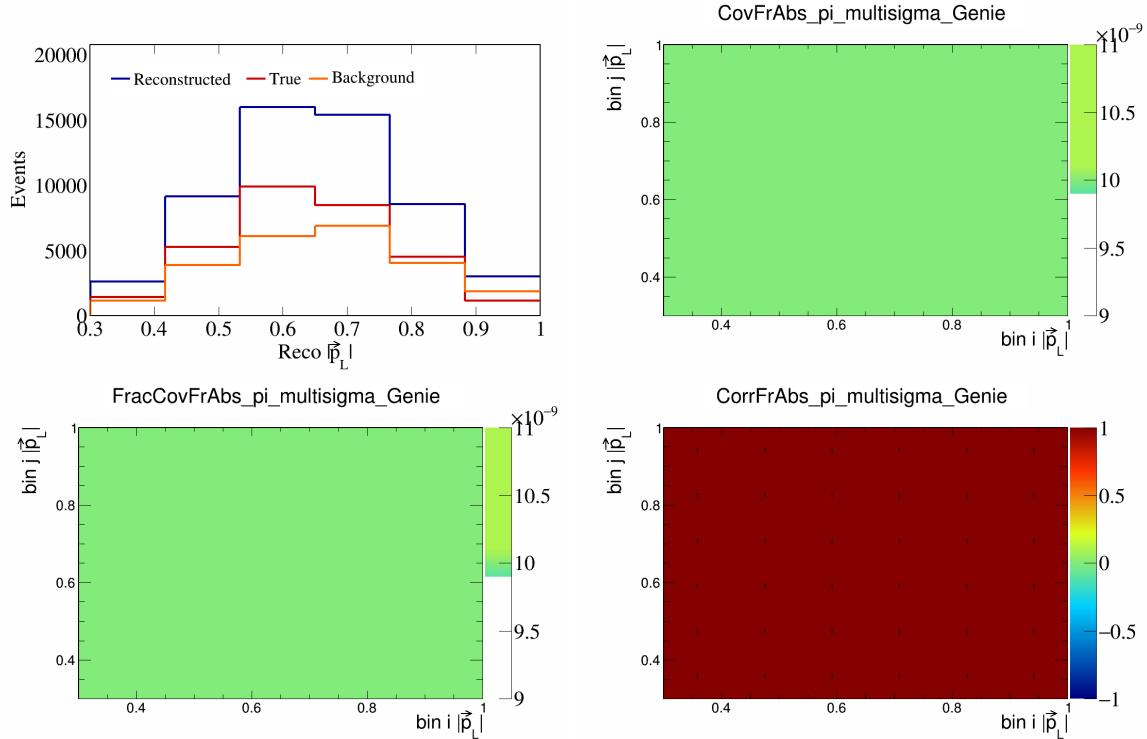


Figure 156: FrAbspi variations for $|\vec{p}_L|$.

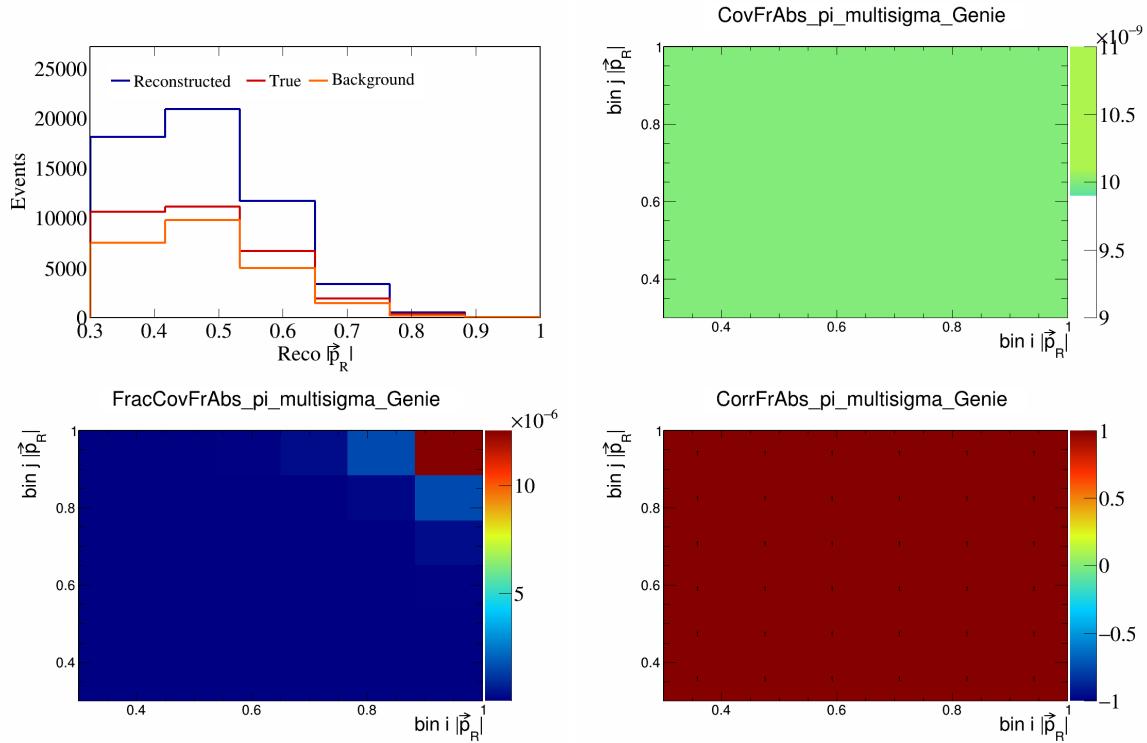


Figure 157: FrAbspi variations for $|\vec{p}_R|$.

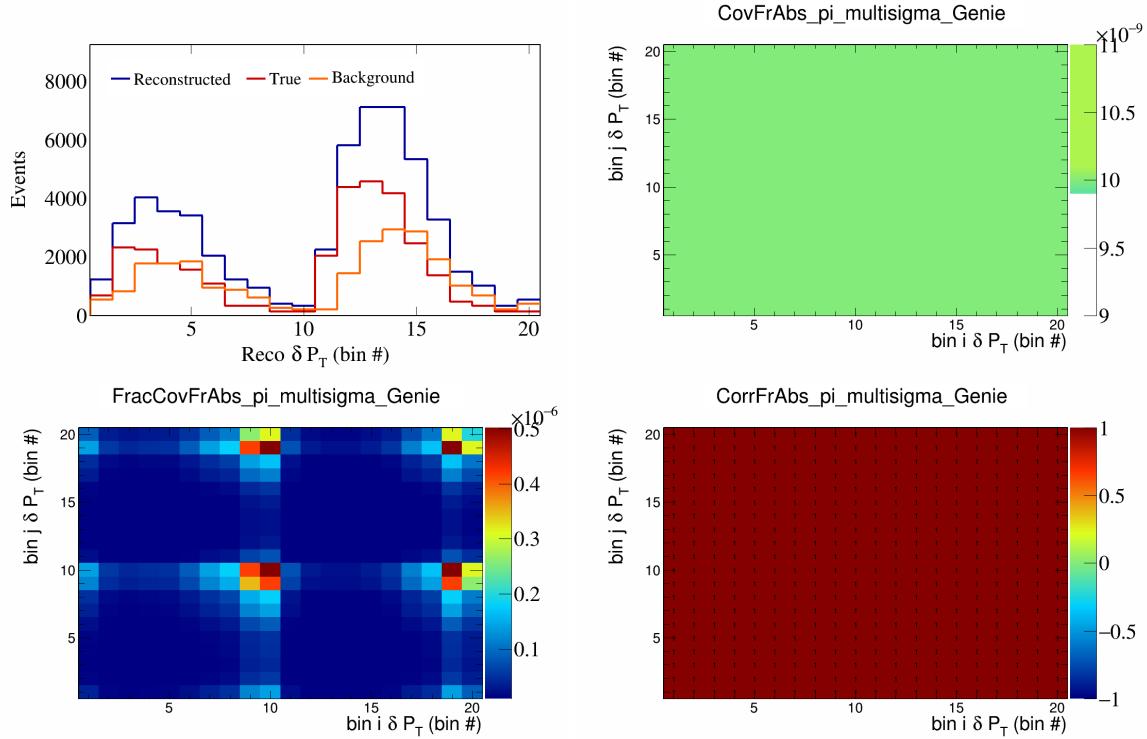


Figure 158: FrAbspi variations for δP_T in $\cos(\theta_{\vec{p}_\mu})$.

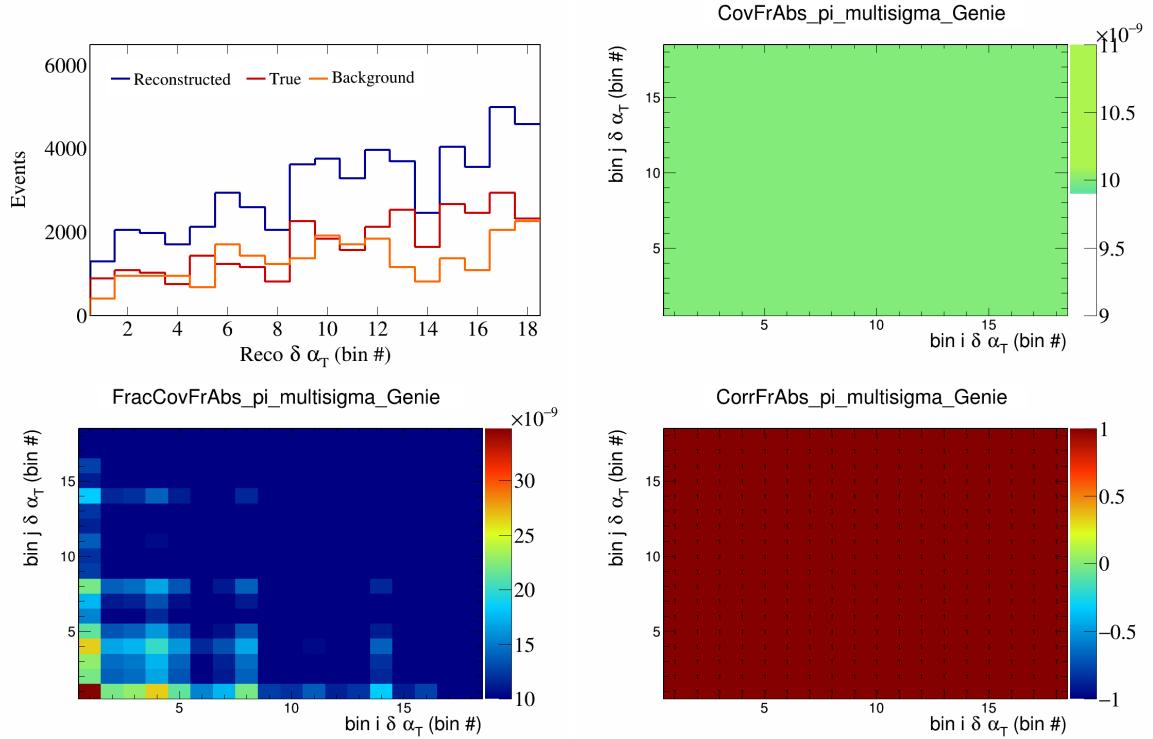


Figure 159: FrAbspi variations for $\delta\alpha_T$ in $\cos(\theta_{\vec{p}_\mu})$.

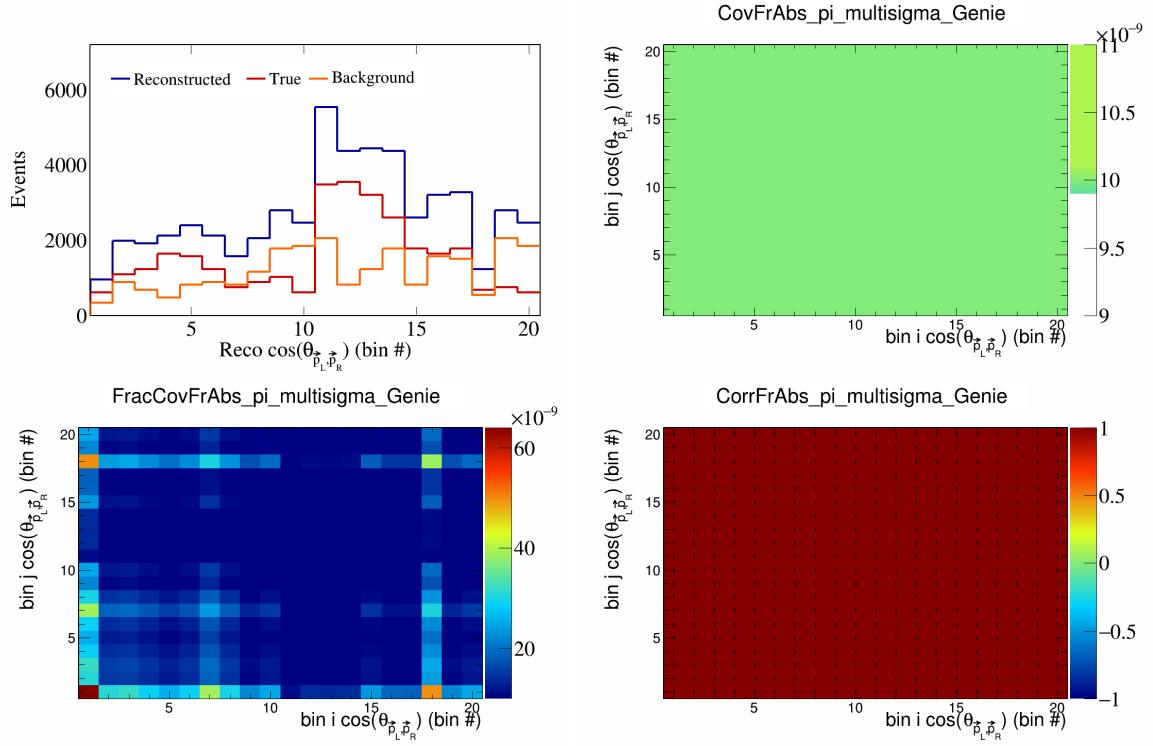


Figure 160: FrAbspi variations for $\cos(\theta_{\vec{p}_L, \vec{p}_R})$ in $\cos(\theta_{\vec{p}_\mu})$.

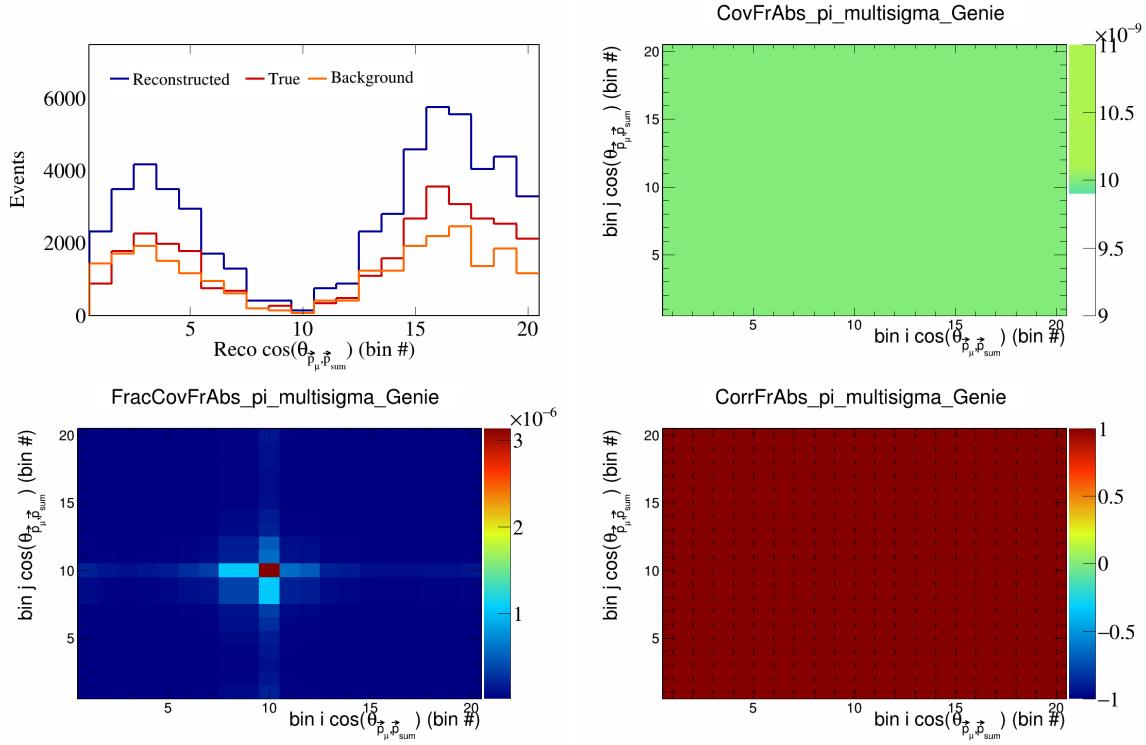


Figure 161: FrAbspi variations for $\cos(\theta_{\vec{p}_\mu})$ in $\cos(\theta_{\vec{p}_\mu})$.

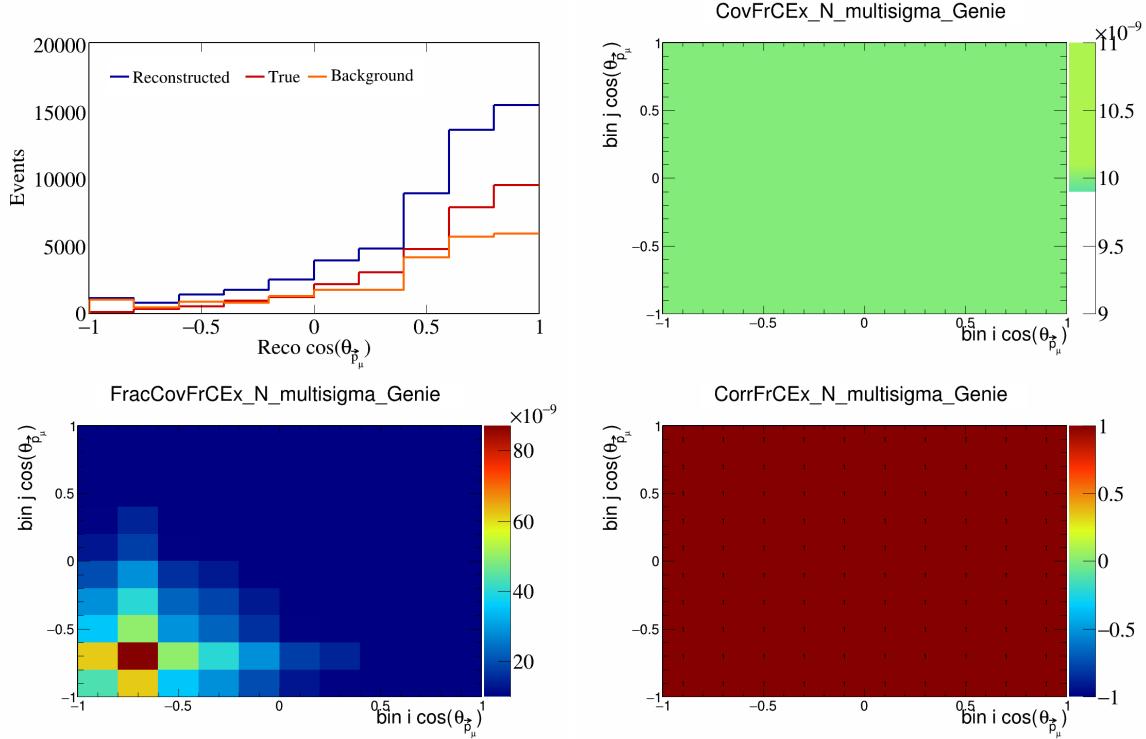


Figure 162: FrCExN variations for $\cos(\theta_{\vec{p}_\mu})$.

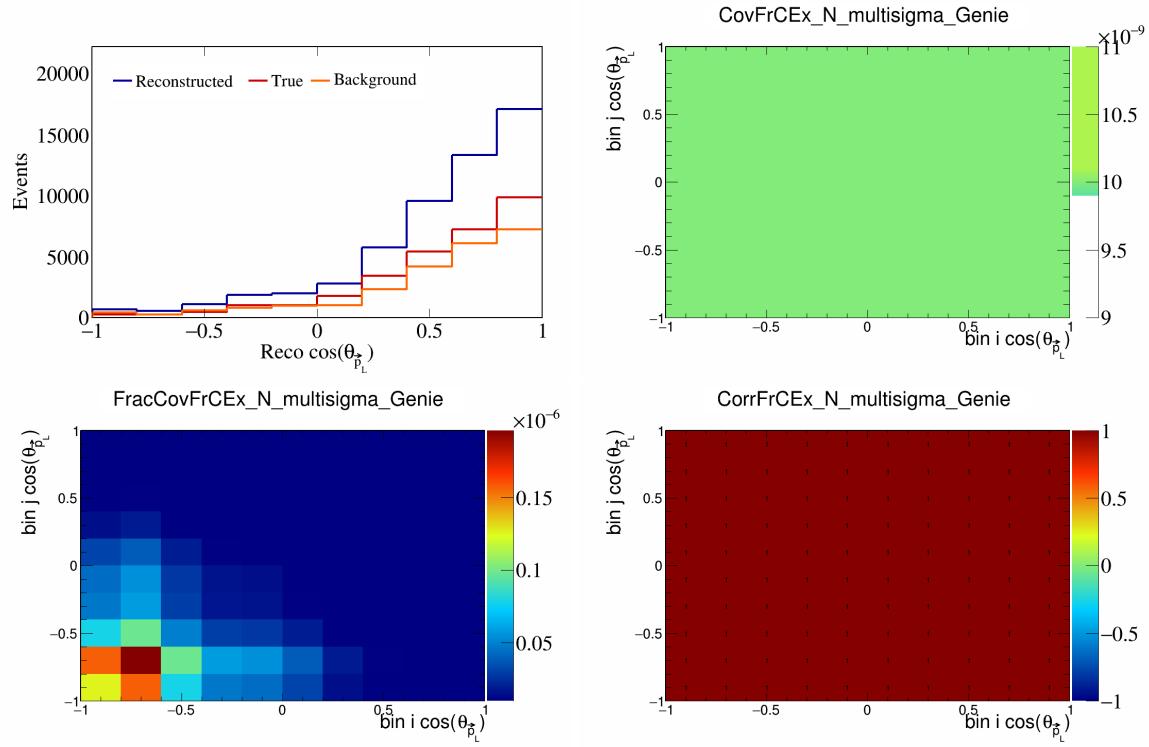


Figure 163: FrCExN variations for $\cos(\theta_{\vec{p}_L})$.

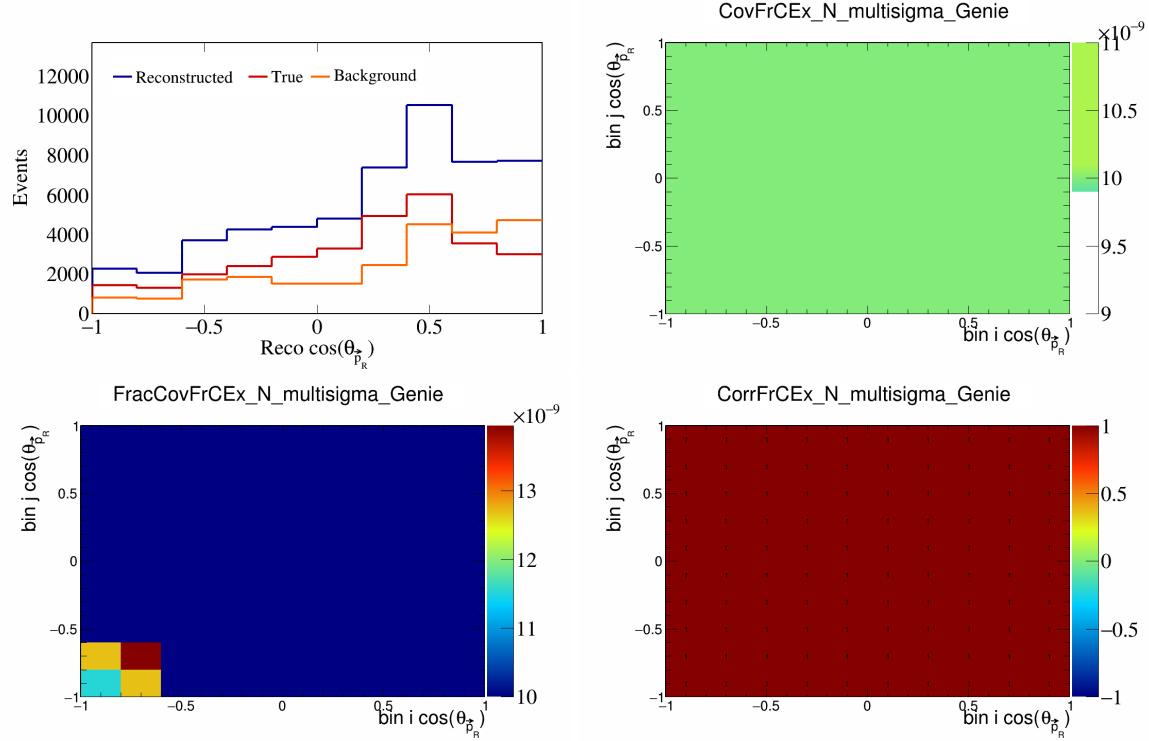


Figure 164: FrCExN variations for $\cos(\theta_{\vec{p}_R})$.

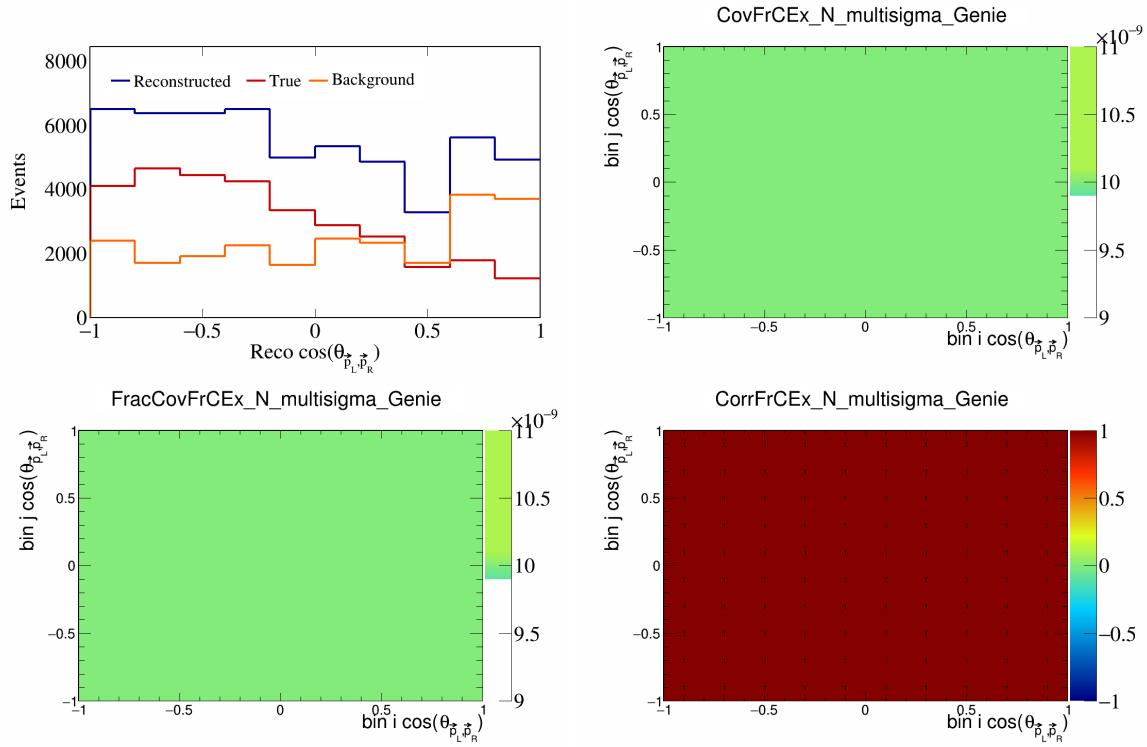


Figure 165: FrCEExN variations for $\cos(\theta_{\vec{p}_L, \vec{p}_R})$.

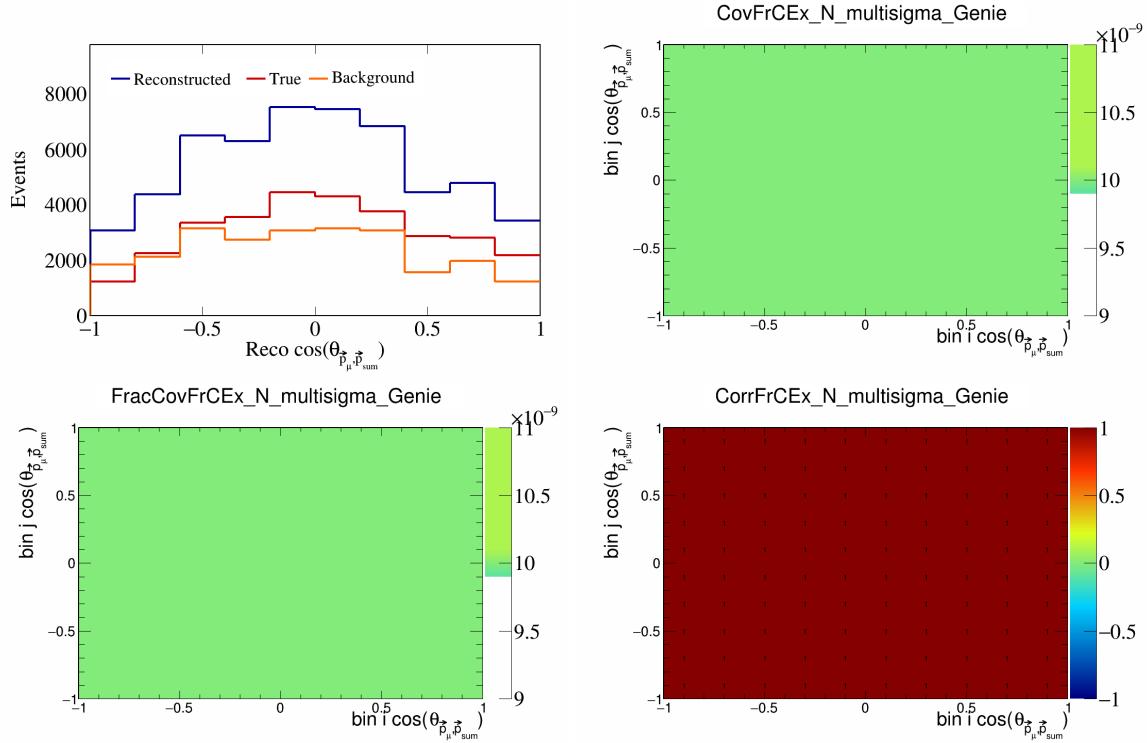


Figure 166: FrCEExN variations for $\cos(\theta_{\vec{p}_\mu, \vec{p}_{\text{sum}}})$.

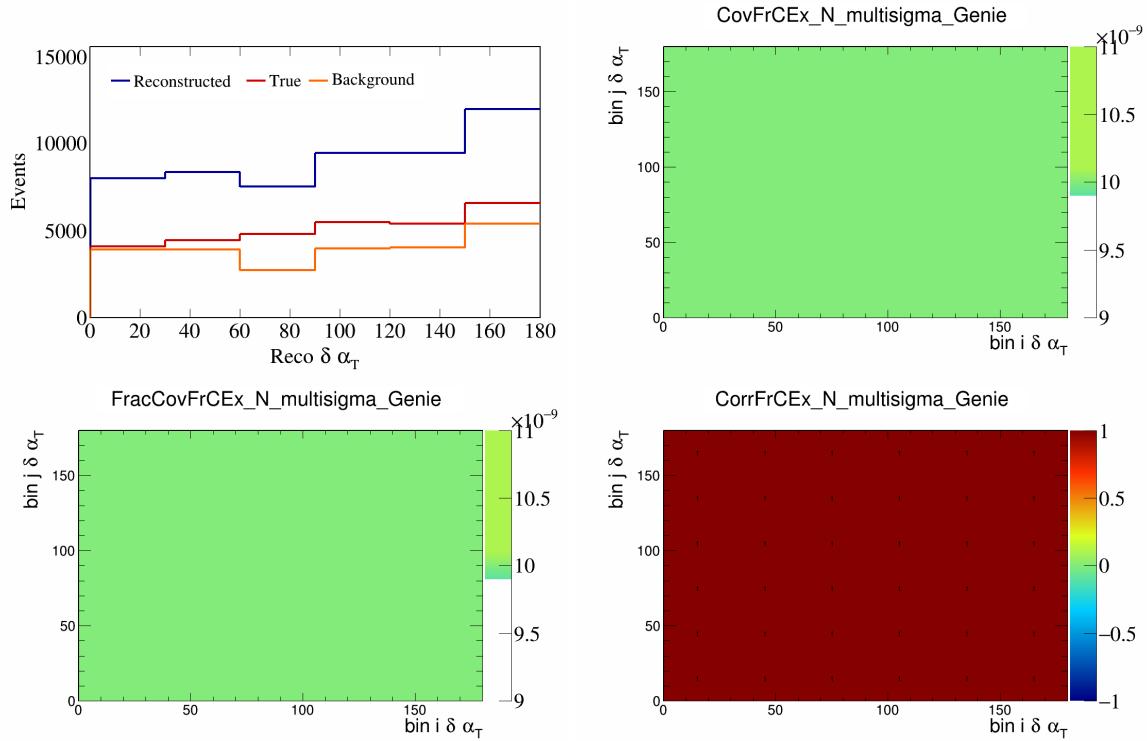


Figure 167: FrCEExN variations for $\delta\alpha_T$.

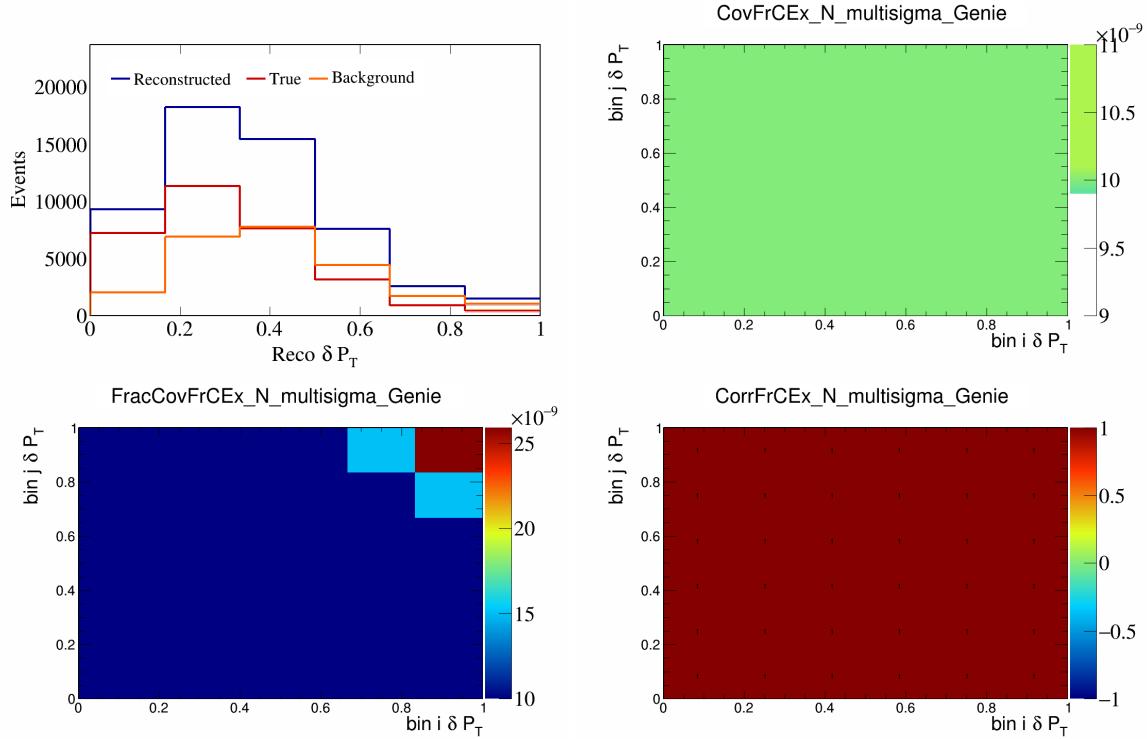


Figure 168: FrCEExN variations for δP_T .

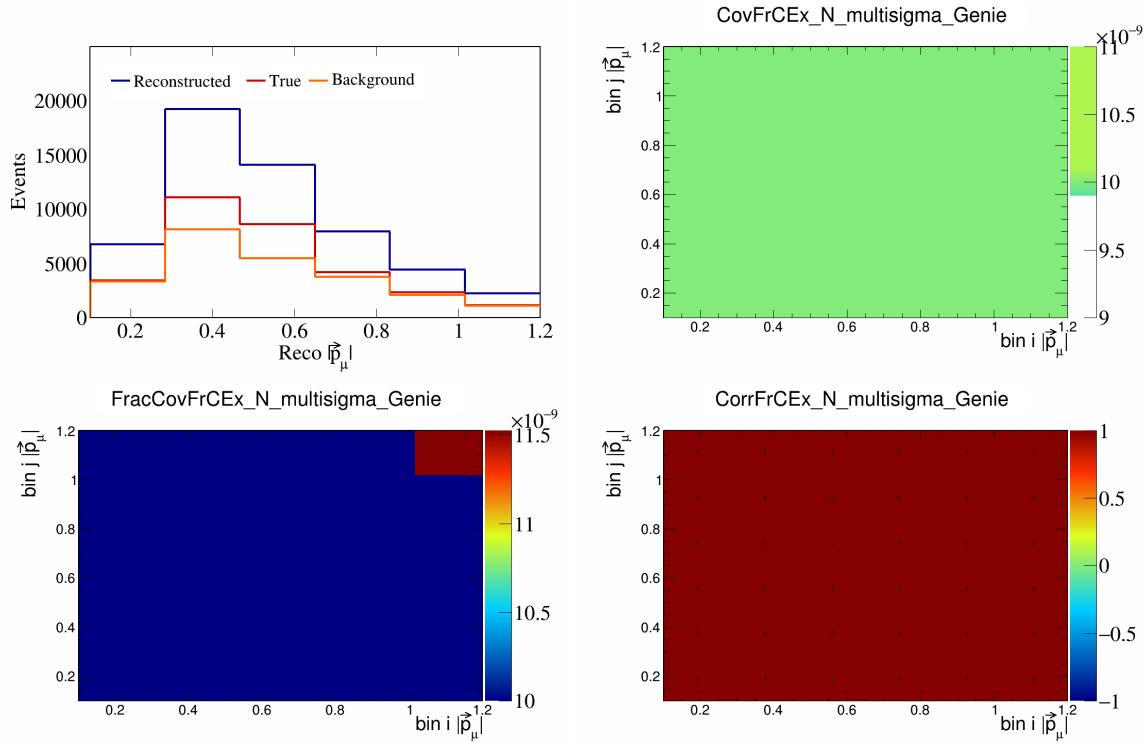


Figure 169: FrCExN variations for $|\vec{p}_\mu|$.

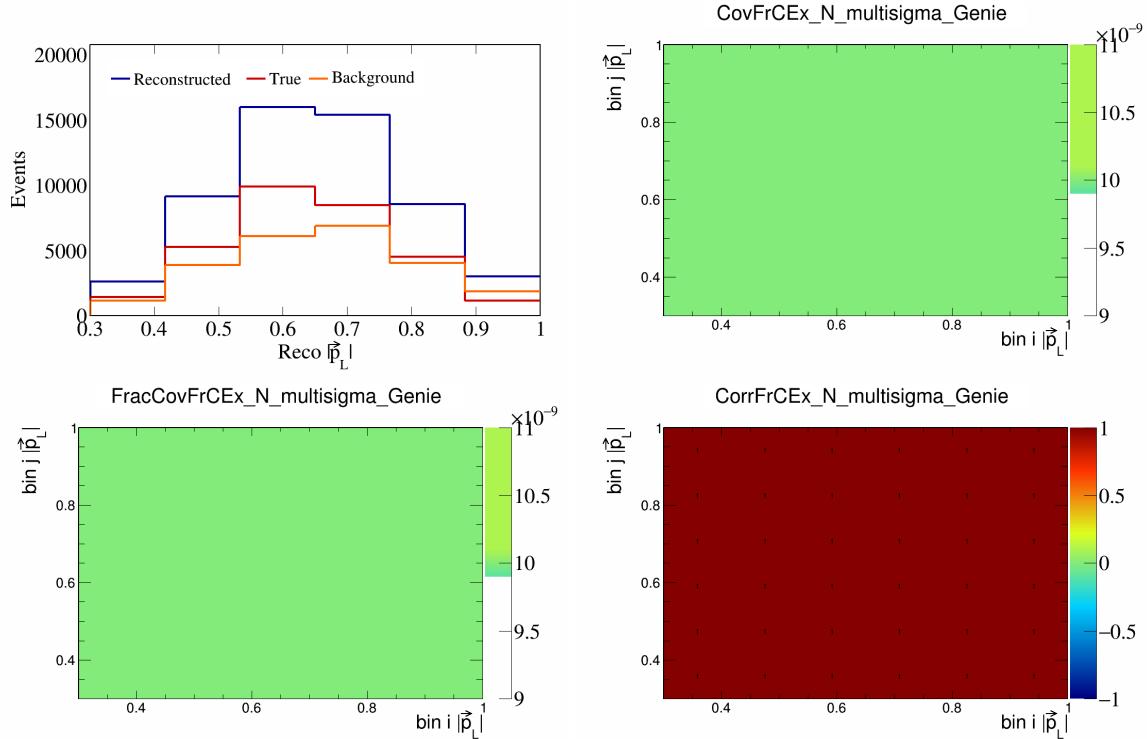


Figure 170: FrCExN variations for $|\vec{p}_L|$.

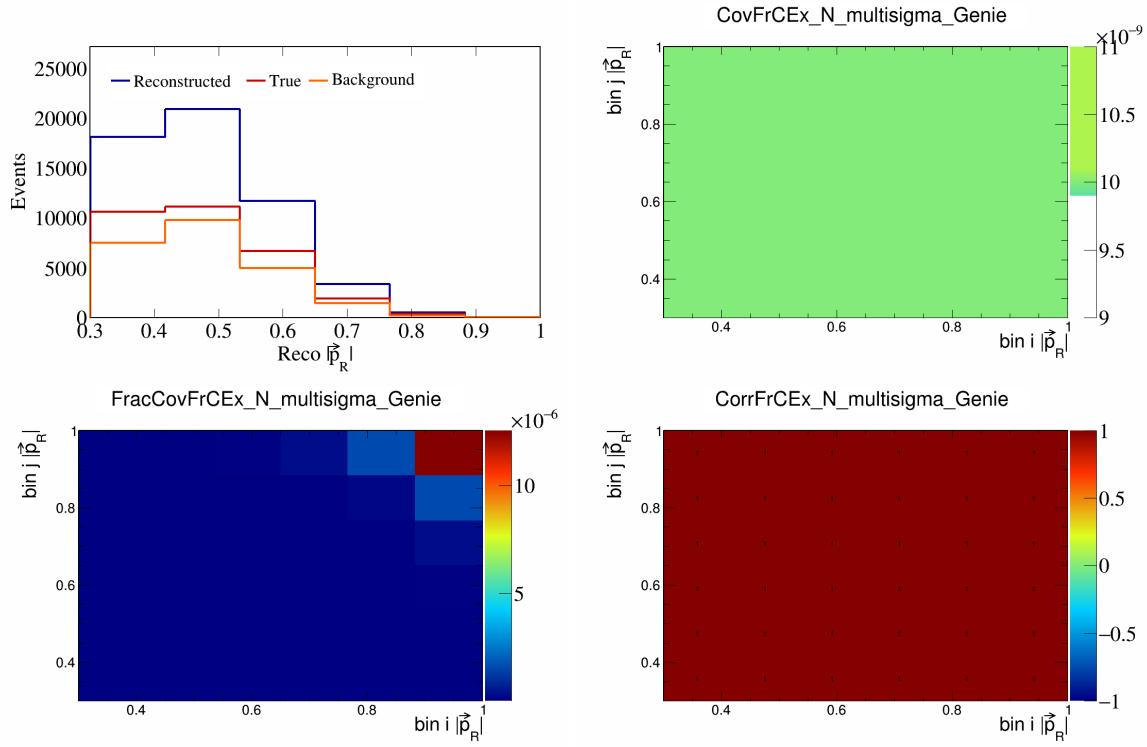


Figure 171: FrCEExN variations for $|\vec{p}_R|$.

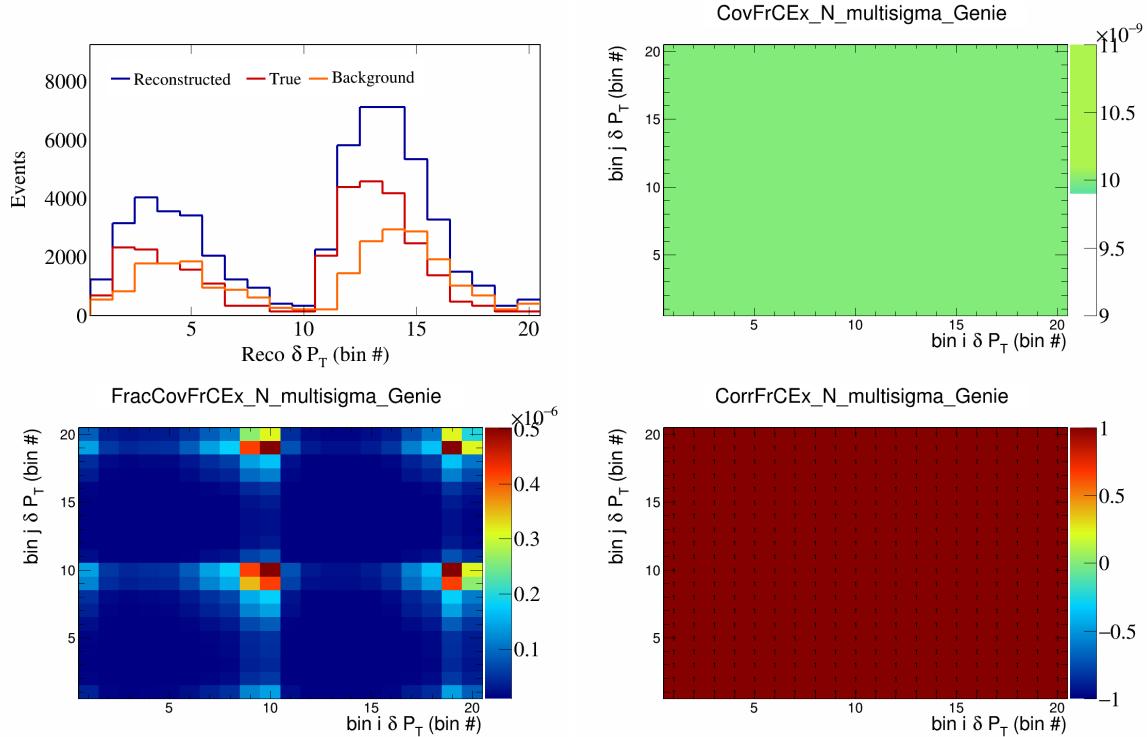


Figure 172: FrCEExN variations for δP_T in $\cos(\theta_{\vec{p}_\mu})$.

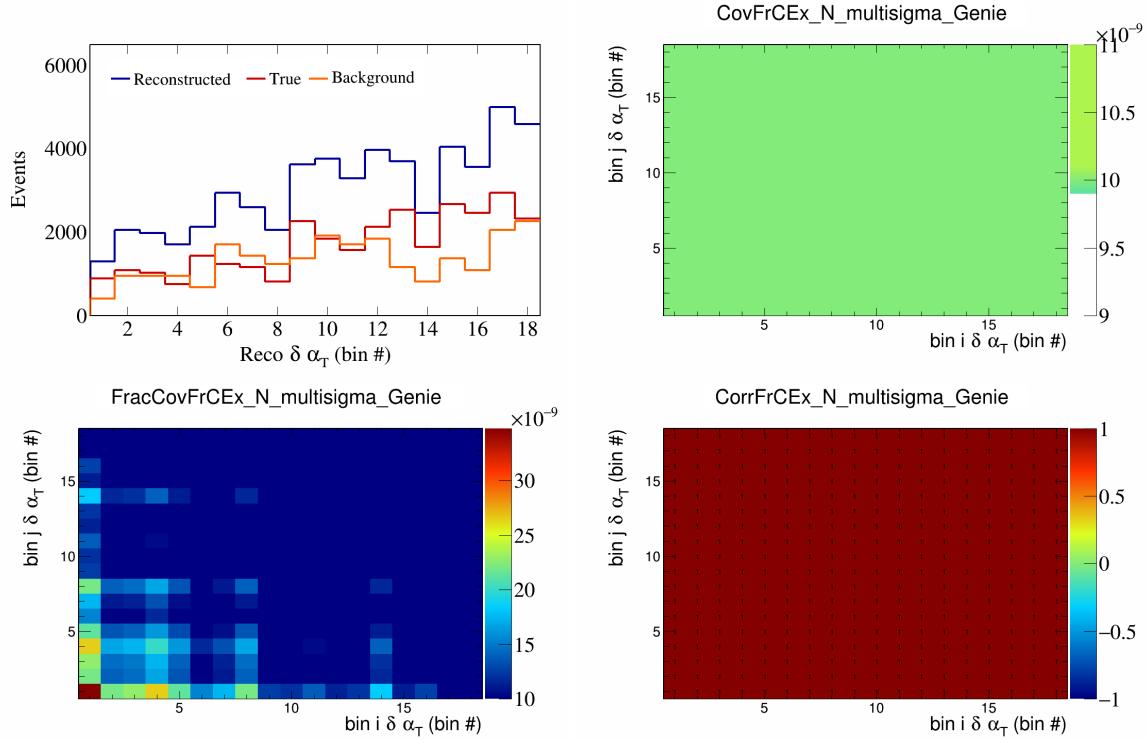


Figure 173: FrCEExN variations for $\delta\alpha_T$ in $\cos(\theta_{\vec{p}_\mu})$.

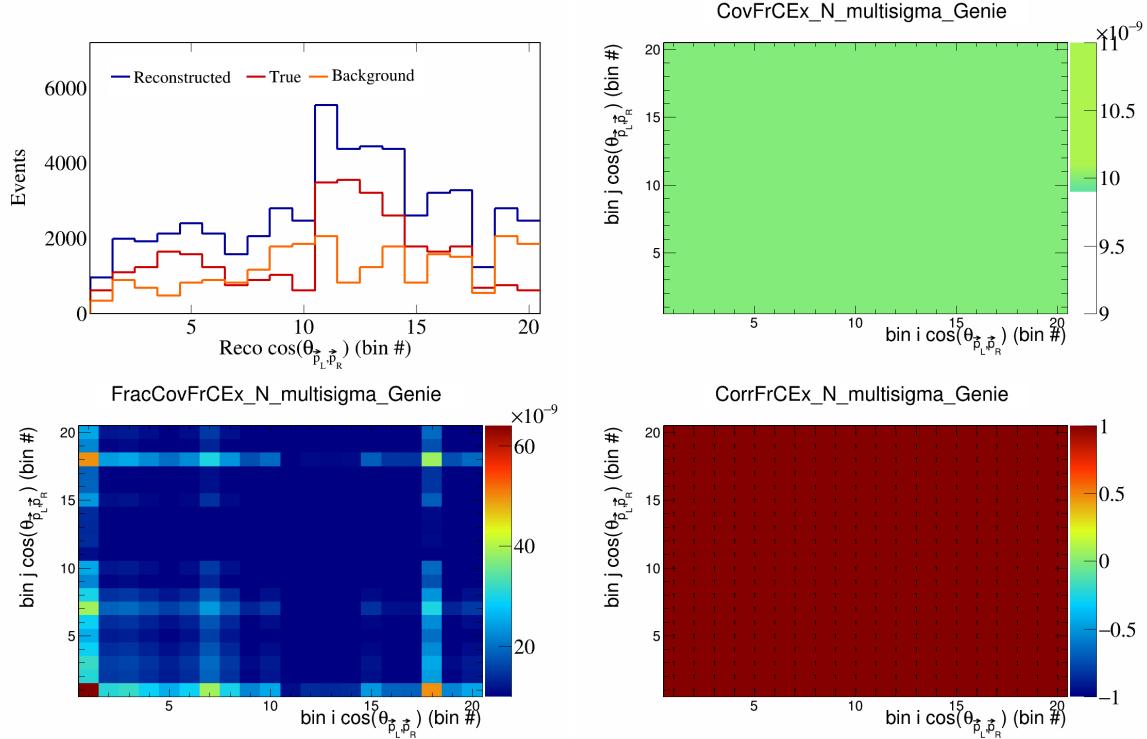


Figure 174: FrCEExN variations for $\cos(\theta_{\vec{p}_L, \vec{p}_R})$ in $\cos(\theta_{\vec{p}_\mu})$.

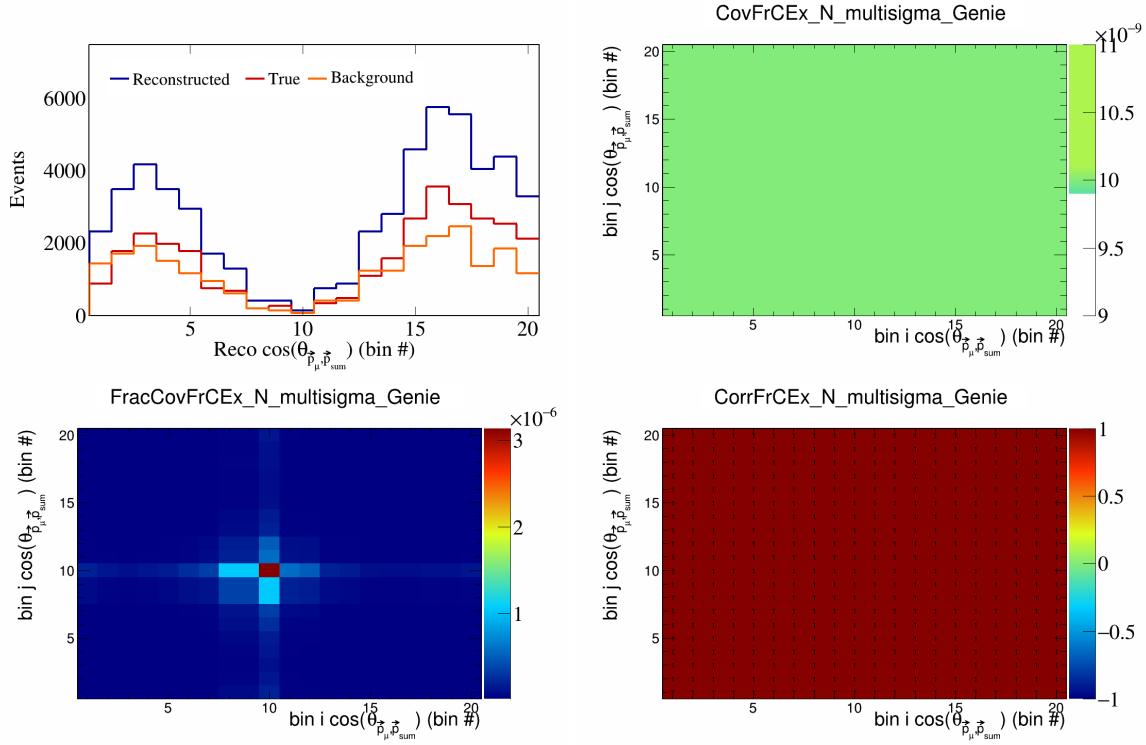


Figure 175: FrCEExN variations for $\cos(\theta_{\vec{p}_\mu, \vec{p}_{\text{sum}}})$ in $\cos(\theta_{\vec{p}_\mu})$.

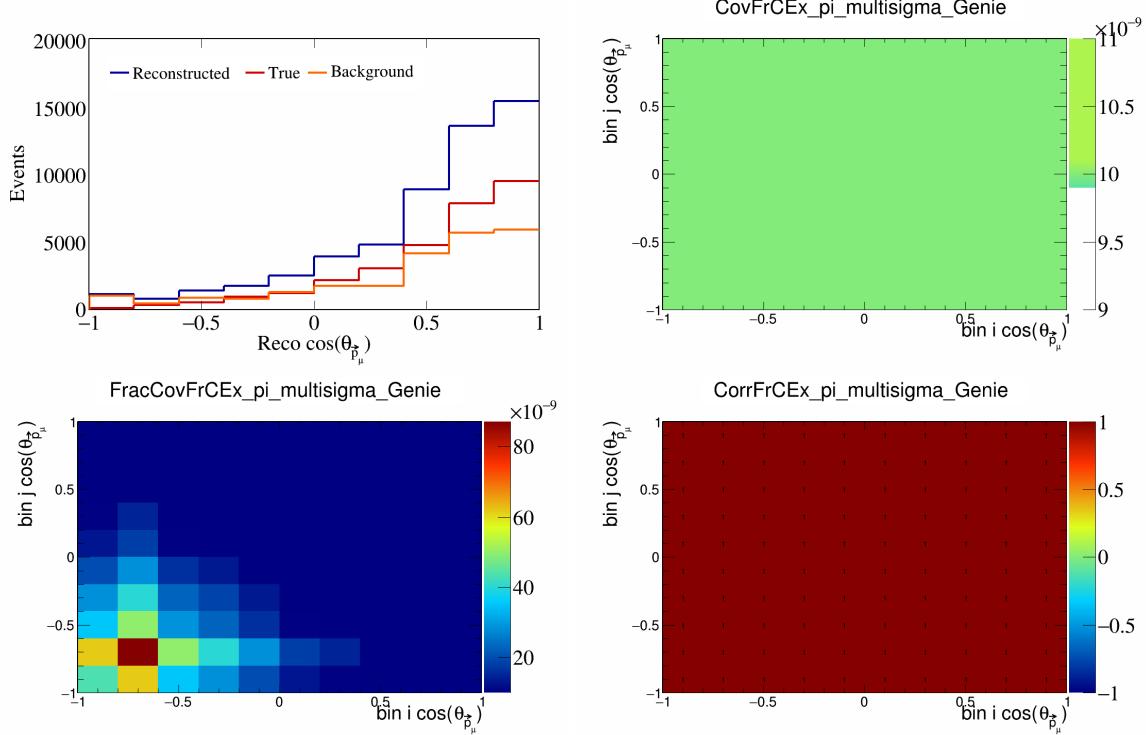


Figure 176: FrCEExpi variations for $\cos(\theta_{\vec{p}_\mu})$.

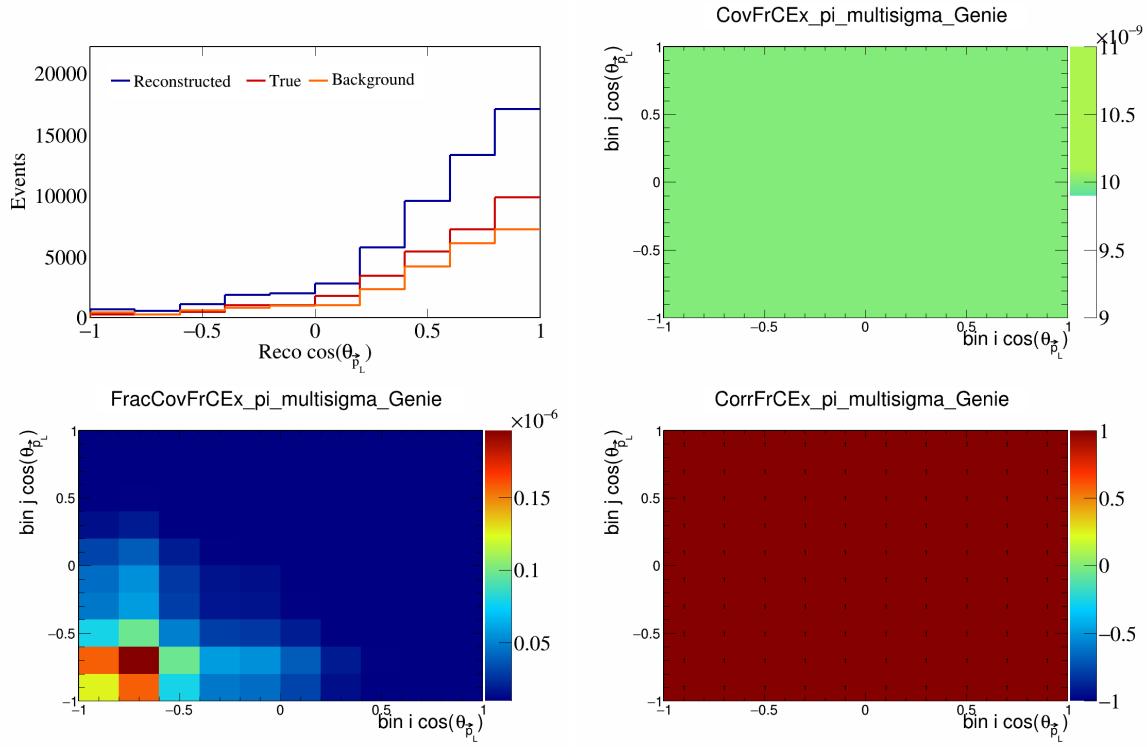


Figure 177: FrCEpi variations for $\cos(\theta_{\vec{p}_L})$.

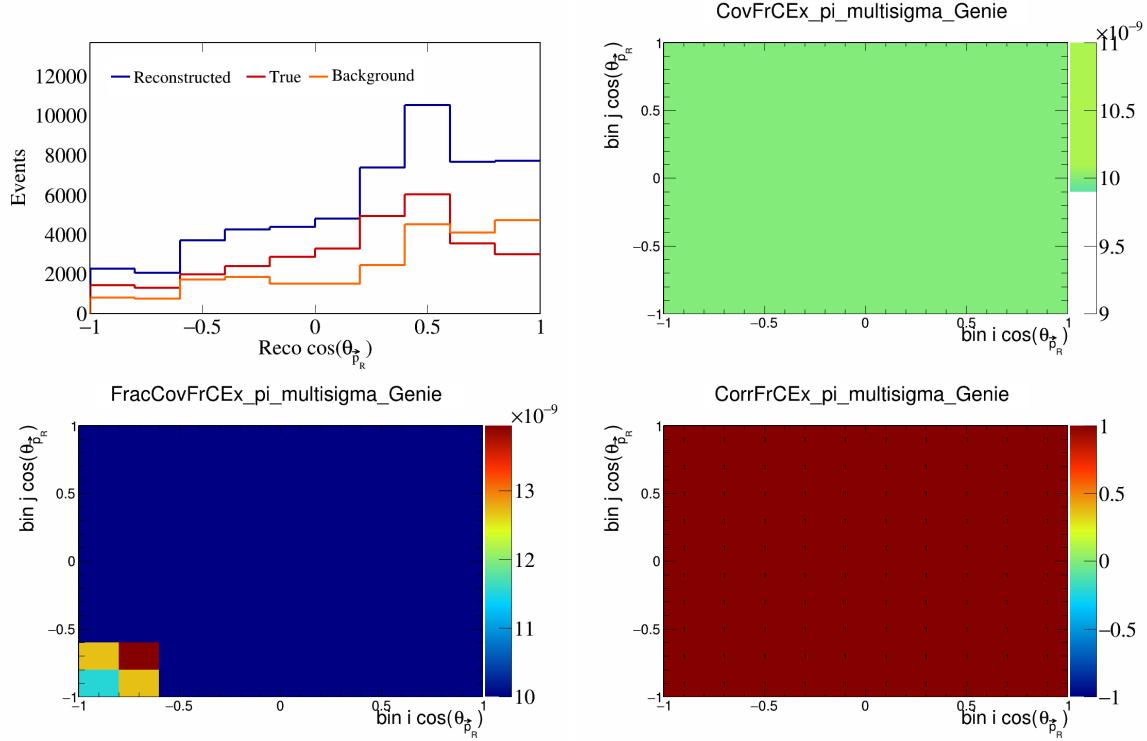


Figure 178: FrCEpi variations for $\cos(\theta_{\vec{p}_R})$.

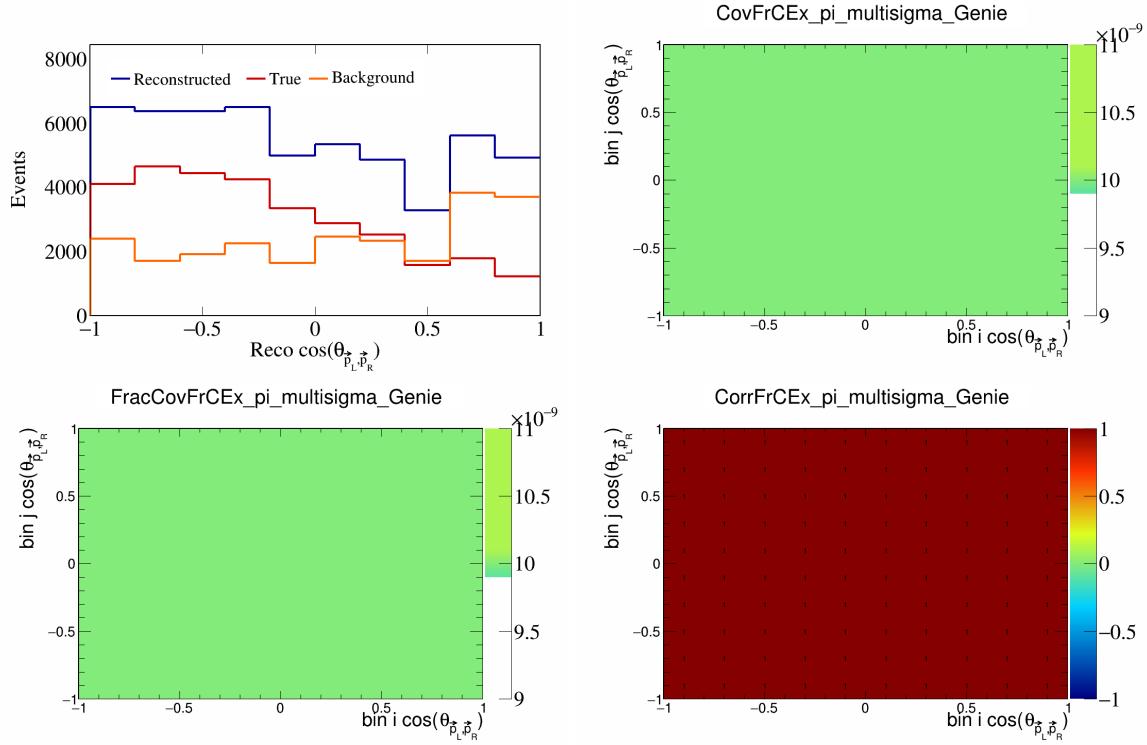


Figure 179: FrCEpi variations for $\cos(\theta_{\vec{p}_L, \vec{p}_R})$.

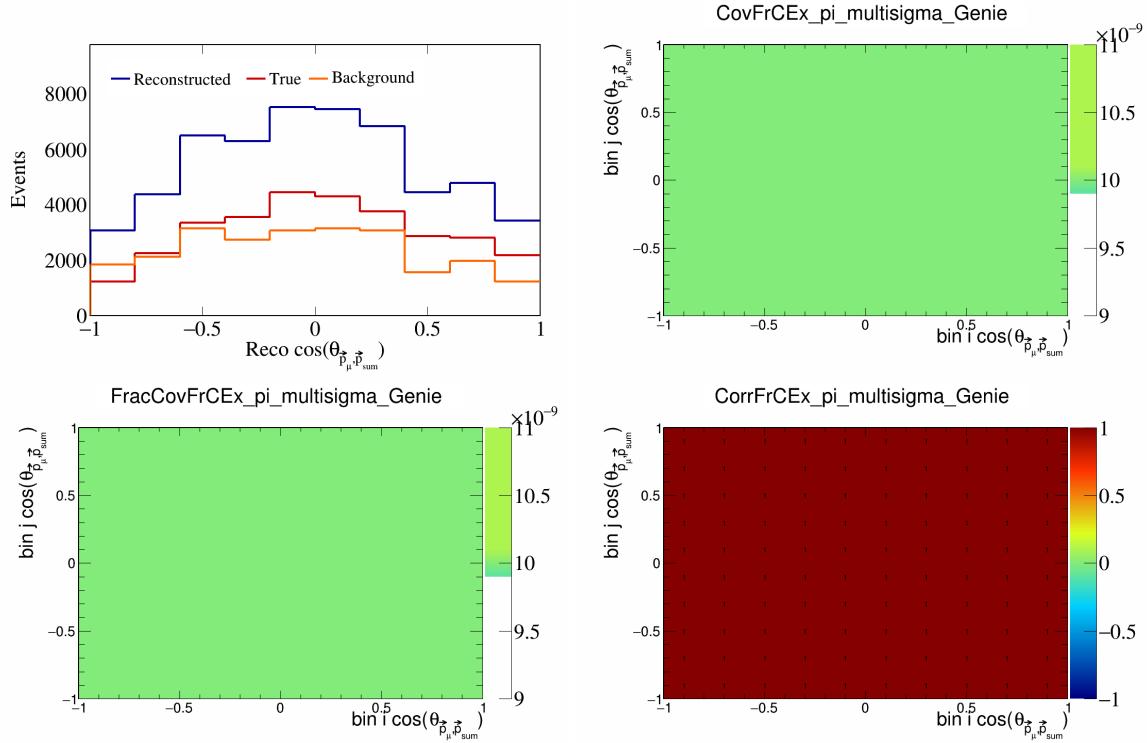


Figure 180: FrCEpi variations for $\cos(\theta_{\vec{p}_\mu, \vec{p}_{\text{sum}}})$.

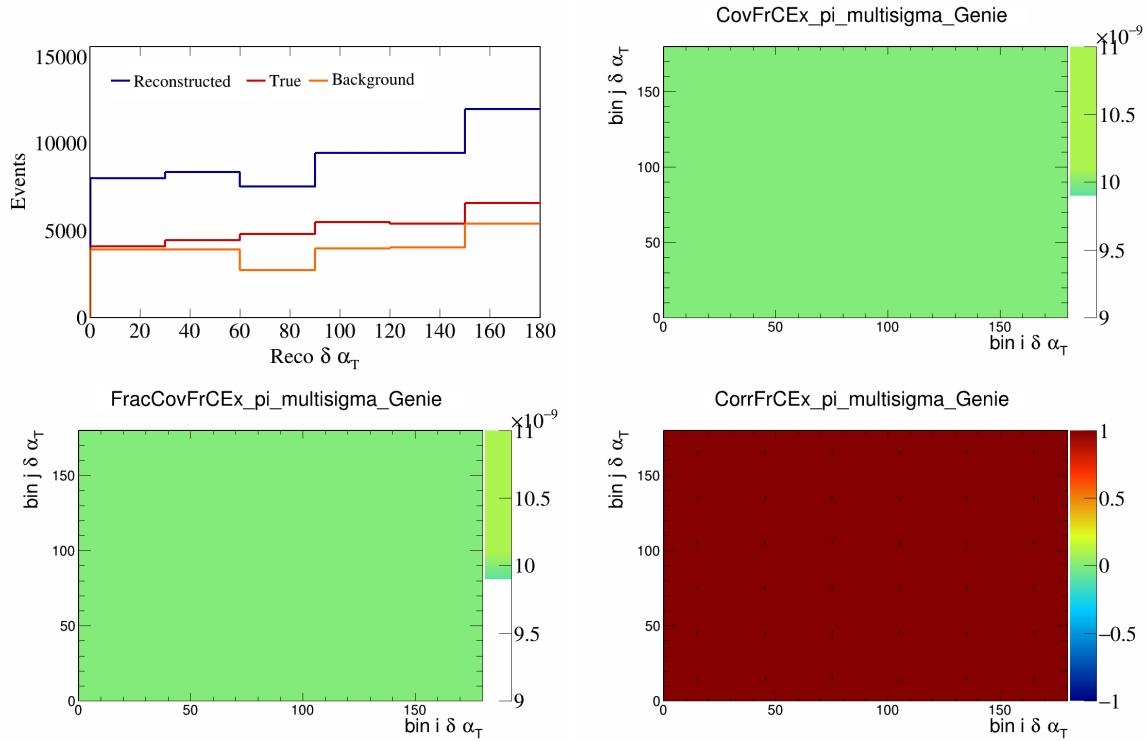


Figure 181: FrCEExpi variations for $\delta\alpha_T$.

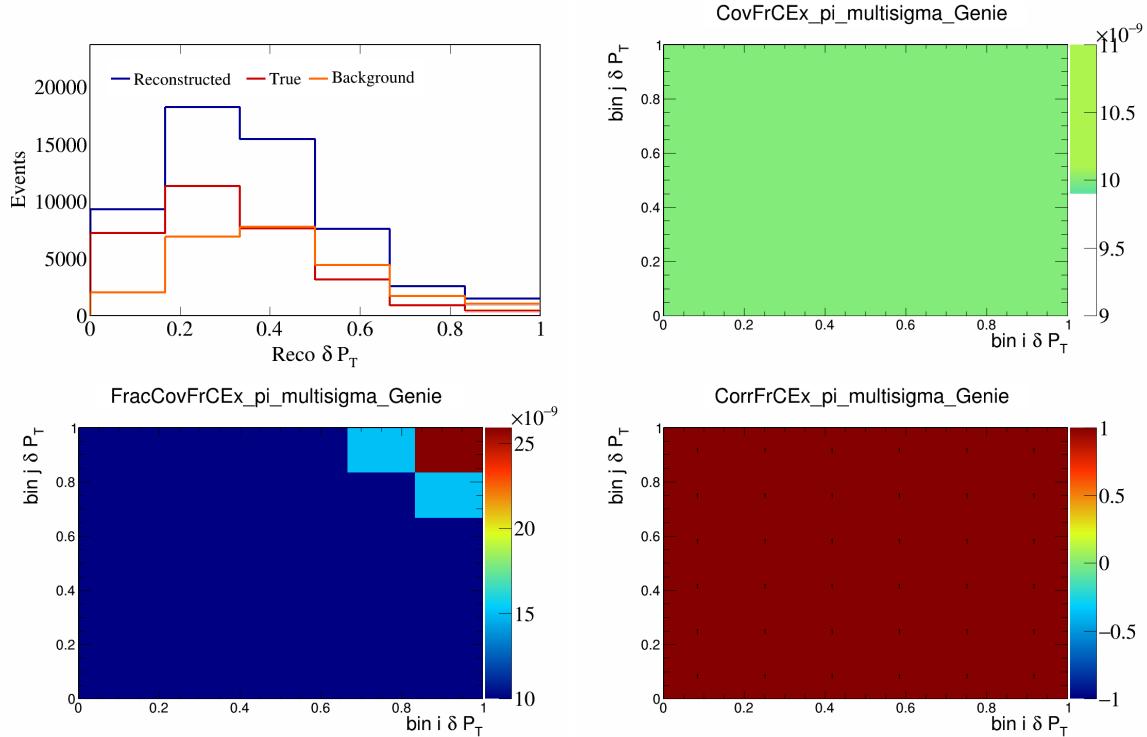


Figure 182: FrCEExpi variations for δP_T .

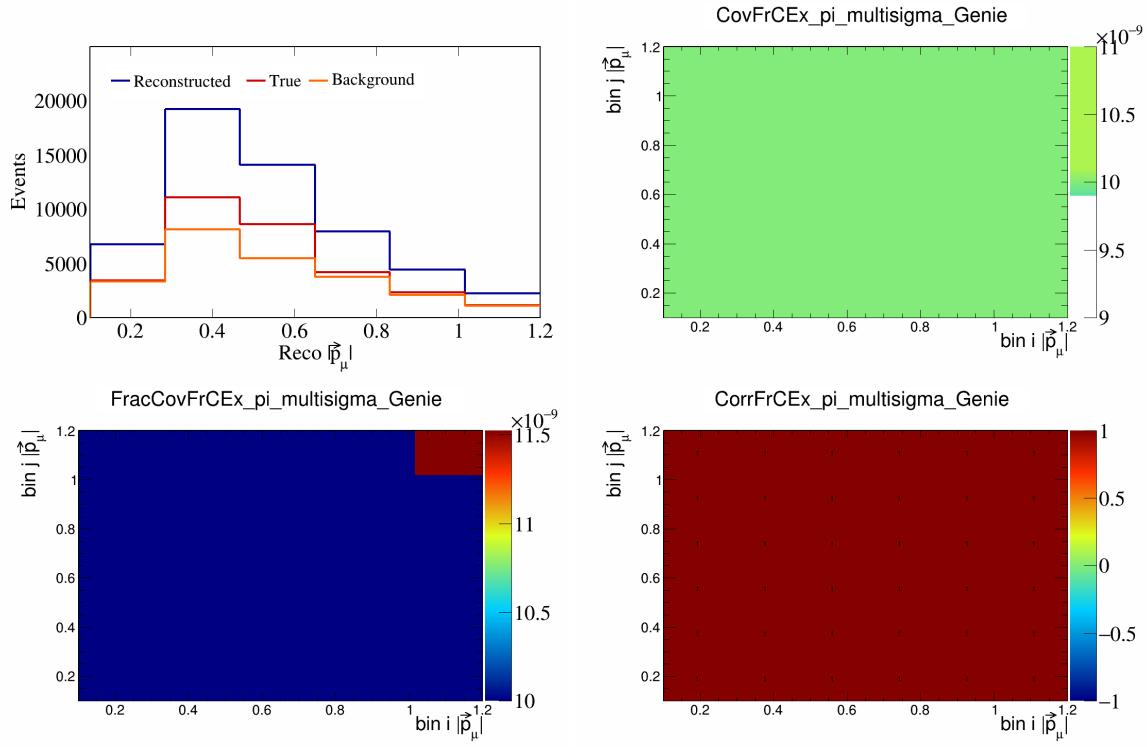


Figure 183: FrCEExpi variations for $|\vec{p}_\mu|$.

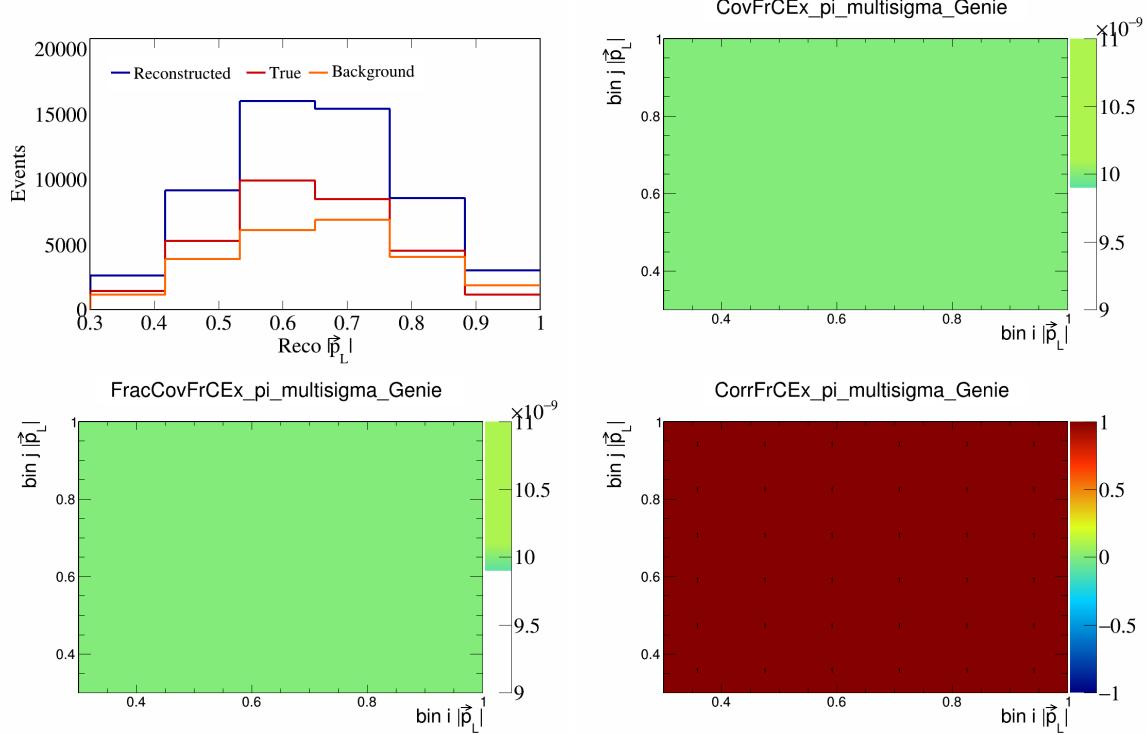


Figure 184: FrCEExpi variations for $|\vec{p}_L|$.

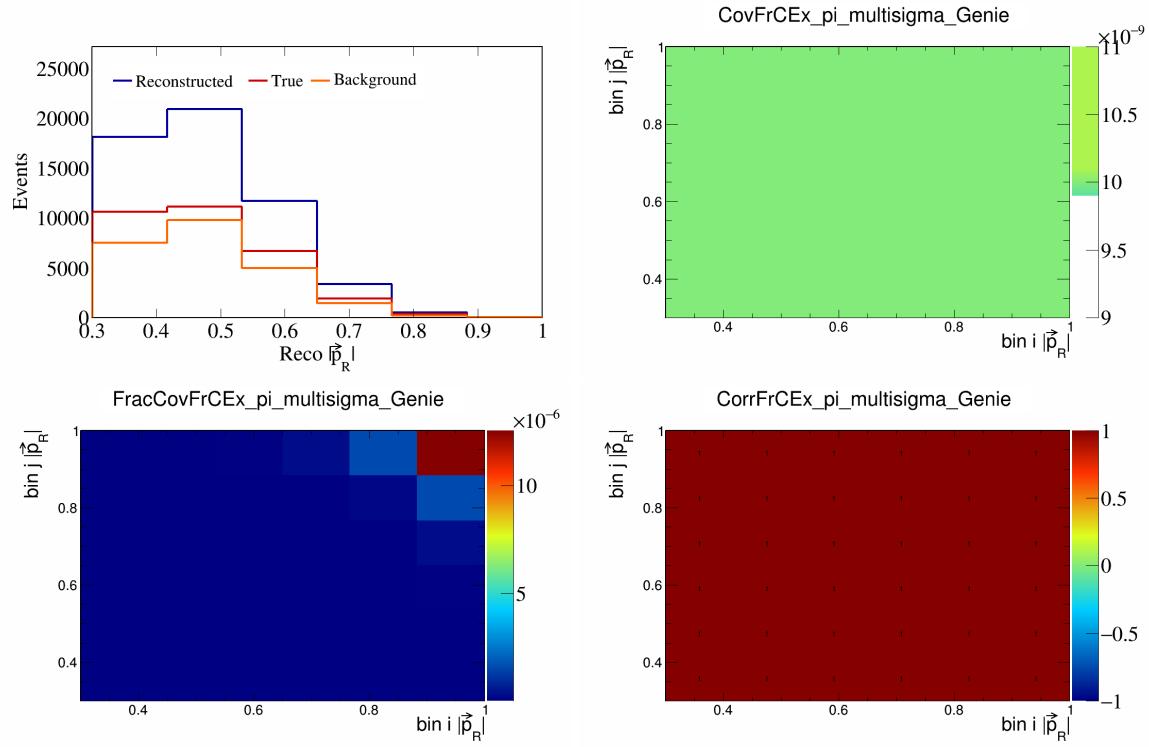


Figure 185: FrCEExpi variations for $|\vec{p}_R|$.

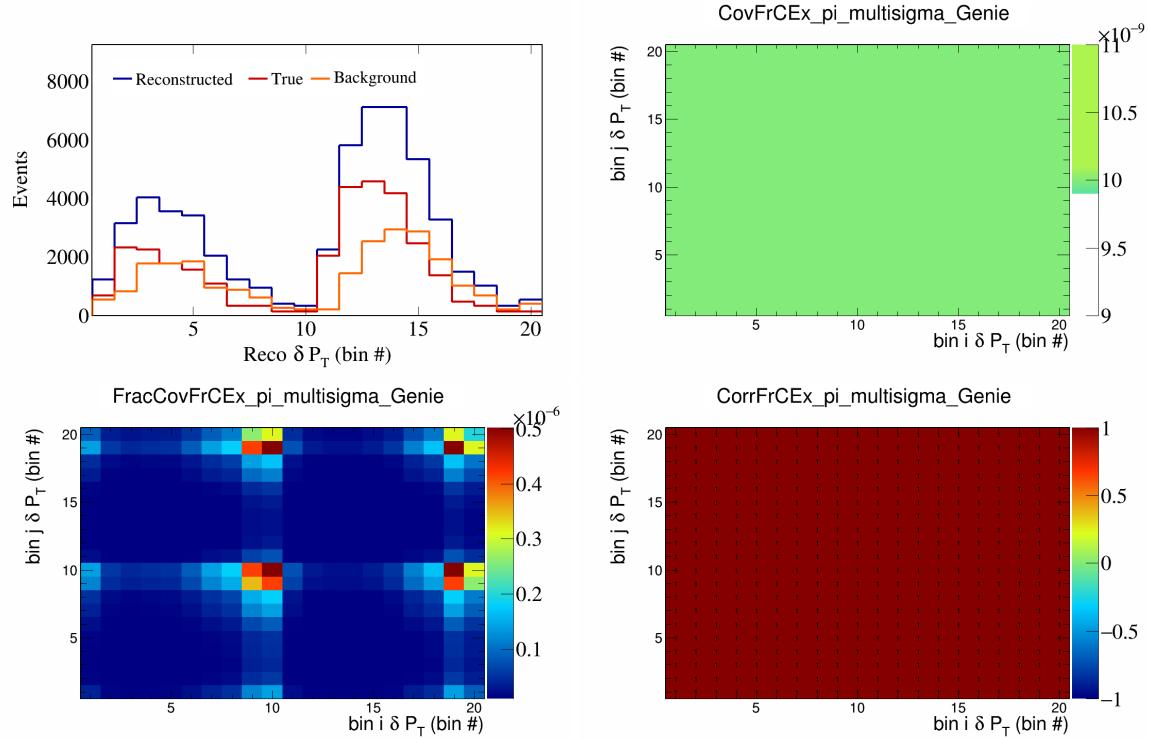


Figure 186: FrCEExpi variations for δP_T in $\cos(\theta_{\vec{p}_\mu})$.

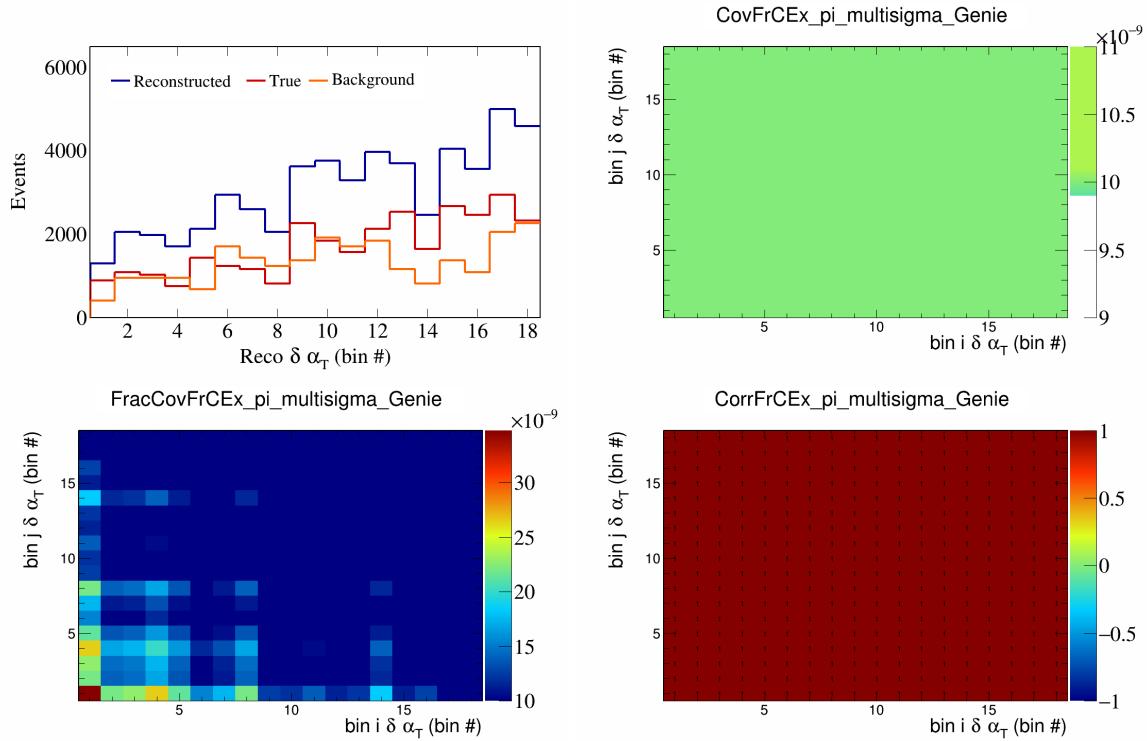


Figure 187: FrCEExpi variations for $\delta\alpha_T$ in $\cos(\theta_{\vec{p}_\mu})$.

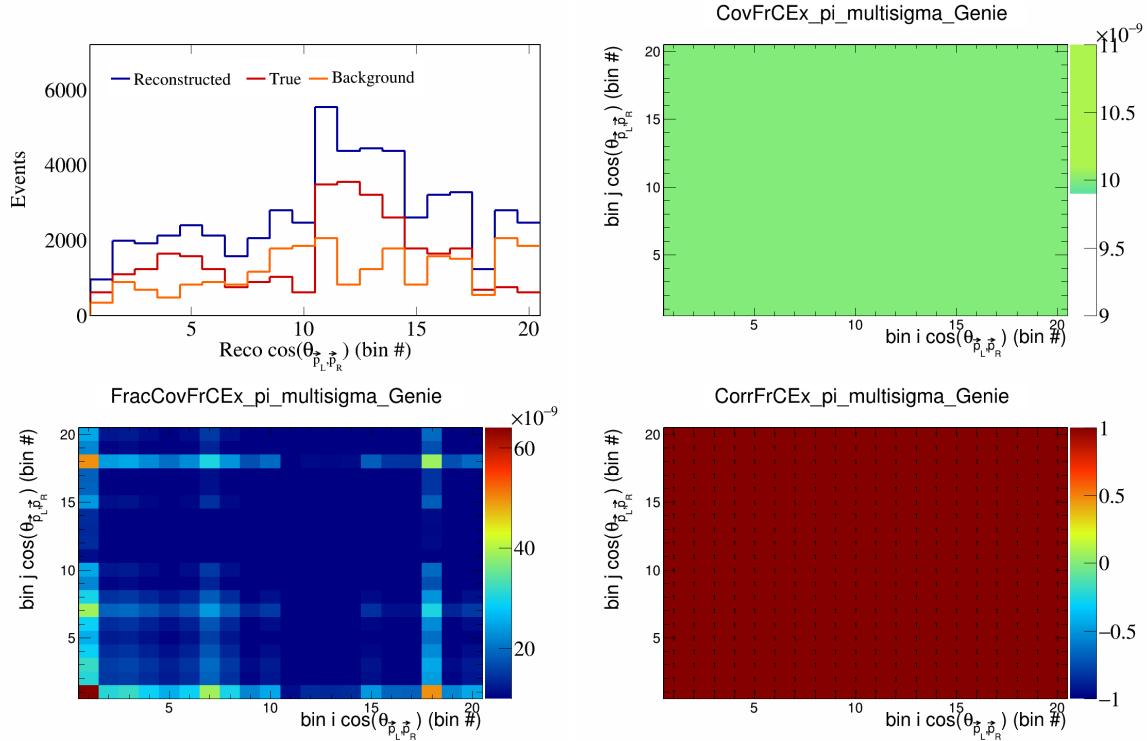


Figure 188: FrCEExpi variations for $\cos(\theta_{\vec{p}_L, \vec{p}_R})$ in $\cos(\theta_{\vec{p}_\mu})$.

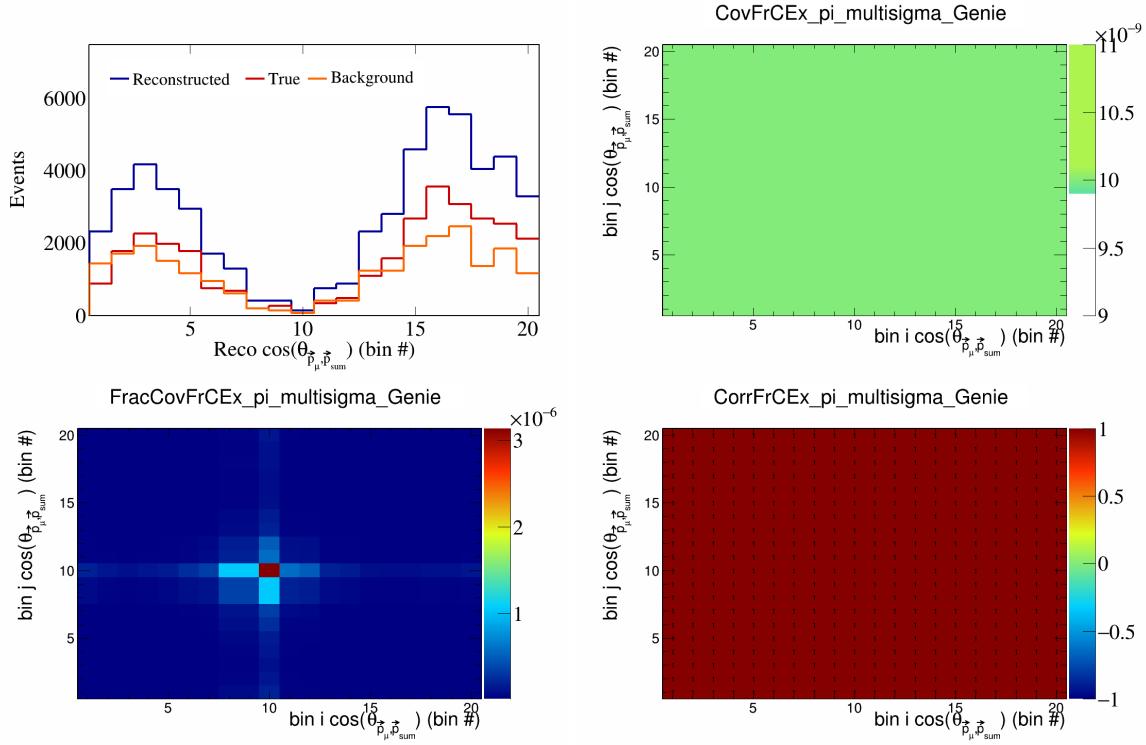


Figure 189: FrCEExpi variations for $\cos(\theta_{\vec{p}_\mu, \vec{p}_{\text{sum}}})$ in $\cos(\theta_{\vec{p}_\mu})$.

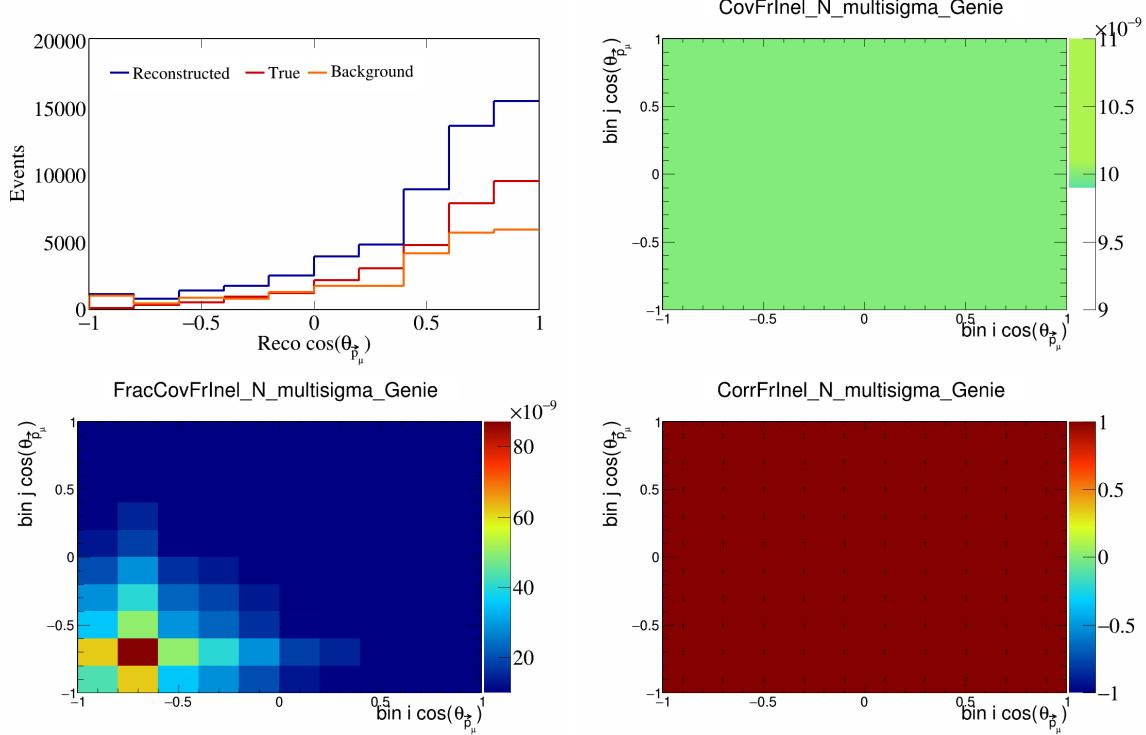


Figure 190: FrInelN variations for $\cos(\theta_{\vec{p}_\mu})$.

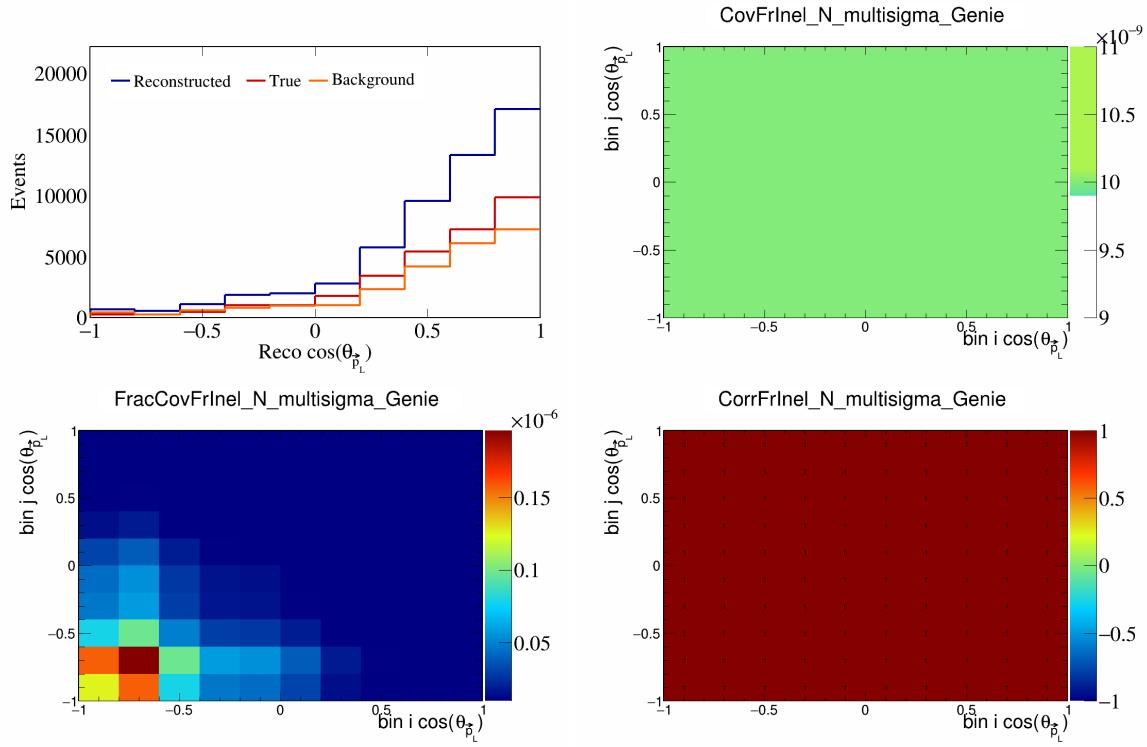


Figure 191: FrInelN variations for $\cos(\theta_{\vec{p}_L})$.

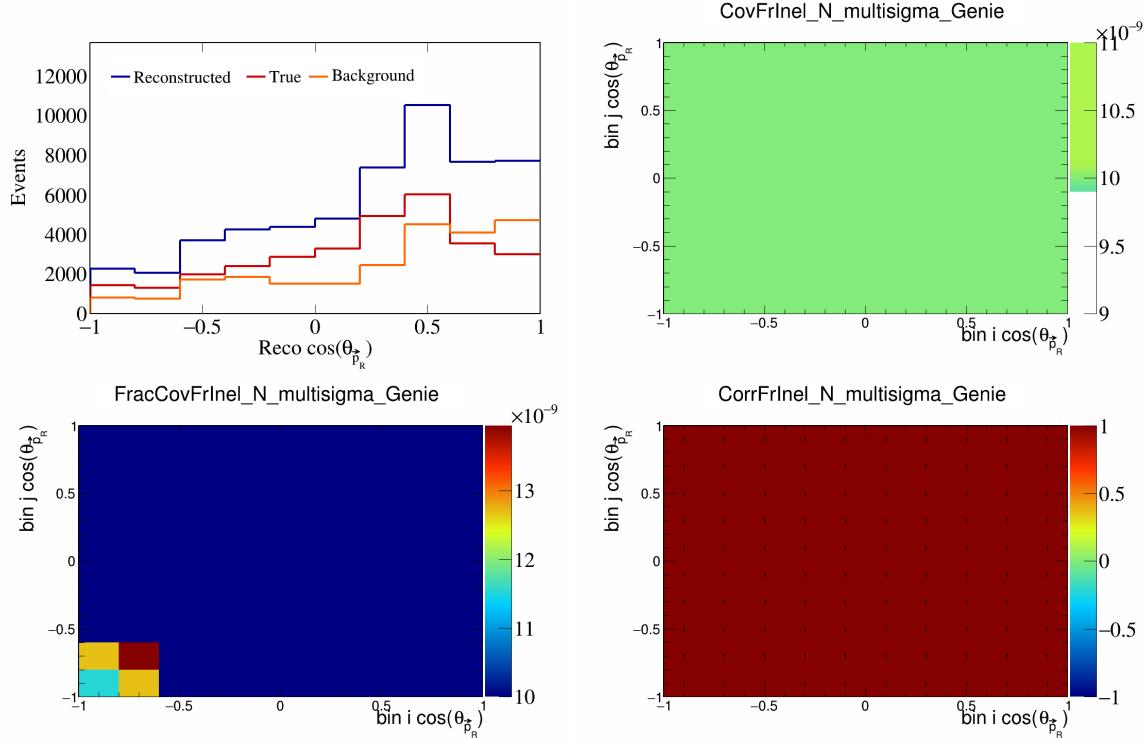


Figure 192: FrInelN variations for $\cos(\theta_{\vec{p}_R})$.

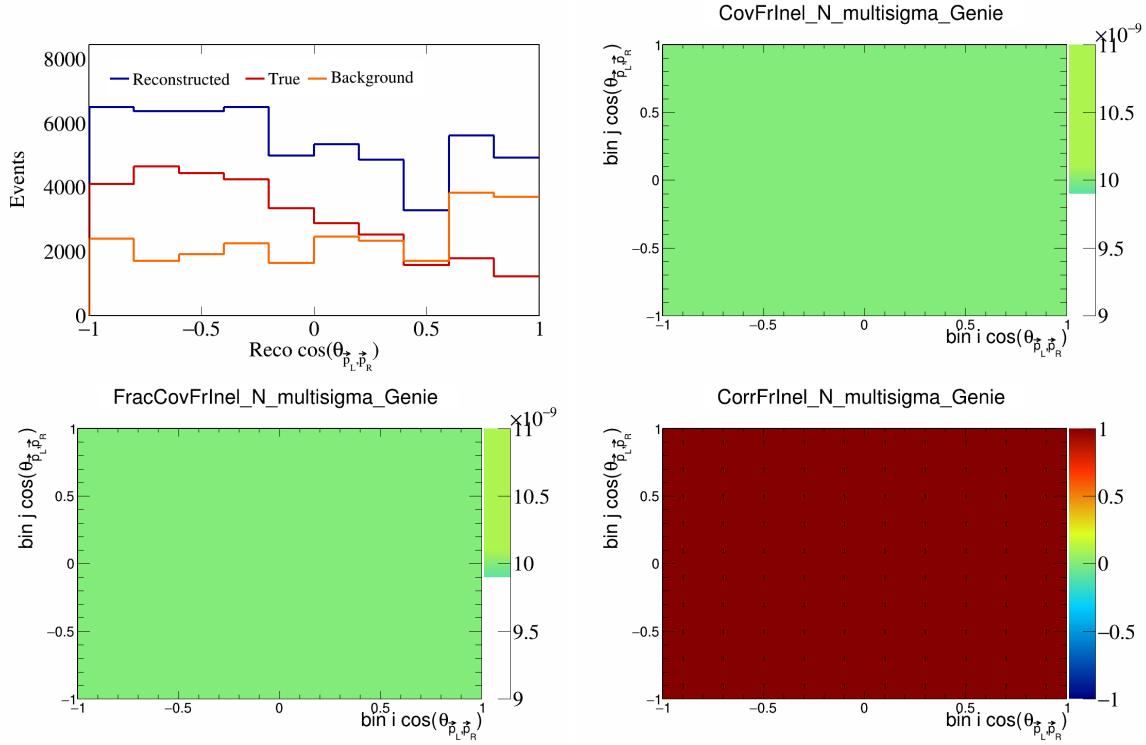


Figure 193: FrInelN variations for $\cos(\theta_{\vec{p}_L, \vec{p}_R})$.

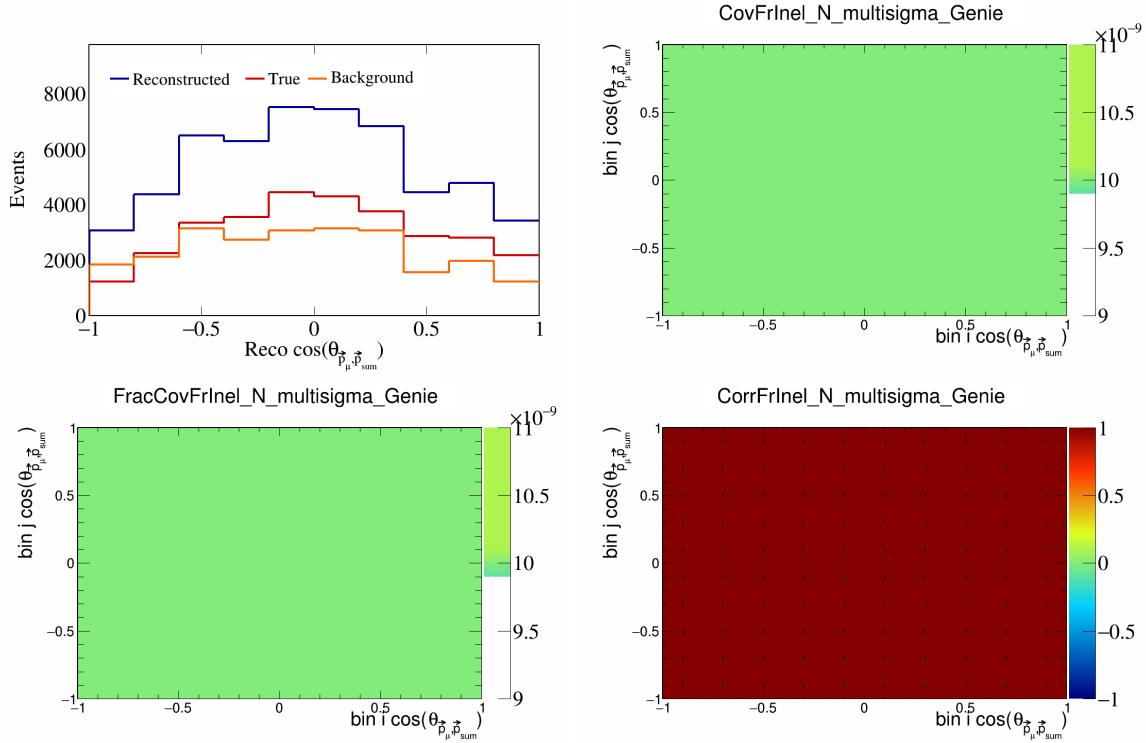


Figure 194: FrInelN variations for $\cos(\theta_{\vec{p}_\mu, \vec{p}_{\text{sum}}})$.

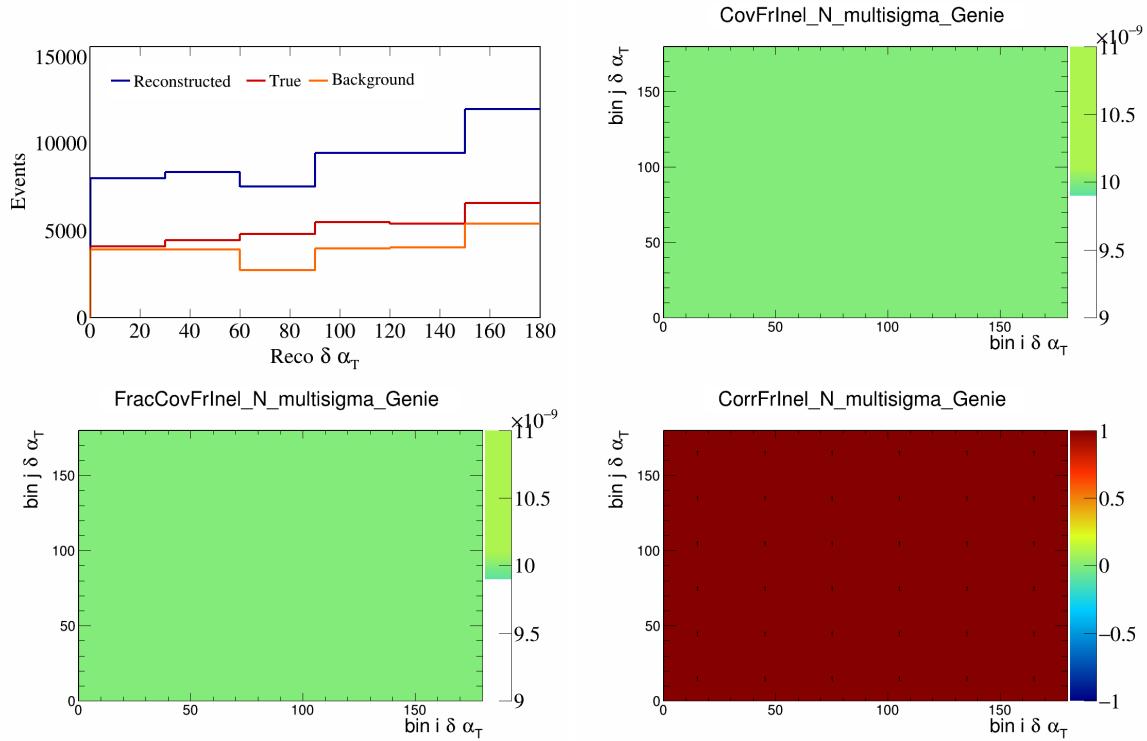


Figure 195: FrInelN variations for $\delta\alpha_T$.

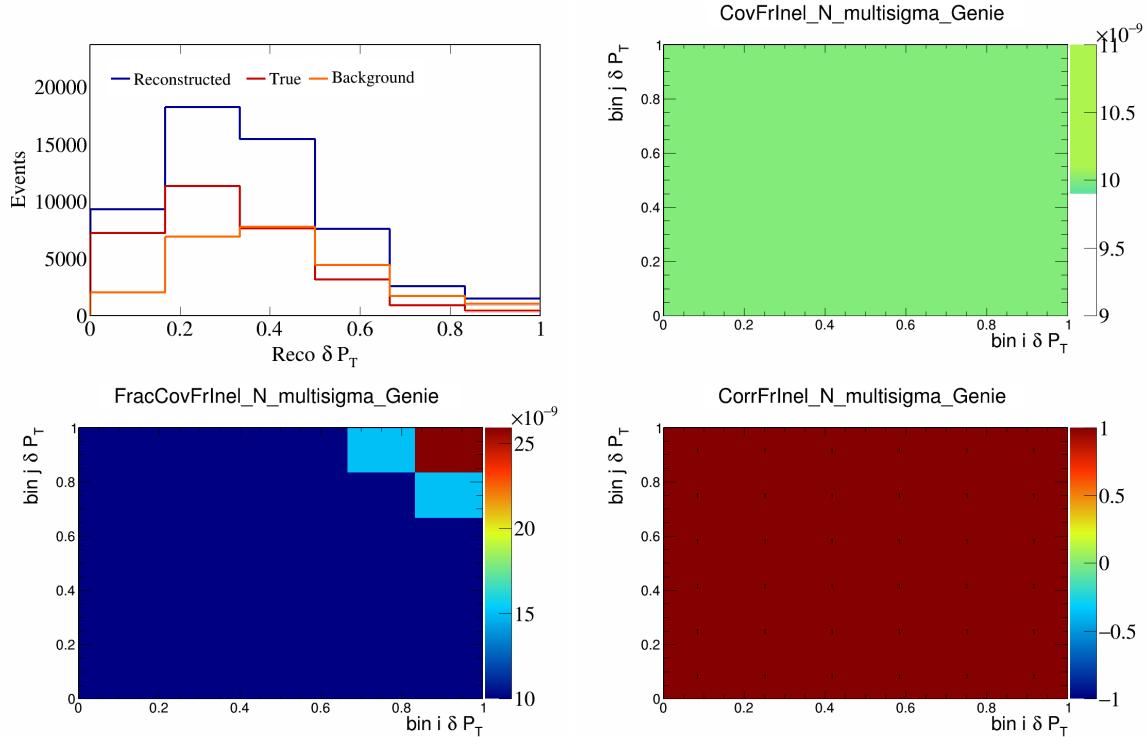


Figure 196: FrInelN variations for δP_T .

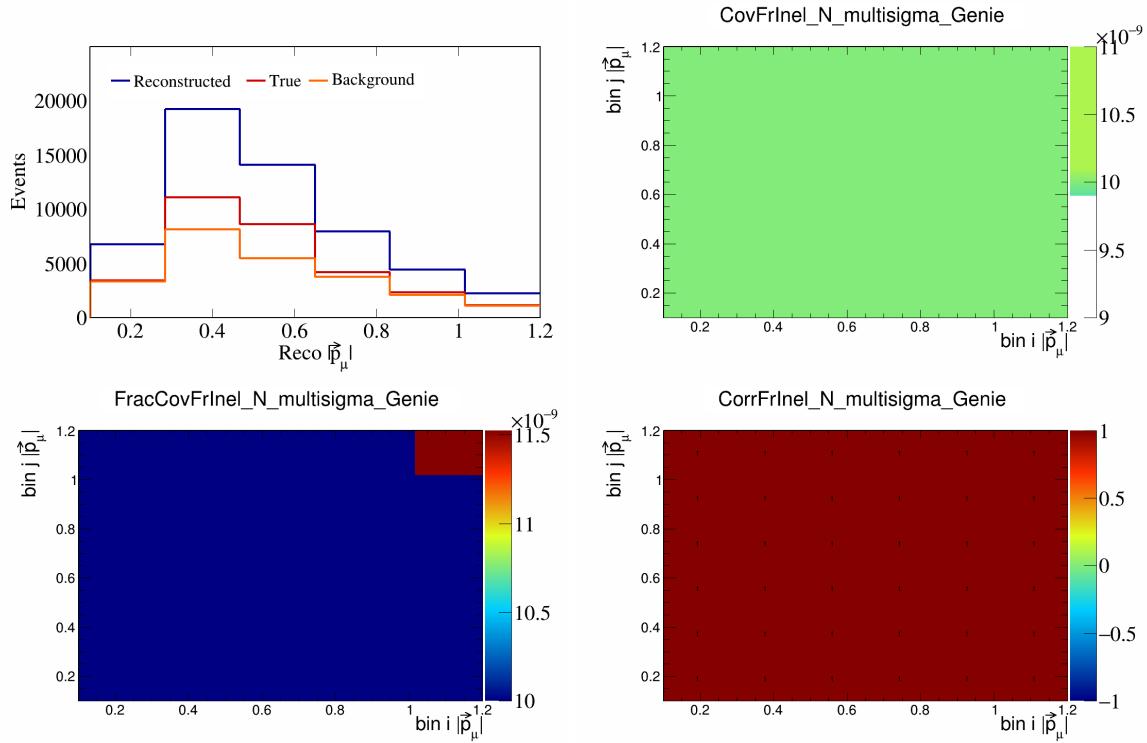


Figure 197: FrInelN variations for $|\vec{p}_\mu|$.

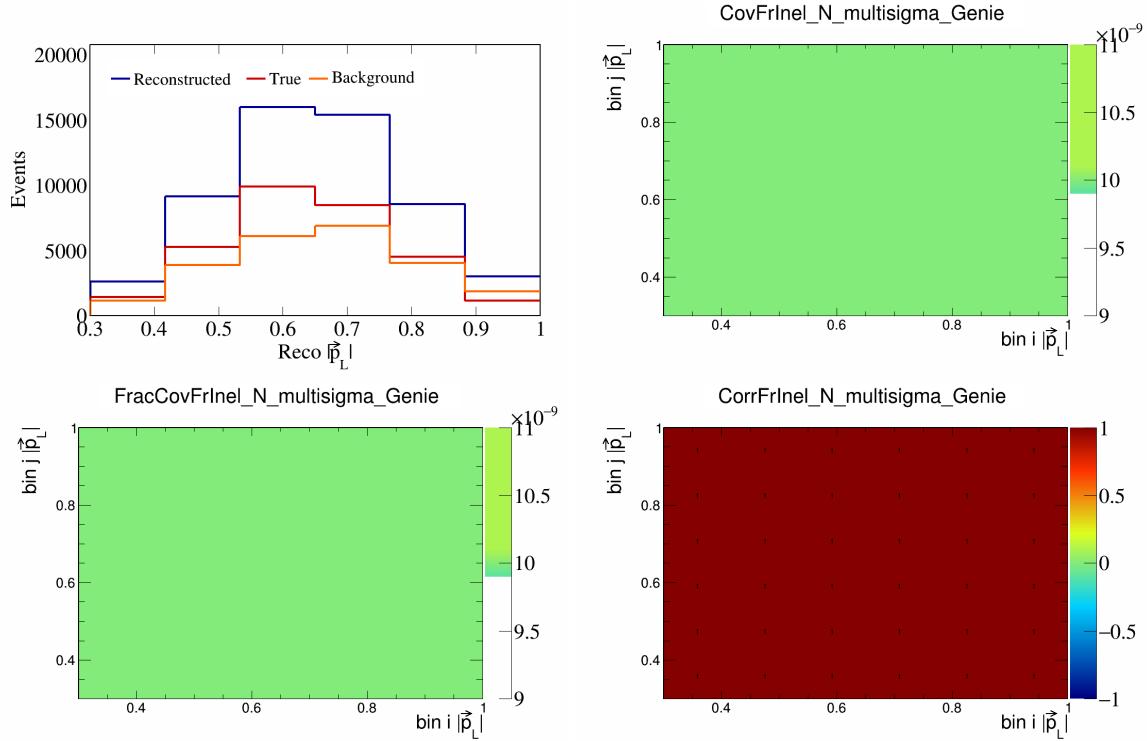


Figure 198: FrInelN variations for $|\vec{p}_L|$.

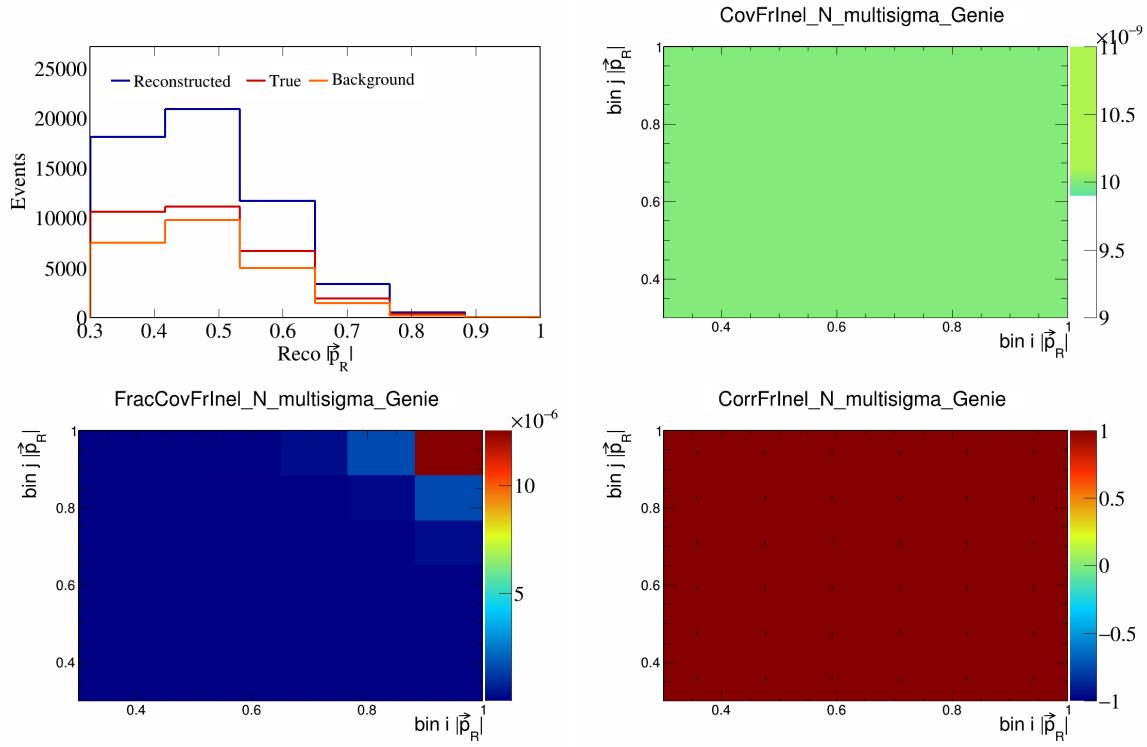


Figure 199: FrInelN variations for $|\vec{p}_R|$.

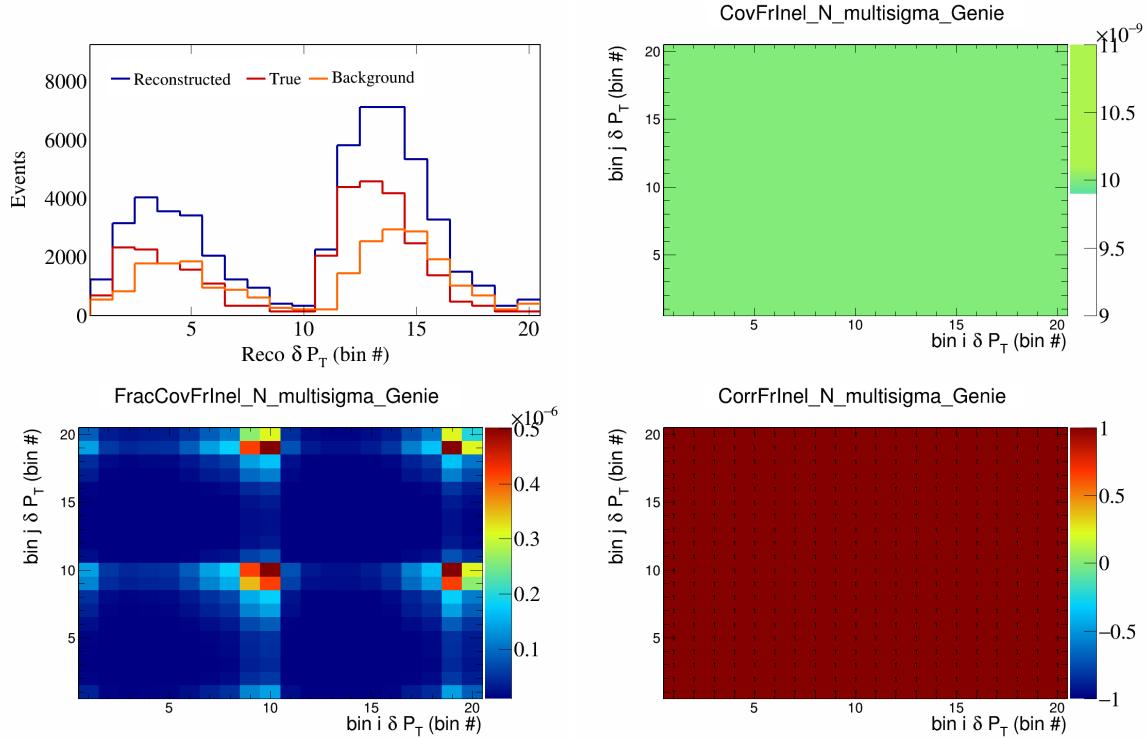


Figure 200: FrInelN variations for δP_T in $\cos(\theta_{\vec{p}_\mu})$.

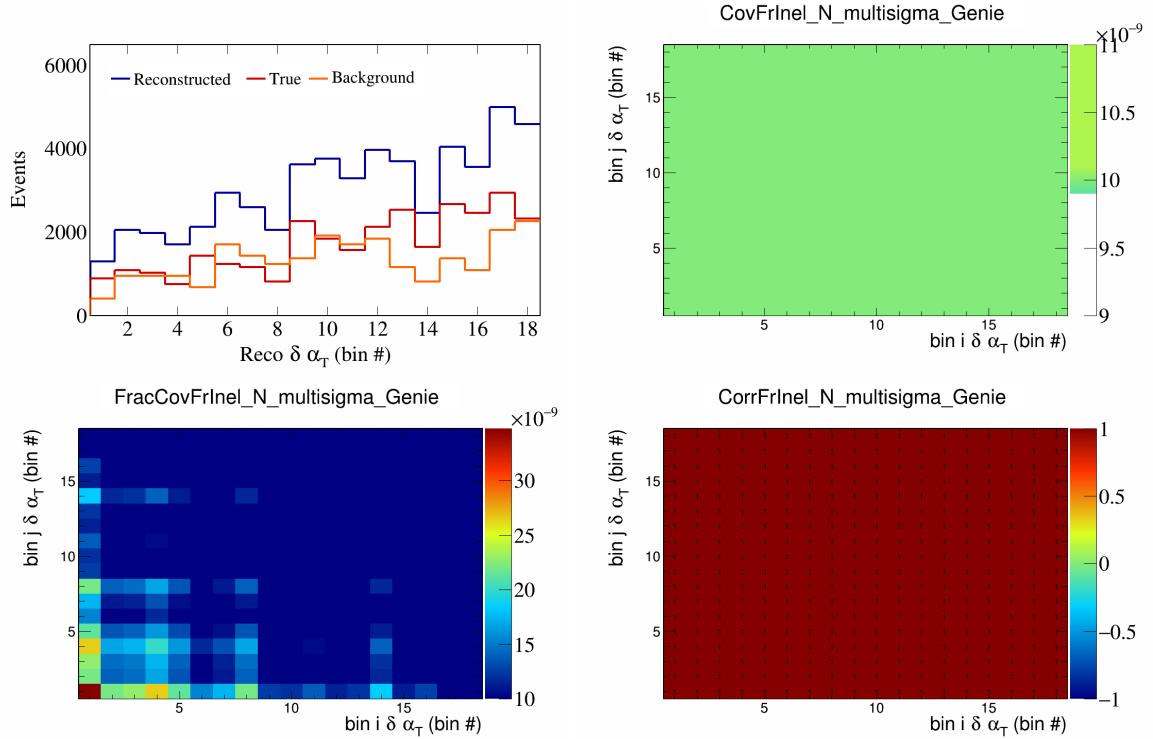


Figure 201: FrInelN variations for $\delta\alpha_T$ in $\cos(\theta_{\vec{p}_\mu})$.

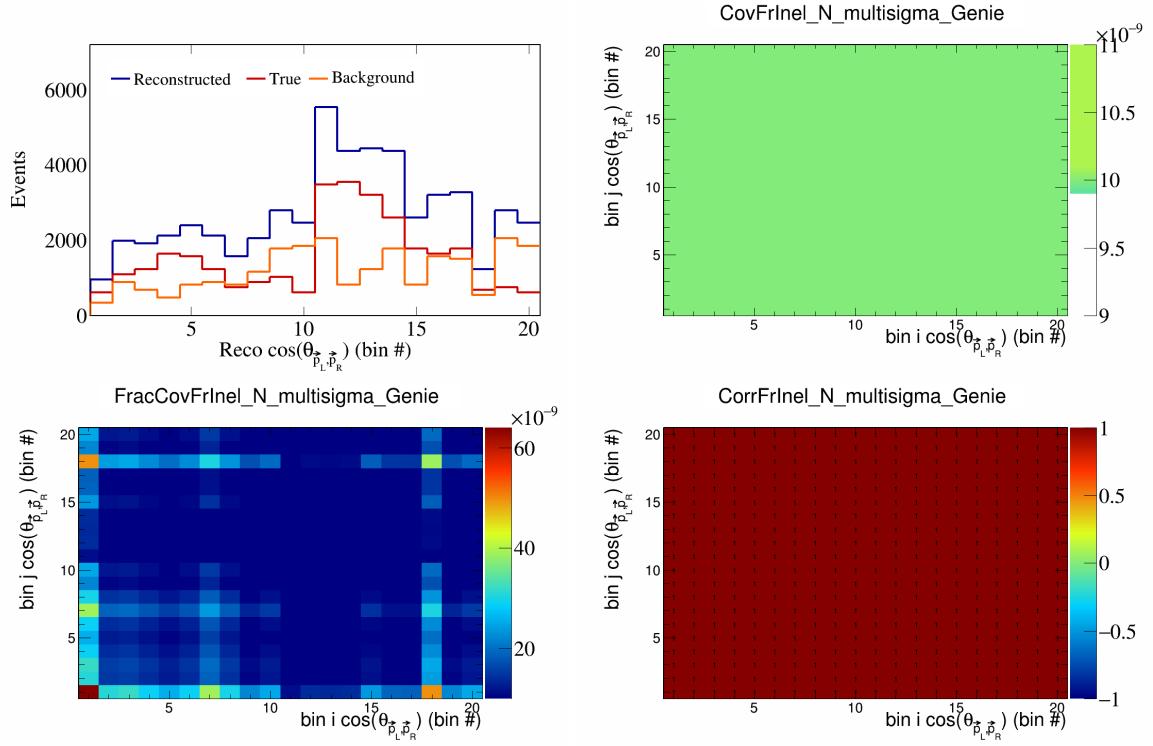


Figure 202: FrInelN variations for $\cos(\theta_{\vec{p}_L, \vec{p}_R})$ in $\cos(\theta_{\vec{p}_\mu})$.

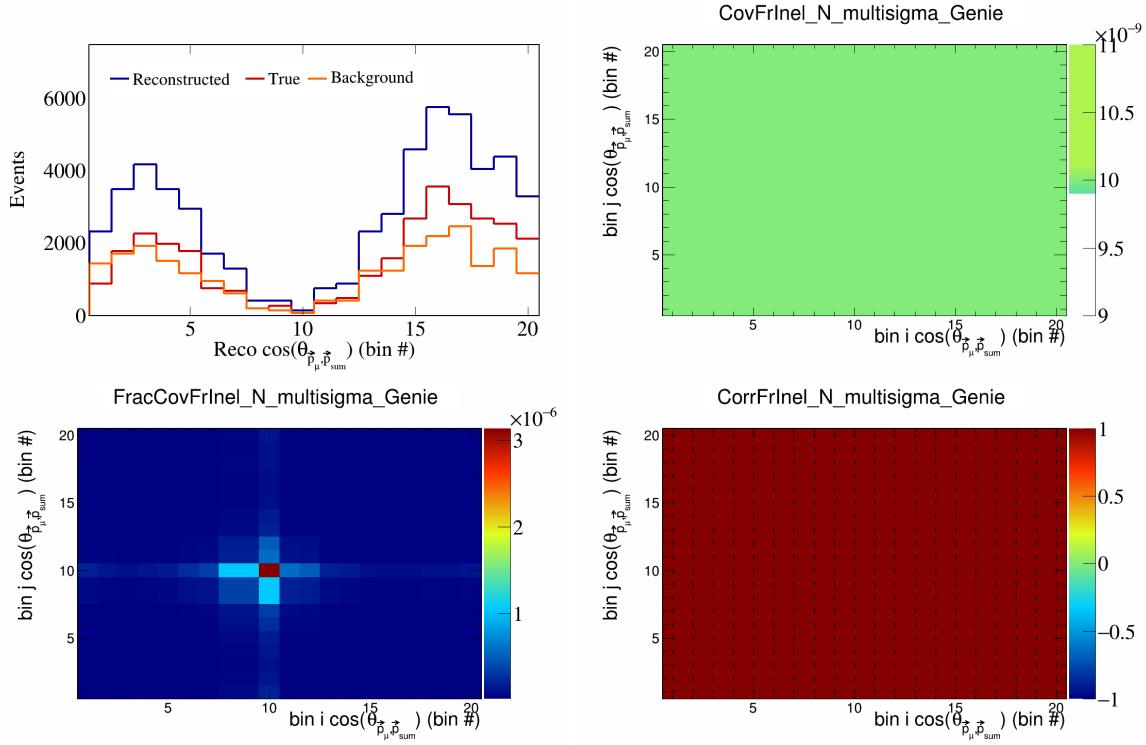


Figure 203: FrInelN variations for $\cos(\theta_{\vec{p}_\mu, \vec{p}_{\text{sum}}})$ in $\cos(\theta_{\vec{p}_\mu})$.

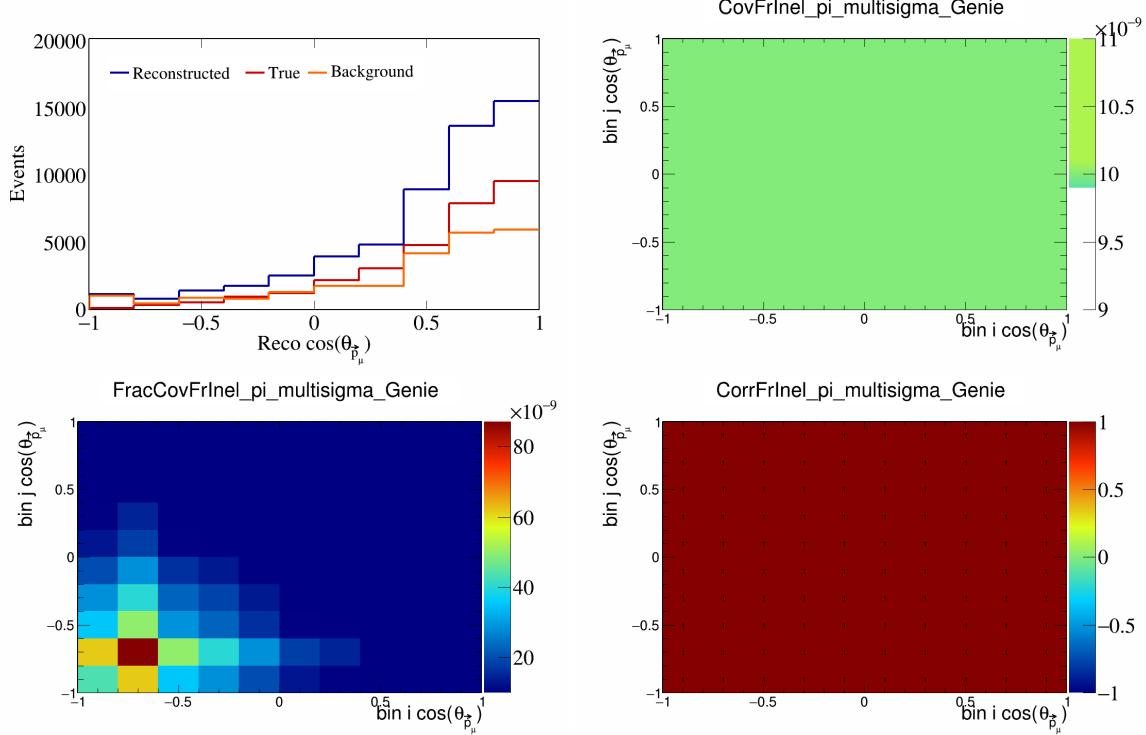


Figure 204: FrInelpi variations for $\cos(\theta_{\vec{p}_\mu})$.

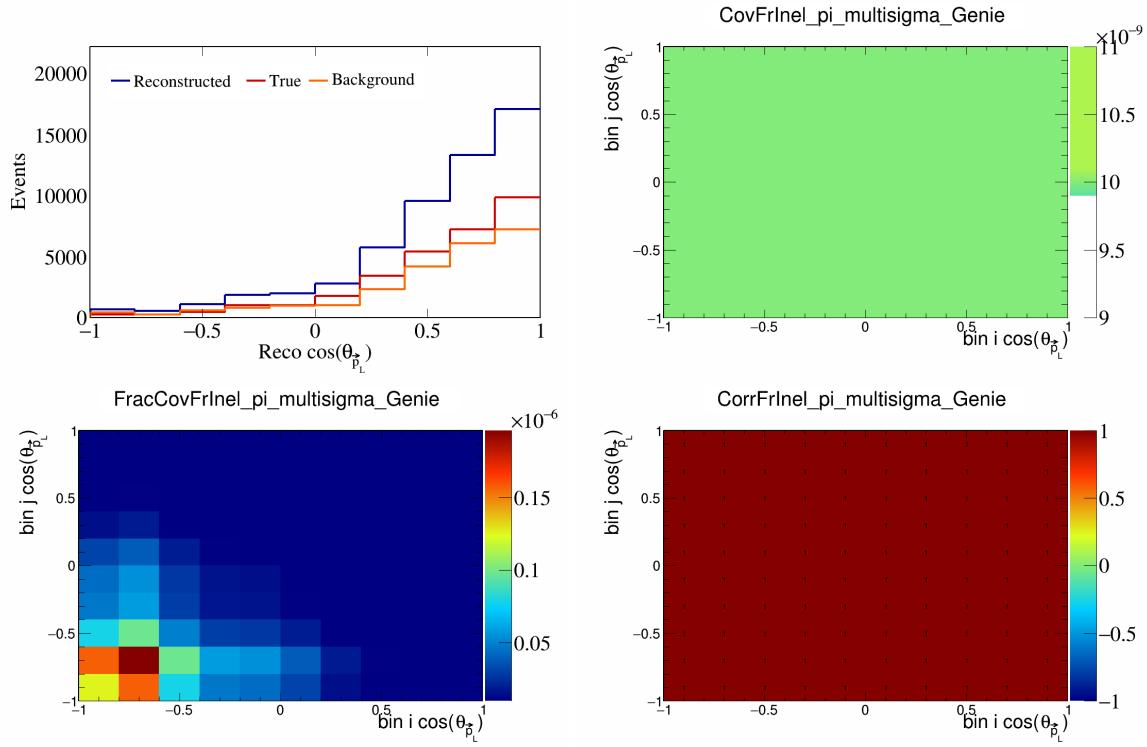


Figure 205: FrInelpi variations for $\cos(\theta_{\vec{p}_L})$.

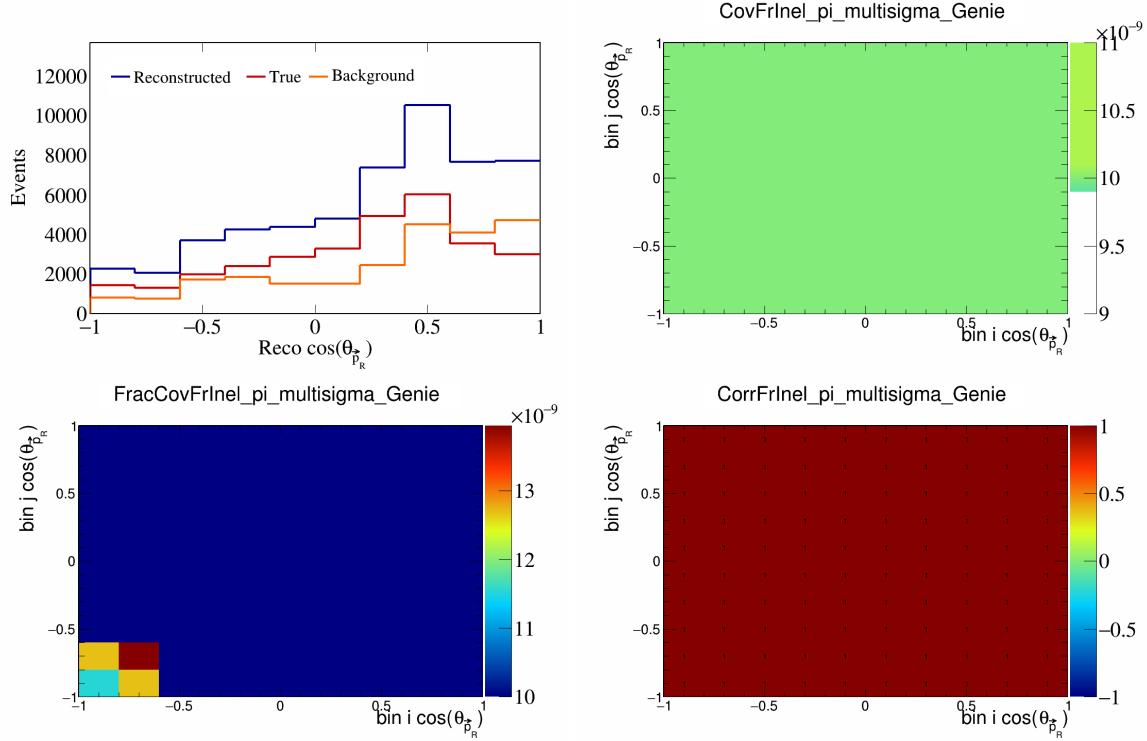


Figure 206: FrInelpi variations for $\cos(\theta_{\vec{p}_R})$.

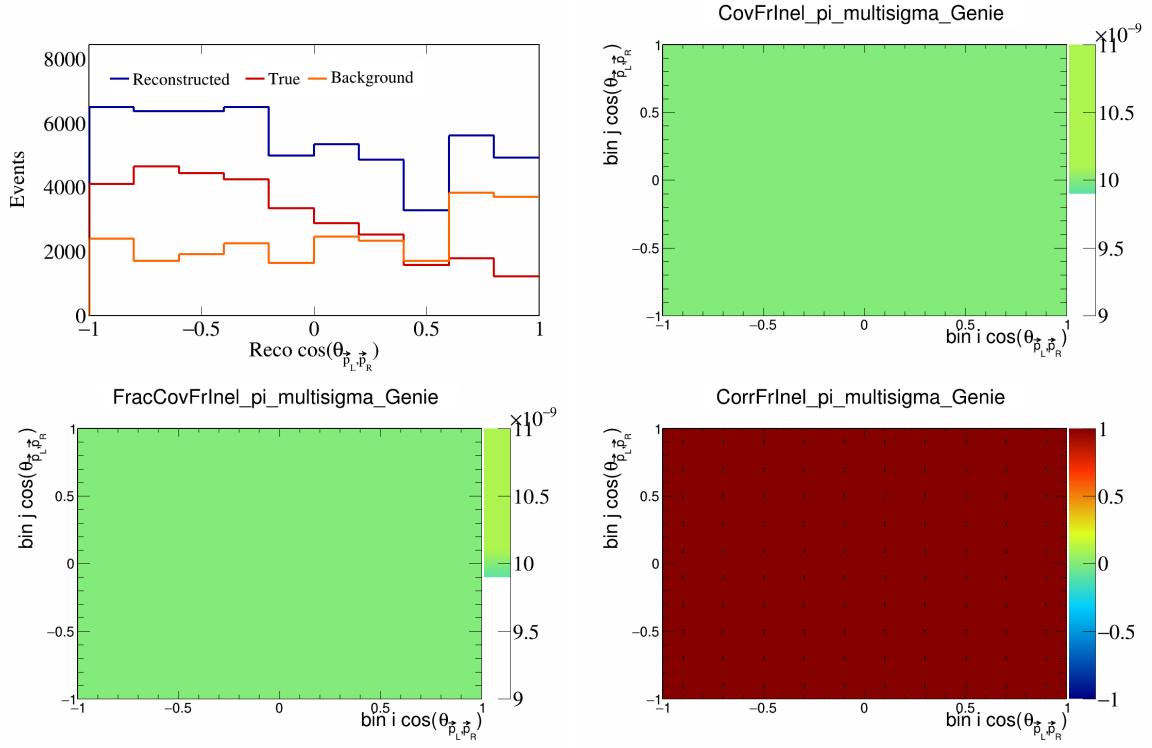


Figure 207: FrInelpi variations for $\cos(\theta_{\vec{p}_L, \vec{p}_R})$.

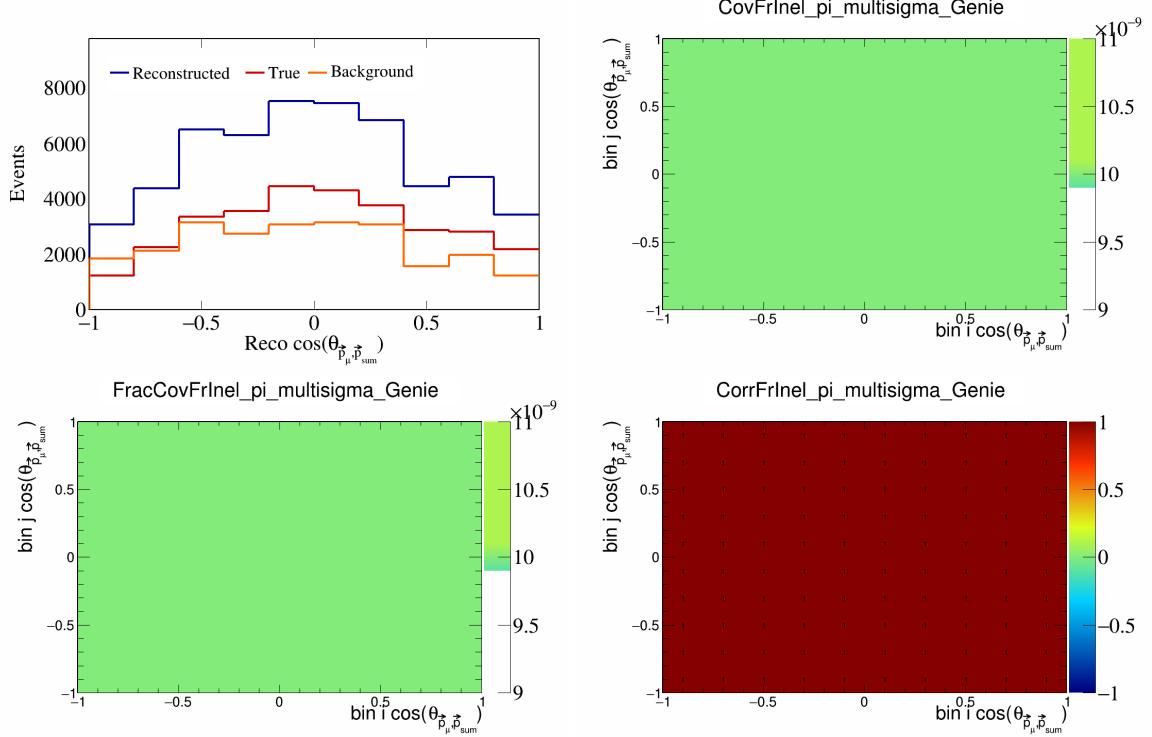


Figure 208: FrInelpi variations for $\cos(\theta_{\vec{p}_\mu, \vec{p}_{\text{sum}}})$.

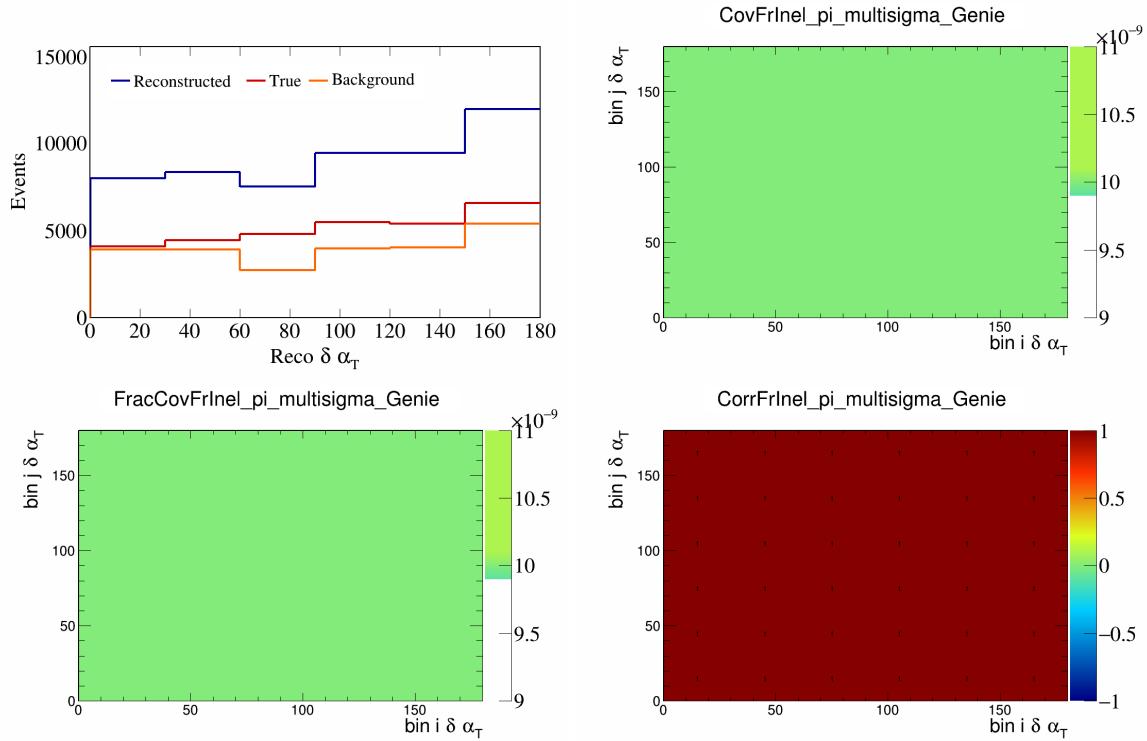


Figure 209: FrInelpi variations for $\delta\alpha_T$.

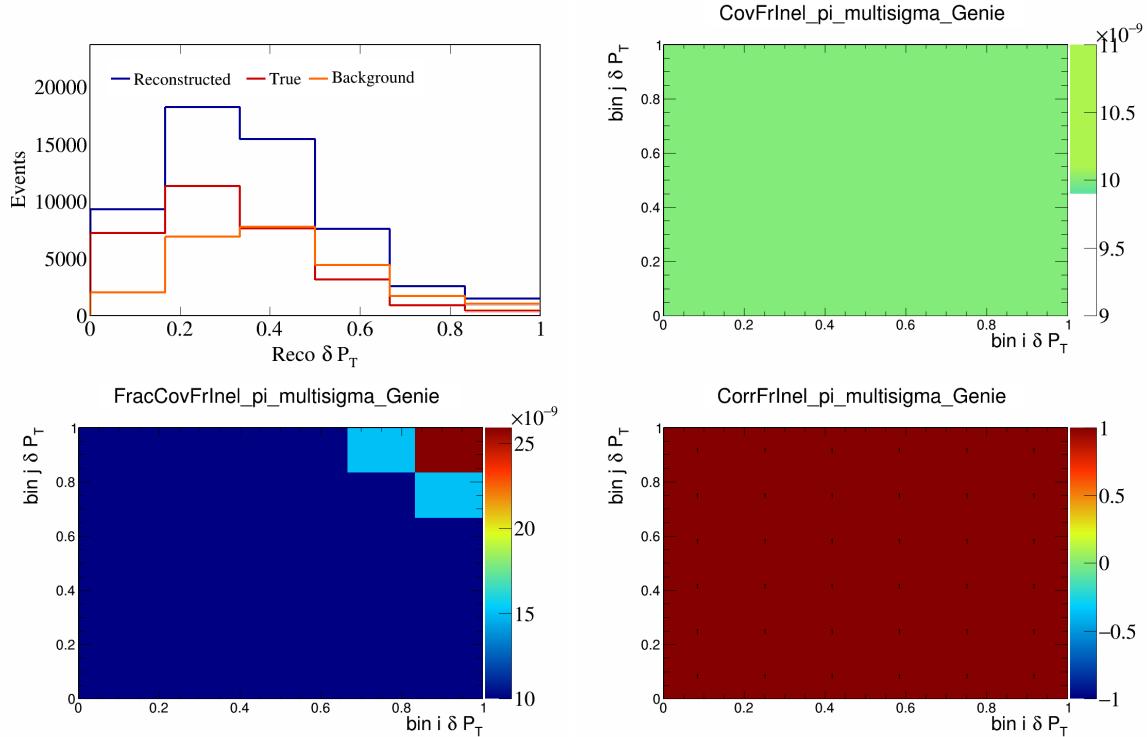


Figure 210: FrInelpi variations for δP_T .

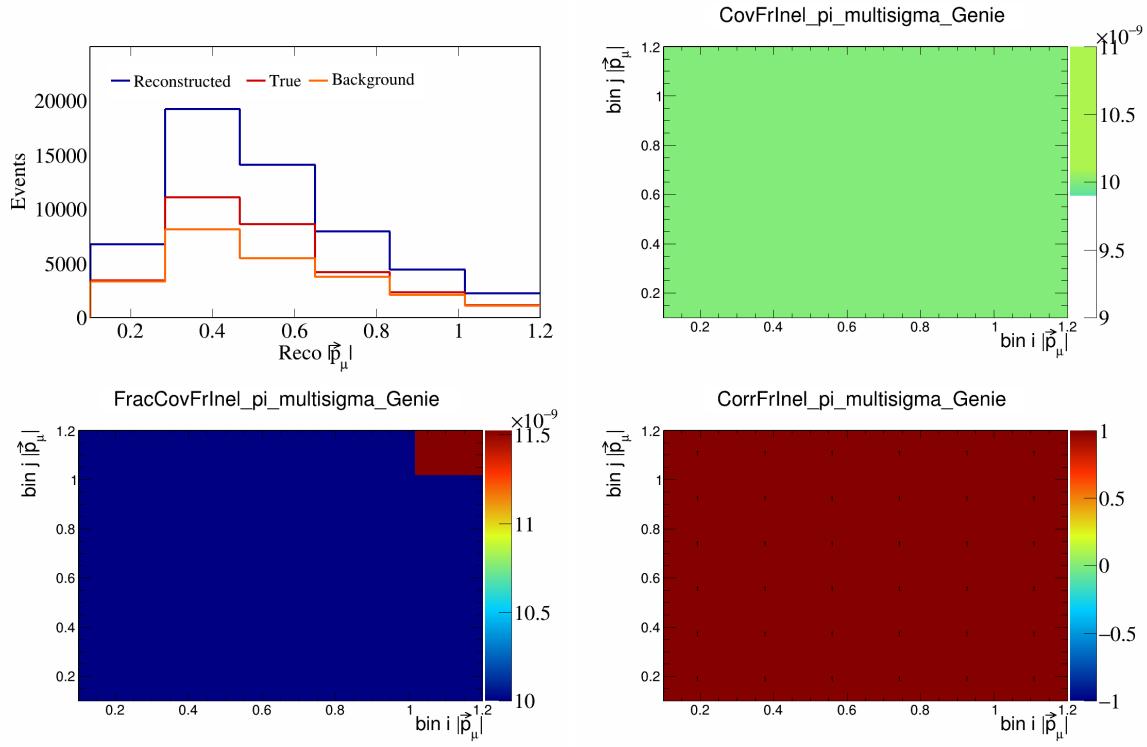


Figure 211: FrInelpi variations for $|\vec{p}_\mu|$.

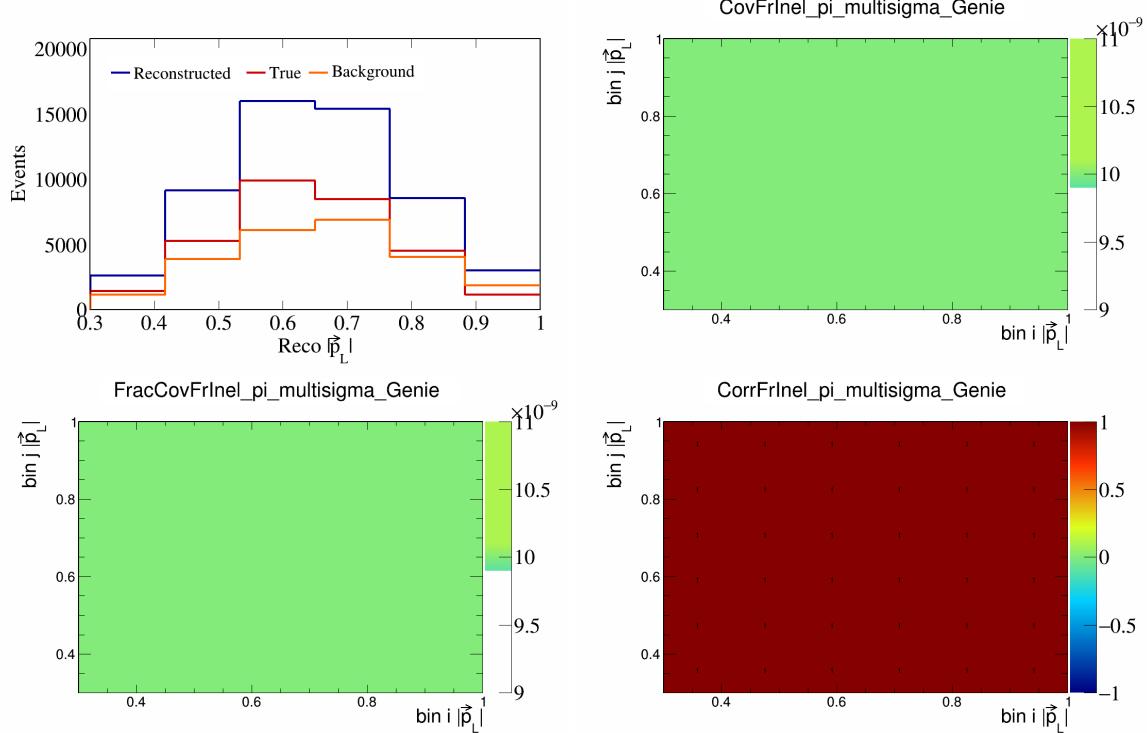


Figure 212: FrInelpi variations for $|\vec{p}_L|$.

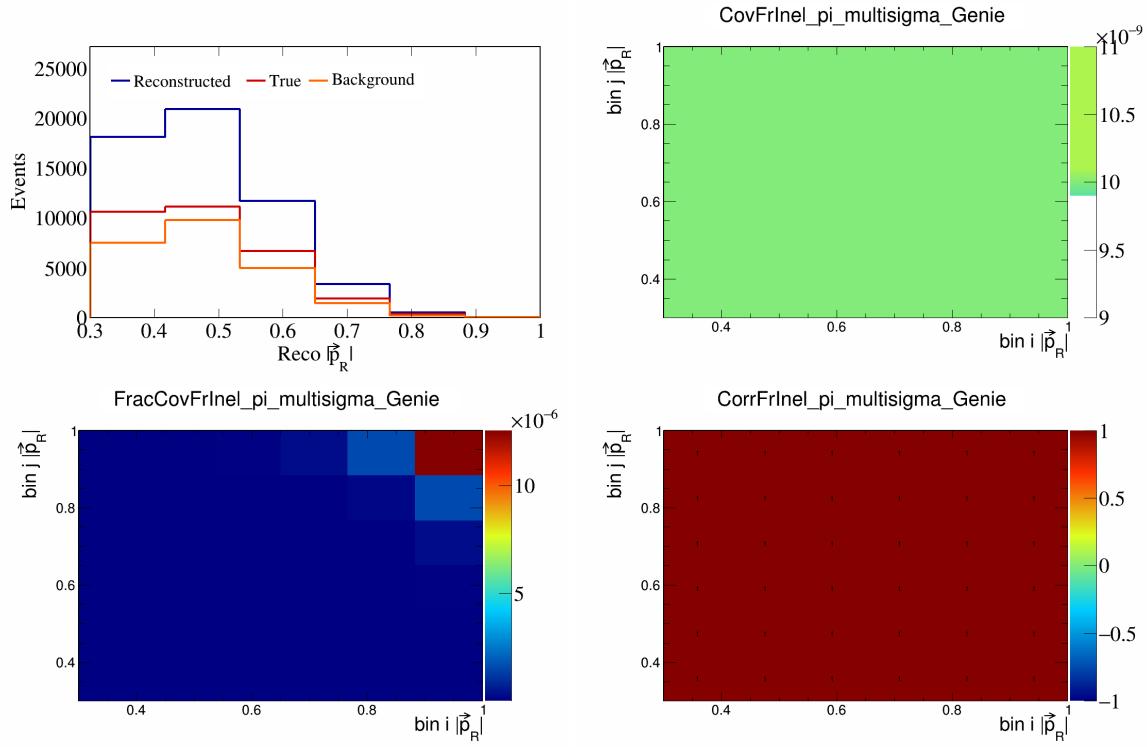


Figure 213: FrInelpi variations for $|\vec{p}_R|$.

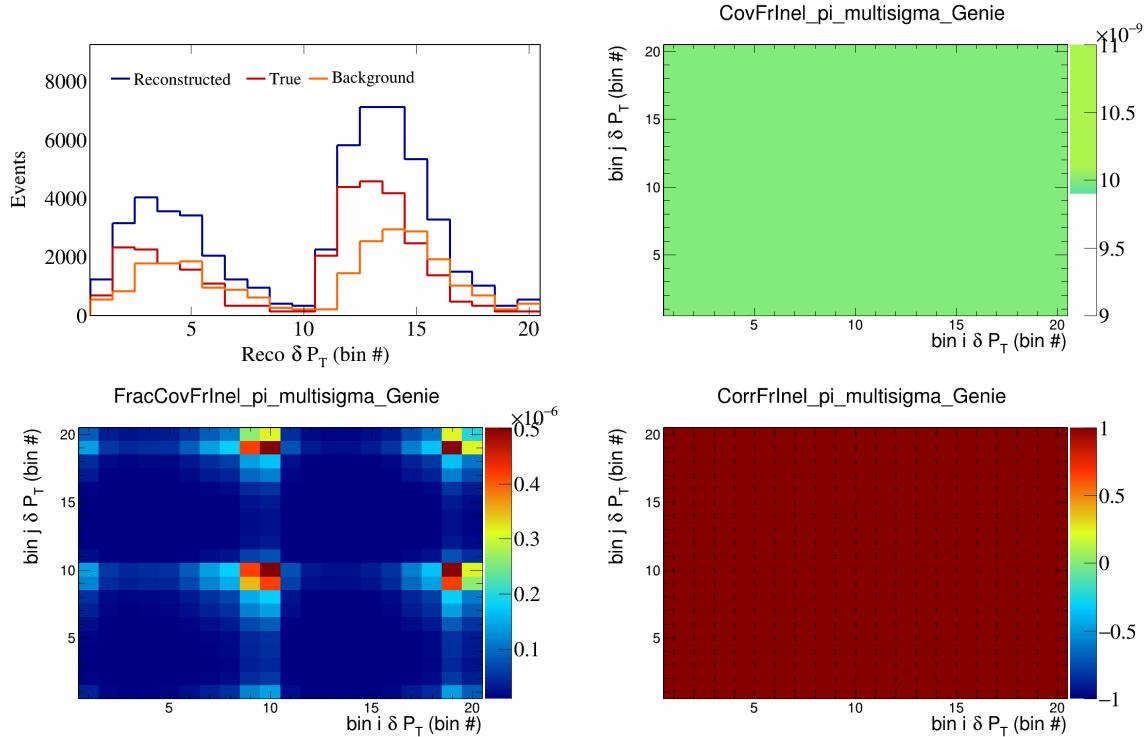


Figure 214: FrInelpi variations for δP_T in $\cos(\theta_{\vec{p}_\mu})$.

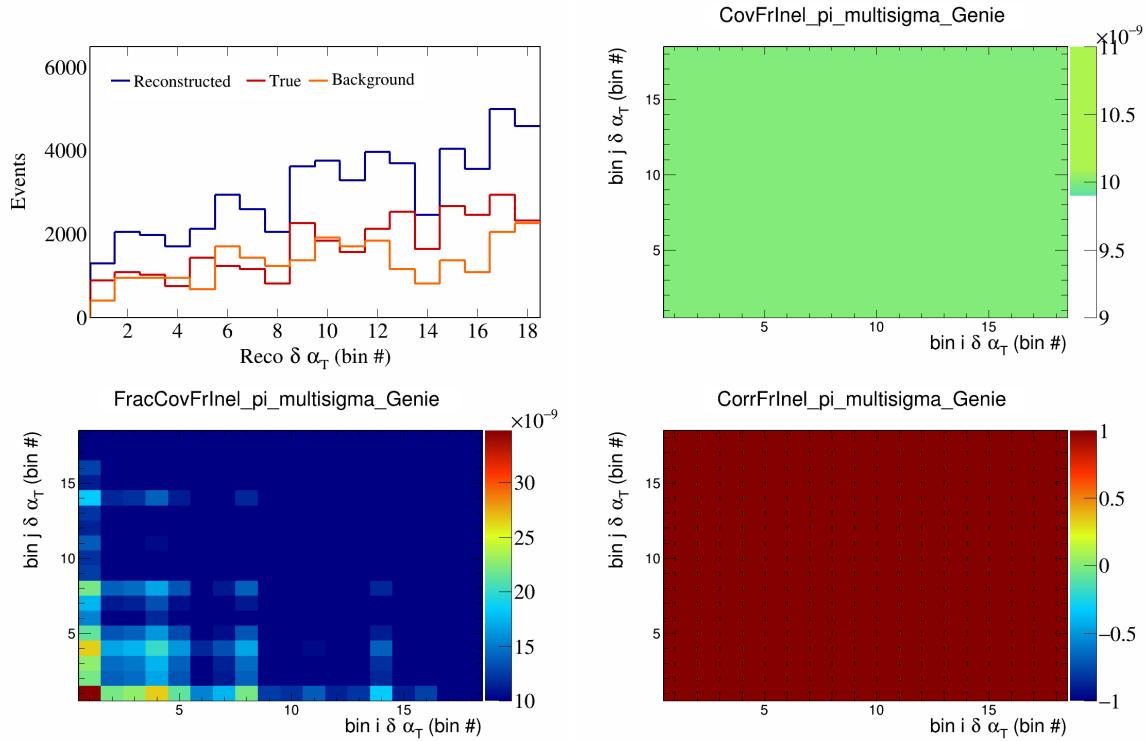


Figure 215: FrInelpi variations for $\delta\alpha_T$ in $\cos(\theta_{\vec{p}_\mu})$.

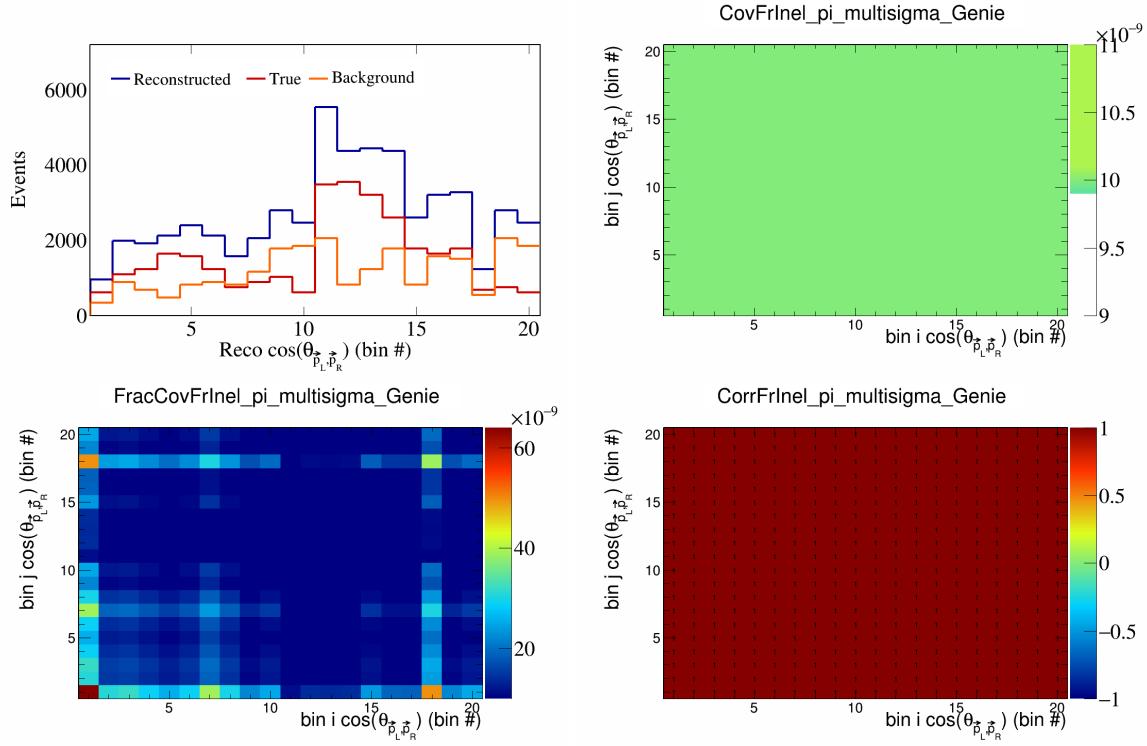


Figure 216: FrInelpi variations for $\cos(\theta_{\vec{p}_L, \vec{p}_R})$ in $\cos(\theta_{\vec{p}_\mu})$.

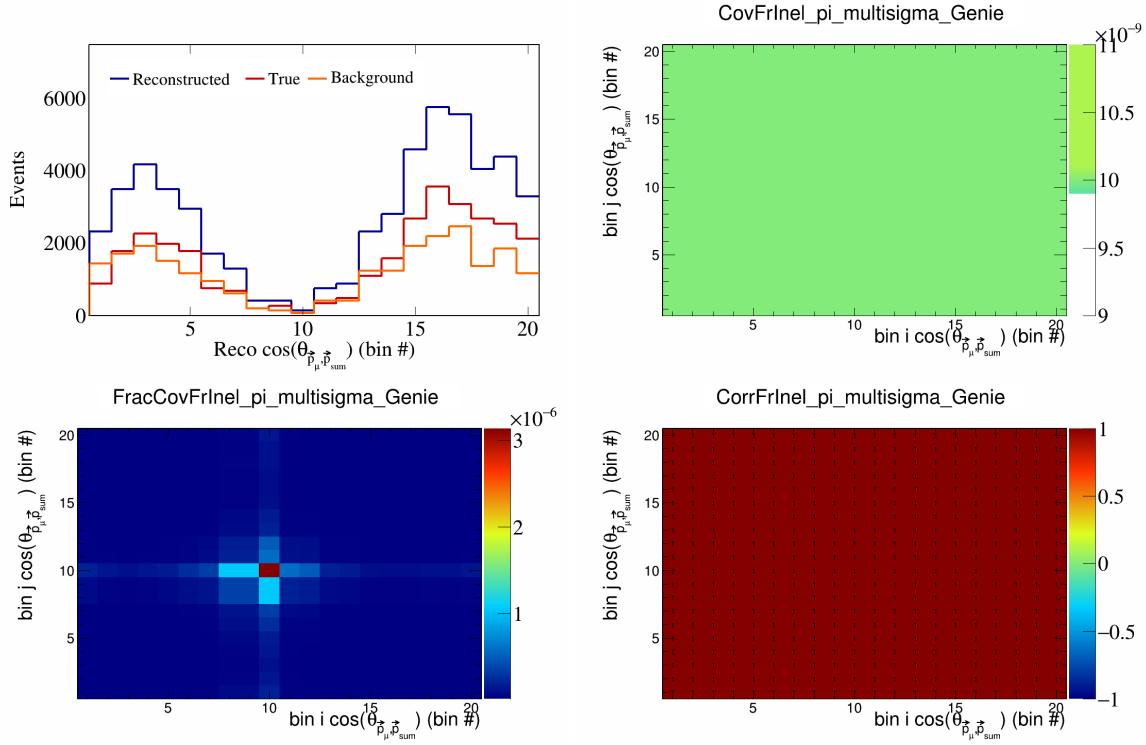


Figure 217: FrInelpi variations for $\cos(\theta_{\vec{p}_\mu, \vec{p}_{\text{sum}}})$ in $\cos(\theta_{\vec{p}_\mu})$.

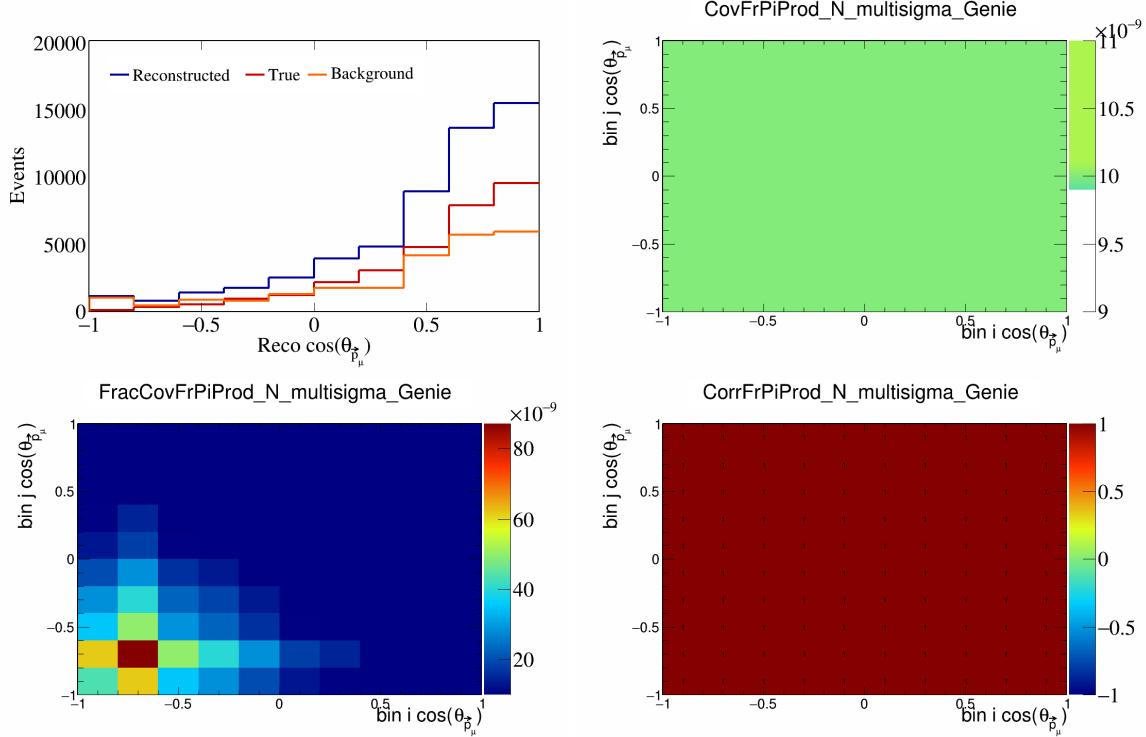


Figure 218: FrPiProdN variations for $\cos(\theta_{\vec{p}_\mu})$.

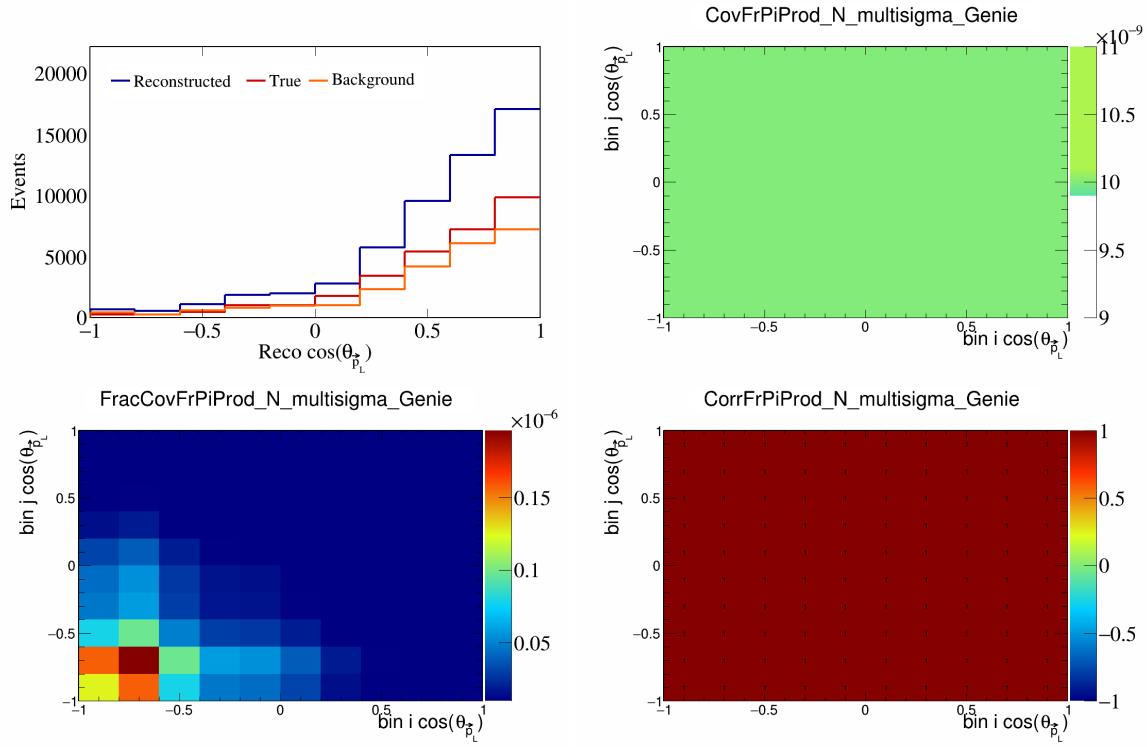


Figure 219: FrPiProdN variations for $\cos(\theta_{\vec{p}_L})$.

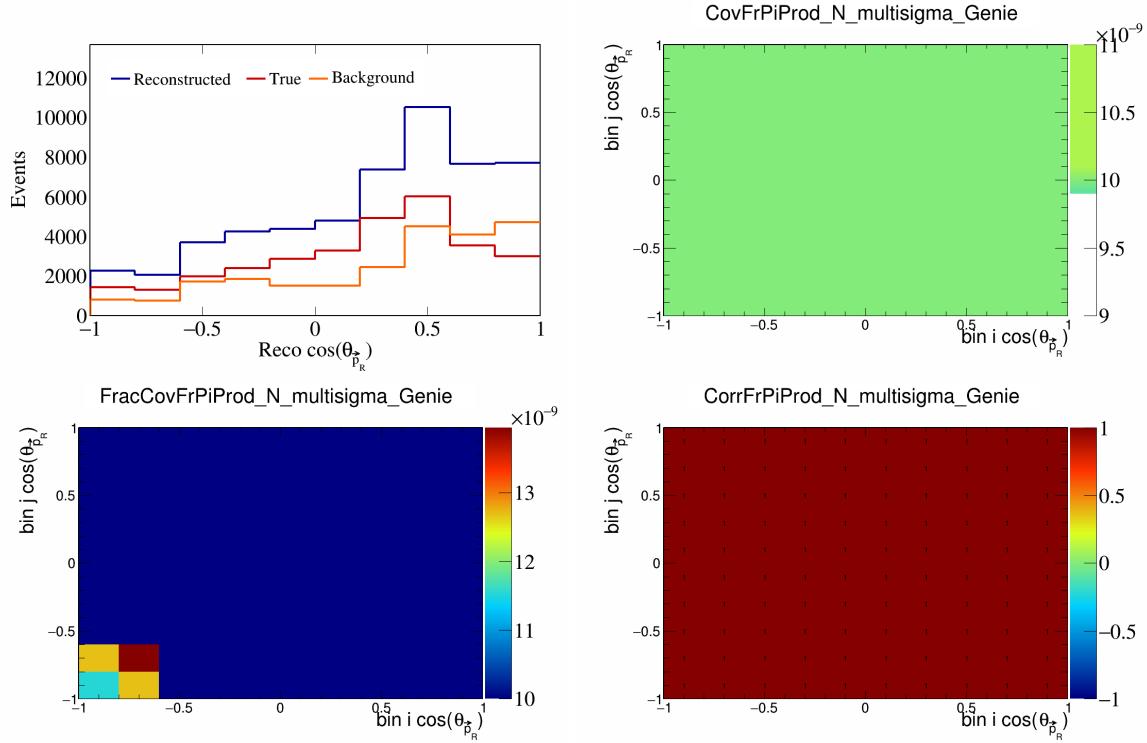


Figure 220: FrPiProdN variations for $\cos(\theta_{\vec{p}_R})$.

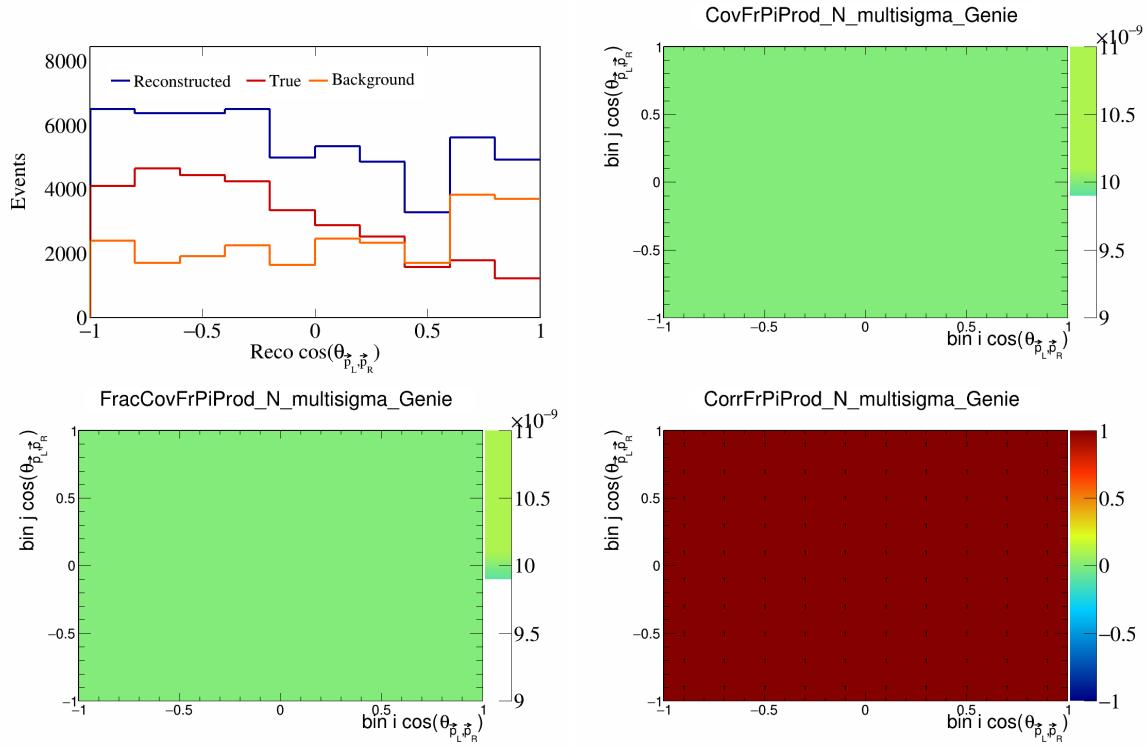


Figure 221: FrPiProdN variations for $\cos(\theta_{\vec{p}_L, \vec{p}_R})$.

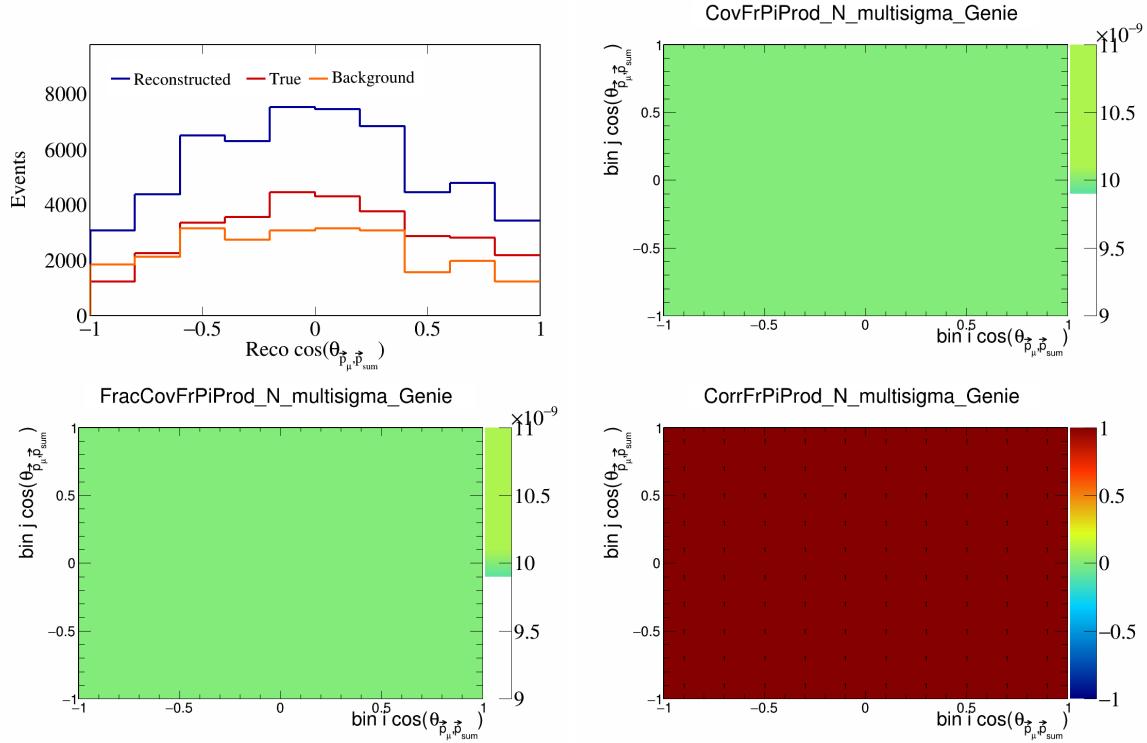


Figure 222: FrPiProdN variations for $\cos(\theta_{\vec{p}_\mu, \vec{p}_{\text{sum}}})$.

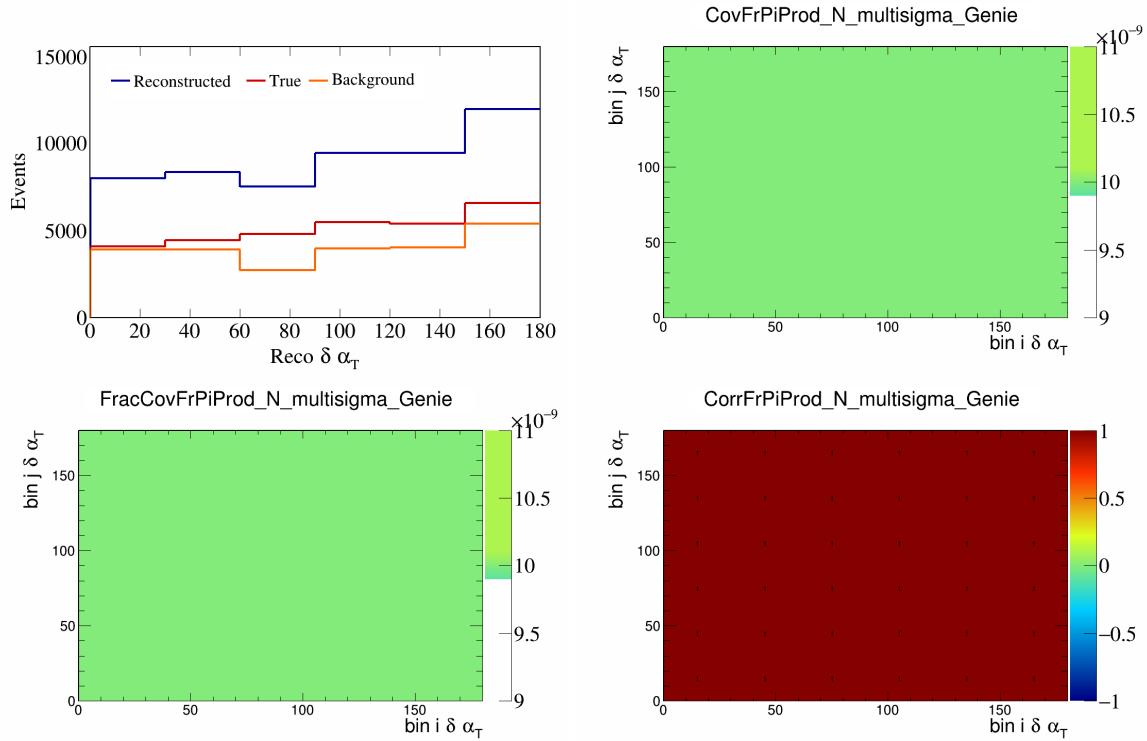


Figure 223: FrPiProdN variations for $\delta\alpha_T$.

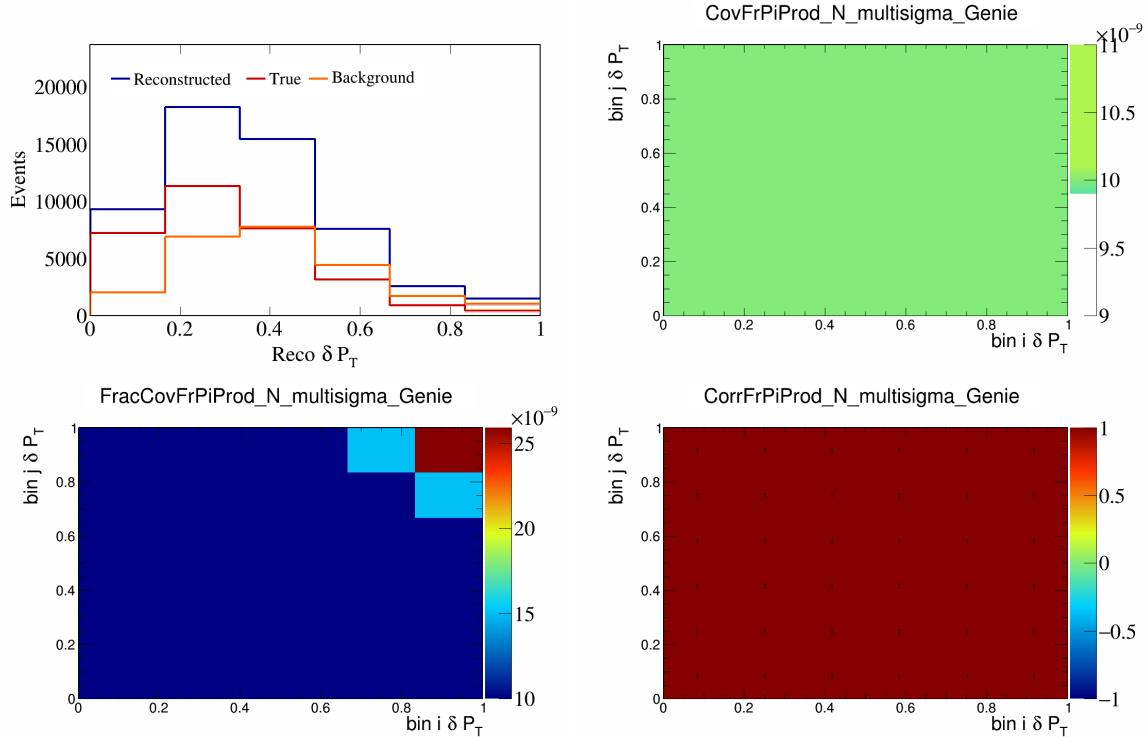


Figure 224: FrPiProdN variations for δP_T .

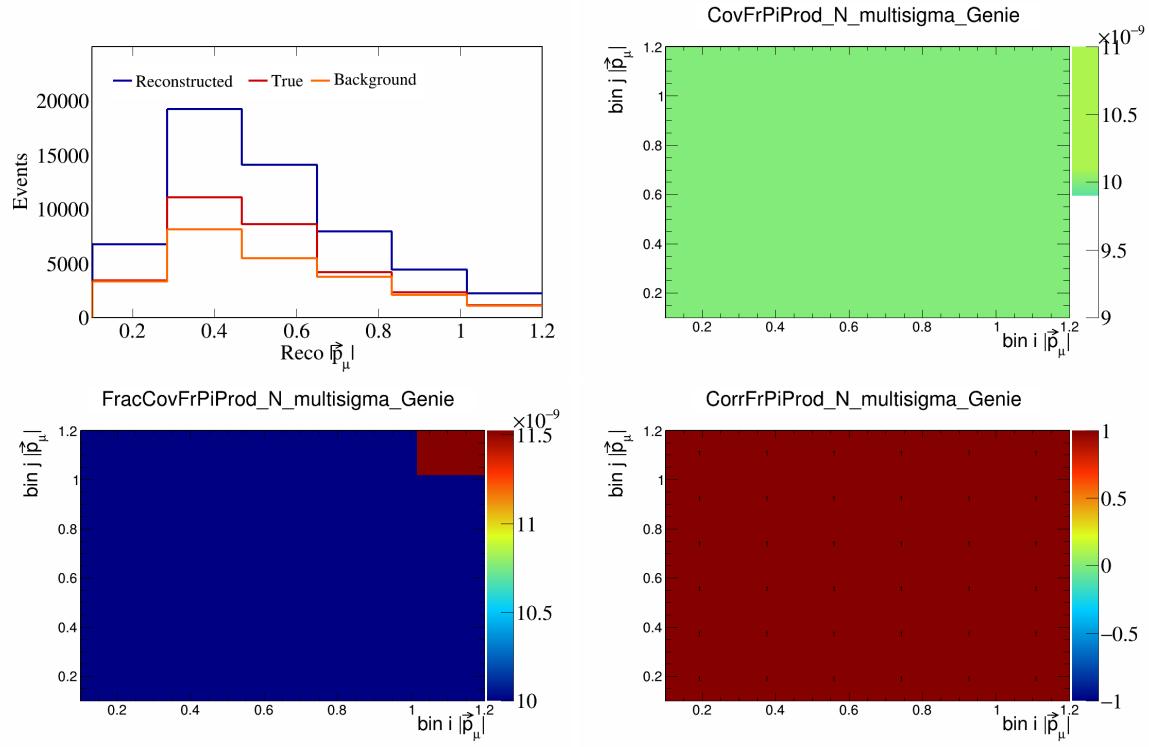


Figure 225: FrPiProdN variations for $|\vec{p}_\mu|$.

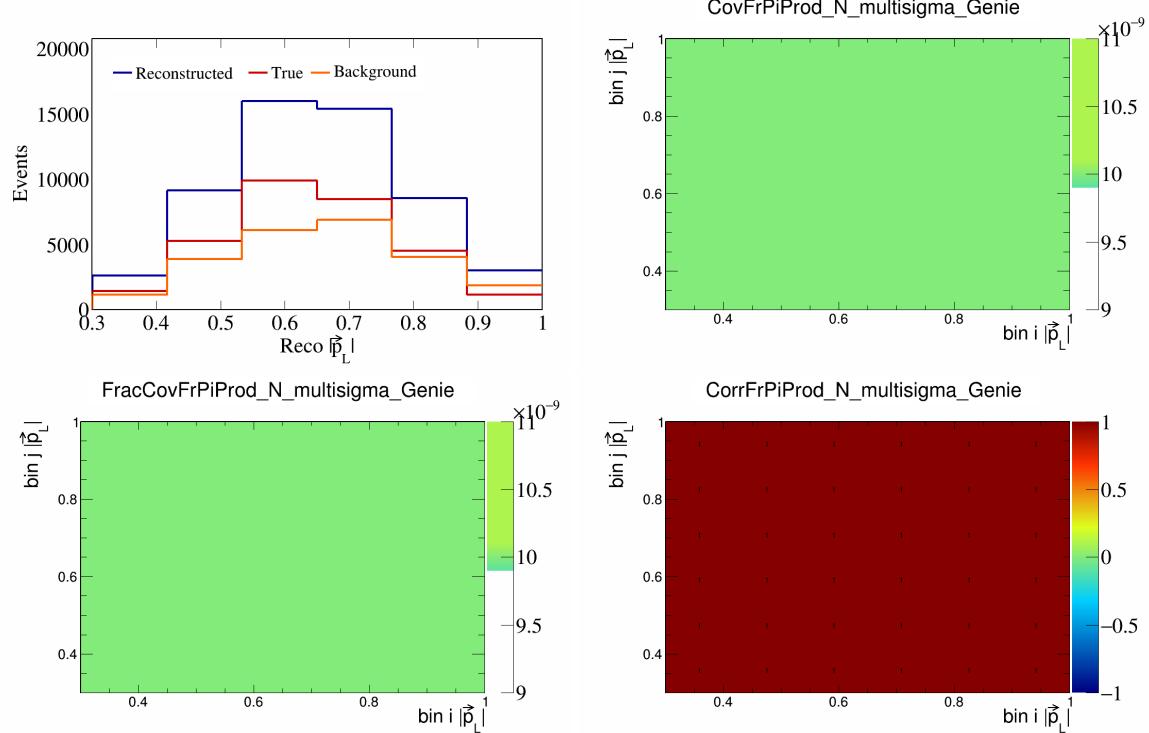


Figure 226: FrPiProdN variations for $|\vec{p}_L|$.

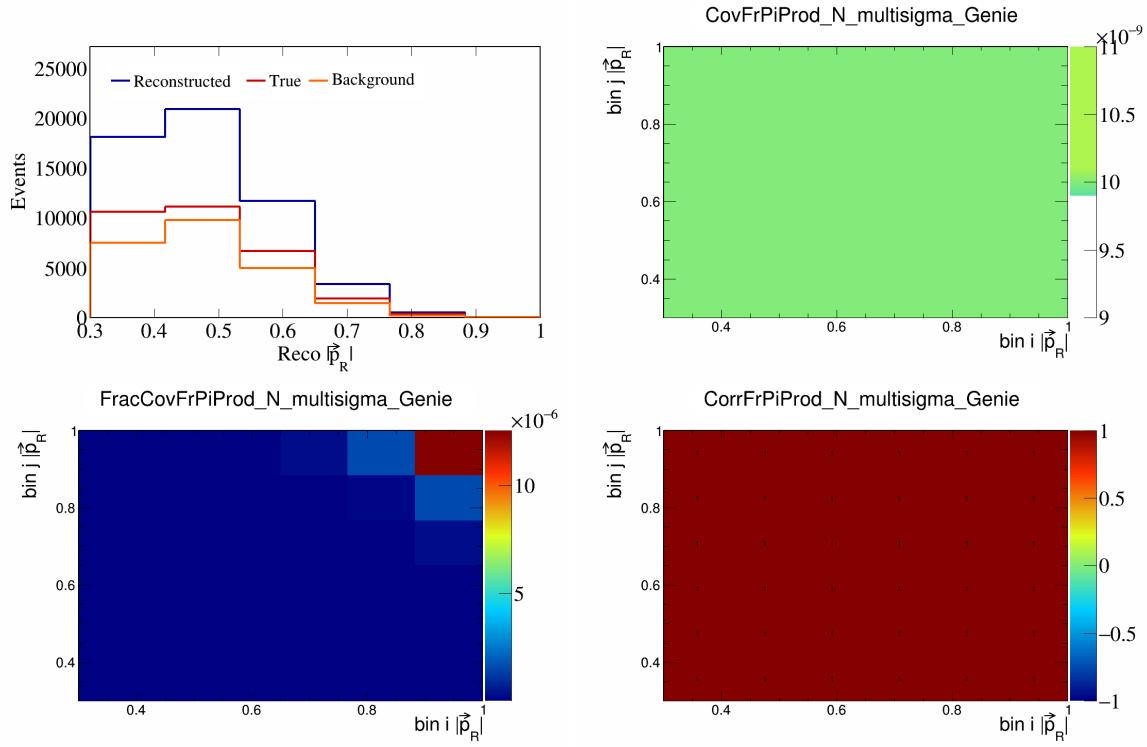


Figure 227: FrPiProdN variations for $|\vec{p}_R|$.

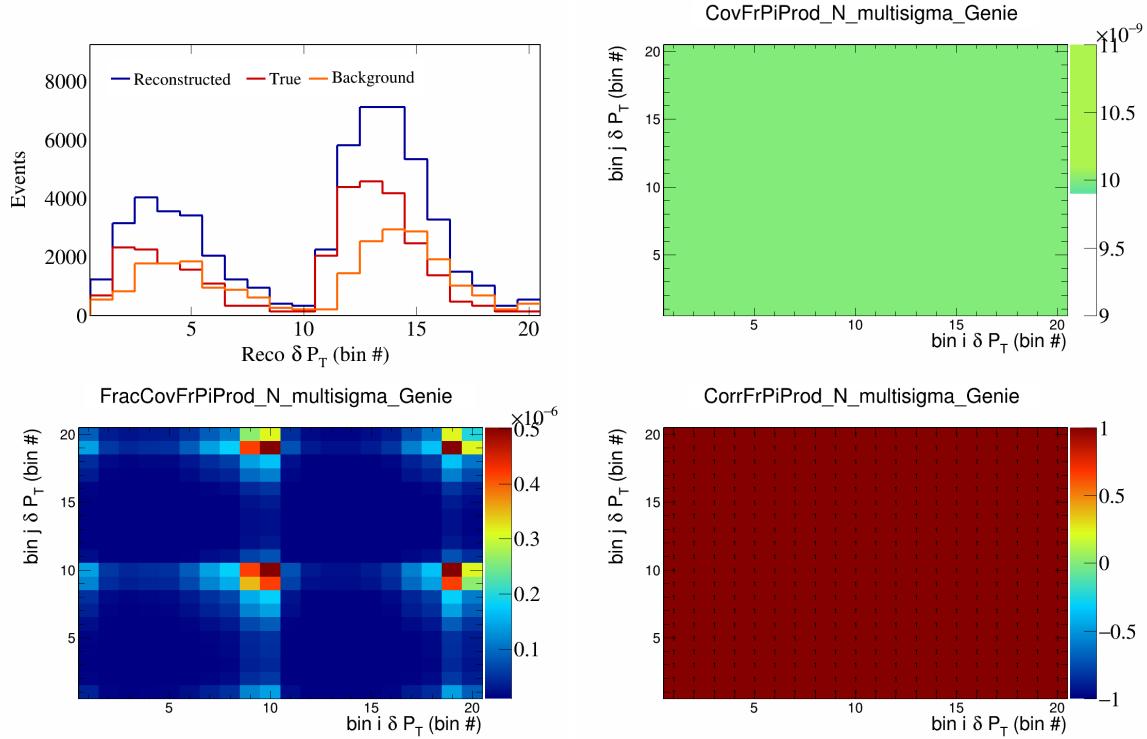


Figure 228: FrPiProdN variations for δP_T in $\cos(\theta_{\vec{p}_\mu})$.

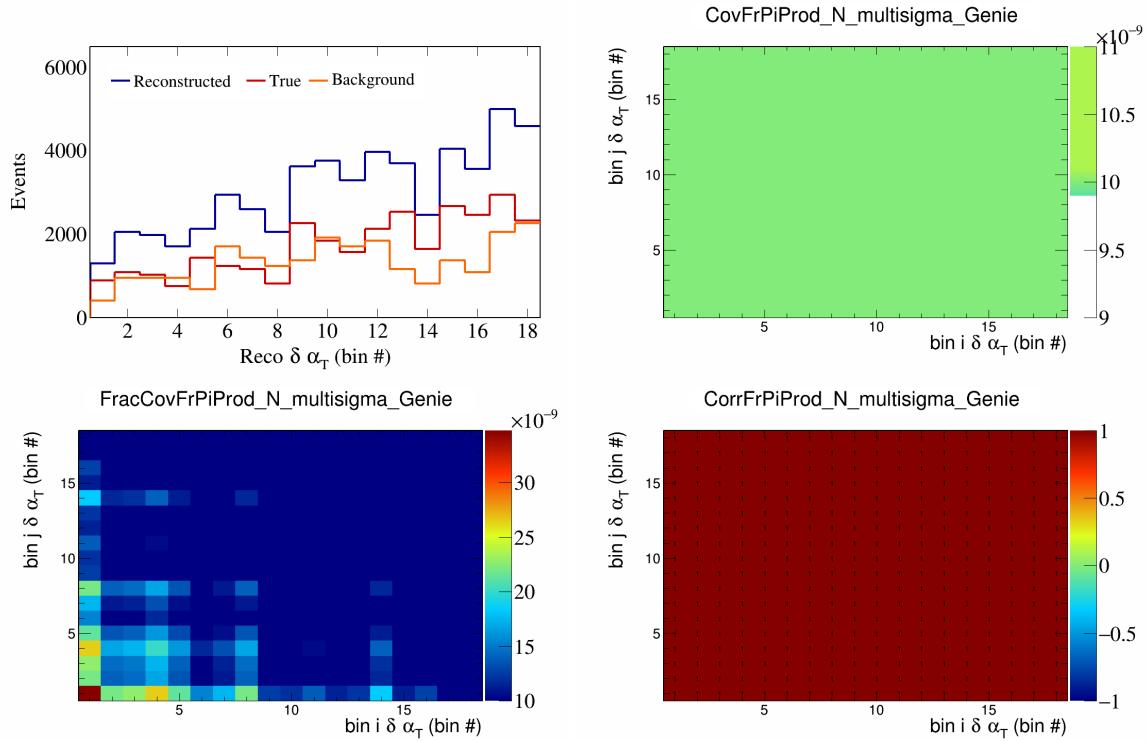


Figure 229: FrPiProdN variations for $\delta\alpha_T$ in $\cos(\theta_{\vec{p}_\mu})$.

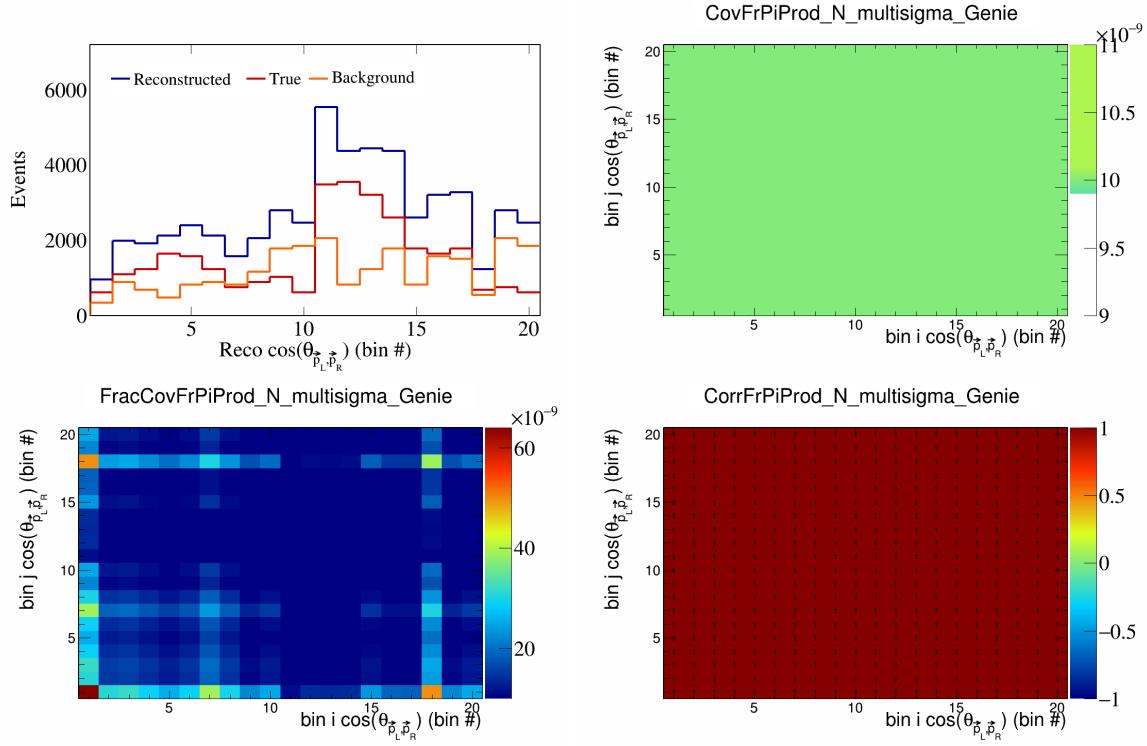


Figure 230: FrPiProdN variations for $\cos(\theta_{\vec{p}_L, \vec{p}_R})$ in $\cos(\theta_{\vec{p}_\mu})$.

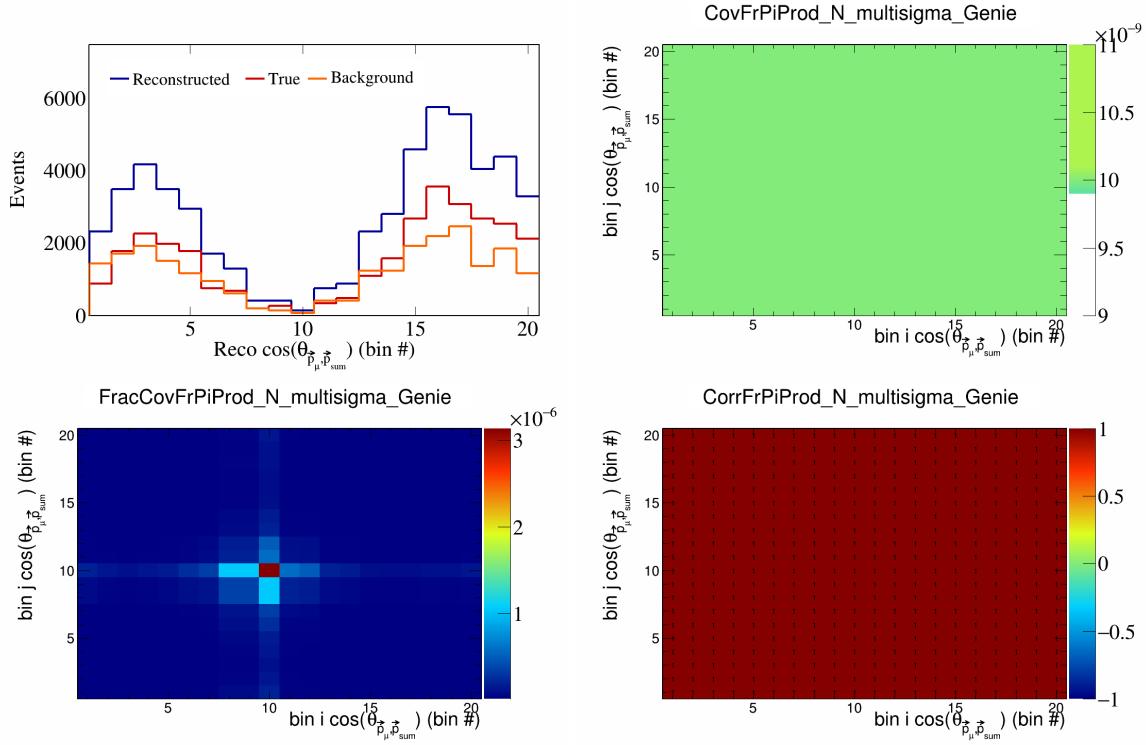


Figure 231: FrPiProdN variations for $\cos(\theta_{\vec{p}_\mu, \vec{p}_{\text{sum}}})$ in $\cos(\theta_{\vec{p}_\mu})$.

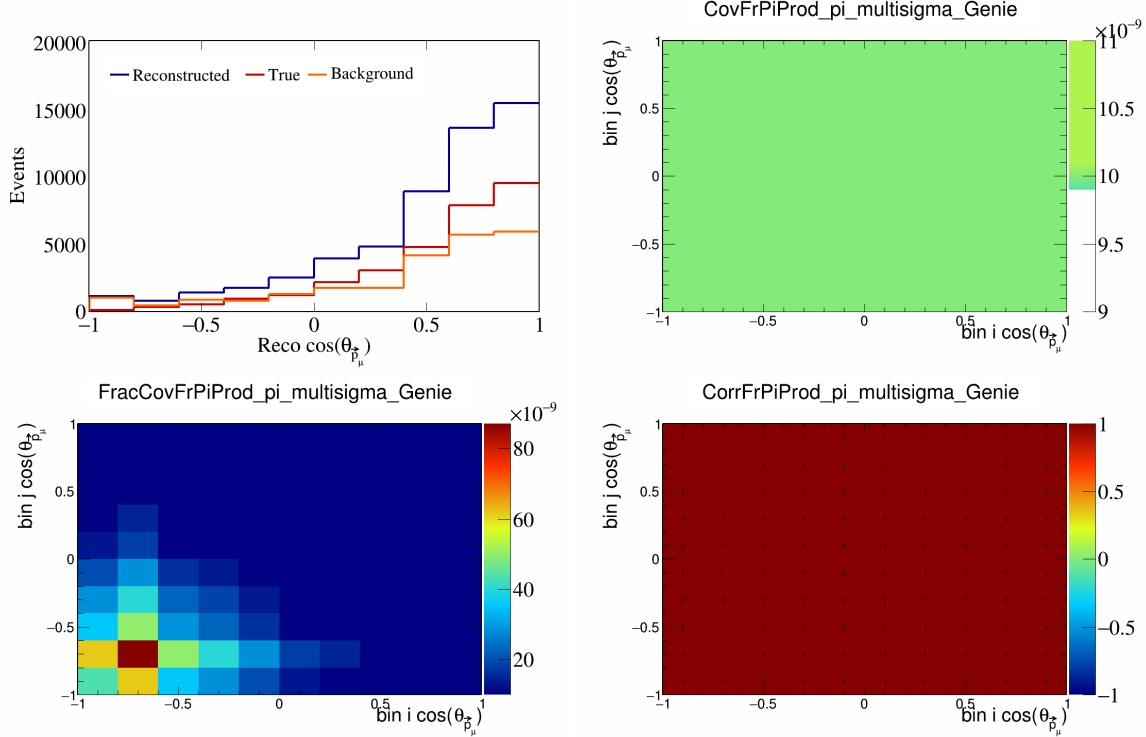


Figure 232: FrPiProdpi variations for $\cos(\theta_{\vec{p}_\mu})$.

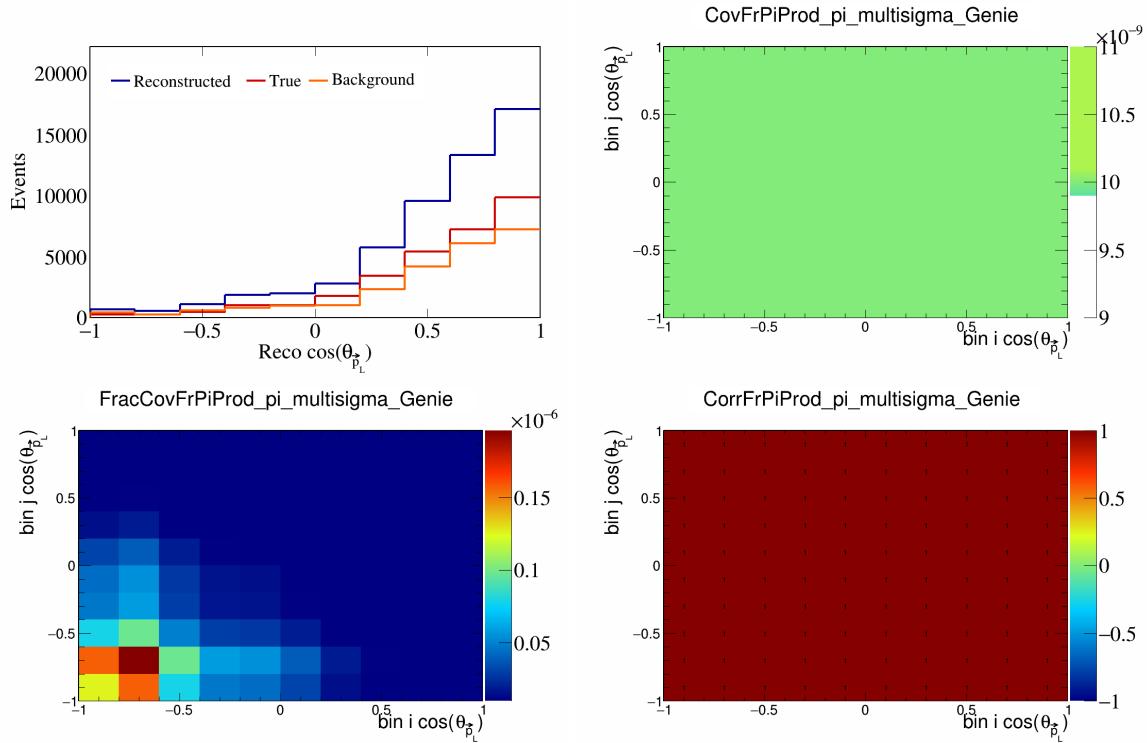


Figure 233: FrPiProdpi variations for $\cos(\theta_{\vec{p}_L})$.

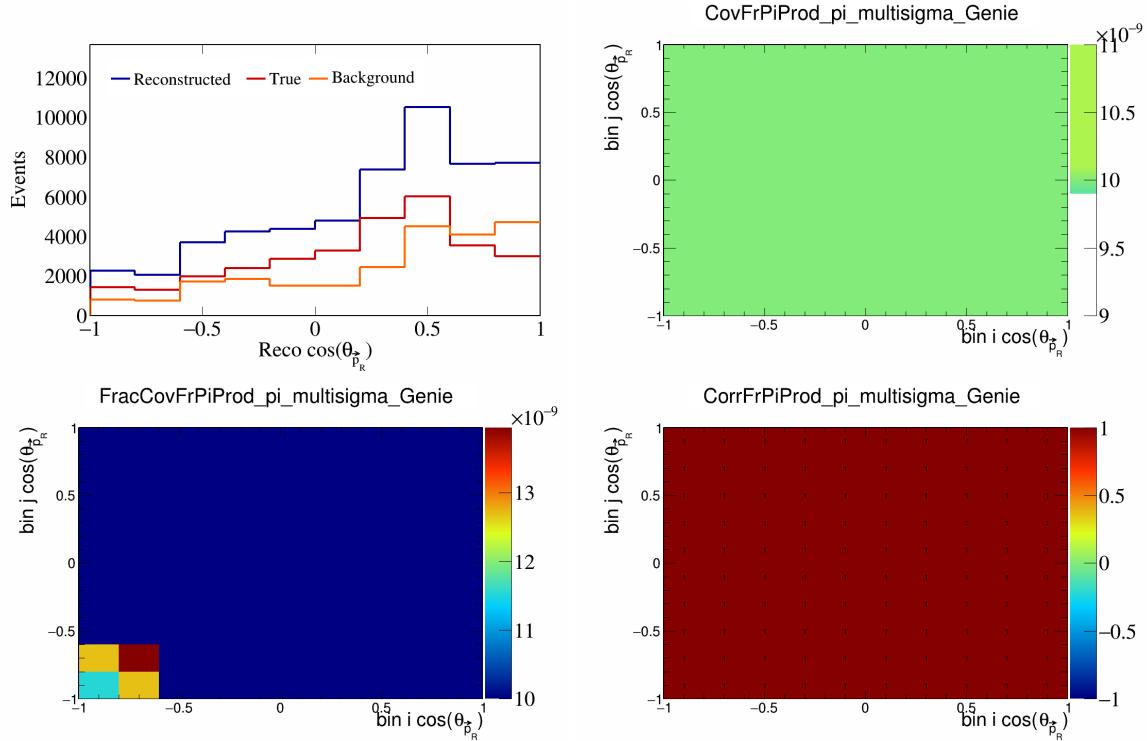


Figure 234: FrPiProdpi variations for $\cos(\theta_{\vec{p}_R})$.

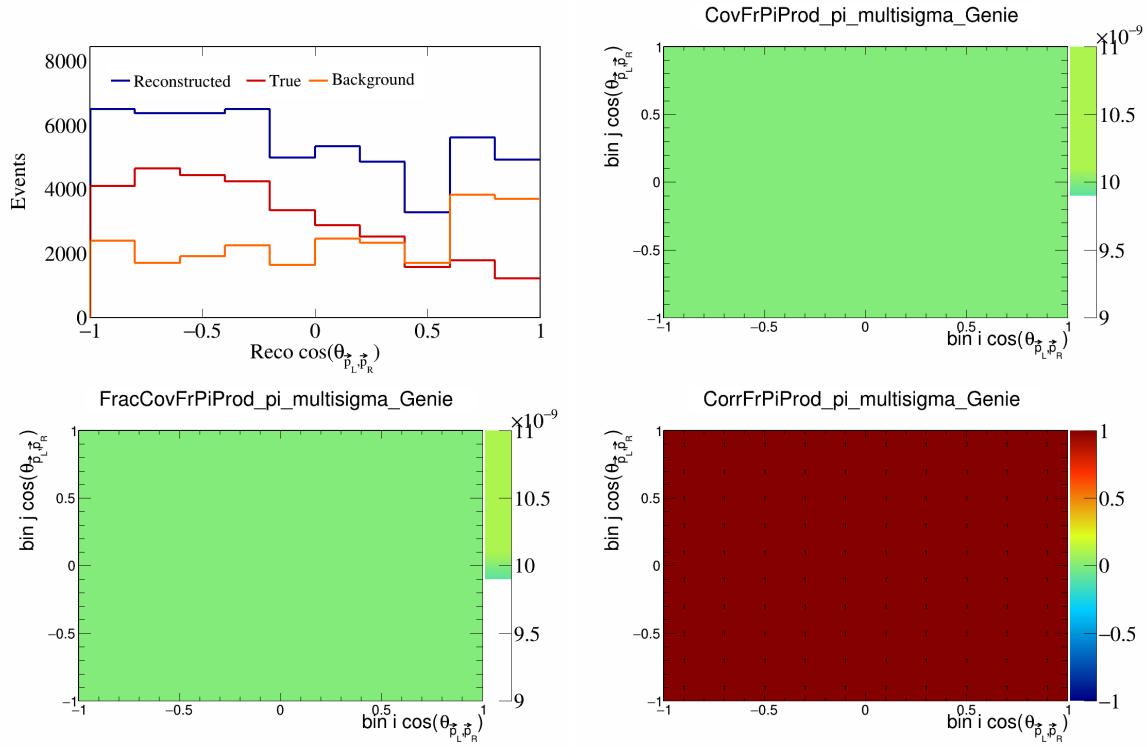


Figure 235: FrPiProdpi variations for $\cos(\theta_{\vec{p}_L, \vec{p}_R})$.

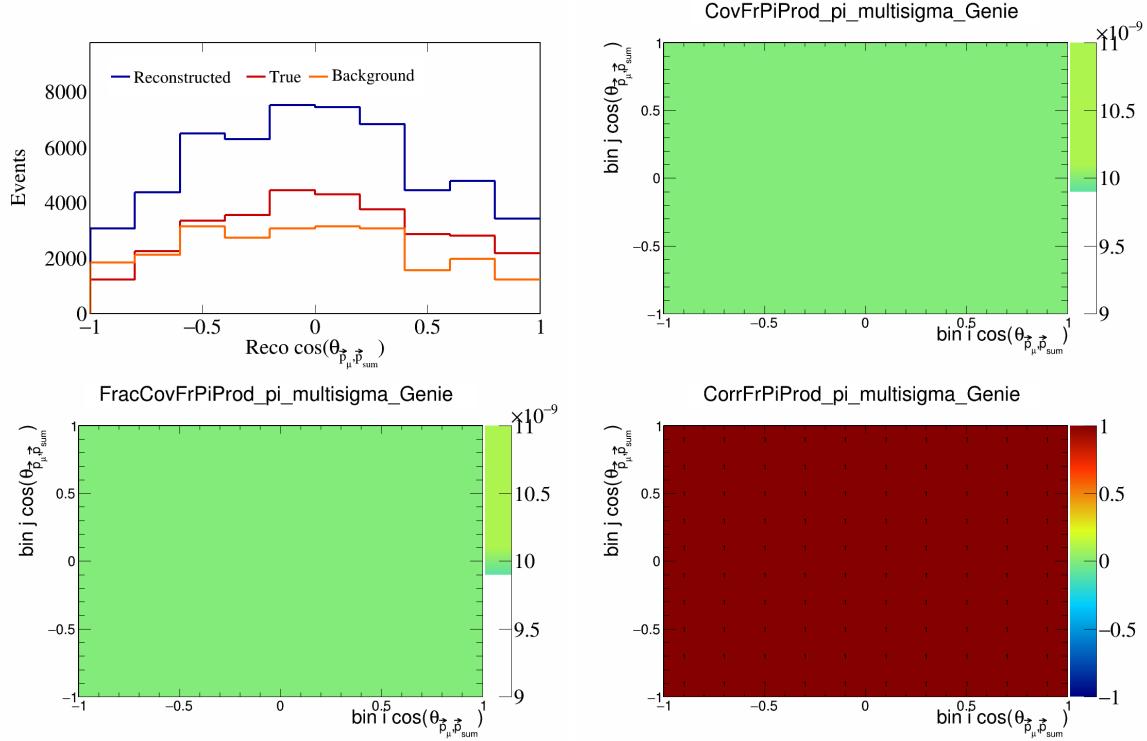


Figure 236: FrPiProdpi variations for $\cos(\theta_{\vec{p}_\mu, \vec{p}_{\text{sum}}})$.

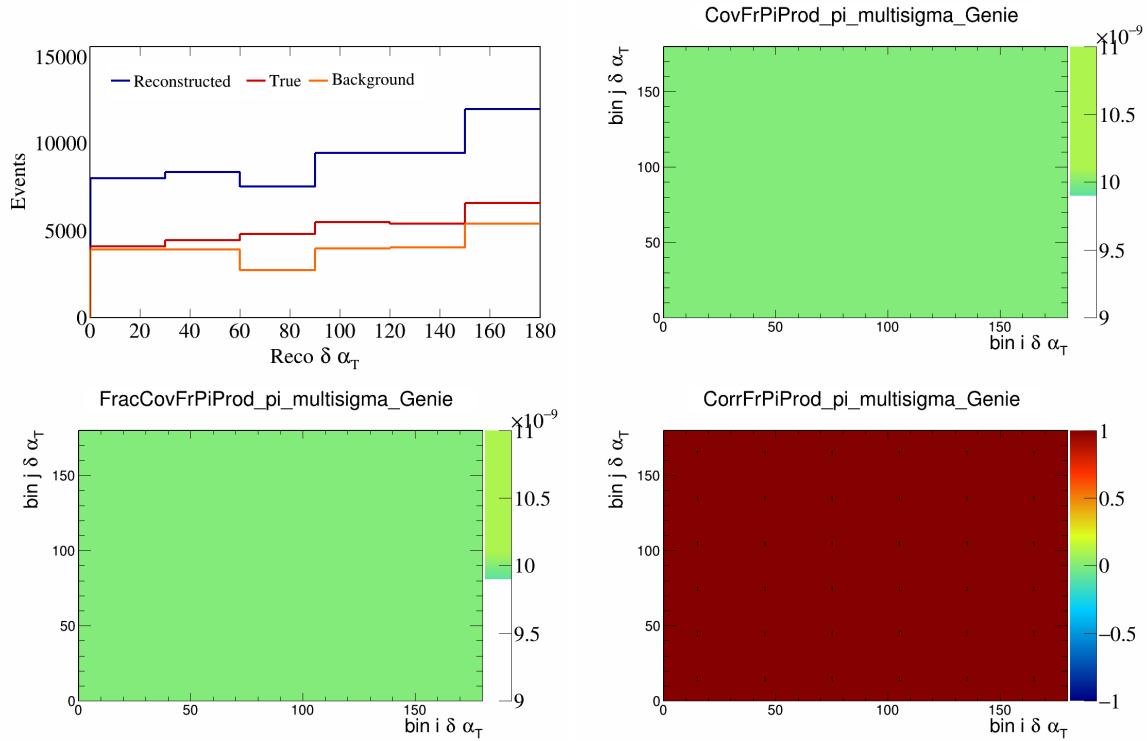


Figure 237: FrPiProdpi variations for $\delta\alpha_T$.

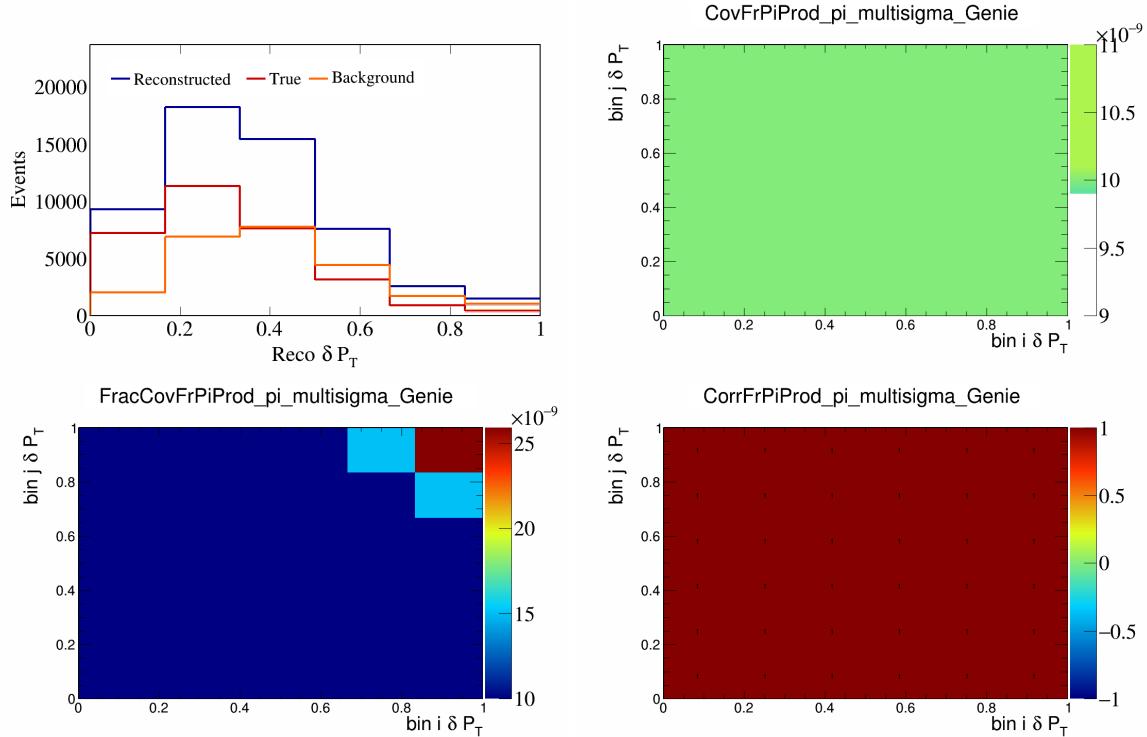


Figure 238: FrPiProdpi variations for δP_T .

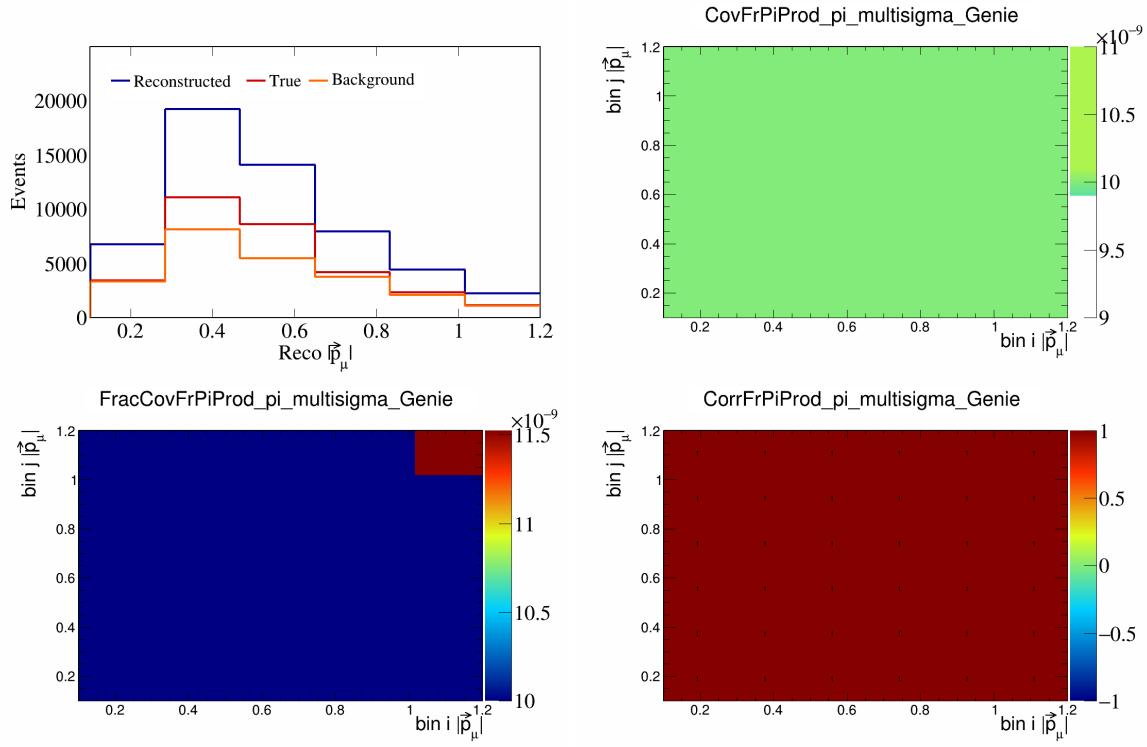


Figure 239: FrPiProdpi variations for $|\vec{p}_\mu|$.

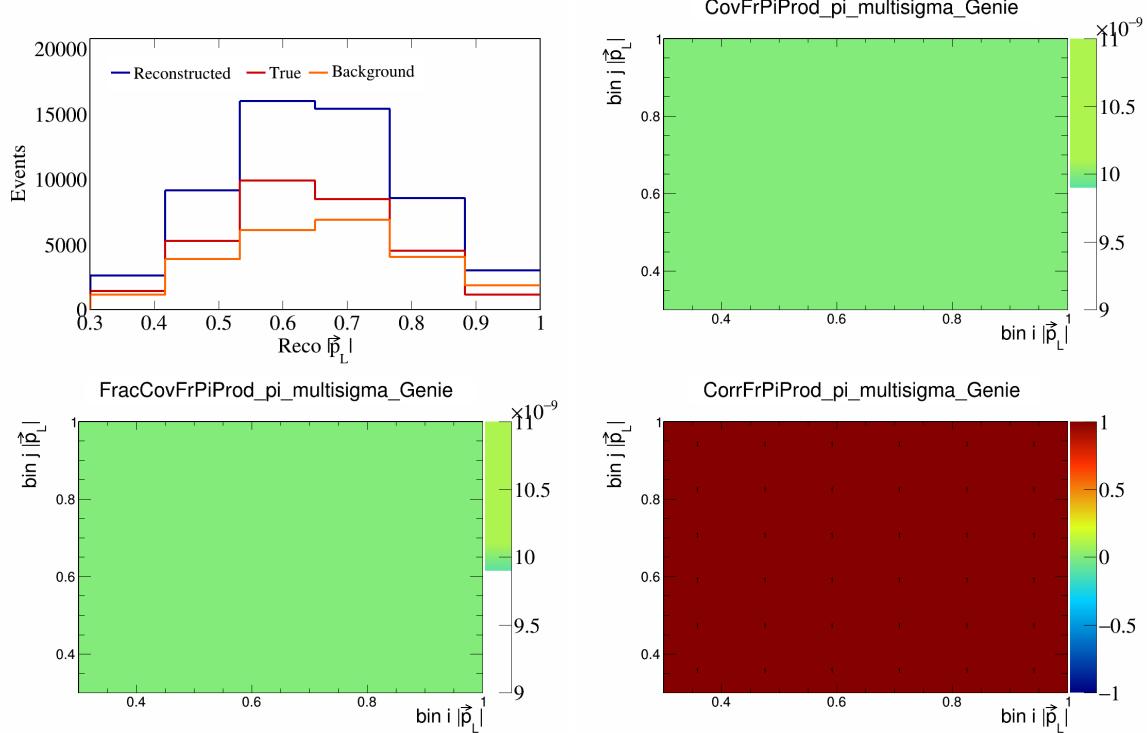


Figure 240: FrPiProdpi variations for $|\vec{p}_L|$.

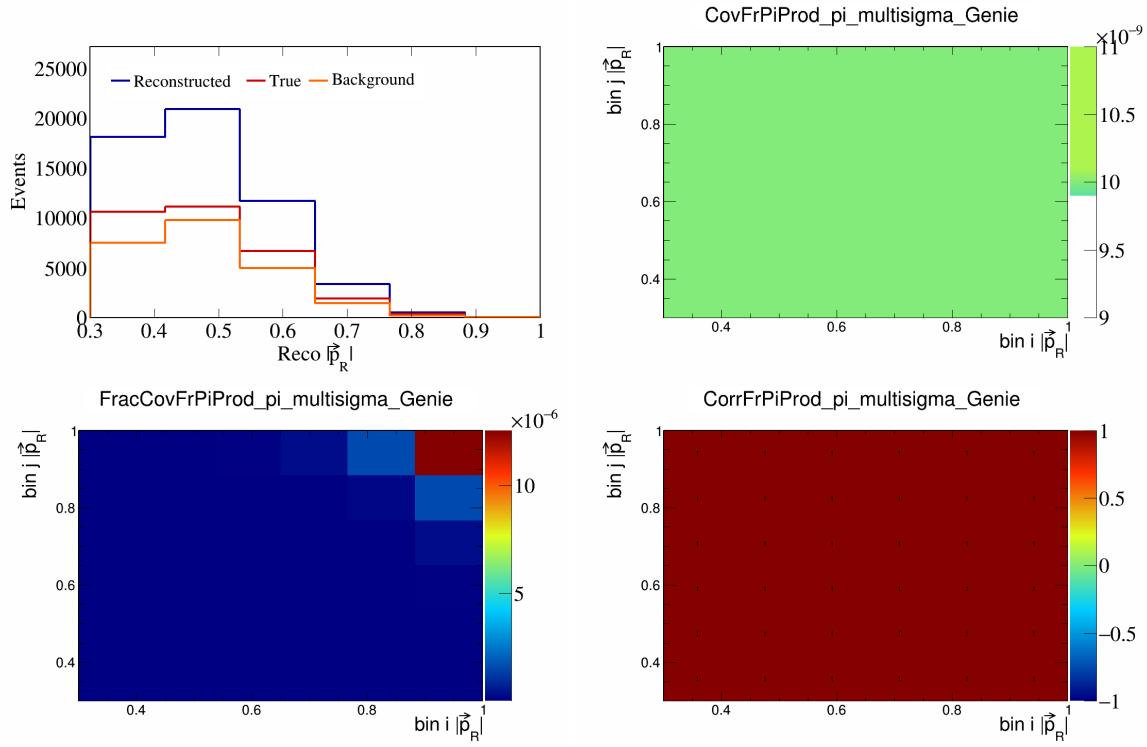


Figure 241: FrPiProdpi variations for $|\vec{p}_R|$.

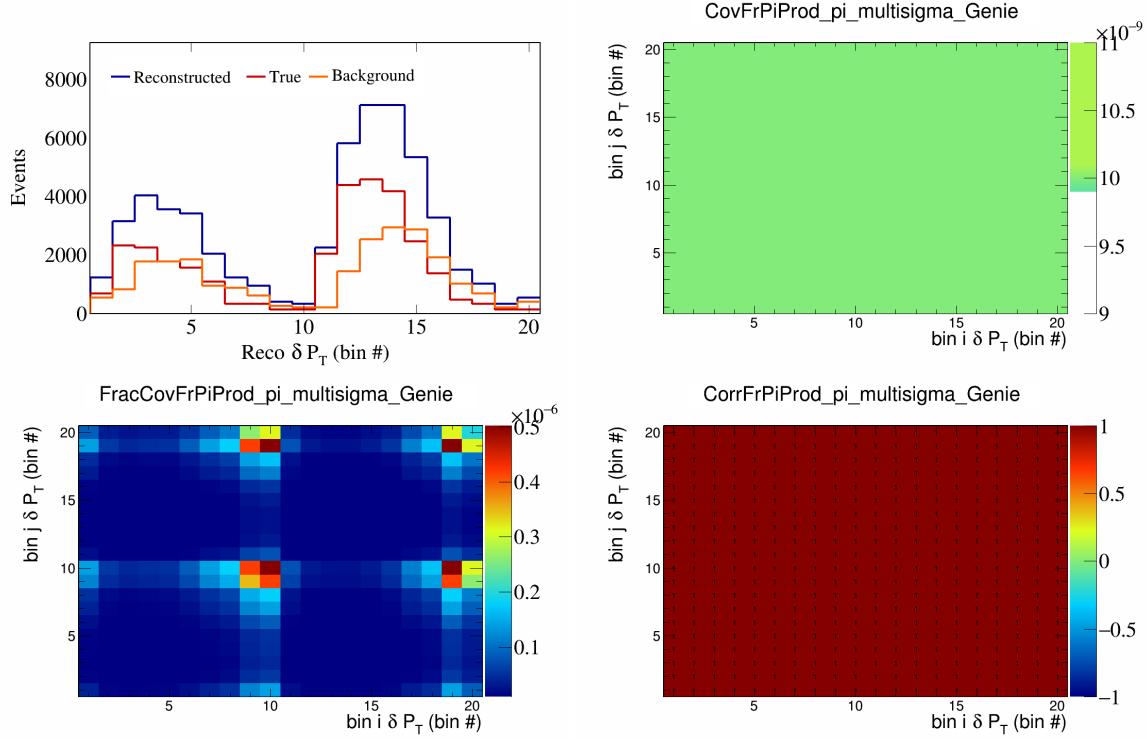


Figure 242: FrPiProdpi variations for δP_T in $\cos(\theta_{\vec{p}_\mu})$.

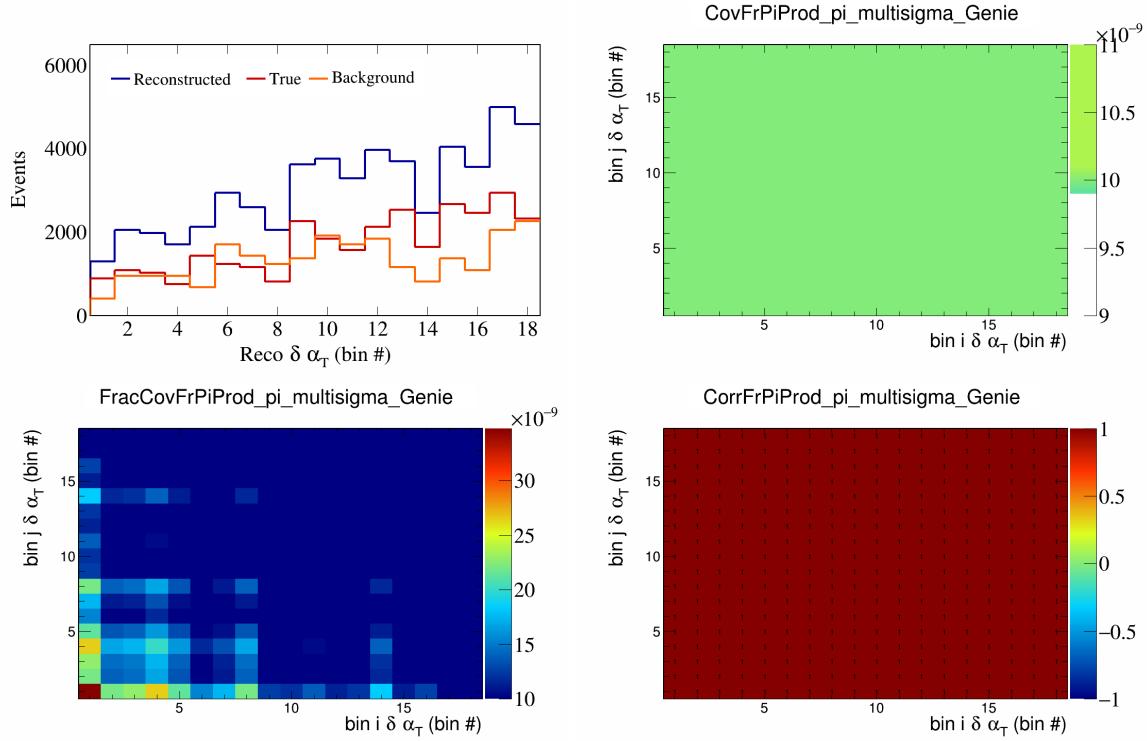


Figure 243: FrPiProdpi variations for $\delta\alpha_T$ in $\cos(\theta_{\vec{p}_\mu})$.

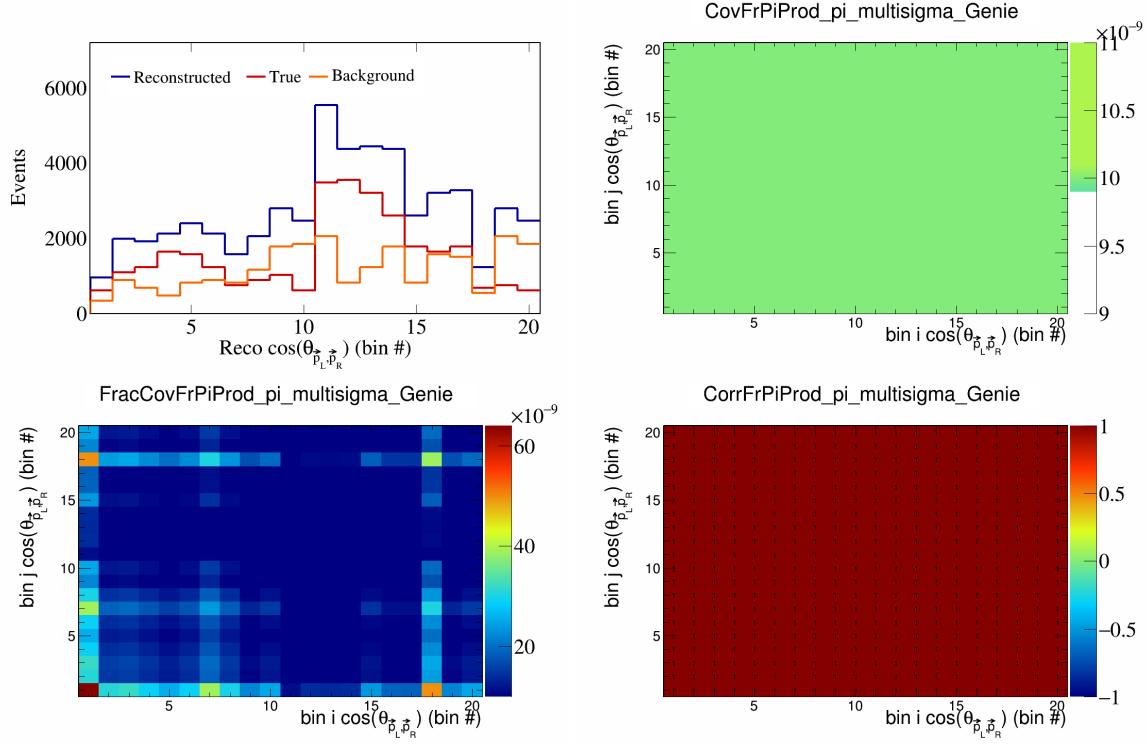


Figure 244: FrPiProdpi variations for $\cos(\theta_{\vec{p}_L, \vec{p}_R})$ in $\cos(\theta_{\vec{p}_\mu})$.

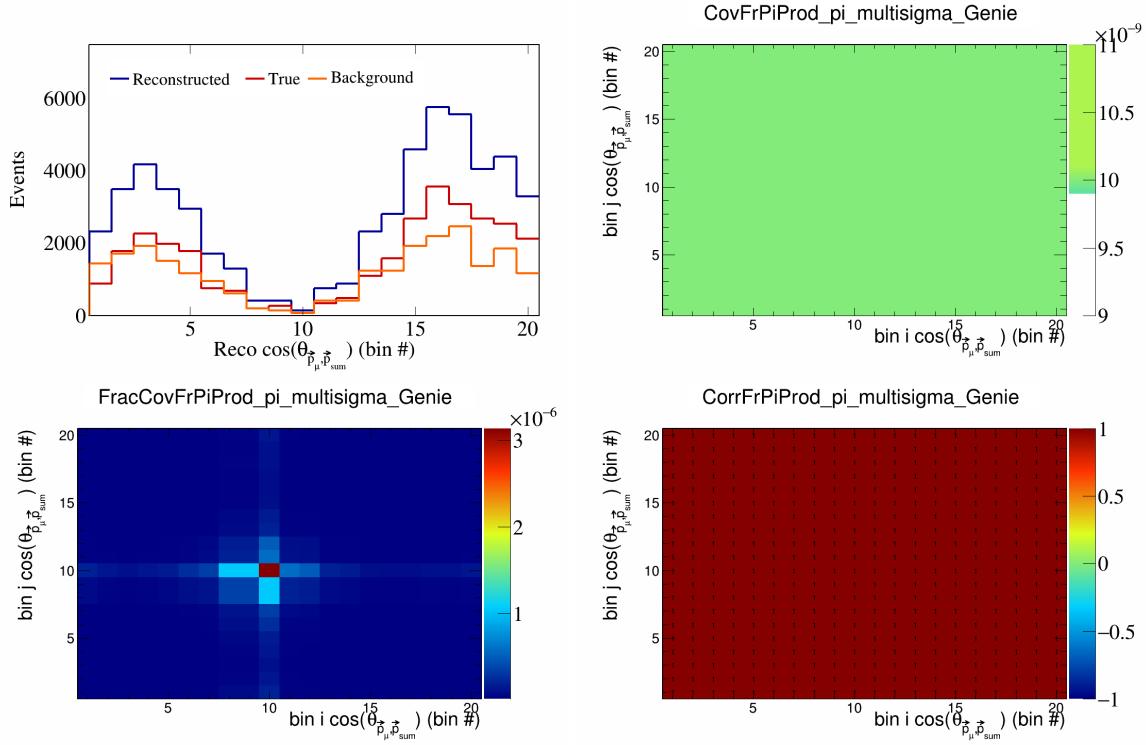


Figure 245: FrPiProdpi variations for $\cos(\theta_{\vec{p}_\mu, \vec{p}_{\text{sum}}})$ in $\cos(\theta_{\vec{p}_\mu})$.

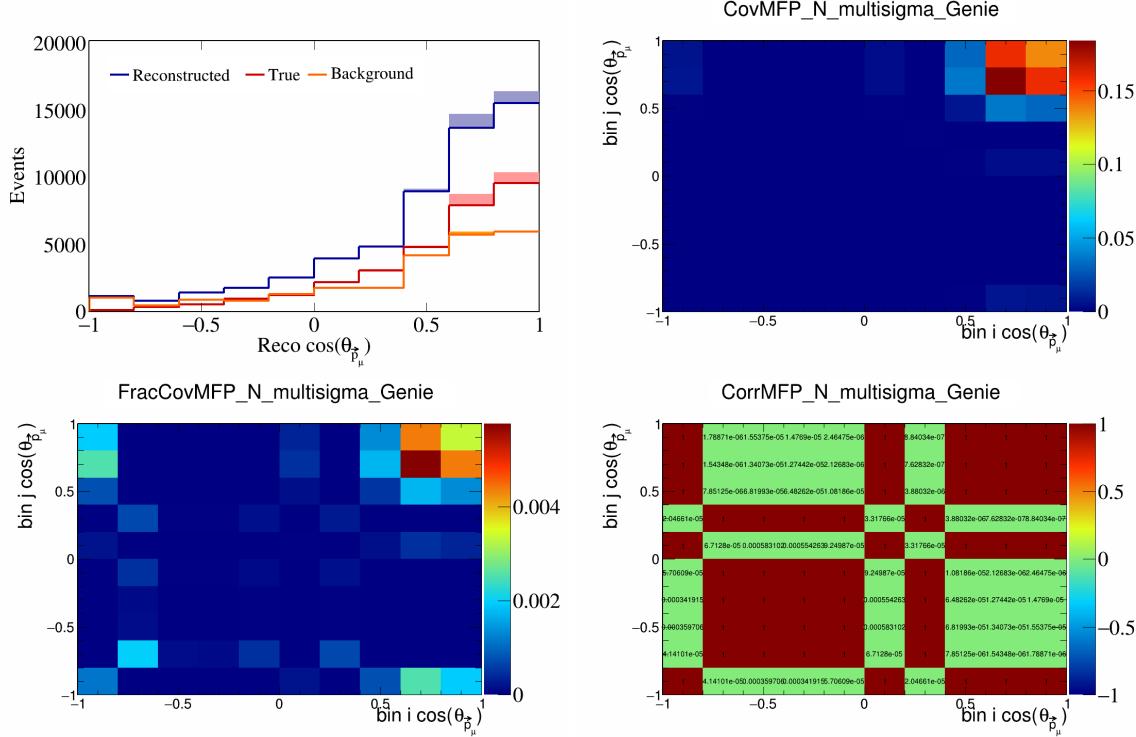


Figure 246: MFPN variations for $\cos(\theta_{\vec{p}_\mu})$.

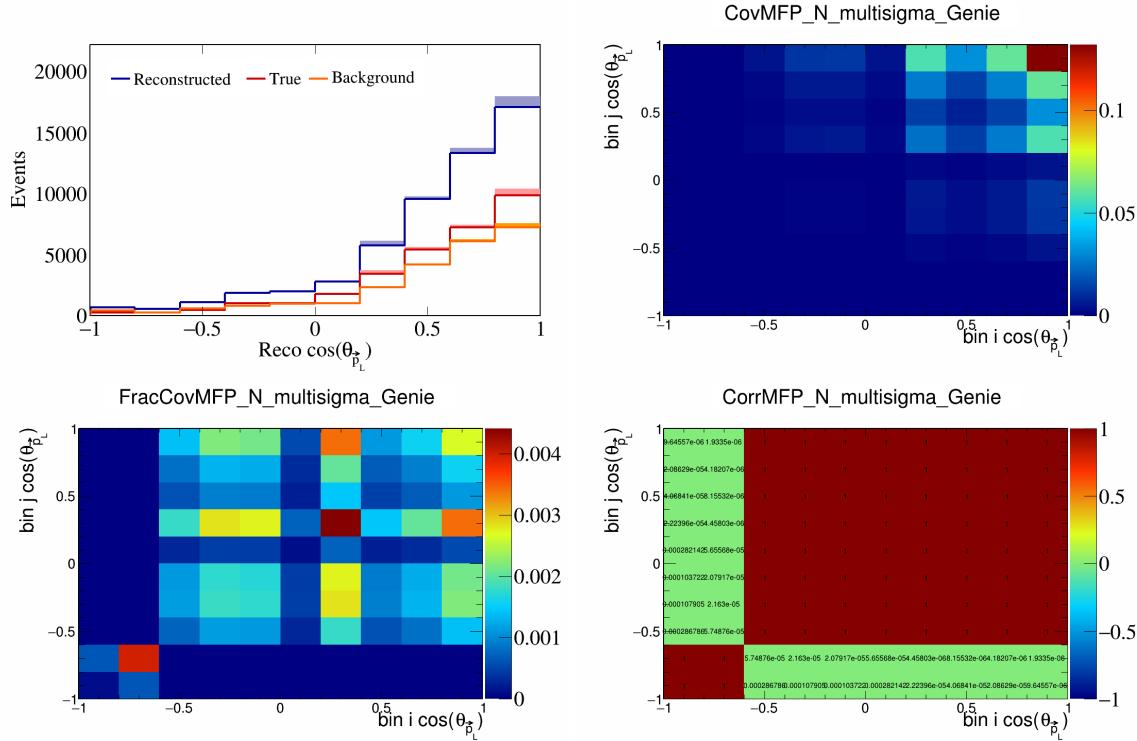


Figure 247: MFPN variations for $\cos(\theta_{\vec{p}_L})$.

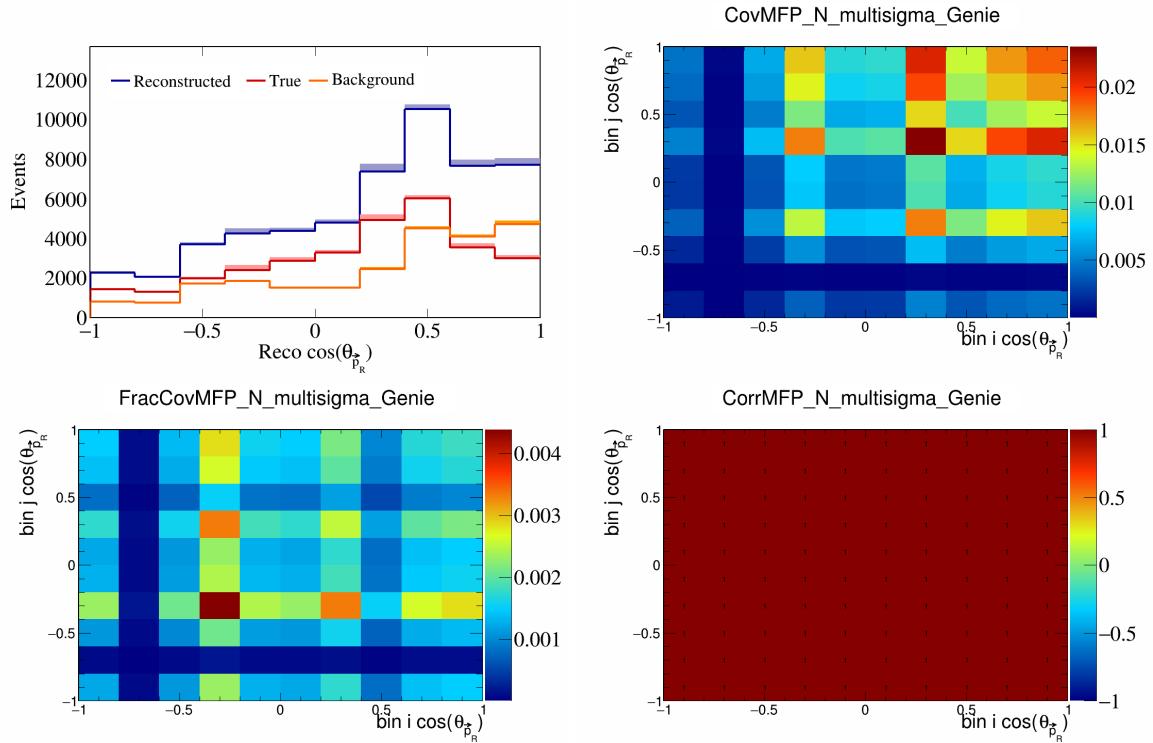


Figure 248: MFPN variations for $\cos(\theta_{\vec{p}_R})$.

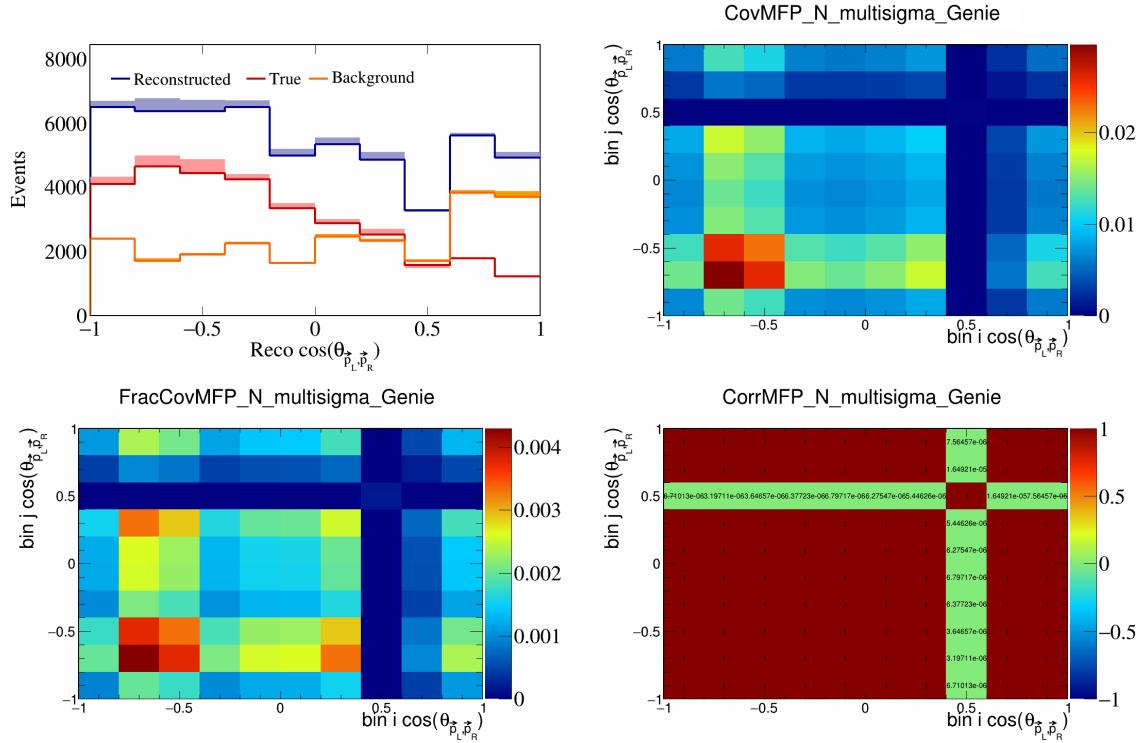


Figure 249: MFPN variations for $\cos(\theta_{\vec{p}_L, \vec{p}_R})$.

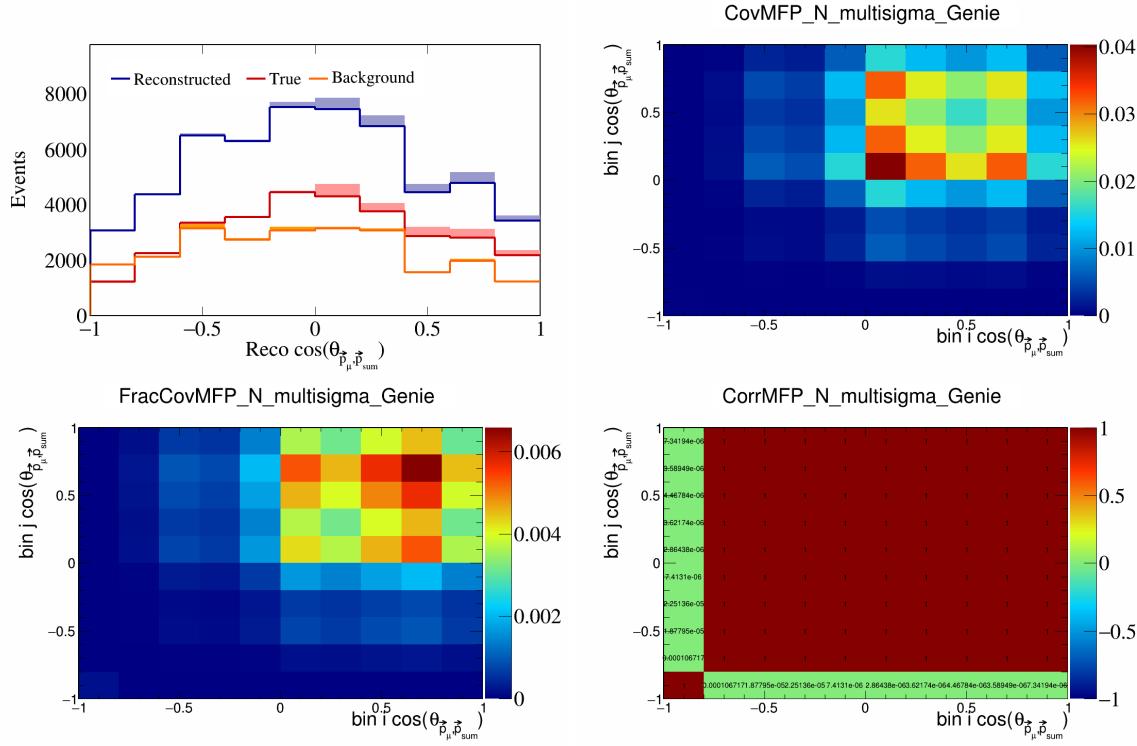


Figure 250: MFPN variations for $\cos(\theta_{\vec{p}_\mu, \vec{p}_{\text{sum}}})$.

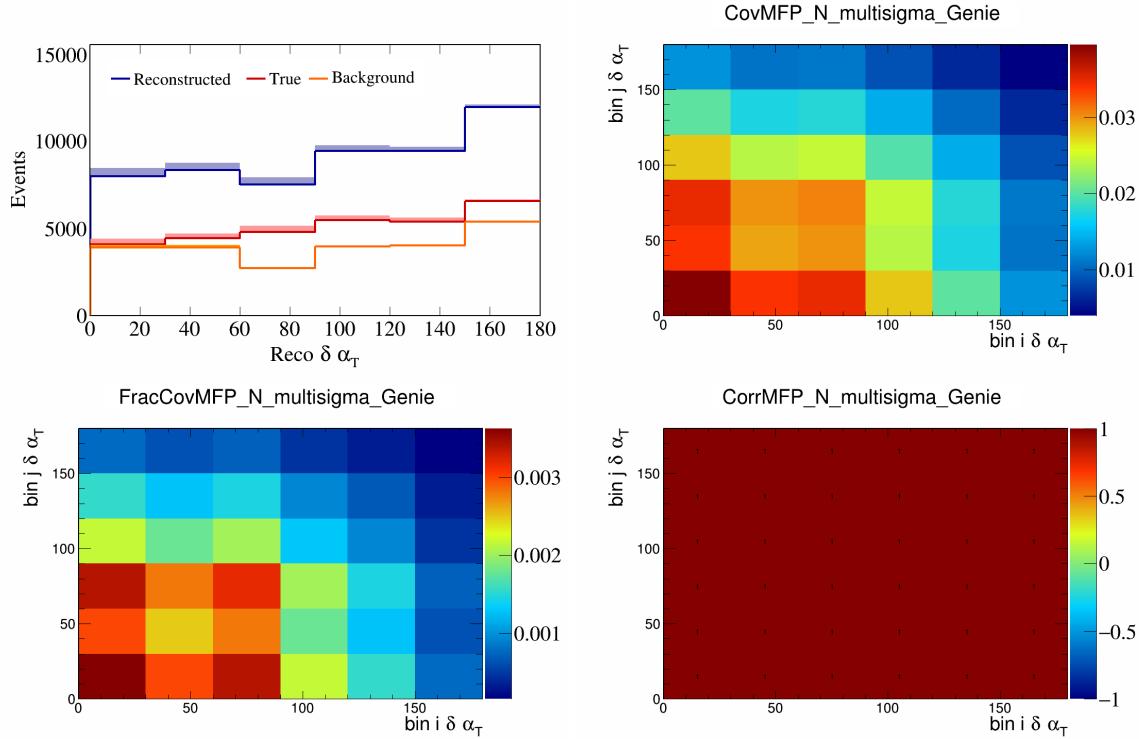


Figure 251: MFPN variations for $\delta\alpha_T$.

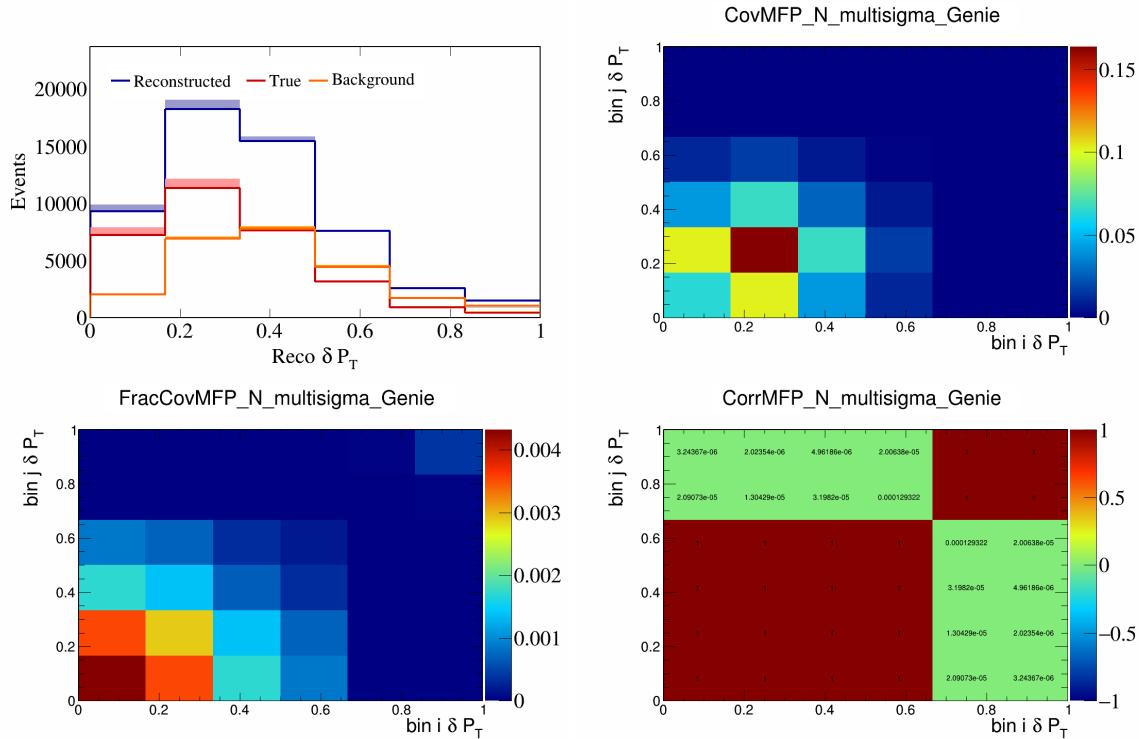


Figure 252: MFPN variations for δP_T .

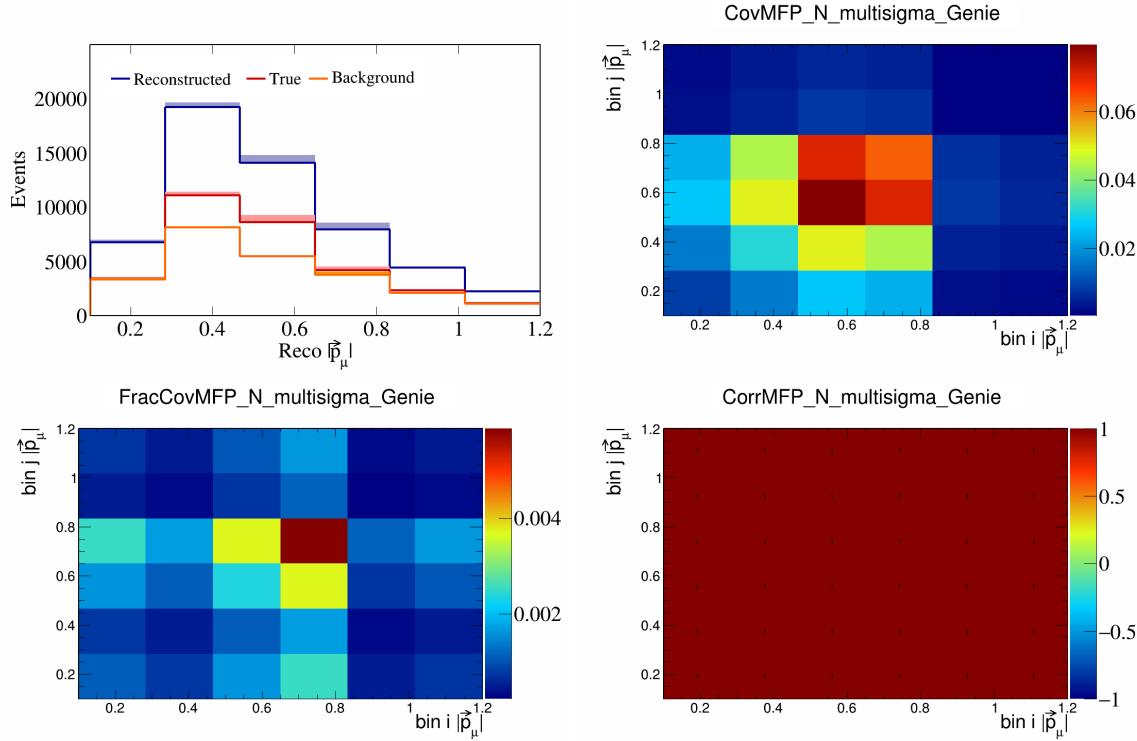


Figure 253: MFPN variations for $|\vec{p}_\mu|$.

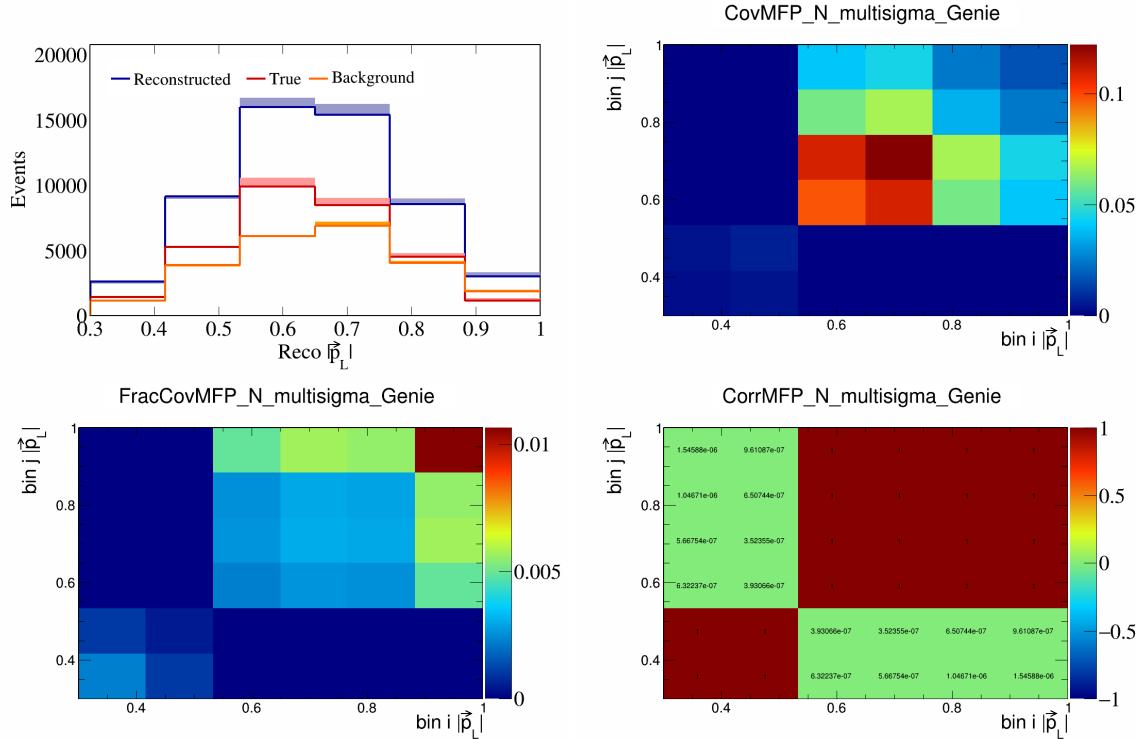


Figure 254: MFPN variations for $|\vec{p}_L|$.

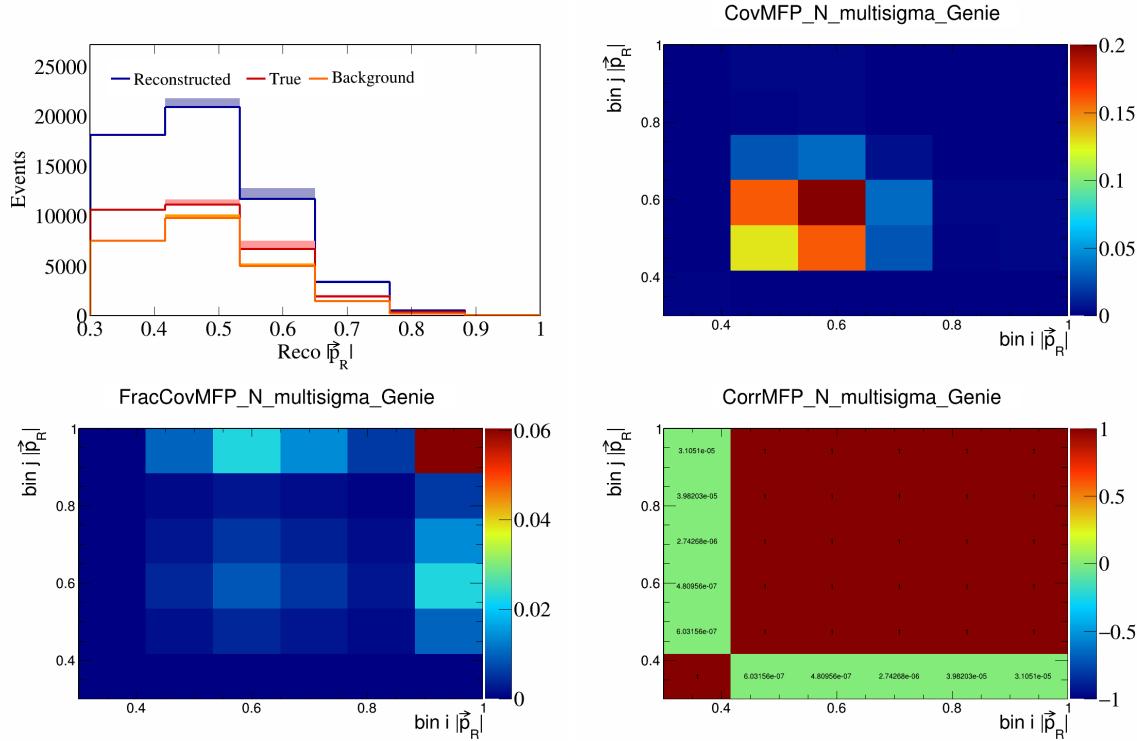


Figure 255: MFPN variations for $|\vec{p}_R|$.

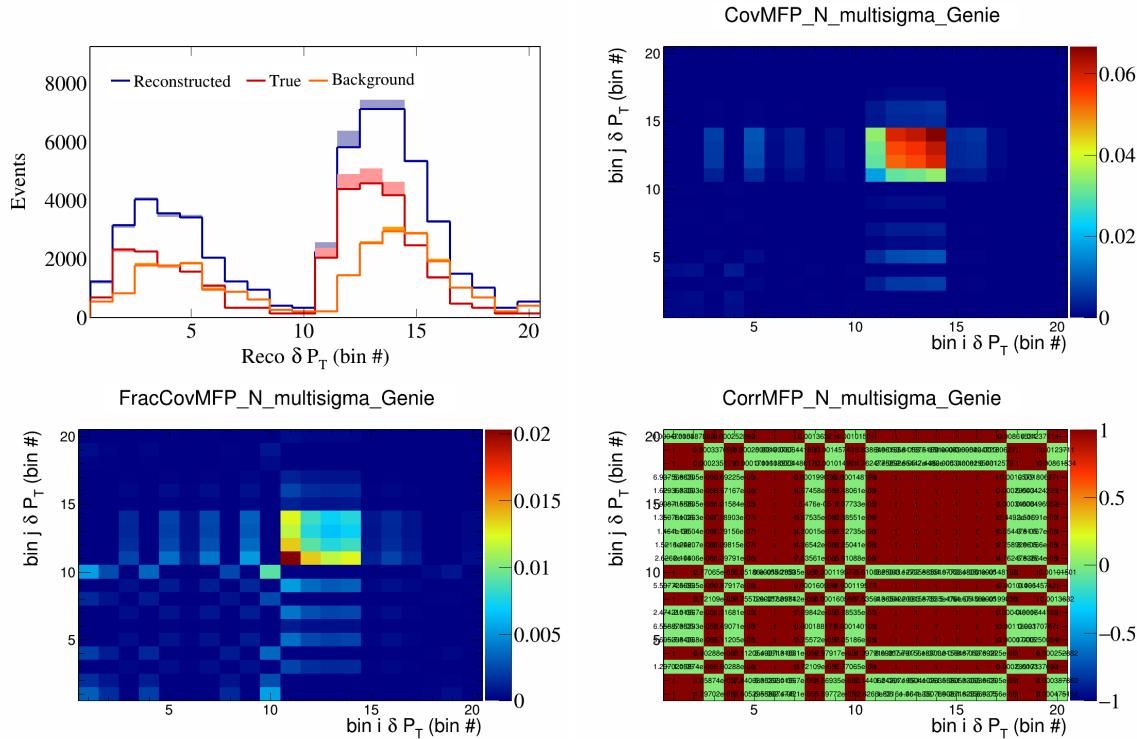


Figure 256: MFPN variations for δP_T in $\cos(\theta_{\vec{p}_\mu})$.

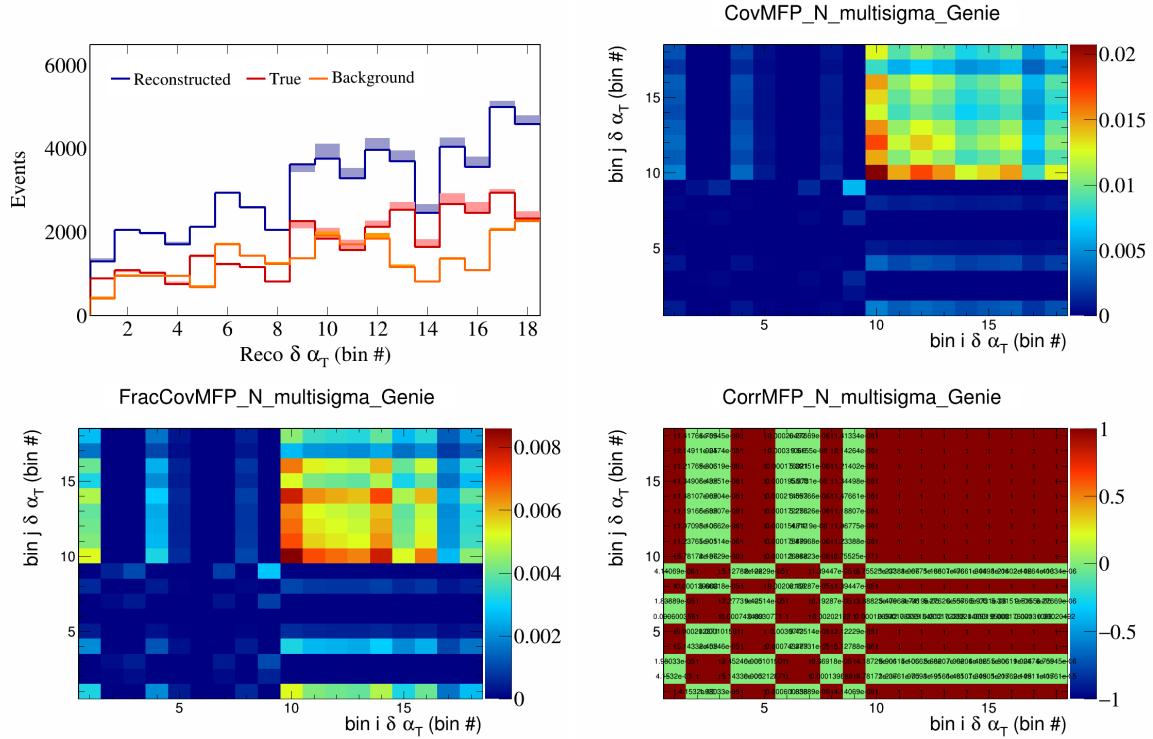


Figure 257: MFPN variations for $\delta\alpha_T$ in $\cos(\theta_{\vec{p}_\mu})$.

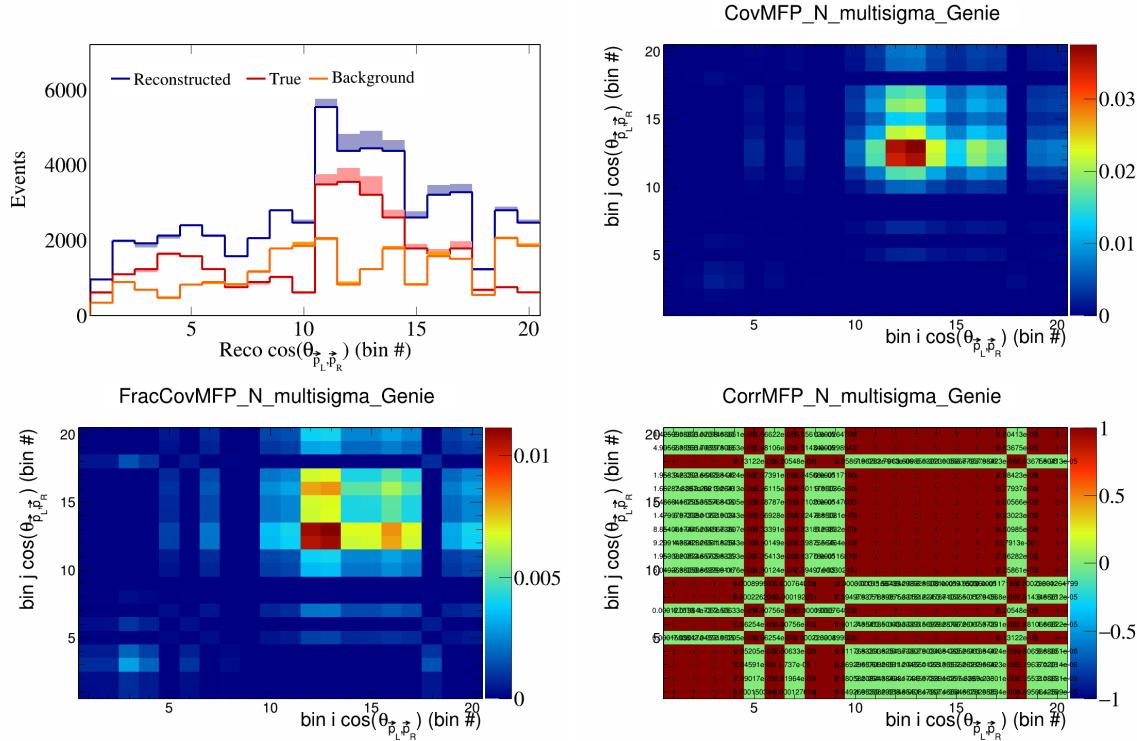


Figure 258: MFPN variations for $\cos(\theta_{\vec{p}_L, \vec{p}_R})$ in $\cos(\theta_{\vec{p}_\mu})$.

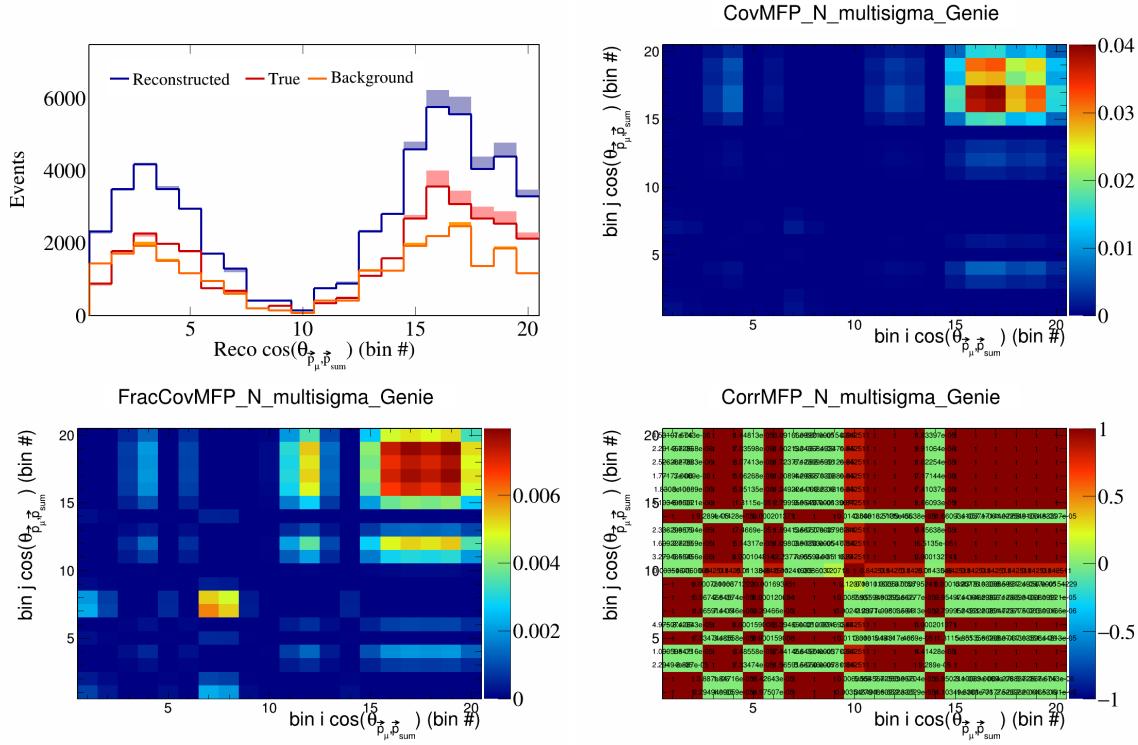


Figure 259: MFPN variations for $\cos(\theta_{\vec{p}_\mu, \vec{p}_{\text{sum}}})$ in $\cos(\theta_{\vec{p}_\mu})$.

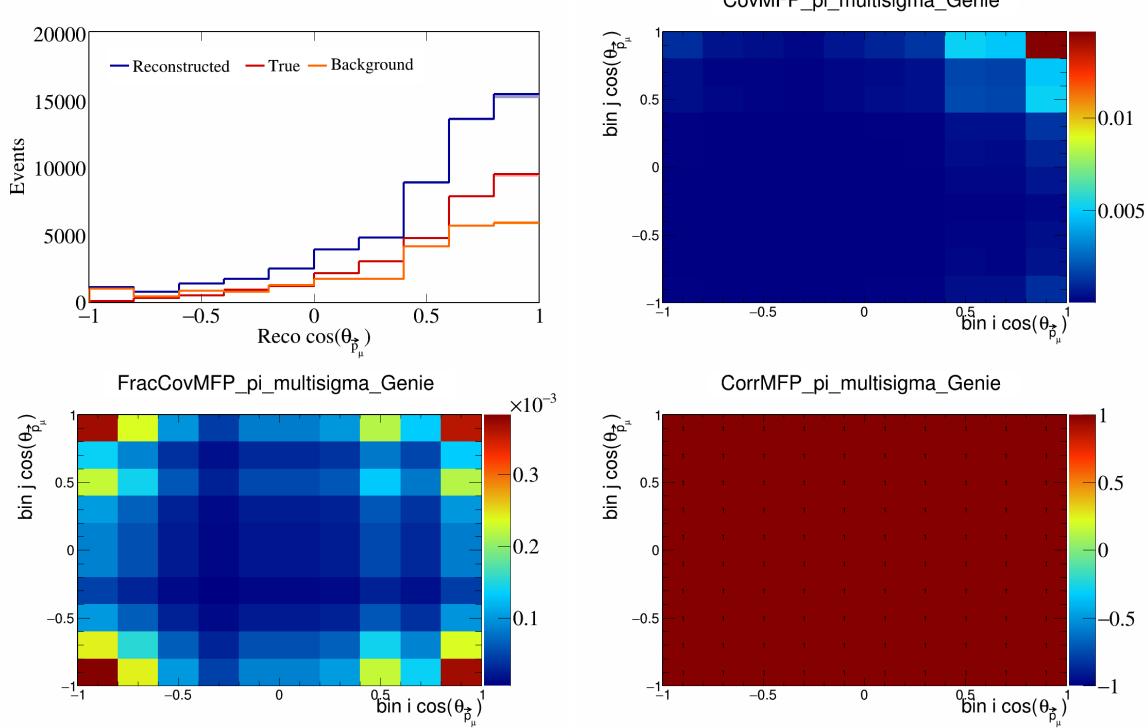


Figure 260: MFPPi variations for $\cos(\theta_{\vec{p}_\mu})$.

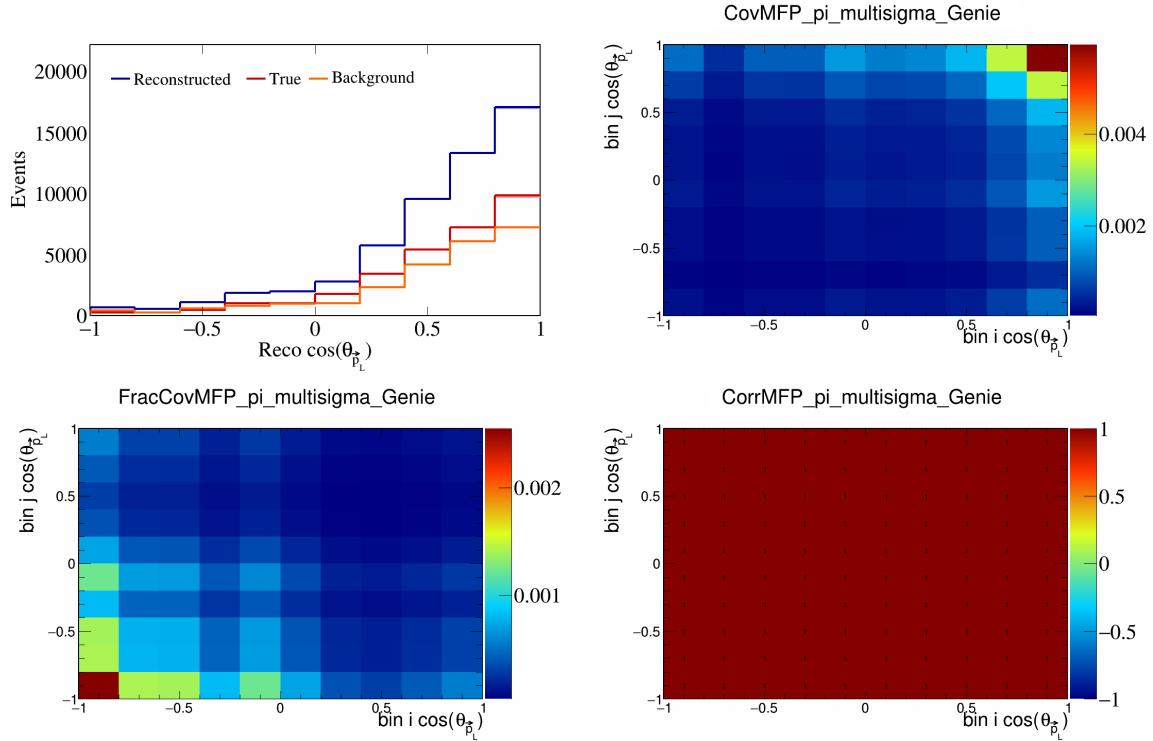


Figure 261: MFPPi variations for $\cos(\theta_{\vec{p}_L})$.

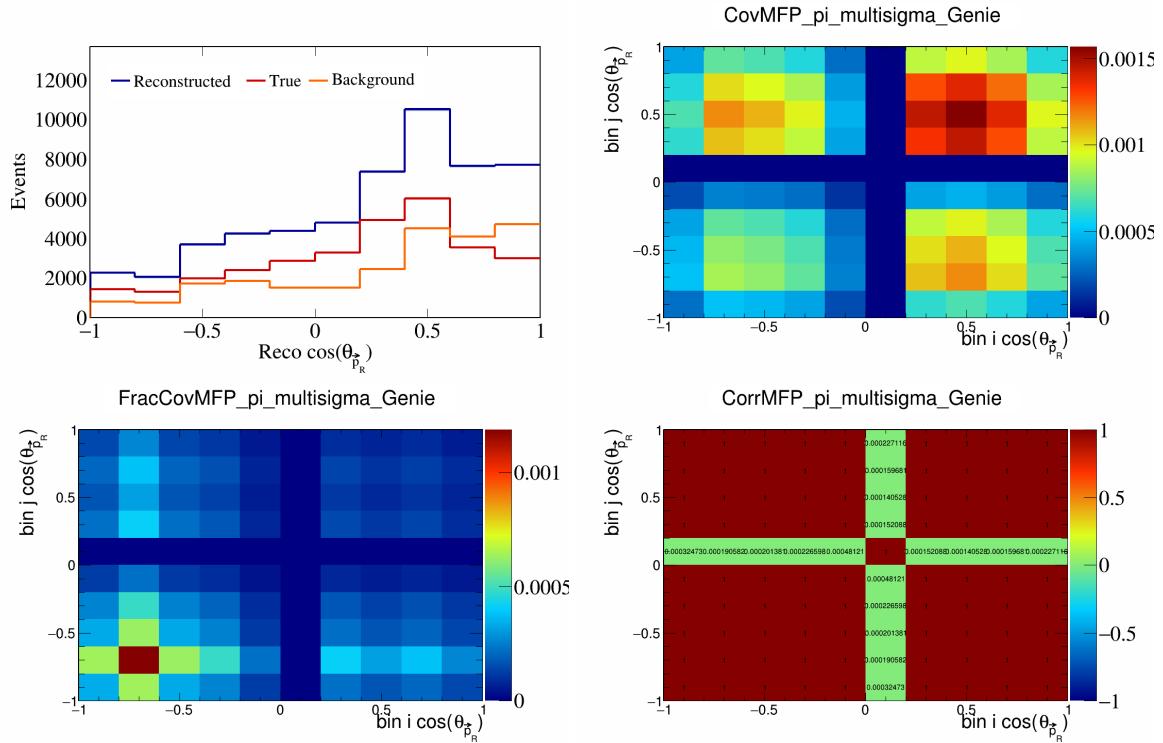


Figure 262: MFPPi variations for $\cos(\theta_{\vec{p}_R})$.

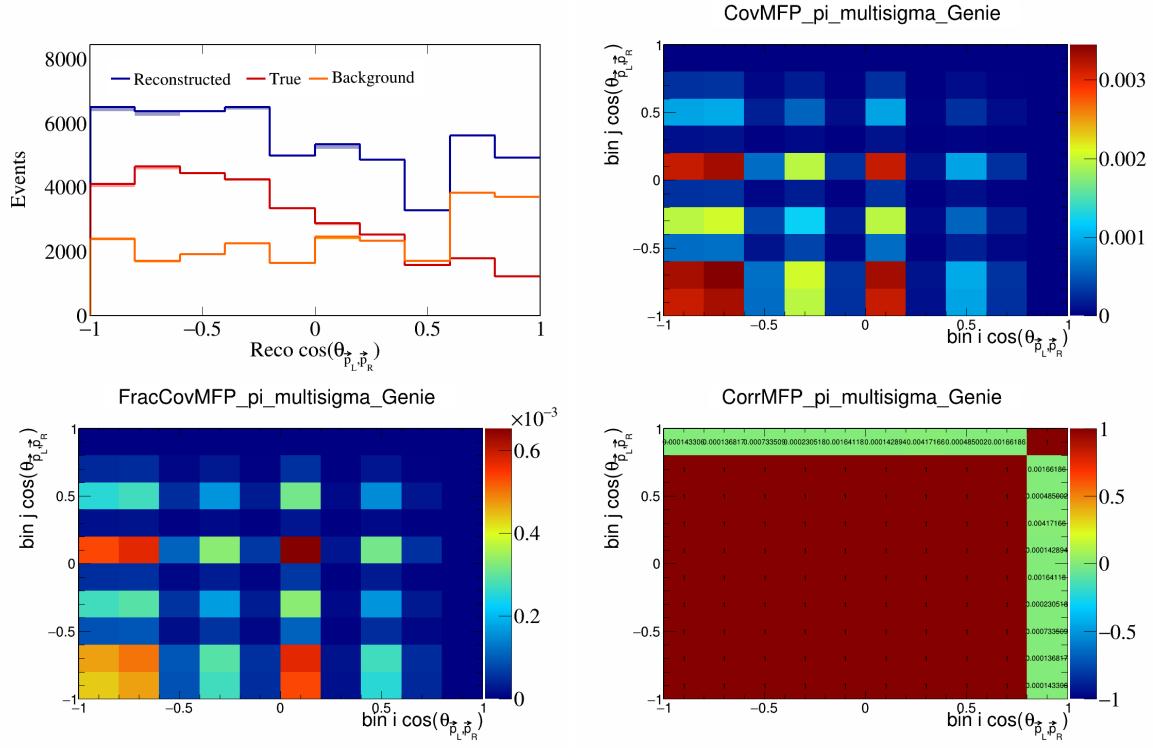


Figure 263: MFPpi variations for $\cos(\theta_{\vec{p}_L, \vec{p}_R})$.

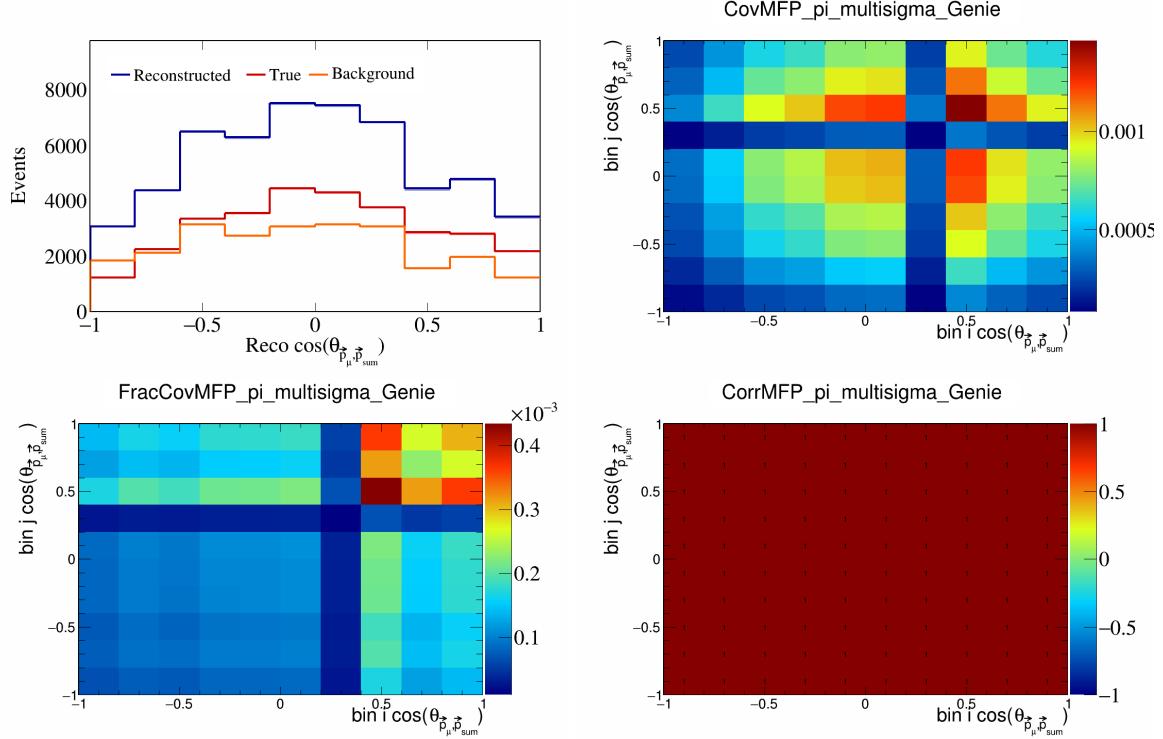


Figure 264: MFPpi variations for $\cos(\theta_{\vec{p}_\mu, \vec{p}_{\text{sum}}})$.

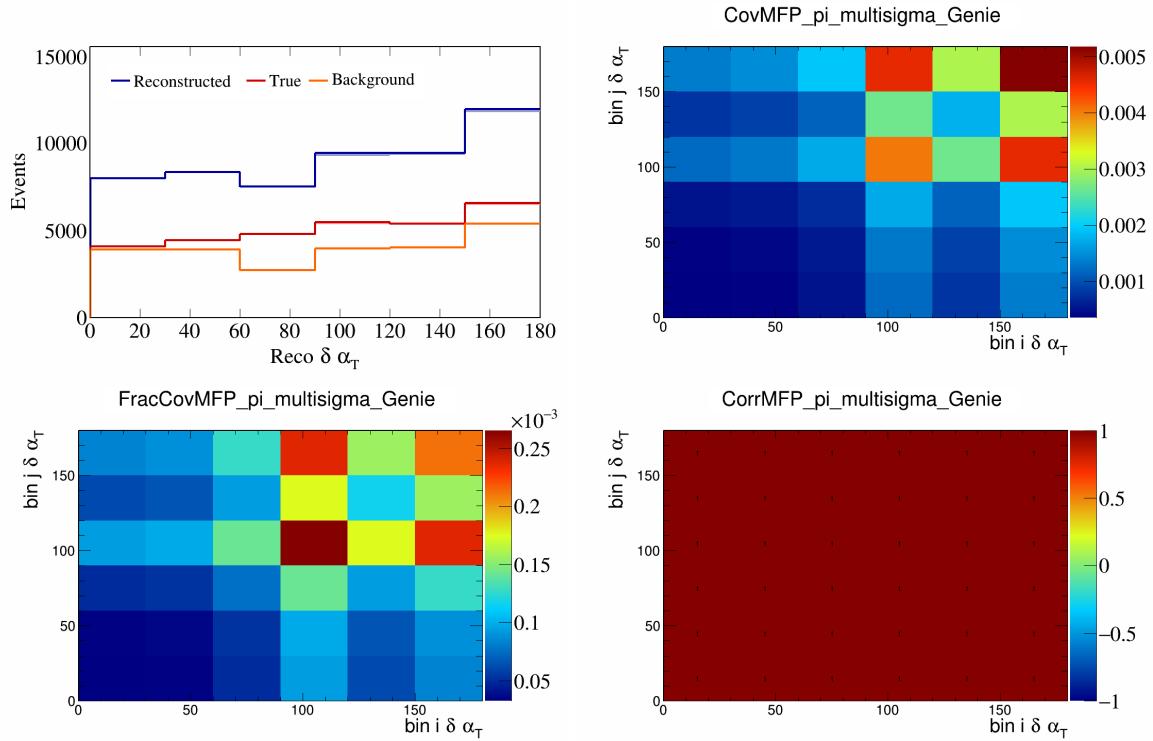


Figure 265: MFPPi variations for $\delta\alpha_T$.

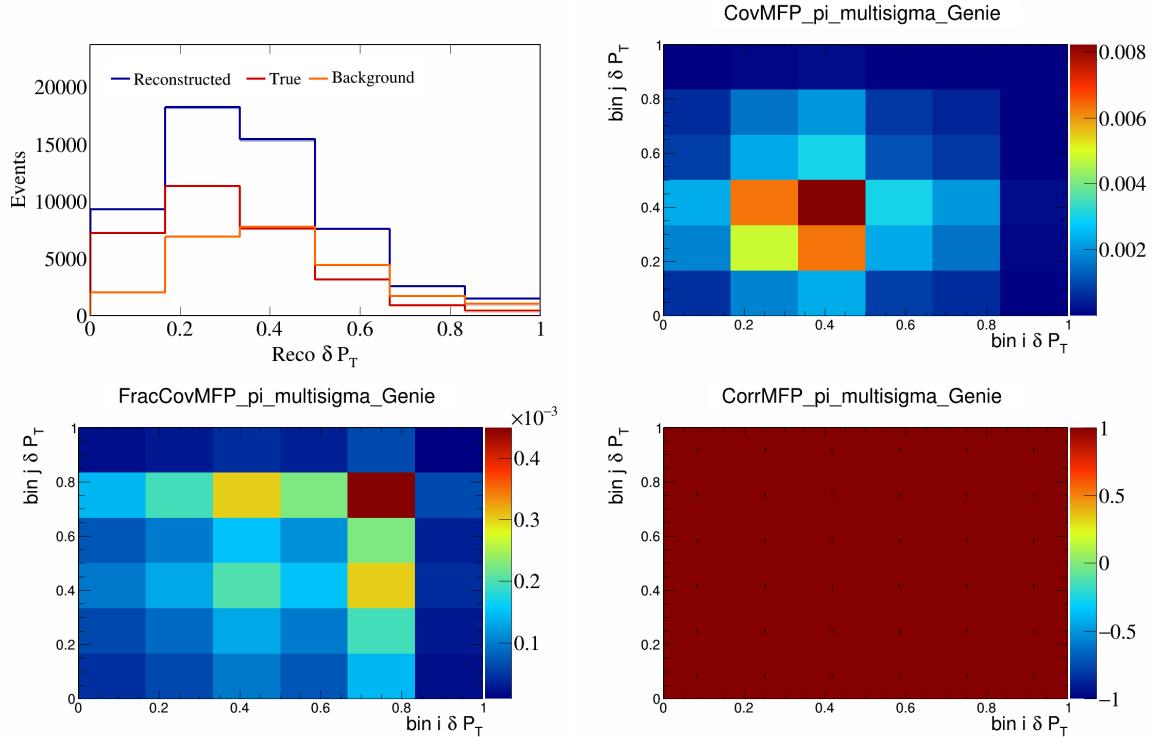


Figure 266: MFPPi variations for δP_T .

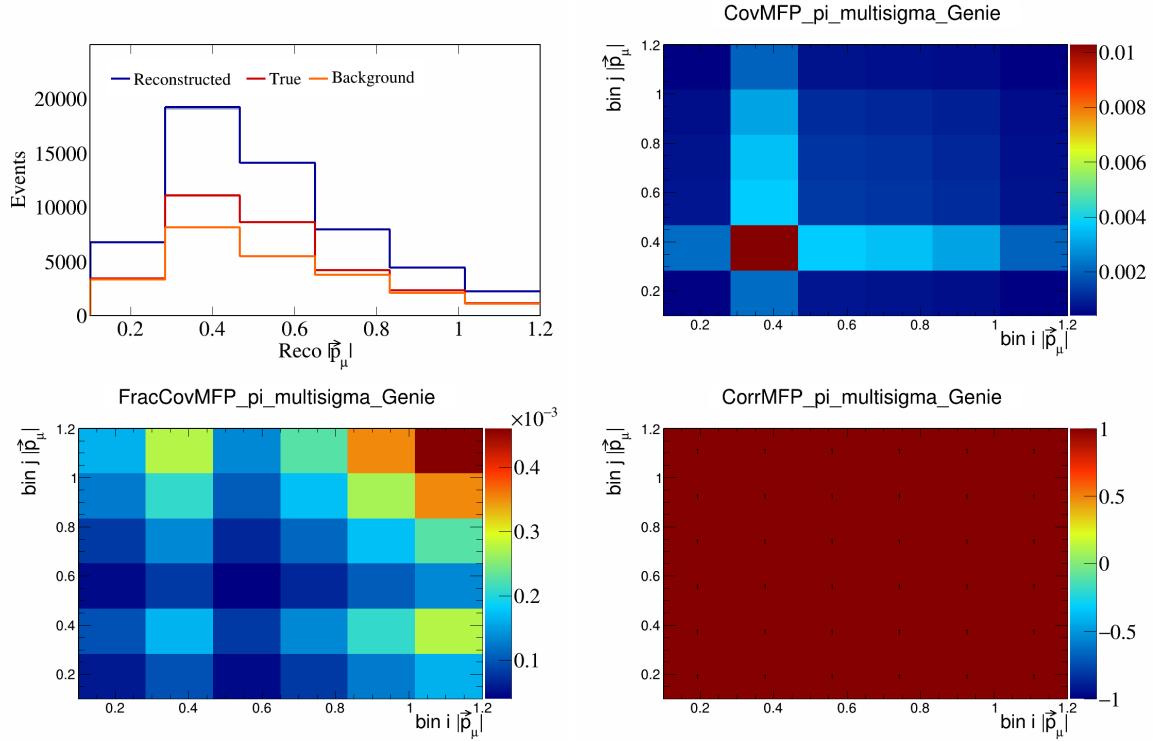


Figure 267: MFPpi variations for $|\vec{p}_\mu|$.

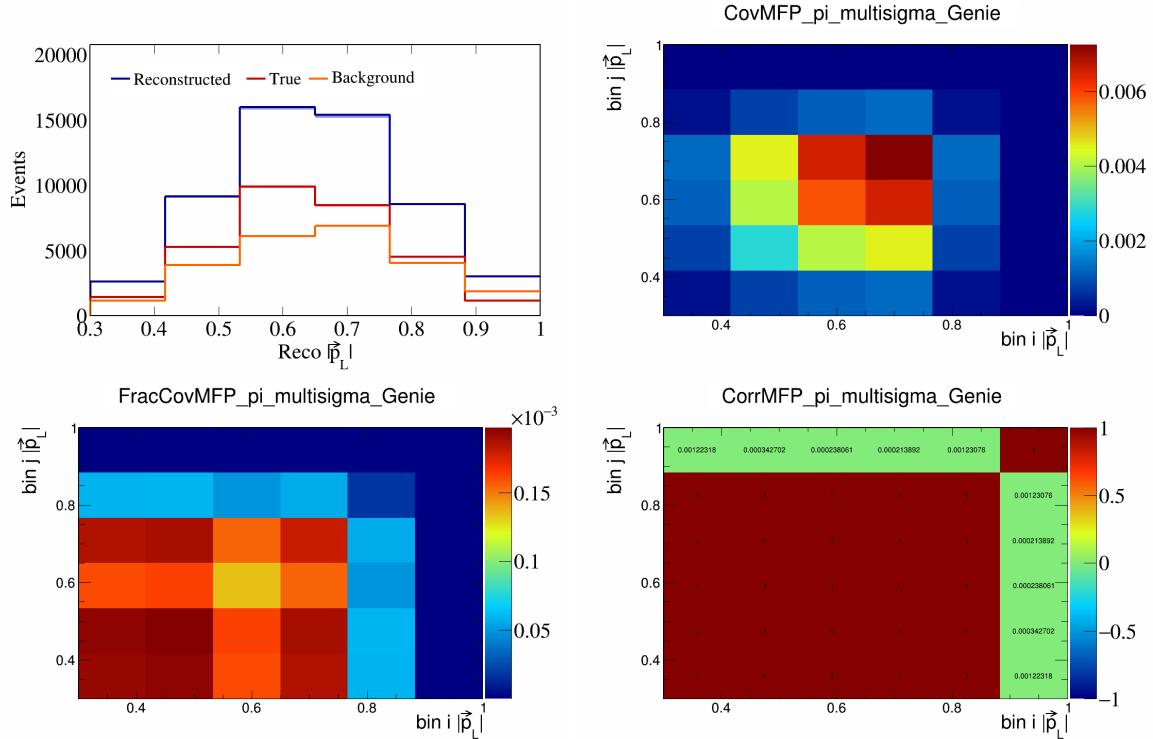


Figure 268: MFPpi variations for $|\vec{p}_L|$.

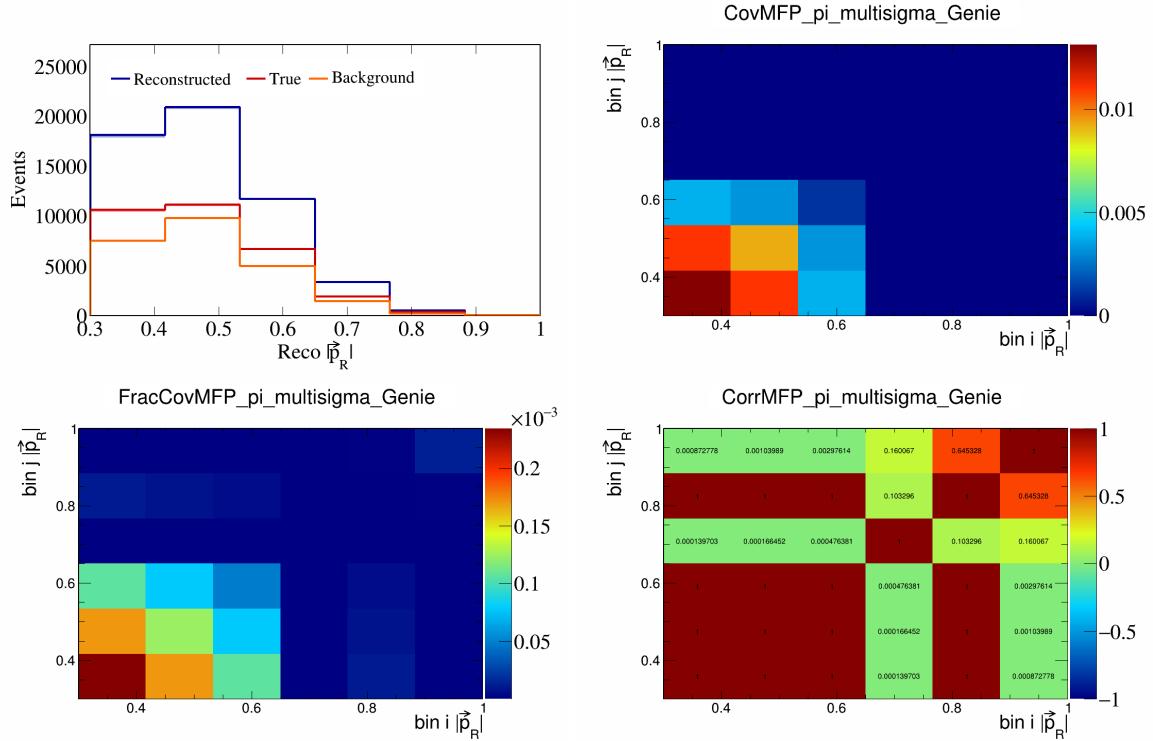


Figure 269: MFPPi variations for $|\vec{p}_R|$.

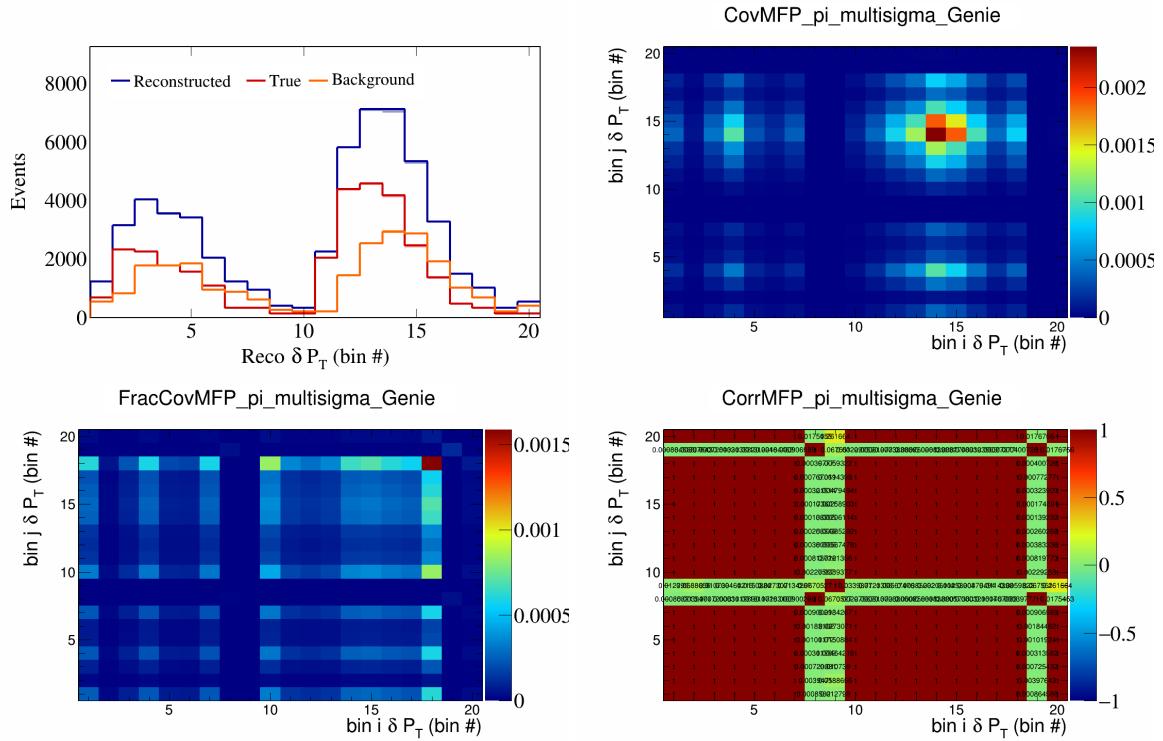


Figure 270: MFPPi variations for δP_T in $\cos(\theta_{\vec{p}_\mu})$.

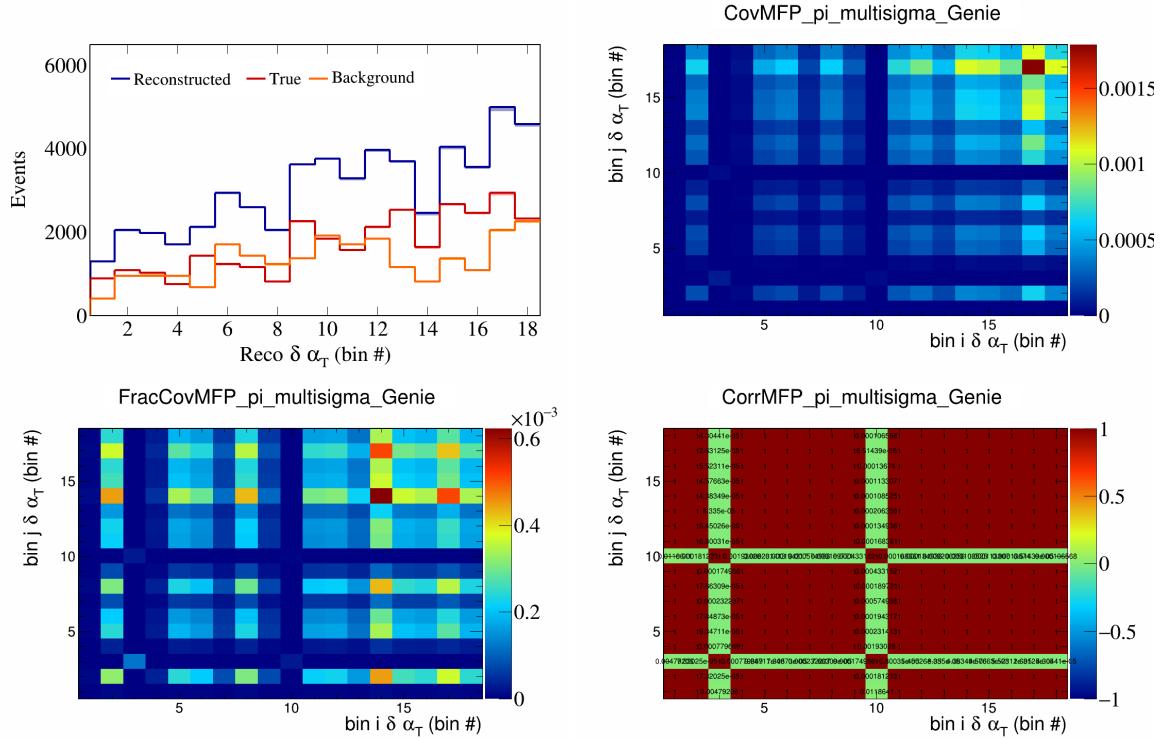


Figure 271: MFPpi variations for $\delta\alpha_T$ in $\cos(\theta_{\vec{p}_\mu})$.

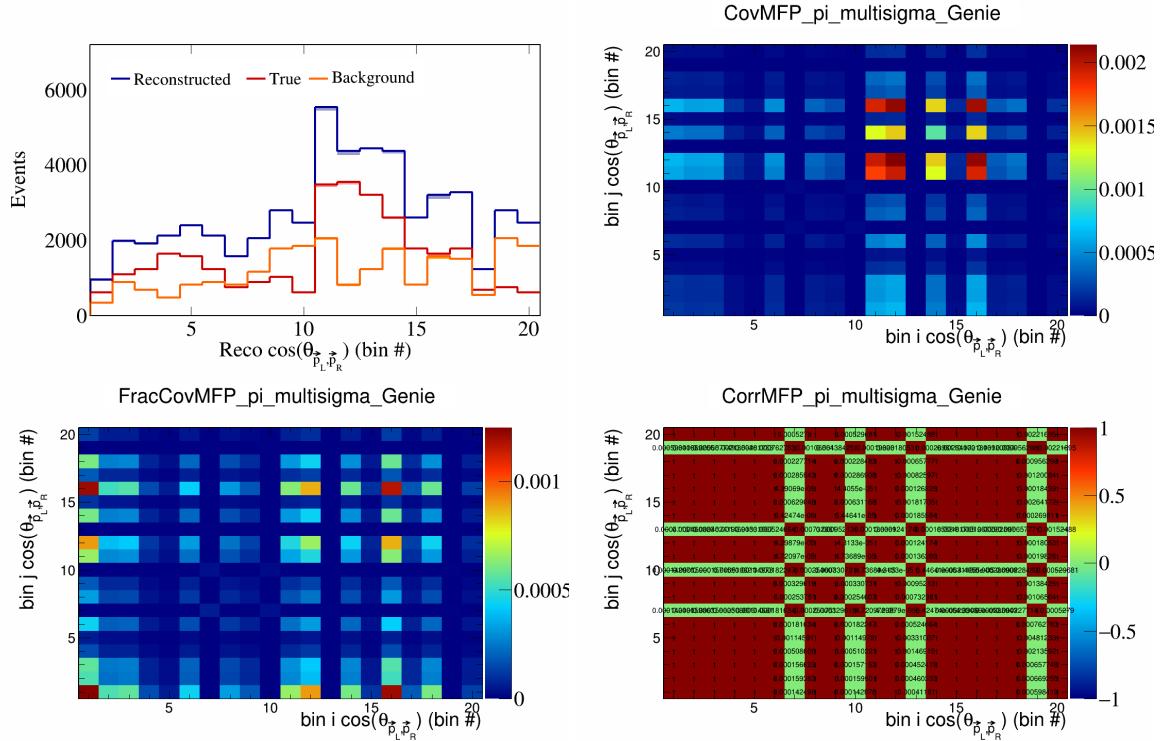


Figure 272: MFPpi variations for $\cos(\theta_{\vec{p}_L, \vec{p}_R})$ in $\cos(\theta_{\vec{p}_\mu})$.

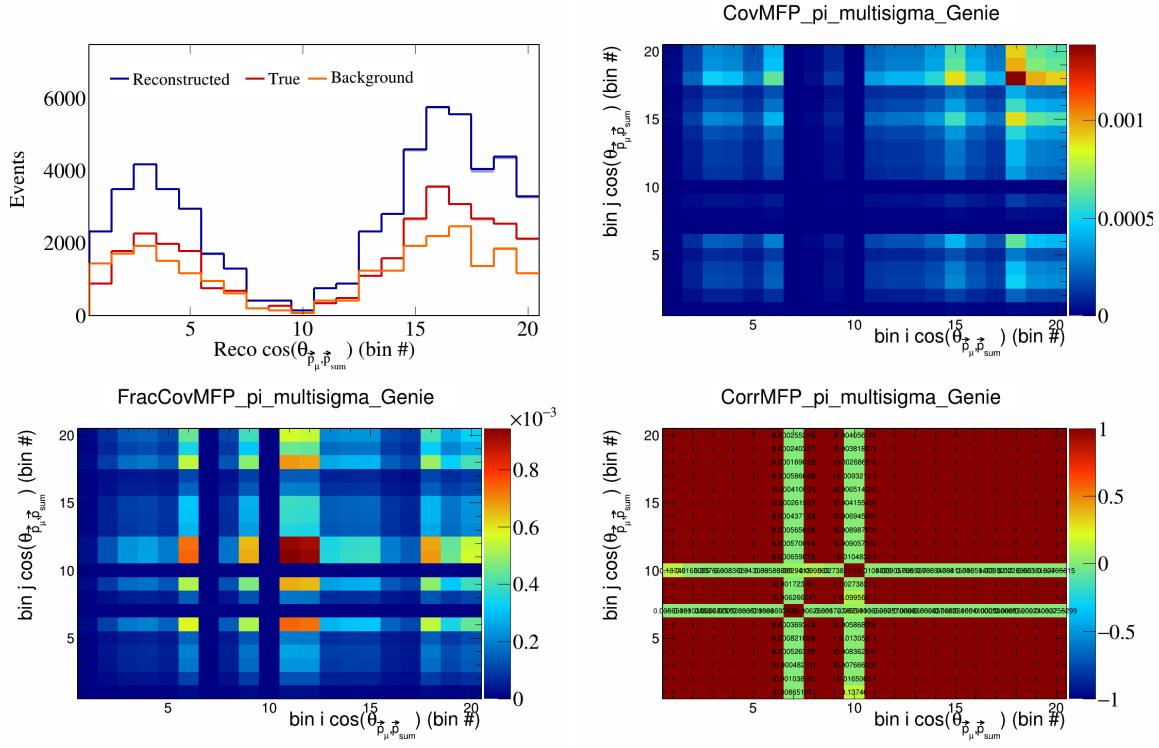


Figure 273: MFPpi variations for $\cos(\theta_{\vec{p}_\mu, \vec{p}_{\text{sum}}})$ in $\cos(\theta_{\vec{p}_\mu})$.

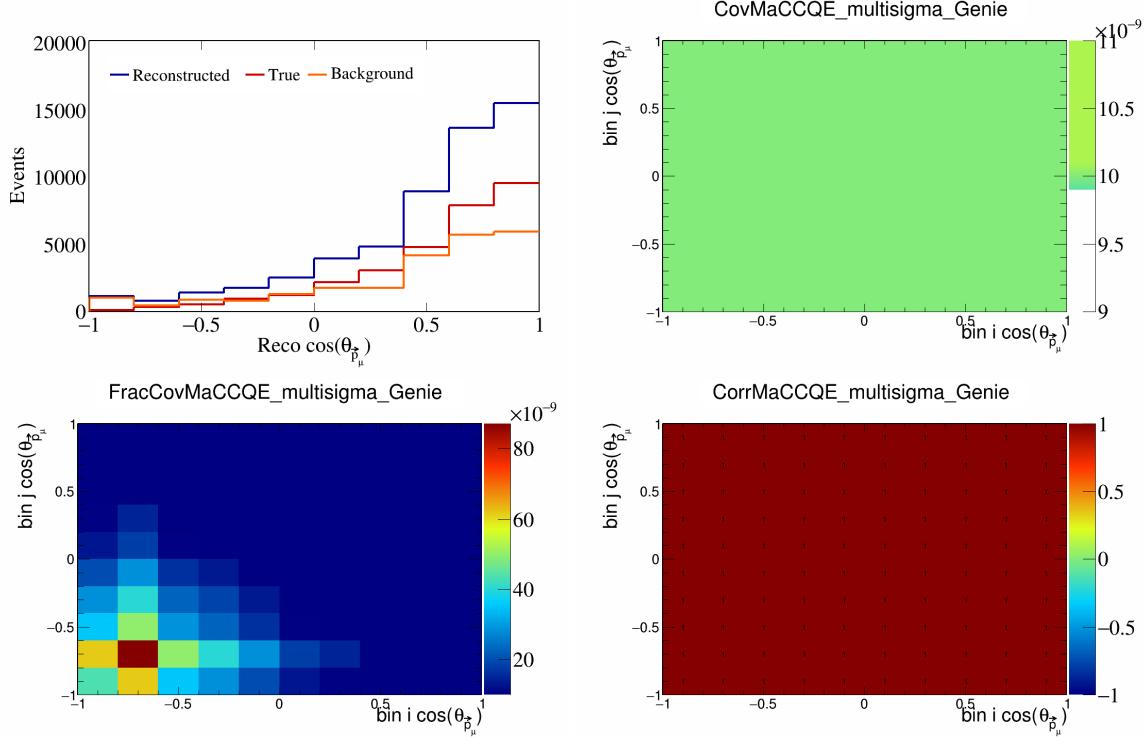


Figure 274: MaCCQE variations for $\cos(\theta_{\vec{p}_\mu})$.

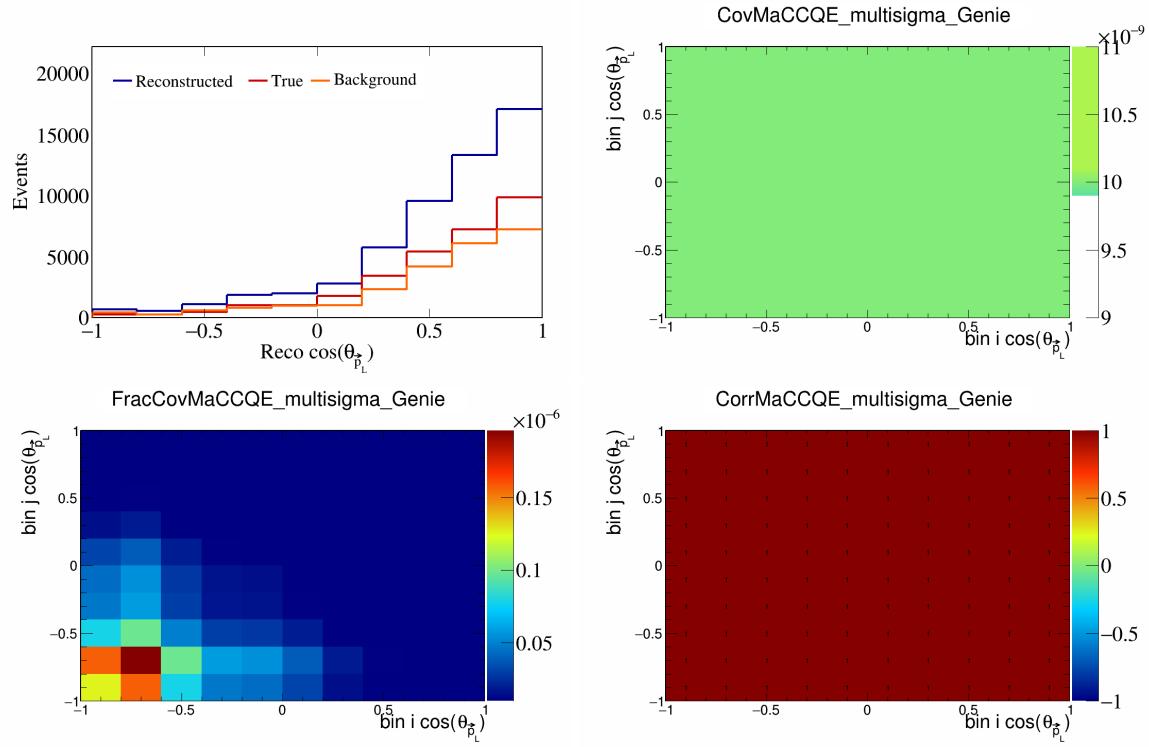


Figure 275: MaCCQE variations for $\cos(\theta_{\vec{p}_L})$.

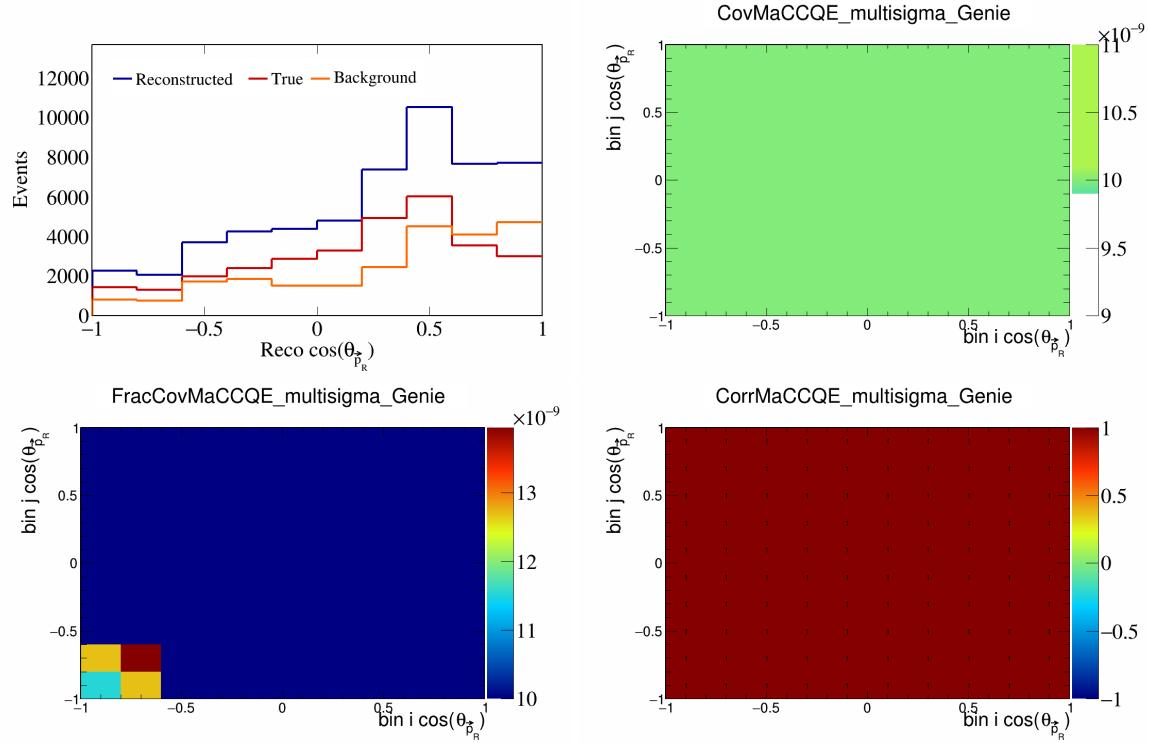


Figure 276: MaCCQE variations for $\cos(\theta_{\vec{p}_R})$.

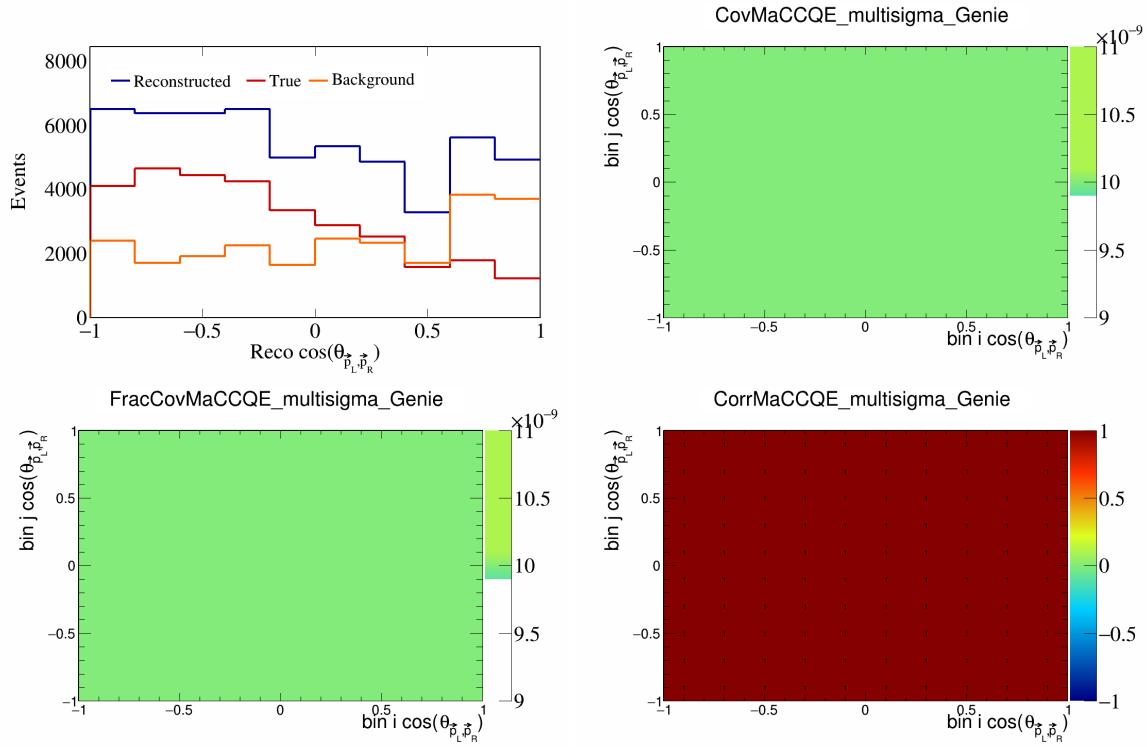


Figure 277: MaCCQE variations for $\cos(\theta_{\vec{p}_L, \vec{p}_R})$.

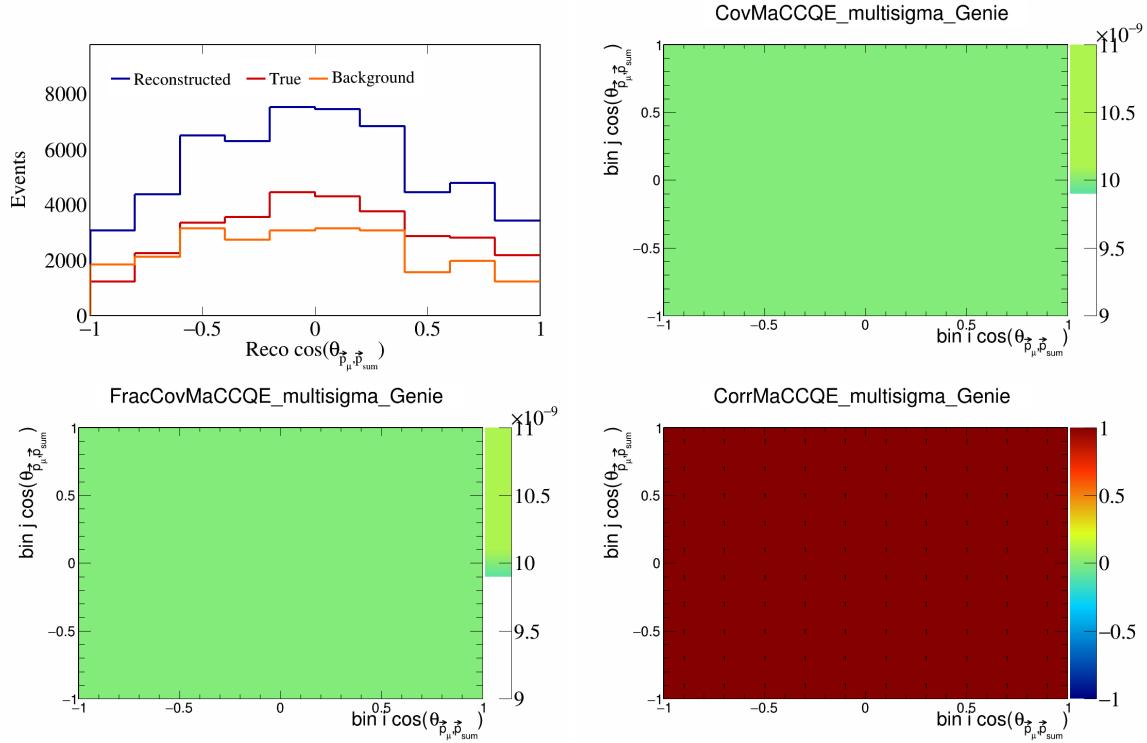


Figure 278: MaCCQE variations for $\cos(\theta_{\vec{p}_\mu, \vec{p}_{\text{sum}}})$.

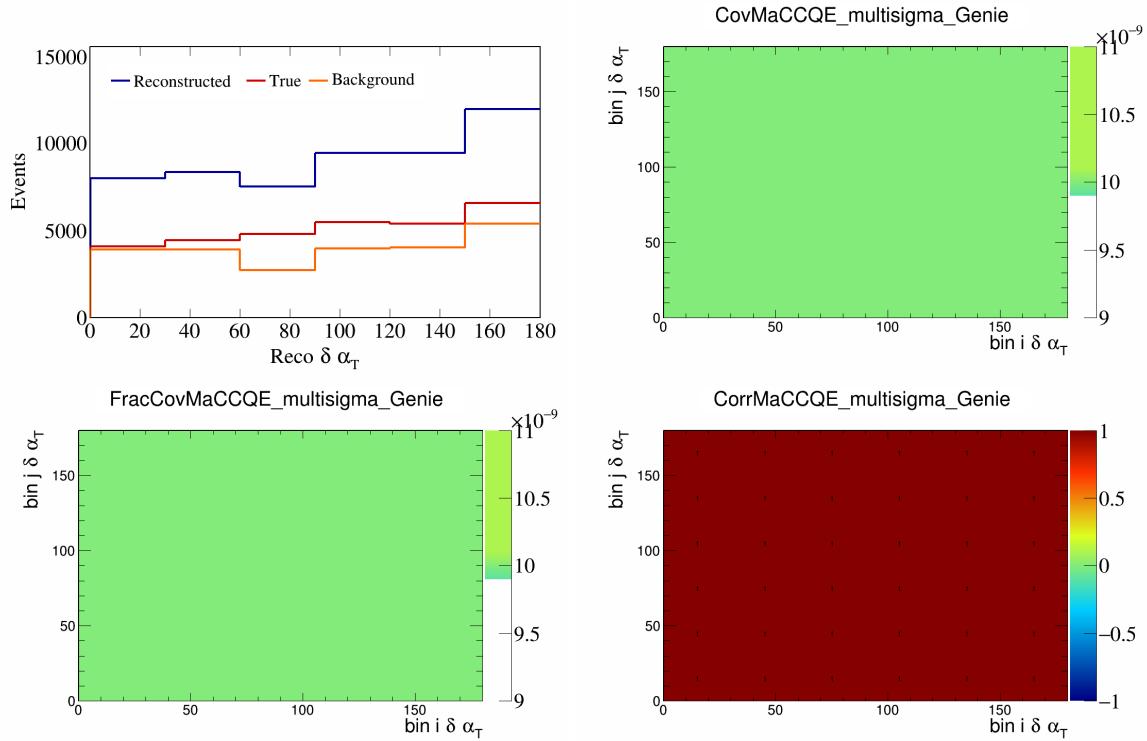


Figure 279: MaCCQE variations for $\delta\alpha_T$.

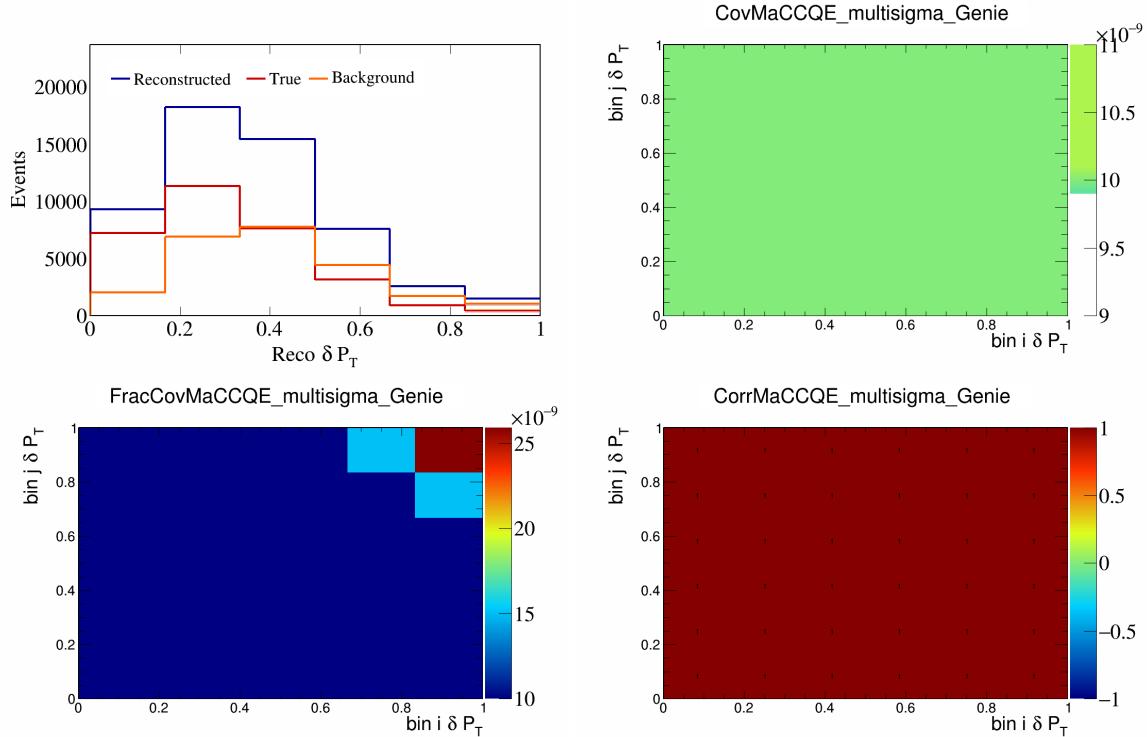


Figure 280: MaCCQE variations for δP_T .

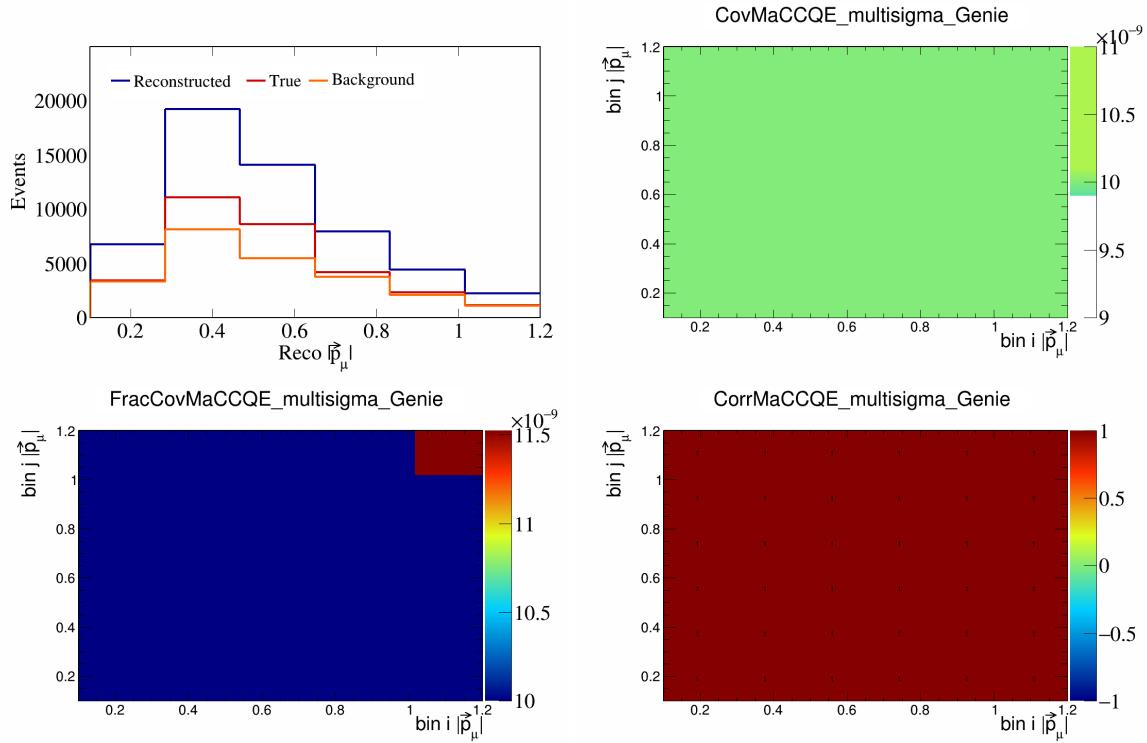


Figure 281: MaCCQE variations for $|\vec{p}_\mu|$.

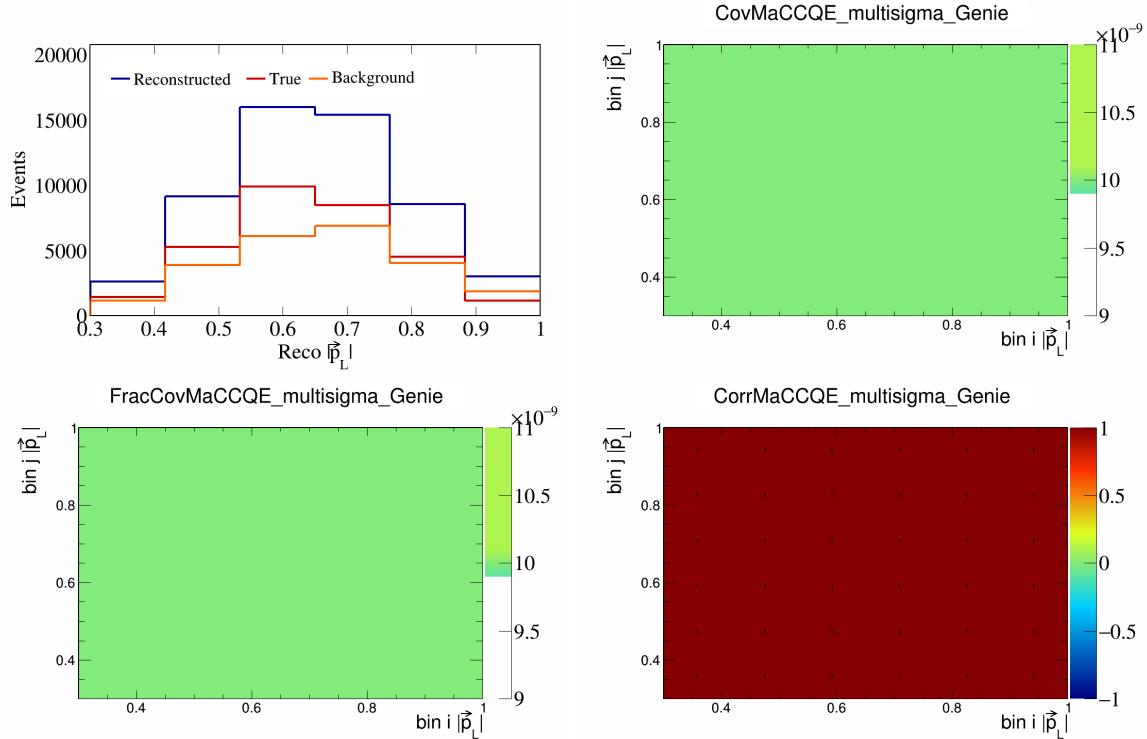


Figure 282: MaCCQE variations for $|\vec{p}_L|$.

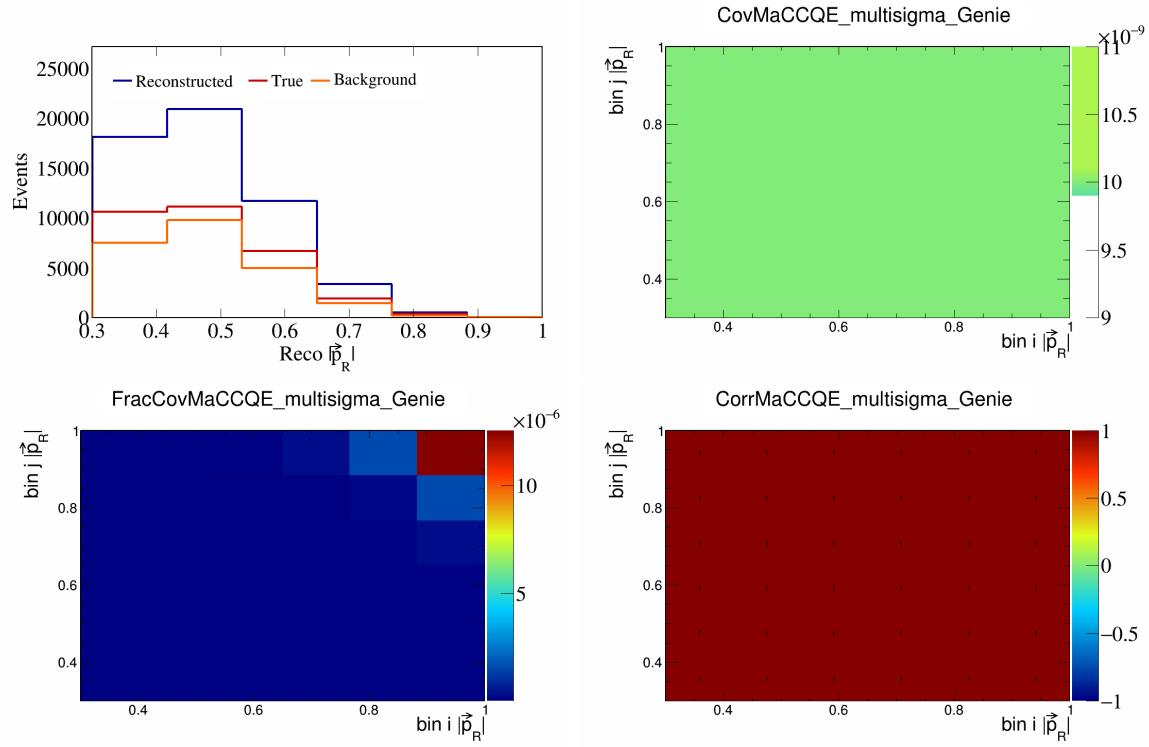


Figure 283: MaCCQE variations for $|\vec{p}_R|$.

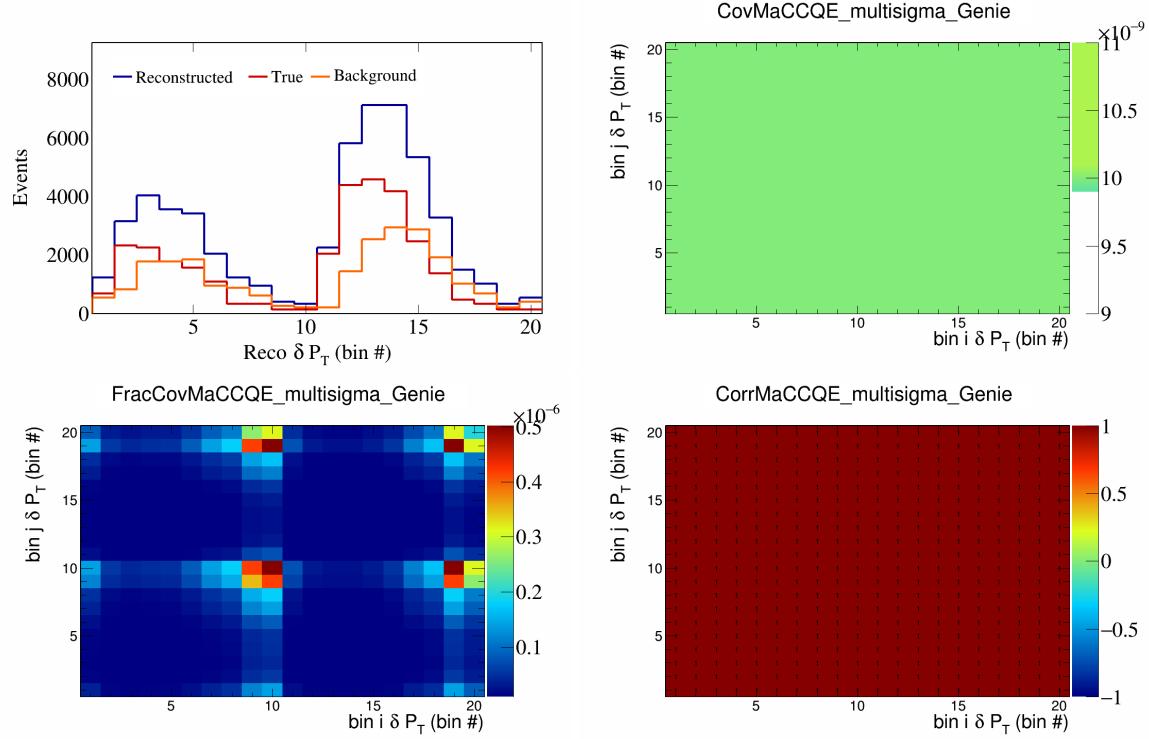


Figure 284: MaCCQE variations for δP_T in $\cos(\theta_{\vec{p}_\mu})$.

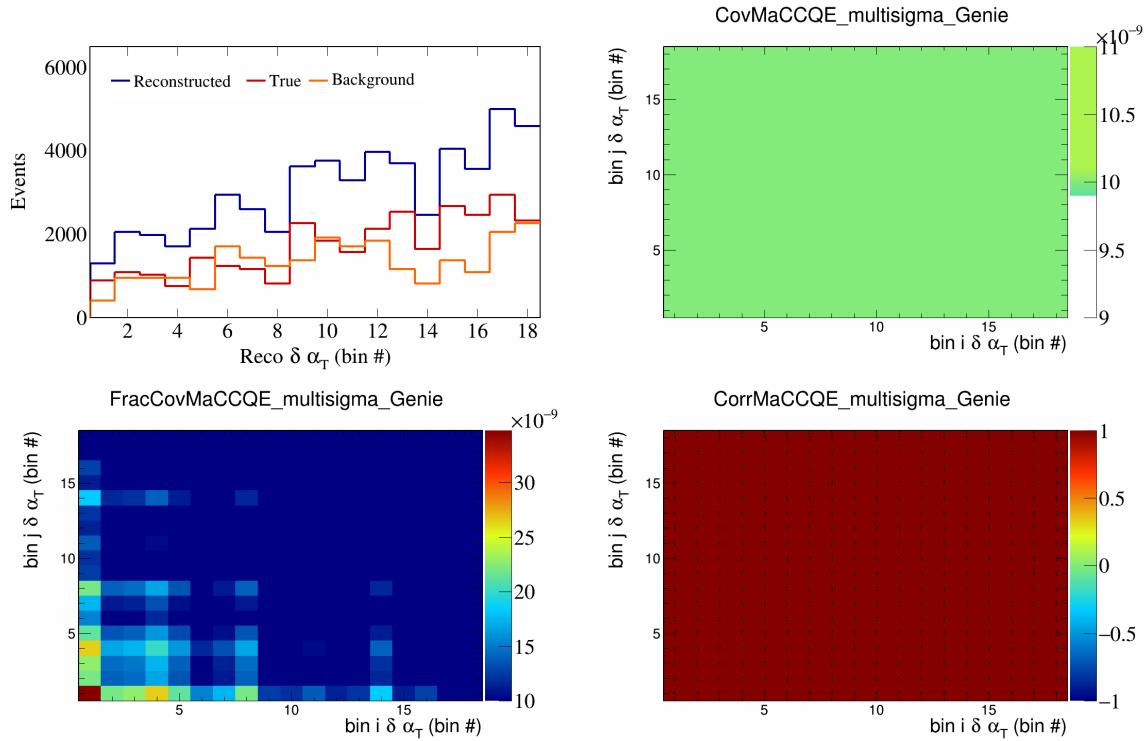


Figure 285: MaCCQE variations for $\delta\alpha_T$ in $\cos(\theta_{\vec{p}_\mu})$.

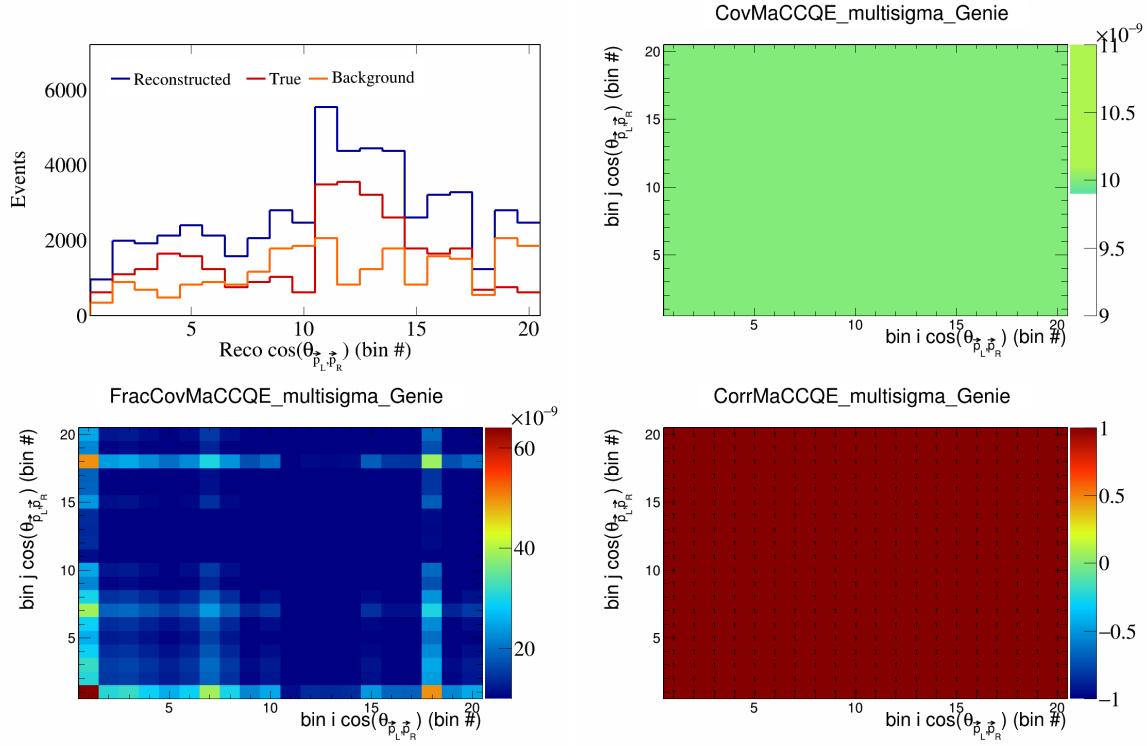


Figure 286: MaCCQE variations for $\cos(\theta_{\vec{p}_L, \vec{p}_R})$ in $\cos(\theta_{\vec{p}_\mu})$.

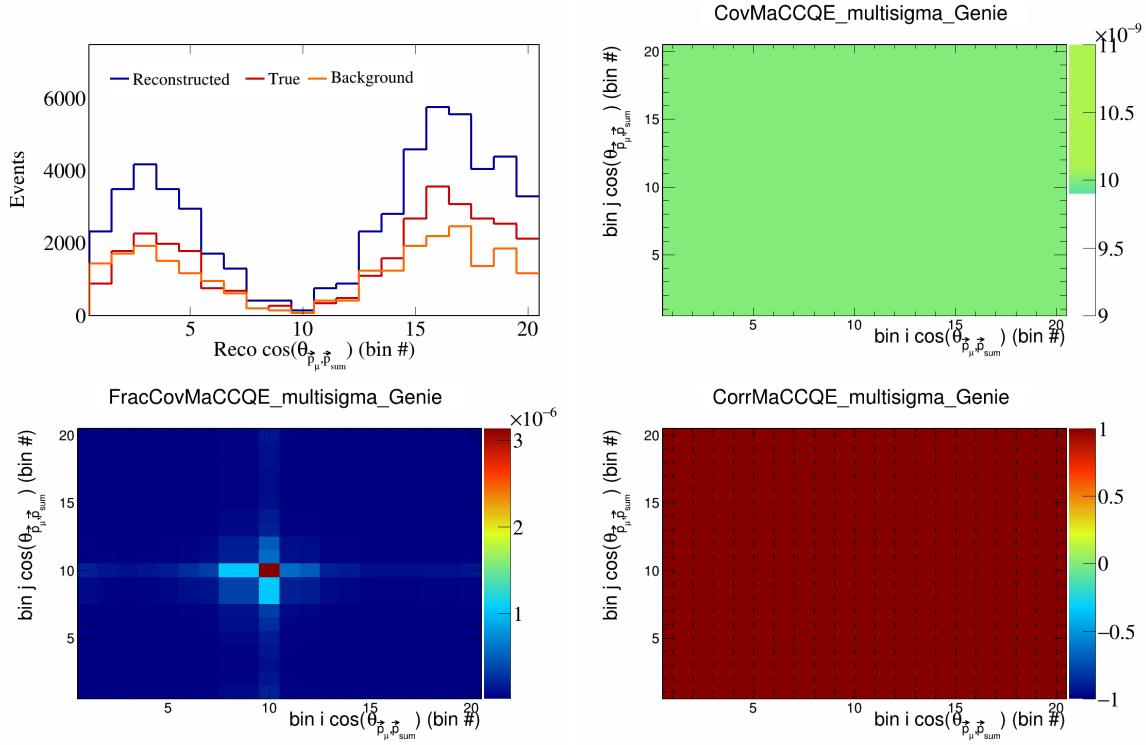


Figure 287: MaCCQE variations for $\cos(\theta_{\vec{p}_\mu, \vec{p}_{\text{sum}}})$ in $\cos(\theta_{\vec{p}_\mu})$.

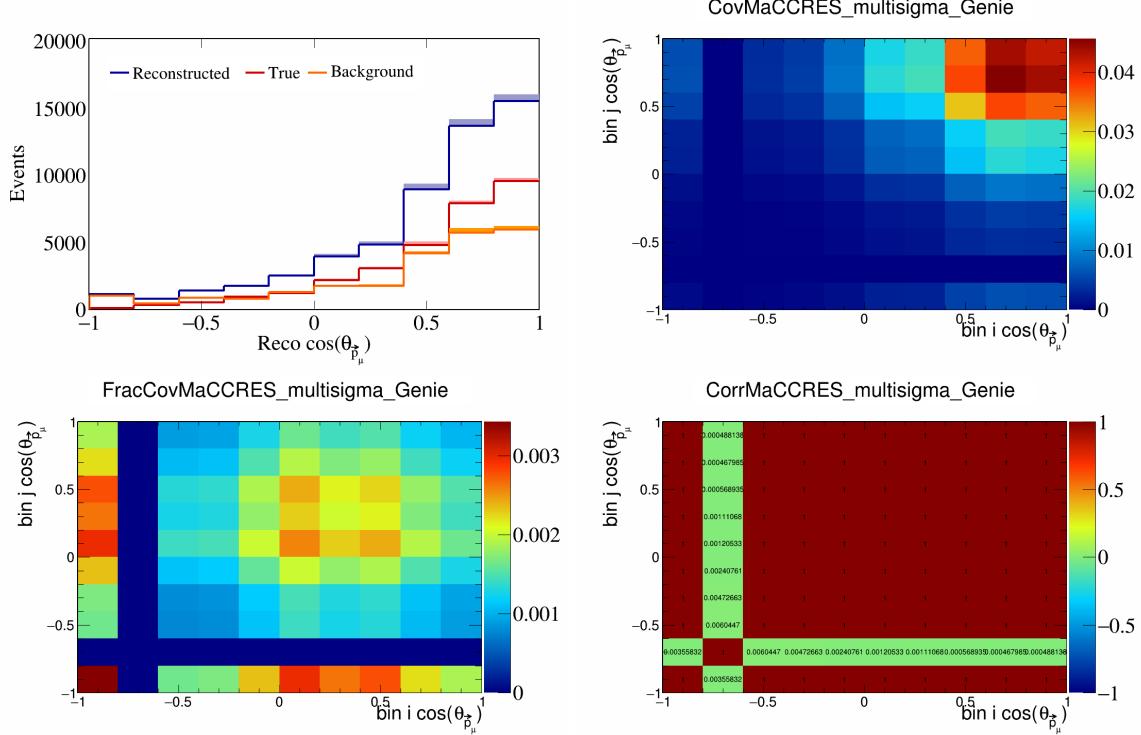


Figure 288: MaCCRES variations for $\cos(\theta_{\vec{p}_\mu, \vec{p}_{\text{sum}}})$ in $\cos(\theta_{\vec{p}_\mu})$.

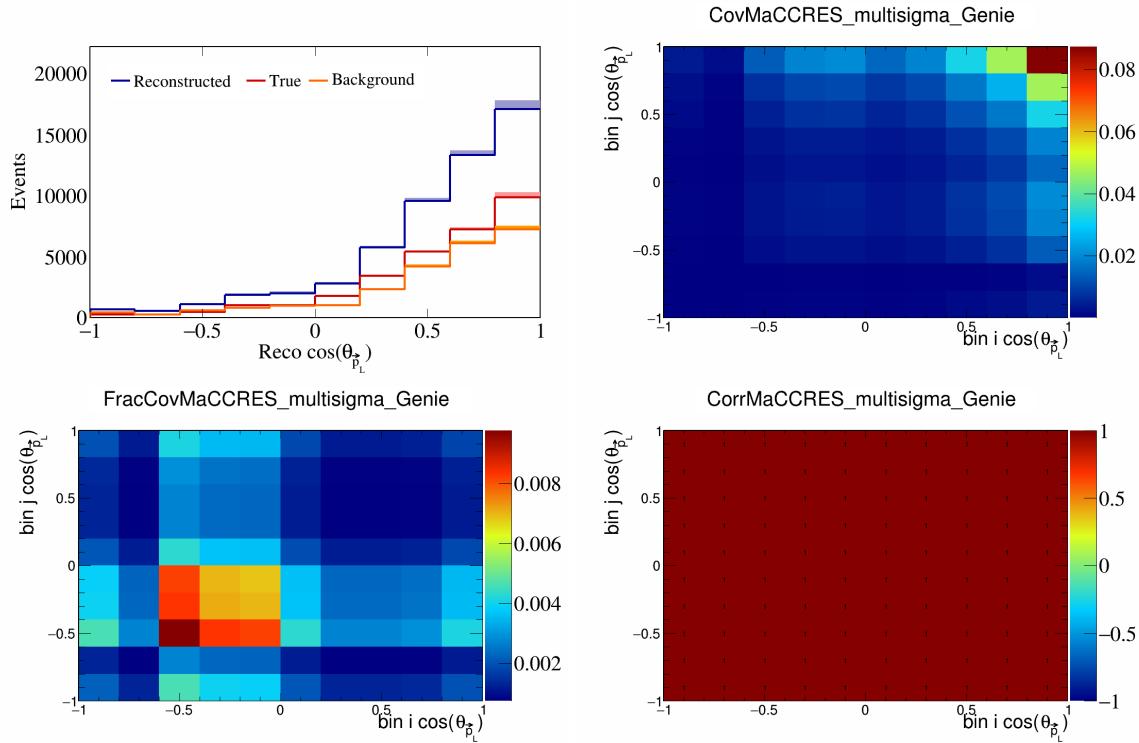


Figure 289: MaCCRES variations for $\cos(\theta_{\vec{p}_L})$.

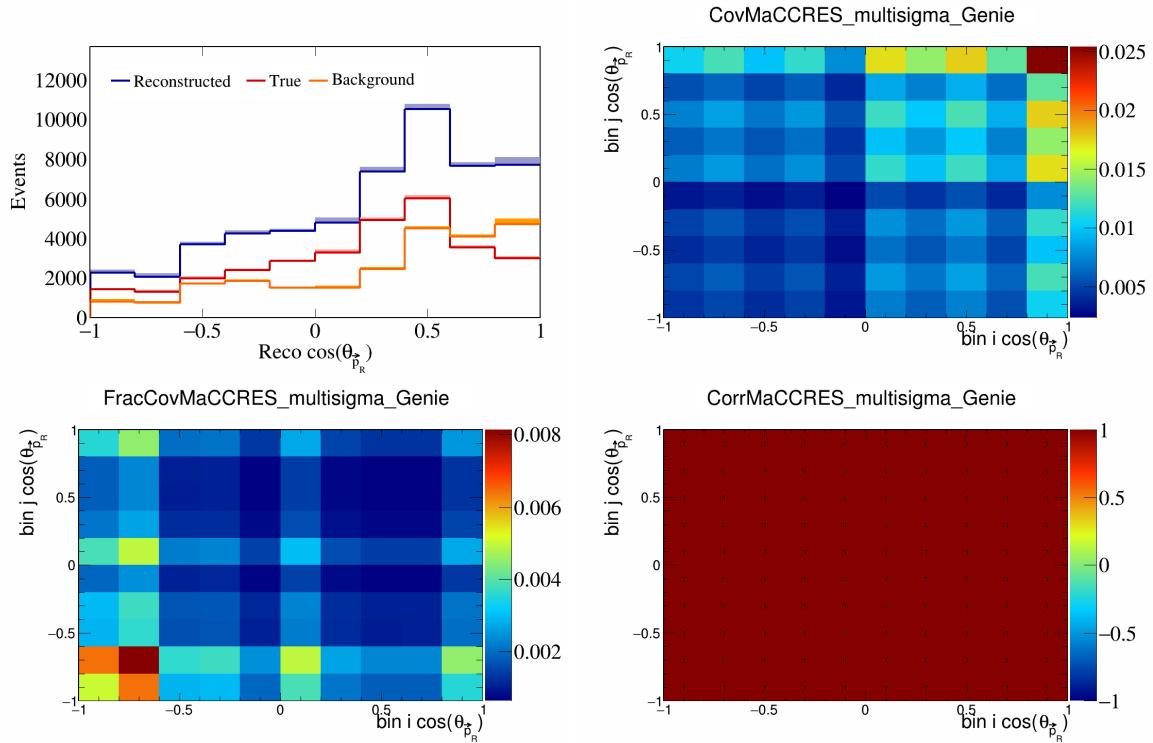


Figure 290: MaCCRES variations for $\cos(\theta_{\vec{p}_R})$.

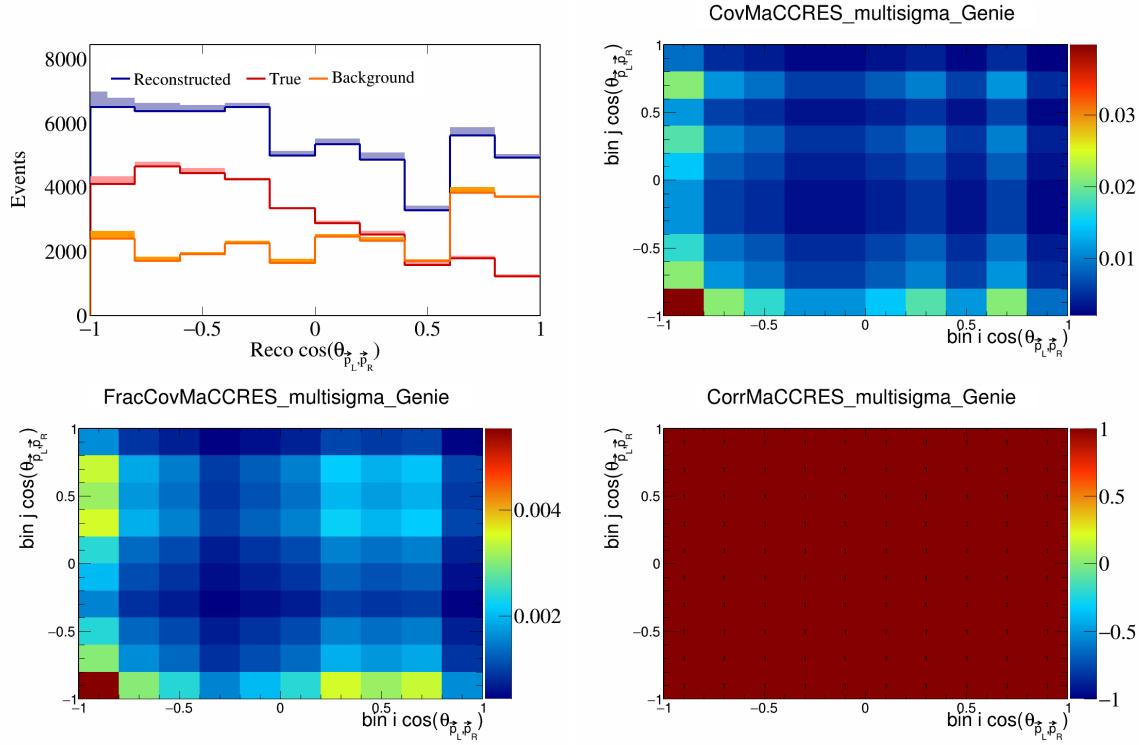


Figure 291: MaCCRES variations for $\cos(\theta_{\vec{p}_L, \vec{p}_R})$.

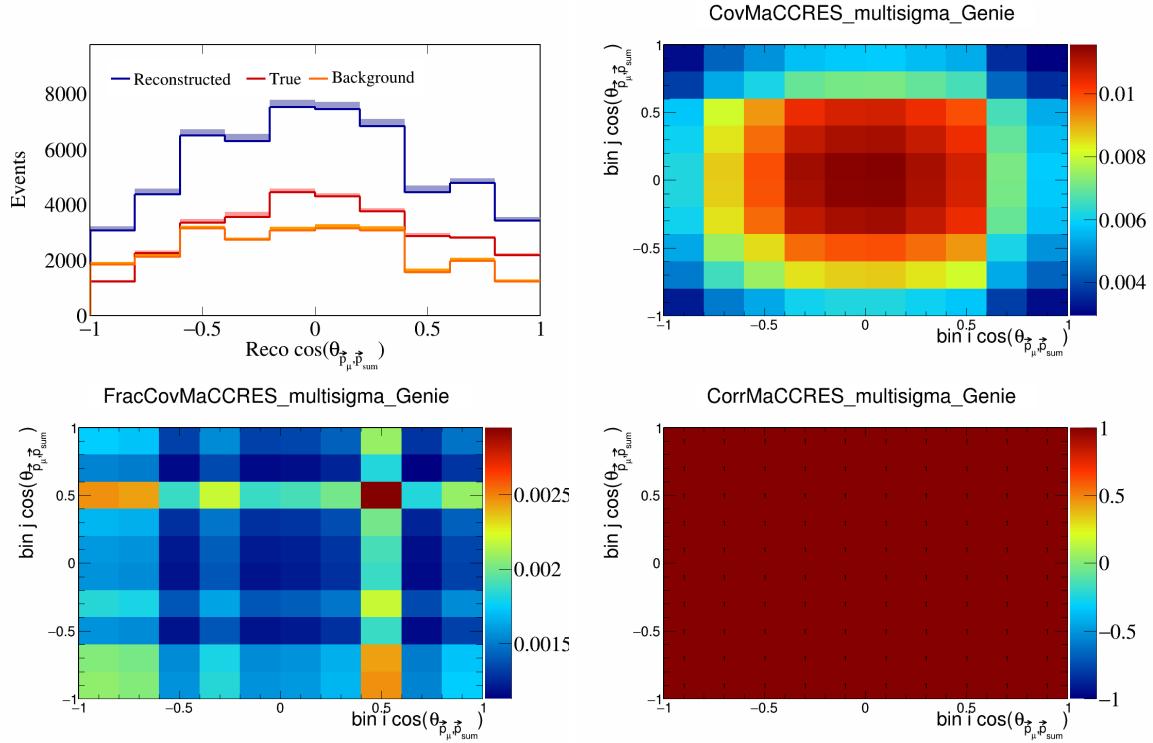


Figure 292: MaCCRES variations for $\cos(\theta_{\vec{p}_\mu, \vec{p}_{\text{sum}}})$.

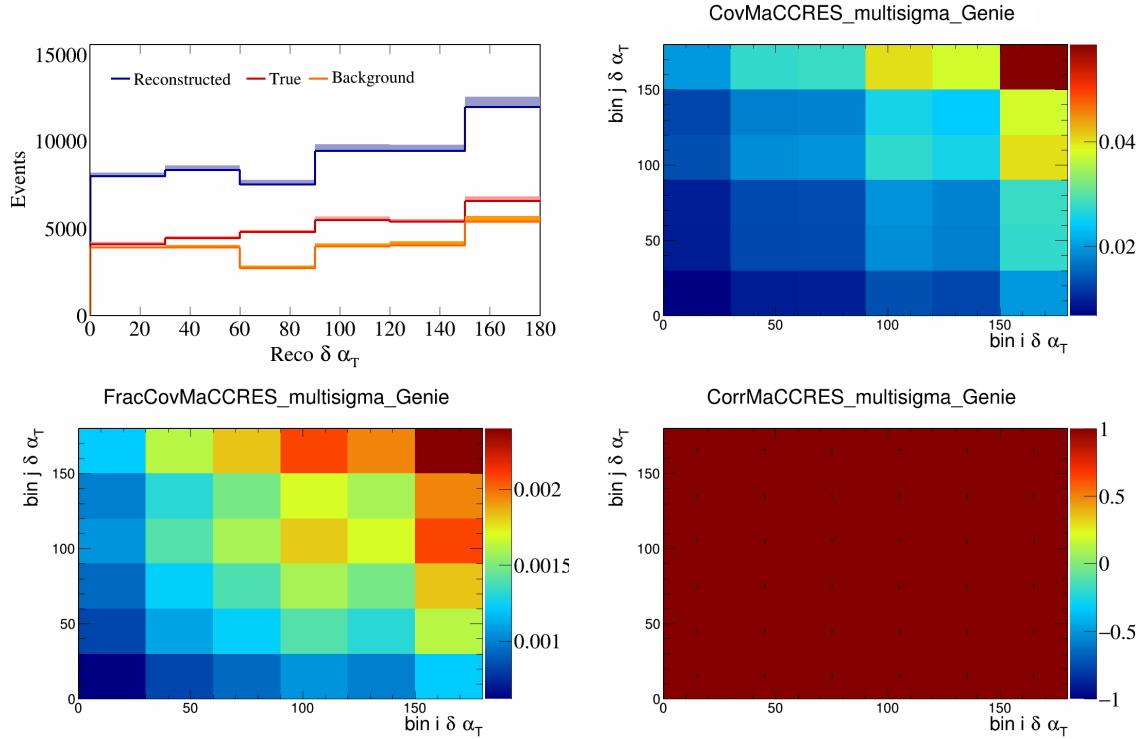


Figure 293: MaCCRES variations for $\delta\alpha_T$.

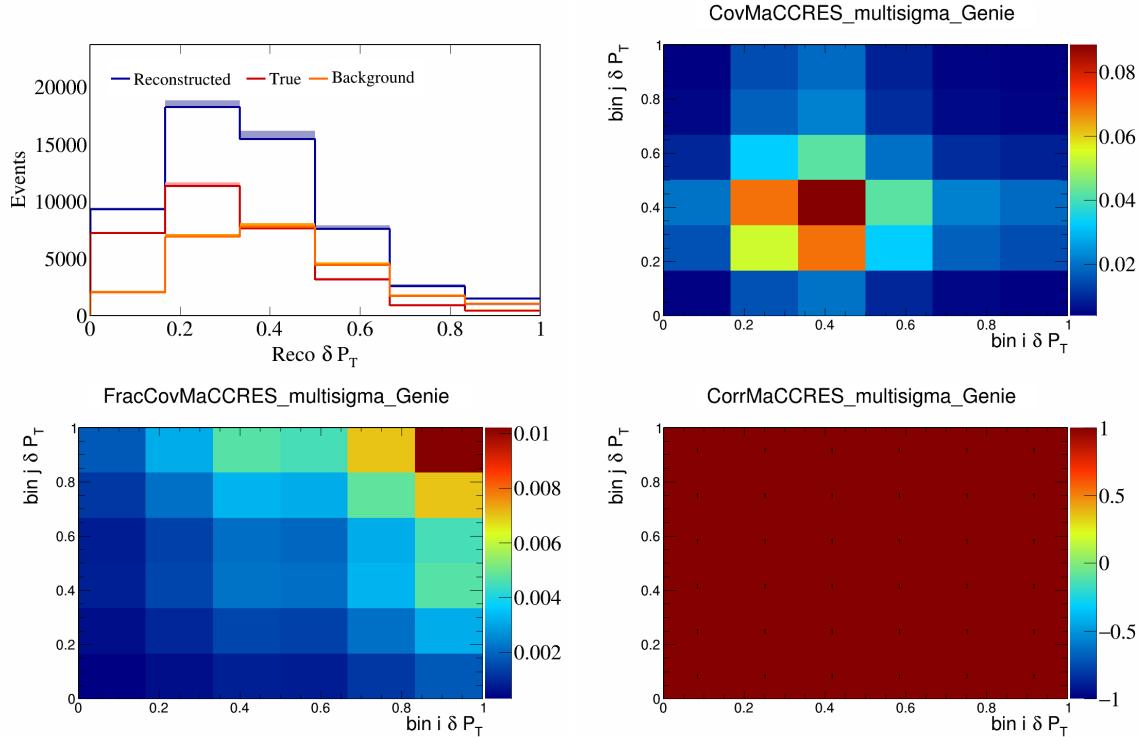


Figure 294: MaCCRES variations for δP_T .

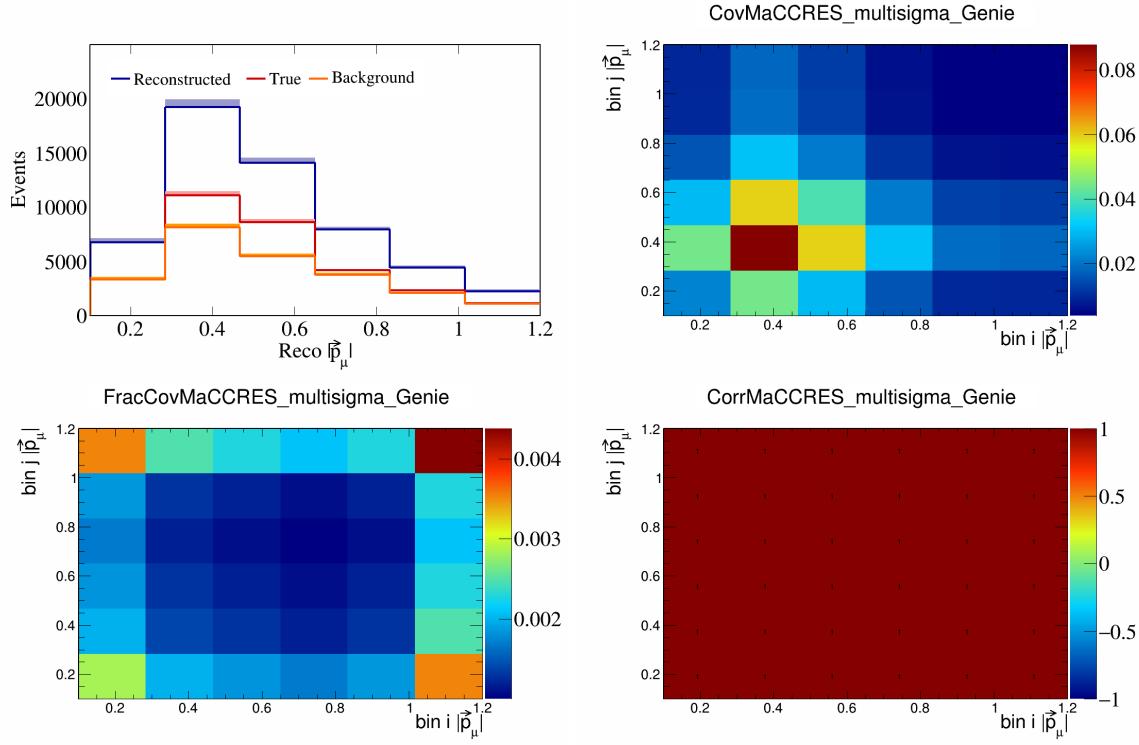


Figure 295: MaCCRES variations for $|\vec{p}_\mu|$.

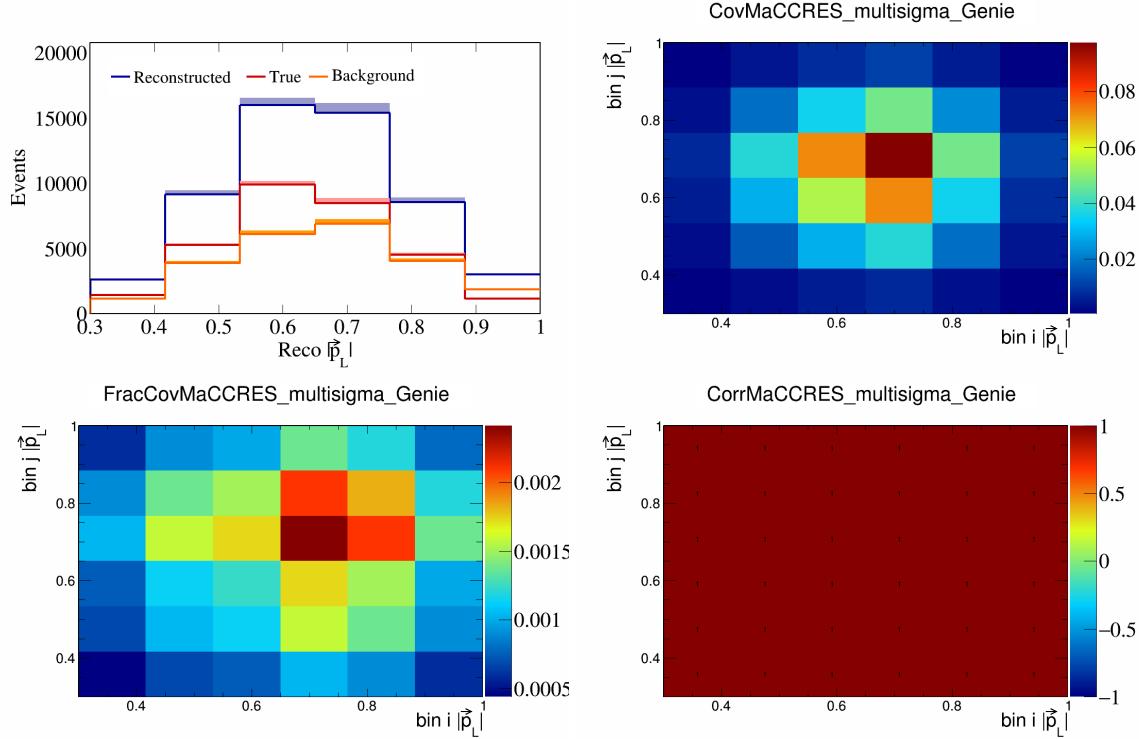


Figure 296: MaCCRES variations for $|\vec{p}_L|$.

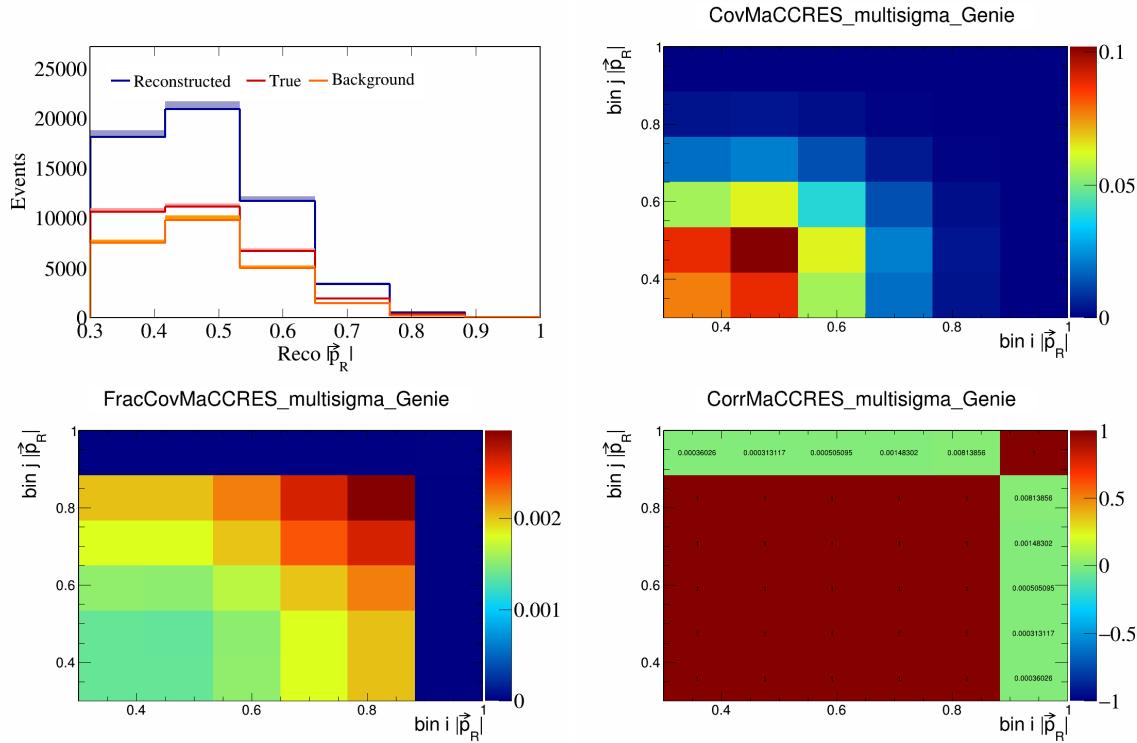


Figure 297: MaCCRES variations for $|\vec{p}_R|$.

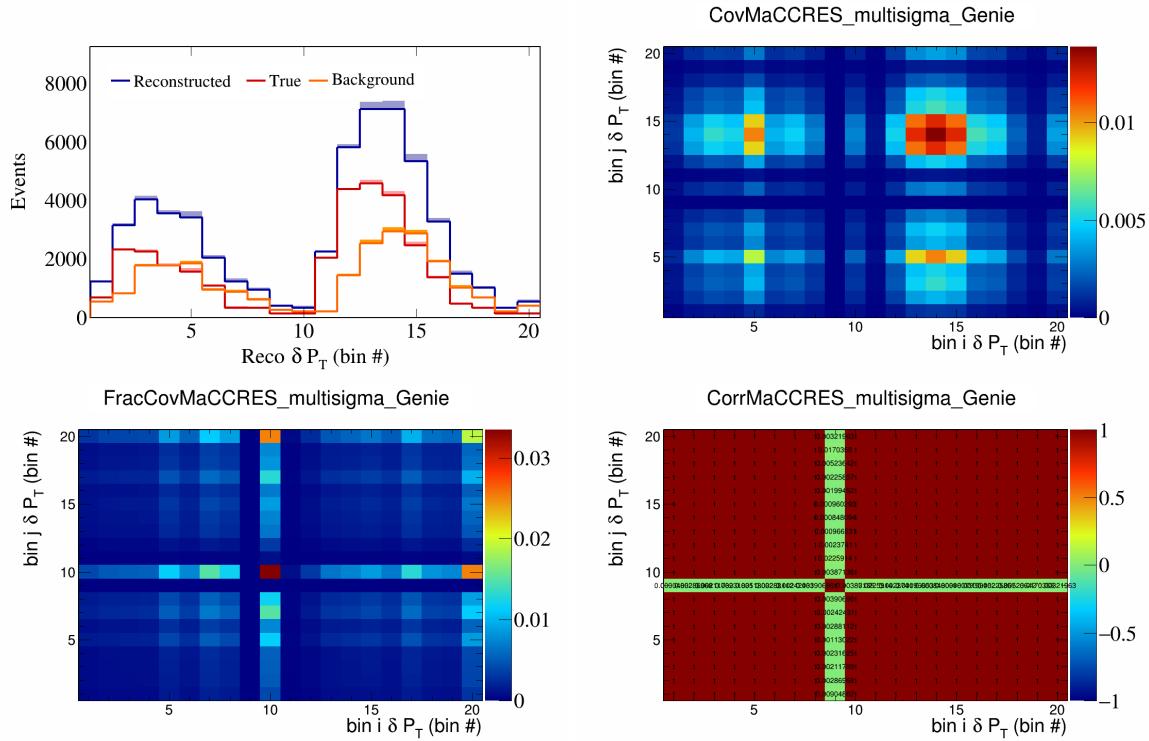


Figure 298: MaCCRES variations for δP_T in $\cos(\theta_{\vec{p}_\mu})$.

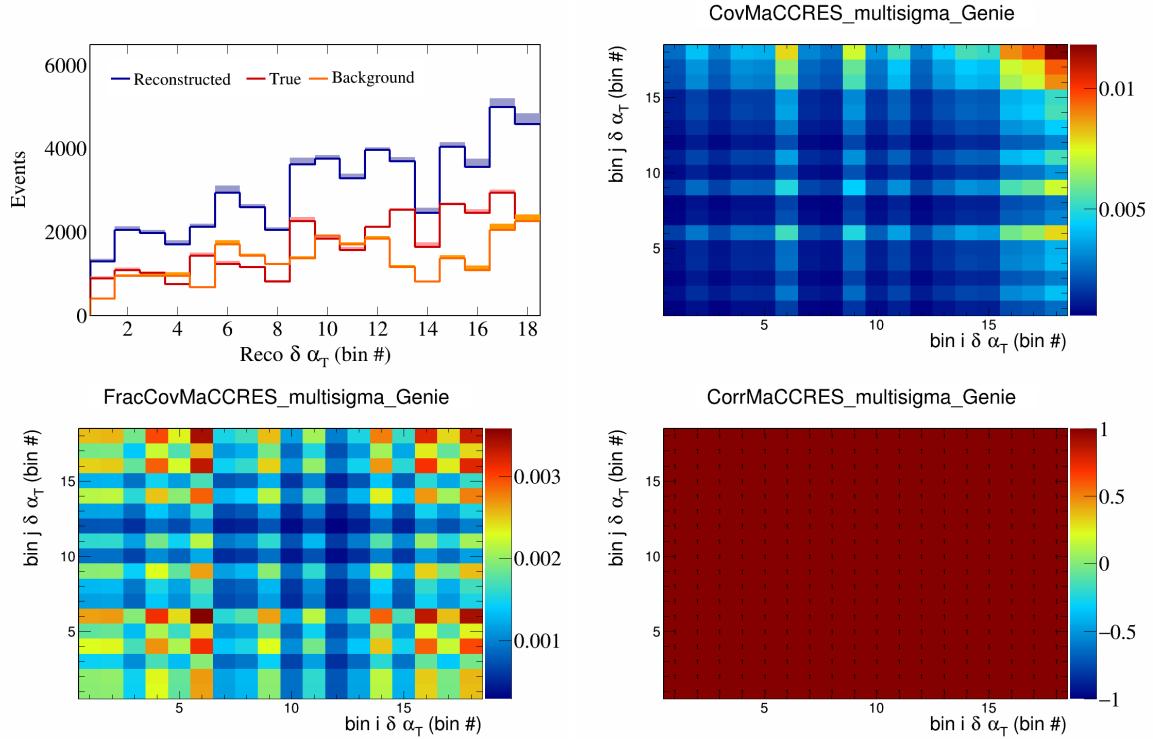


Figure 299: MaCCRES variations for $\delta \alpha_T$ in $\cos(\theta_{\vec{p}_\mu})$.

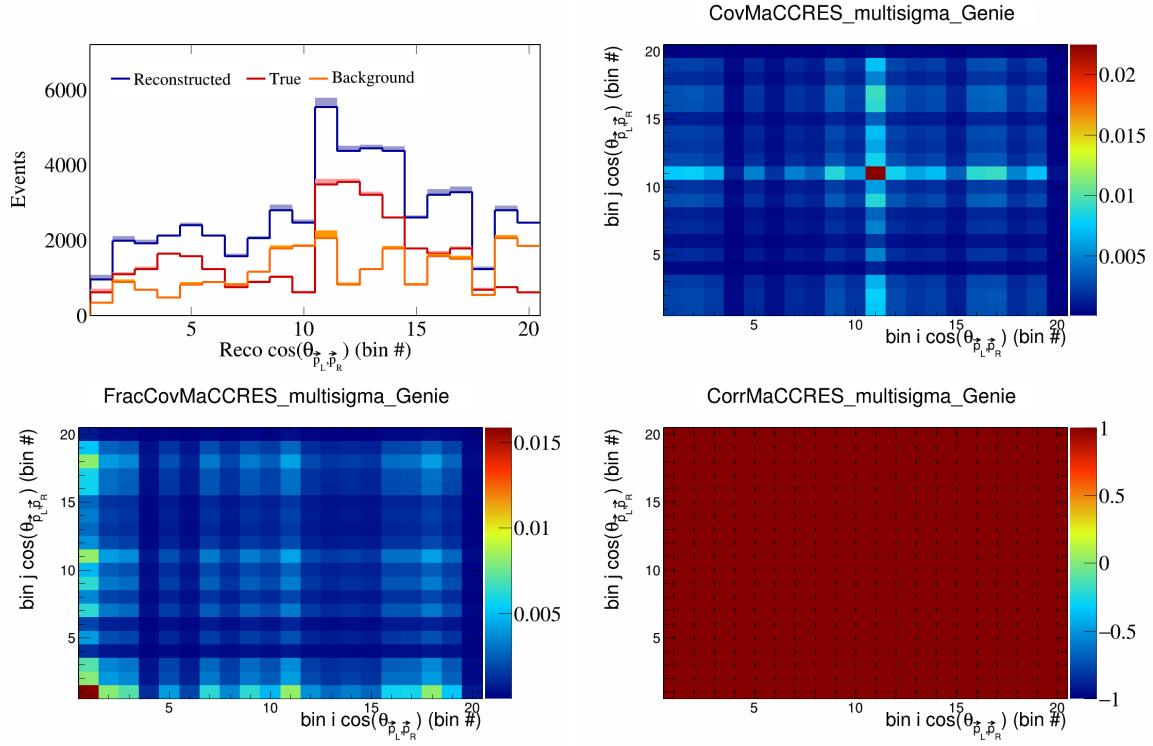


Figure 300: MaCCRES variations for $\cos(\theta_{\vec{p}_L, \vec{p}_R})$ in $\cos(\theta_{\vec{p}_\mu})$.

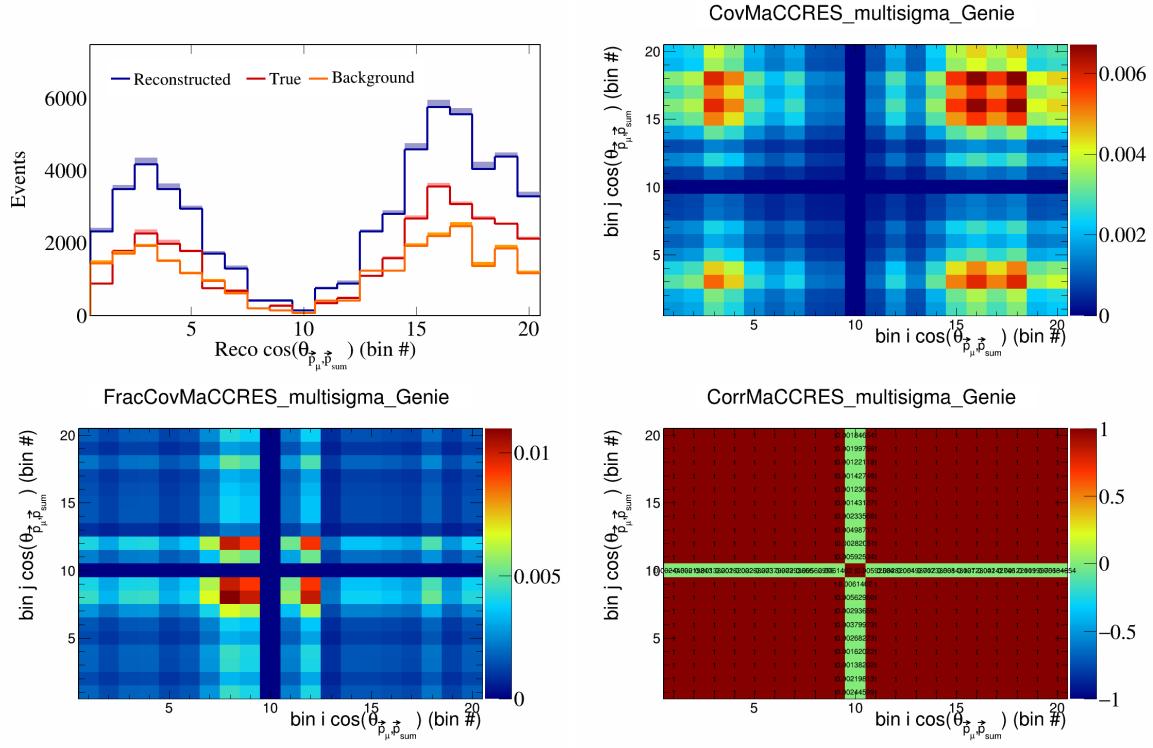


Figure 301: MaCCRES variations for $\cos(\theta_{\vec{p}_\mu, \vec{p}_{\text{sum}}})$ in $\cos(\theta_{\vec{p}_\mu})$.

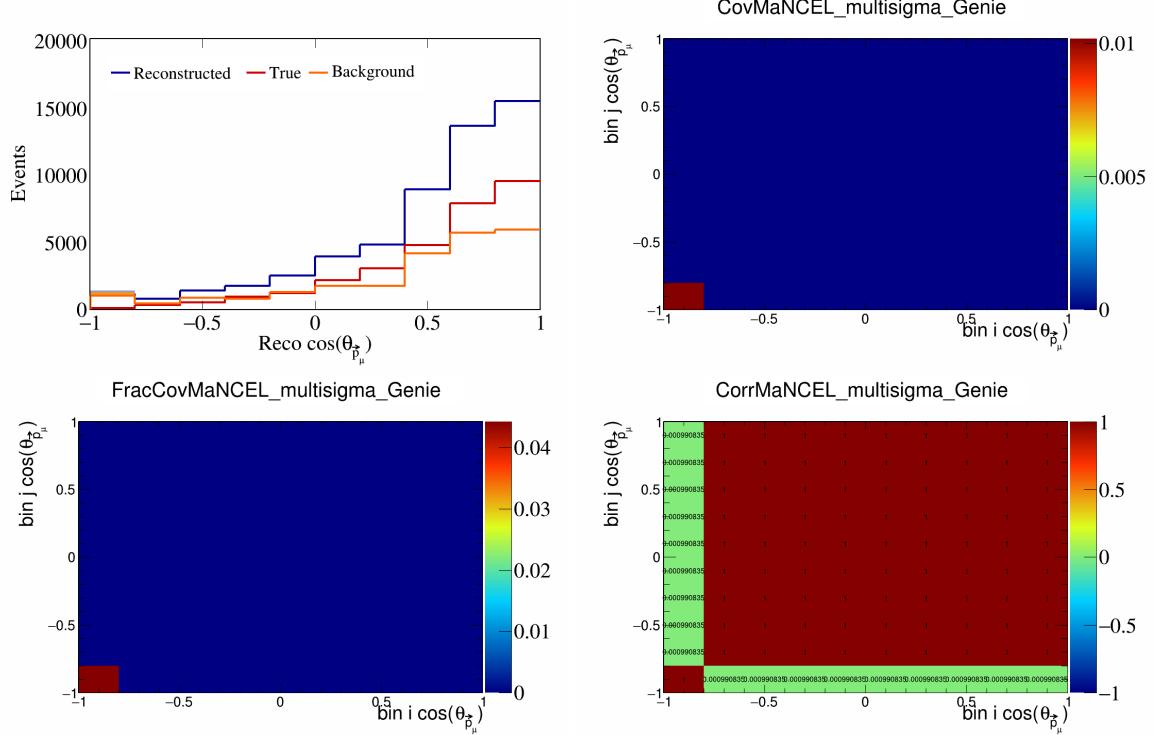


Figure 302: MaNCEL variations for $\cos(\theta_{\vec{p}_\mu})$.

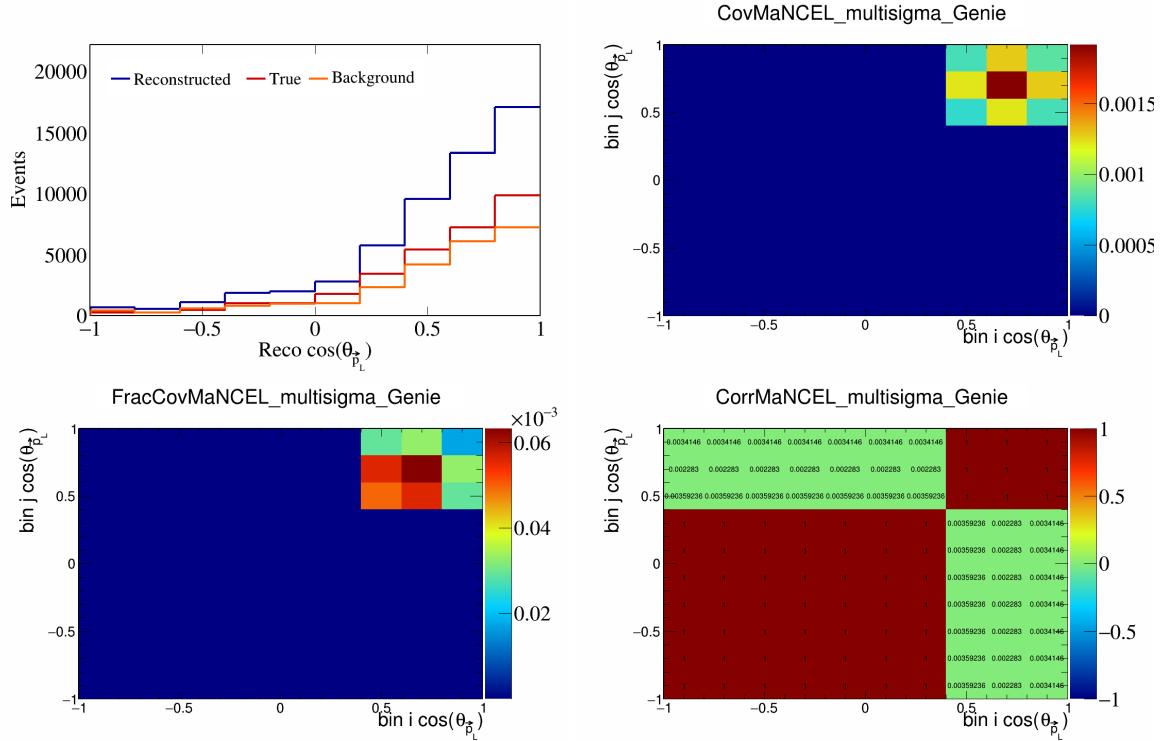


Figure 303: MaNCEL variations for $\cos(\theta_{\vec{p}_L})$.

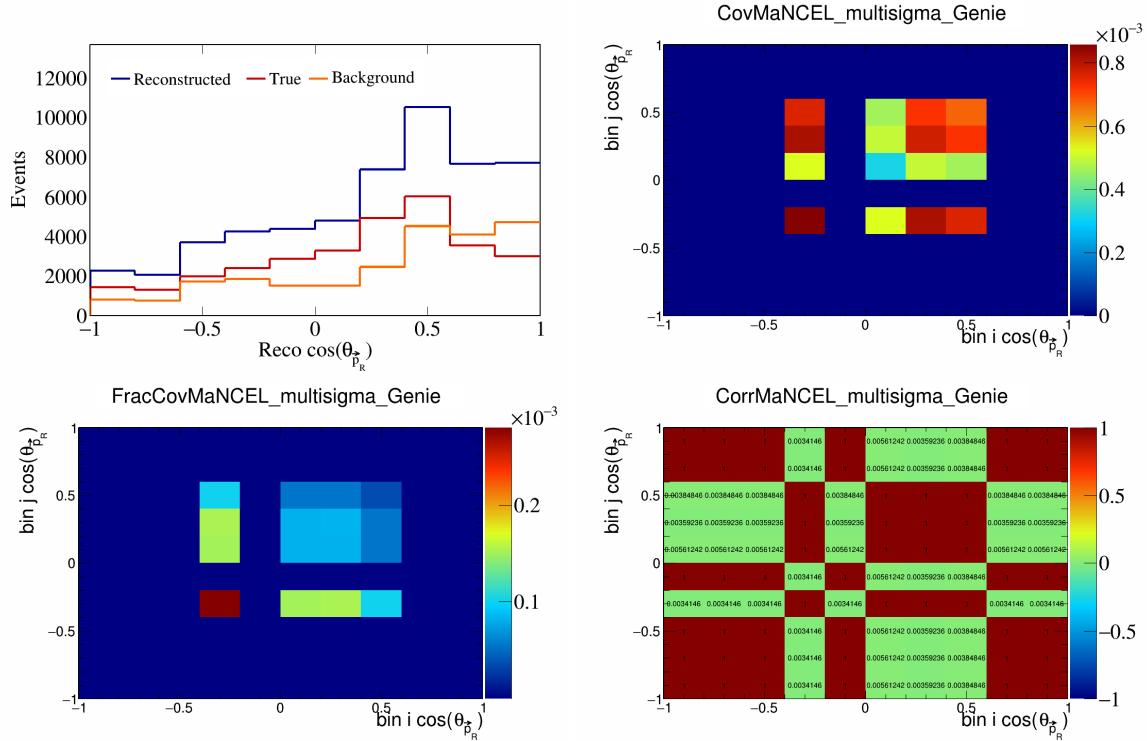


Figure 304: MaNCEL variations for $\cos(\theta_{\vec{p}_R})$.

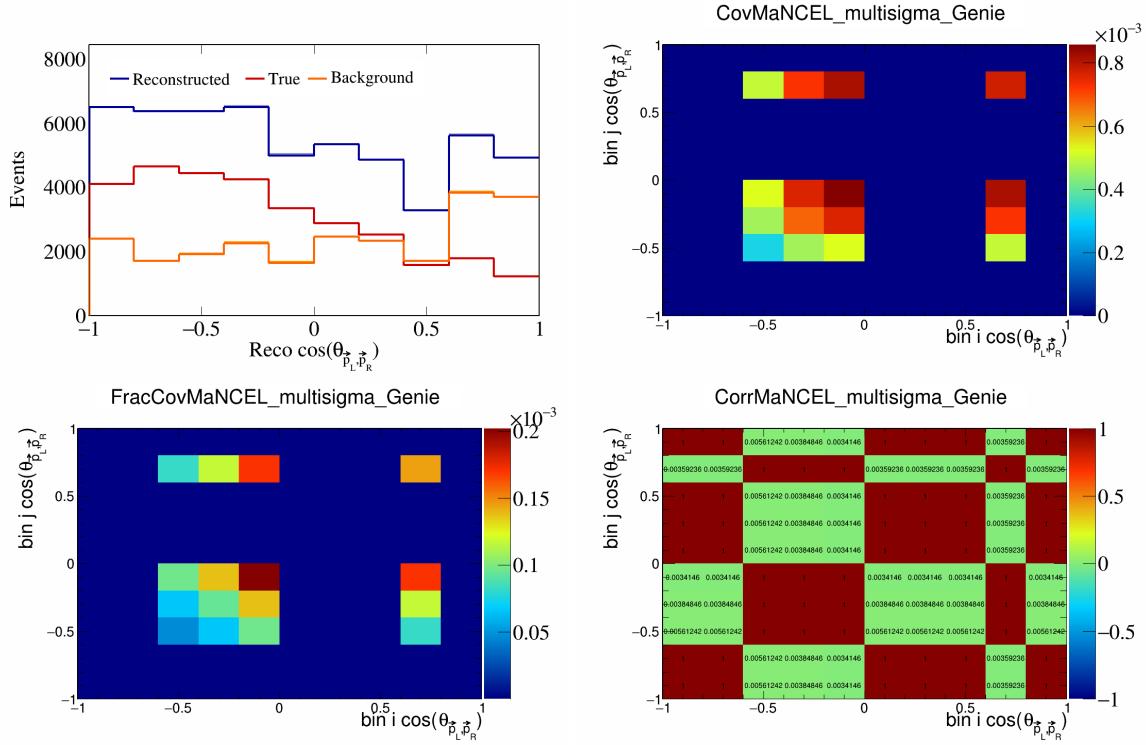


Figure 305: MaNCEL variations for $\cos(\theta_{\vec{p}_L, \vec{p}_R})$.

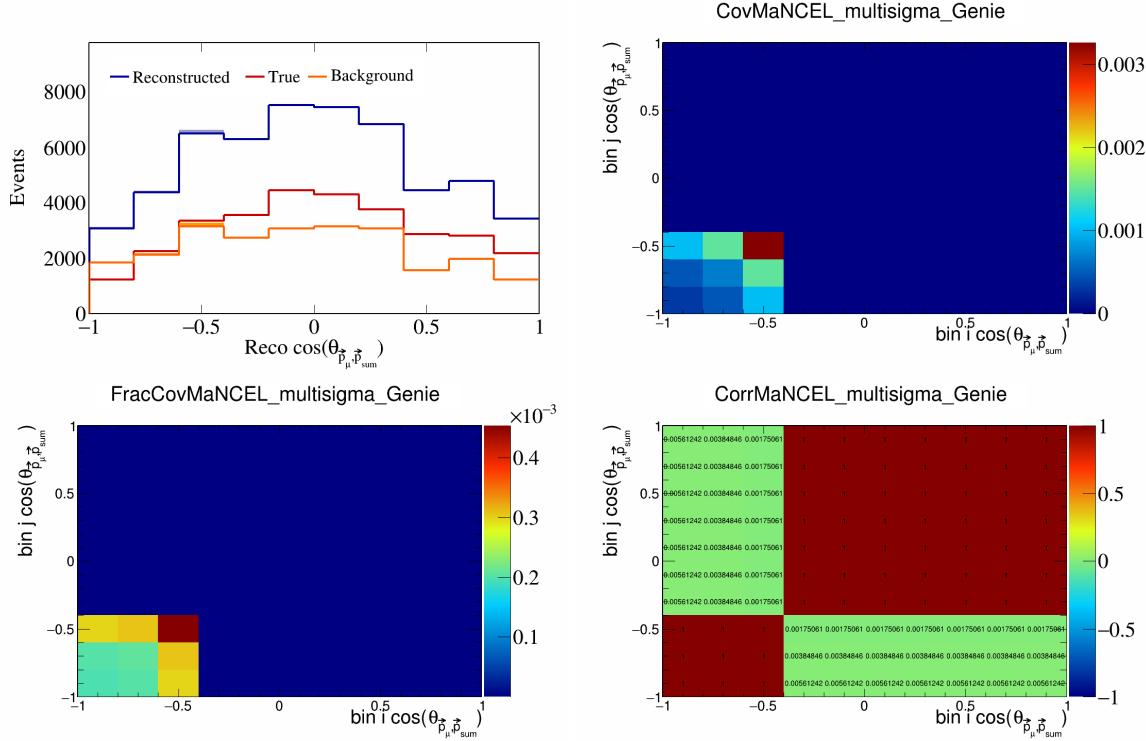


Figure 306: MaNCEL variations for $\cos(\theta_{\vec{p}_\mu, \vec{p}_{\text{sum}}})$.

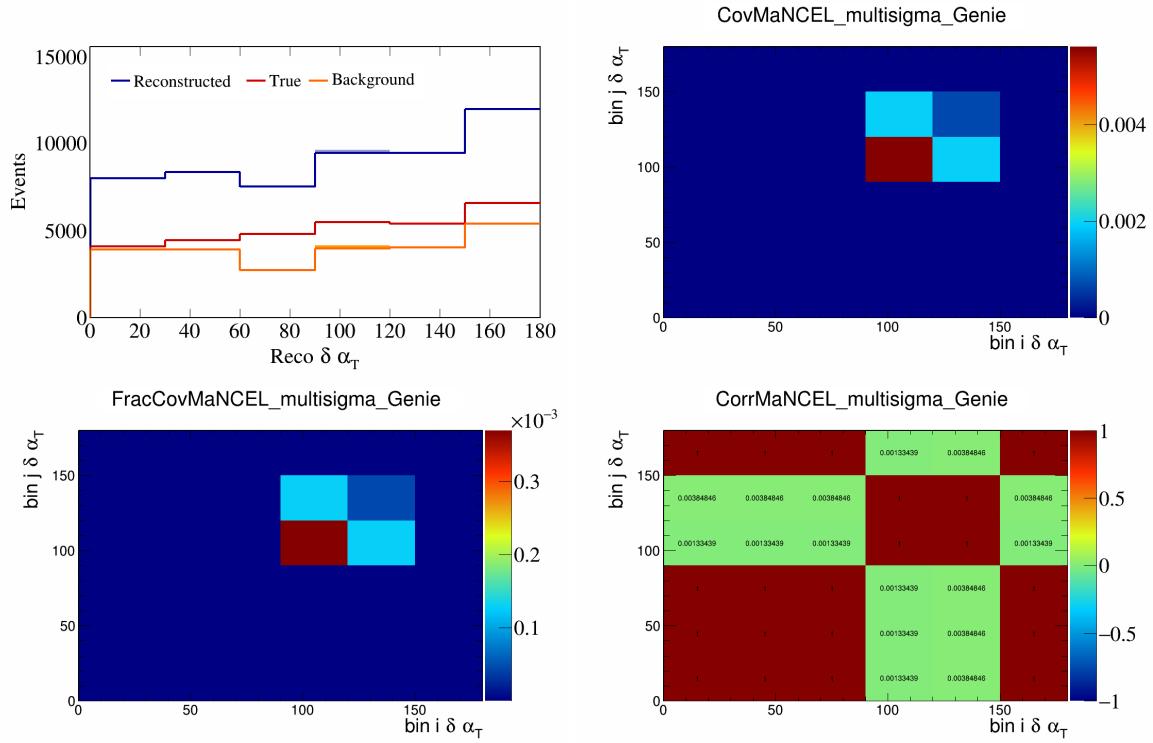


Figure 307: MaNCEL variations for $\delta\alpha_T$.

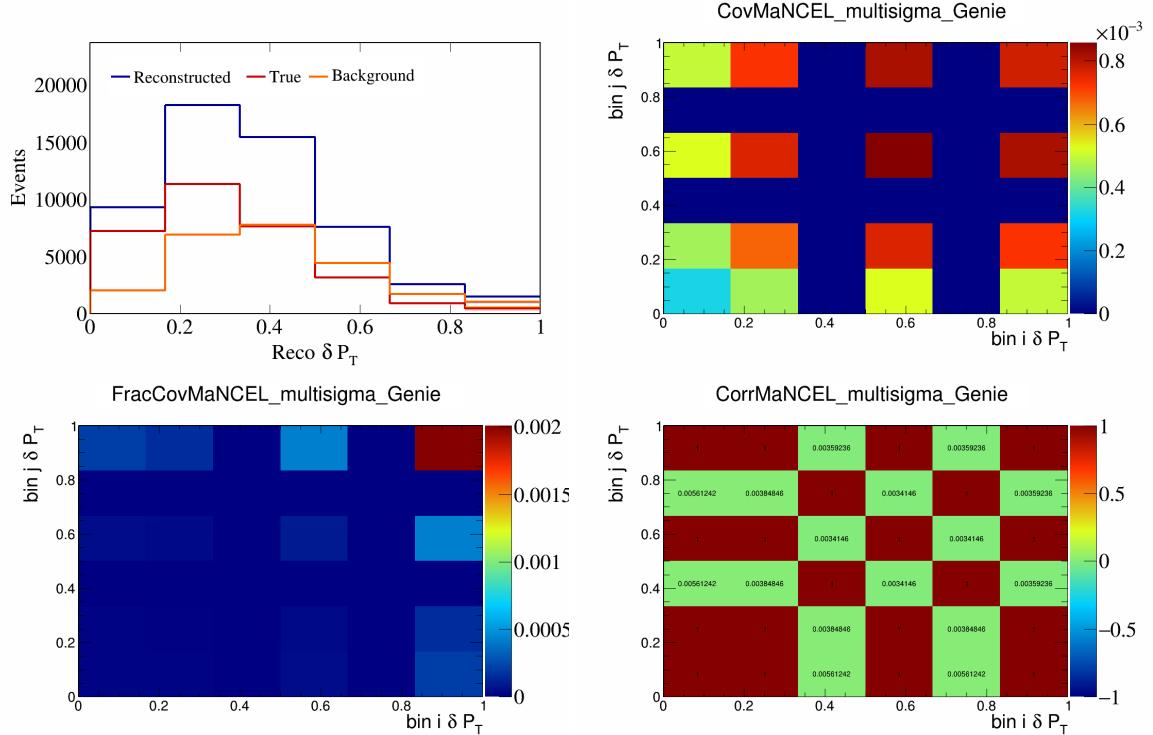


Figure 308: MaNCEL variations for δP_T .

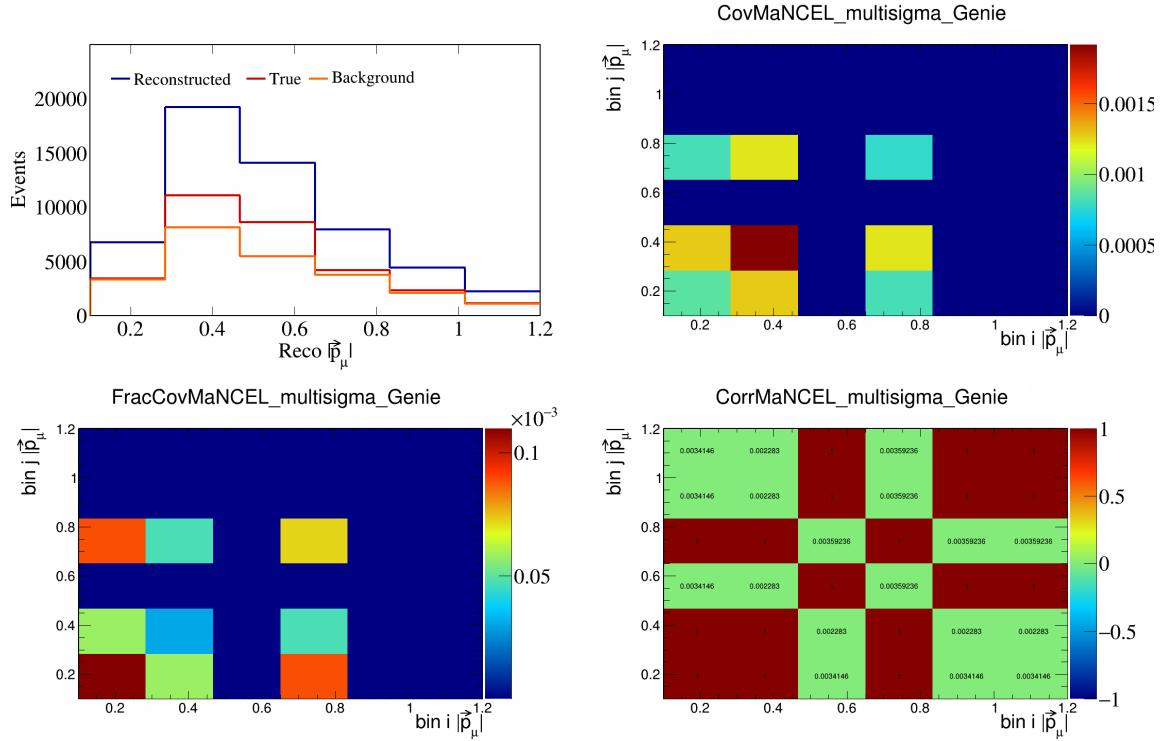


Figure 309: MaNCEL variations for $|\vec{p}_\mu|$.

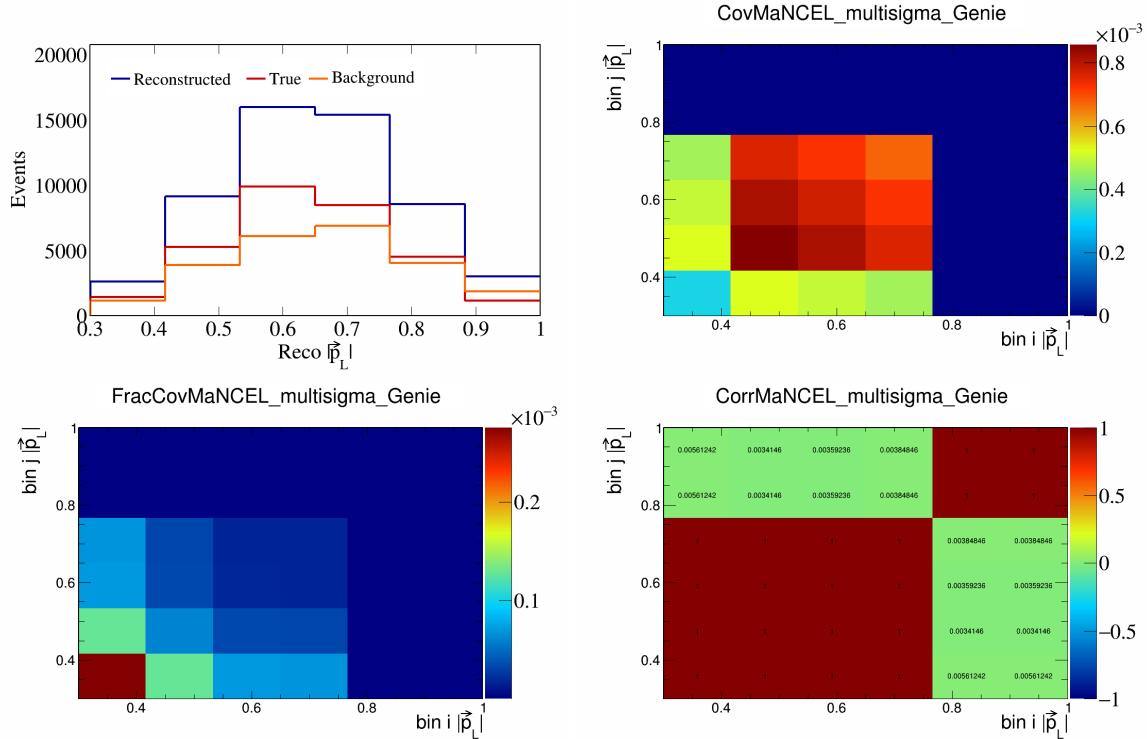


Figure 310: MaNCEL variations for $|\vec{p}_L|$.

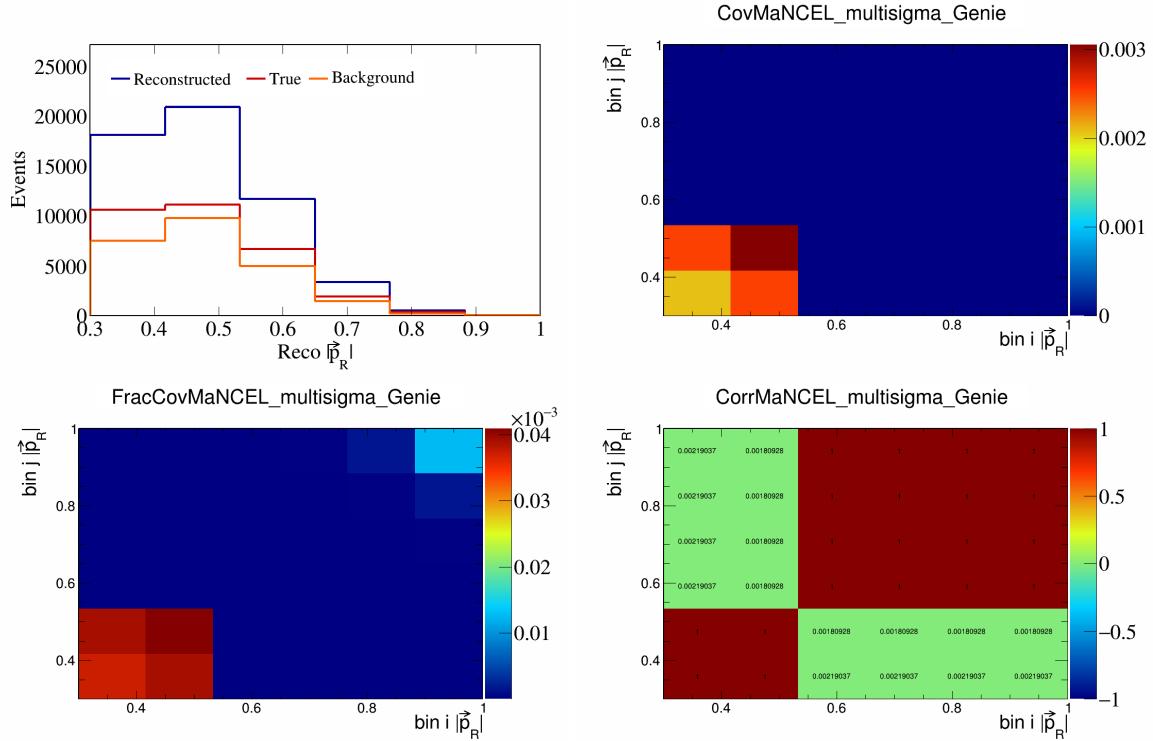


Figure 311: MaNCEL variations for $|\vec{p}_R|$.

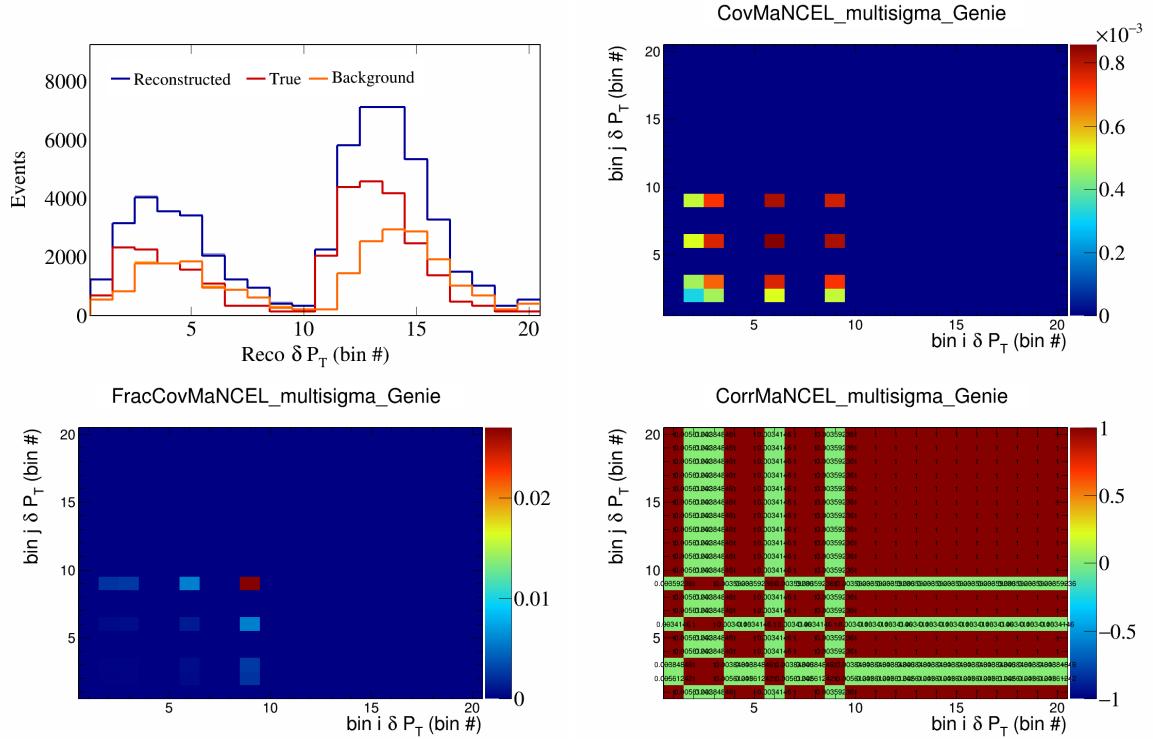


Figure 312: MaNCEL variations for δP_T in $\cos(\theta_{\vec{p}_\mu})$.

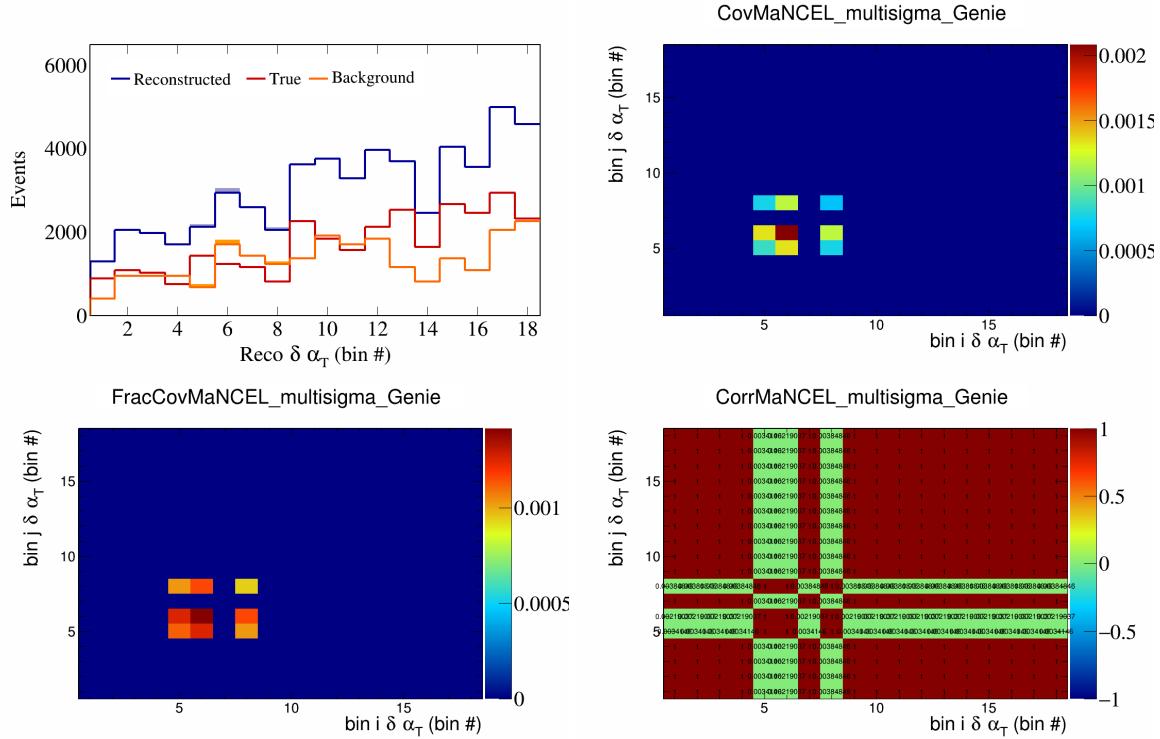


Figure 313: MaNCEL variations for $\delta\alpha_T$ in $\cos(\theta_{\vec{p}_\mu})$.

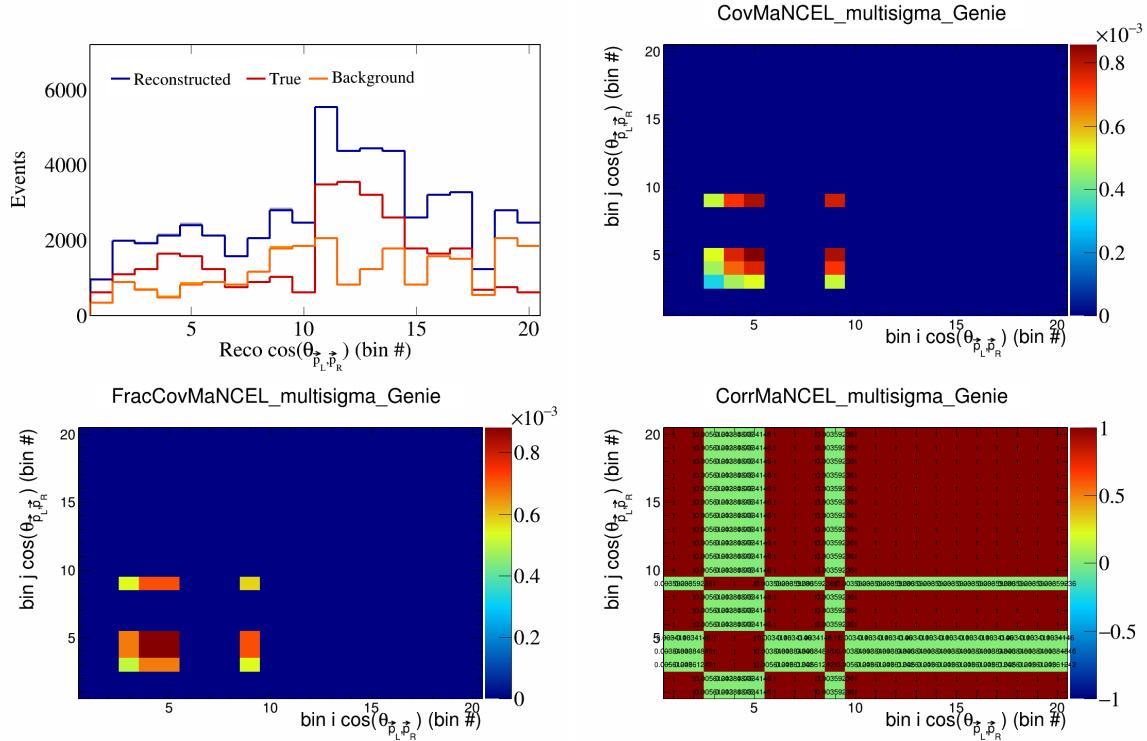


Figure 314: MaNCEL variations for $\cos(\theta_{\vec{p}_L, \vec{p}_R})$ in $\cos(\theta_{\vec{p}_\mu})$.

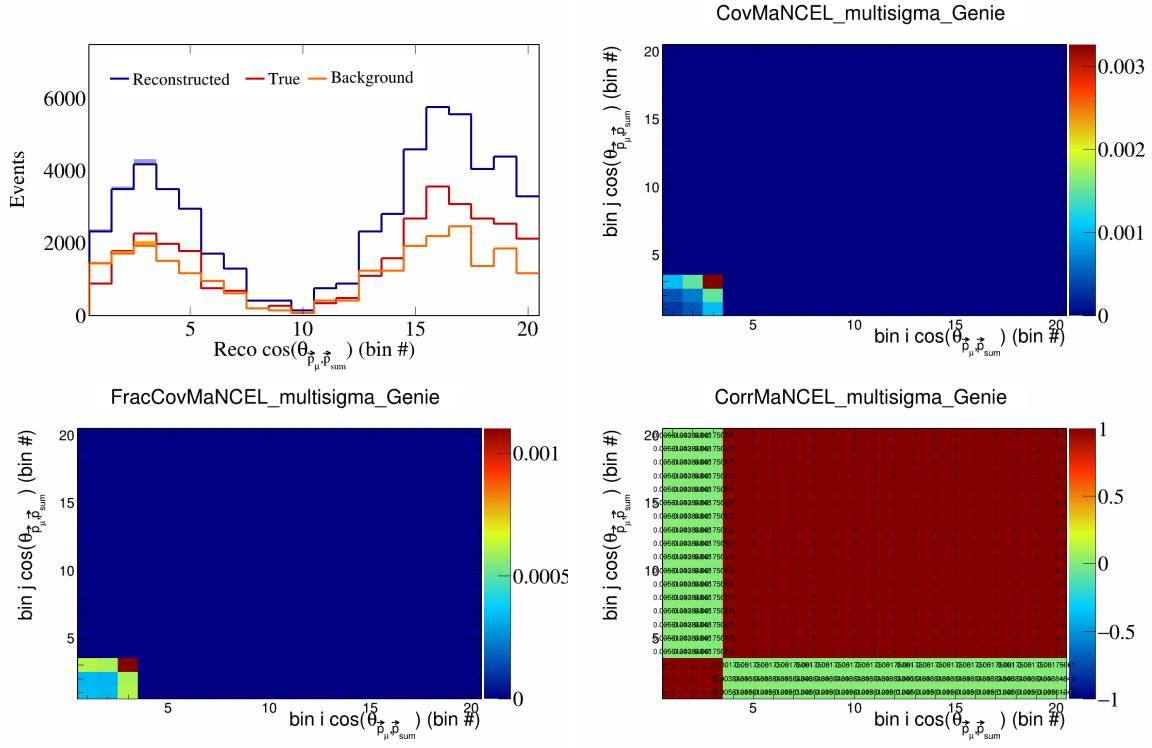


Figure 315: MaNCEL variations for $\cos(\theta_{\vec{p}_\mu, \vec{p}_{\text{sum}}})$ in $\cos(\theta_{\vec{p}_\mu})$.

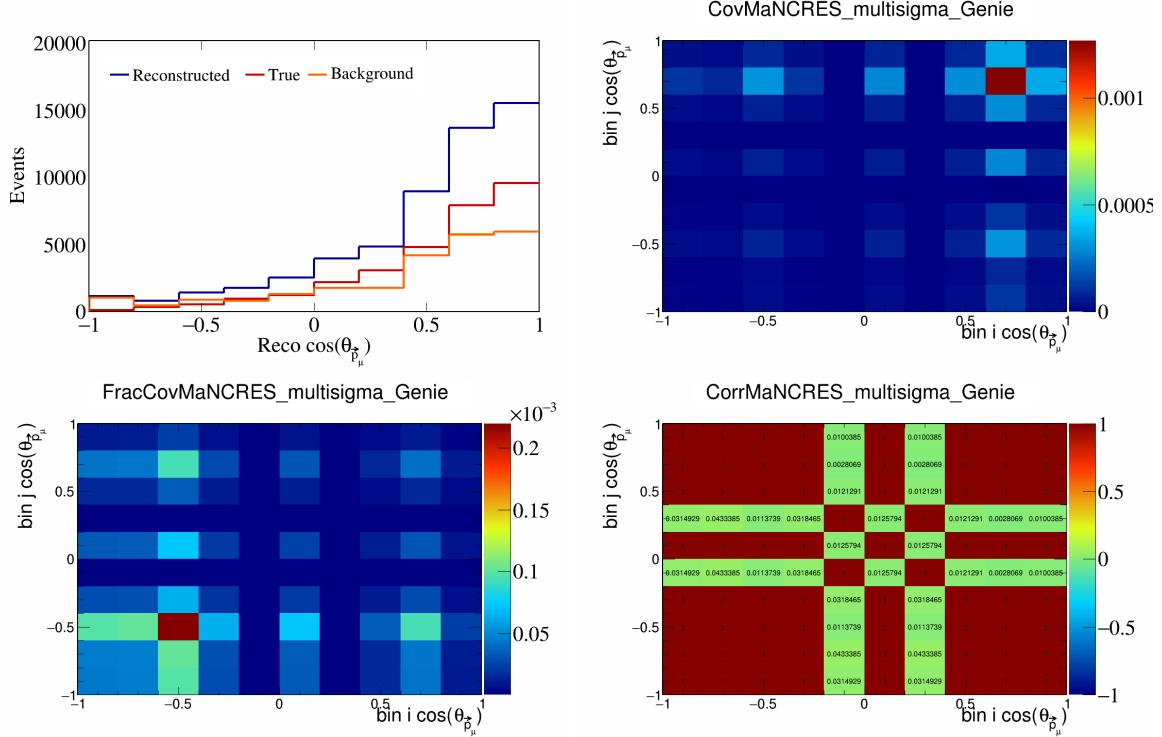


Figure 316: MaNCRES variations for $\cos(\theta_{\vec{p}_\mu})$.

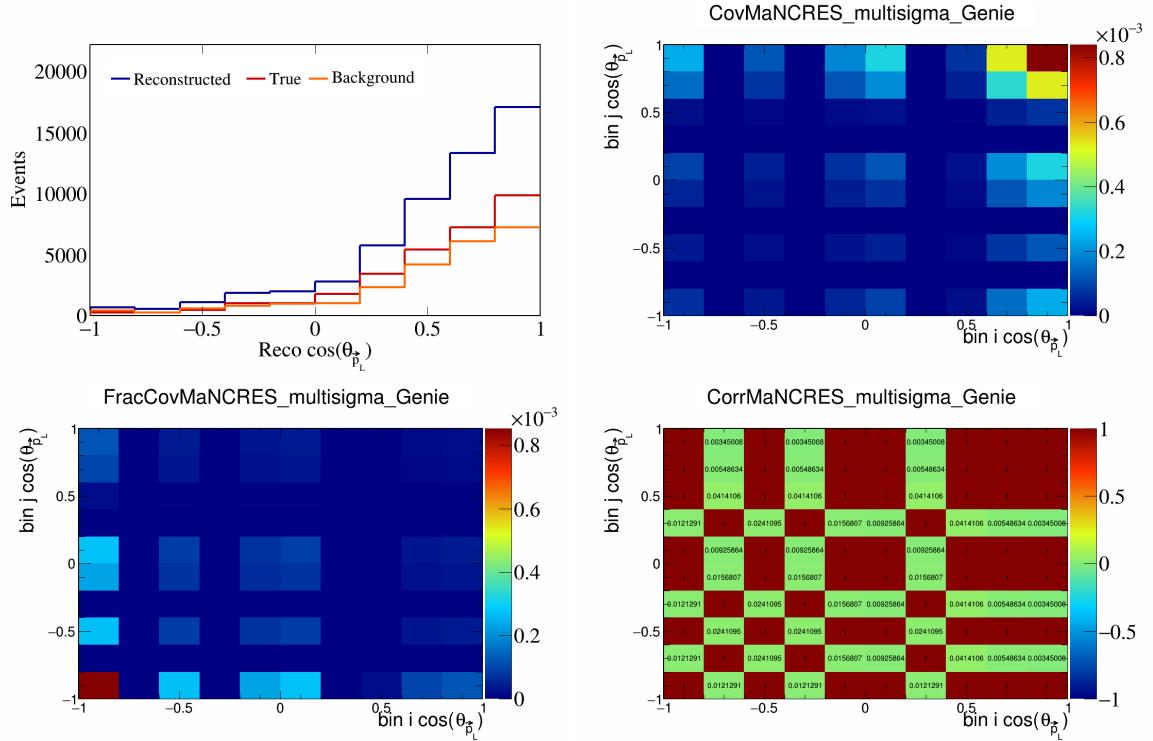


Figure 317: MaNCRES variations for $\cos(\theta_{\vec{p}_L})$.

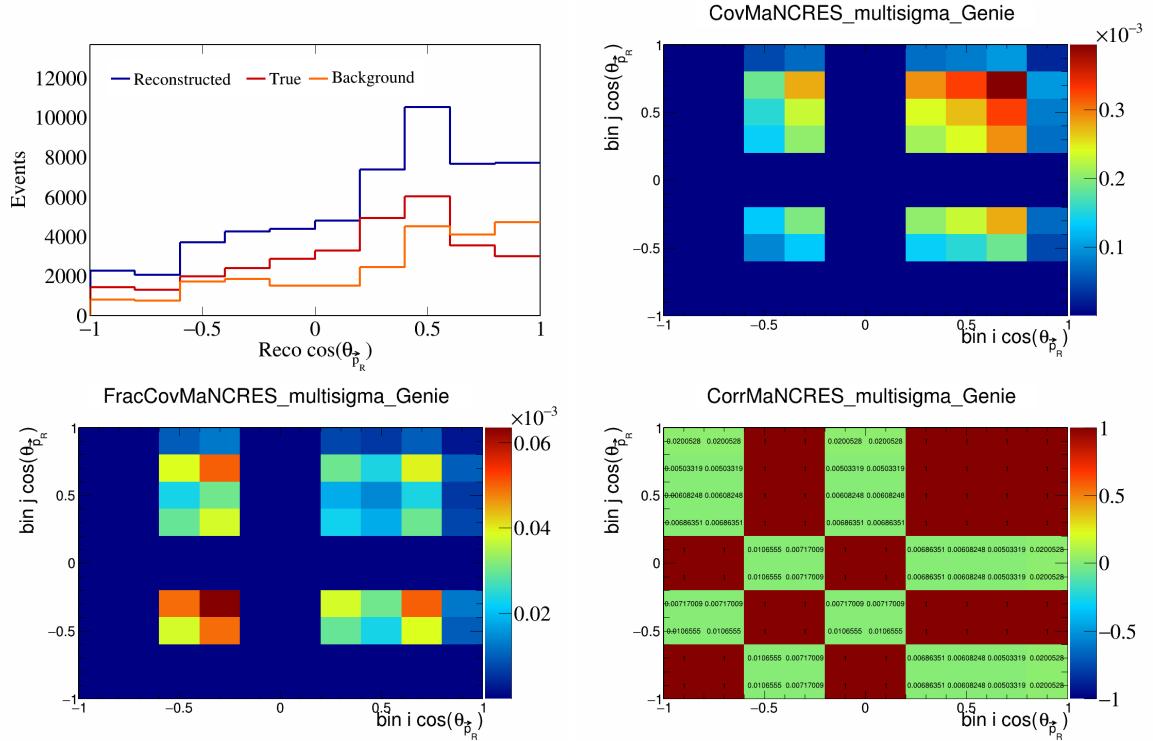


Figure 318: MaNCRES variations for $\cos(\theta_{\vec{p}_R})$.

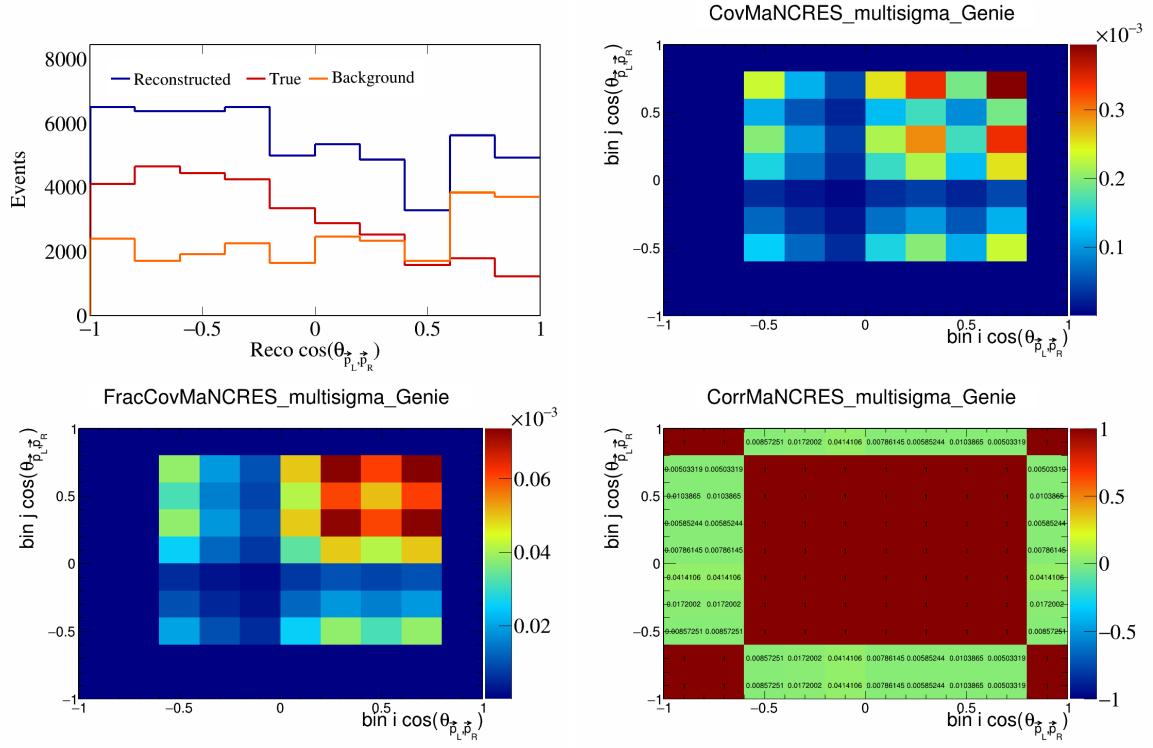


Figure 319: MaNCRES variations for $\cos(\theta_{\vec{p}_L, \vec{p}_R})$.

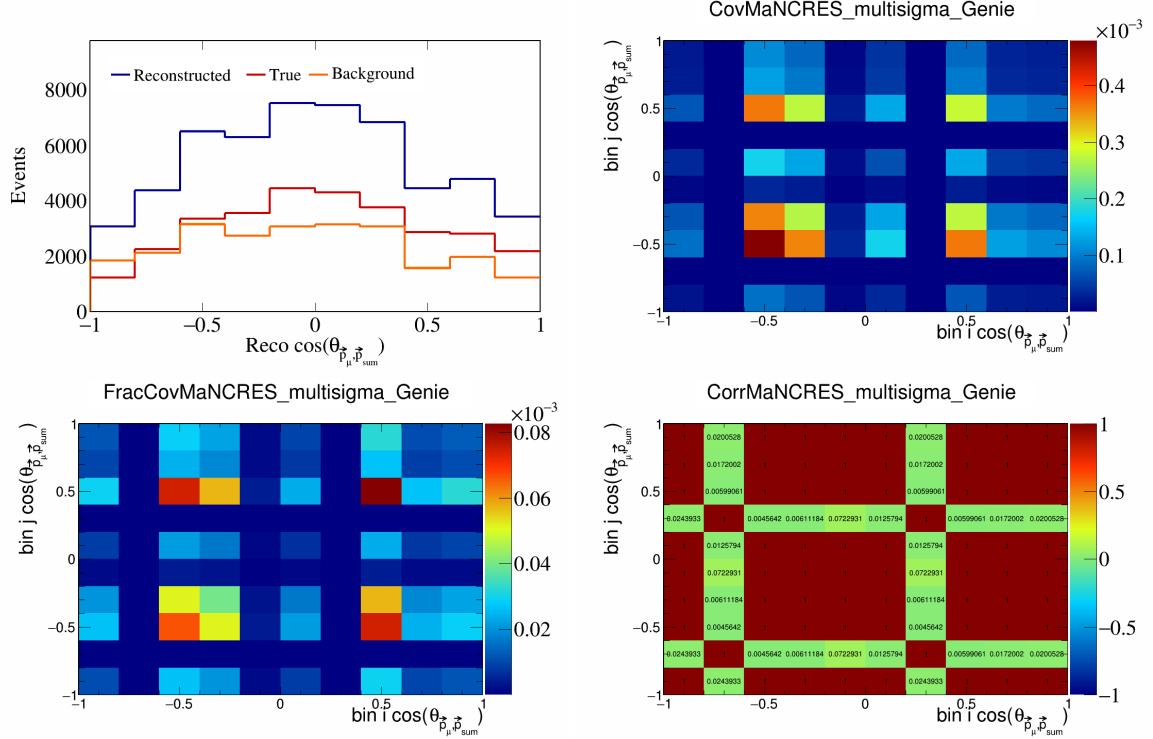


Figure 320: MaNCRES variations for $\cos(\theta_{\vec{p}_\mu, \vec{p}_{\text{sum}}})$.

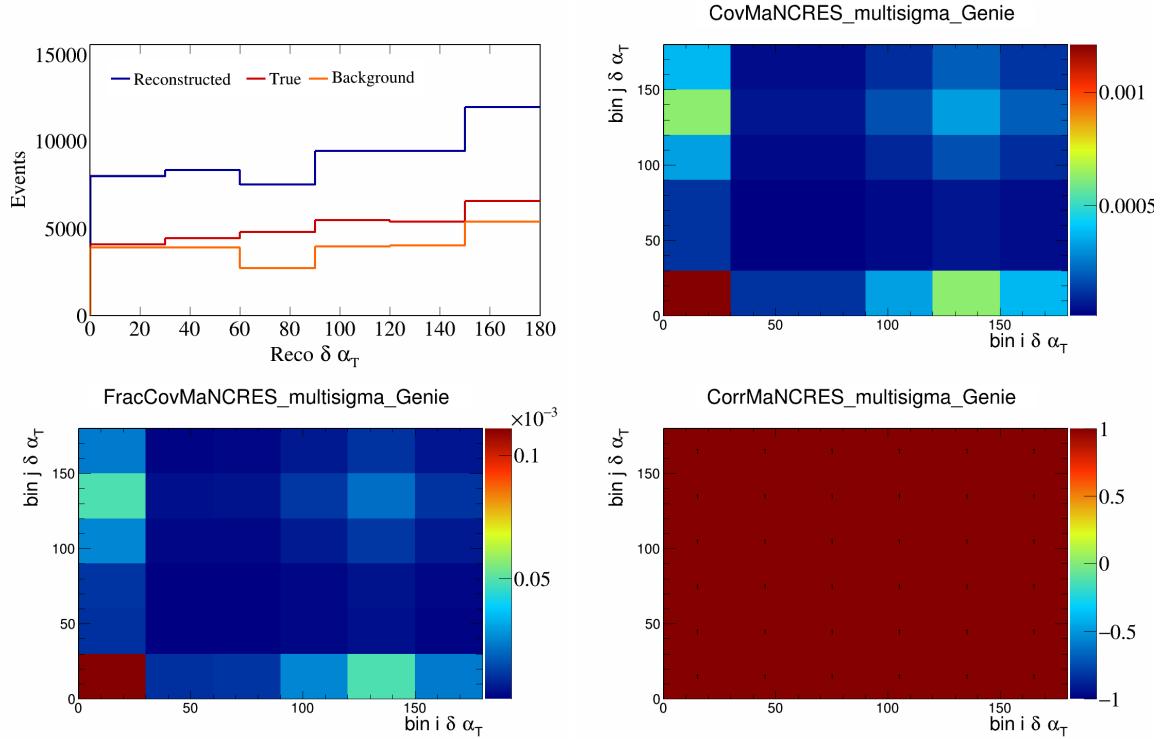


Figure 321: MaNCRES variations for $\delta\alpha_T$.

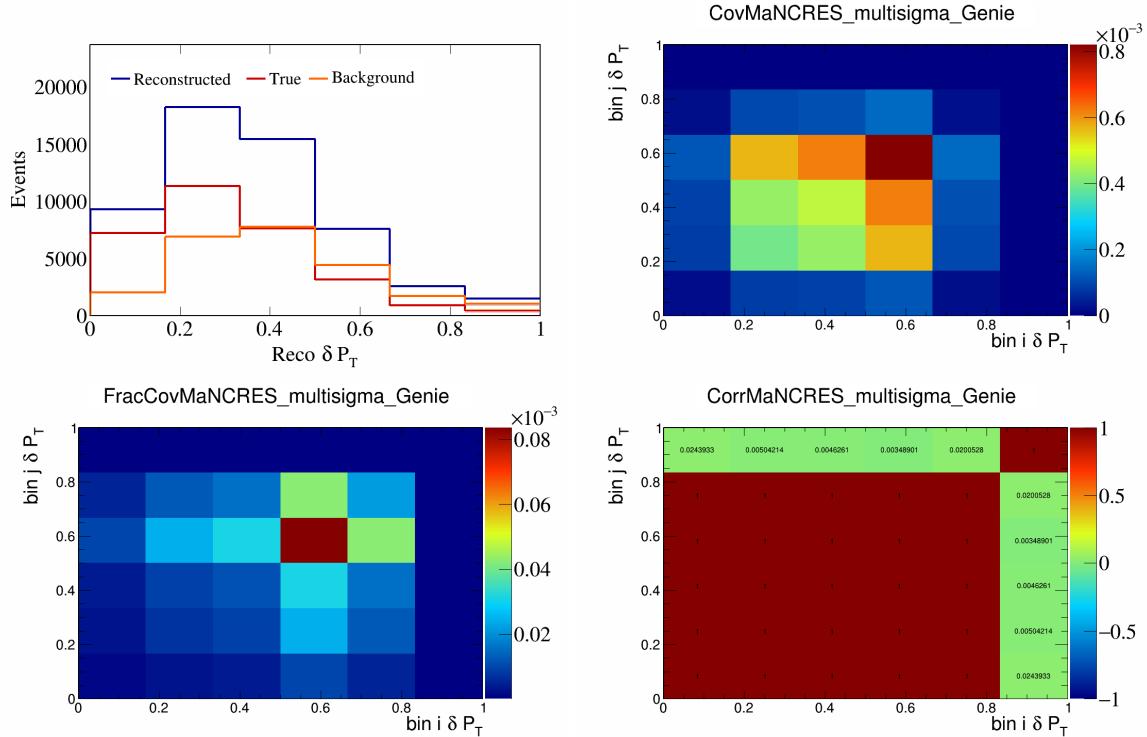


Figure 322: MaNCRES variations for δP_T .

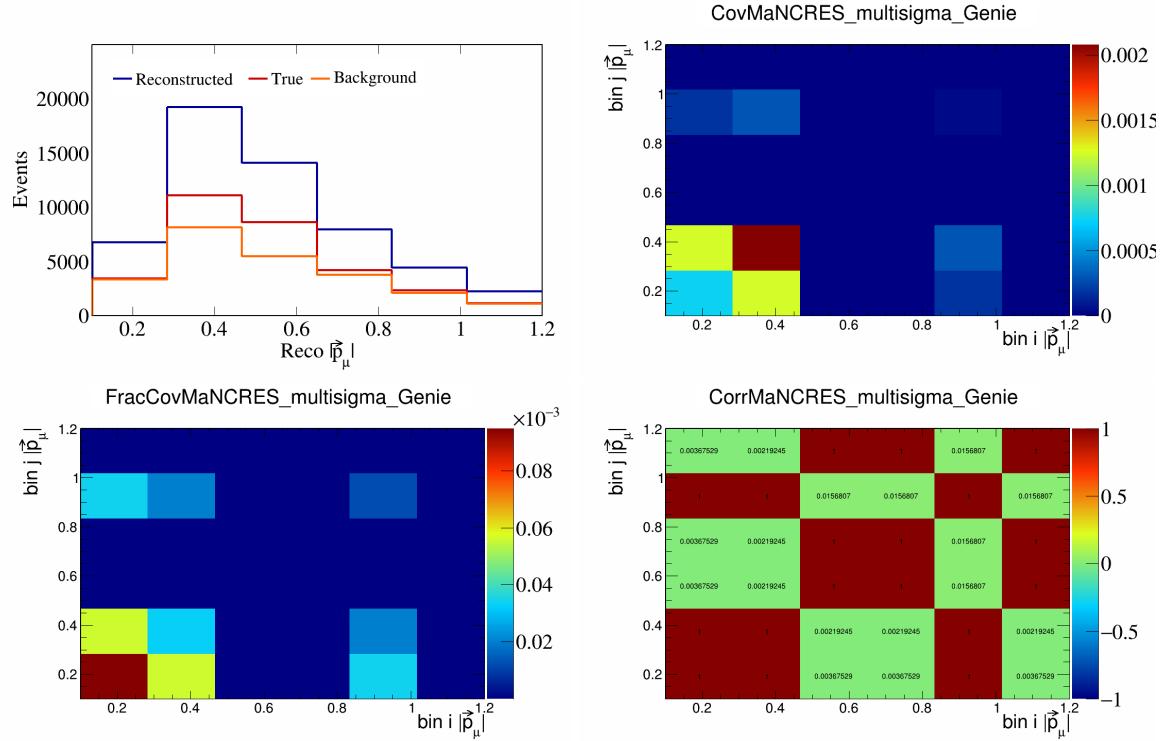


Figure 323: MaNCRES variations for $|\vec{p}_\mu|$.

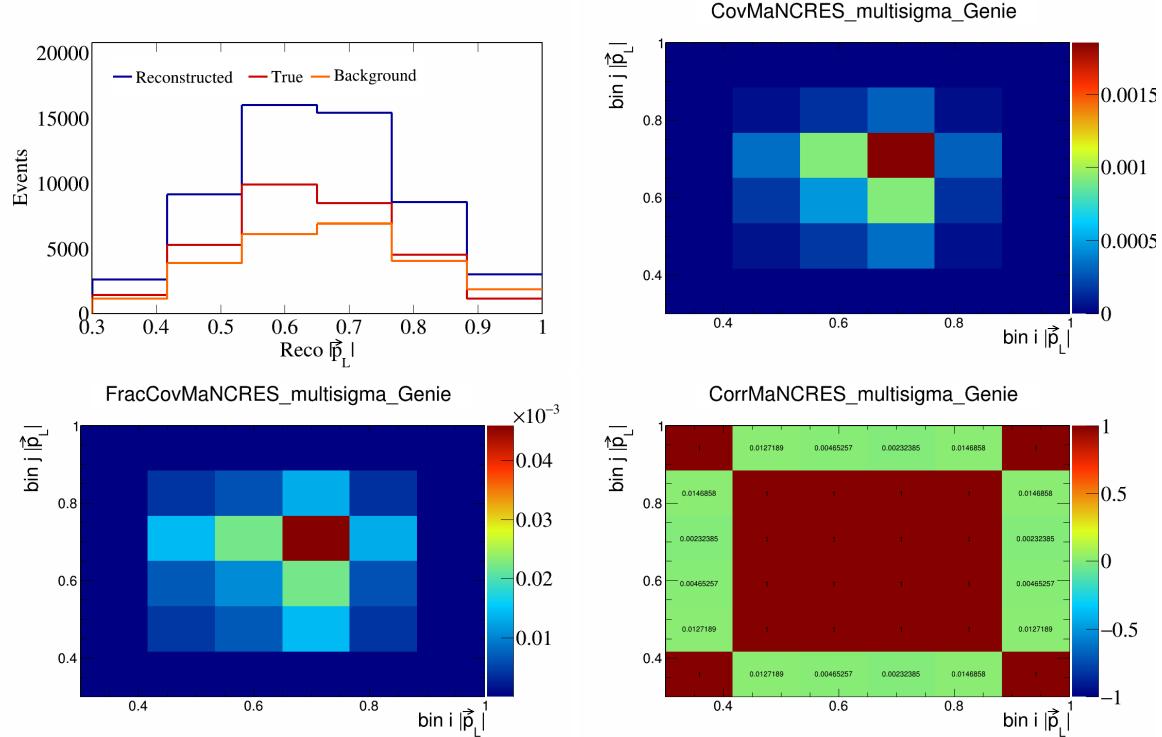


Figure 324: MaNCRES variations for $|\vec{p}_L|$.

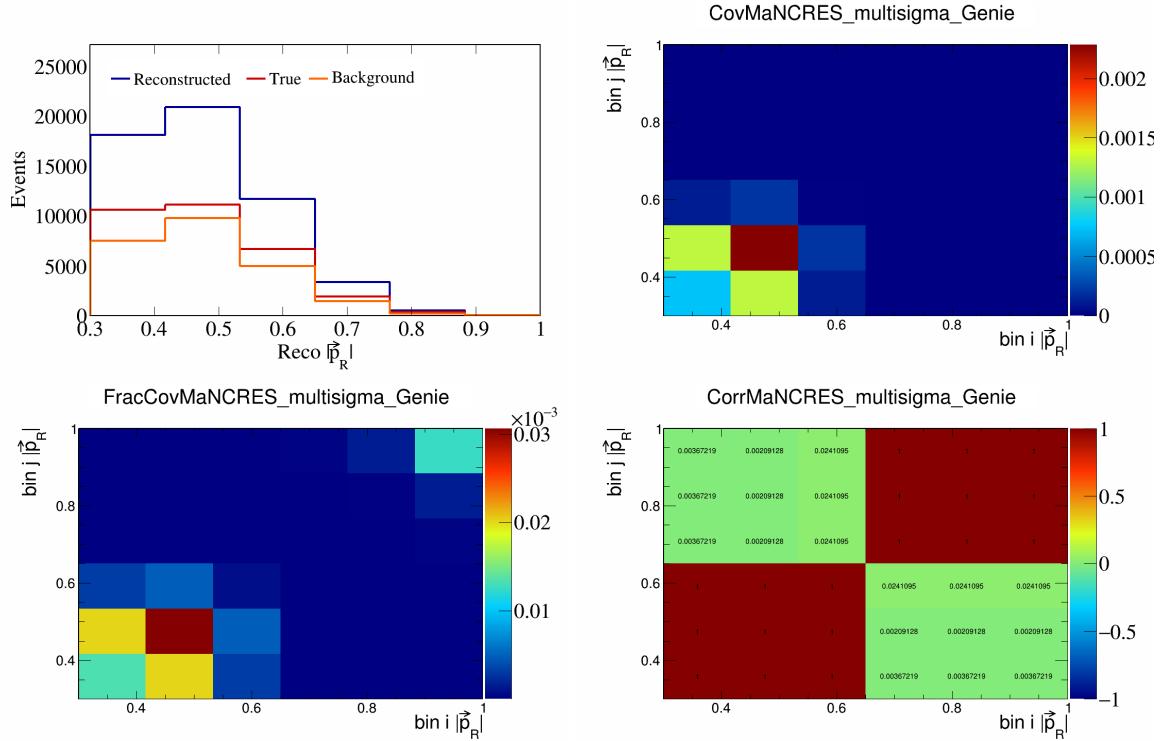


Figure 325: MaNCRES variations for $|\vec{p}_R|$.

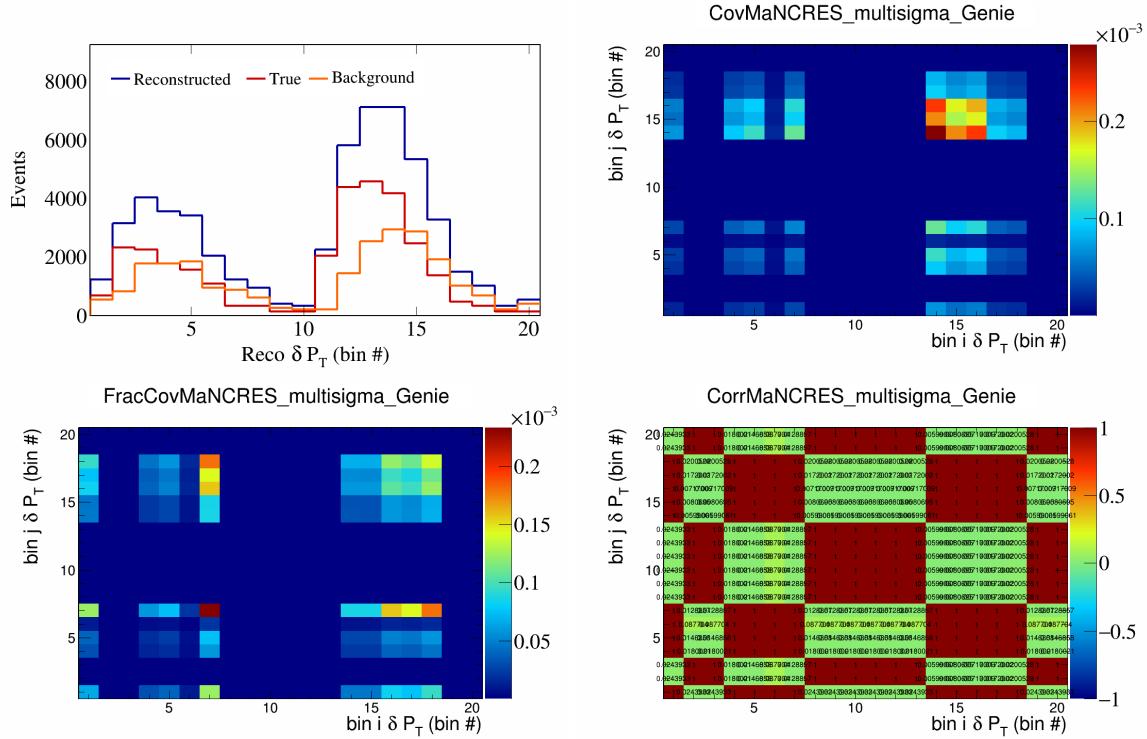


Figure 326: MaNCRES variations for δP_T in $\cos(\theta_{\vec{p}_\mu})$.

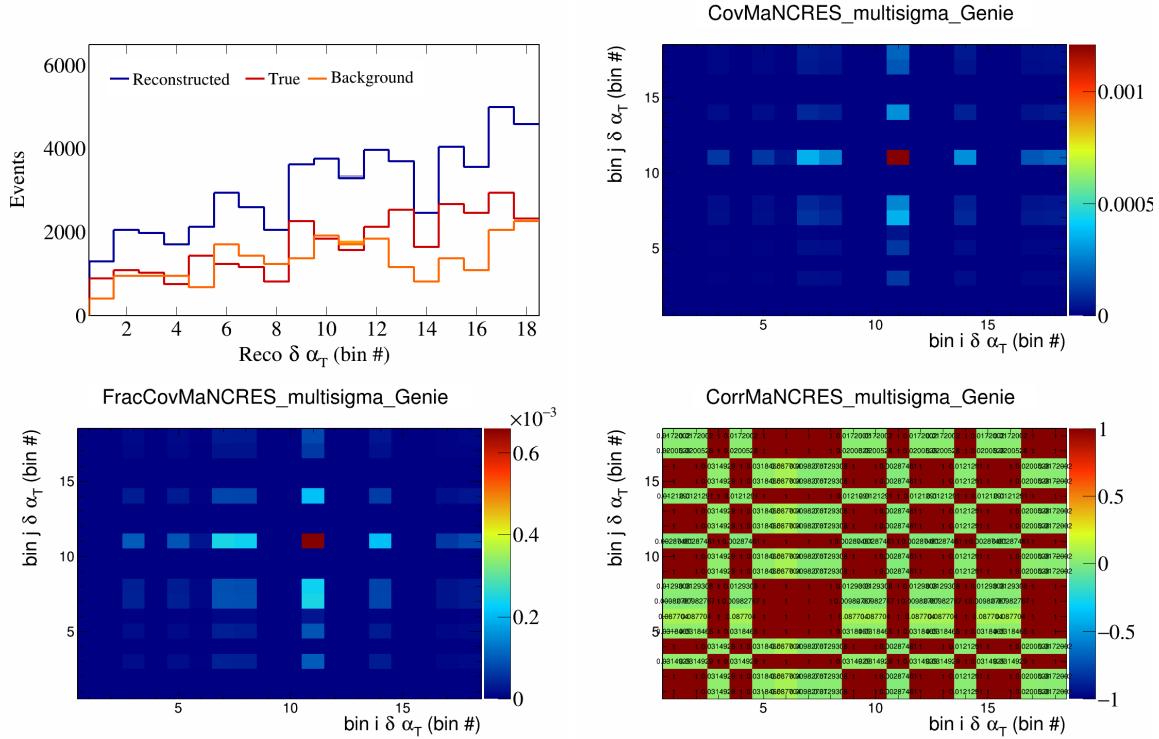


Figure 327: MaNCRES variations for $\delta \alpha_T$ in $\cos(\theta_{\vec{p}_\mu})$.

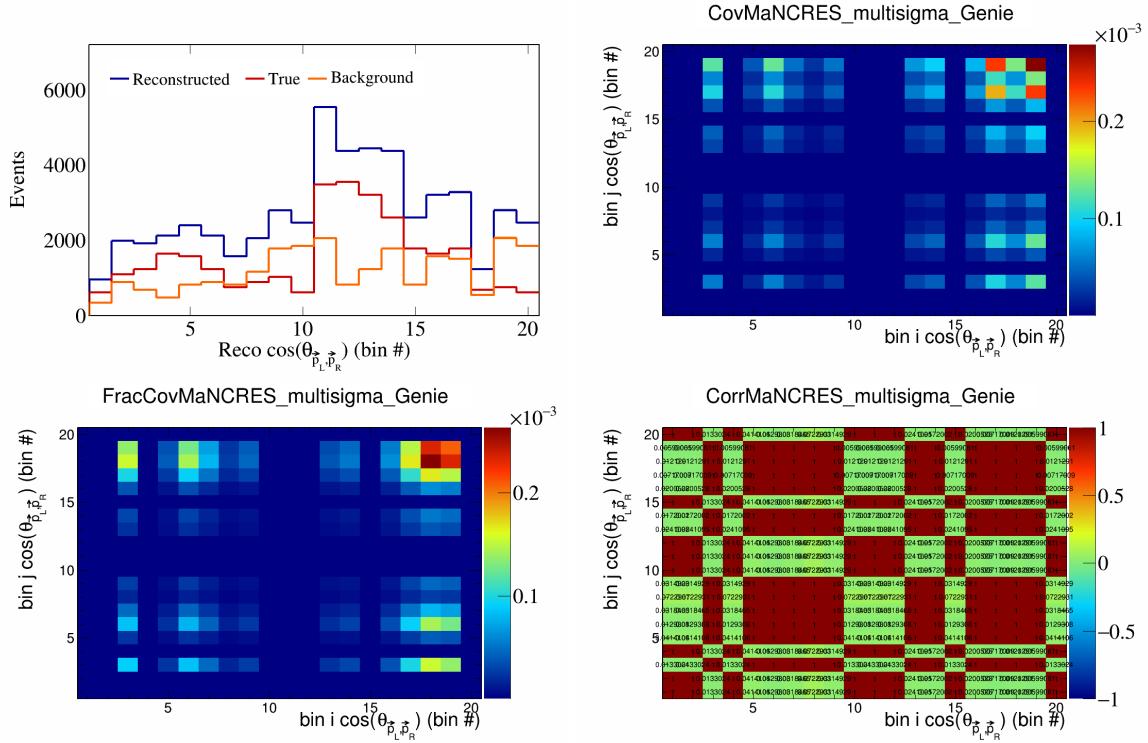


Figure 328: MaNCRES variations for $\cos(\theta_{\vec{p}_L, \vec{p}_R})$ in $\cos(\theta_{\vec{p}_\mu})$.

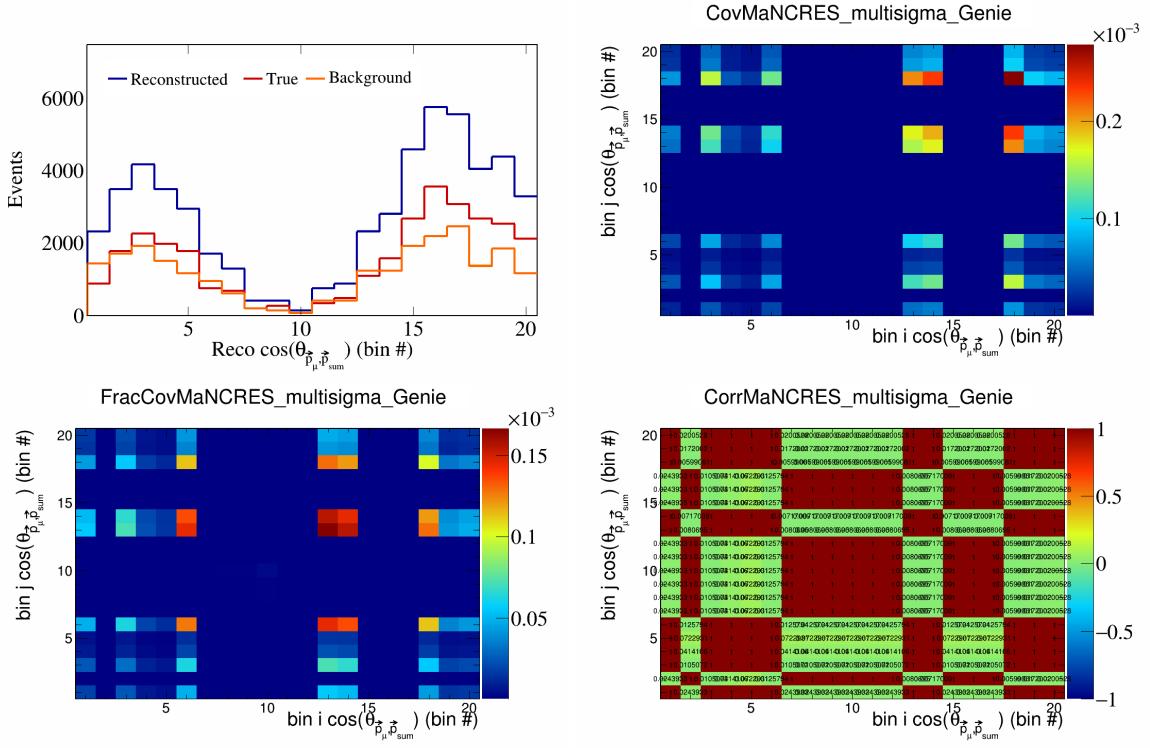


Figure 329: MaNCRES variations for $\cos(\theta_{\vec{p}_\mu, \vec{p}_{\text{sum}}})$ in $\cos(\theta_{\vec{p}_\mu})$.

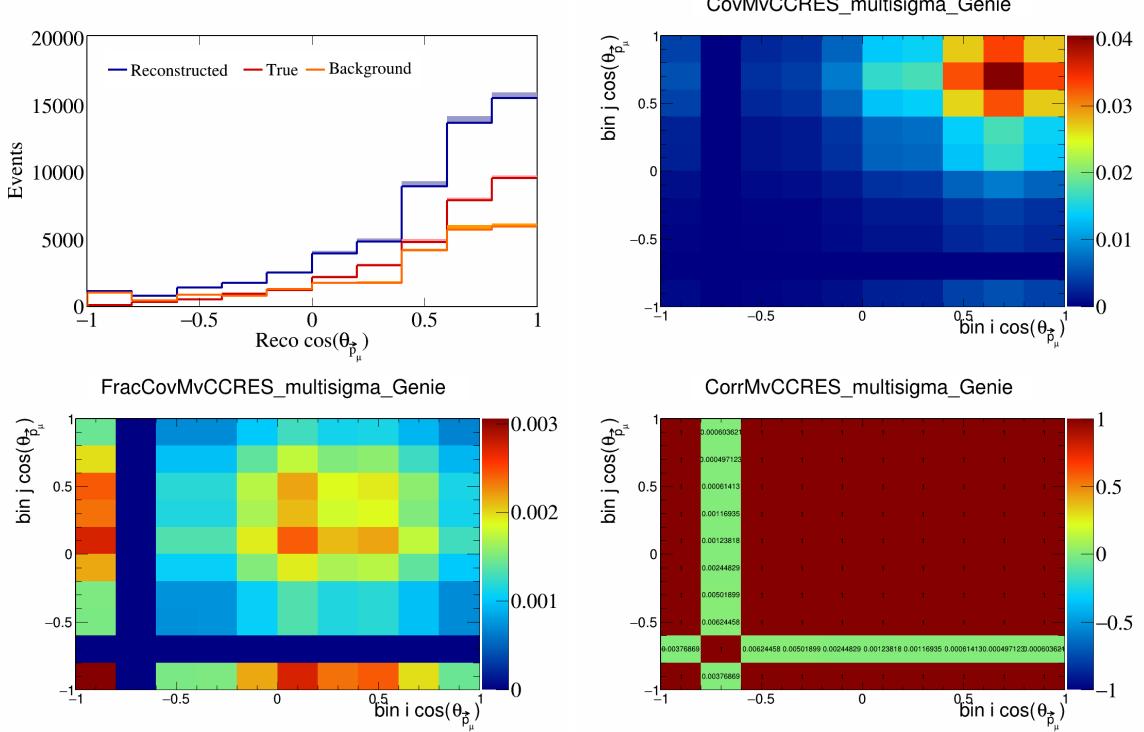


Figure 330: MvCCRES variations for $\cos(\theta_{\vec{p}_\mu})$.

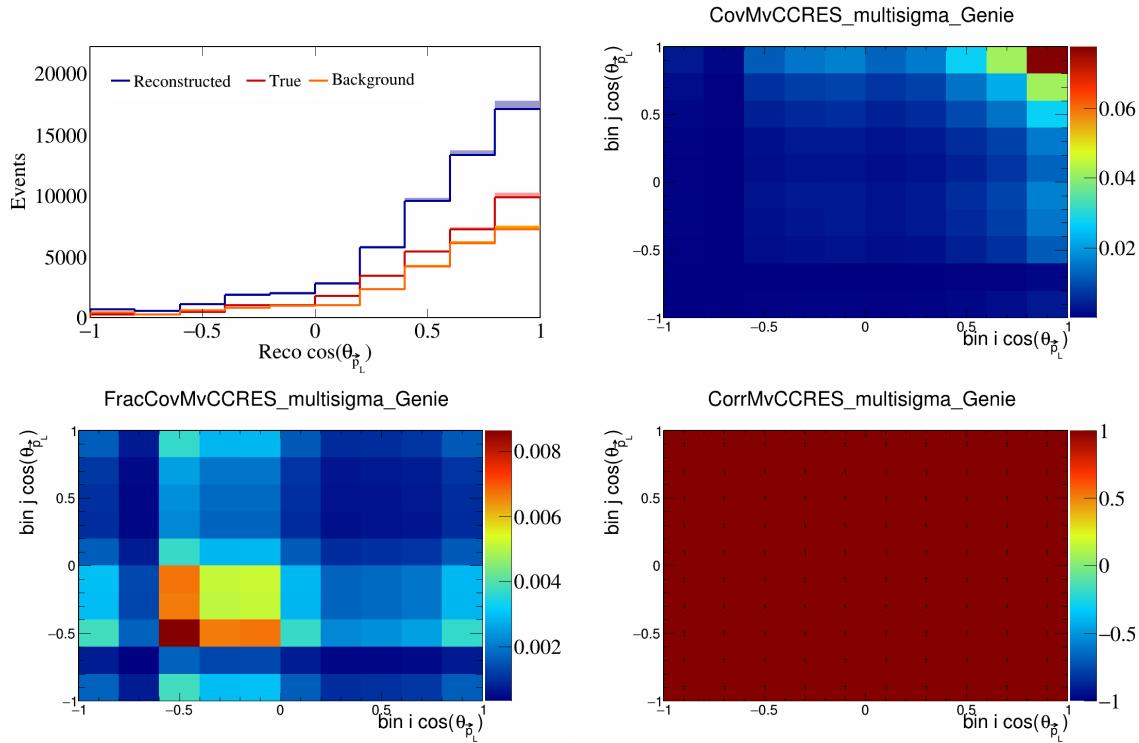


Figure 331: MvCCRES variations for $\cos(\theta_{\vec{p}_L})$.

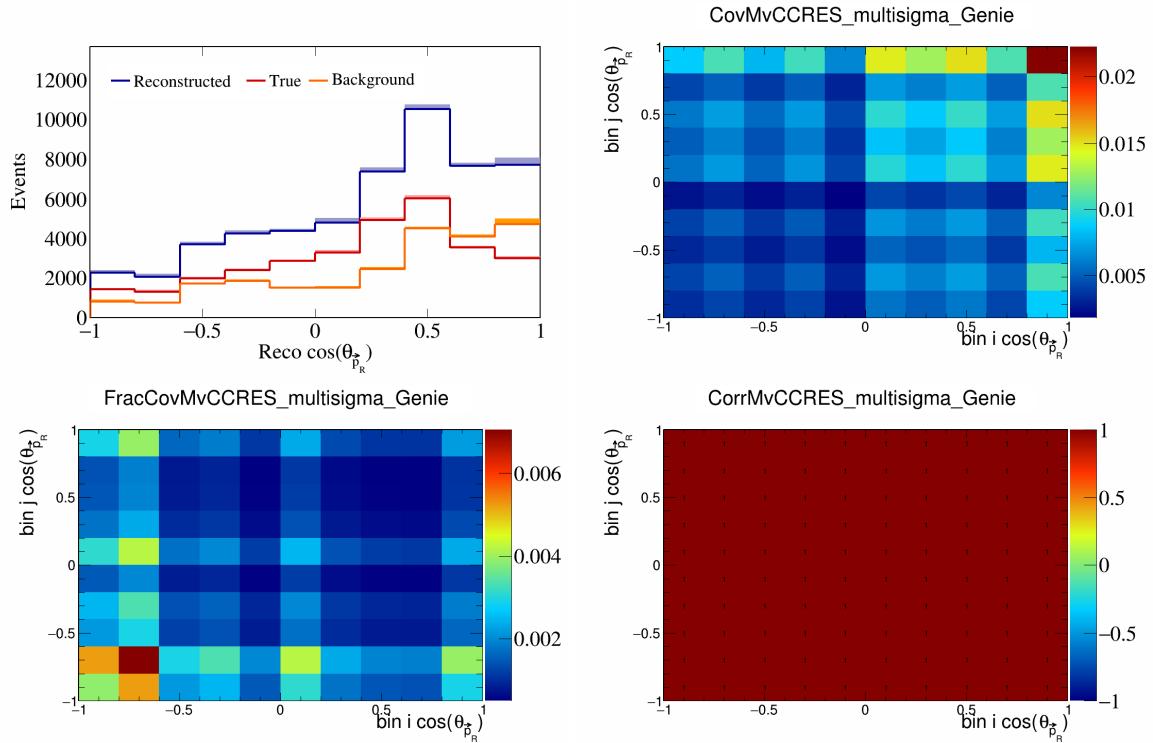


Figure 332: MvCCRES variations for $\cos(\theta_{\vec{p}_R})$.

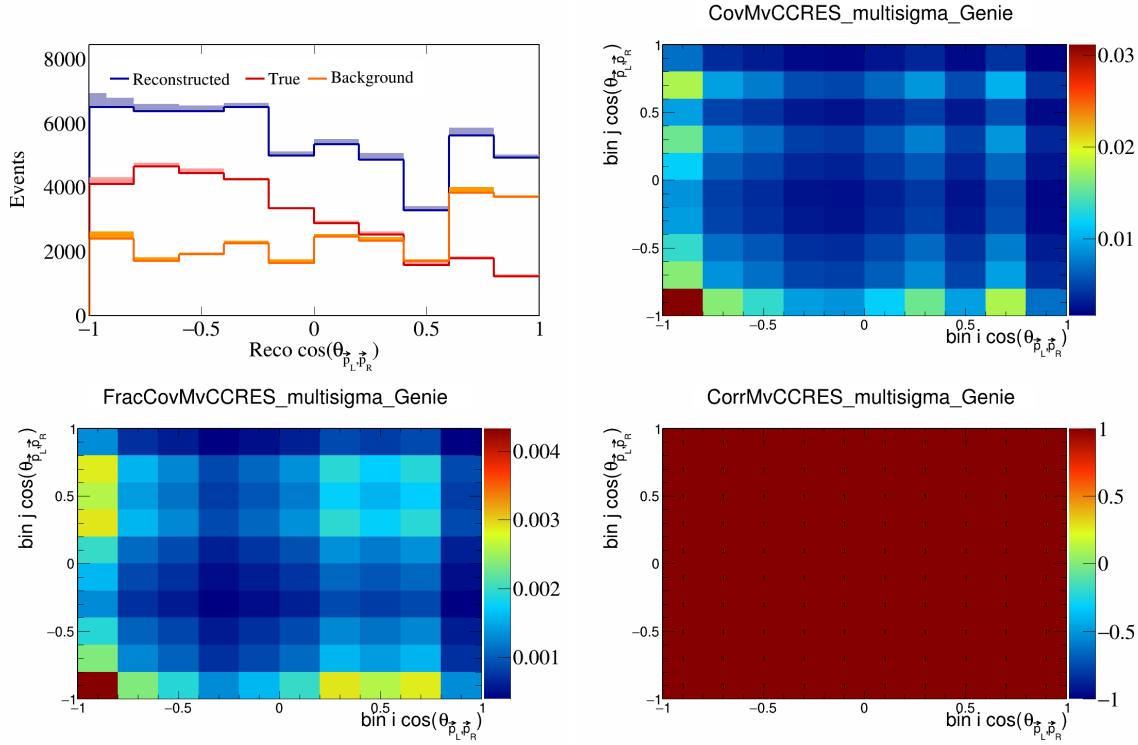


Figure 333: MvCCRES variations for $\cos(\theta_{\vec{p}_L, \vec{p}_R})$.

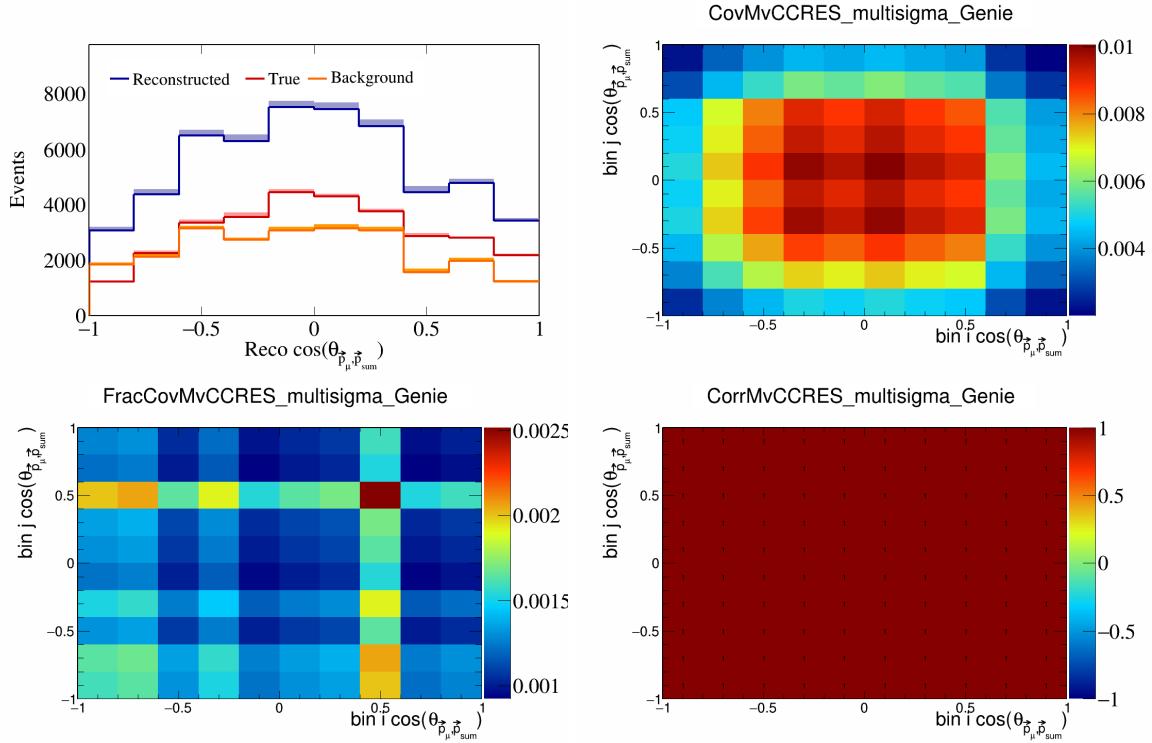


Figure 334: MvCCRES variations for $\cos(\theta_{\vec{p}_\mu, \vec{p}_{\text{sum}}})$.

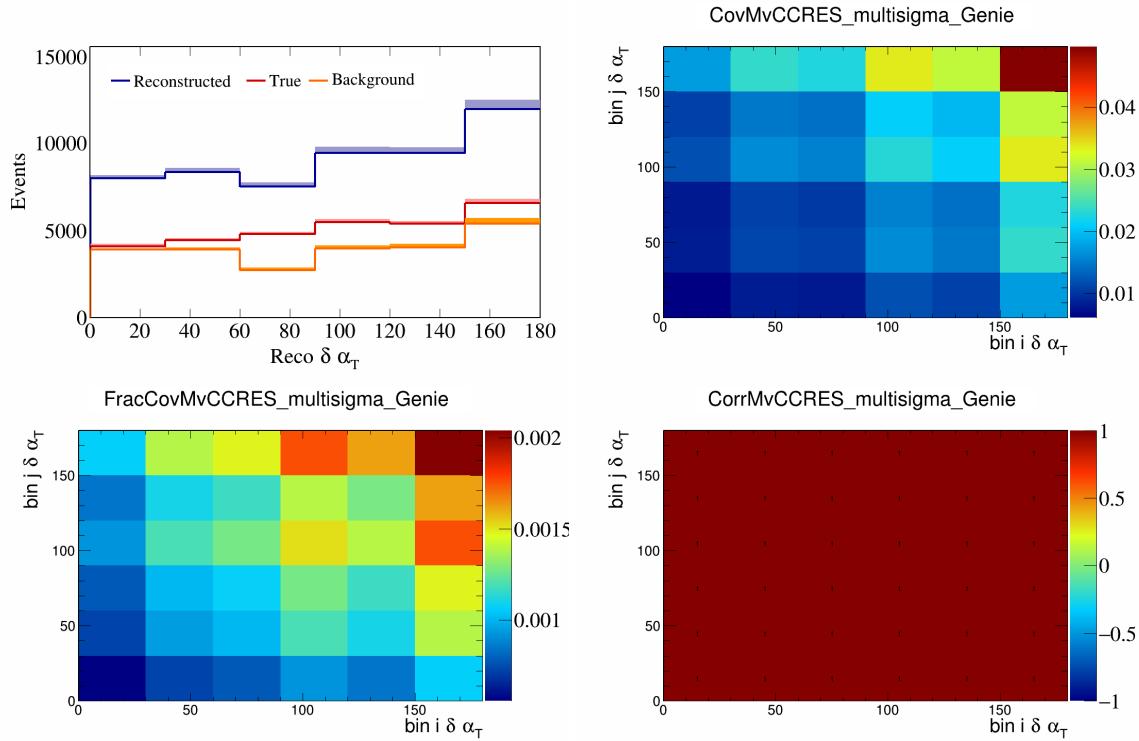


Figure 335: MvCCRES variations for $\delta\alpha_T$.

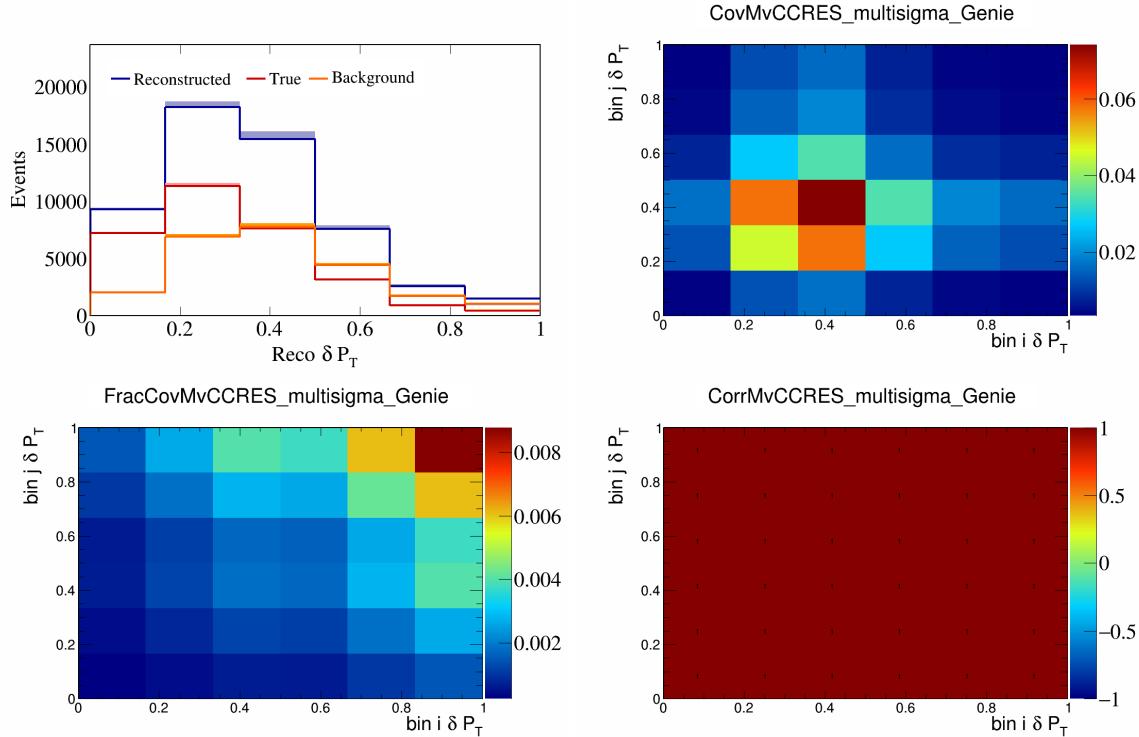


Figure 336: MvCCRES variations for δP_T .

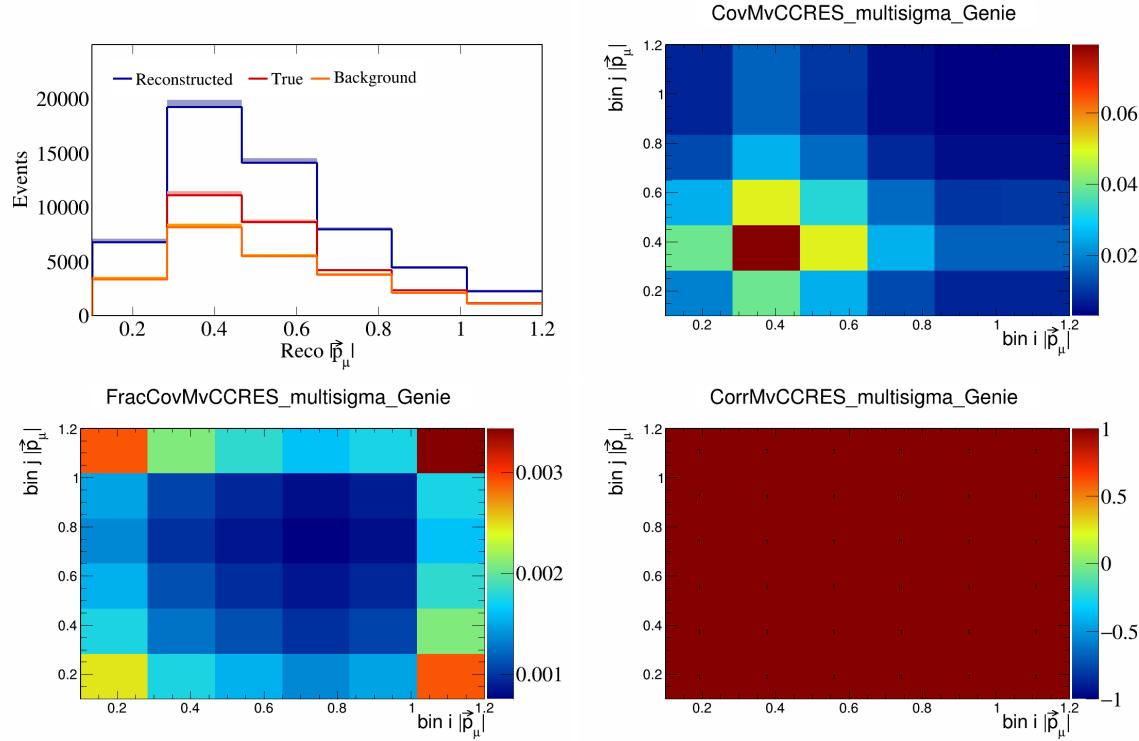


Figure 337: MvCCRES variations for $|\vec{p}_\mu|$.

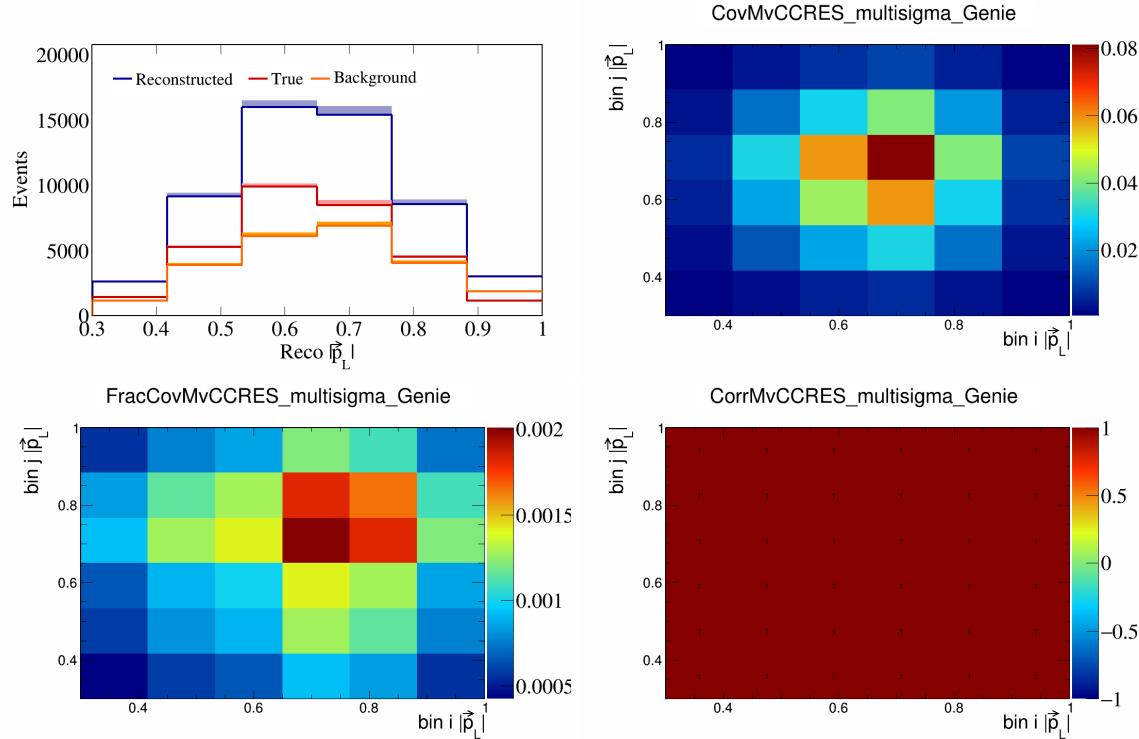


Figure 338: MvCCRES variations for $|\vec{p}_L|$.

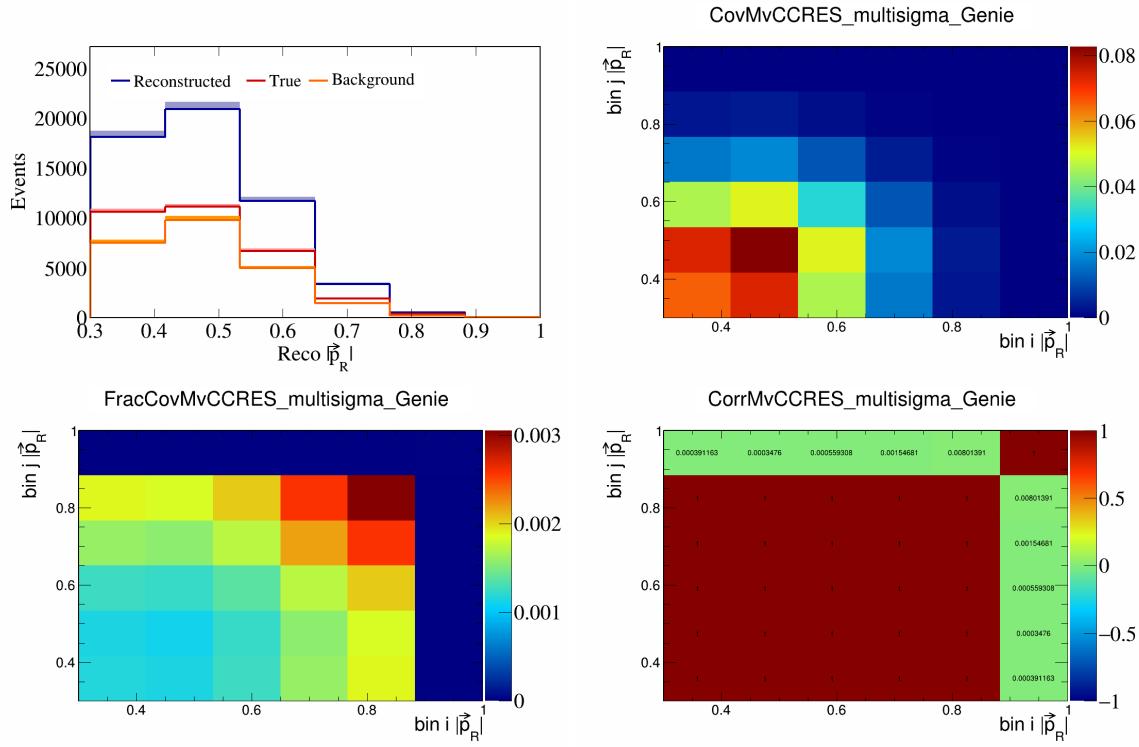


Figure 339: MvCCRES variations for $|\vec{p}_R|$.

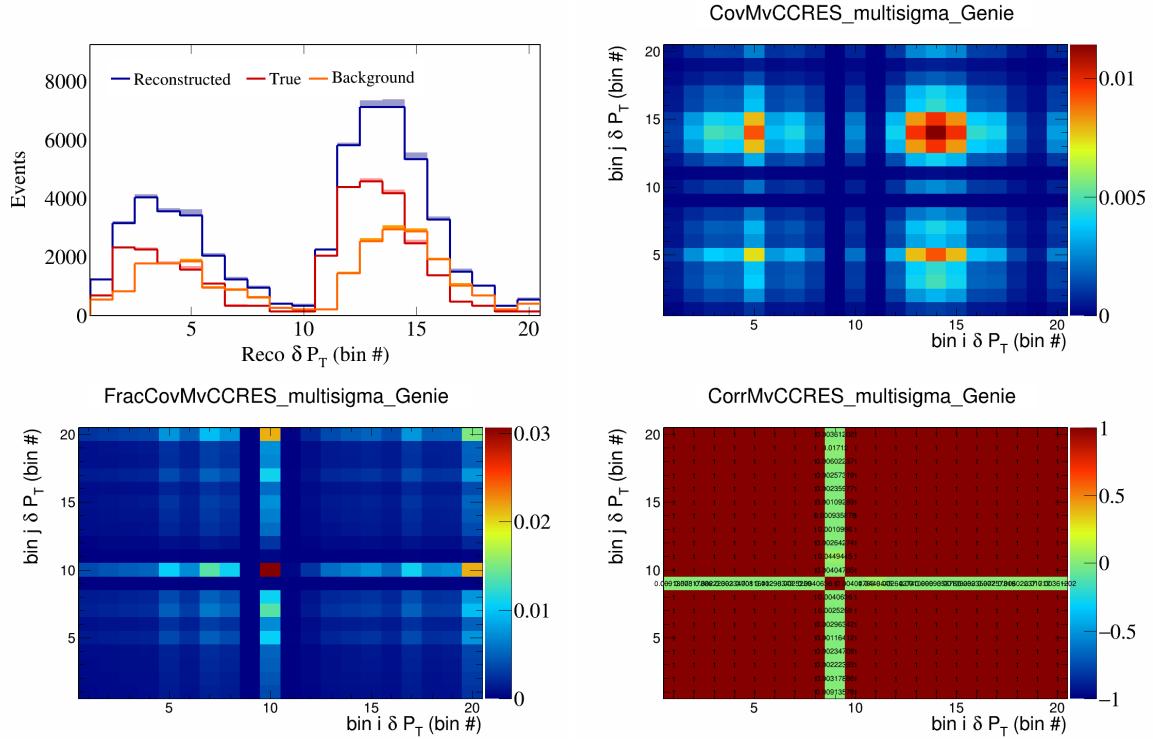


Figure 340: MvCCRES variations for δP_T in $\cos(\theta_{\vec{p}_\mu})$.

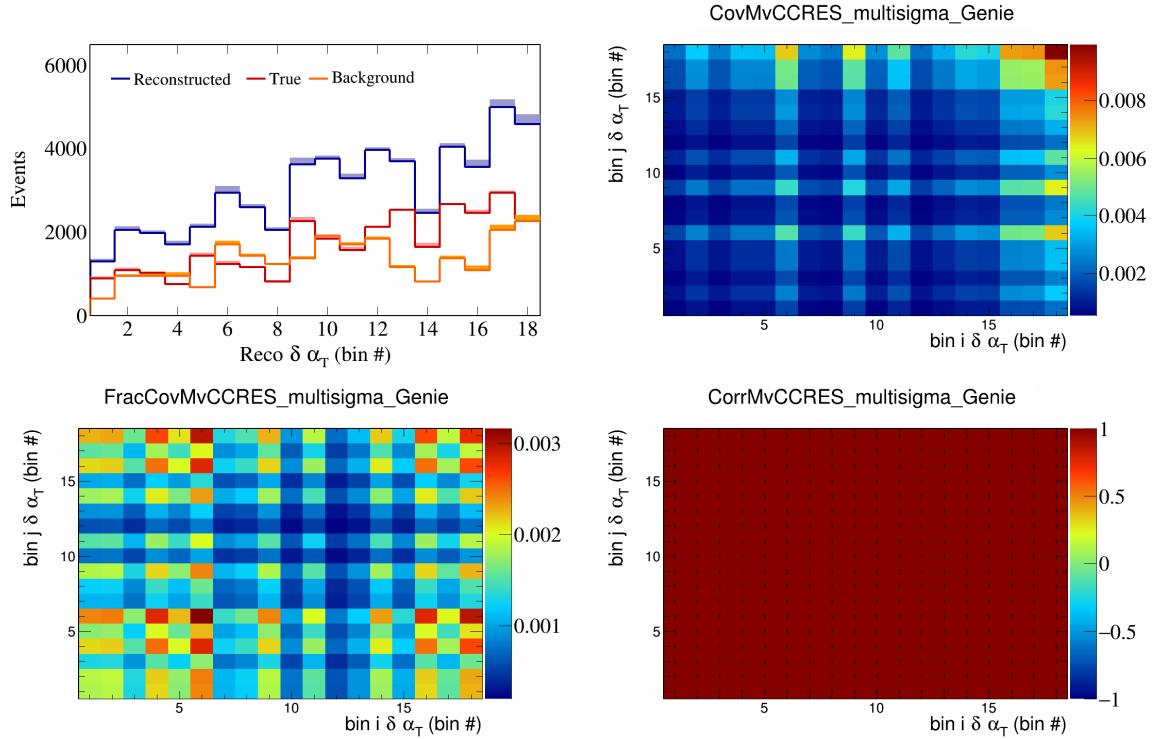


Figure 341: MvCCRES variations for $\delta\alpha_T$ in $\cos(\theta_{\vec{p}_\mu})$.

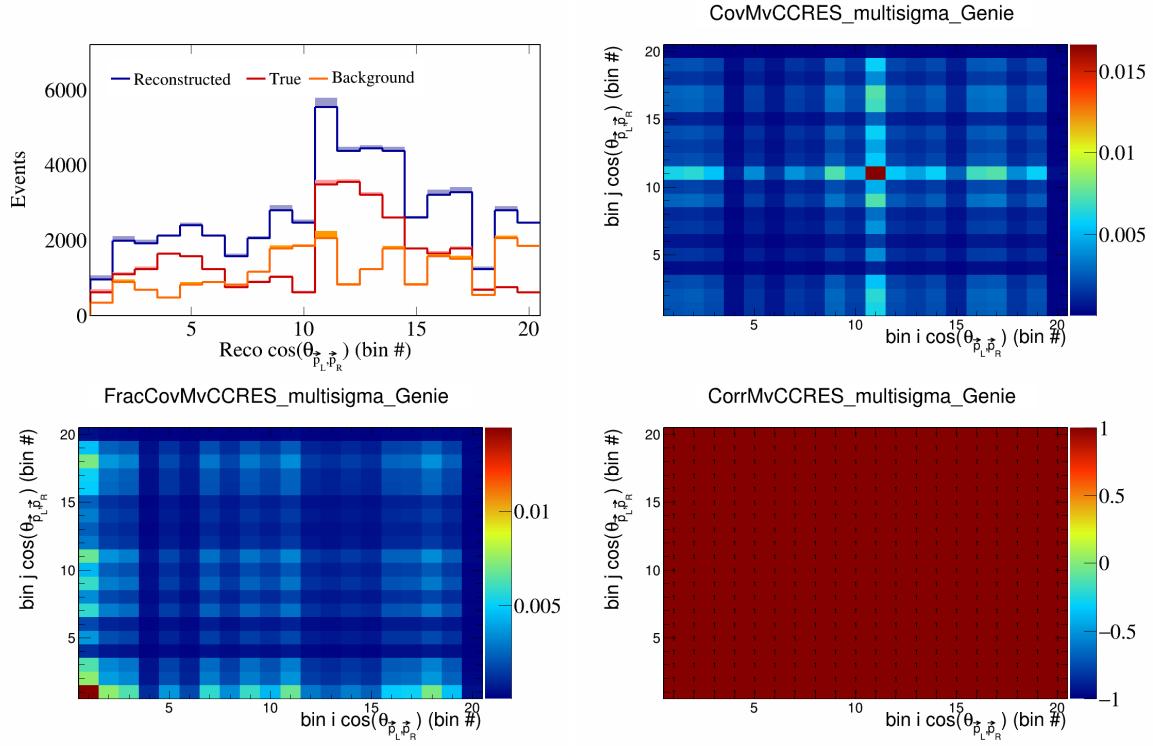


Figure 342: MvCCRES variations for $\cos(\theta_{\vec{p}_L, \vec{p}_R})$ in $\cos(\theta_{\vec{p}_\mu})$.

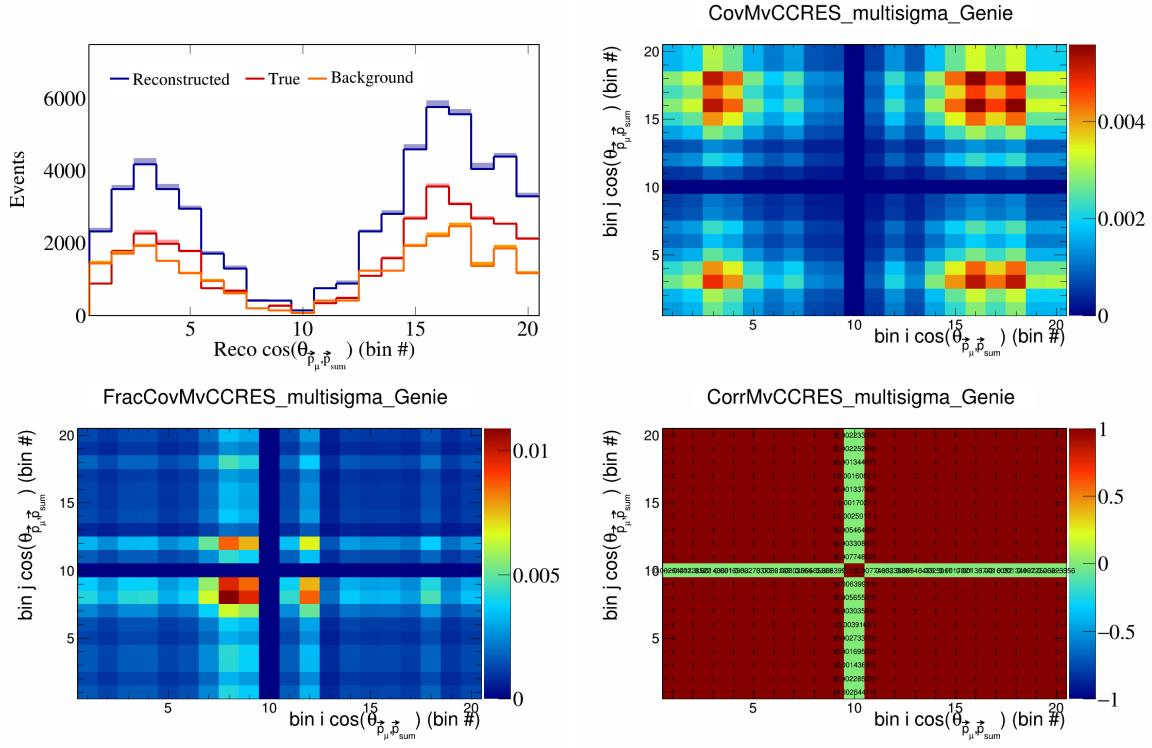


Figure 343: MvCCRES variations for $\cos(\theta_{\vec{p}_\mu, \vec{p}_{\text{sum}}})$ in $\cos(\theta_{\vec{p}_\mu})$.

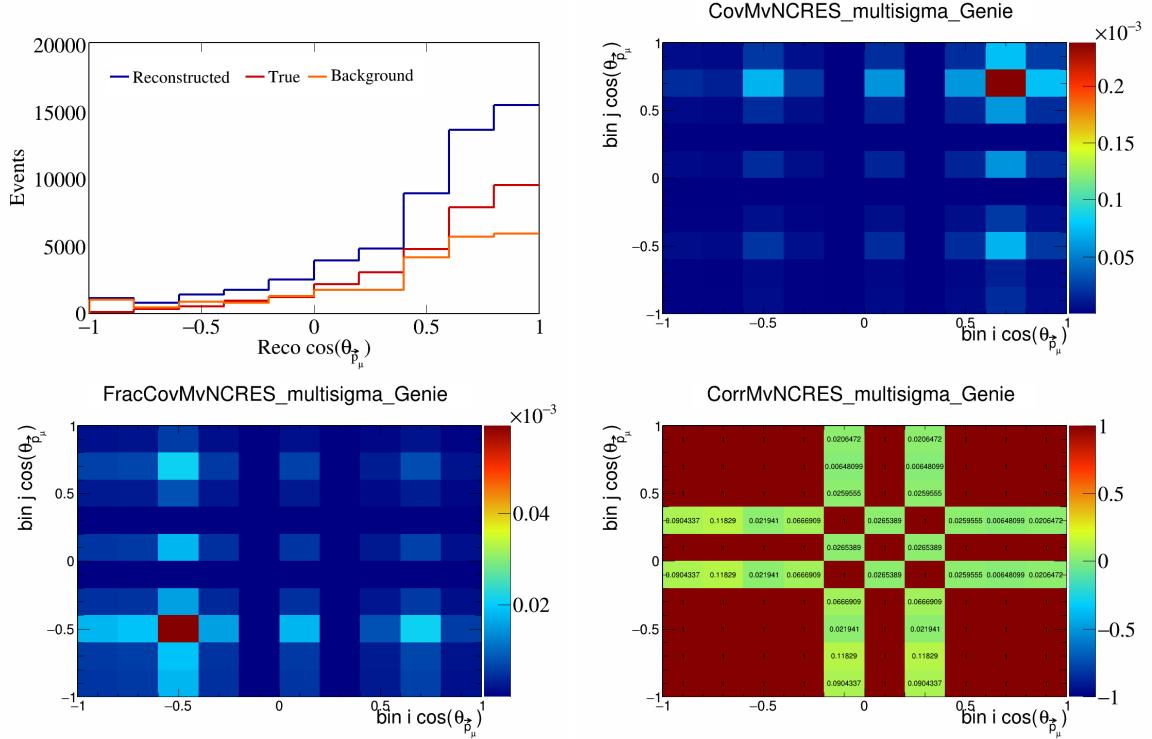


Figure 344: MvNCRES variations for $\cos(\theta_{\vec{p}_\mu})$.

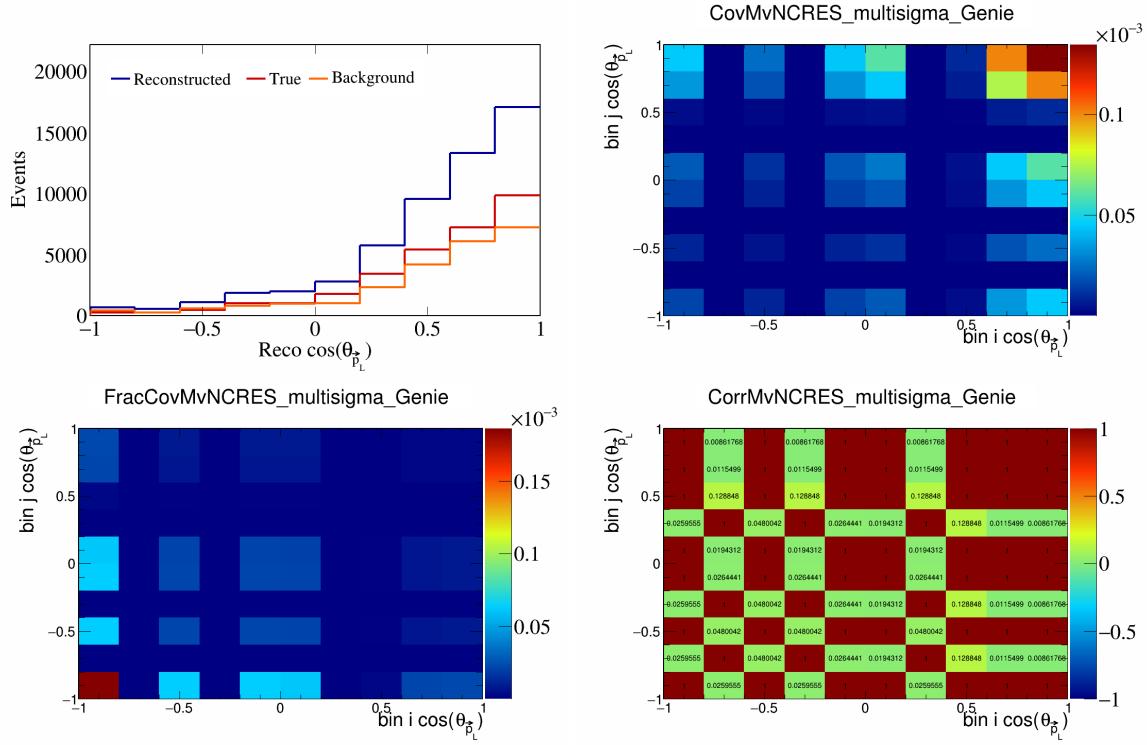


Figure 345: MvNCRES variations for $\cos(\theta_{\vec{p}_L})$.

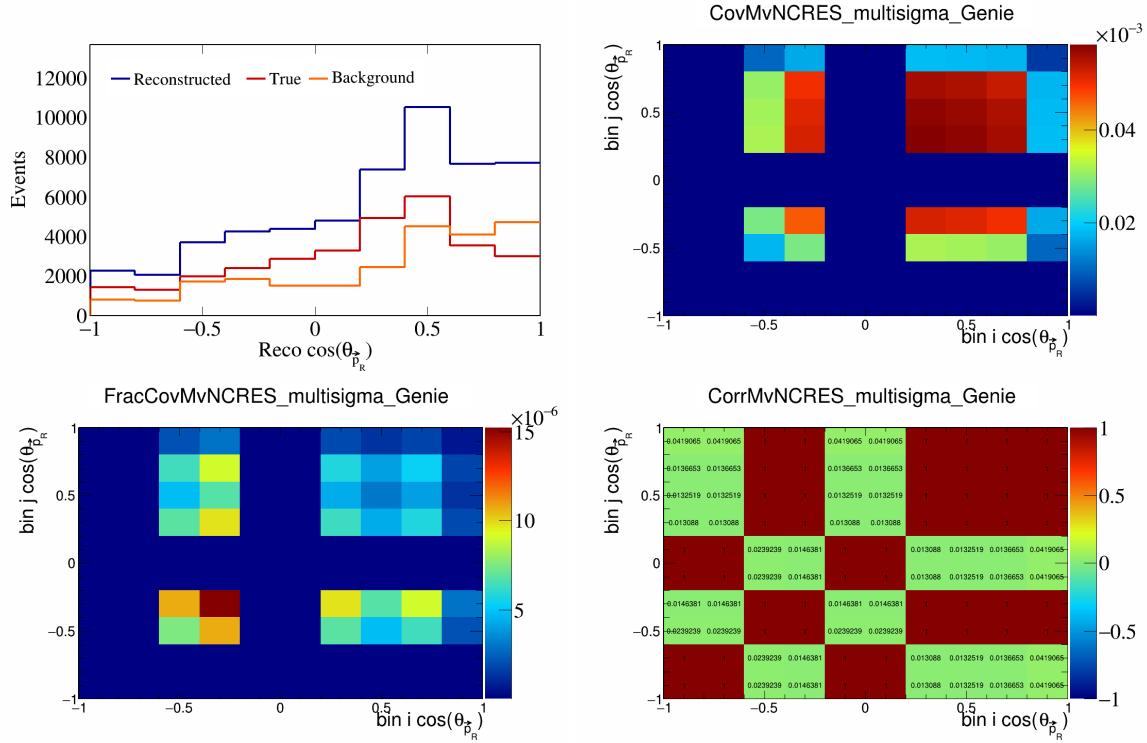


Figure 346: MvNCRES variations for $\cos(\theta_{\vec{p}_R})$.

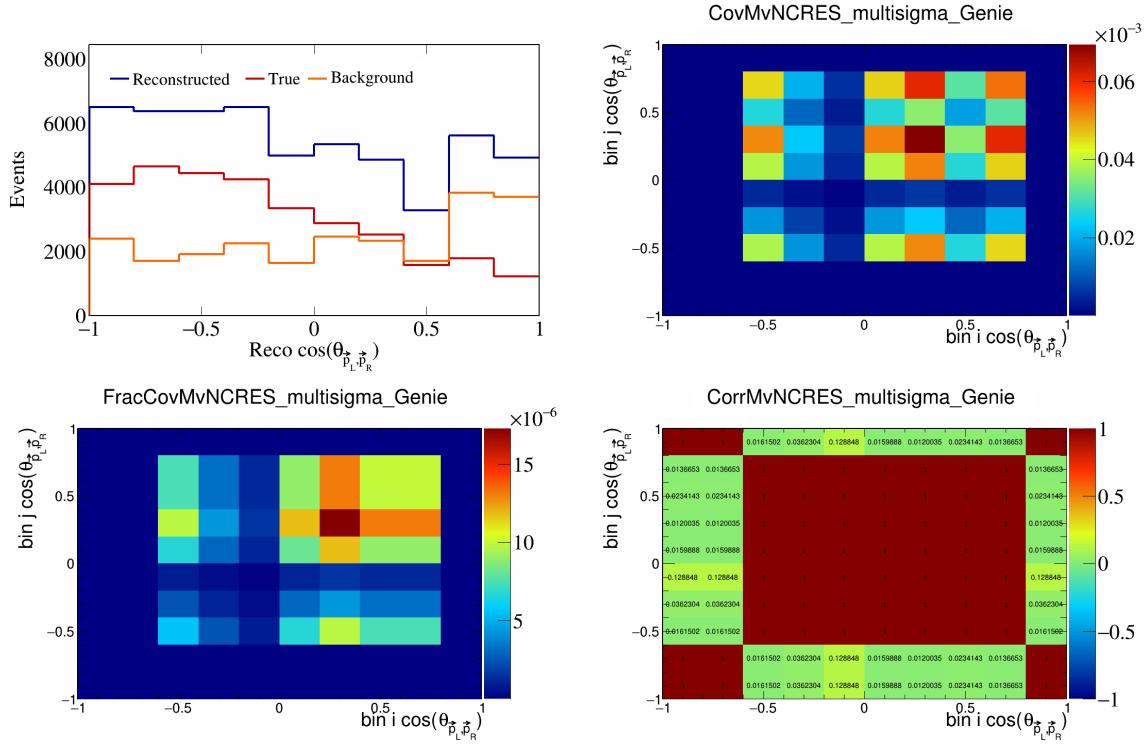


Figure 347: MvNCRES variations for $\cos(\theta_{\vec{p}_L, \vec{p}_R})$.

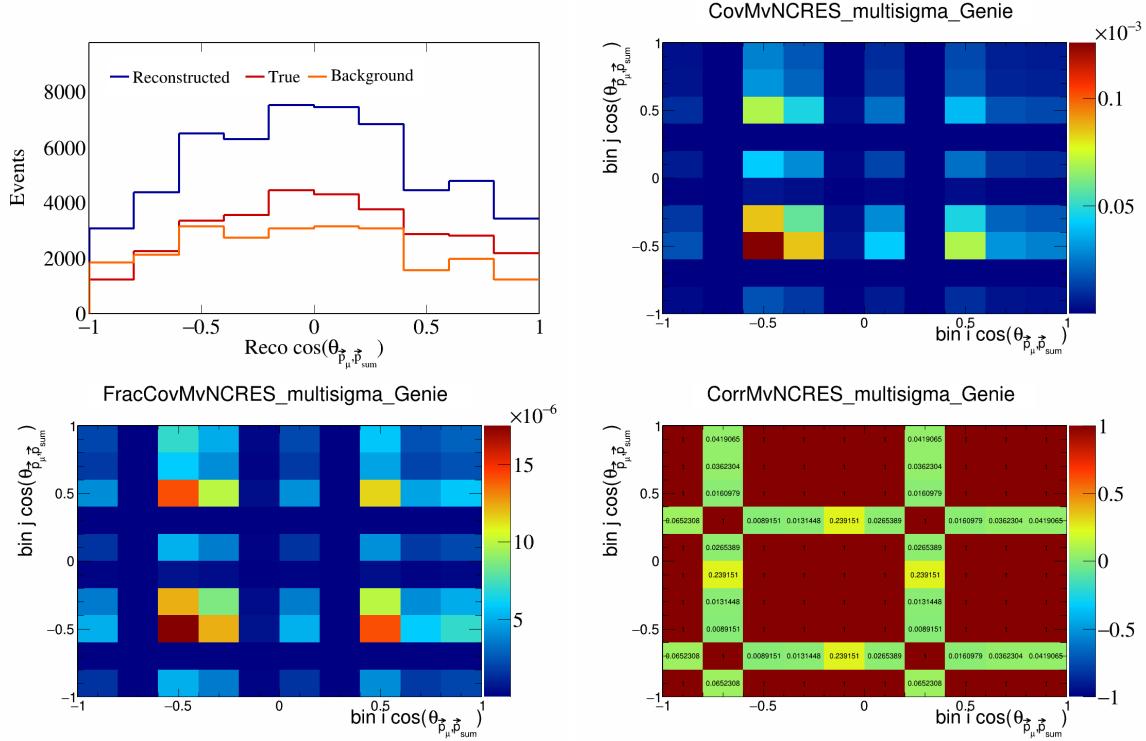


Figure 348: MvNCRES variations for $\cos(\theta_{\vec{p}_\mu, \vec{p}_{\text{sum}}})$.

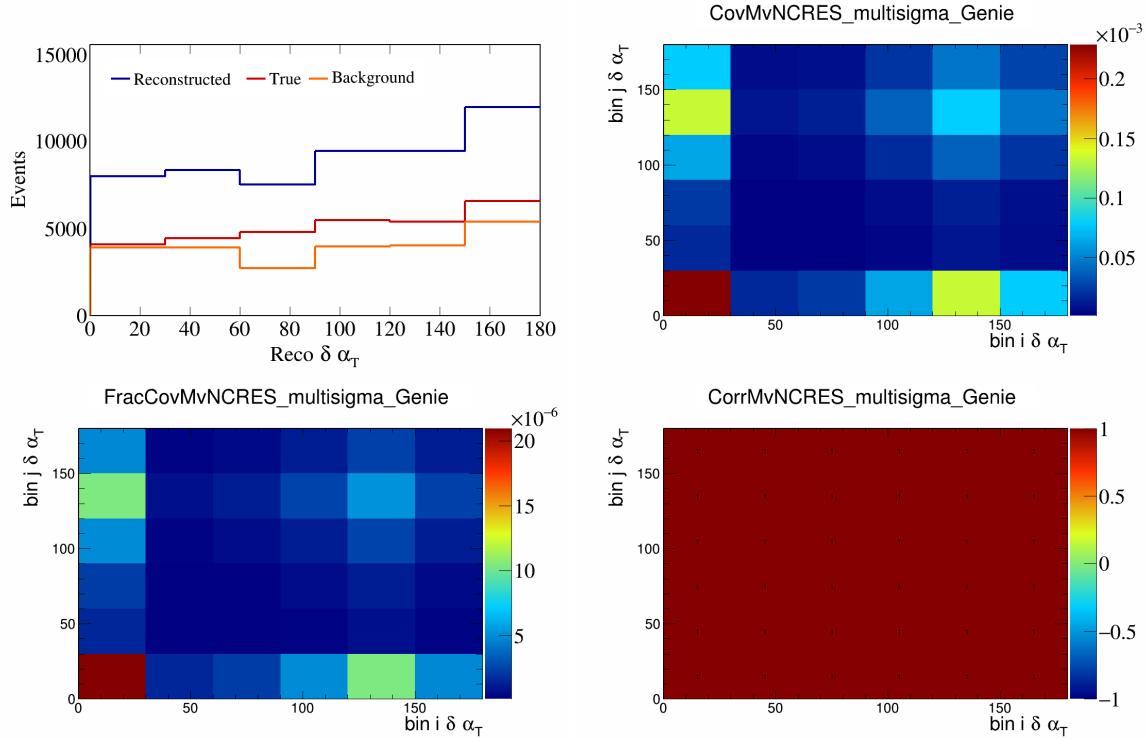


Figure 349: MvNCRES variations for $\delta\alpha_T$.

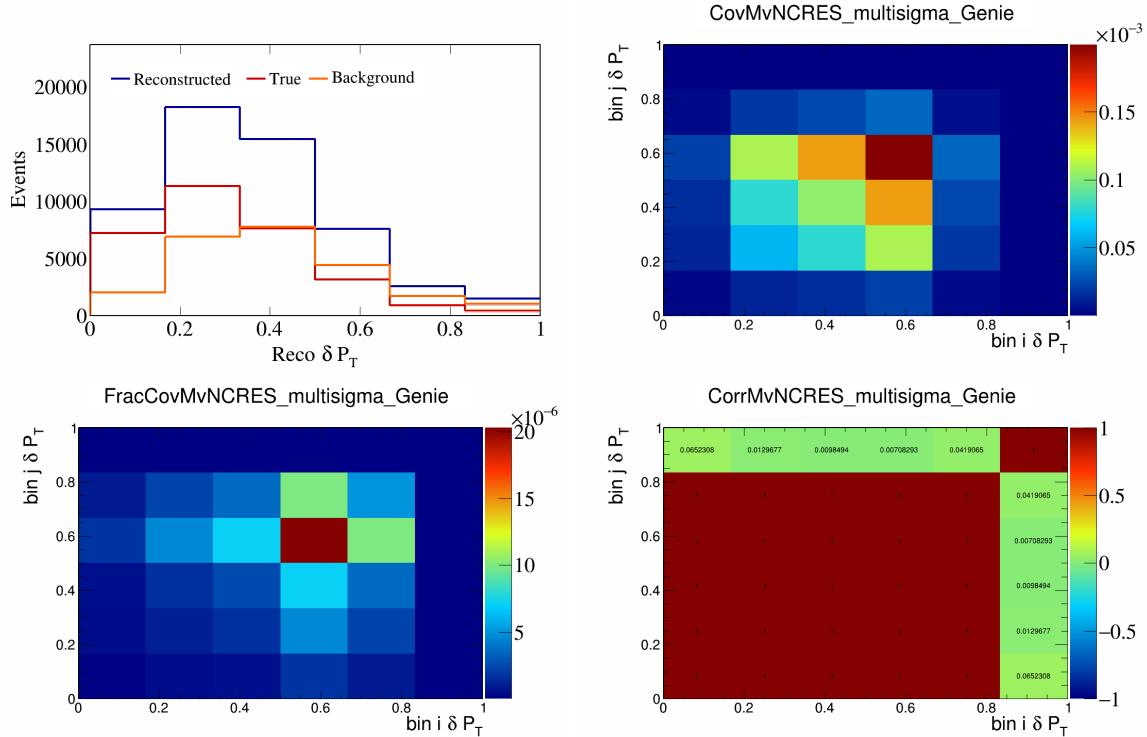


Figure 350: MvNCRES variations for δP_T .

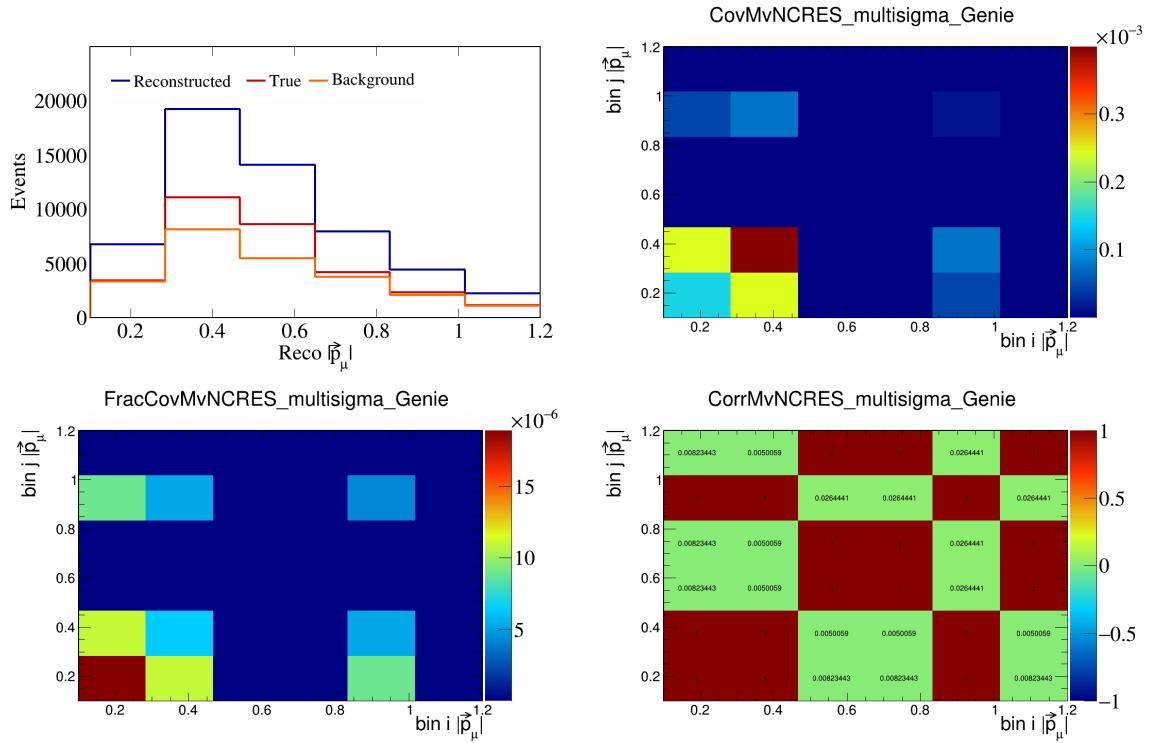


Figure 351: MvNCRES variations for $|\vec{p}_\mu|$.

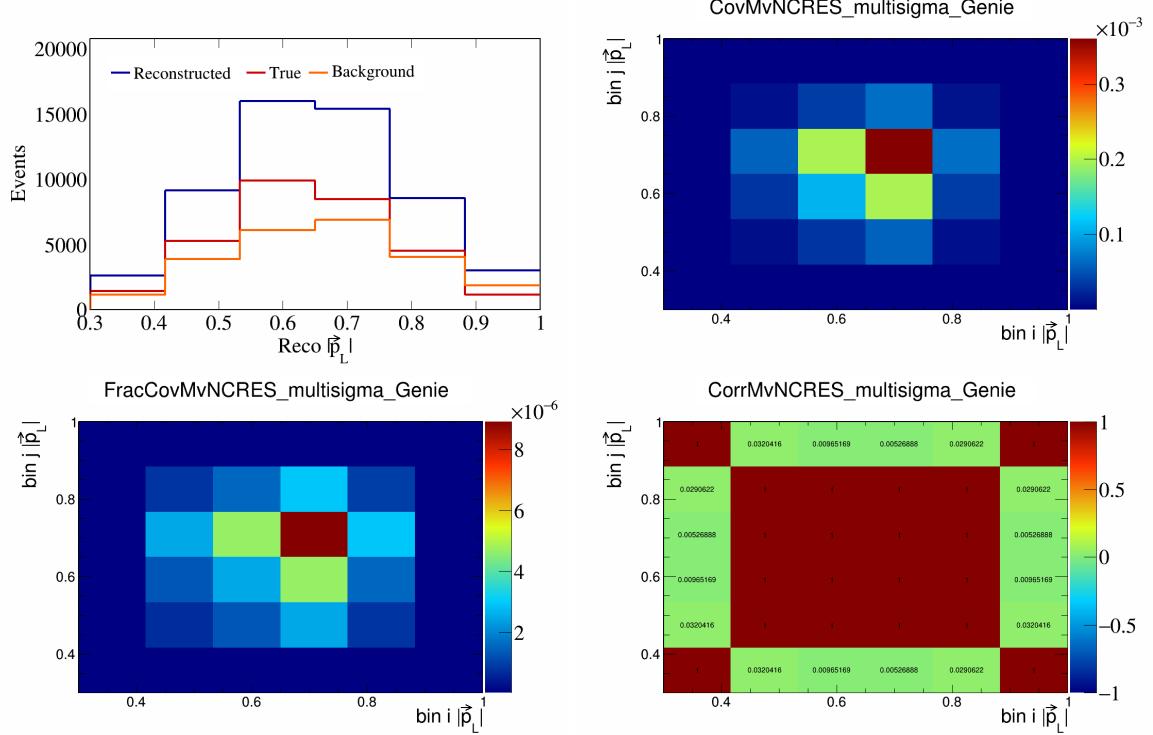


Figure 352: MvNCRES variations for $|\vec{p}_L|$.

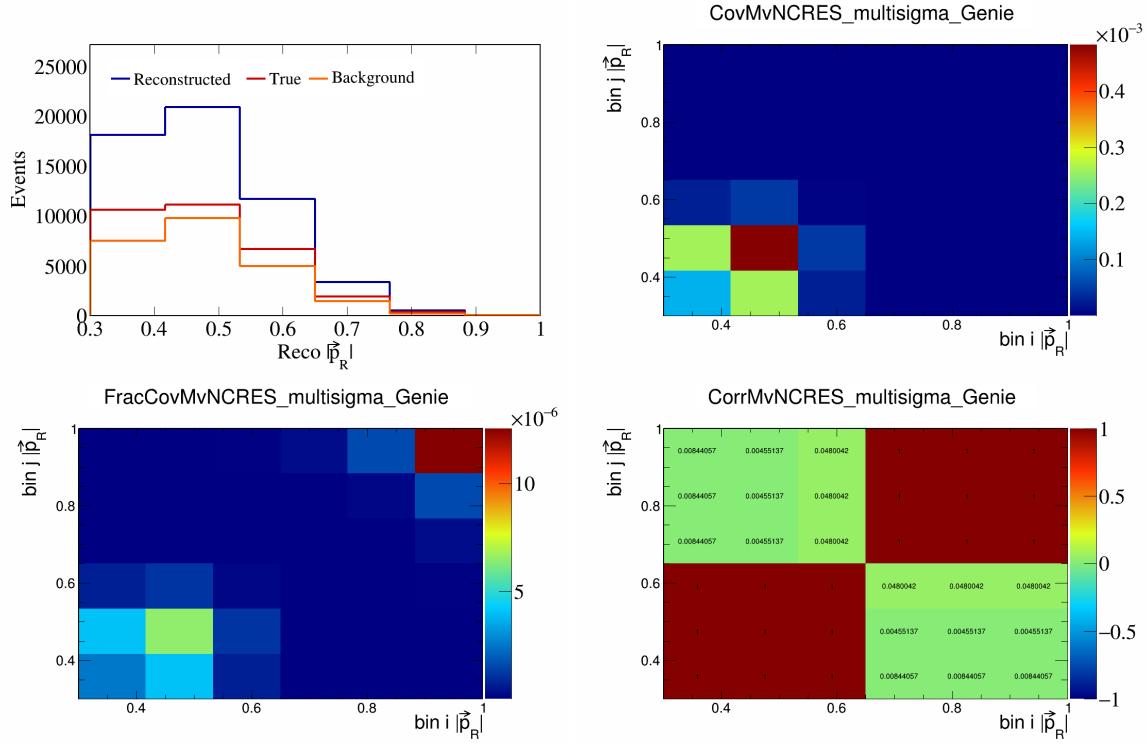


Figure 353: MvNCRES variations for $|\vec{p}_R|$.

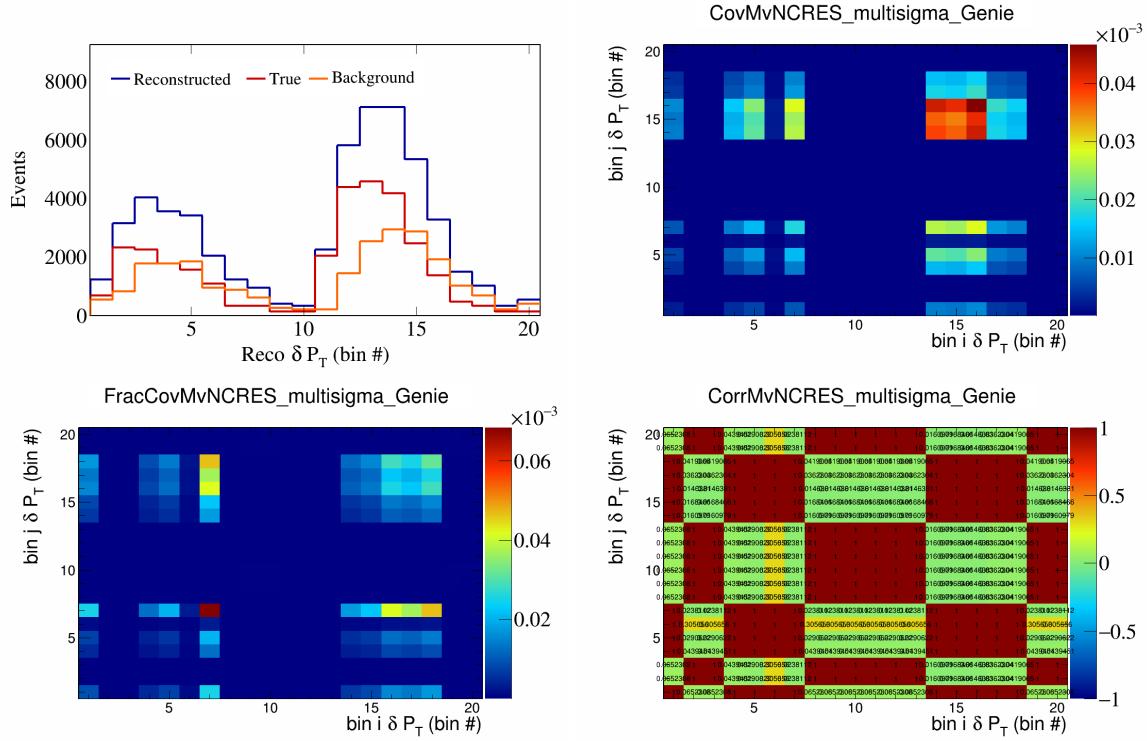


Figure 354: MvNCRES variations for δP_T in $\cos(\theta_{\vec{p}_\mu})$.

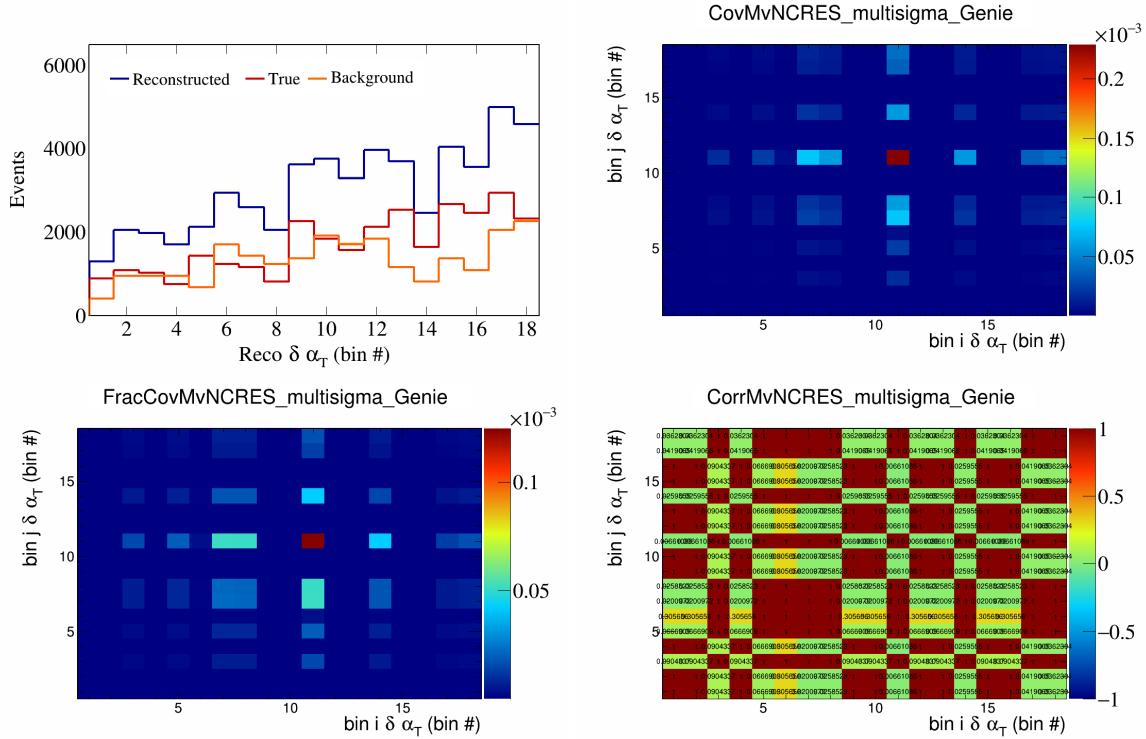


Figure 355: MvNCRES variations for $\delta\alpha_T$ in $\cos(\theta_{\vec{p}_\mu})$.

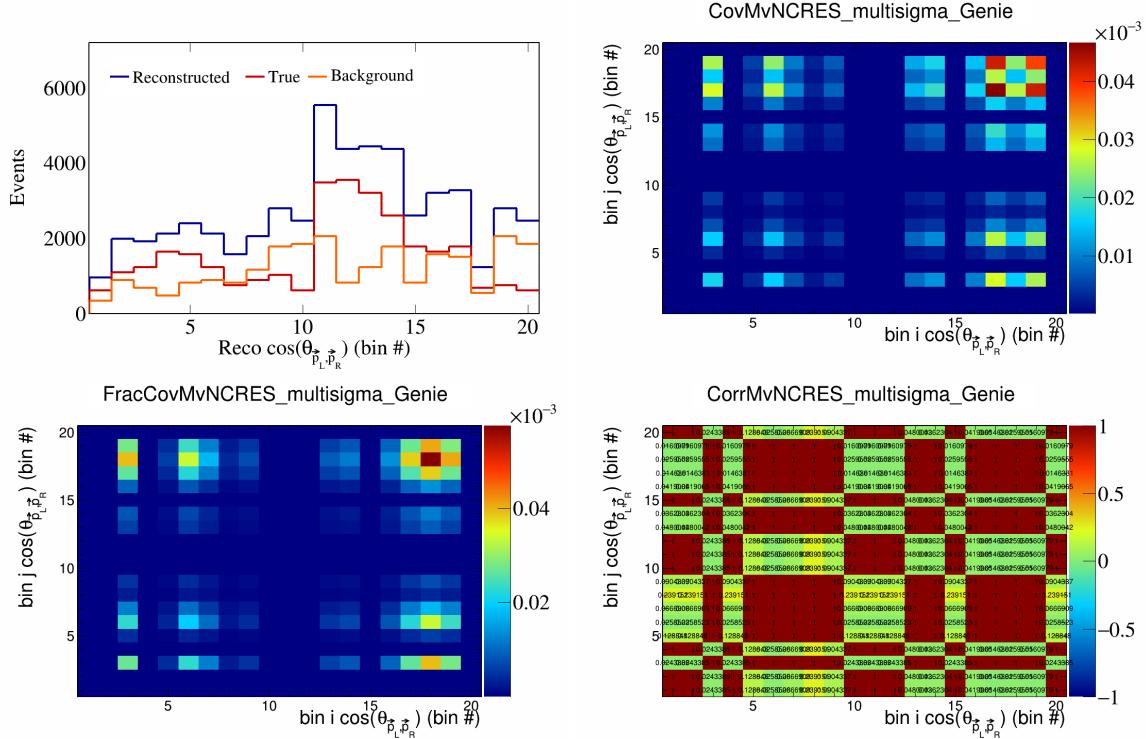


Figure 356: MvNCRES variations for $\cos(\theta_{\vec{p}_L, \vec{p}_R})$ in $\cos(\theta_{\vec{p}_\mu})$.

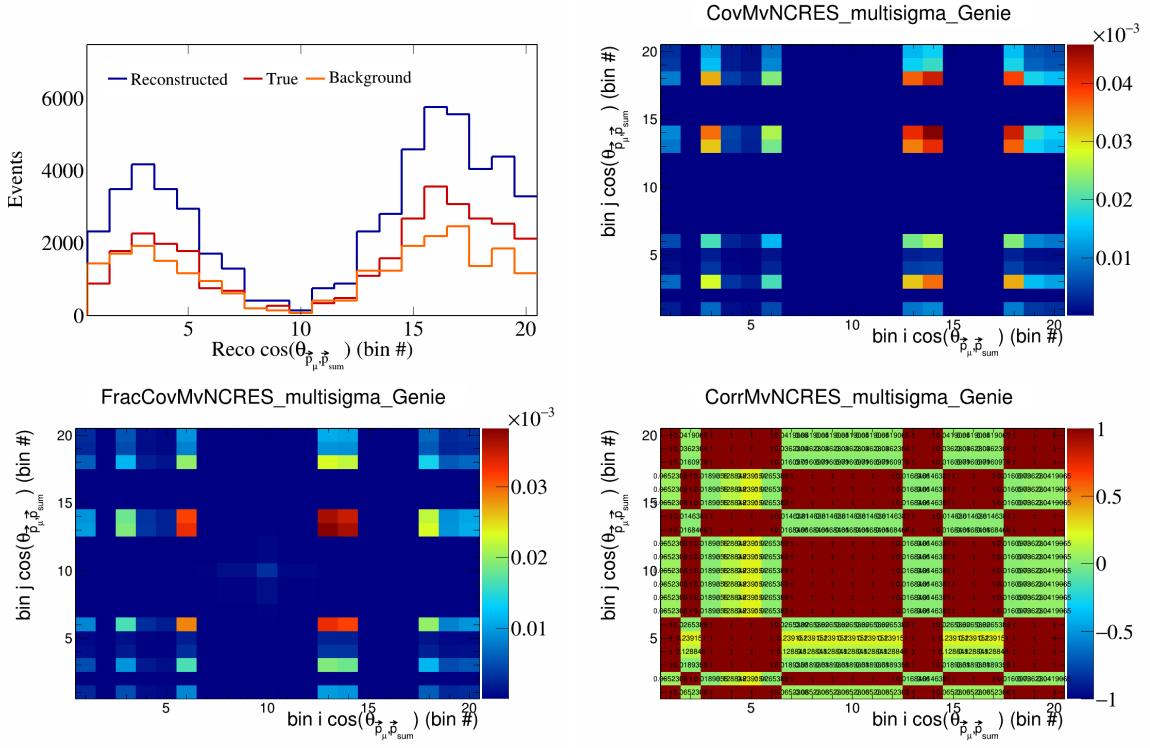


Figure 357: MyNCRES variations for $\cos(\theta_{\vec{p}_\mu, \vec{p}_{\text{sum}}})$ in $\cos(\theta_{\vec{p}_\mu})$.

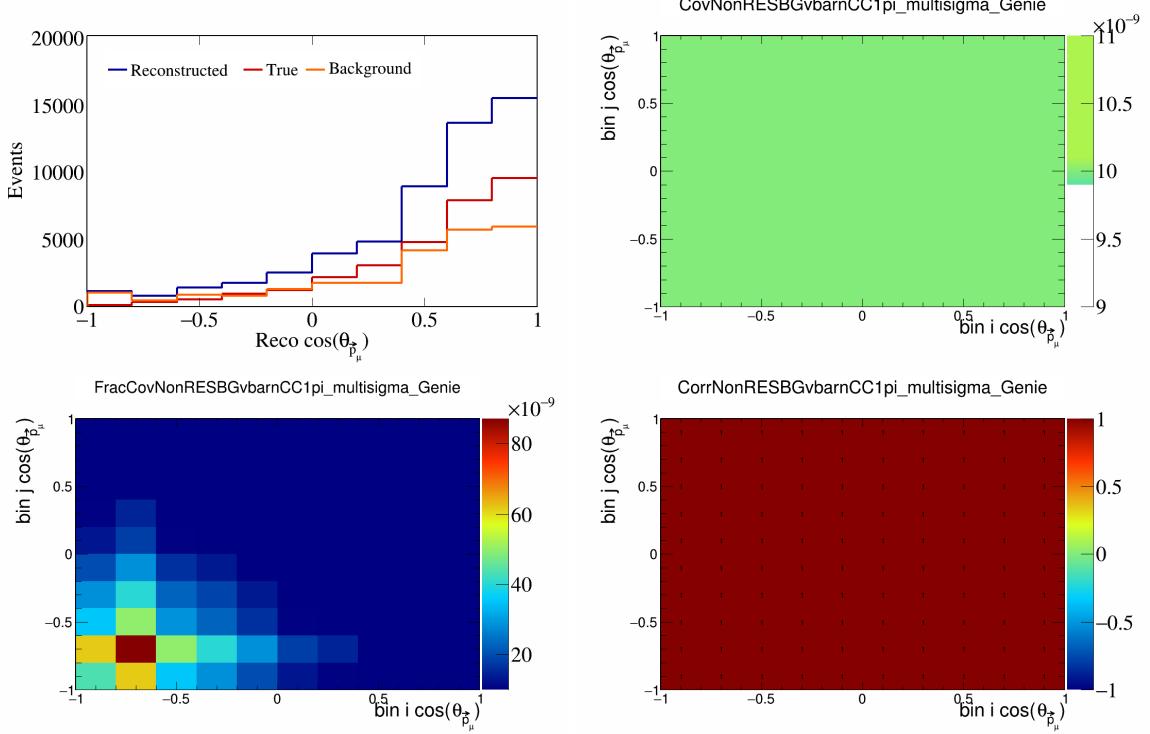


Figure 358: NonRESBGvbarCC1pi variations for $\cos(\theta_{\vec{p}_\mu})$.

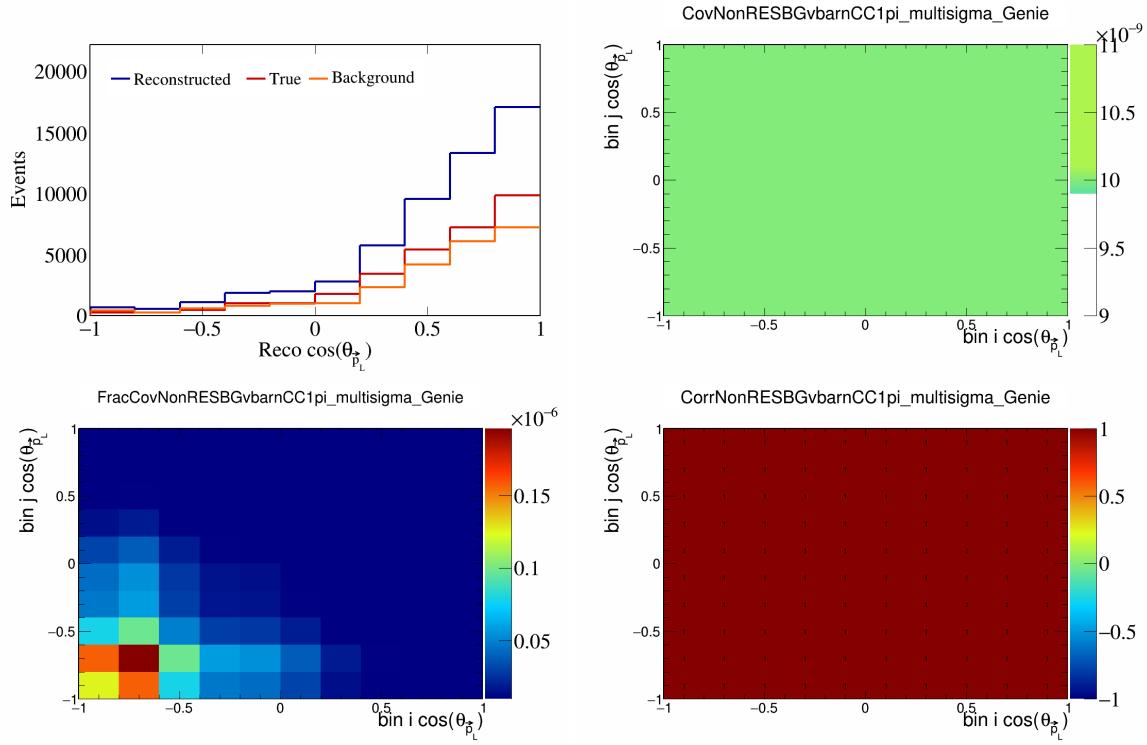


Figure 359: NonRESBGvbarCC1pi variations for $\cos(\theta_{\vec{p}_L})$.

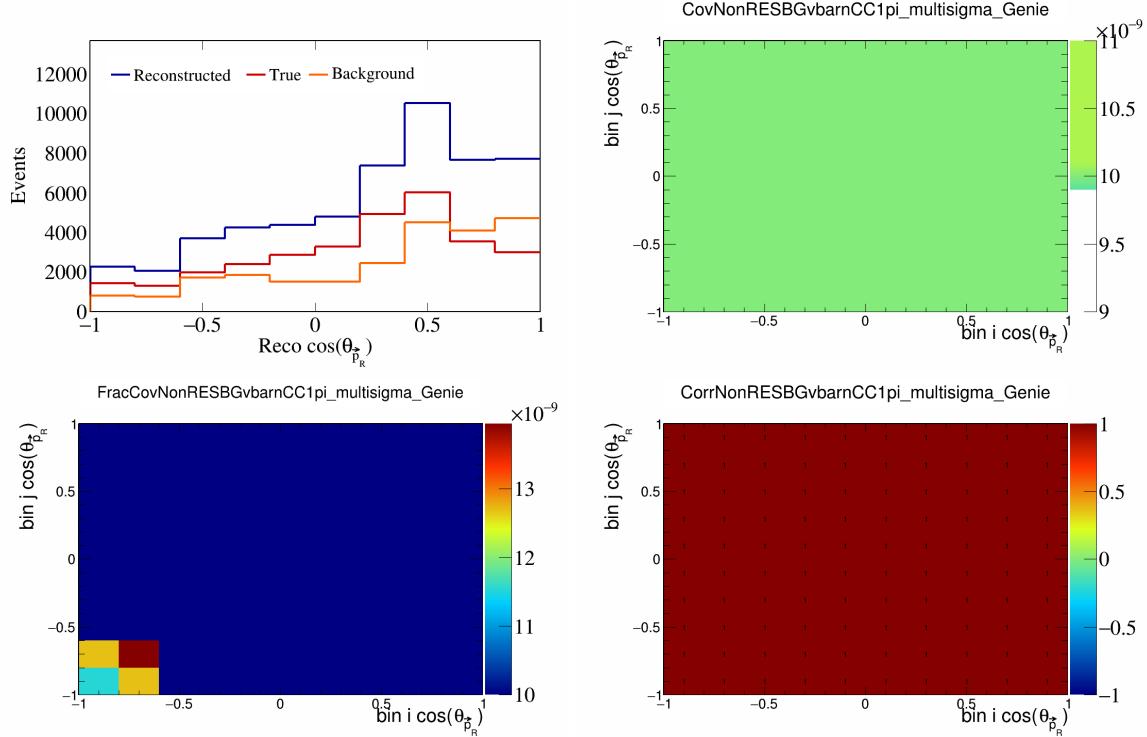


Figure 360: NonRESBGvbarCC1pi variations for $\cos(\theta_{\vec{p}_R})$.

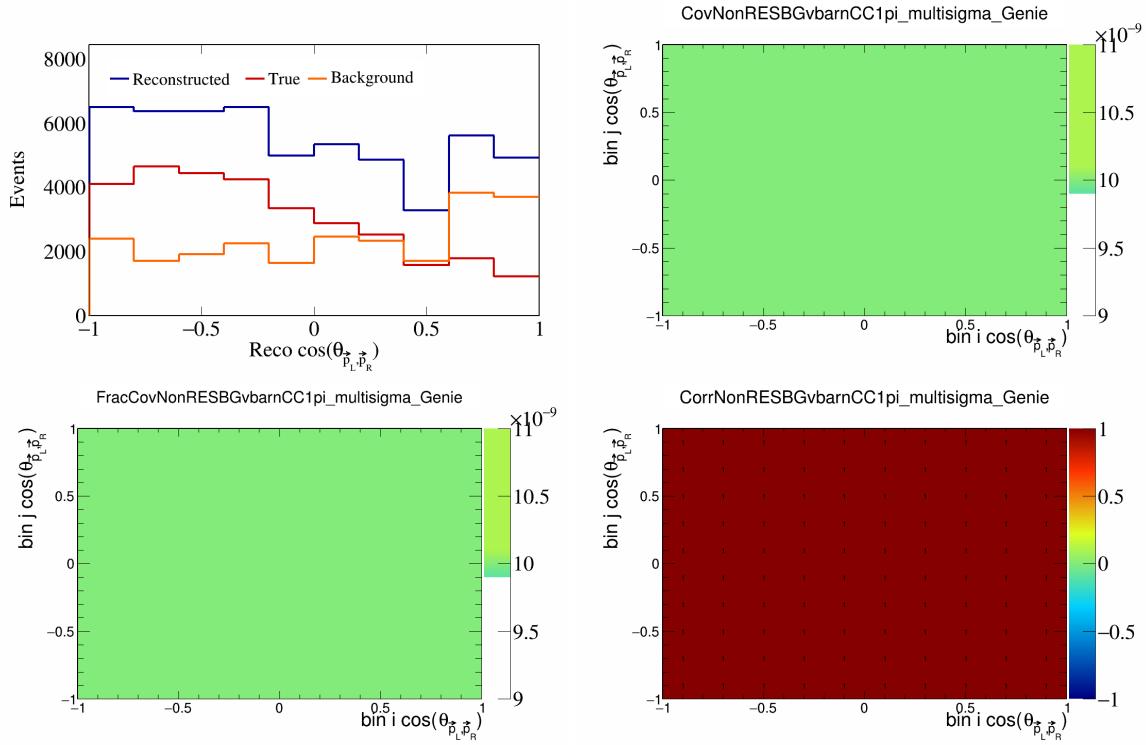


Figure 361: NonRESBGvbarCC1pi variations for $\cos(\theta_{\vec{p}_L, \vec{p}_R})$.

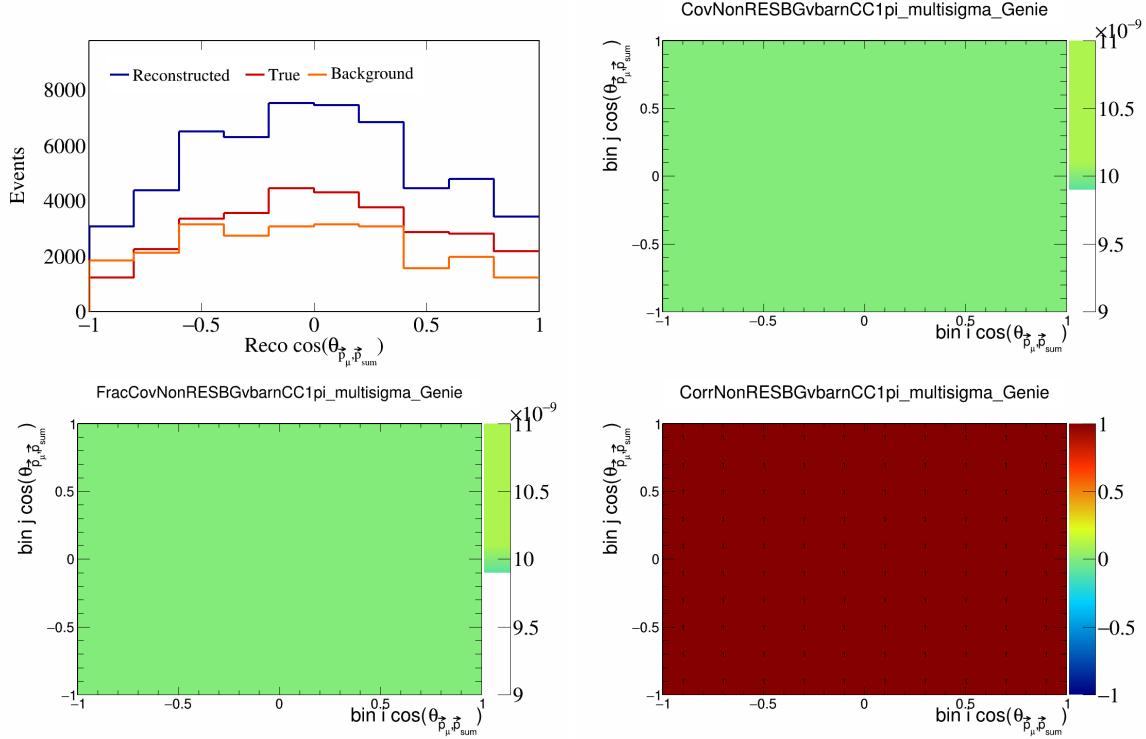


Figure 362: NonRESBGvbarCC1pi variations for $\cos(\theta_{\vec{p}_\mu, \vec{p}_{\text{sum}}})$.

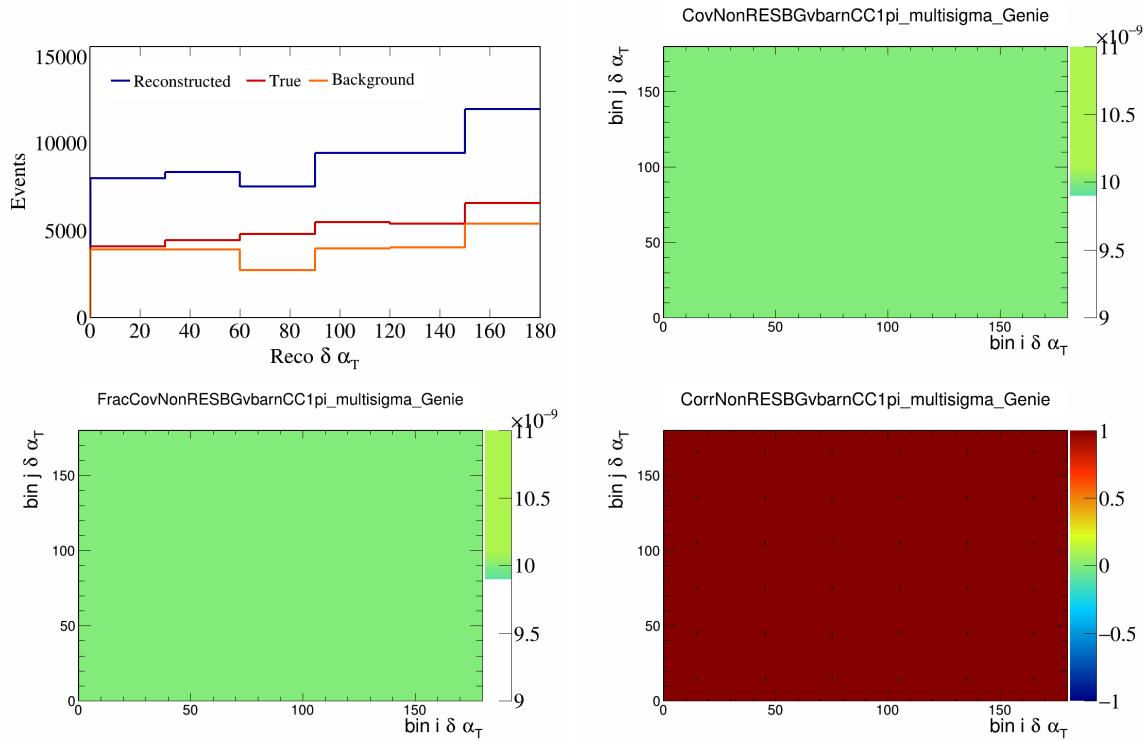


Figure 363: NonRESBGvbarCC1pi variations for $\delta\alpha_T$.

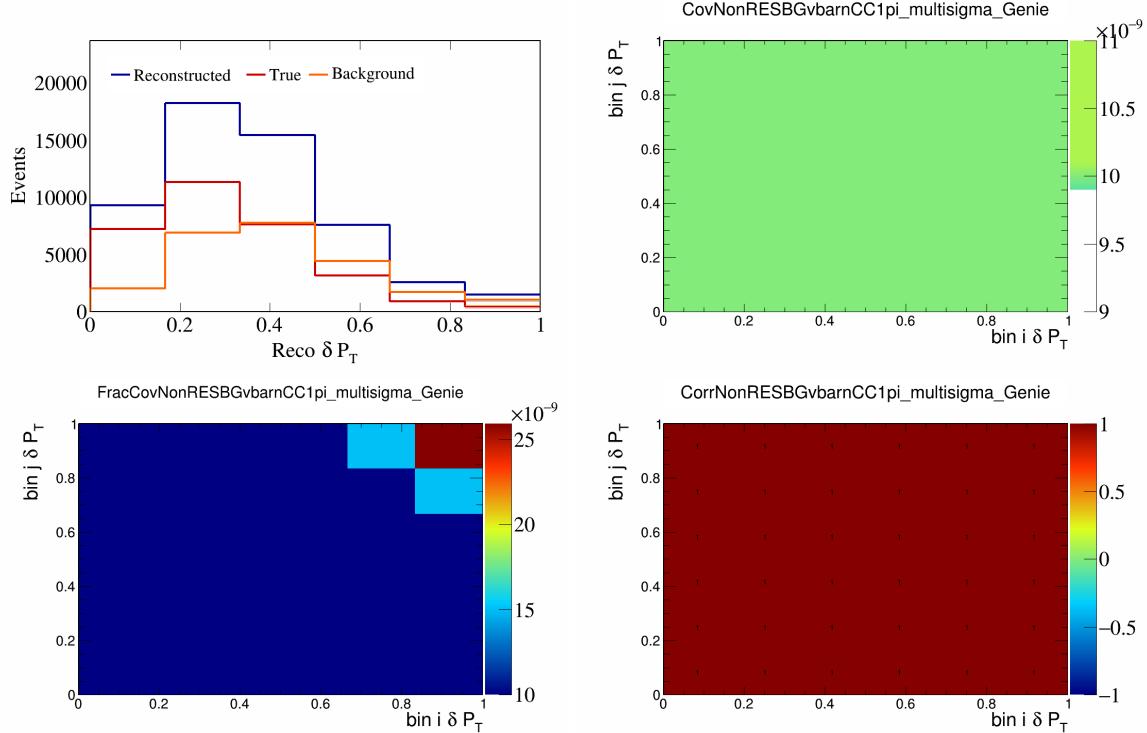


Figure 364: NonRESBGvbarCC1pi variations for δP_T .

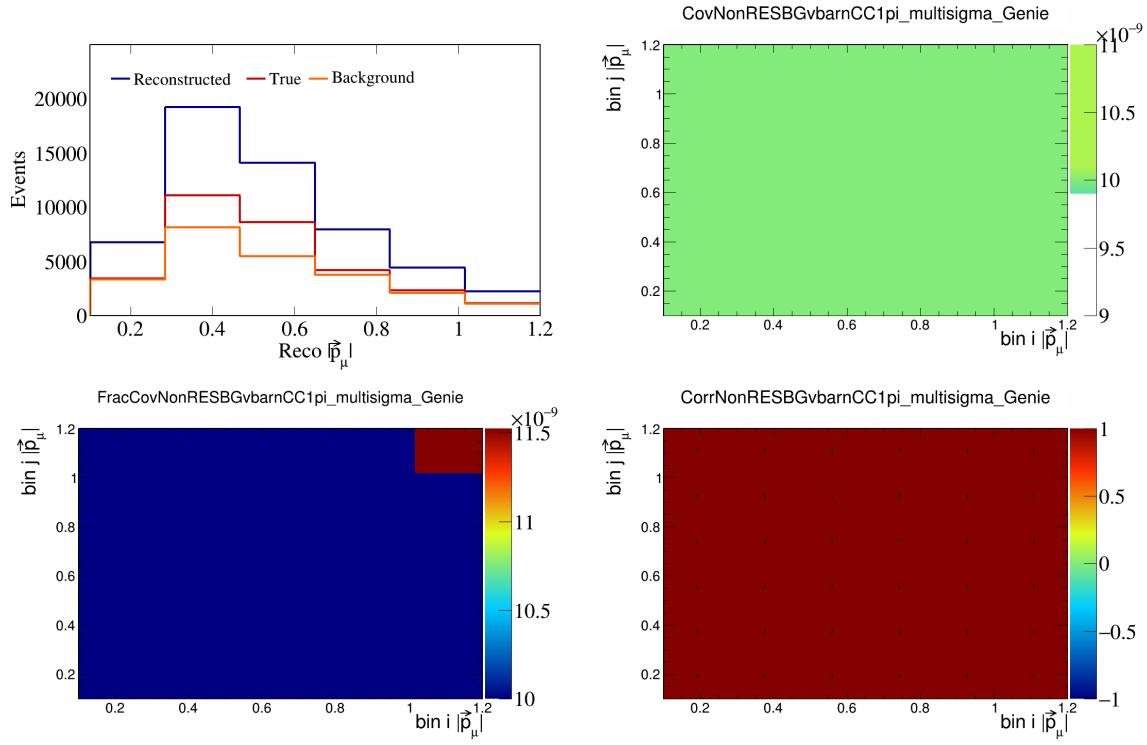


Figure 365: NonRESBGvbarCC1pi variations for $|\vec{p}_\mu|$.

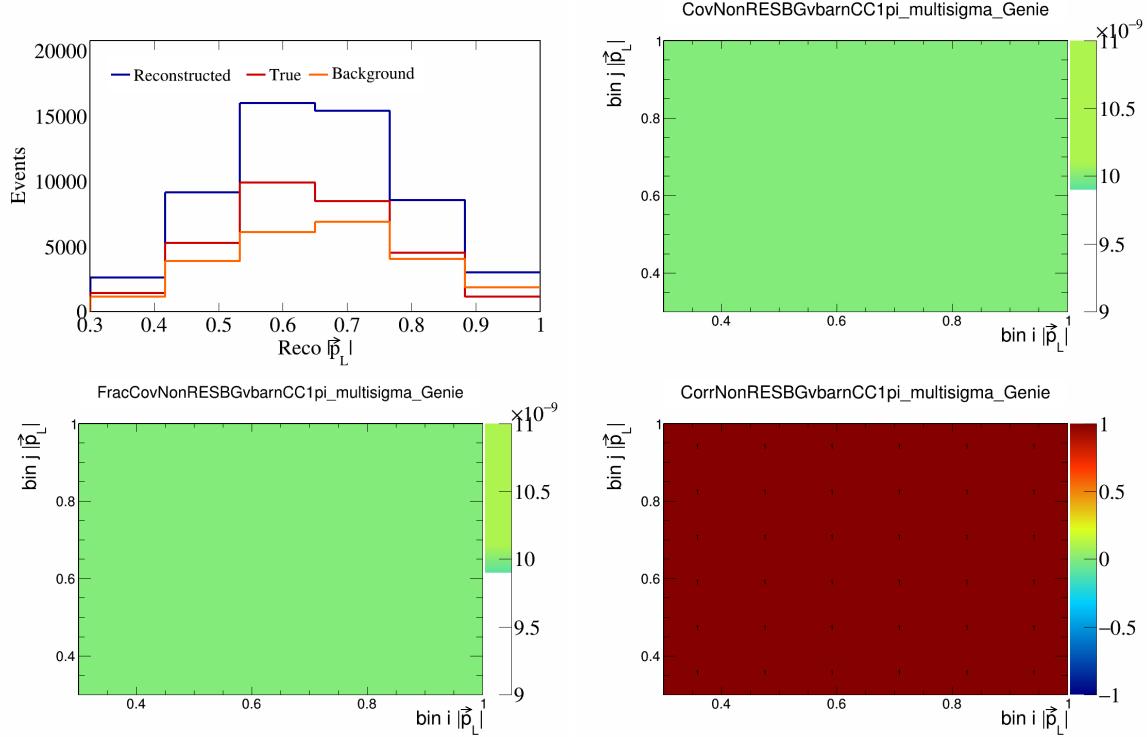


Figure 366: NonRESBGvbarCC1pi variations for $|\vec{p}_L|$.

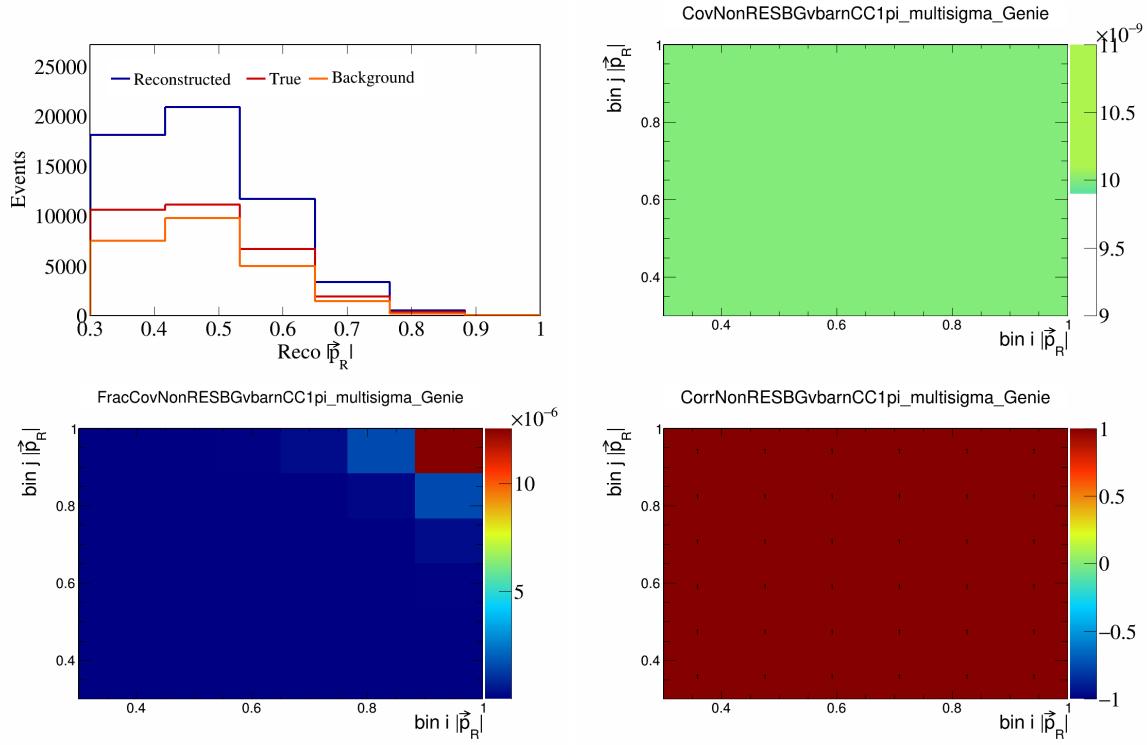


Figure 367: NonRESBGvbarCC1pi variations for $|\vec{p}_R|$.

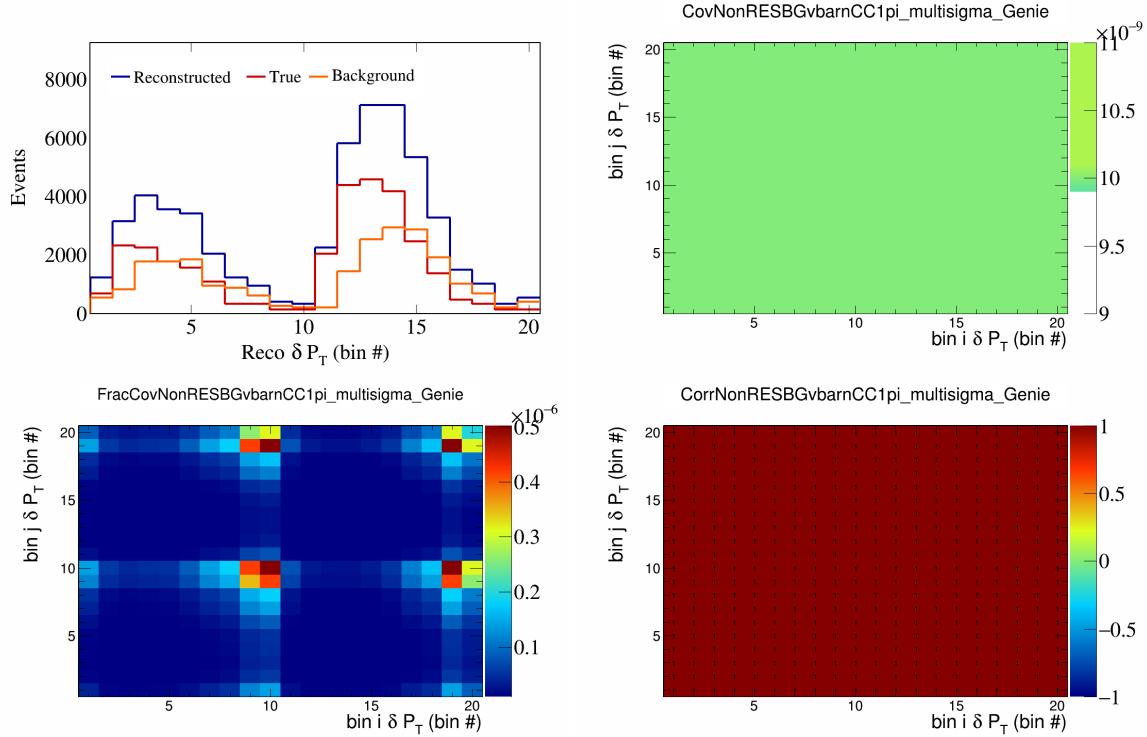


Figure 368: NonRESBGvbarCC1pi variations for δP_T in $\cos(\theta_{\vec{p}_\mu})$.

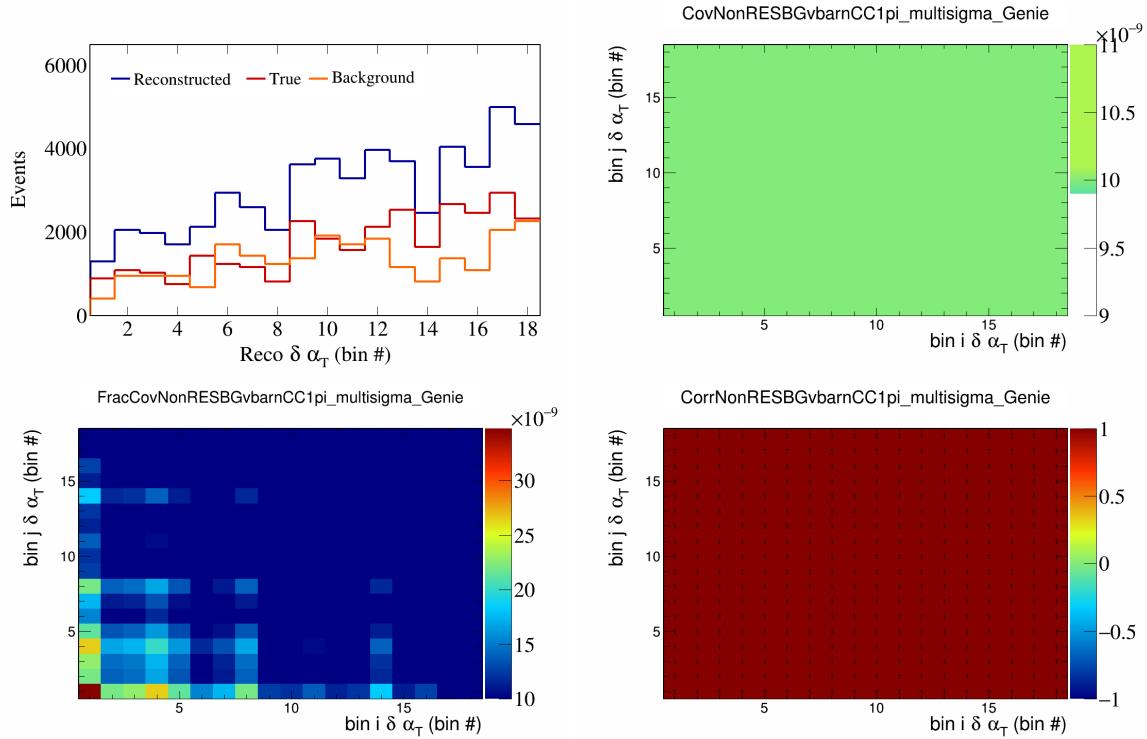


Figure 369: NonRESBGvbarCC1pi variations for $\delta\alpha_T$ in $\cos(\theta_{\vec{p}_\mu})$.

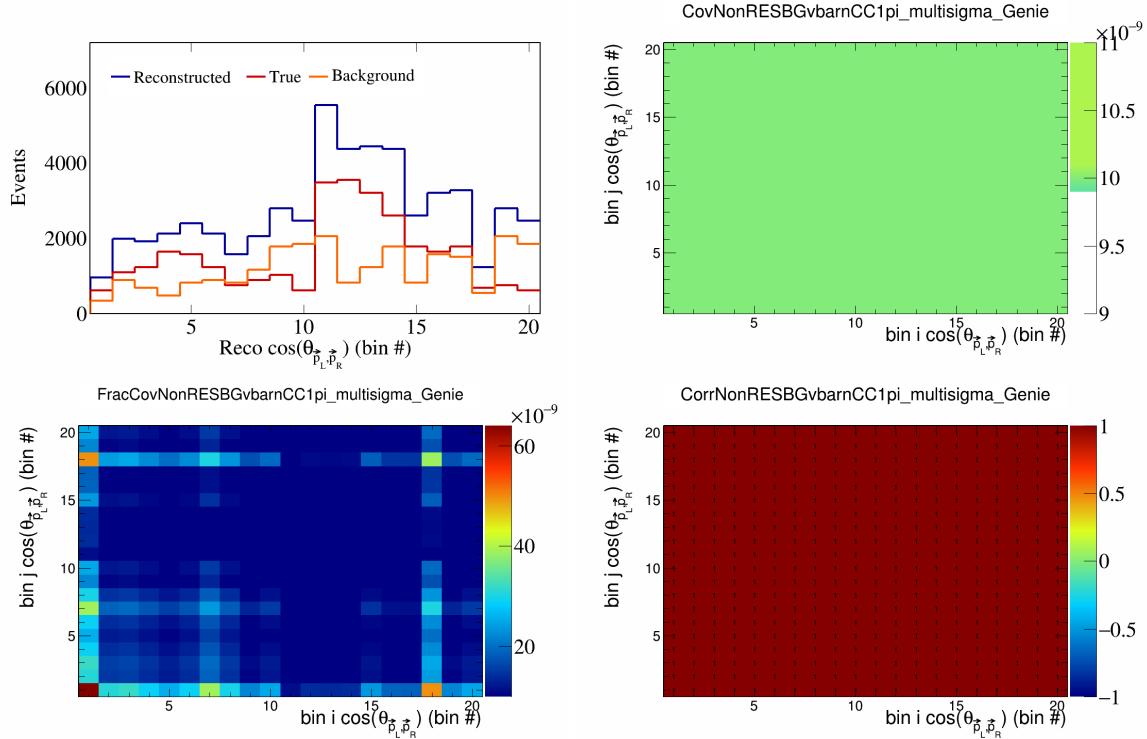


Figure 370: NonRESBGvbarCC1pi variations for $\cos(\theta_{\vec{p}_L, \vec{p}_R})$ in $\cos(\theta_{\vec{p}_\mu})$.

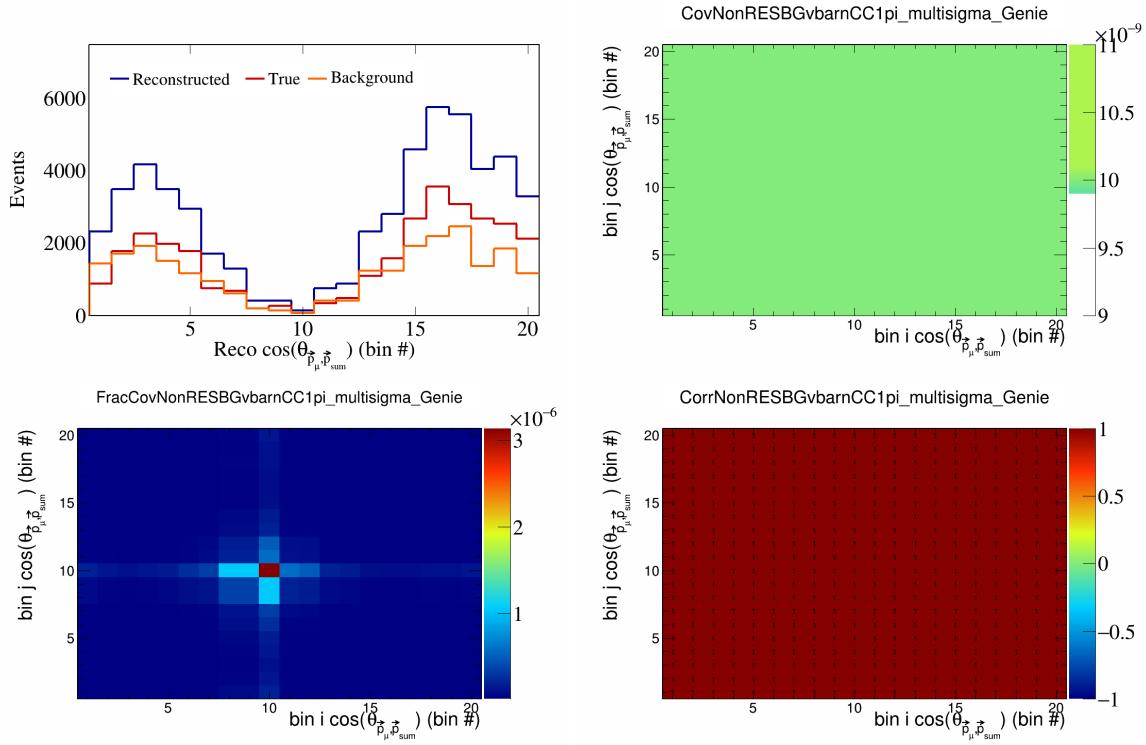


Figure 371: NonRESBGvbarCC1pi variations for $\cos(\theta_{\vec{p}_\mu, \vec{p}_{\text{sum}}})$ in $\cos(\theta_{\vec{p}_\mu})$.

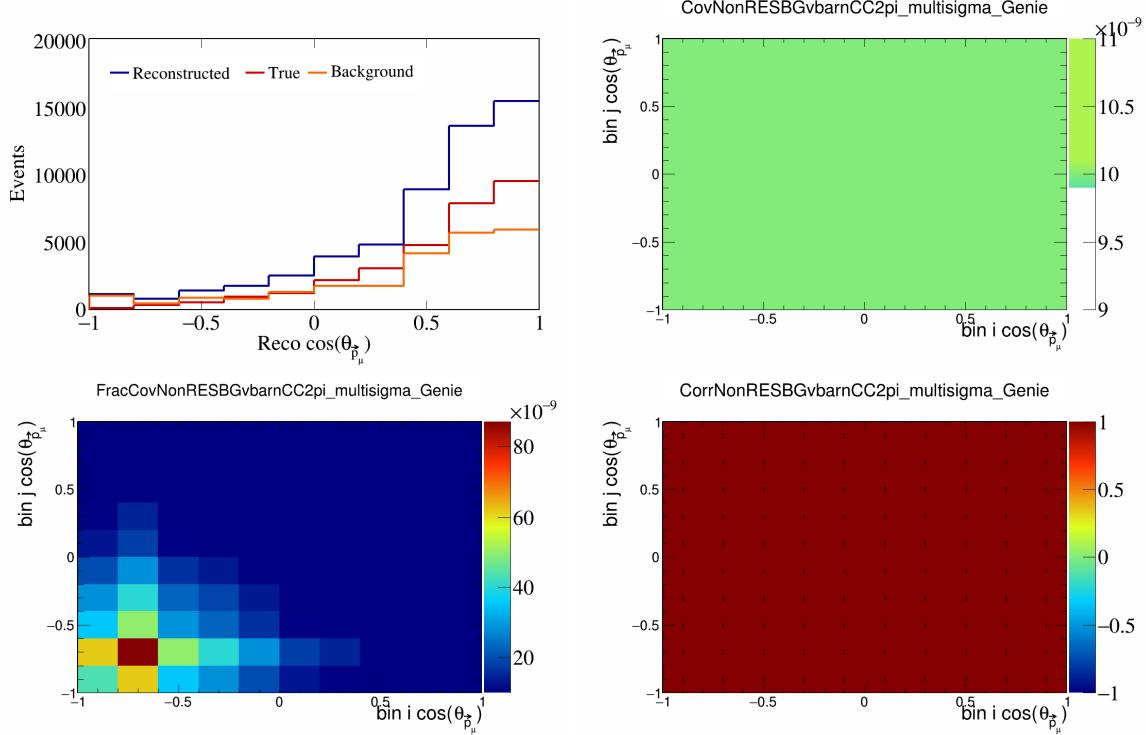


Figure 372: NonRESBGvbarCC2pi variations for $\cos(\theta_{\vec{p}_\mu})$.

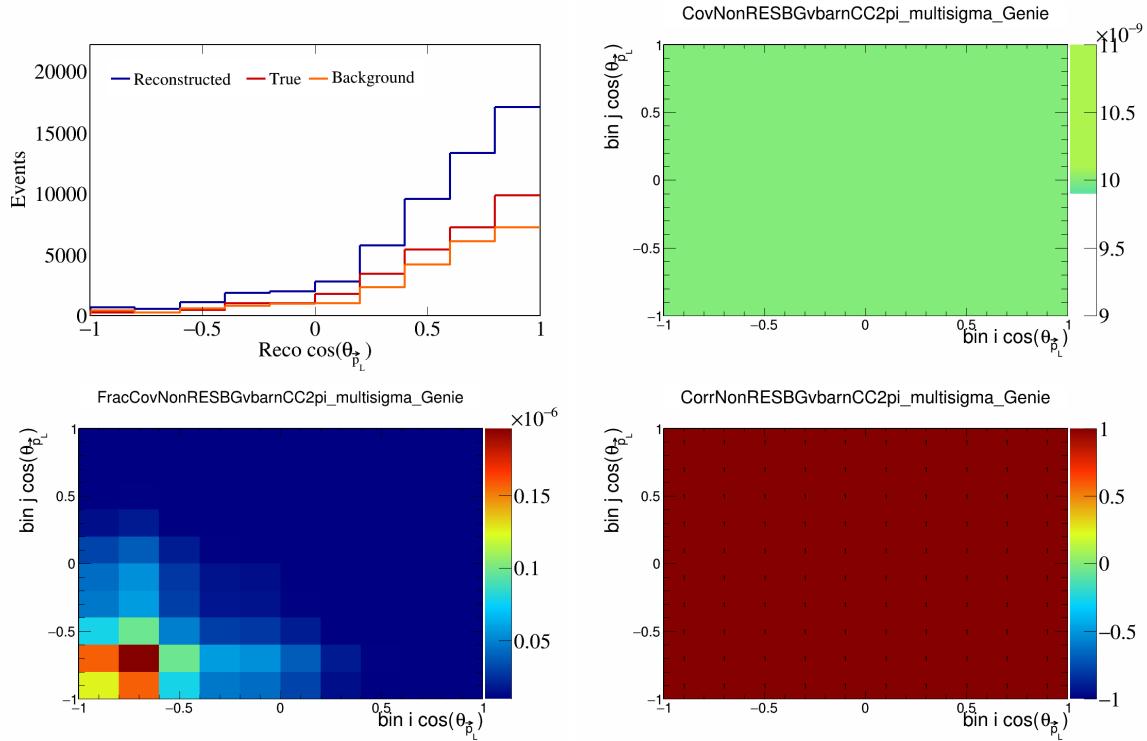


Figure 373: NonRESBGvbarCC2pi variations for $\cos(\theta_{\vec{p}_L})$.

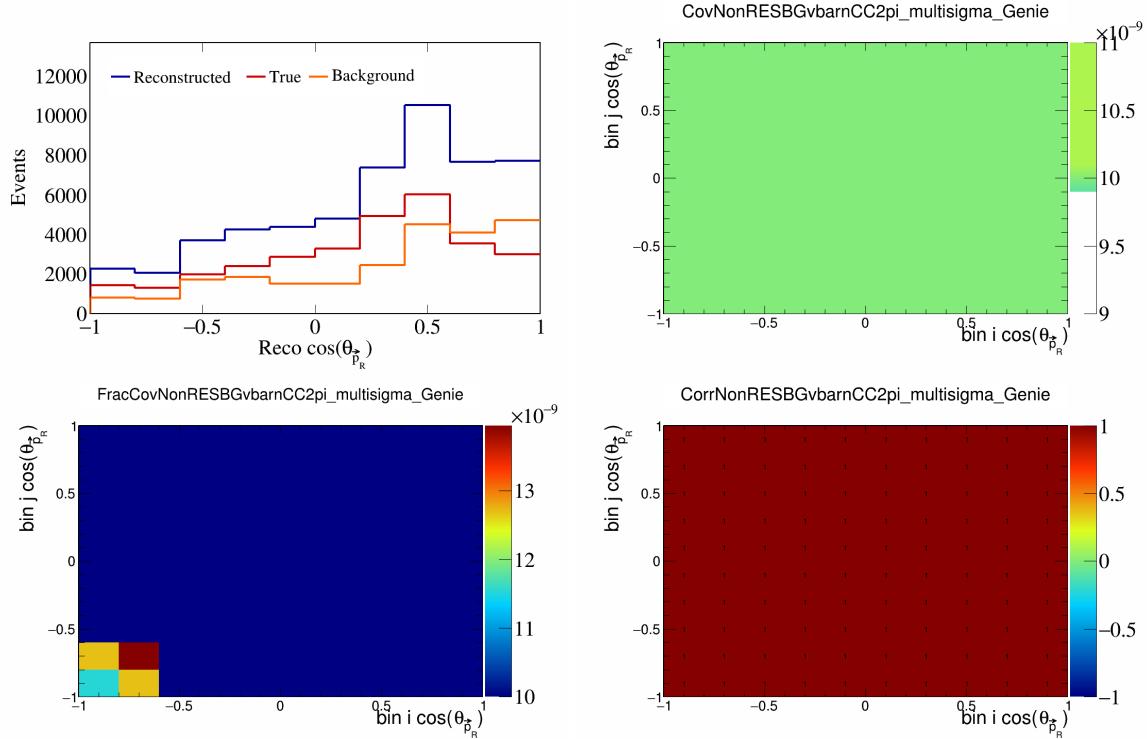


Figure 374: NonRESBGvbarCC2pi variations for $\cos(\theta_{\vec{p}_R})$.

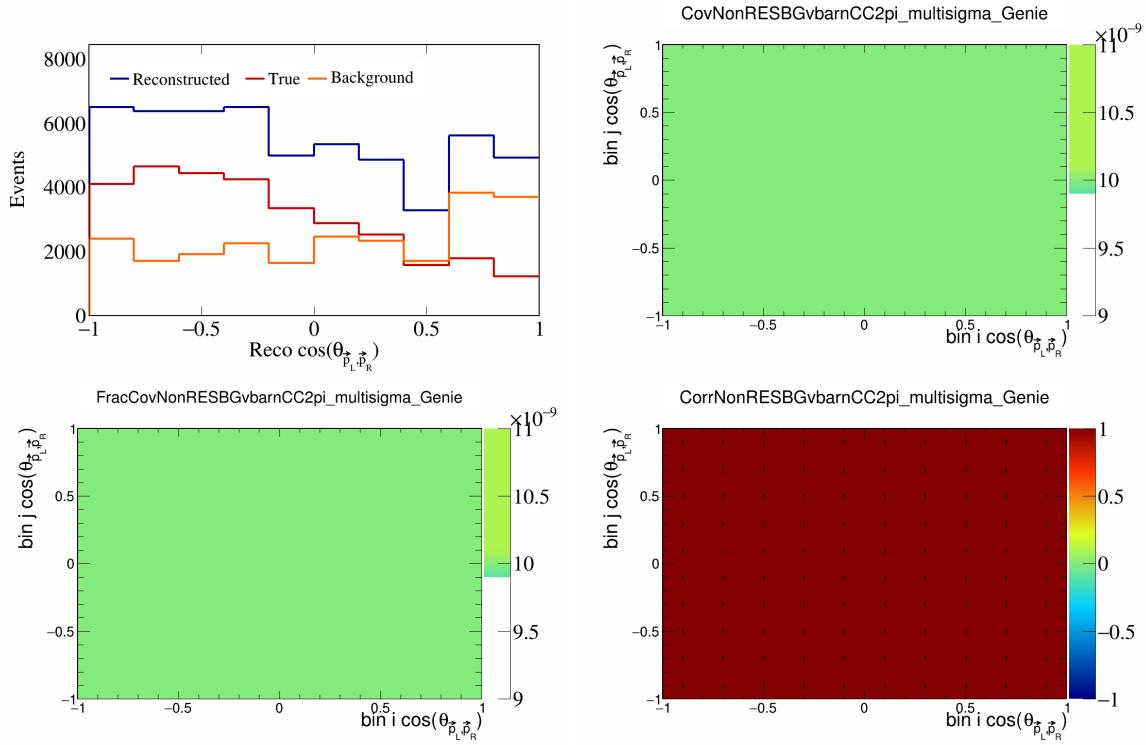


Figure 375: NonRESBGvbarCC2pi variations for $\cos(\theta_{\vec{p}_L, \vec{p}_R})$.

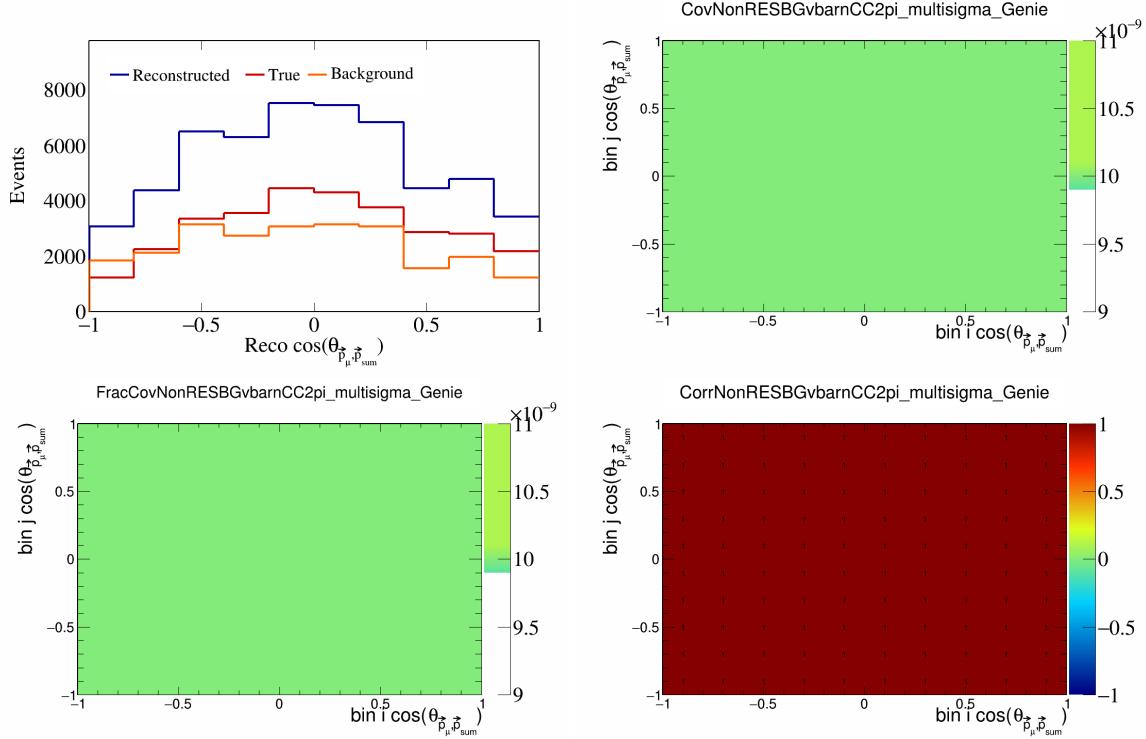


Figure 376: NonRESBGvbarCC2pi variations for $\cos(\theta_{\vec{p}_\mu, \vec{p}_{\text{sum}}})$.

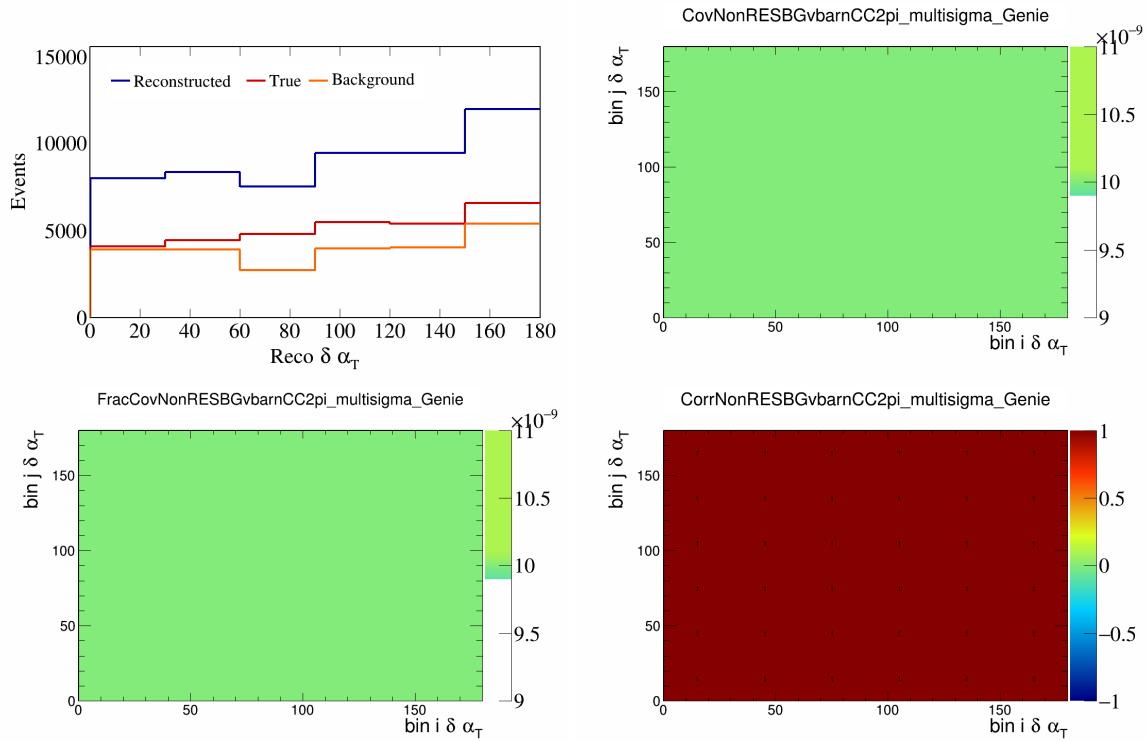


Figure 377: NonRESBGvbarCC2pi variations for $\delta\alpha_T$.

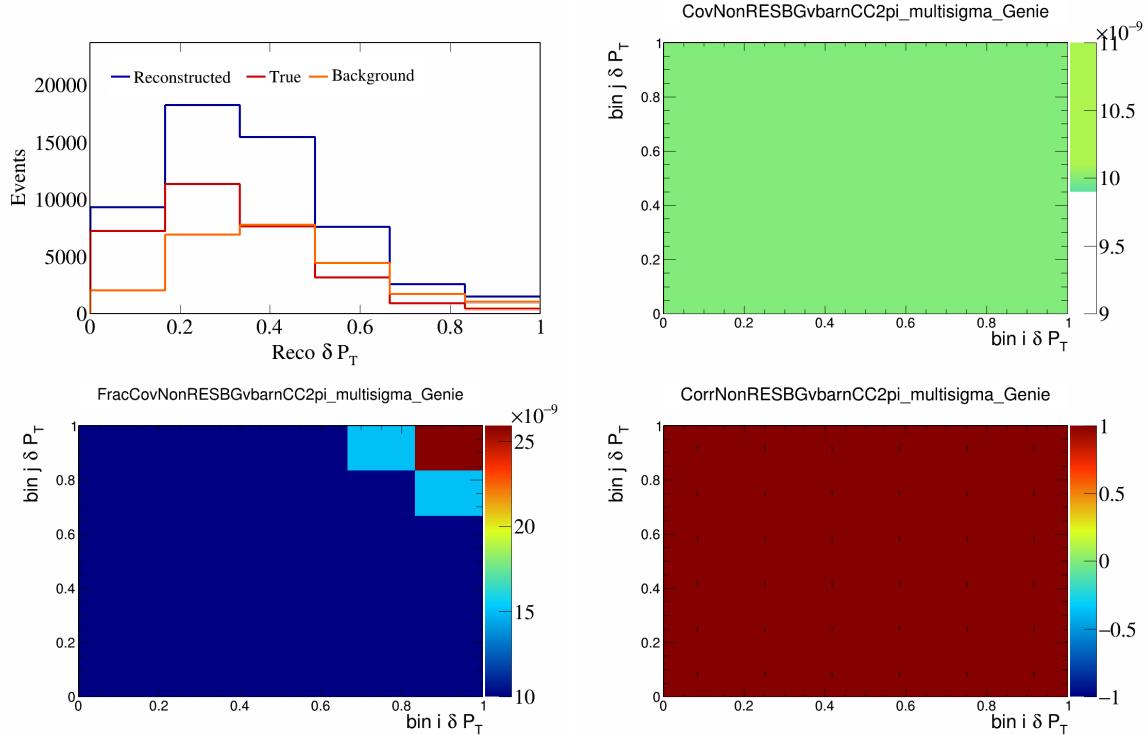


Figure 378: NonRESBGvbarCC2pi variations for δP_T .

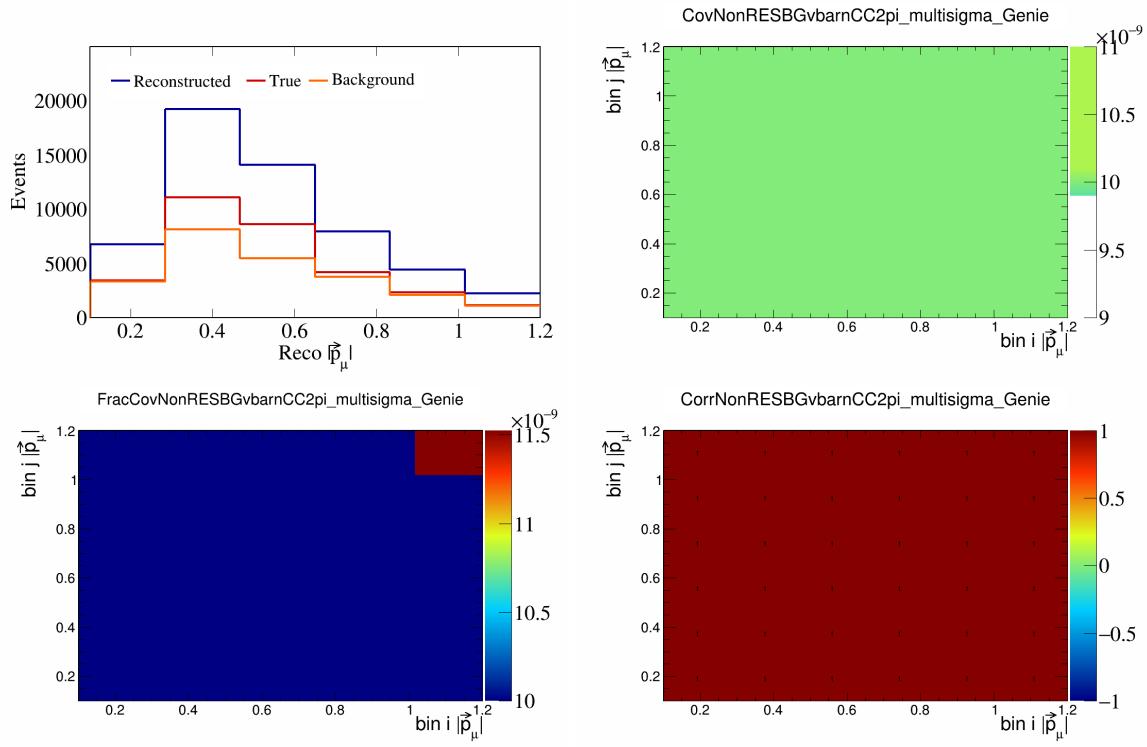


Figure 379: NonRESBGvbarCC2pi variations for $|\vec{p}_\mu|$.

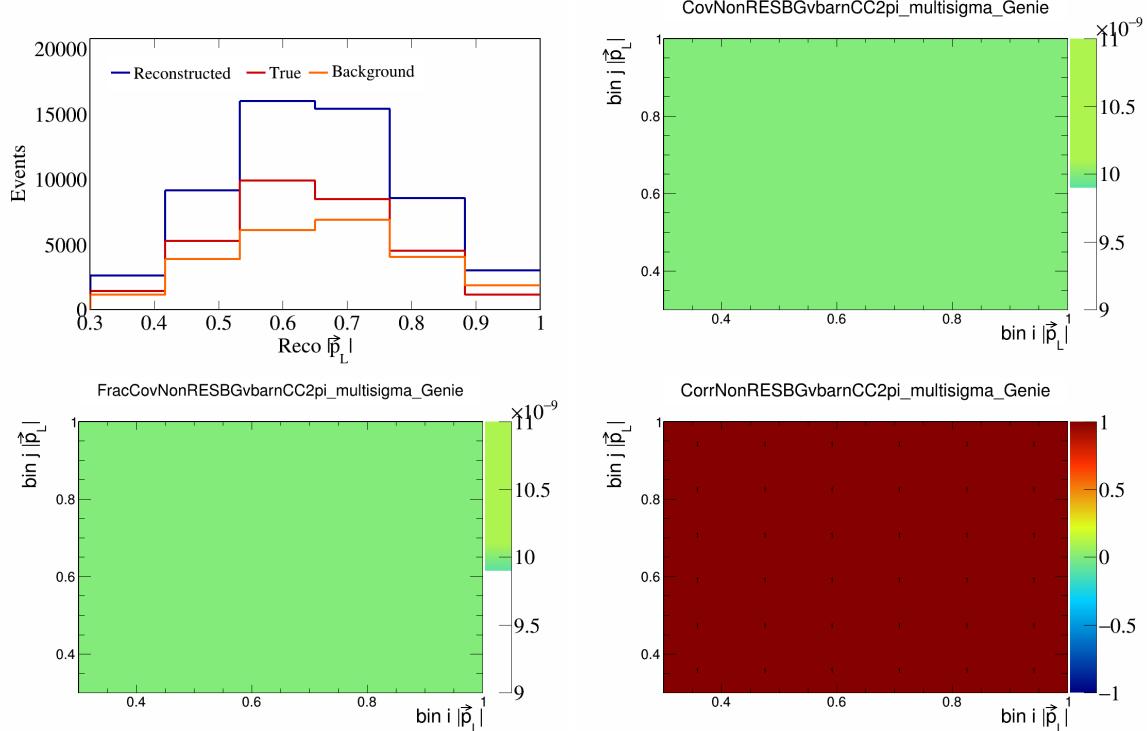


Figure 380: NonRESBGvbarCC2pi variations for $|\vec{p}_L|$.

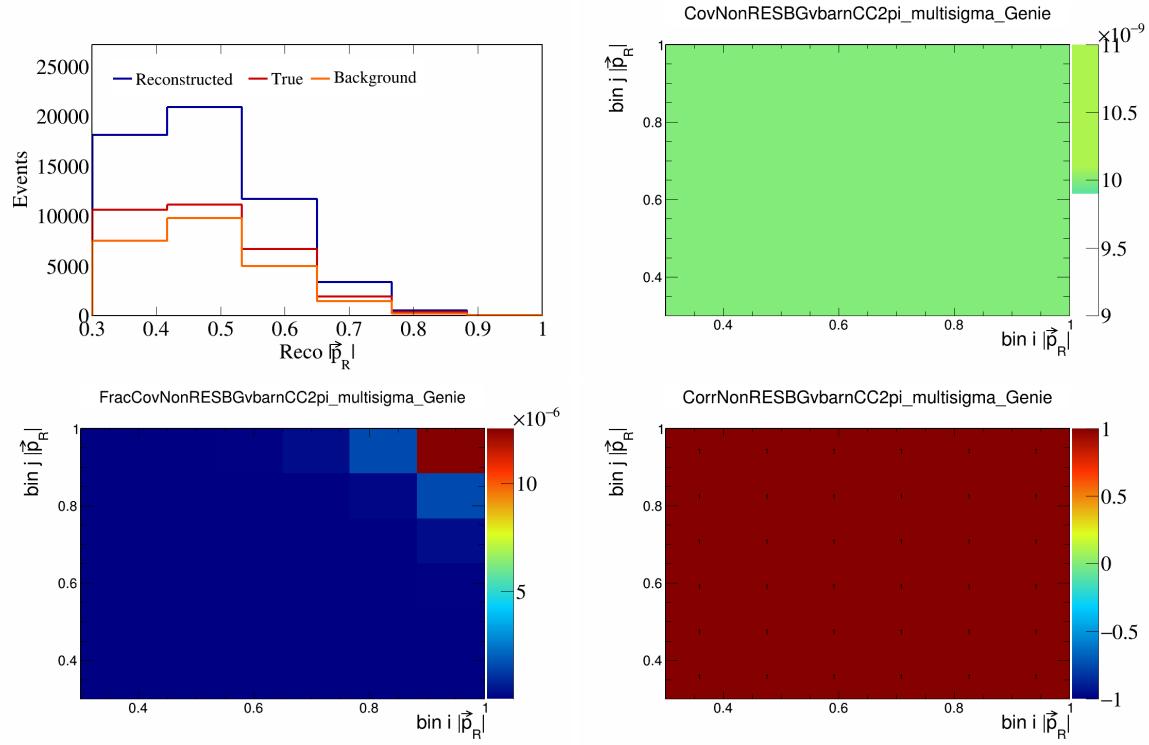


Figure 381: NonRESBGvbarCC2pi variations for $|\vec{p}_R|$.

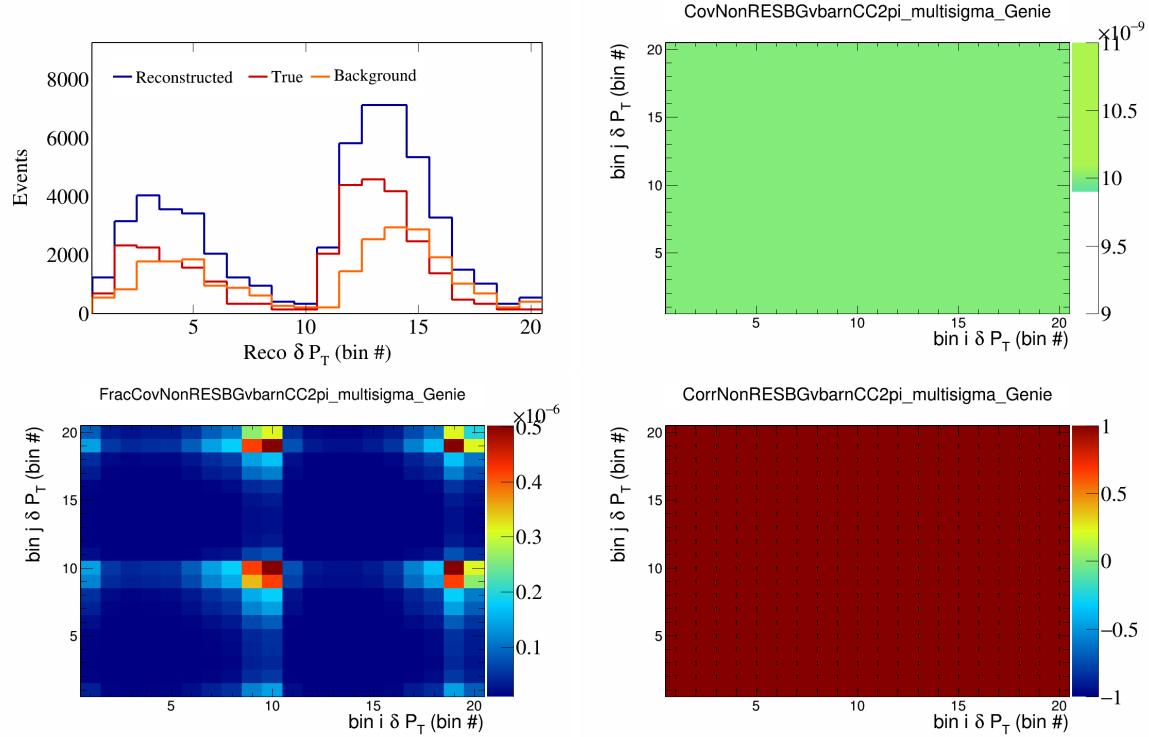


Figure 382: NonRESBGvbarCC2pi variations for δP_T in $\cos(\theta_{\vec{p}_\mu})$.

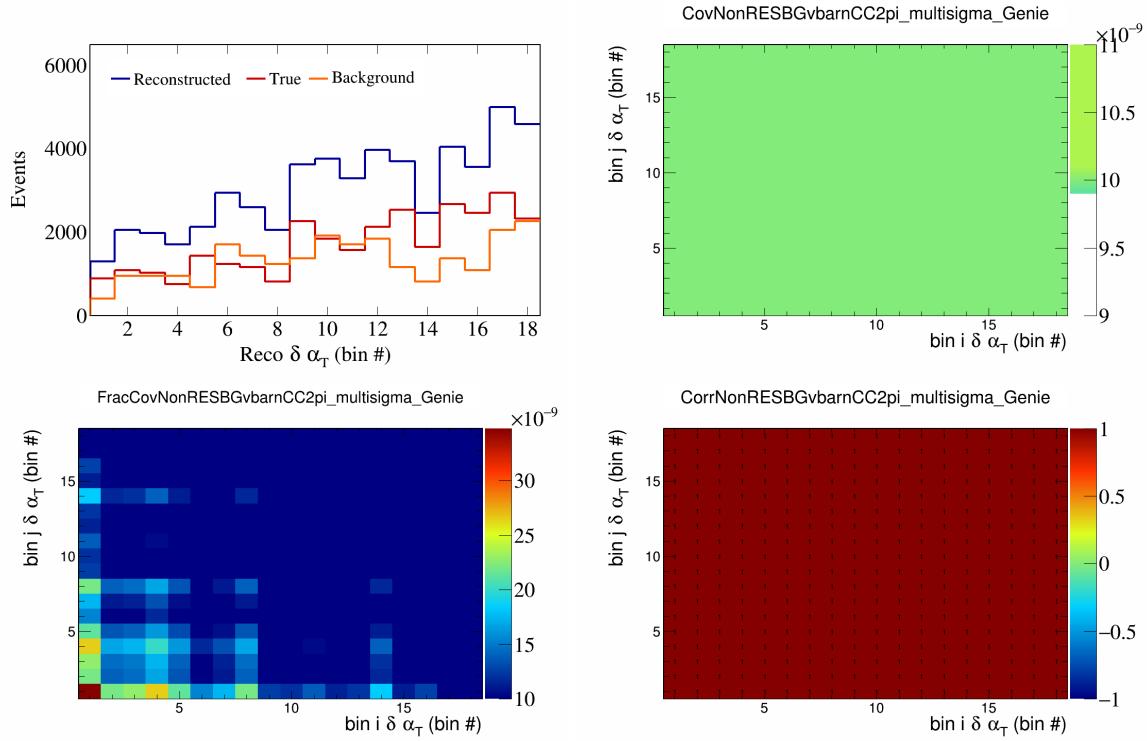


Figure 383: NonRESBGvbarCC2pi variations for $\delta\alpha_T$ in $\cos(\theta_{\vec{p}_\mu})$.

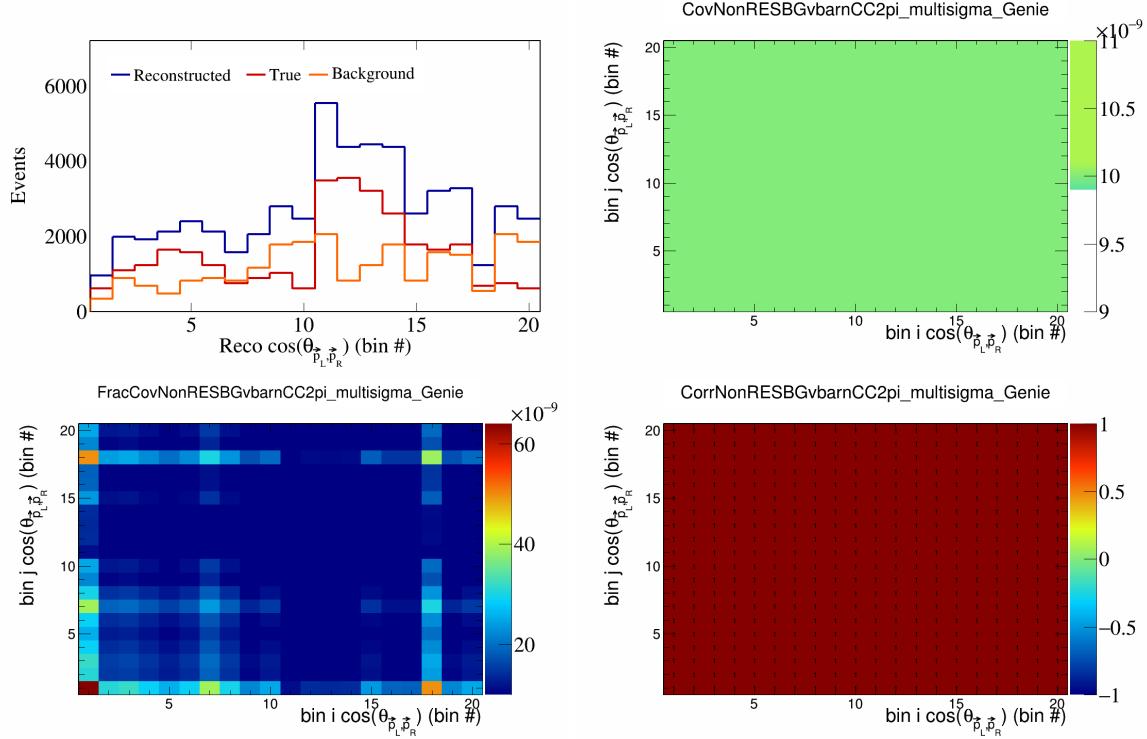


Figure 384: NonRESBGvbarCC2pi variations for $\cos(\theta_{\vec{p}_L, \vec{p}_R})$ in $\cos(\theta_{\vec{p}_\mu})$.

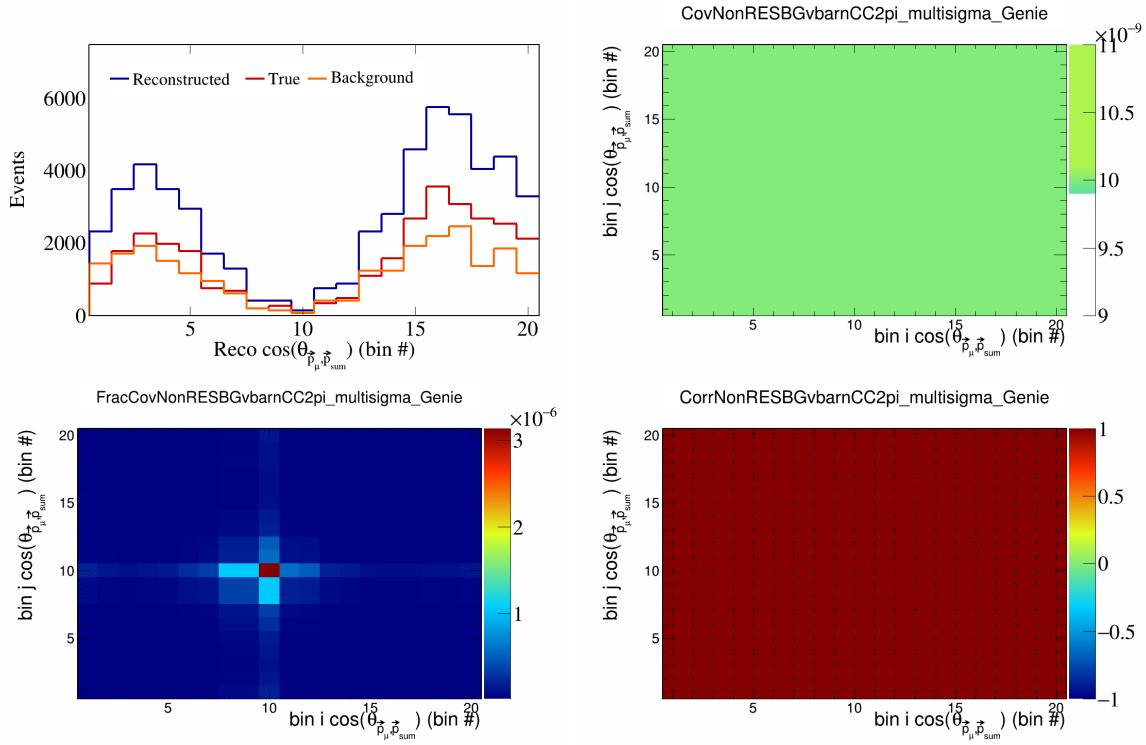


Figure 385: NonRESBGvbarCC2pi variations for $\cos(\theta_{\vec{p}_\mu})$ in $\cos(\theta_{\vec{p}_\mu})$.

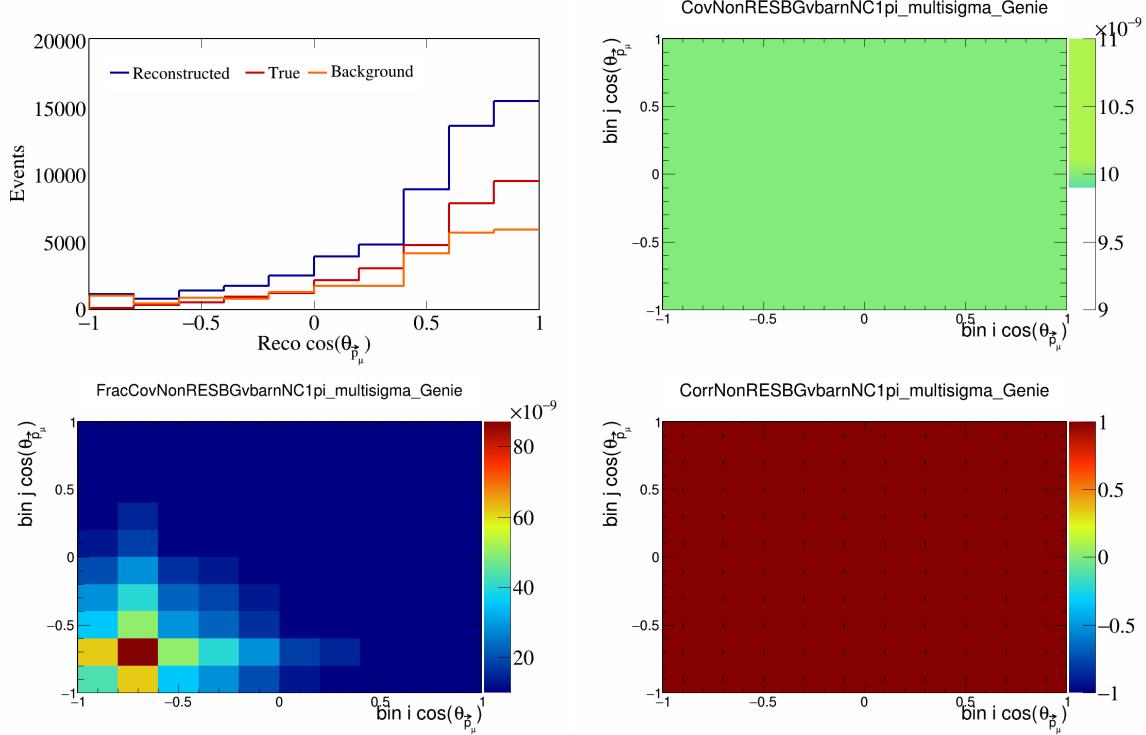


Figure 386: NonRESBGvbarNC1pi variations for $\cos(\theta_{\vec{p}_\mu})$.

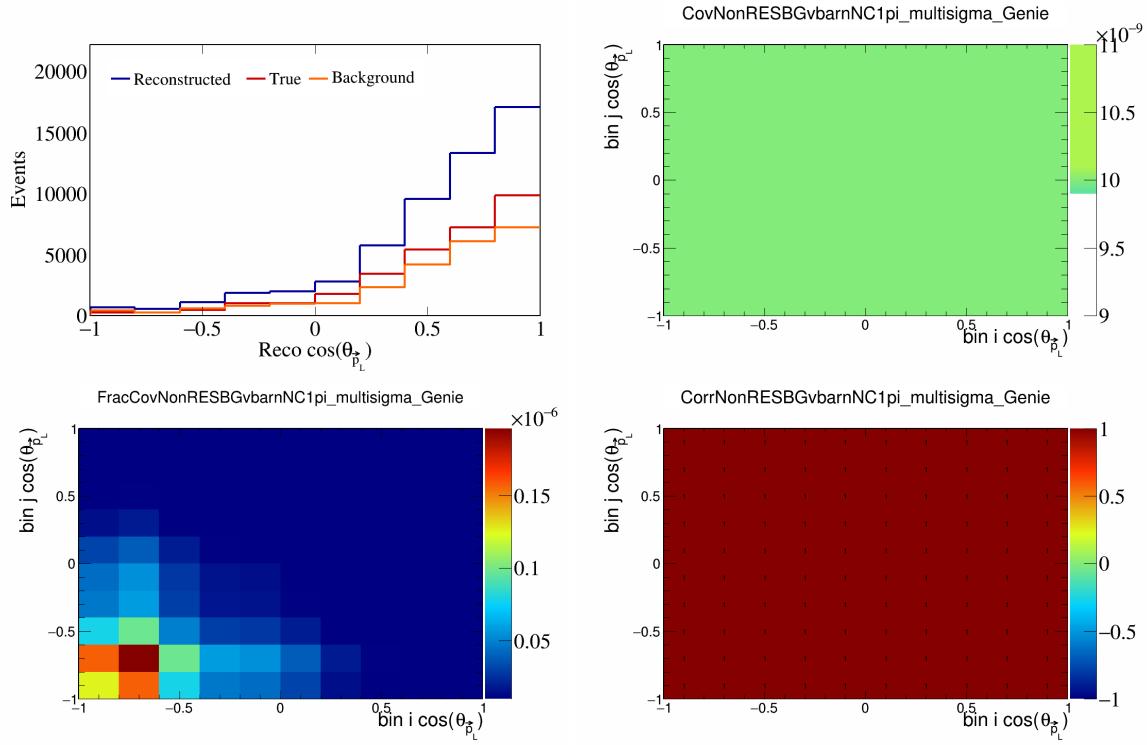


Figure 387: NonRESBGvbarNC1pi variations for $\cos(\theta_{\vec{p}_L})$.

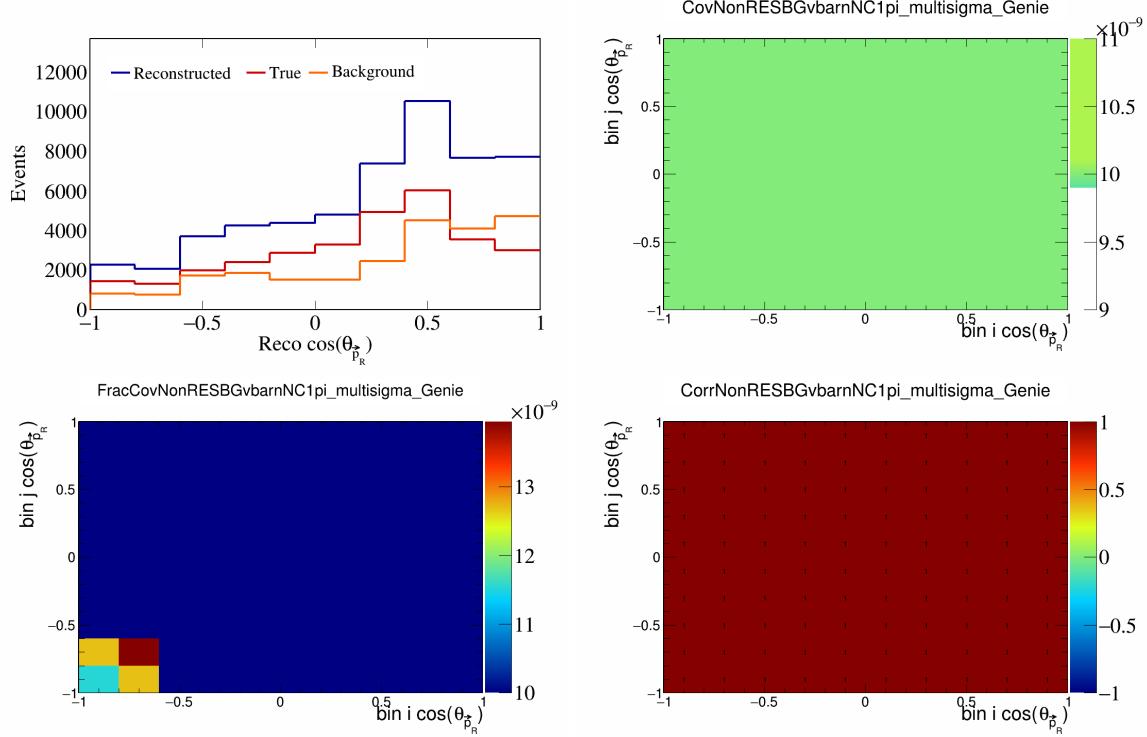


Figure 388: NonRESBGvbarNC1pi variations for $\cos(\theta_{\vec{p}_R})$.

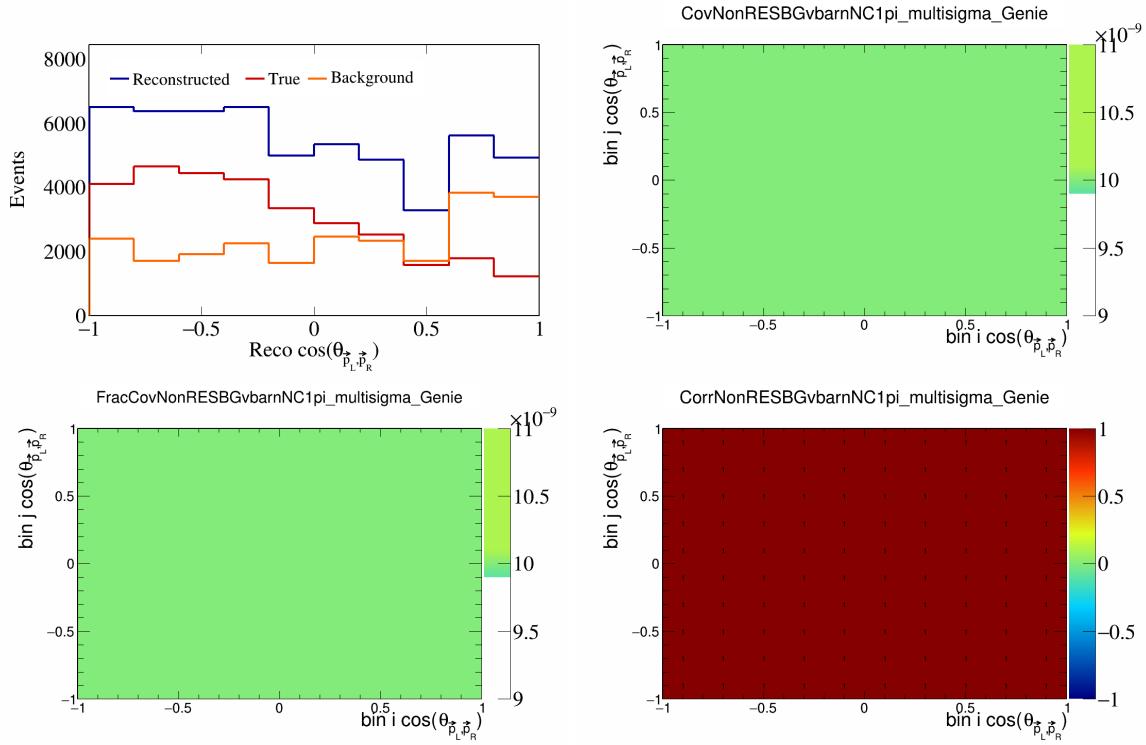


Figure 389: NonRESBGvbarNC1pi variations for $\cos(\theta_{\vec{p}_L, \vec{p}_R})$.

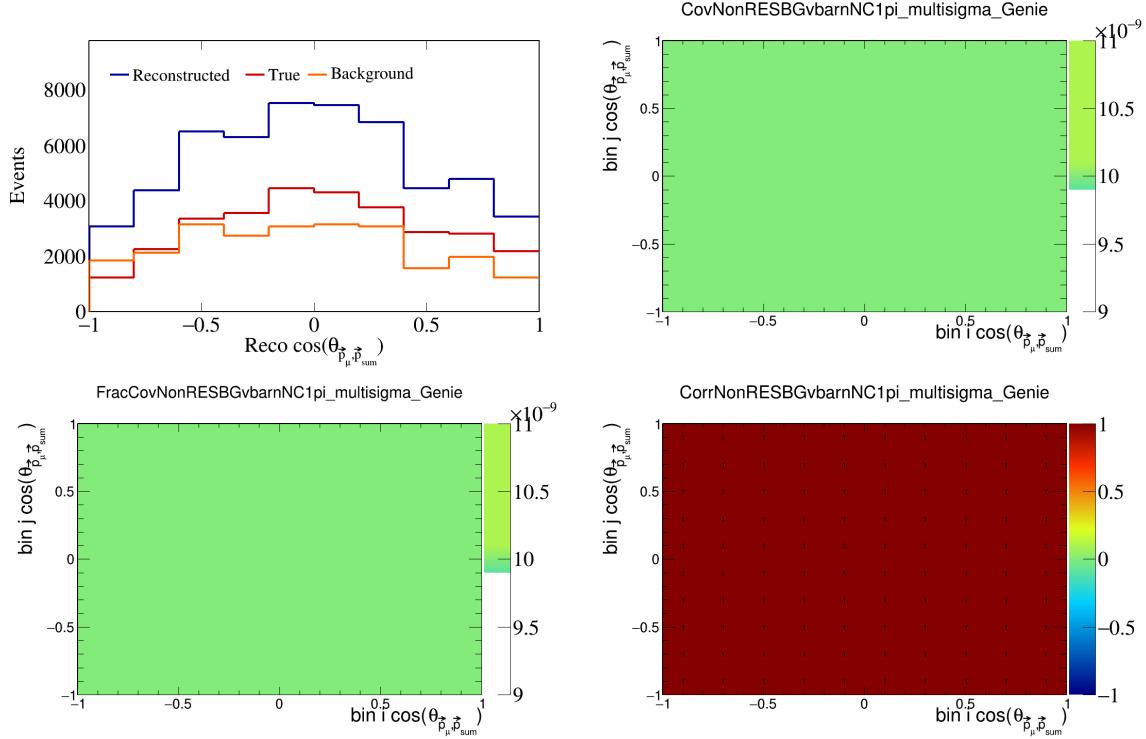


Figure 390: NonRESBGvbarNC1pi variations for $\cos(\theta_{\vec{p}_\mu, \vec{p}_{\text{sum}}})$.

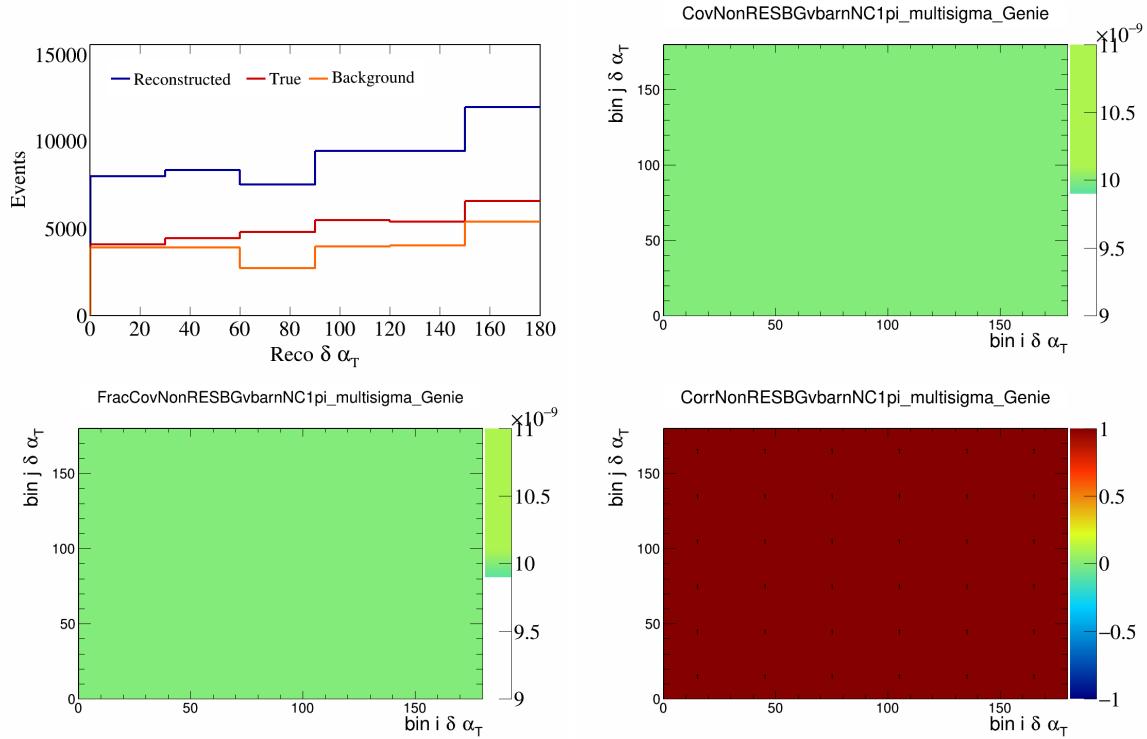


Figure 391: NonRESBGvbarNC1pi variations for $\delta\alpha_T$.

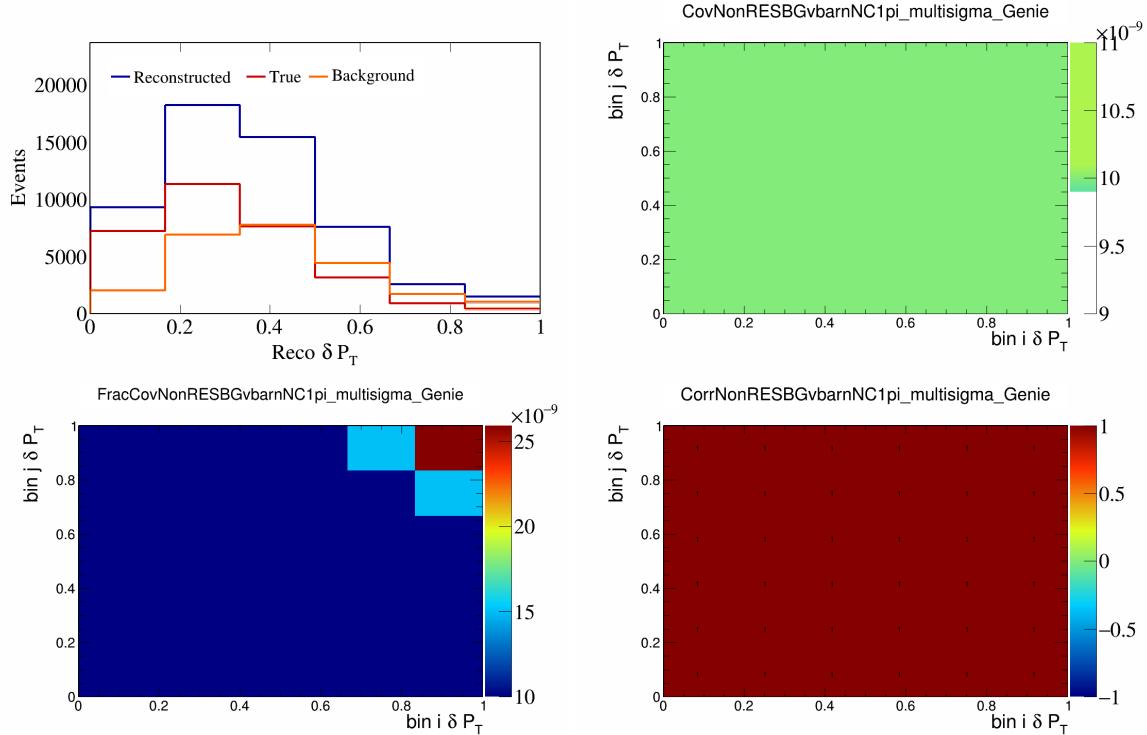


Figure 392: NonRESBGvbarNC1pi variations for δP_T .

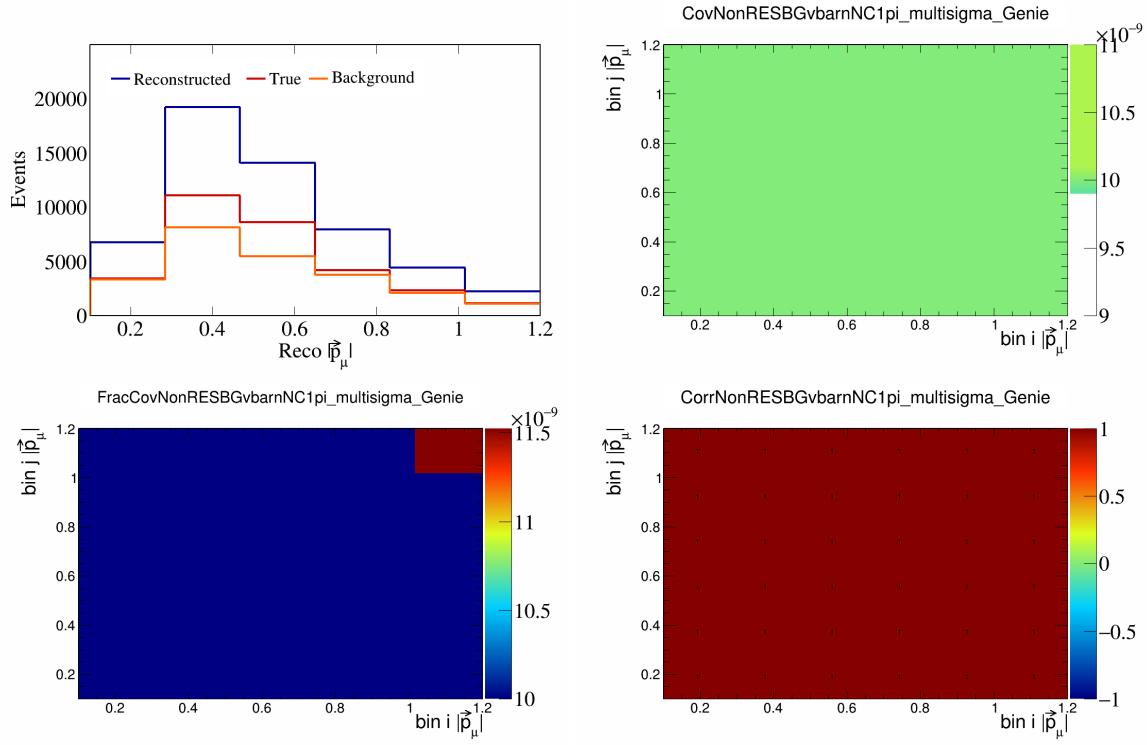


Figure 393: NonRESBGvbarNC1pi variations for $|\vec{p}_\mu|$.

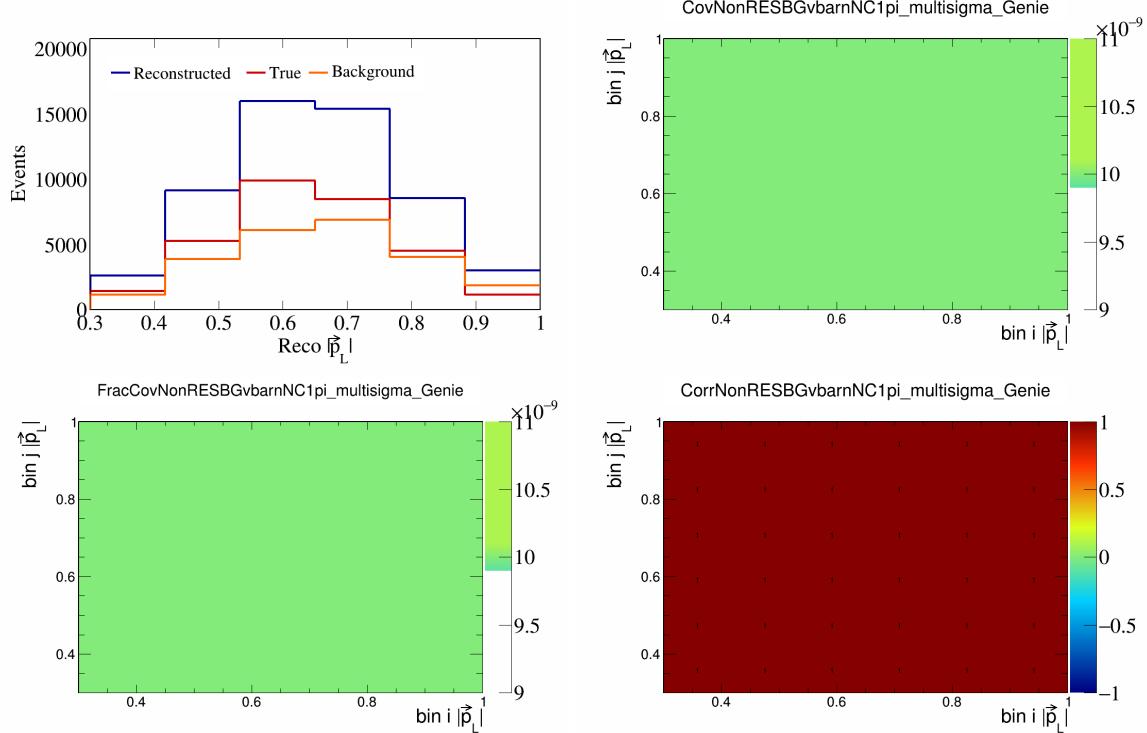


Figure 394: NonRESBGvbarNC1pi variations for $|\vec{p}_L|$.

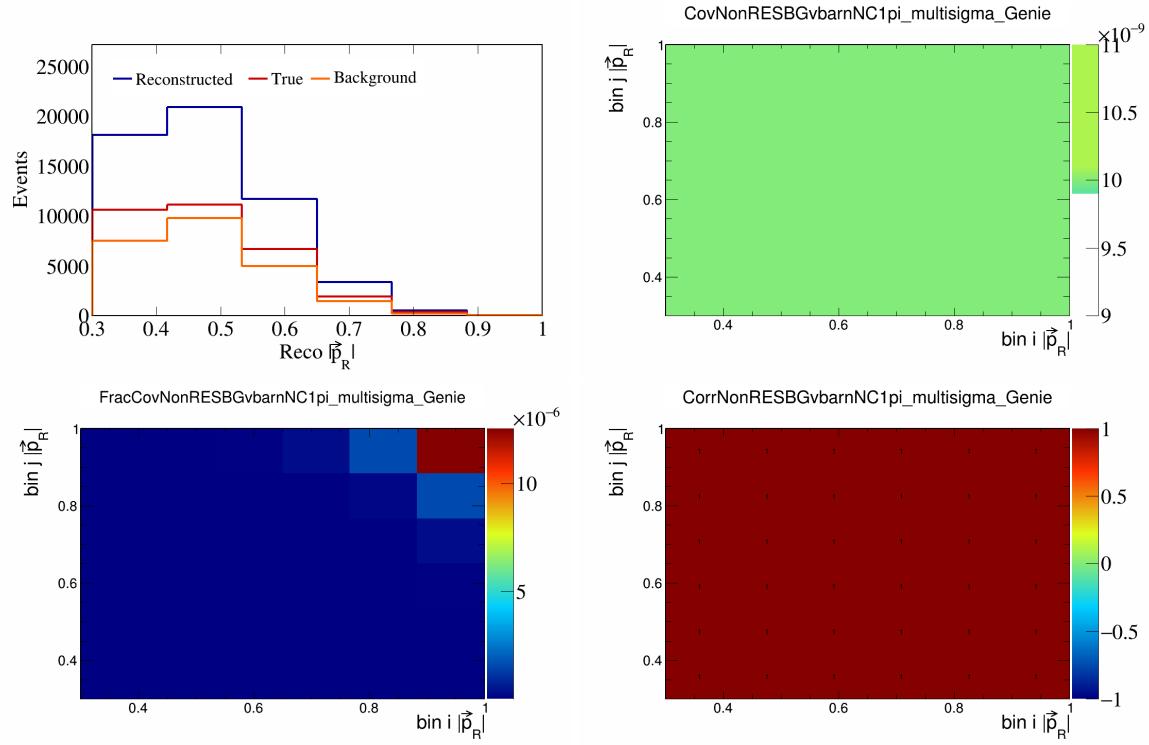


Figure 395: NonRESBGvbarNC1pi variations for $|\vec{p}_R|$.

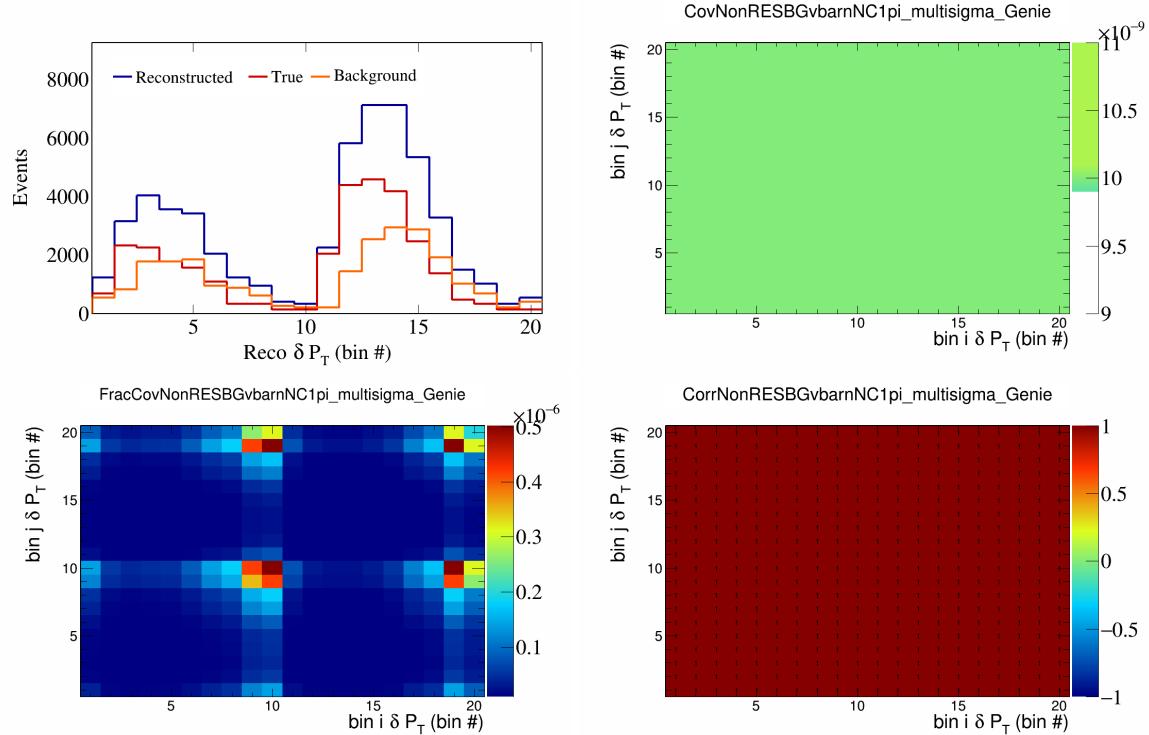


Figure 396: NonRESBGvbarNC1pi variations for δP_T in $\cos(\theta_{\vec{p}_\mu})$.

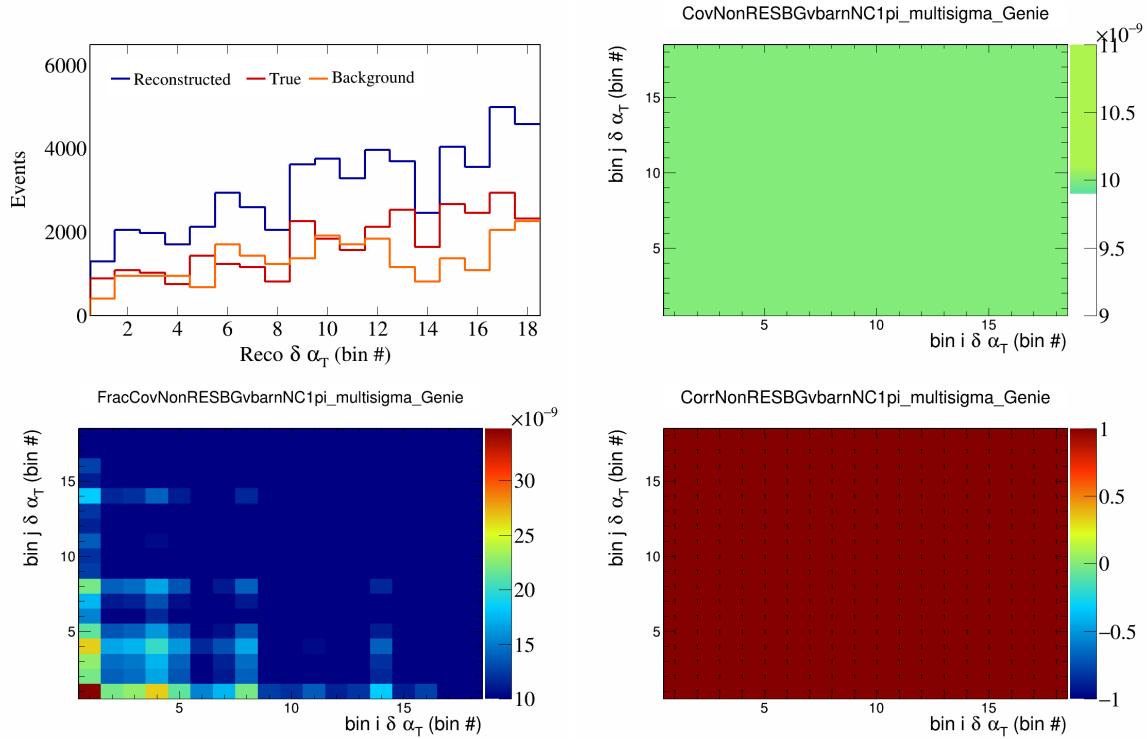


Figure 397: NonRESBGvbarNC1pi variations for $\delta\alpha_T$ in $\cos(\theta_{\vec{p}_\mu})$.

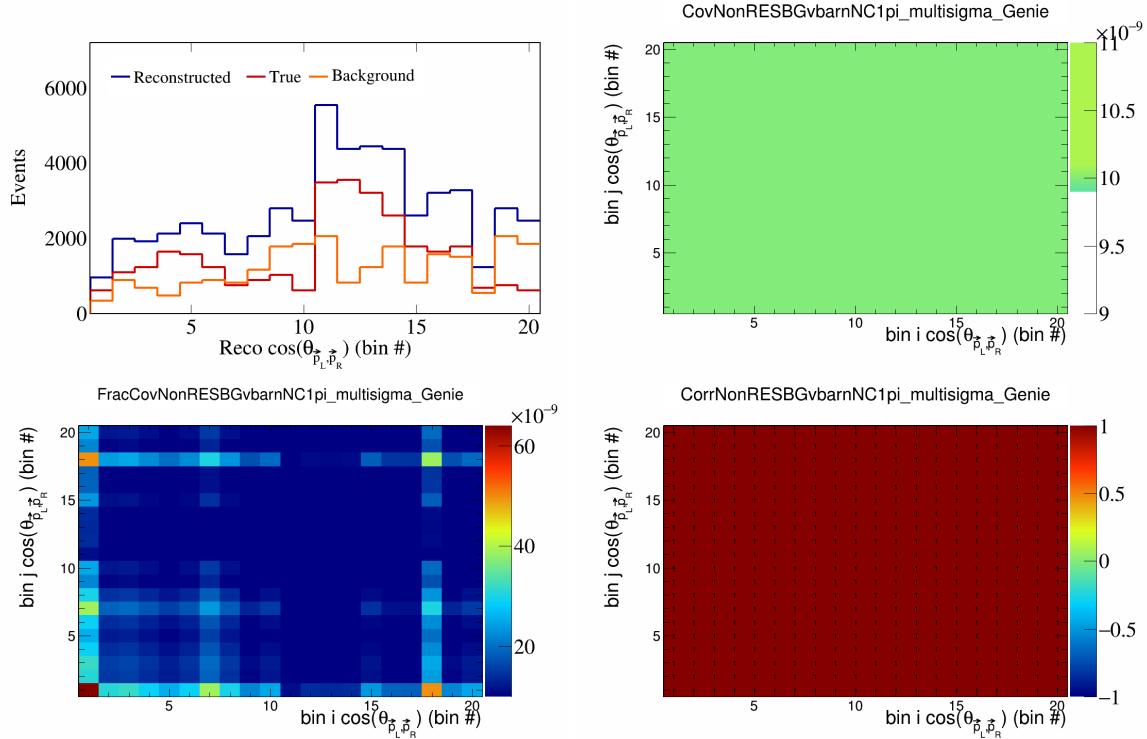


Figure 398: NonRESBGvbarNC1pi variations for $\cos(\theta_{\vec{p}_L, \vec{p}_R})$ in $\cos(\theta_{\vec{p}_\mu})$.

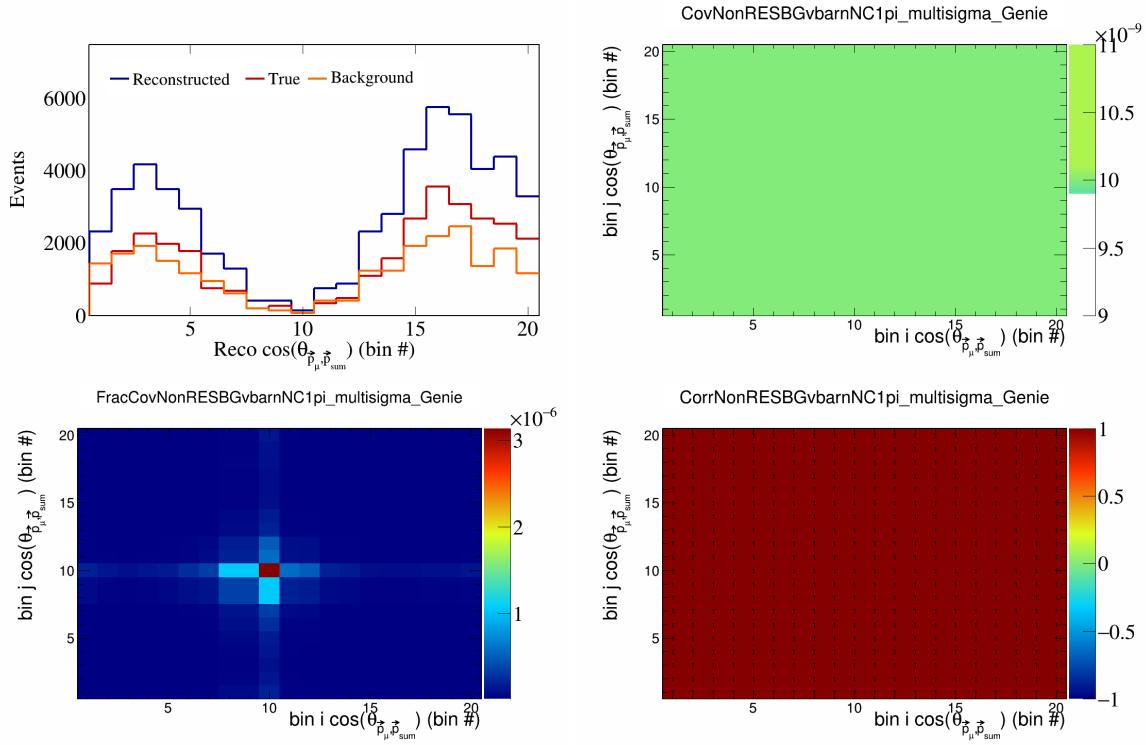


Figure 399: NonRESBGvbarNC1pi variations for $\cos(\theta_{\vec{p}_\mu, \vec{p}_{\text{sum}}})$ in $\cos(\theta_{\vec{p}_\mu})$.

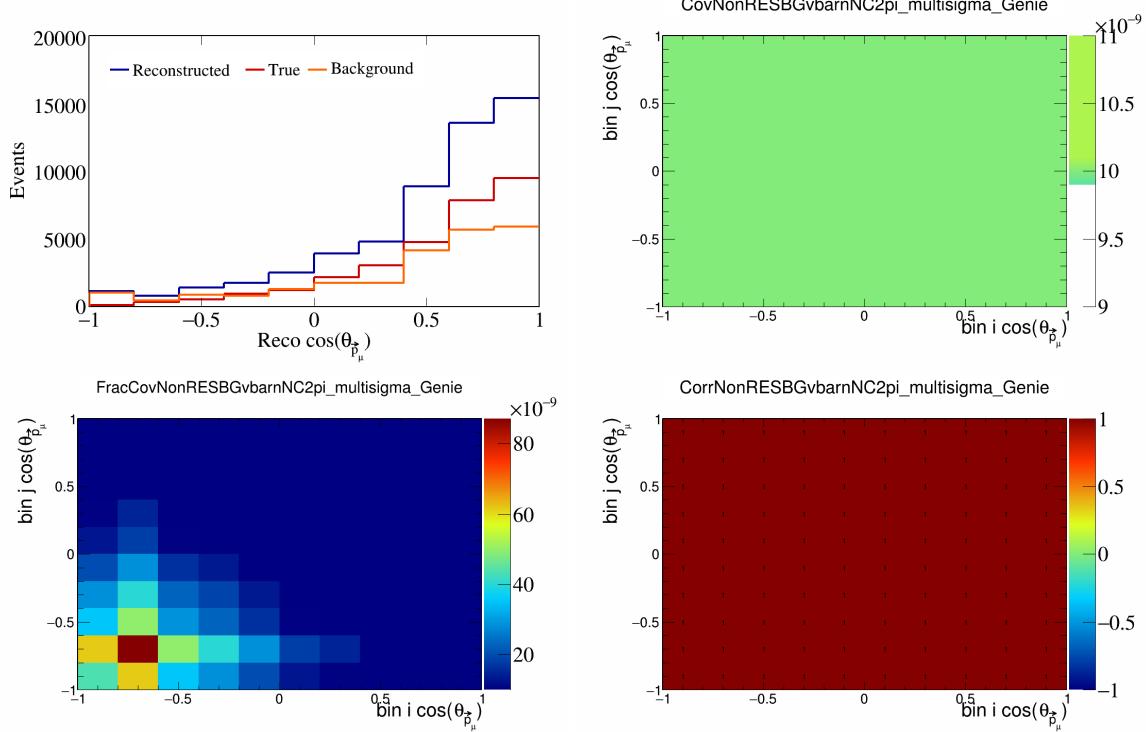


Figure 400: NonRESBGvbarNC2pi variations for $\cos(\theta_{\vec{p}_\mu})$.

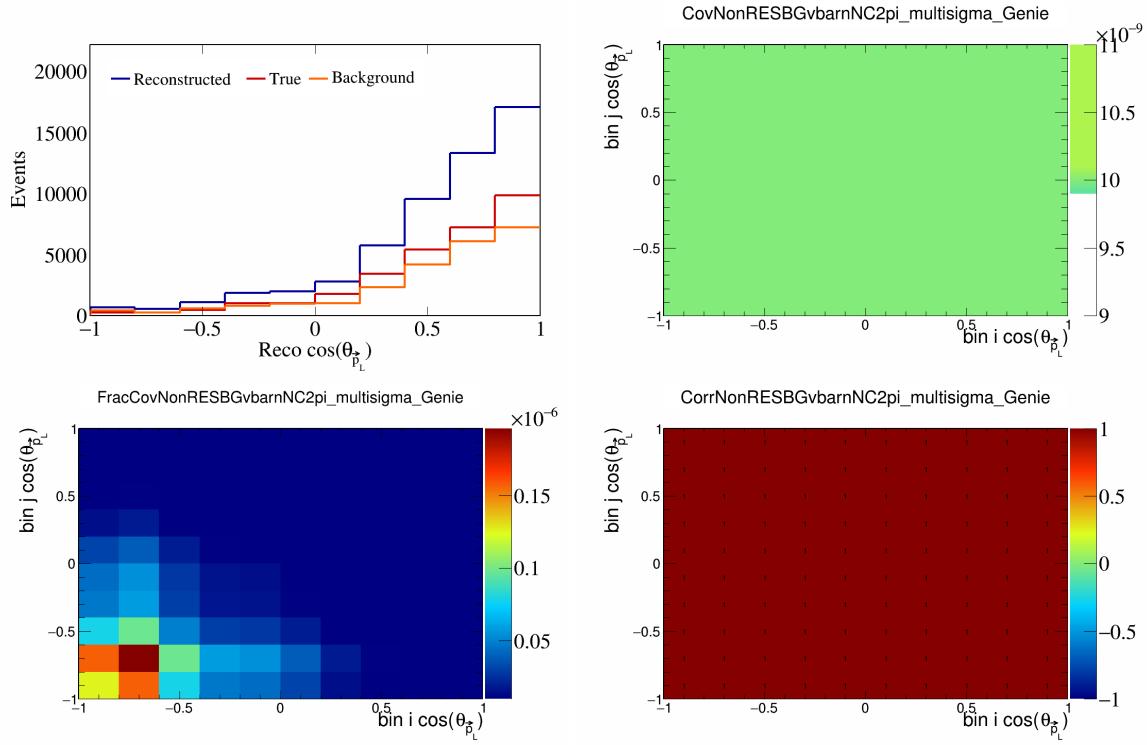


Figure 401: NonRESBGvbarNC2pi variations for $\cos(\theta_{\vec{p}_L})$.

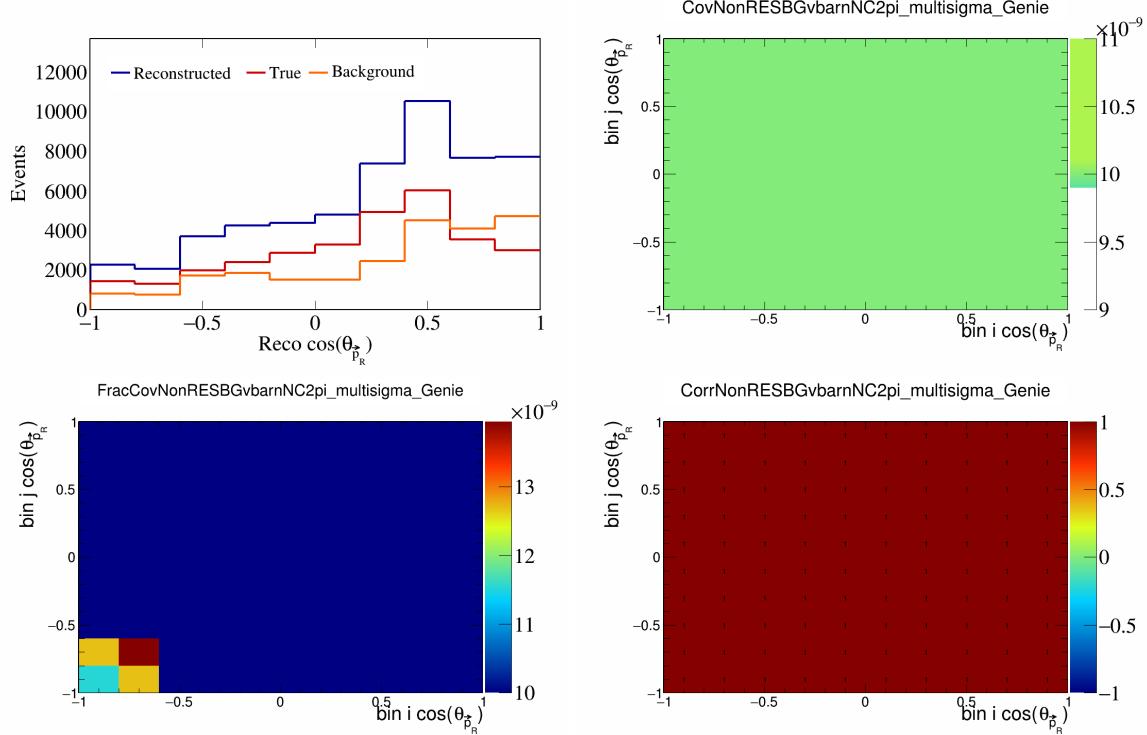


Figure 402: NonRESBGvbarNC2pi variations for $\cos(\theta_{\vec{p}_R})$.

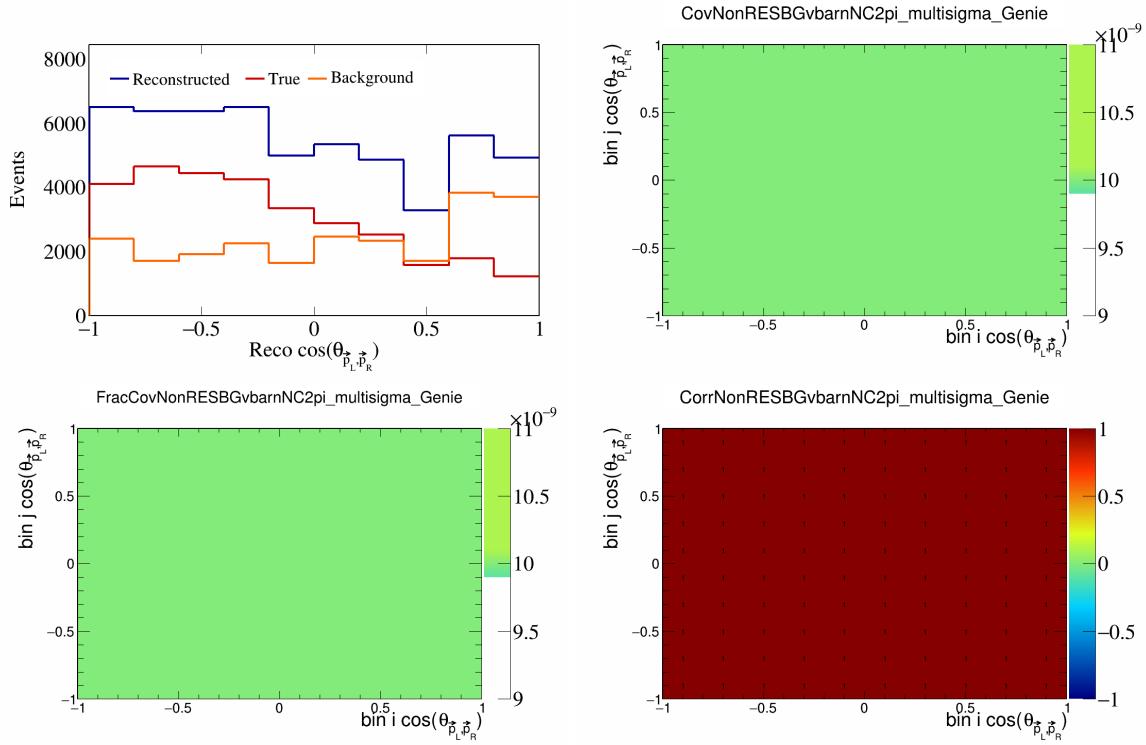


Figure 403: NonRESBGvbarNC2pi variations for $\cos(\theta_{\vec{p}_L, \vec{p}_R})$.

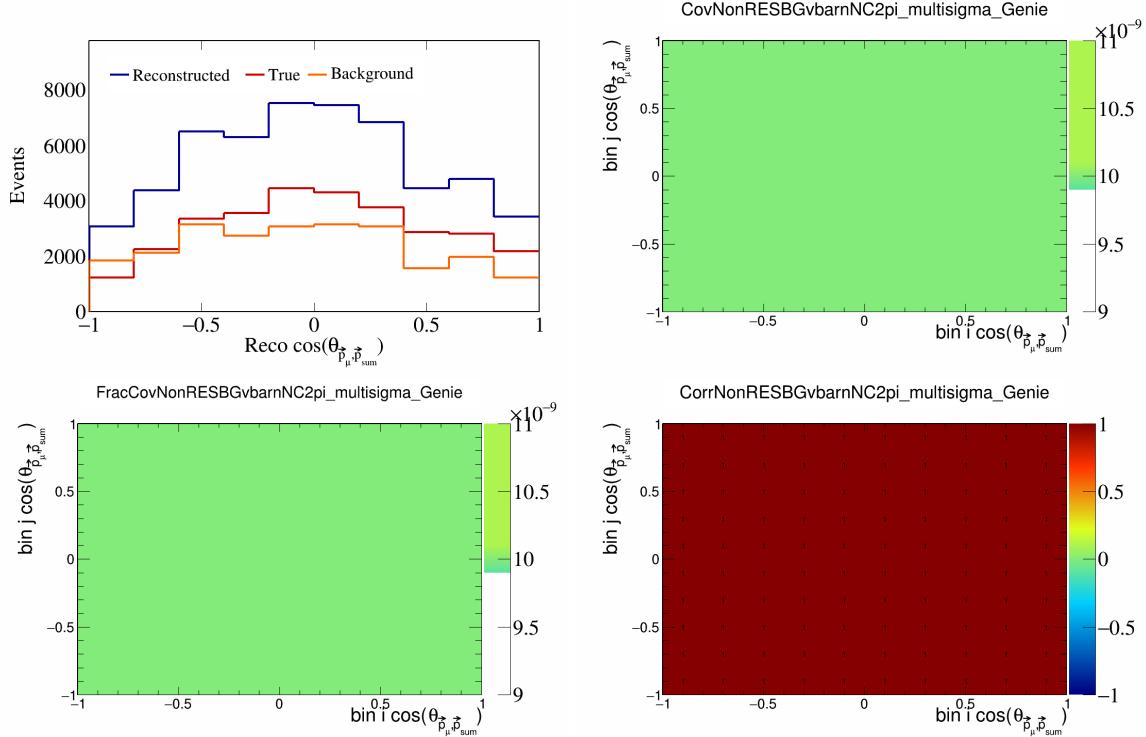


Figure 404: NonRESBGvbarNC2pi variations for $\cos(\theta_{\vec{p}_\mu, \vec{p}_{\text{sum}}})$.

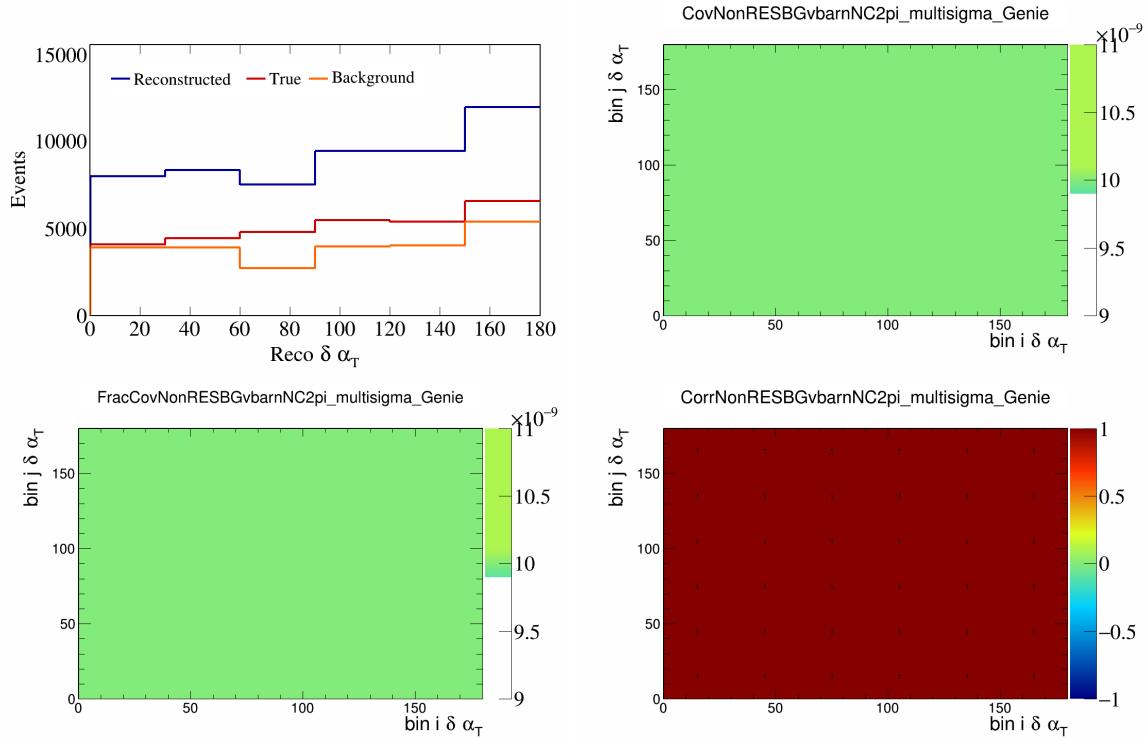


Figure 405: NonRESBGvbarNC2pi variations for $\delta\alpha_T$.

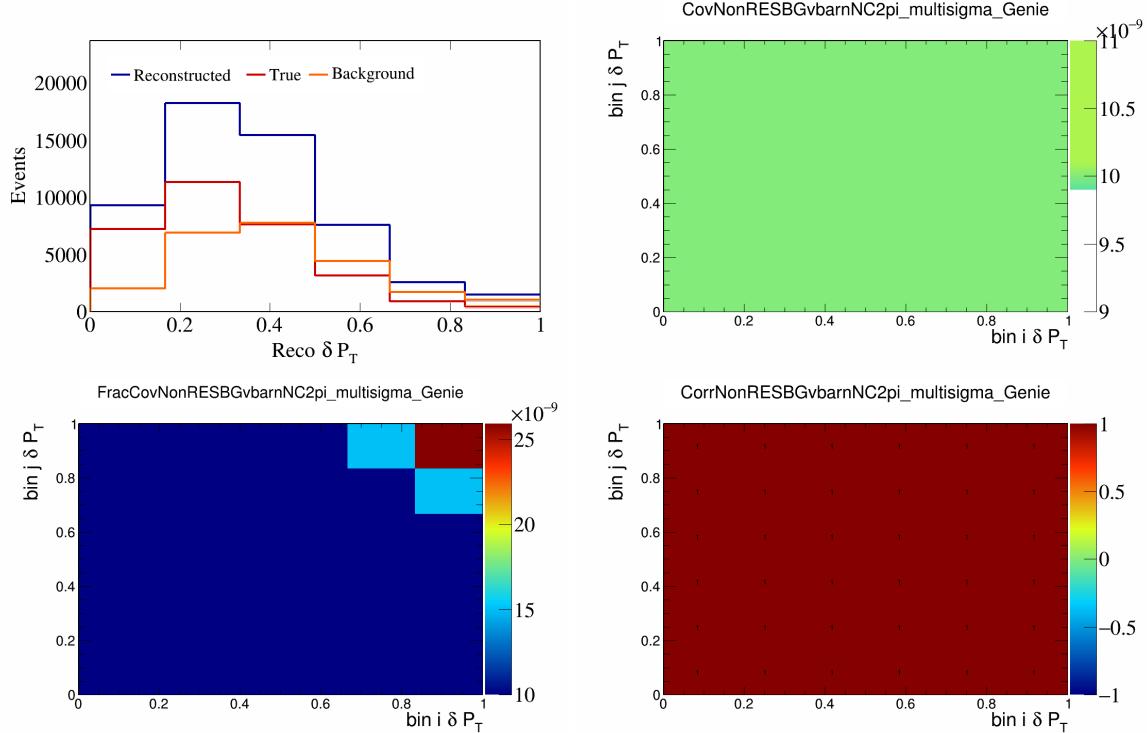


Figure 406: NonRESBGvbarNC2pi variations for δP_T .

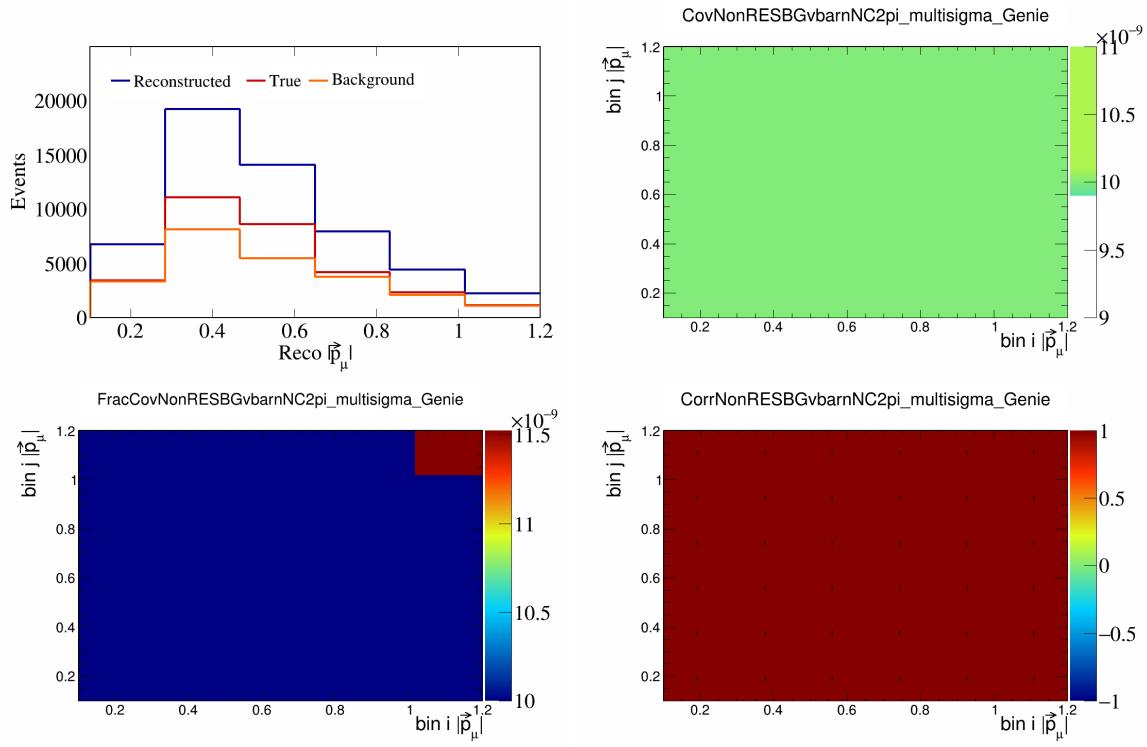


Figure 407: NonRESBGvbarNC2pi variations for $|\vec{p}_\mu|$.

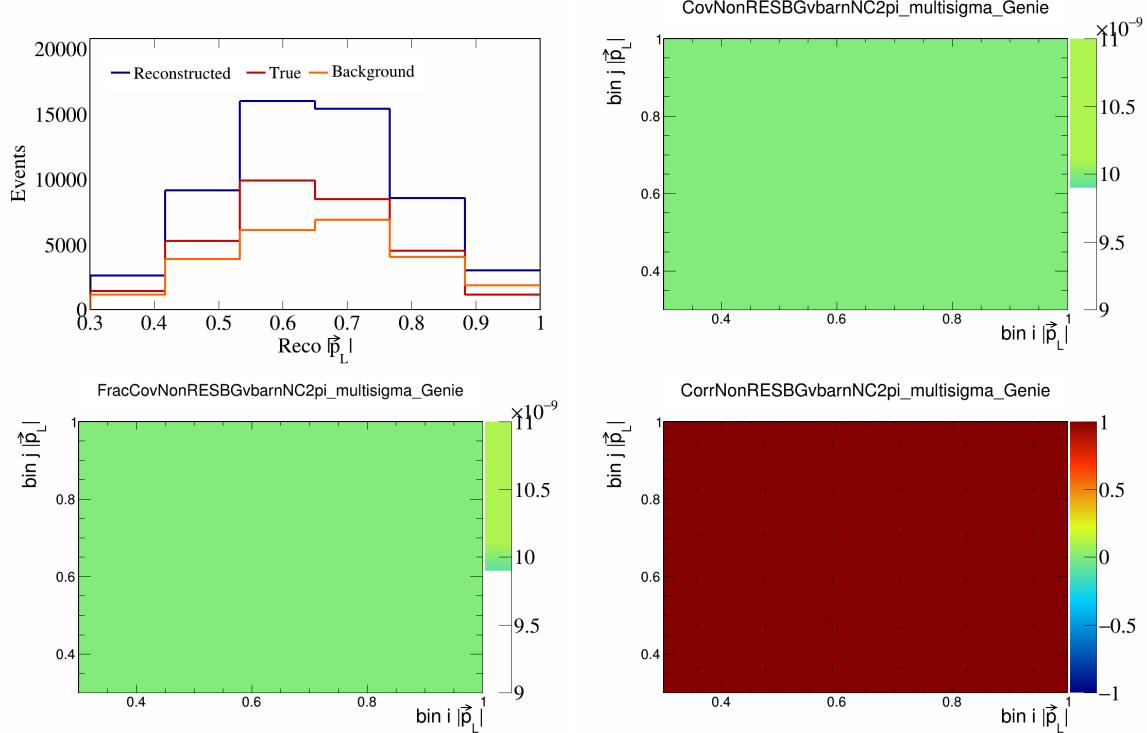


Figure 408: NonRESBGvbarNC2pi variations for $|\vec{p}_L|$.

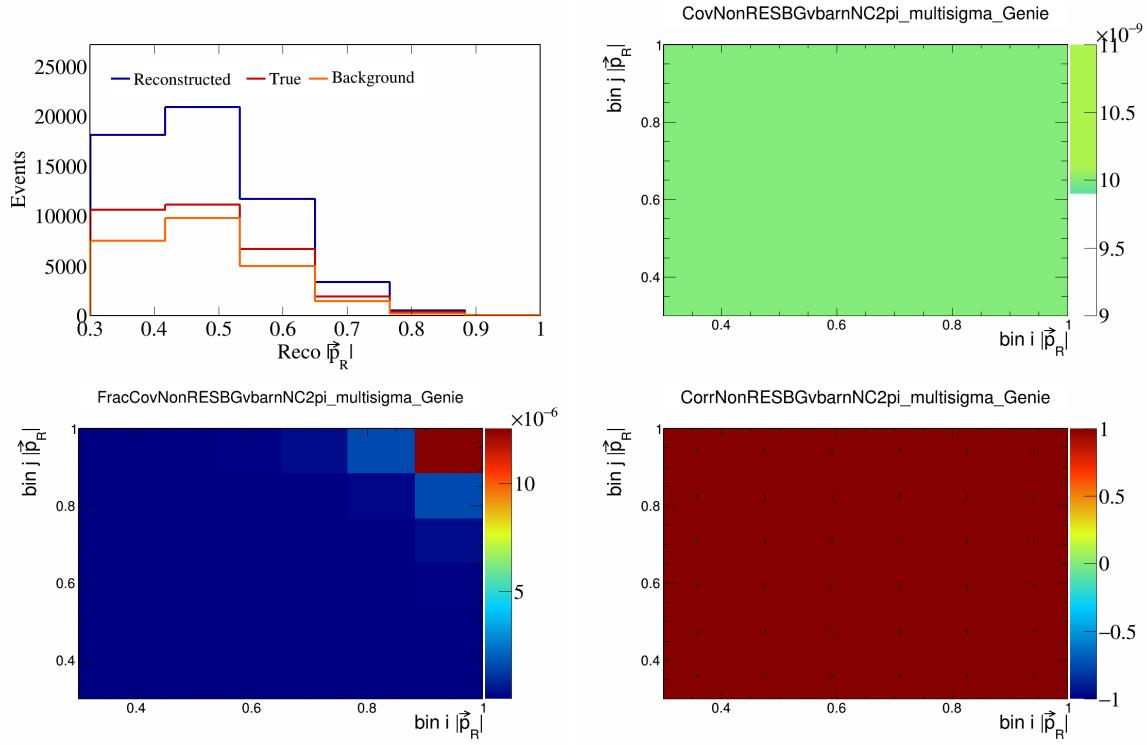


Figure 409: NonRESBGvbarNC2pi variations for $|\vec{p}_R|$.

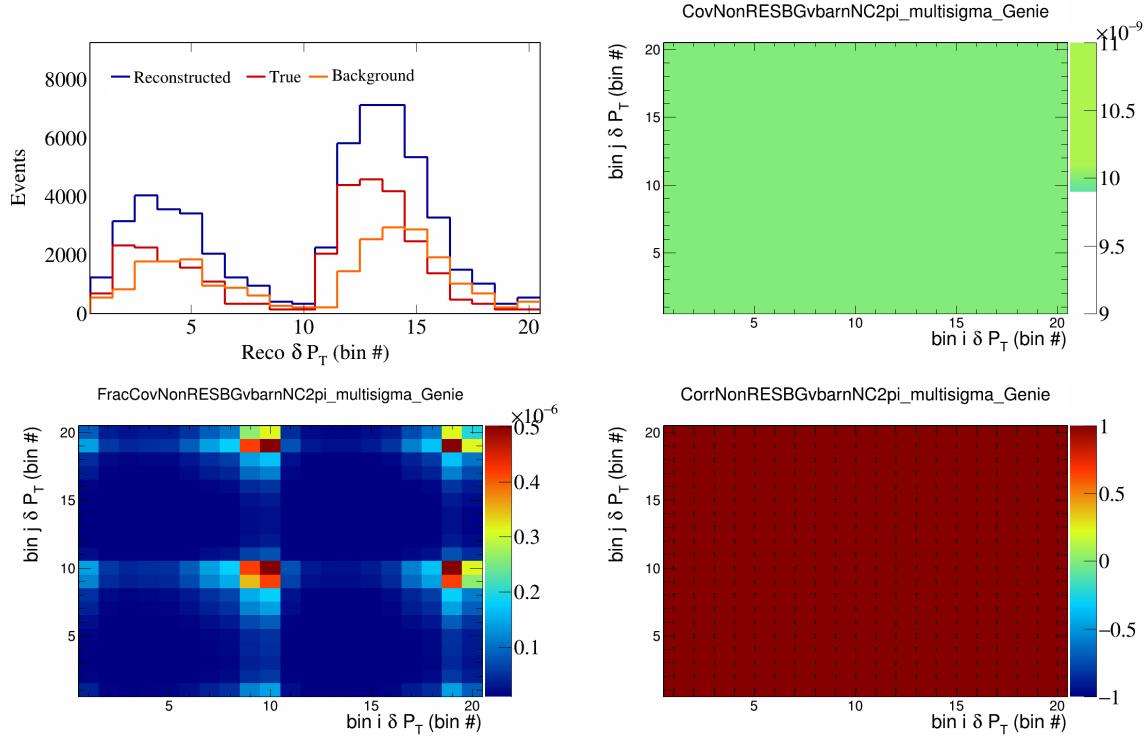


Figure 410: NonRESBGvbarNC2pi variations for δP_T in $\cos(\theta_{\vec{p}_\mu})$.

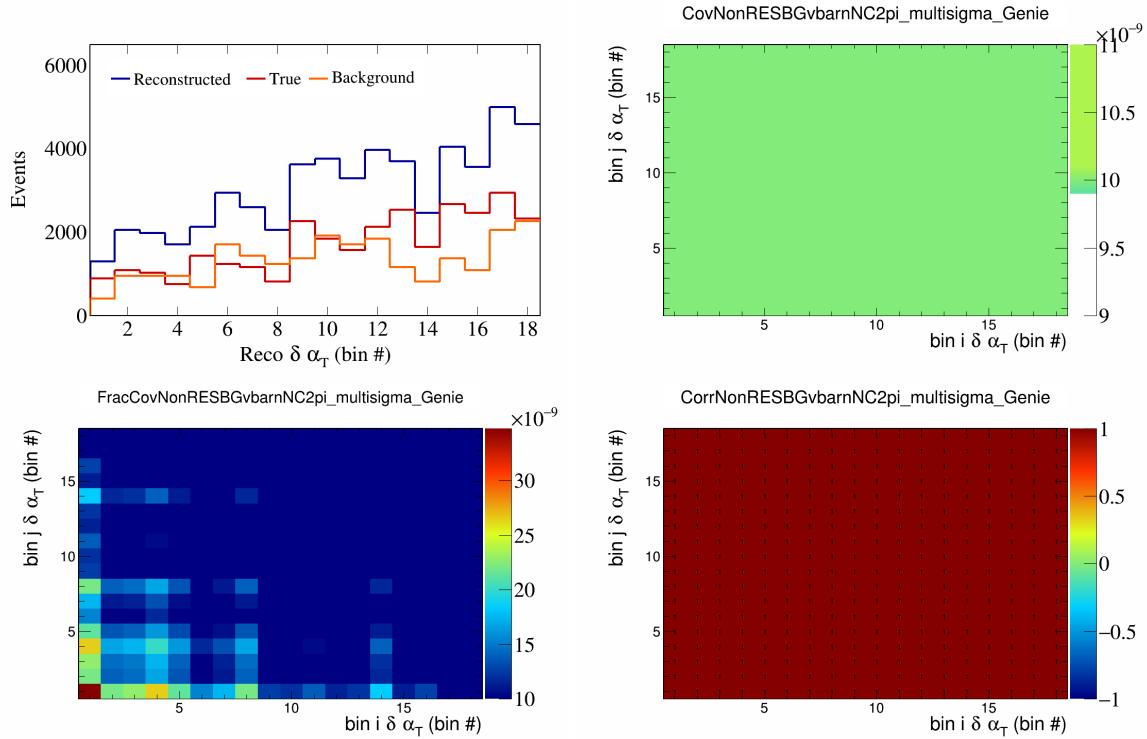


Figure 411: NonRESBGvbarNC2pi variations for $\delta\alpha_T$ in $\cos(\theta_{\vec{p}_\mu})$.

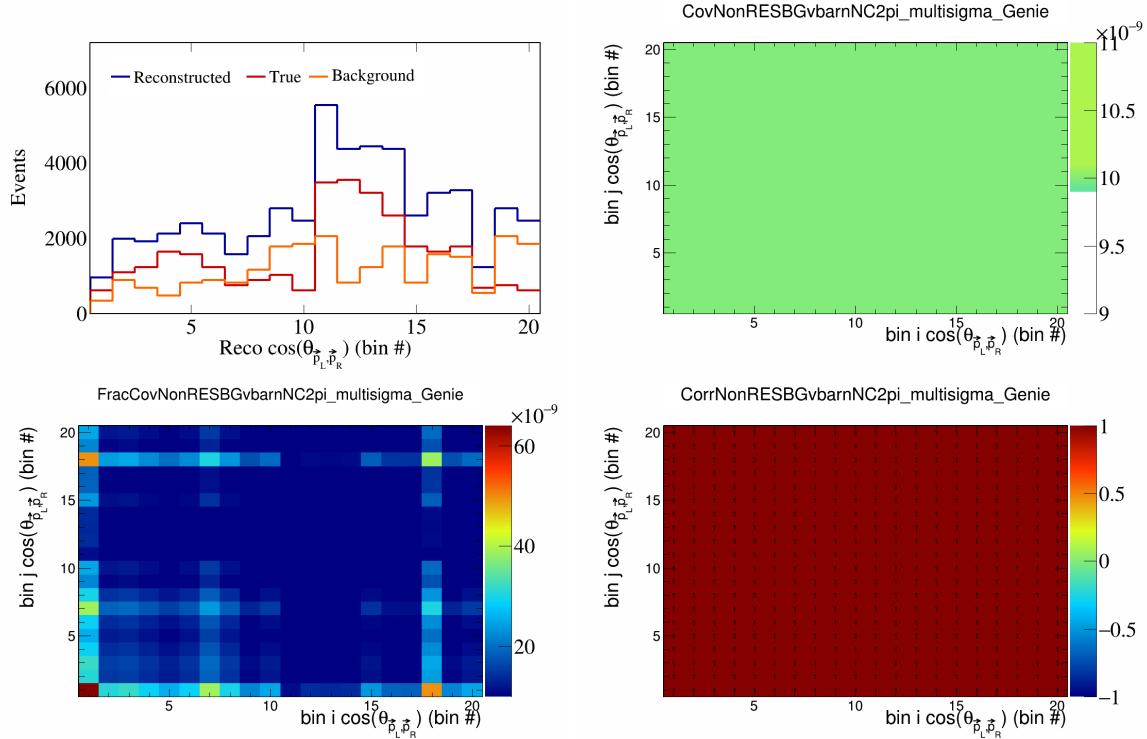


Figure 412: NonRESBGvbarNC2pi variations for $\cos(\theta_{\vec{p}_L, \vec{p}_R})$ in $\cos(\theta_{\vec{p}_\mu})$.

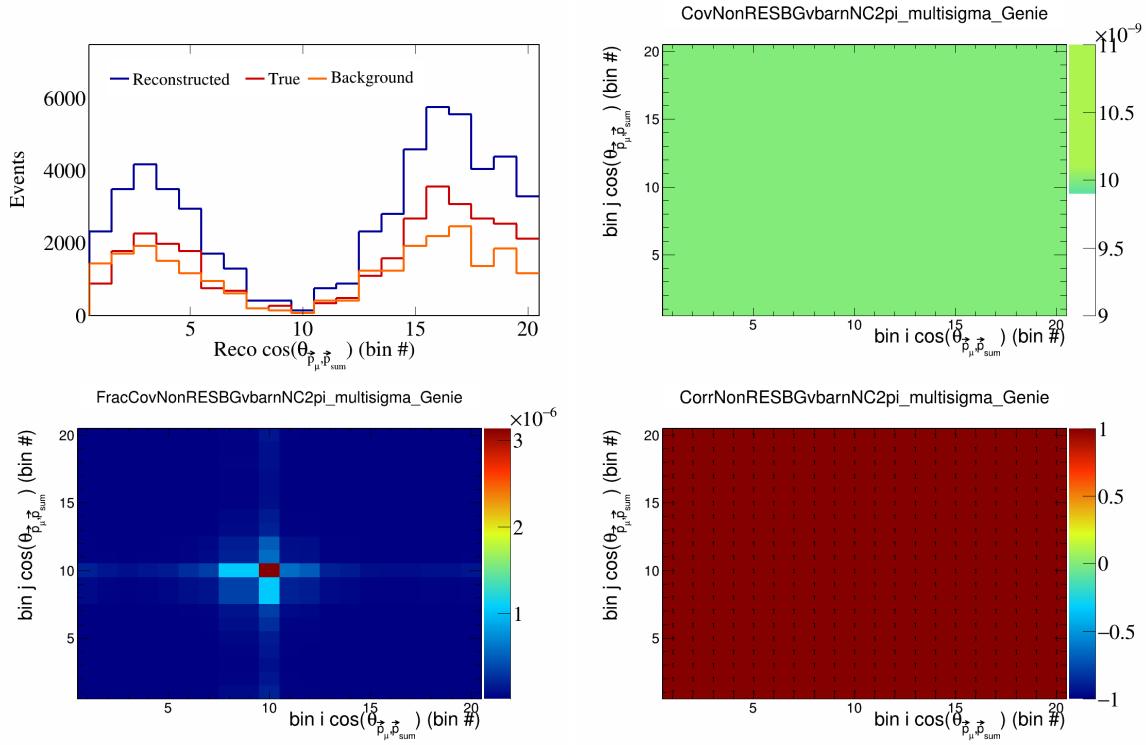


Figure 413: NonRESBGvbarNC2pi variations for $\cos(\theta_{\vec{p}_\mu, \vec{p}_{\text{sum}}})$ in $\cos(\theta_{\vec{p}_\mu})$.

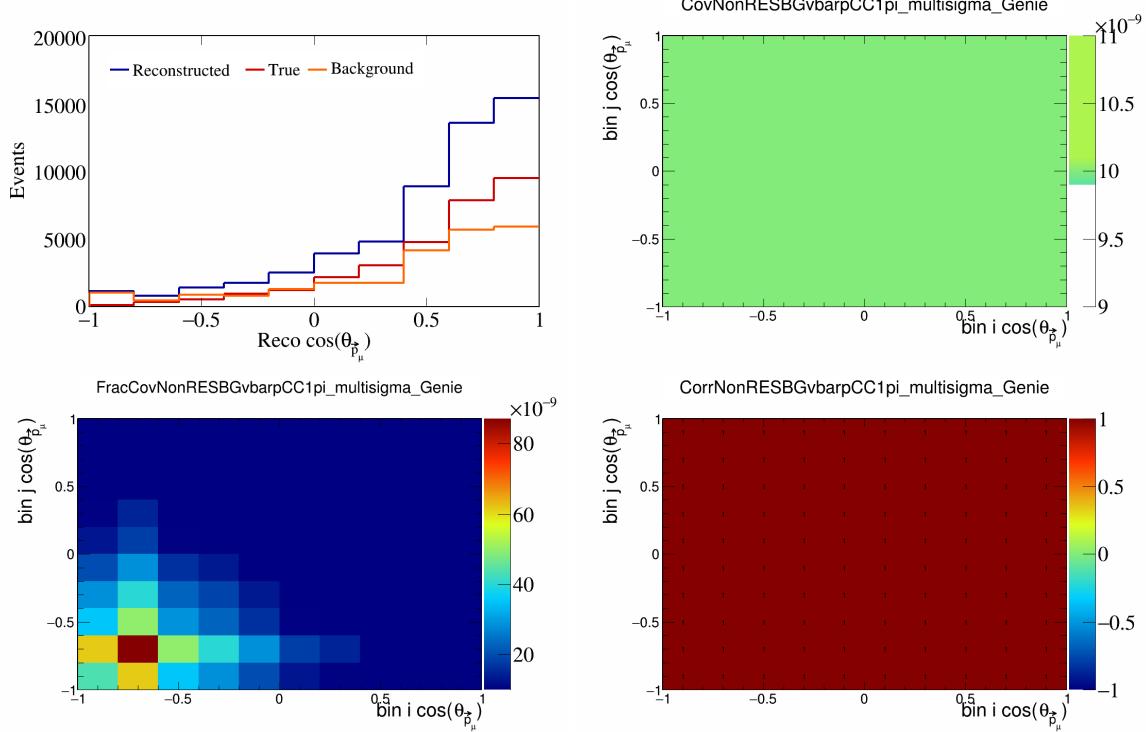


Figure 414: NonRESBGvbarCC1pi variations for $\cos(\theta_{\vec{p}_\mu})$.

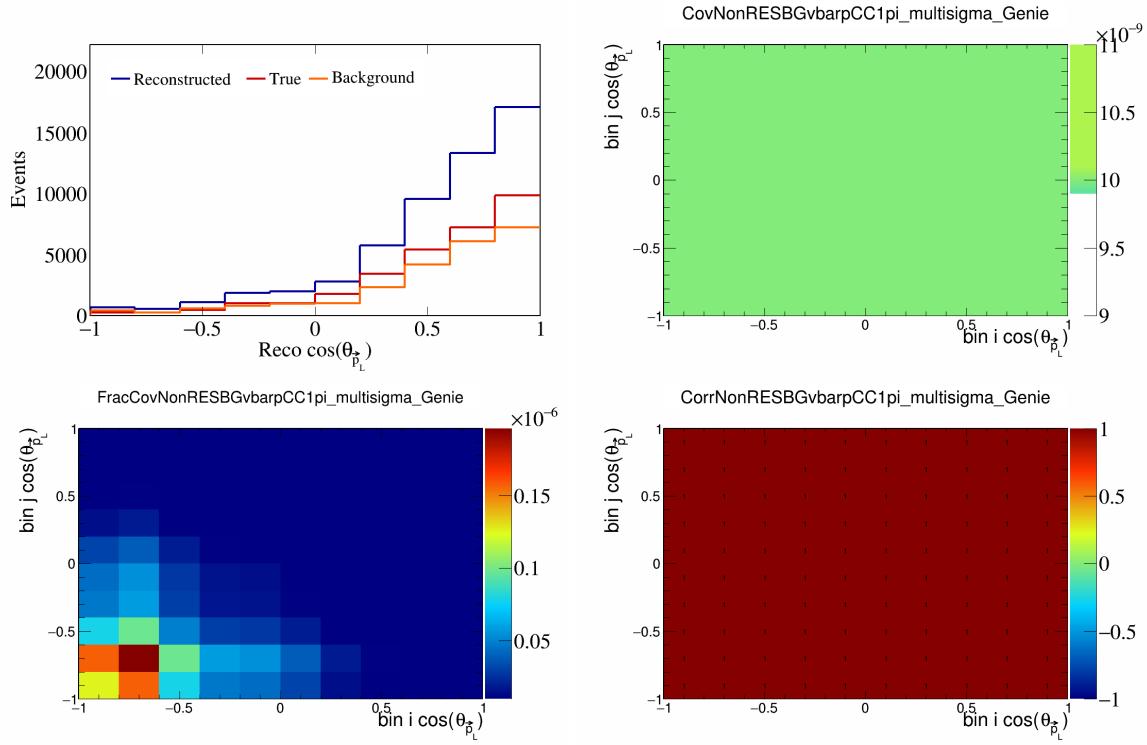


Figure 415: NonRESBGvbarpCC1pi variations for $\cos(\theta_{\vec{p}_L})$.

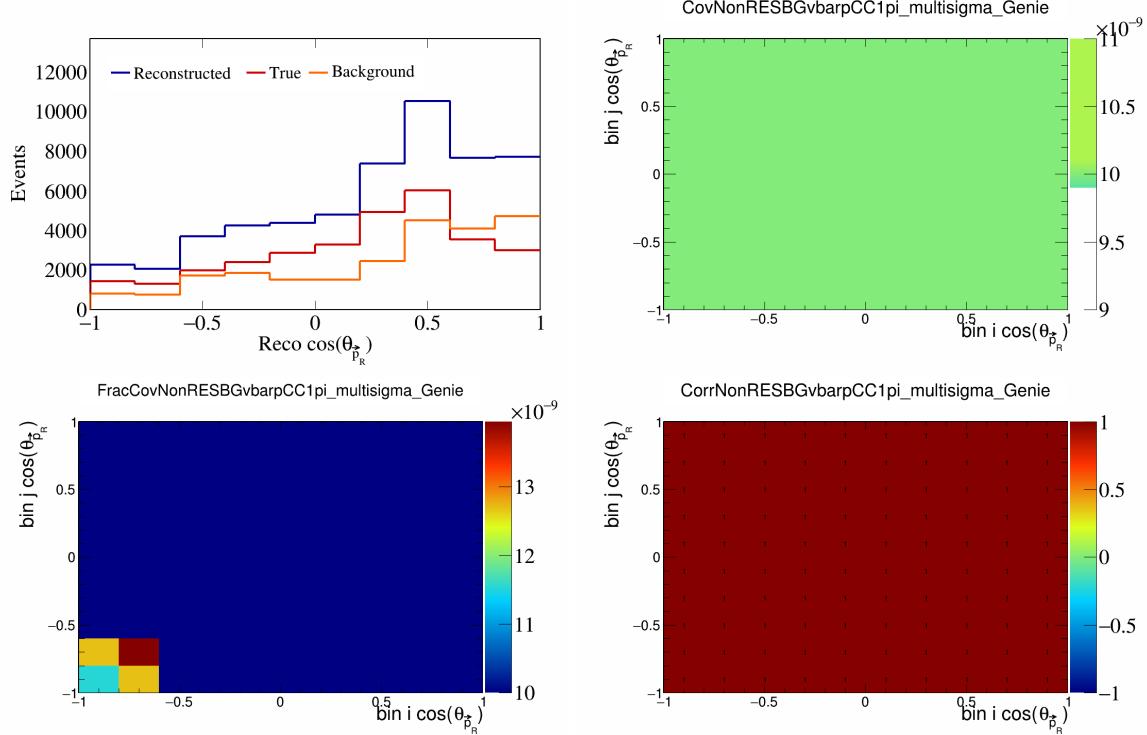


Figure 416: NonRESBGvbarpCC1pi variations for $\cos(\theta_{\vec{p}_R})$.

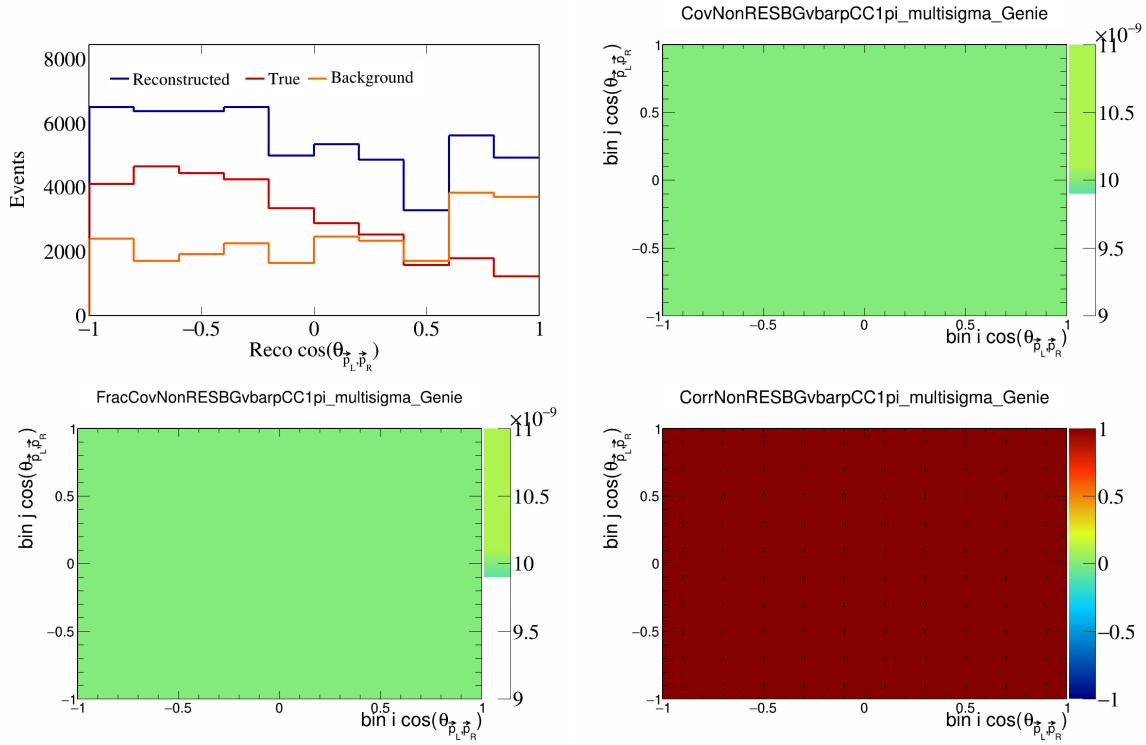


Figure 417: NonRESBGvbarpCC1pi variations for $\cos(\theta_{\vec{p}_L, \vec{p}_R})$.

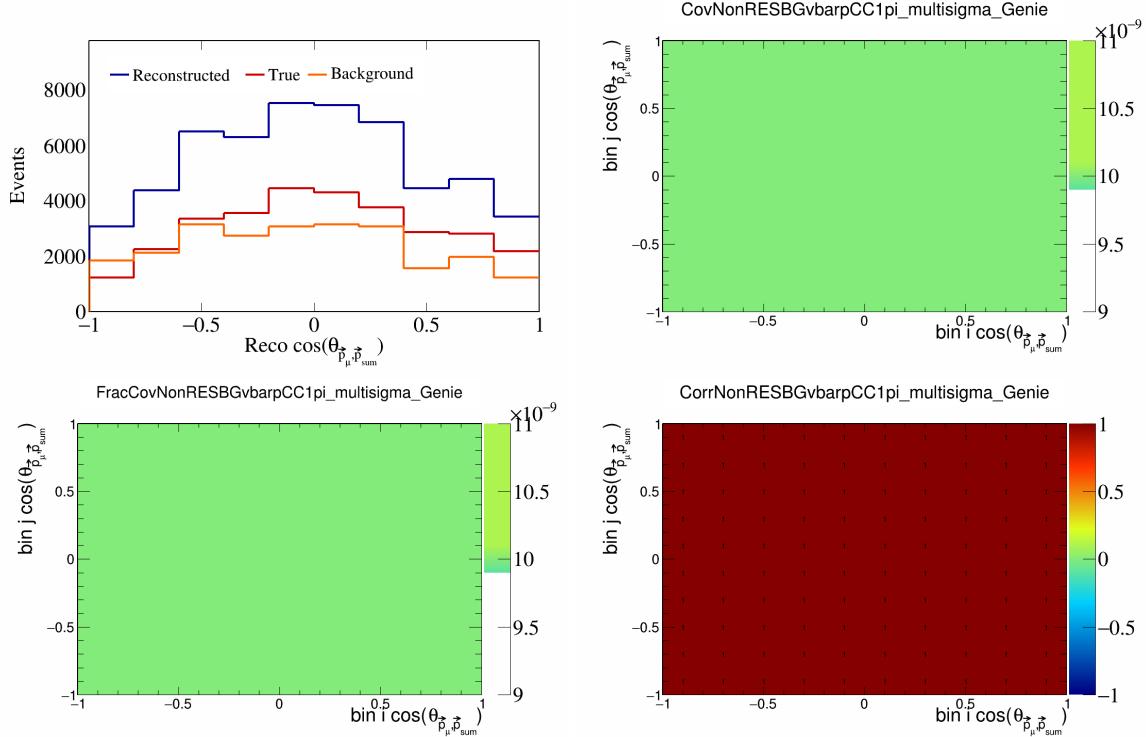


Figure 418: NonRESBGvbarpCC1pi variations for $\cos(\theta_{\vec{p}_\mu, \vec{p}_{\text{sum}}})$.

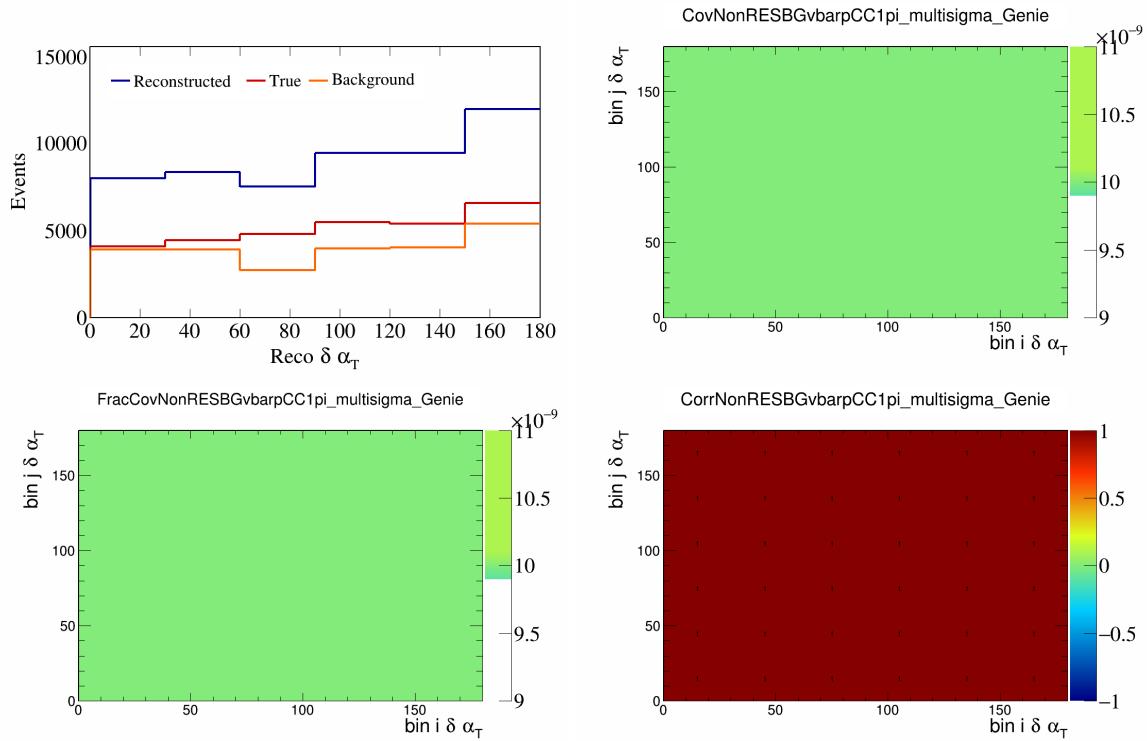


Figure 419: NonRESBGvbarpCC1pi variations for $\delta\alpha_T$.

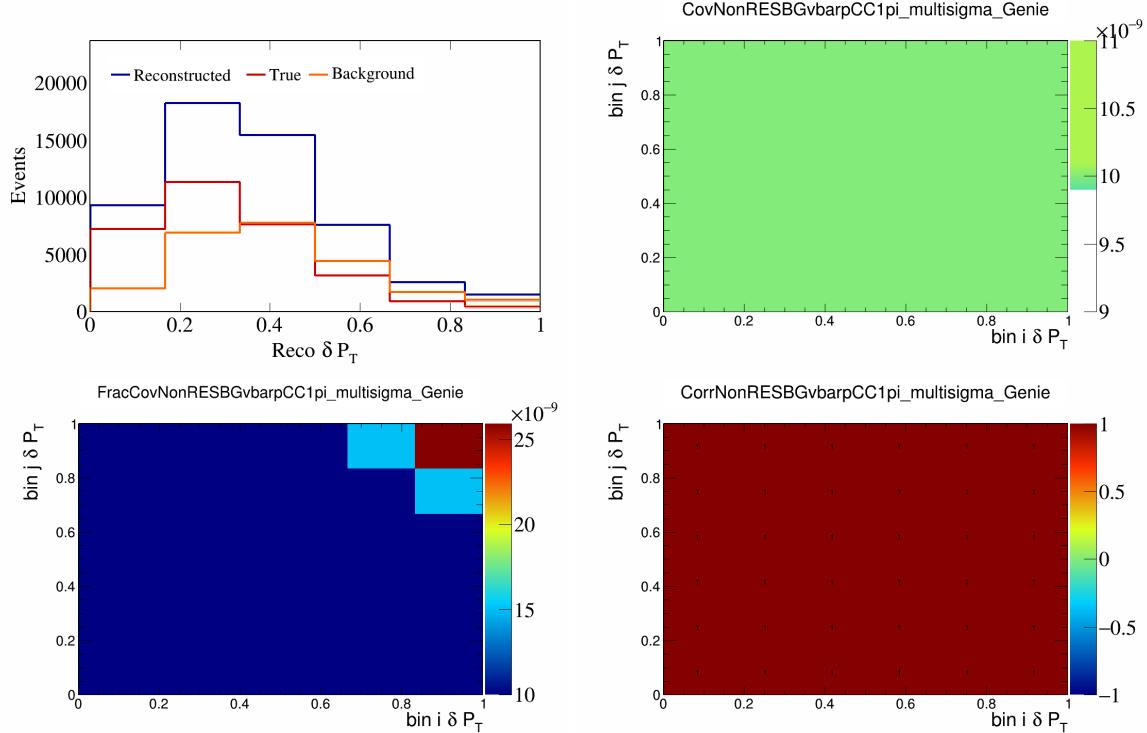


Figure 420: NonRESBGvbarpCC1pi variations for δP_T .

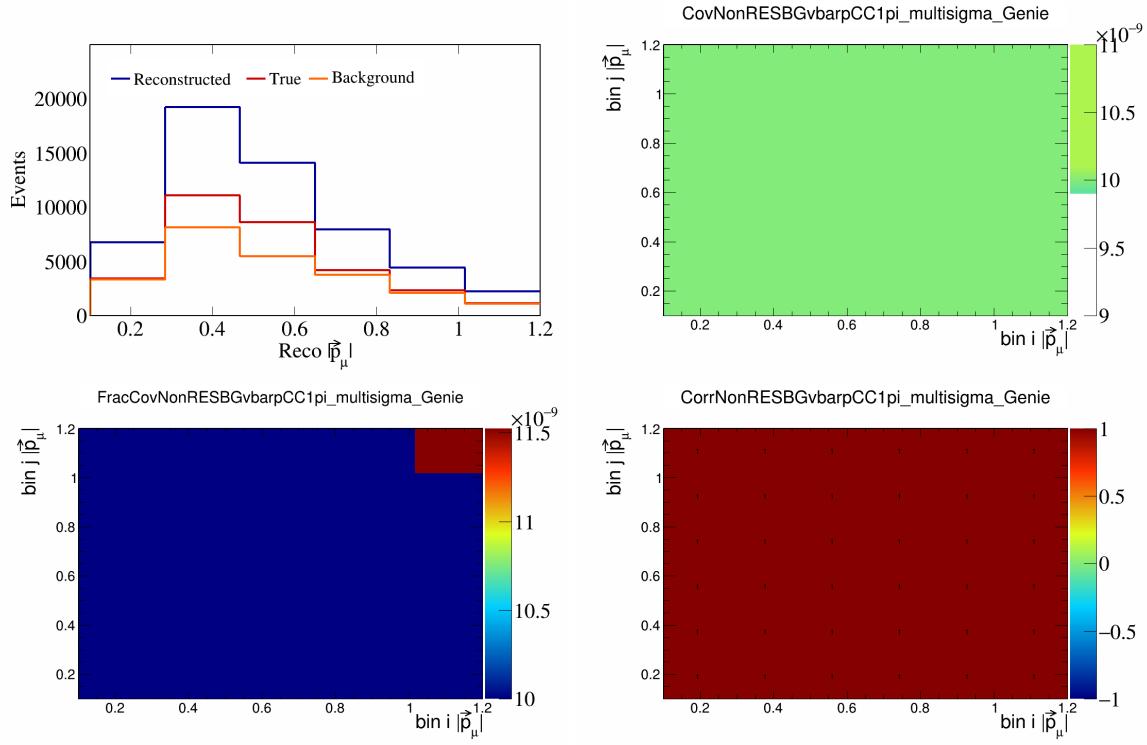


Figure 421: NonRESBGvbarpCC1pi variations for $|\vec{p}_\mu|$.

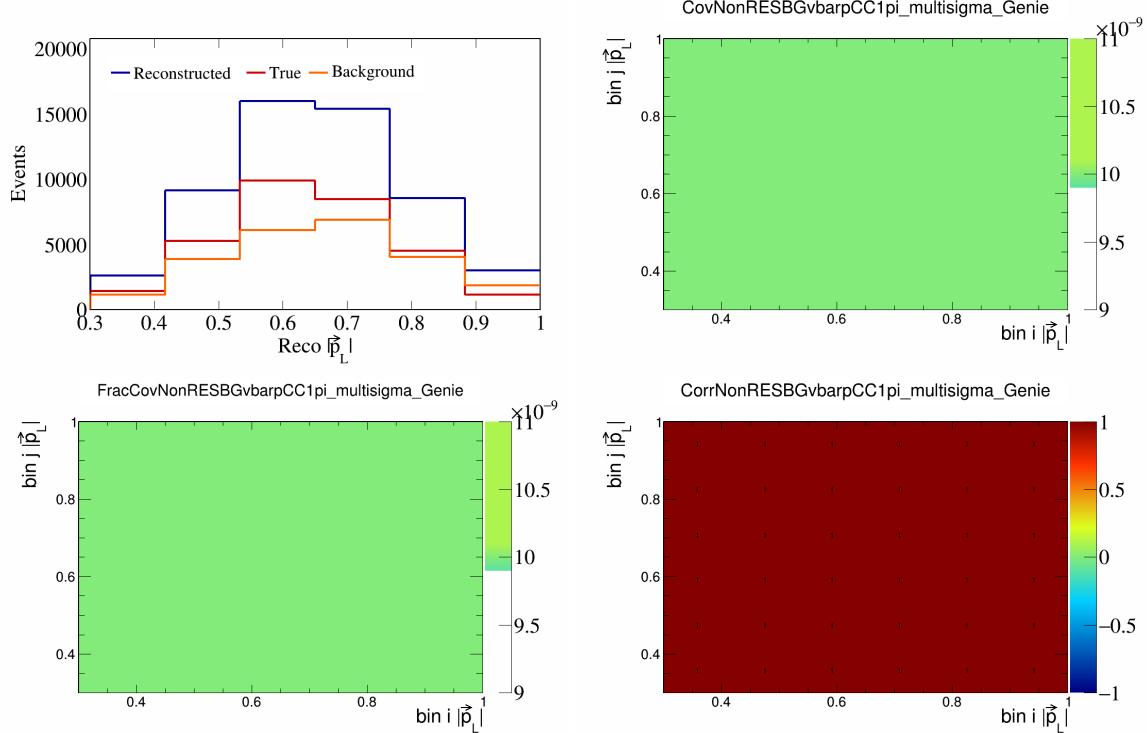


Figure 422: NonRESBGvbarpCC1pi variations for $|\vec{p}_L|$.

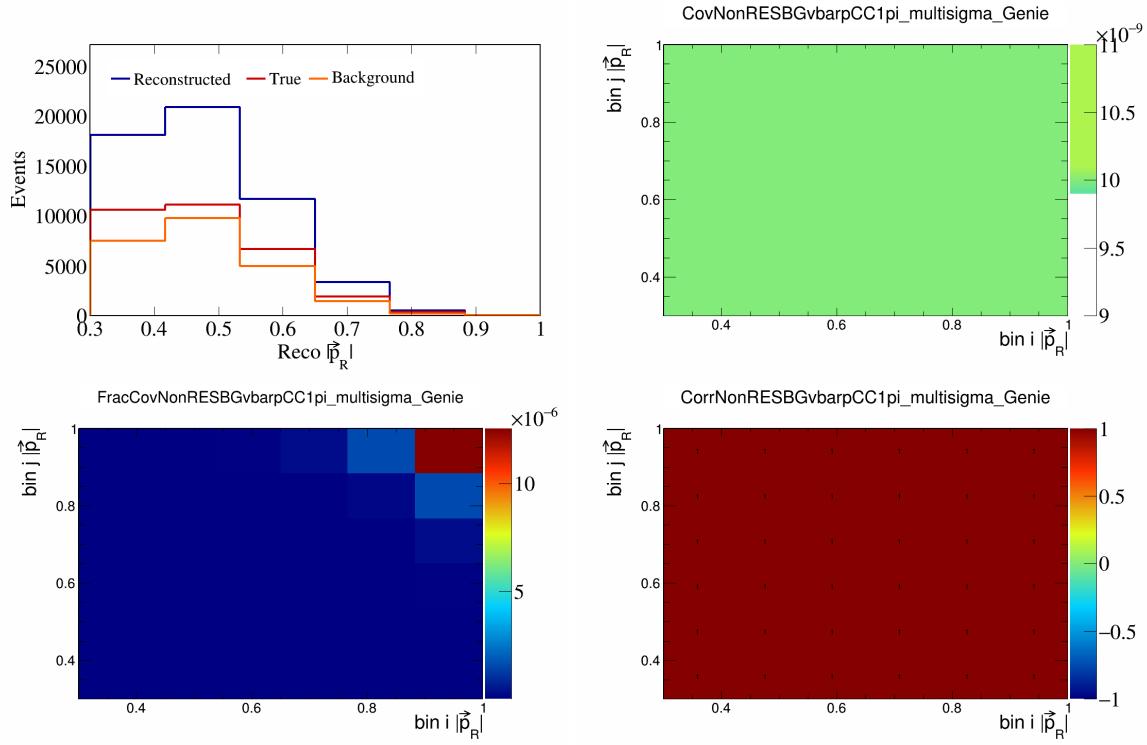


Figure 423: NonRESBGvbarpCC1pi variations for $|\vec{p}_R|$.

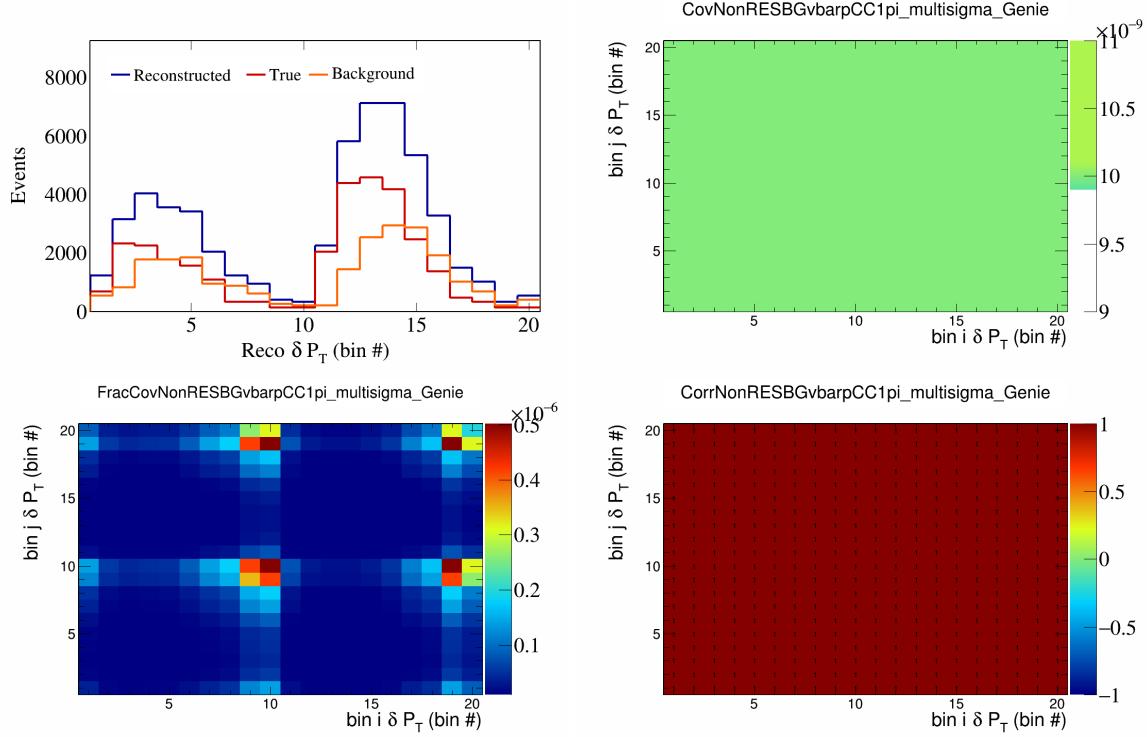


Figure 424: NonRESBGvbarpCC1pi variations for δP_T in $\cos(\theta_{\vec{p}_\mu})$.

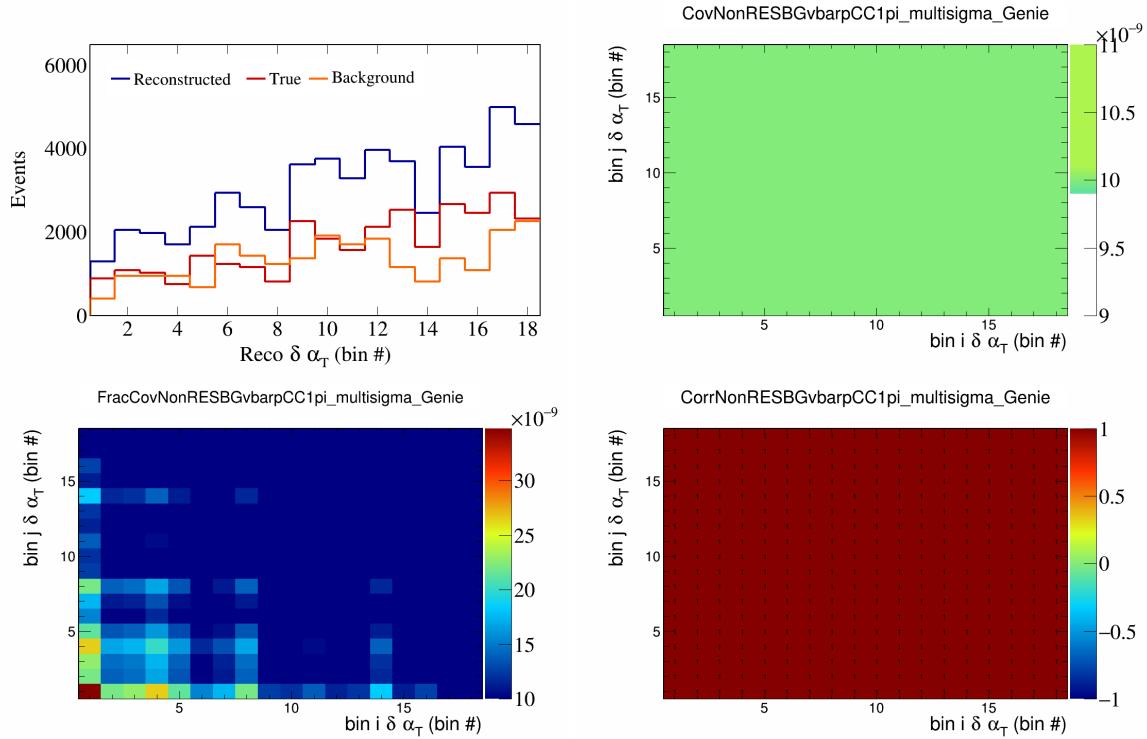


Figure 425: NonRESBGvbarpCC1pi variations for $\delta\alpha_T$ in $\cos(\theta_{\vec{p}_\mu})$.

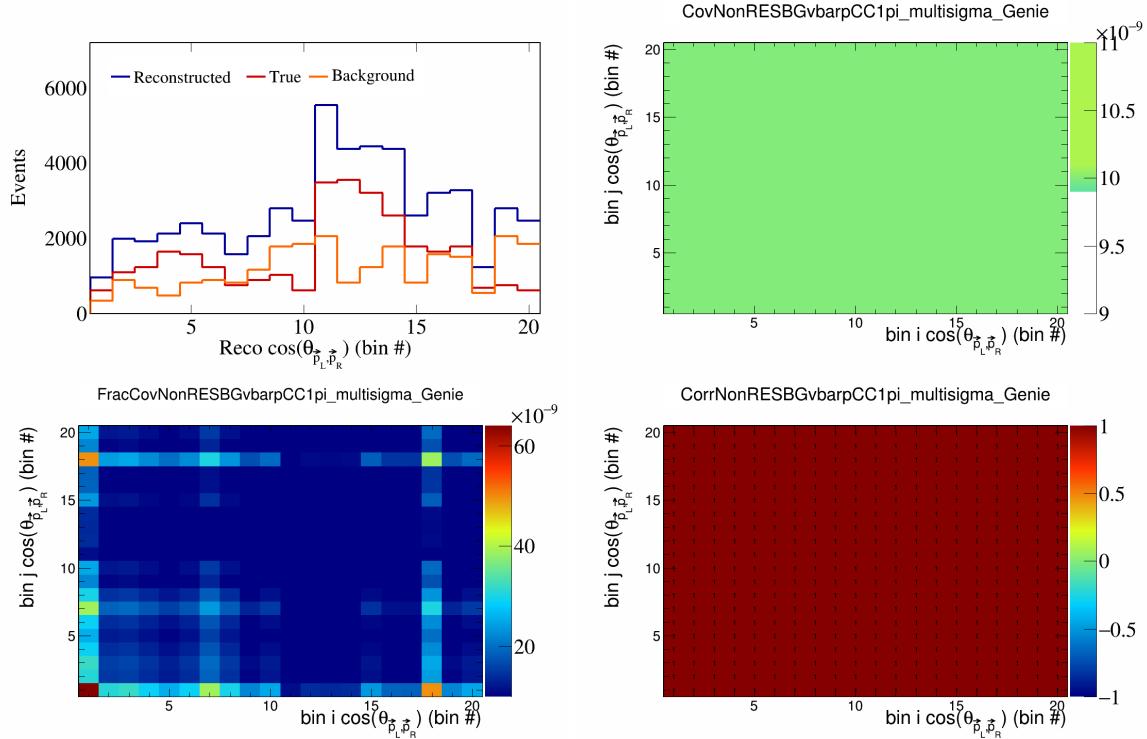


Figure 426: NonRESBGvbarpCC1pi variations for $\cos(\theta_{\vec{p}_L, \vec{p}_R})$ in $\cos(\theta_{\vec{p}_\mu})$.

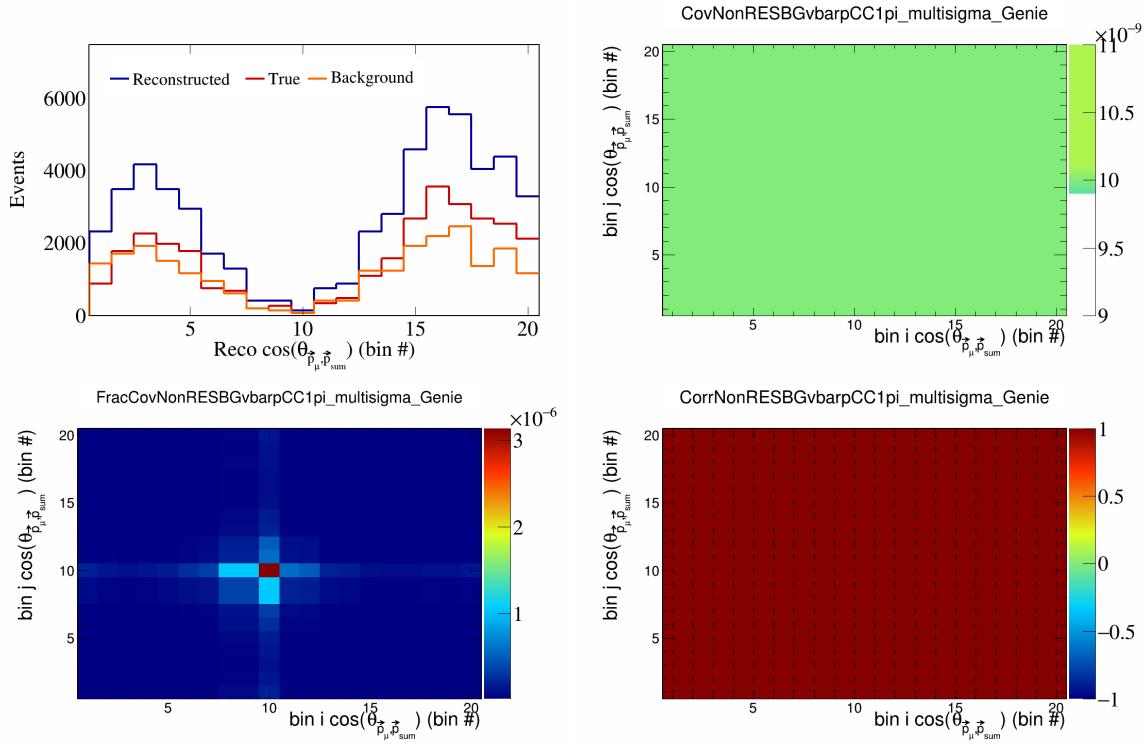


Figure 427: NonRESBGvbarpCC1pi variations for $\cos(\theta_{\vec{p}_\mu})$ in $\cos(\theta_{\vec{p}_\mu})$.

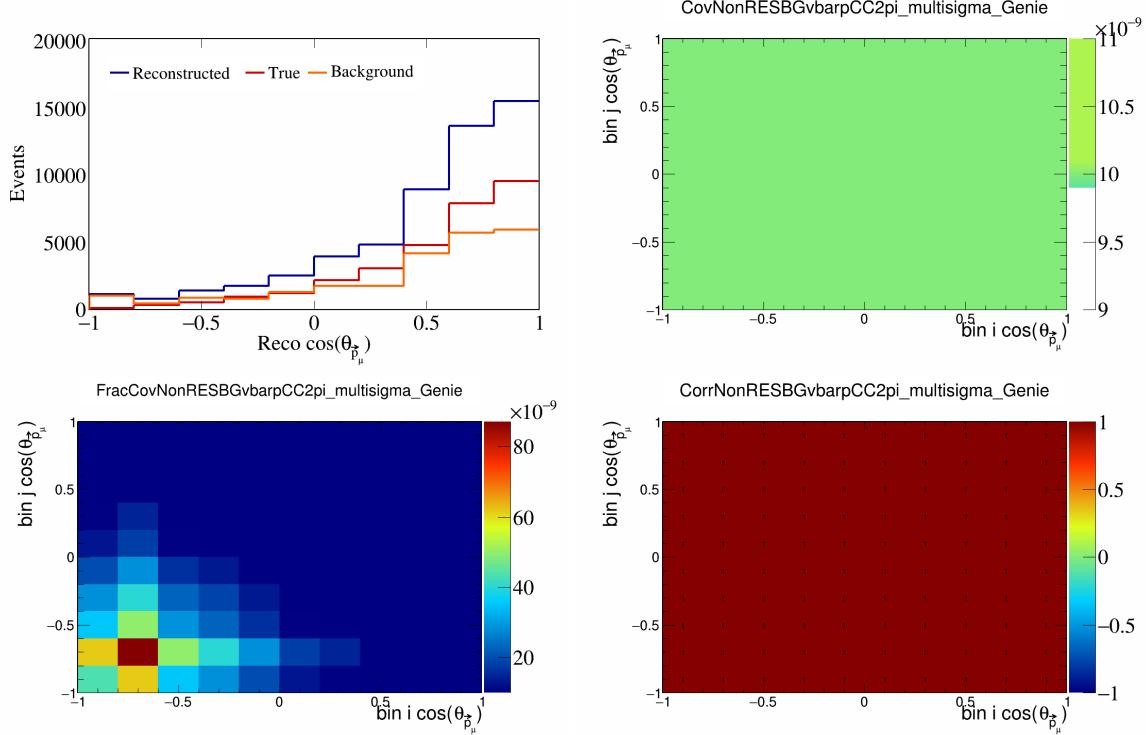


Figure 428: NonRESBGvbarpCC2pi variations for $\cos(\theta_{\vec{p}_\mu})$.

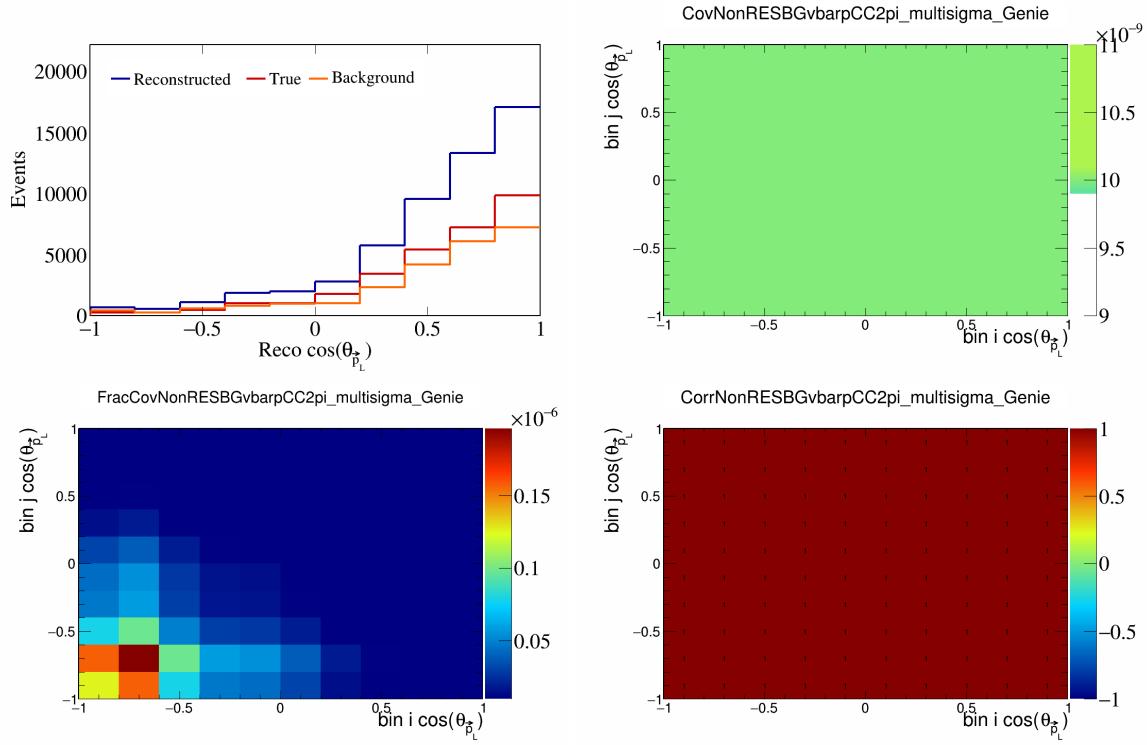


Figure 429: NonRESBGvbarpCC2pi variations for $\cos(\theta_{\vec{p}_L})$.

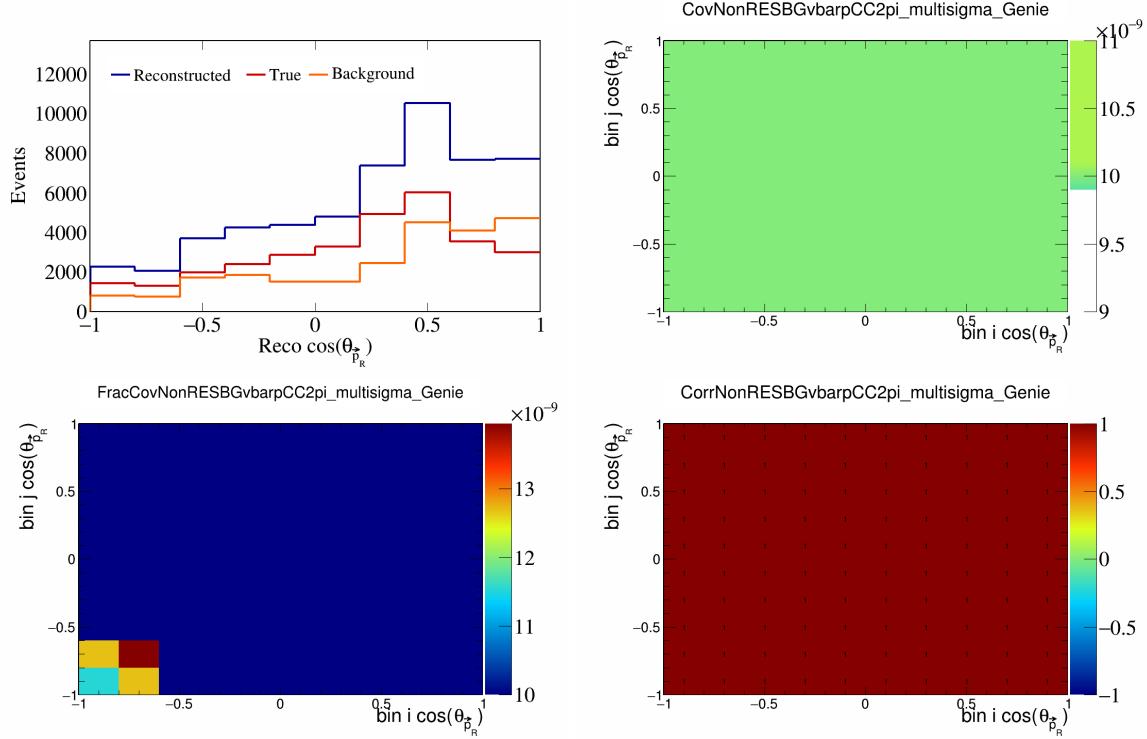


Figure 430: NonRESBGvbarpCC2pi variations for $\cos(\theta_{\vec{p}_R})$.

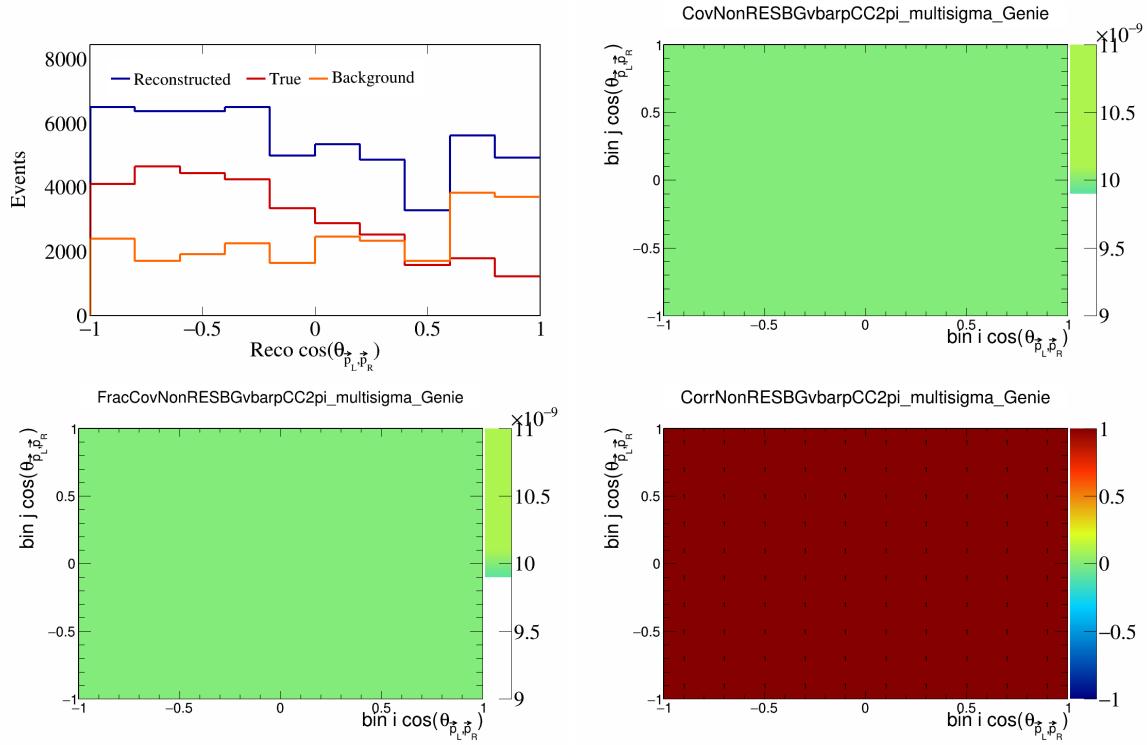


Figure 431: NonRESBGvbarpCC2pi variations for $\cos(\theta_{\vec{p}_L, \vec{p}_R})$.

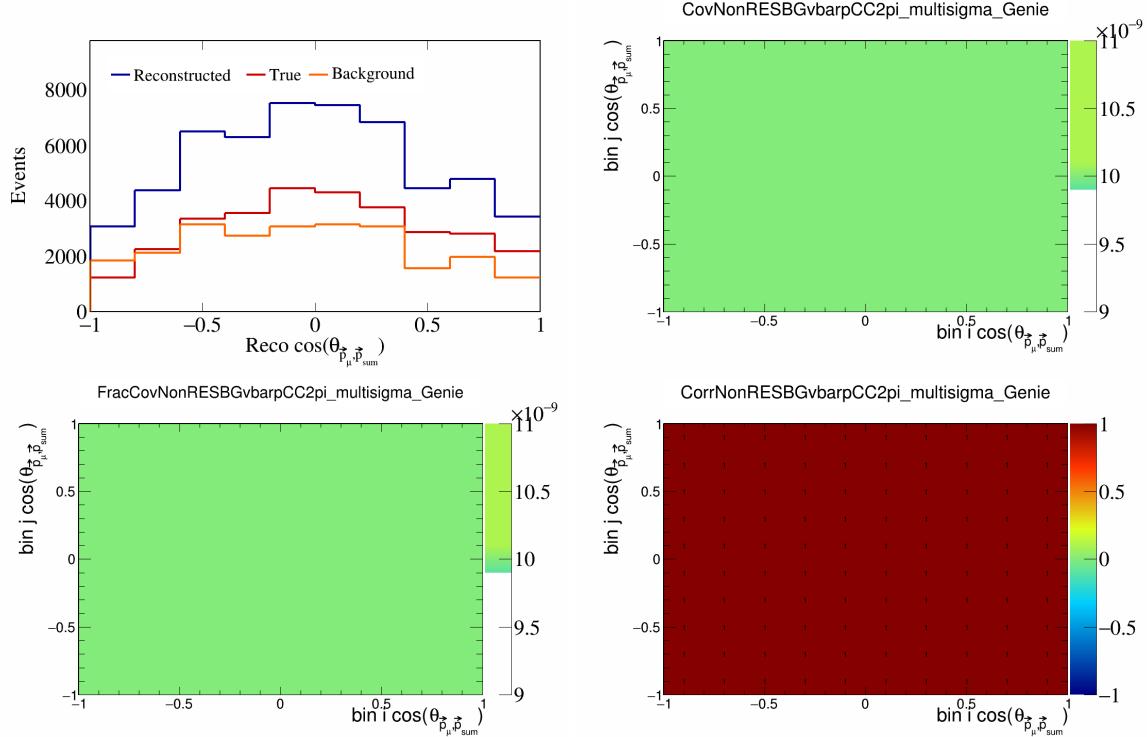


Figure 432: NonRESBGvbarpCC2pi variations for $\cos(\theta_{\vec{p}_\mu, \vec{p}_{\text{sum}}})$.

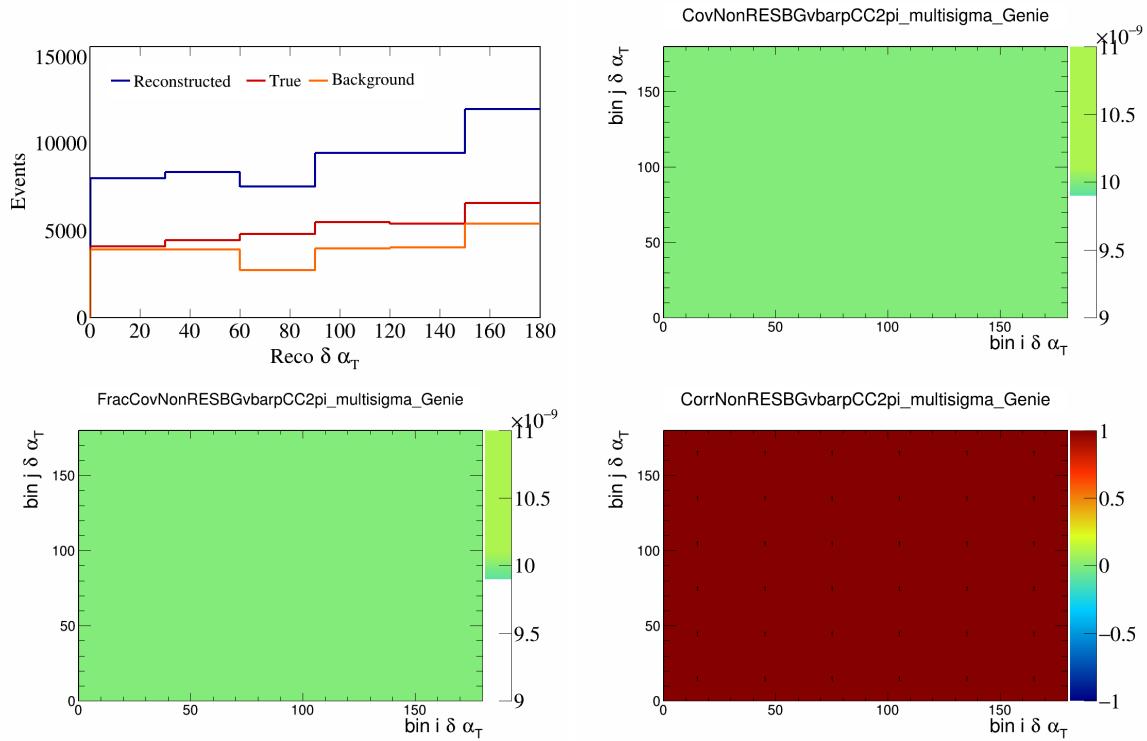


Figure 433: NonRESBGvbarpCC2pi variations for $\delta\alpha_T$.

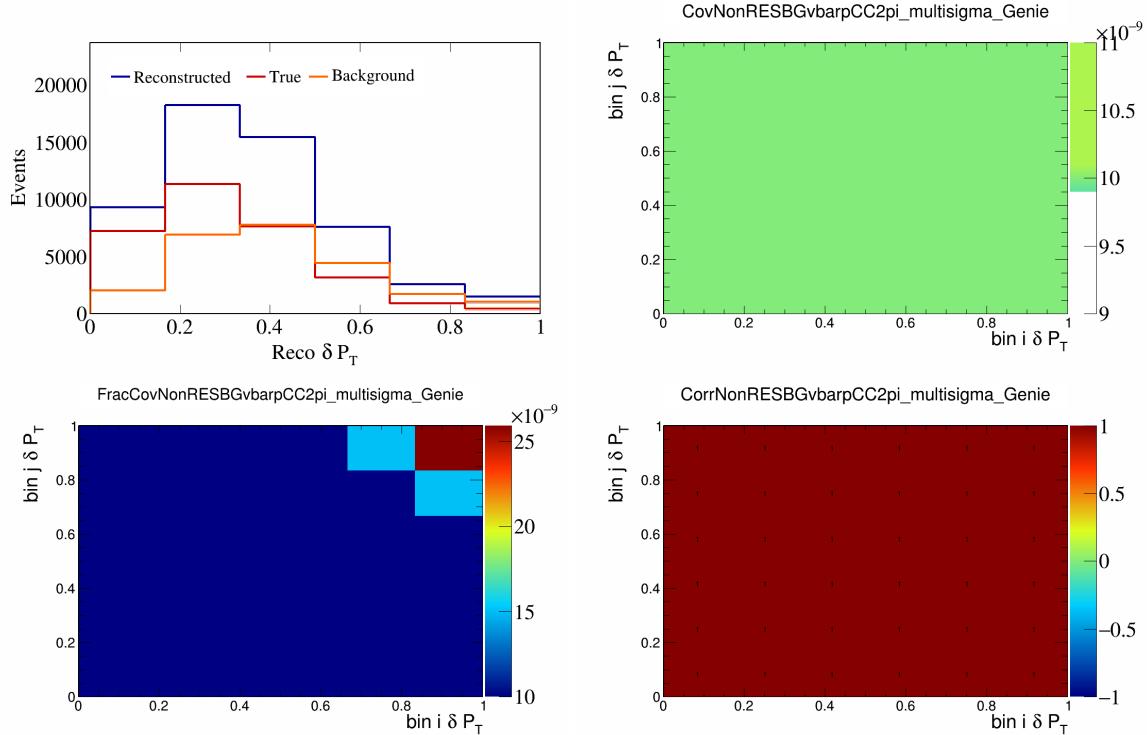


Figure 434: NonRESBGvbarpCC2pi variations for δP_T .

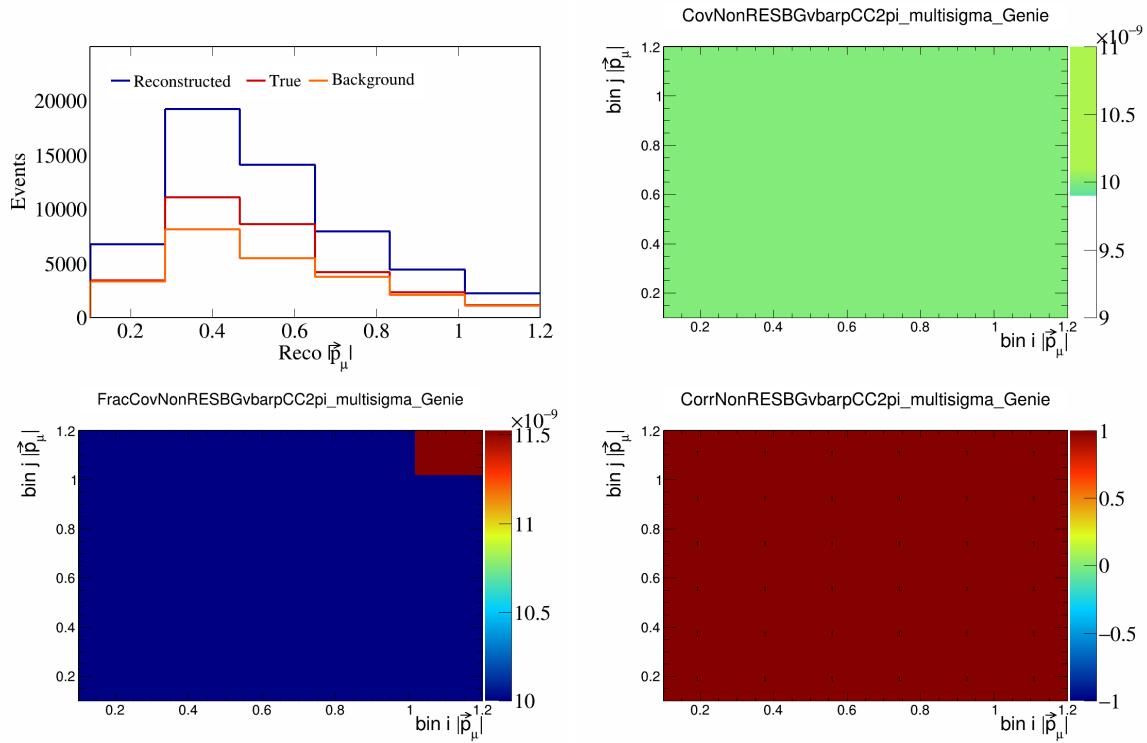


Figure 435: NonRESBGvbarpCC2pi variations for $|\vec{p}_\mu|$.

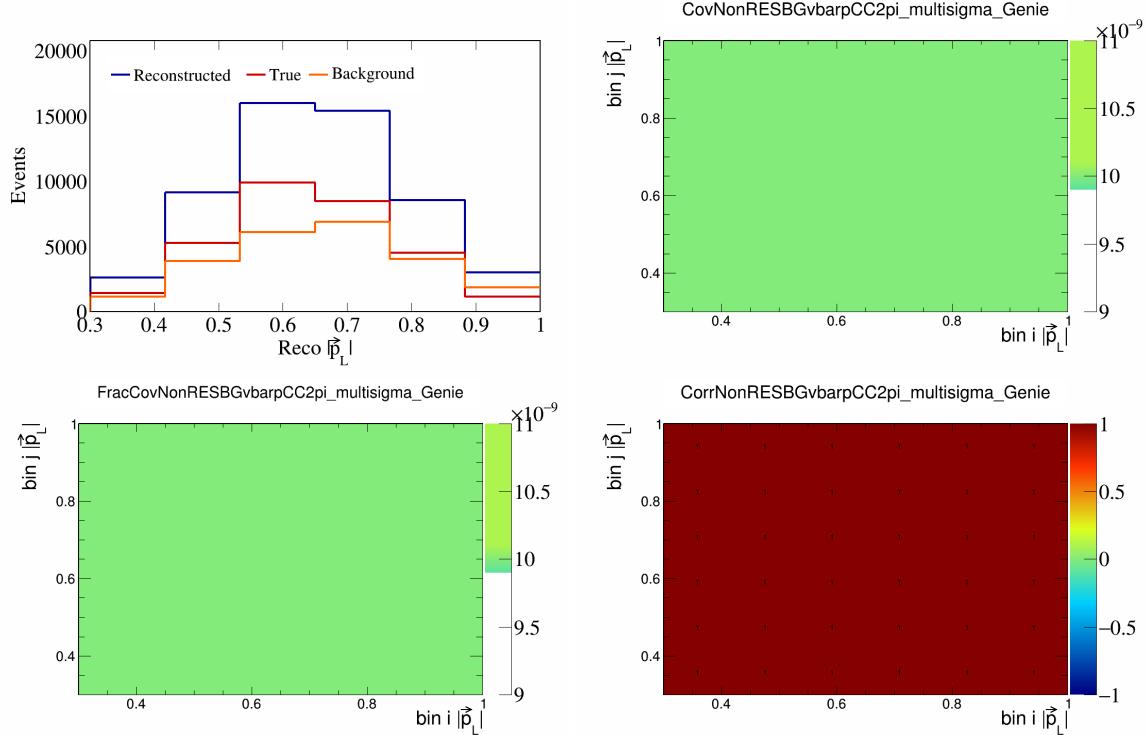


Figure 436: NonRESBGvbarpCC2pi variations for $|\vec{p}_L|$.

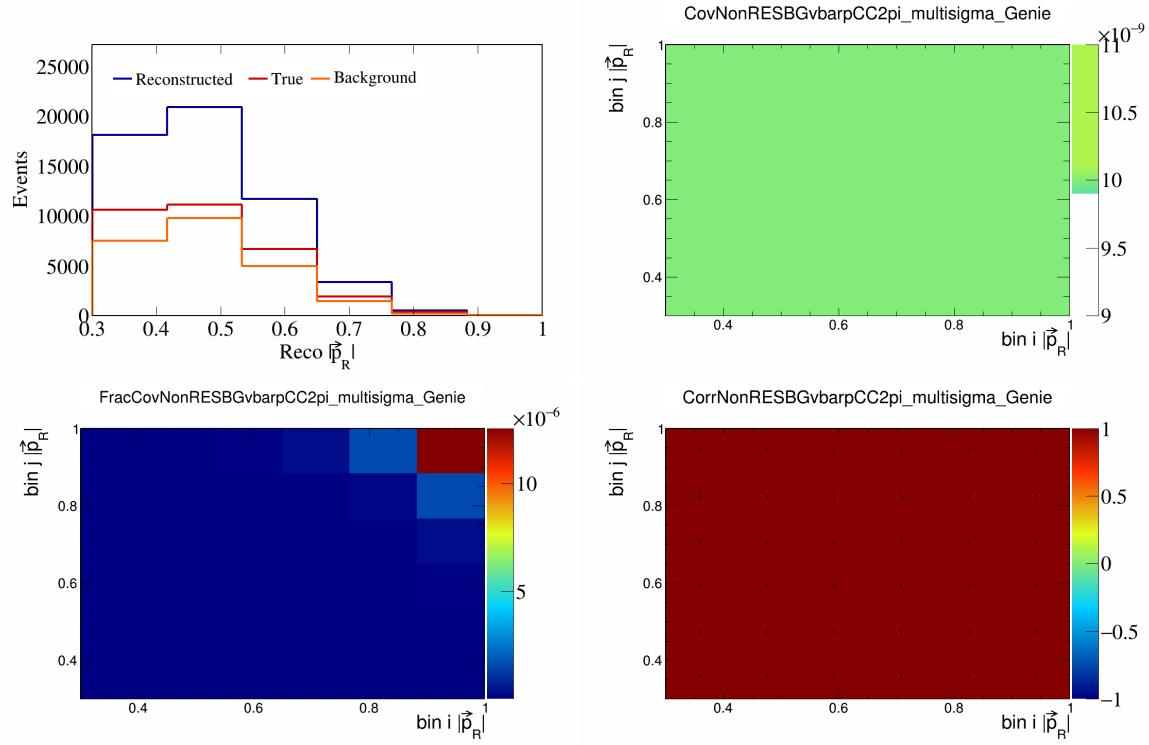


Figure 437: NonRESBGvbarpCC2pi variations for $|\vec{p}_R|$.

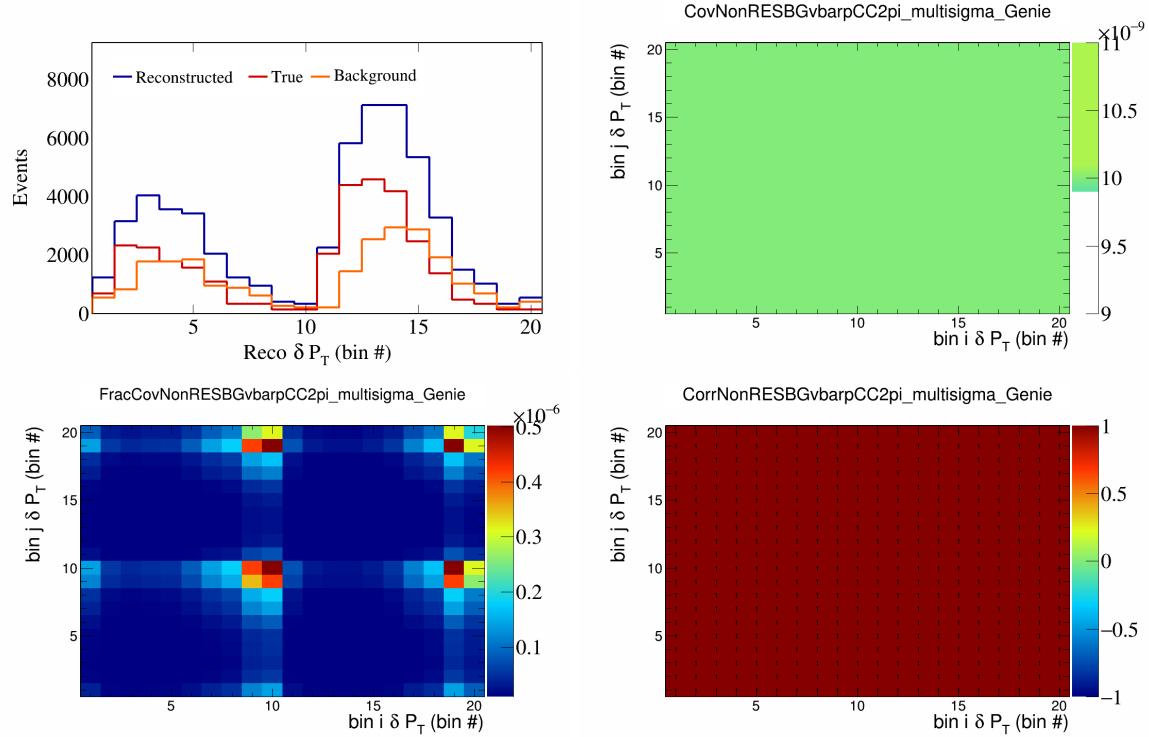


Figure 438: NonRESBGvbarpCC2pi variations for δP_T in $\cos(\theta_{\vec{p}_\mu})$.

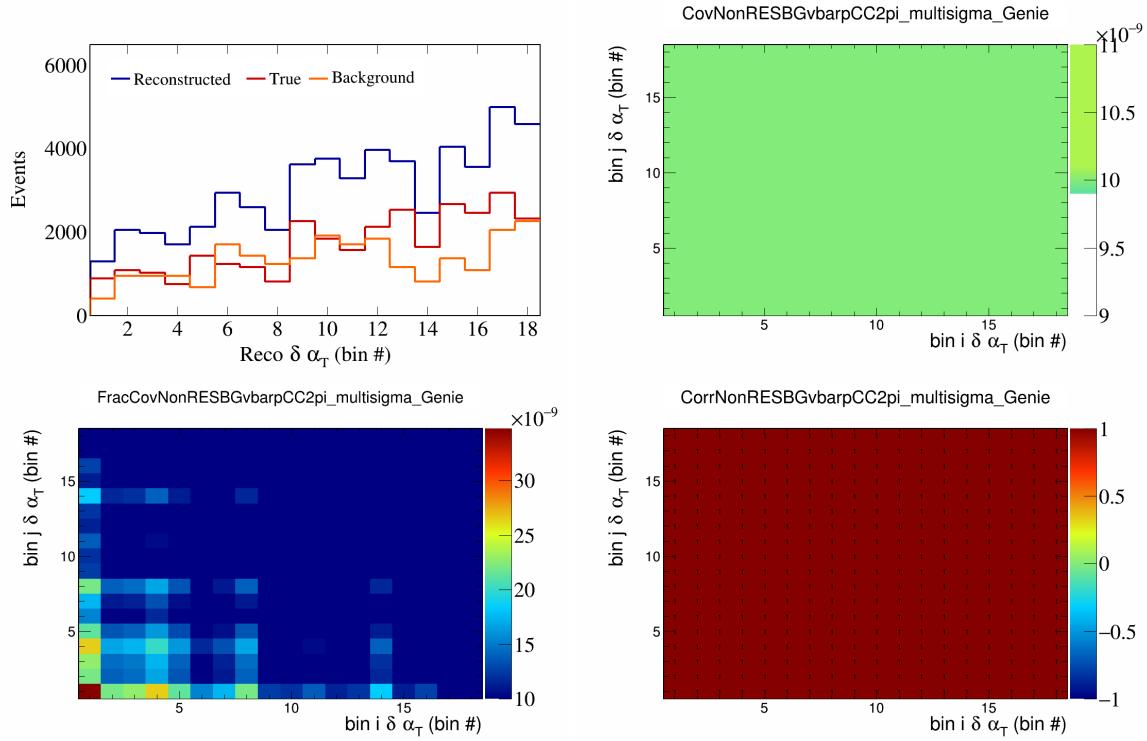


Figure 439: NonRESBGvbarpCC2pi variations for $\delta\alpha_T$ in $\cos(\theta_{\vec{p}_\mu})$.

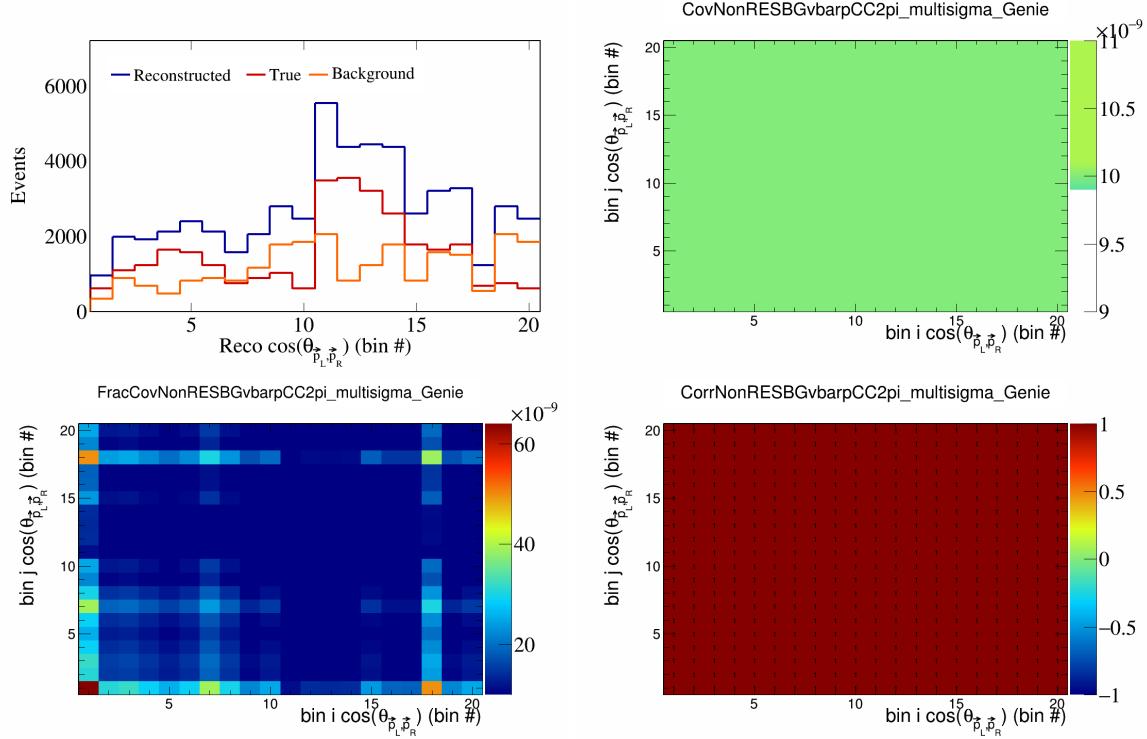


Figure 440: NonRESBGvbarpCC2pi variations for $\cos(\theta_{\vec{p}_L, \vec{p}_R})$ in $\cos(\theta_{\vec{p}_\mu})$.

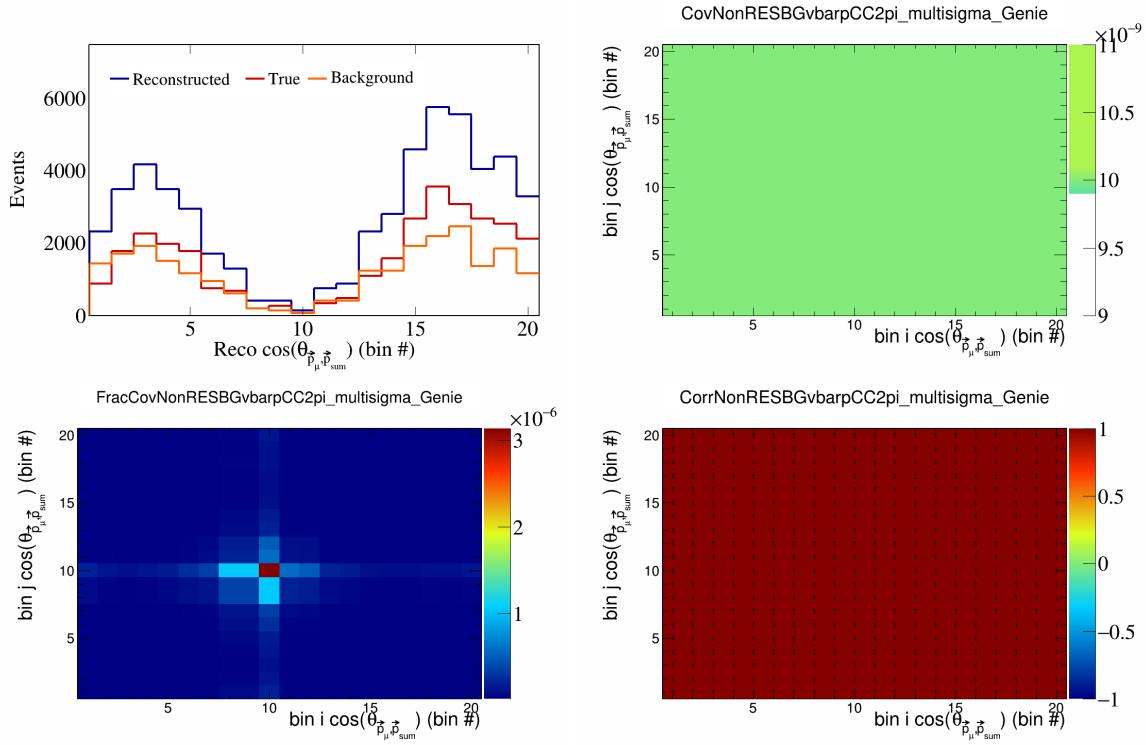


Figure 441: NonRESBGvbarpCC2pi variations for $\cos(\theta_{\vec{p}_\mu})$ in $\cos(\theta_{\vec{p}_\mu})$.

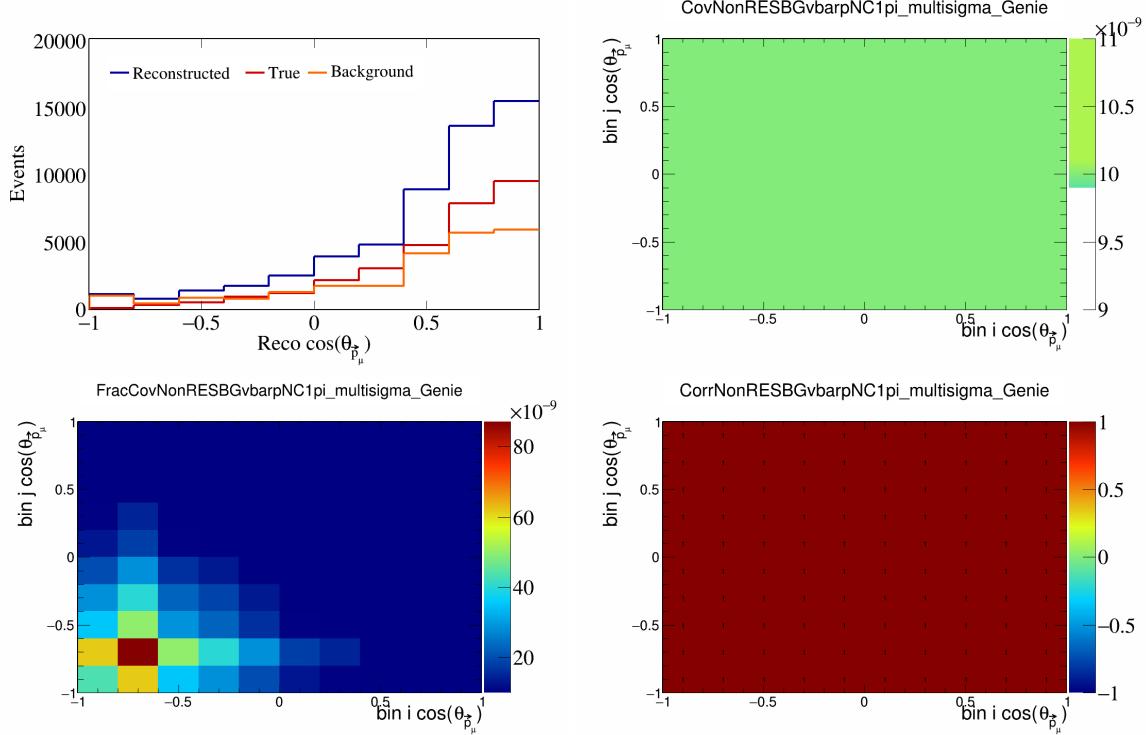


Figure 442: NonRESBGvbarpNC1pi variations for $\cos(\theta_{\vec{p}_\mu})$.

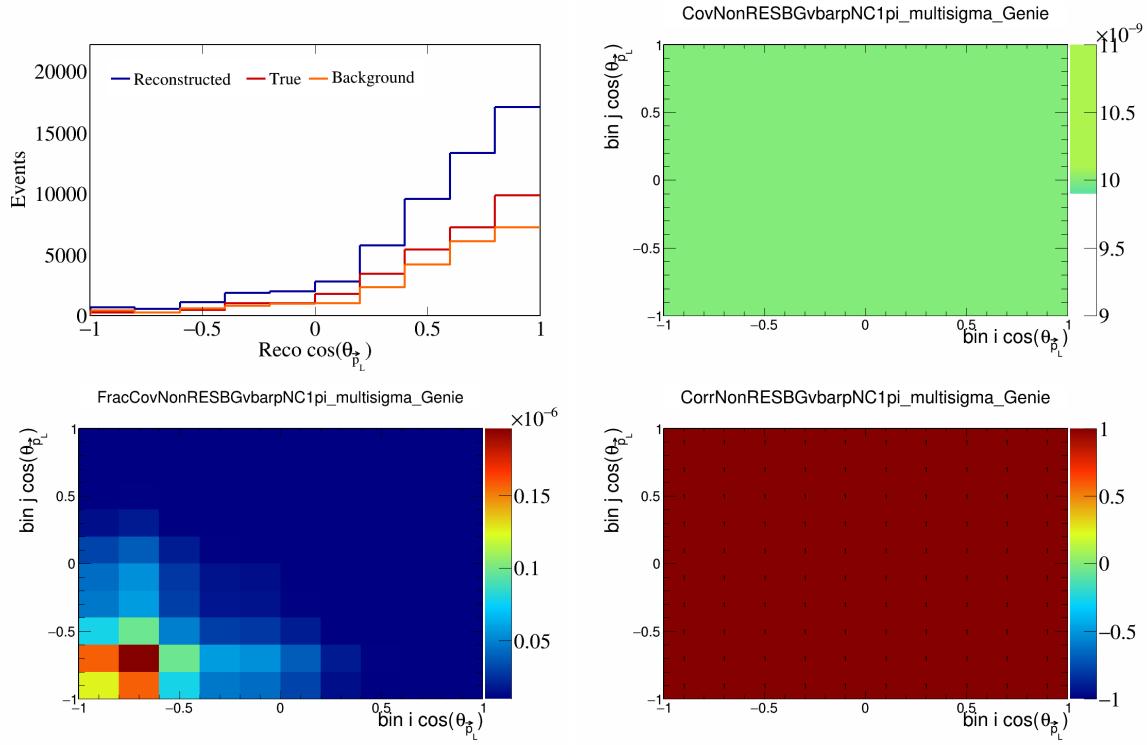


Figure 443: NonRESBGvbarpNC1pi variations for $\cos(\theta_{\vec{p}_L})$.

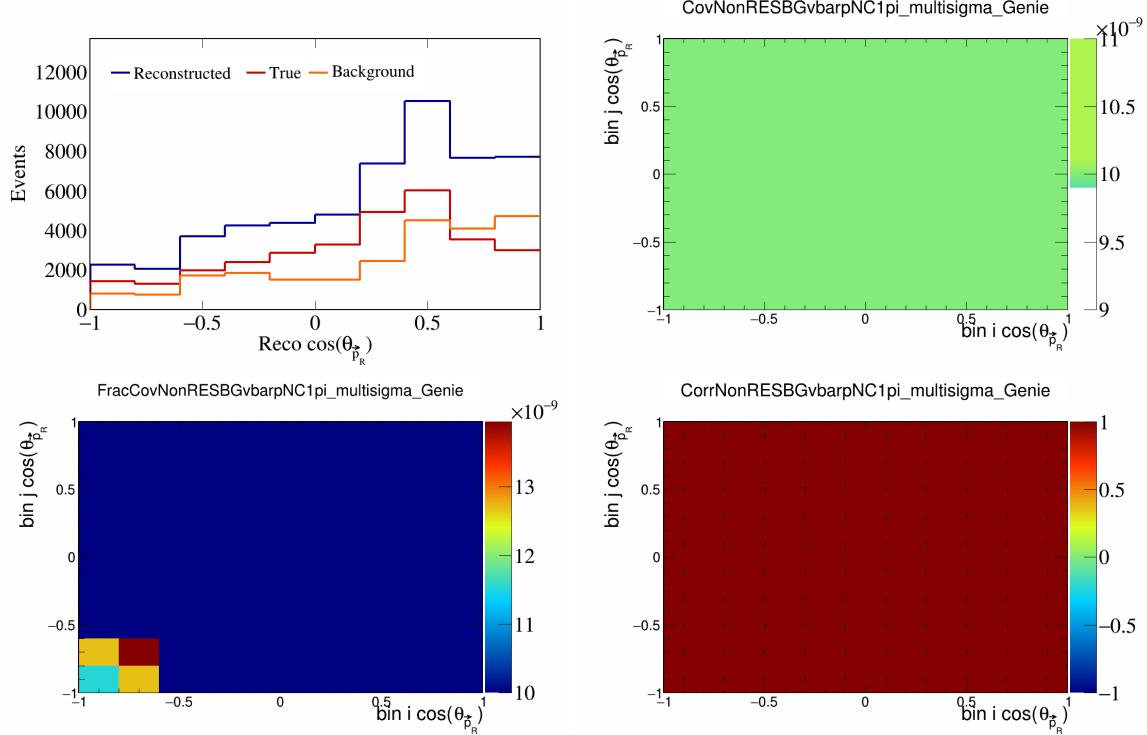


Figure 444: NonRESBGvbarpNC1pi variations for $\cos(\theta_{\vec{p}_R})$.

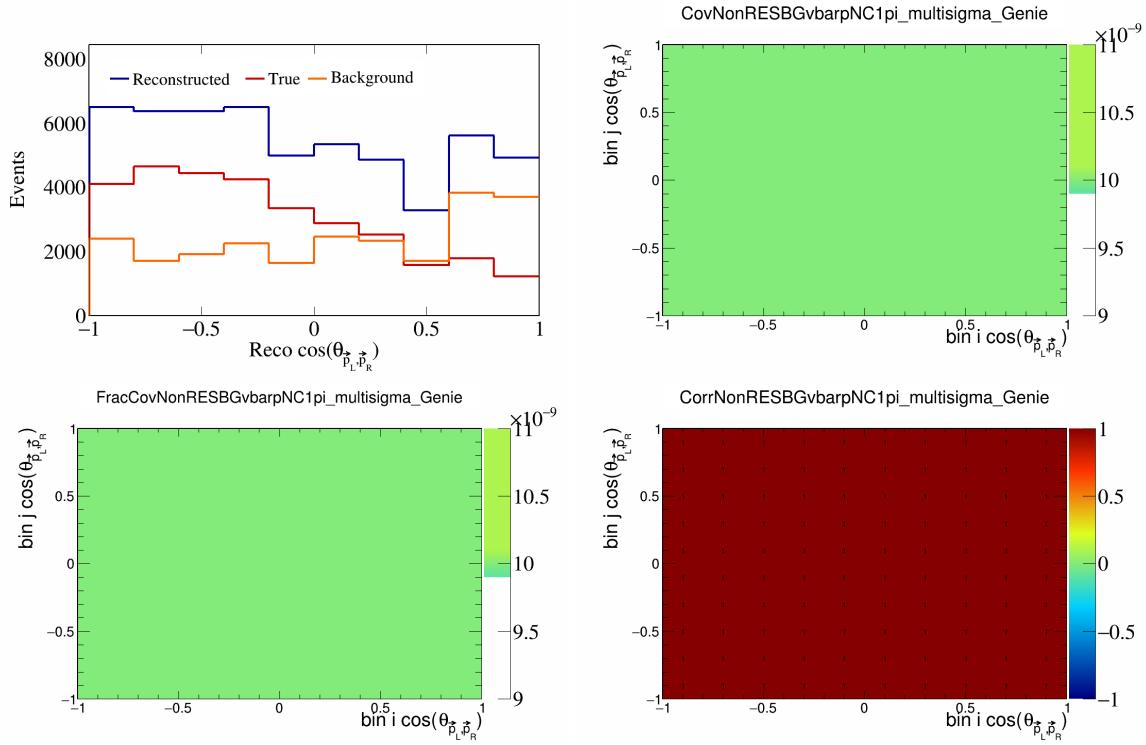


Figure 445: NonRESBGvbarpNC1pi variations for $\cos(\theta_{\vec{p}_L, \vec{p}_R})$.

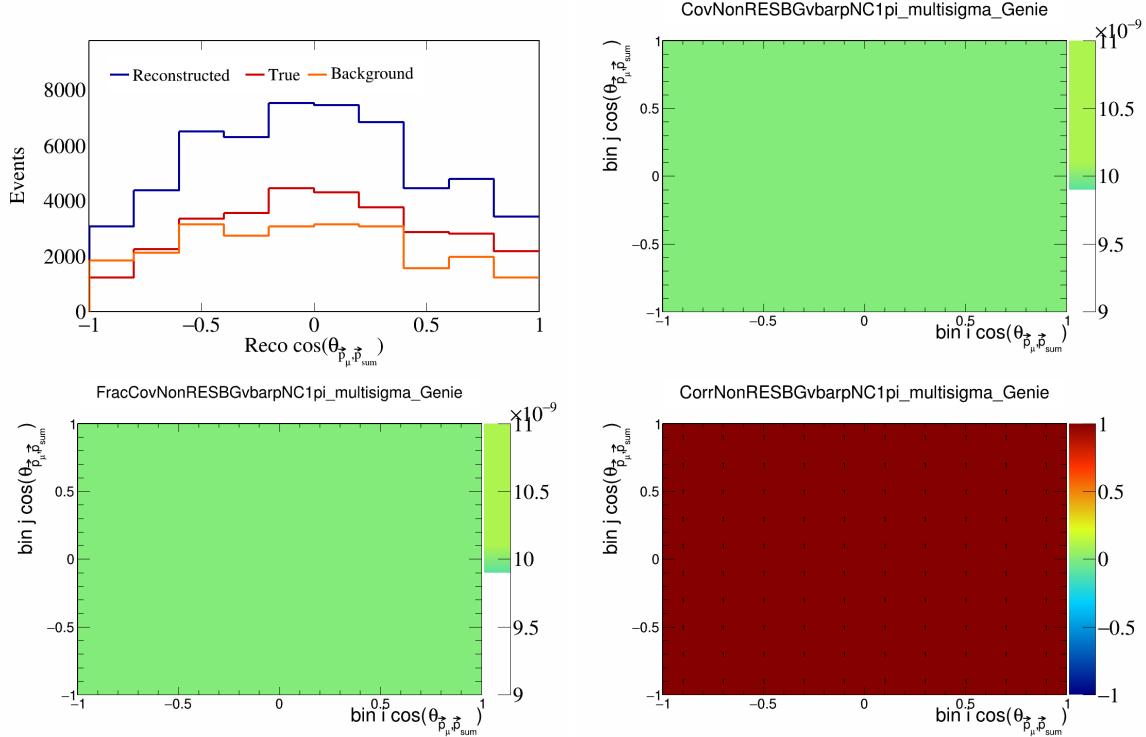


Figure 446: NonRESBGvbarpNC1pi variations for $\cos(\theta_{\vec{p}_\mu, \vec{p}_{\text{sum}}})$.

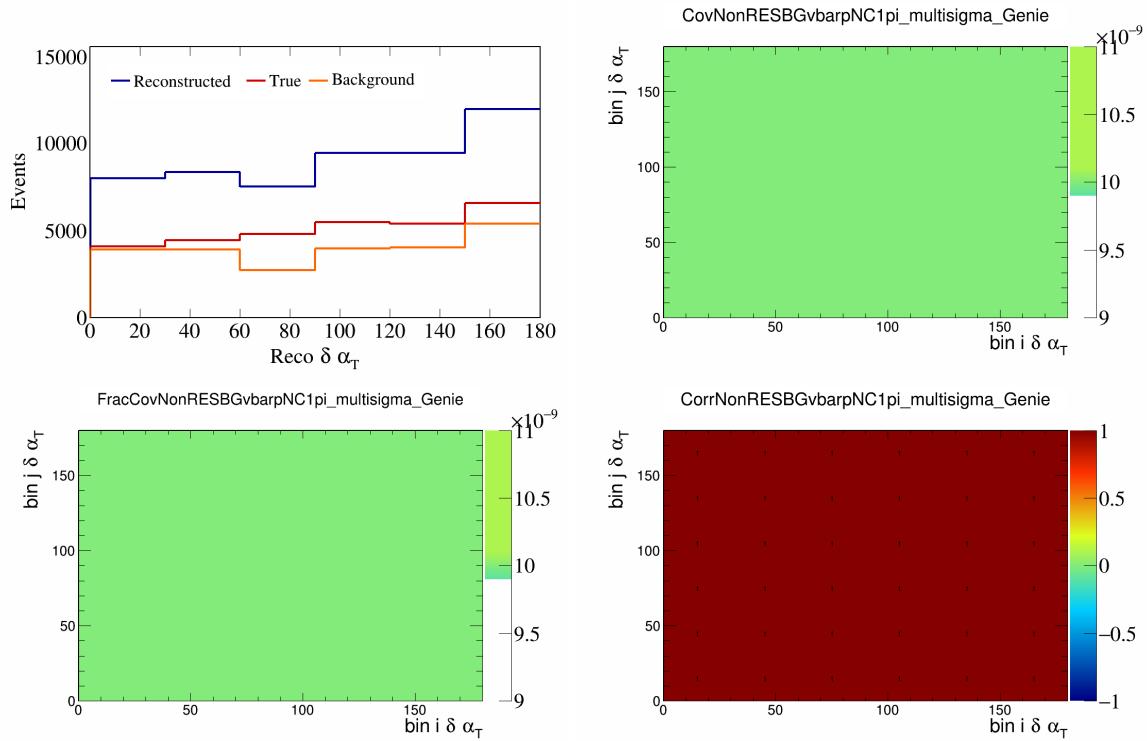


Figure 447: NonRESBGvbarpNC1pi variations for $\delta\alpha_T$.

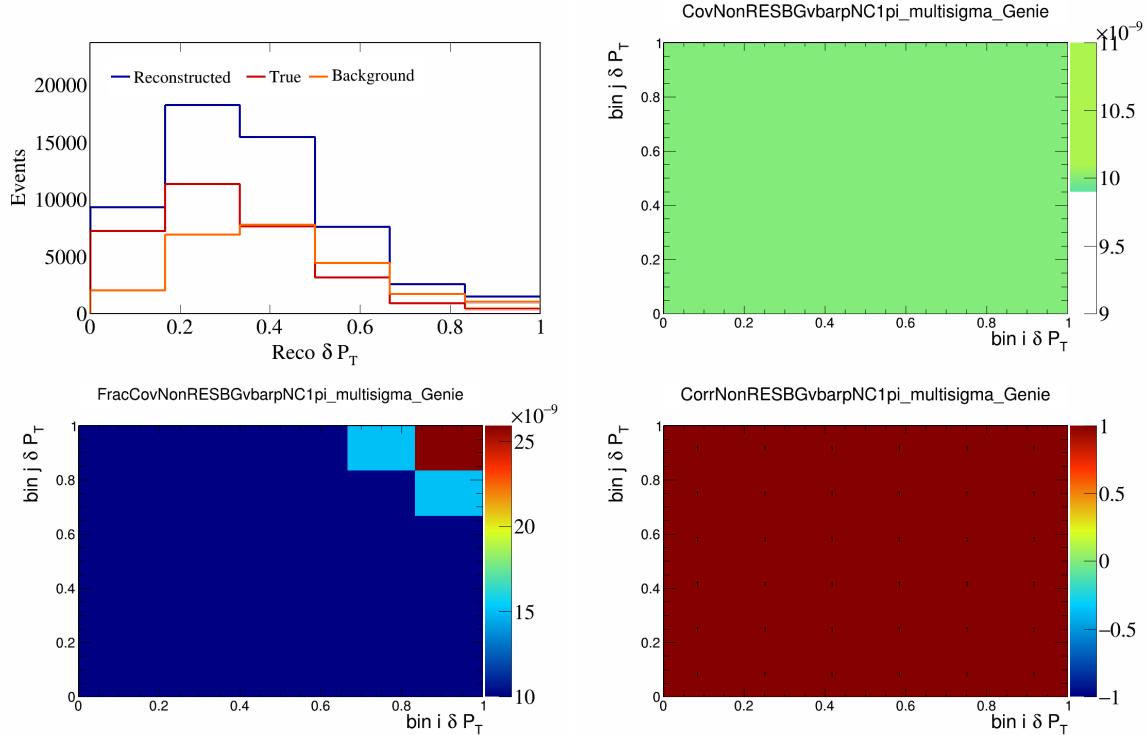


Figure 448: NonRESBGvbarpNC1pi variations for δP_T .

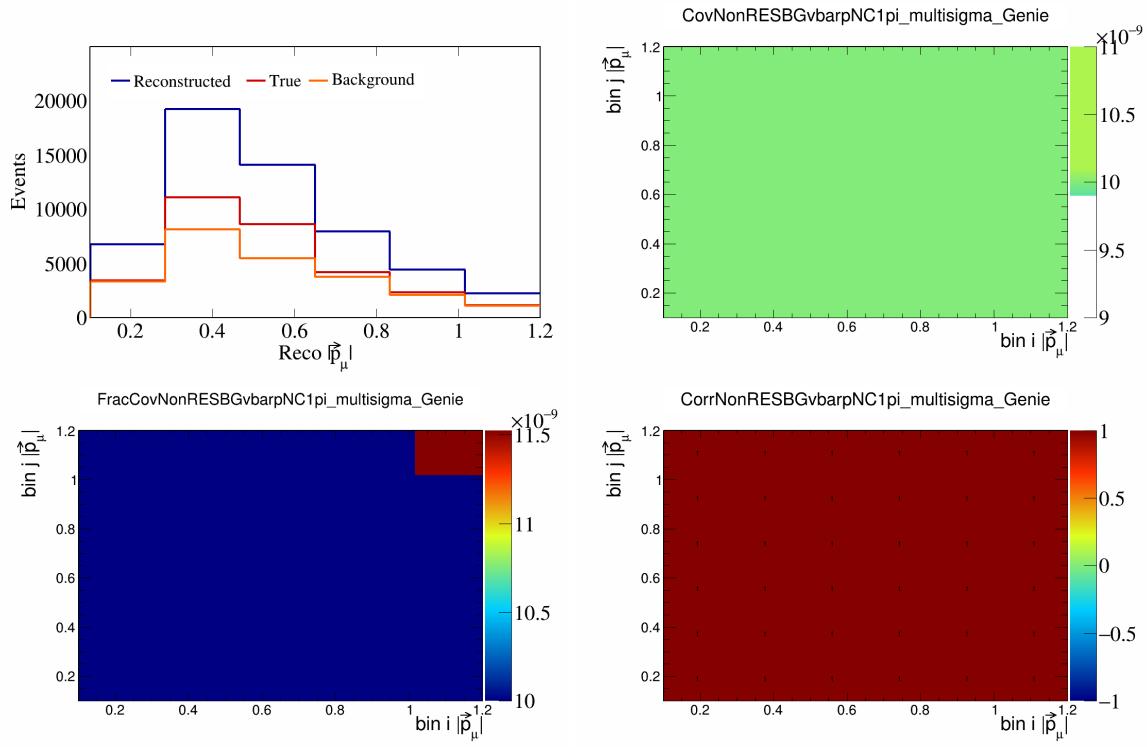


Figure 449: NonRESBGvbarpNC1pi variations for $|\vec{p}_\mu|$.

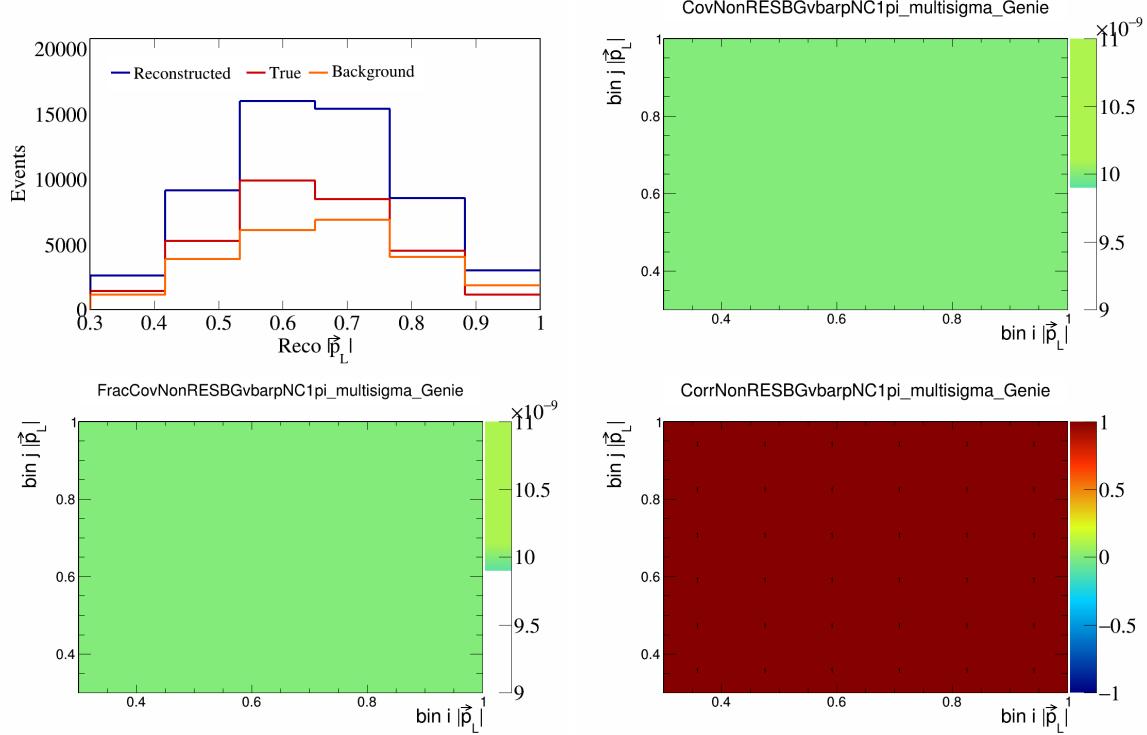


Figure 450: NonRESBGvbarpNC1pi variations for $|\vec{p}_L|$.

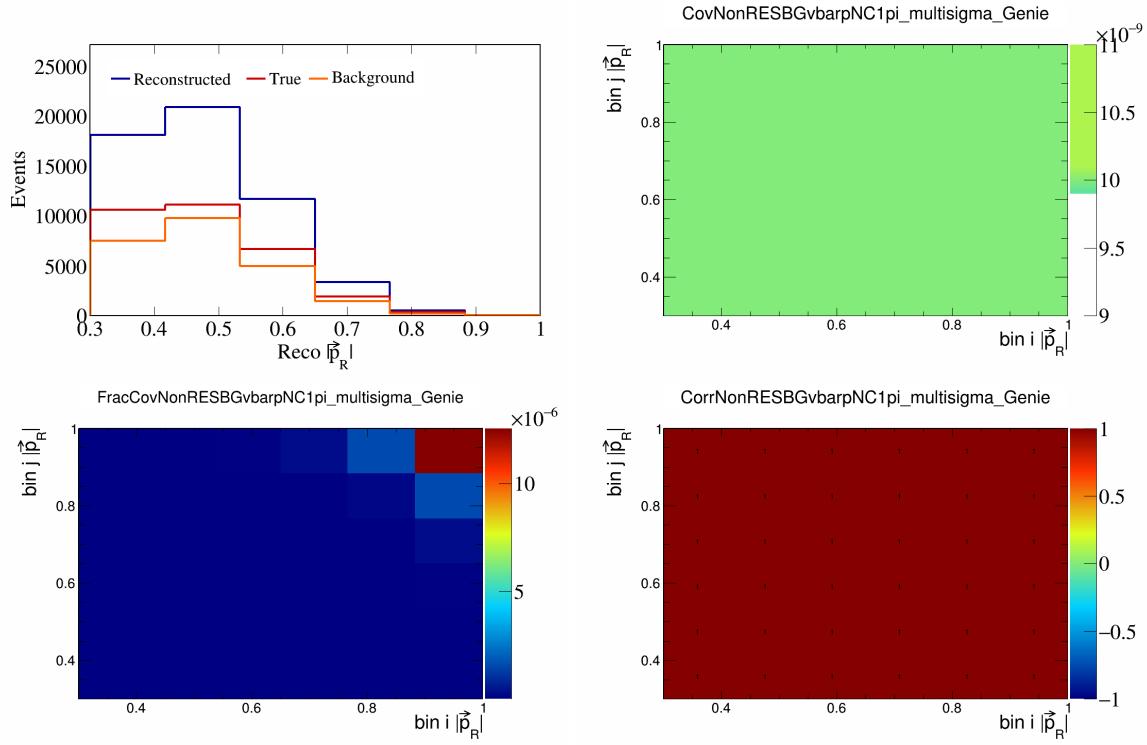


Figure 451: NonRESBGvbarpNC1pi variations for $|\vec{p}_R|$.

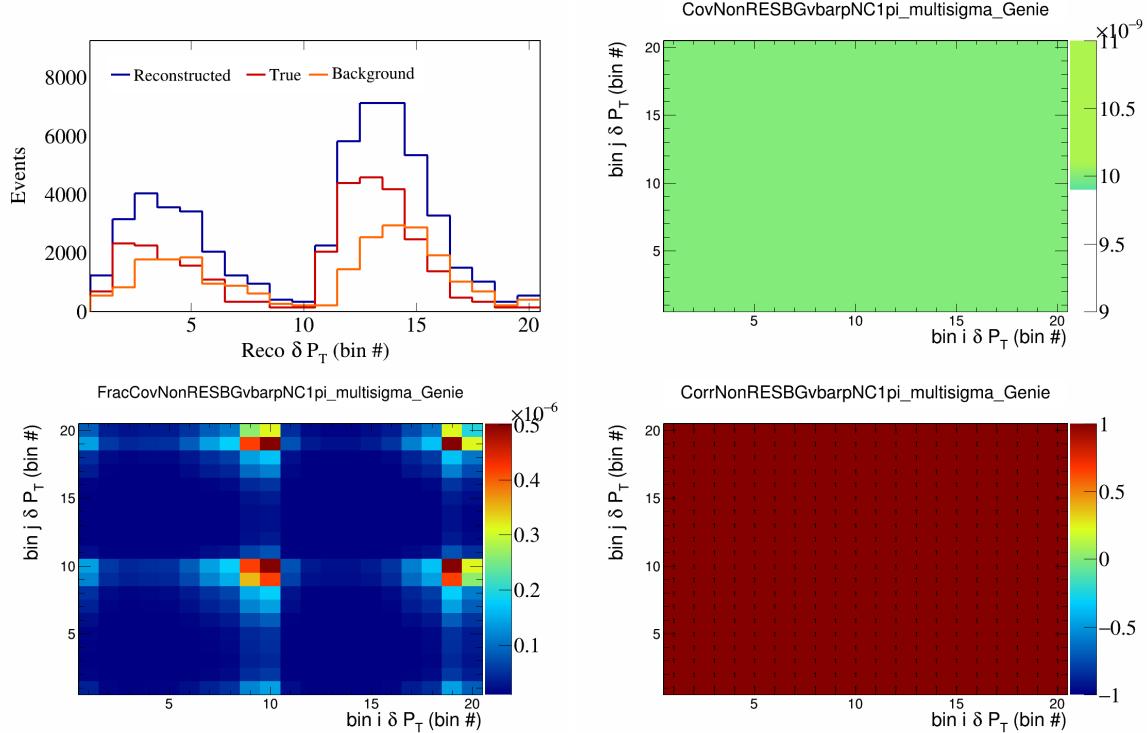


Figure 452: NonRESBGvbarpNC1pi variations for δP_T in $\cos(\theta_{\vec{p}_\mu})$.

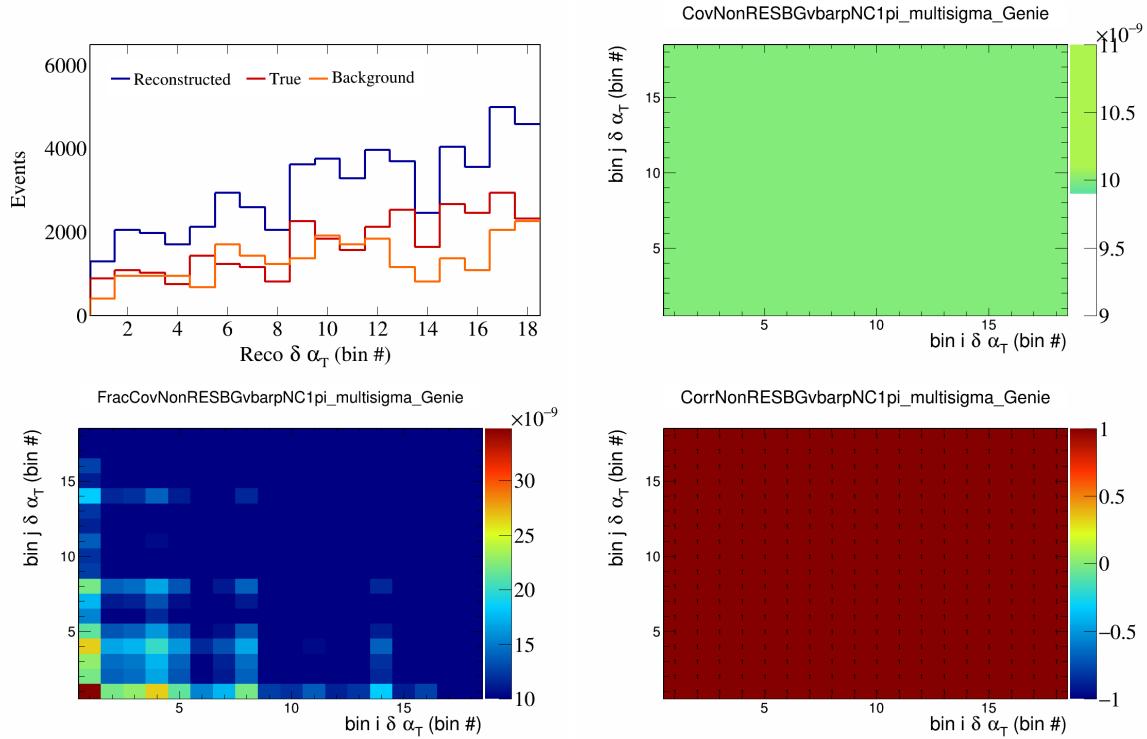


Figure 453: NonRESBGvbarpNC1pi variations for $\delta \alpha_T$ in $\cos(\theta_{\vec{p}_\mu})$.

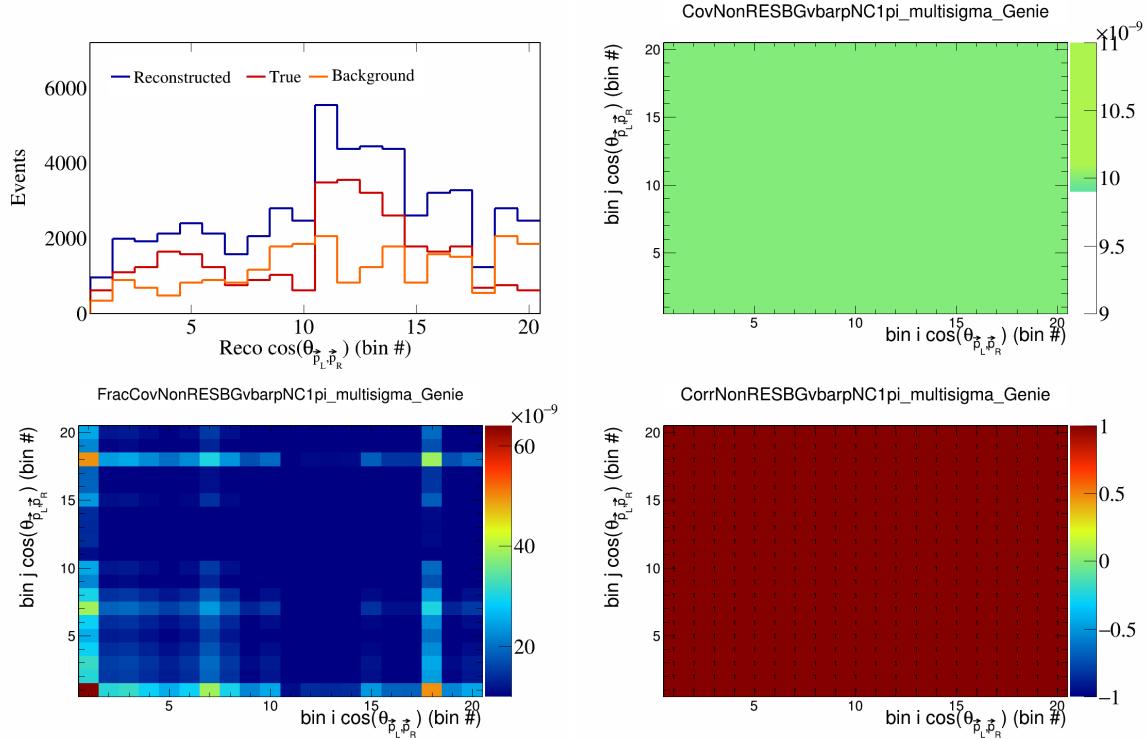


Figure 454: NonRESBGvbarpNC1pi variations for $\cos(\theta_{\vec{p}_L, \vec{p}_R})$ in $\cos(\theta_{\vec{p}_\mu})$.

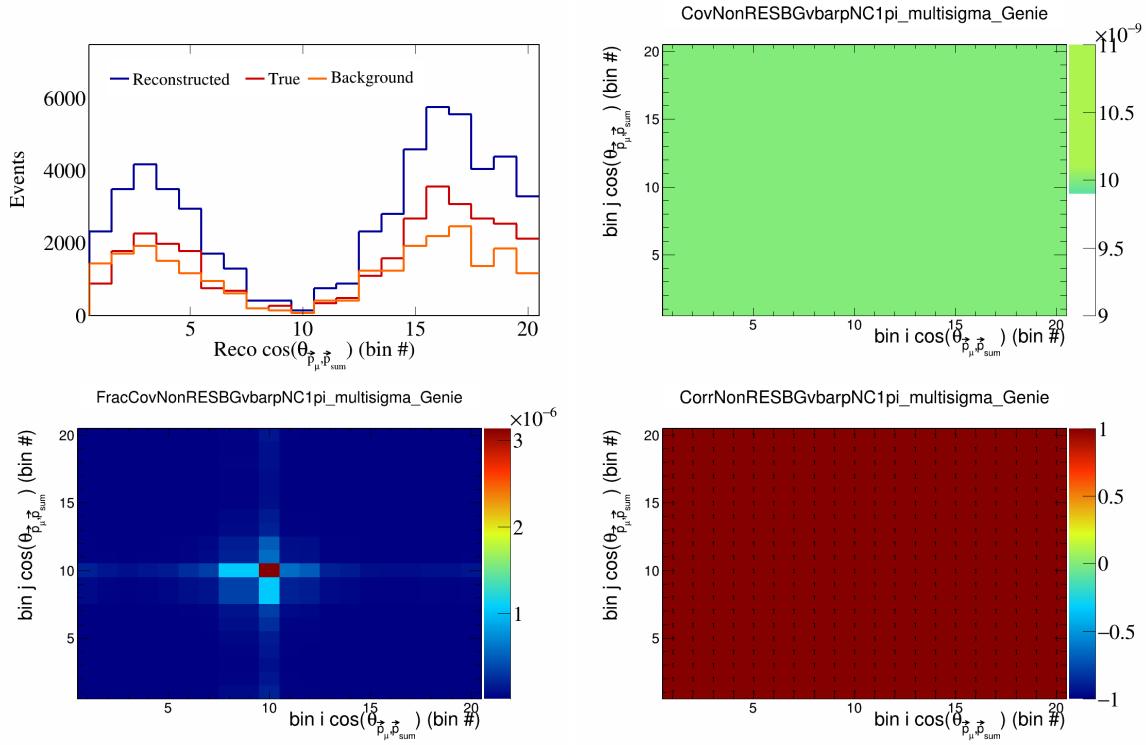


Figure 455: NonRESBGvbarpNC1pi variations for $\cos(\theta_{\vec{p}_\mu})$ in $\cos(\theta_{\vec{p}_\mu})$.

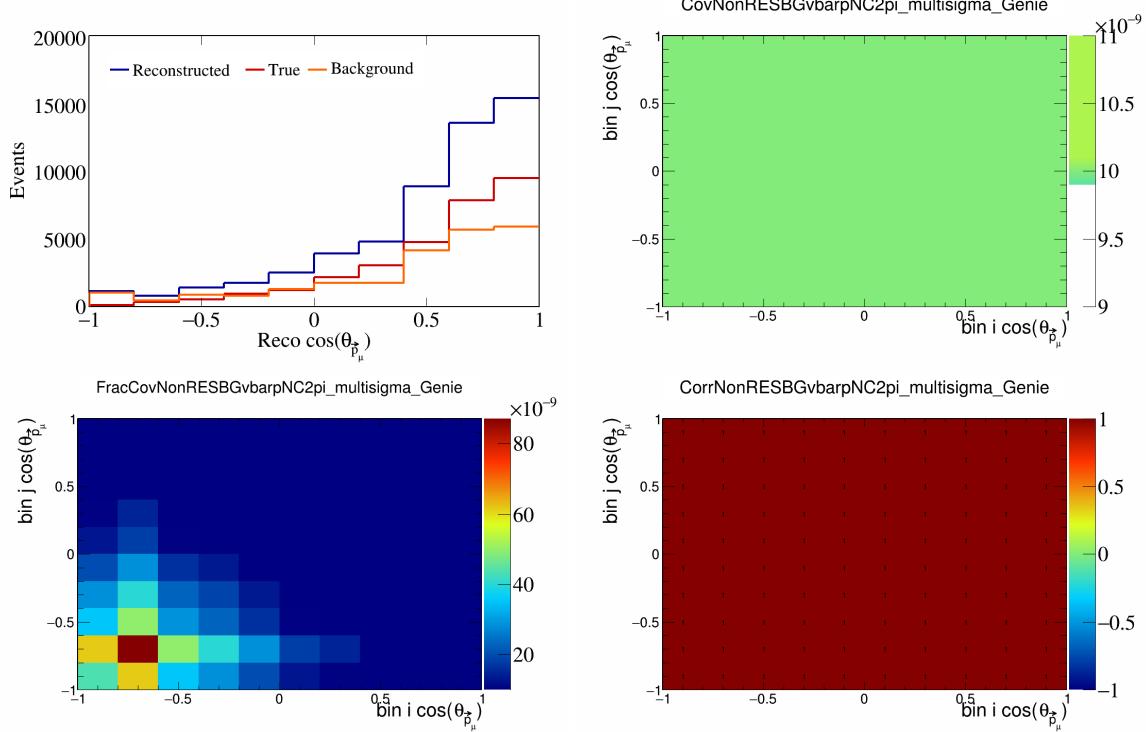


Figure 456: NonRESBGvbarpNC2pi variations for $\cos(\theta_{\vec{p}_\mu})$.

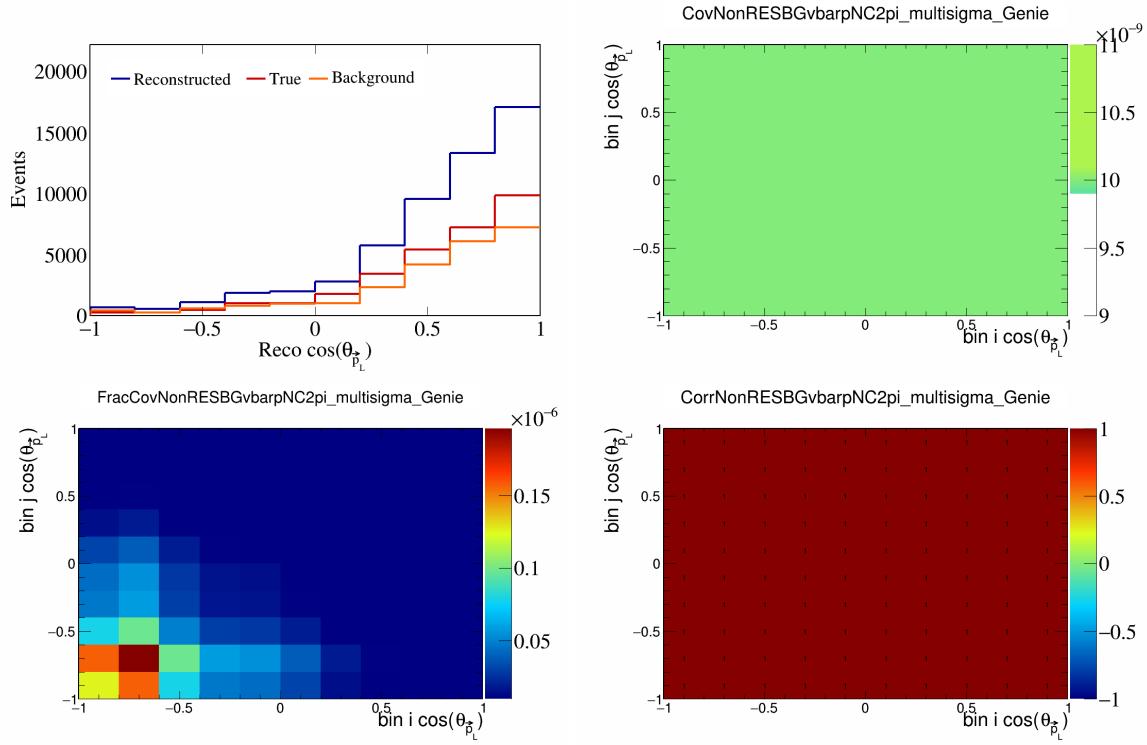


Figure 457: NonRESBGvbarpiNC2pi variations for $\cos(\theta_{\vec{p}_L})$.

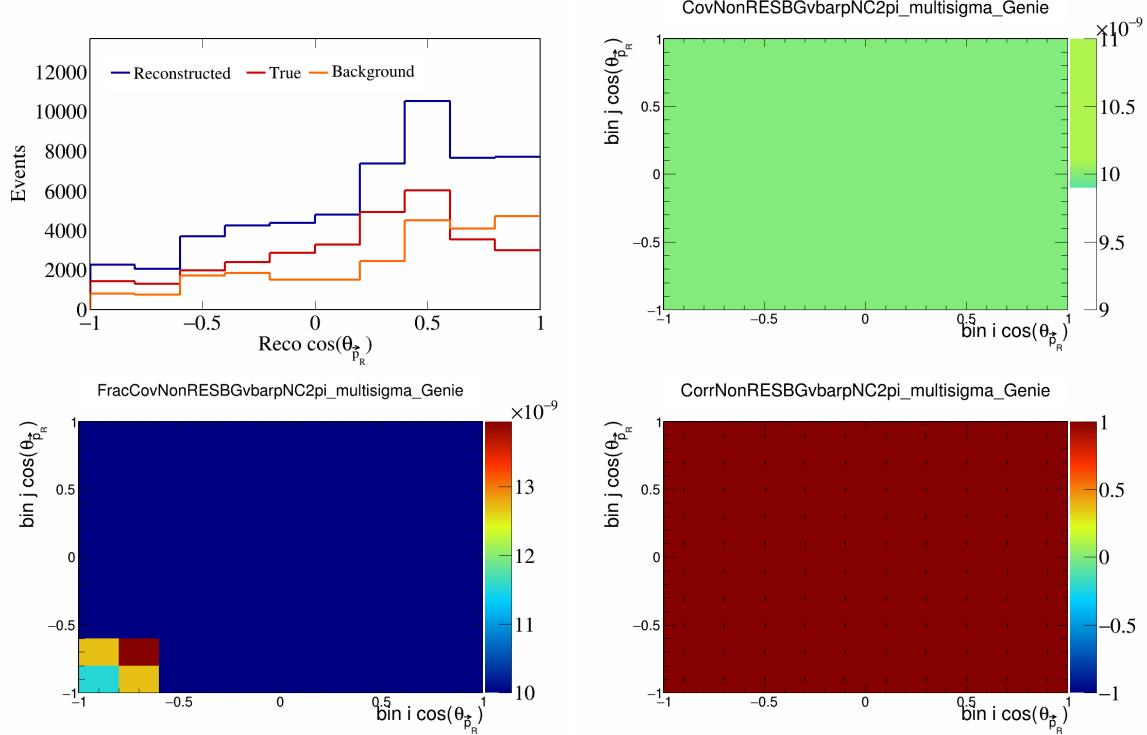


Figure 458: NonRESBGvbarpiNC2pi variations for $\cos(\theta_{\vec{p}_R})$.

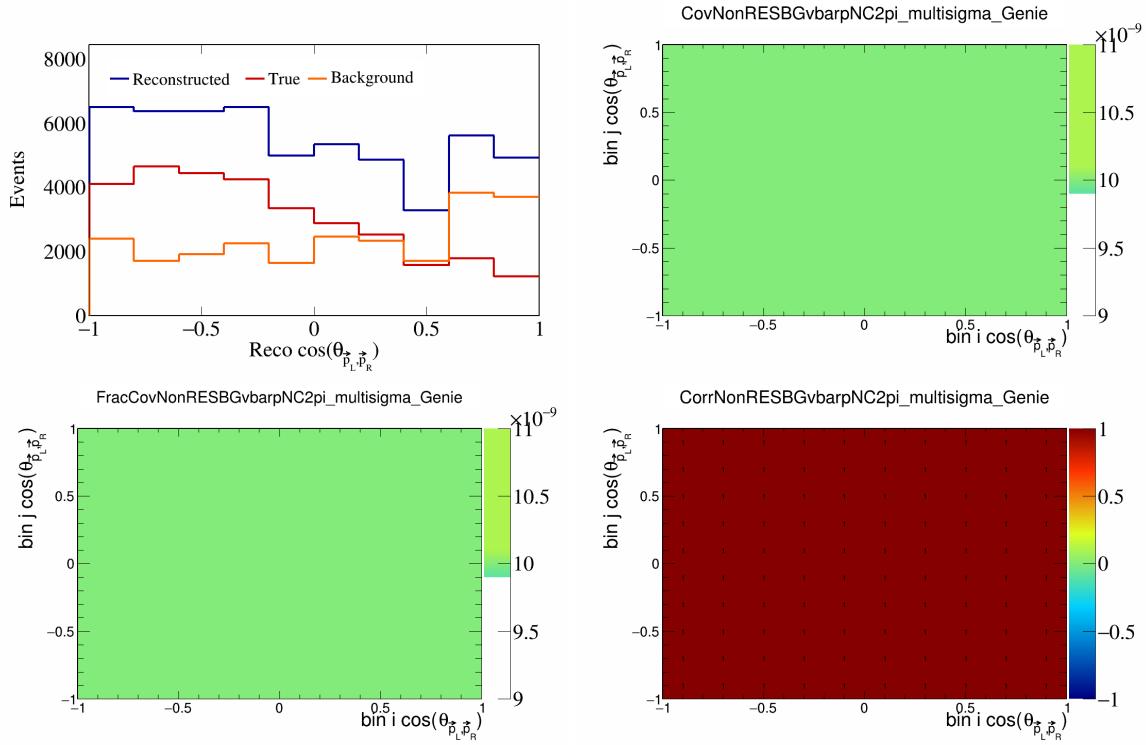


Figure 459: NonRESBGvbarpNC2pi variations for $\cos(\theta_{\vec{p}_L, \vec{p}_R})$.

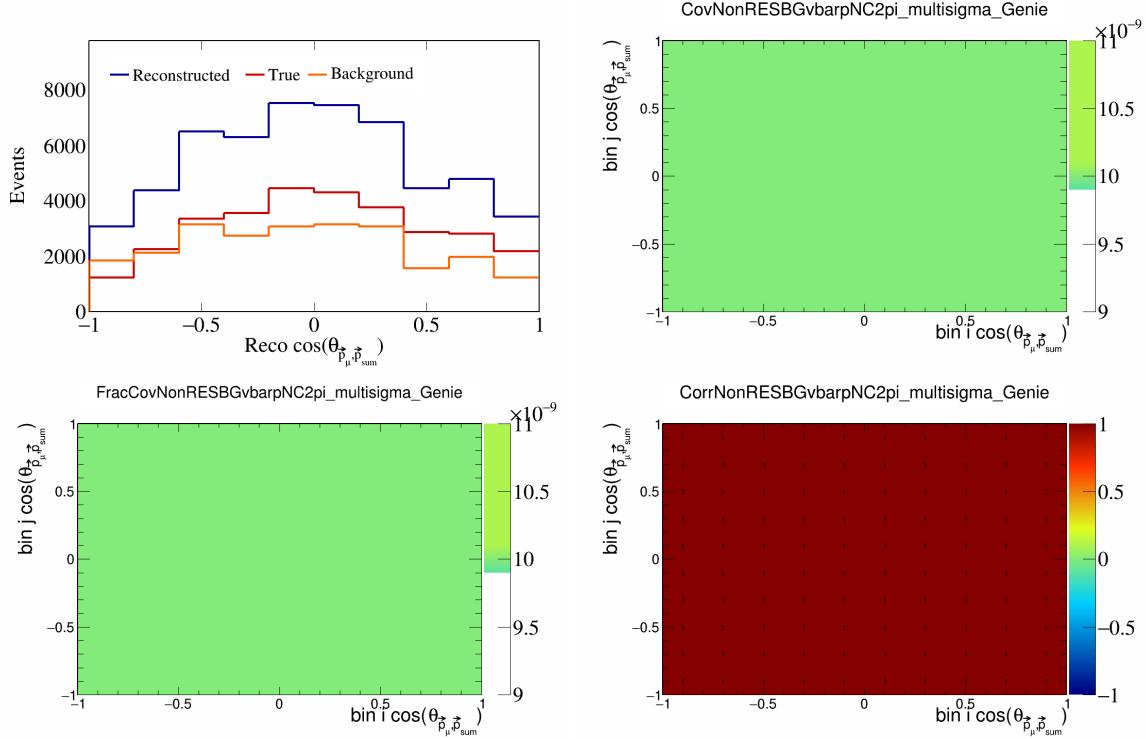


Figure 460: NonRESBGvbarpNC2pi variations for $\cos(\theta_{\vec{p}_\mu, \vec{p}_{\text{sum}}})$.

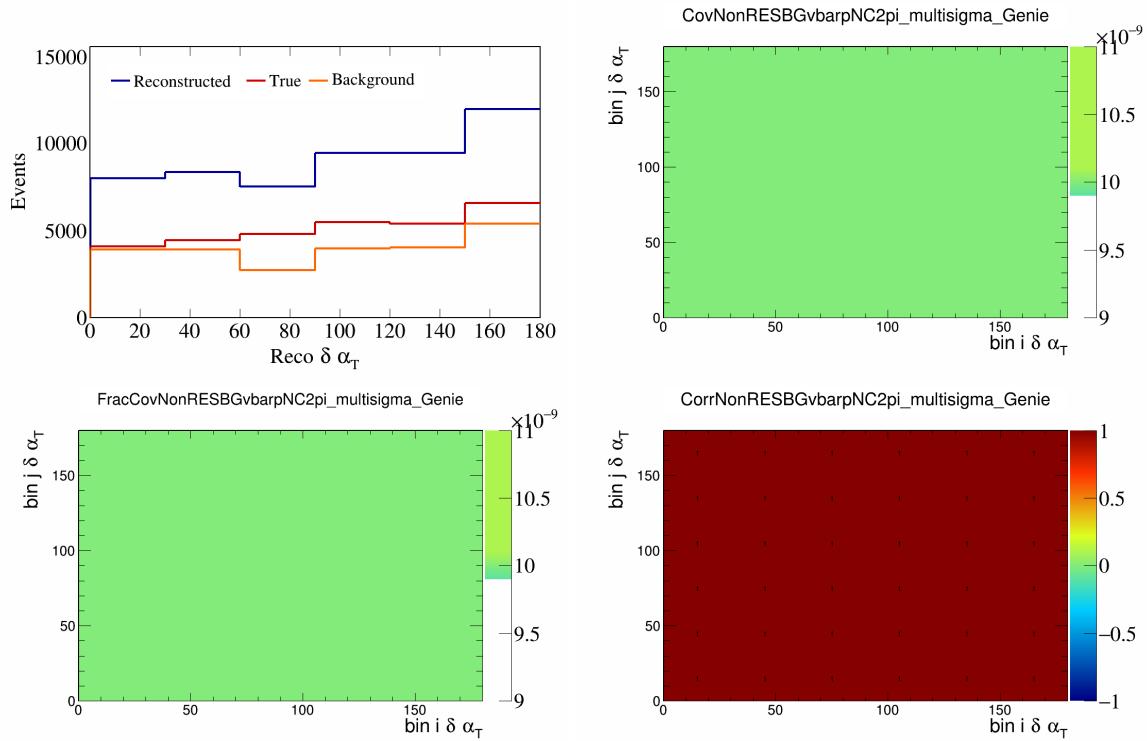


Figure 461: NonRESBGvbarpNC2pi variations for $\delta\alpha_T$.

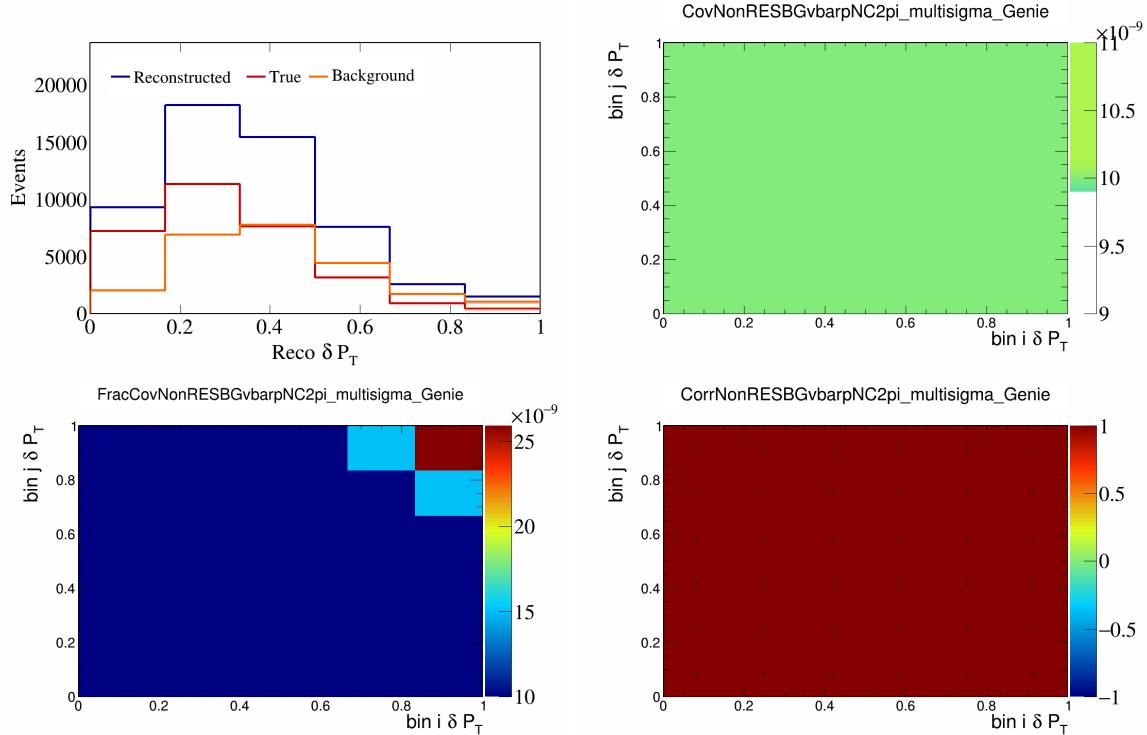


Figure 462: NonRESBGvbarpNC2pi variations for δP_T .

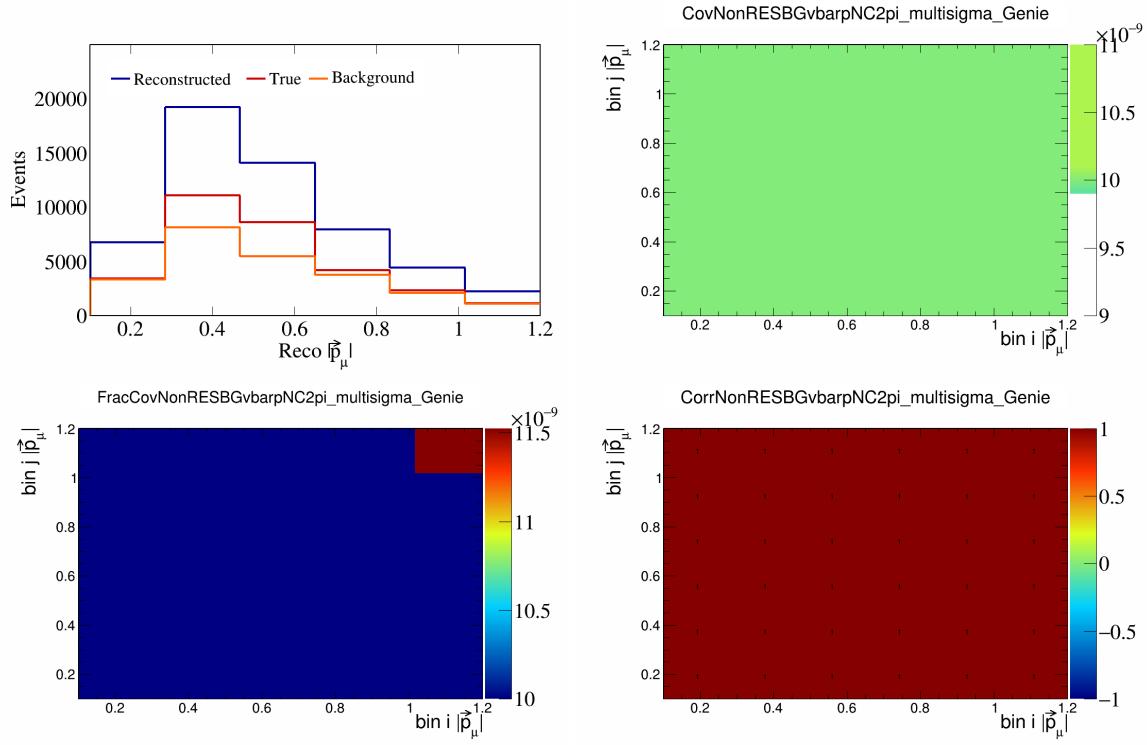


Figure 463: NonRESBGvbarpNC2pi variations for $|\vec{p}_\mu|$.

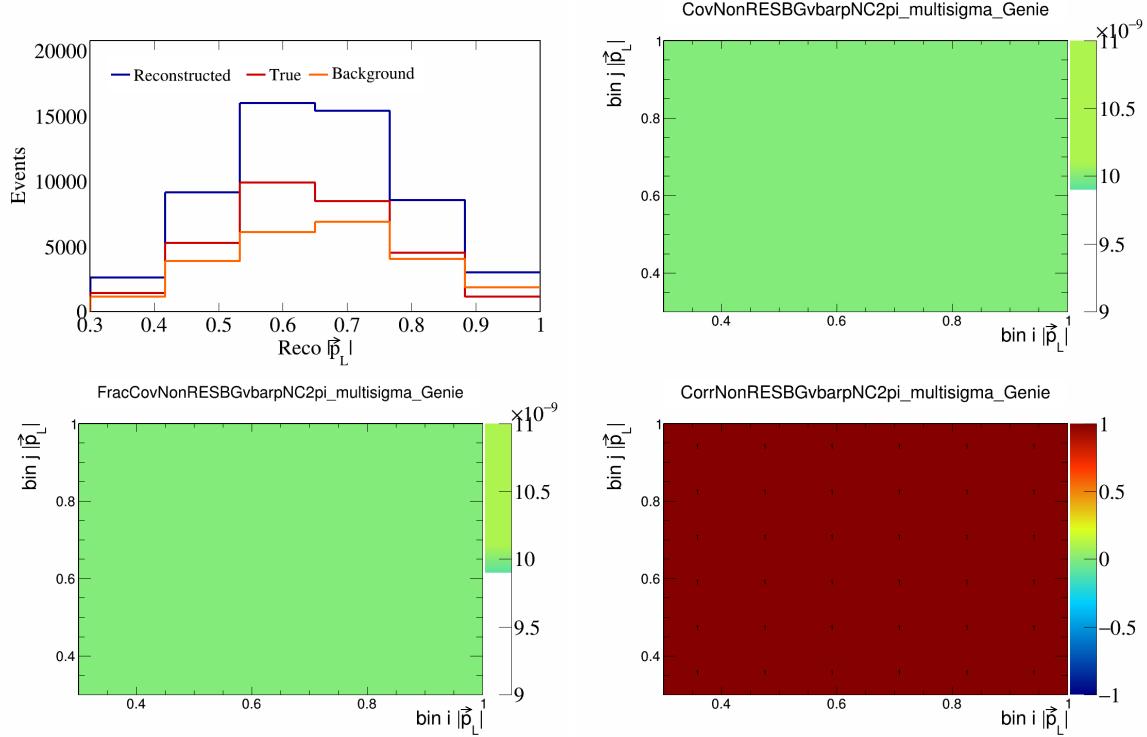


Figure 464: NonRESBGvbarpNC2pi variations for $|\vec{p}_L|$.

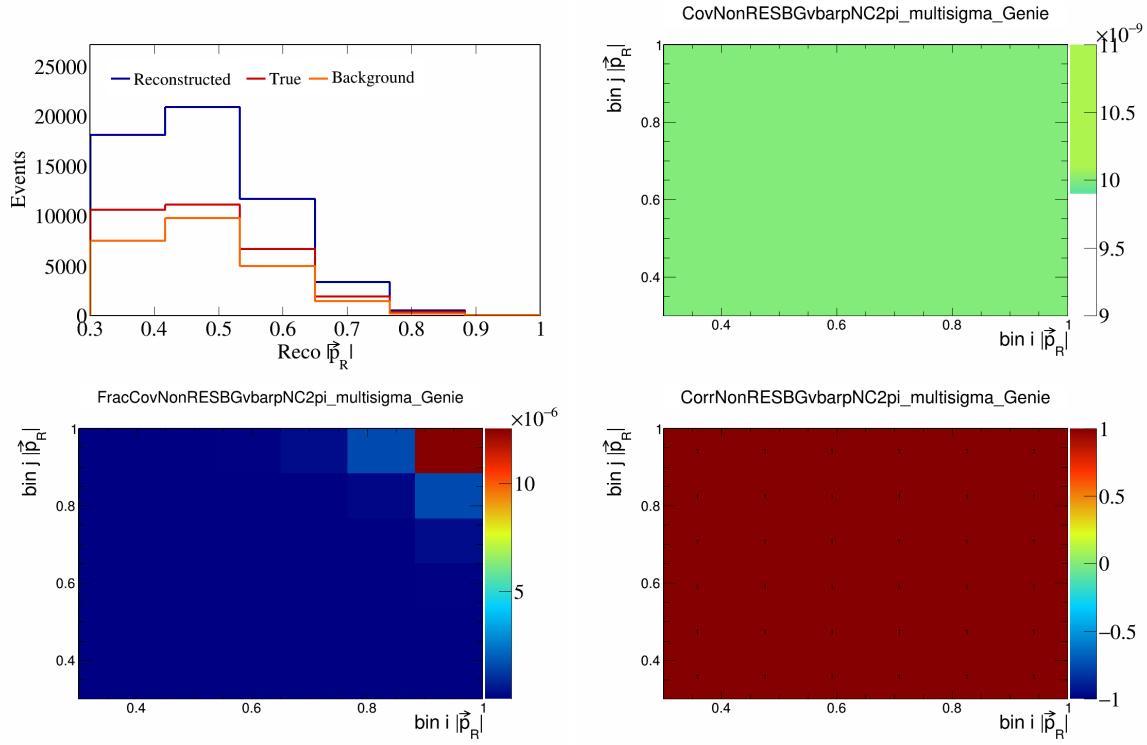


Figure 465: NonRESBGvbarpNC2pi variations for $|\vec{p}_R|$.

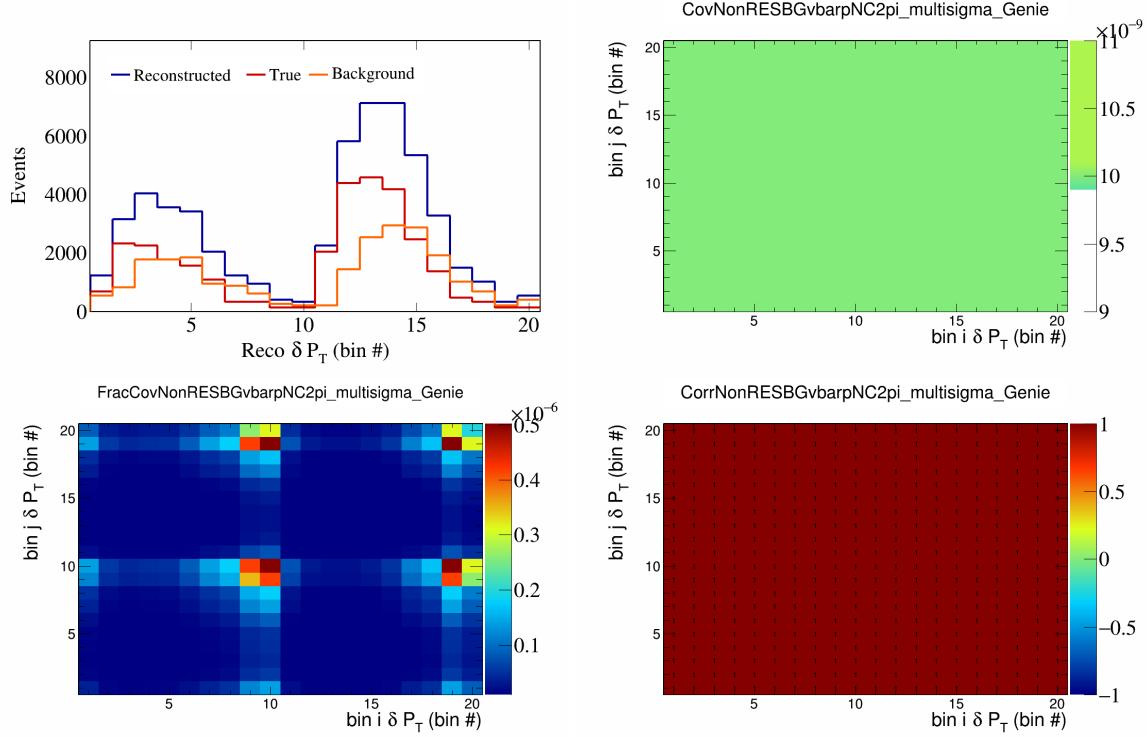


Figure 466: NonRESBGvbarpNC2pi variations for δP_T in $\cos(\theta_{\vec{p}_\mu})$.

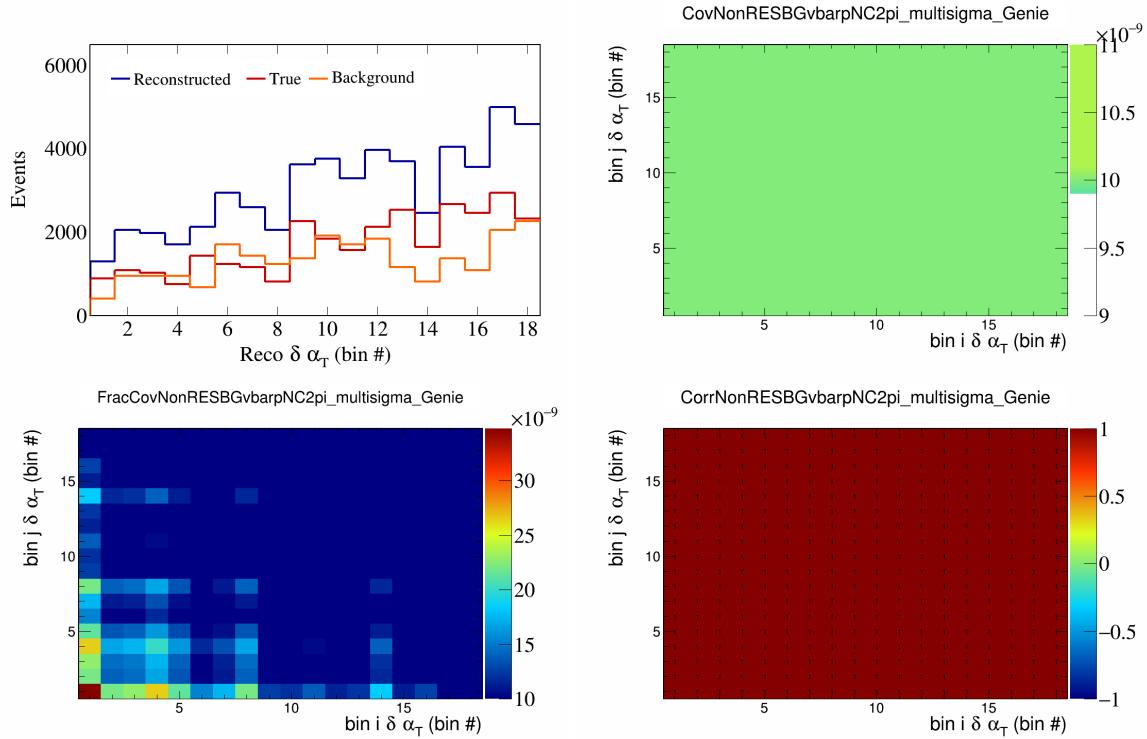


Figure 467: NonRESBGvbarNC2pi variations for $\delta\alpha_T$ in $\cos(\theta_{\vec{p}_\mu})$.

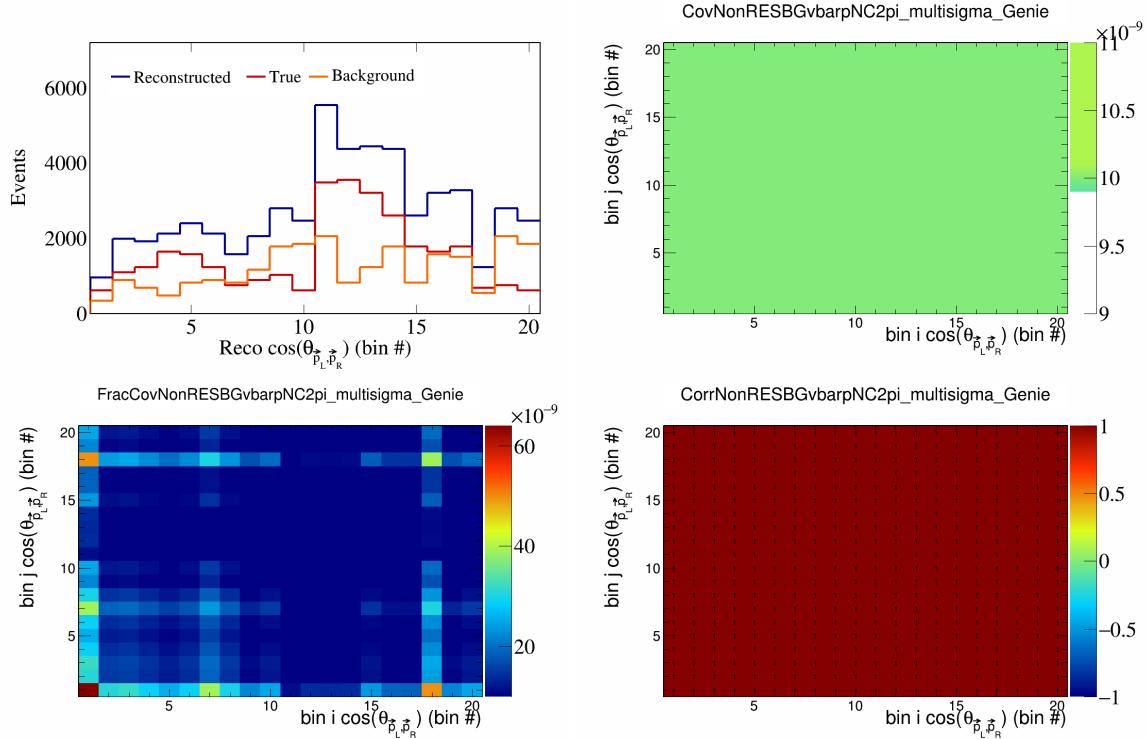


Figure 468: NonRESBGvbarNC2pi variations for $\cos(\theta_{\vec{p}_L, \vec{p}_R})$ in $\cos(\theta_{\vec{p}_\mu})$.

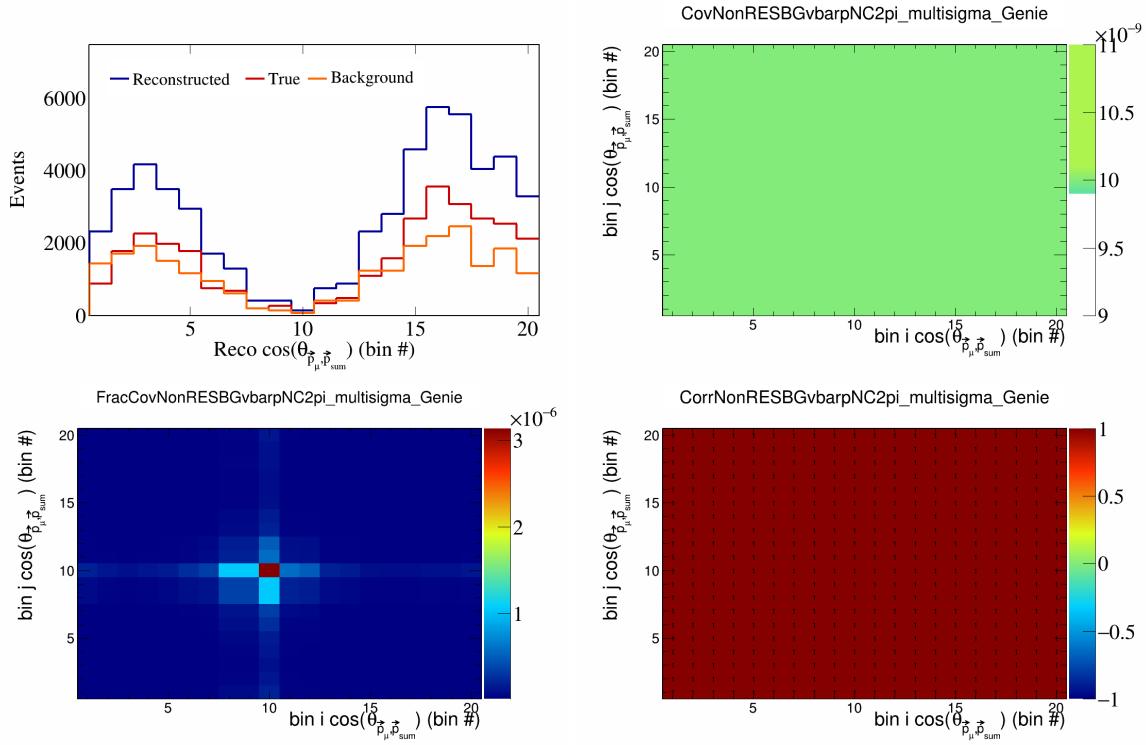


Figure 469: NonRESBGvbarpNC2pi variations for $\cos(\theta_{\vec{p}_\mu} \cdot \vec{p}_{\text{sum}})$ in $\cos(\theta_{\vec{p}_\mu})$.

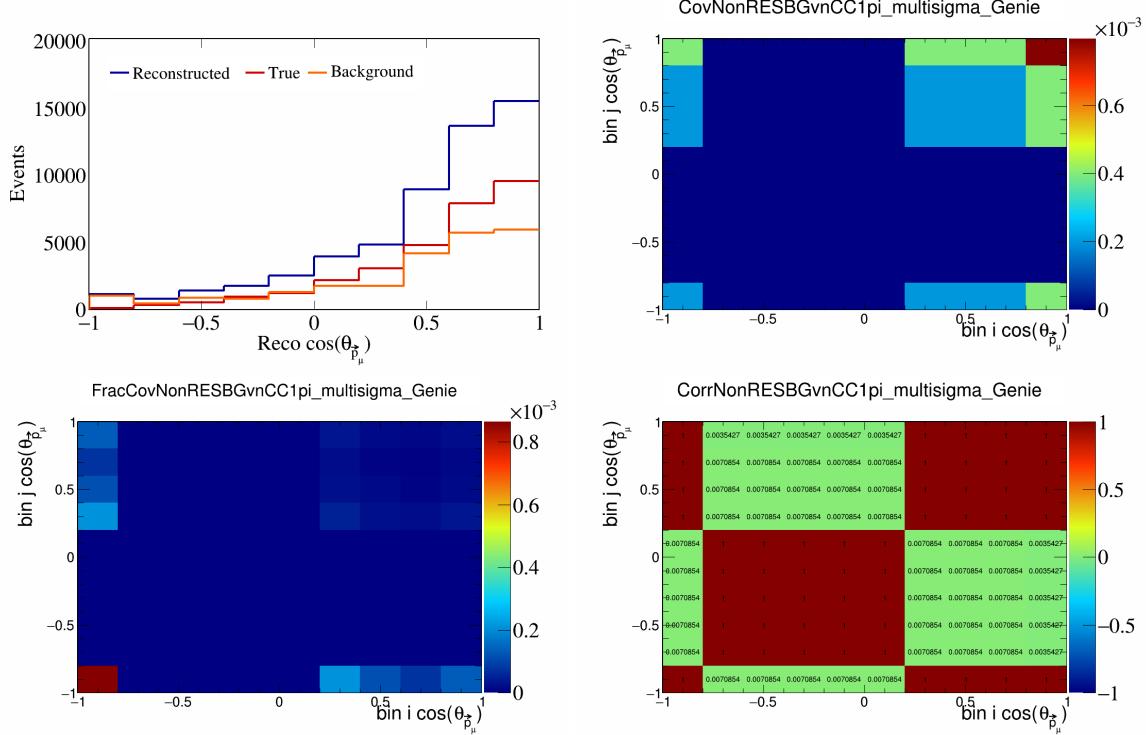


Figure 470: NonRESBGvnCC1pi variations for $\cos(\theta_{\vec{p}_\mu})$.

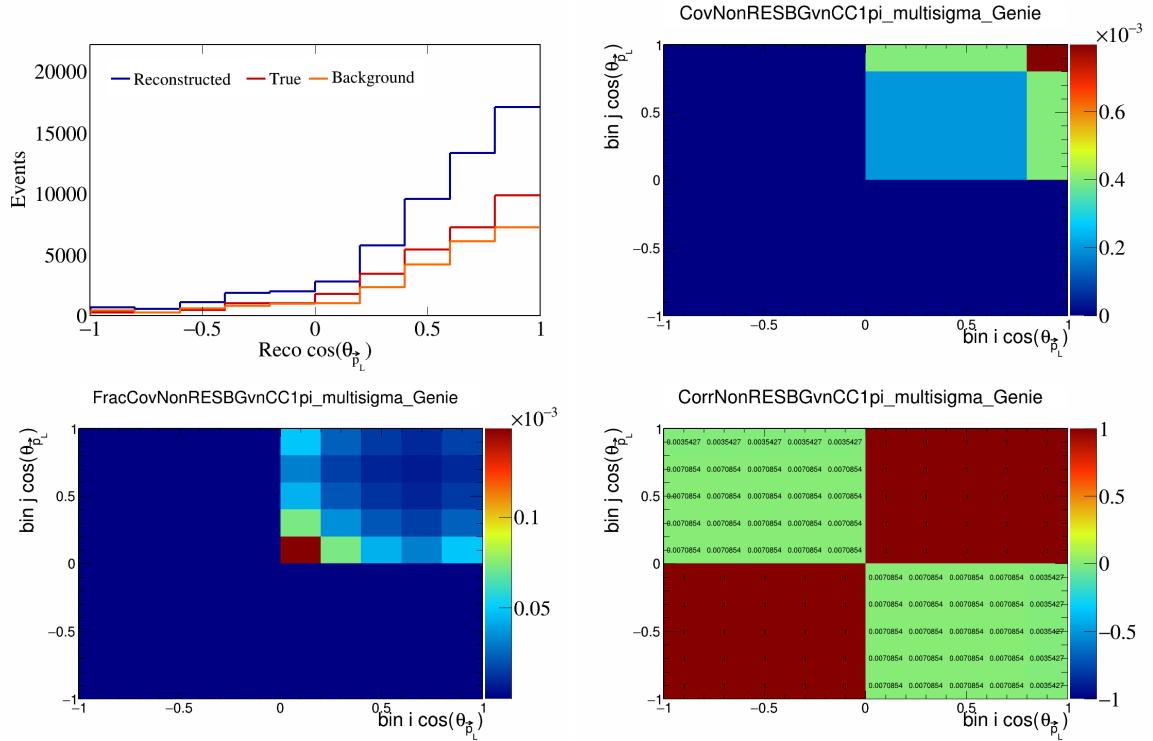


Figure 471: NonRESBGvnCC1pi variations for $\cos(\theta_{\vec{p}_L})$.

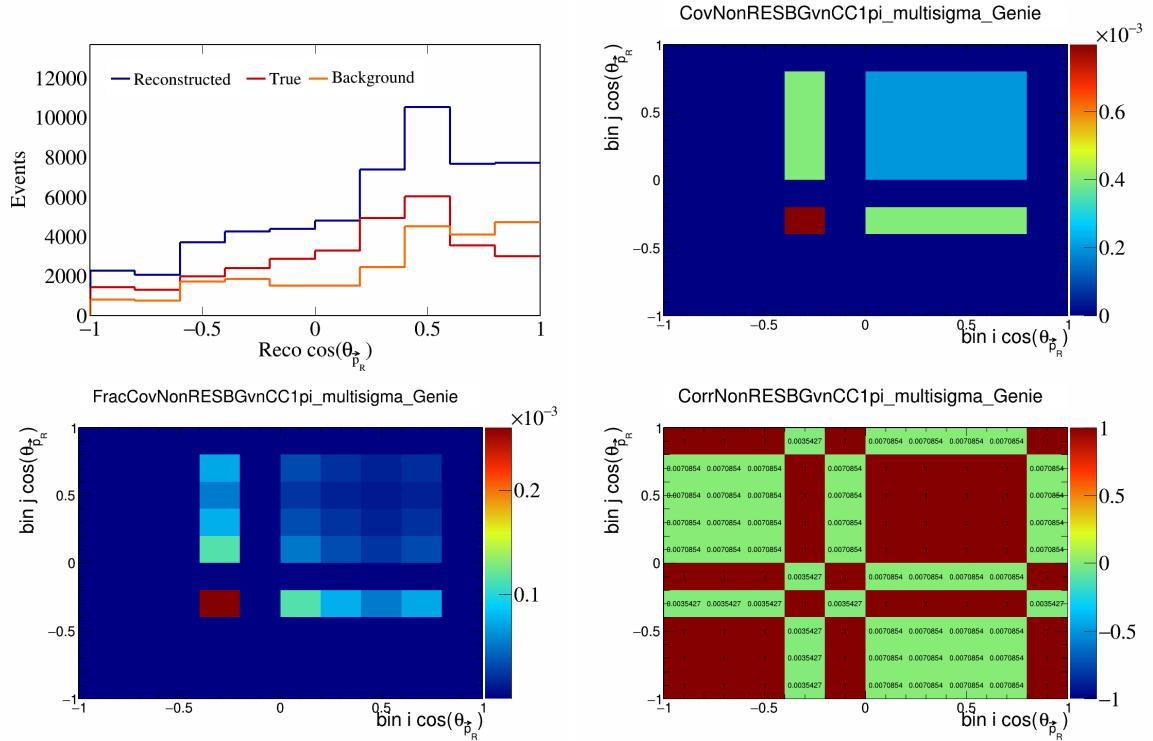


Figure 472: NonRESBGvnCC1pi variations for $\cos(\theta_{\vec{p}_R})$.

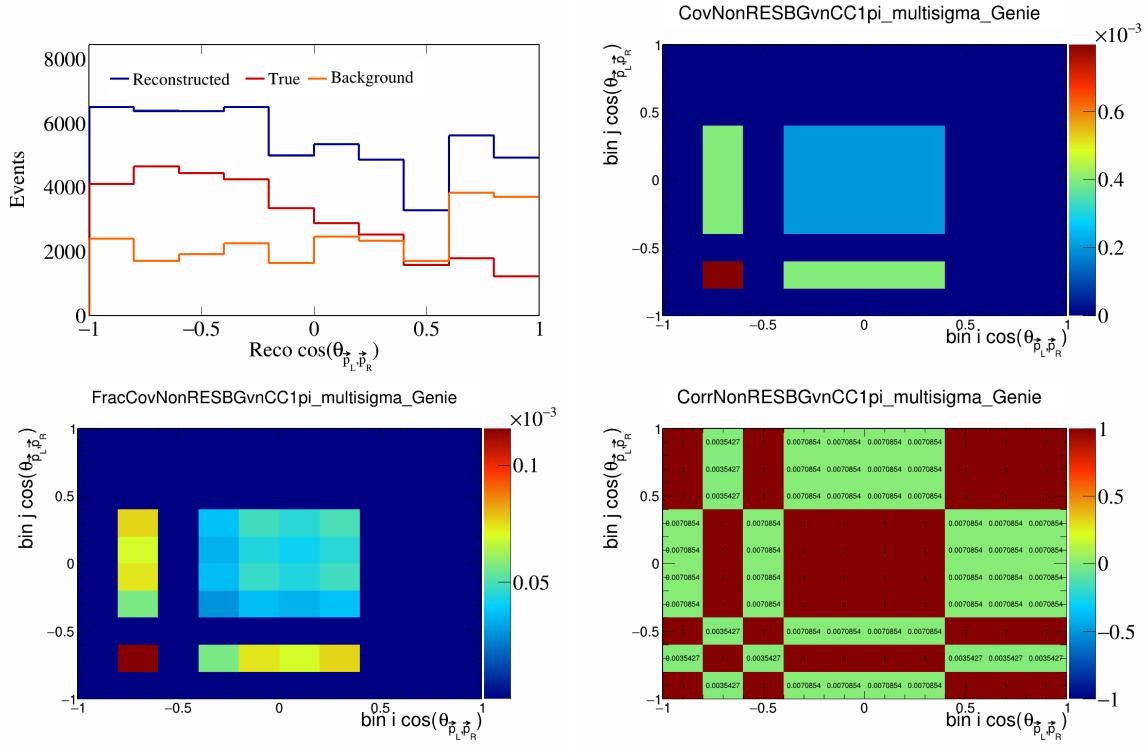


Figure 473: NonRESBGvnCC1pi variations for $\cos(\theta_{\vec{p}_L, \vec{p}_R})$.

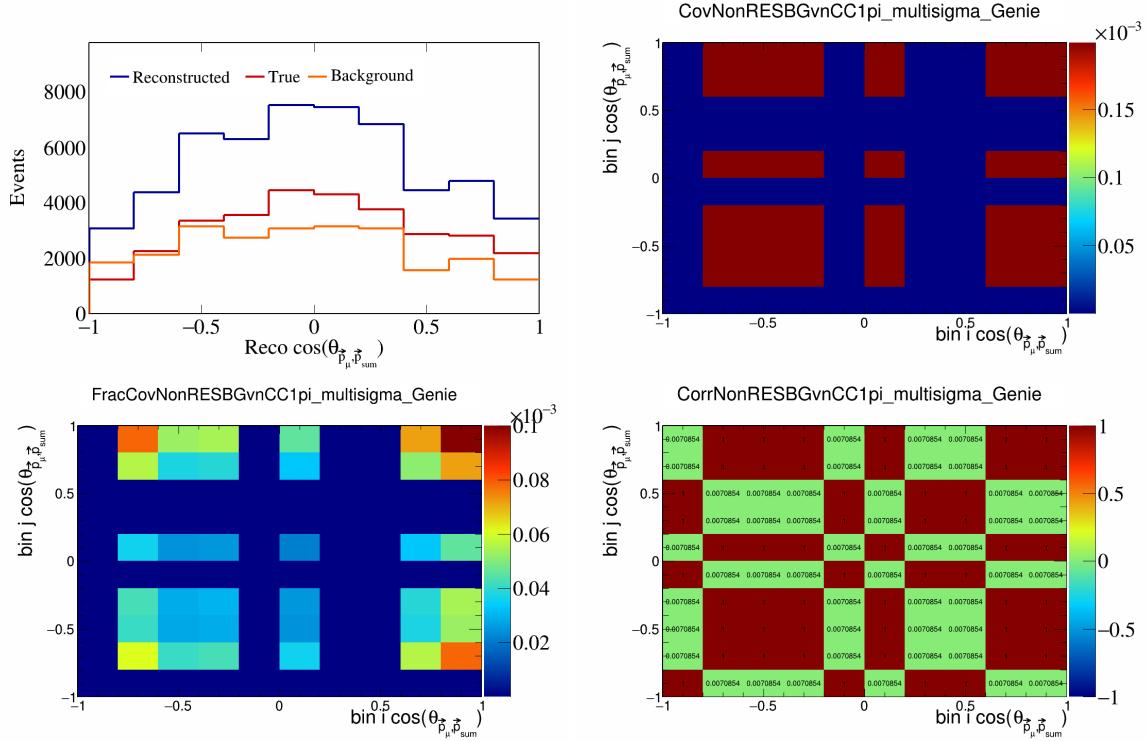


Figure 474: NonRESBGvnCC1pi variations for $\cos(\theta_{\vec{p}_\mu, \vec{p}_{\text{sum}}})$.

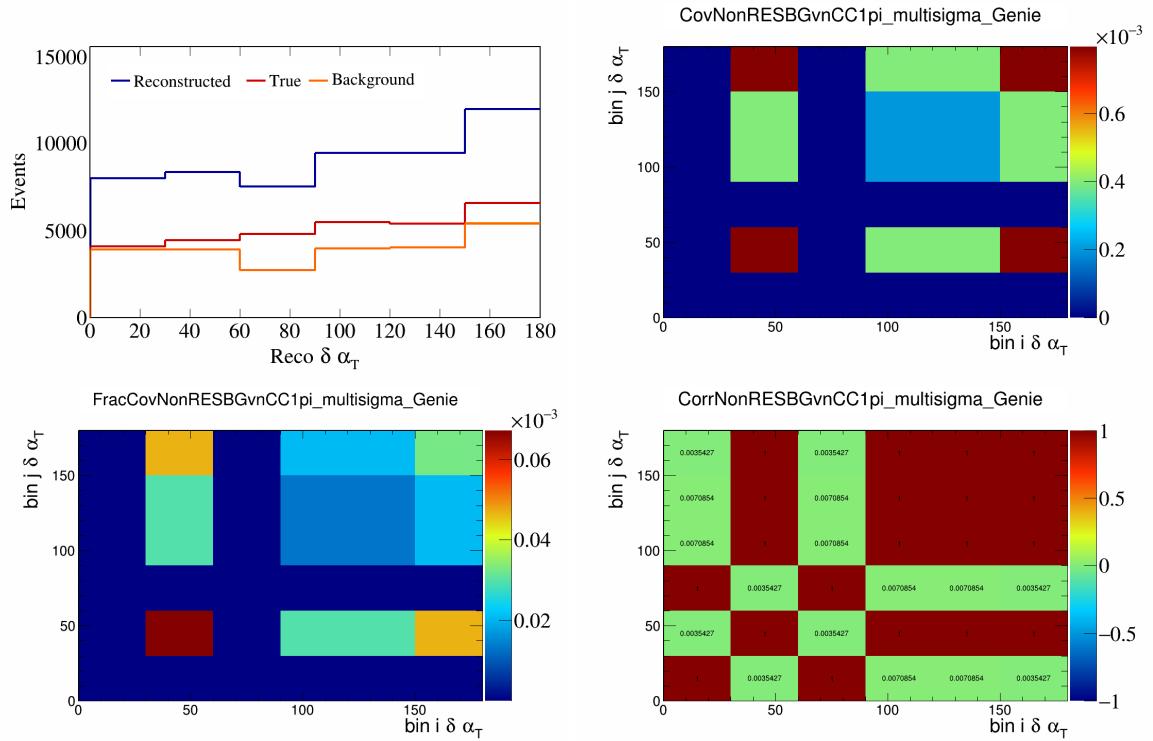


Figure 475: NonRESBGvnCC1pi variations for $\delta \alpha_T$.

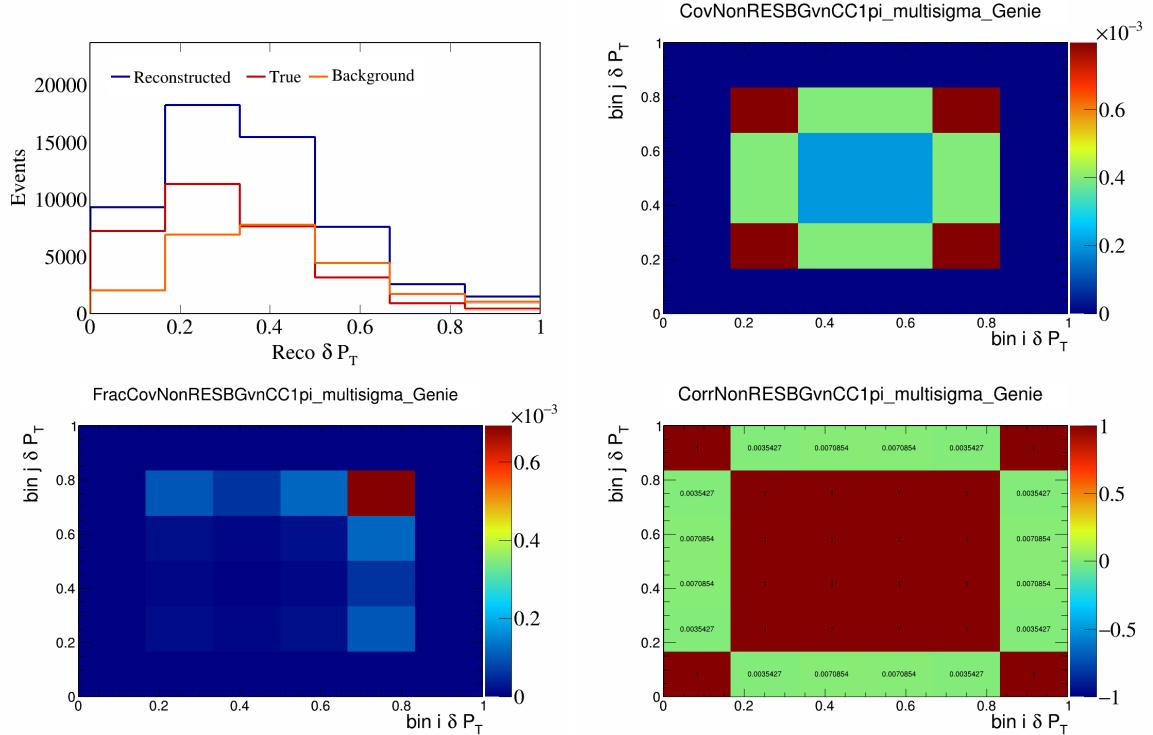


Figure 476: NonRESBGvnCC1pi variations for δP_T .

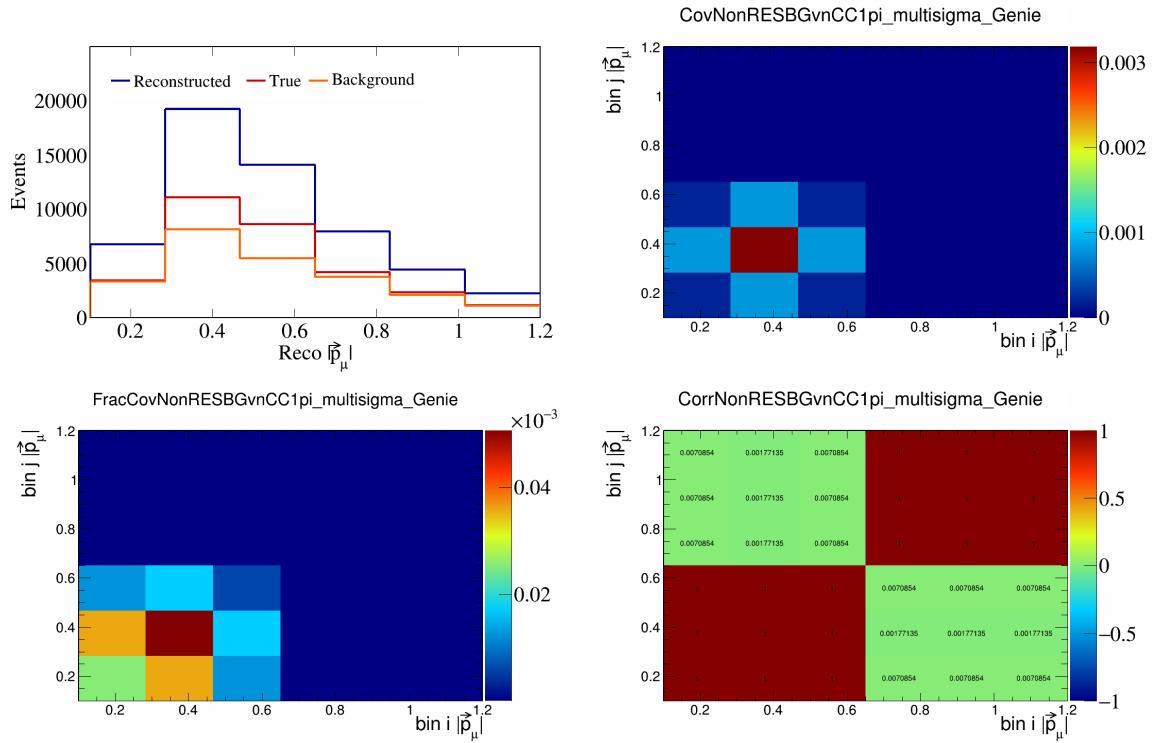


Figure 477: NonRESBGvnCC1pi variations for $|\vec{p}_\mu|$.

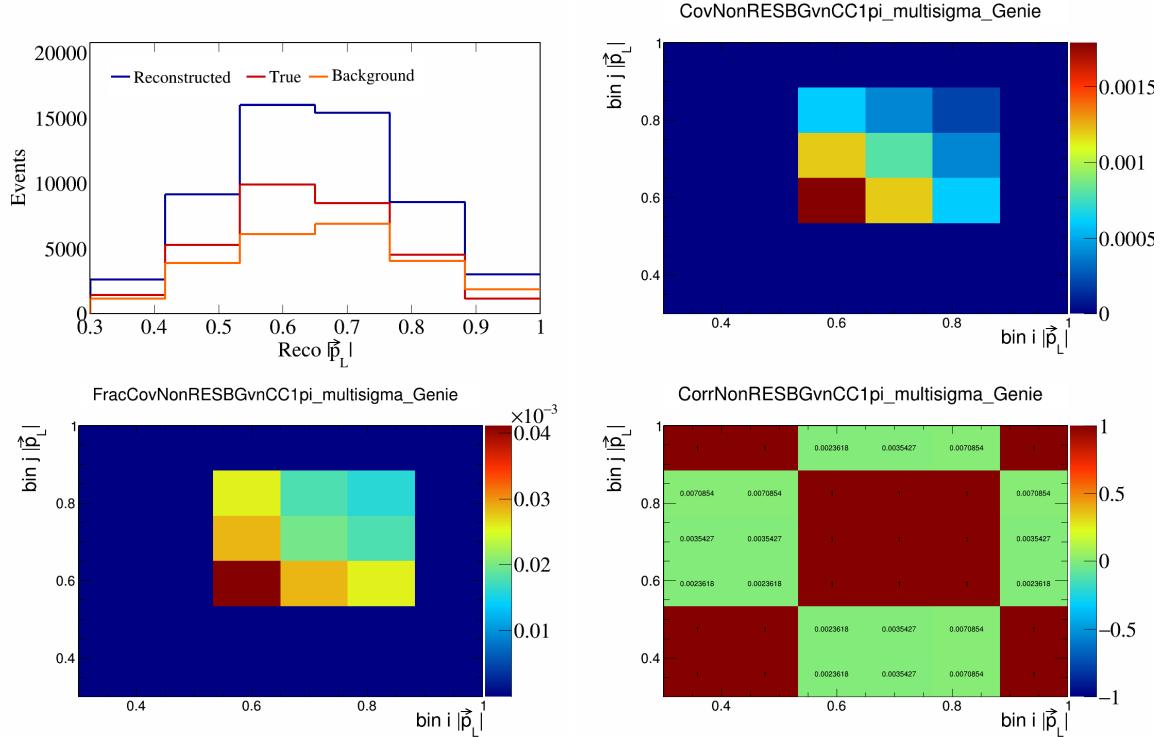


Figure 478: NonRESBGvnCC1pi variations for $|\vec{p}_L|$.

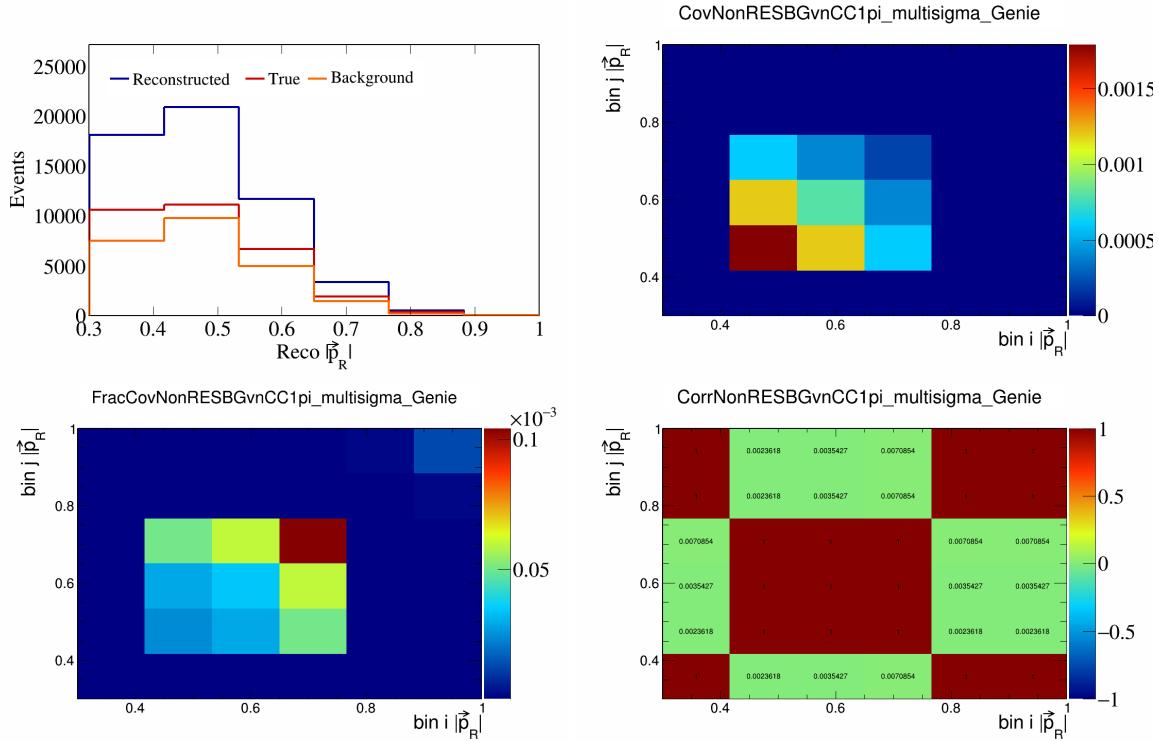


Figure 479: NonRESBGvnCC1pi variations for $|\vec{p}_R|$.

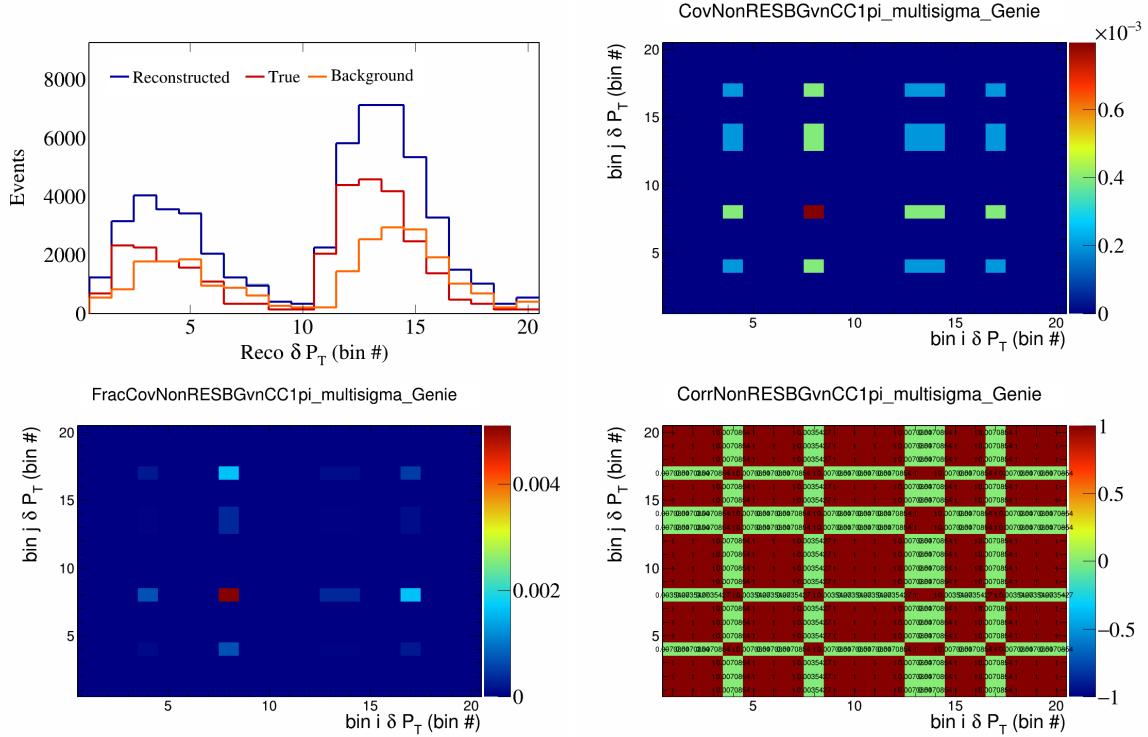


Figure 480: NonRESBGvnCC1pi variations for δP_T in $\cos(\theta_{\vec{p}_\mu})$.

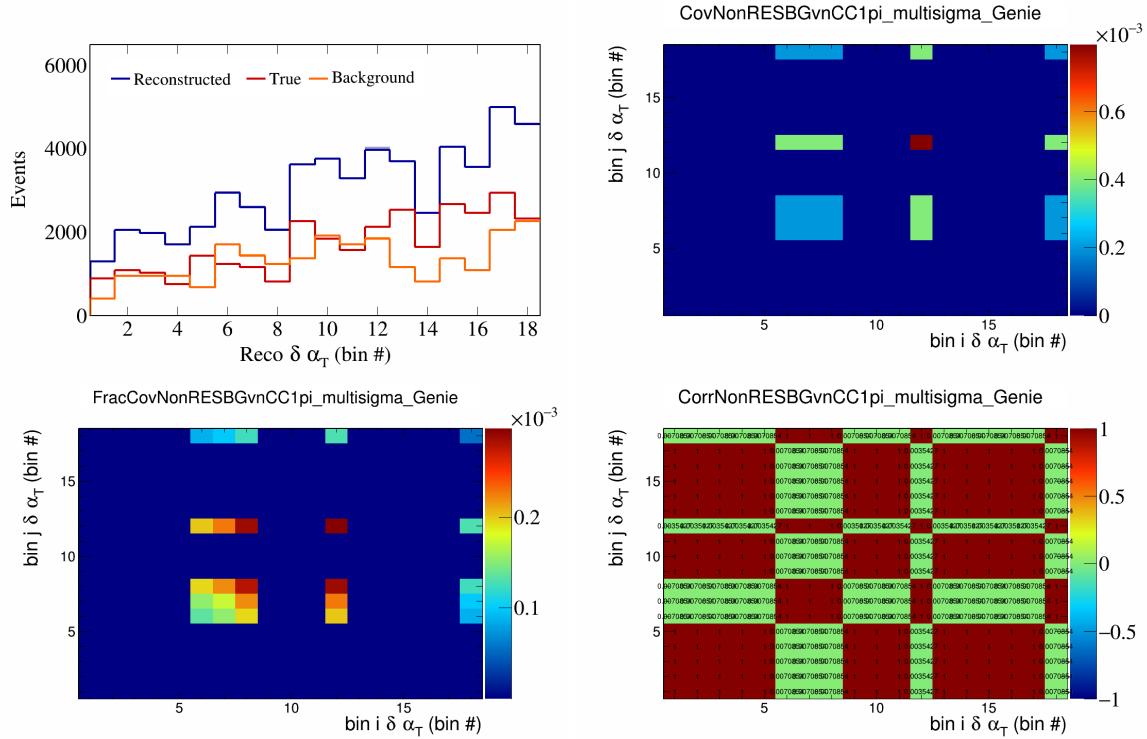


Figure 481: NonRESBGvnCC1pi variations for $\delta\alpha_T$ in $\cos(\theta_{\vec{p}_\mu})$.

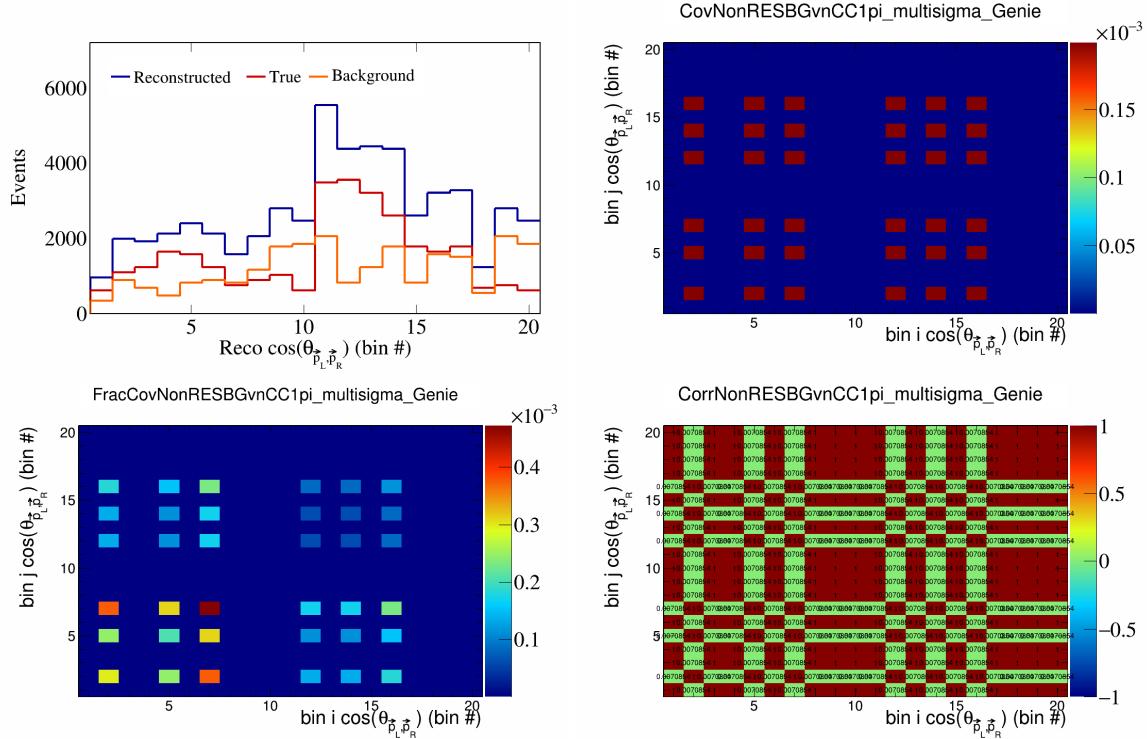


Figure 482: NonRESBGvnCC1pi variations for $\cos(\theta_{\vec{p}_L, \vec{p}_R})$ in $\cos(\theta_{\vec{p}_\mu})$.

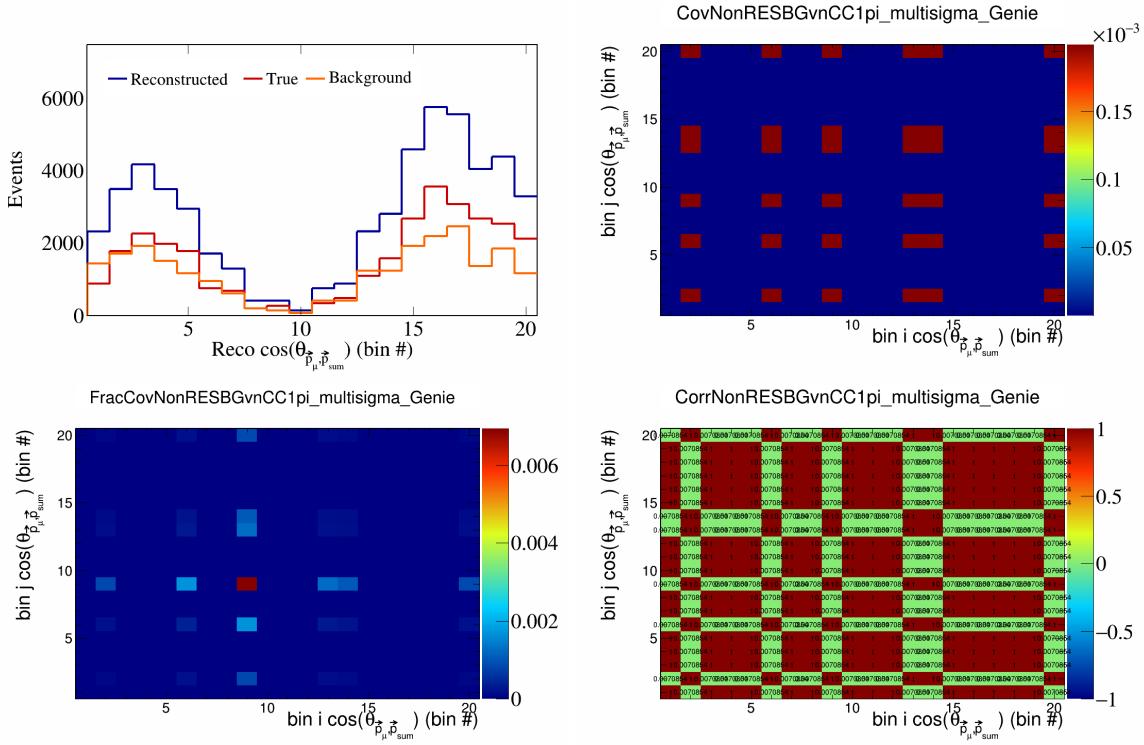


Figure 483: NonRESBGvnCC1pi variations for $\cos(\theta_{\vec{p}_\mu, \vec{p}_{\text{sum}}})$ in $\cos(\theta_{\vec{p}_\mu})$.

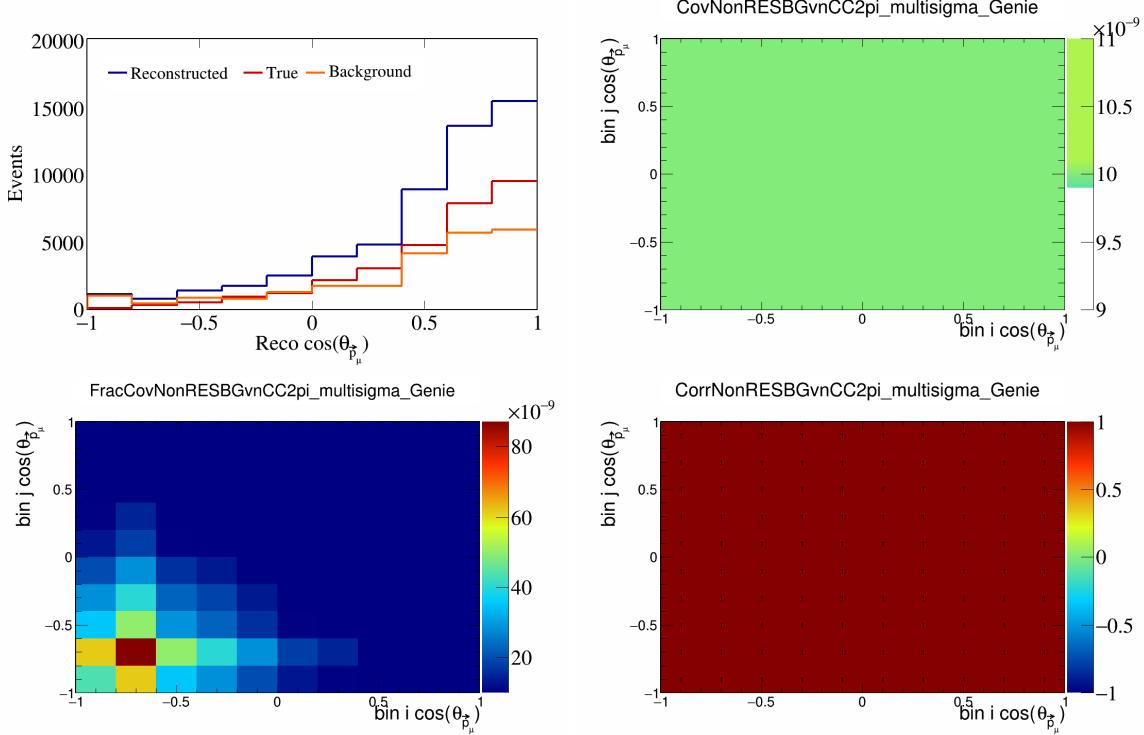


Figure 484: NonRESBGvnCC2pi variations for $\cos(\theta_{\vec{p}_\mu})$.

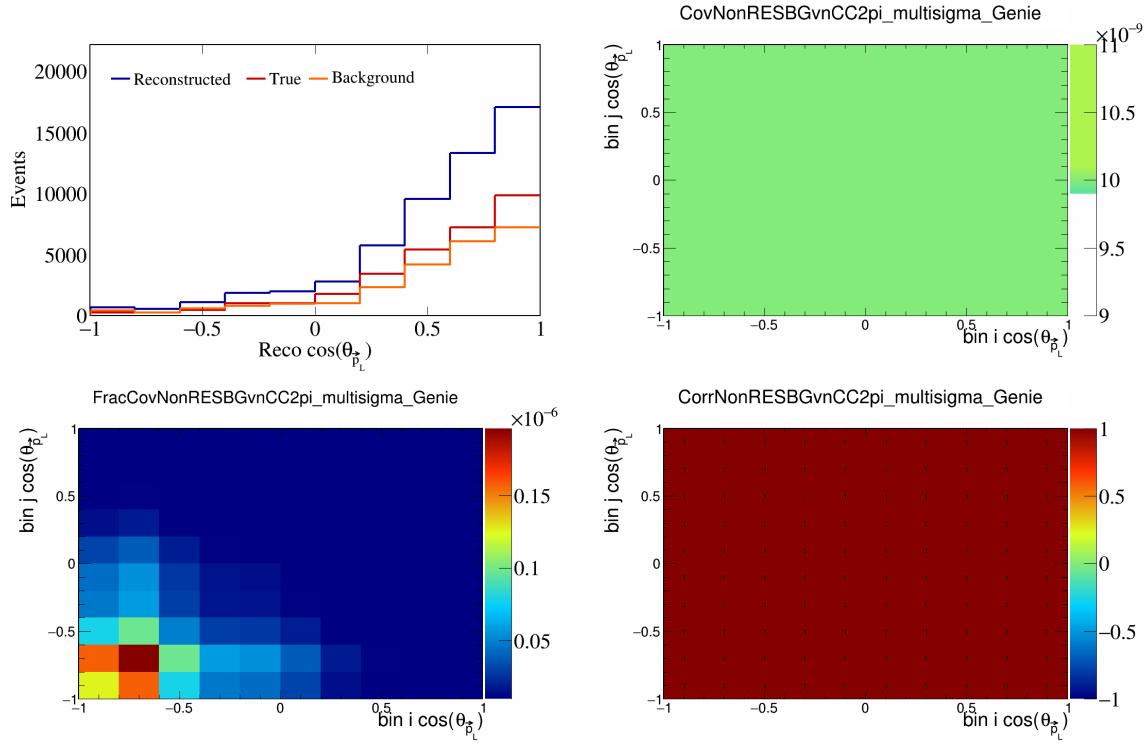


Figure 485: NonRESBGvnCC2pi variations for $\cos(\theta_{\vec{p}_L})$.

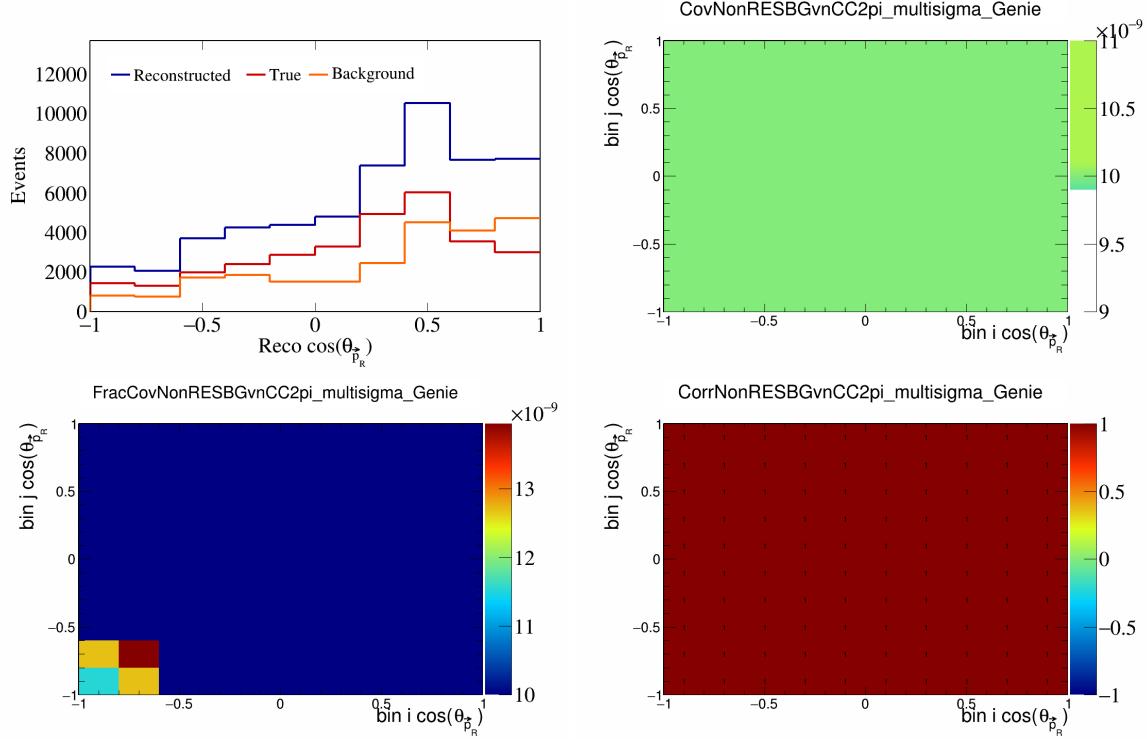


Figure 486: NonRESBGvnCC2pi variations for $\cos(\theta_{\vec{p}_R})$.

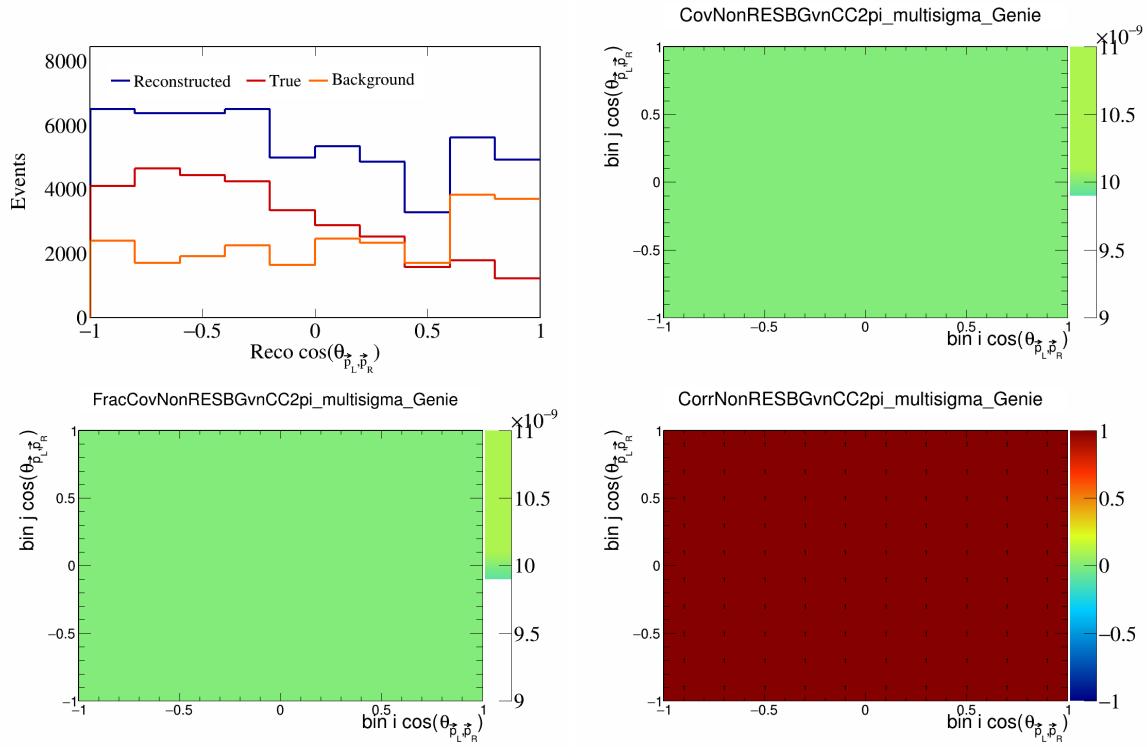


Figure 487: NonRESBGvnCC2pi variations for $\cos(\theta_{\vec{p}_L, \vec{p}_R})$.

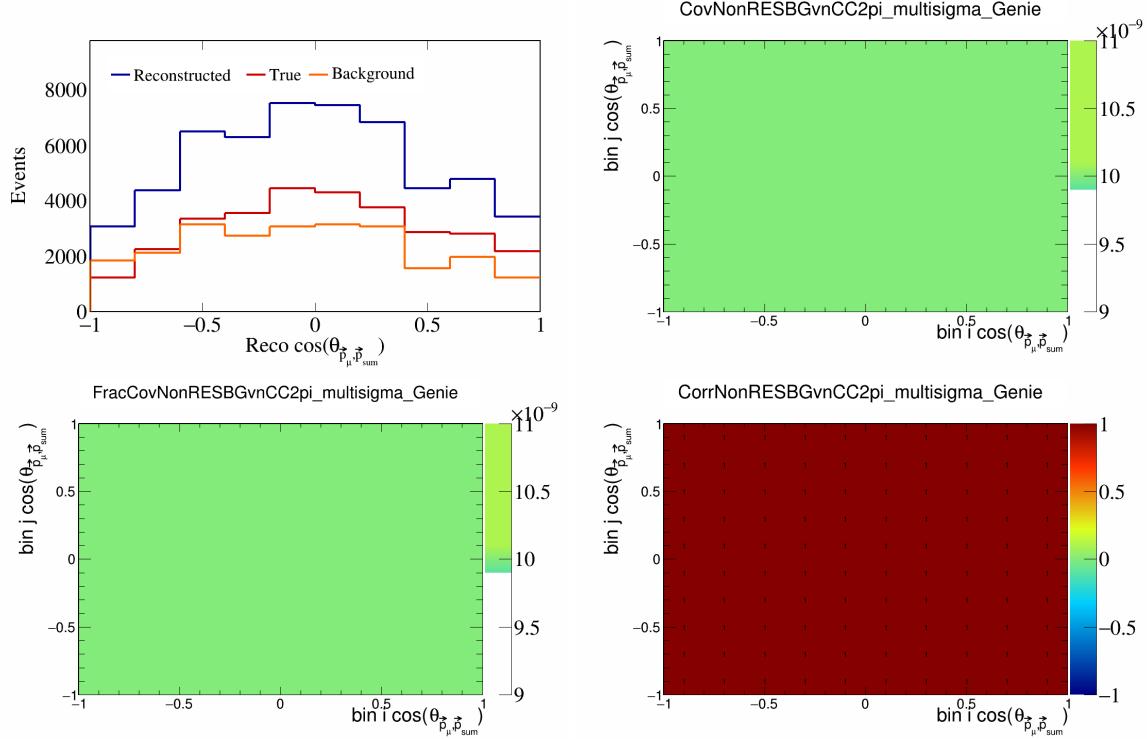


Figure 488: NonRESBGvnCC2pi variations for $\cos(\theta_{\vec{p}_\mu, \vec{p}_{\text{sum}}})$.

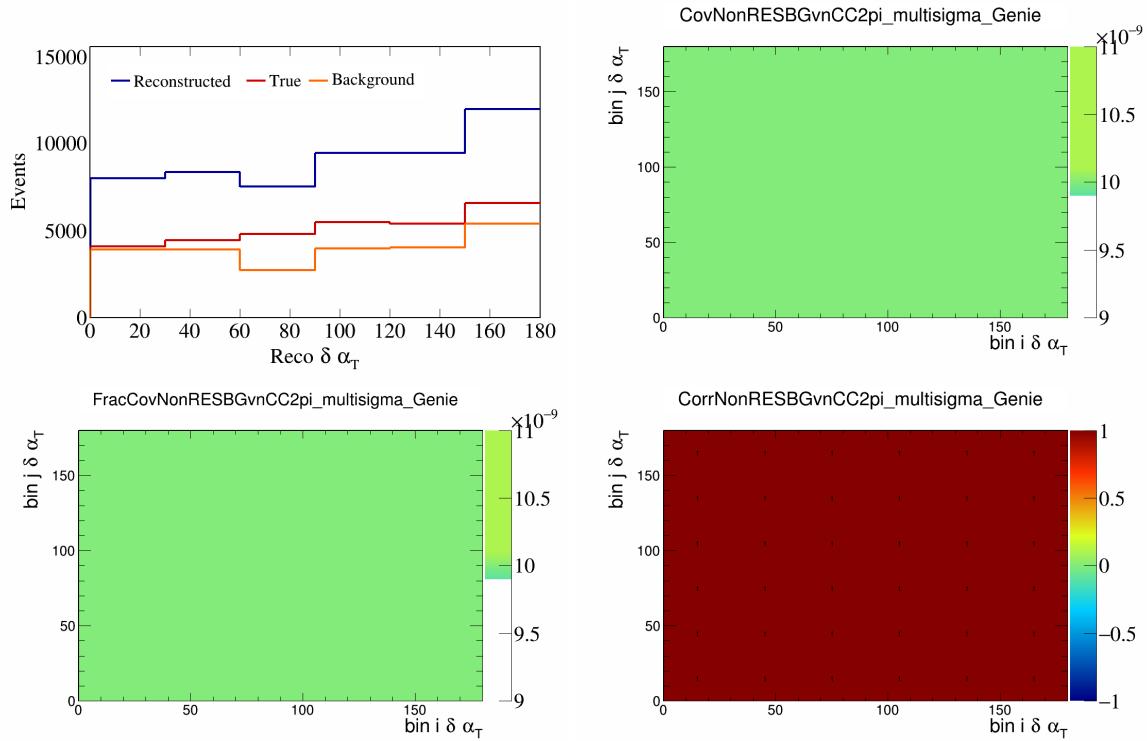


Figure 489: NonRESBGvnCC2pi variations for $\delta\alpha_T$.

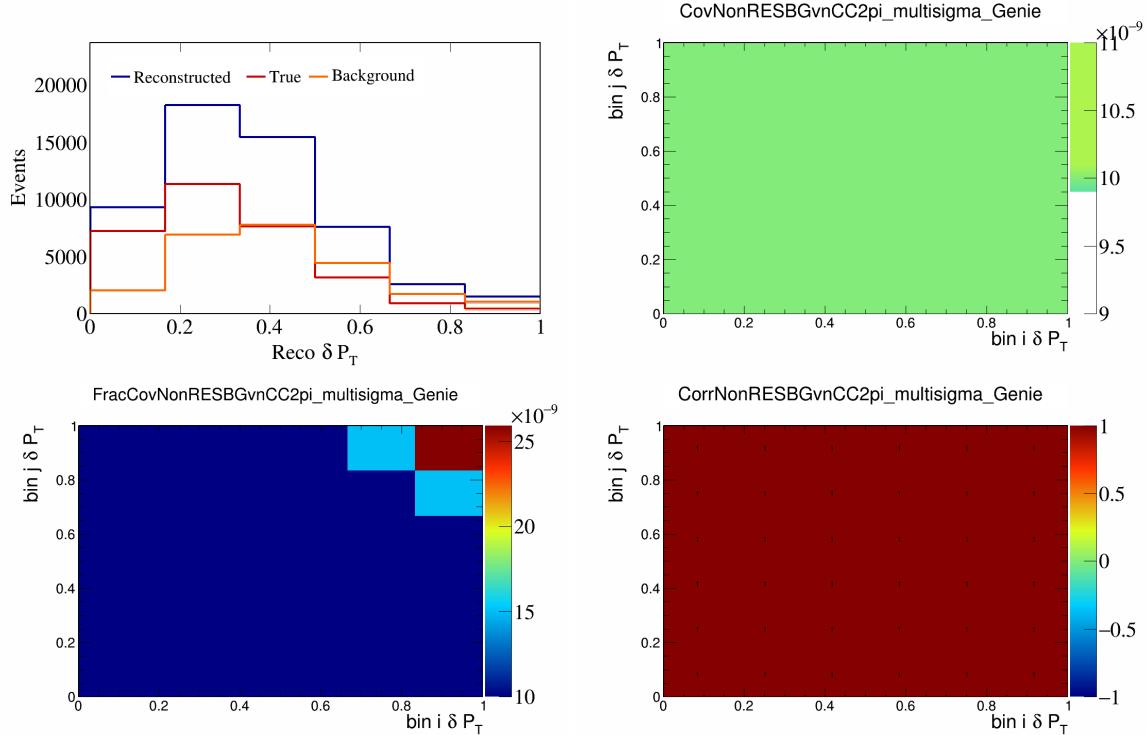


Figure 490: NonRESBGvnCC2pi variations for δP_T .

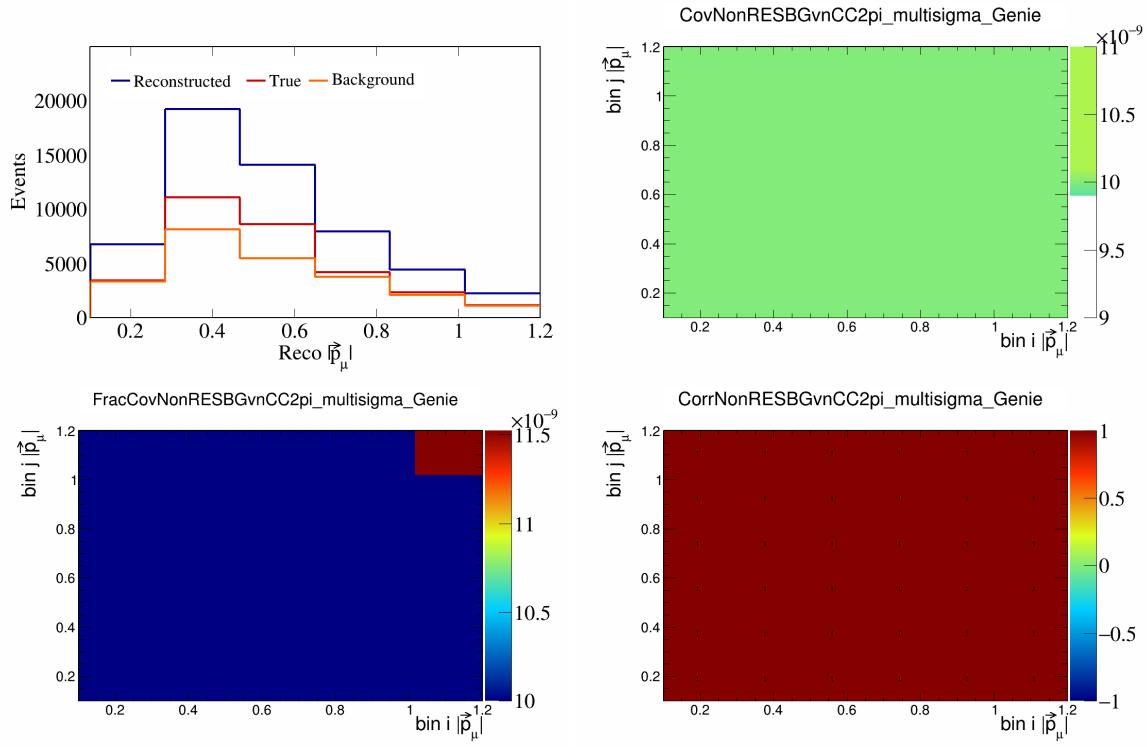


Figure 491: NonRESBGvnCC2pi variations for $|\vec{p}_\mu|$.

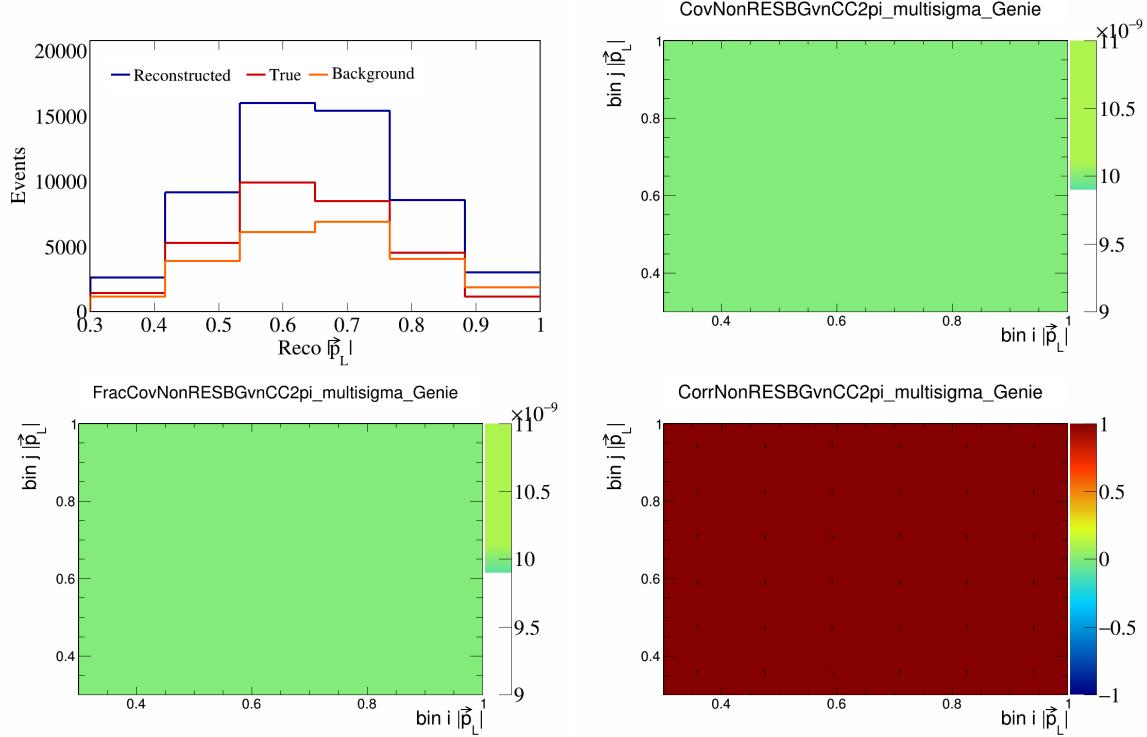


Figure 492: NonRESBGvnCC2pi variations for $|\vec{p}_L|$.

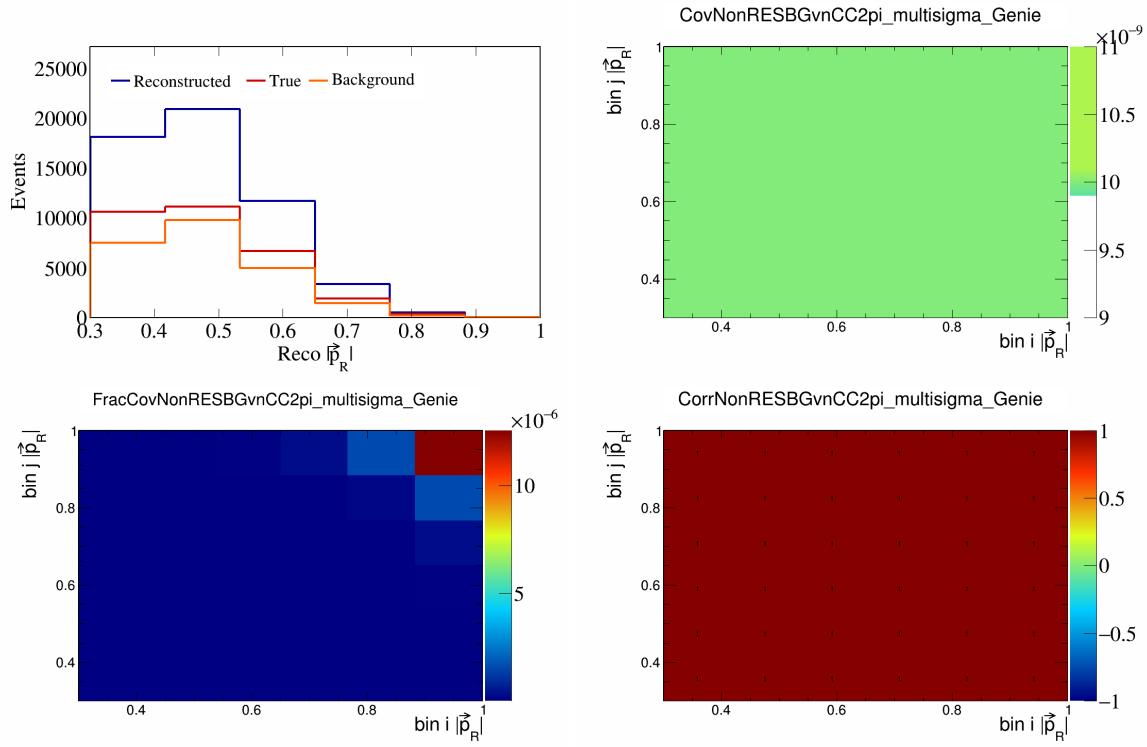


Figure 493: NonRESBGvnCC2pi variations for $|\vec{p}_R|$.

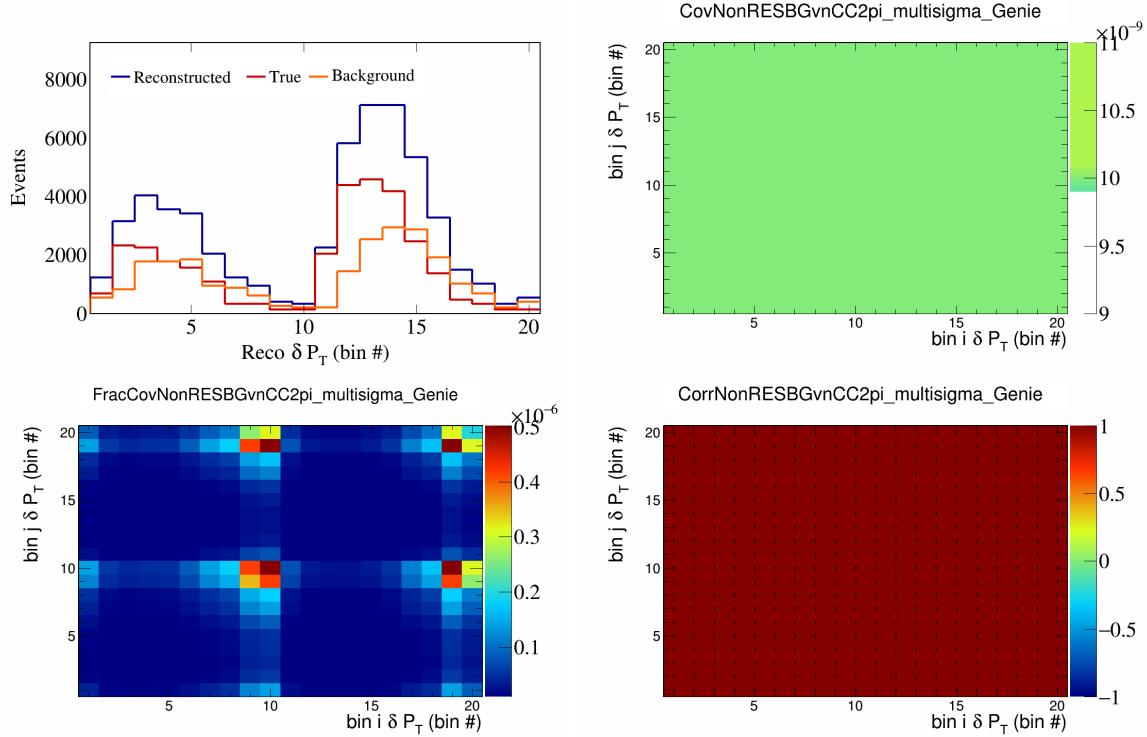


Figure 494: NonRESBGvnCC2pi variations for δP_T in $\cos(\theta_{\vec{p}_\mu})$.

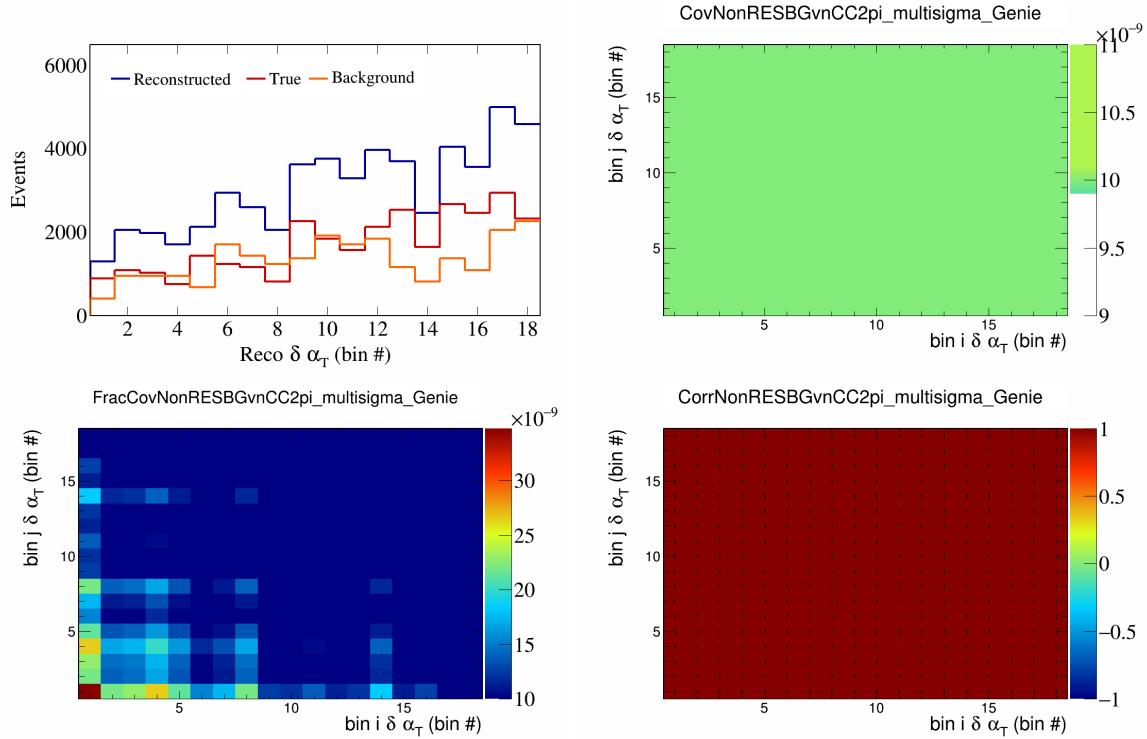


Figure 495: NonRESBGvnCC2pi variations for $\delta\alpha_T$ in $\cos(\theta_{\vec{p}_\mu})$.

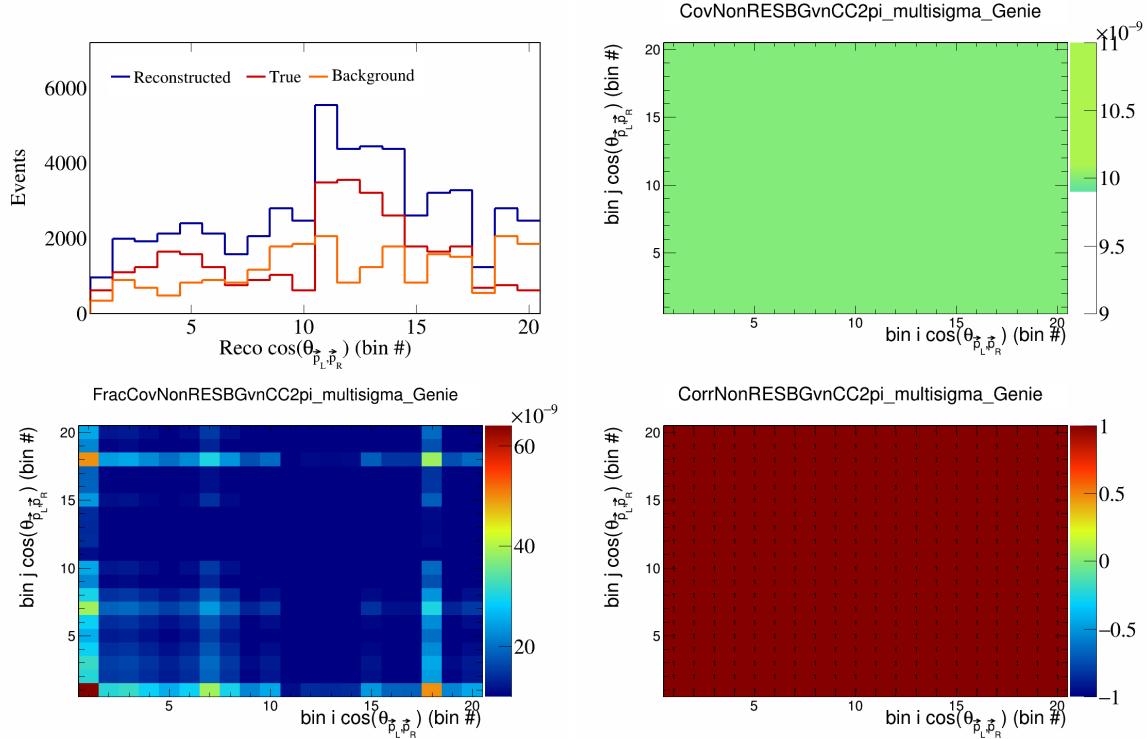


Figure 496: NonRESBGvnCC2pi variations for $\cos(\theta_{\vec{p}_L, \vec{p}_R})$ in $\cos(\theta_{\vec{p}_\mu})$.

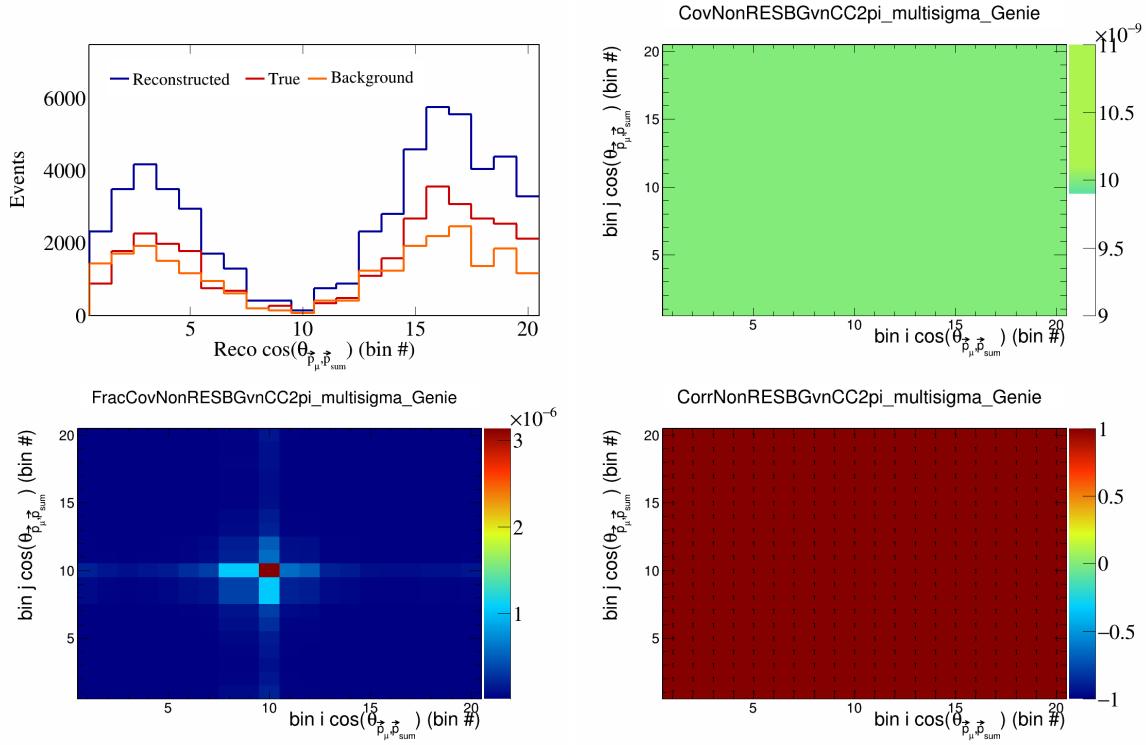


Figure 497: NonRESBGvnCC2pi variations for $\cos(\theta_{\vec{p}_\mu, \vec{p}_{\text{sum}}})$ in $\cos(\theta_{\vec{p}_\mu})$.

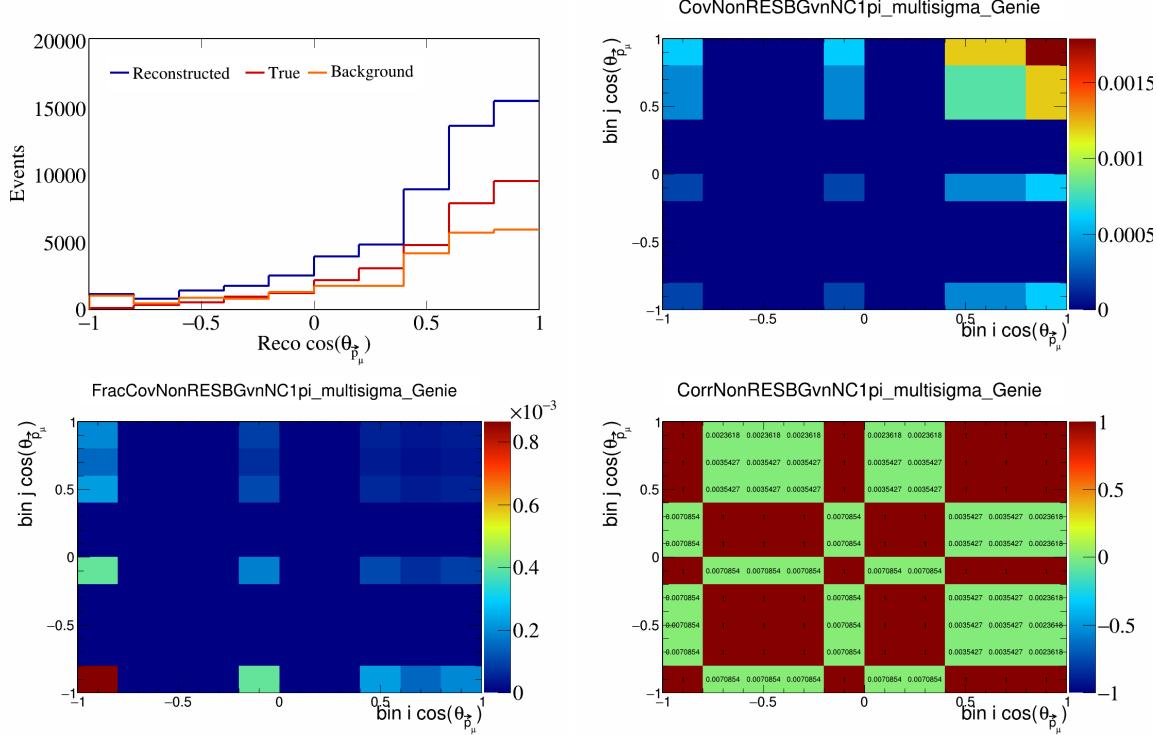


Figure 498: NonRESBGvnNC1pi variations for $\cos(\theta_{\vec{p}_\mu})$.

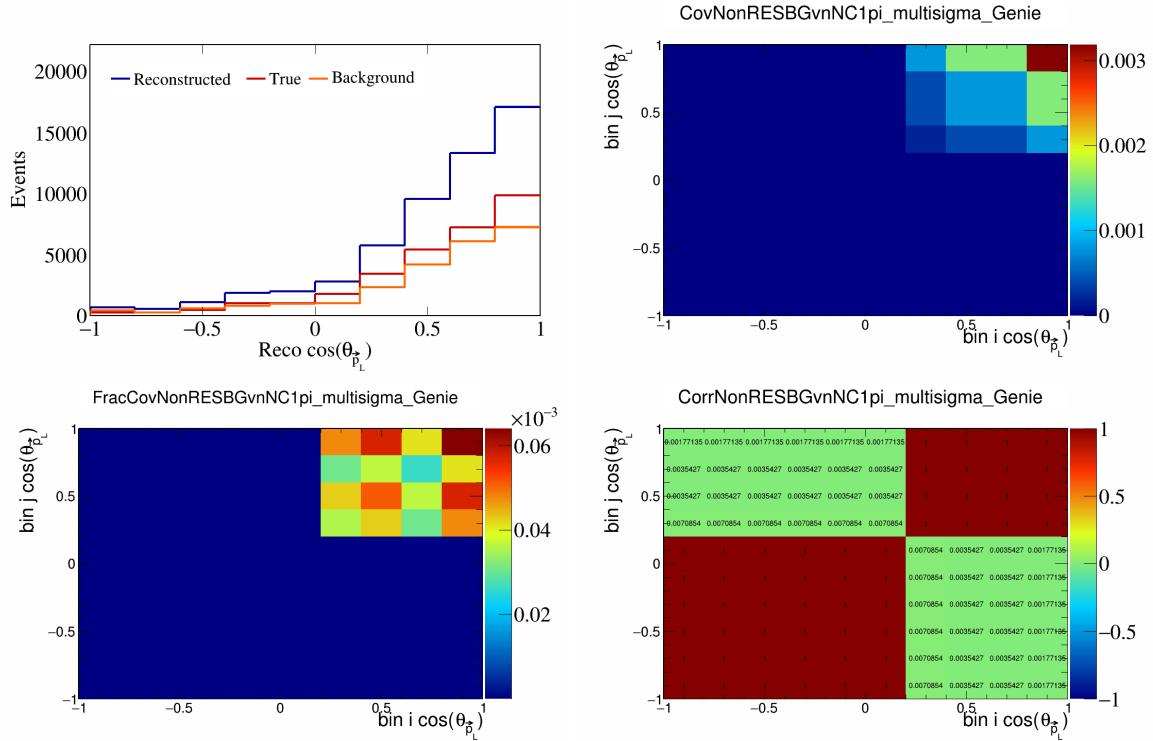


Figure 499: NonRESBGvnNC1pi variations for $\cos(\theta_{\vec{p}_L})$.

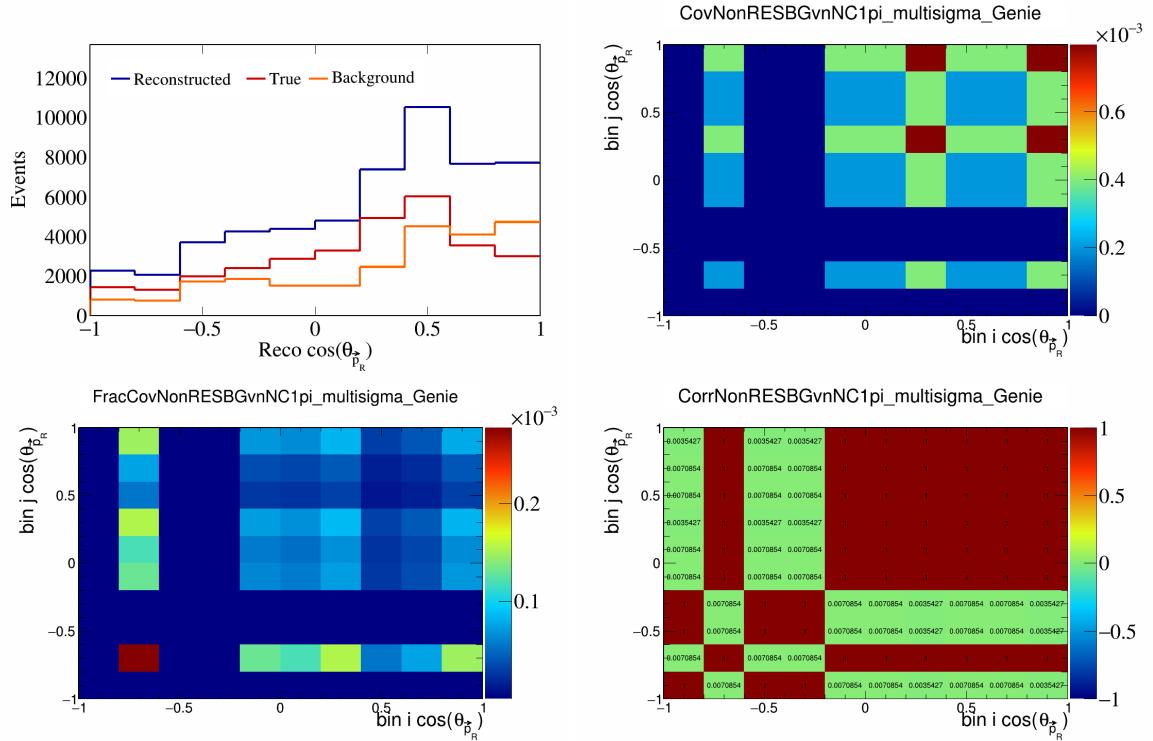


Figure 500: NonRESBGvnNC1pi variations for $\cos(\theta_{\vec{p}_R})$.

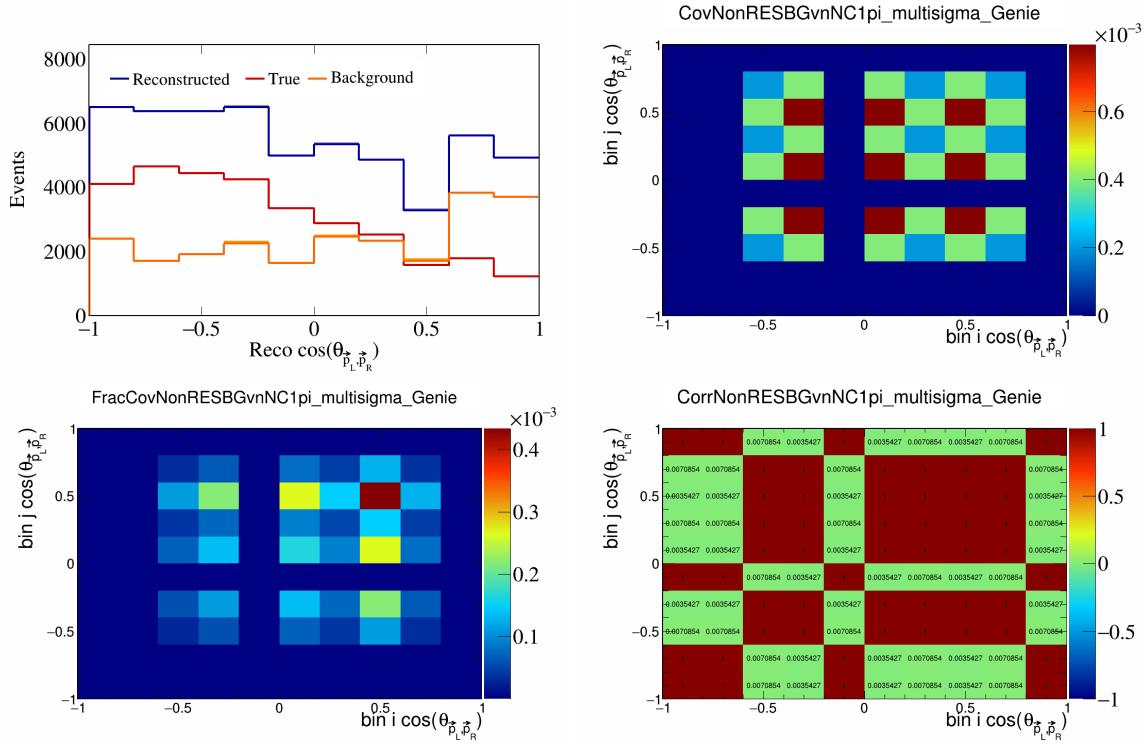


Figure 501: NonRESBGvnNC1pi variations for $\cos(\theta_{\vec{p}_L, \vec{p}_R})$.

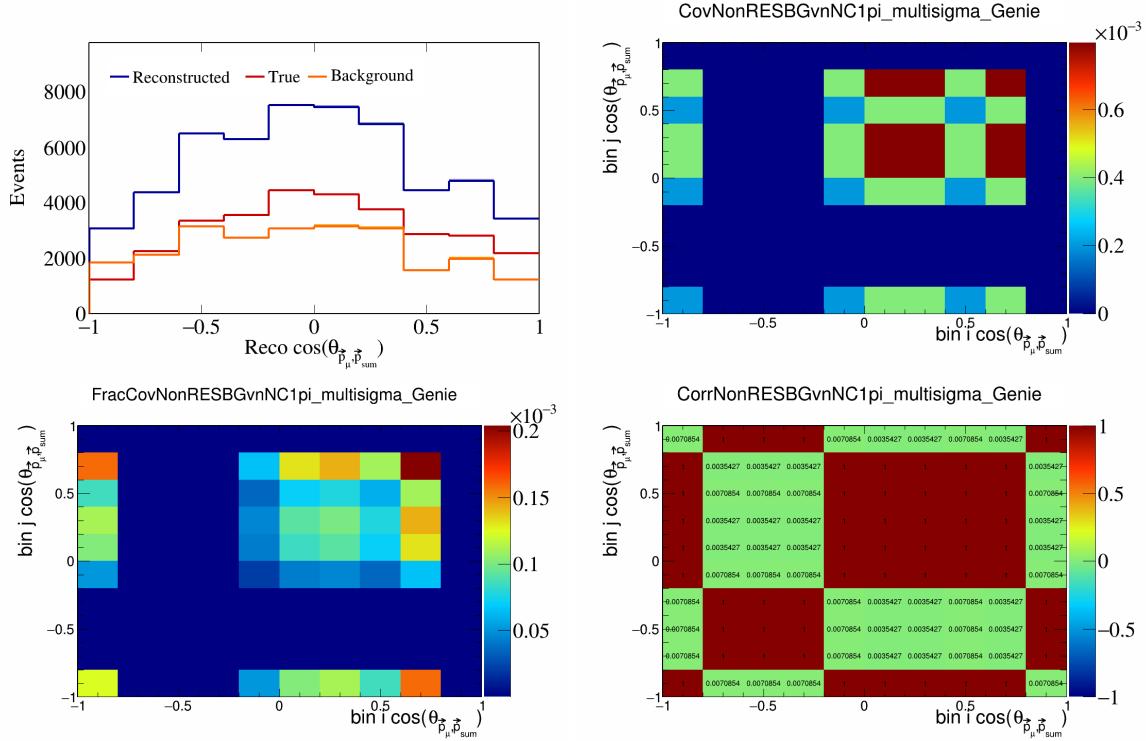


Figure 502: NonRESBGvnNC1pi variations for $\cos(\theta_{\vec{p}_\mu, \vec{p}_{\text{sum}}})$.

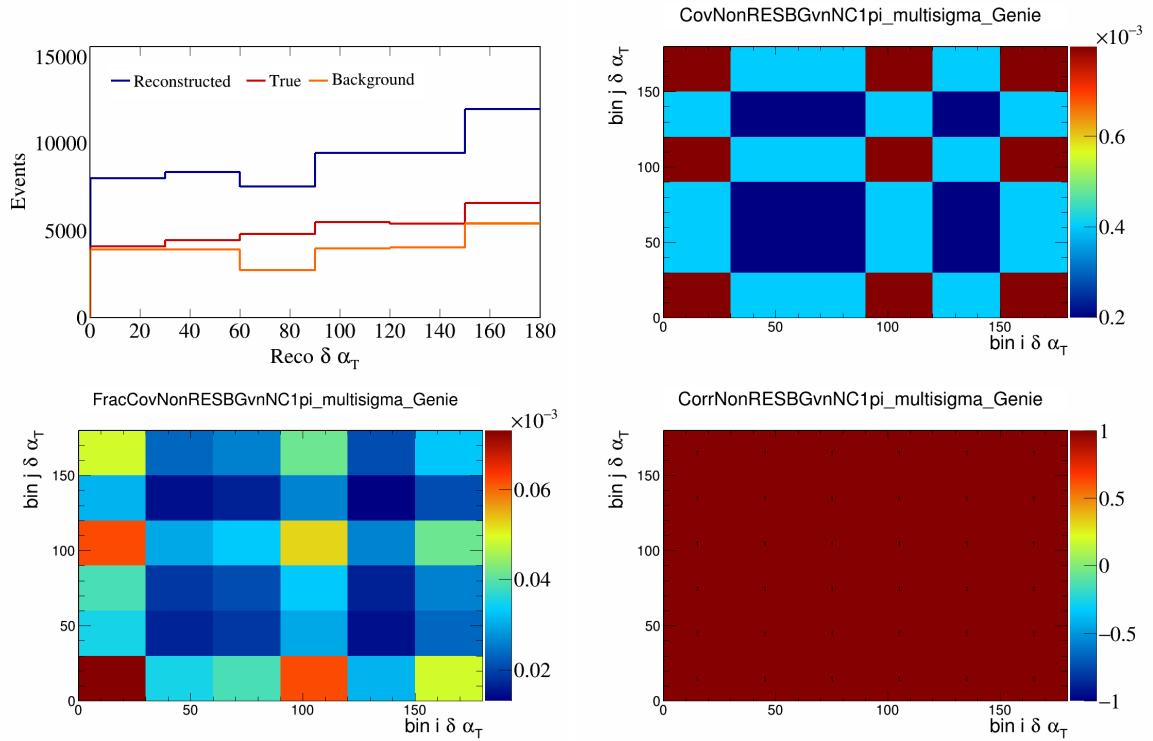


Figure 503: NonRESBGvnNC1pi variations for $\delta\alpha_T$.

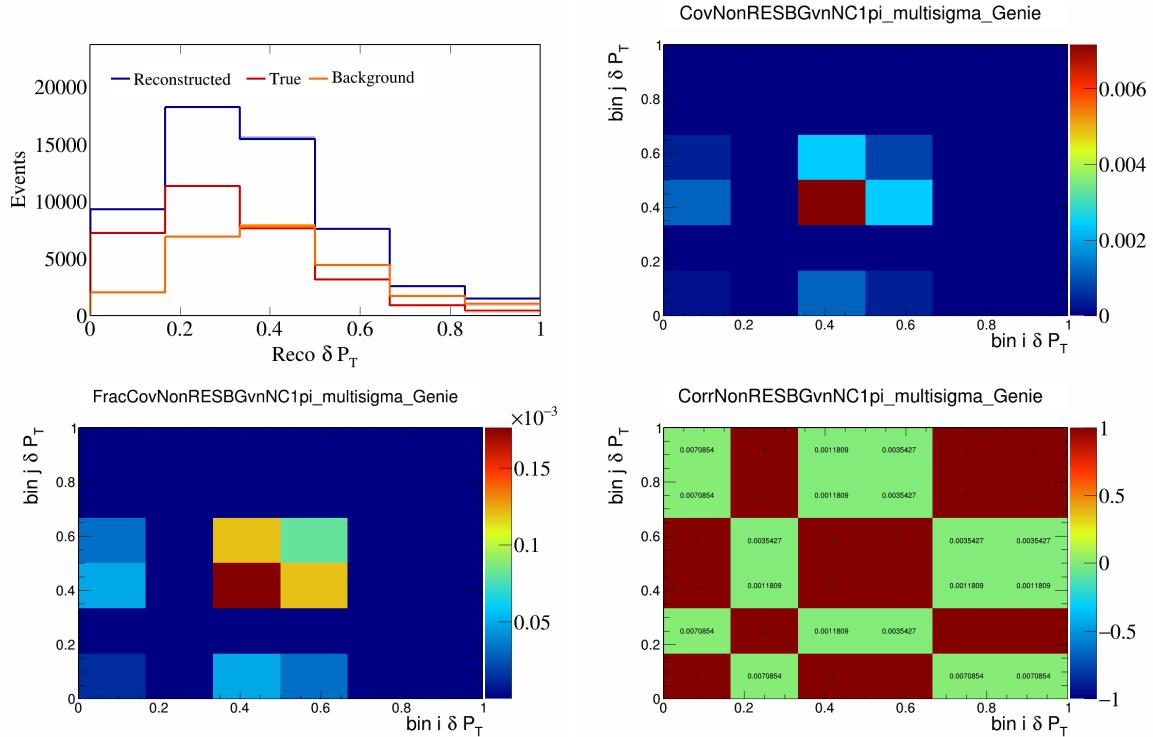


Figure 504: NonRESBGvnNC1pi variations for δP_T .

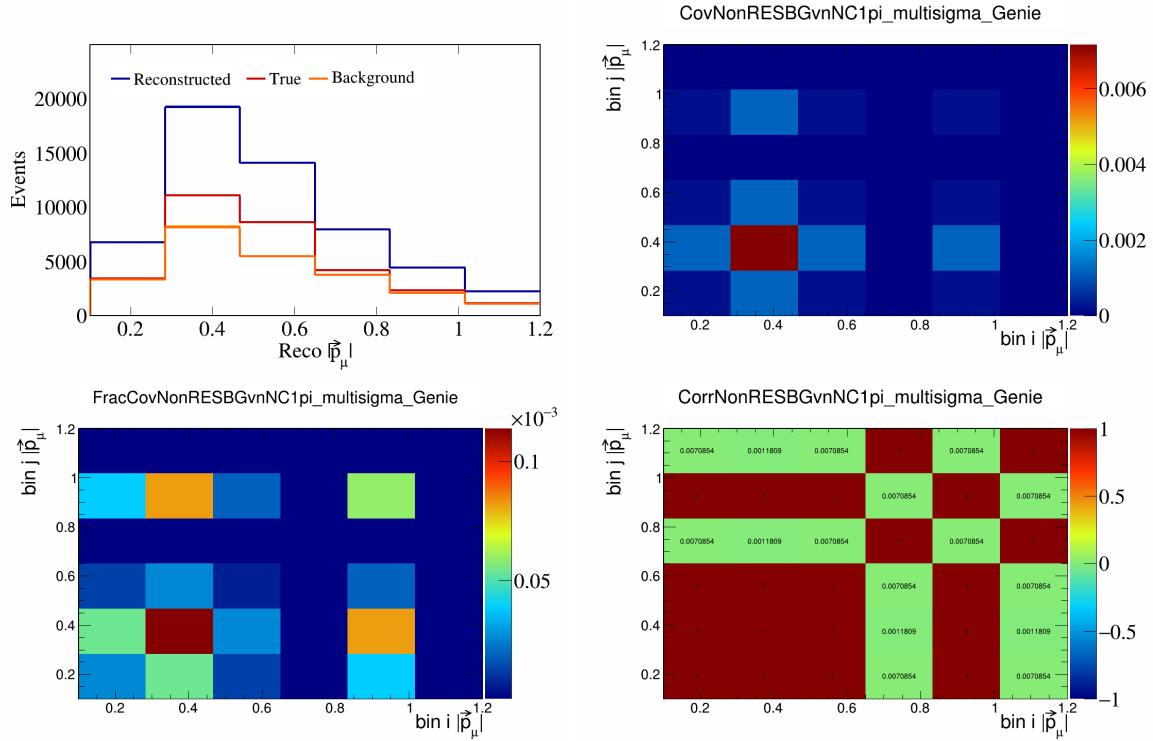


Figure 505: NonRESBGvnNC1pi variations for $|\vec{p}_\mu|$.

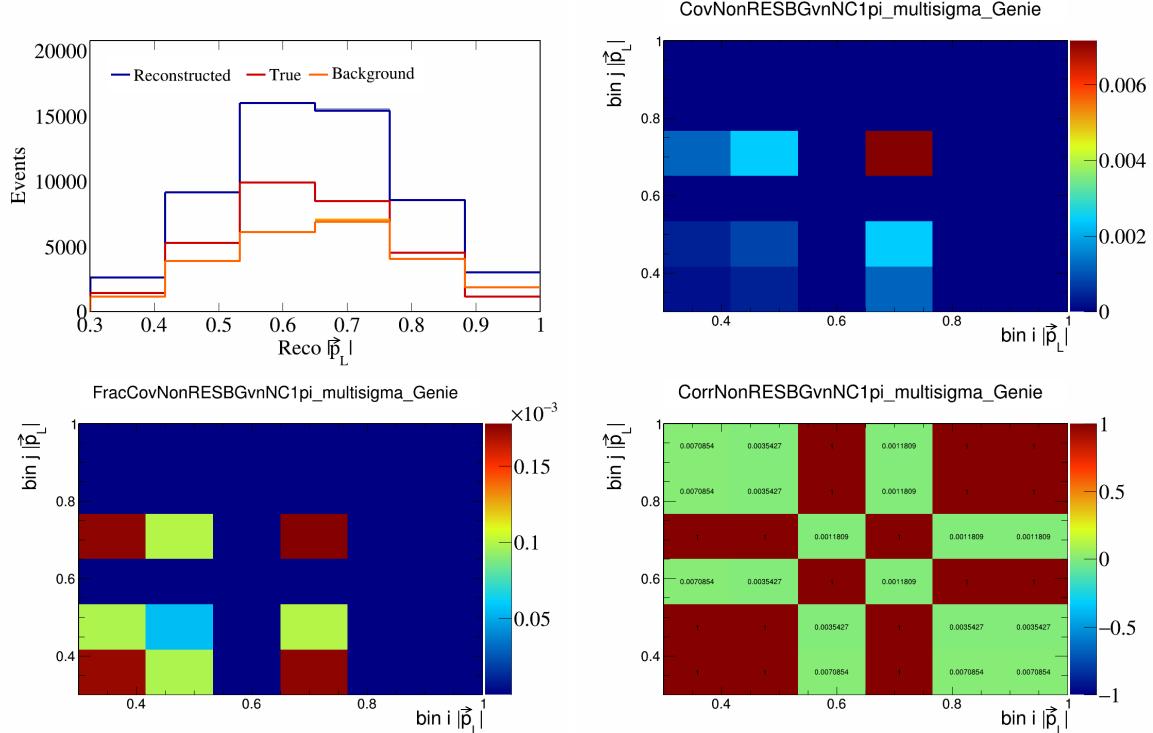


Figure 506: NonRESBGvnNC1pi variations for $|\vec{p}_L|$.

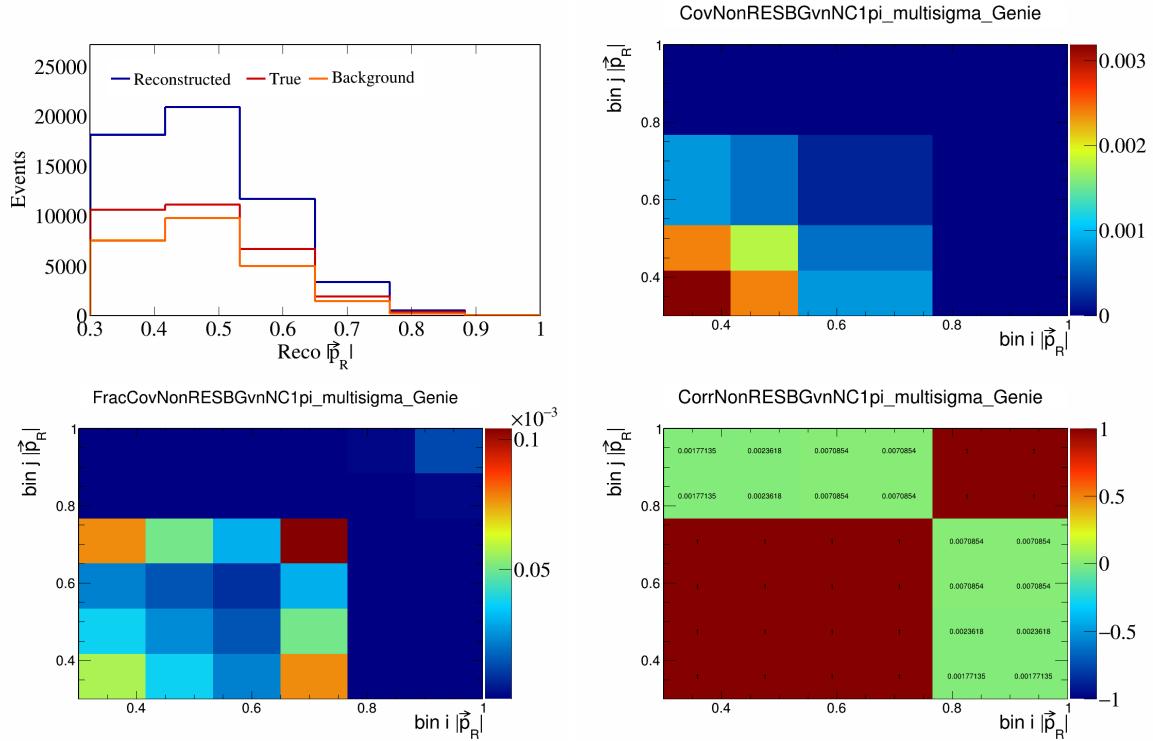


Figure 507: NonRESBGvnNC1pi variations for $|\vec{p}_R|$.

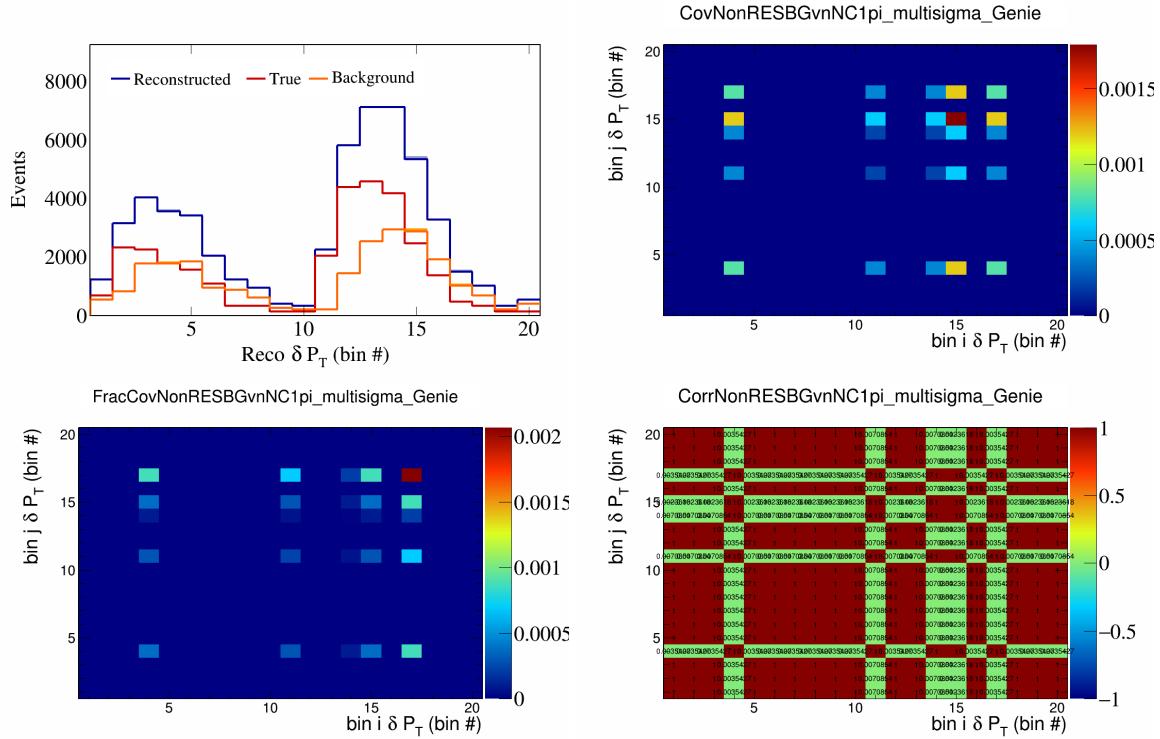


Figure 508: NonRESBGvnNC1pi variations for δP_T in $\cos(\theta_{\vec{p}_\mu})$.

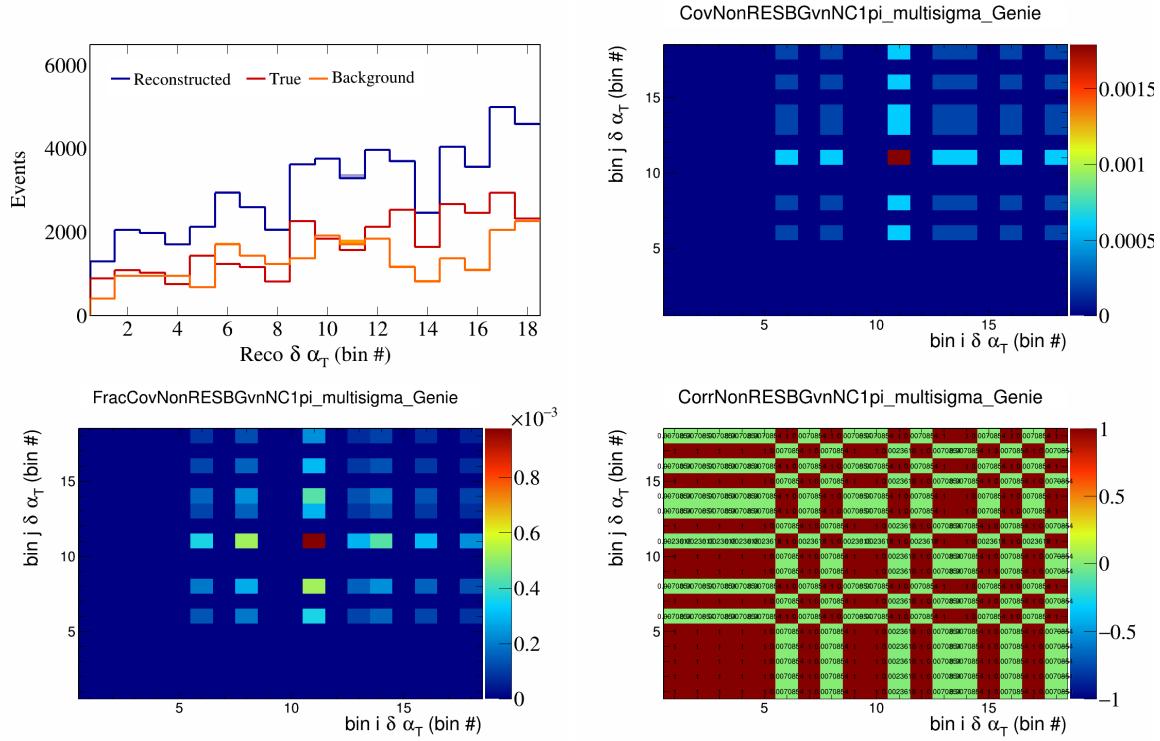


Figure 509: NonRESBGvnNC1pi variations for $\delta\alpha_T$ in $\cos(\theta_{\vec{p}_\mu})$.

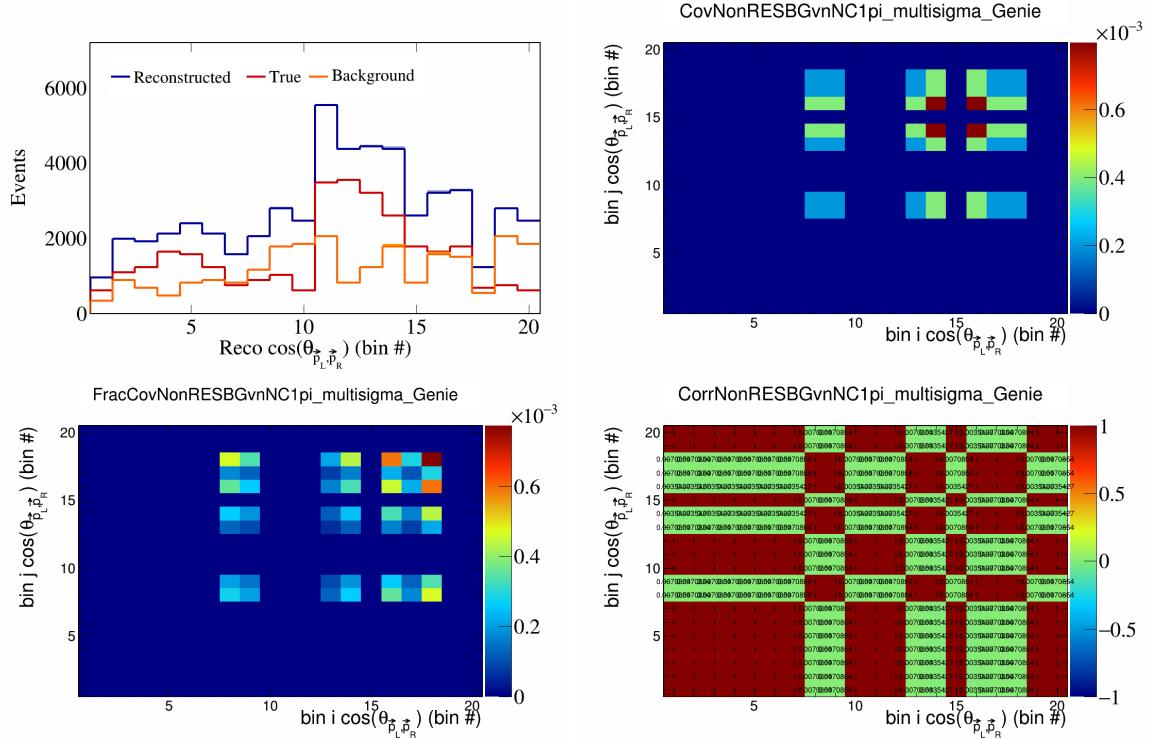


Figure 510: NonRESBGvnNC1pi variations for $\cos(\theta_{\vec{p}_L, \vec{p}_R})$ in $\cos(\theta_{\vec{p}_\mu})$.

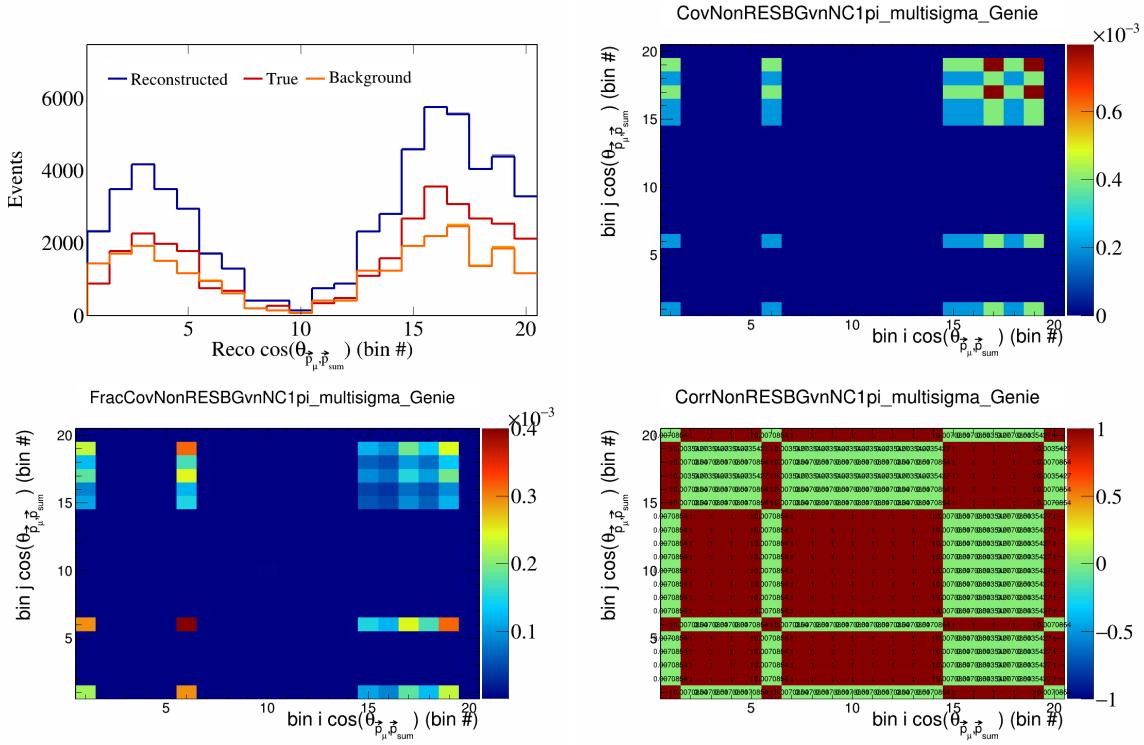


Figure 511: NonRESBGvnNC1pi variations for $\cos(\theta_{\vec{p}_\mu, \vec{p}_{\text{sum}}})$ in $\cos(\theta_{\vec{p}_\mu})$.

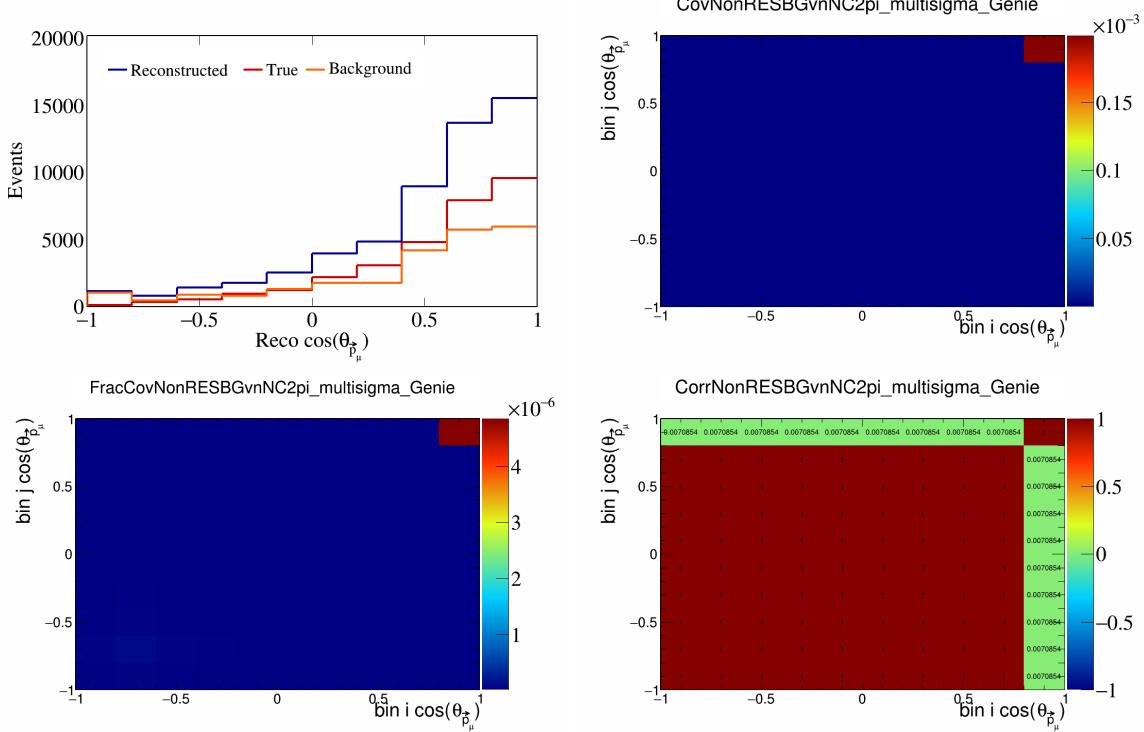


Figure 512: NonRESBGvnNC2pi variations for $\cos(\theta_{\vec{p}_\mu})$.

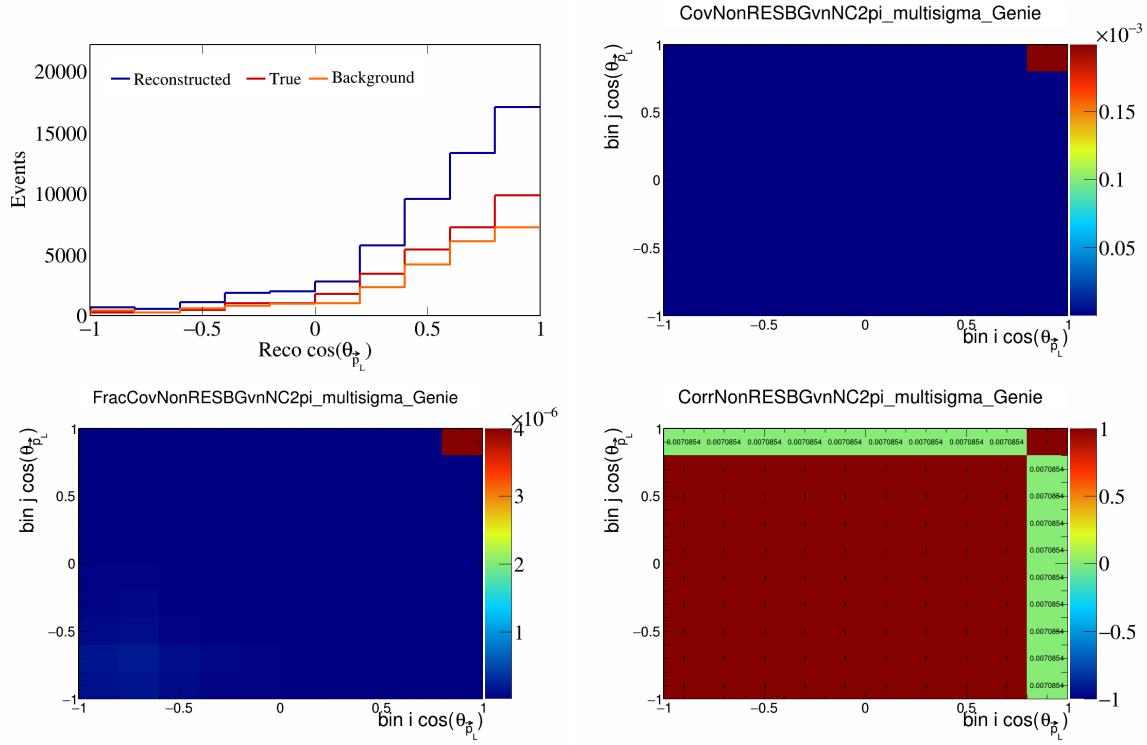


Figure 513: NonRESBGvnNC2pi variations for $\cos(\theta_{\vec{p}_L})$.

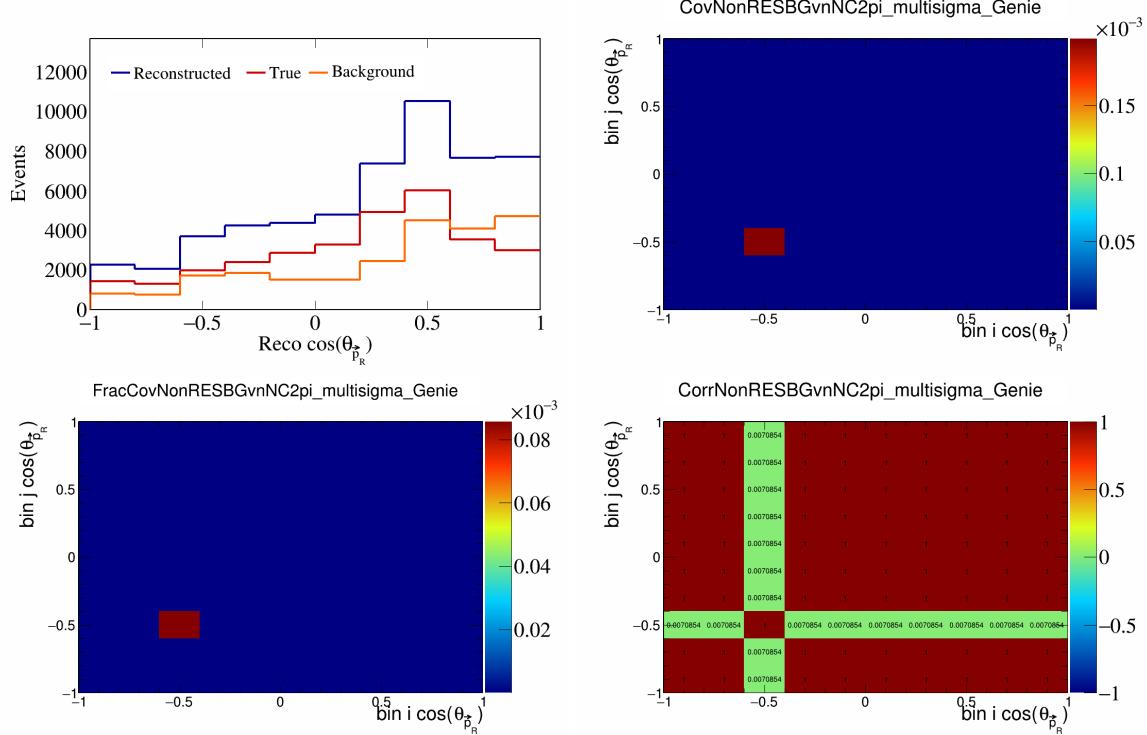


Figure 514: NonRESBGvnNC2pi variations for $\cos(\theta_{\vec{p}_R})$.

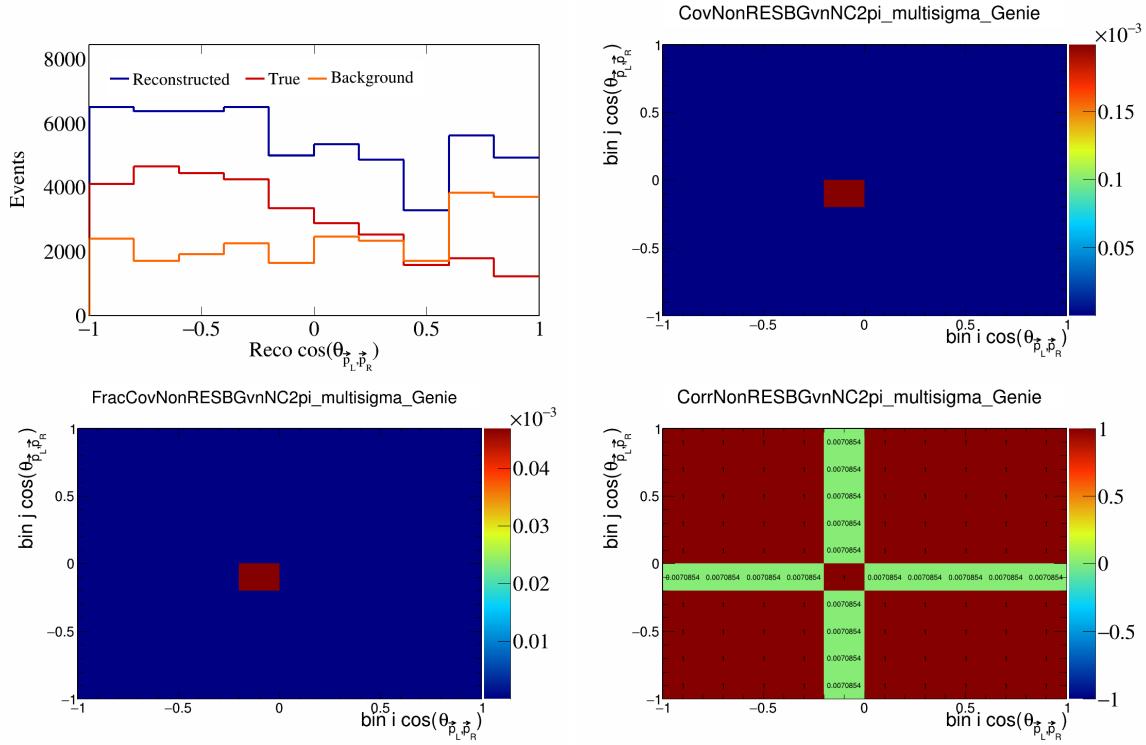


Figure 515: NonRESBGvnNC2pi variations for $\cos(\theta_{\vec{p}_L, \vec{p}_R})$.

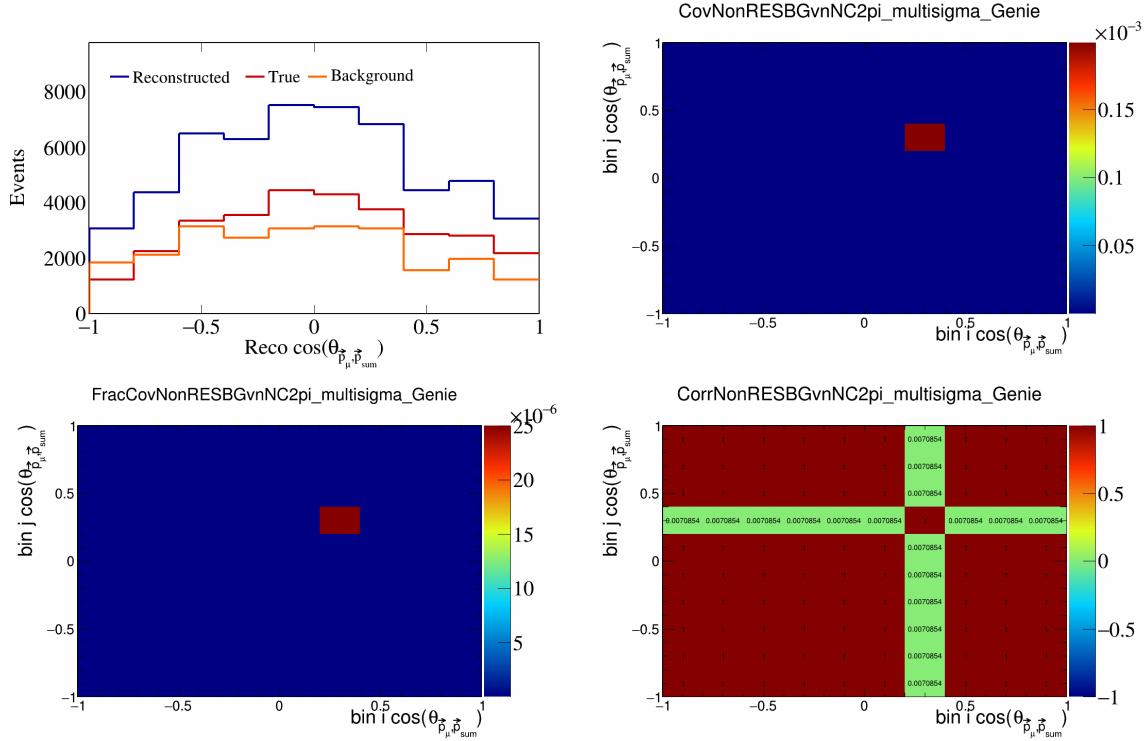


Figure 516: NonRESBGvnNC2pi variations for $\cos(\theta_{\vec{p}_\mu, \vec{p}_{\text{sum}}})$.

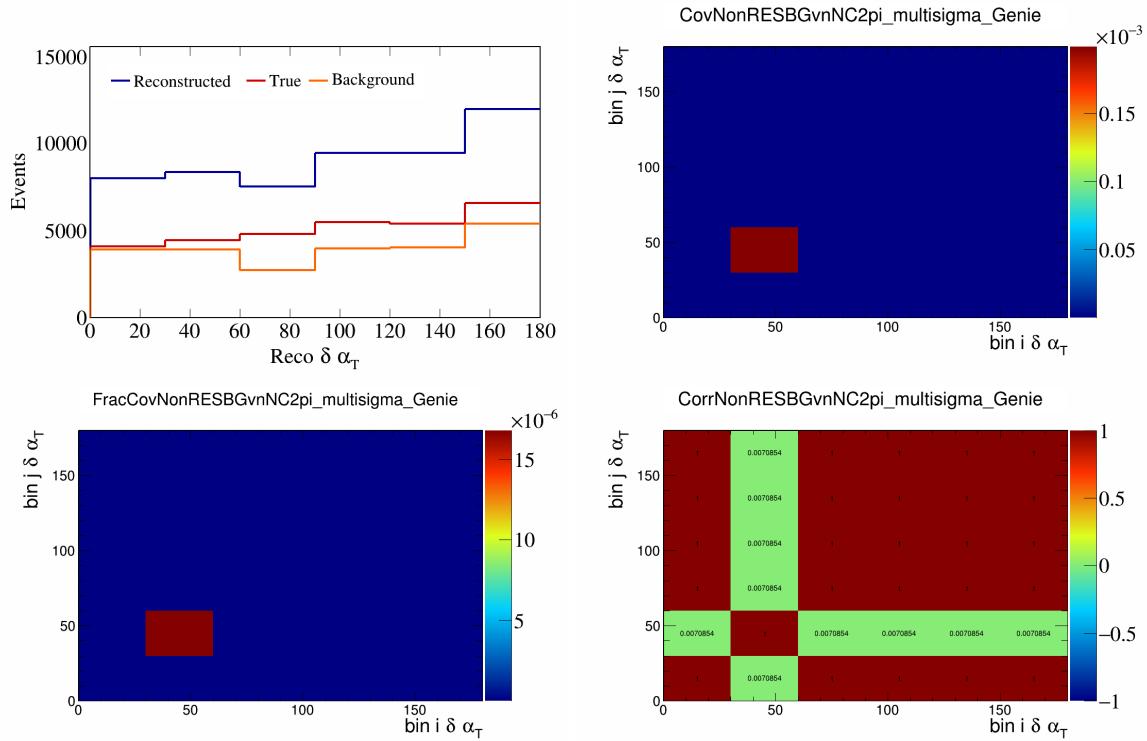


Figure 517: NonRESBGvnNC2pi variations for $\delta \alpha_T$.

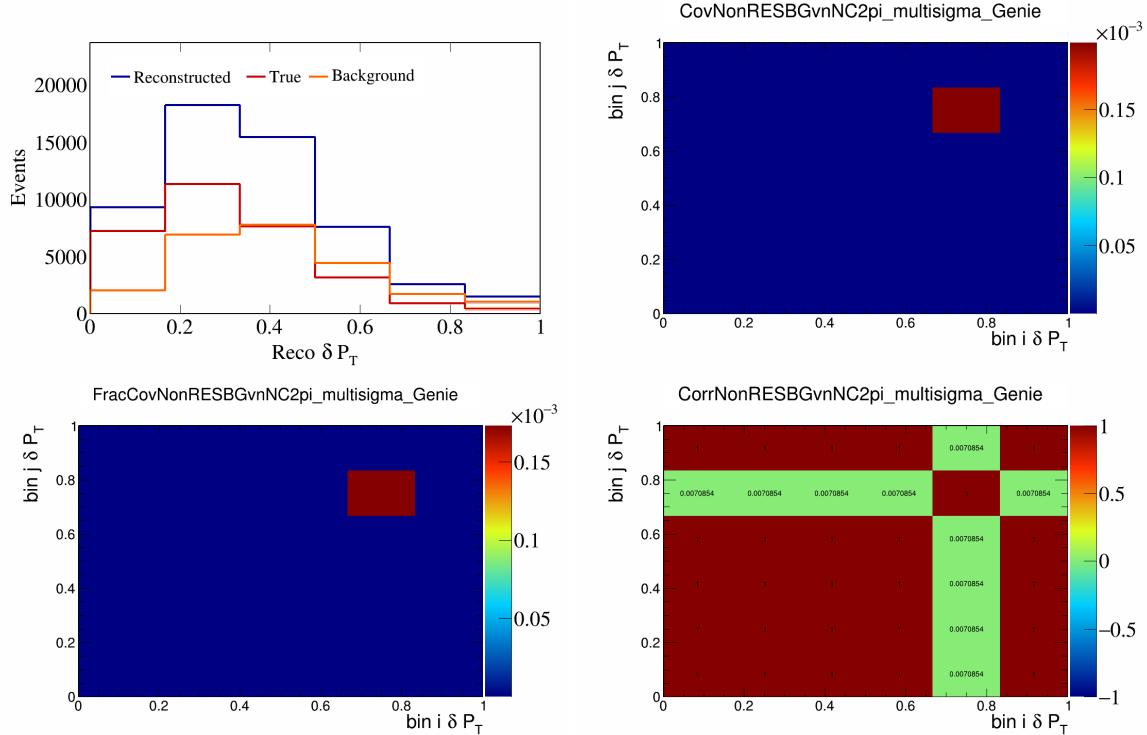


Figure 518: NonRESBGvnNC2pi variations for δP_T .

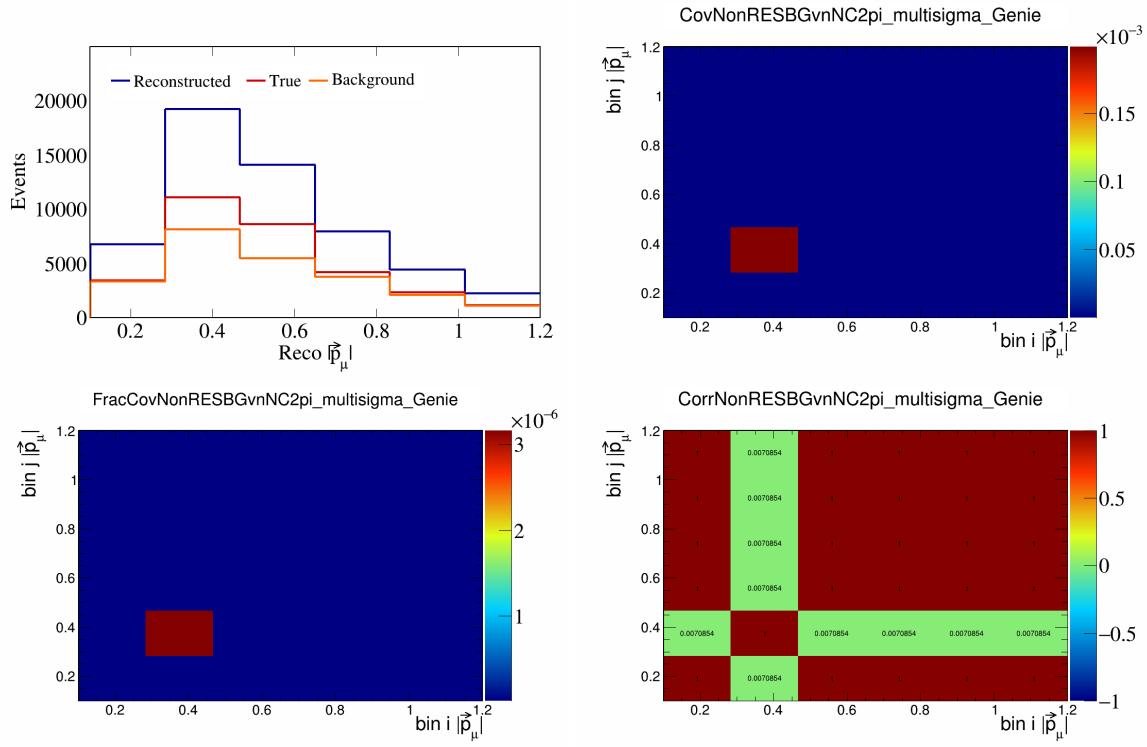


Figure 519: NonRESBGvnNC2pi variations for $|\vec{p}_\mu|$.

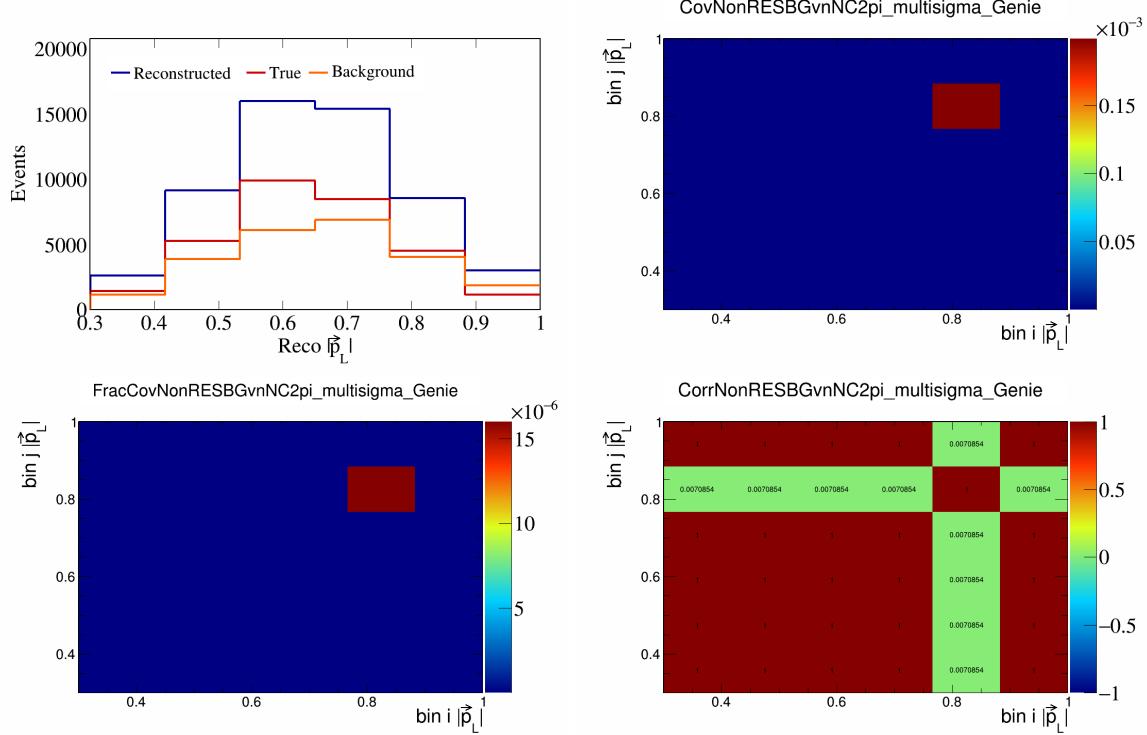


Figure 520: NonRESBGvnNC2pi variations for $|\vec{p}_L|$.

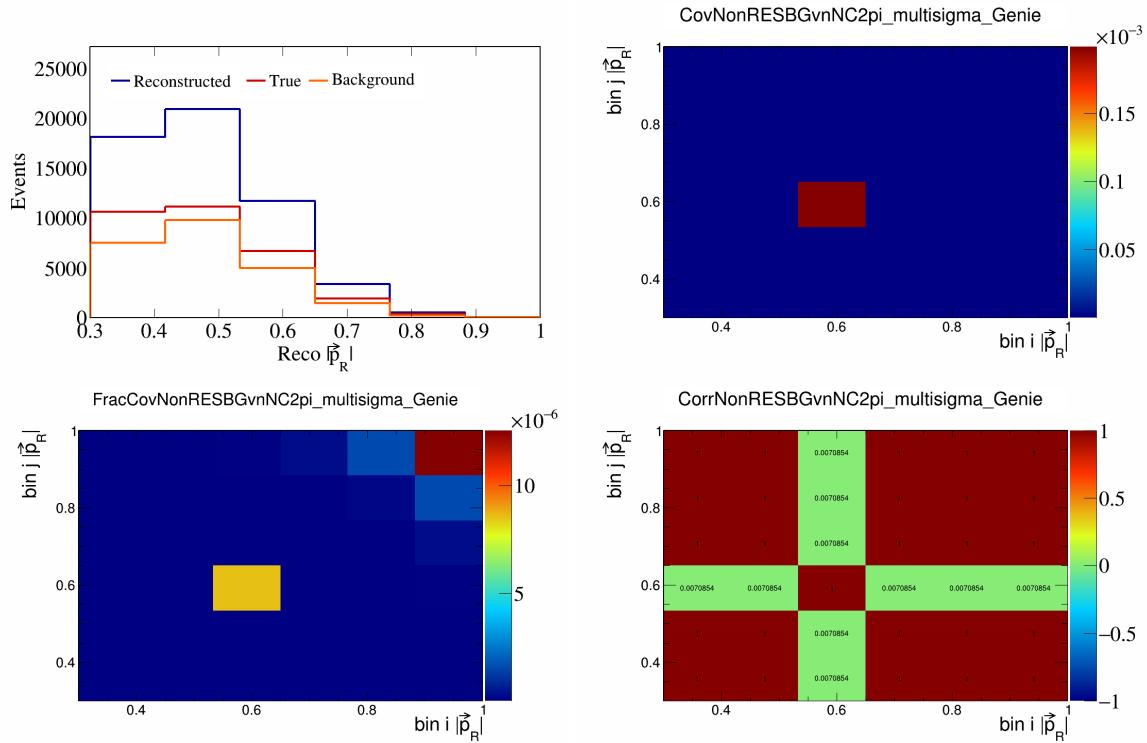


Figure 521: NonRESBGvnNC2pi variations for $|\vec{p}_R|$.

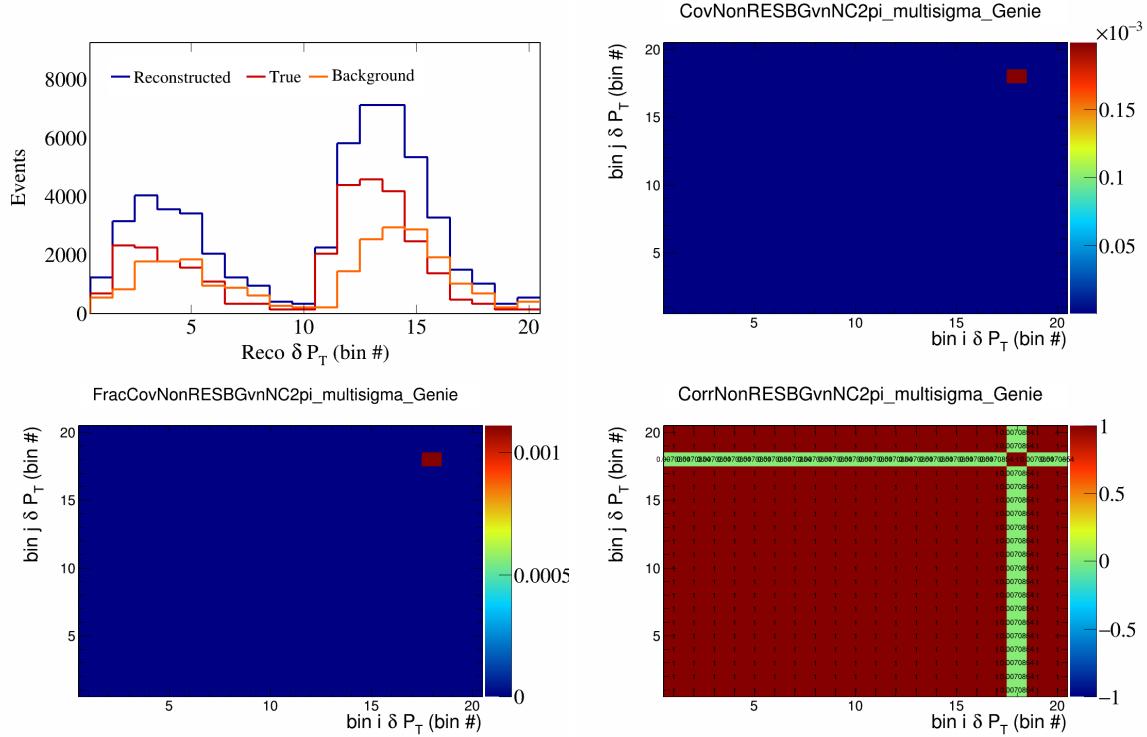


Figure 522: NonRESBGvnNC2pi variations for δP_T in $\cos(\theta_{\vec{p}_\mu})$.

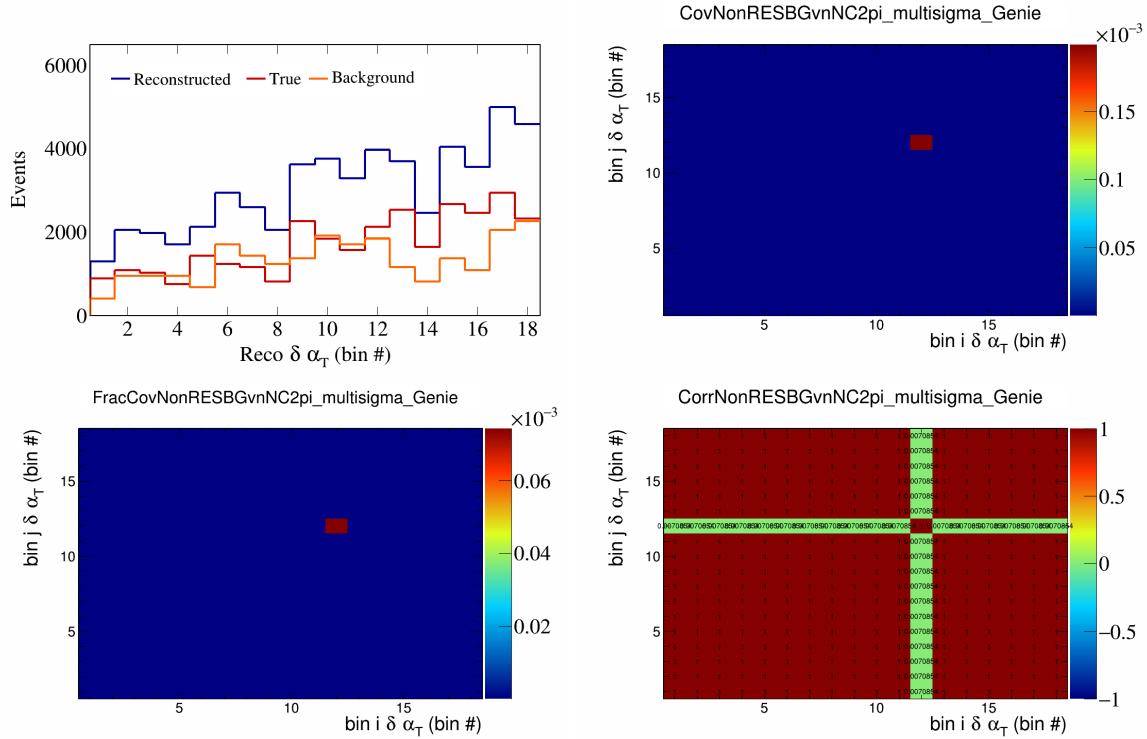


Figure 523: NonRESBGvnNC2pi variations for $\delta \alpha_T$ in $\cos(\theta_{\vec{p}_\mu})$.

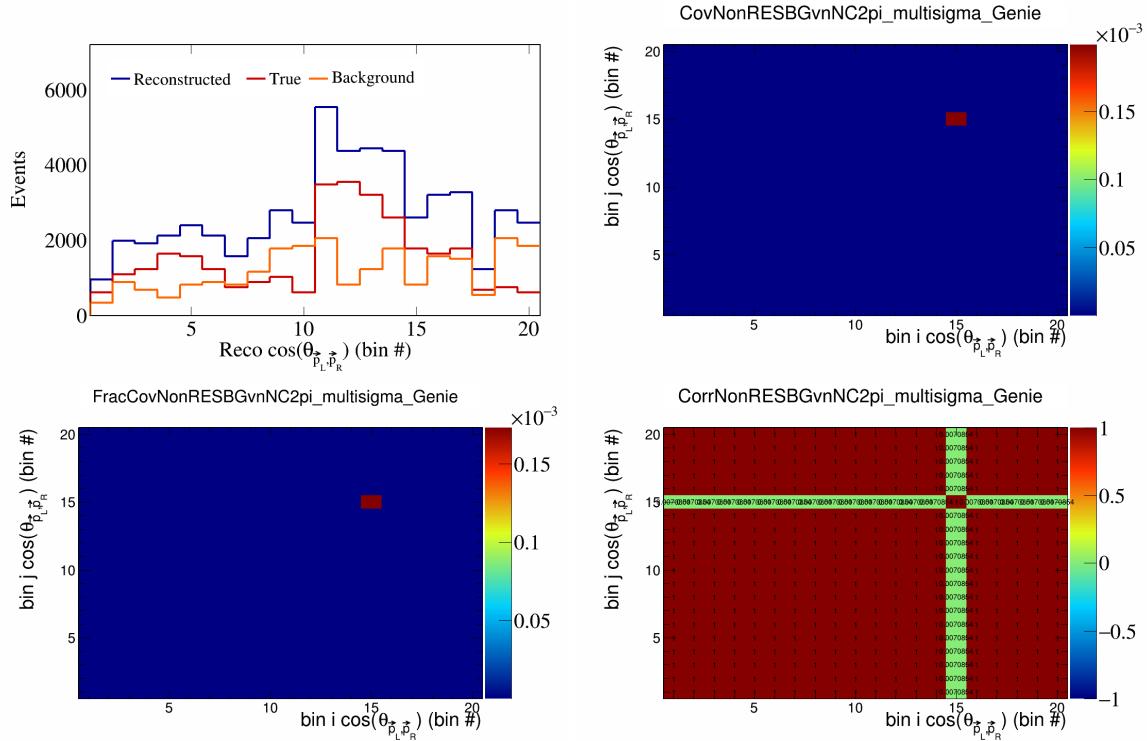


Figure 524: NonRESBGvnNC2pi variations for $\cos(\theta_{\vec{p}_L, \vec{p}_R})$ in $\cos(\theta_{\vec{p}_\mu})$.

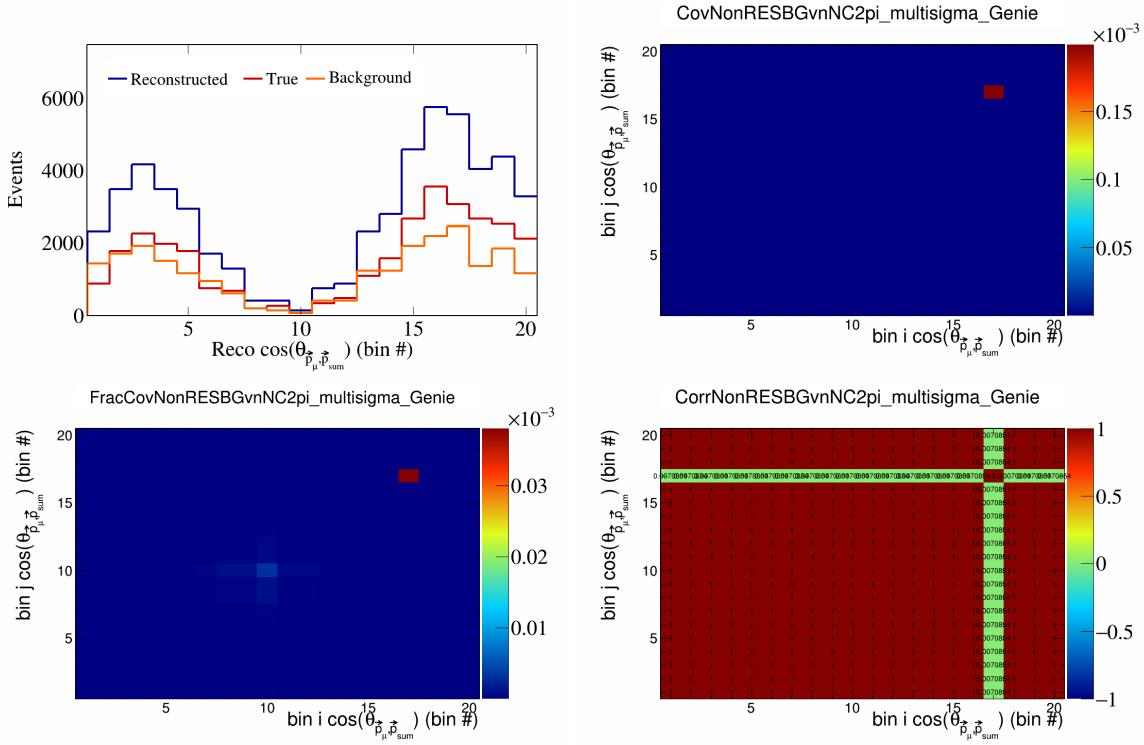


Figure 525: NonRESBGvnNC2pi variations for $\cos(\theta_{\vec{p}_\mu, \vec{p}_{\text{sum}}})$ in $\cos(\theta_{\vec{p}_\mu})$.

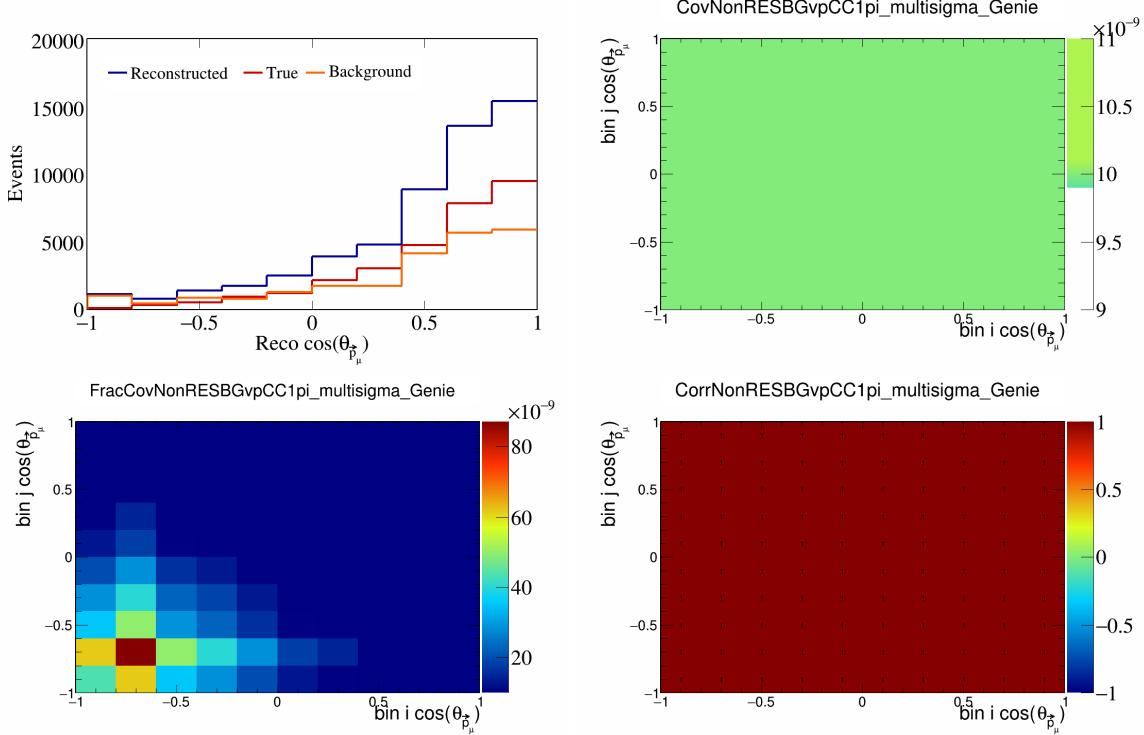


Figure 526: NonRESBGvpCC1pi variations for $\cos(\theta_{\vec{p}_\mu})$.

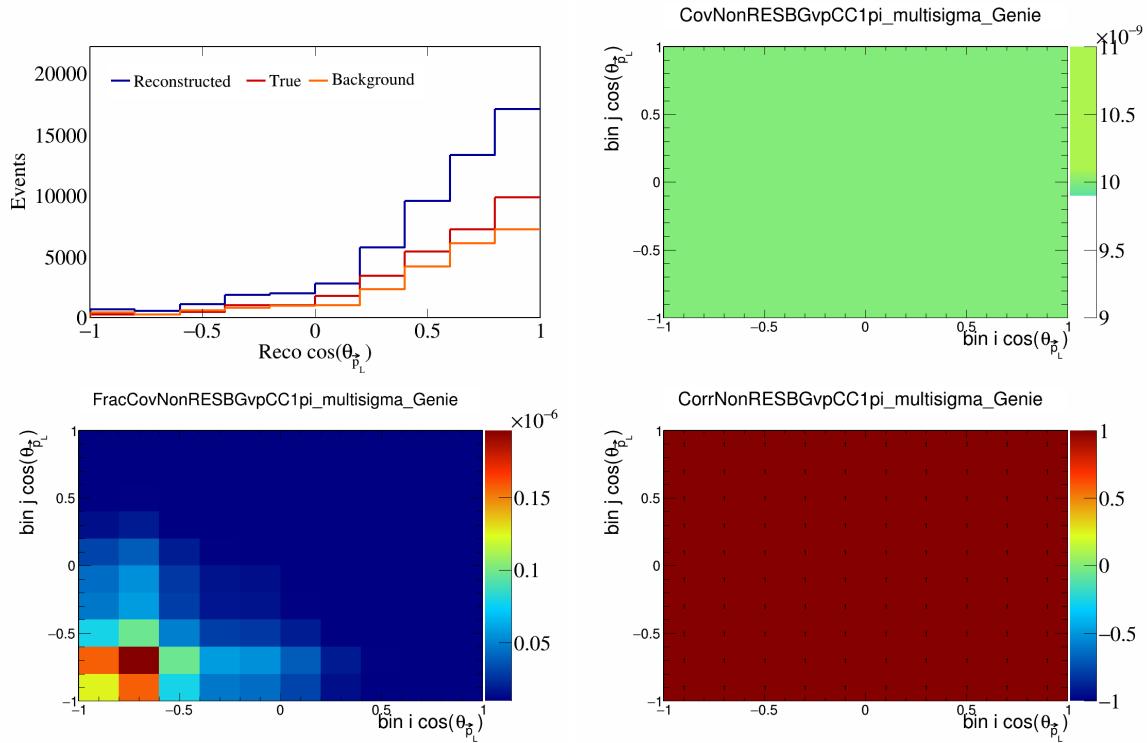


Figure 527: NonRESBGvpCC1pi variations for $\cos(\theta_{\vec{p}_L})$.

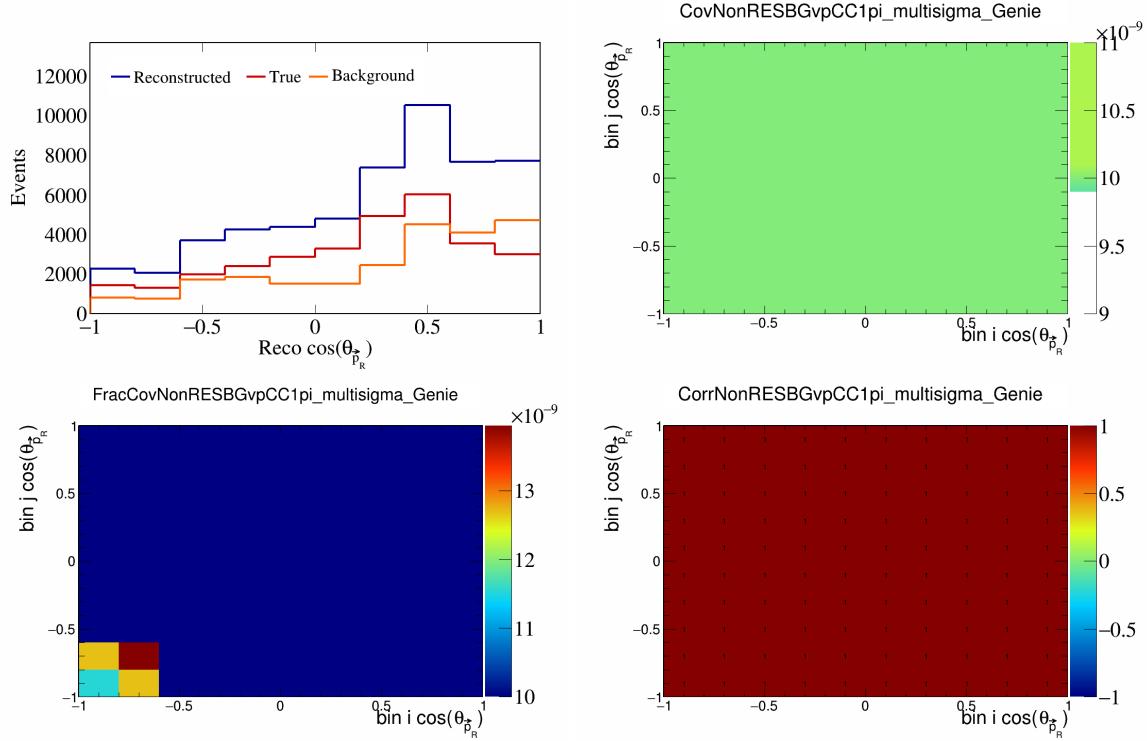


Figure 528: NonRESBGvpCC1pi variations for $\cos(\theta_{\vec{p}_R})$.

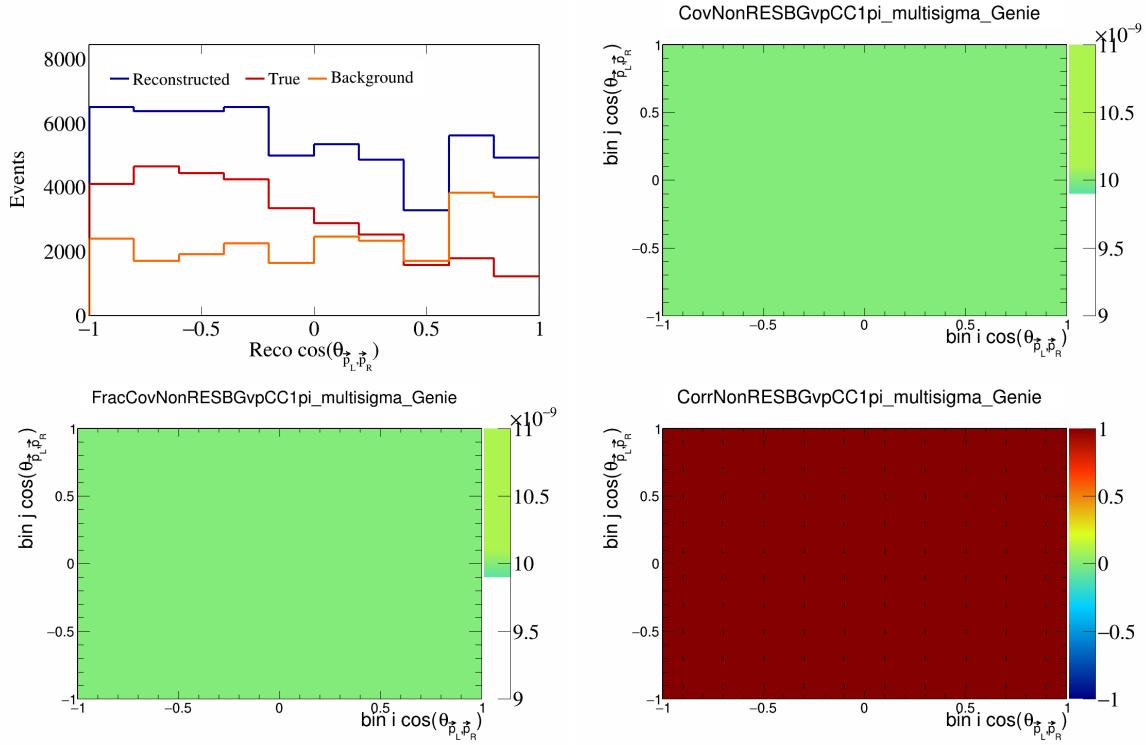


Figure 529: NonRESBGvpCC1pi variations for $\cos(\theta_{\vec{p}_L, \vec{p}_R})$.

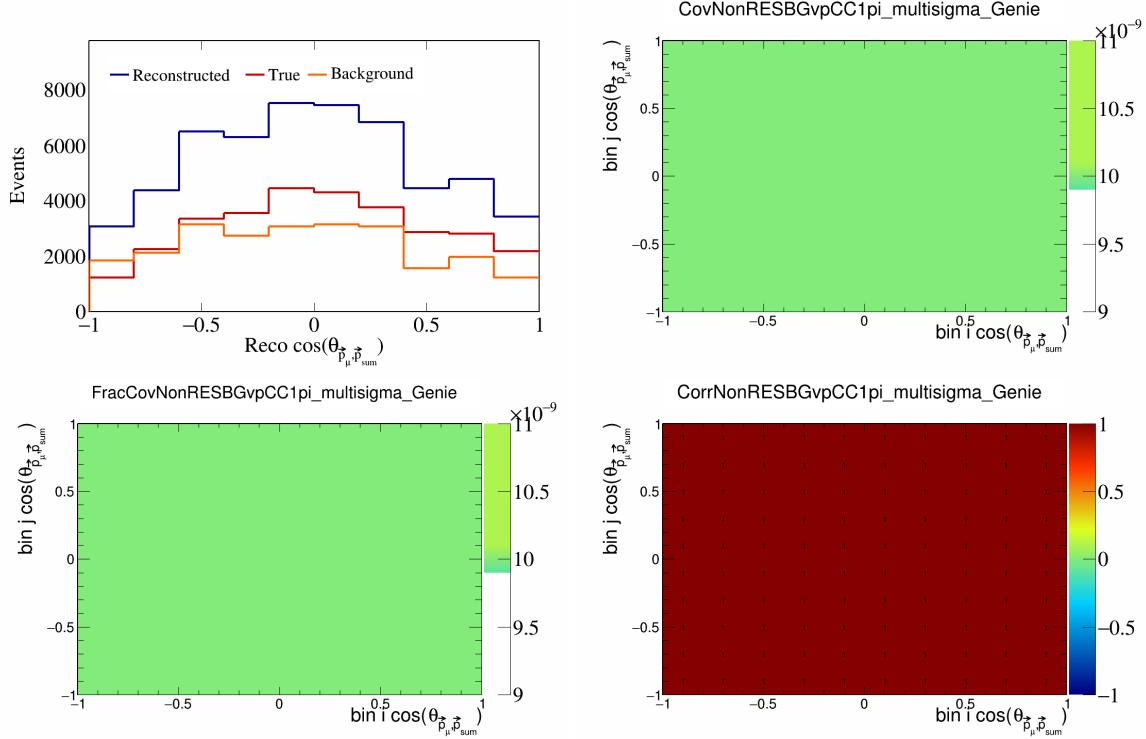


Figure 530: NonRESBGvpCC1pi variations for $\cos(\theta_{\vec{p}_\mu, \vec{p}_{\text{sum}}})$.

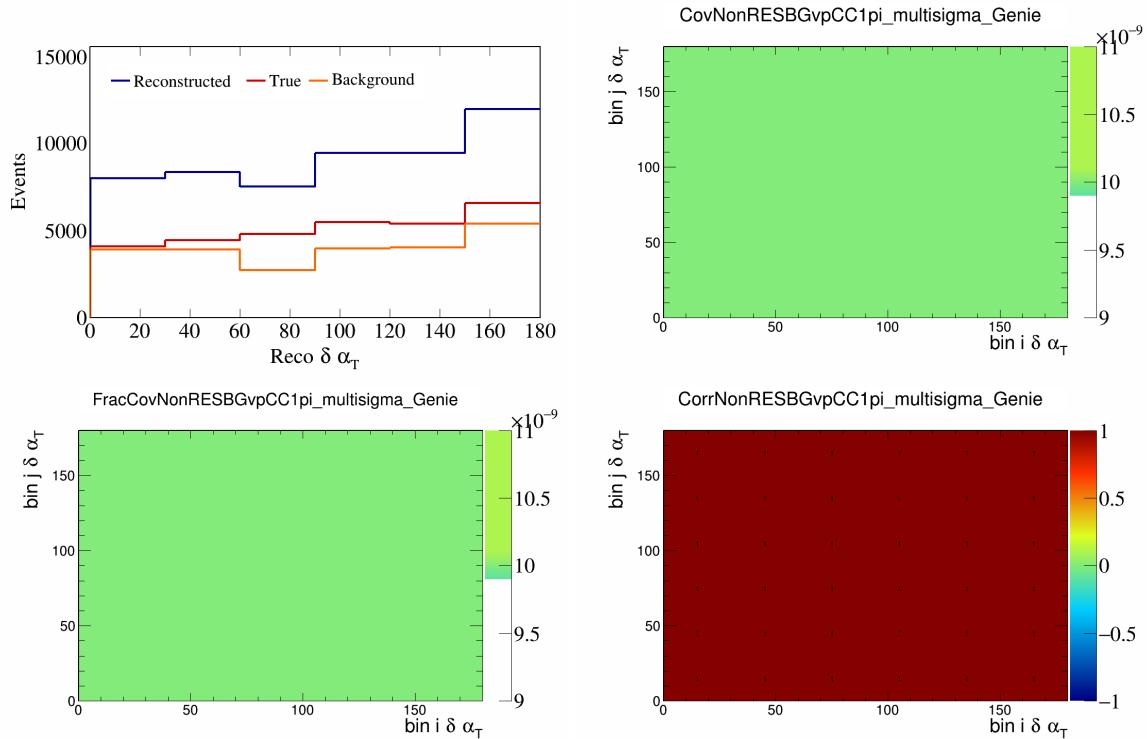


Figure 531: NonRESBGvpCC1pi variations for $\delta\alpha_T$.

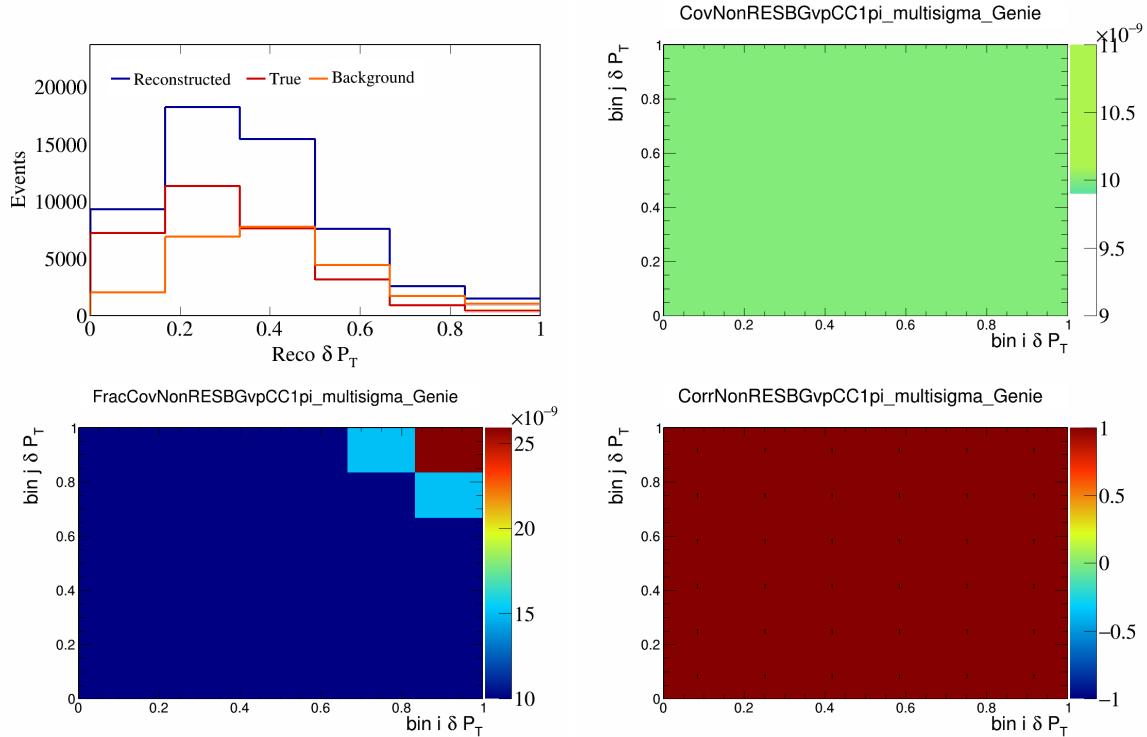


Figure 532: NonRESBGvpCC1pi variations for δP_T .

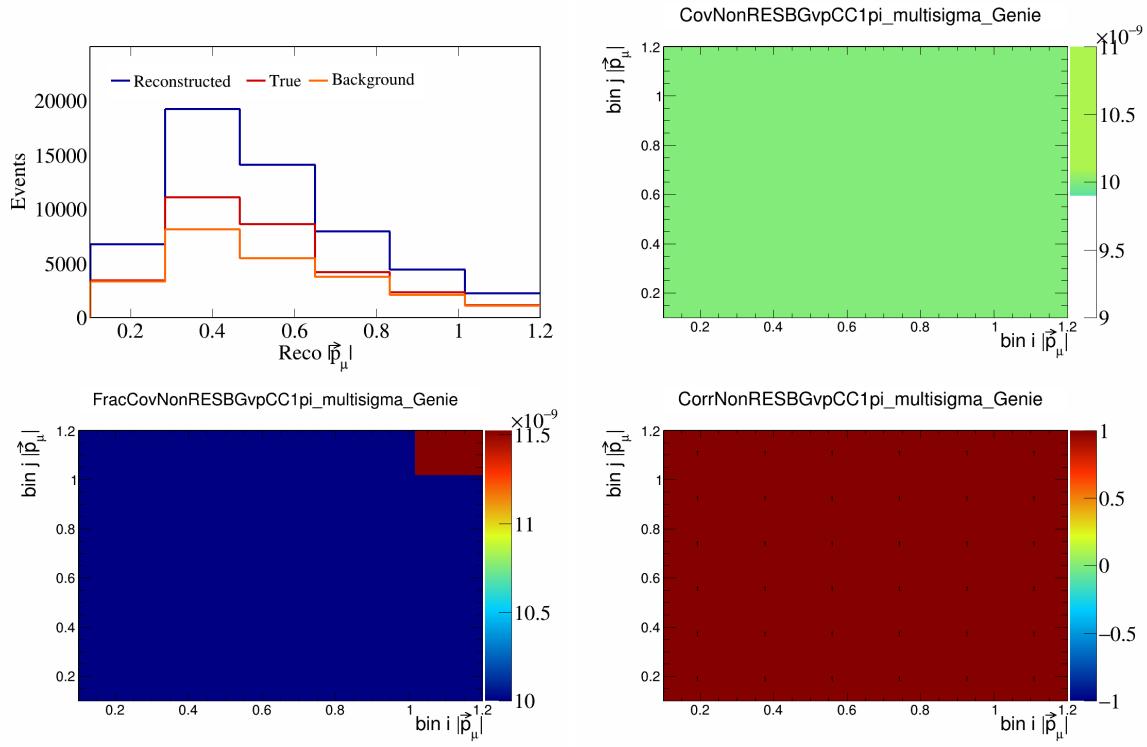


Figure 533: NonRESBGvpCC1pi variations for $|\vec{p}_\mu|$.

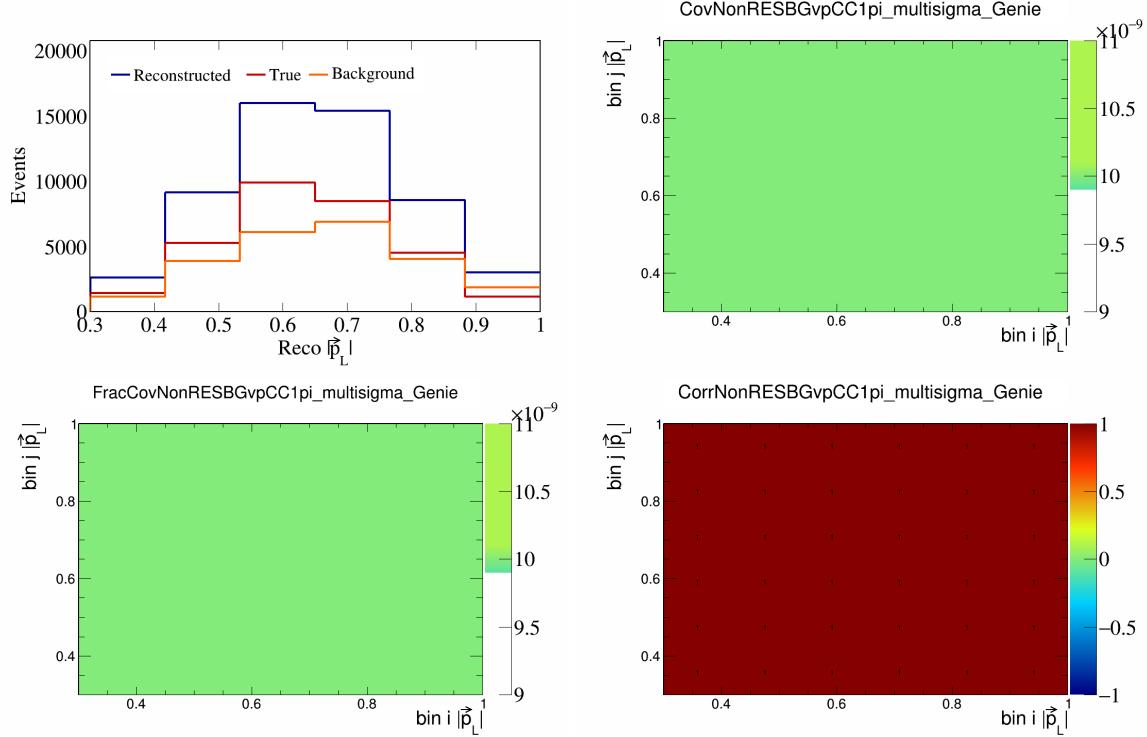


Figure 534: NonRESBGvpCC1pi variations for $|\vec{p}_L|$.

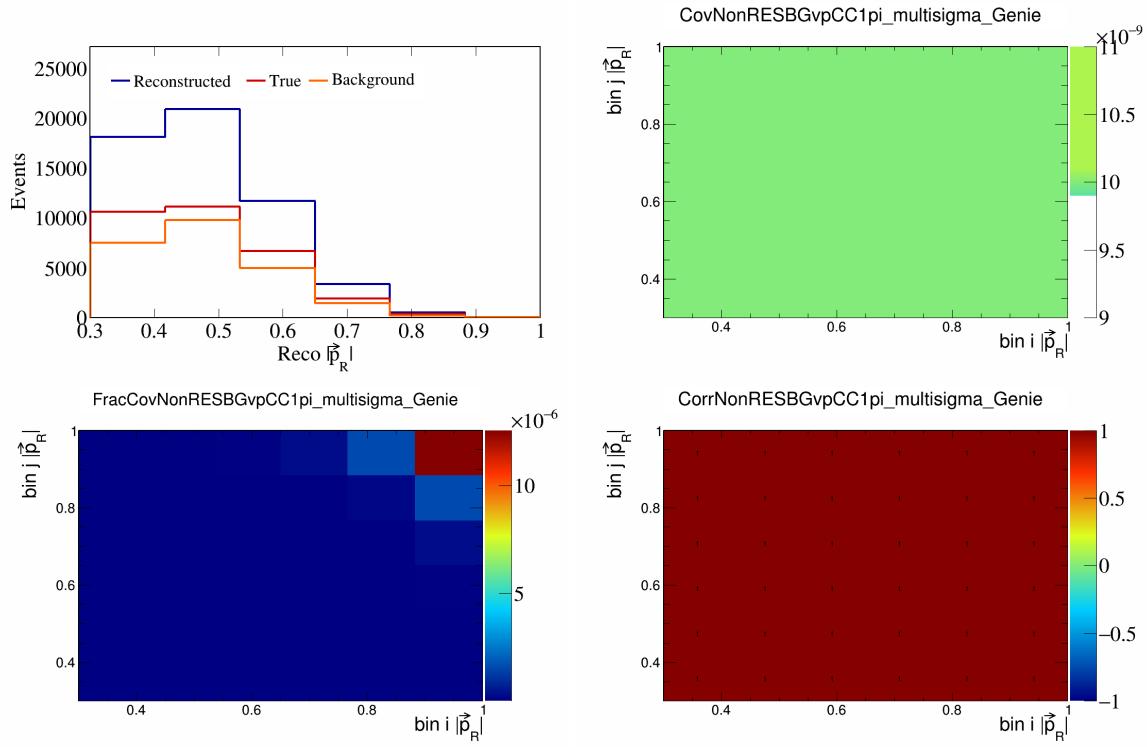


Figure 535: NonRESBGvpCC1pi variations for $|\vec{p}_R|$.

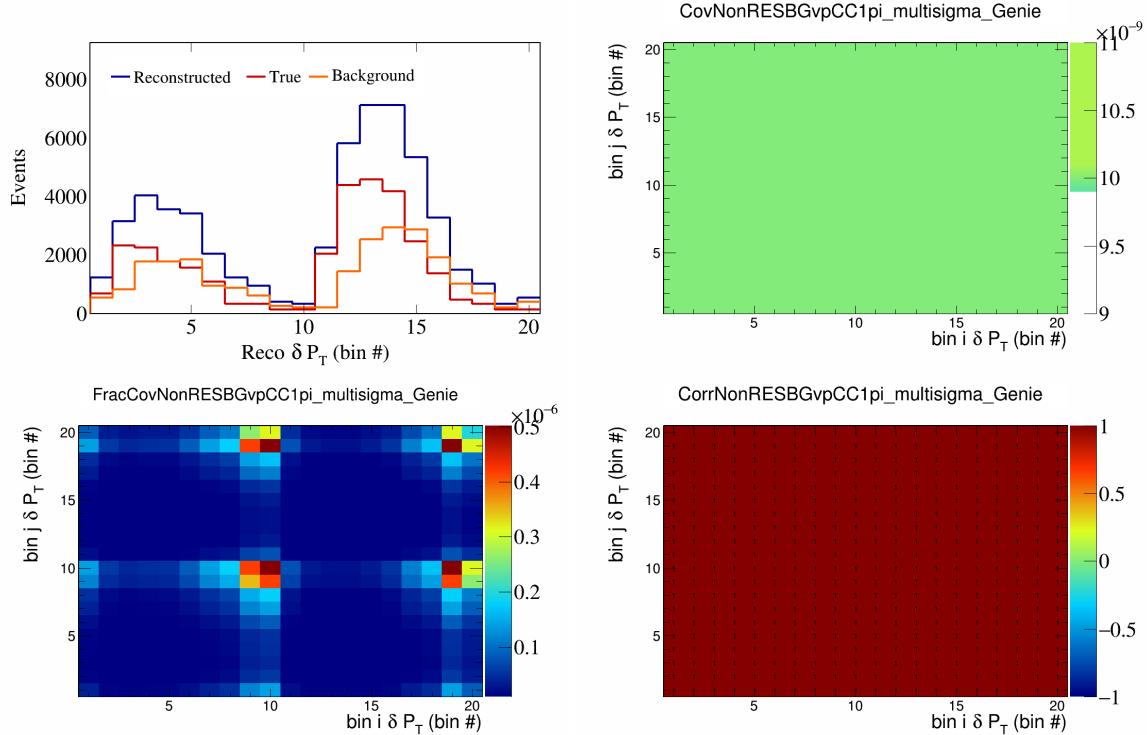


Figure 536: NonRESBGvpCC1pi variations for δP_T in $\cos(\theta_{\vec{p}_\mu})$.

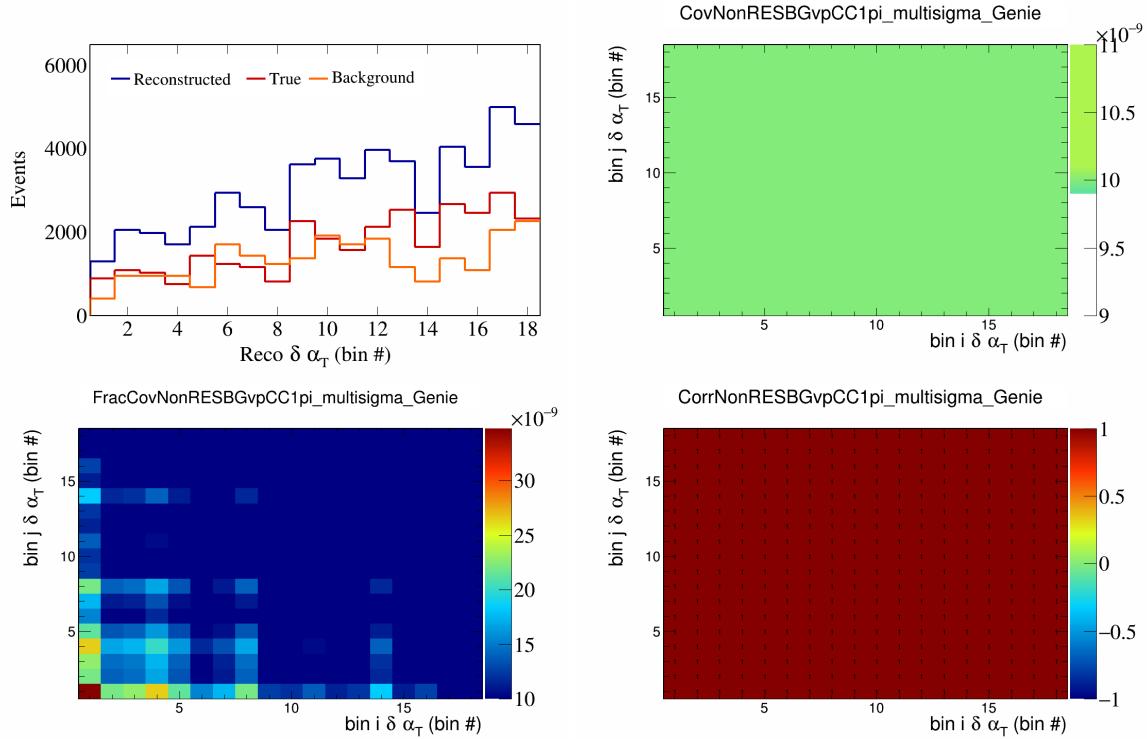


Figure 537: NonRESBGvpCC1pi variations for $\delta\alpha_T$ in $\cos(\theta_{\vec{p}_\mu})$.

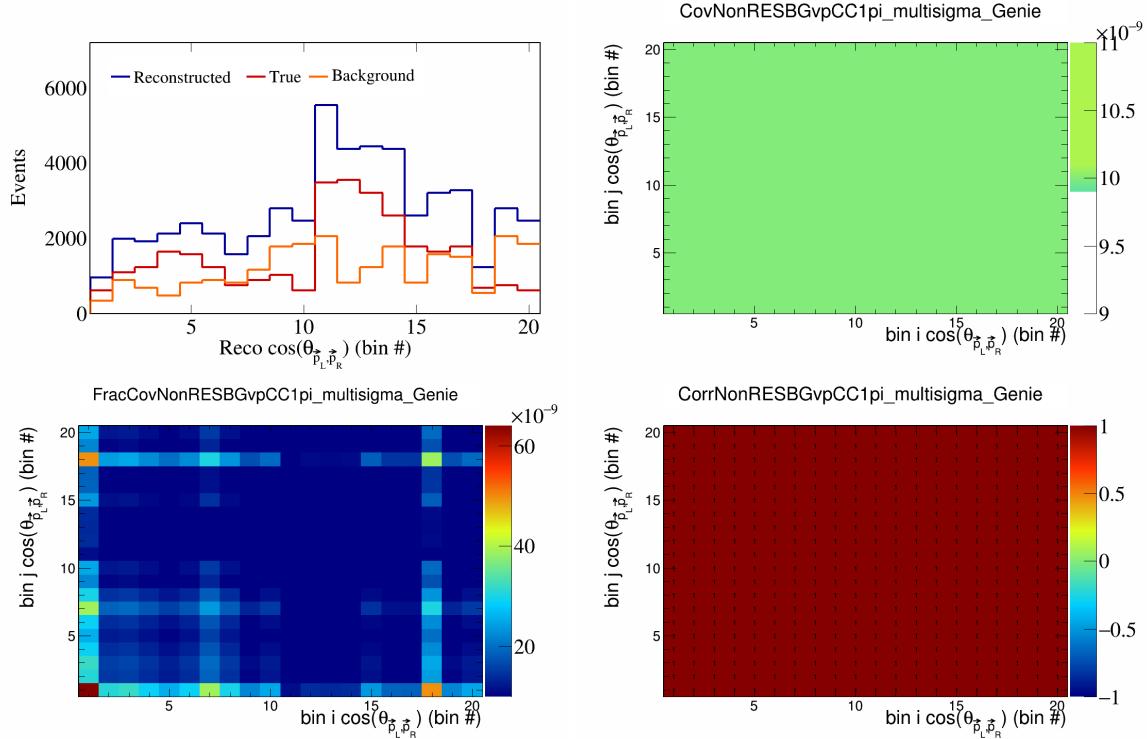


Figure 538: NonRESBGvpCC1pi variations for $\cos(\theta_{\vec{p}_L, \vec{p}_R})$ in $\cos(\theta_{\vec{p}_\mu})$.

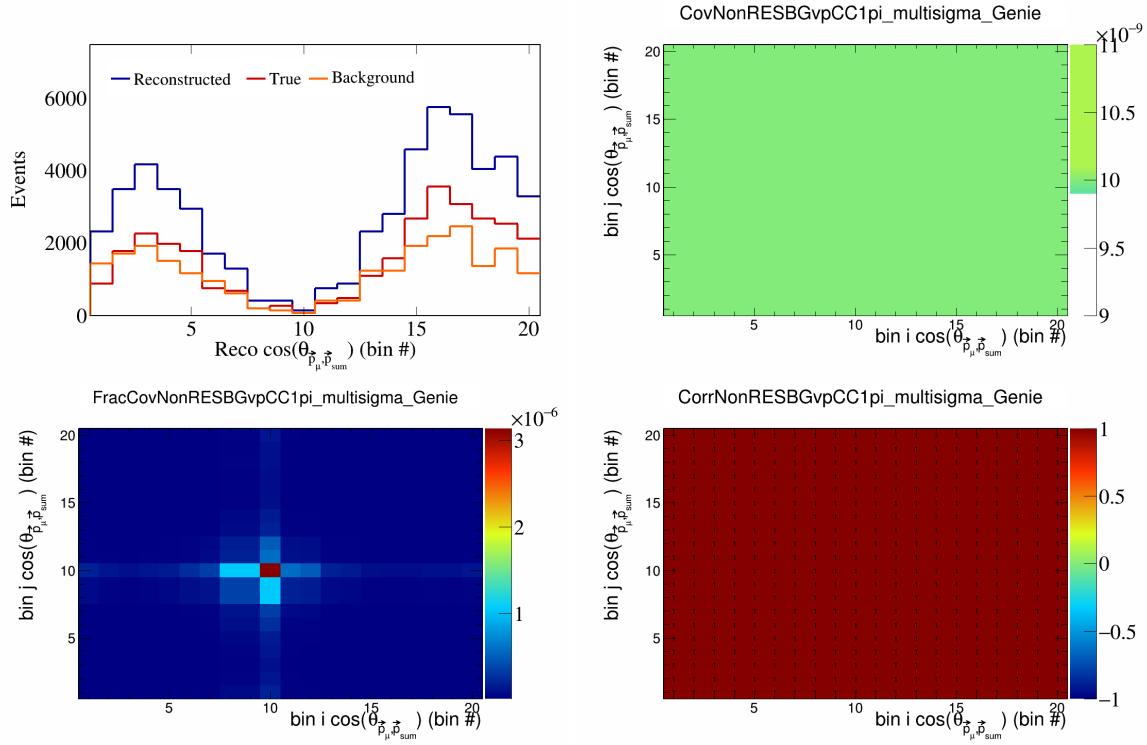


Figure 539: NonRESBGvpCC1pi variations for $\cos(\theta_{\vec{p}_\mu, \vec{p}_{\text{sum}}})$ in $\cos(\theta_{\vec{p}_\mu})$.

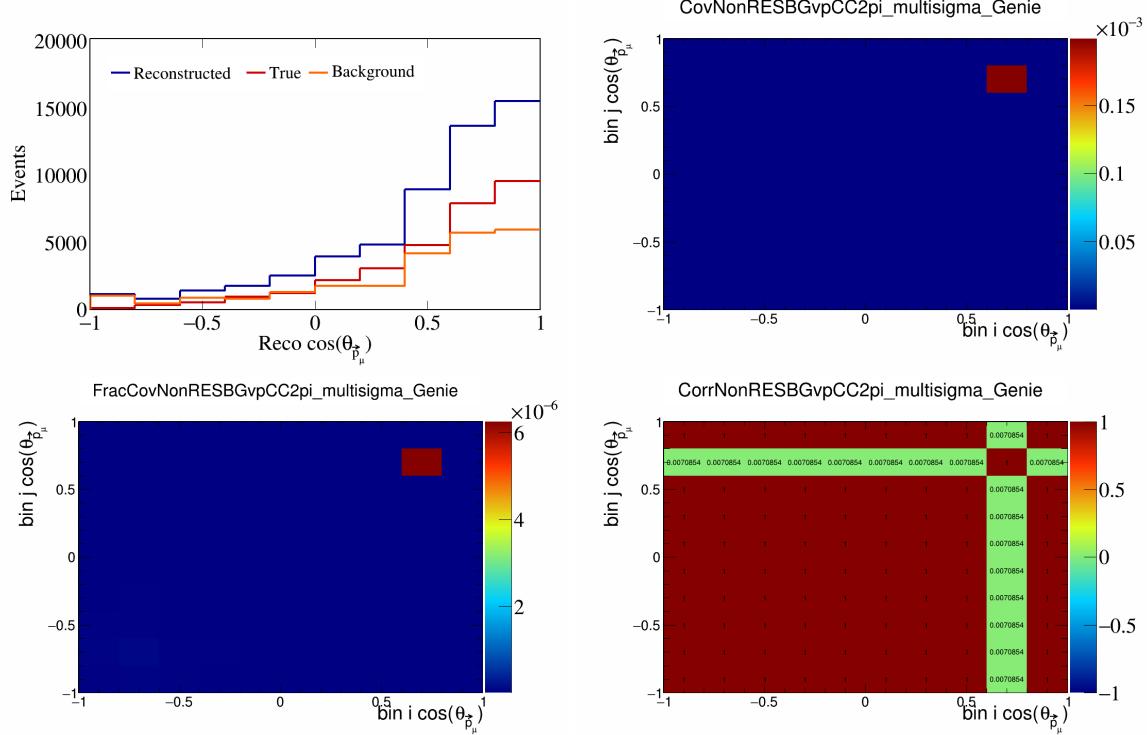


Figure 540: NonRESBGvpCC2pi variations for $\cos(\theta_{\vec{p}_\mu})$.

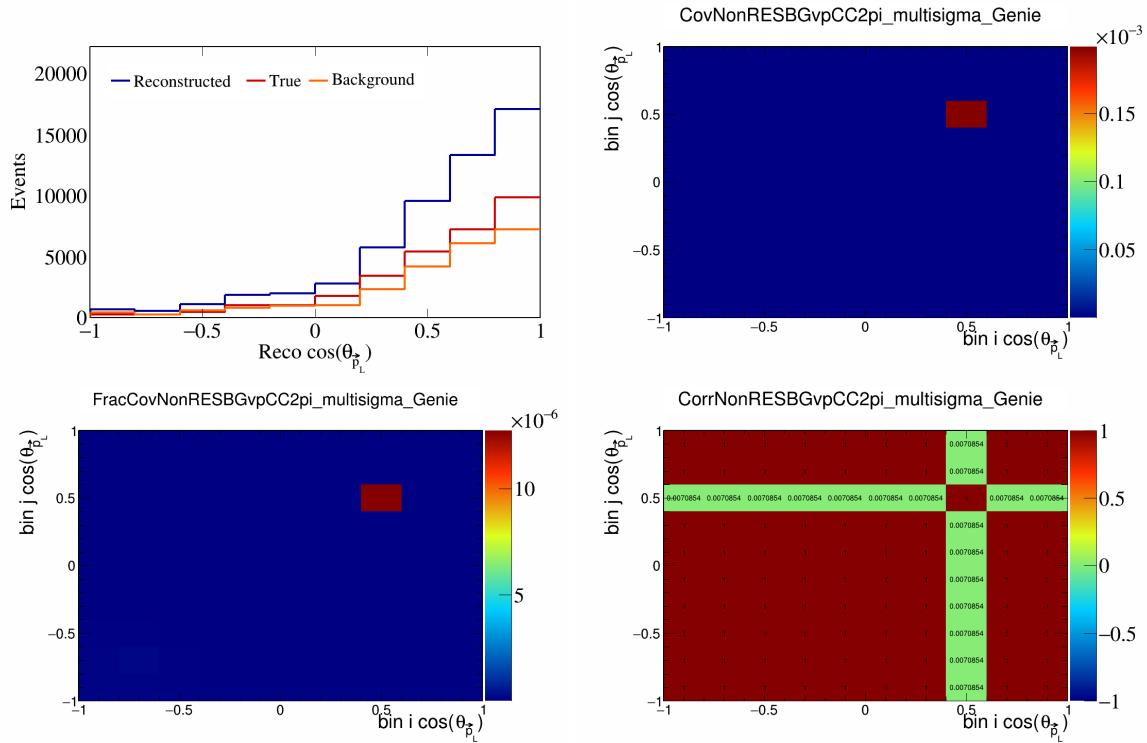


Figure 541: NonRESBGvpCC2pi variations for $\cos(\theta_{\vec{p}_L})$.

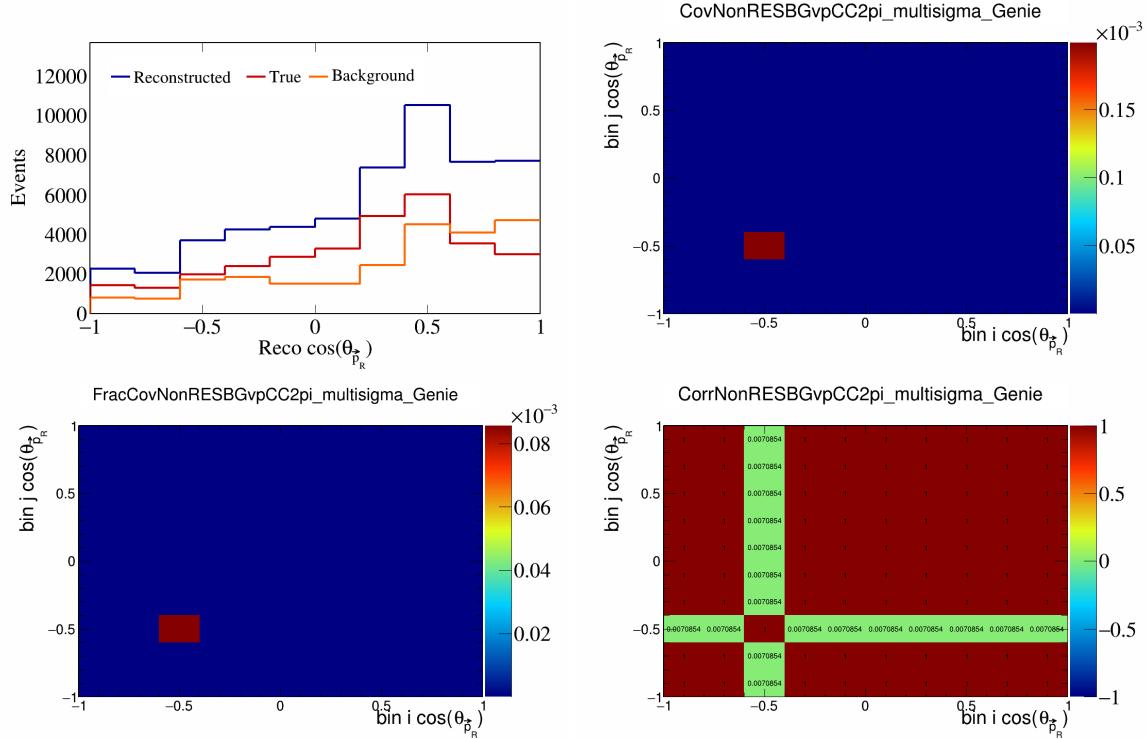


Figure 542: NonRESBGvpCC2pi variations for $\cos(\theta_{\vec{p}_R})$.

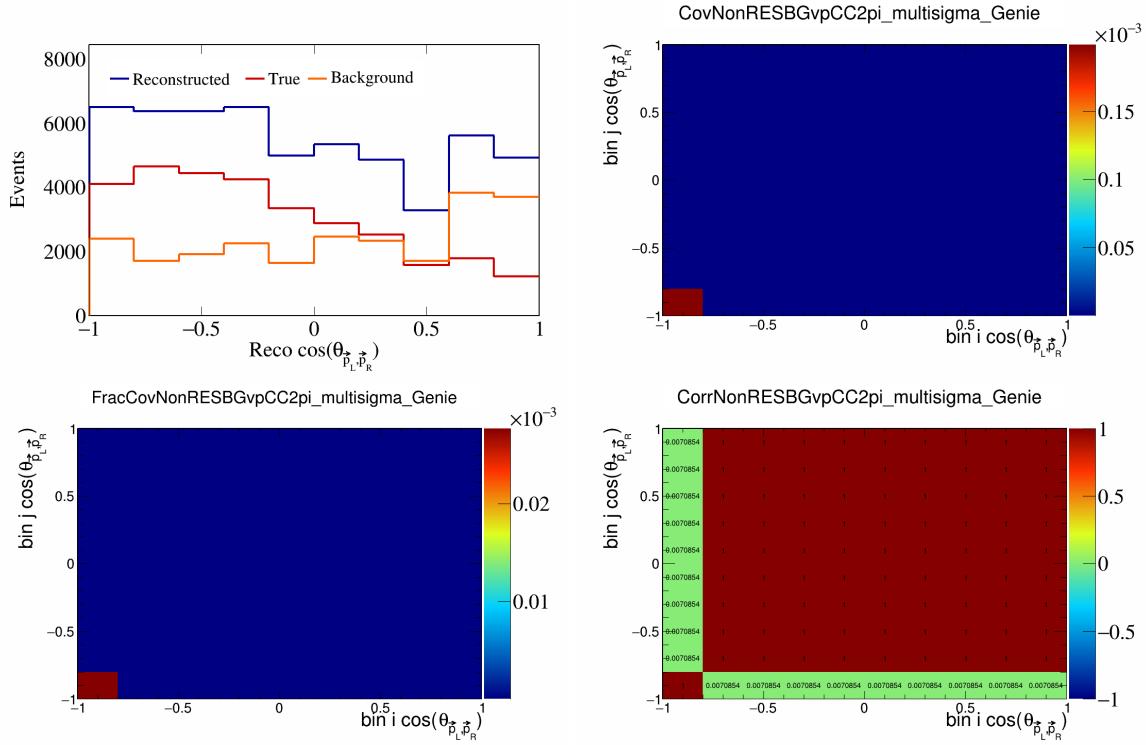


Figure 543: NonRESBGvpCC2pi variations for $\cos(\theta_{\vec{p}_L, \vec{p}_R})$.

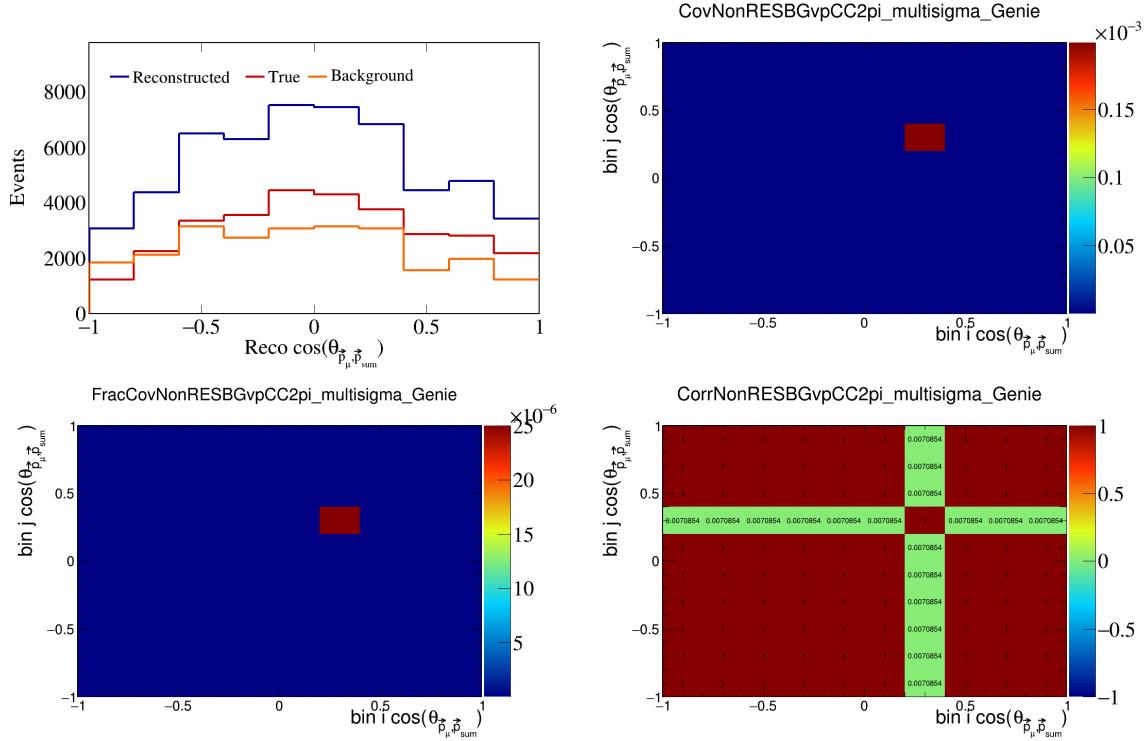


Figure 544: NonRESBGvpCC2pi variations for $\cos(\theta_{\vec{p}_\mu, \vec{p}_{\text{sum}}})$.

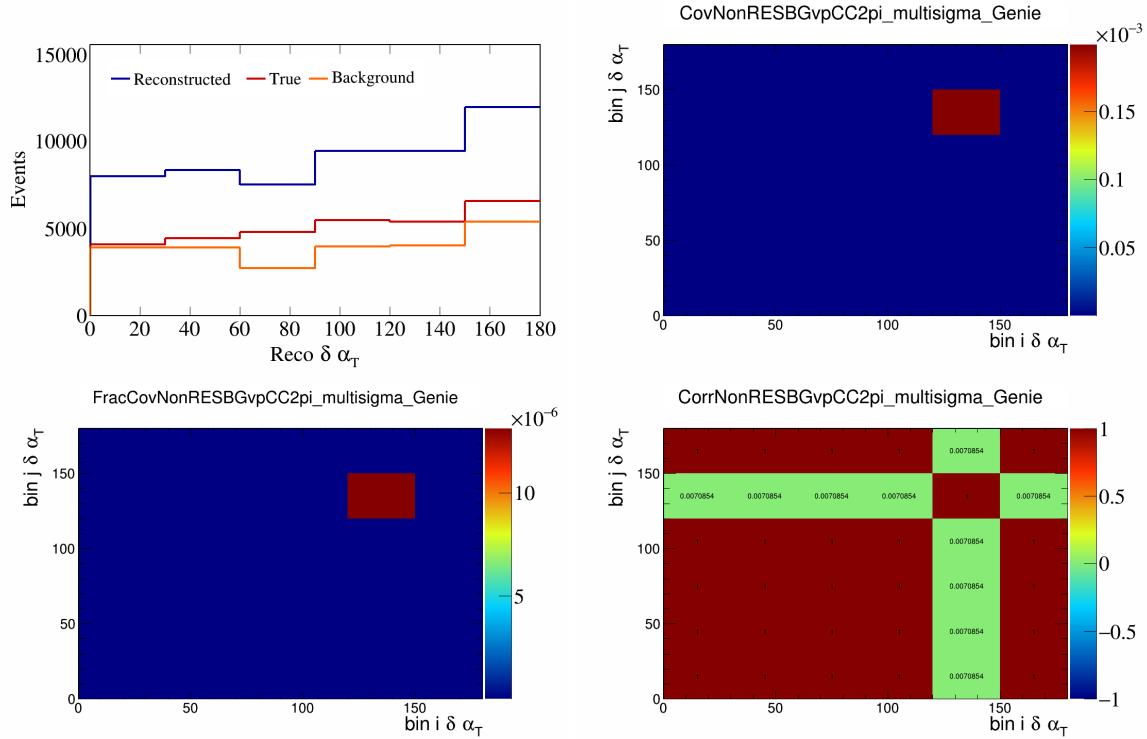


Figure 545: NonRESBGvpCC2pi variations for $\delta\alpha_T$.

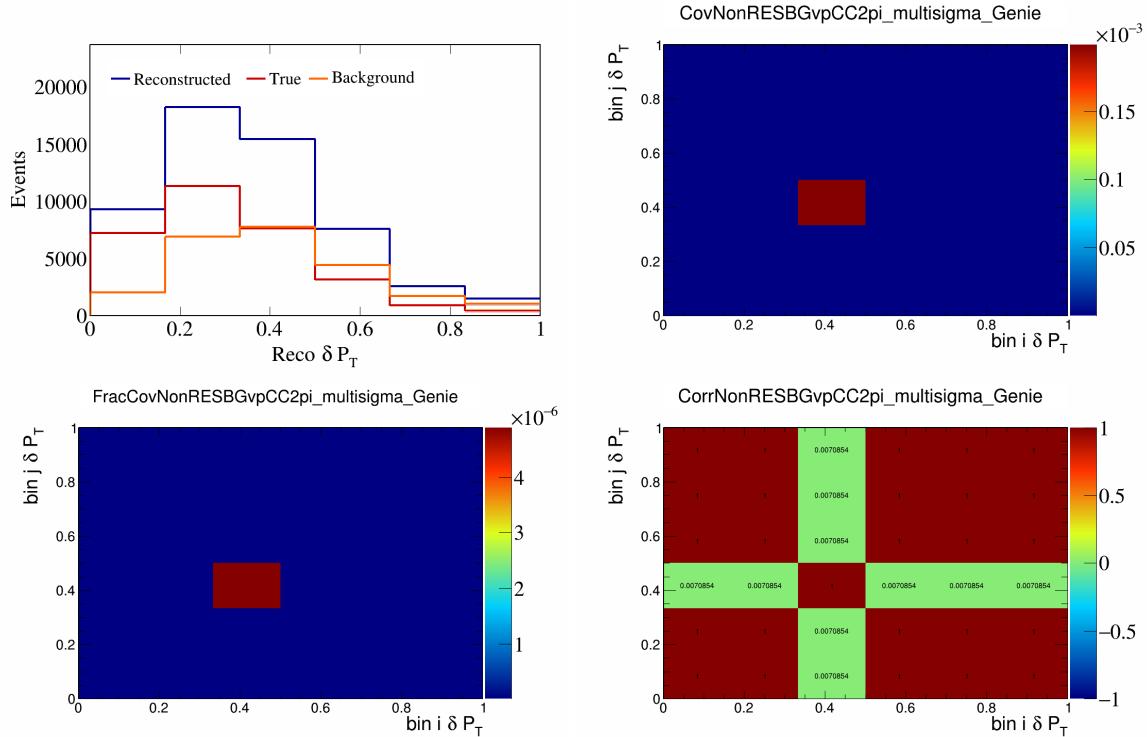


Figure 546: NonRESBGvpCC2pi variations for δP_T .

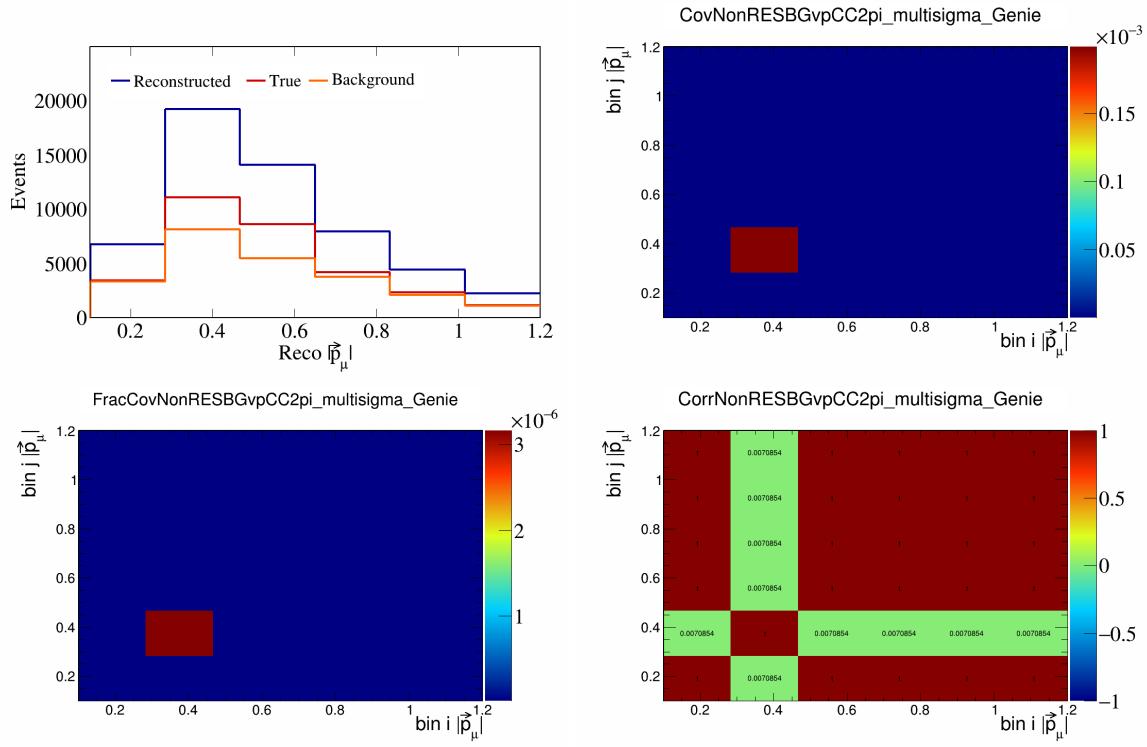


Figure 547: NonRESBGvpCC2pi variations for $|\vec{p}_\mu|$.

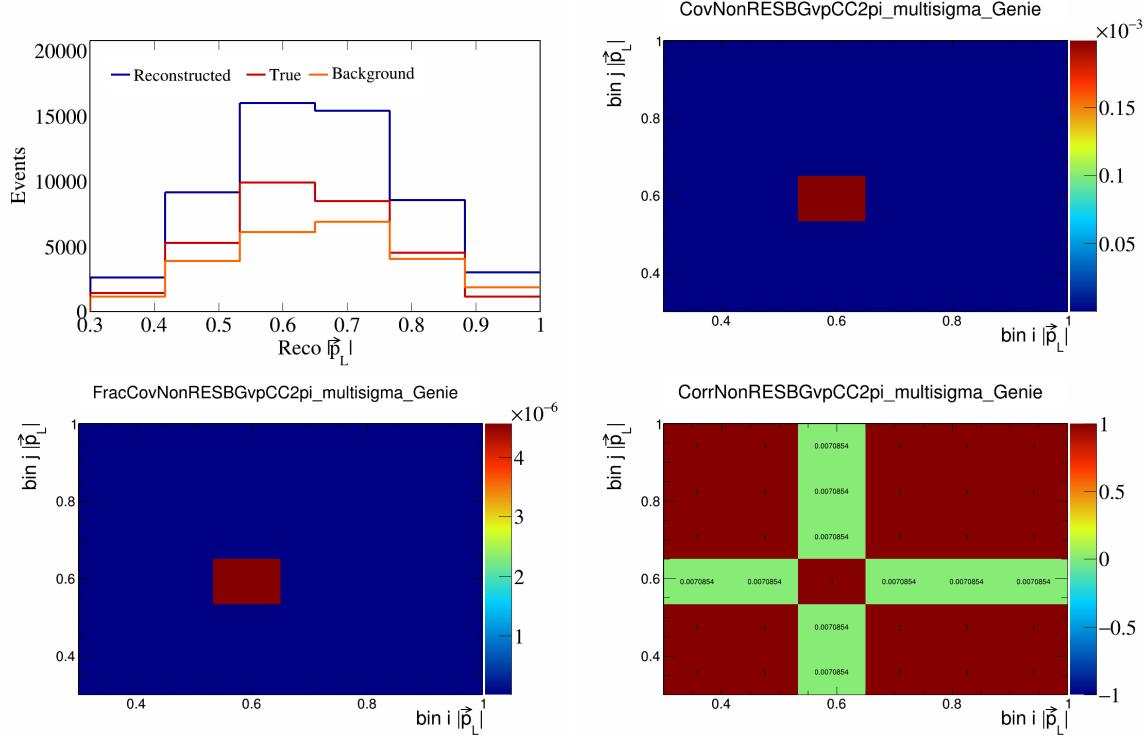


Figure 548: NonRESBGvpCC2pi variations for $|\vec{p}_L|$.

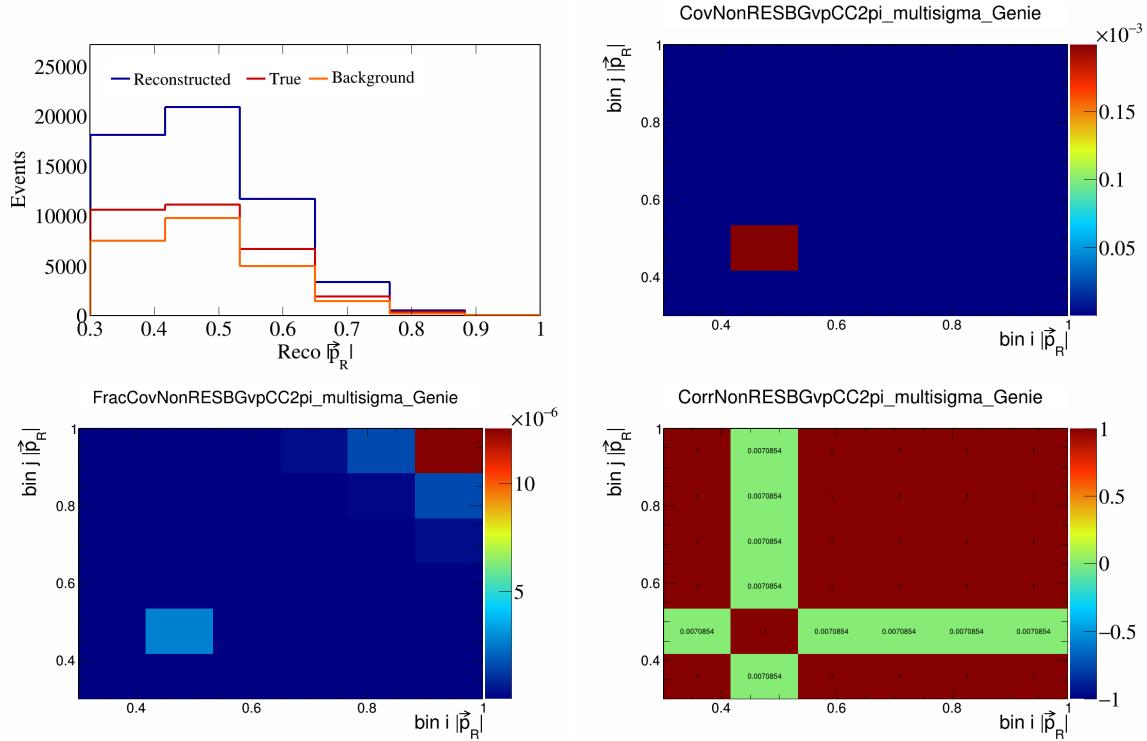


Figure 549: NonRESBGvpCC2pi variations for $|\vec{p}_R|$.

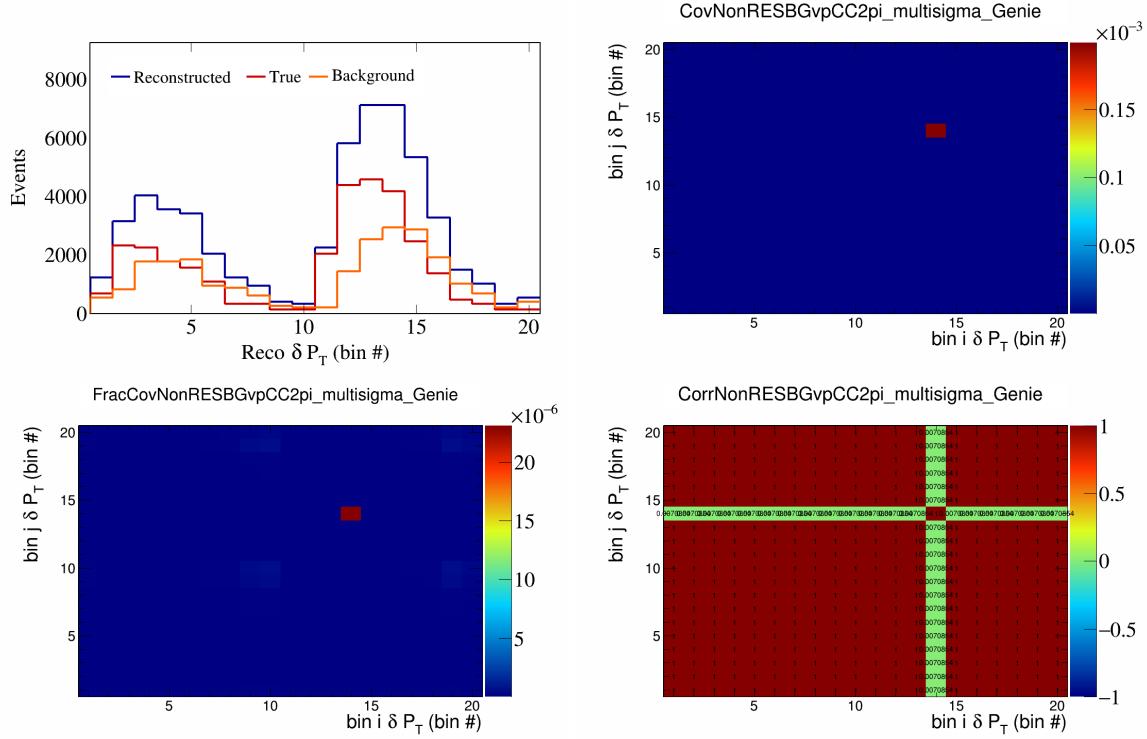


Figure 550: NonRESBGvpCC2pi variations for δP_T in $\cos(\theta_{\vec{p}_\mu})$.

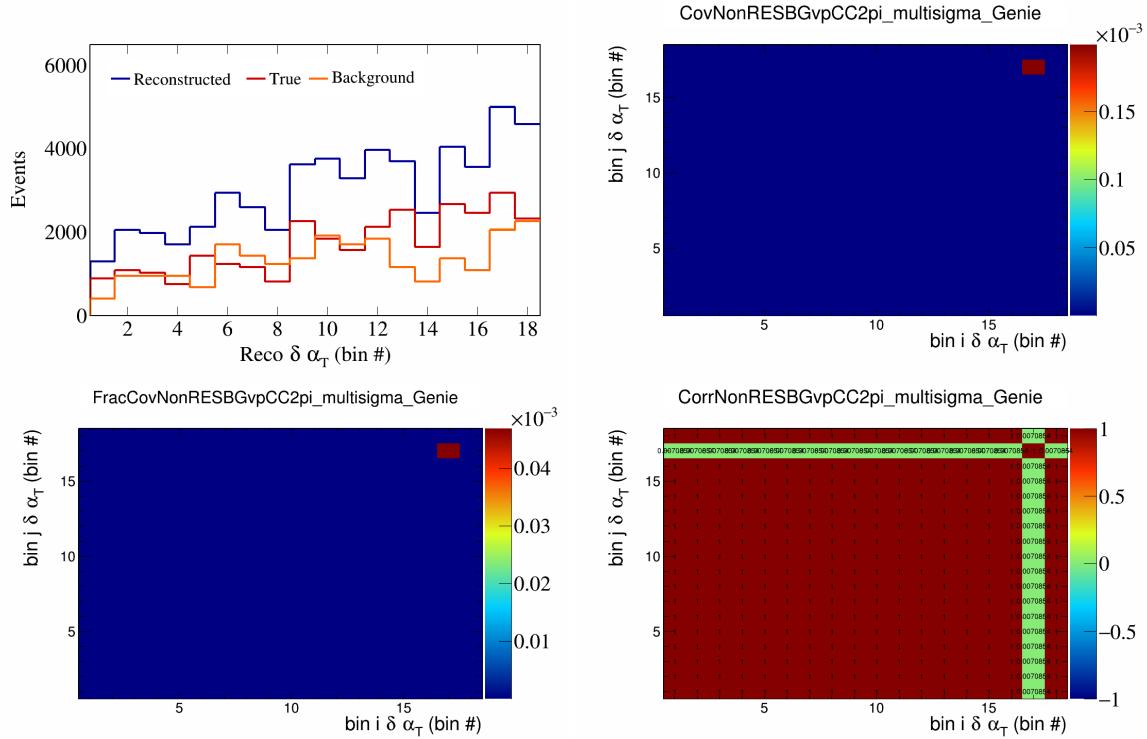


Figure 551: NonRESBGvpCC2pi variations for $\delta \alpha_T$ in $\cos(\theta_{\vec{p}_\mu})$.

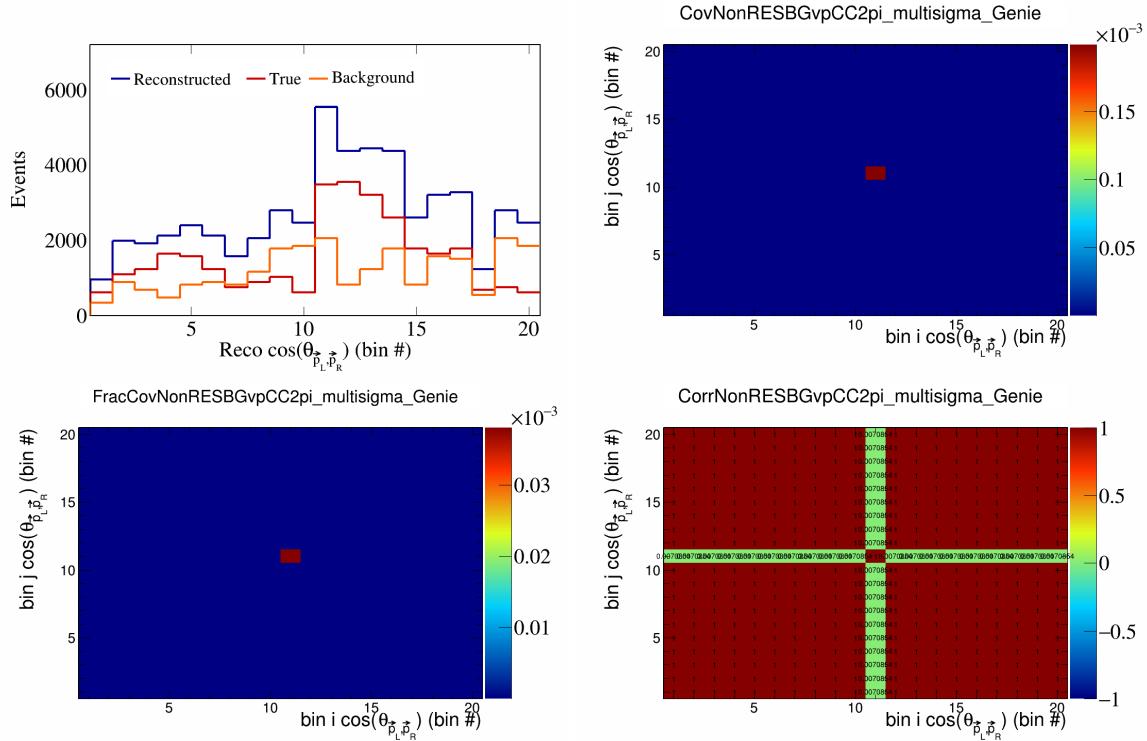


Figure 552: NonRESBGvpCC2pi variations for $\cos(\theta_{\vec{p}_L, \vec{p}_R})$ in $\cos(\theta_{\vec{p}_\mu})$.

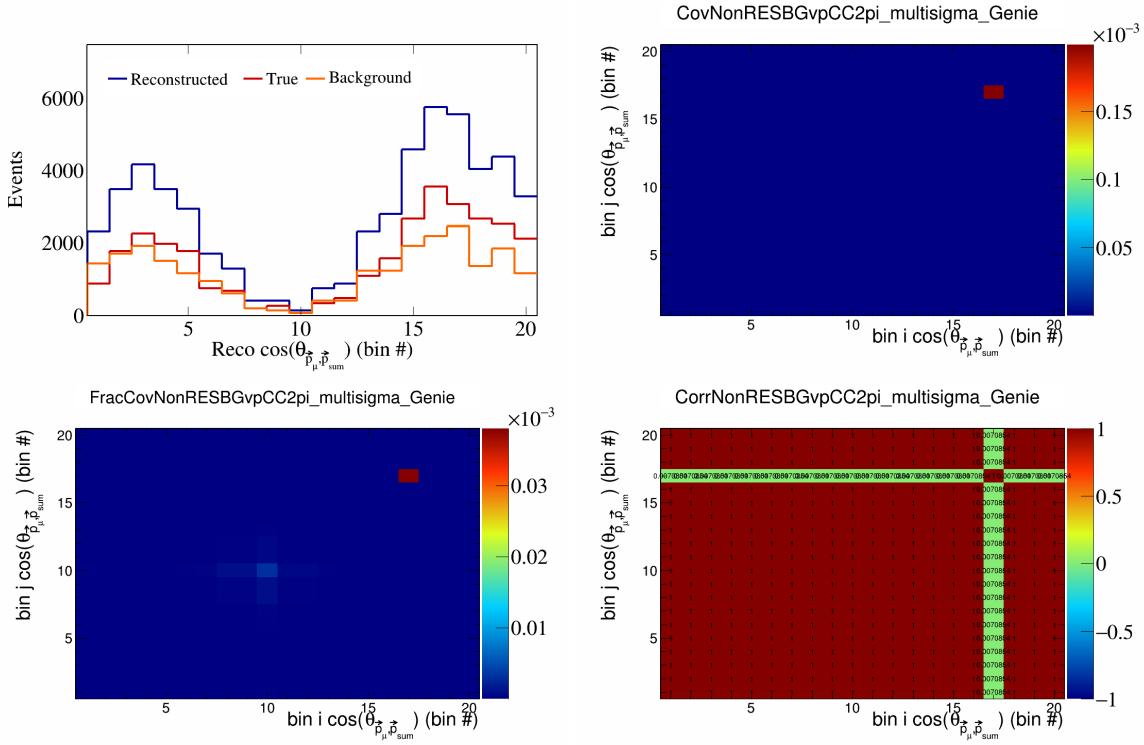


Figure 553: NonRESBGvpCC2pi variations for $\cos(\theta_{\vec{p}_\mu, \vec{p}_{\text{sum}}})$ in $\cos(\theta_{\vec{p}_\mu})$.

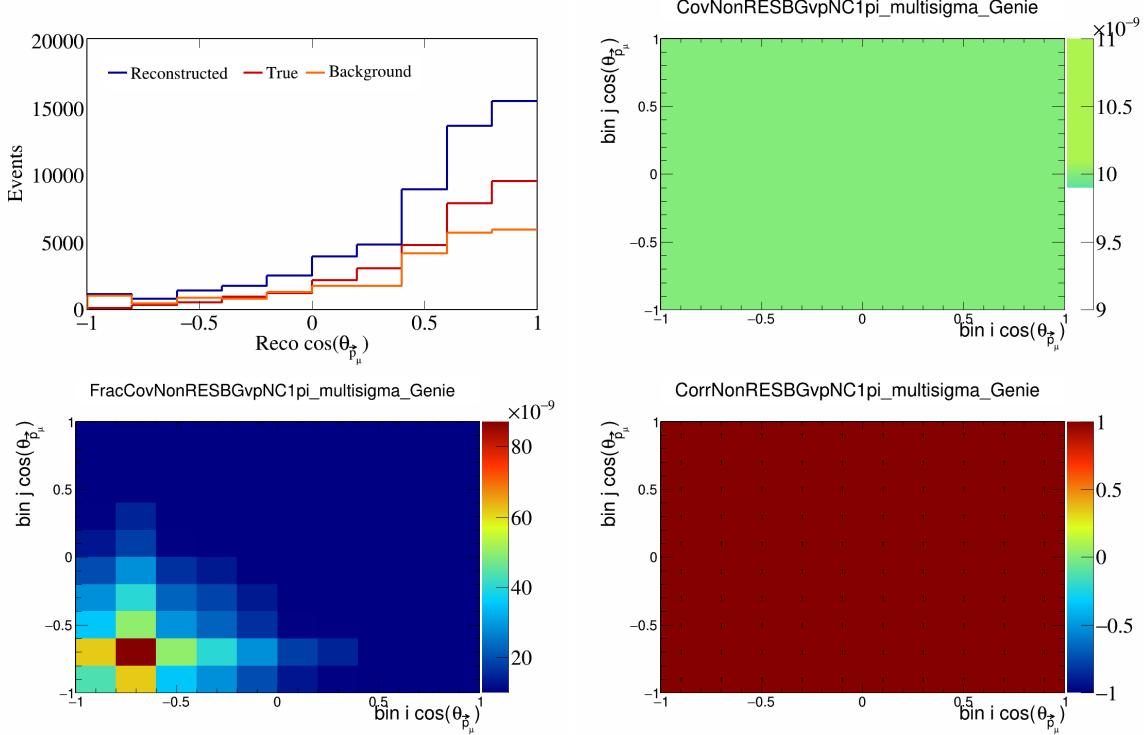


Figure 554: NonRESBGvpNC1pi variations for $\cos(\theta_{\vec{p}_\mu})$.

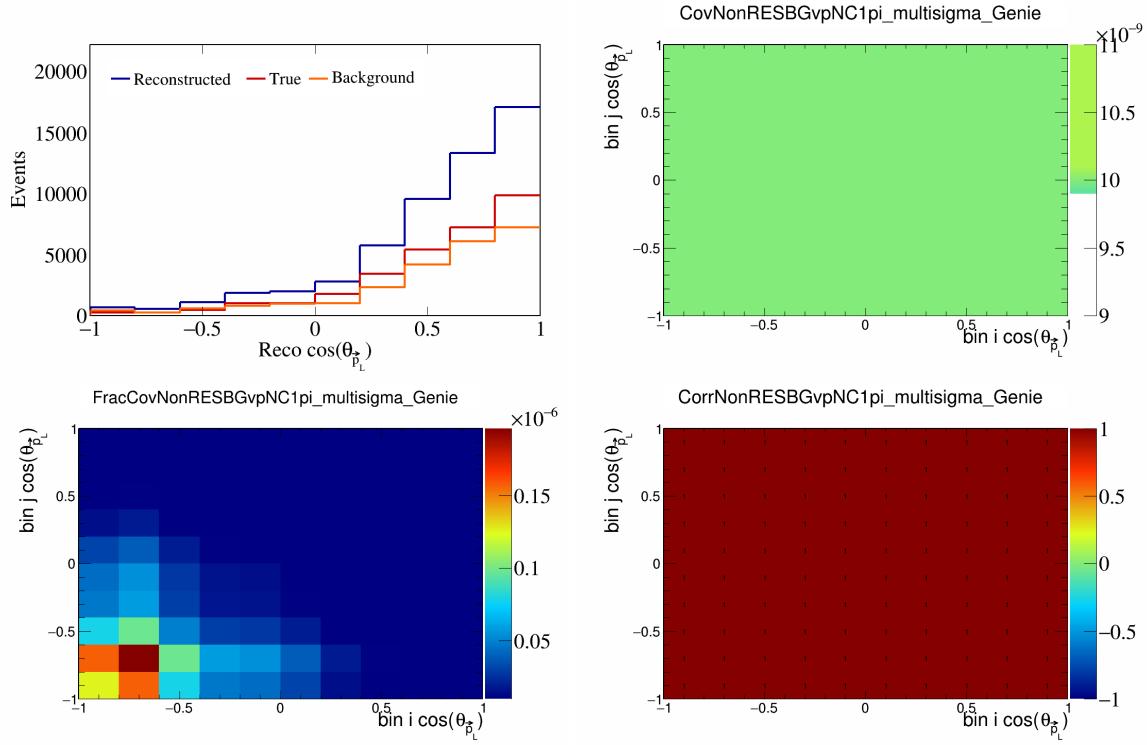


Figure 555: NonRESBGvpNC1pi variations for $\cos(\theta_{\vec{p}_L})$.

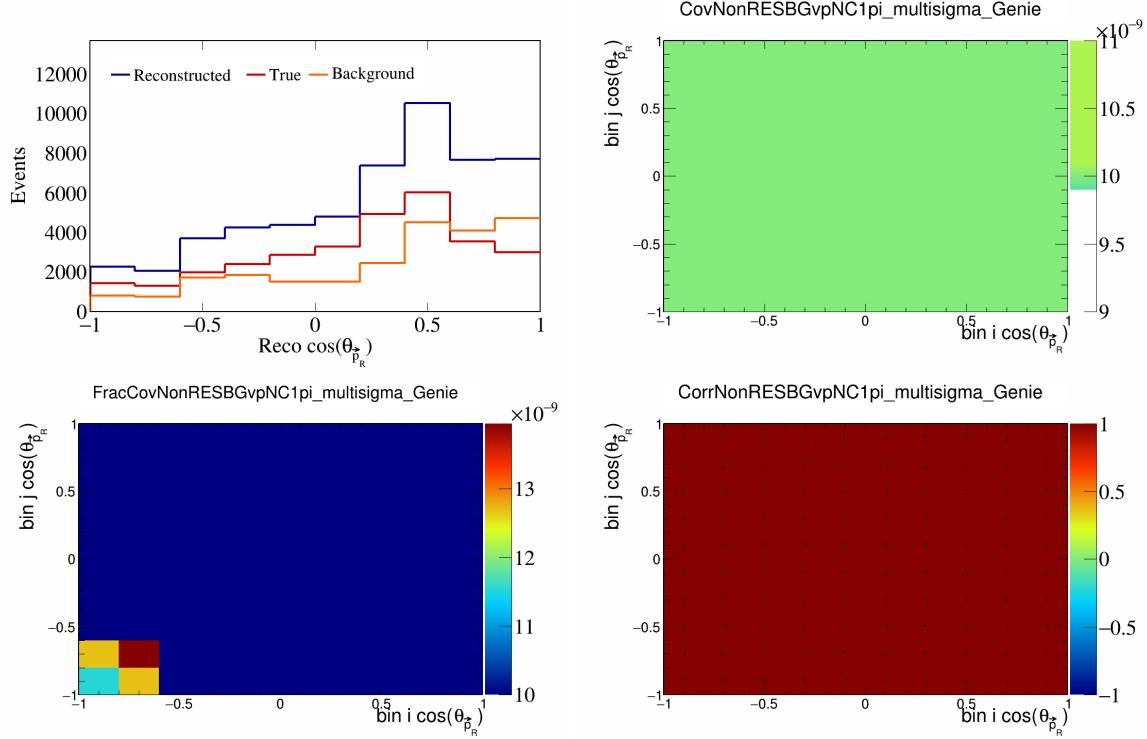


Figure 556: NonRESBGvpNC1pi variations for $\cos(\theta_{\vec{p}_R})$.

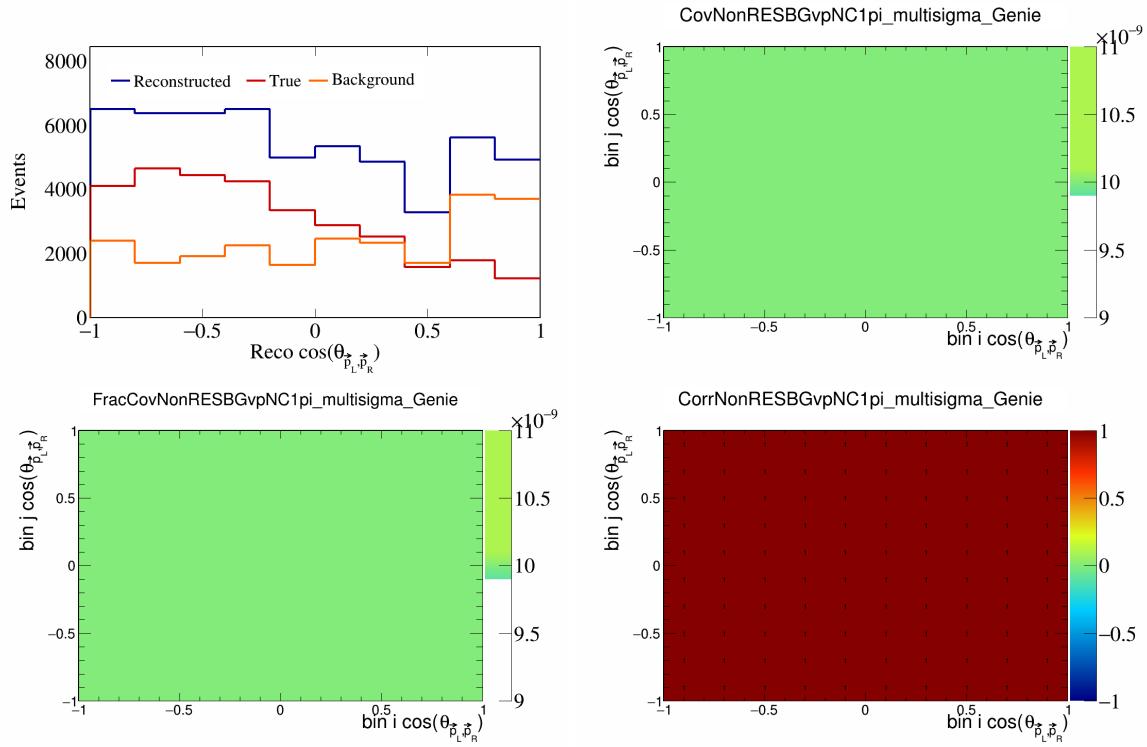


Figure 557: NonRESBGvpNC1pi variations for $\cos(\theta_{\vec{p}_L, \vec{p}_R})$.

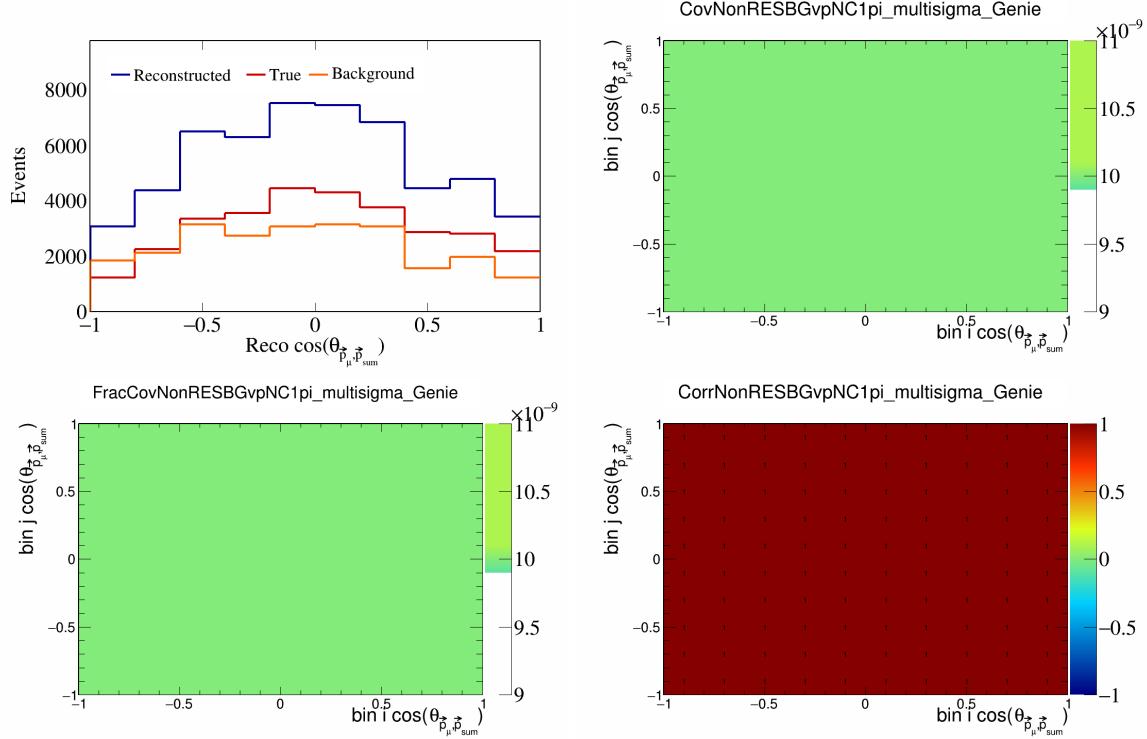


Figure 558: NonRESBGvpNC1pi variations for $\cos(\theta_{\vec{p}_\mu, \vec{p}_{\text{sum}}})$.

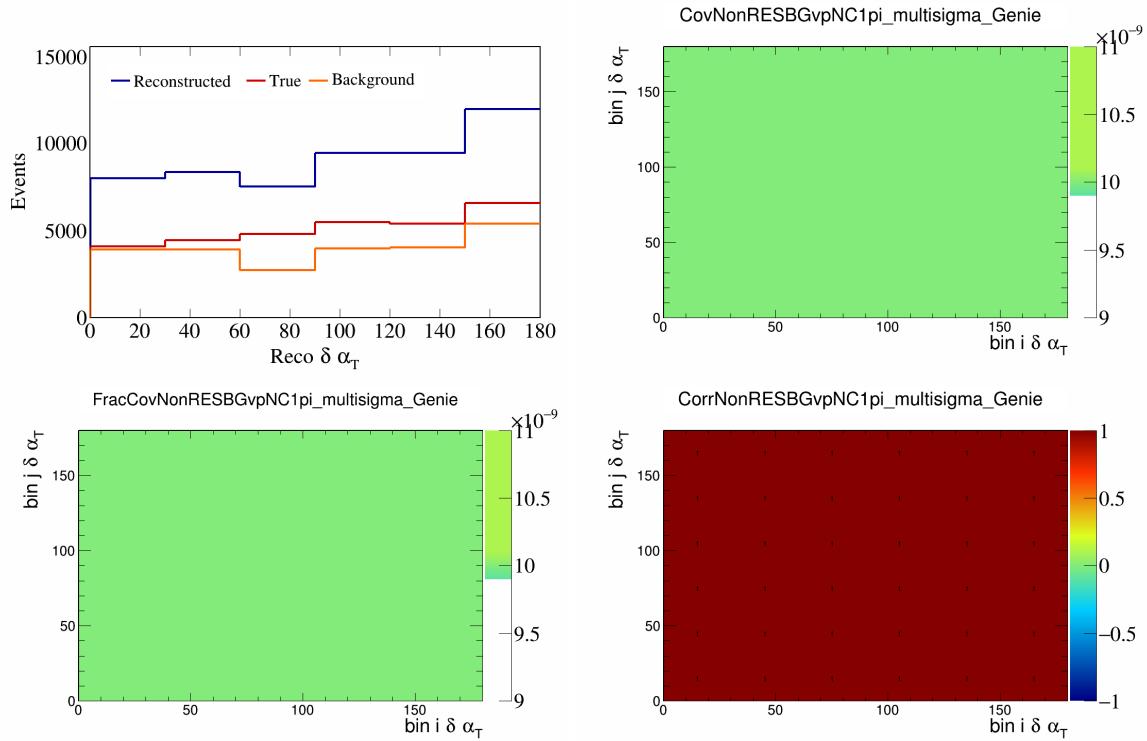


Figure 559: NonRESBGvpNC1pi variations for $\delta\alpha_T$.

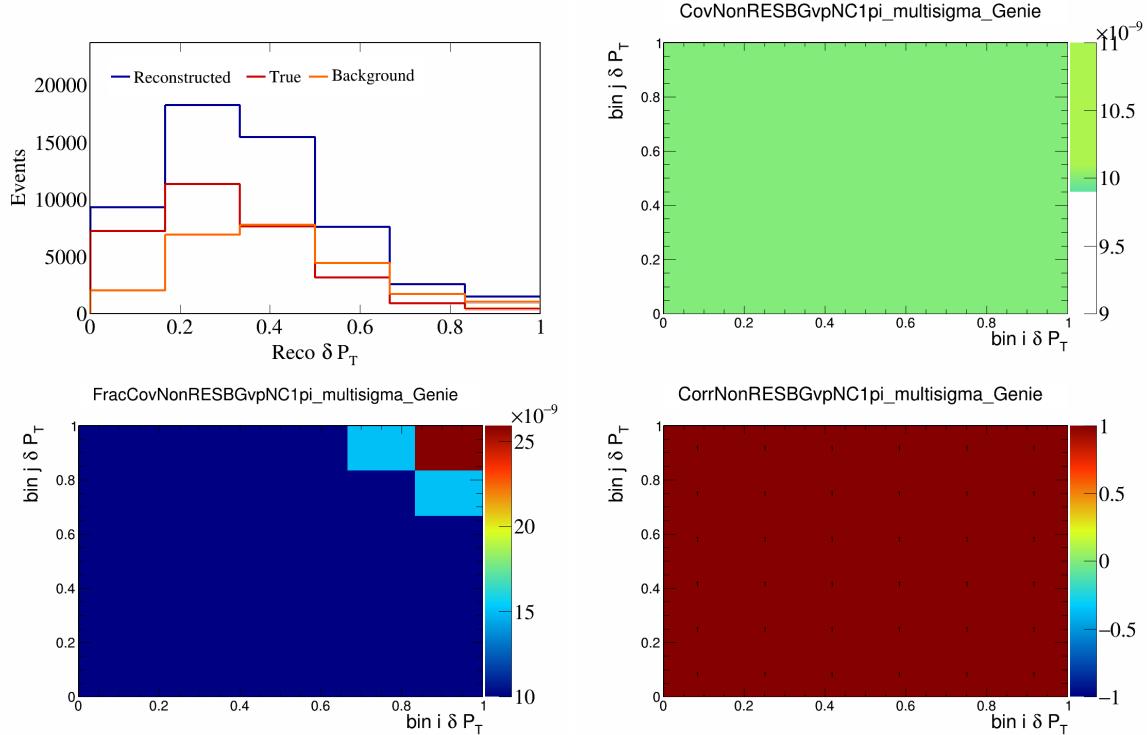


Figure 560: NonRESBGvpNC1pi variations for δP_T .

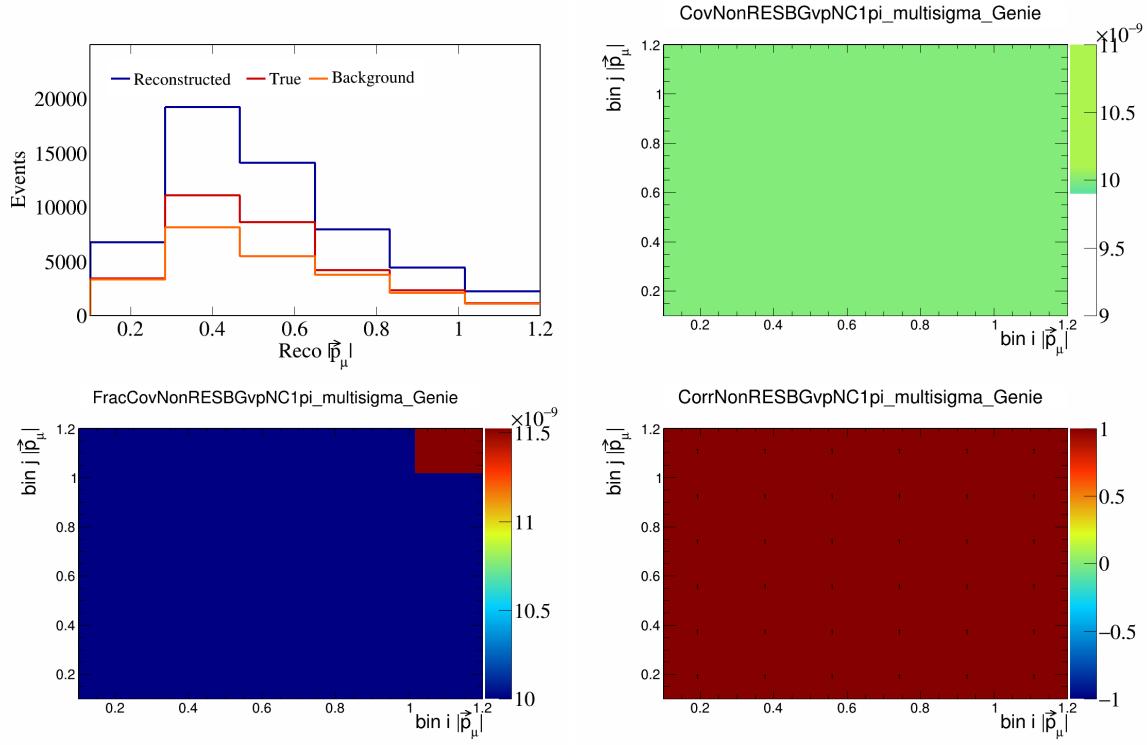


Figure 561: NonRESBGvpNC1pi variations for $|\vec{p}_\mu|$.

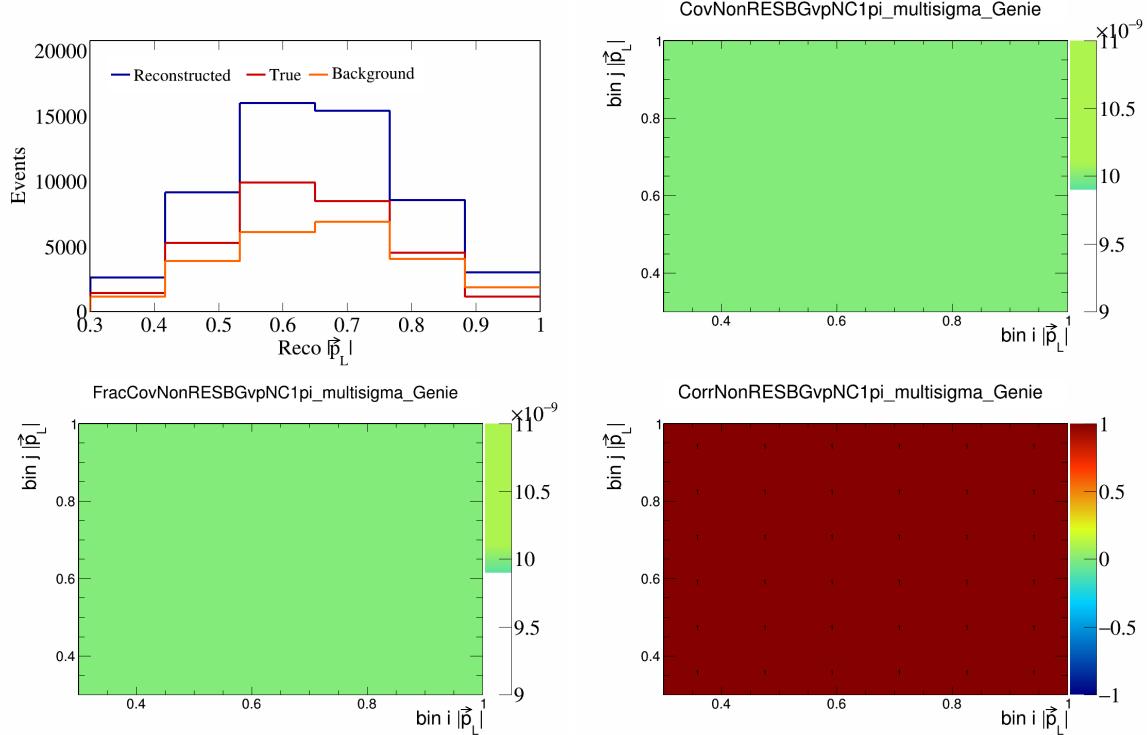


Figure 562: NonRESBGvpNC1pi variations for $|\vec{p}_L|$.

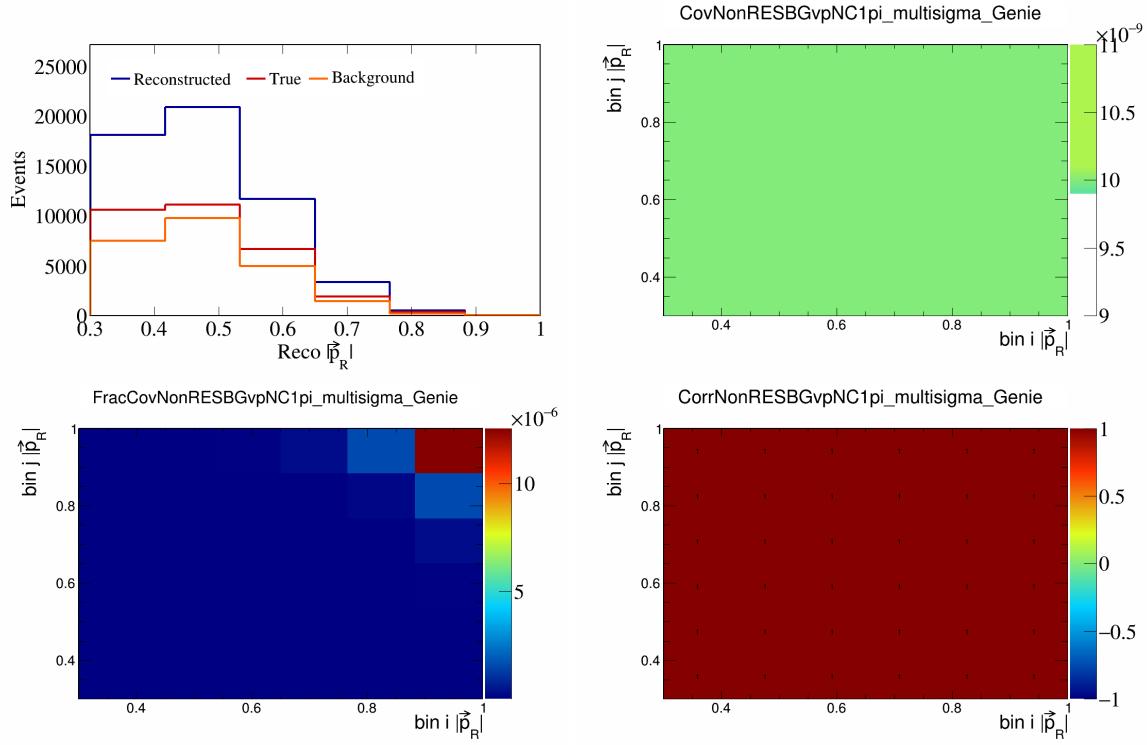


Figure 563: NonRESBGvpNC1pi variations for $|\vec{p}_R|$.

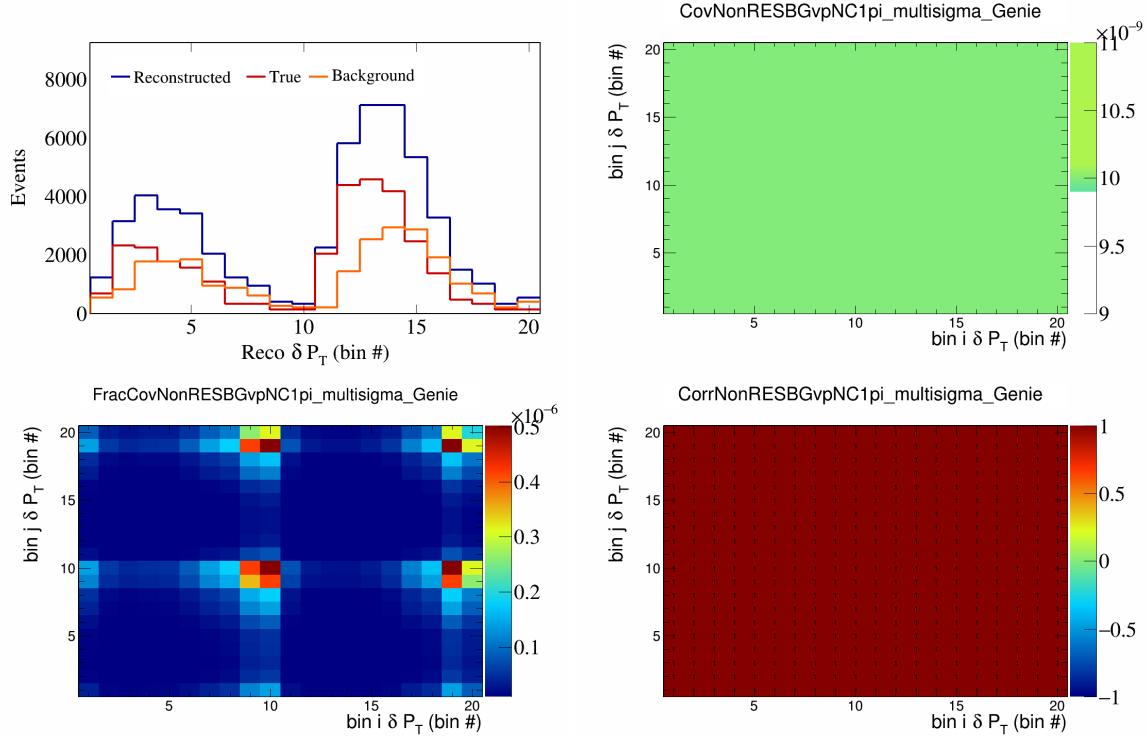


Figure 564: NonRESBGvpNC1pi variations for δP_T in $\cos(\theta_{\vec{p}_\mu})$.

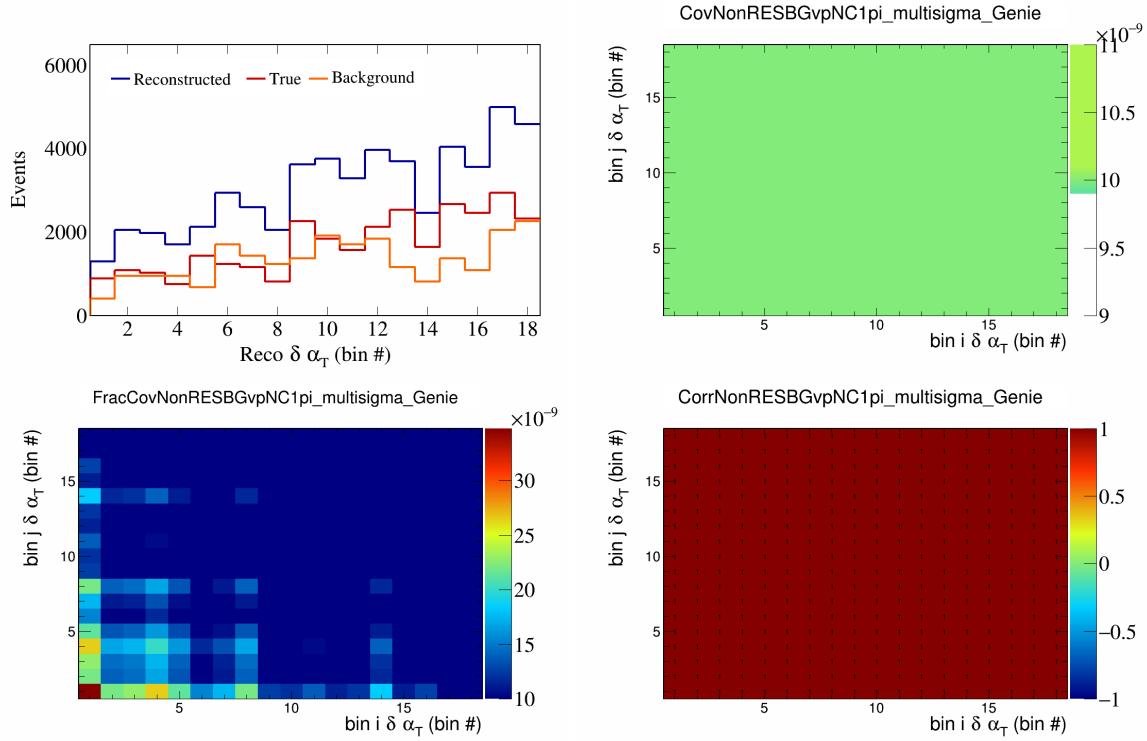


Figure 565: NonRESBGvpNC1pi variations for $\delta\alpha_T$ in $\cos(\theta_{\vec{p}_\mu})$.

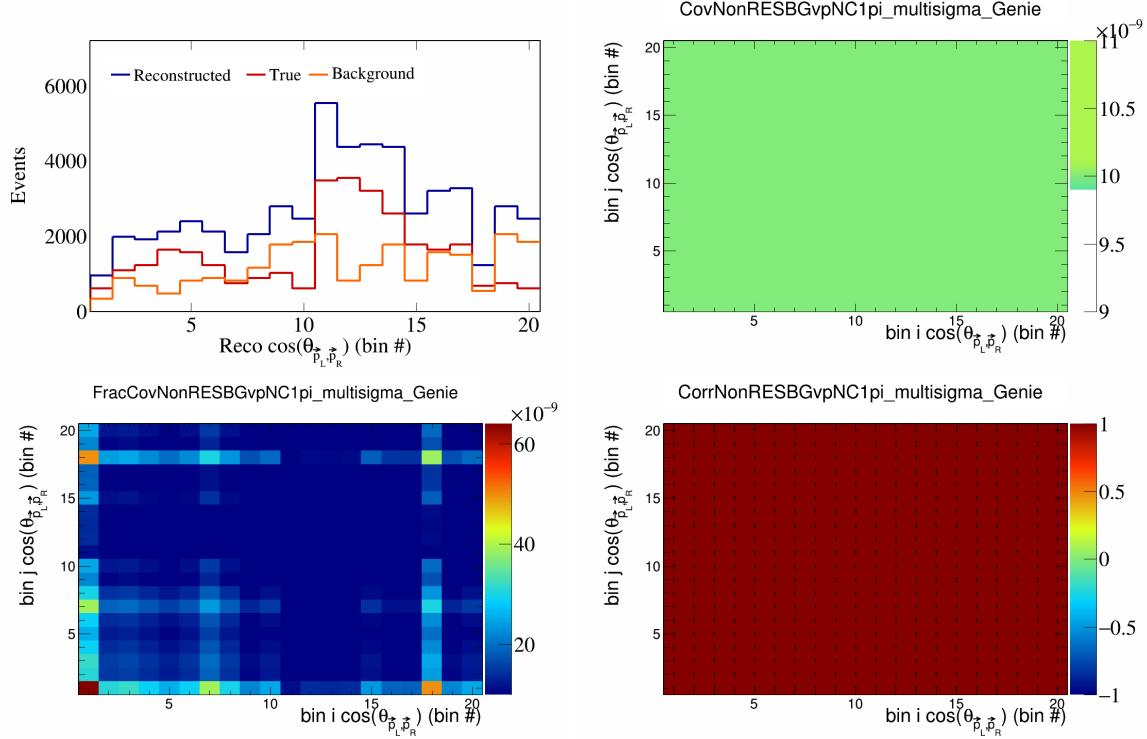


Figure 566: NonRESBGvpNC1pi variations for $\cos(\theta_{\vec{p}_L, \vec{p}_R})$ in $\cos(\theta_{\vec{p}_\mu})$.

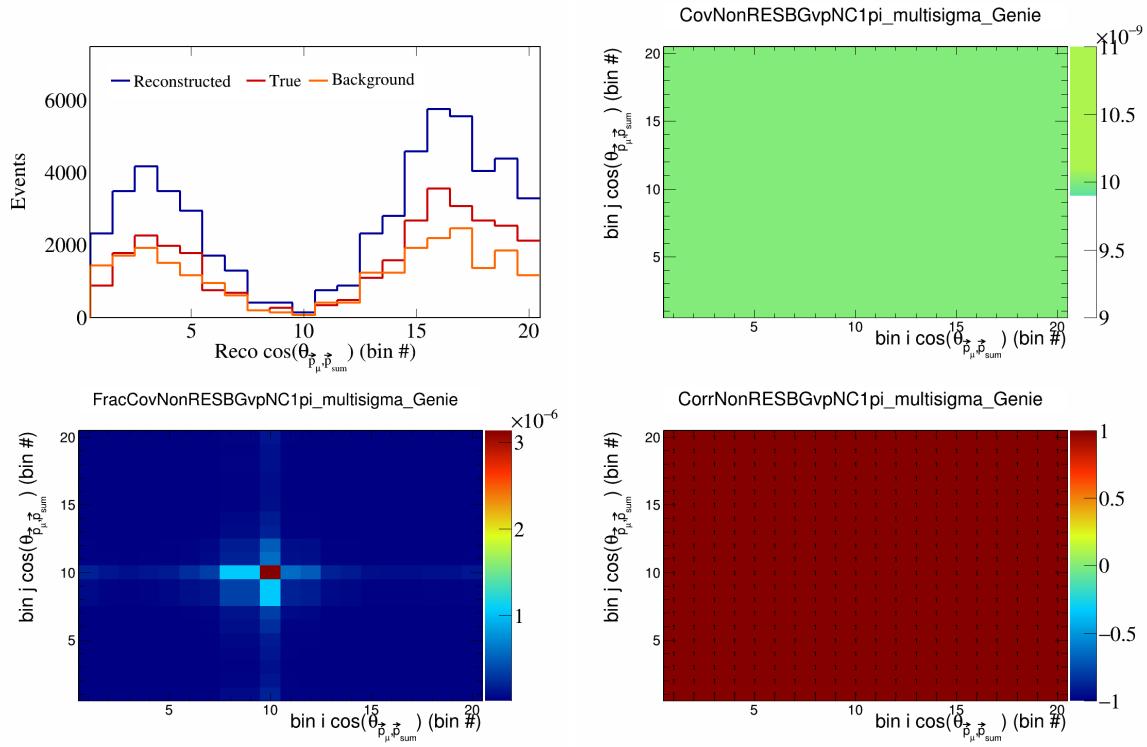


Figure 567: NonRESBGvpNC1pi variations for $\cos(\theta_{\vec{p}_\mu, \vec{p}_{\text{sum}}})$ in $\cos(\theta_{\vec{p}_\mu})$.

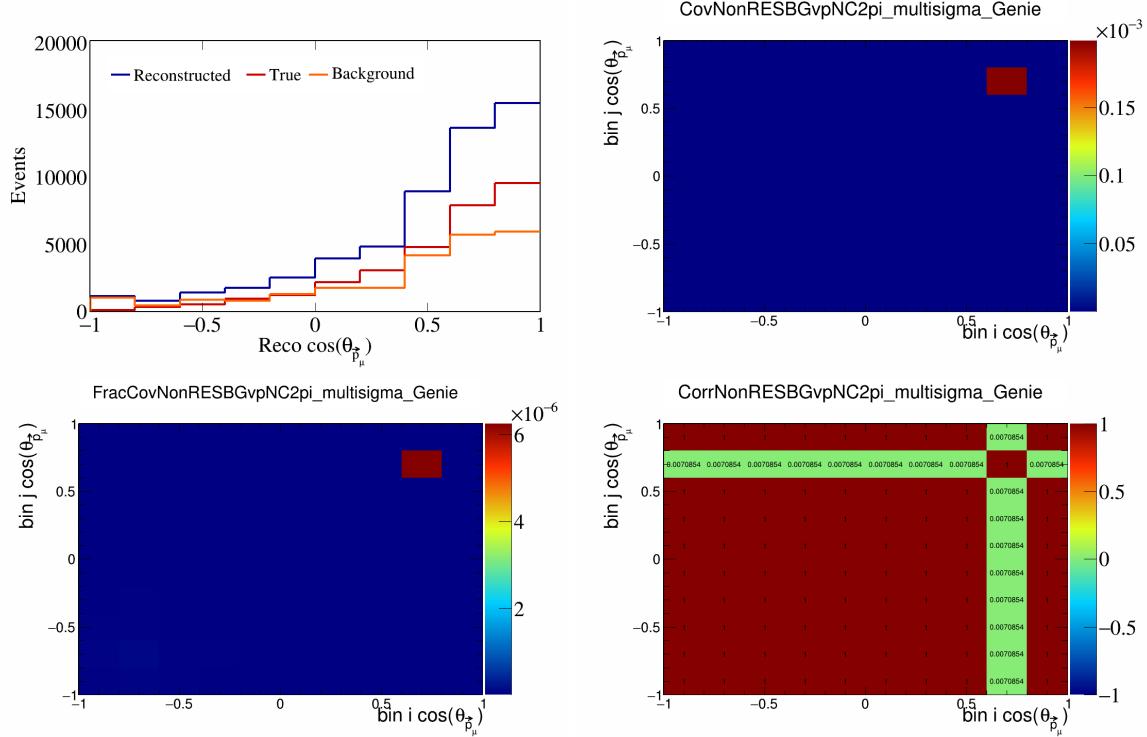


Figure 568: NonRESBGvpNC2pi variations for $\cos(\theta_{\vec{p}_\mu})$.

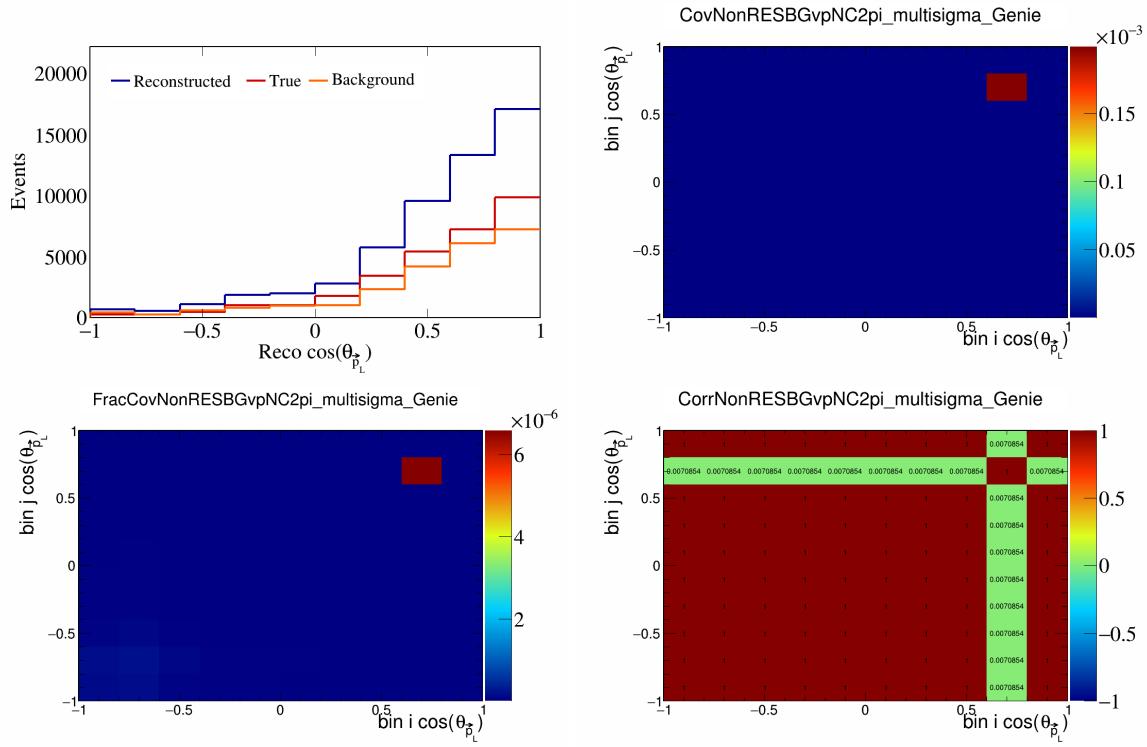


Figure 569: NonRESBGvpNC2pi variations for $\cos(\theta_{\vec{p}_L})$.

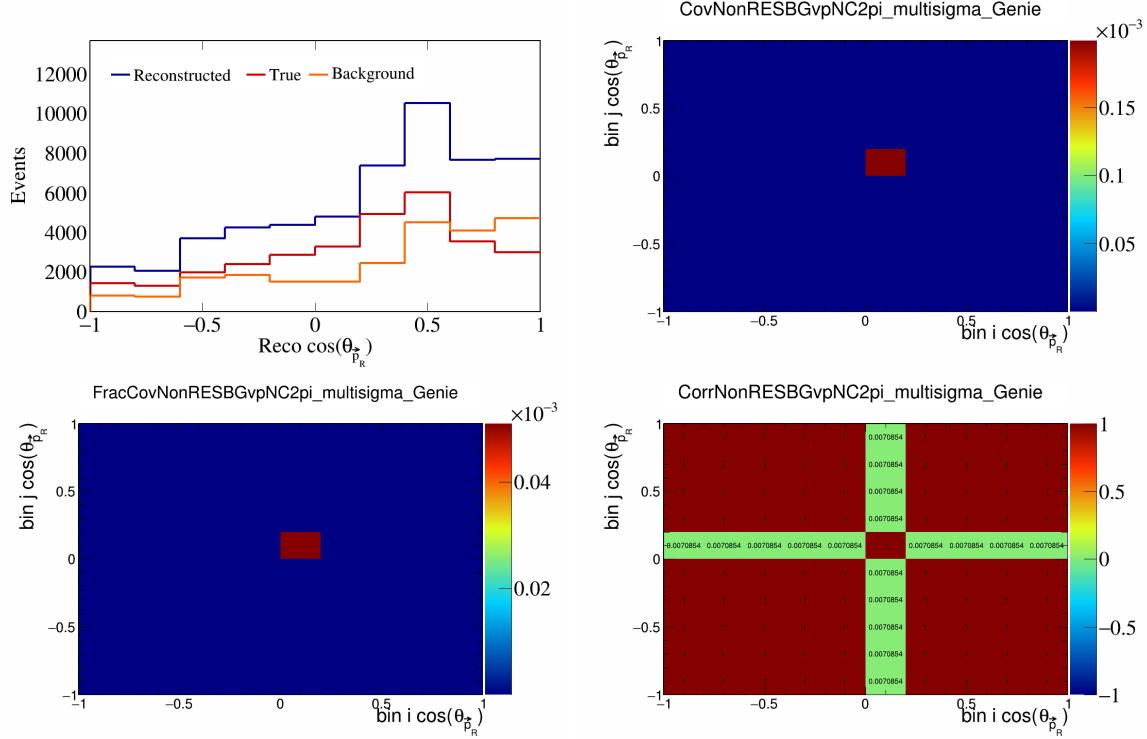


Figure 570: NonRESBGvpNC2pi variations for $\cos(\theta_{\vec{p}_R})$.

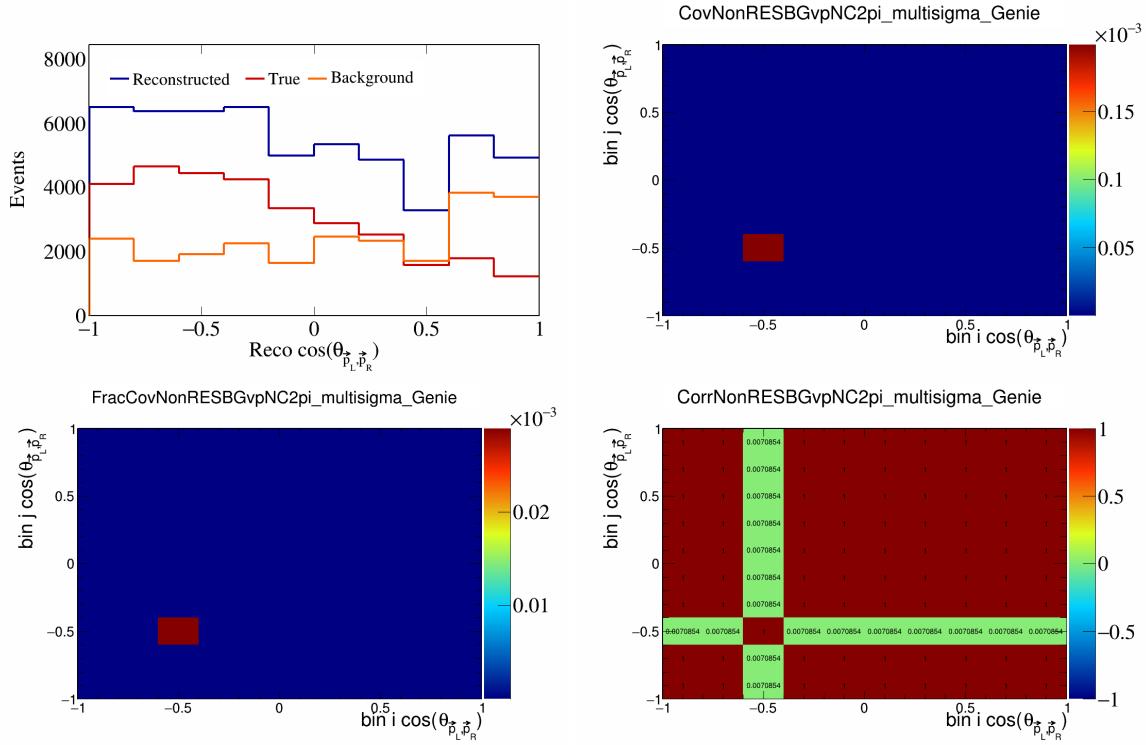


Figure 571: NonRESBGvpNC2pi variations for $\cos(\theta_{\vec{p}_L, \vec{p}_R})$.

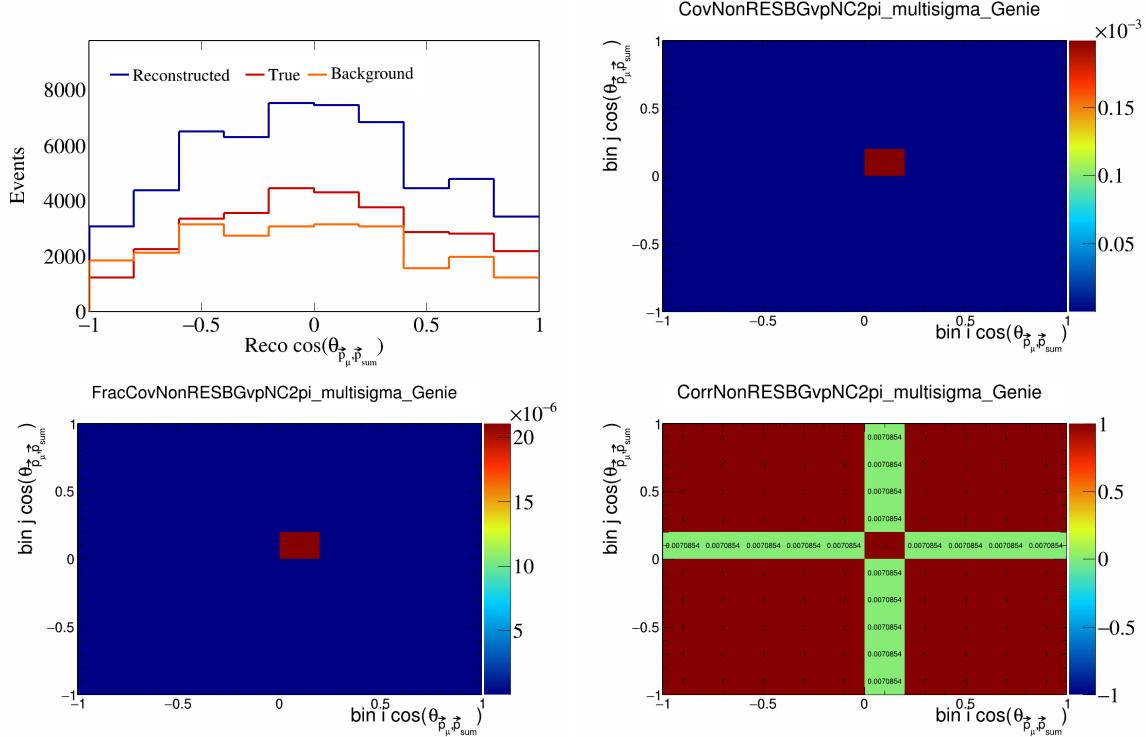


Figure 572: NonRESBGvpNC2pi variations for $\cos(\theta_{\vec{p}_\mu, \vec{p}_{\text{sum}}})$.

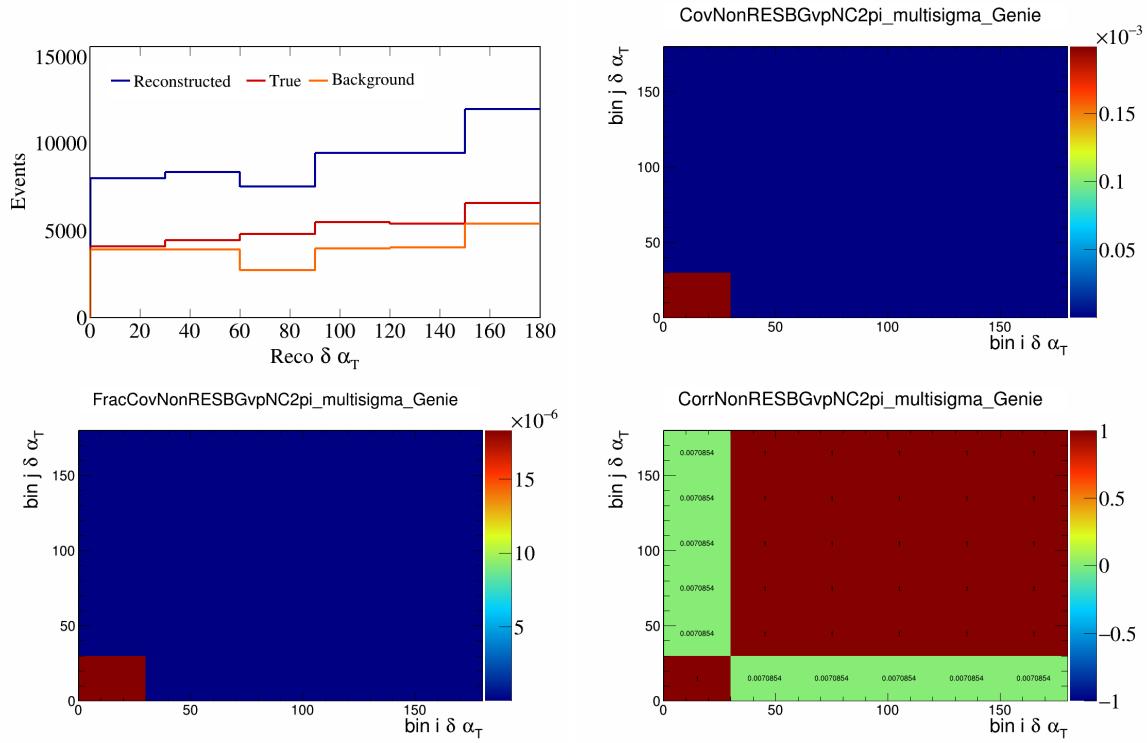


Figure 573: NonRESBGvpNC2pi variations for $\delta\alpha_T$.

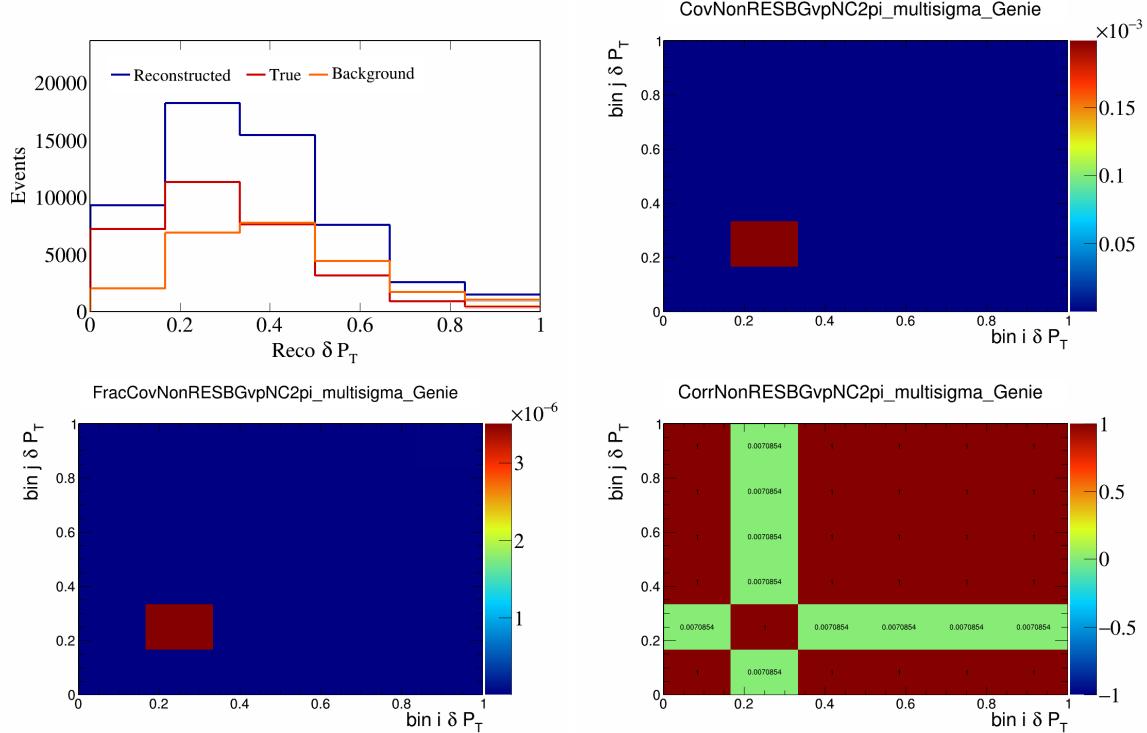


Figure 574: NonRESBGvpNC2pi variations for δP_T .

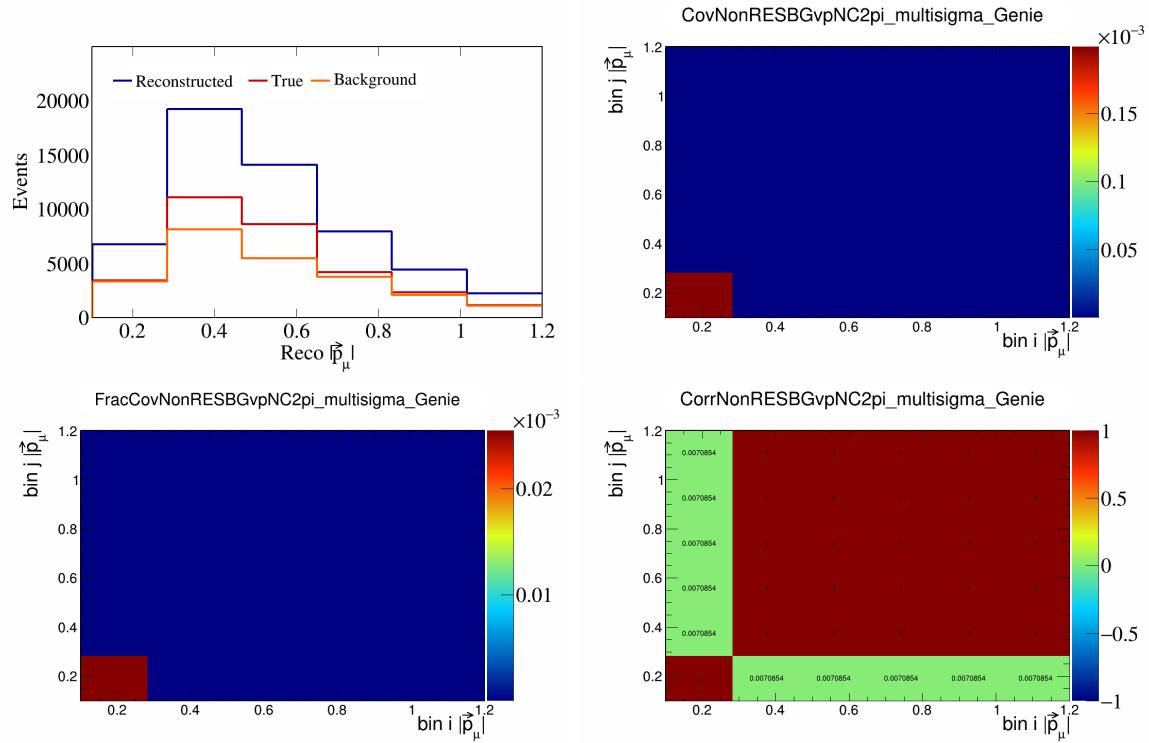


Figure 575: NonRESBGvpNC2pi variations for $|\vec{p}_\mu|$.

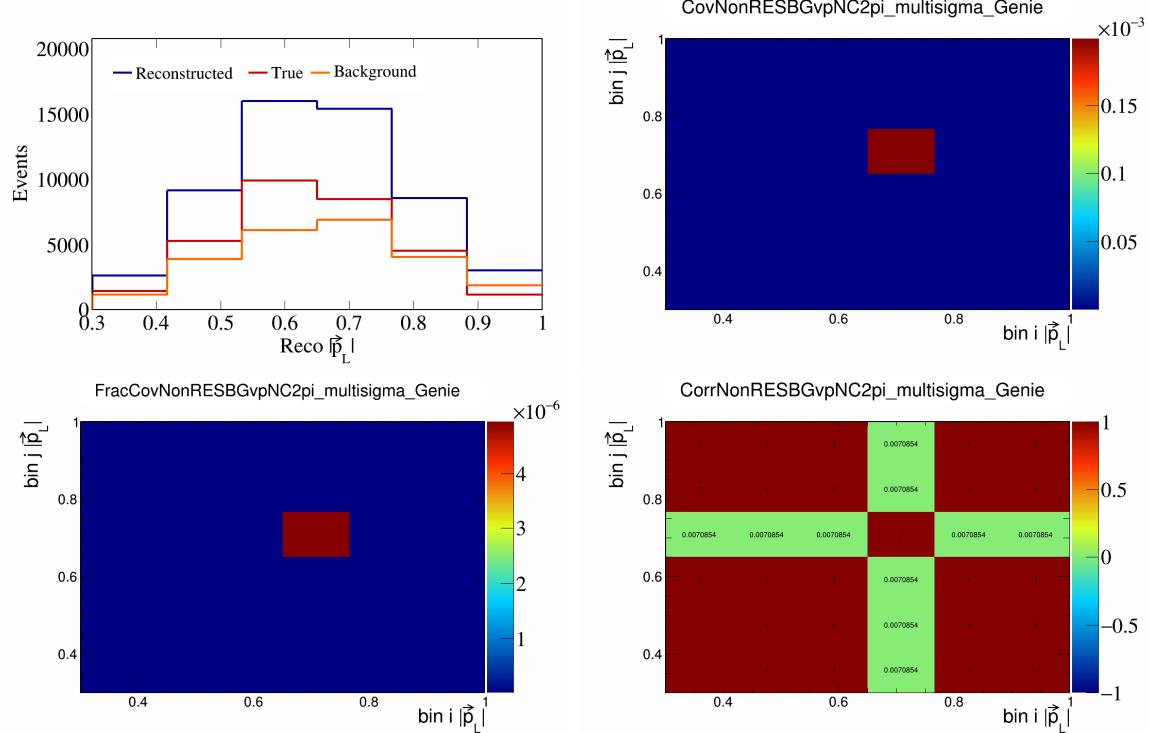


Figure 576: NonRESBGvpNC2pi variations for $|\vec{p}_L|$.

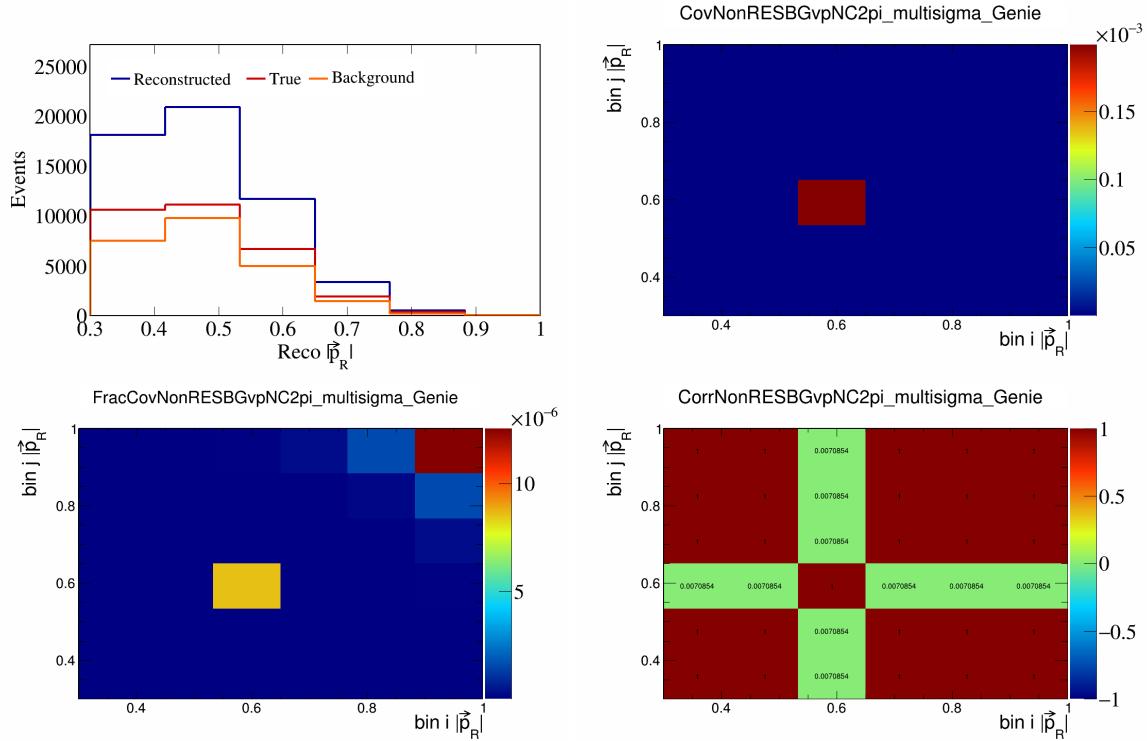


Figure 577: NonRESBGvpNC2pi variations for $|\vec{p}_R|$.

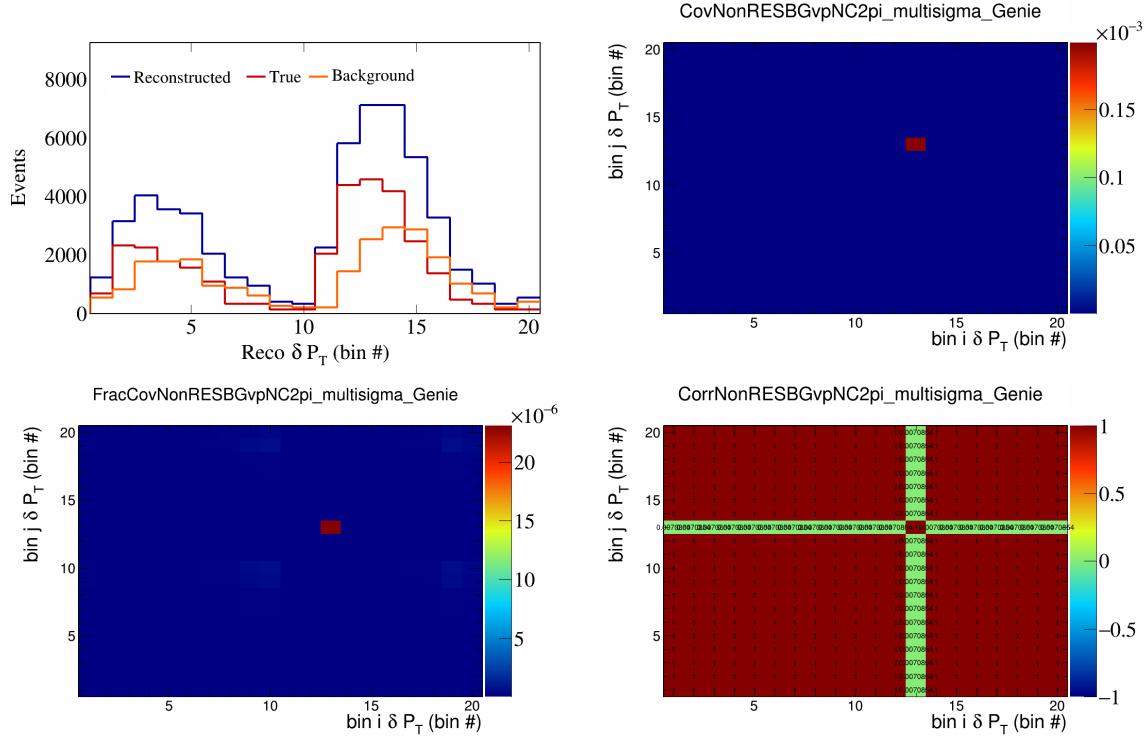


Figure 578: NonRESBGvpNC2pi variations for δP_T in $\cos(\theta_{\vec{p}_\mu})$.

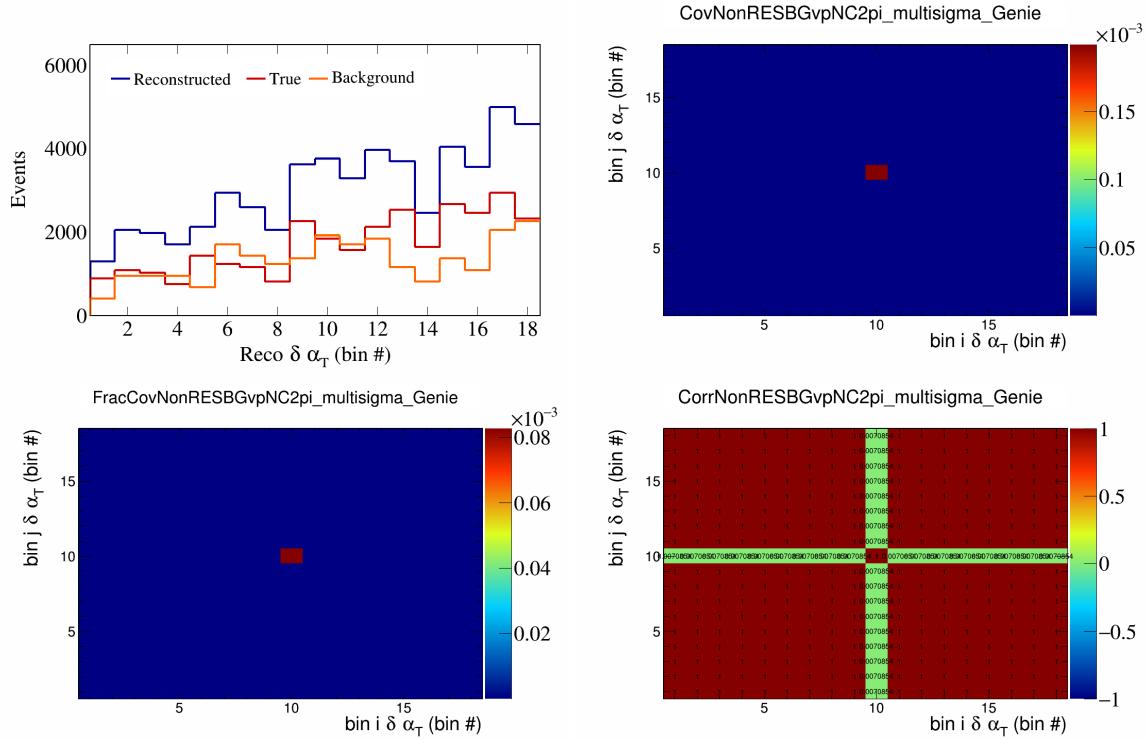


Figure 579: NonRESBGvpNC2pi variations for $\delta\alpha_T$ in $\cos(\theta_{\vec{p}_\mu})$.

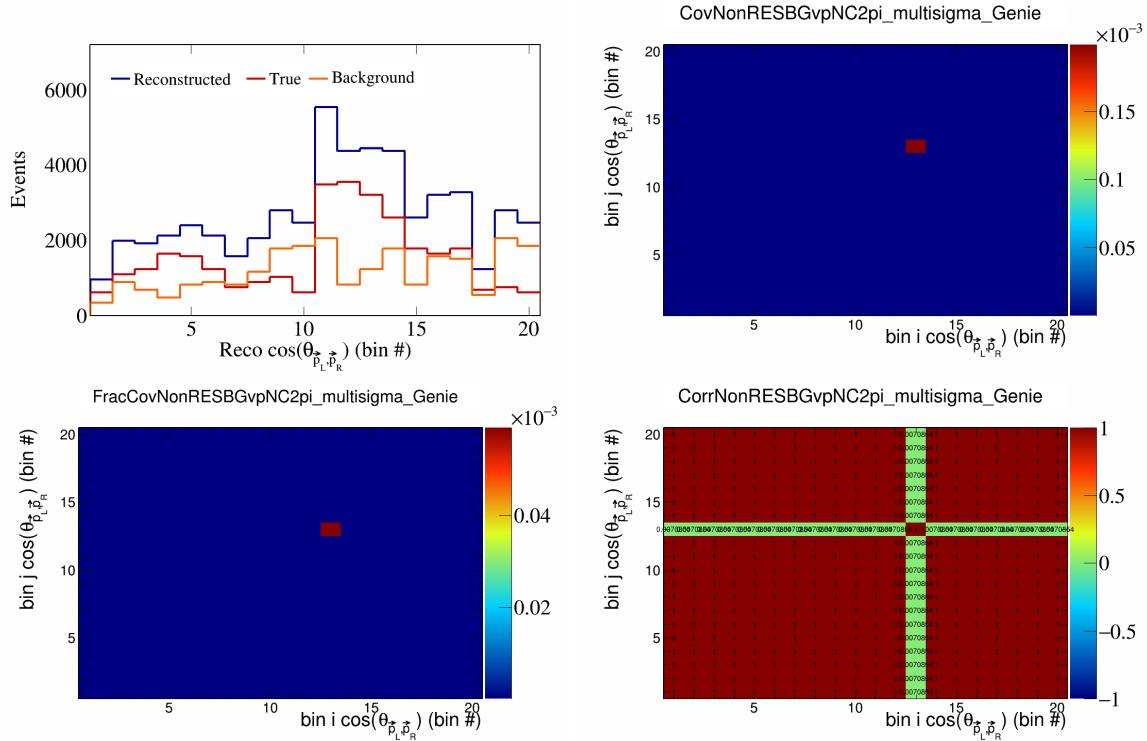


Figure 580: NonRESBGvpNC2pi variations for $\cos(\theta_{\vec{p}_L, \vec{p}_R})$ in $\cos(\theta_{\vec{p}_\mu})$.

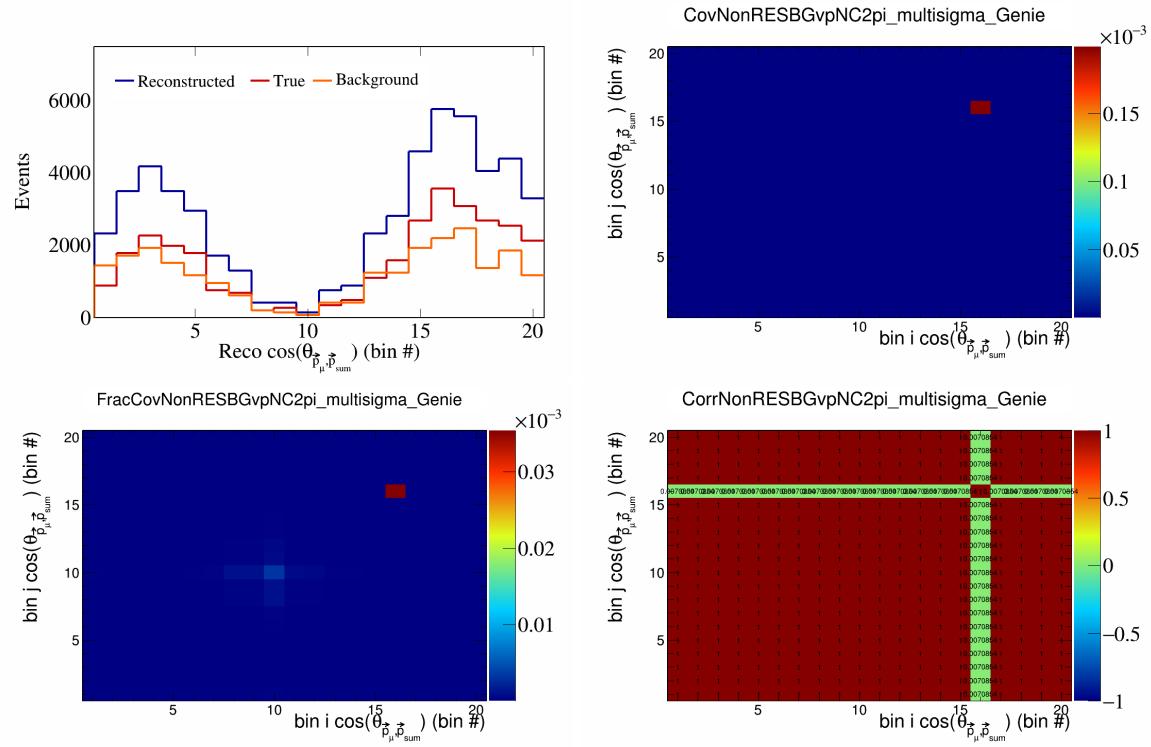


Figure 581: NonRESBGvpNC2pi variations for $\cos(\theta_{\vec{p}_\mu, \vec{p}_{\text{sum}}})$ in $\cos(\theta_{\vec{p}_\mu})$.

217 5.2 Flux systematics

218 In this appendix, the variations, covariance matrices, fractional covariance matrices, and correlation matrices
 219 are plotted for all of the flux systematics and variables.

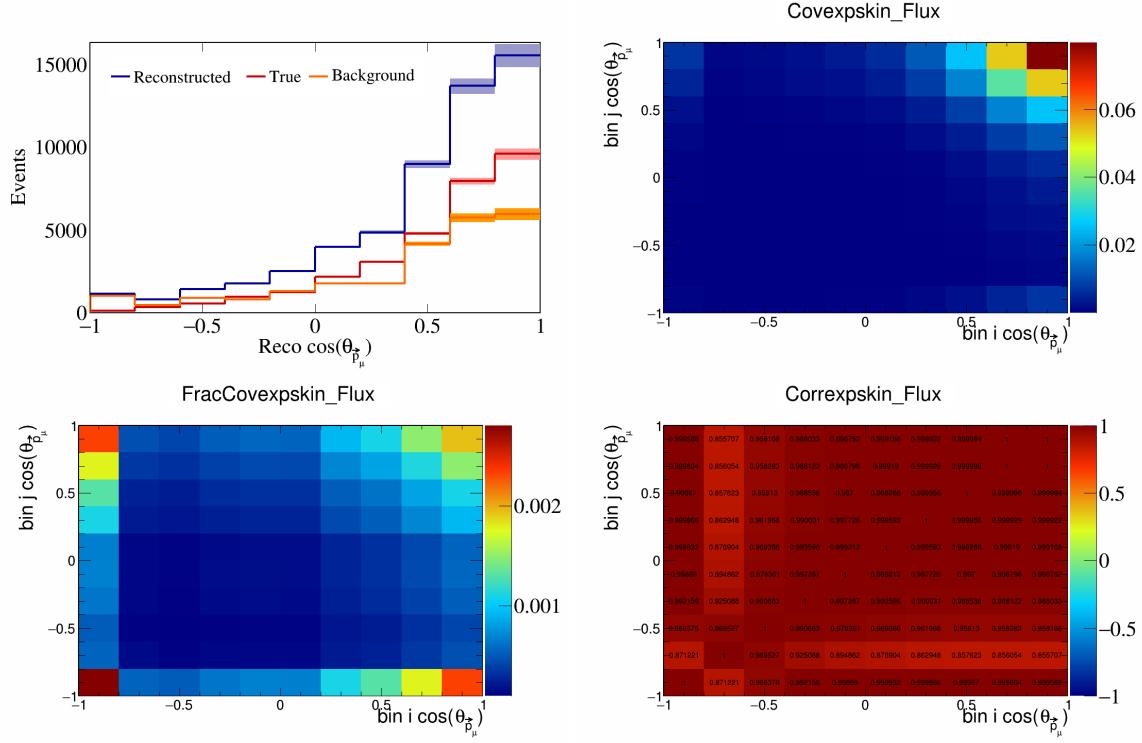


Figure 582: Epskin variations for $\cos(\theta_{\vec{p}_\mu})$.

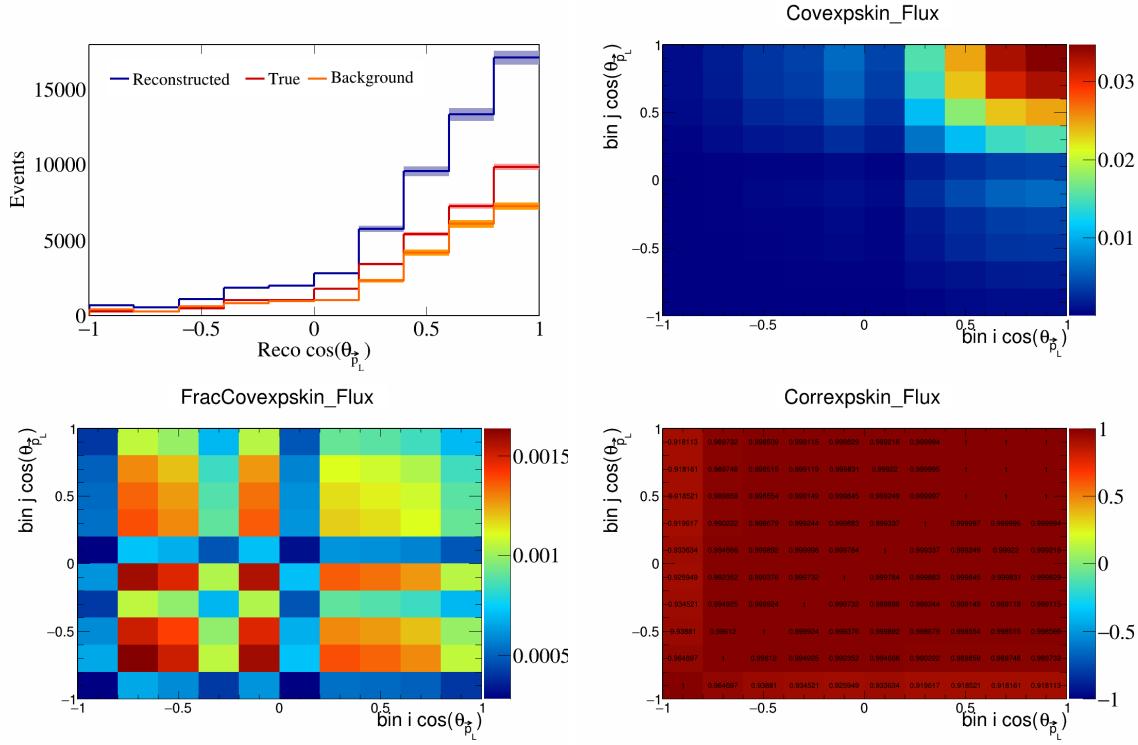


Figure 583: Expskin variations for $\cos(\theta_{\vec{p}_L})$.

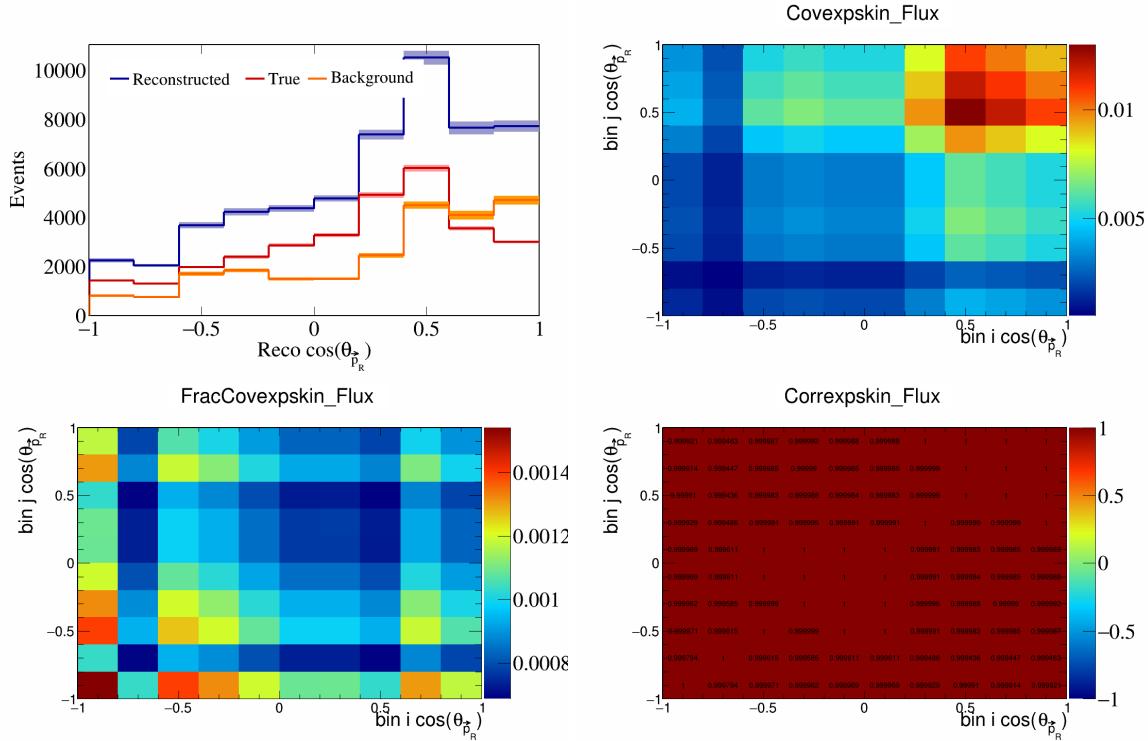


Figure 584: Expskin variations for $\cos(\theta_{\vec{p}_R})$.

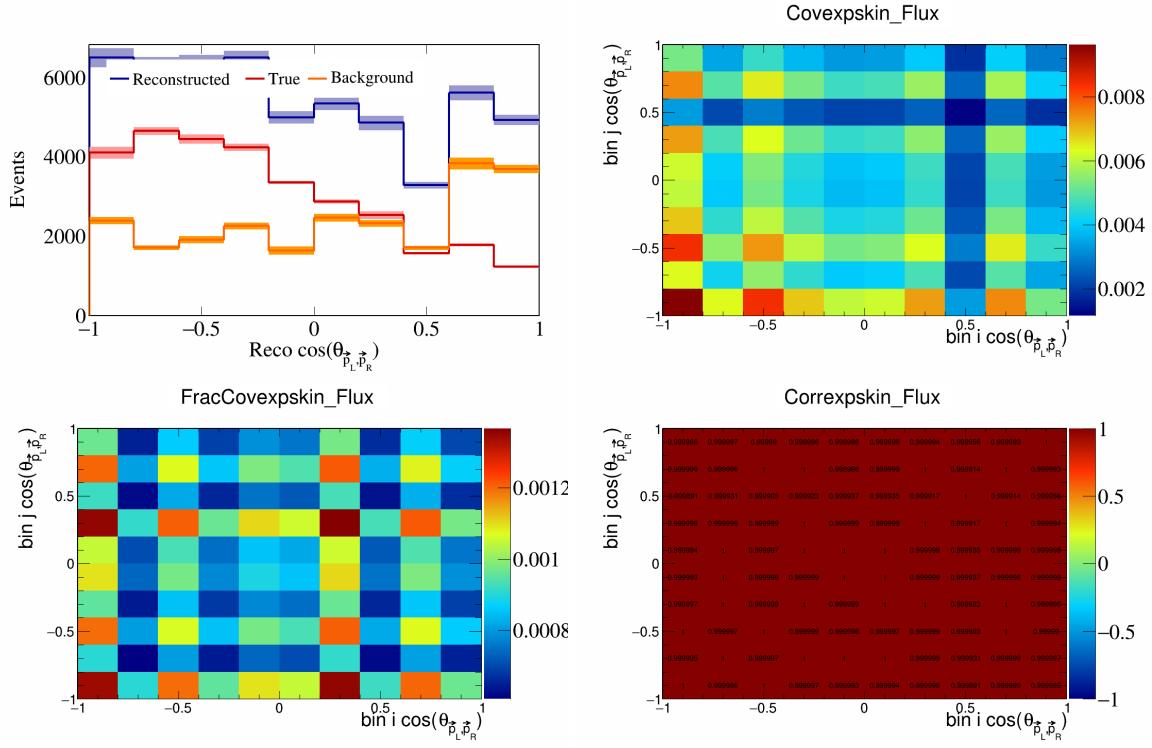


Figure 585: ExpSkin variations for $\cos(\theta_{\vec{p}_L, \vec{p}_R})$.

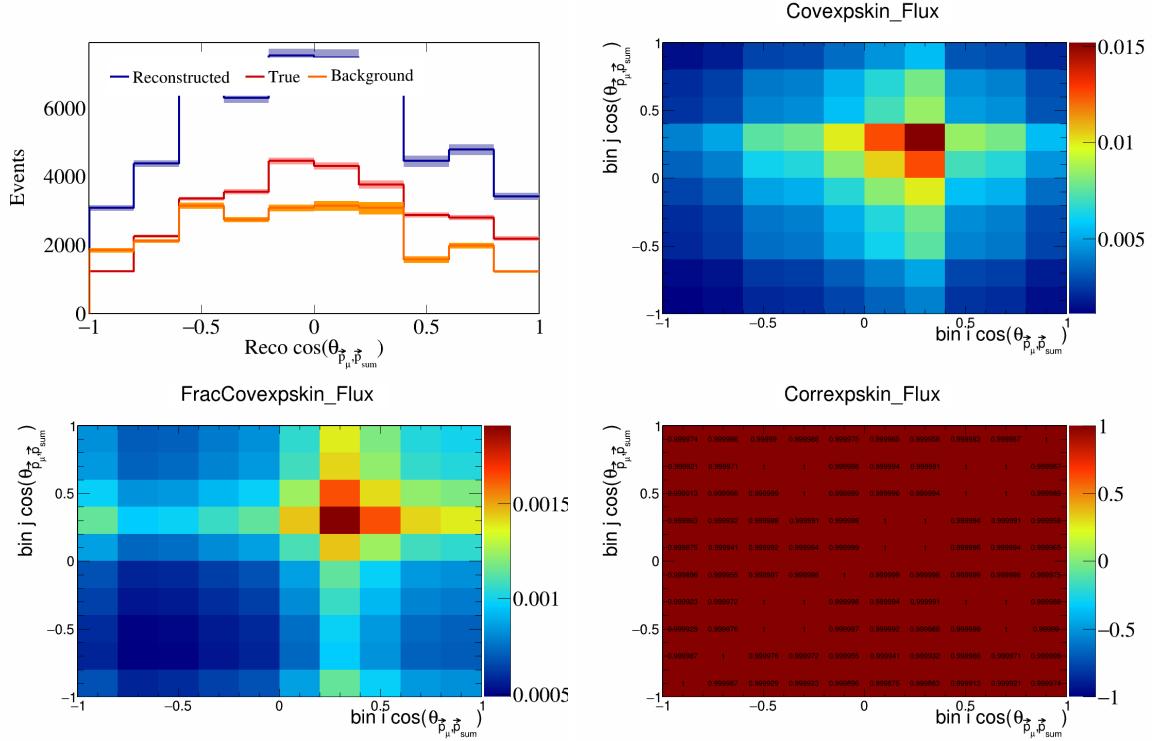


Figure 586: ExpSkin variations for $\cos(\theta_{\vec{p}_\mu, \vec{p}_{\text{sum}}})$.

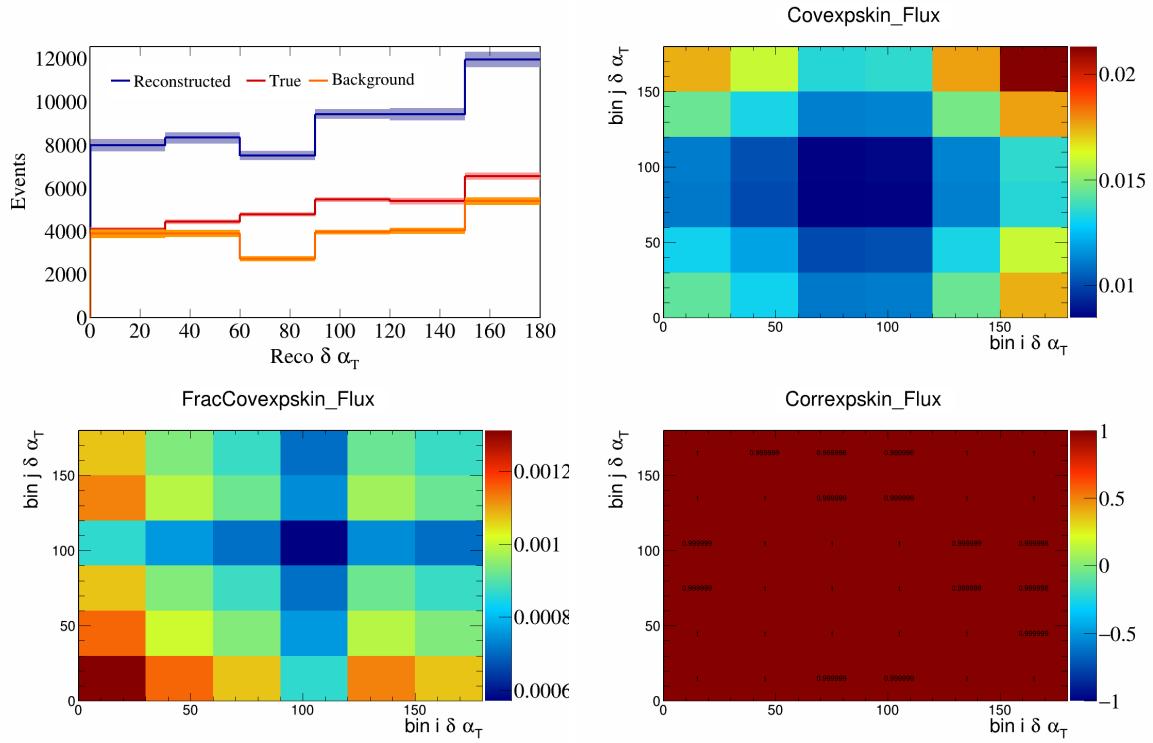


Figure 587: Expskin variations for $\delta \alpha_T$.

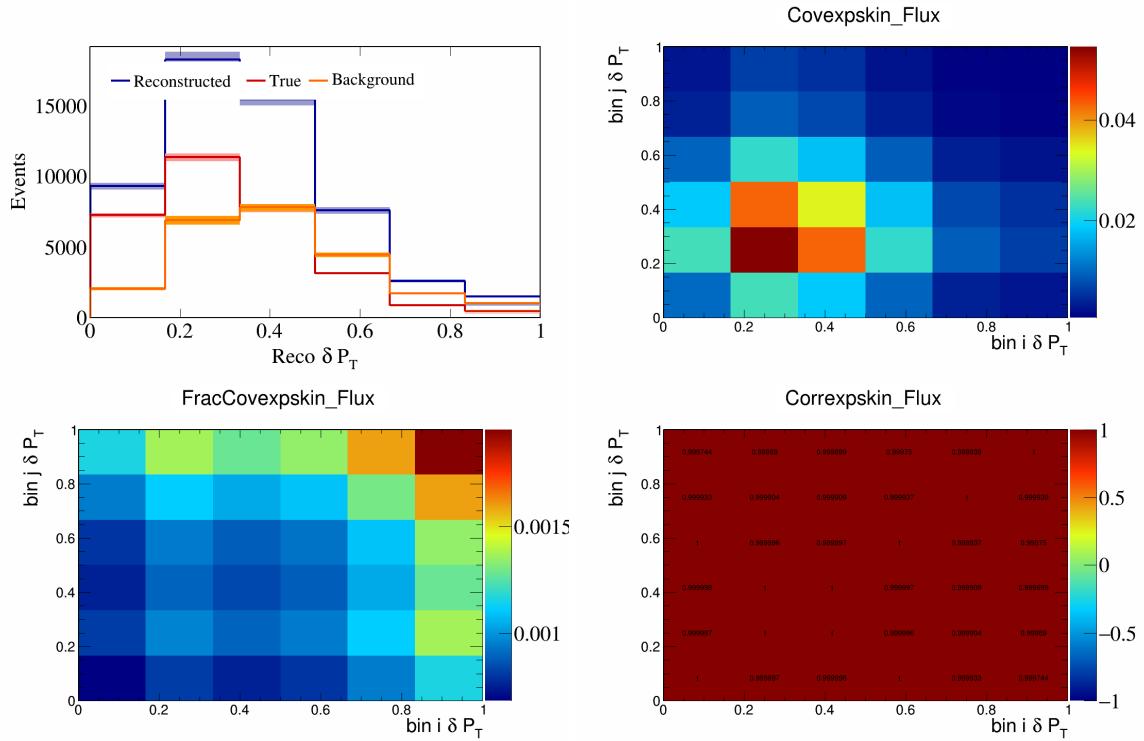


Figure 588: Expskin variations for δP_T .

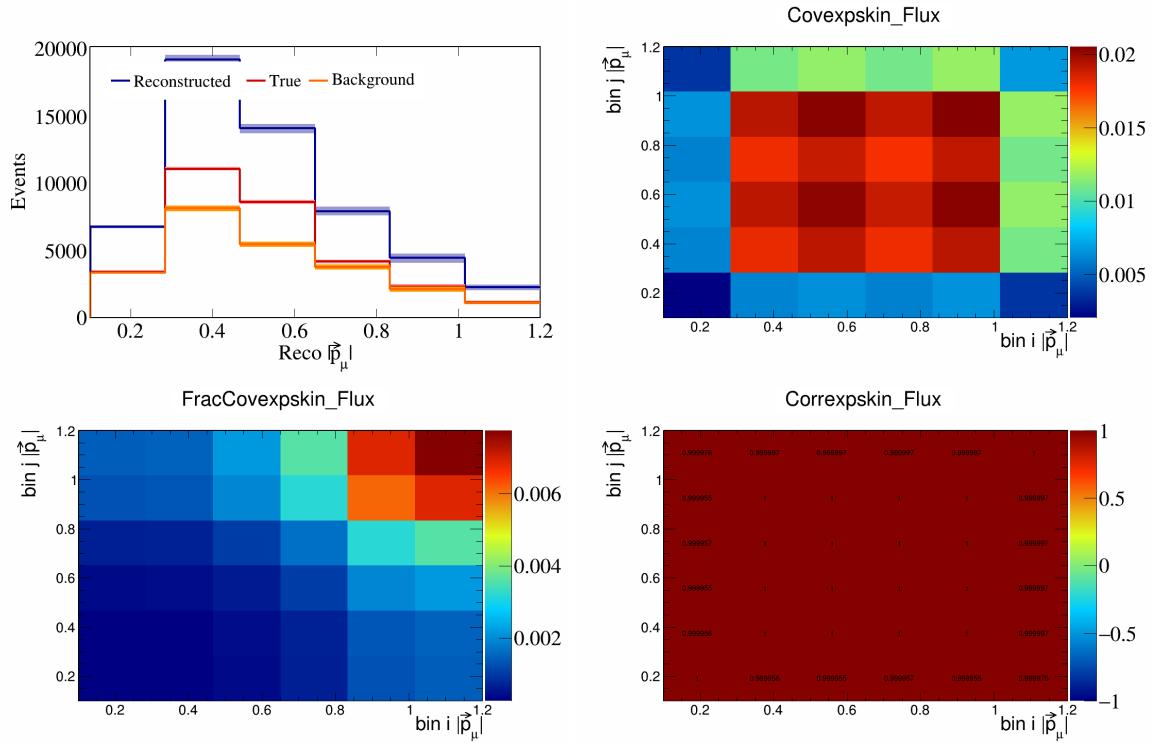


Figure 589: Expskin variations for $|\vec{p}_\mu|$.

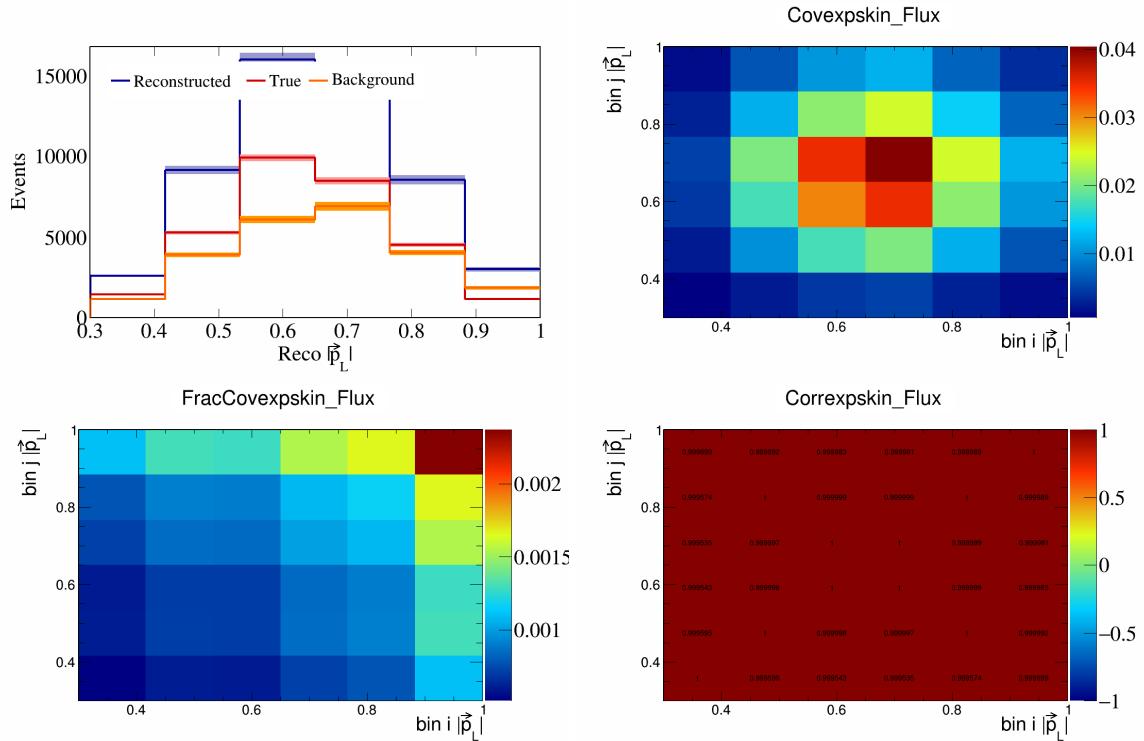


Figure 590: Expskin variations for $|\vec{p}_L|$.

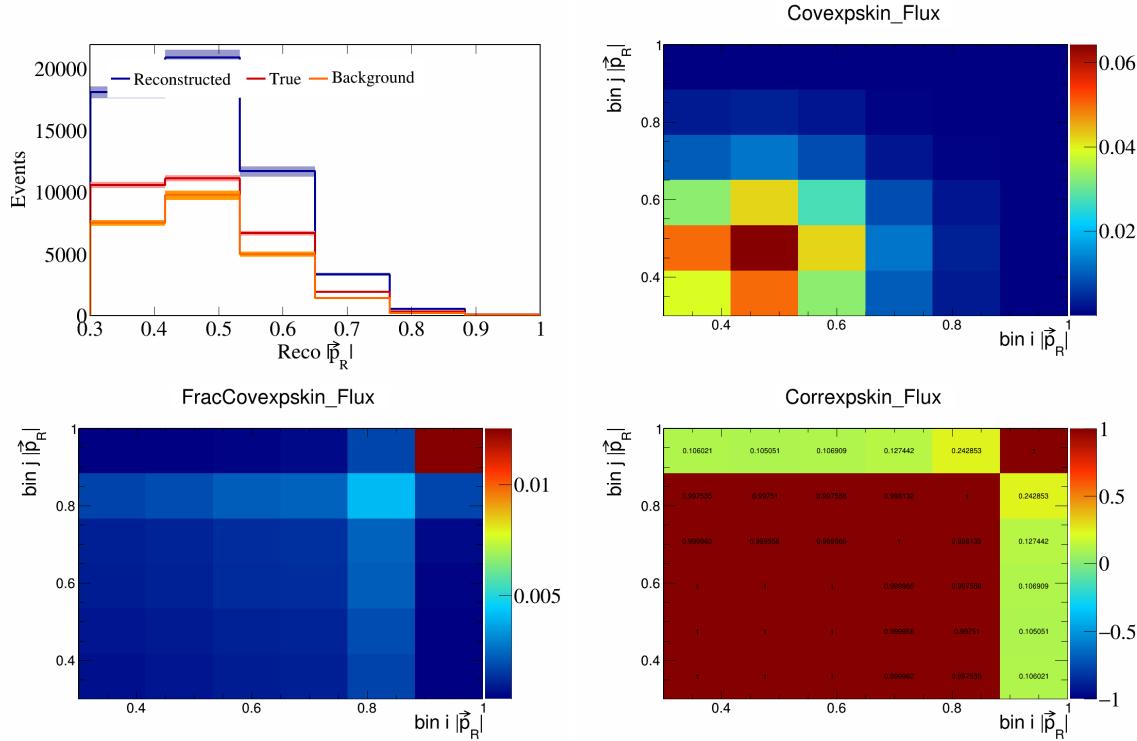


Figure 591: Expskin variations for $|\vec{p}_R|$.

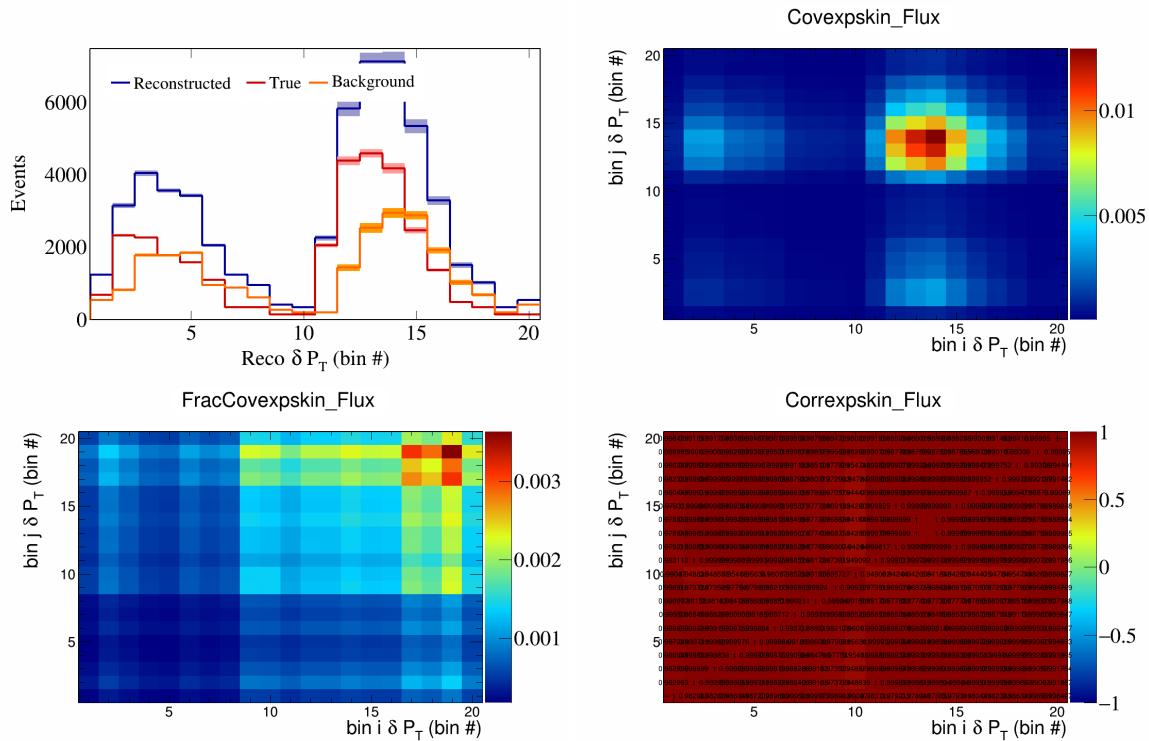


Figure 592: Expskin variations for δP_T in $\cos(\theta_{\vec{p}_\mu})$.

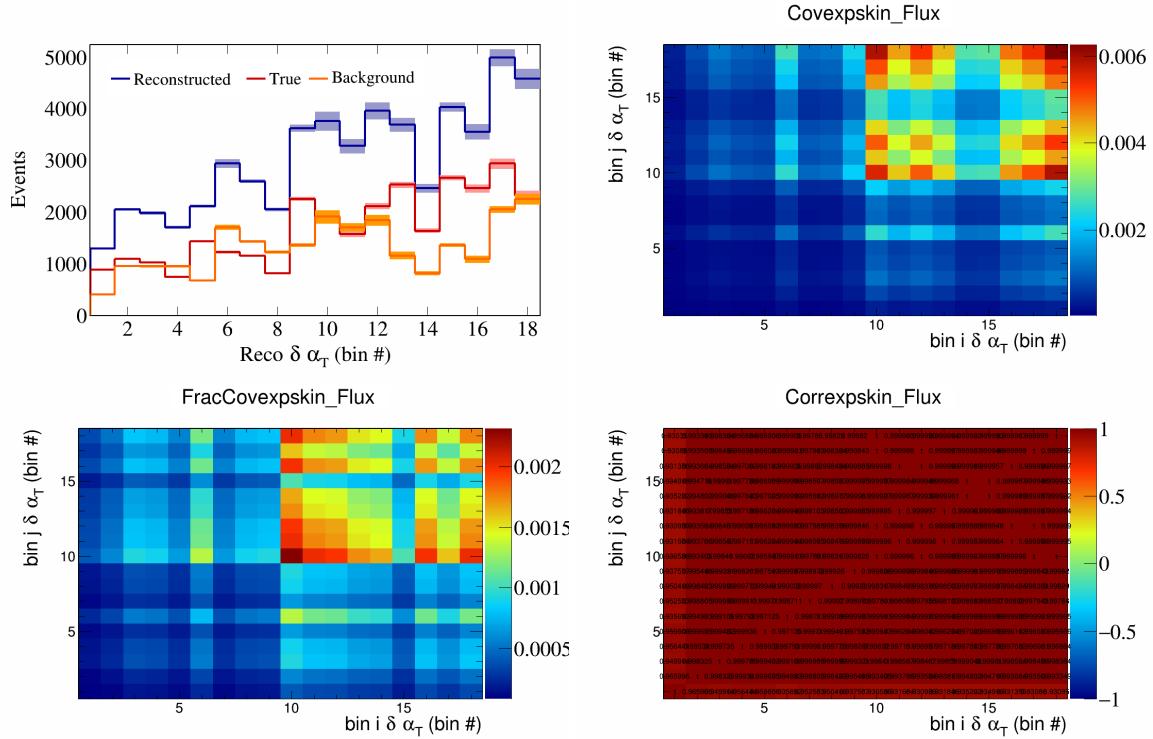


Figure 593: Expskin variations for $\delta\alpha_T$ in $\cos(\theta_{\vec{p}_\mu})$.

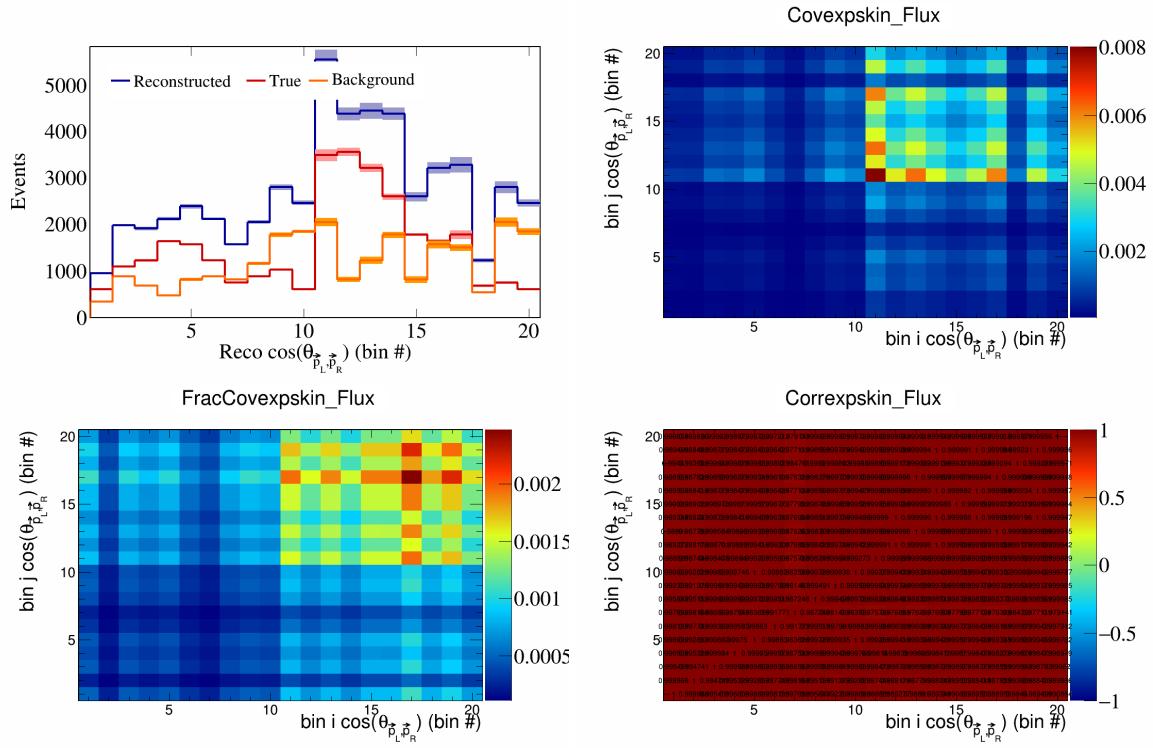


Figure 594: Expskin variations for $\cos(\theta_{\vec{p}_L, \vec{p}_R})$ in $\cos(\theta_{\vec{p}_\mu})$.

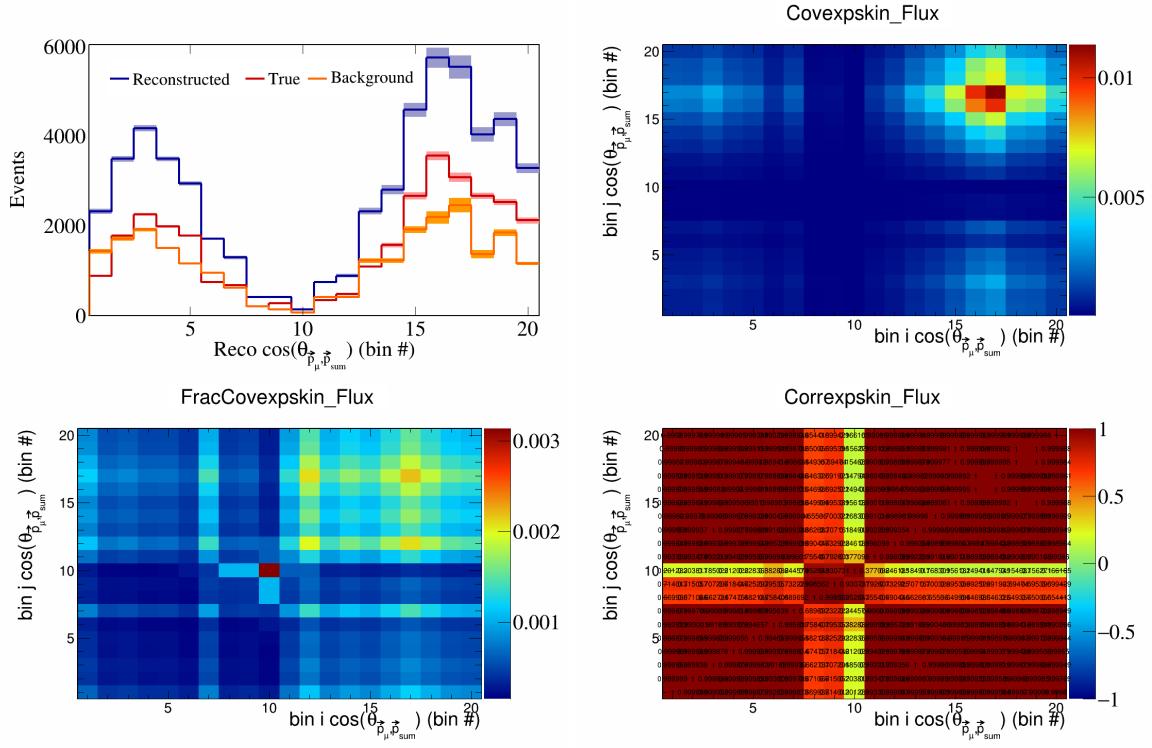


Figure 595: Expskin variations for $\cos(\theta_{\vec{p}_\mu})$ in $\cos(\theta_{\vec{p}_\mu})$.

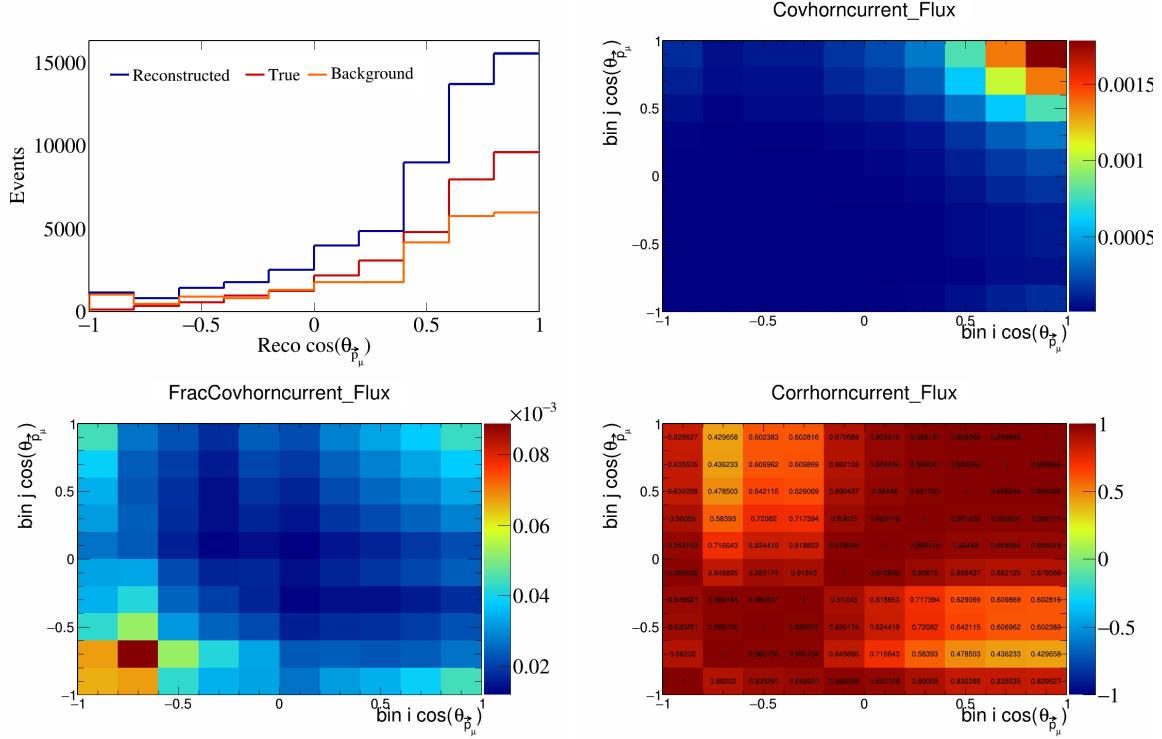


Figure 596: HornCurrent variations for $\cos(\theta_{\vec{p}_\mu})$.

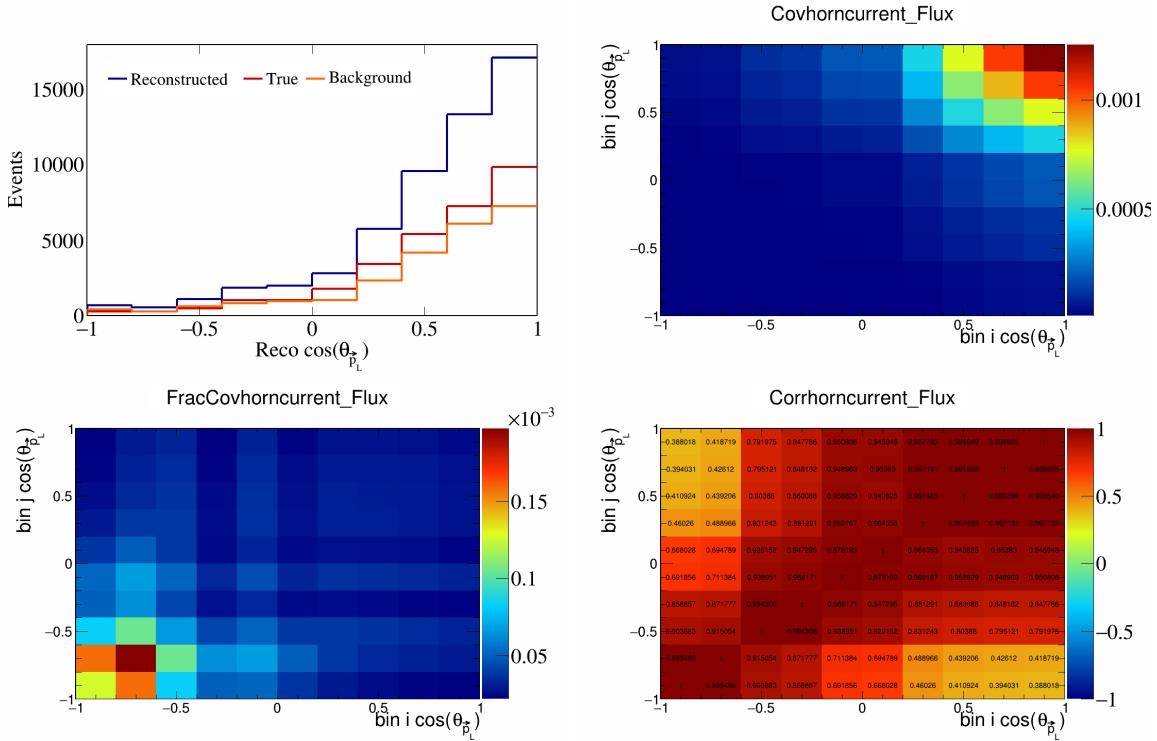


Figure 597: HornCurrent variations for $\cos(\theta_{\vec{p}_L})$.

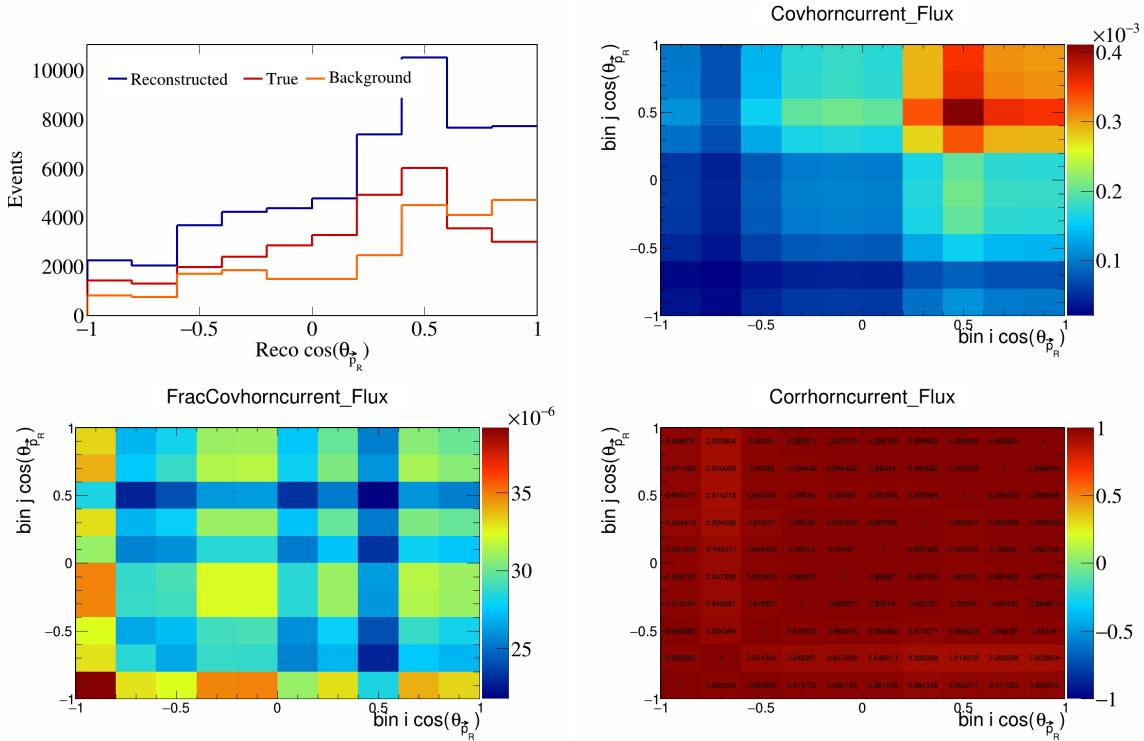


Figure 598: HornCurrent variations for $\cos(\theta_{\vec{p}_R})$.

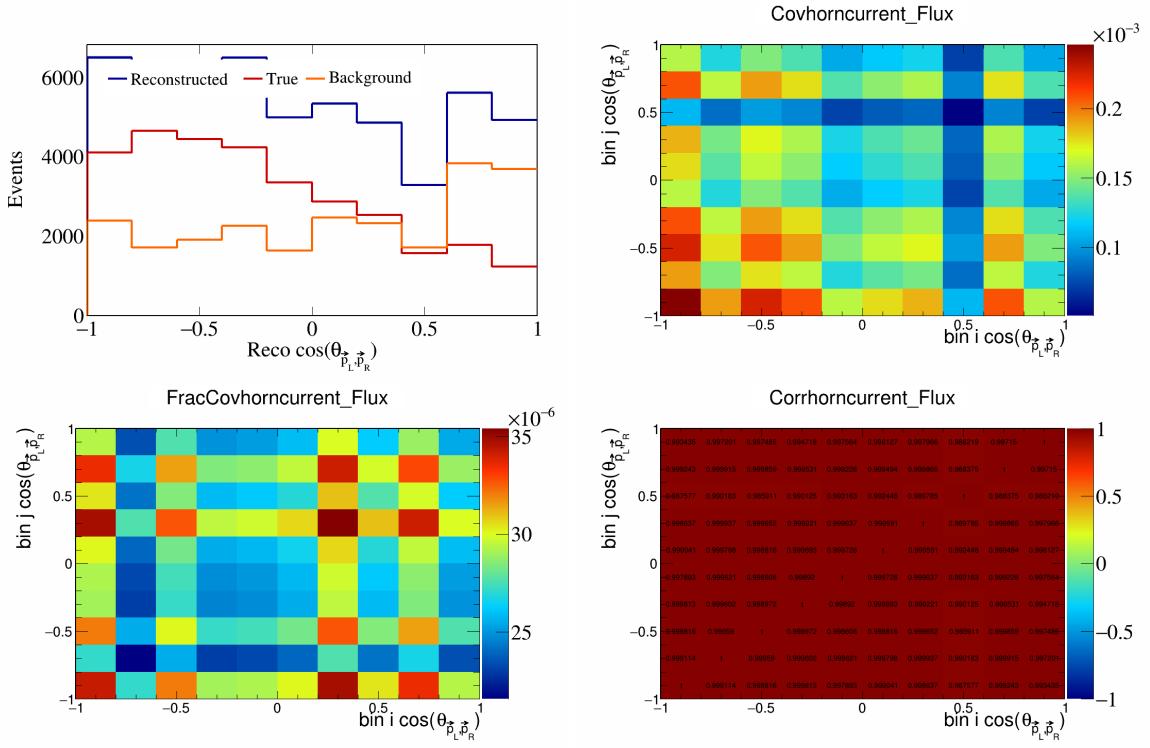


Figure 599: HornCurrent variations for $\cos(\theta_{\vec{p}_L, \vec{p}_R})$.

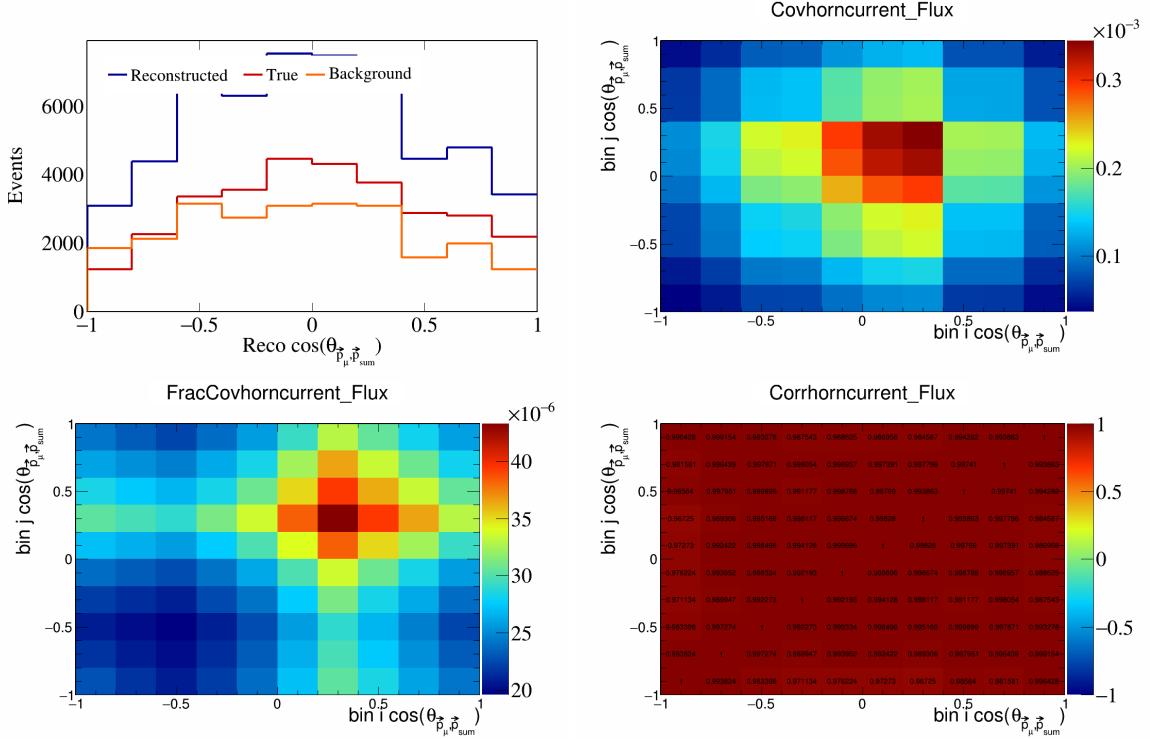


Figure 600: HornCurrent variations for $\cos(\theta_{\vec{p}_\mu, \vec{p}_{\text{sum}}})$.

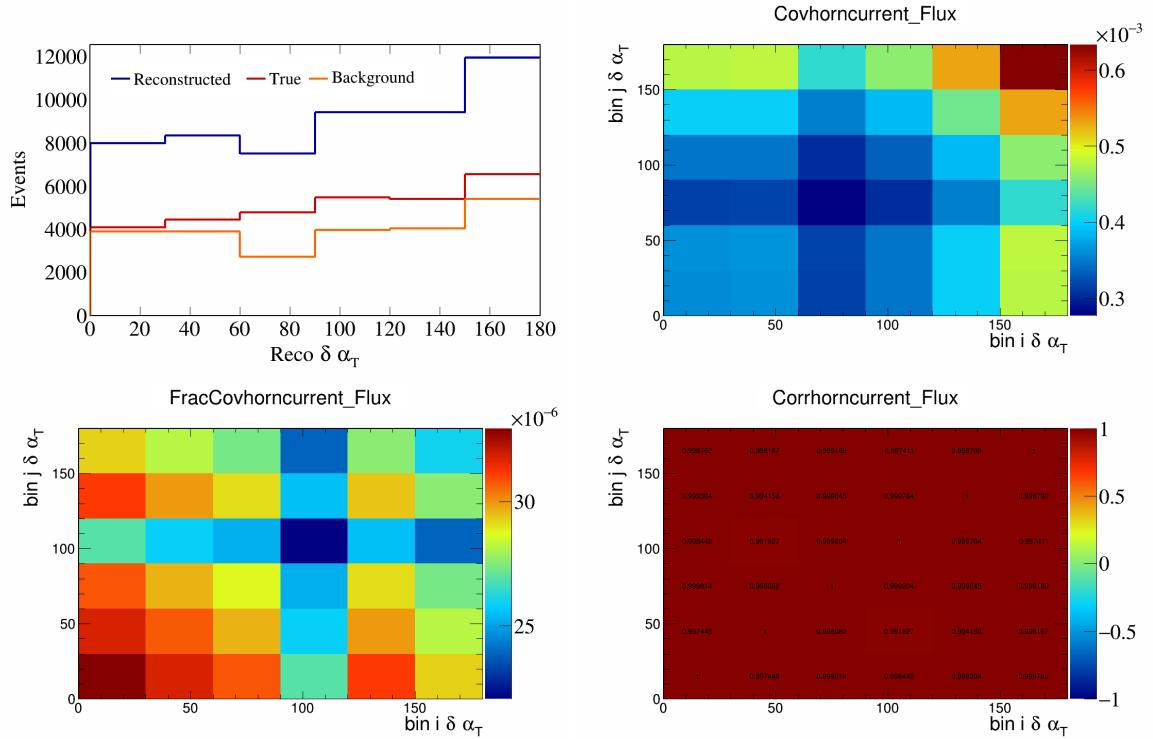


Figure 601: HornCurrent variations for $\delta\alpha_T$.

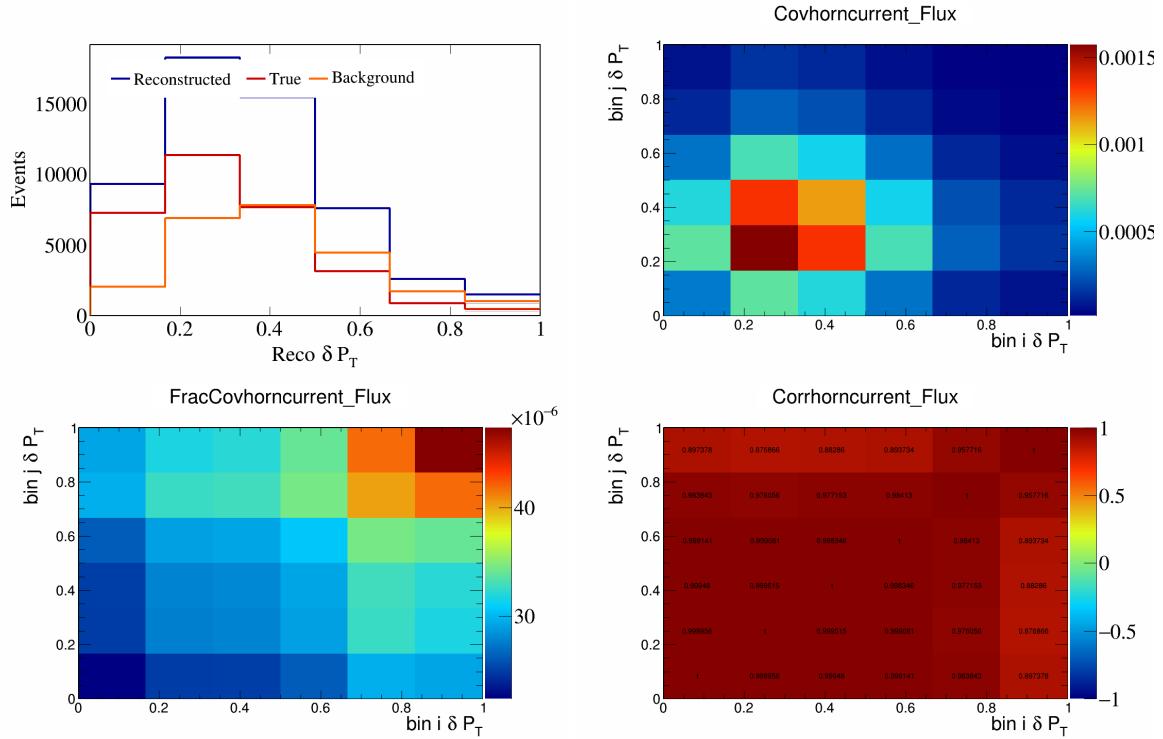


Figure 602: HornCurrent variations for δP_T .

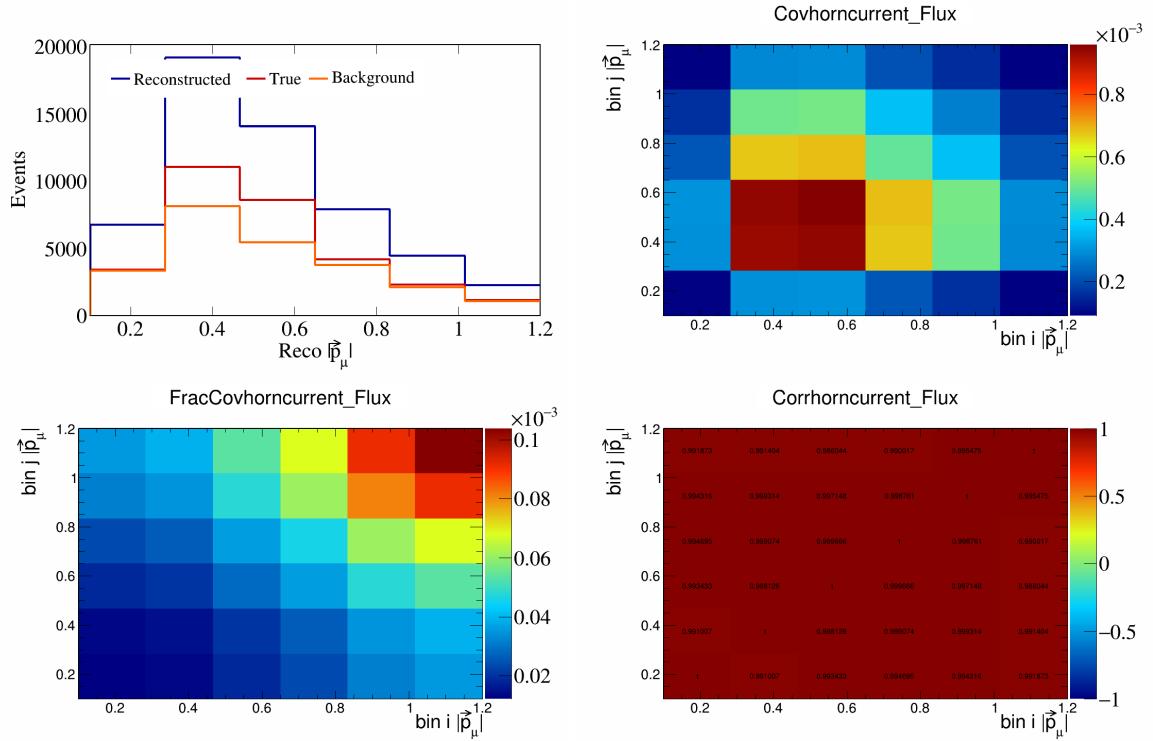


Figure 603: HornCurrent variations for $|\vec{p}_\mu|$.

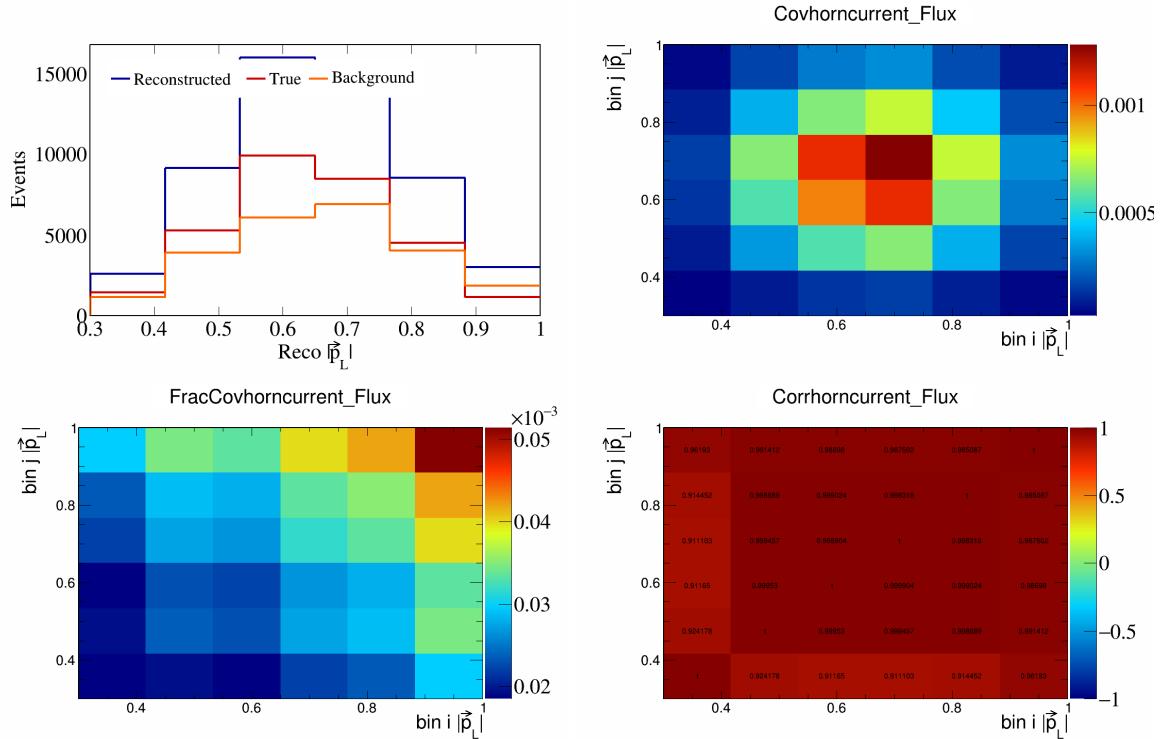


Figure 604: HornCurrent variations for $|\vec{p}_L|$.

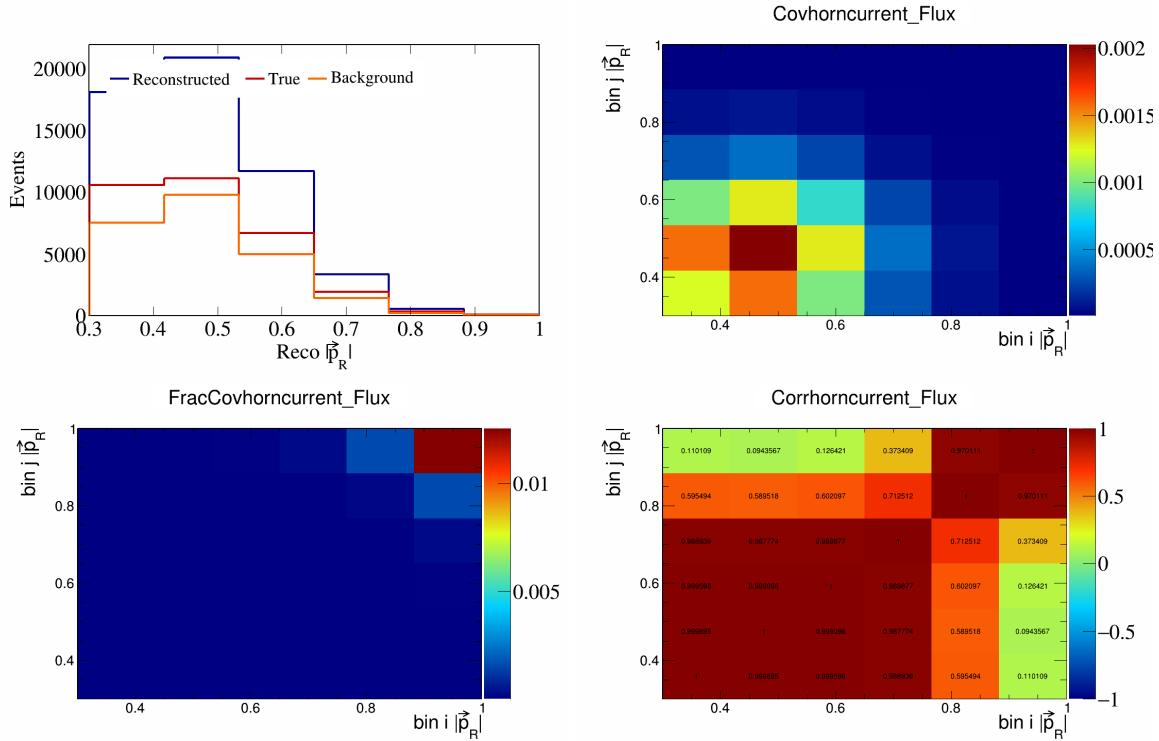


Figure 605: HornCurrent variations for $|\vec{p}_R|$.

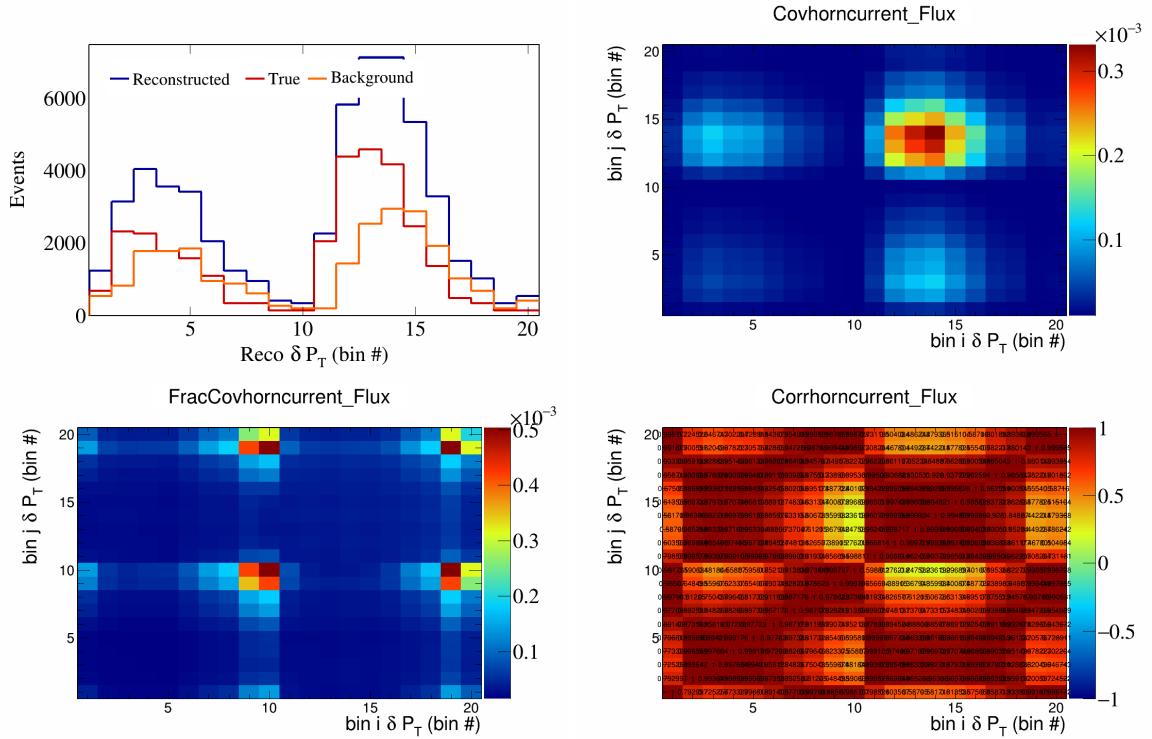


Figure 606: HornCurrent variations for δP_T in $\cos(\theta_{\vec{p}_\mu})$.

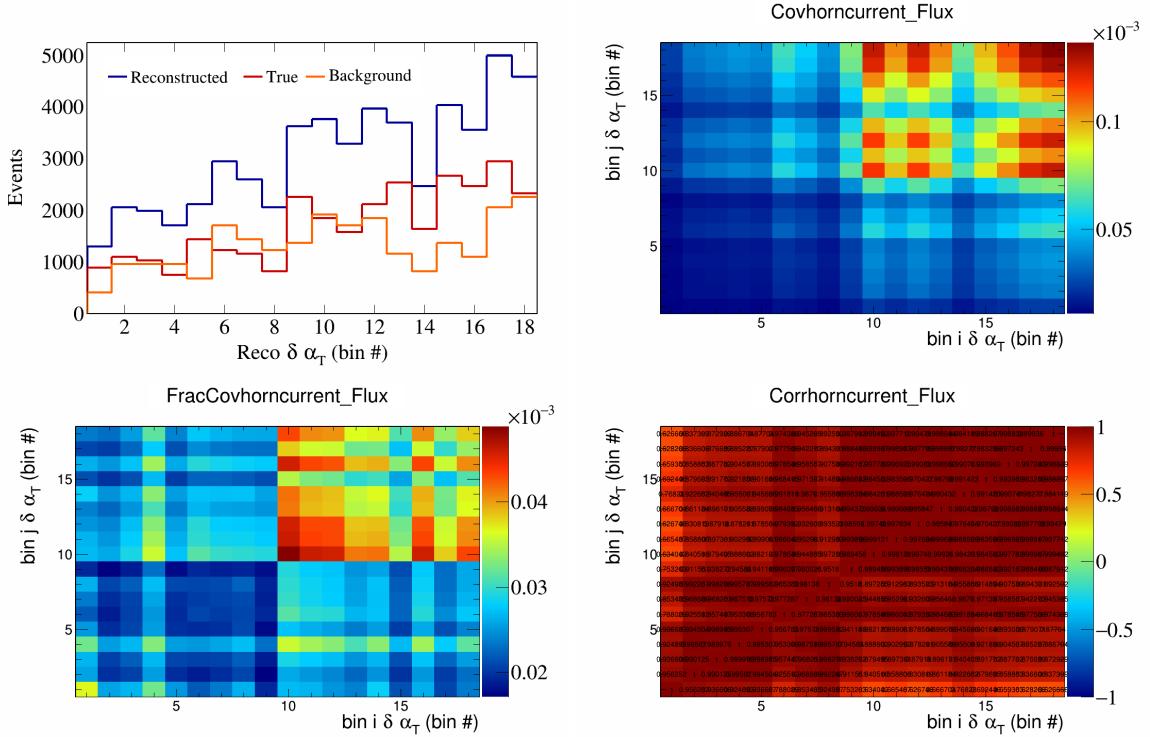


Figure 607: HornCurrent variations for $\delta\alpha_T$ in $\cos(\theta_{\vec{p}_\mu})$.

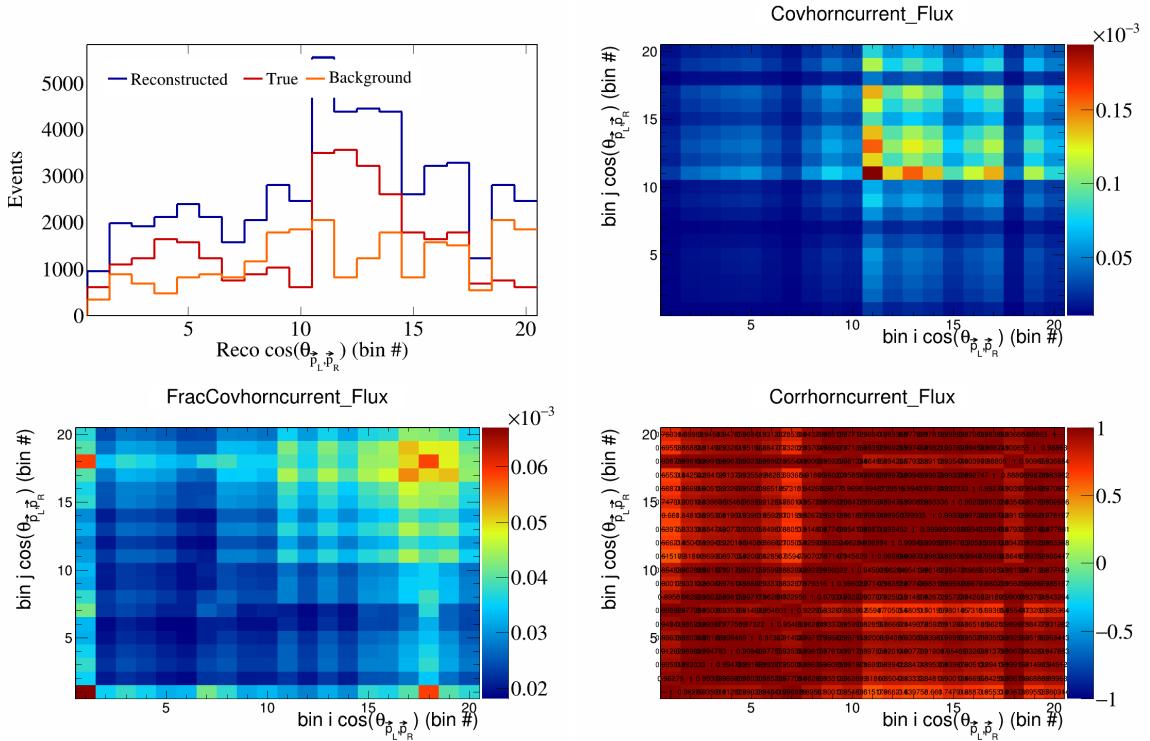


Figure 608: HornCurrent variations for $\cos(\theta_{\vec{p}_L, \vec{p}_R})$ in $\cos(\theta_{\vec{p}_\mu})$.

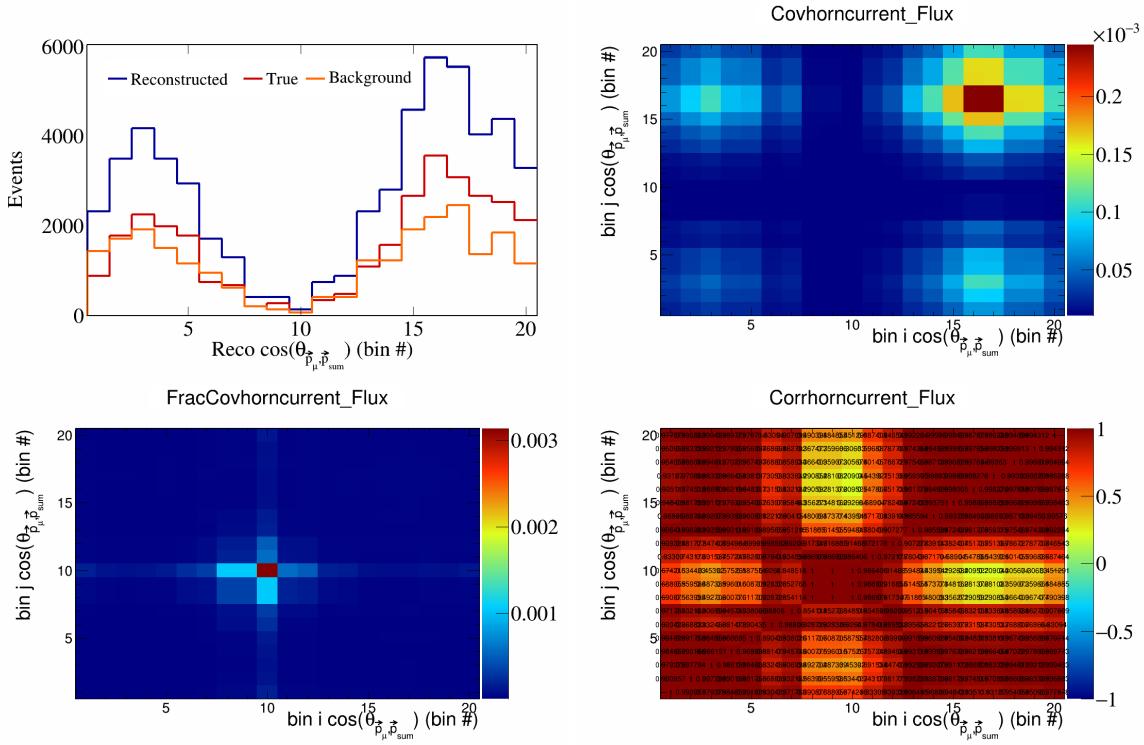


Figure 609: HornCurrent variations for $\cos(\theta_{\vec{p}_\mu \vec{p}_{\text{sum}}})$ in $\cos(\theta_{\vec{p}_\mu})$.

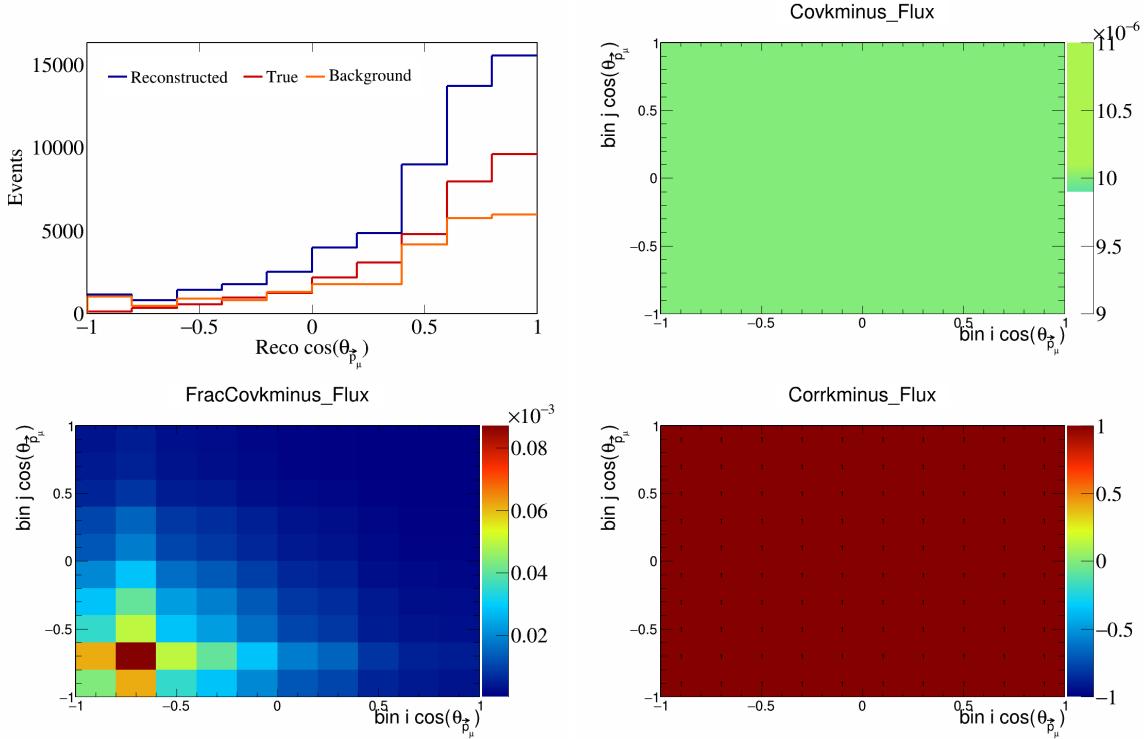


Figure 610: KMinus variations for $\cos(\theta_{\vec{p}_\mu})$.

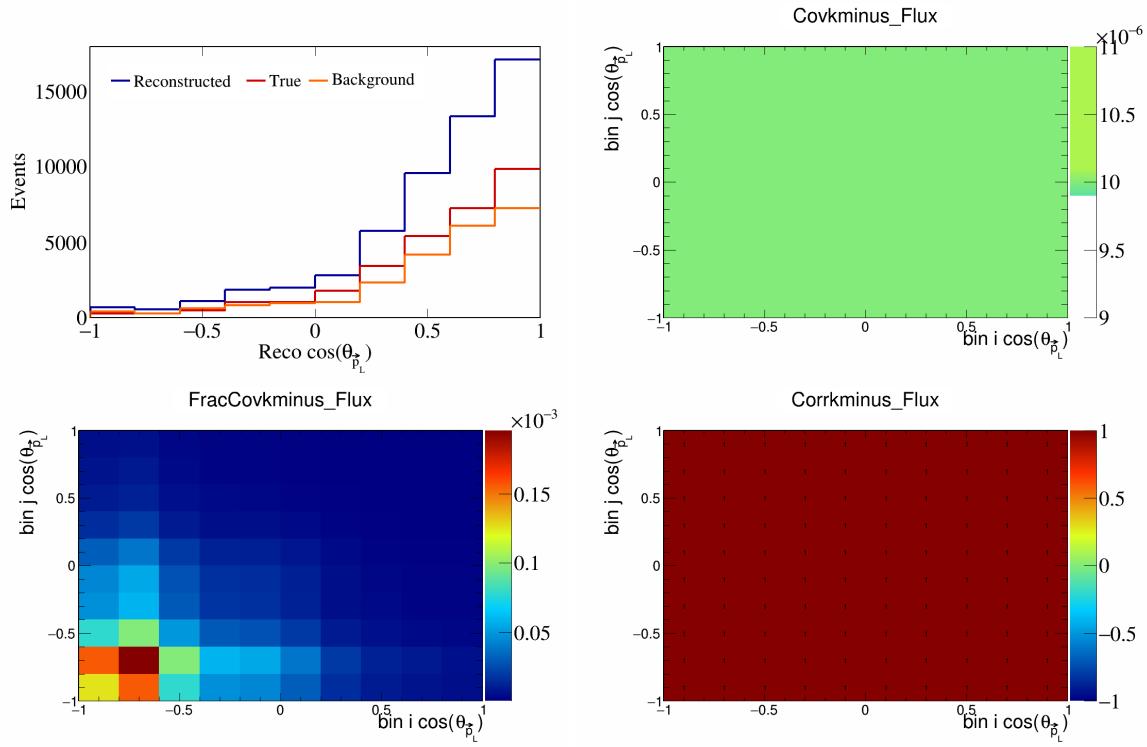


Figure 611: KMinus variations for $\cos(\theta_{\vec{p}_L})$.

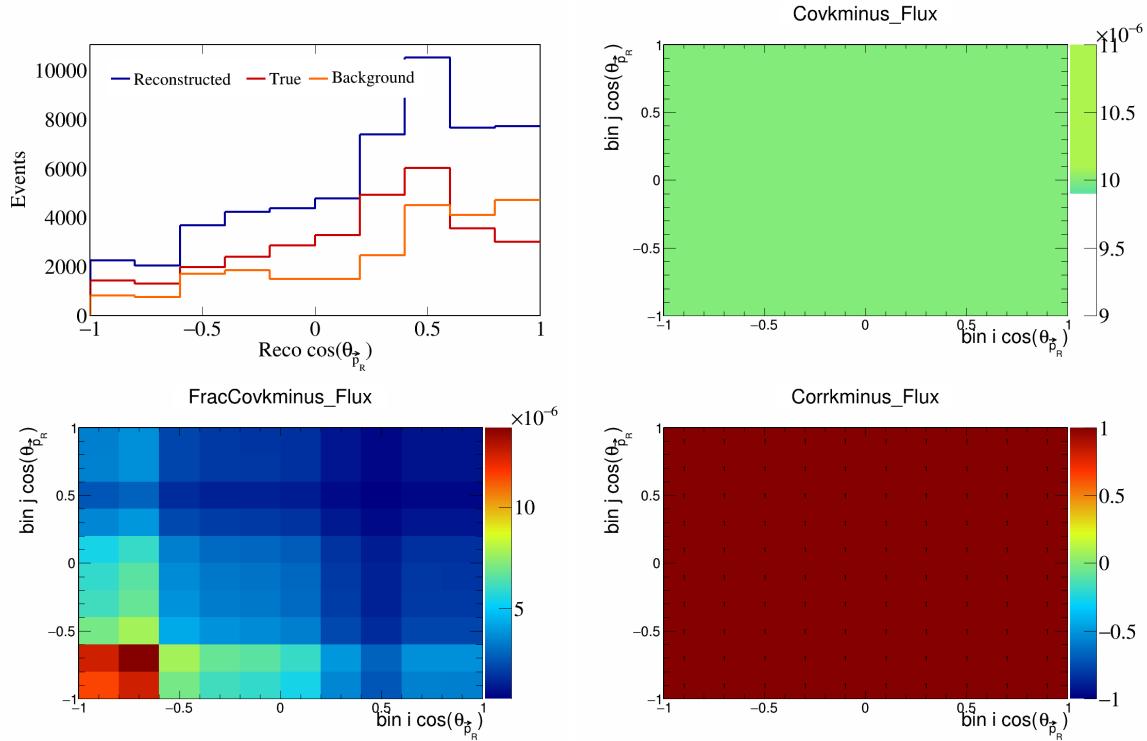


Figure 612: KMinus variations for $\cos(\theta_{\vec{p}_R})$.

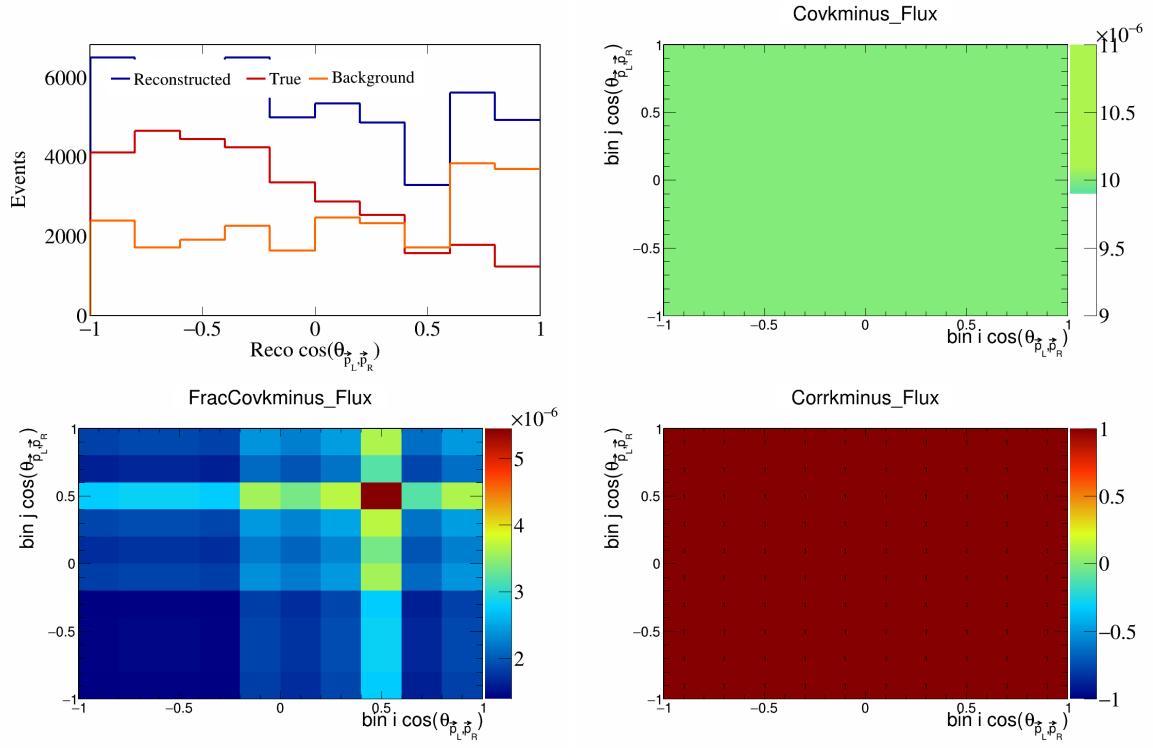


Figure 613: KMinus variations for $\cos(\theta_{\vec{p}_L, \vec{p}_R})$.

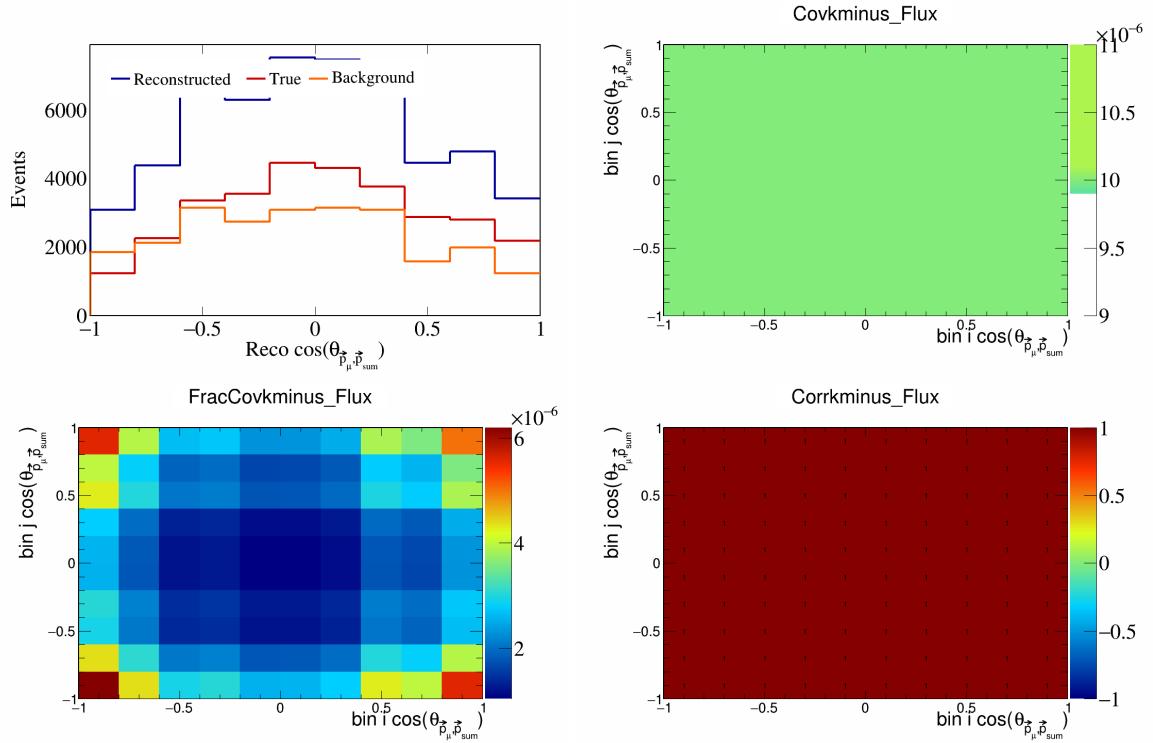


Figure 614: KMinus variations for $\cos(\theta_{\vec{p}_\mu, \vec{p}_{\text{sum}}})$.

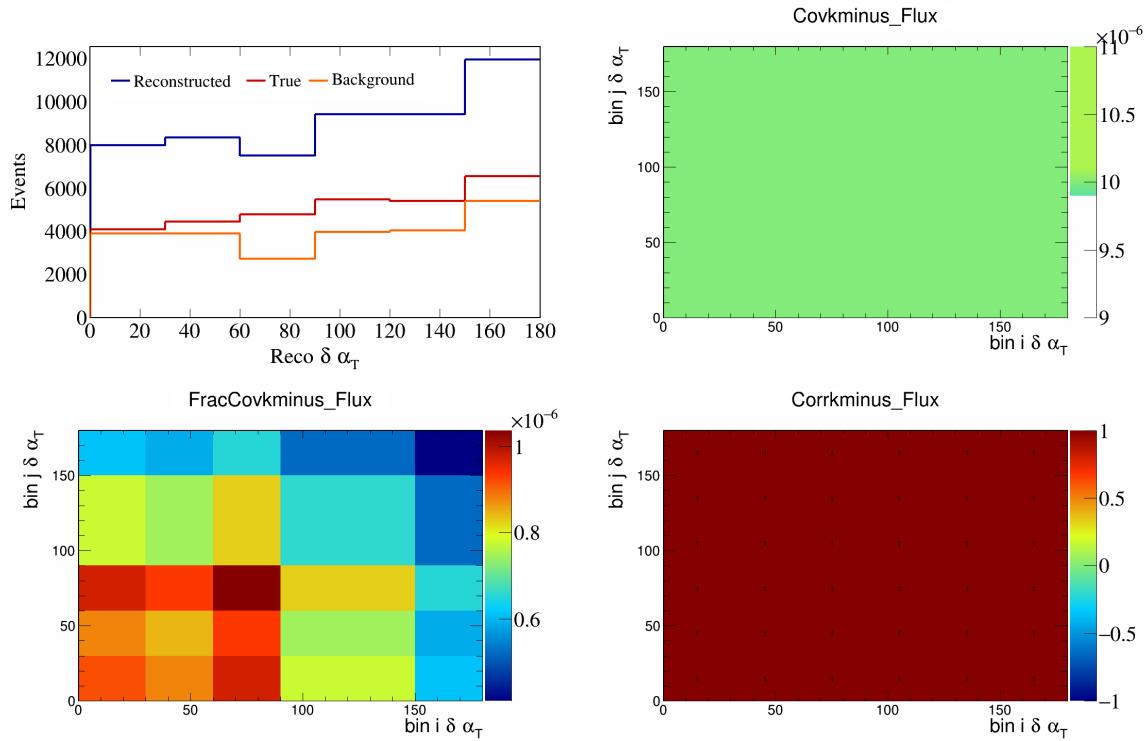


Figure 615: KMinus variations for $\delta\alpha_T$.

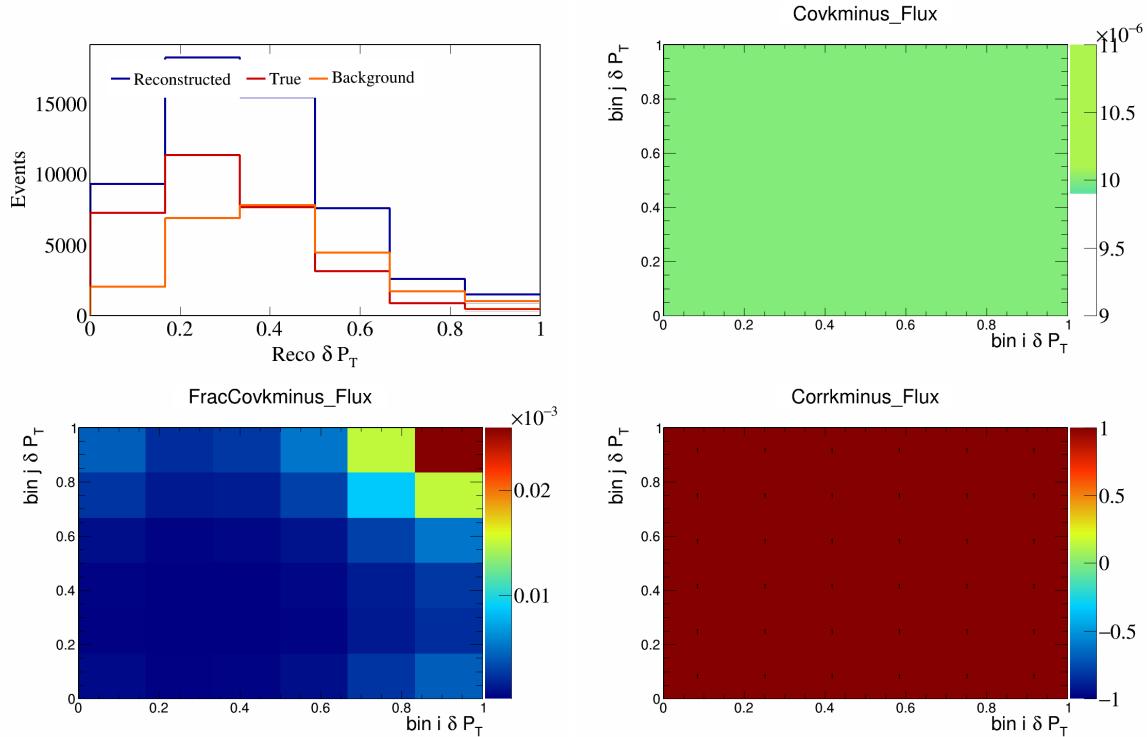


Figure 616: KMinus variations for δP_T .

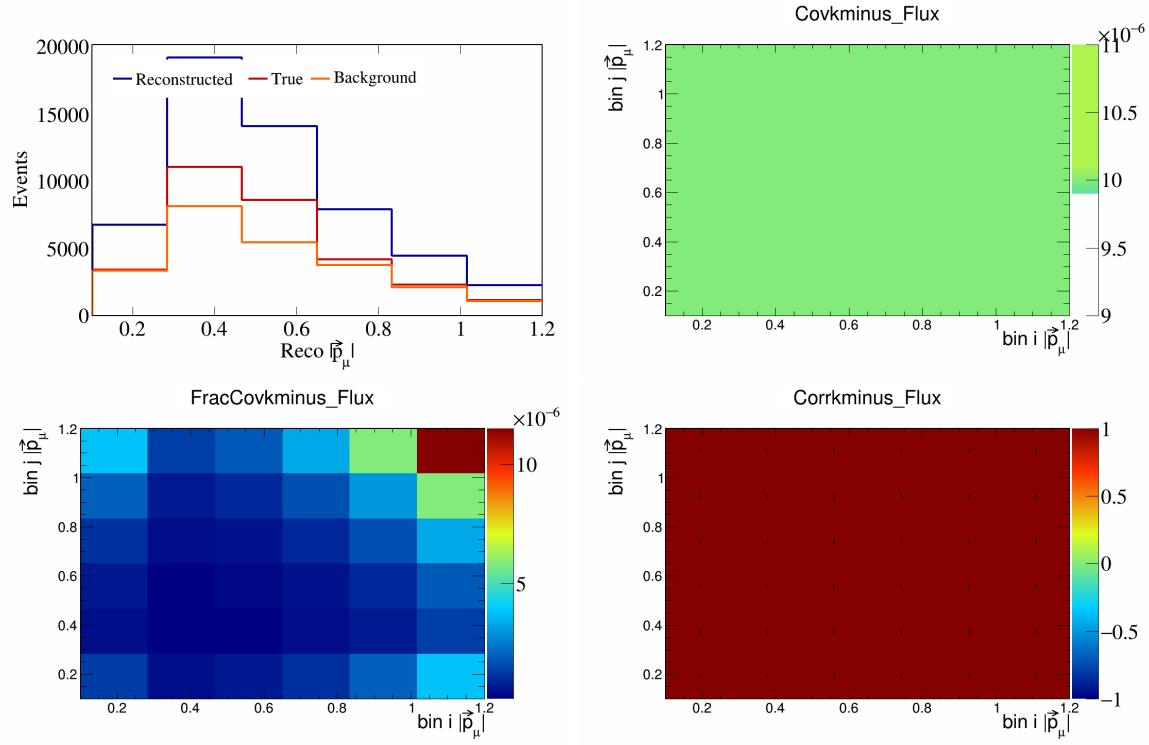


Figure 617: KMinus variations for $|\vec{p}_\mu|$.

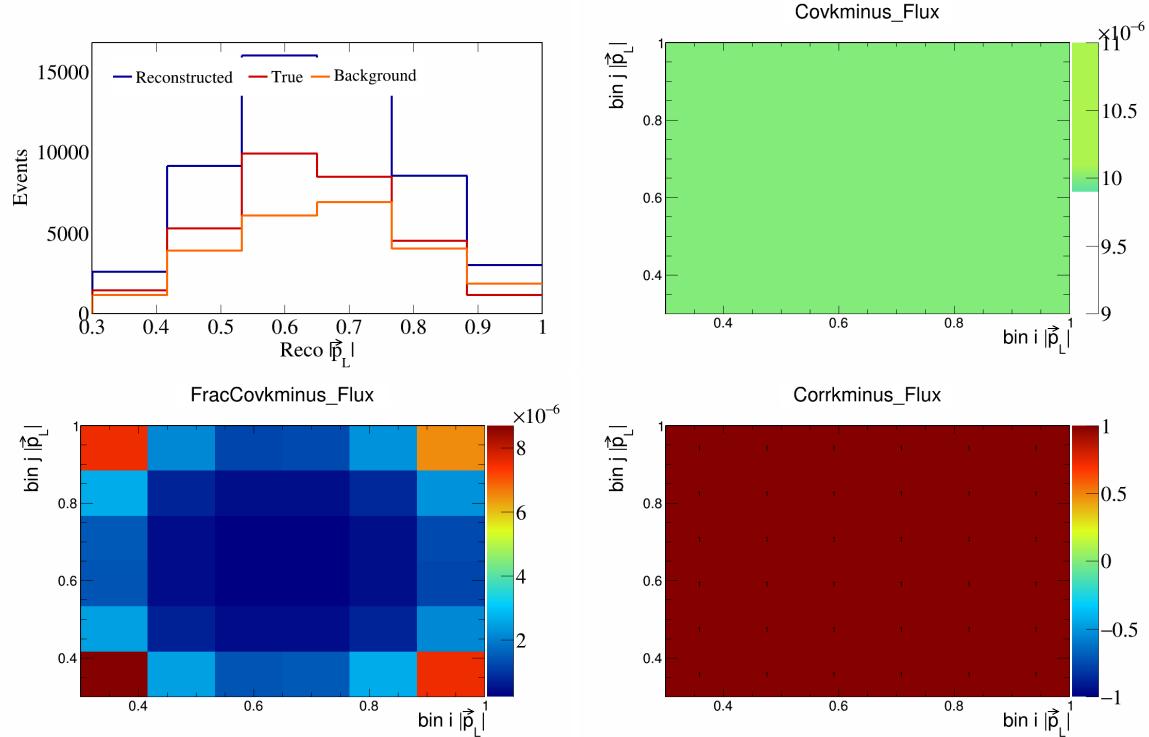


Figure 618: KMinus variations for $|\vec{p}_L|$.

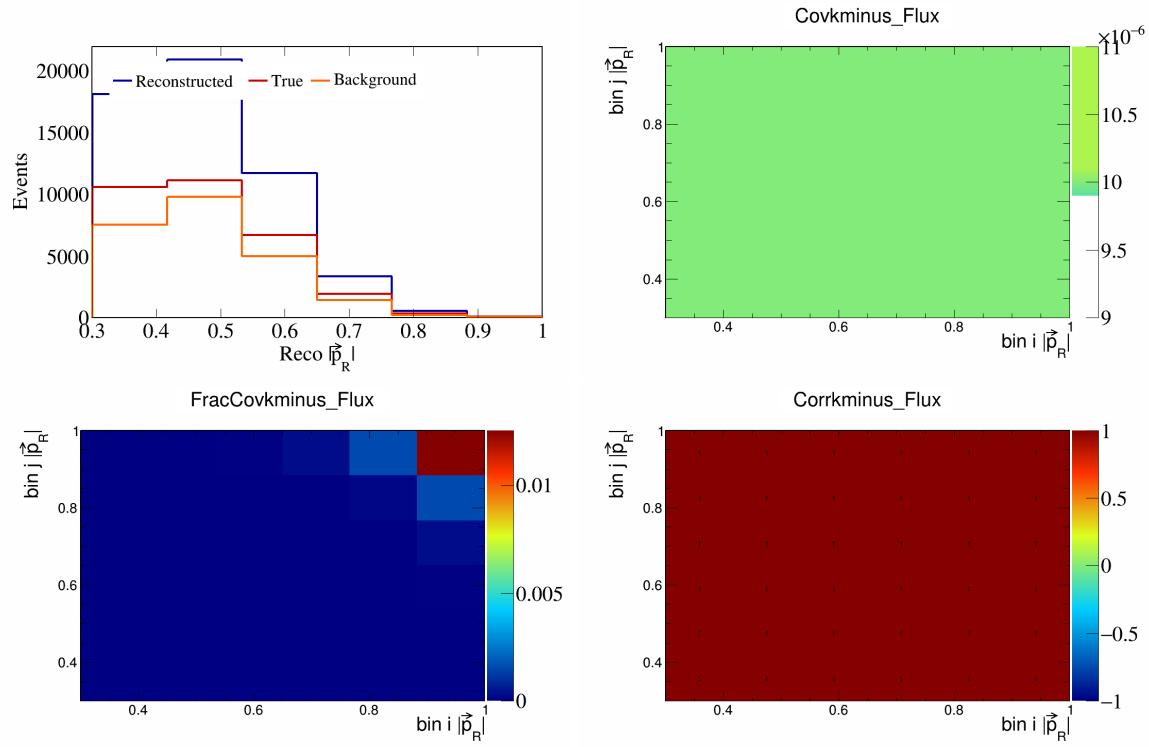


Figure 619: KMinus variations for $|\vec{p}_R|$.

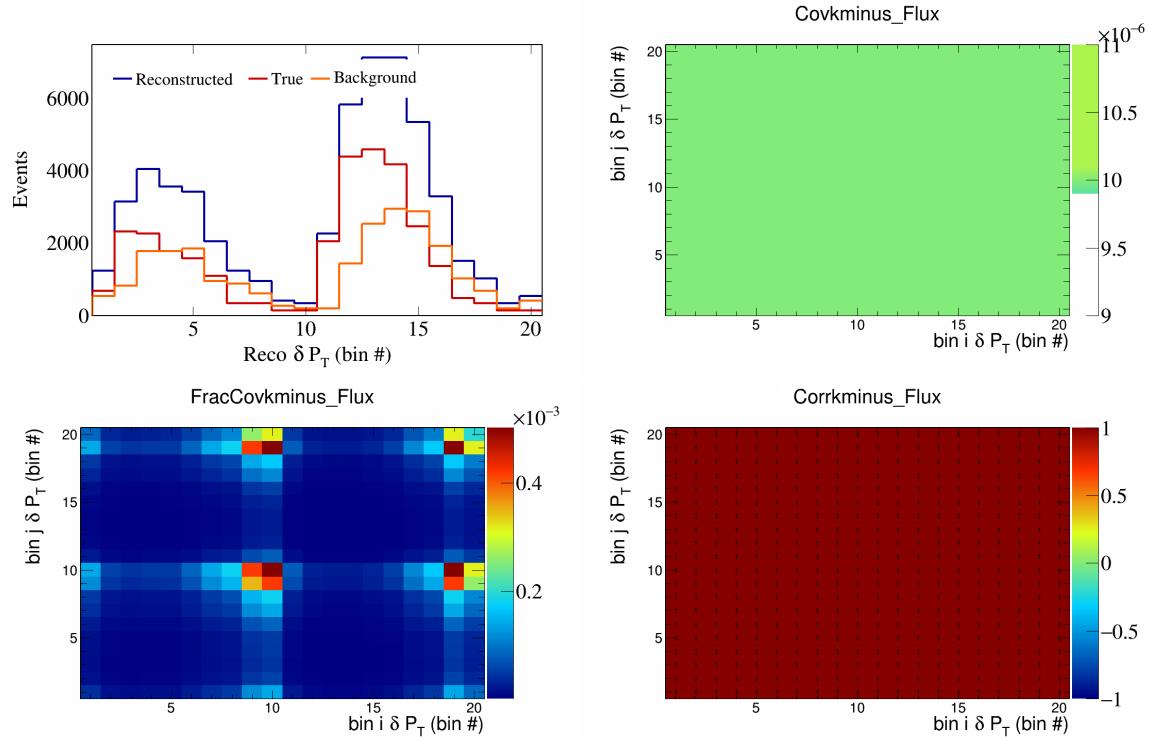


Figure 620: KMinus variations for δP_T in $\cos(\theta_{\vec{p}_\mu})$.

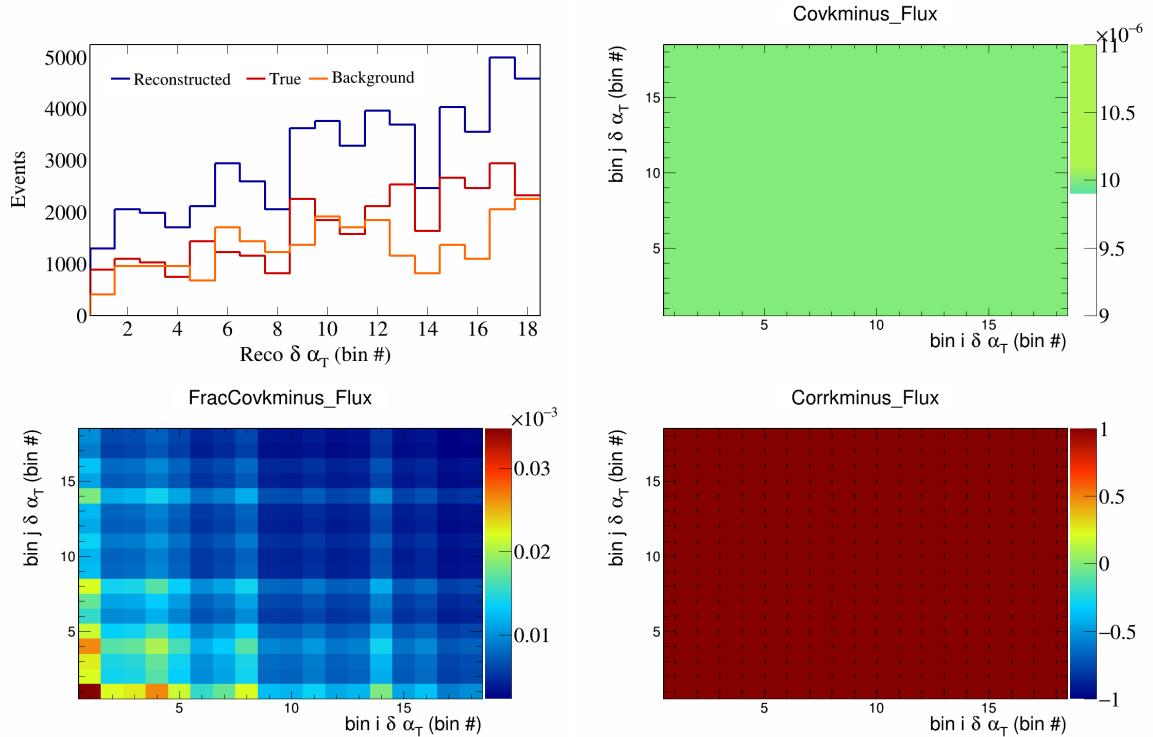


Figure 621: KMinus variations for $\delta\alpha_T$ in $\cos(\theta_{\vec{p}_\mu})$.

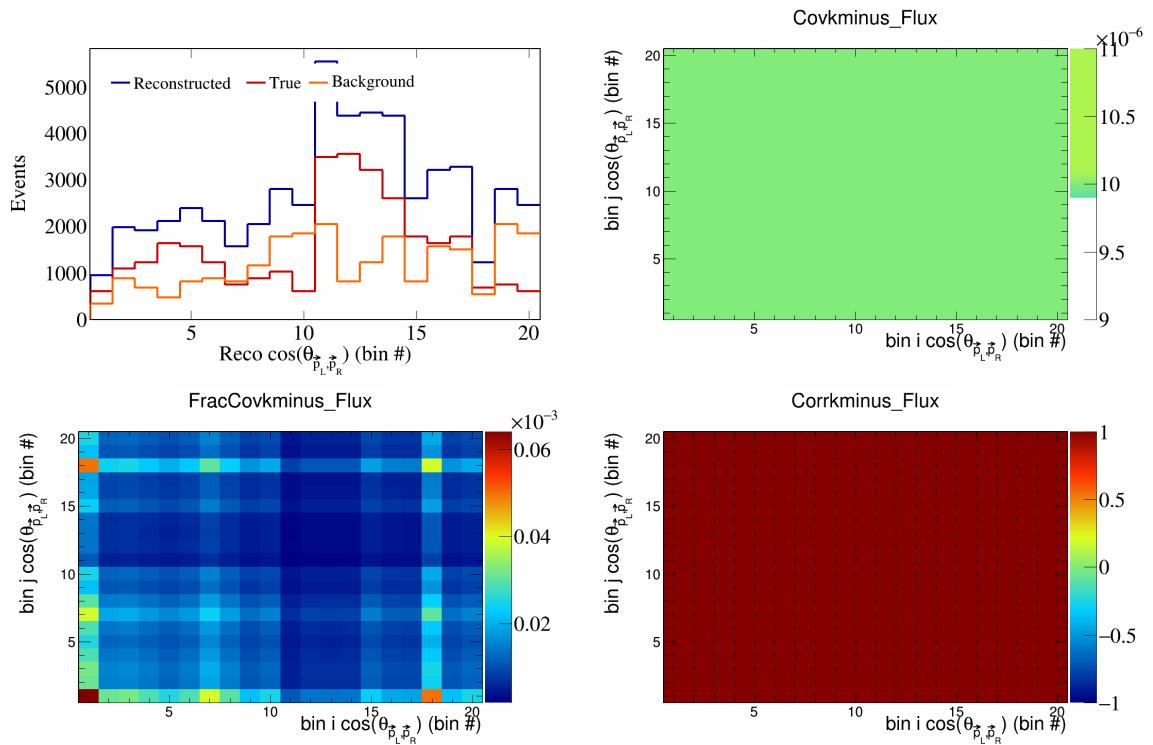


Figure 622: KMinus variations for $\cos(\theta_{\vec{p}_L, \vec{p}_R})$ in $\cos(\theta_{\vec{p}_\mu})$.

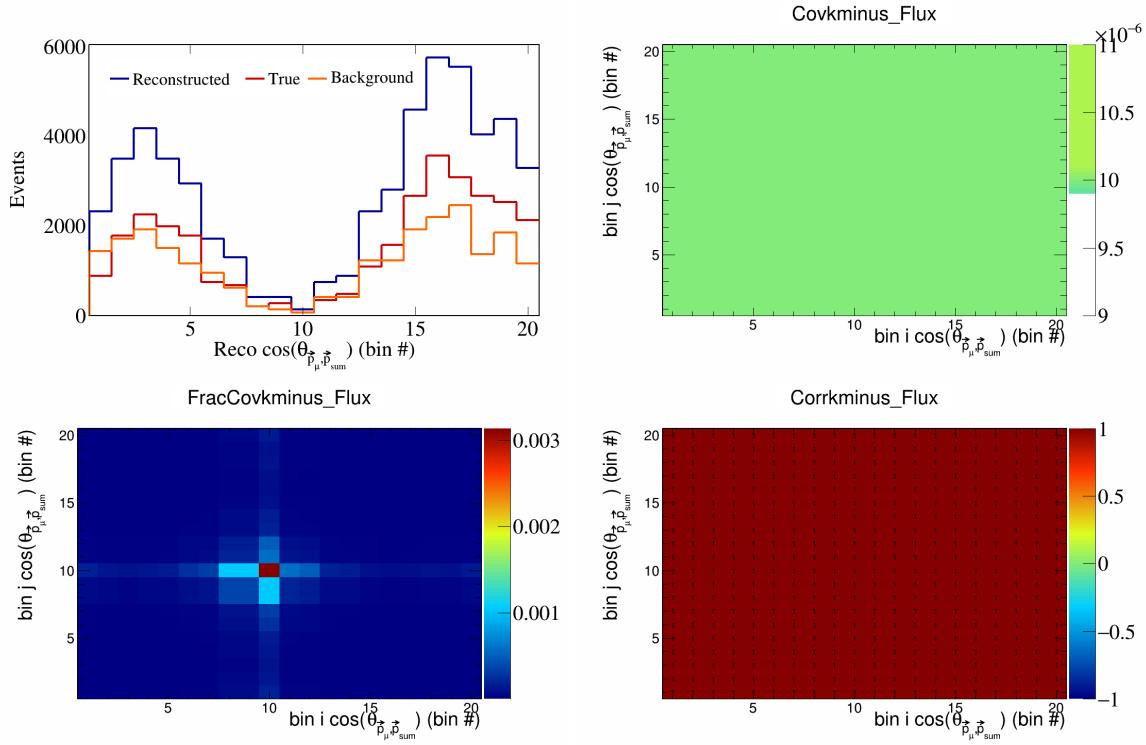


Figure 623: KMinus variations for $\cos(\theta_{\vec{p}_\mu} \vec{p}_{\text{sum}})$ in $\cos(\theta_{\vec{p}_\mu})$.

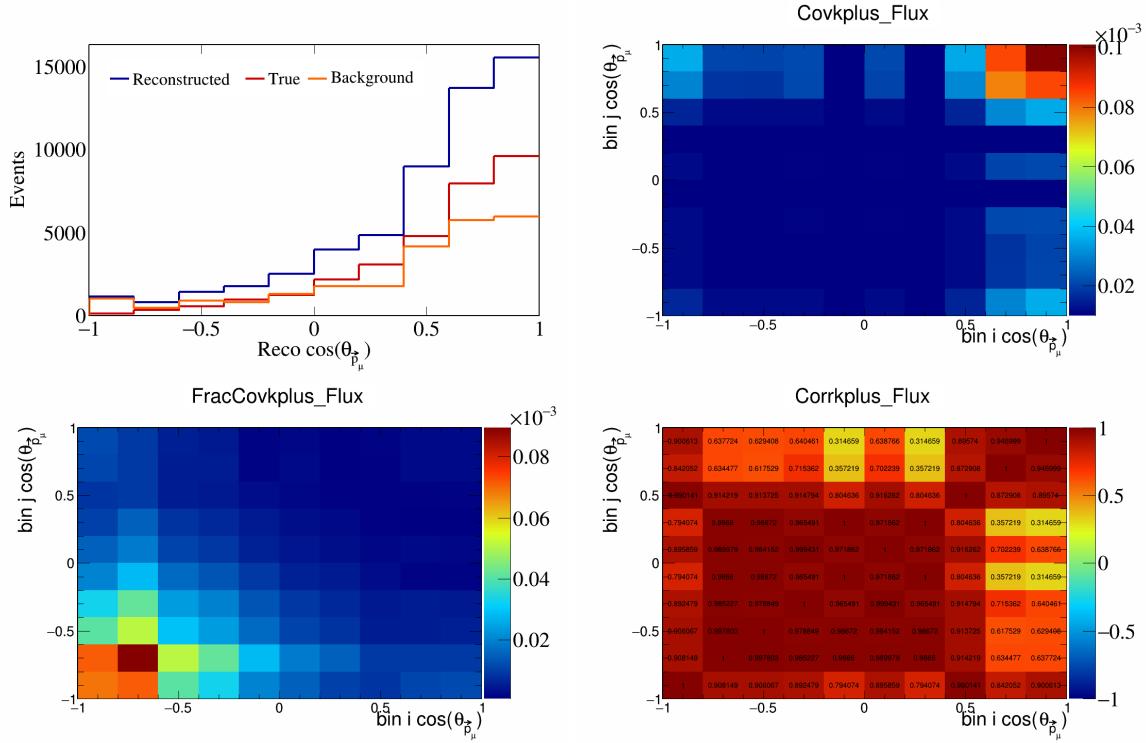


Figure 624: KPlus variations for $\cos(\theta_{\vec{p}_\mu} \vec{p}_{\text{sum}})$ in $\cos(\theta_{\vec{p}_\mu})$.

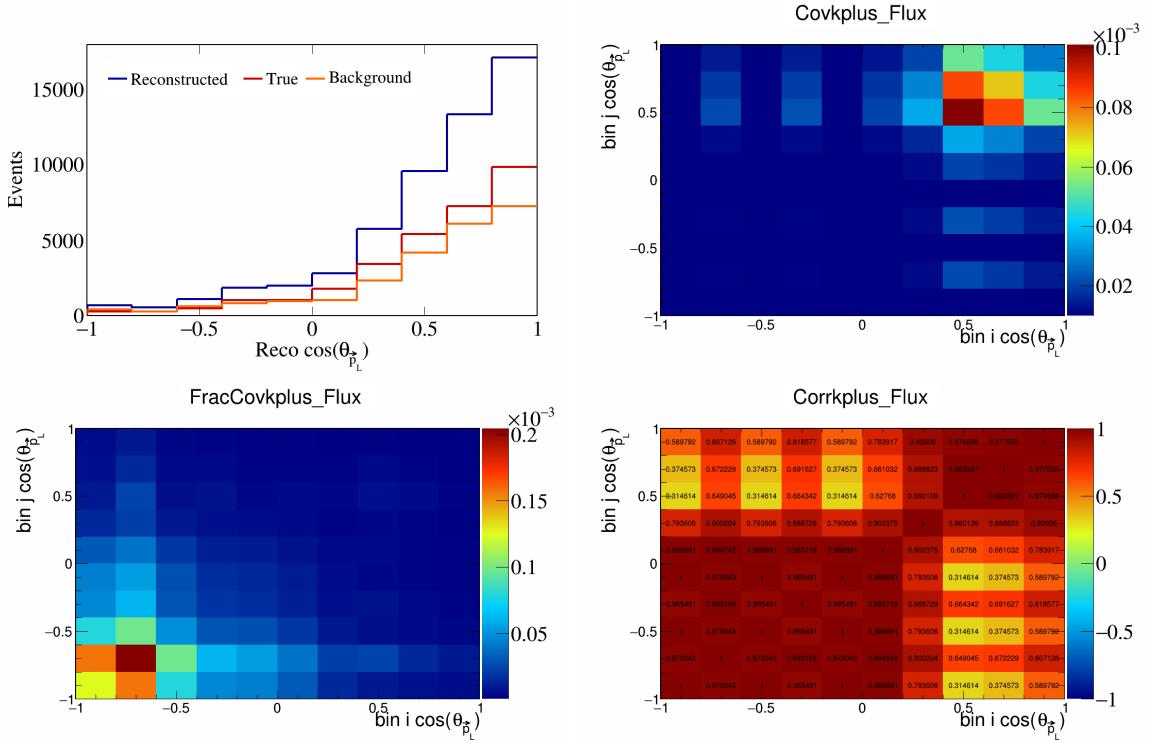


Figure 625: KPlus variations for $\cos(\theta_{\vec{p}_L})$.

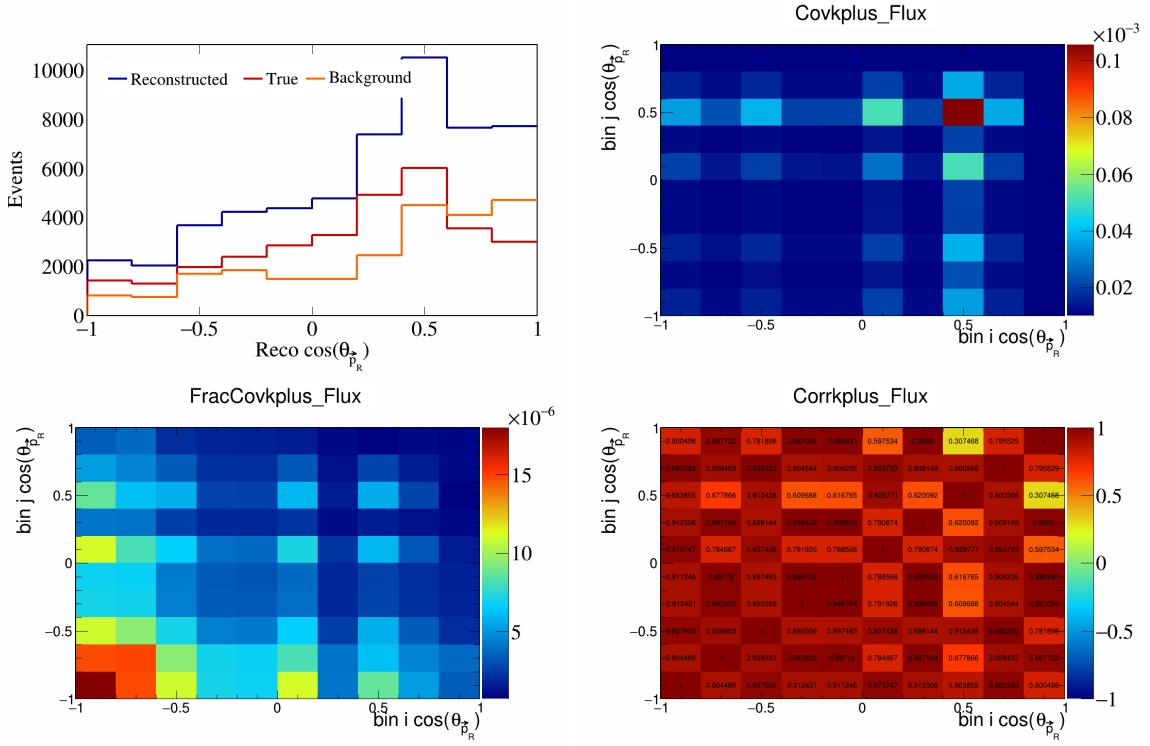


Figure 626: KPlus variations for $\cos(\theta_{\vec{p}_R})$.

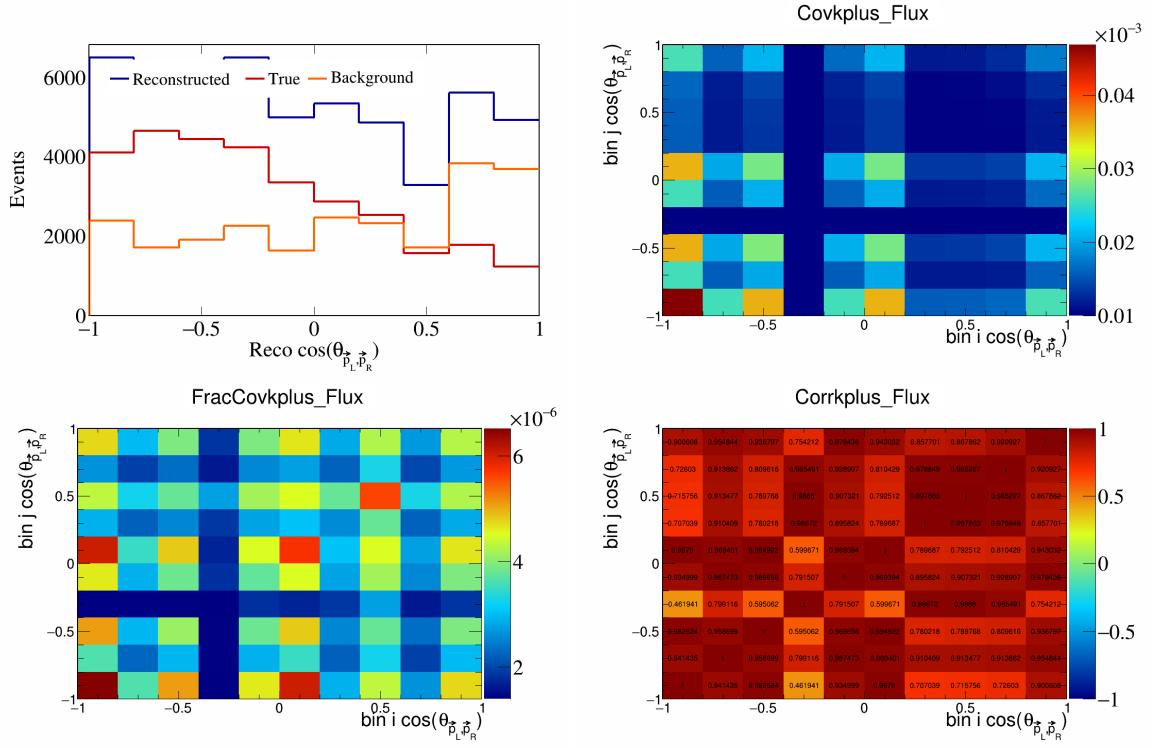


Figure 627: KPlus variations for $\cos(\theta_{\vec{p}_L, \vec{p}_R})$.

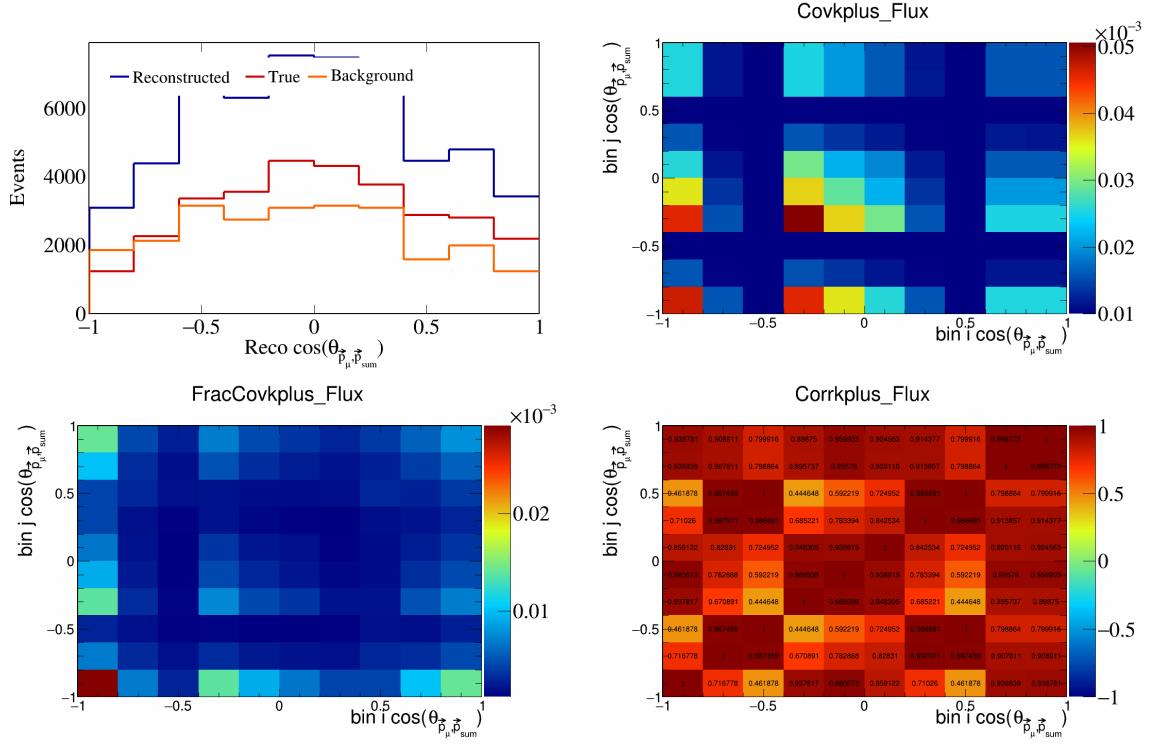


Figure 628: KPlus variations for $\cos(\theta_{\vec{p}_\mu, \vec{p}_{\text{sum}}})$.

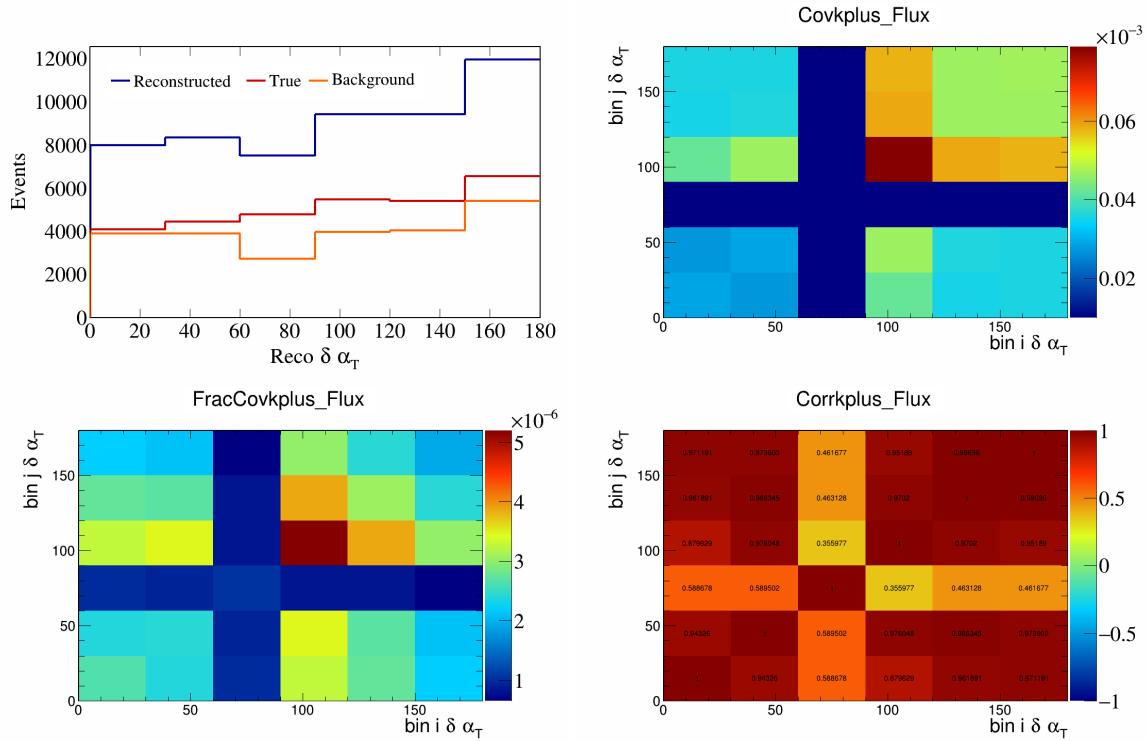


Figure 629: KPlus variations for $\delta\alpha_T$.

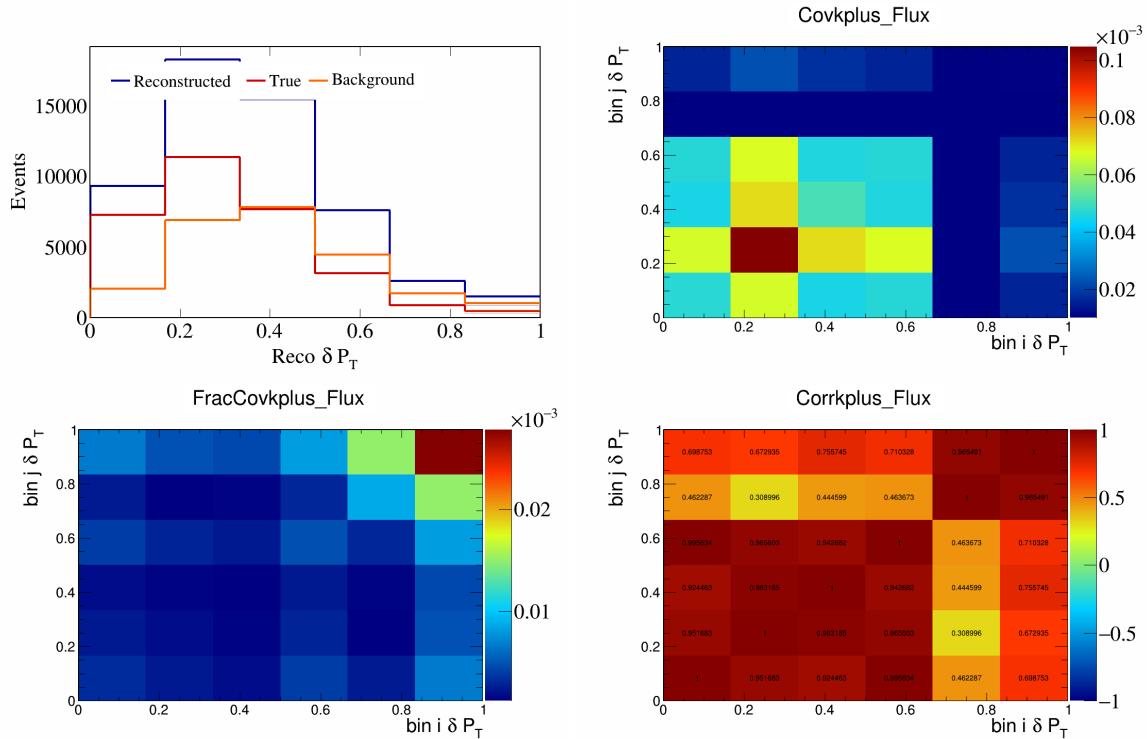


Figure 630: KPlus variations for δP_T .

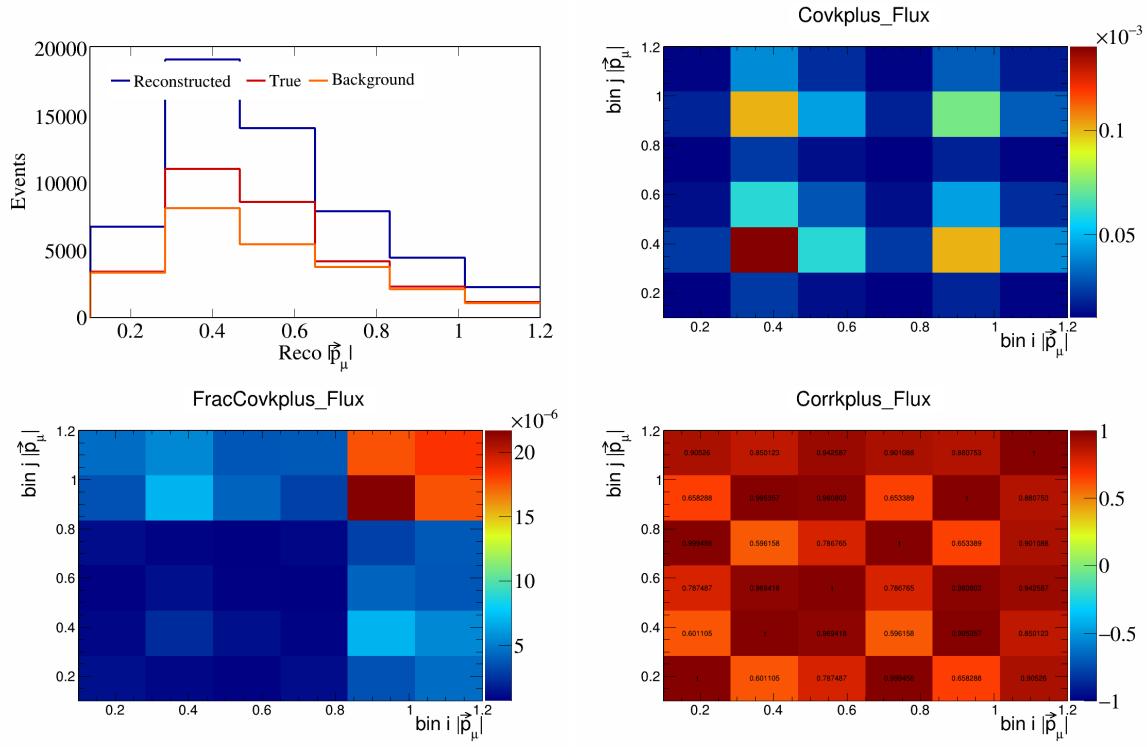


Figure 631: KPlus variations for $|\vec{p}_\mu|$.

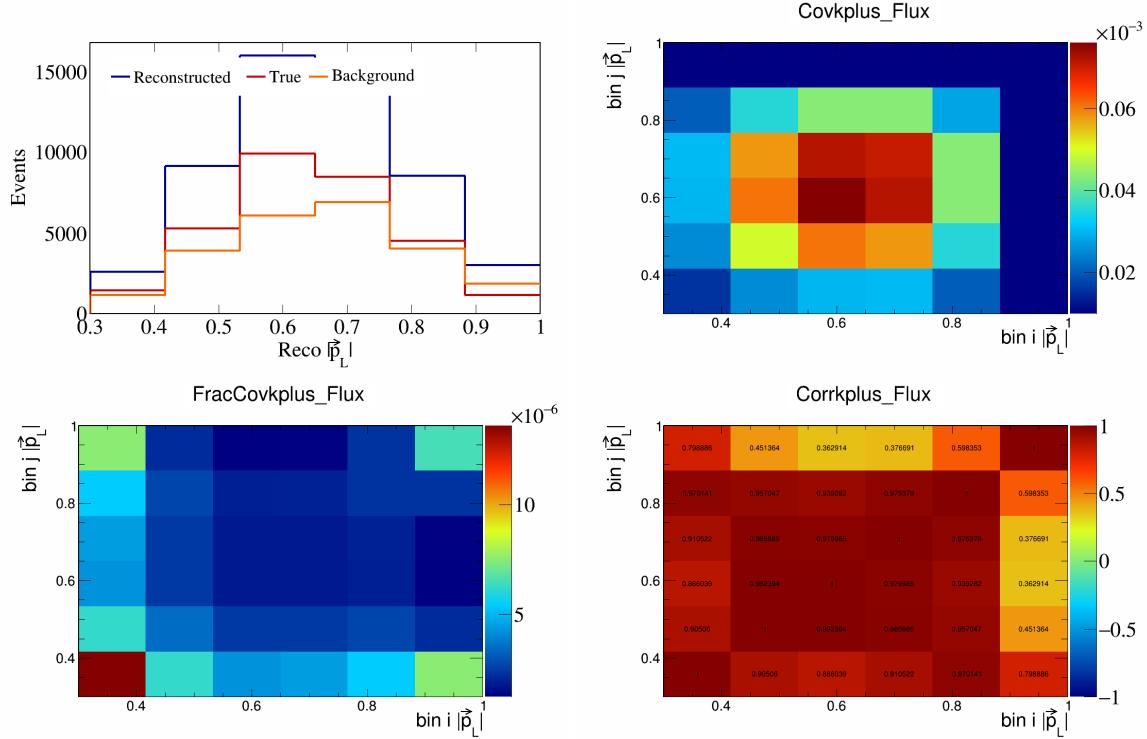


Figure 632: KPlus variations for $|\vec{p}_L|$.

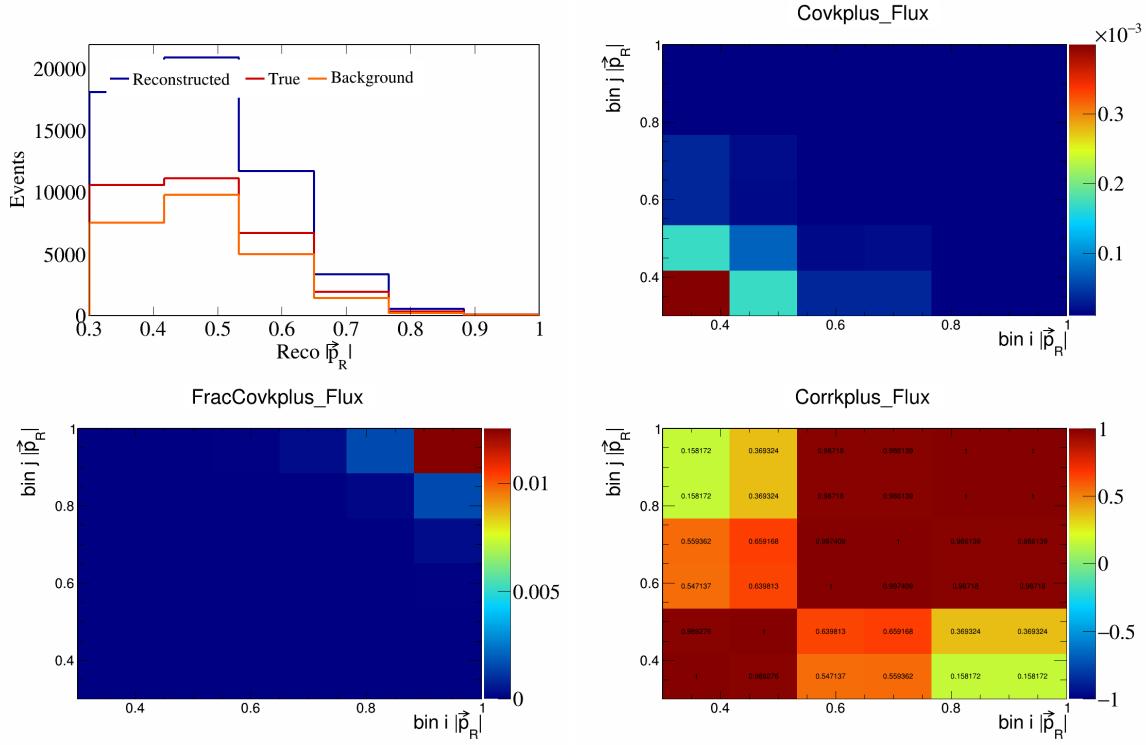


Figure 633: KPlus variations for $|\vec{p}_R|$.

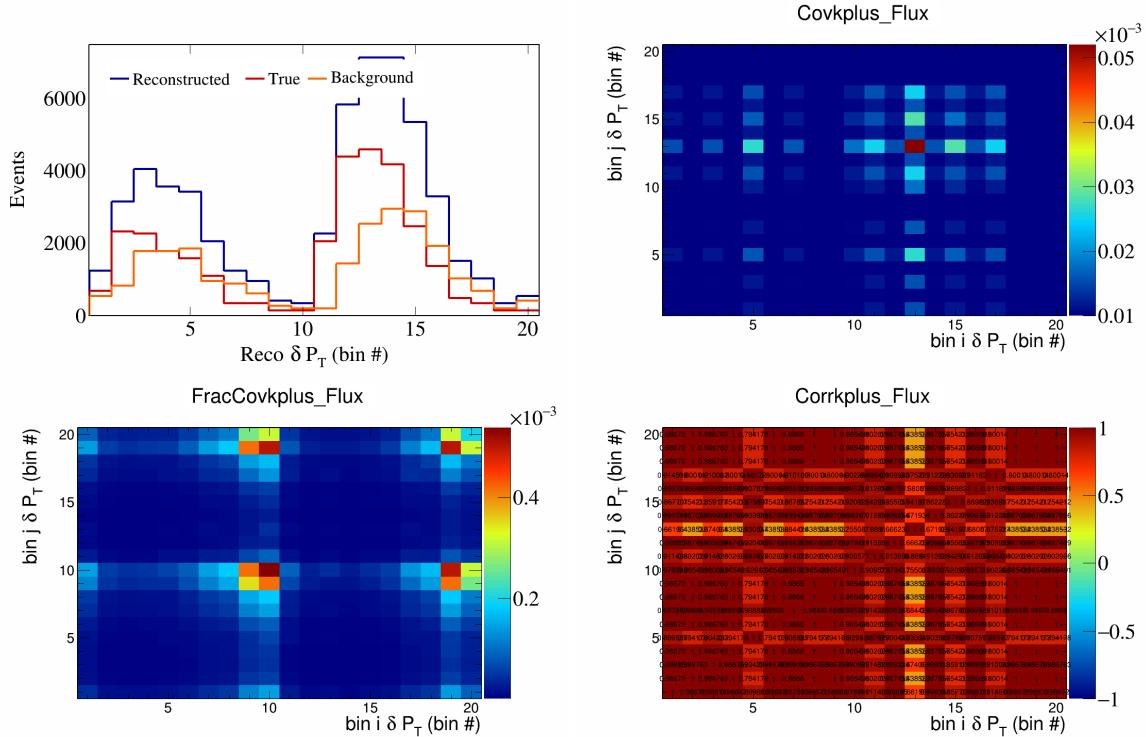


Figure 634: KPlus variations for δP_T in $\cos(\theta_{\vec{p}_\mu})$.

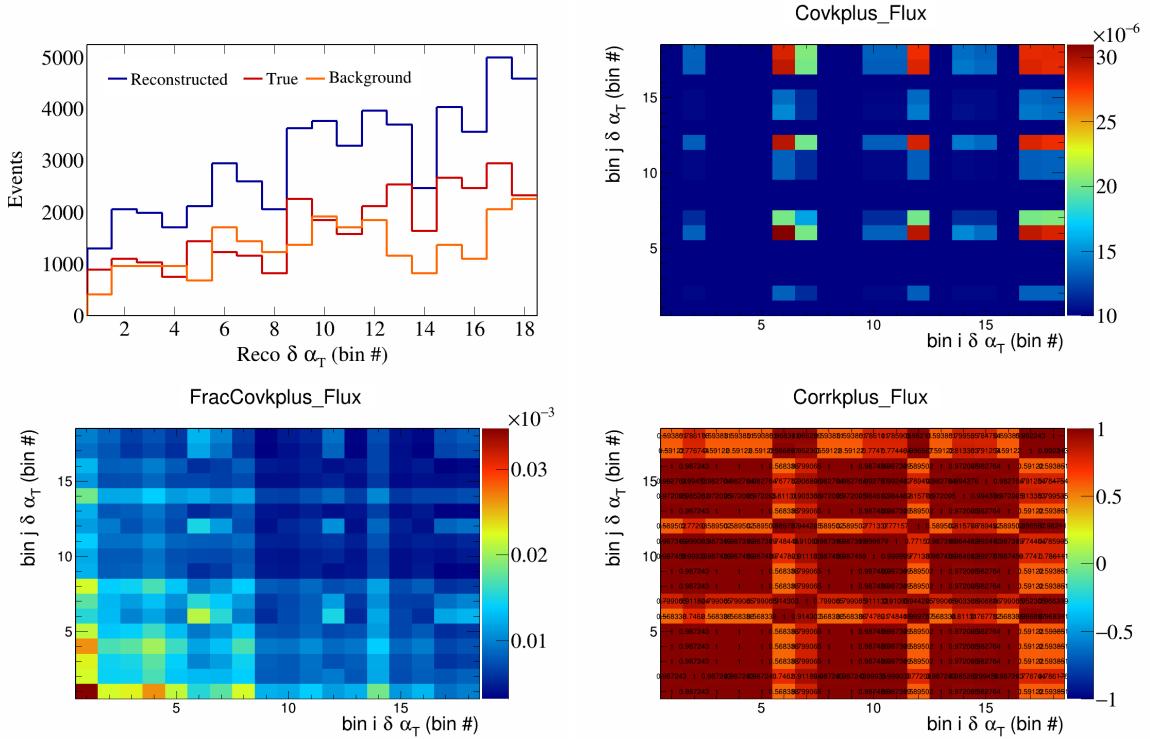


Figure 635: KPlus variations for $\delta\alpha_T$ in $\cos(\theta_{\vec{p}_\mu})$.

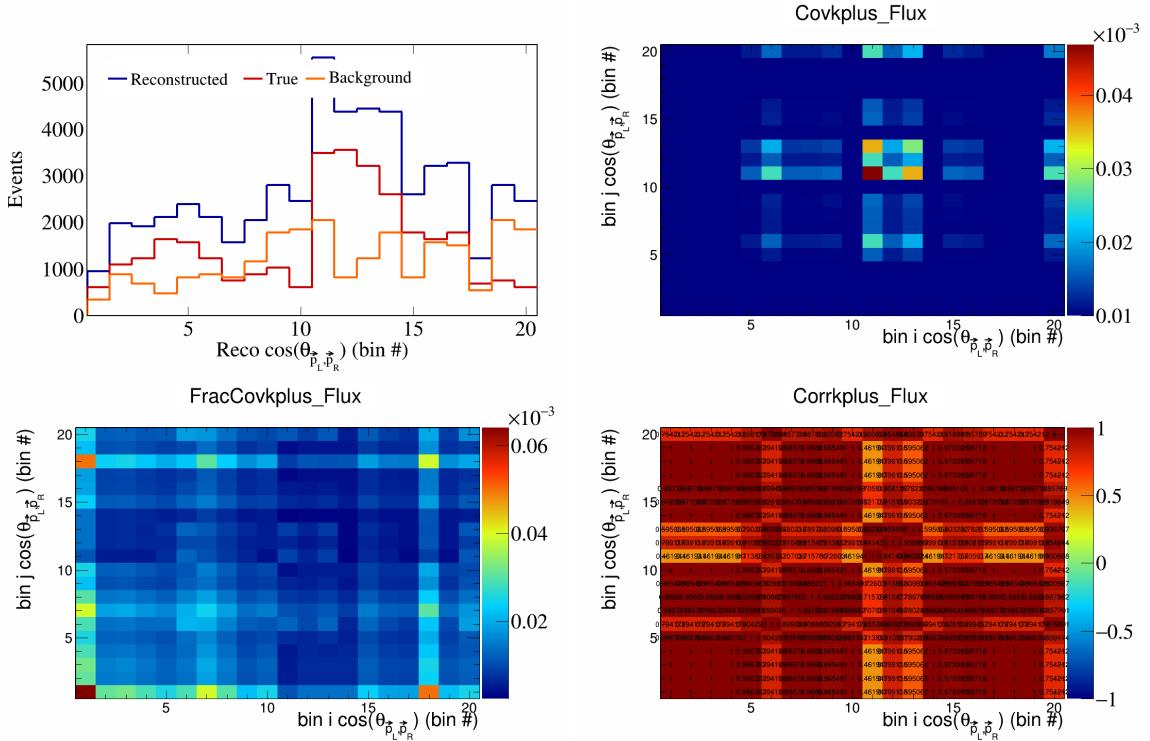


Figure 636: KPlus variations for $\cos(\theta_{p_L, p_R})$ in $\cos(\theta_{\vec{p}_\mu})$.

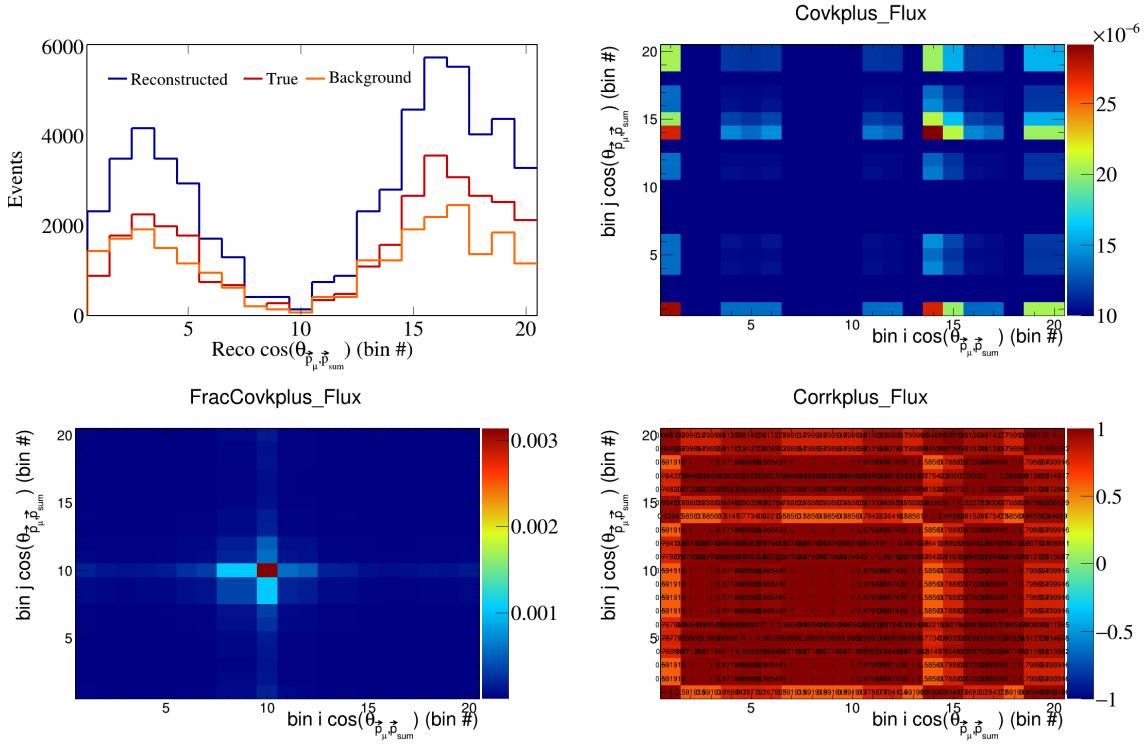


Figure 637: KPlus variations for $\cos(\theta_{\vec{p}_\mu}^i, \vec{p}_{\mu}^j)$ in $\cos(\theta_{\vec{p}_\mu})$.

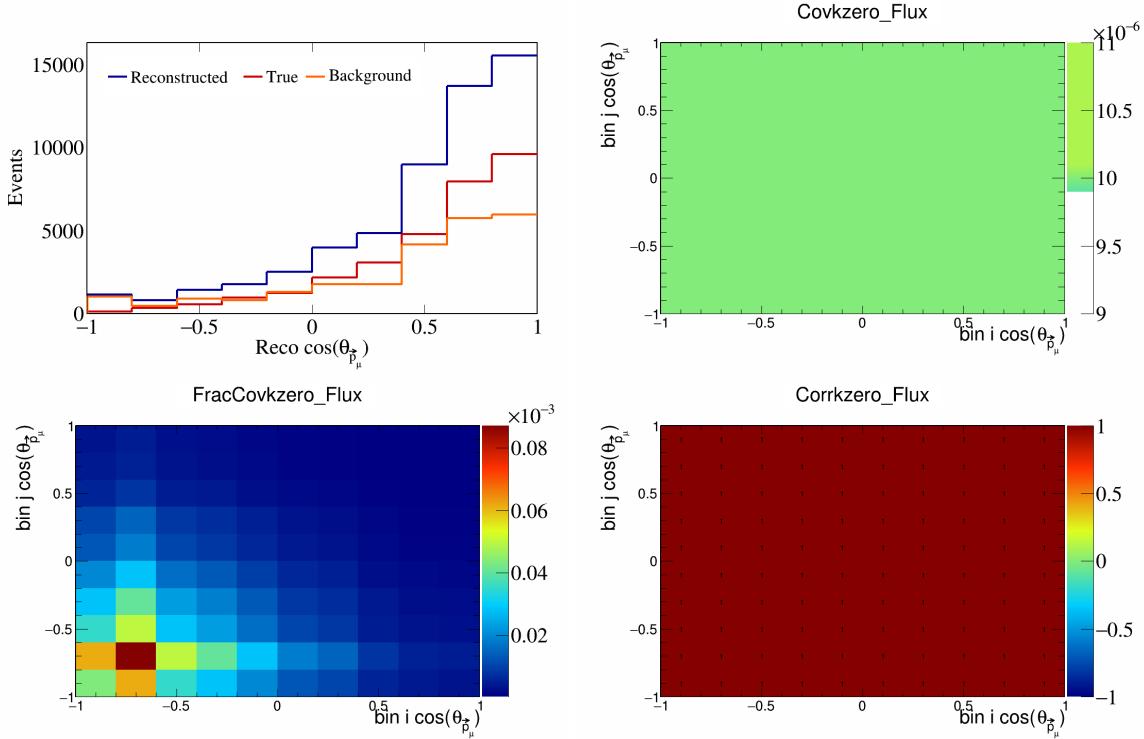


Figure 638: KZero variations for $\cos(\theta_{\vec{p}_\mu}^i, \vec{p}_{\mu}^j)$.

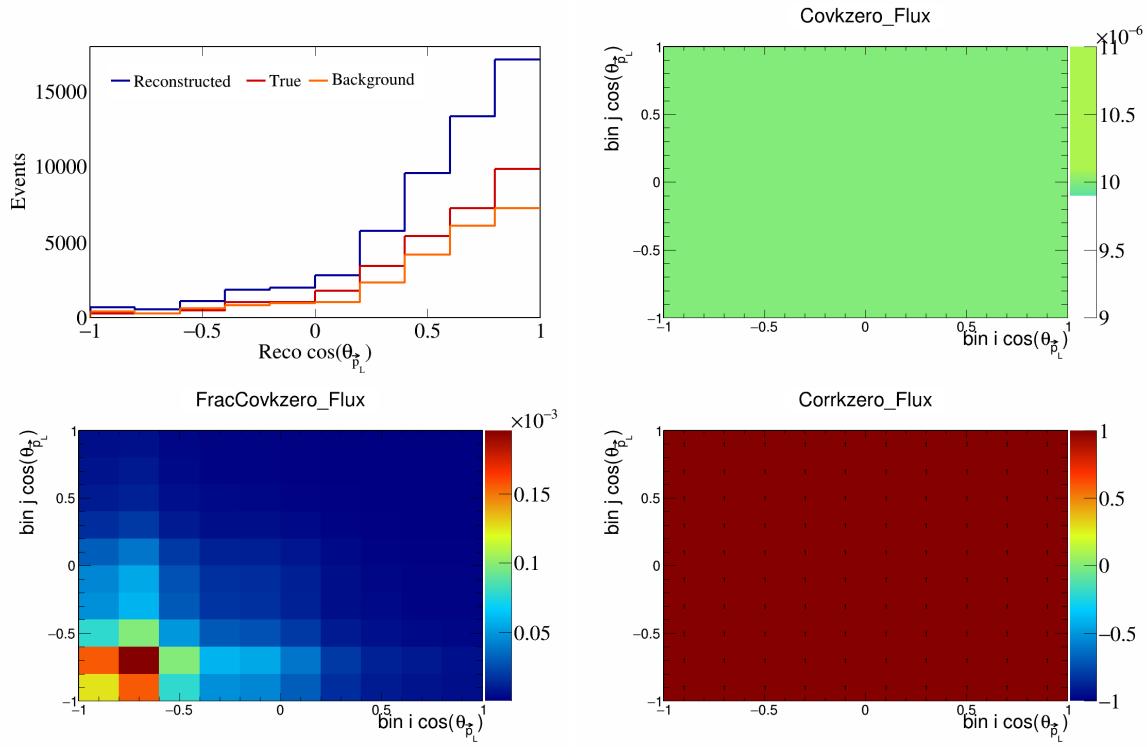


Figure 639: KZero variations for $\cos(\theta_{\vec{p}_L})$.

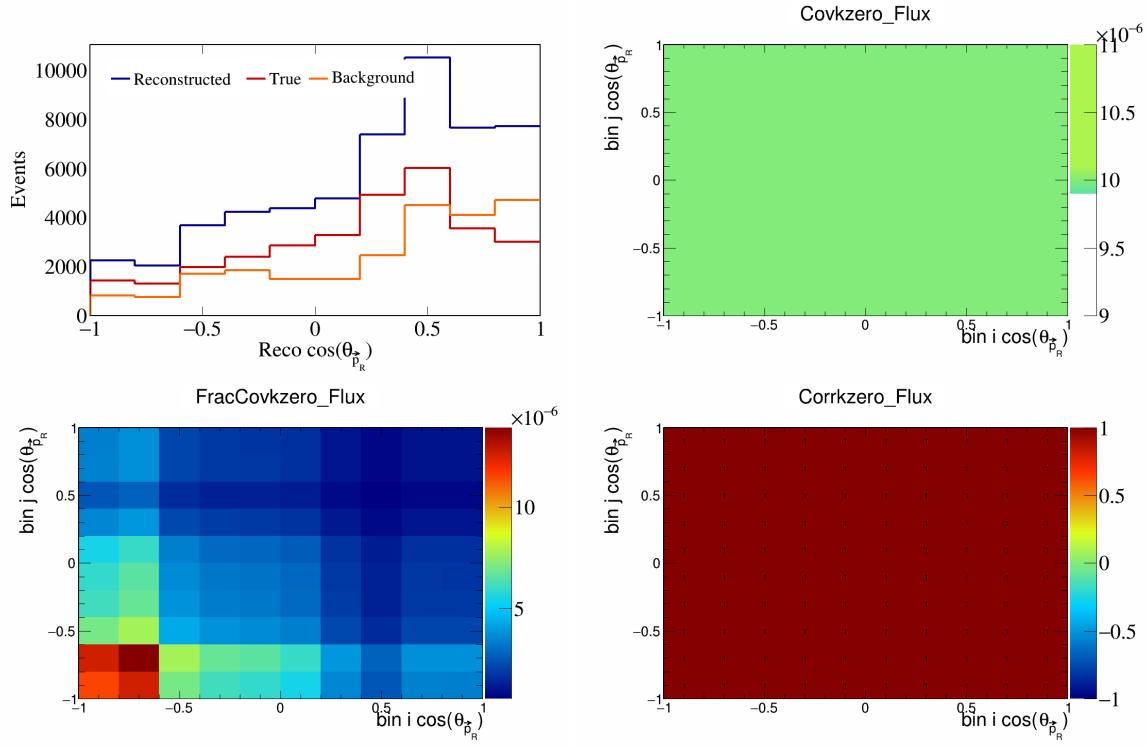


Figure 640: KZero variations for $\cos(\theta_{\vec{p}_R})$.

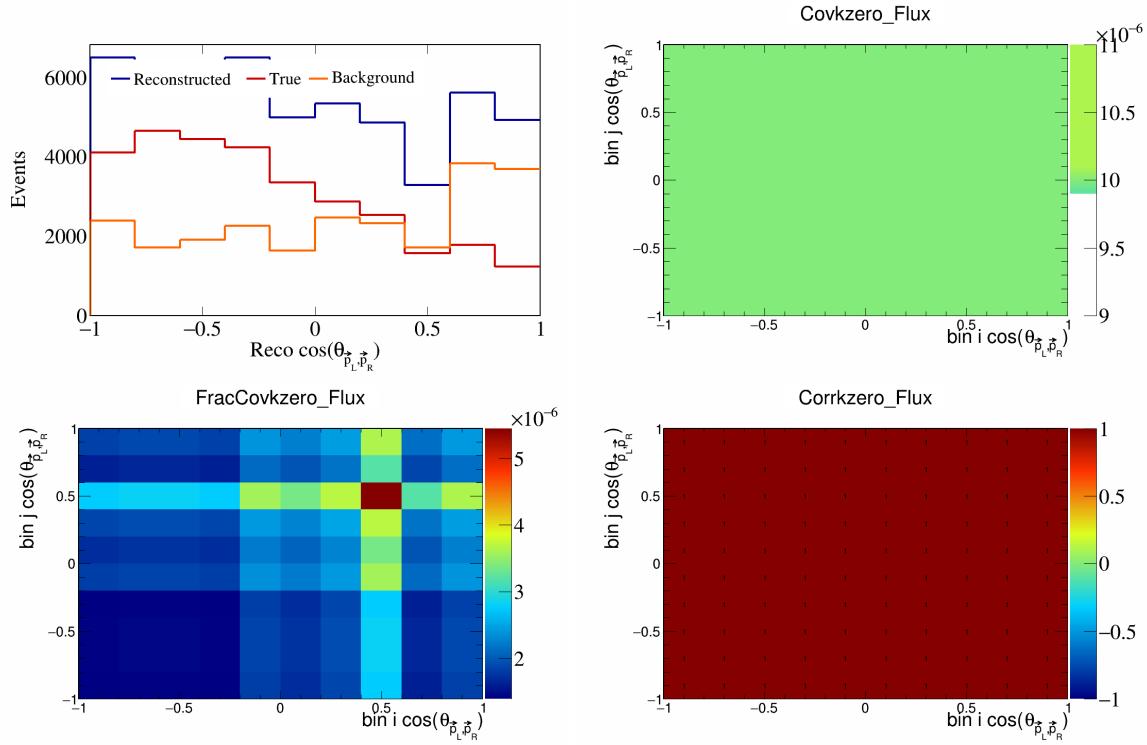


Figure 641: KZero variations for $\cos(\theta_{\vec{p}_L, \vec{p}_R})$.

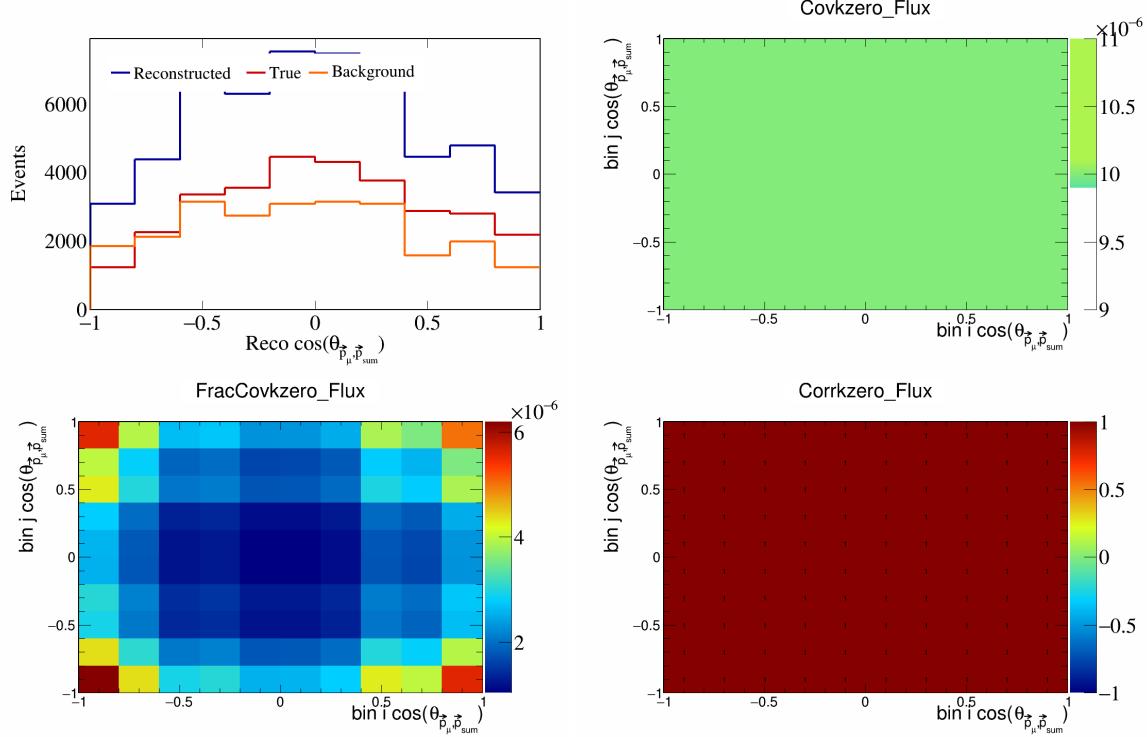


Figure 642: KZero variations for $\cos(\theta_{\vec{p}_\mu, \vec{p}_{\text{sum}}})$.

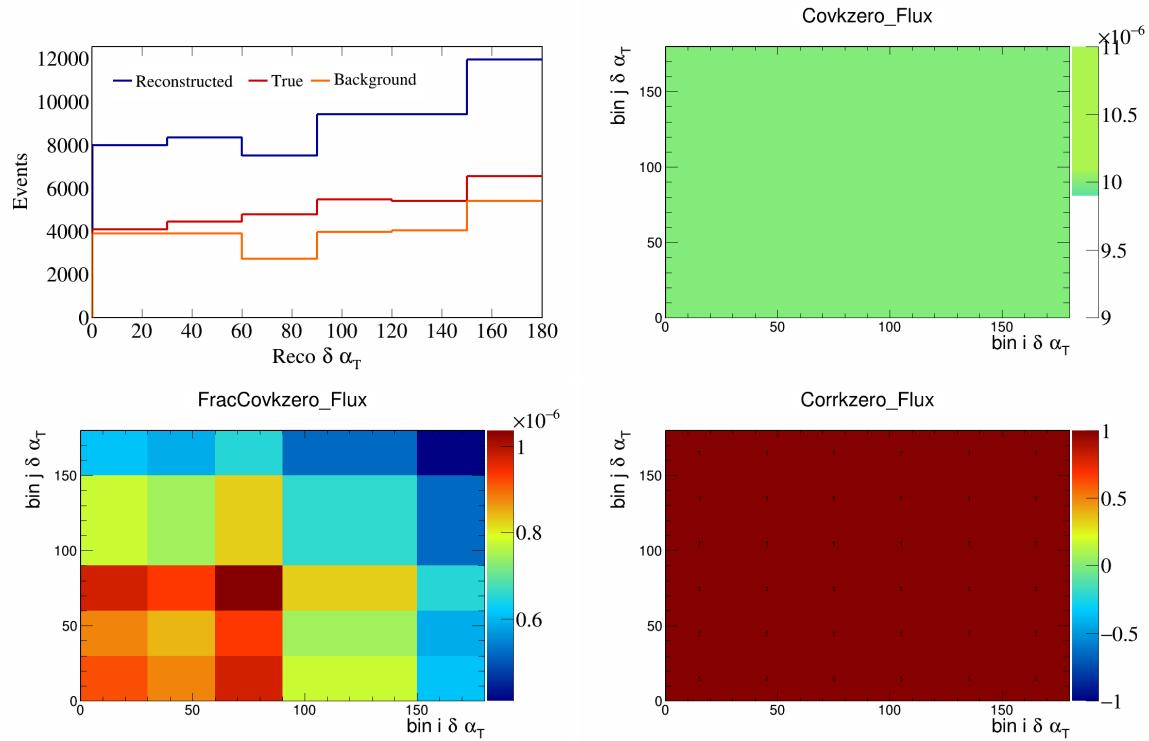


Figure 643: KZero variations for $\delta\alpha_T$.

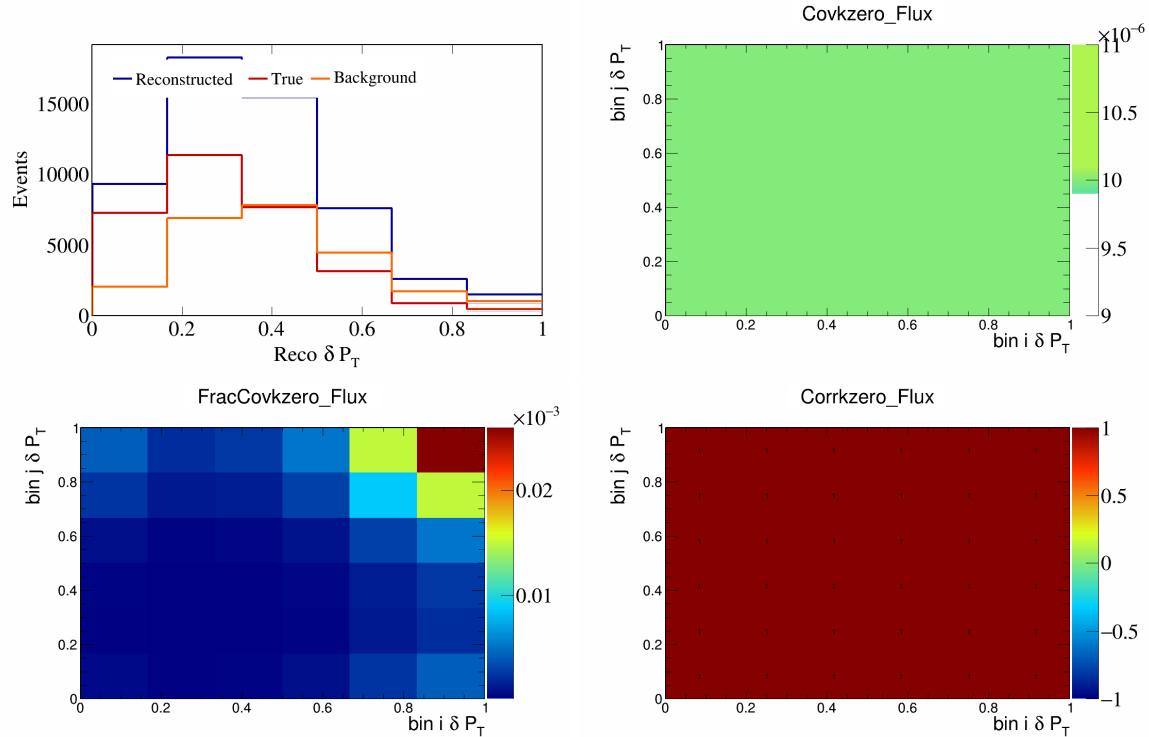


Figure 644: KZero variations for δP_T .

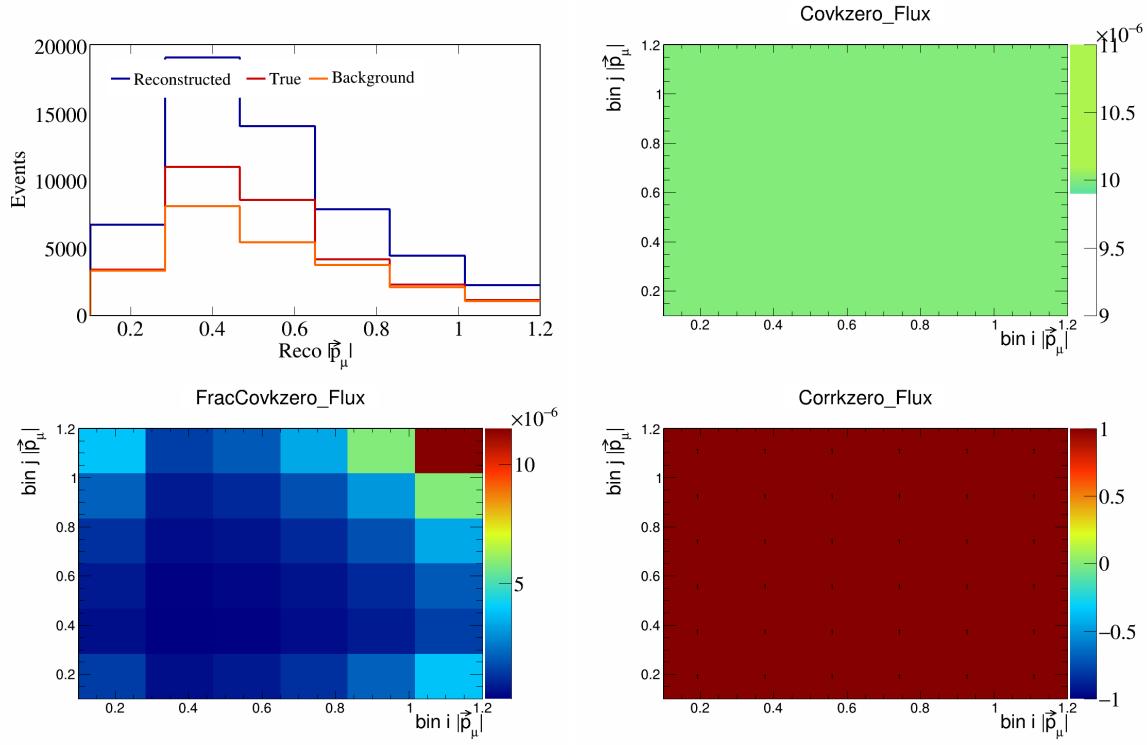


Figure 645: KZero variations for $|\vec{p}_\mu|$.

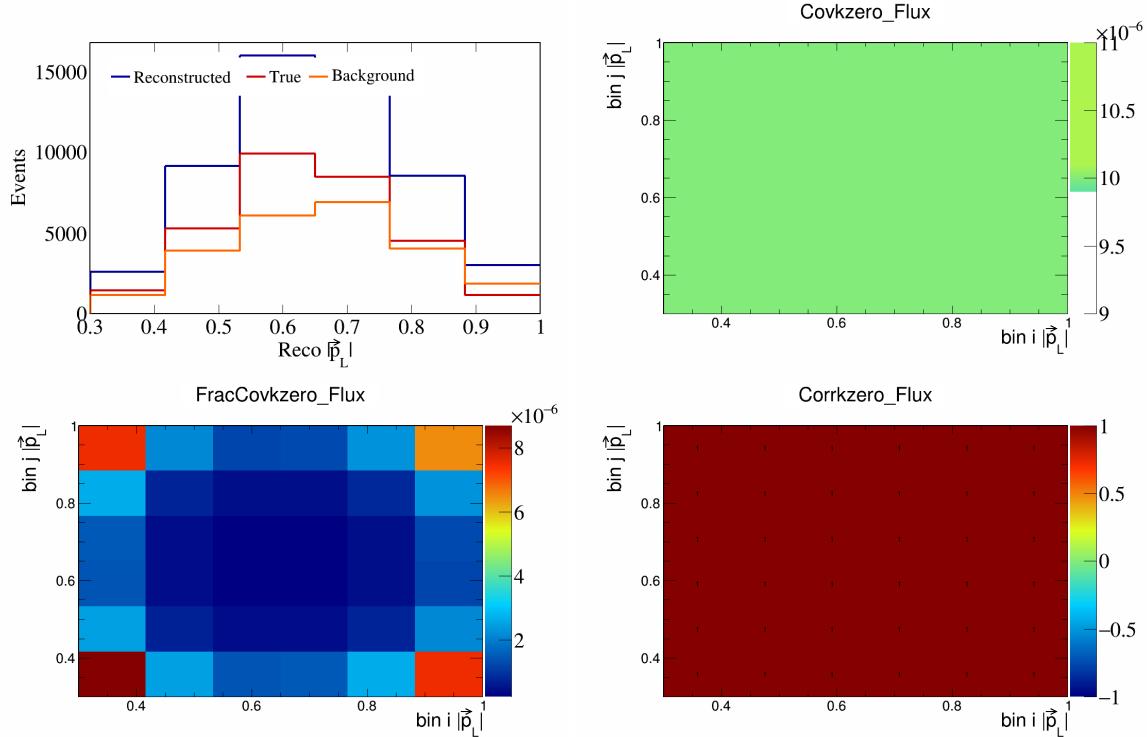


Figure 646: KZero variations for $|\vec{p}_L|$.

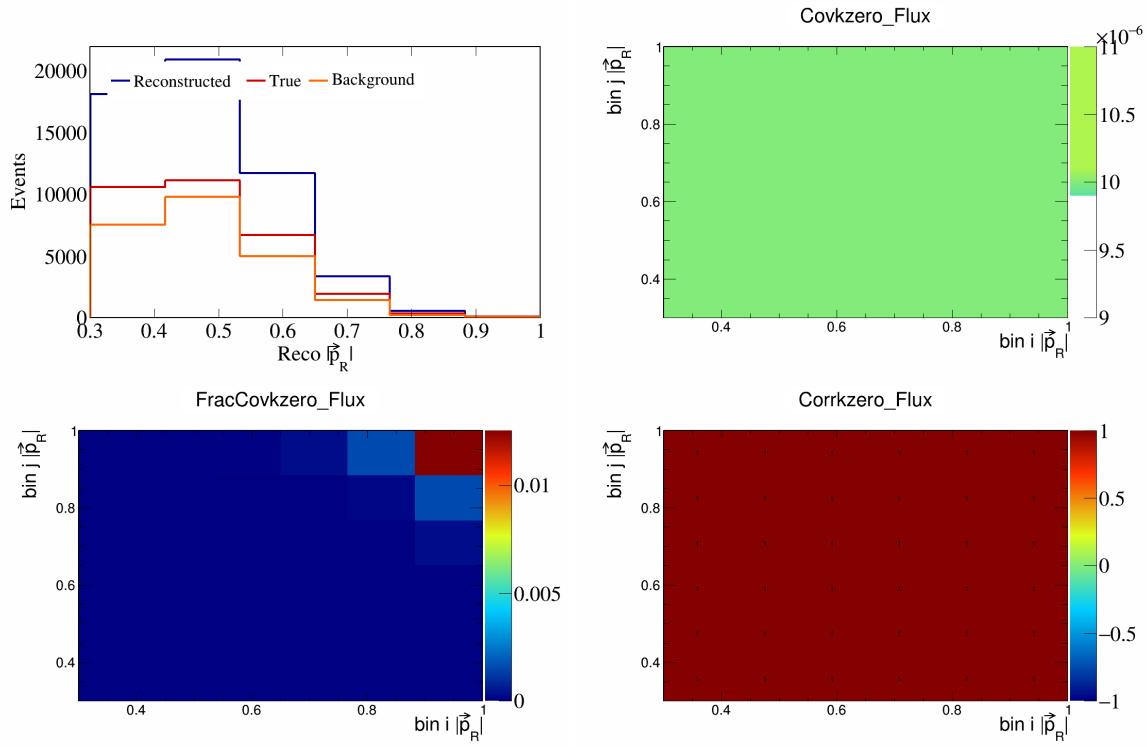


Figure 647: KZero variations for $|\vec{p}_R|$.

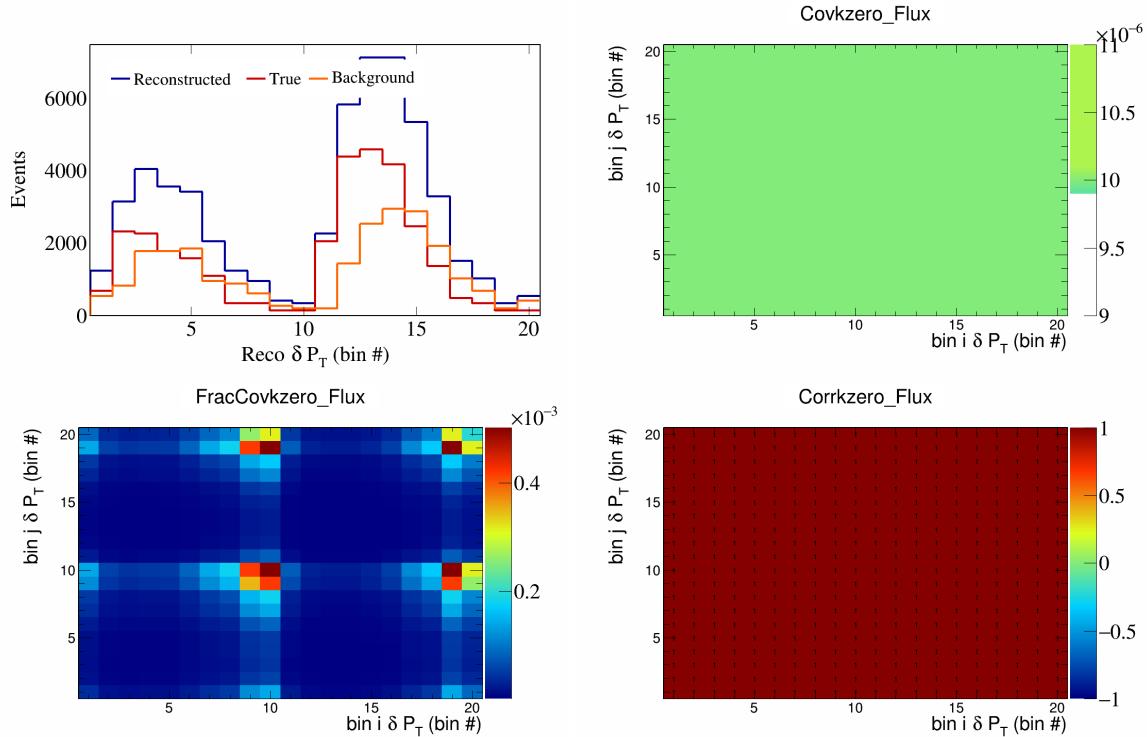


Figure 648: KZero variations for δP_T in $\cos(\theta_{\vec{p}_\mu})$.

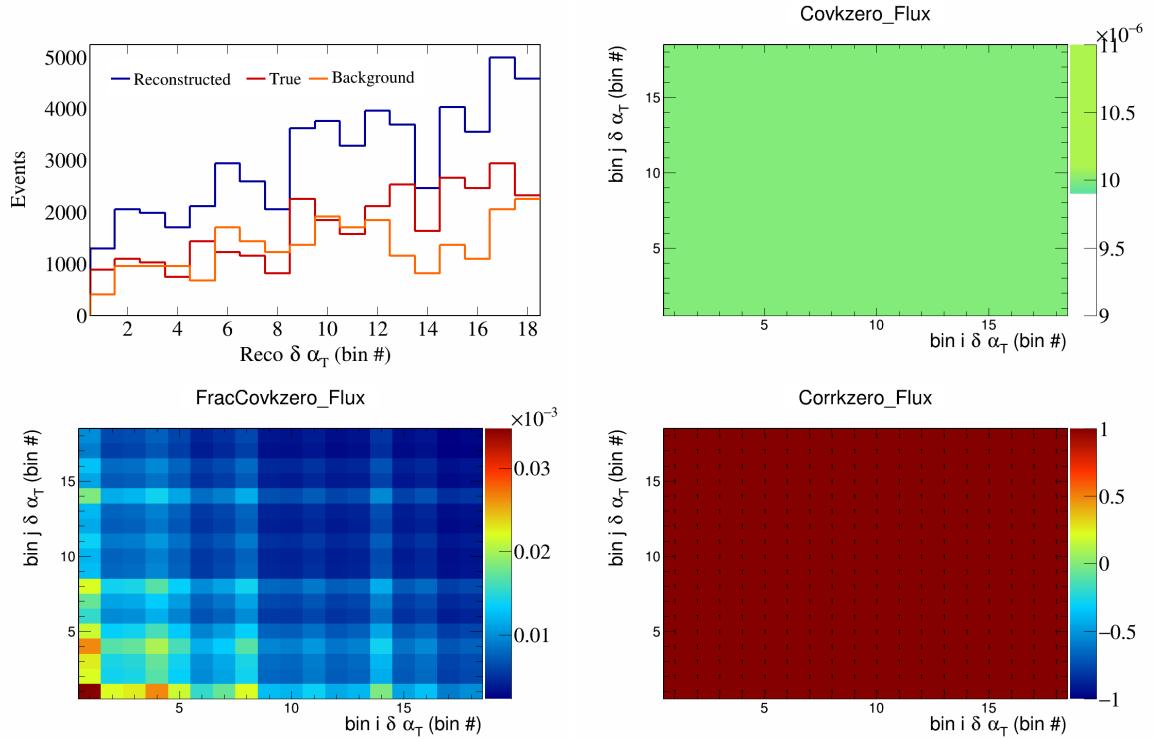


Figure 649: KZero variations for $\delta\alpha_T$ in $\cos(\theta_{\vec{p}_\mu})$.

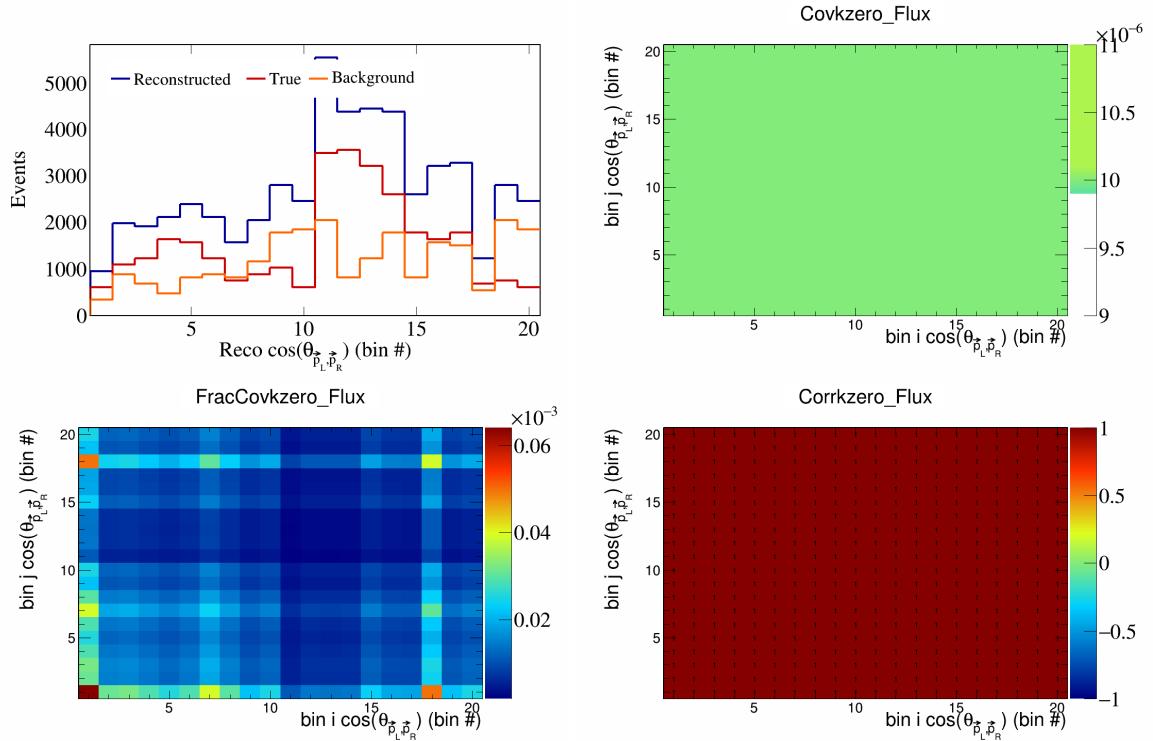


Figure 650: KZero variations for $\cos(\theta_{\vec{p}_L, \vec{p}_R})$ in $\cos(\theta_{\vec{p}_\mu})$.

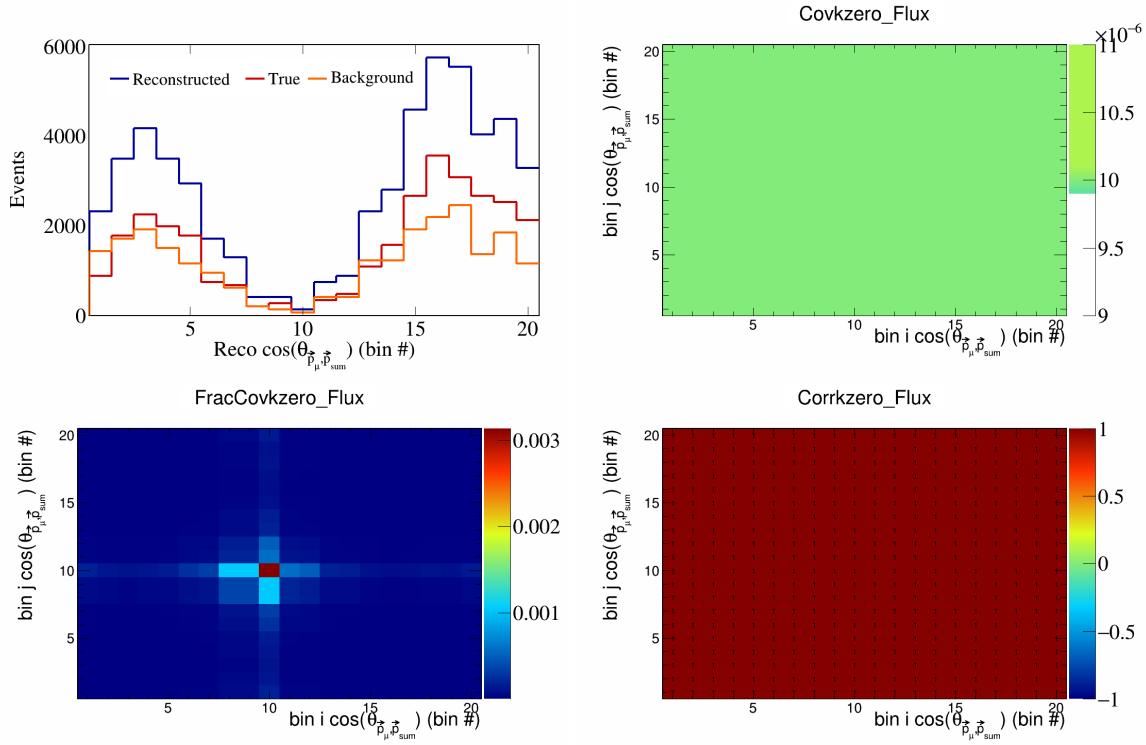


Figure 651: KZero variations for $\cos(\theta_{\vec{p}_\mu, \vec{p}_{\text{sum}}})$ in $\cos(\theta_{\vec{p}_\mu})$.

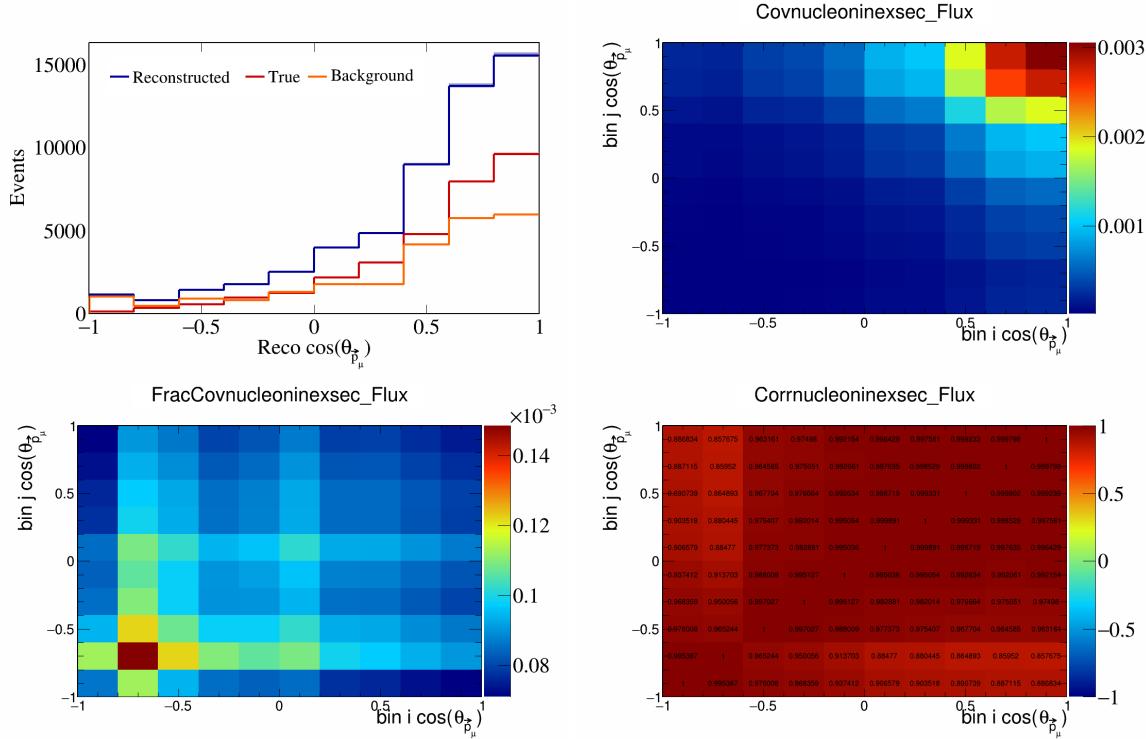


Figure 652: NucleonIneXSec variations for $\cos(\theta_{\vec{p}_\mu})$.

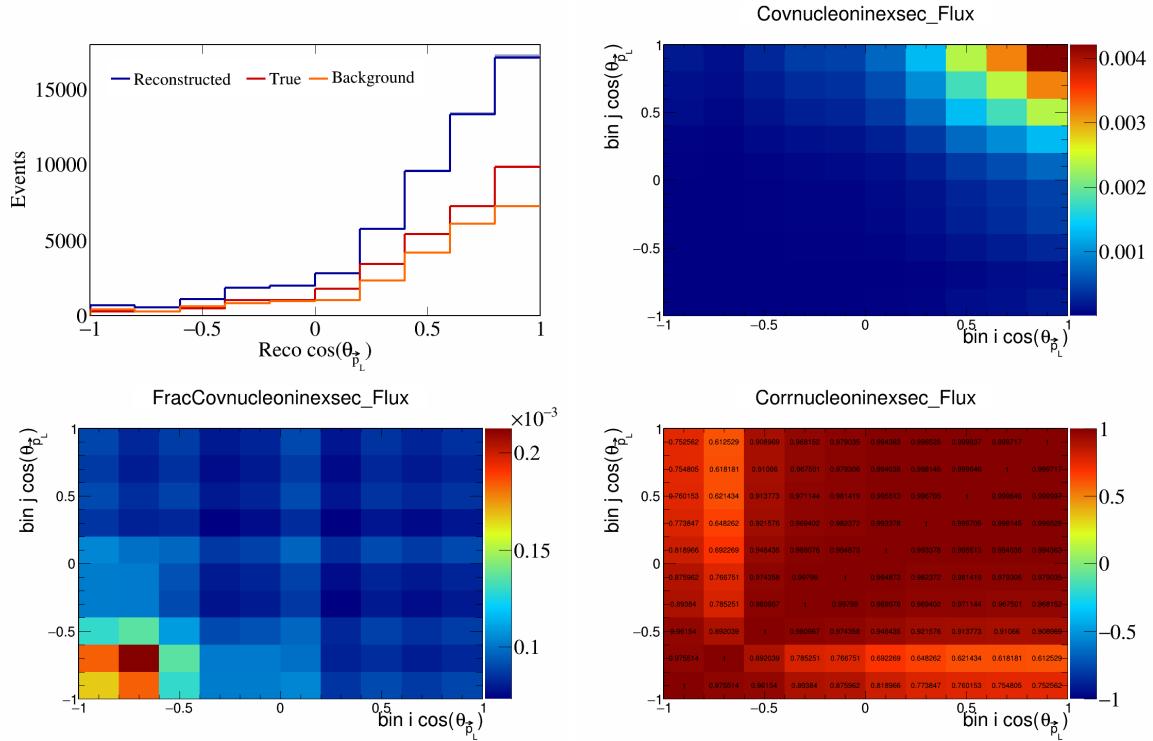


Figure 653: NucleonIneXSec variations for $\cos(\theta_{\vec{p}_L})$.

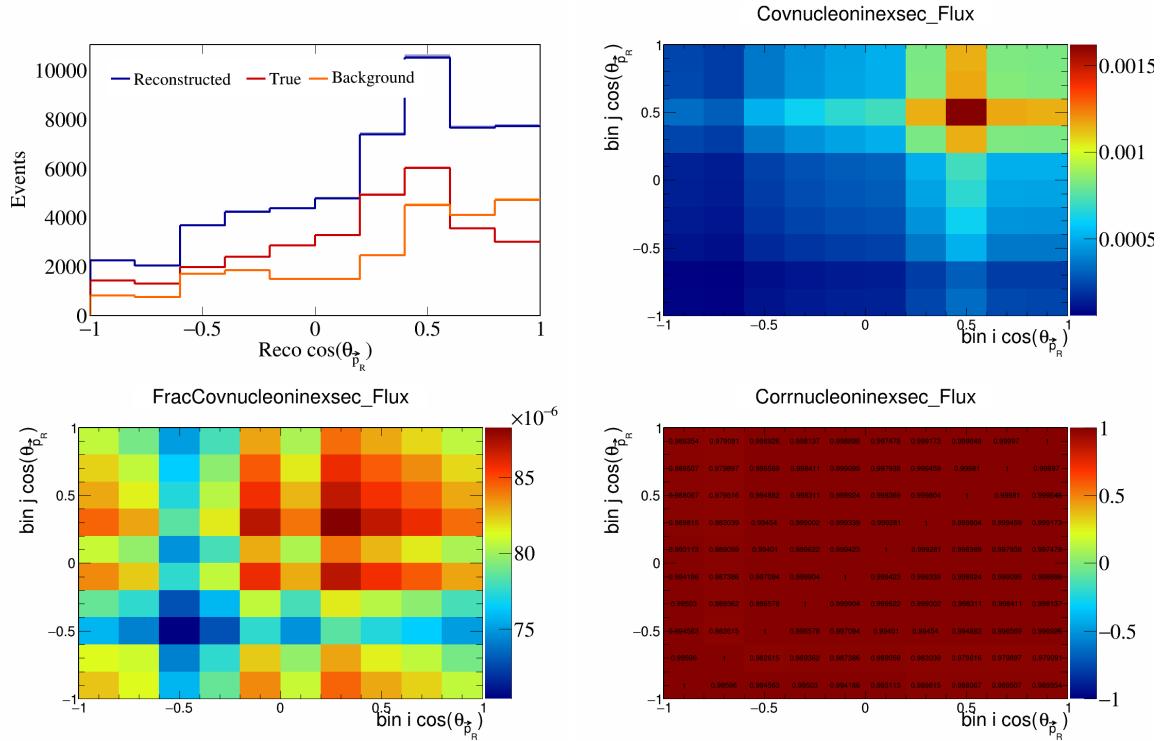


Figure 654: NucleonIneXSec variations for $\cos(\theta_{\vec{p}_R})$.

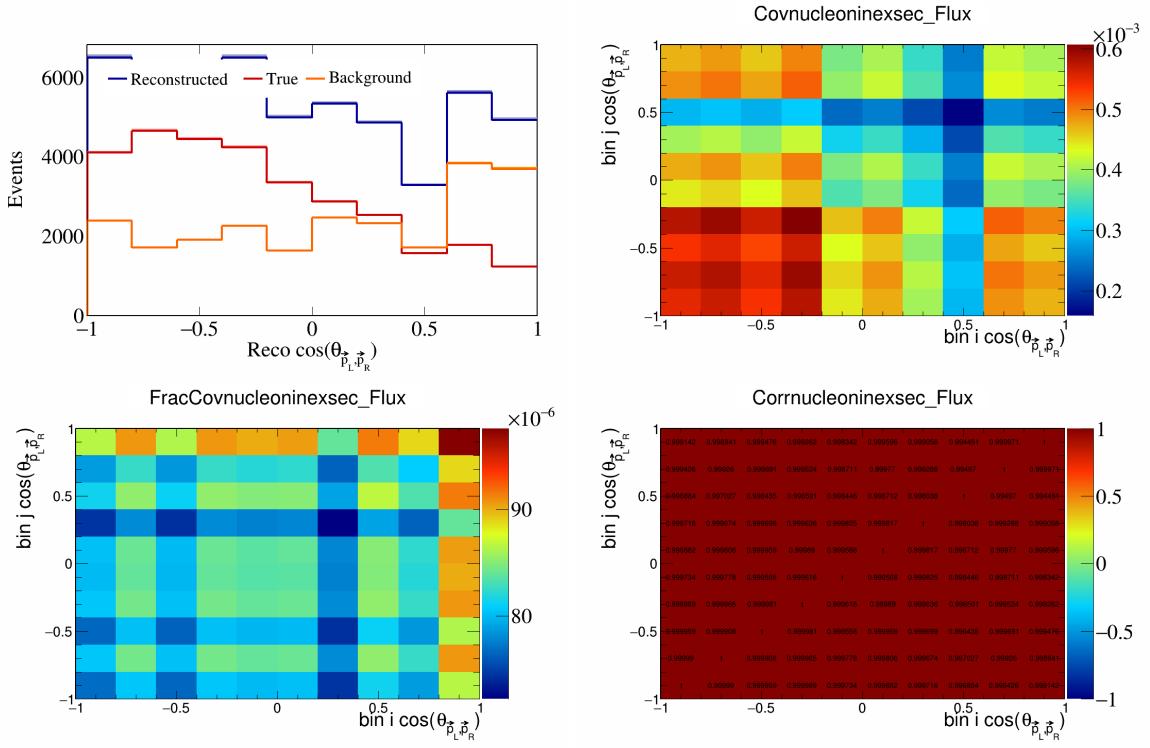


Figure 655: NucleonIneXSec variations for $\cos(\theta_{\vec{p}_L, \vec{p}_R})$.

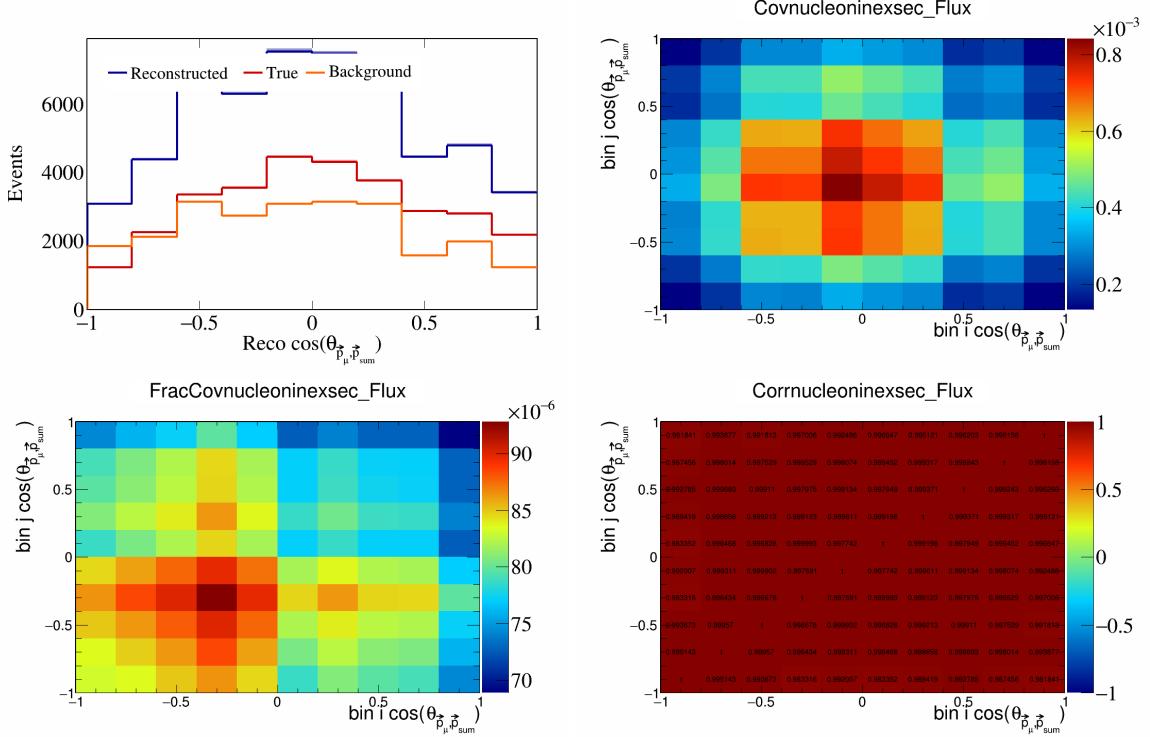


Figure 656: NucleonIneXSec variations for $\cos(\theta_{\vec{p}_\mu, \vec{p}_{\text{sum}}})$.

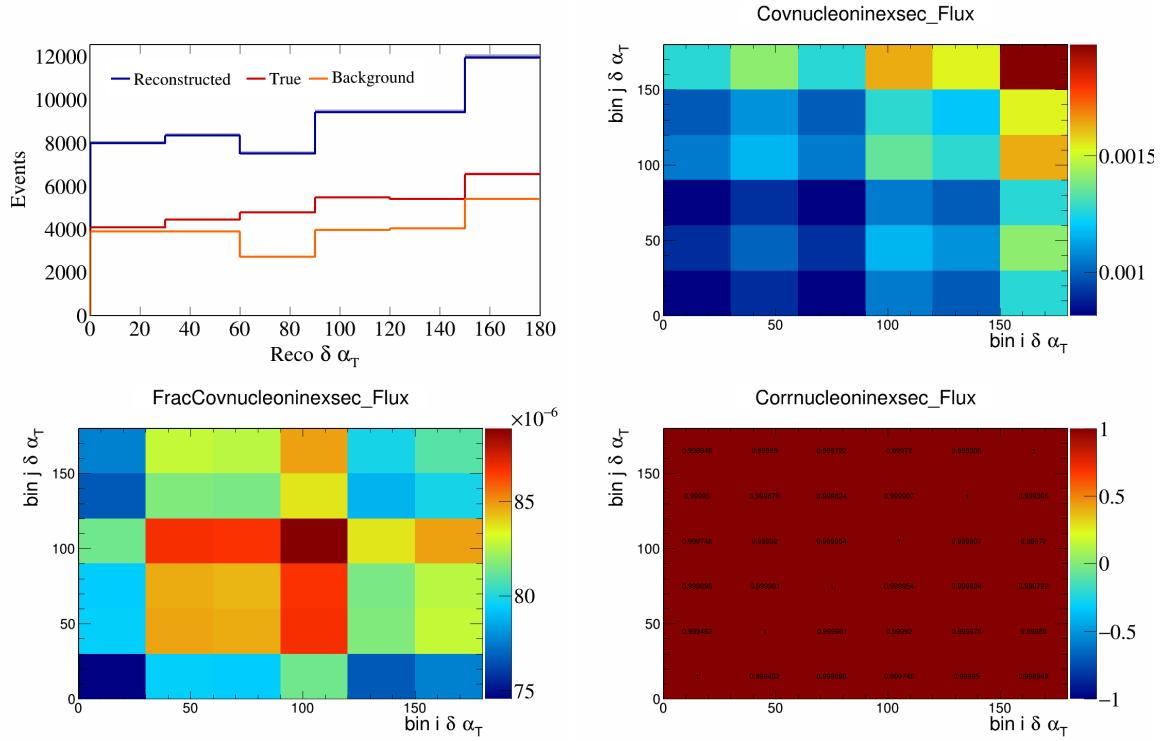


Figure 657: NucleonIneXSec variations for $\delta \alpha_T$.

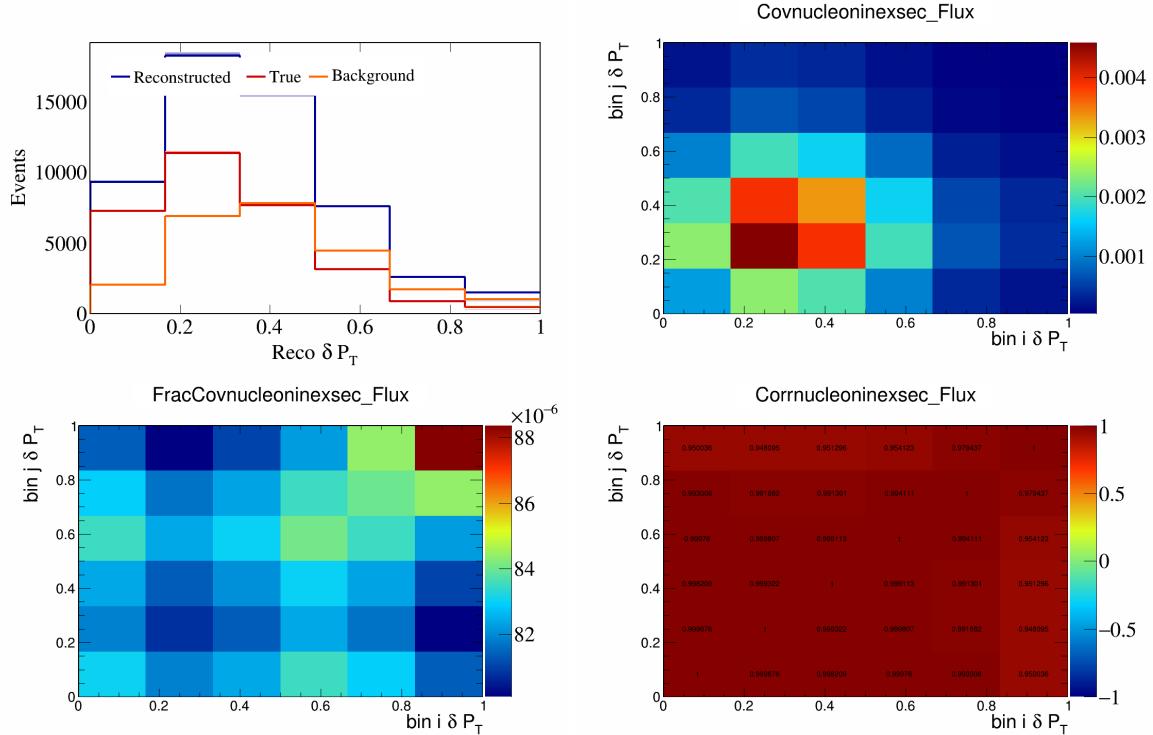


Figure 658: NucleonIneXSec variations for δP_T .

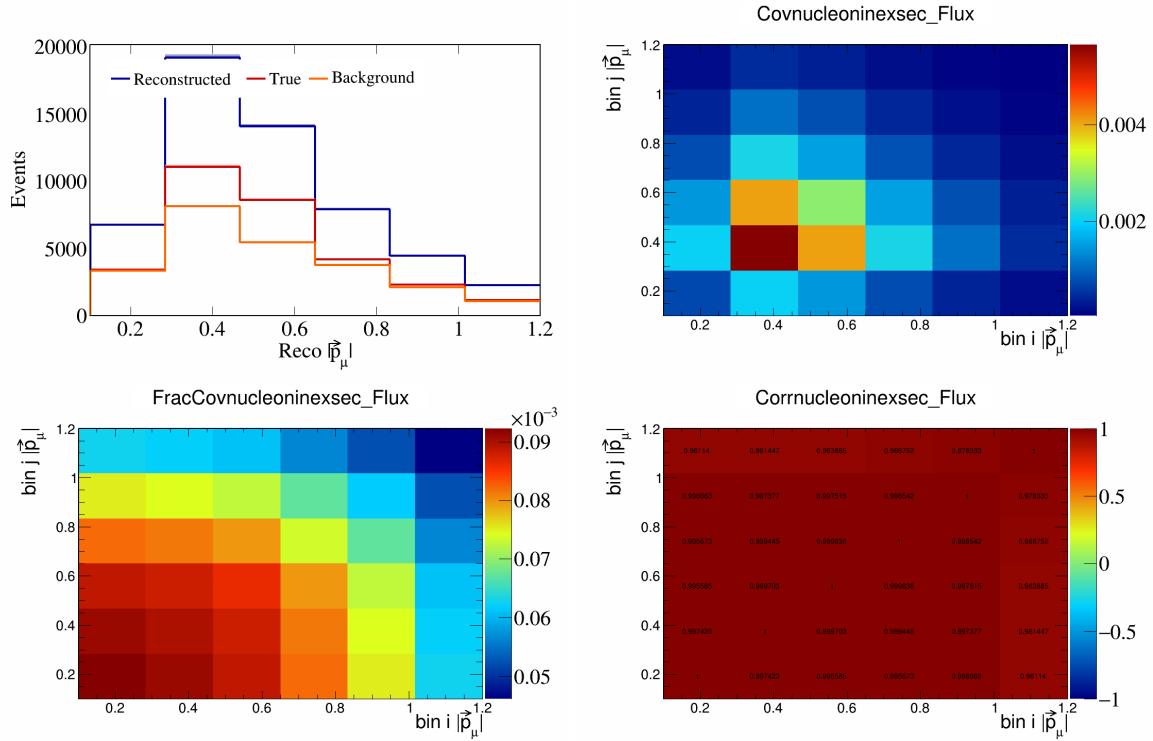


Figure 659: NucleonIneXSec variations for $|\vec{p}_\mu|$.

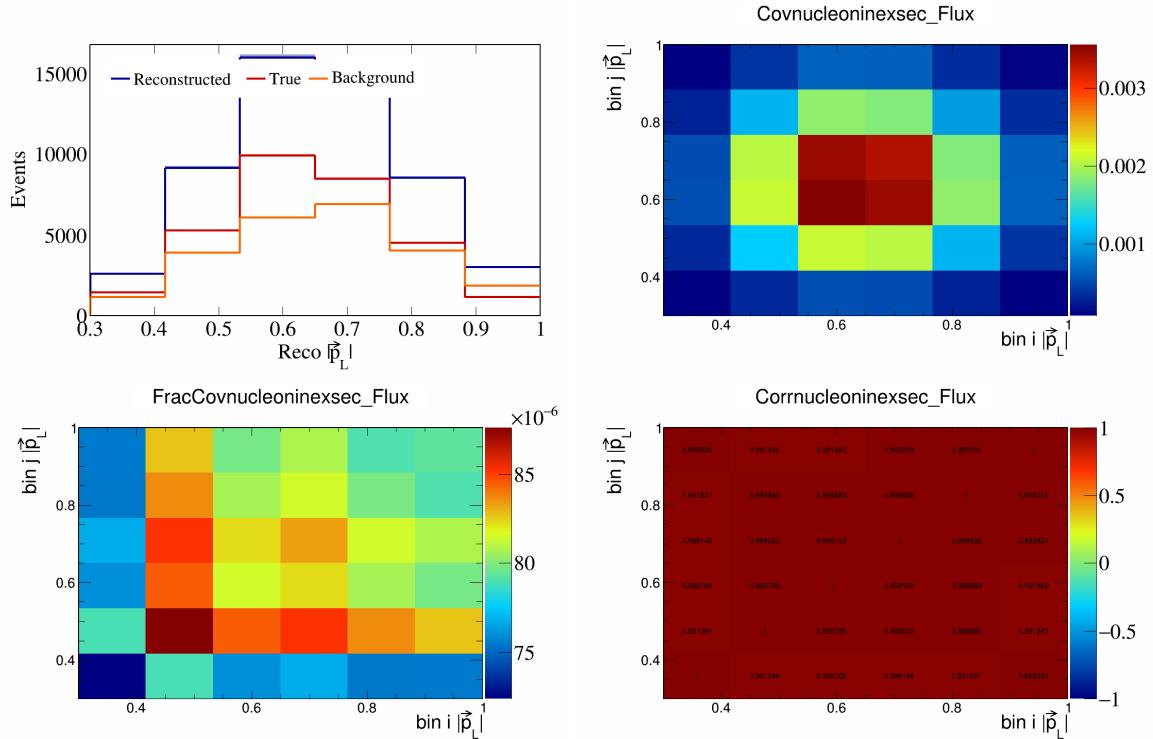


Figure 660: NucleonIneXSec variations for $|\vec{p}_L|$.

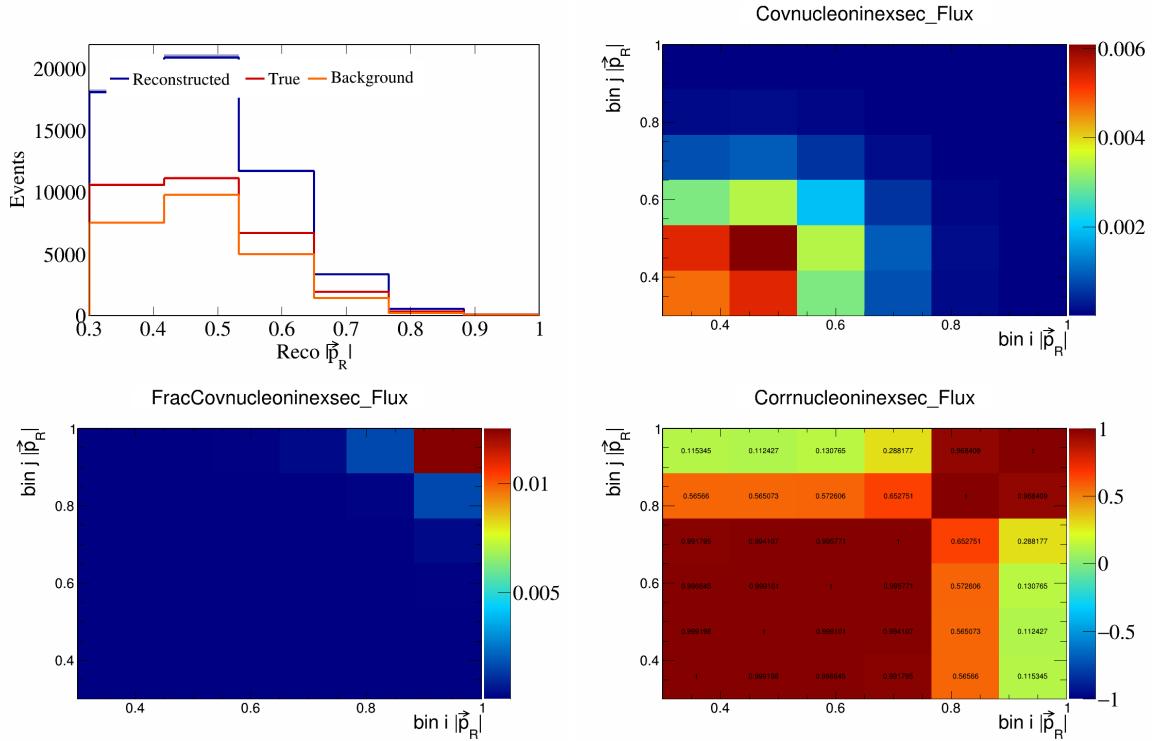


Figure 661: NucleonIneXSec variations for $|\vec{p}_R|$.

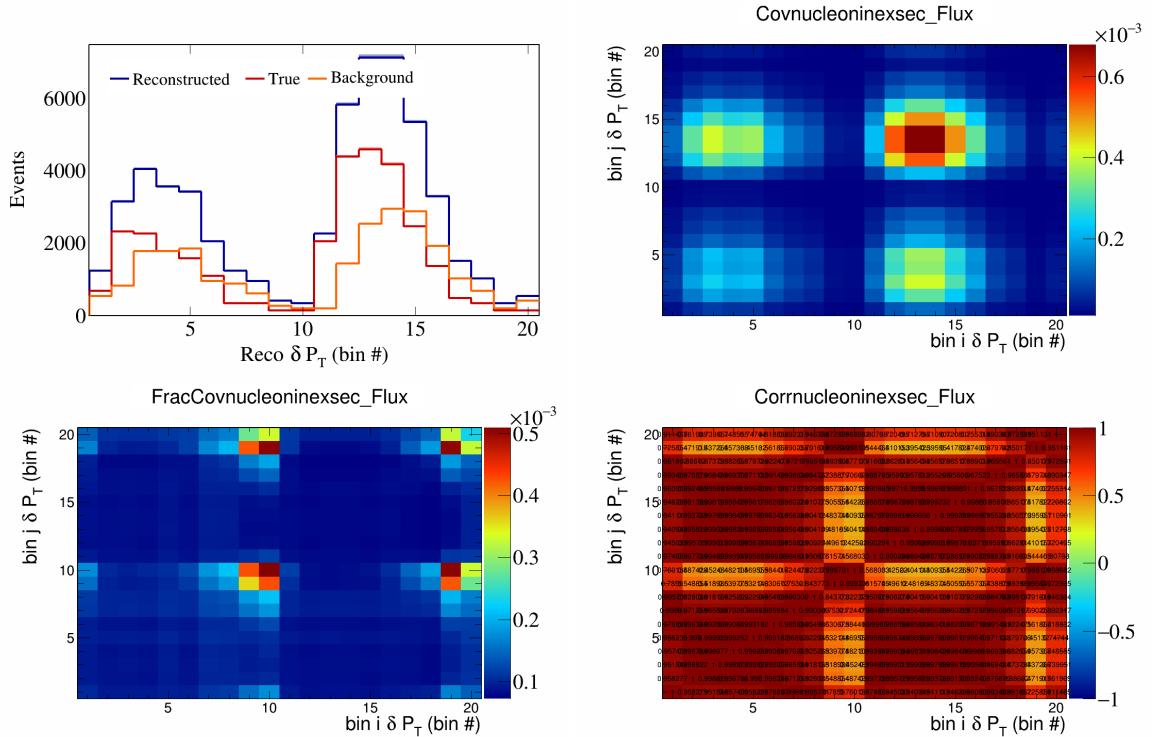


Figure 662: NucleonIneXSec variations for δP_T in $\cos(\theta_{\vec{p}_\mu})$.

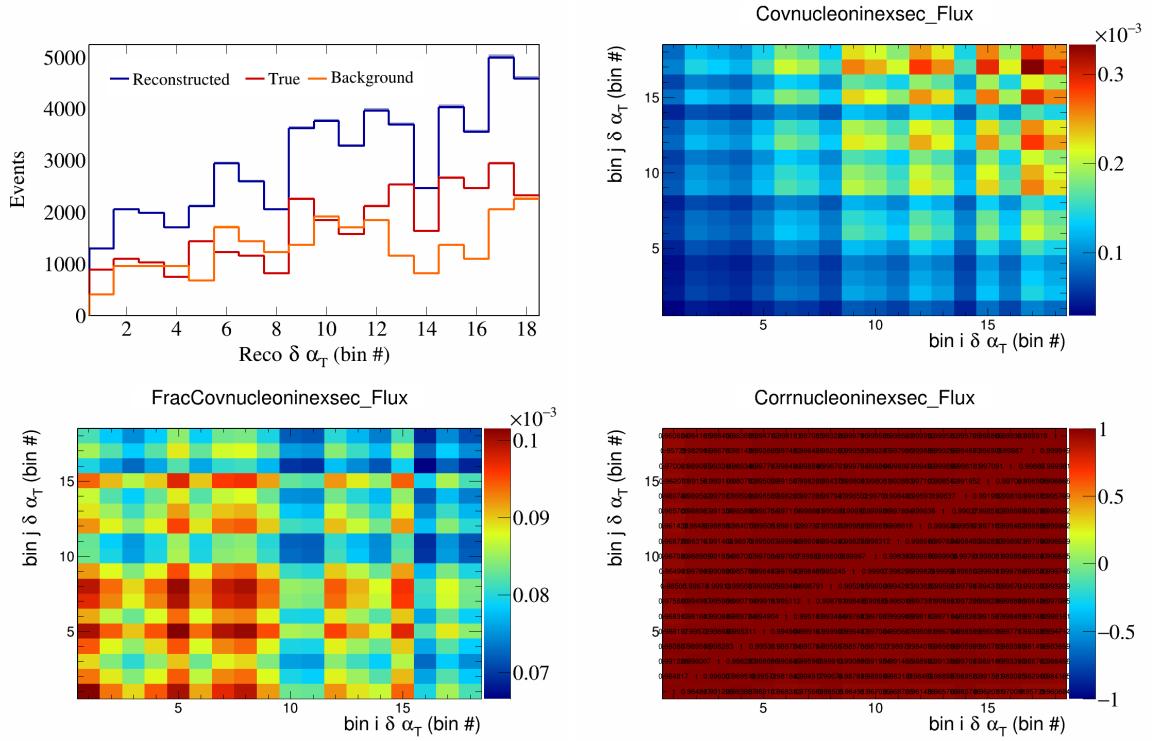


Figure 663: NucleonIneXSec variations for $\delta\alpha_T$ in $\cos(\theta_{\vec{p}_\mu})$.

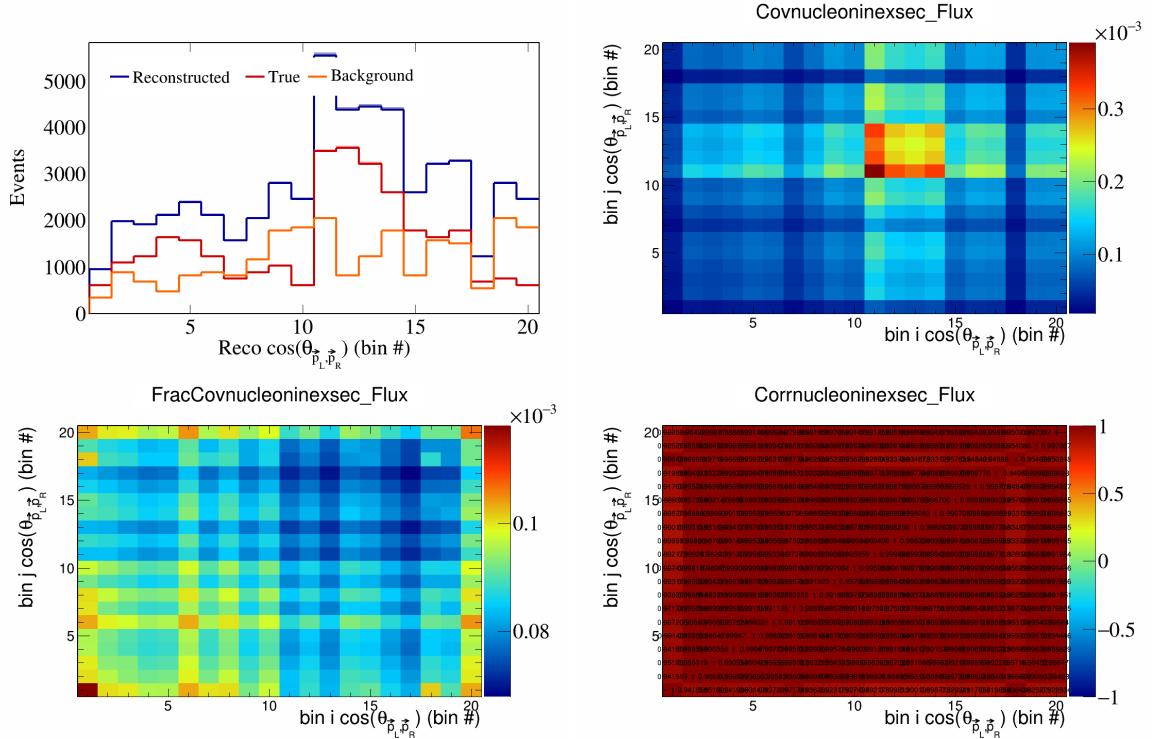


Figure 664: NucleonIneXSec variations for $\cos(\theta_{\vec{p}_L, \vec{p}_R})$ in $\cos(\theta_{\vec{p}_\mu})$.

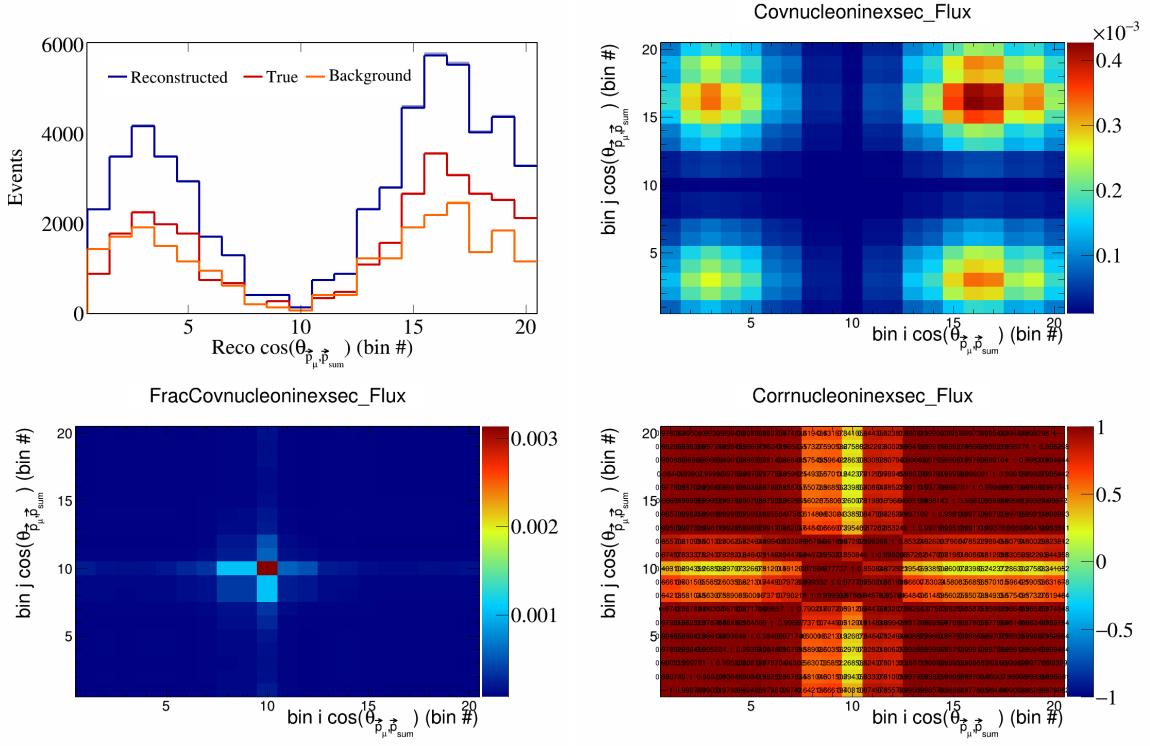


Figure 665: NucleonIneXSec variations for $\cos(\theta_{\vec{p}_\mu, \vec{p}_{\text{sum}}})$ in $\cos(\theta_{\vec{p}_\mu})$.

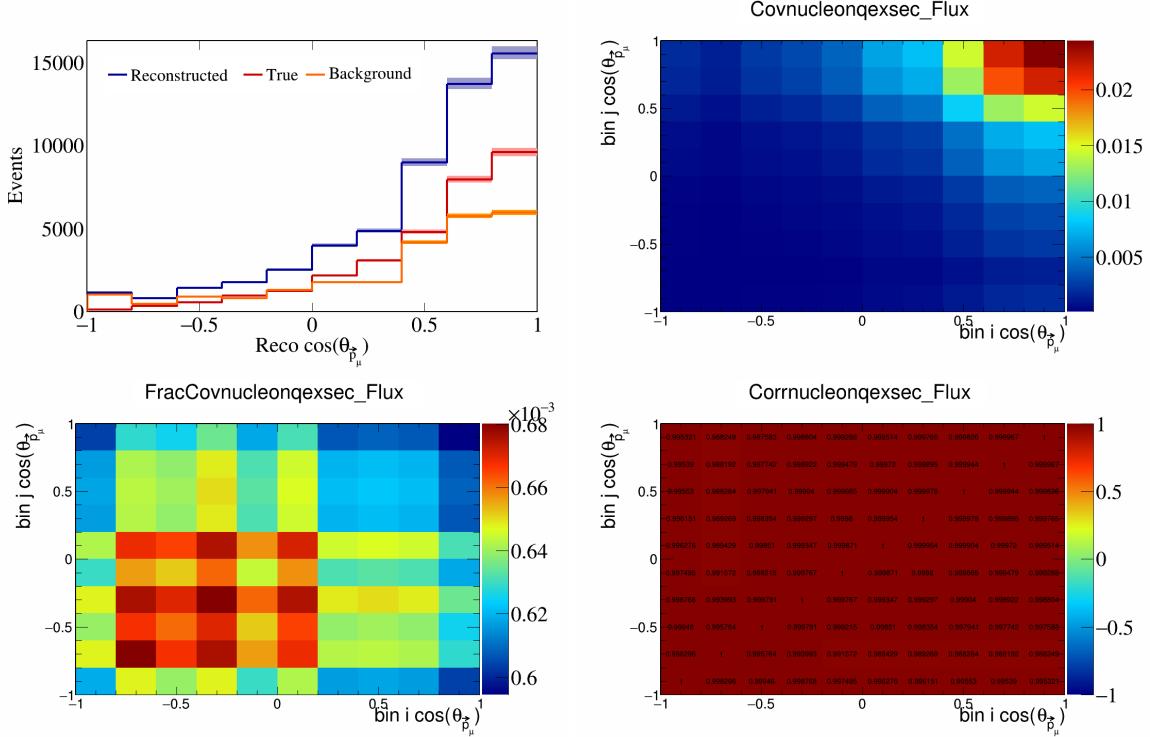


Figure 666: NucleonQeXSec variations for $\cos(\theta_{\vec{p}_\mu})$.

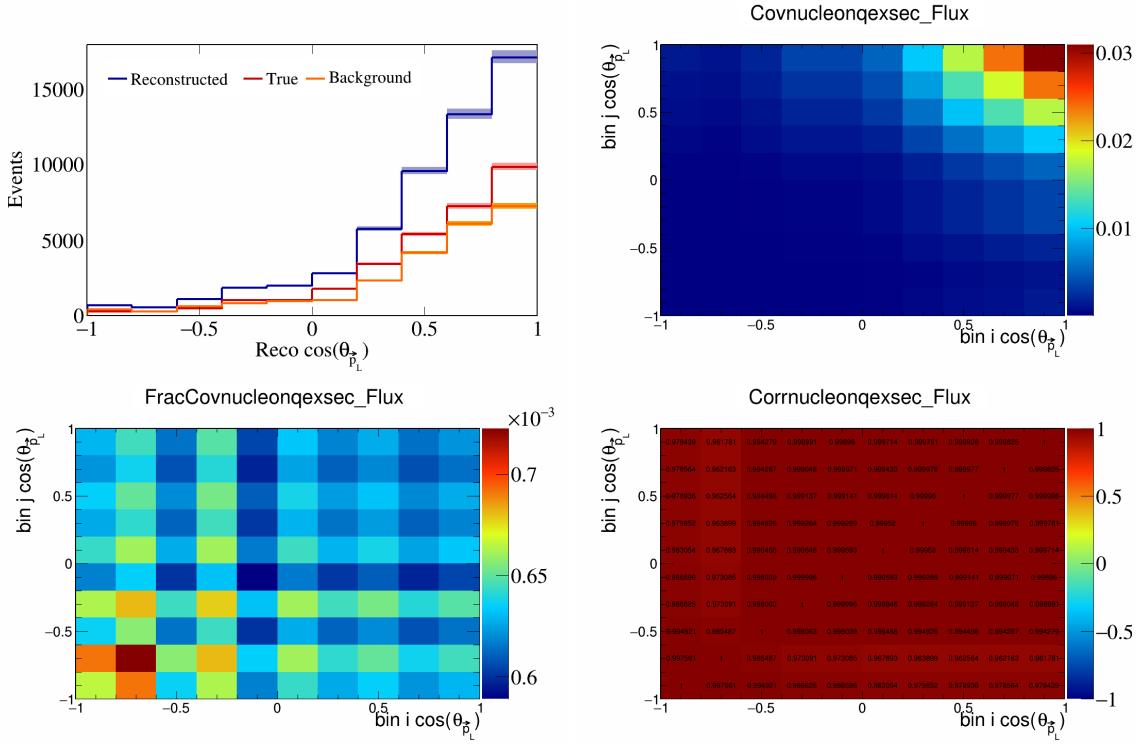


Figure 667: NucleonQeXSec variations for $\cos(\theta_{\vec{p}_L})$.

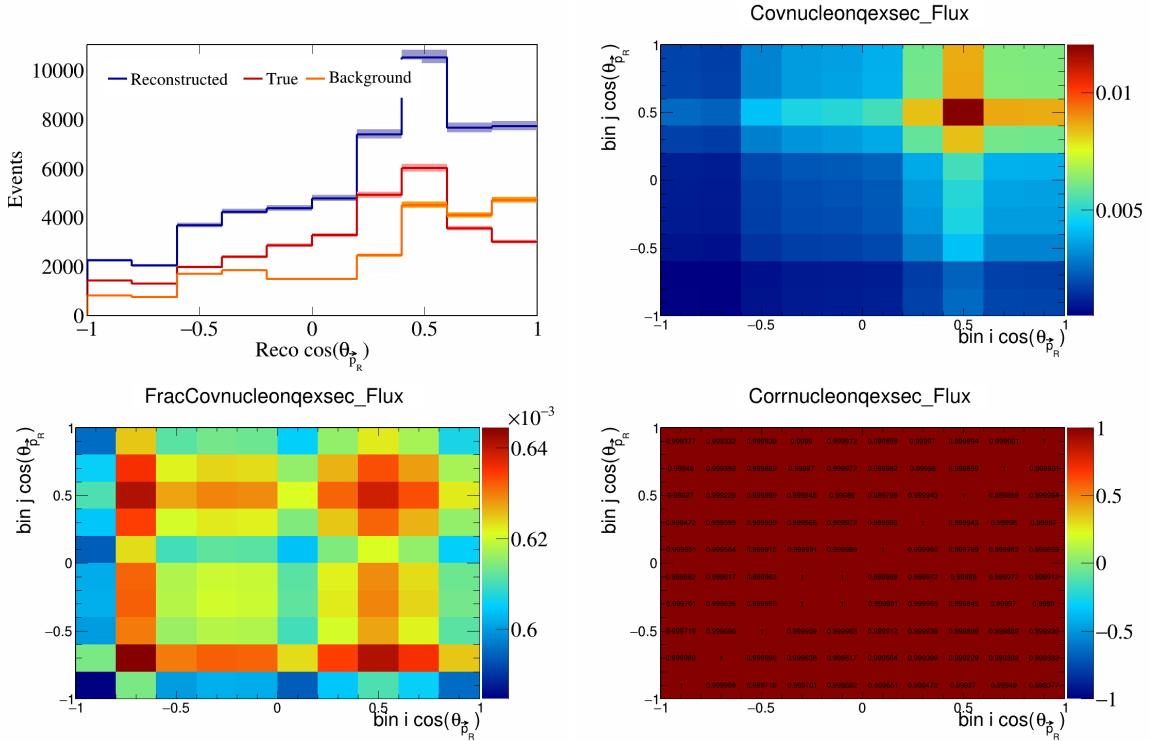


Figure 668: NucleonQeXSec variations for $\cos(\theta_{\vec{p}_R})$.

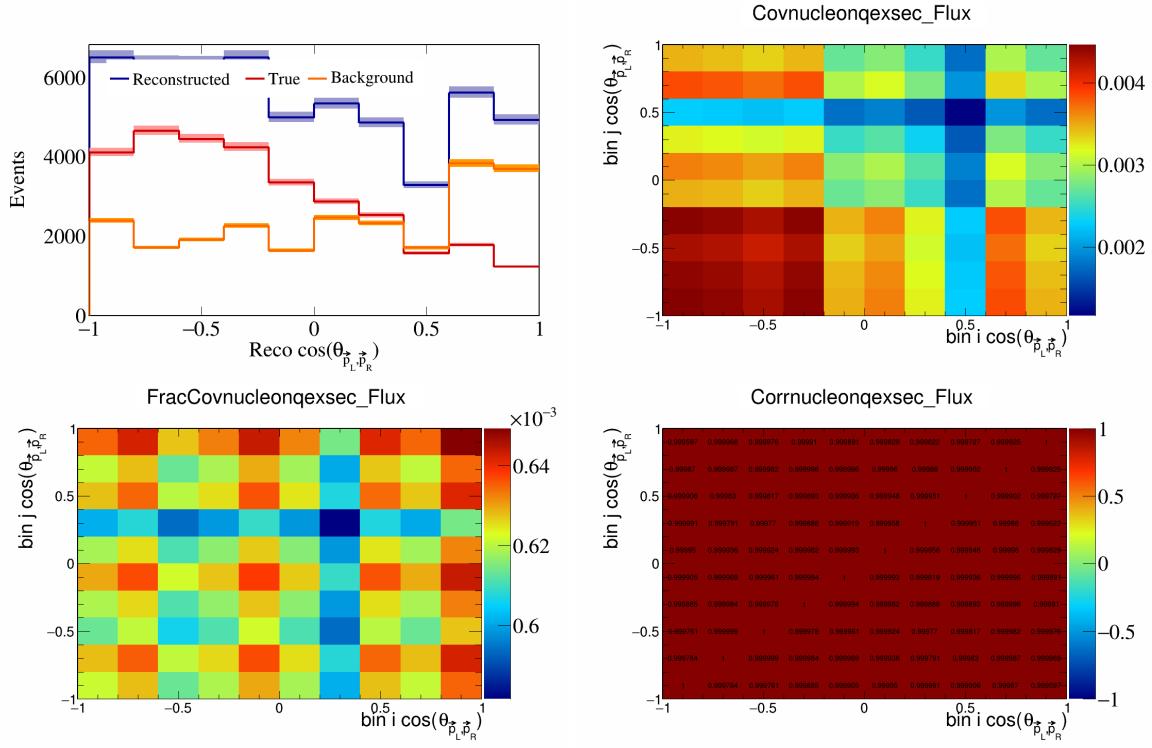


Figure 669: NucleonQeXSec variations for $\cos(\theta_{\vec{p}_L, \vec{p}_R})$.

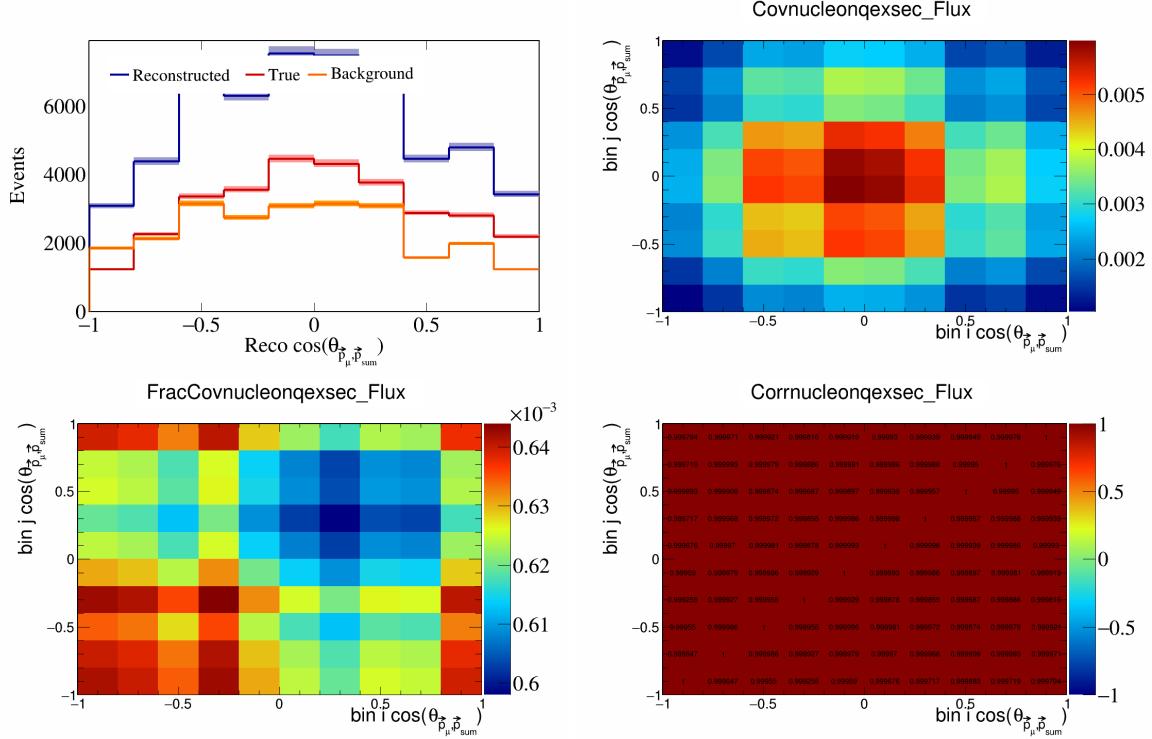


Figure 670: NucleonQeXSec variations for $\cos(\theta_{\vec{p}_\mu, \vec{p}_{\text{sum}}})$.

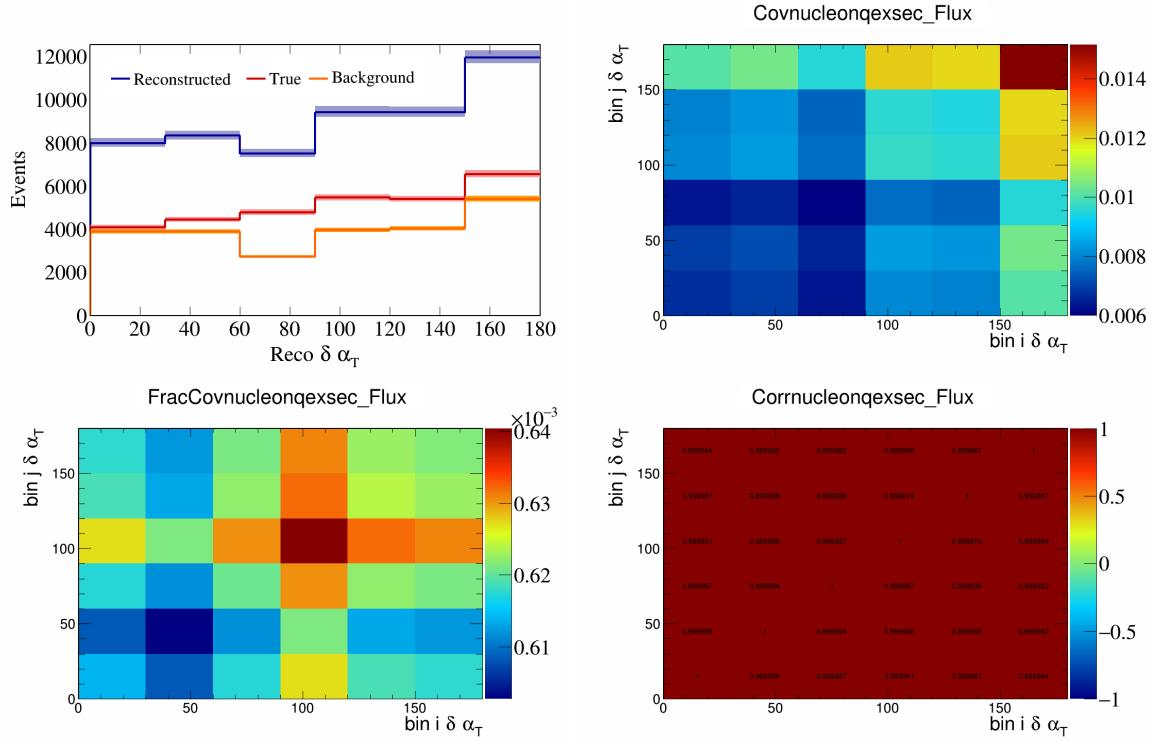


Figure 671: NucleonQeXSec variations for $\delta\alpha_T$.

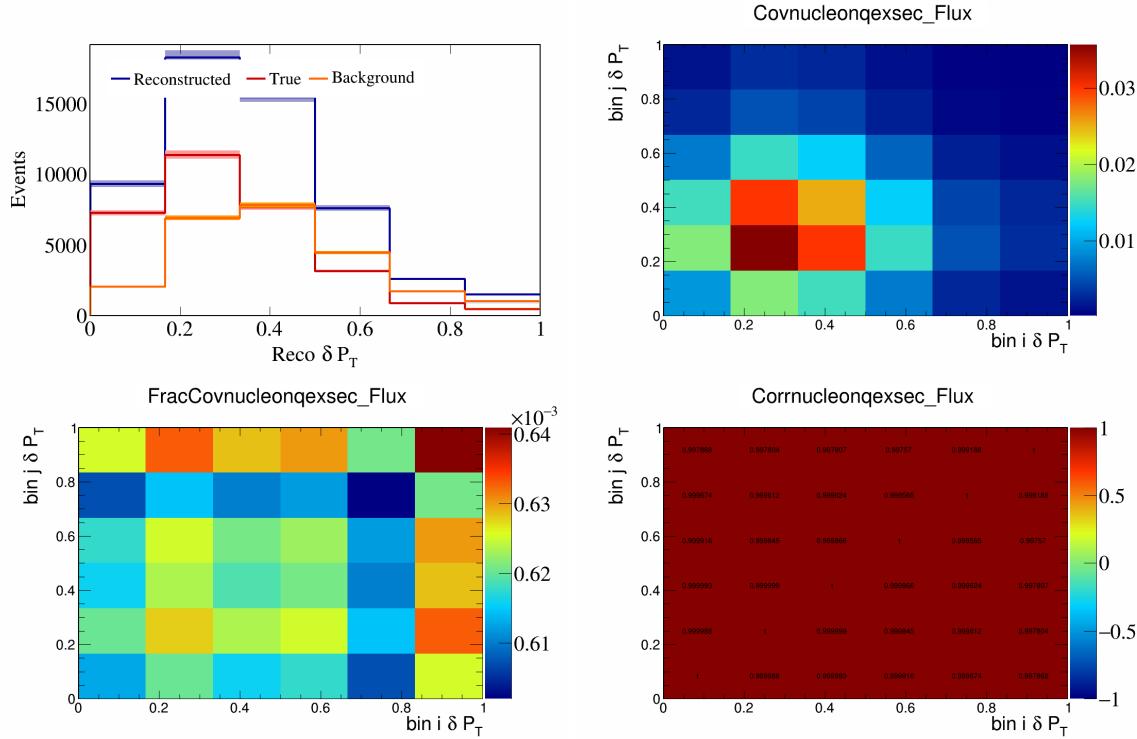


Figure 672: NucleonQeXSec variations for δP_T .

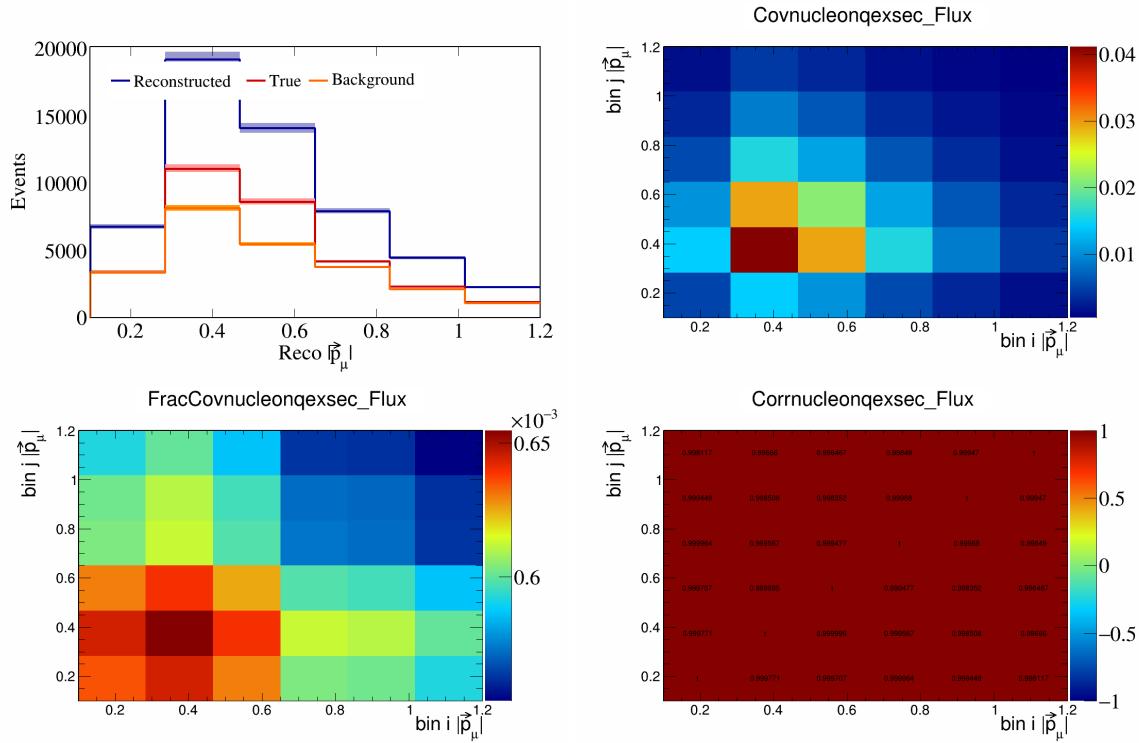


Figure 673: NucleonQeXSec variations for $|\vec{p}_\mu|$.

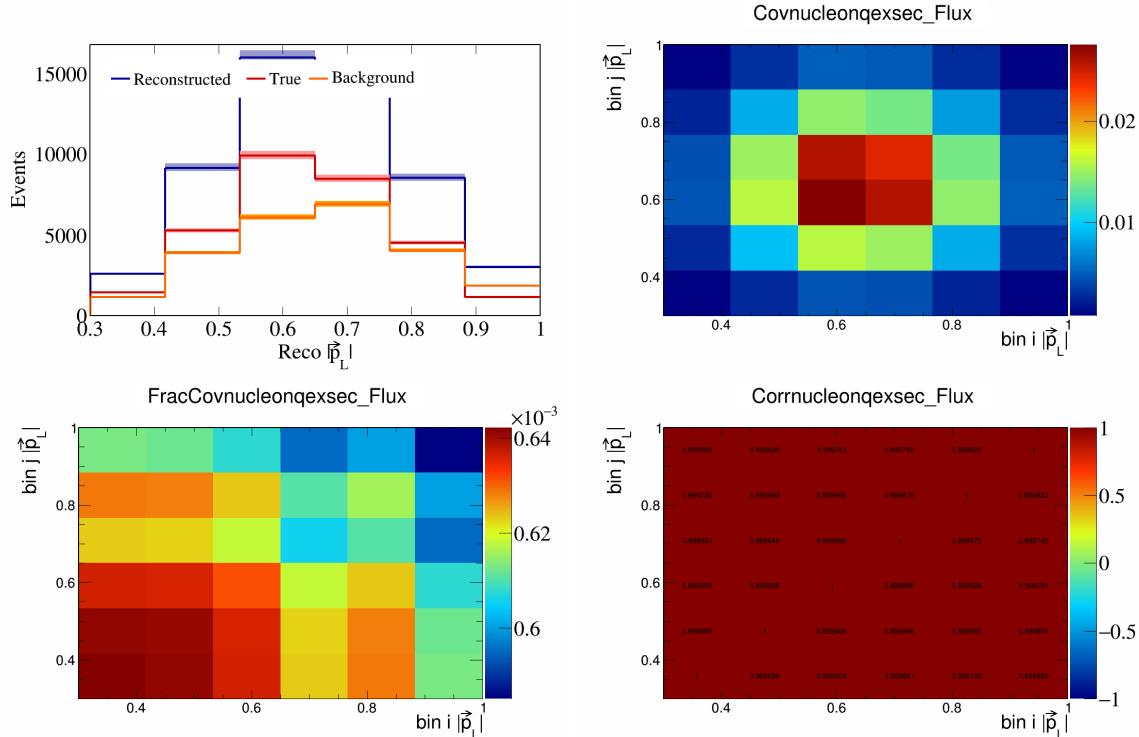


Figure 674: NucleonQeXSec variations for $|\vec{p}_L|$.

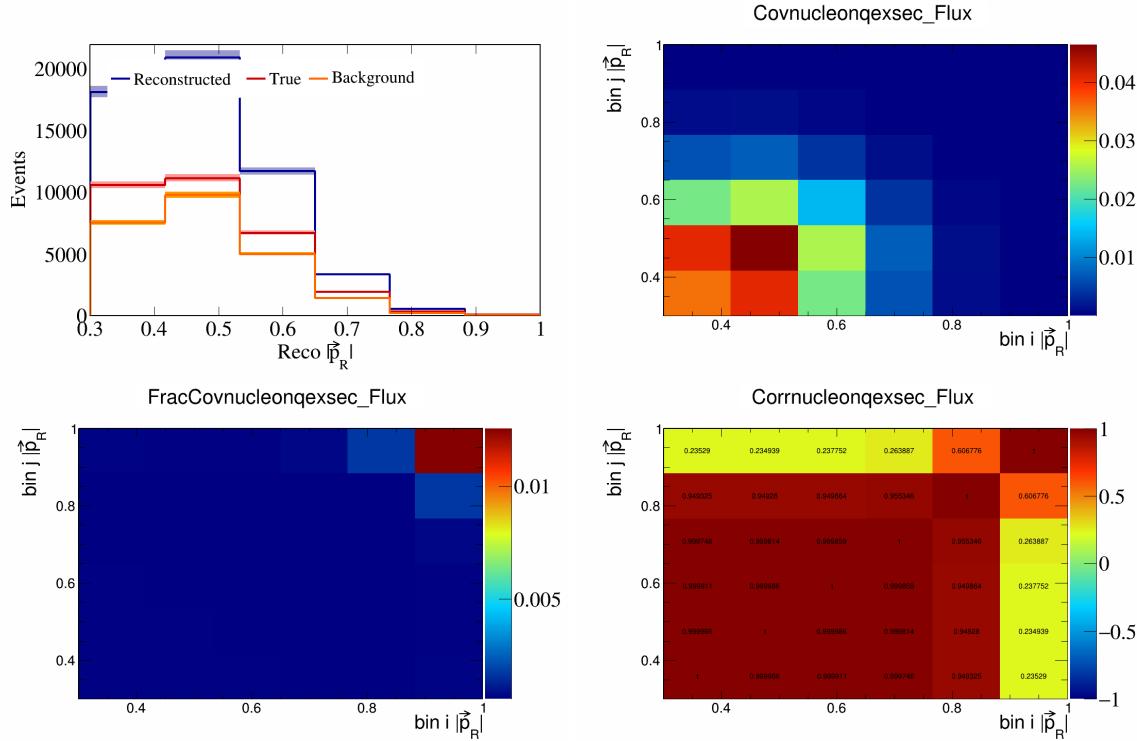


Figure 675: NucleonQeXSec variations for $|\vec{p}_R|$.

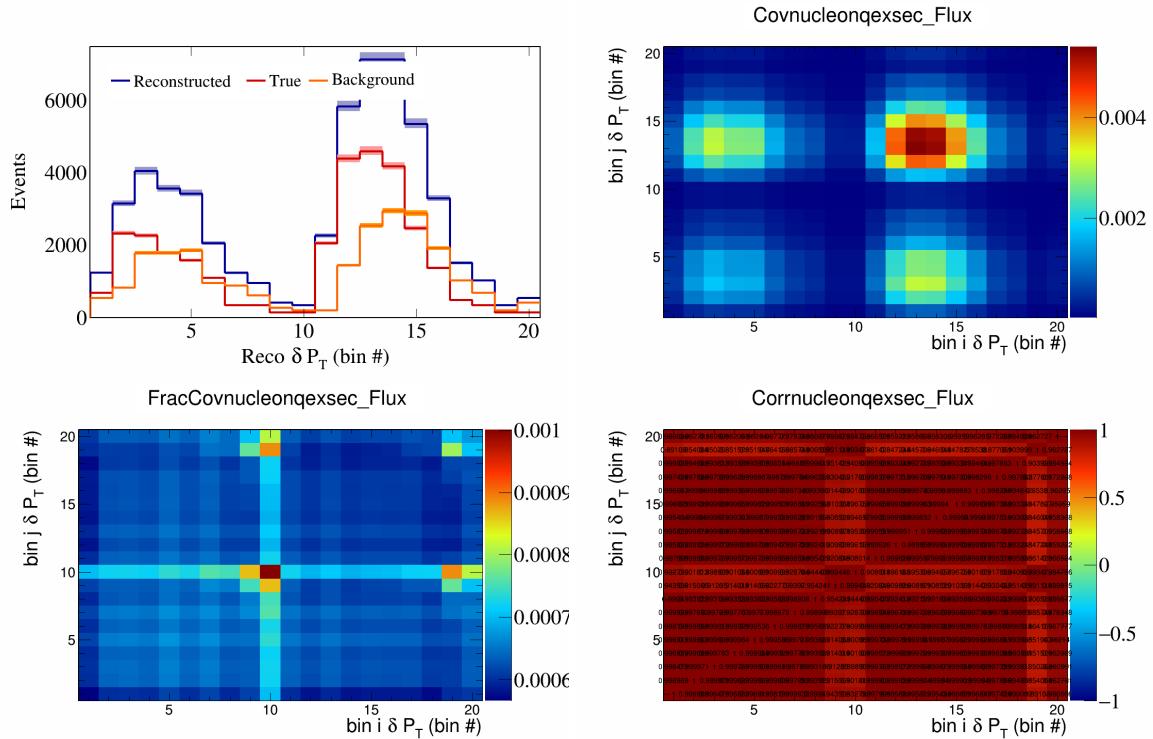


Figure 676: NucleonQeXSec variations for δP_T in $\cos(\theta_{\vec{p}_\mu})$.

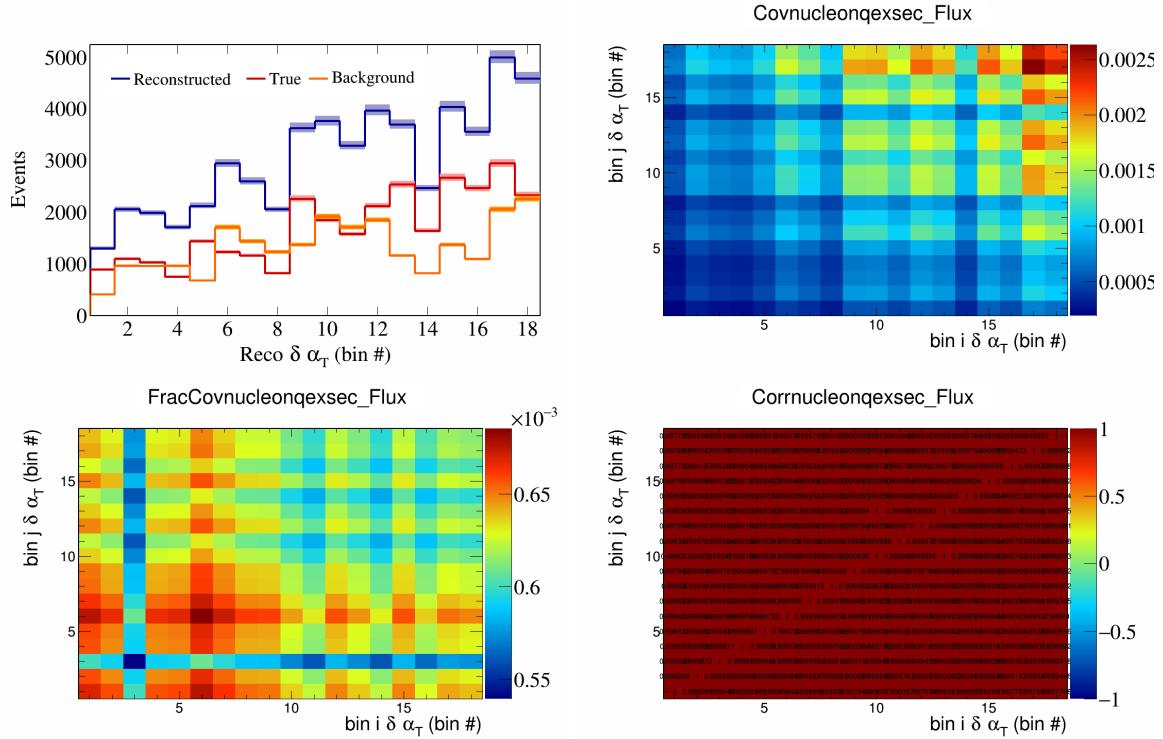


Figure 677: NucleonQeXSec variations for $\delta\alpha_T$ in $\cos(\theta_{\vec{p}_\mu})$.

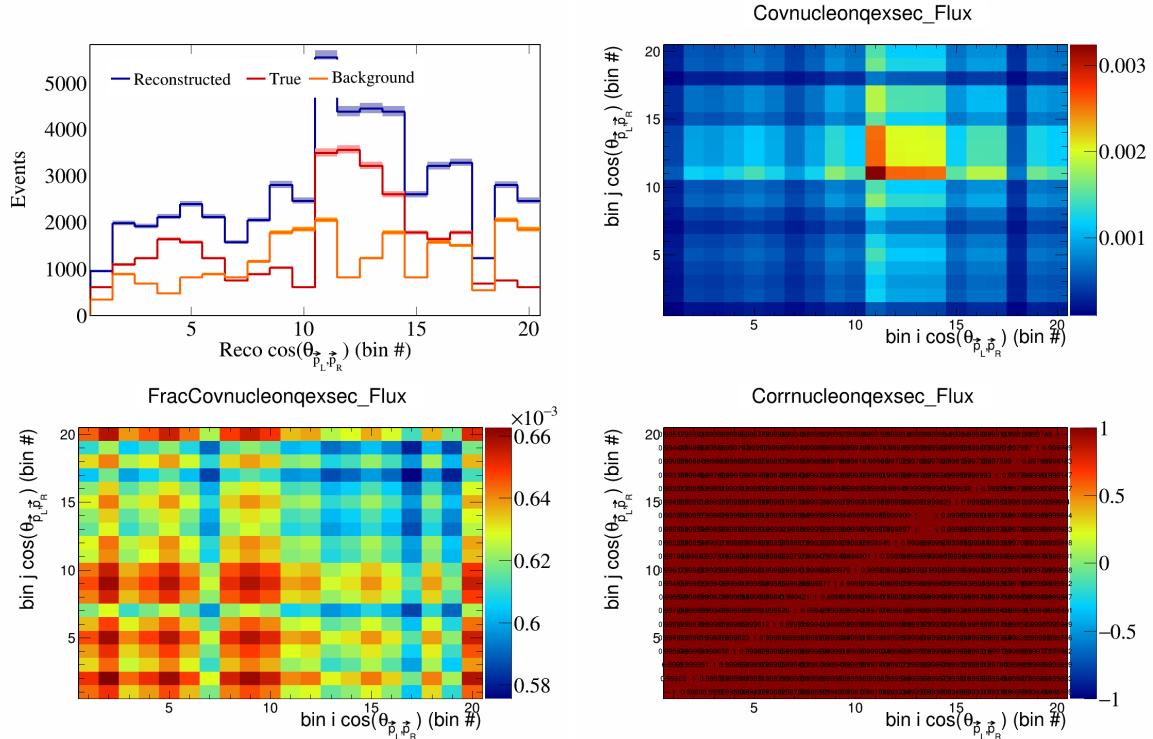


Figure 678: NucleonQeXSec variations for $\cos(\theta_{\vec{p}_L, \vec{p}_R})$ in $\cos(\theta_{\vec{p}_\mu})$.

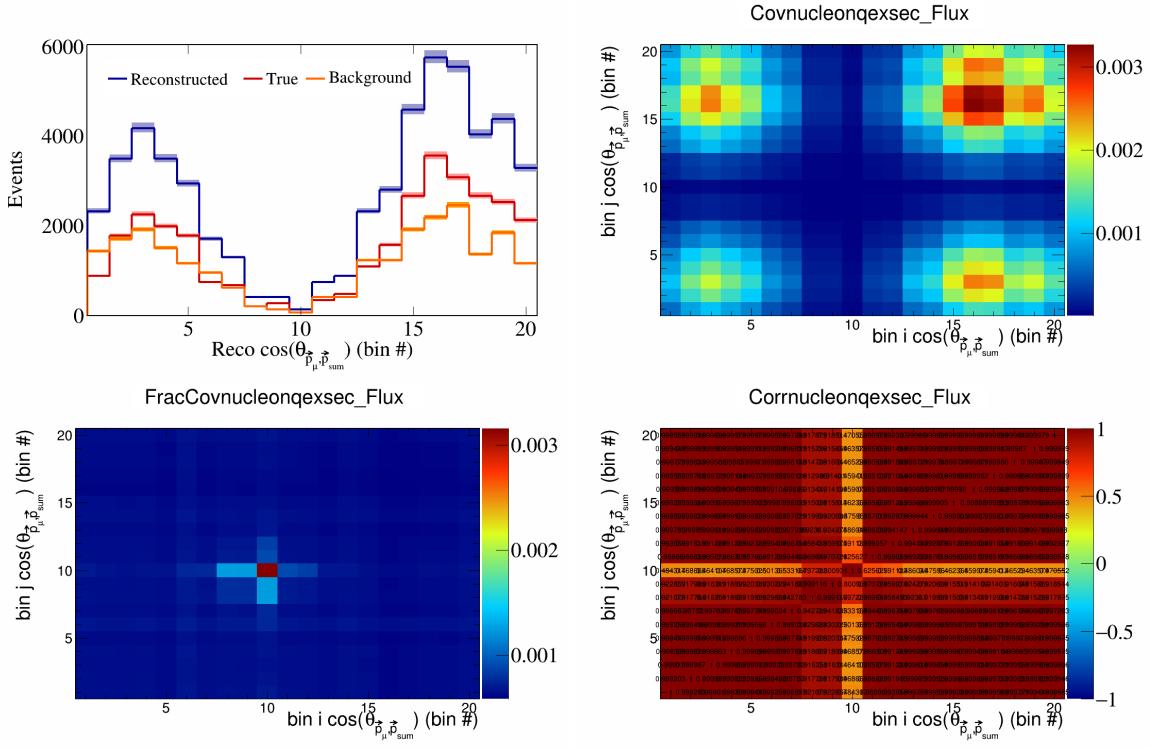


Figure 679: NucleonQeXSec variations for $\cos(\theta_{\vec{p}_\mu, \vec{p}_{\text{sum}}})$ in $\cos(\theta_{\vec{p}_\mu})$.

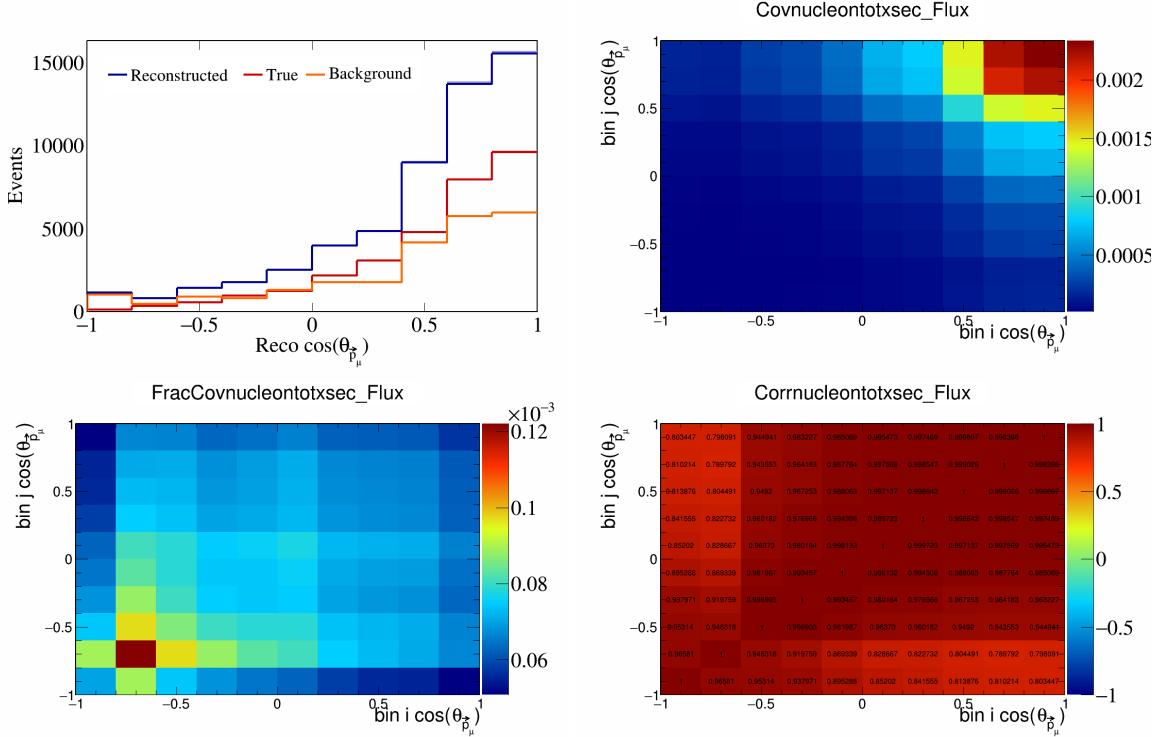


Figure 680: NucleonTotXSec variations for $\cos(\theta_{\vec{p}_\mu})$.

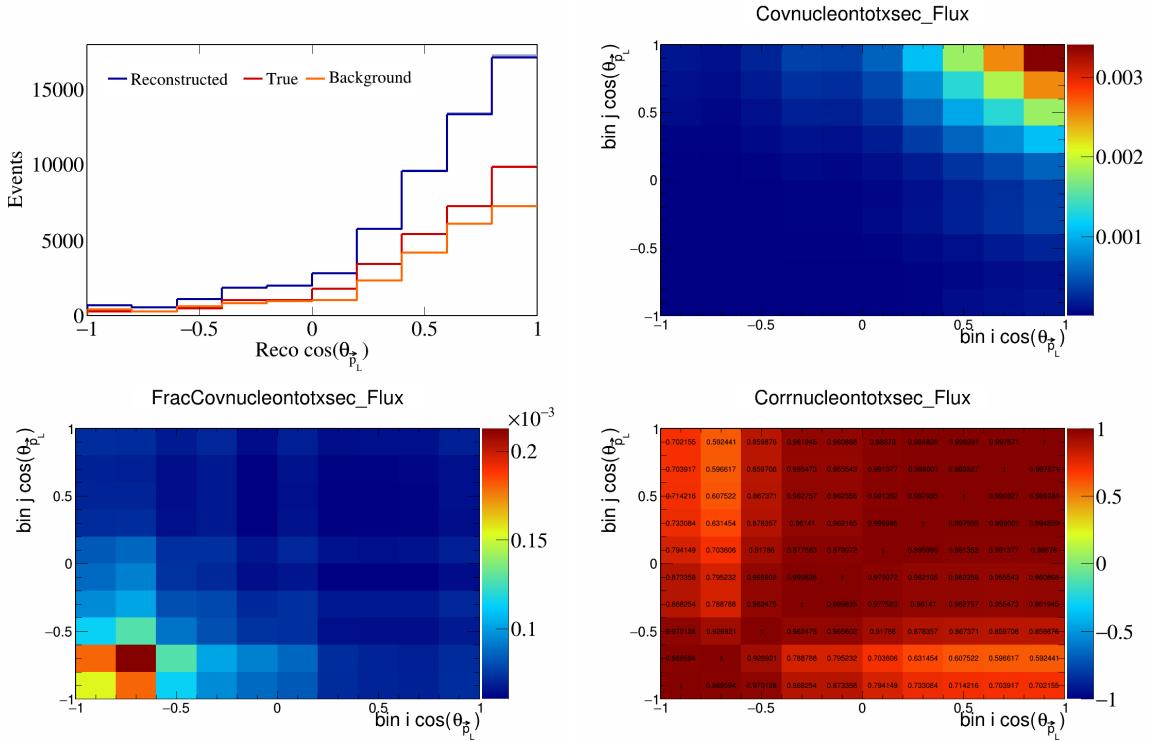


Figure 681: NucleonTotXSec variations for $\cos(\theta_{\vec{p}_L})$.

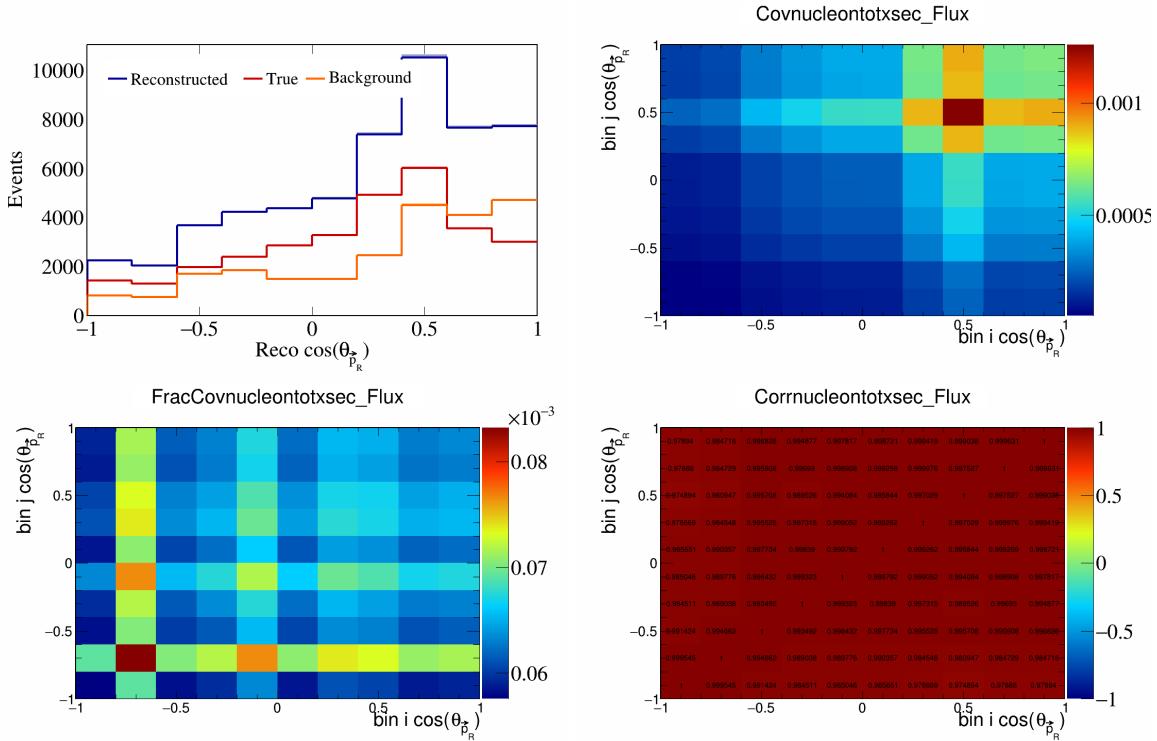


Figure 682: NucleonTotXSec variations for $\cos(\theta_{\vec{p}_R})$.

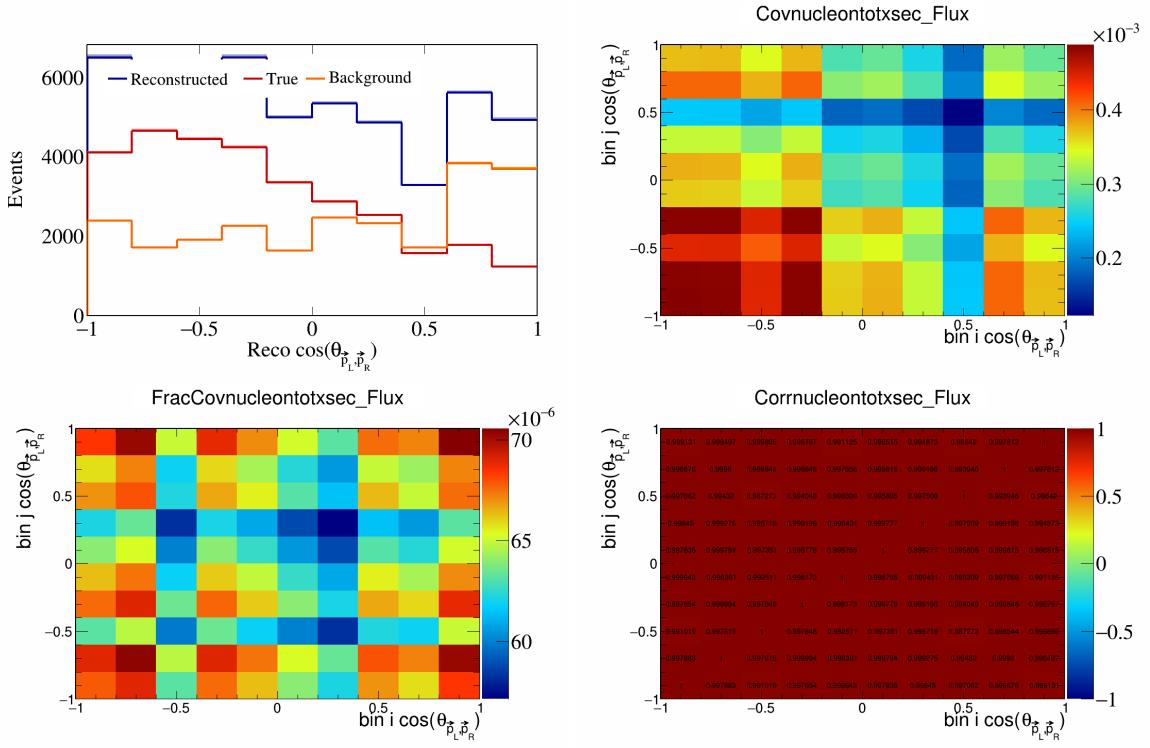


Figure 683: NucleonTotXSec variations for $\cos(\theta_{\vec{p}_L, \vec{p}_R})$.

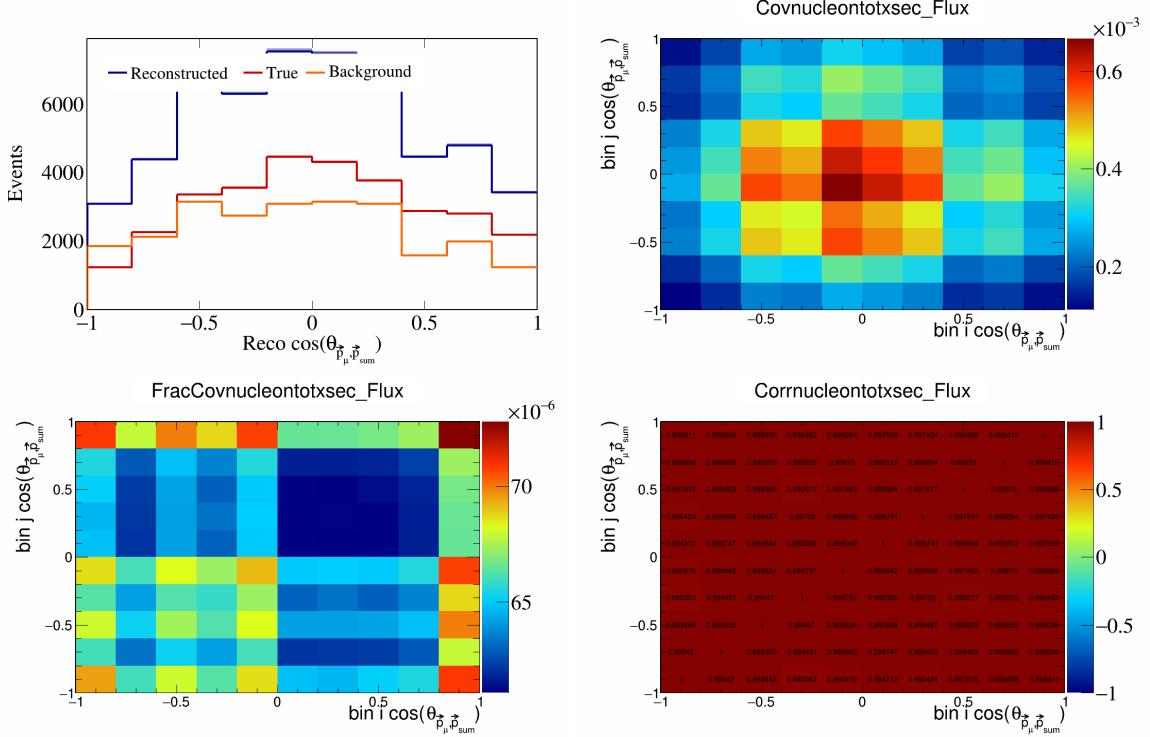


Figure 684: NucleonTotXSec variations for $\cos(\theta_{\vec{p}_\mu, \vec{p}_{\text{sum}}})$.

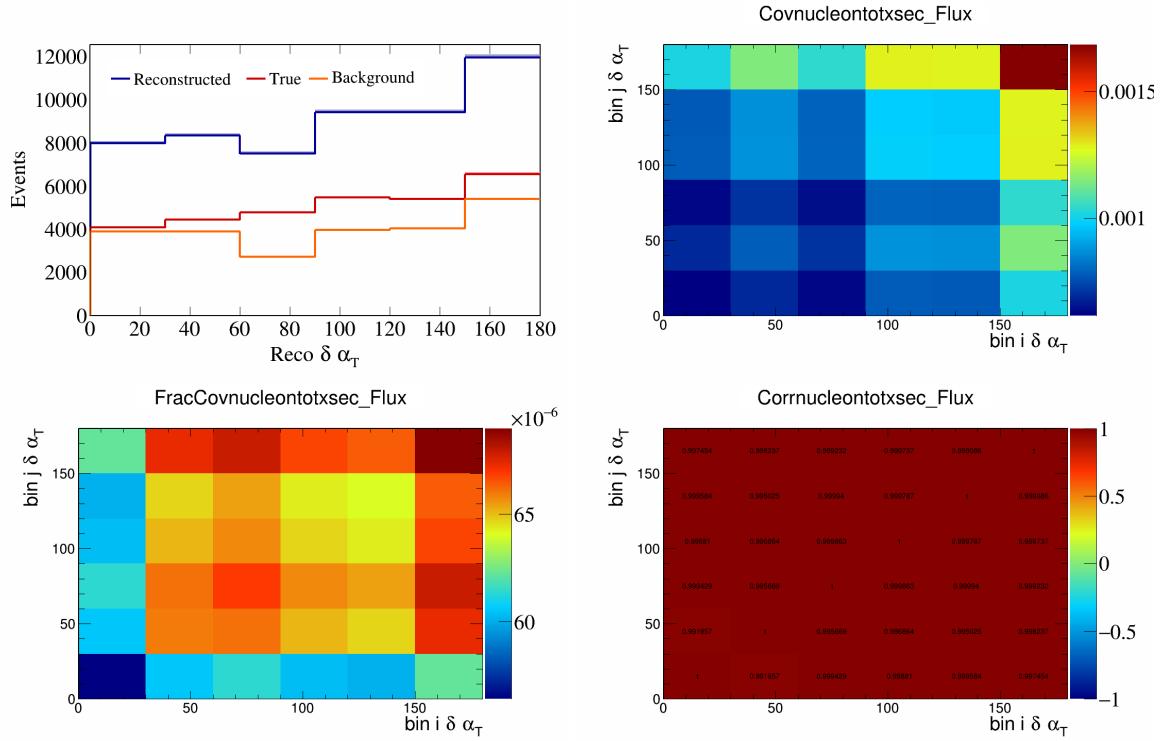


Figure 685: NucleonTotXSec variations for $\delta \alpha_T$.

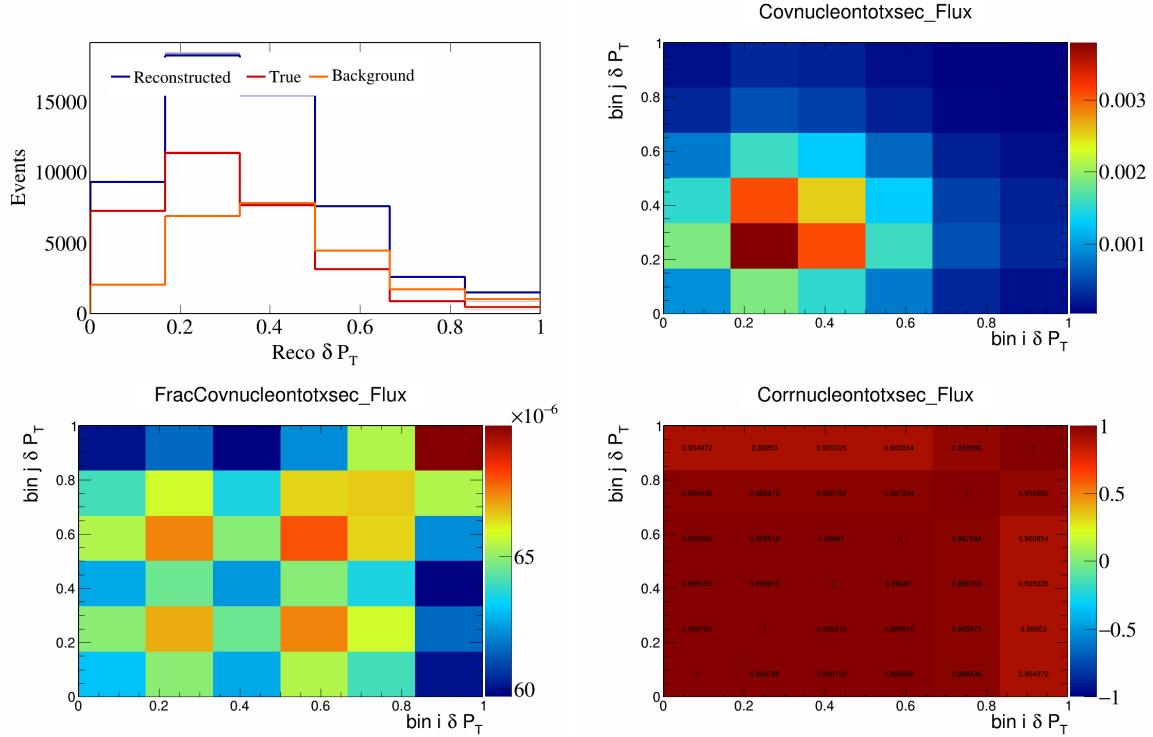


Figure 686: NucleonTotXSec variations for δP_T .

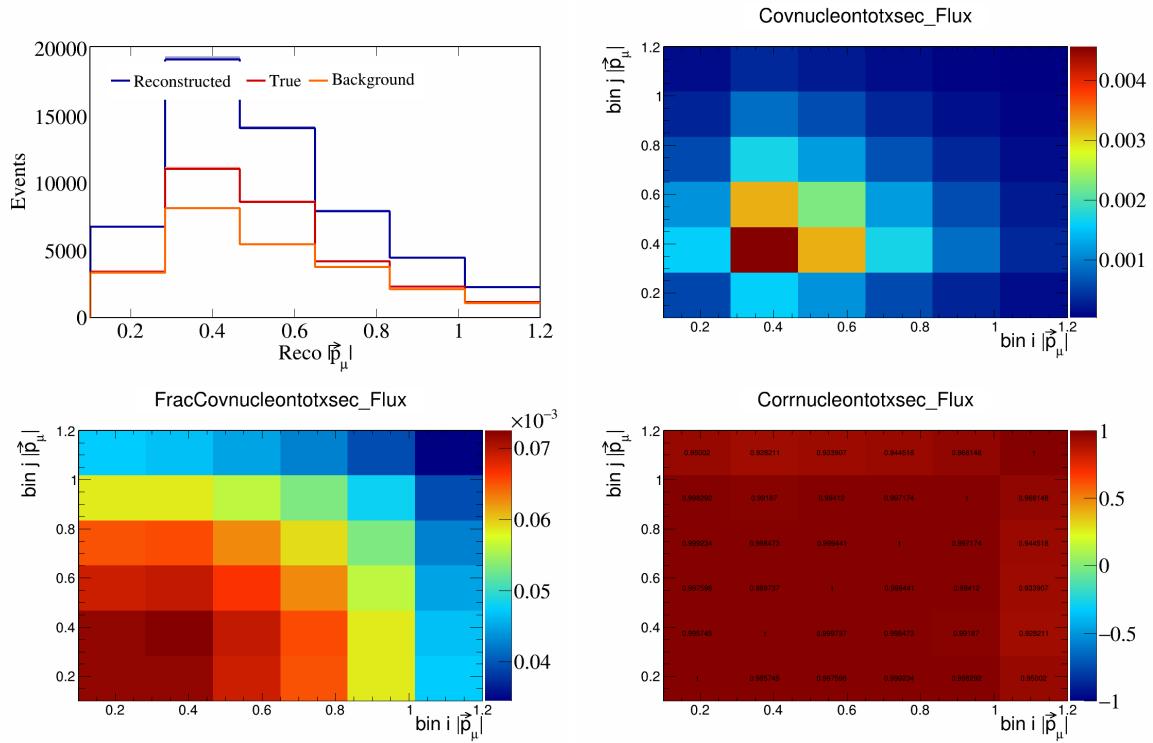


Figure 687: NucleonTotXSec variations for $|\vec{p}_\mu|$.

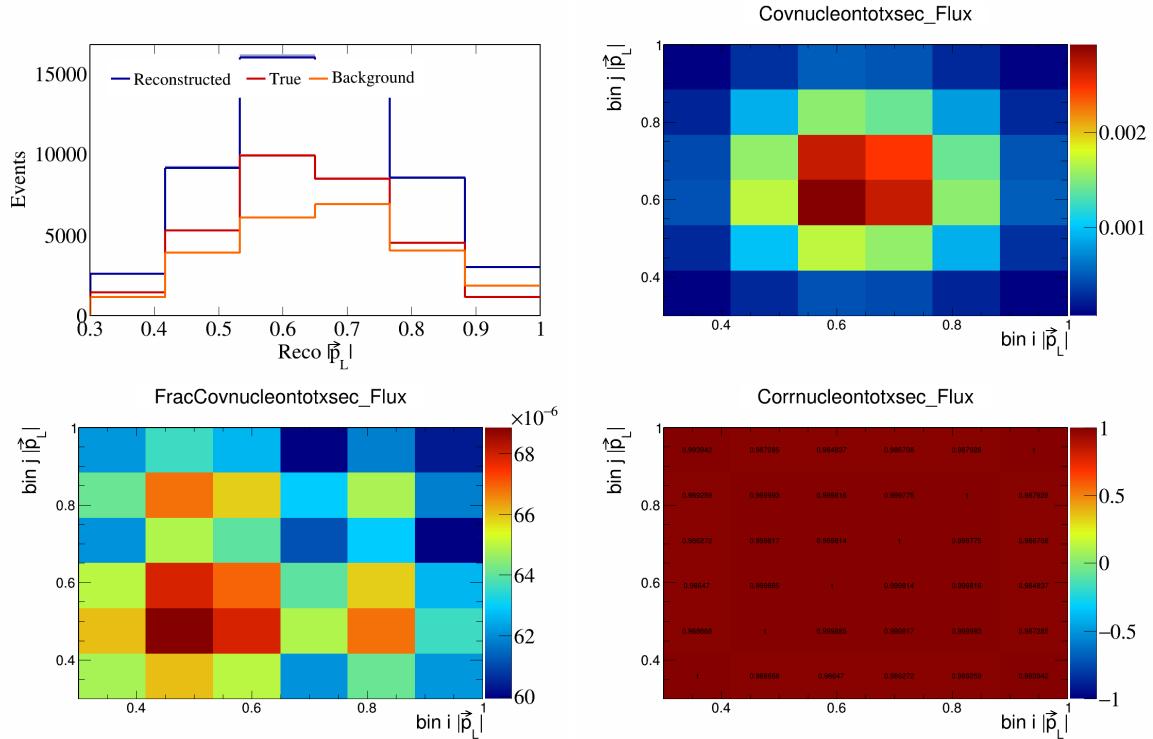


Figure 688: NucleonTotXSec variations for $|\vec{p}_L|$.

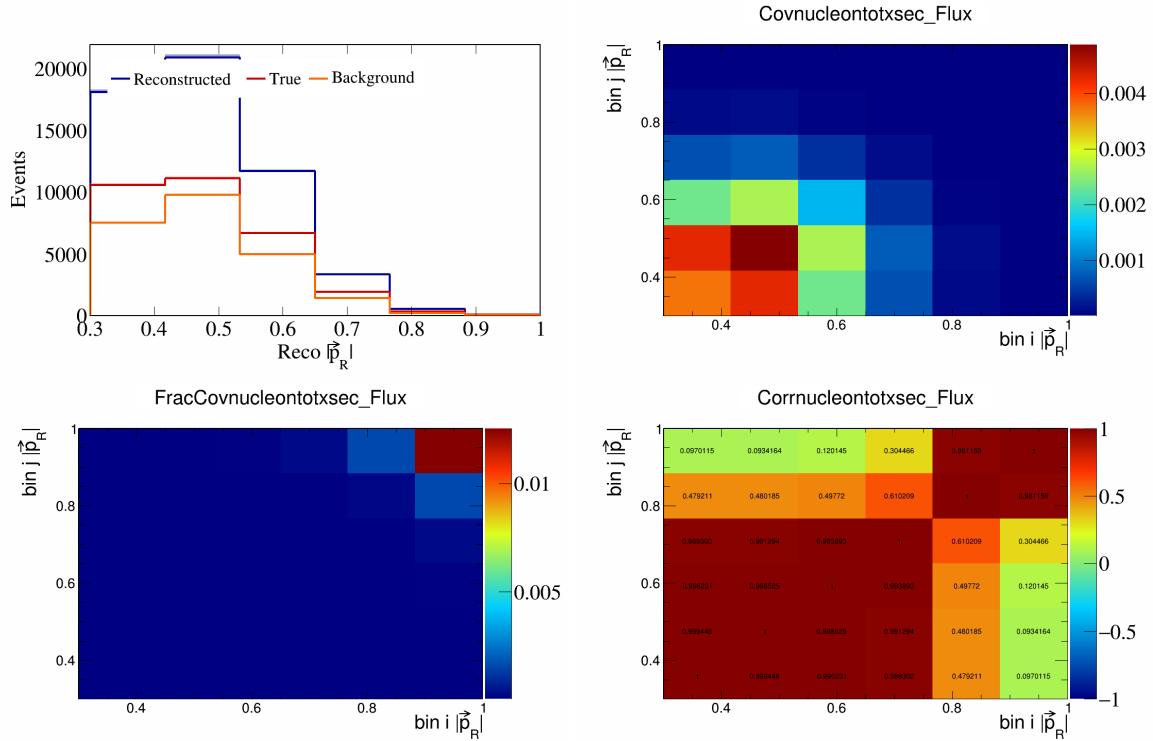


Figure 689: NucleonTotXSec variations for $|\vec{p}_R|$.

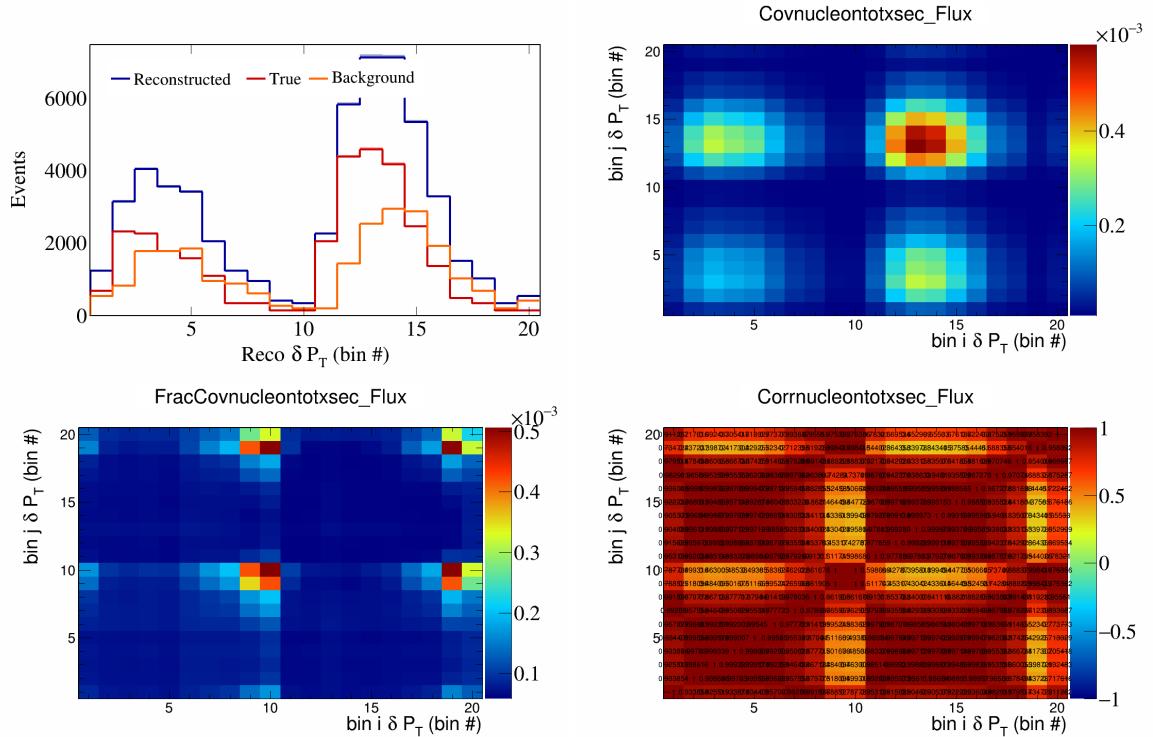


Figure 690: NucleonTotXSec variations for δP_T in $\cos(\theta_{\vec{p}_\mu})$.

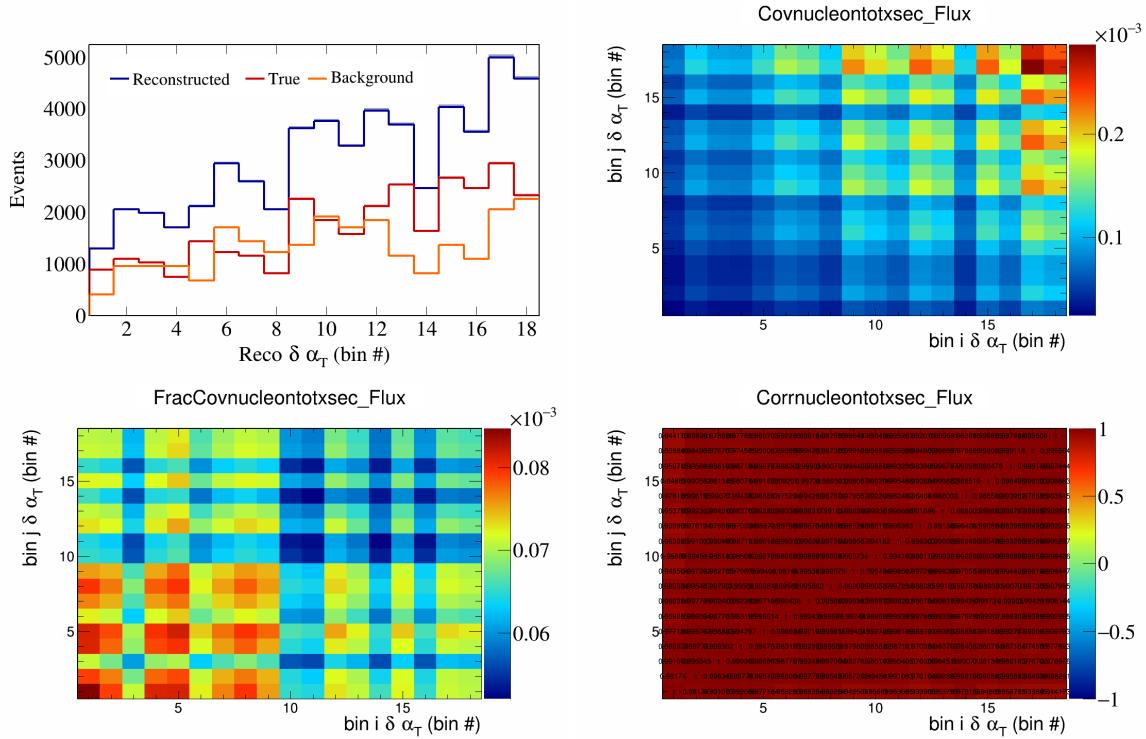


Figure 691: NucleonTotXSec variations for $\delta\alpha_T$ in $\cos(\theta_{\vec{p}_\mu})$.

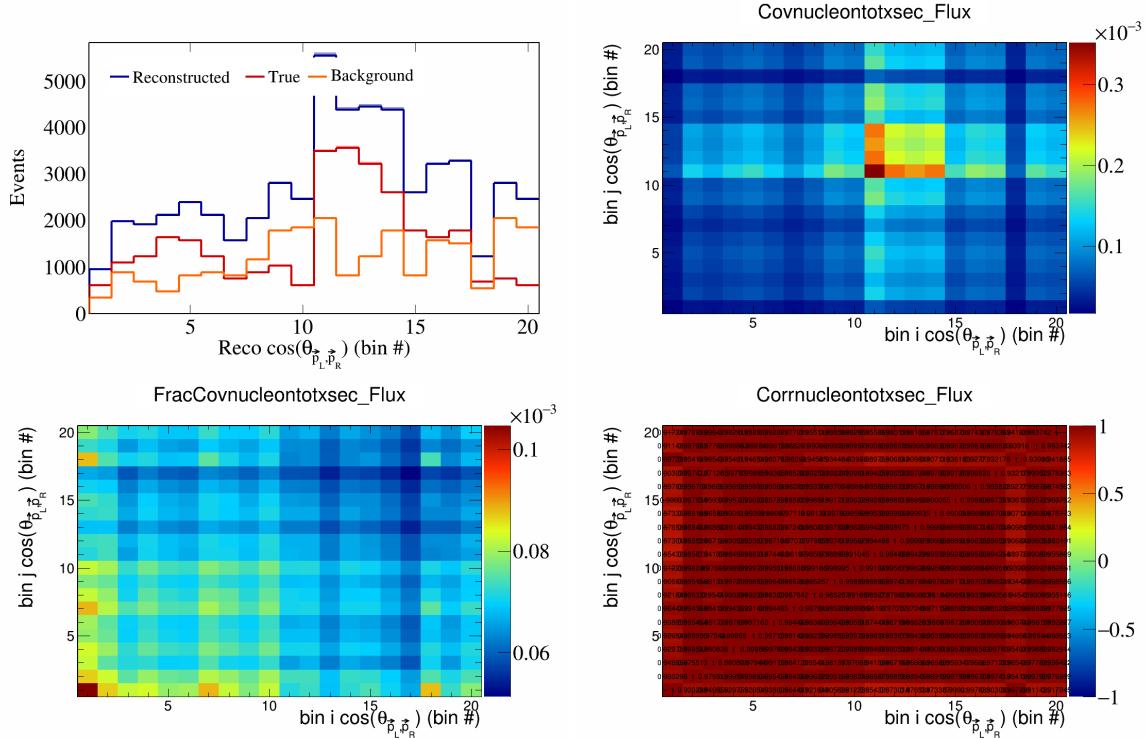


Figure 692: NucleonTotXSec variations for $\cos(\theta_{p_L, p_R})$ in $\cos(\theta_{\vec{p}_\mu})$.

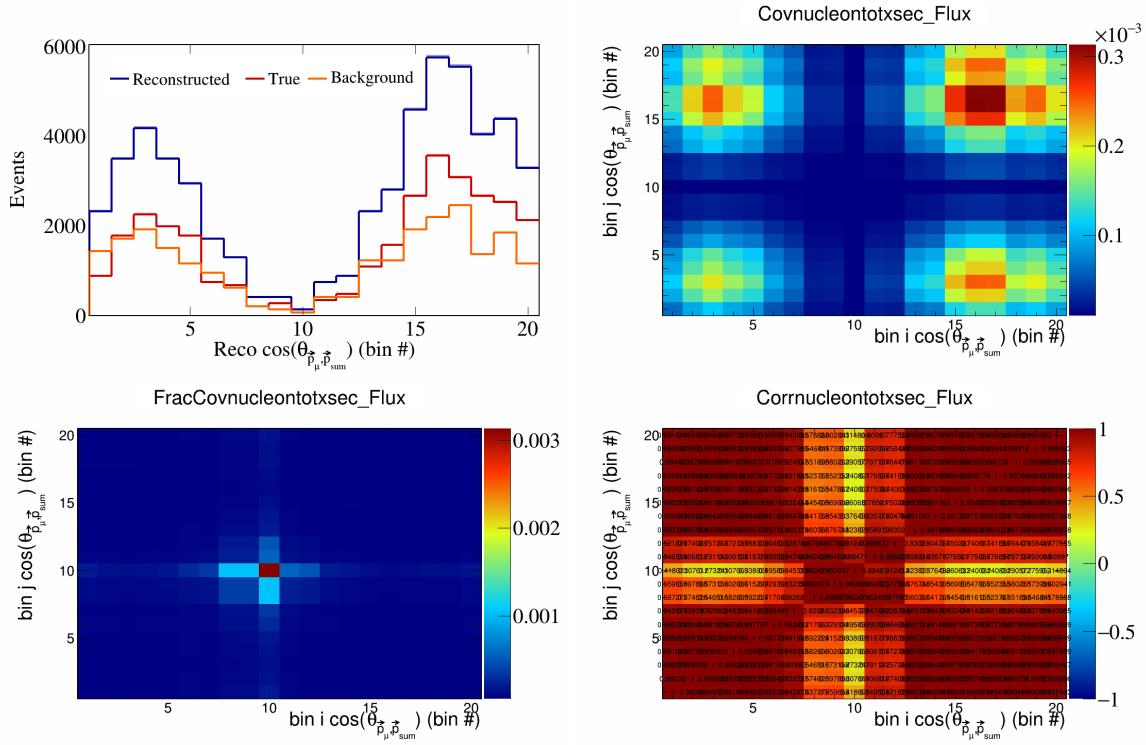


Figure 693: NucleonTotXSec variations for $\cos(\theta_{\vec{p}_\mu, \vec{p}_{\text{sum}}})$ in $\cos(\theta_{\vec{p}_\mu})$.

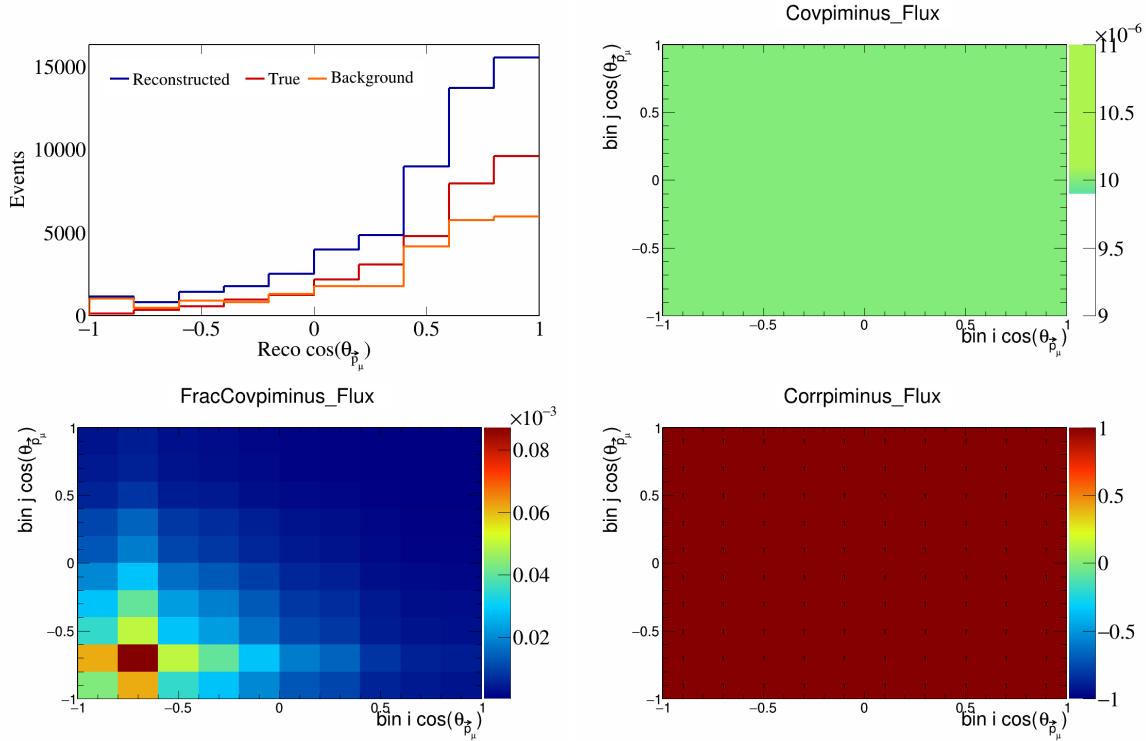


Figure 694: PiMinus variations for $\cos(\theta_{\vec{p}_\mu})$.

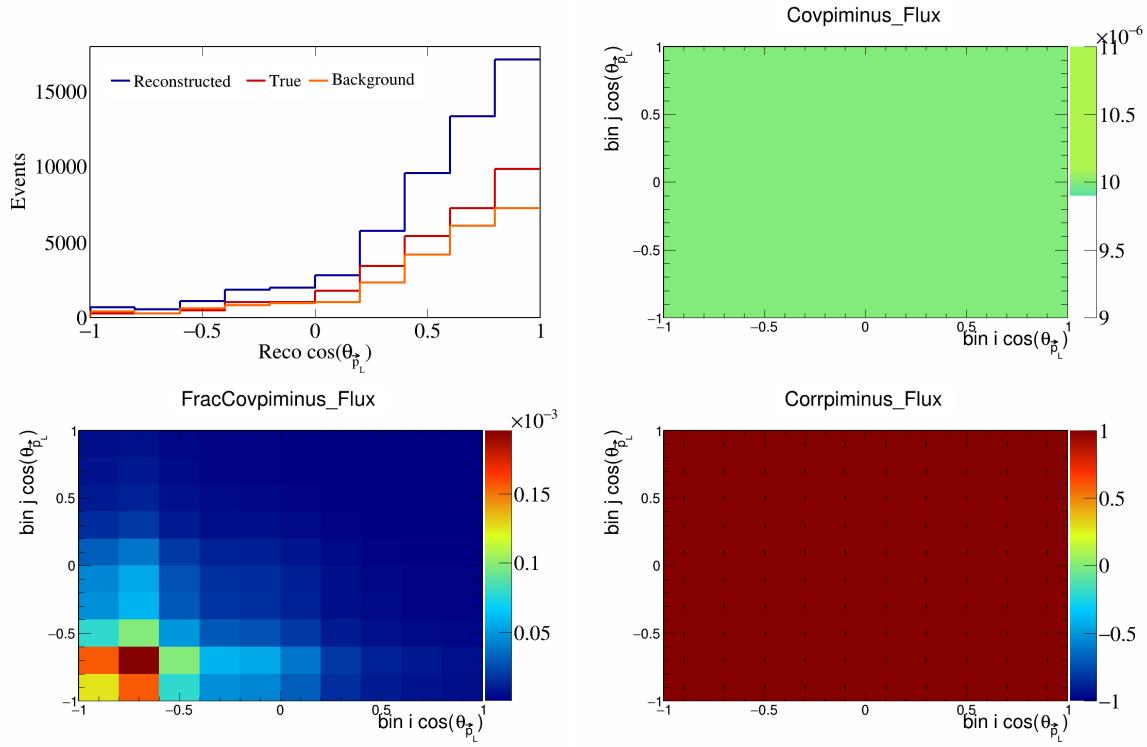


Figure 695: PiMinus variations for $\cos(\theta_{\vec{p}_L})$.

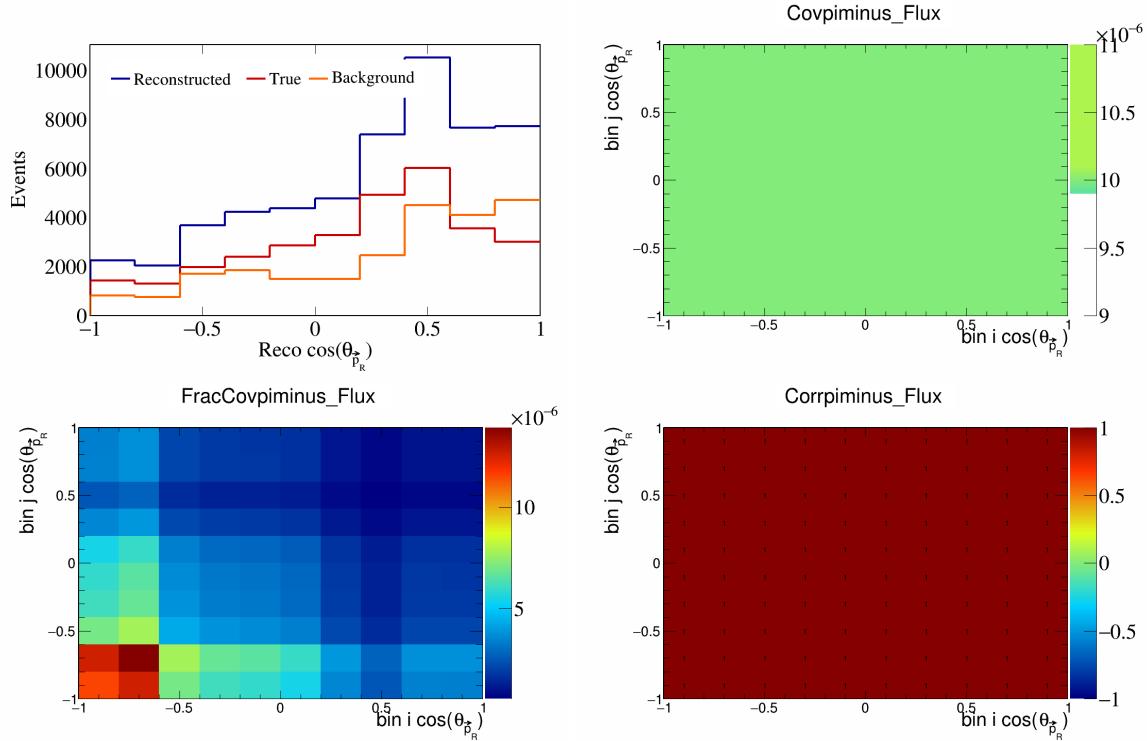


Figure 696: PiMinus variations for $\cos(\theta_{\vec{p}_R})$.

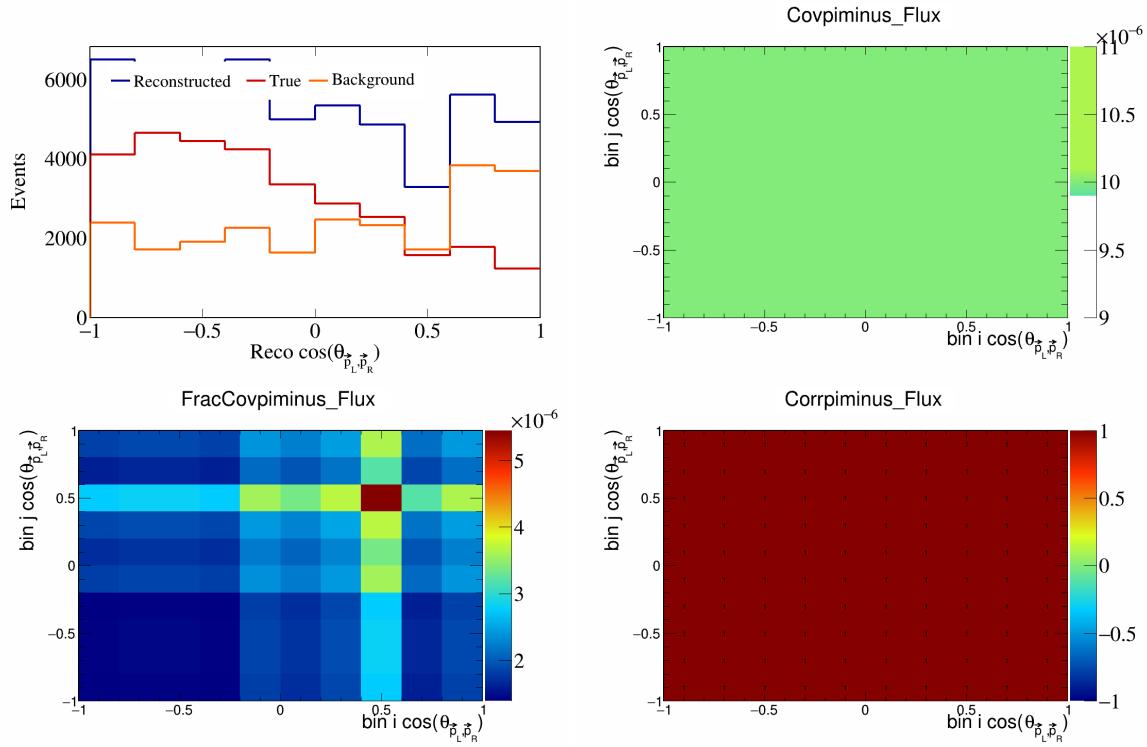


Figure 697: PiMinus variations for $\cos(\theta_{\vec{p}_L, \vec{p}_R})$.

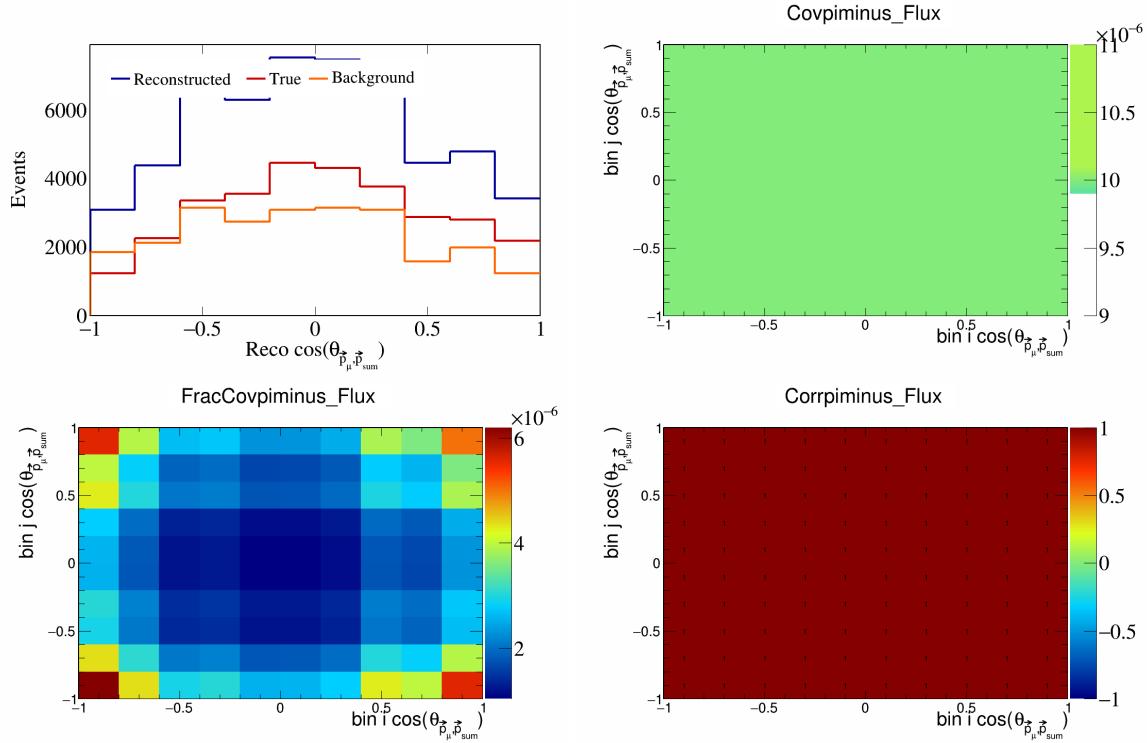


Figure 698: PiMinus variations for $\cos(\theta_{\vec{p}_\mu, \vec{p}_{\text{sum}}})$.

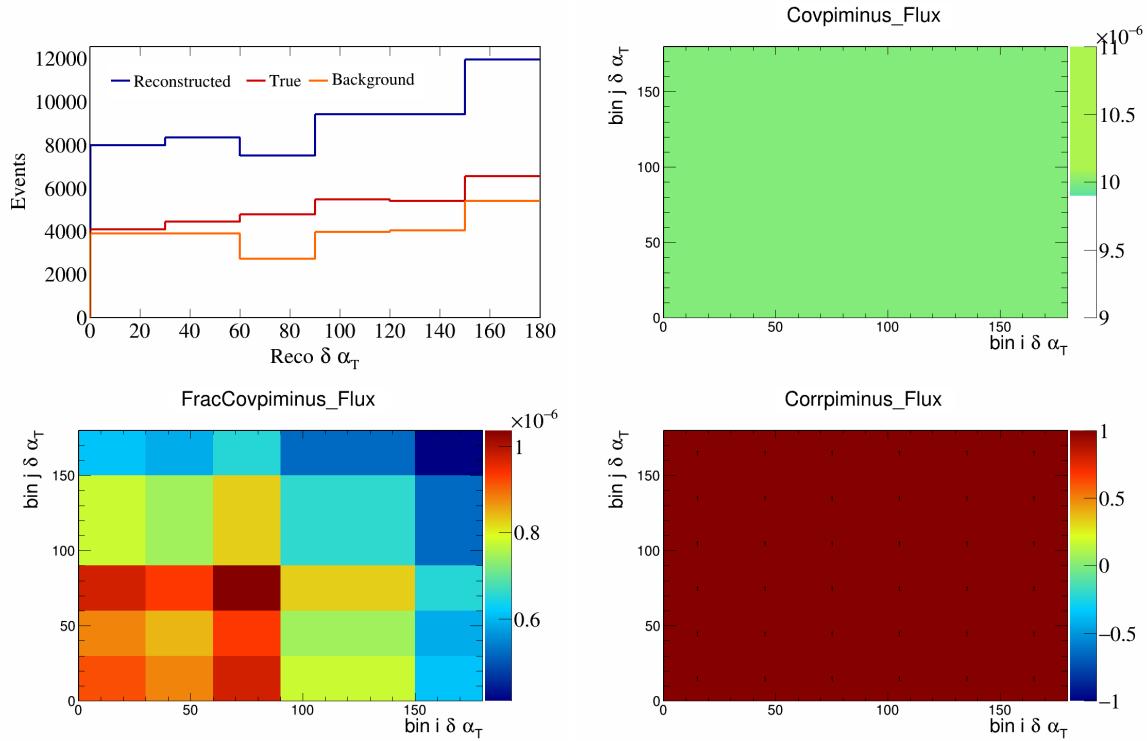


Figure 699: PiMinus variations for $\delta\alpha_T$.

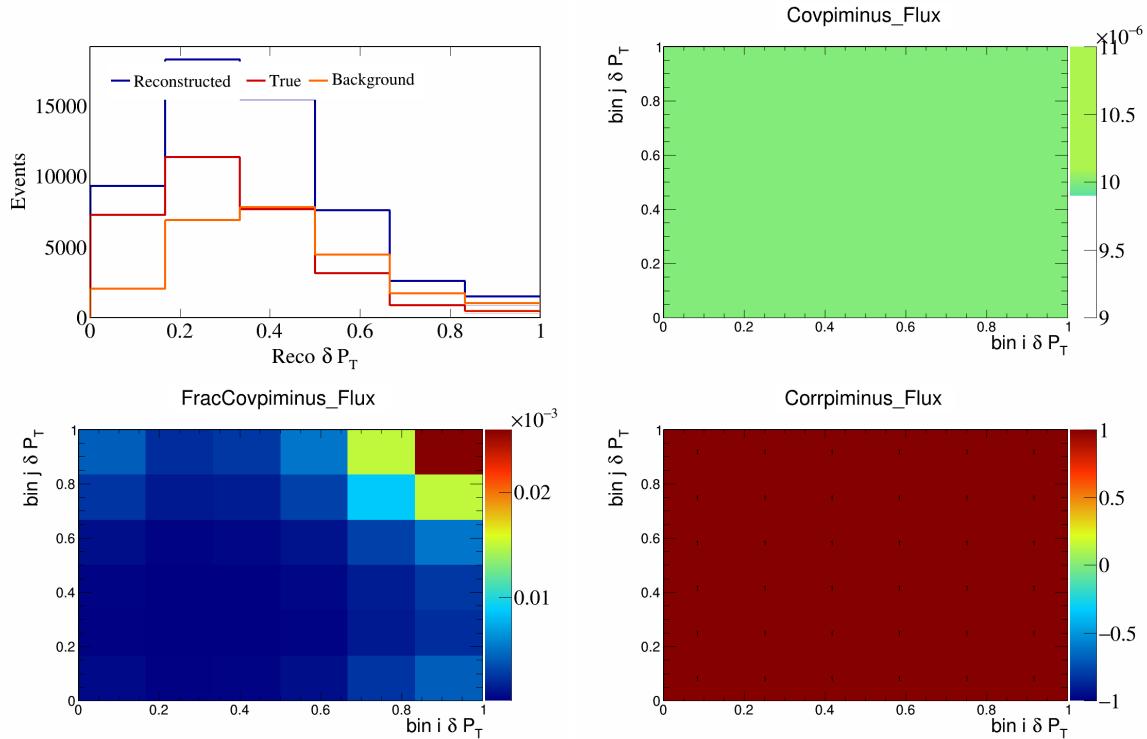


Figure 700: PiMinus variations for δP_T .

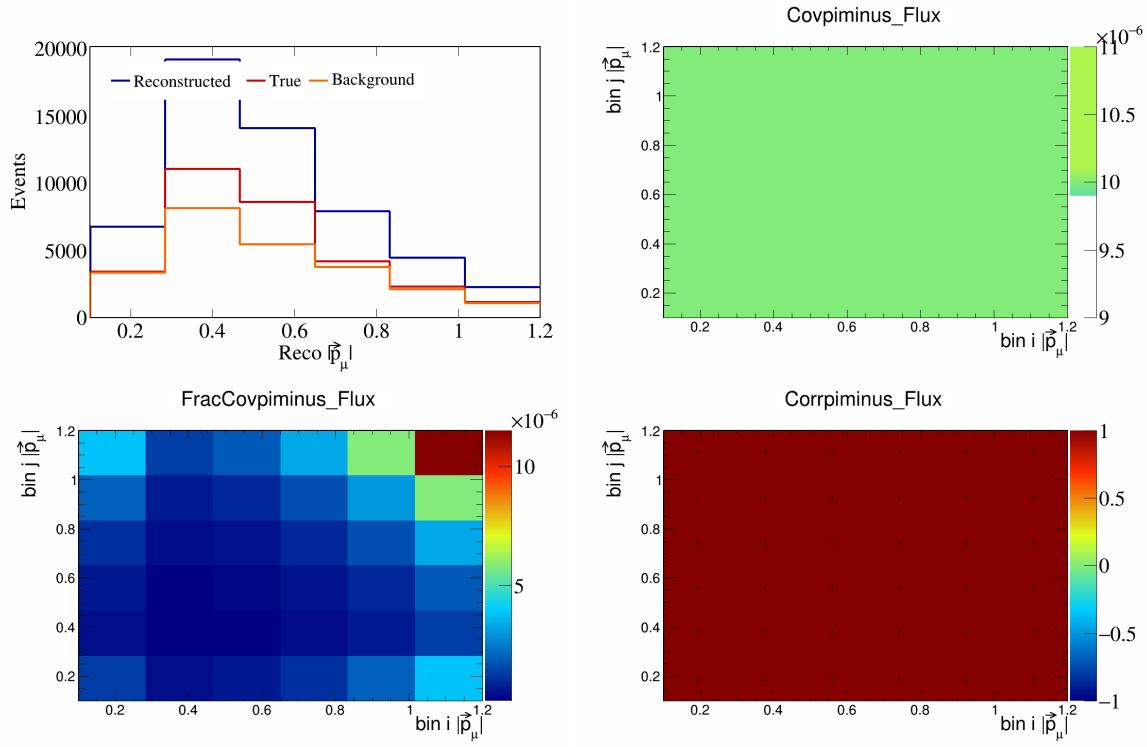


Figure 701: PiMinus variations for $|\vec{p}_\mu|$.

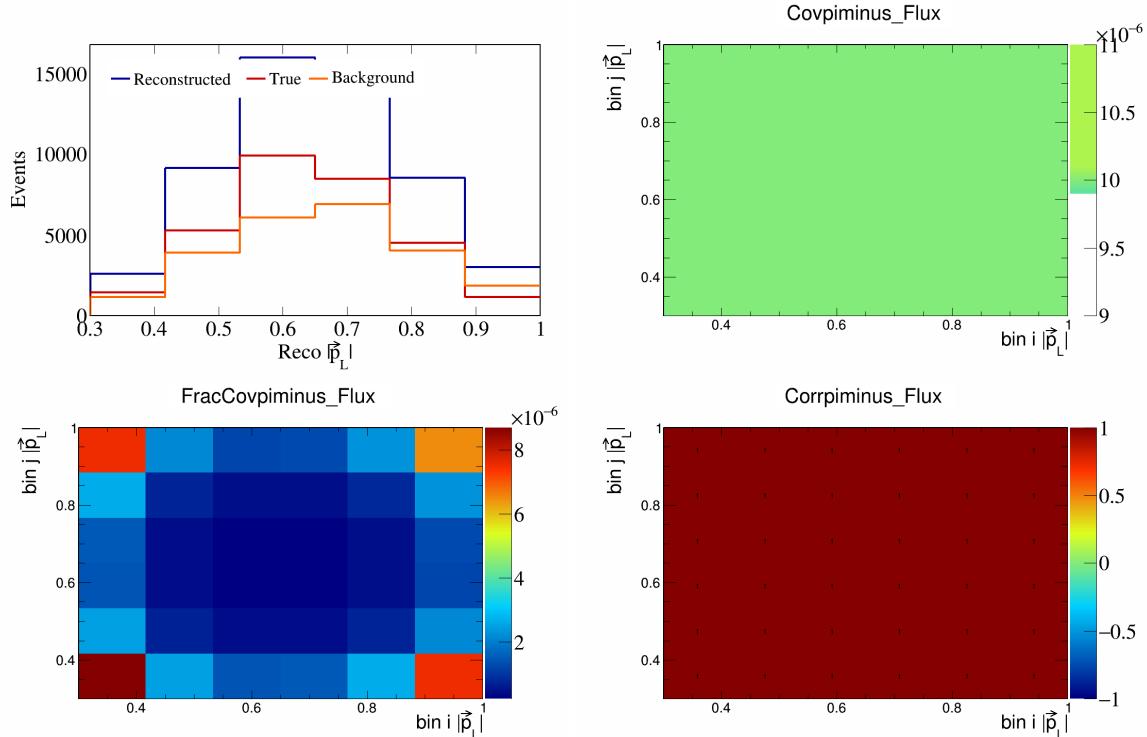


Figure 702: PiMinus variations for $|\vec{p}_L|$.

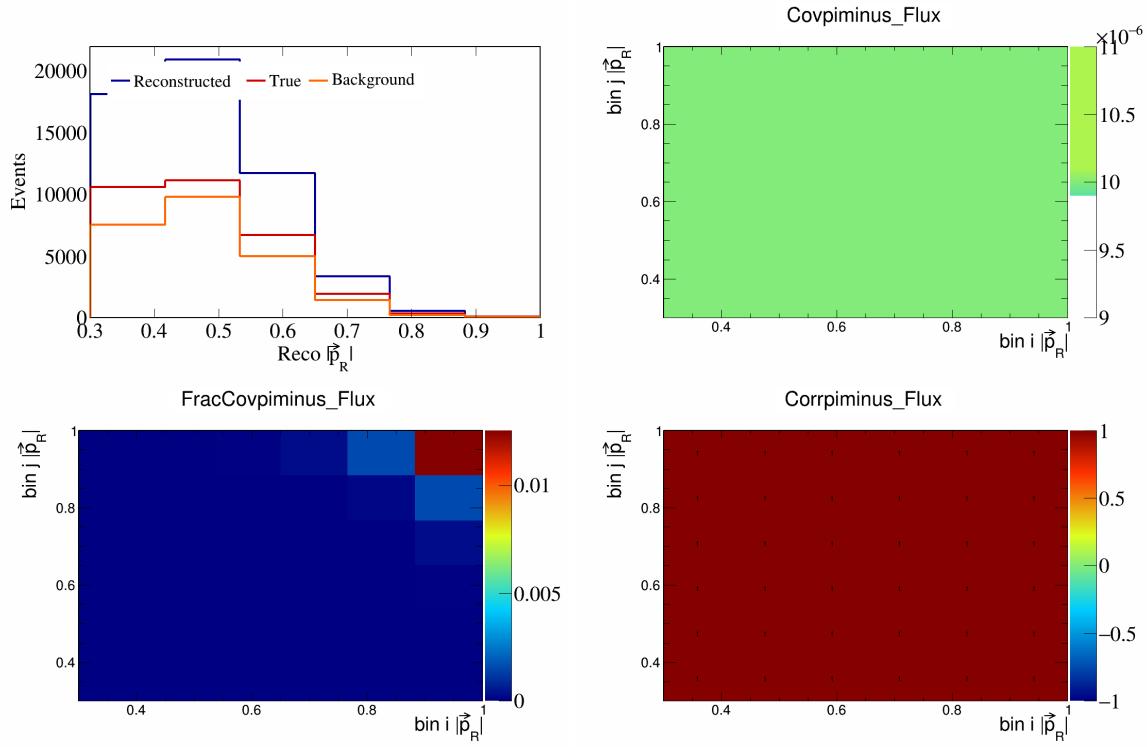


Figure 703: PiMinus variations for $|\vec{p}_R|$.

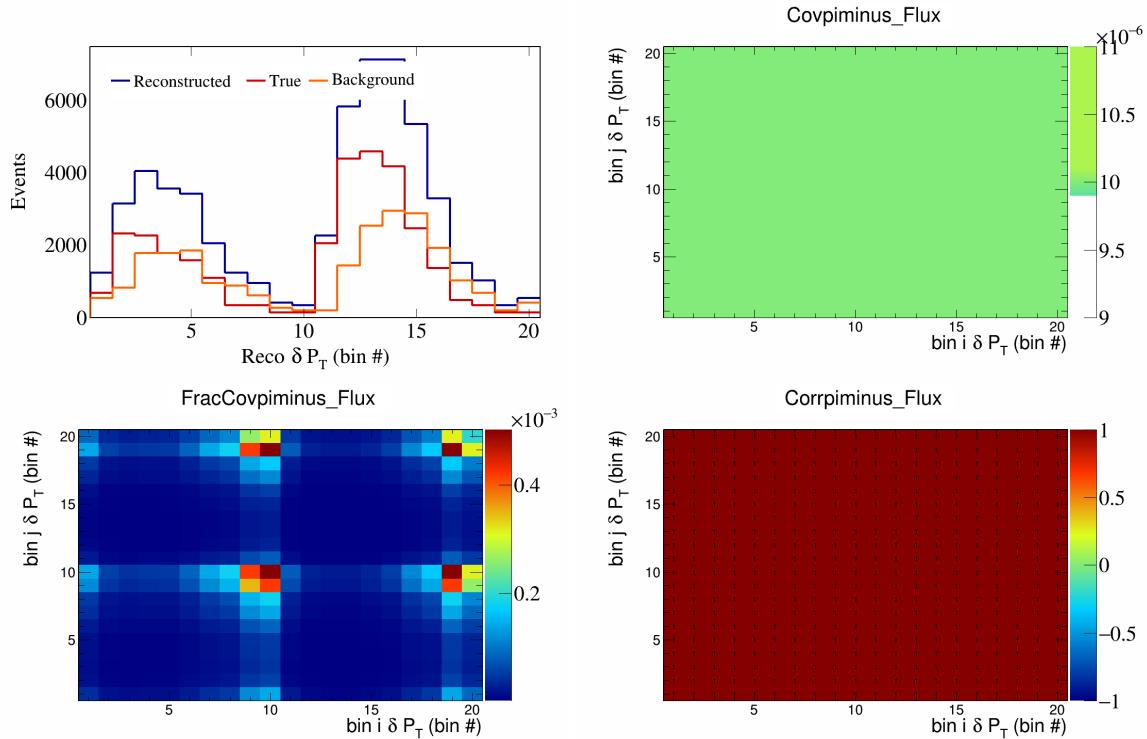


Figure 704: PiMinus variations for δP_T in $\cos(\theta_{\vec{p}_\mu})$.

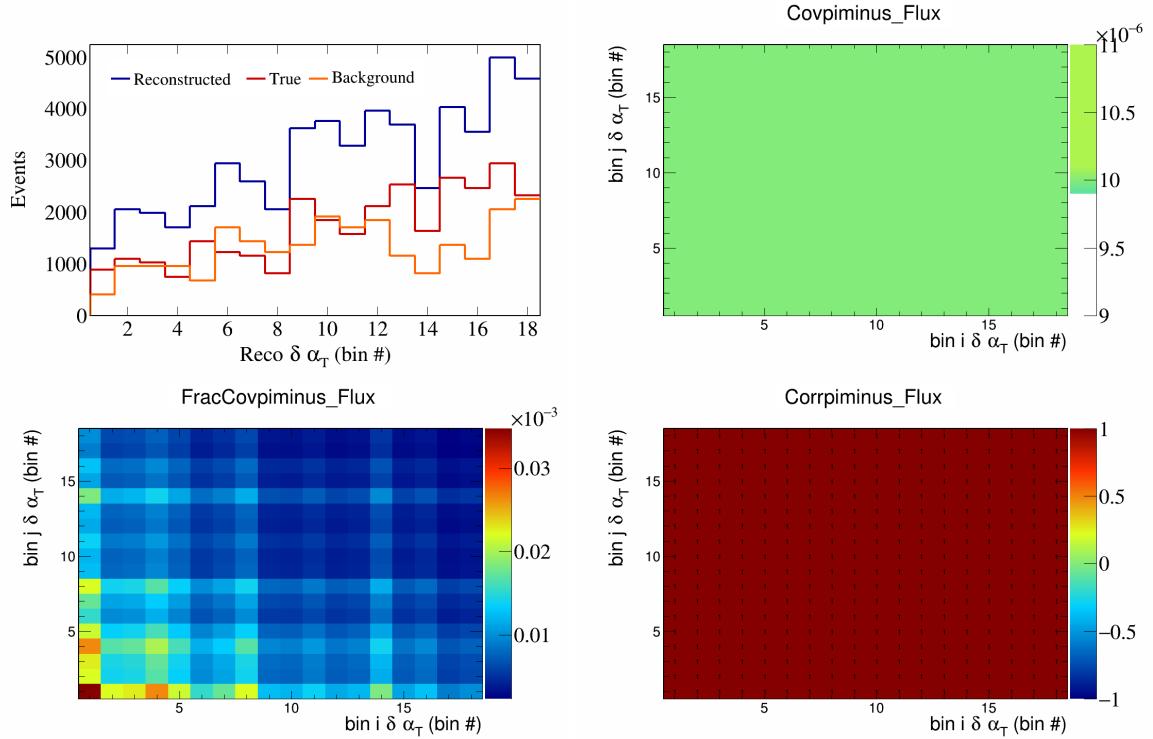


Figure 705: PiMinus variations for $\delta\alpha_T$ in $\cos(\theta_{\vec{p}_\mu})$.

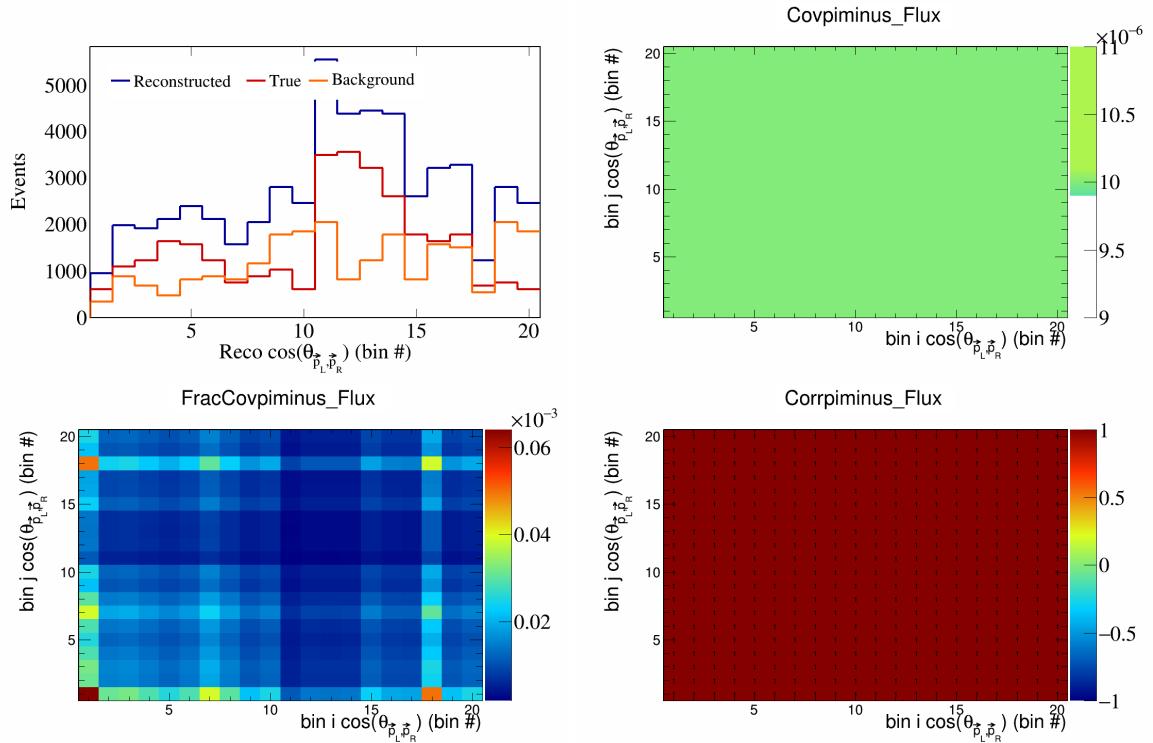


Figure 706: PiMinus variations for $\cos(\theta_{\vec{p}_L, \vec{p}_R})$ in $\cos(\theta_{\vec{p}_\mu})$.

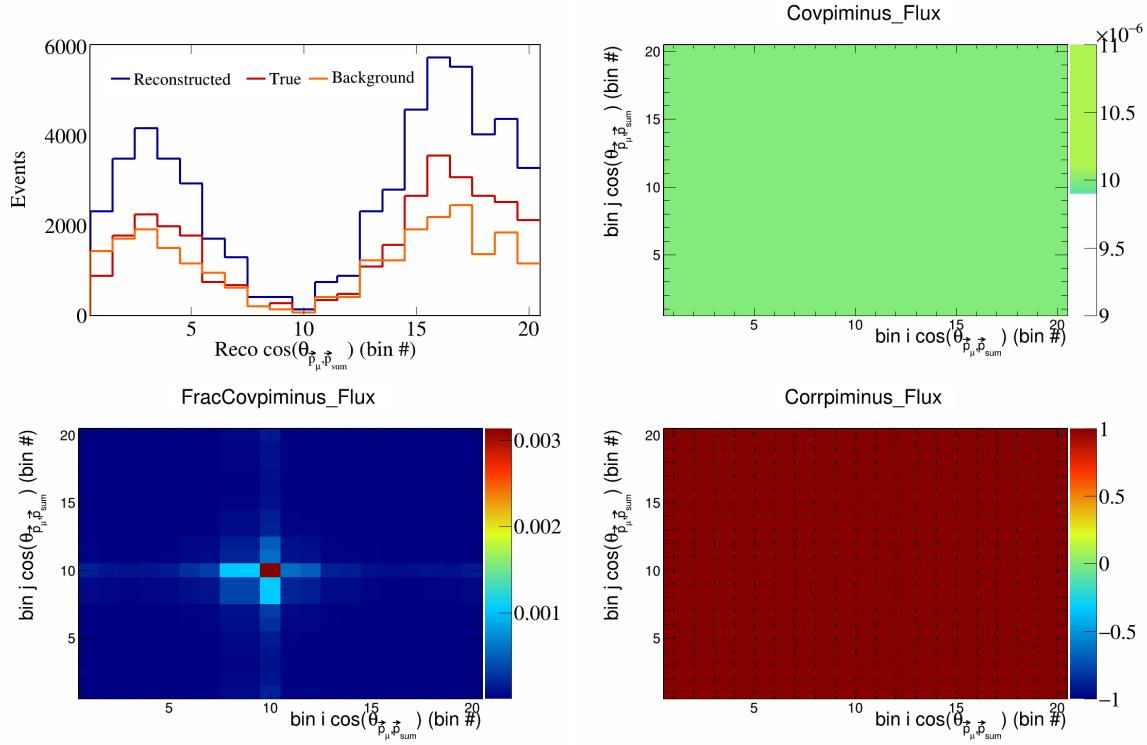


Figure 707: PiMinus variations for $\cos(\theta_{\vec{p}_\mu, \vec{p}_{\text{sum}}})$ in $\cos(\theta_{\vec{p}_\mu})$.

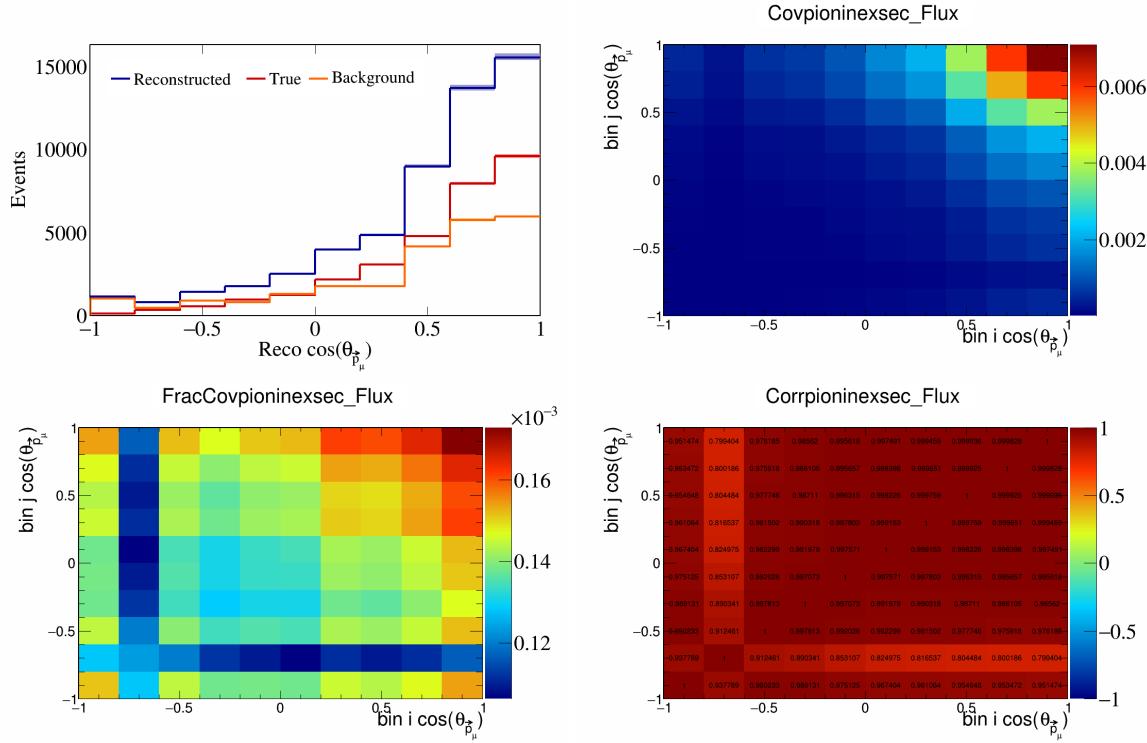


Figure 708: PionIneXSec variations for $\cos(\theta_{\vec{p}_\mu})$.

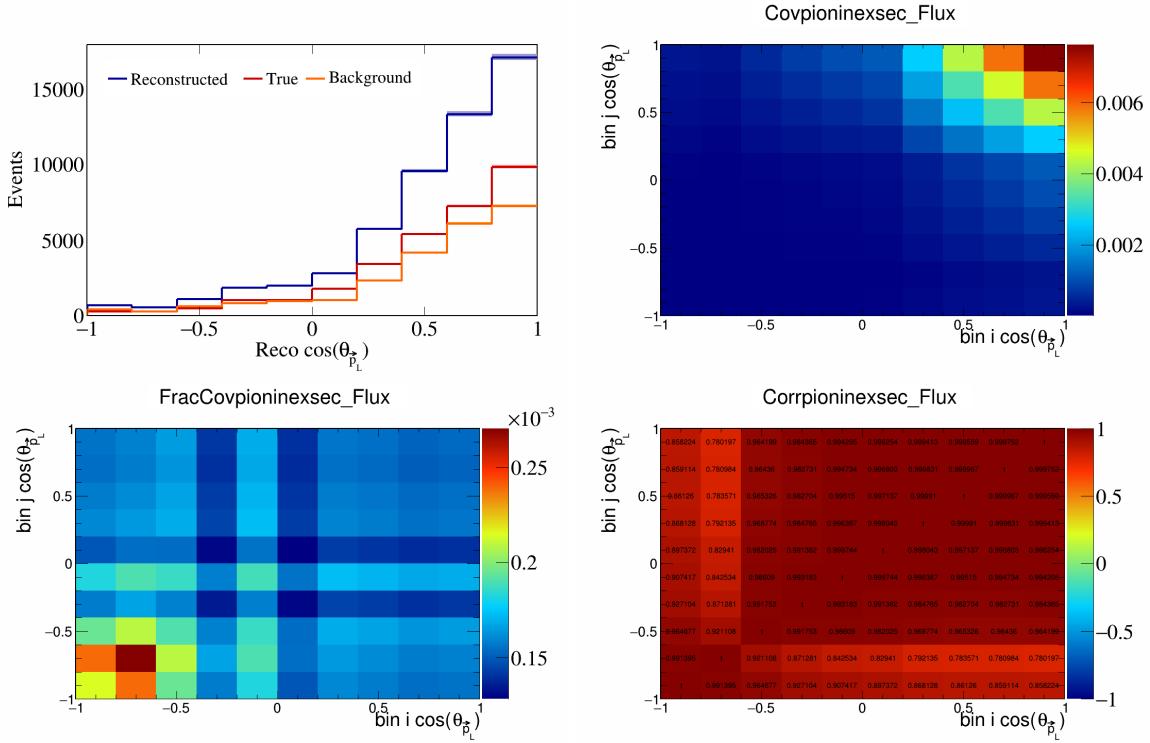


Figure 709: PionIneXSec variations for $\cos(\theta_{\vec{p}_L})$.

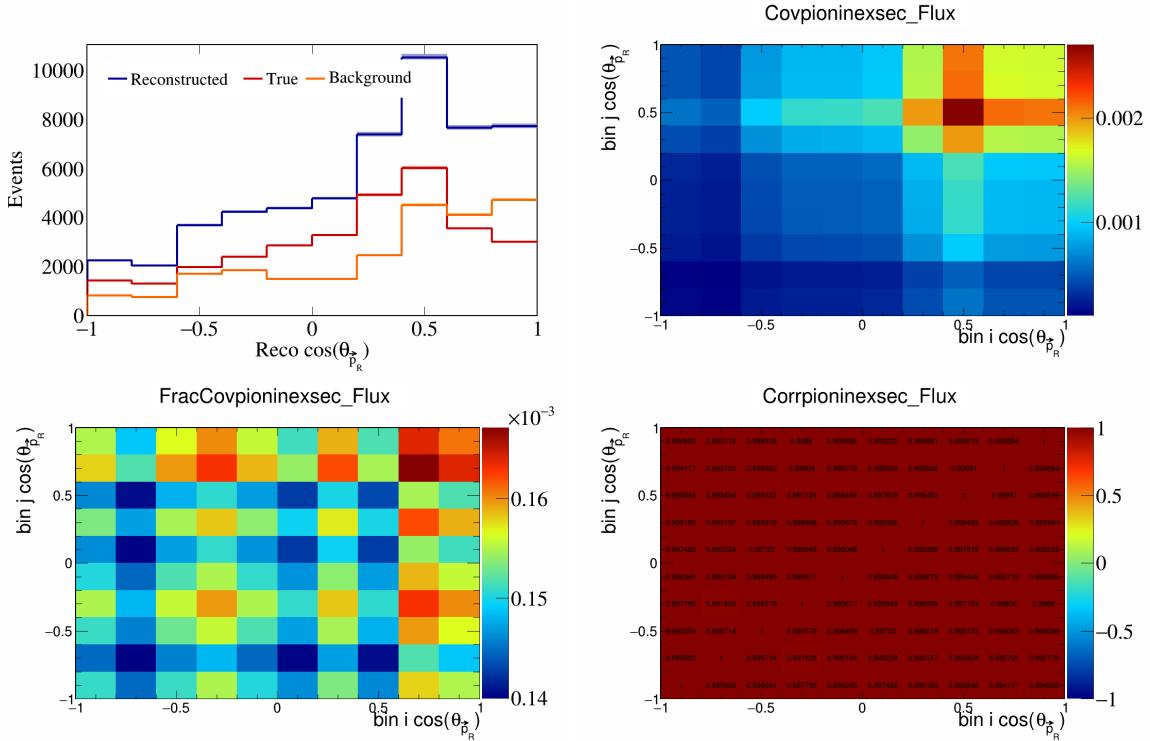


Figure 710: PionIneXSec variations for $\cos(\theta_{\vec{p}_R})$.

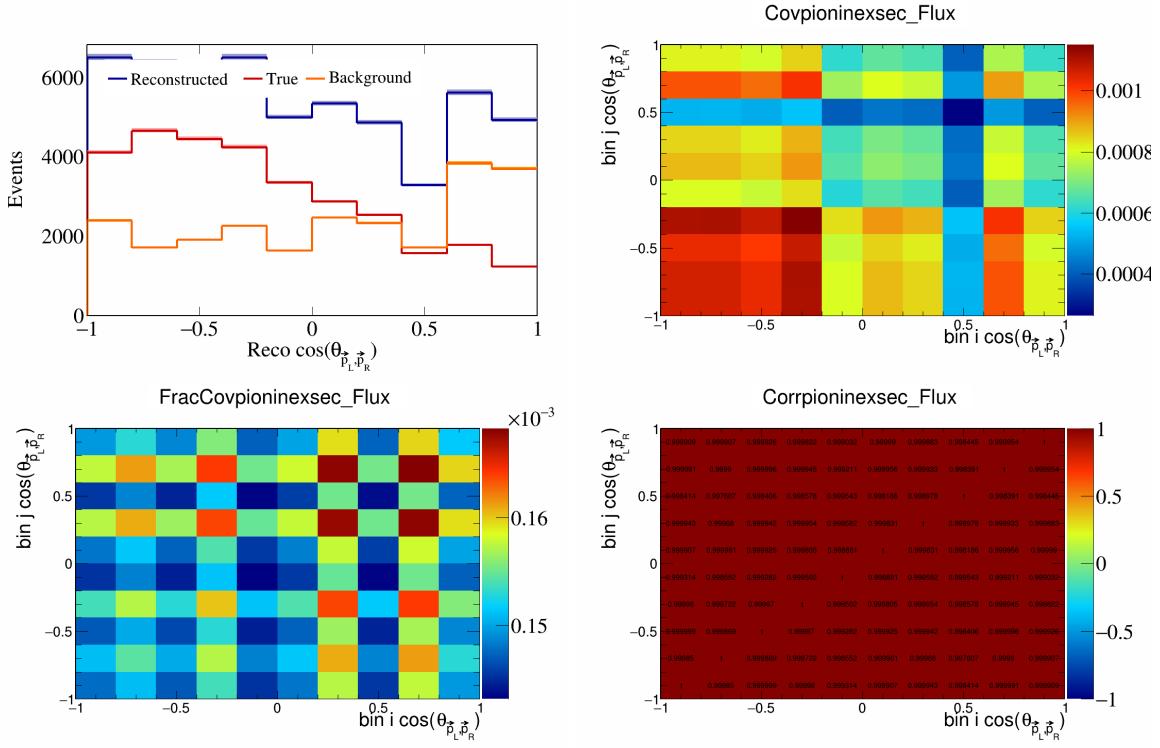


Figure 711: PionIneXSec variations for $\cos(\theta_{\vec{p}_L, \vec{p}_R})$.

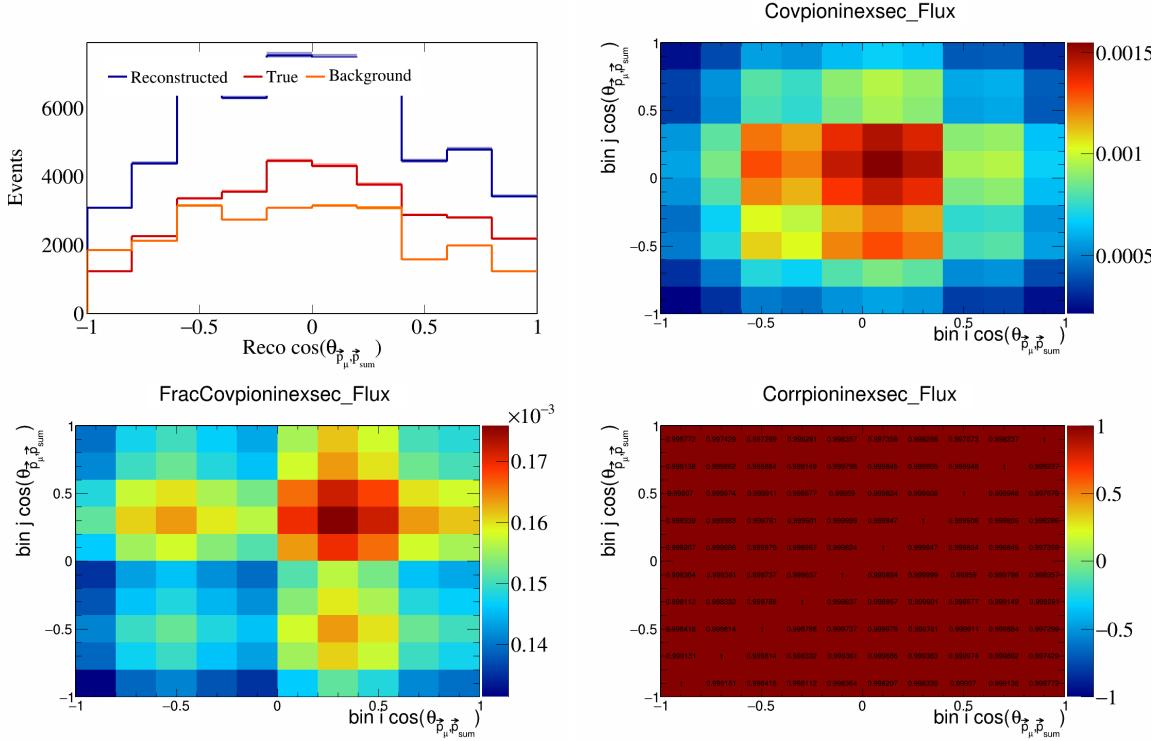


Figure 712: PionIneXSec variations for $\cos(\theta_{\vec{p}_\mu, \vec{p}_{\text{sum}}})$.

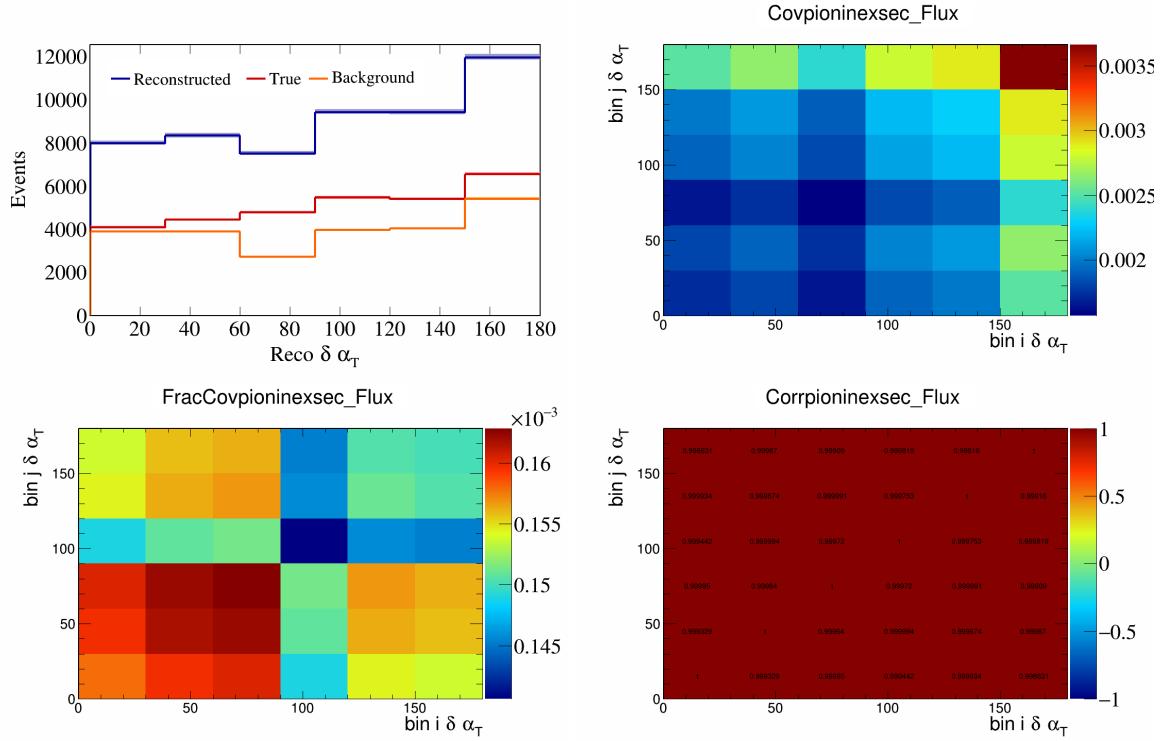


Figure 713: PionIneXSec variations for $\delta\alpha_T$.

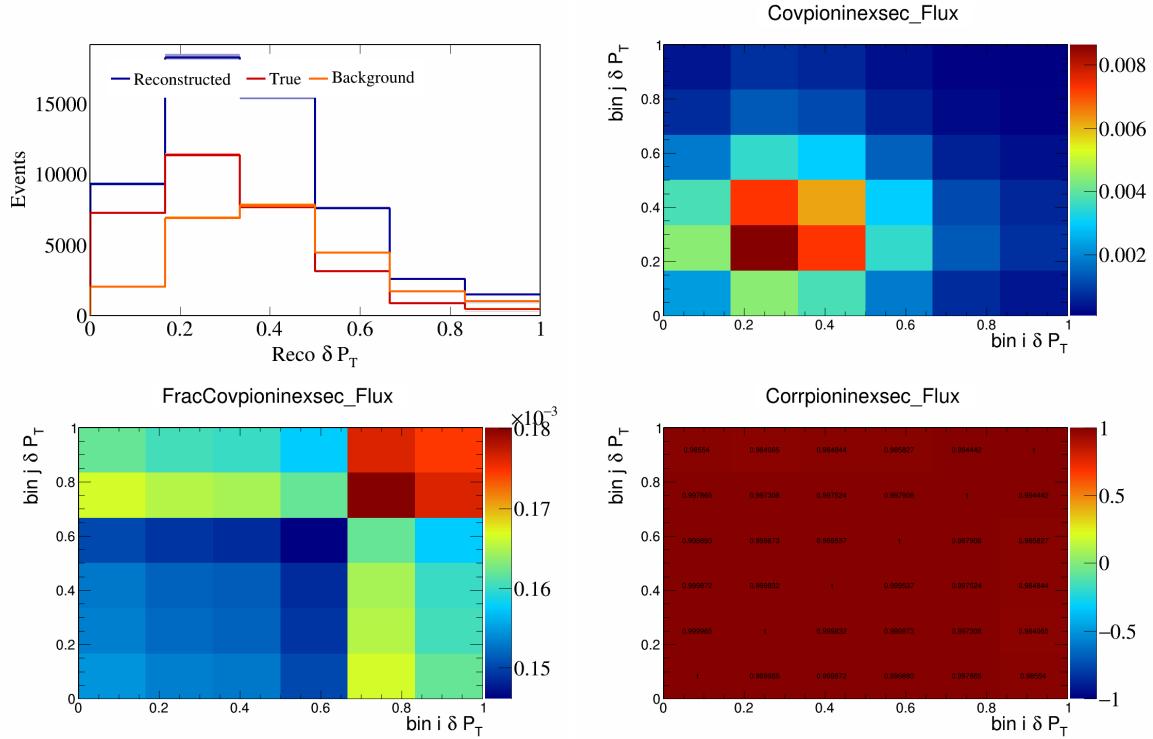


Figure 714: PionIneXSec variations for δP_T .

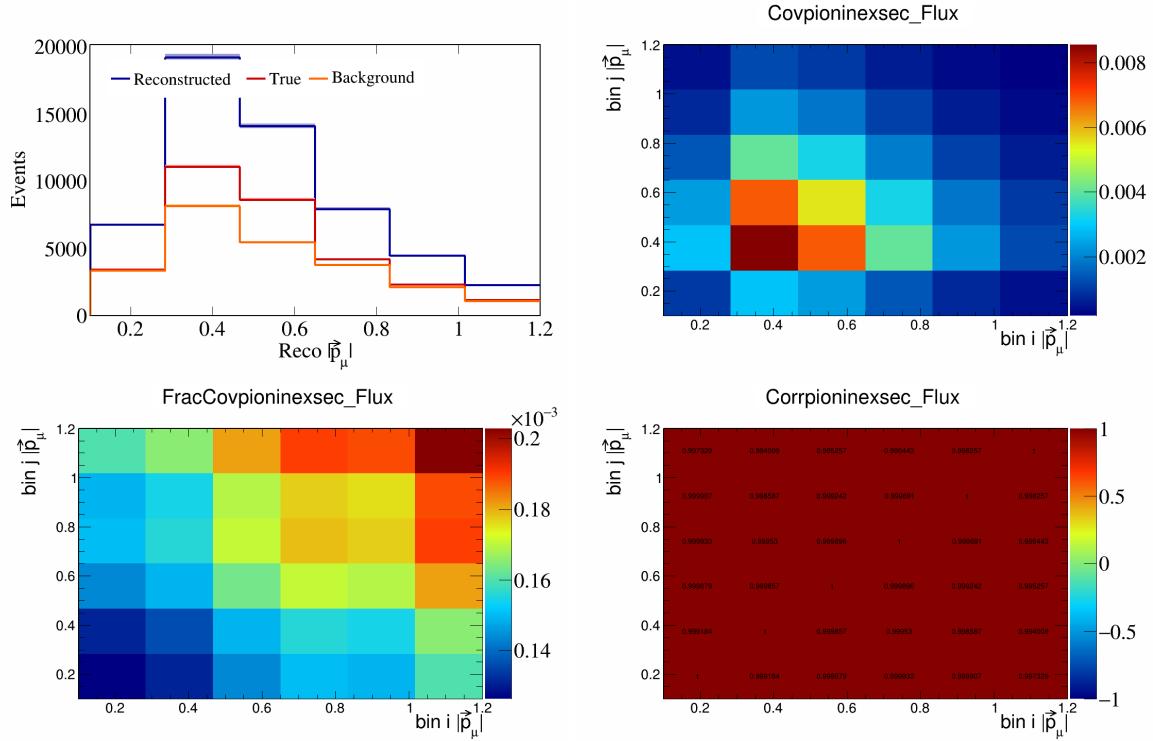


Figure 715: PionIneXSec variations for $|\vec{p}_\mu|$.

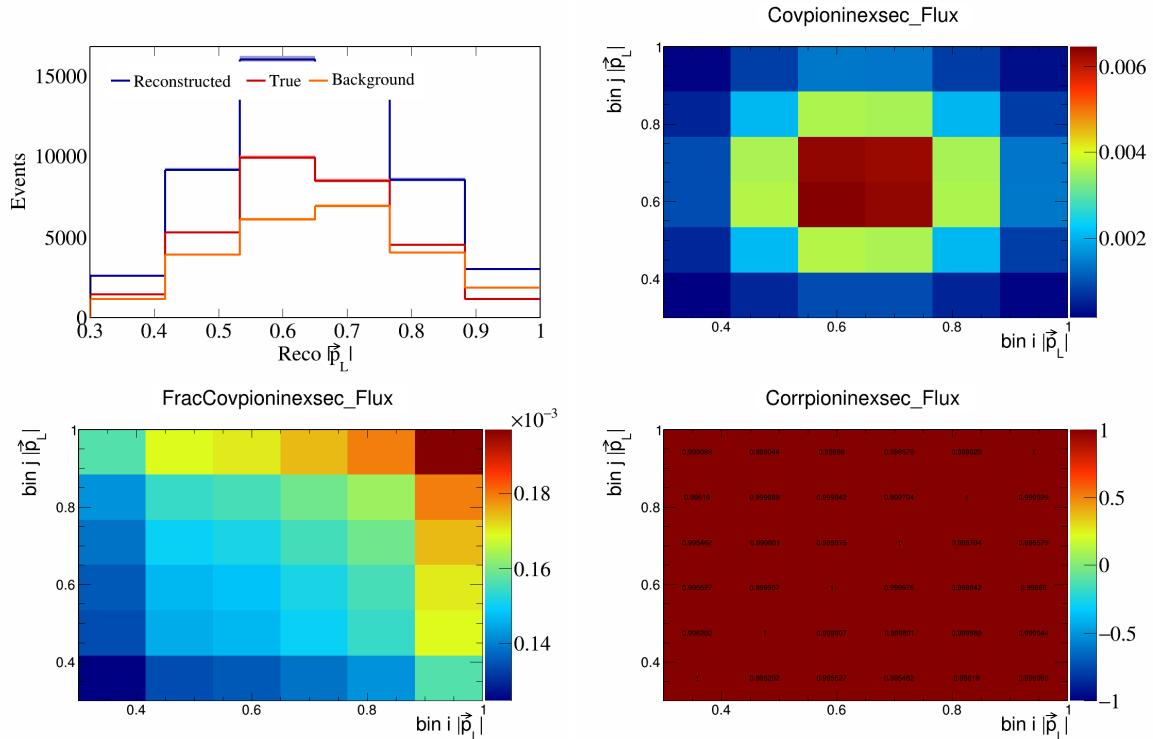


Figure 716: PionIneXSec variations for $|\vec{p}_L|$.

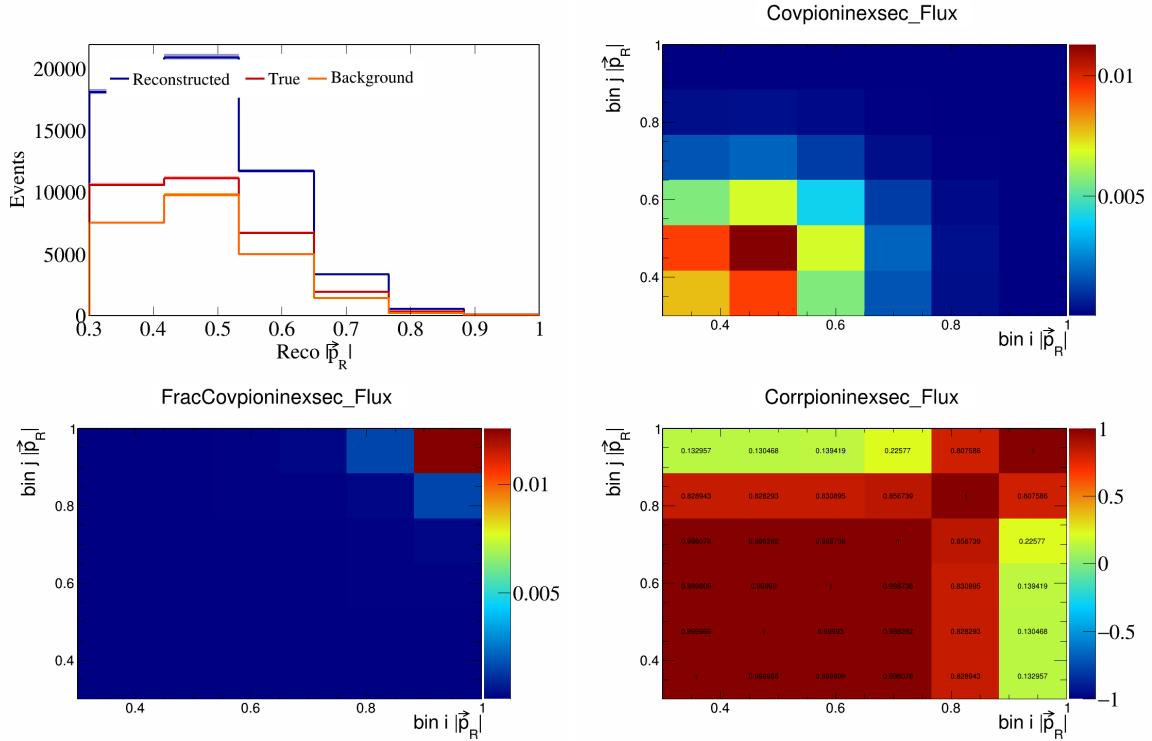


Figure 717: PionIneXSec variations for $|\vec{p}_R|$.

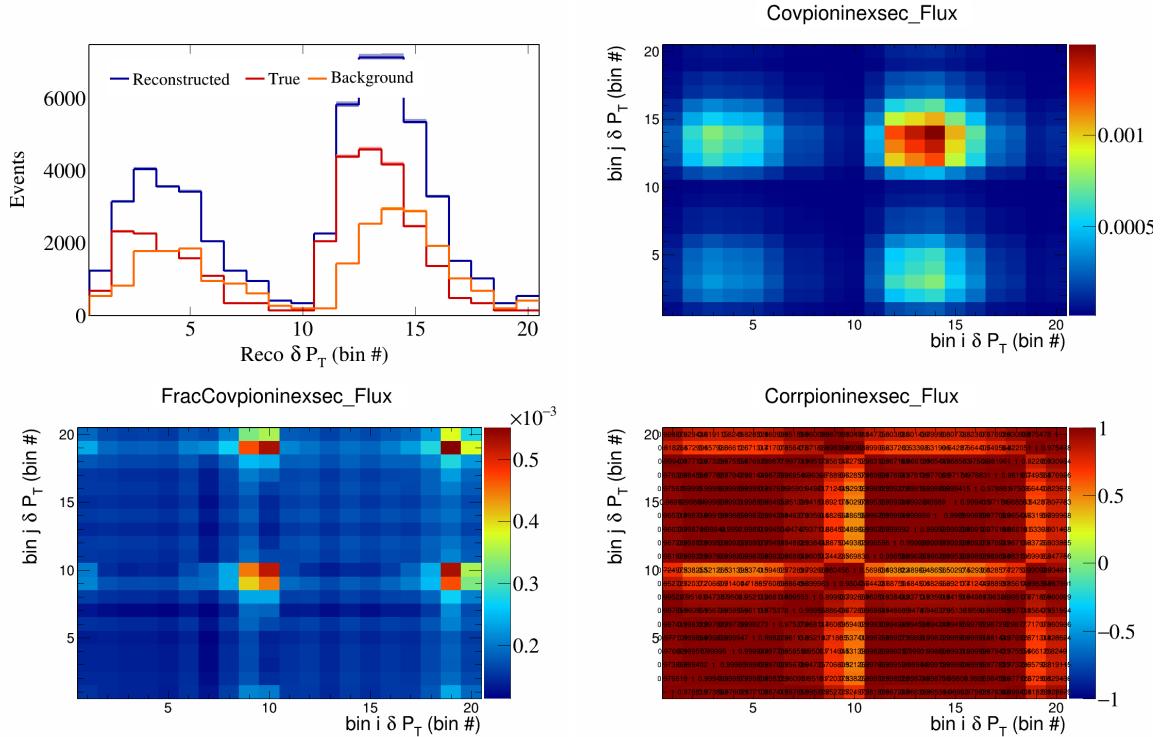


Figure 718: PionIneXSec variations for δP_T in $\cos(\theta_{\vec{p}_\mu})$.

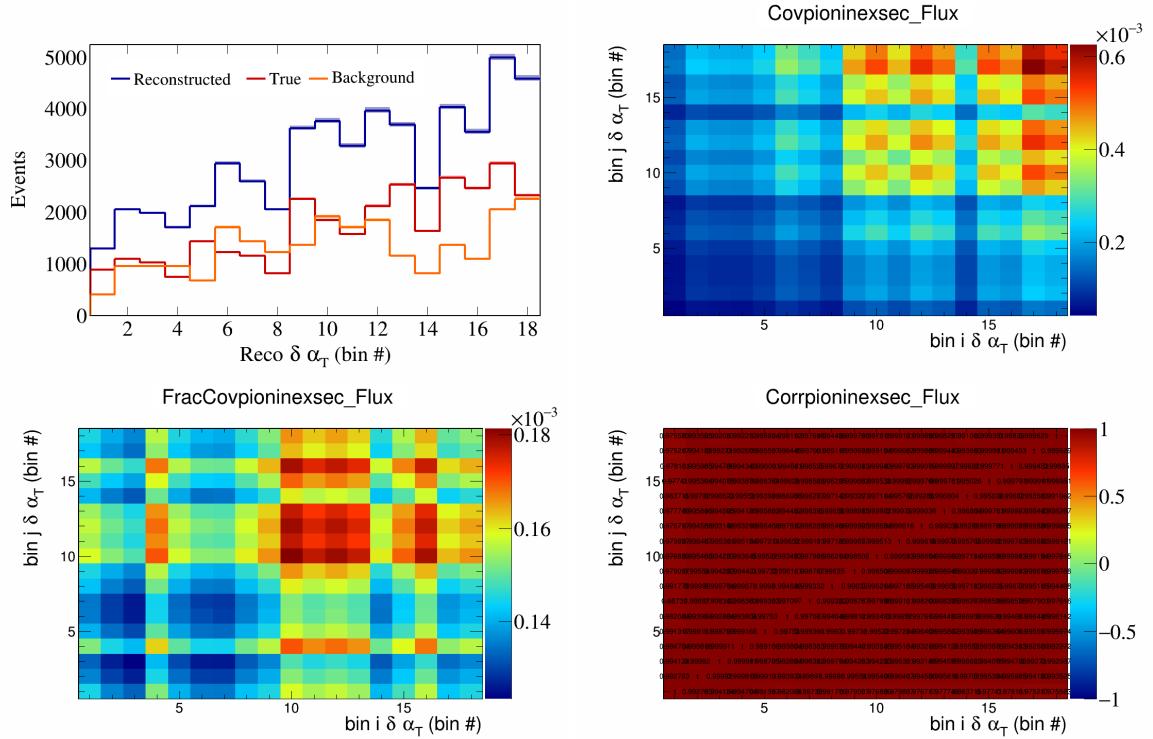


Figure 719: PionIneXSec variations for $\delta \alpha_T$ in $\cos(\theta_{\vec{p}_\mu})$.

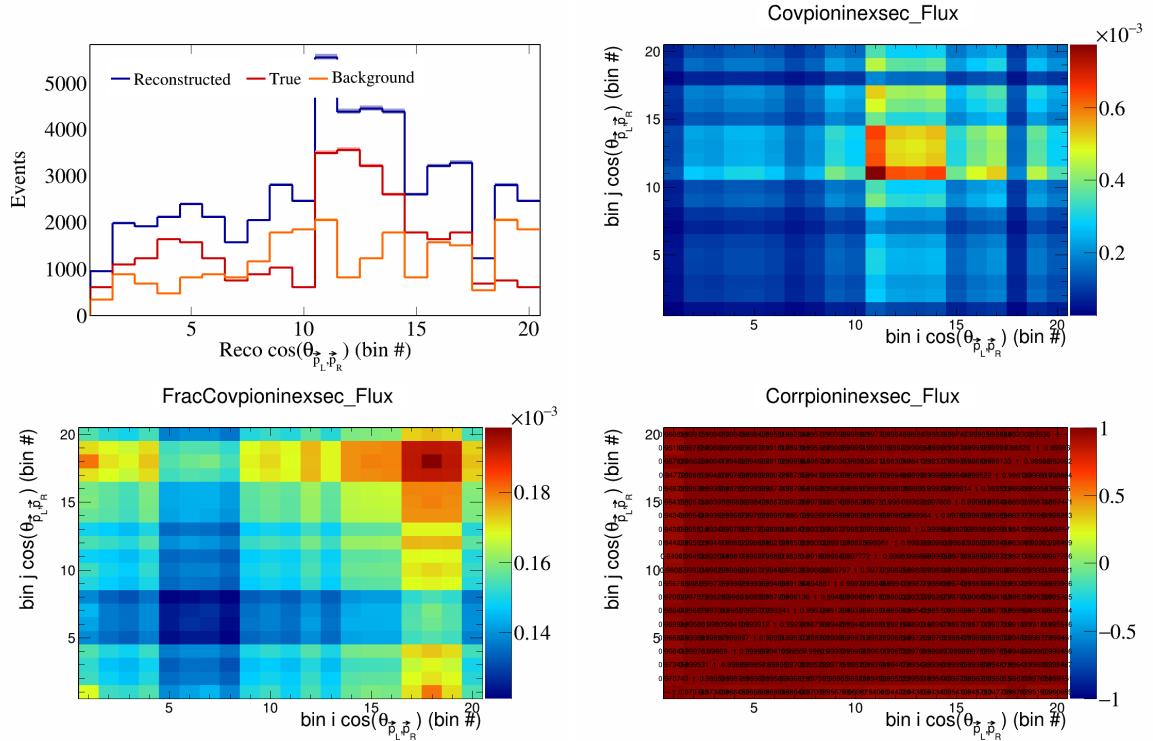


Figure 720: PionIneXSec variations for $\cos(\theta_{\vec{p}_L, \vec{p}_R})$ in $\cos(\theta_{\vec{p}_\mu})$.

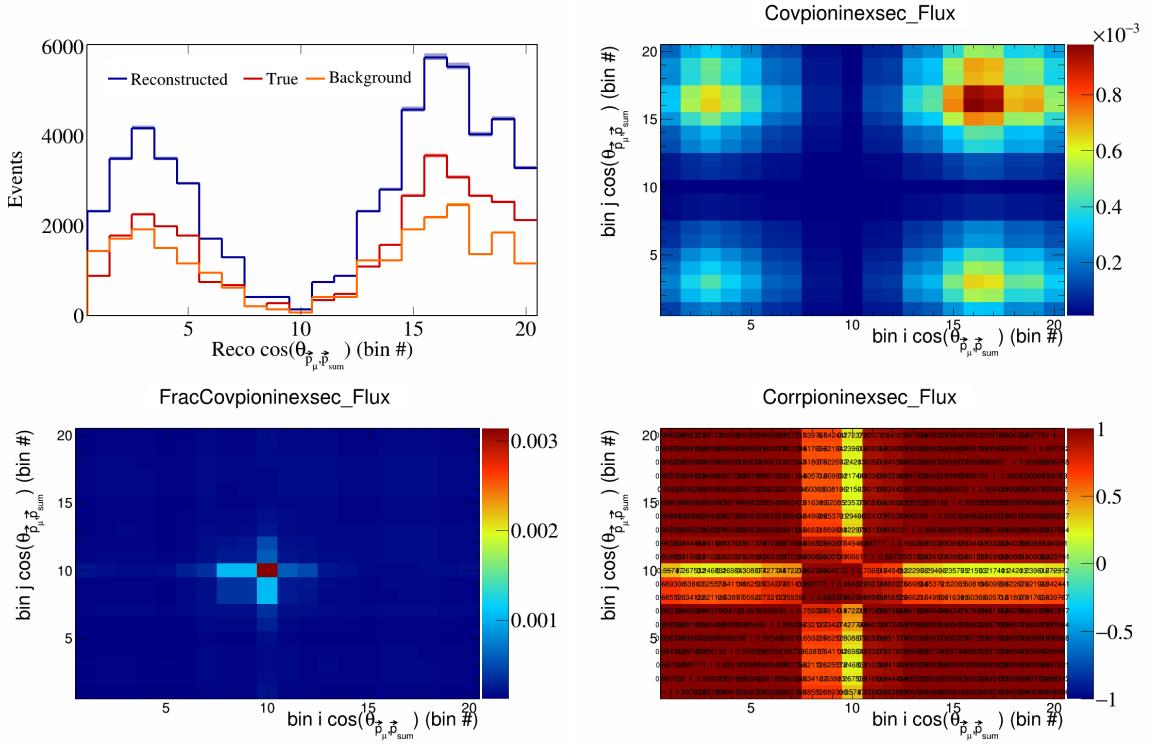


Figure 721: PionIneXSec variations for $\cos(\theta_{\vec{p}_\mu} \vec{p}_{\text{sum}})$ in $\cos(\theta_{\vec{p}_\mu})$.

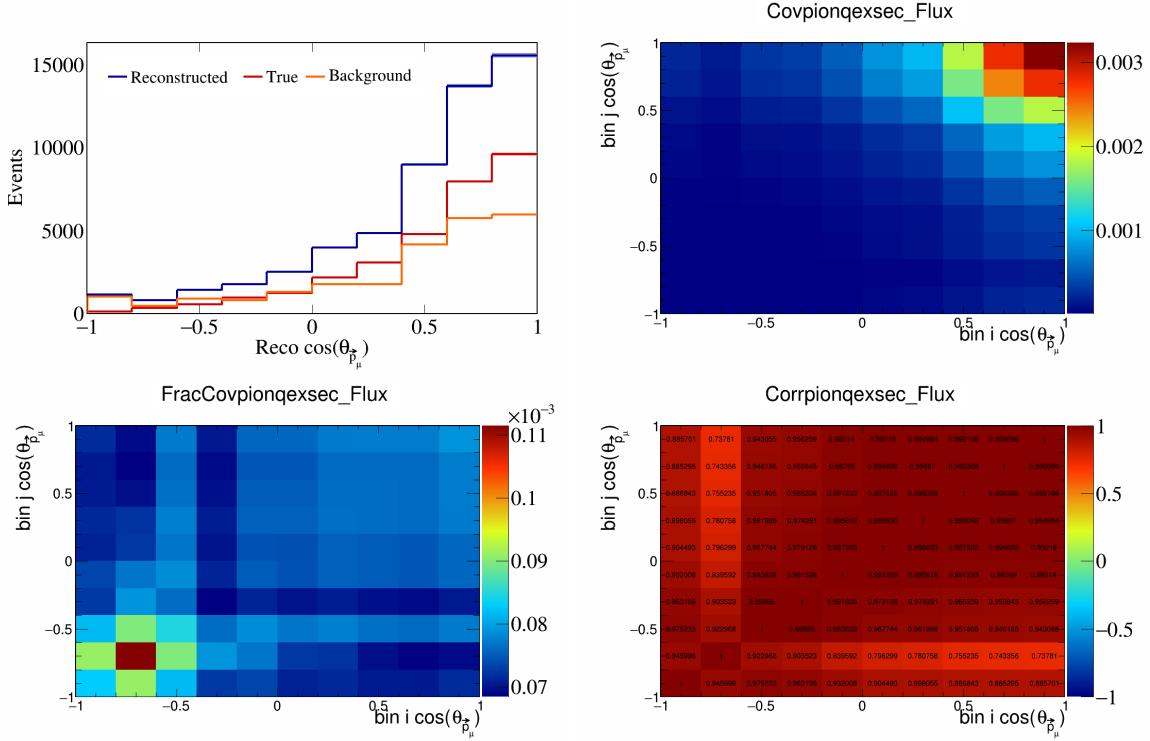


Figure 722: PionQeXSec variations for $\cos(\theta_{\vec{p}_\mu})$.

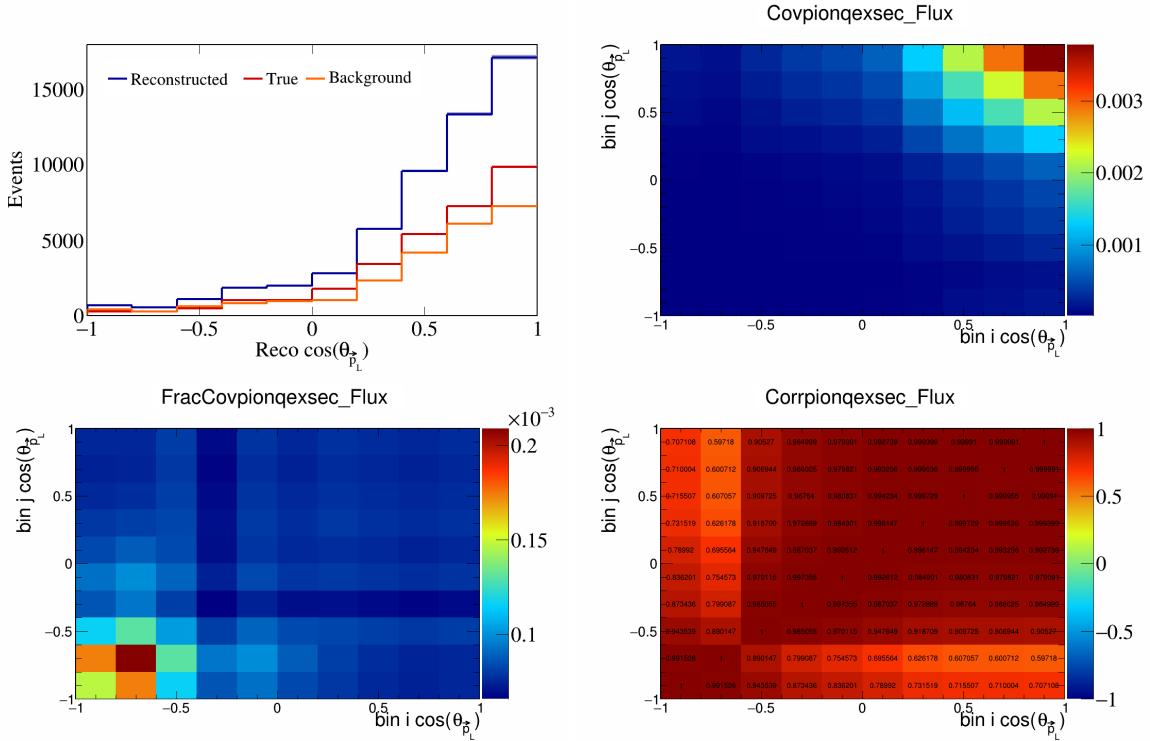


Figure 723: PionQeXSec variations for $\cos(\theta_{\vec{p}_L})$.

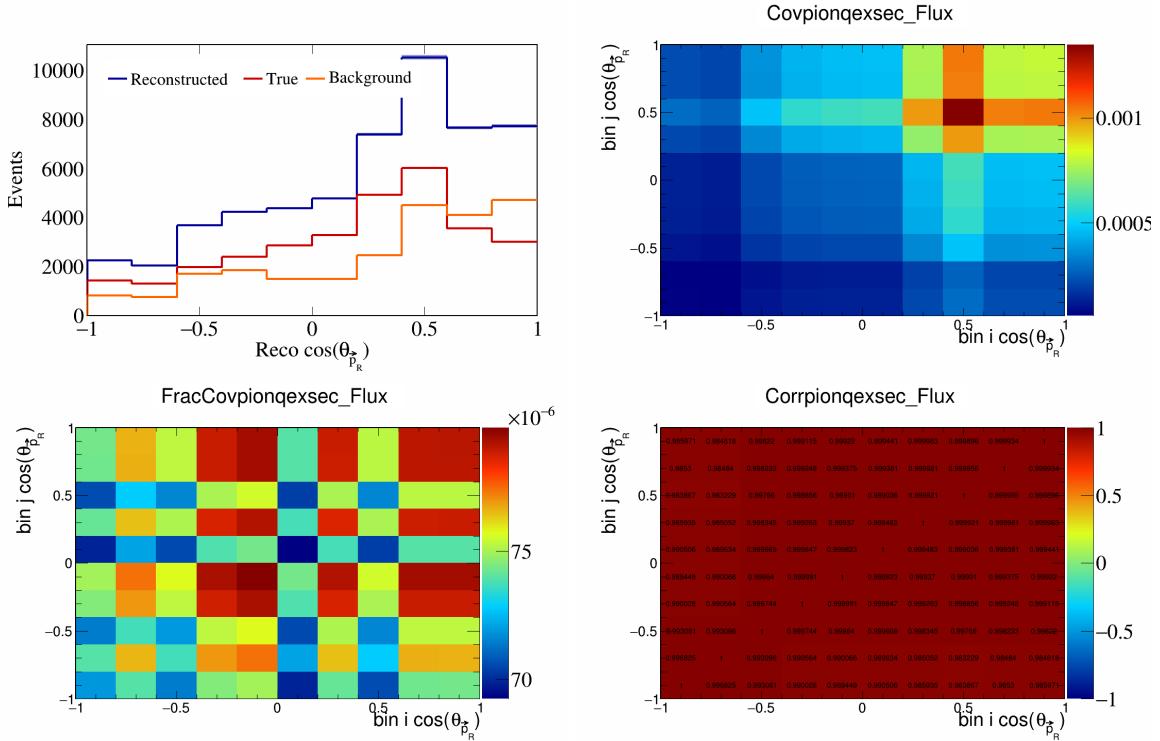


Figure 724: PionQeXSec variations for $\cos(\theta_{\vec{p}_R})$.

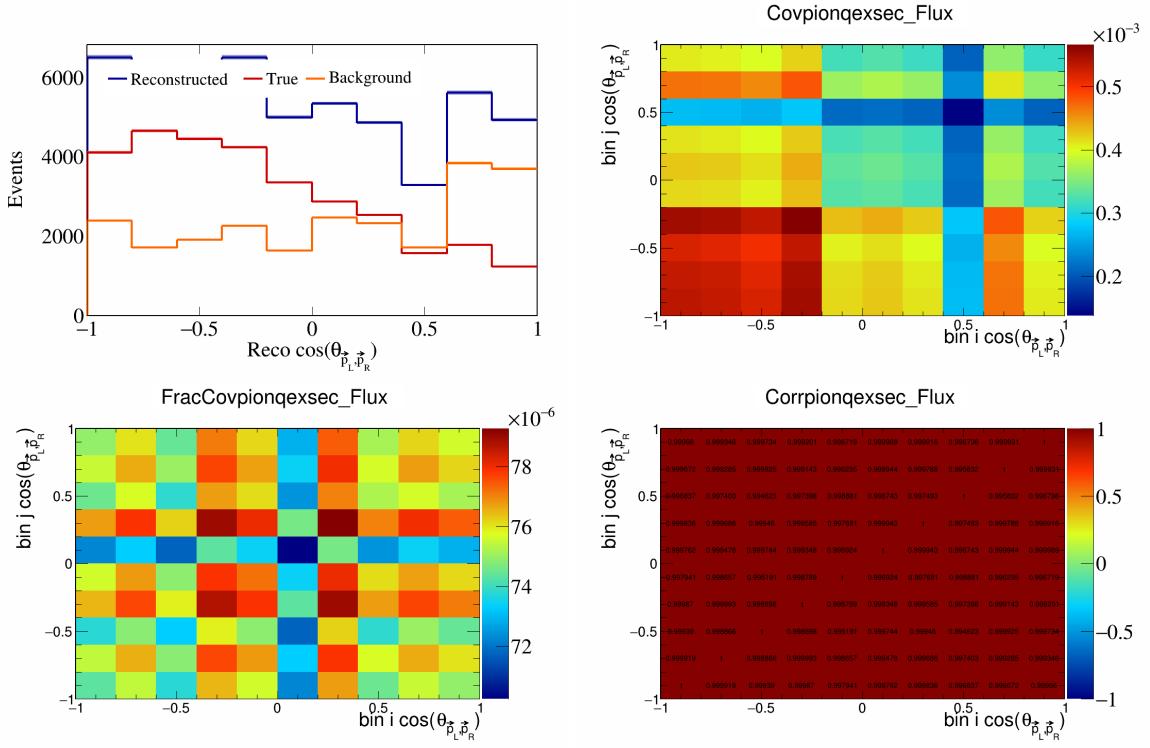


Figure 725: PionQeXSec variations for $\cos(\theta_{\vec{p}_L, \vec{p}_R})$.

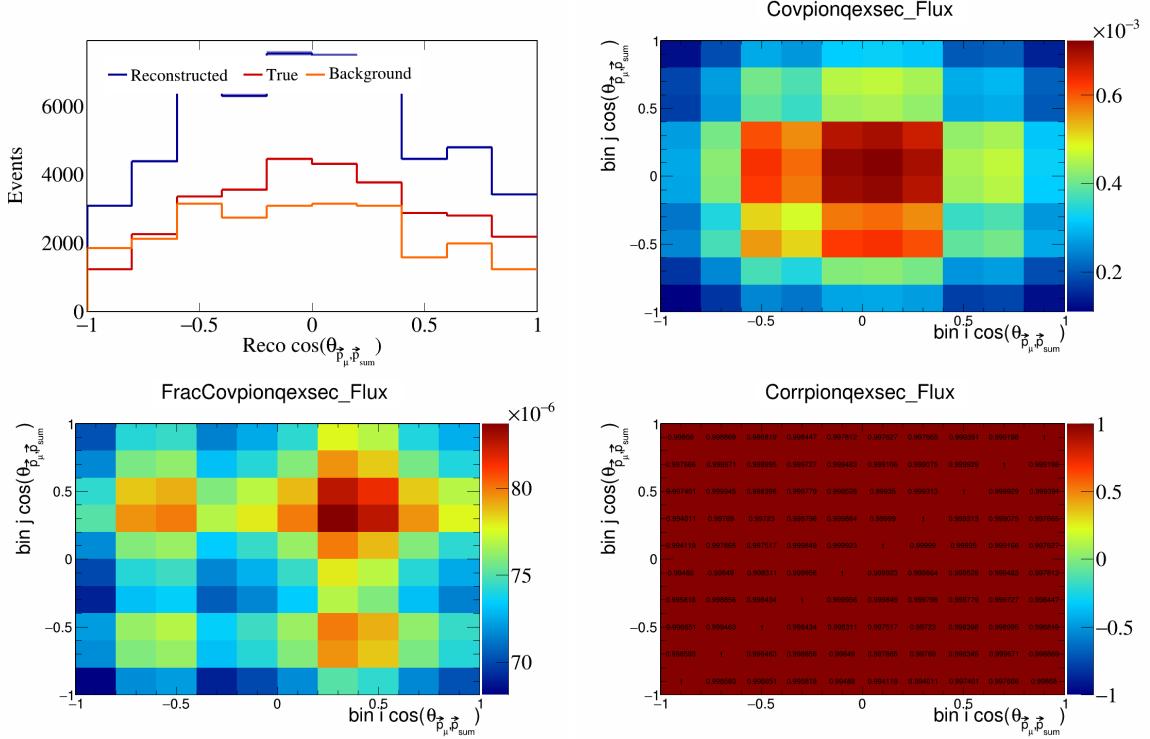


Figure 726: PionQeXSec variations for $\cos(\theta_{\vec{p}_\mu, \vec{p}_{\text{sum}}})$.

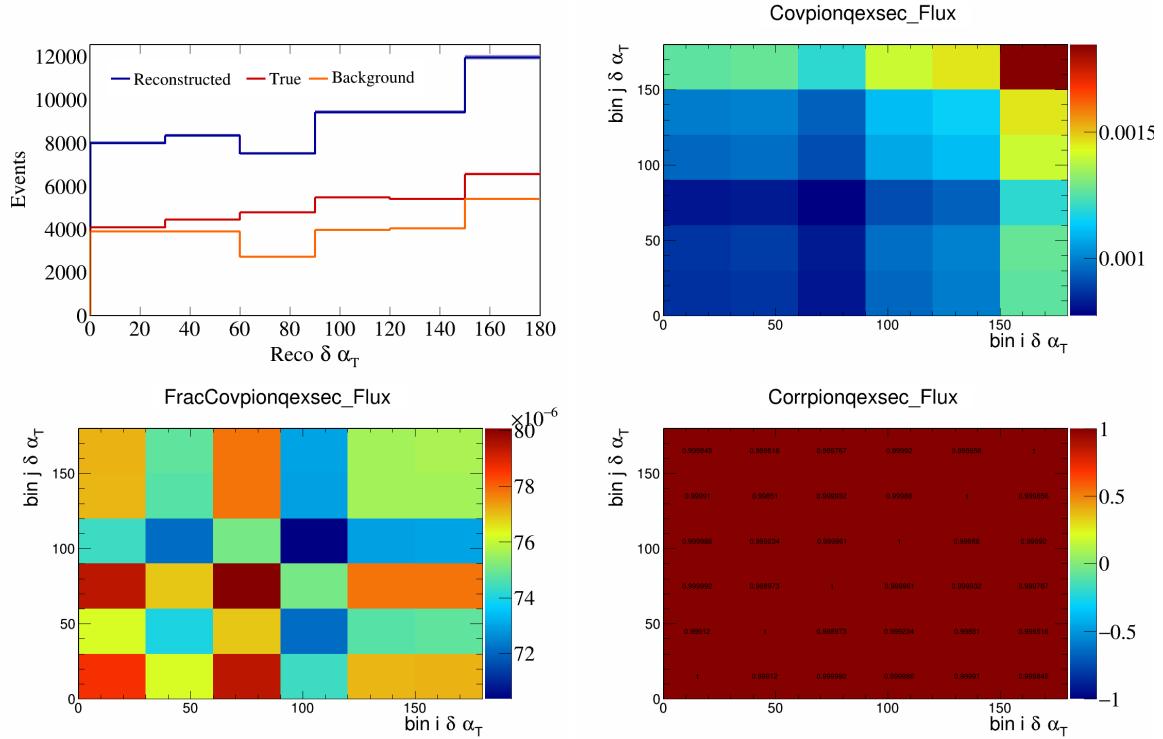


Figure 727: PionQeXSec variations for $\delta\alpha_T$.

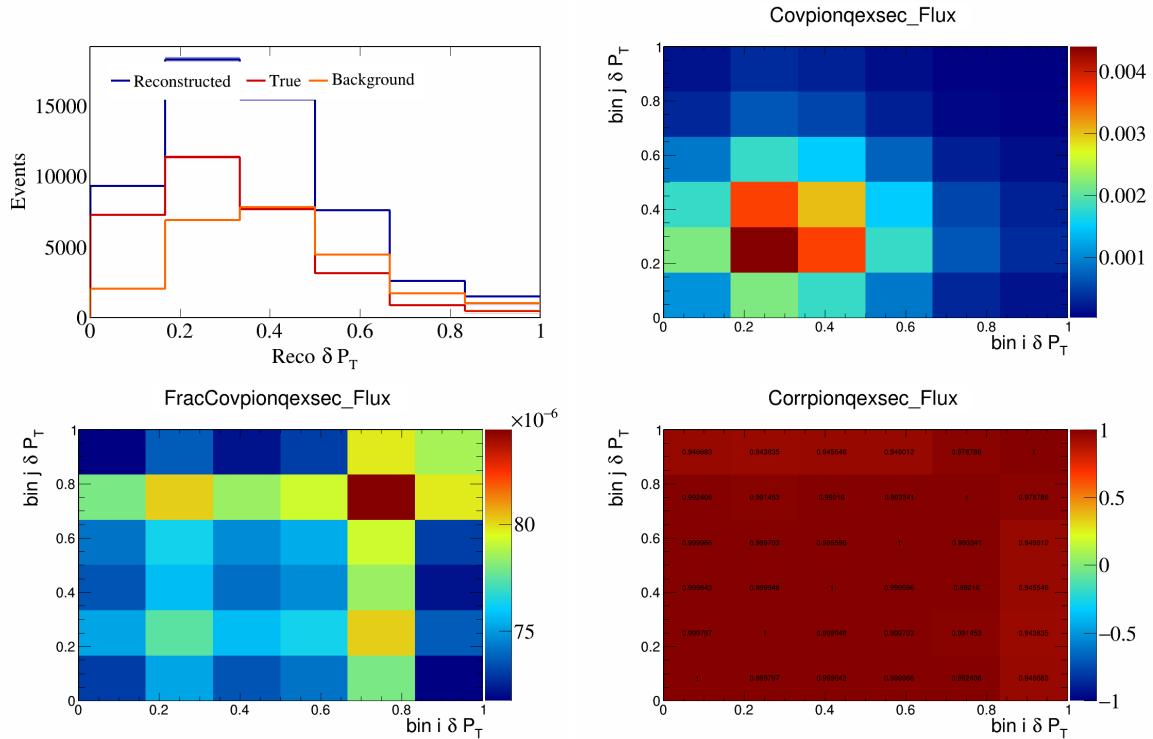


Figure 728: PionQeXSec variations for δP_T .

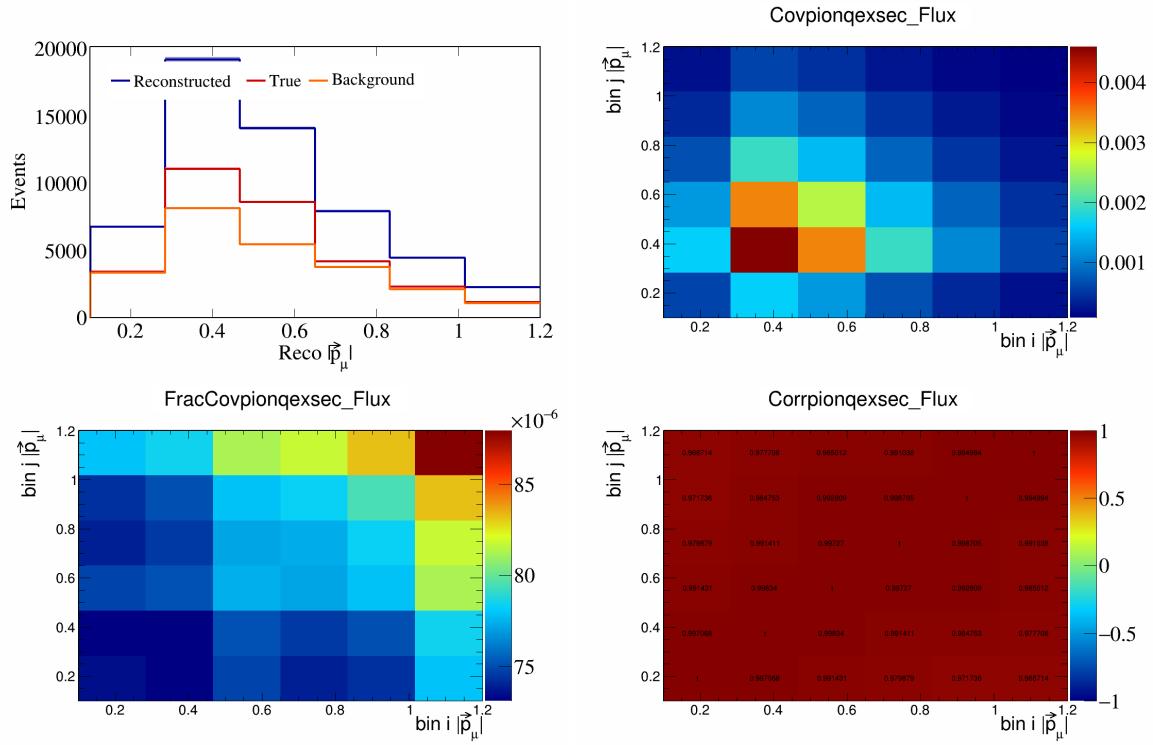


Figure 729: PionQeXSec variations for $|\vec{p}_\mu|$.

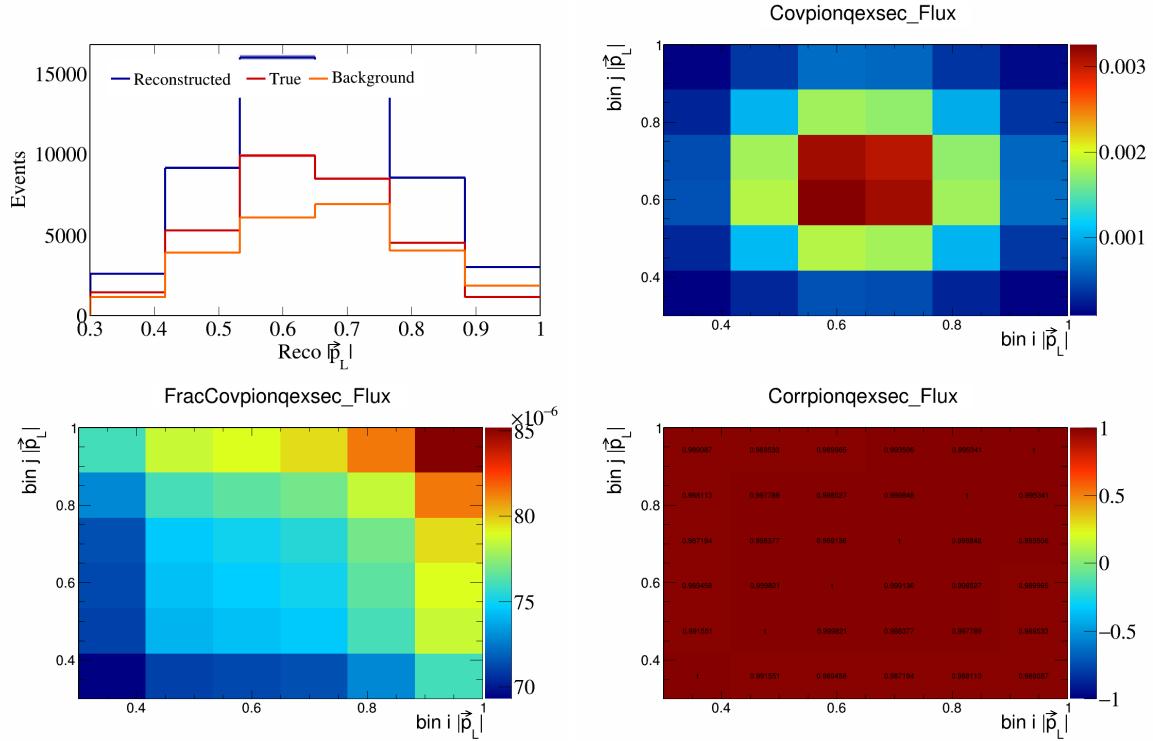


Figure 730: PionQeXSec variations for $|\vec{p}_L|$.

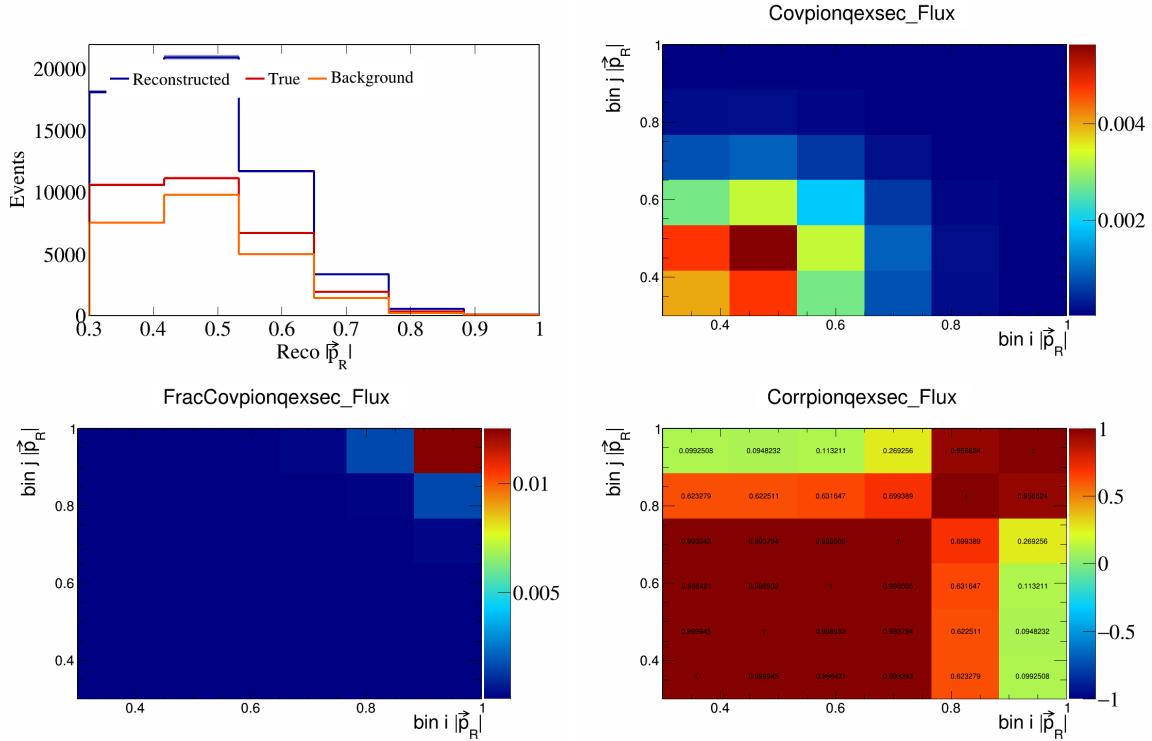


Figure 731: PionQeXSec variations for $|\vec{p}_R|$.

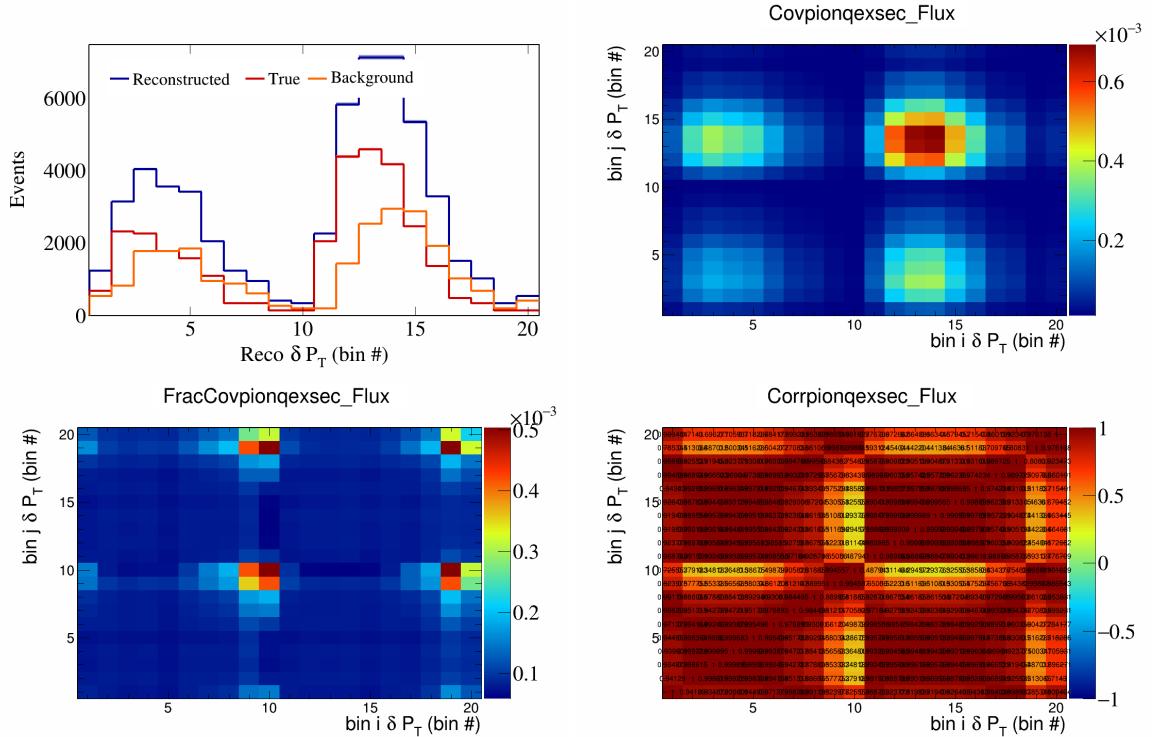


Figure 732: PionQeXSec variations for δP_T in $\cos(\theta_{\vec{p}_\mu})$.

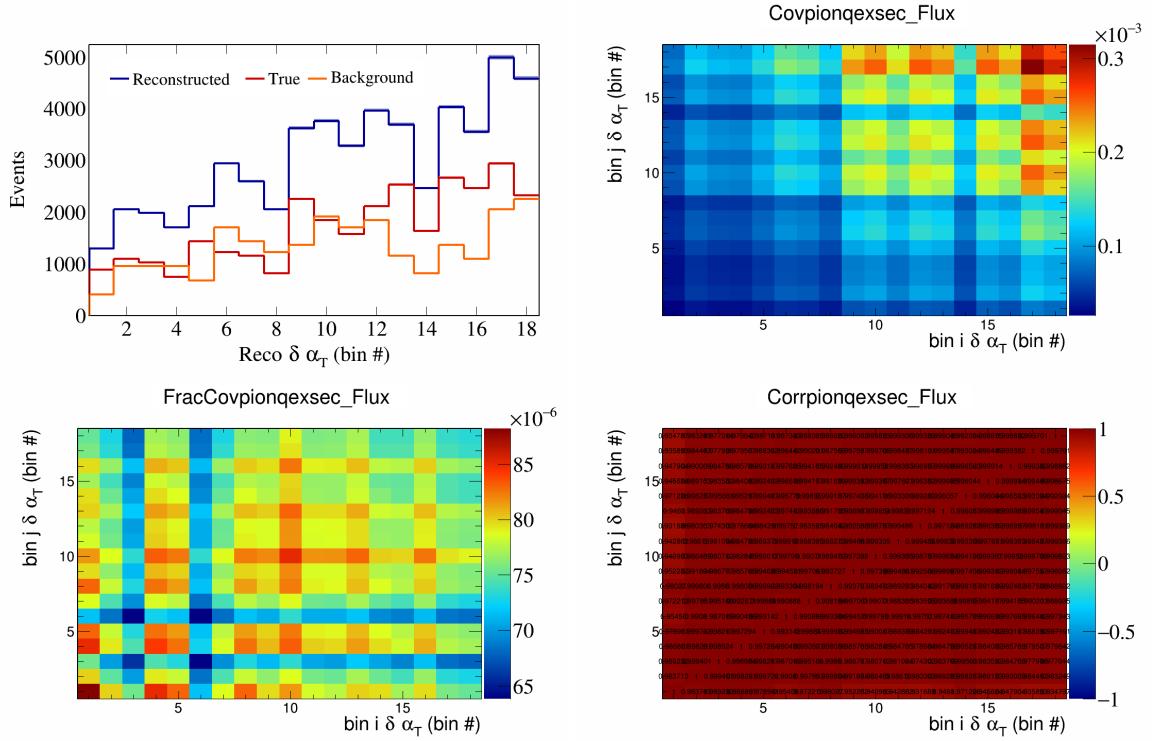


Figure 733: PionQeXSec variations for $\delta \alpha_T$ in $\cos(\theta_{\vec{p}_\mu})$.

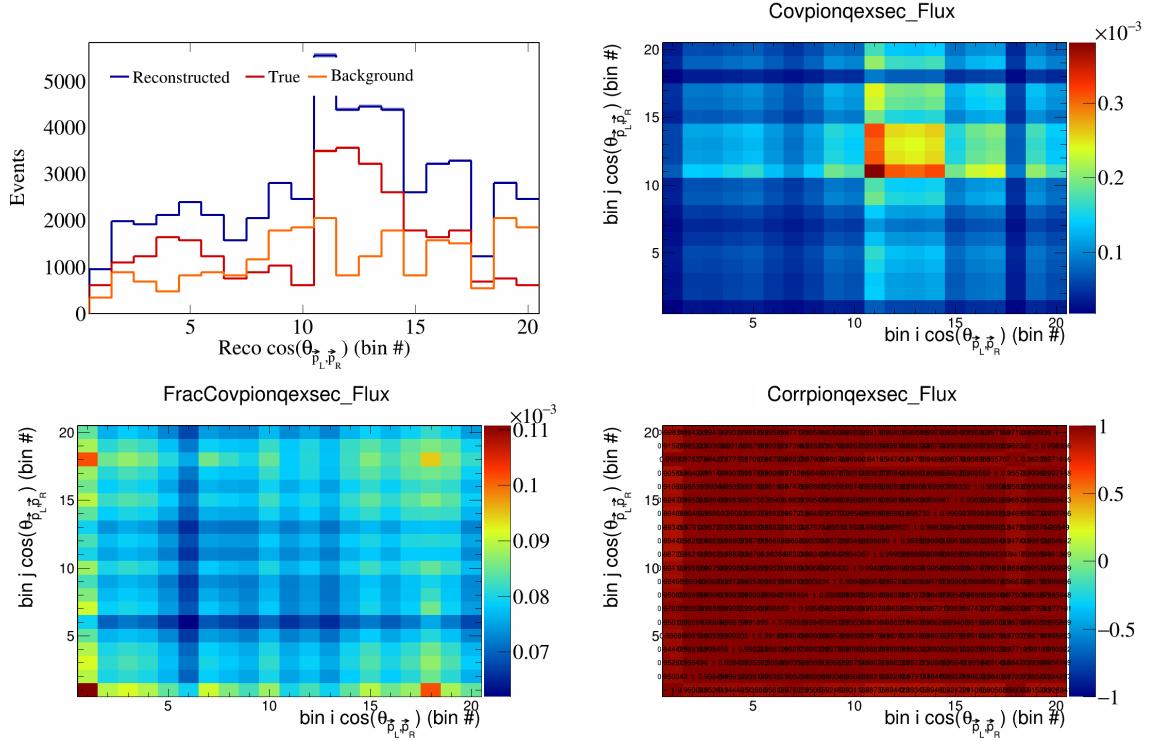


Figure 734: PionQeXSec variations for $\cos(\theta_{\vec{p}_L, \vec{p}_R})$ in $\cos(\theta_{\vec{p}_\mu})$.

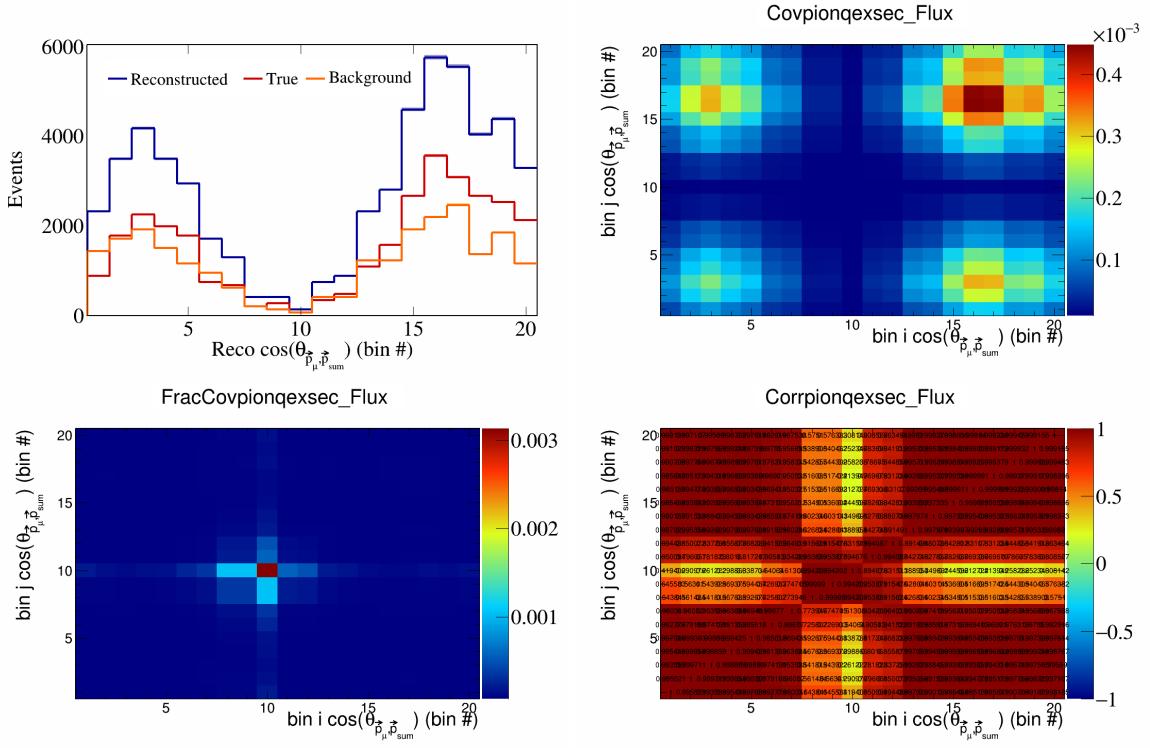


Figure 735: PionQeXSec variations for $\cos(\theta_{\vec{p}_\mu \vec{p}_{\text{sum}}})$ in $\cos(\theta_{\vec{p}_\mu})$.

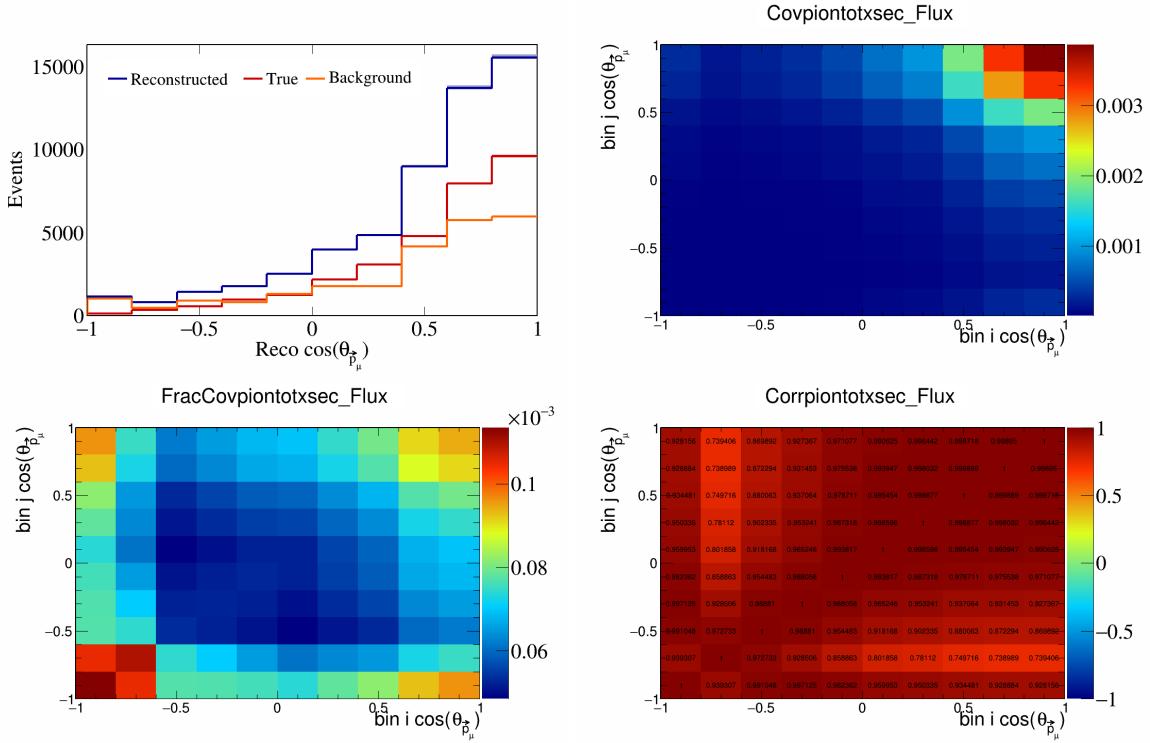


Figure 736: PionTotXSec variations for $\cos(\theta_{\vec{p}_\mu})$.

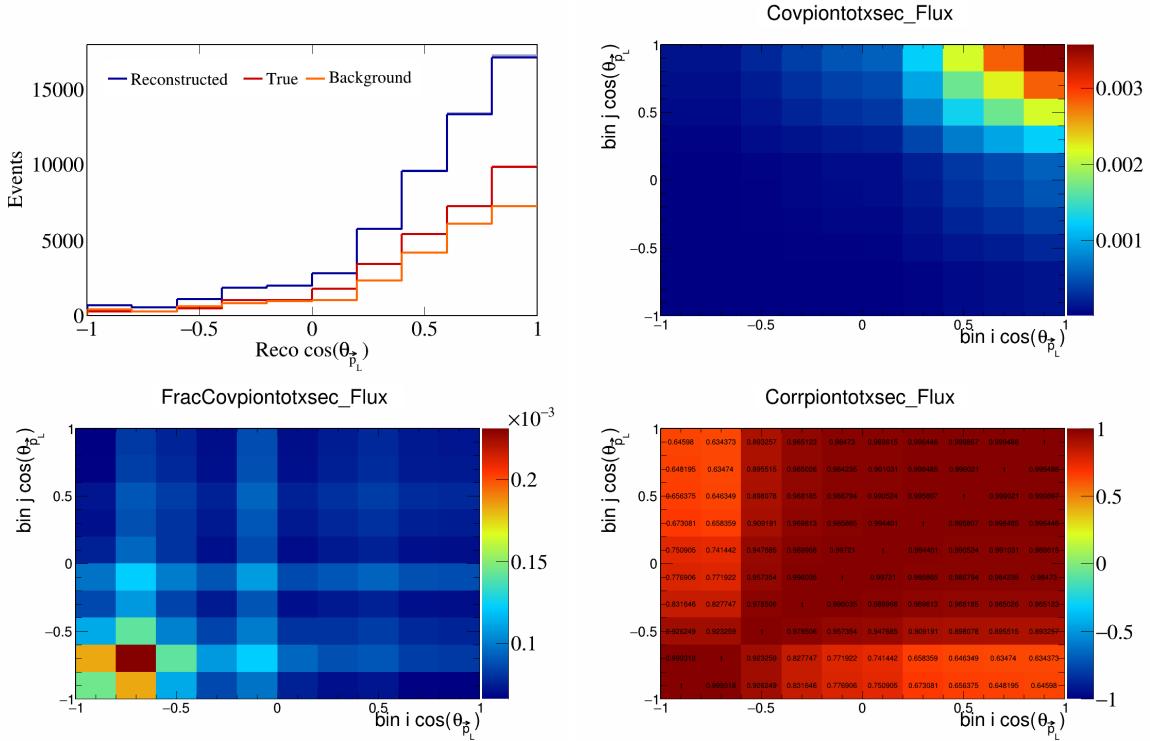


Figure 737: PionTotXSec variations for $\cos(\theta_{\vec{p}_L})$.

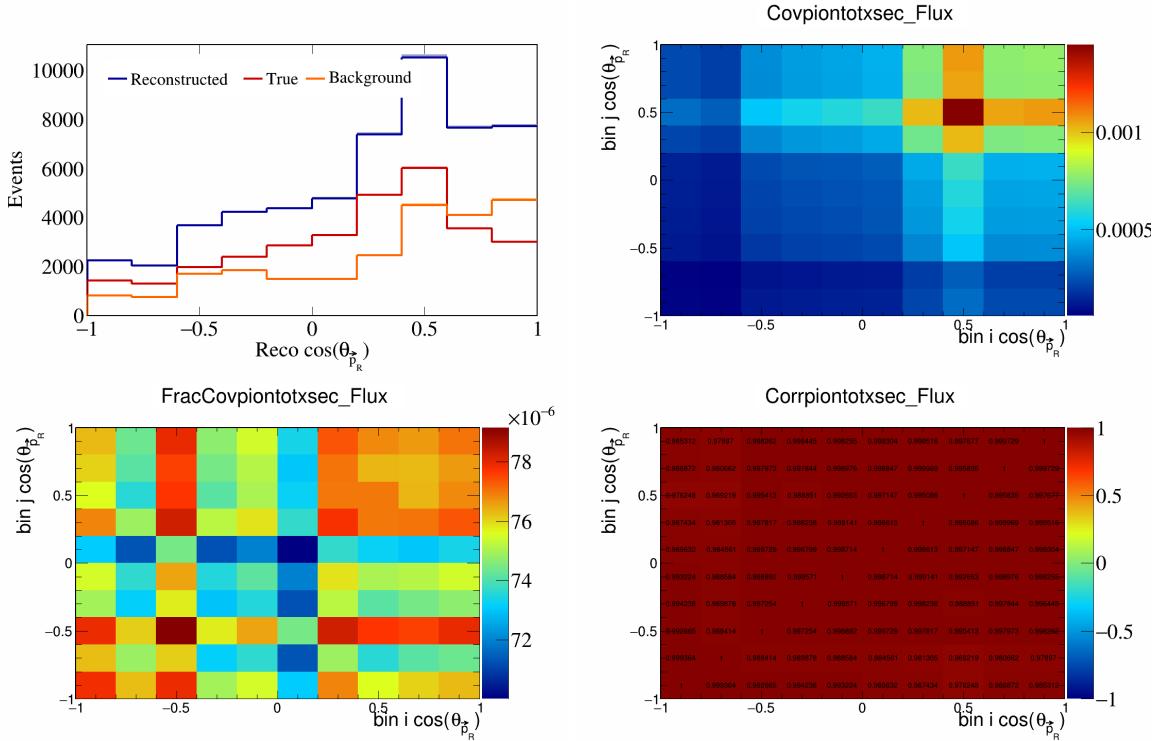


Figure 738: PionTotXSec variations for $\cos(\theta_{\vec{p}_R})$.

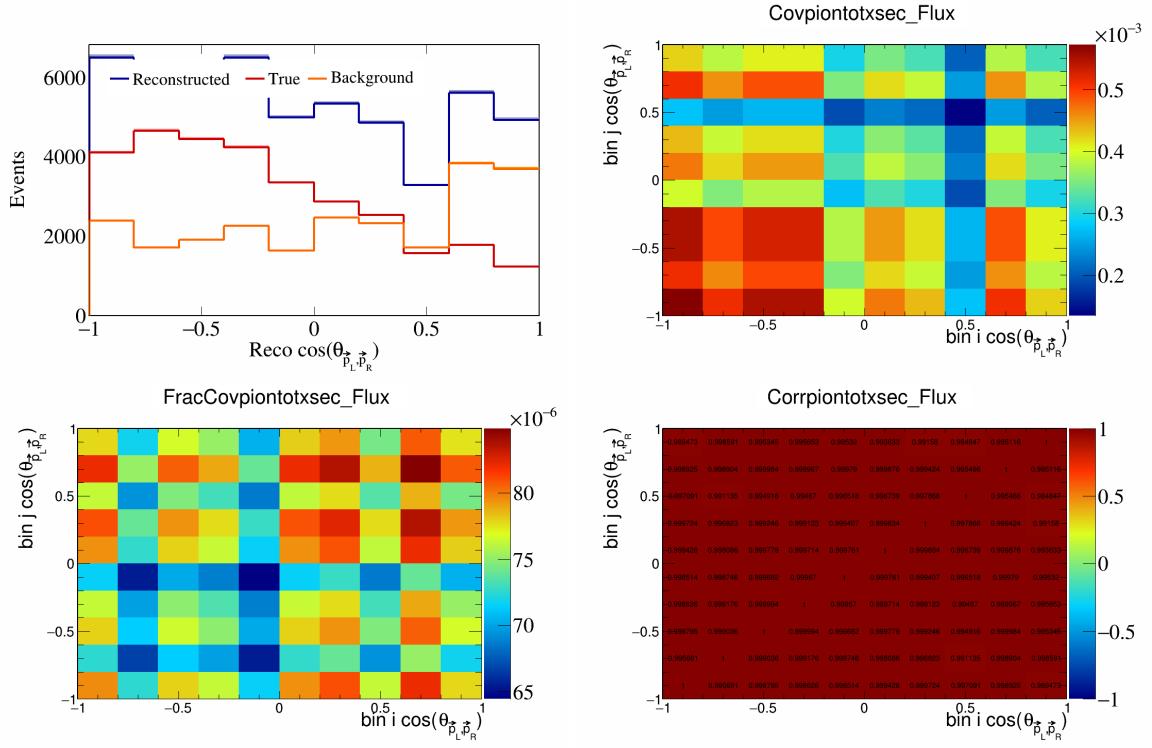


Figure 739: PionTotXSec variations for $\cos(\theta_{\vec{p}_L, \vec{p}_R})$.

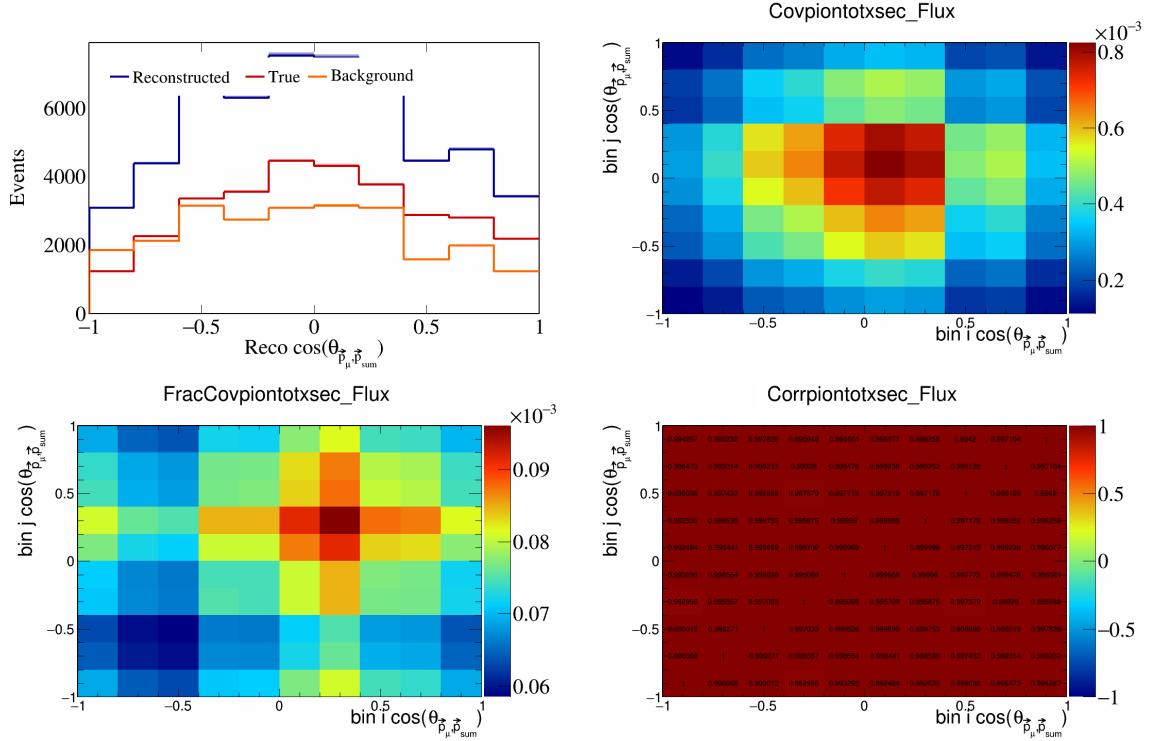


Figure 740: PionTotXSec variations for $\cos(\theta_{\vec{p}_\mu, \vec{p}_{\text{sum}}})$.

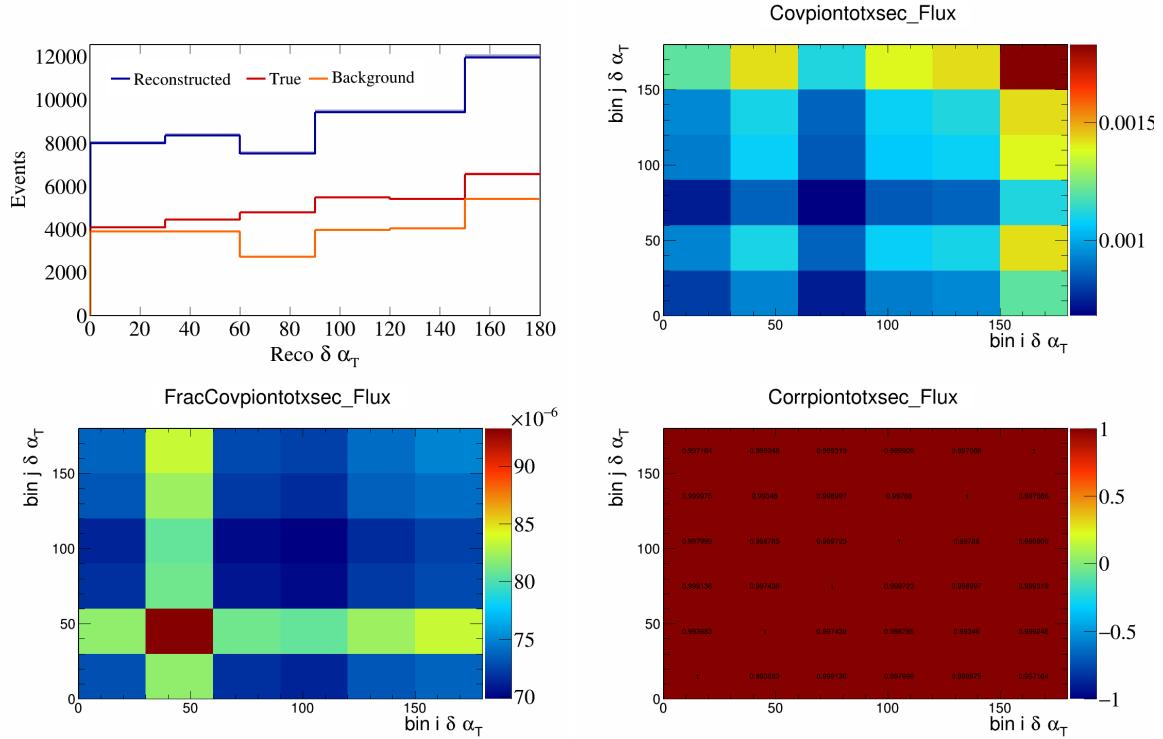


Figure 741: PionTotXSec variations for $\delta\alpha_T$.

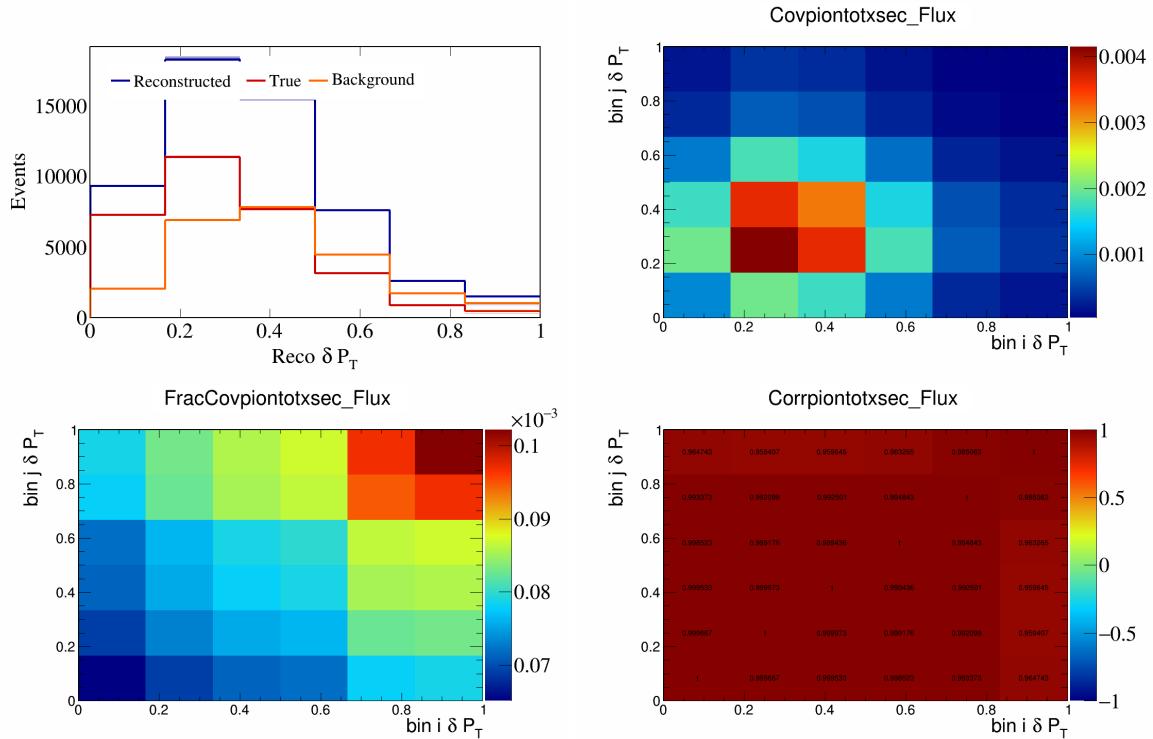


Figure 742: PionTotXSec variations for δP_T .

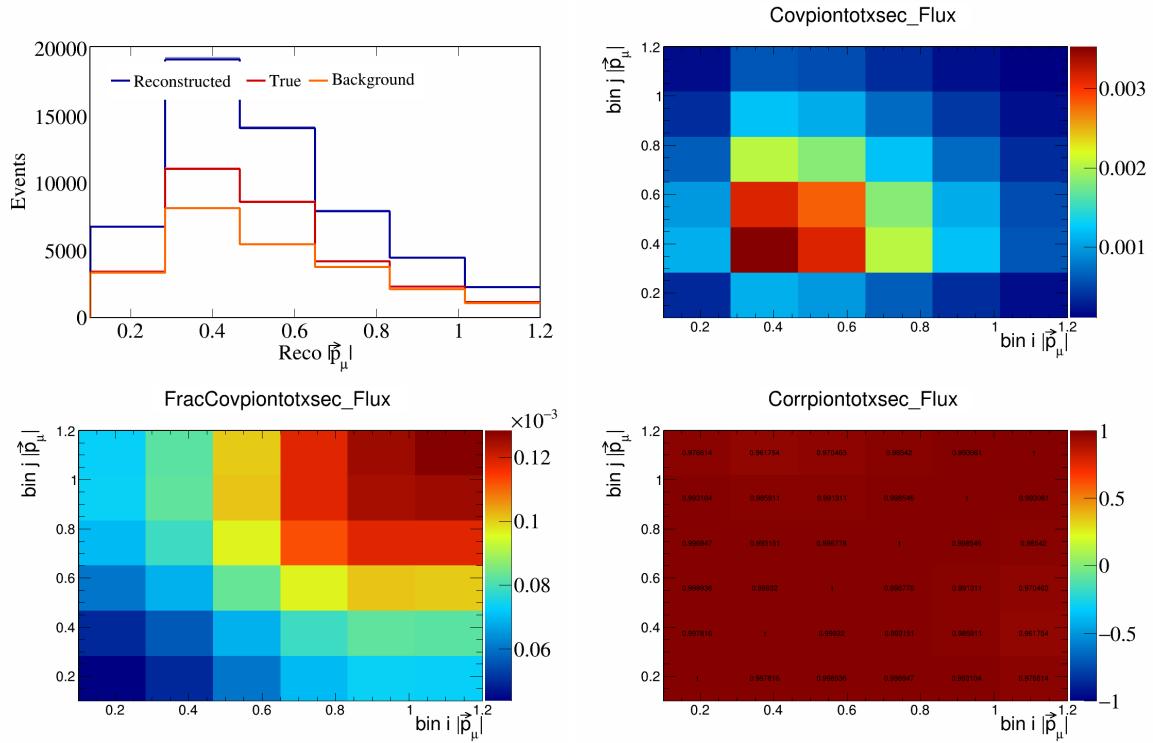


Figure 743: PionTotXSec variations for $|\vec{p}_\mu|$.

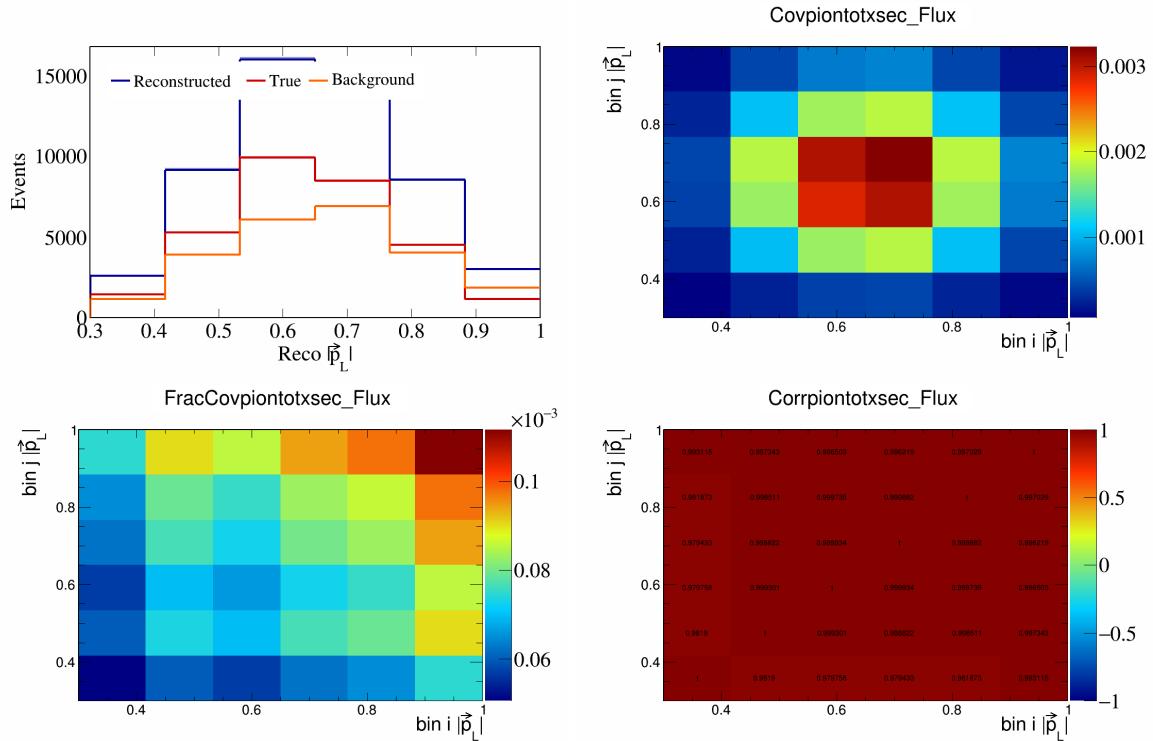


Figure 744: PionTotXSec variations for $|\vec{p}_L|$.

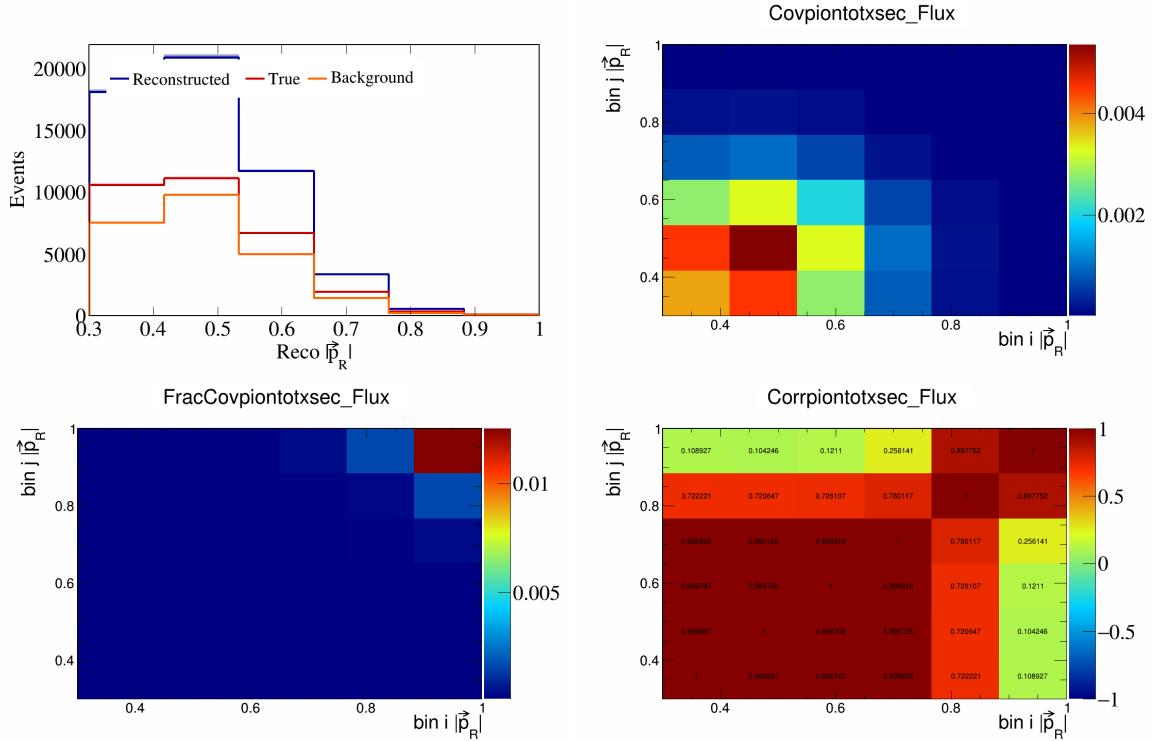


Figure 745: PionTotXSec variations for $|\vec{p}_R|$.

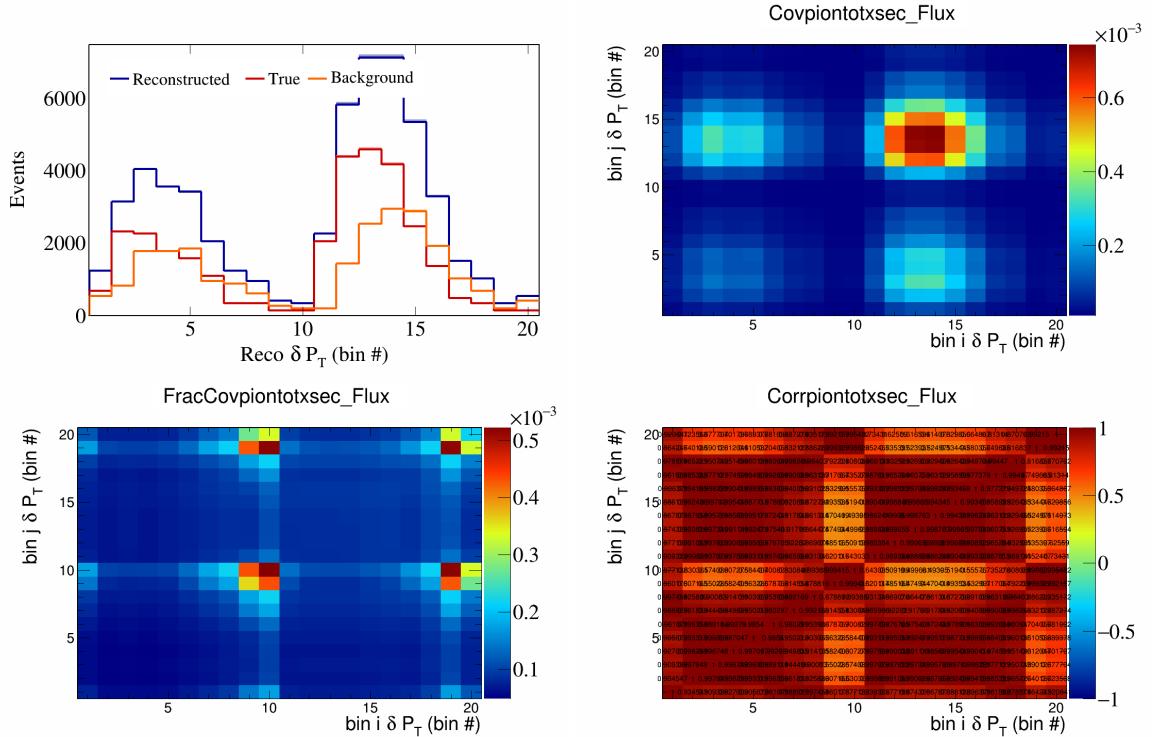


Figure 746: PionTotXSec variations for δP_T in $\cos(\theta_{\vec{p}_\mu})$.

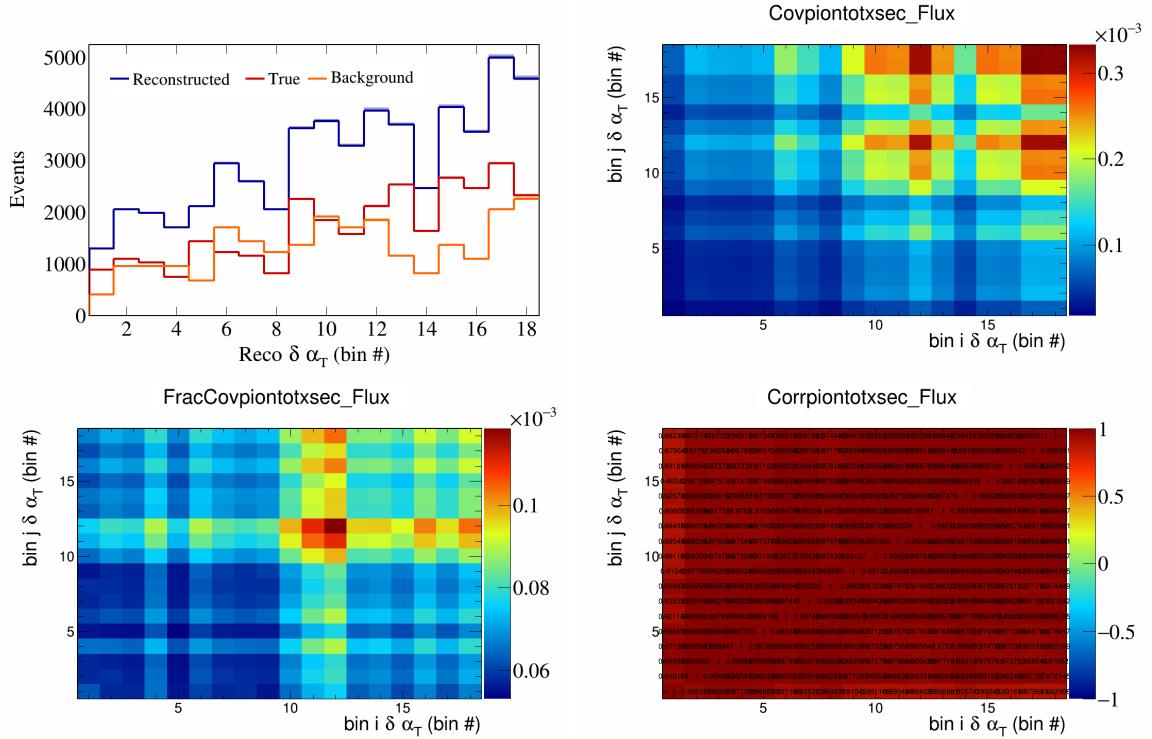


Figure 747: PionTotXSec variations for $\delta \alpha_T$ in $\cos(\theta_{\vec{p}_\mu})$.

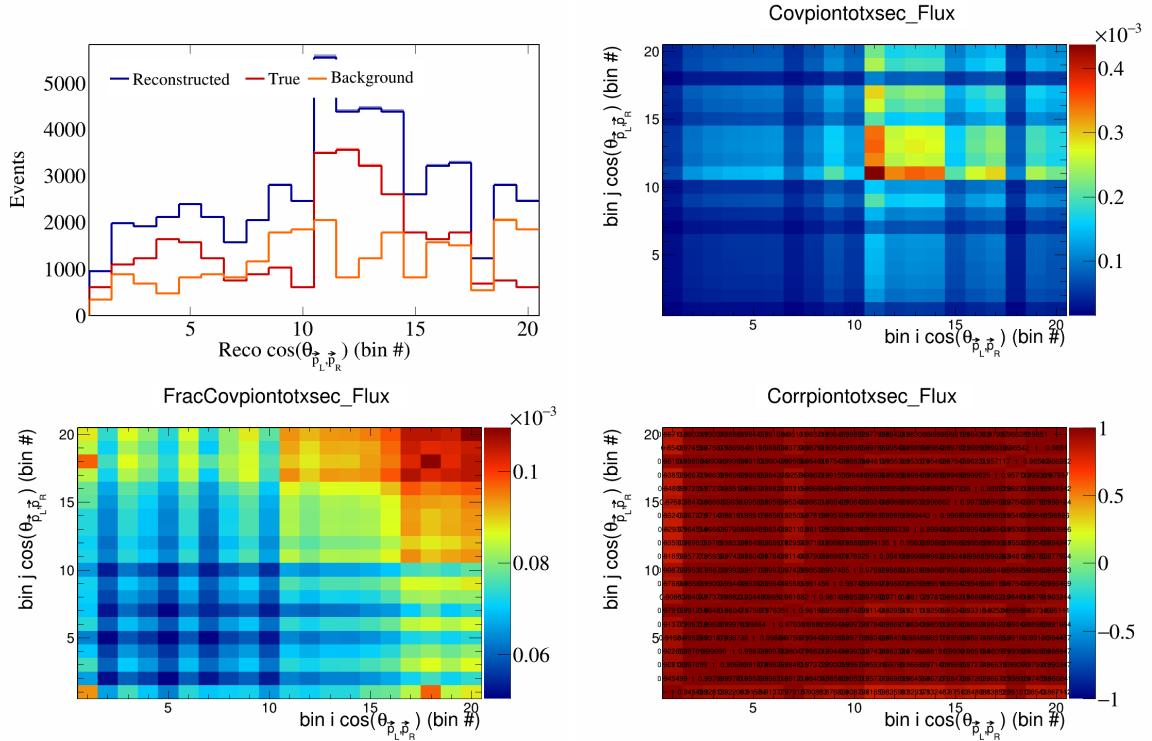


Figure 748: PionTotXSec variations for $\cos(\theta_{\vec{p}_L, \vec{p}_R})$ in $\cos(\theta_{\vec{p}_\mu})$.

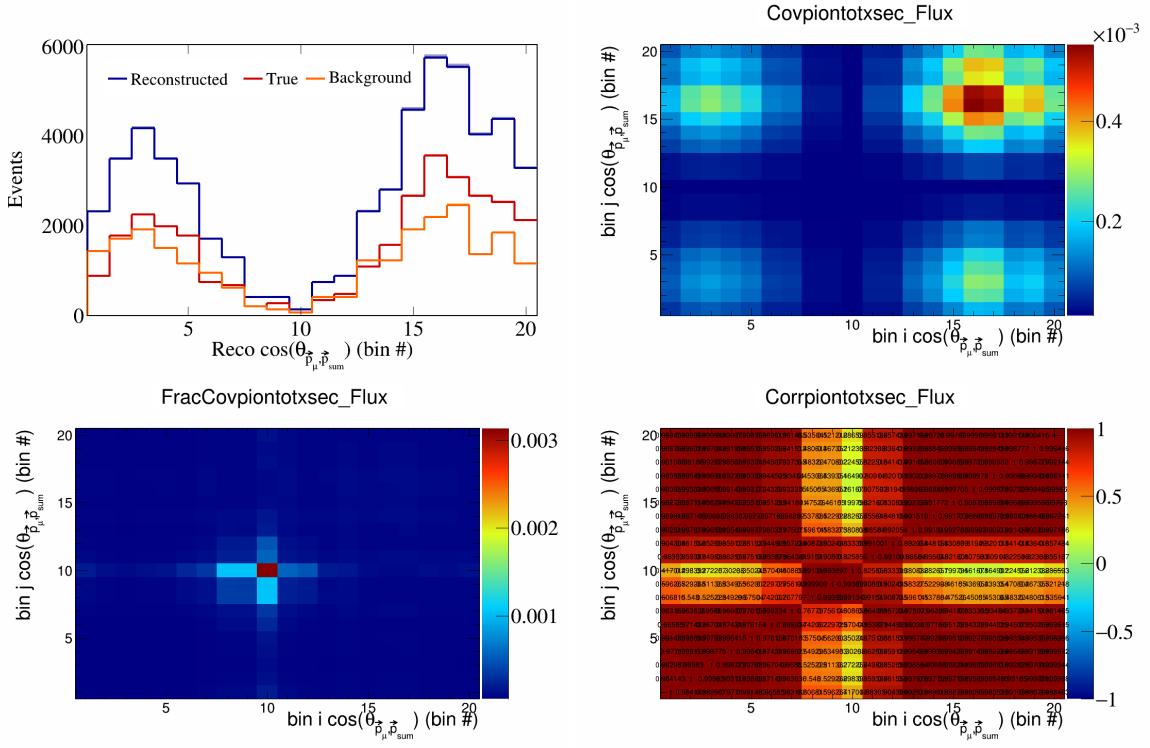


Figure 749: PionTotXSec variations for $\cos(\theta_{\vec{p}_\mu, \vec{p}_{\text{sum}}})$ in $\cos(\theta_{\vec{p}_\mu})$.

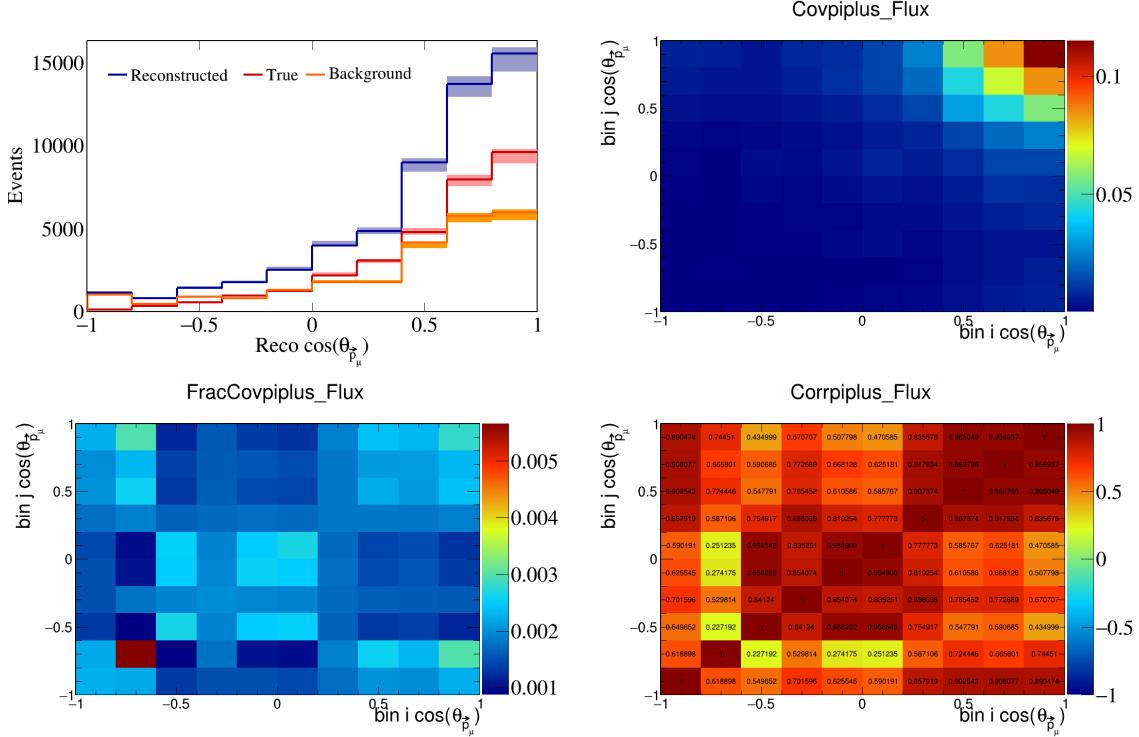


Figure 750: PiPlus variations for $\cos(\theta_{\vec{p}_\mu})$.

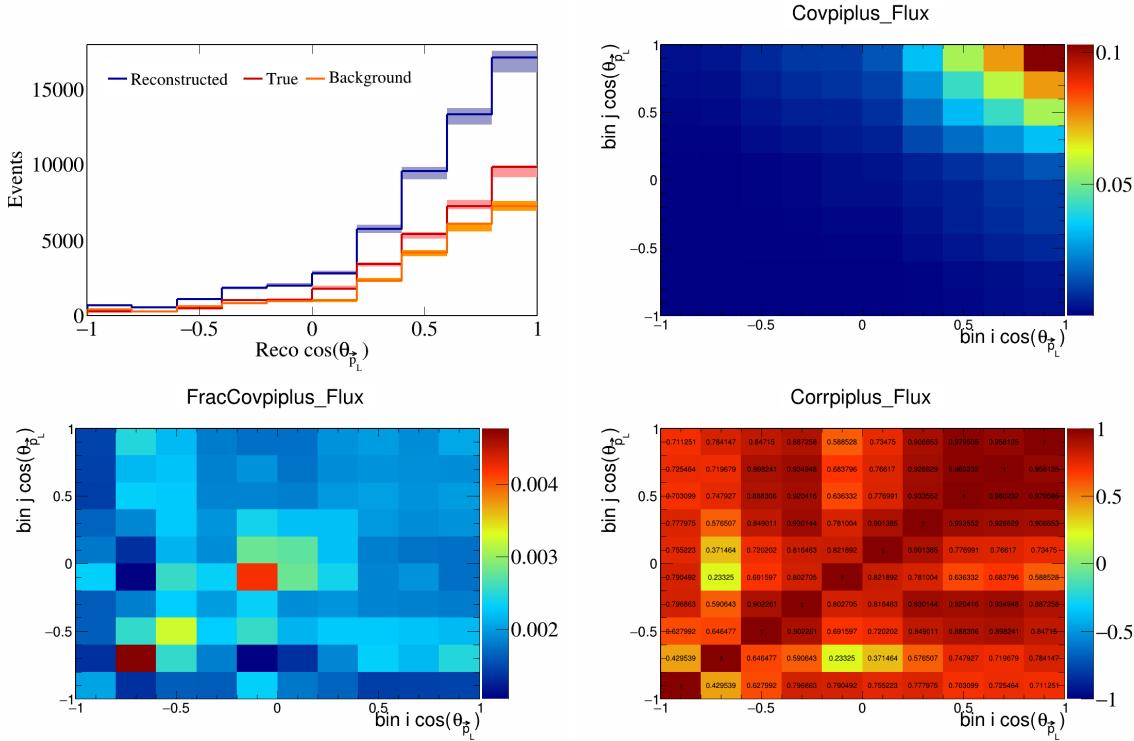


Figure 751: PiPlus variations for $\cos(\theta_{\vec{p}_L})$.

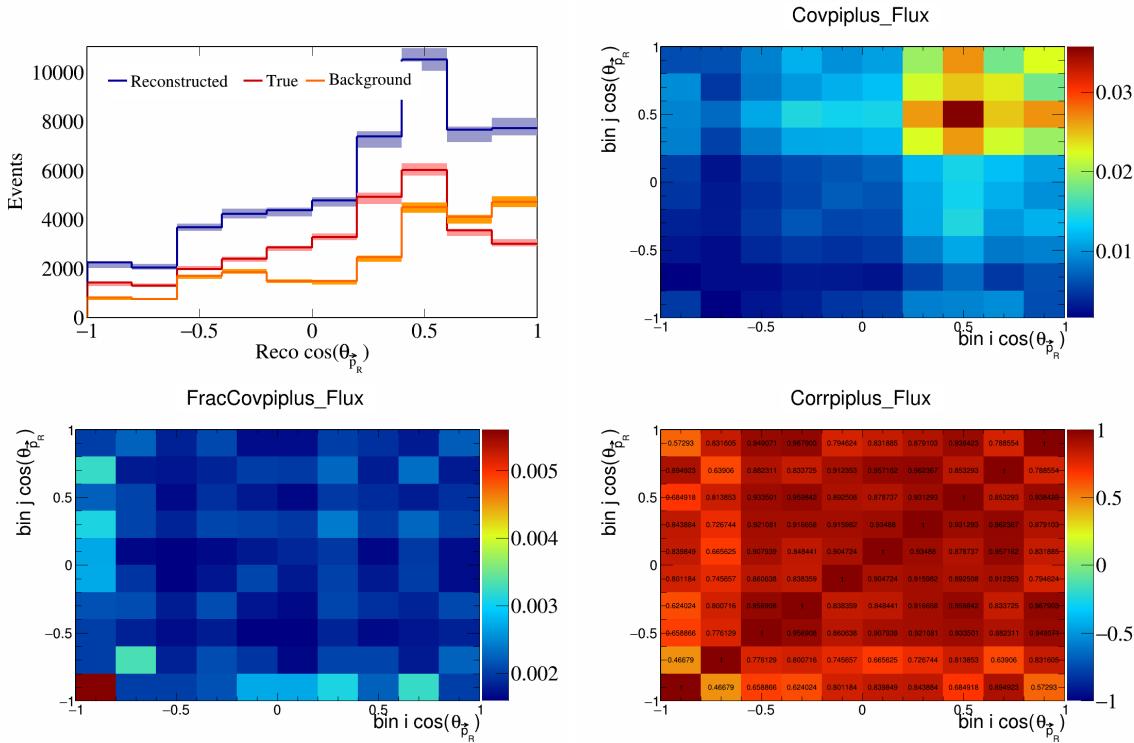


Figure 752: PiPlus variations for $\cos(\theta_{\vec{p}_R})$.

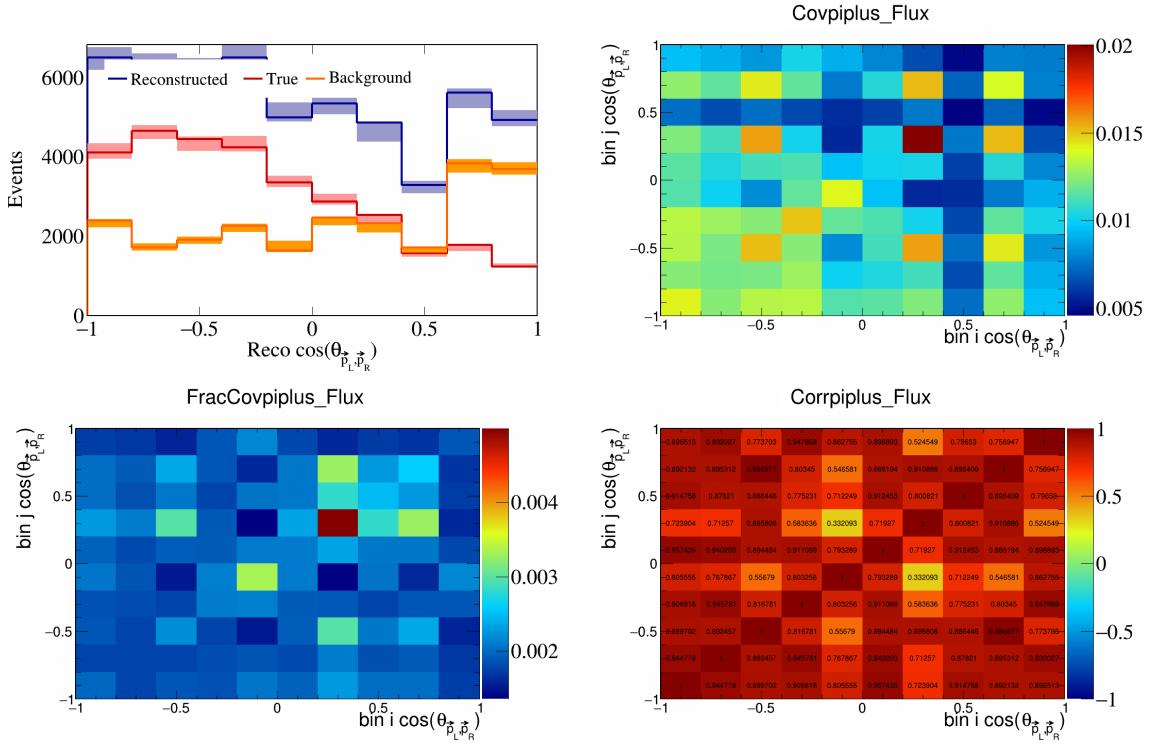


Figure 753: PiPlus variations for $\cos(\theta_{\vec{p}_L, \vec{p}_R})$.

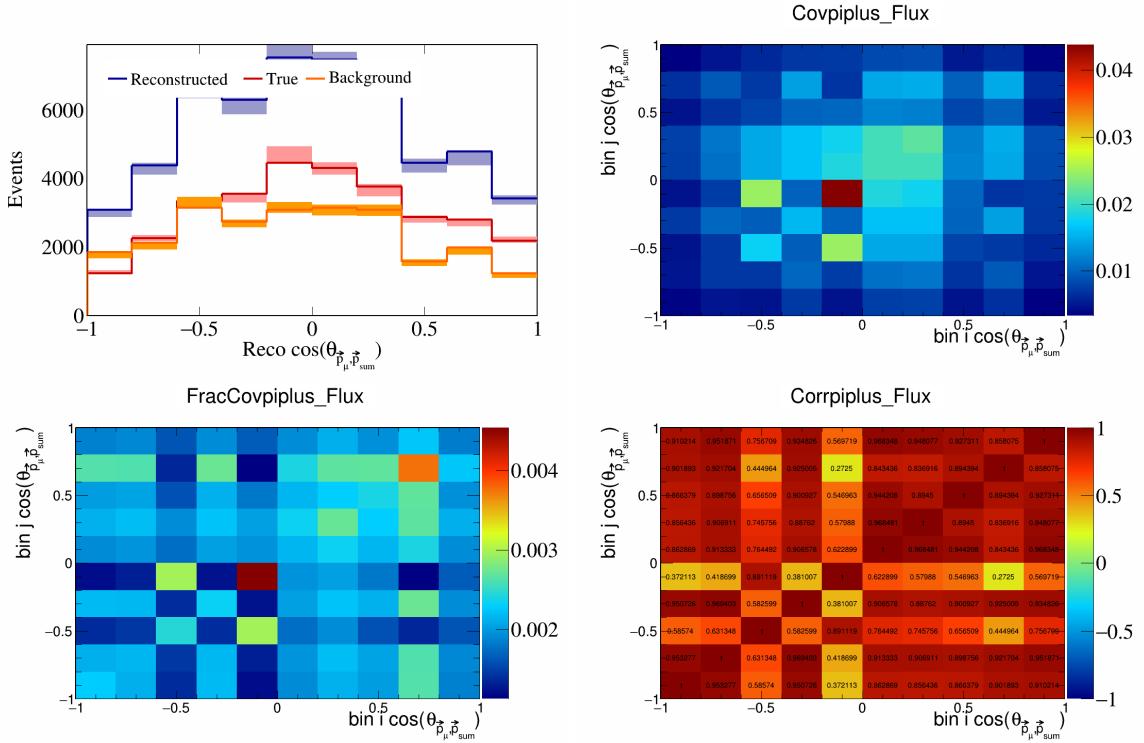


Figure 754: PiPlus variations for $\cos(\theta_{\vec{p}_\mu, \vec{p}_{\text{sum}}})$.

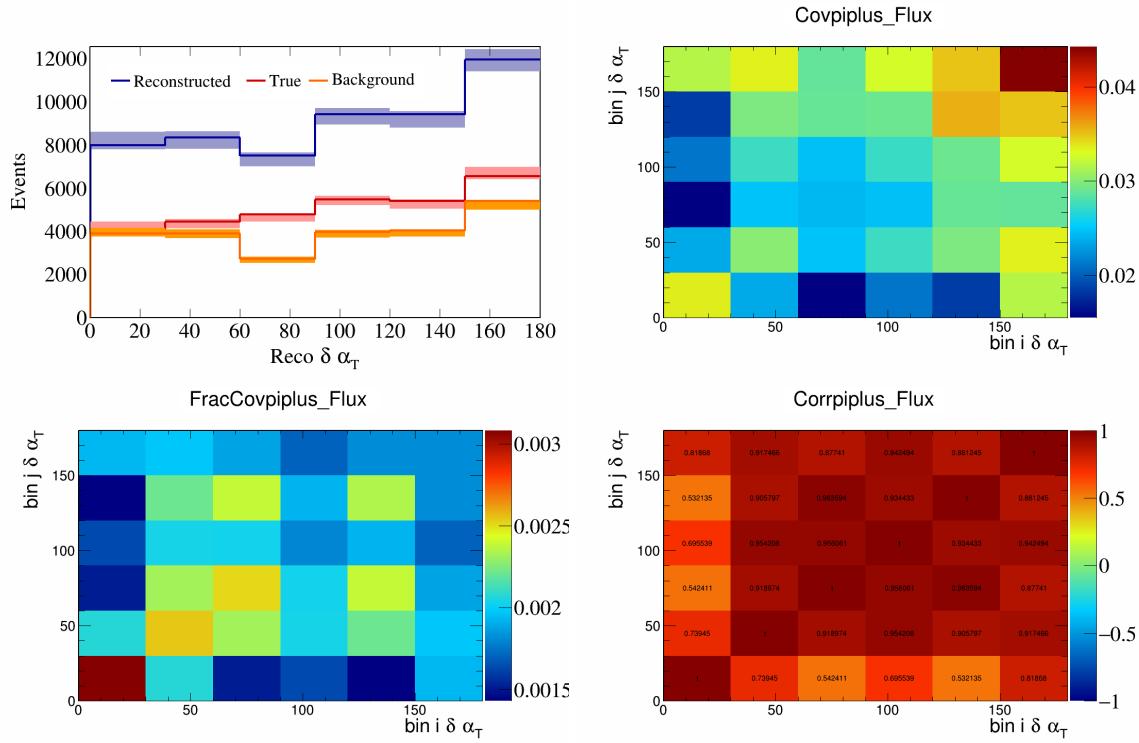


Figure 755: PiPlus variations for $\delta\alpha_T$.

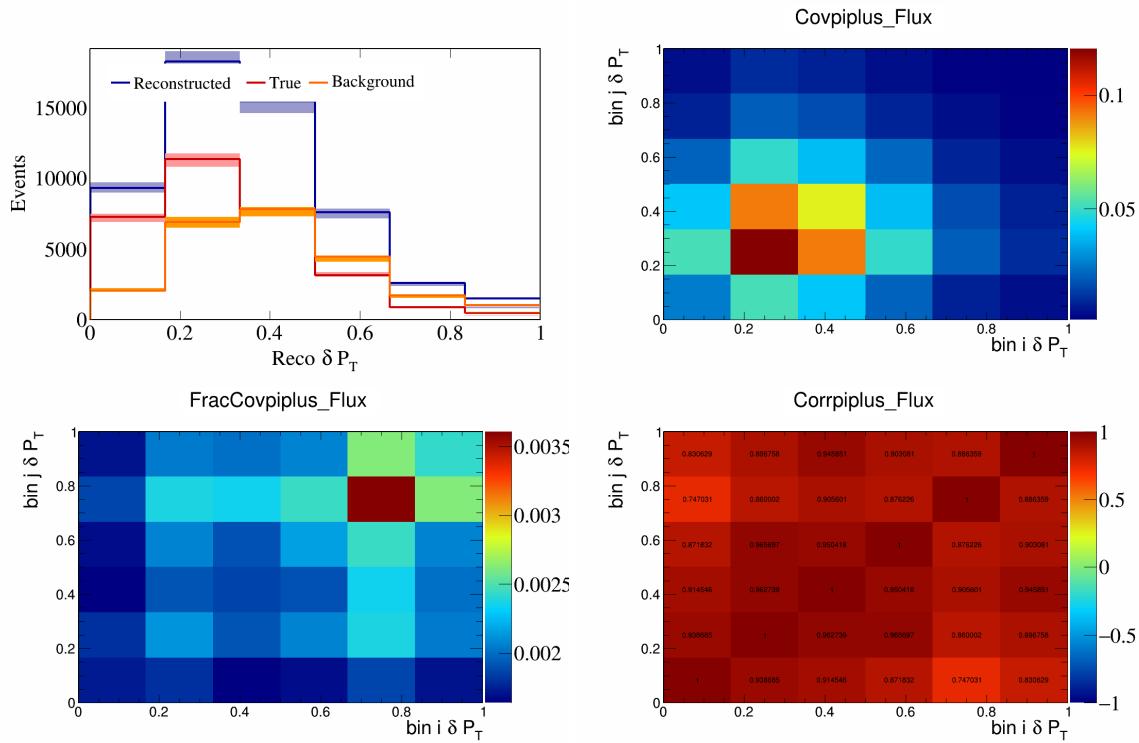


Figure 756: PiPlus variations for δP_T .

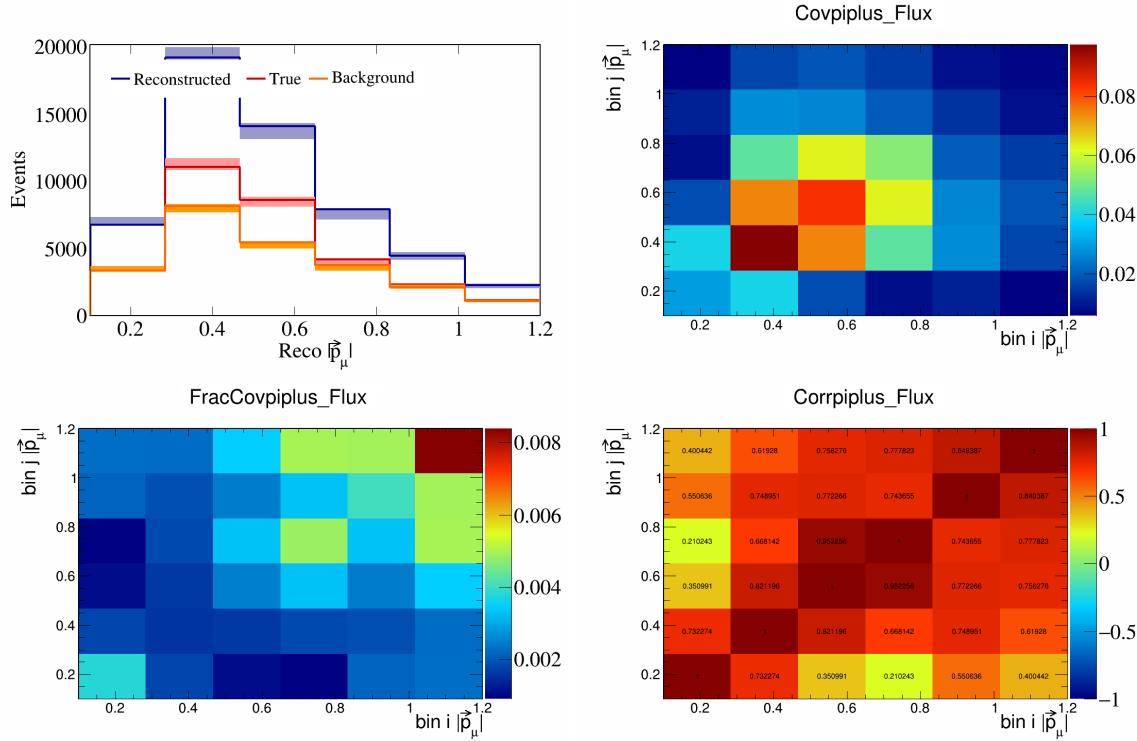


Figure 757: PiPlus variations for $|\vec{p}_\mu|$.

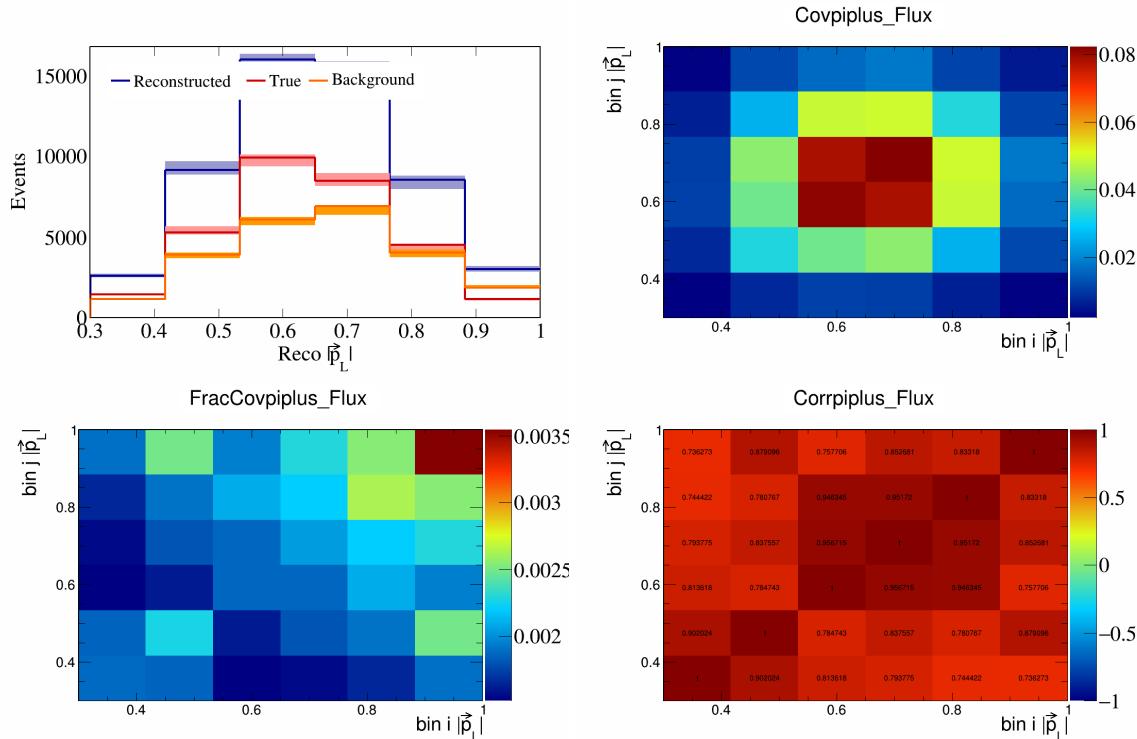


Figure 758: PiPlus variations for $|\vec{p}_L|$.

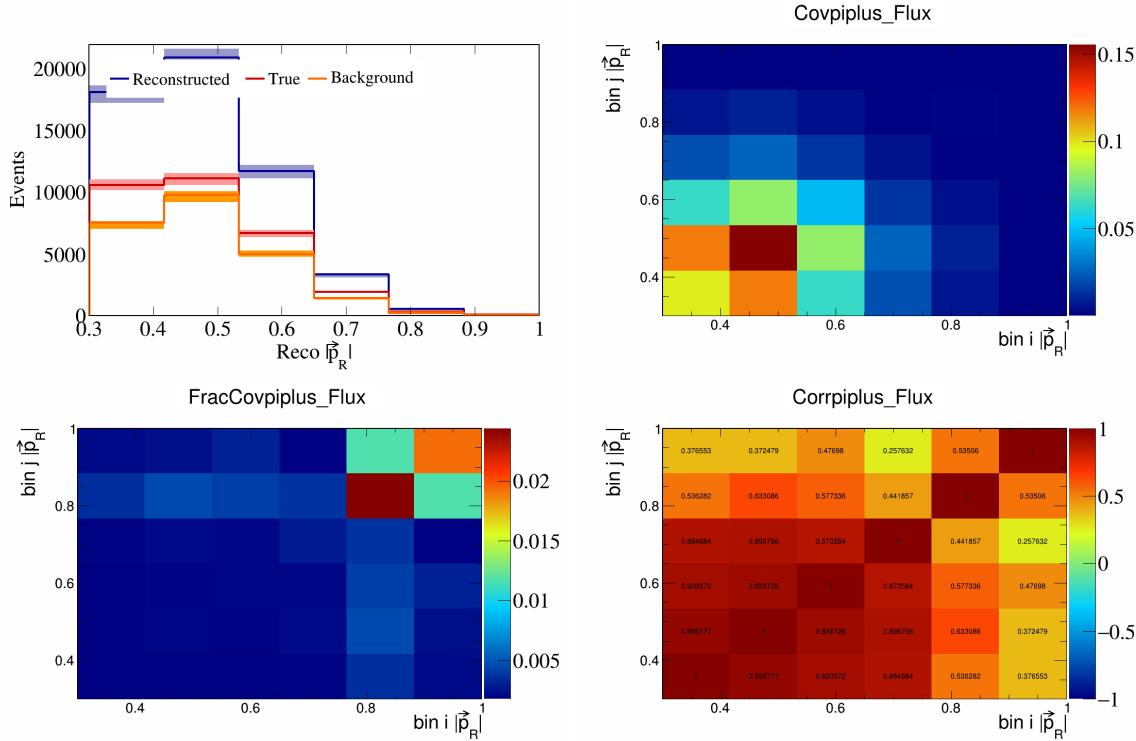


Figure 759: PiPlus variations for $|\vec{p}_R|$.

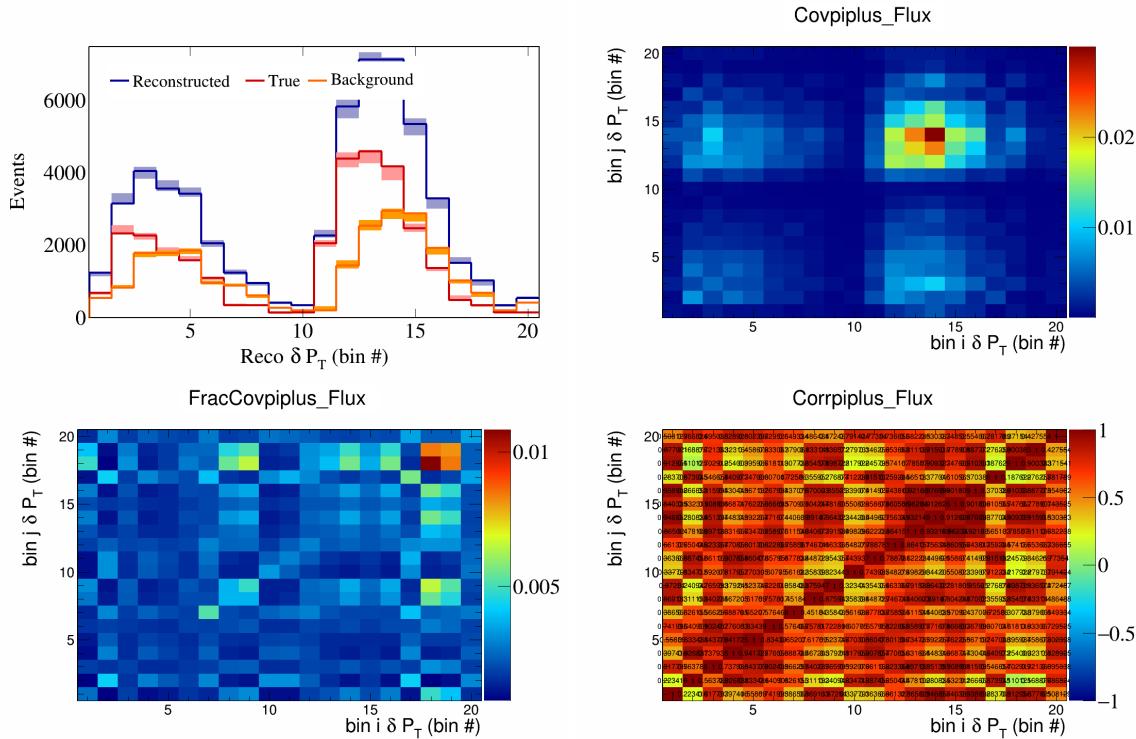


Figure 760: PiPlus variations for δP_T in $\cos(\theta_{\vec{p}_\mu})$.

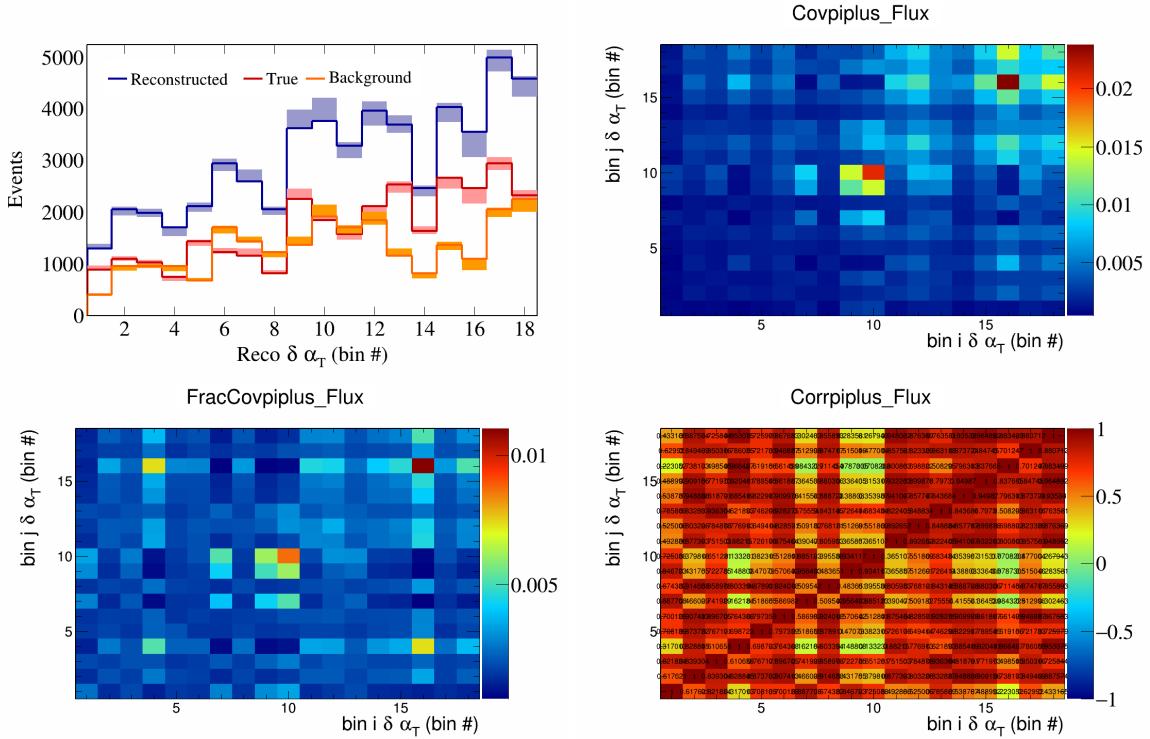


Figure 761: PiPlus variations for $\delta \alpha_T$ in $\cos(\theta_{\vec{p}_\mu})$.

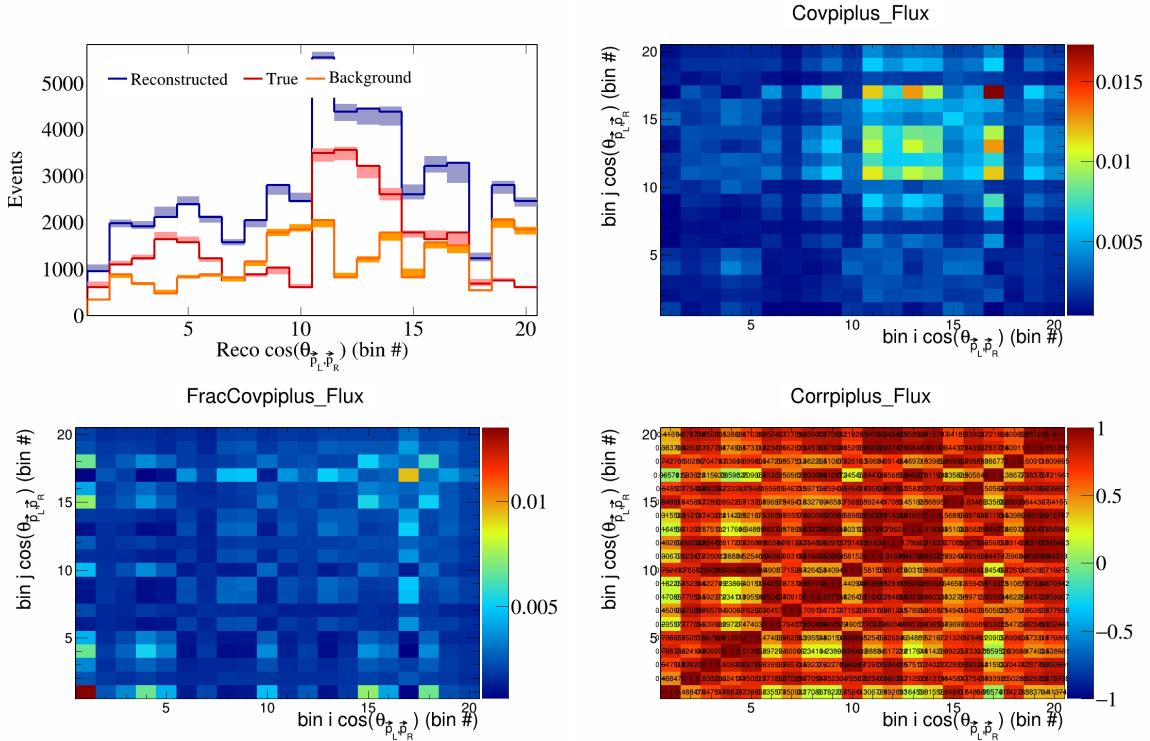


Figure 762: PiPlus variations for $\cos(\theta_{\vec{p}_L, \vec{p}_R})$ in $\cos(\theta_{\vec{p}_\mu})$.

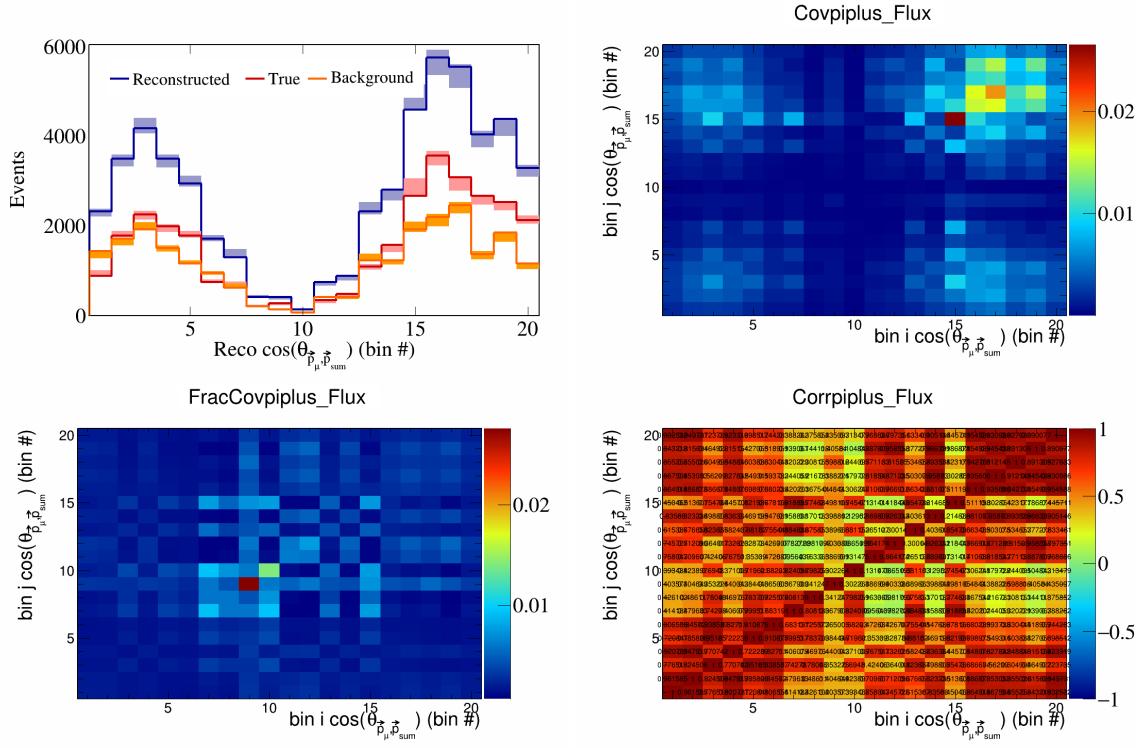


Figure 763: PiPlus variations for $\cos(\theta_{\vec{p}_\mu, \vec{p}_{\text{sum}}})$ in $\cos(\theta_{\vec{p}_\mu})$.

220 5.3 Statistical systematics

221 In this appendix, the covariance matrices for the statistical systematics are plotted.

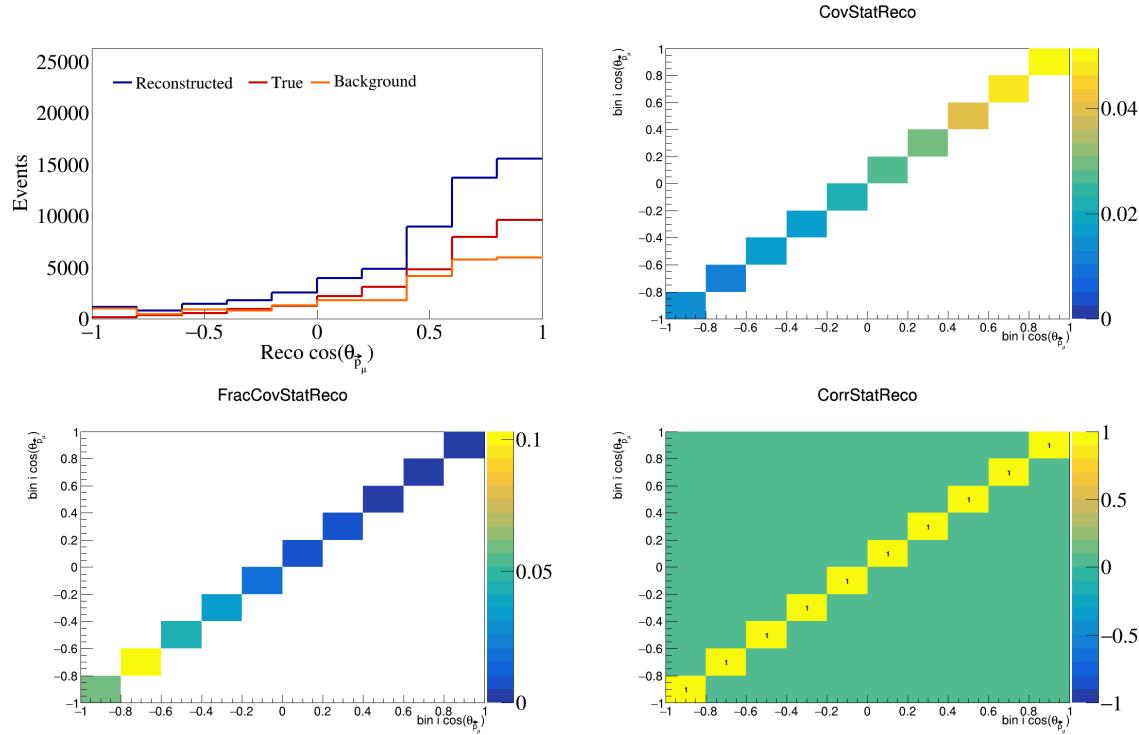


Figure 764: Statistical variations for $\cos(\theta_{\vec{p}_\mu})$.

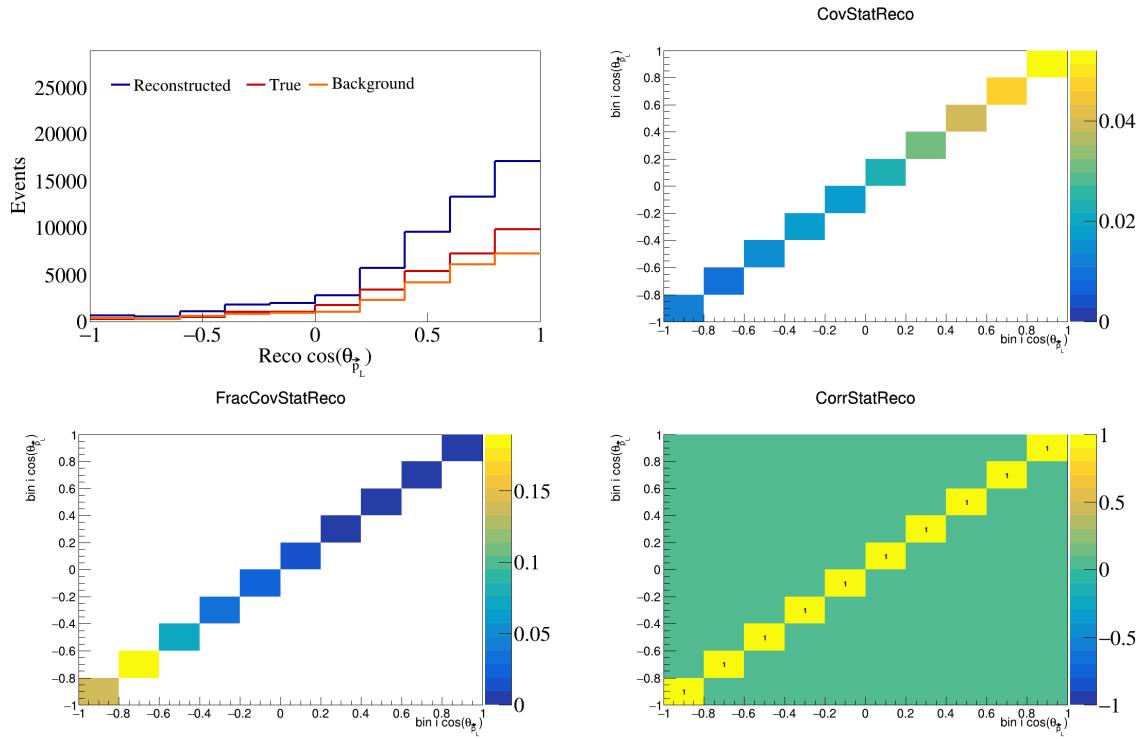


Figure 765: Statistical variations for $\cos(\theta_{\vec{p}_L})$.

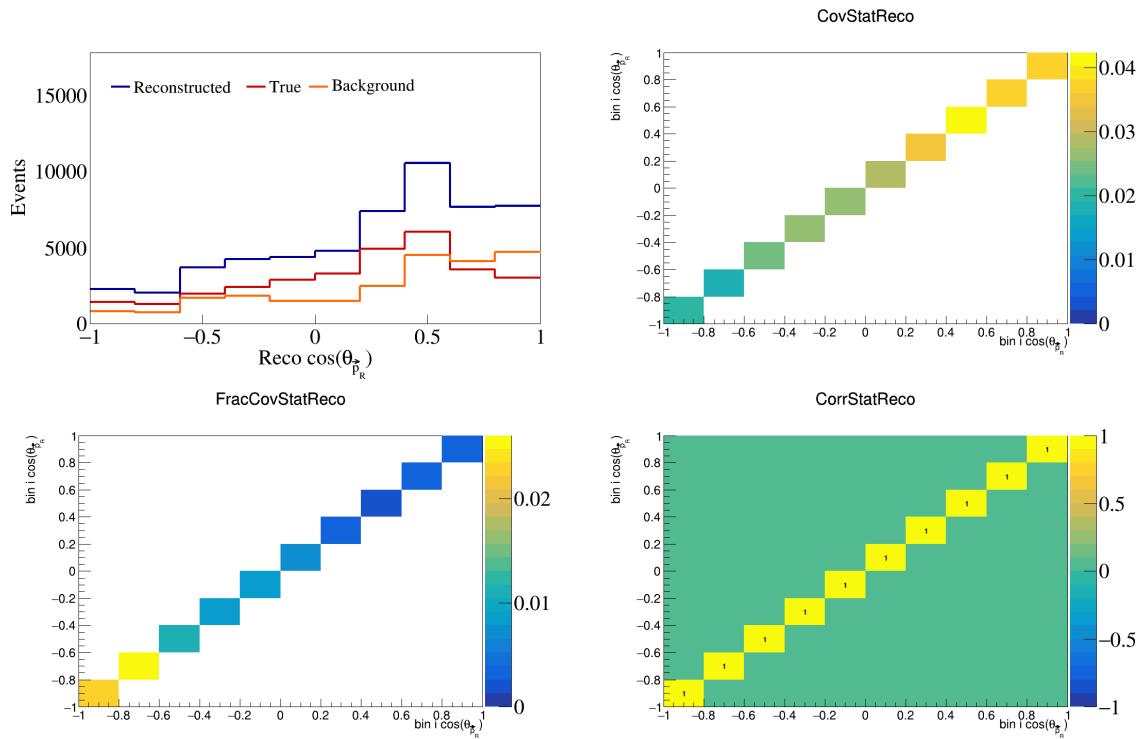


Figure 766: Statistical variations for $\cos(\theta_{\vec{p}_R})$.

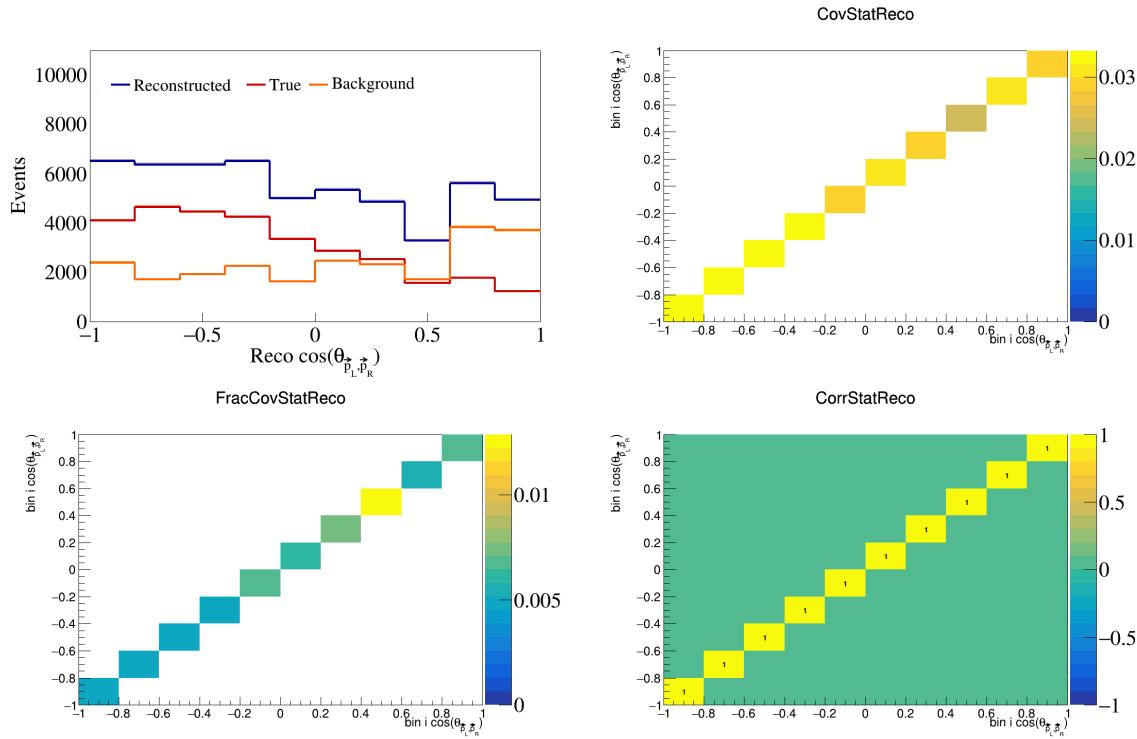


Figure 767: Statistical variations for $\cos(\theta_{\vec{p}_L, \vec{p}_R})$.

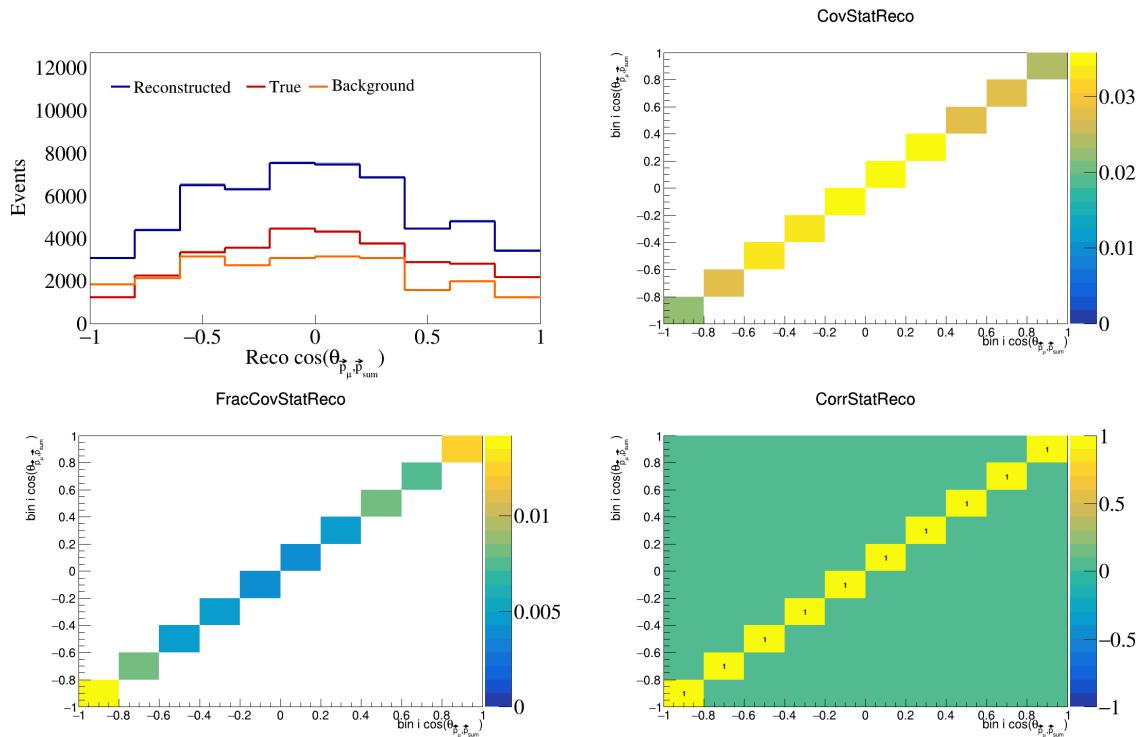


Figure 768: Statistical variations for $\cos(\theta_{\vec{p}_\mu, \vec{p}_{\text{sum}}})$.

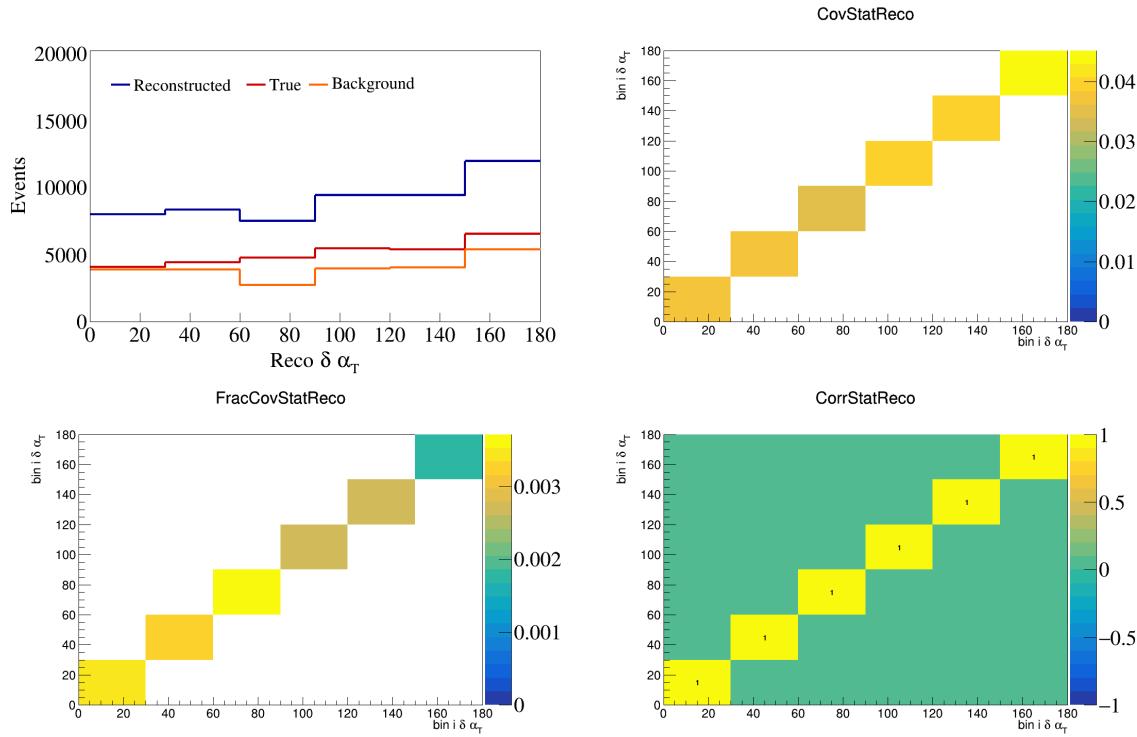


Figure 769: Statistical variations for $\delta\alpha_T$.

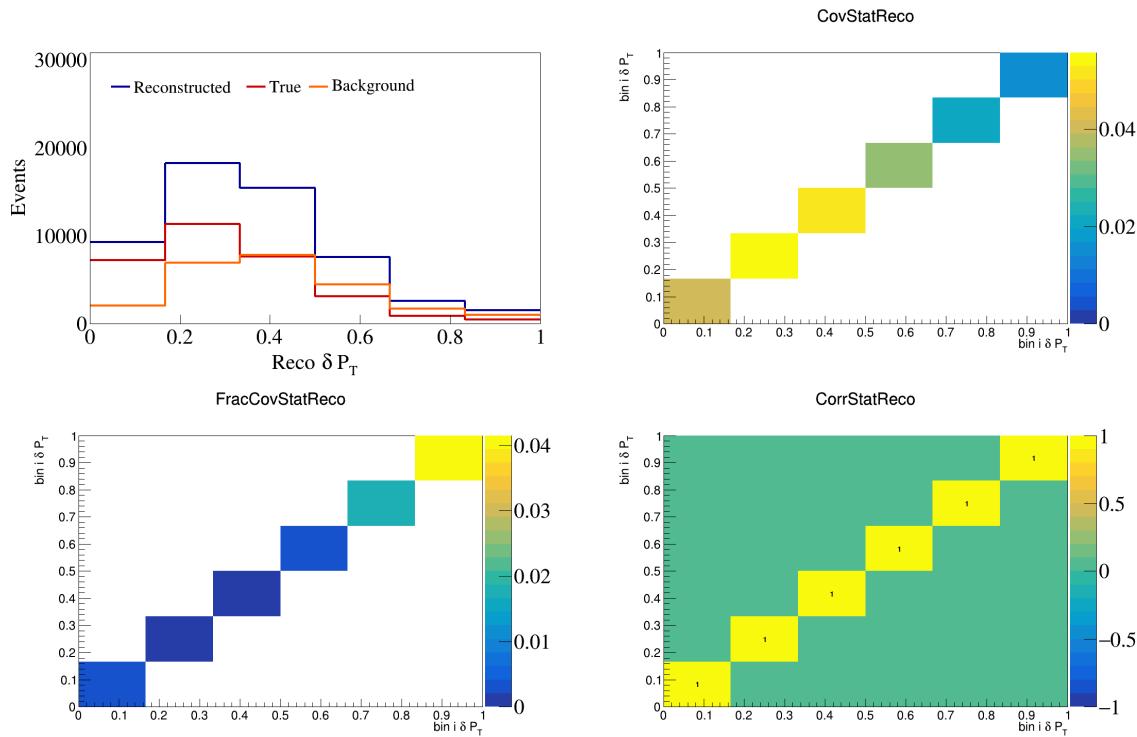


Figure 770: Statistical variations for δP_T .

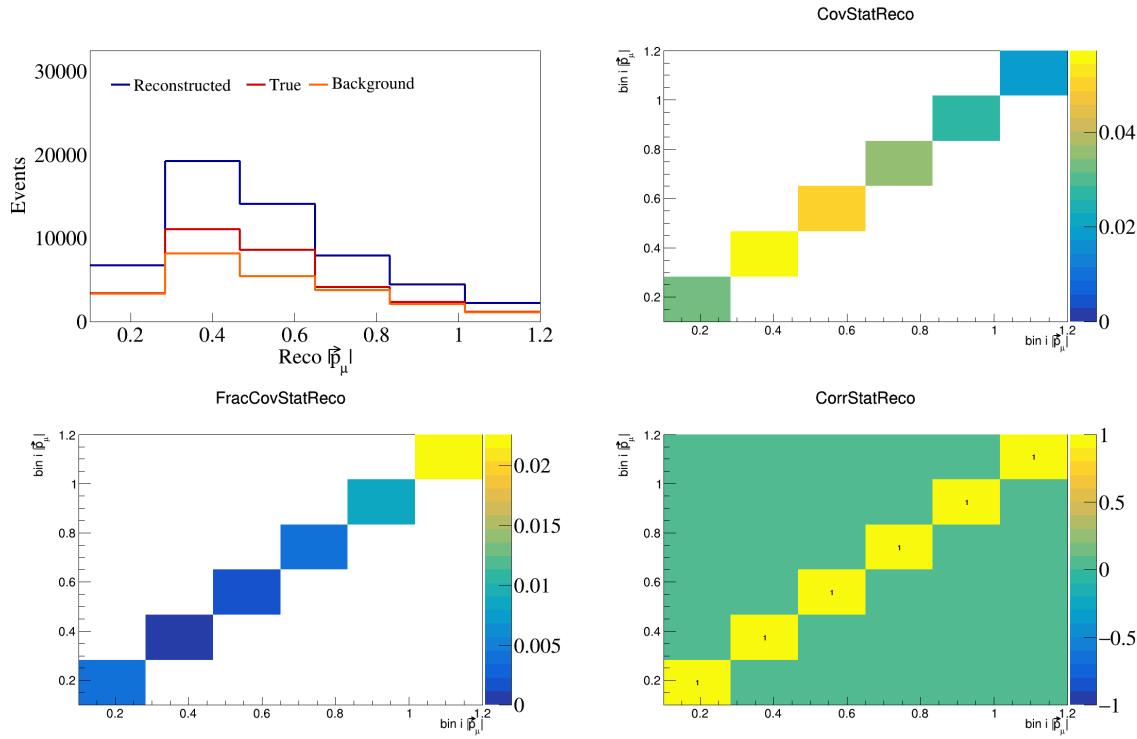


Figure 771: Statistical variations for $|\vec{p}_\mu|$.

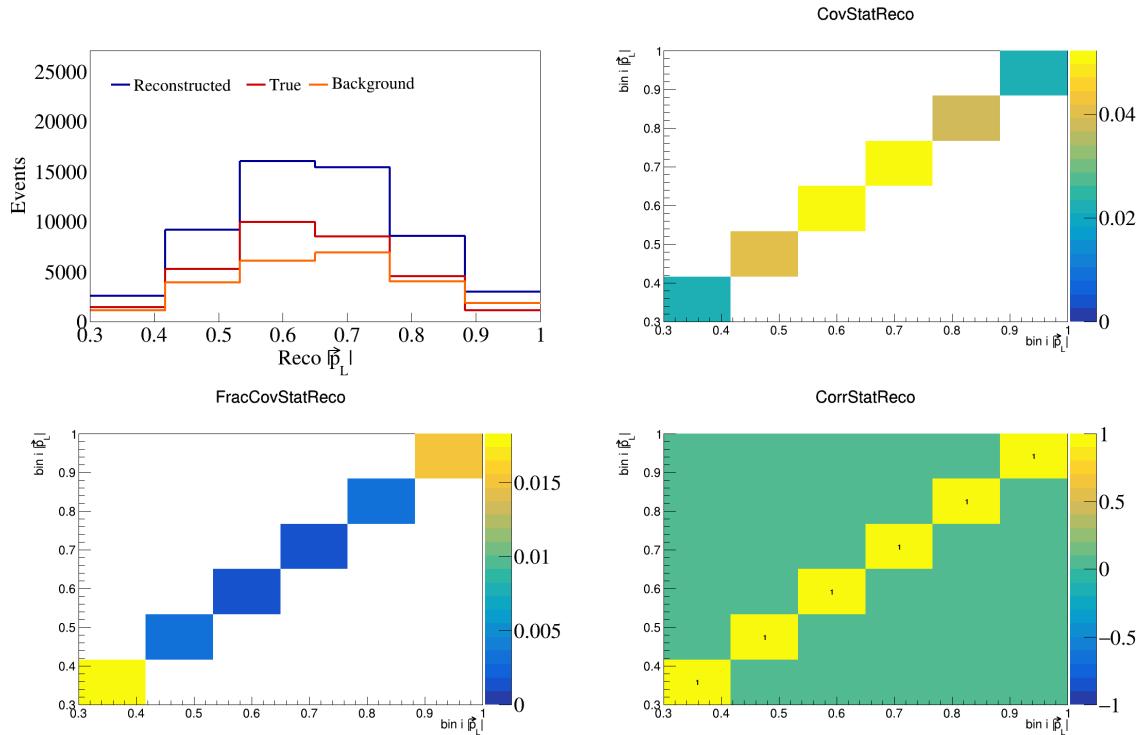


Figure 772: Statistical variations for $|\vec{p}_L|$.

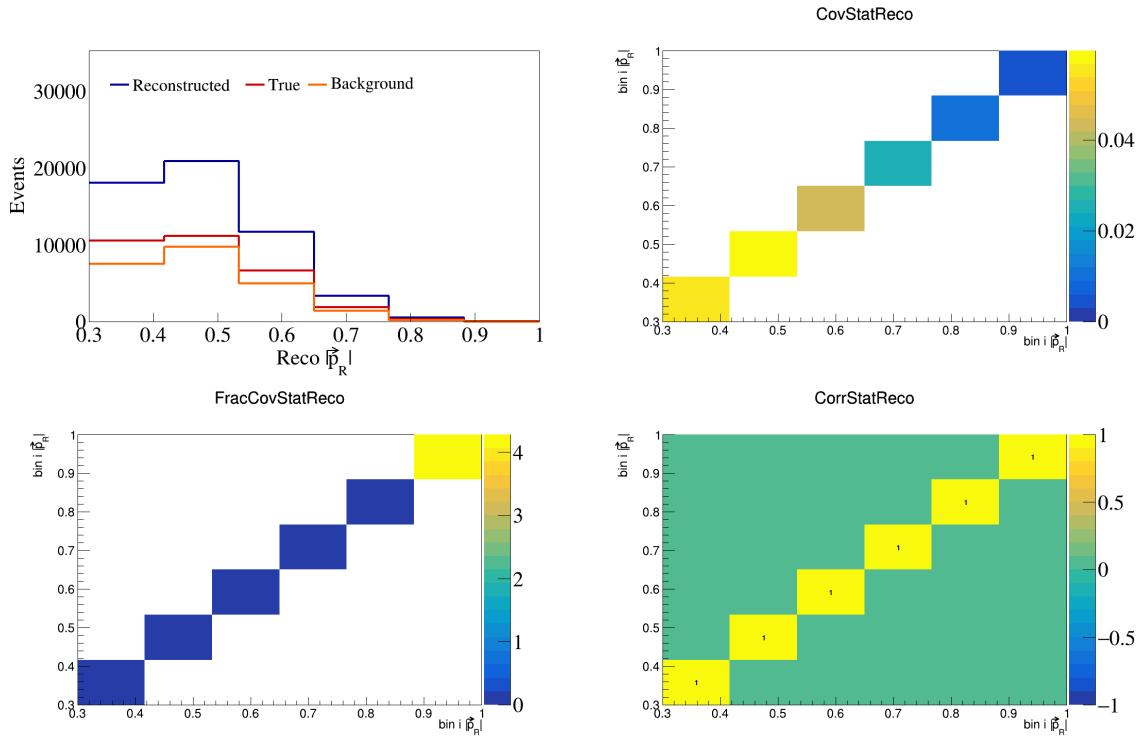


Figure 773: Statistical variations for $|\vec{p}_R|$.

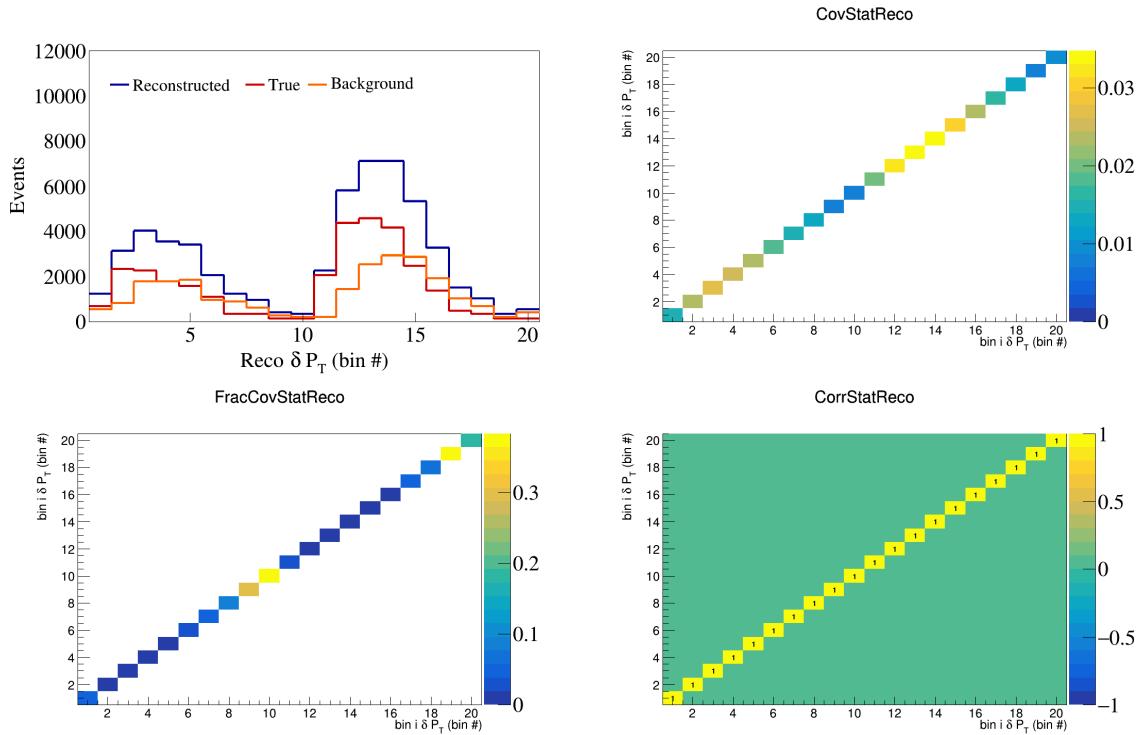


Figure 774: Statistical variations for δP_T in $\cos(\theta_{\vec{p}_\mu})$.

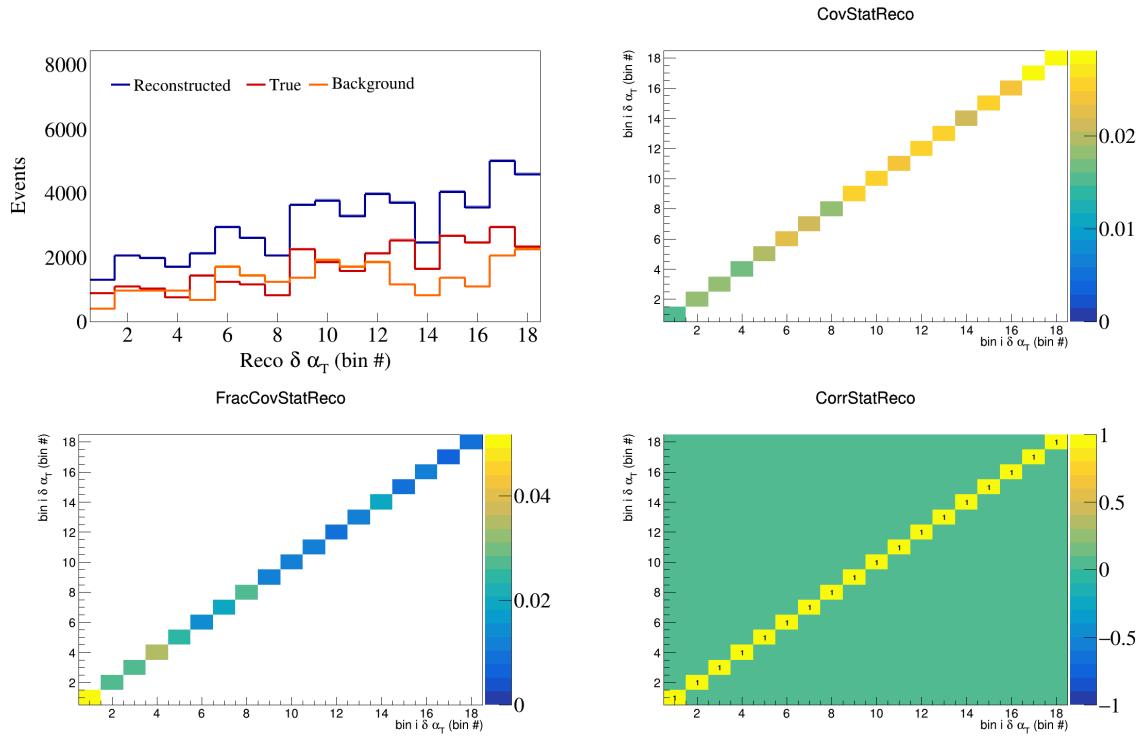


Figure 775: Statistical variations for $\delta\alpha_T$ in $\cos(\theta_{\vec{p}_\mu})$.

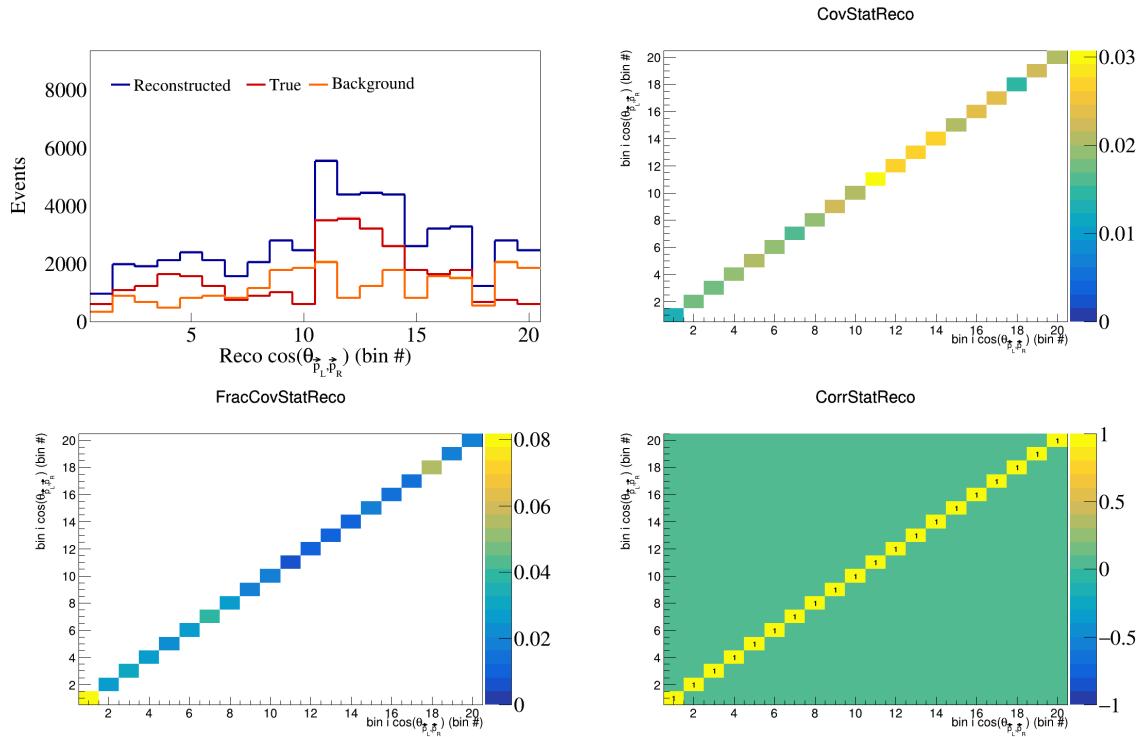


Figure 776: Statistical variations for $\cos(\theta_{\vec{p}_L, \vec{p}_R})$ in $\cos(\theta_{\vec{p}_\mu})$.

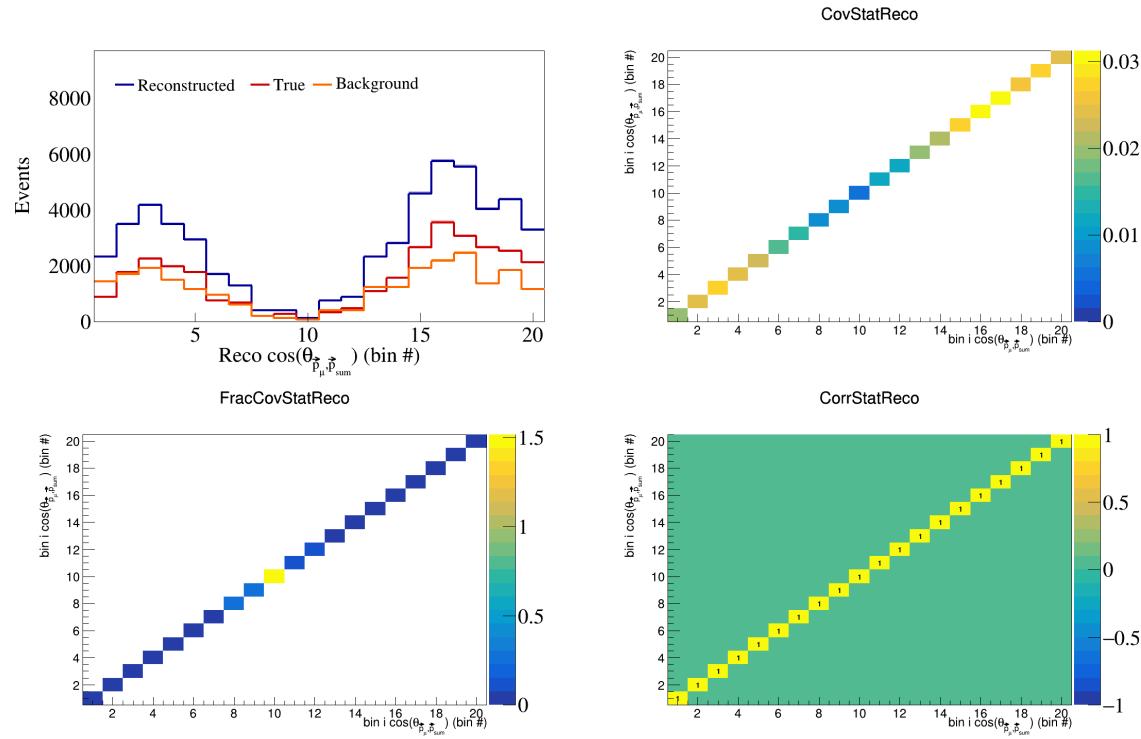


Figure 777: Statistical variations for $\cos(\theta_{\vec{p}_\mu, \vec{p}_{\text{sum}}})$ in $\cos(\theta_{\vec{p}_\mu})$.

222 6 References

- 223 [1] R. Acciarri, C. Adams, J. Asaadi, B. Baller, T. Bolton, C. Bromberg, F. Cavanna, E. Church, D. Edmunds, A. Ereditato, S. Farooq, B. Fleming, H. Greenlee, G. Horton-Smith, C. James, E. Klein, K. Lang, P. Laurens, R. Mehdiyev, B. Page, O. Palamara, K. Partyka, G. Rameika, B. Rebel, M. Soderberg, J. Spitz, A. M. Szelc, M. Weber, T. Yang, and G. P. Zeller. Detection of back-to-back proton pairs in charged-current neutrino interactions with the argoneut detector in the numi low energy beam line. *Phys. Rev. D*, 90:012008, Jul 2014.
- 224 [2] C. Andreopoulos, A. Bell, D. Bhattacharya, F. Cavanna, J. Dobson, S. Dytman, H. Gallagher, P. Guzowski, R. Hatcher, P. Kehayias, A. Meregaglia, D. Naples, G. Pearce, A. Rubbia, M. Whalley, and T. Yang. The genie neutrino monte carlo generator. *Nuclear Instruments and Methods in Physics Research Section A: Accelerators, Spectrometers, Detectors and Associated Equipment*, 614(1):87–104, 2010.
- 234 [3] Costas Andreopoulos, Christopher Barry, Steve Dytman, Hugh Gallagher, Tomasz Golan, Robert Hatcher, Gabriel Perdue, and Julia Yarba. The genie neutrino monte carlo generator: Physics and user manual, 2015.
- 235 [4] D. Ashery, I. Navon, G. Azuelos, H. K. Walter, H. J. Pfeiffer, and F. W. Schlepütz. True absorption and scattering of pions on nuclei. *Phys. Rev. C*, 23:2173–2185, May 1981.
- 239 [5] P. S. Auchincloss, R. Blair, C. Haber, E. Oltman, W. C. Leung, M. Ruiz, S. R. Mishra, P. Z. Quintas, F. J. Sciulli, M. H. Shaevitz, W. H. Smith, F. S. Merritt, M. Oreglia, P. Reutens, R. Coleman, H. E. Fisk, D. Levinthal, D. D. Yovanovitch, W. Marsh, P. A. Rapidis, H. B. White, A. Bodek, F. Borcherding, N. Giokaris, K. Lang, and I. E. Stockdale. Measurement of the inclusive charged-current cross section for neutrino and antineutrino scattering on isoscalar nucleons. *Zeitschrift für Physik C Particles and Fields*, 48(3):411–431, Sep 1990.
- 245 [6] Ch. Berger and L. M. Sehgal. Lepton mass effects in single pion production by neutrinos. *Phys. Rev. D*, 76:113004, Dec 2007.
- 247 [7] Ch. Berger and L. M. Sehgal. Partially conserved axial vector current and coherent pion production by low energy neutrinos. *Phys. Rev. D*, 79:053003, Mar 2009.
- 249 [8] B. Bourguille, J. Nieves, and F. Sánchez. Inclusive and exclusive neutrino-nucleus cross sections and the reconstruction of the interaction kinematics. *Journal of High Energy Physics*, 2021(4):4, Apr 2021.
- 251 [9] R.C. Carrasco and E. Oset. Interaction of real photons with nuclei from 100 to 500 mev. *Nuclear Physics A*, 536(3):445–508, 1992.
- 253 [10] R. Cruz-Torres, D. Lonardoni, R. Weiss, N. Barnea, D. W. Higinbotham, E. Piasetzky, A. Schmidt, L. B. Weinstein, R. B. Wiringa, and O. Hen. Many-body factorization and position-momentum equivalence of nuclear short-range correlations. *Nature Phys.*, 17(3):306–310, 2021.
- 256 [11] Jonathan Engel. Approximate treatment of lepton distortion in charged-current neutrino scattering from nuclei. *Phys. Rev. C*, 57:2004–2009, Apr 1998.
- 258 [12] T. Golan, J.T. Sobczyk, and J. Źmuda. Nuwro: the wrocław monte carlo generator of neutrino interactions. *Nuclear Physics B - Proceedings Supplements*, 229-232:499, 2012. Neutrino 2010.
- 260 [13] Krzysztof M. Graczyk and Jan T. Sobczyk. Form factors in the quark resonance model. *Phys. Rev. D*, 77:053001, Mar 2008.
- 262 [14] Yoshinari Hayato and Luke Pickering. The neut neutrino interaction simulation program library. *The European Physical Journal Special Topics*, 230(24):4469–4481, Dec 2021.
- 264 [15] Teppei Katori. Meson exchange current (MEC) models in neutrino interaction generators. *AIP Conference Proceedings*, 1663(1):030001, 05 2015.

- 266 [16] Konstantin S. Kuzmin, Vladimir V. Lyubushkin, and Vadim A. Naumov. Lepton polarization in neutrino–nucleon interactions. *Modern Physics Letters A*, 19(38):2815–2829, 2004.
- 267
- 268 [17] T. Leitner, L. Alvarez-Ruso, and U. Mosel. Charged current neutrino-nucleus interactions at intermediate energies. *Phys. Rev. C*, 73:065502, Jun 2006.
- 269
- 270 [18] C.H. Llewellyn Smith. Neutrino reactions at accelerator energies. *Physics Reports*, 3(5):261–379, 1972.
- 271 [19] Selection of numu charged current induced interactions with $N > 0$ protons and performance of events with $N = 2$ protons in the final state in the MicroBooNE detector from the BNB, Oct 2018.
- 272
- 273 [20] First Extraction of Single Differential Cross-Sections on Argon for CC1 μ 2p0 π Event Topologies in the MicroBooNE Detector. May 2022.
- 274
- 275 [21] Ulrich Mosel. Neutrino event generators: foundation, status and future. *Journal of Physics G: Nuclear and Particle Physics*, 46(11):113001, Sep 2019.
- 276
- 277 [22] J. Nieves, J. E. Amaro, and M. Valverde. Inclusive quasielastic charged-current neutrino-nucleus reactions. *Phys. Rev. C*, 70:055503, Nov 2004.
- 278
- 279 [23] J. Nieves, F. Sánchez, I. Ruiz Simo, and M. J. Vicente Vacas. Neutrino energy reconstruction and the shape of the charged current quasielastic-like total cross section. *Phys. Rev. D*, 85:113008, Jun 2012.
- 280
- 281 [24] J. Nieves, I. Ruiz Simo, and M. J. Vicente Vacas. Inclusive charged-current neutrino-nucleus reactions. *Phys. Rev. C*, 83:045501, Apr 2011.
- 282
- 283 [25] J. Schwehr, D. Cherdack, and R. Gran. Genie implementation of ific valencia model for qe-like 2p2h neutrino-nucleus cross section, 2017.
- 284
- 285 [26] Torbjörn Sjöstrand, Stephen Mrenna, and Peter Skands. Pythia 6.4 physics and manual. *Journal of High Energy Physics*, 2006(05):026, may 2006.
- 286
- 287 [27] W. Tang, X. Li, X. Qian, H. Wei, and C. Zhang. Data unfolding with wiener-svd method. *Journal of Instrumentation*, 12(10):P10002–P10002, October 2017.
- 288
- 289 [28] Júlia Tena-Vidal, Costas Andreopoulos, Adi Ashkenazi, Christopher Barry, Steve Dennis, Steve Dytman, Hugh Gallagher, Steven Gardiner, Walter Giele, Robert Hatcher, Or Hen, Libo Jiang, Igor D. Kakorin, Konstantin S. Kuzmin, Anselmo Meregaglia, Vadim A. Naumov, Afroditi Papadopoulou, Gabriel Perdue, Marco Roda, Vladyslav Syrotenko, and Jeremy Wolcott. Neutrino-nucleon cross-section model tuning in genie v3. *Phys. Rev. D*, 104:072009, Oct 2021.
- 290
- 291 [29] U. K. Yang and A. Bodek. Parton distributions, d/u , and higher twist effects at high x . *Phys. Rev. Lett.*, 82:2467–2470, Mar 1999.
- 292
- 293
- 294
- 295